Lecture Notes in Electrical Engineering 851

Biplab Sikdar
Santi Prasad Maity
Jagannath Samanta
Avisankar Roy *Editors*

Proceedings of the 3rd International Conference on Communication, Devices and Computing

ICCDC 2021

Springer

Lecture Notes in Electrical Engineering

Volume 851

The book series *Lecture Notes in Electrical Engineering* (LNEE) publishes the latest developments in Electrical Engineering - quickly, informally and in high quality. While original research reported in proceedings and monographs has traditionally formed the core of LNEE, we also encourage authors to submit books devoted to supporting student education and professional training in the various fields and applications areas of electrical engineering. The series cover classical and emerging topics concerning:

- Communication Engineering, Information Theory and Networks
- Electronics Engineering and Microelectronics
- Signal, Image and Speech Processing
- Wireless and Mobile Communication
- Circuits and Systems
- Energy Systems, Power Electronics and Electrical Machines
- Electro-optical Engineering
- Instrumentation Engineering
- Avionics Engineering
- Control Systems
- Internet-of-Things and Cybersecurity
- Biomedical Devices, MEMS and NEMS

For general information about this book series, comments or suggestions, please contact leontina.dicecco@springer.com.

To submit a proposal or request further information, please contact the Publishing Editor in your country:

China

Jasmine Dou, Editor (jasmine.dou@springer.com)

India, Japan, Rest of Asia

Swati Meherishi, Editorial Director (Swati.Meherishi@springer.com)

Southeast Asia, Australia, New Zealand

Ramesh Nath Premnath, Editor (ramesh.premnath@springernature.com)

USA, Canada:

Michael Luby, Senior Editor (michael.luby@springer.com)

All other Countries:

Leontina Di Cecco, Senior Editor (leontina.dicecco@springer.com)

**** This series is indexed by EI Compendex and Scopus databases. ****

More information about this series at https://link.springer.com/bookseries/7818

Biplab Sikdar · Santi Prasad Maity ·
Jagannath Samanta · Avisankar Roy
Editors

Proceedings of the 3rd International Conference on Communication, Devices and Computing

ICCDC 2021

Springer

Editors
Biplab Sikdar
Department of Communications
and Networks
National University of Singapore
Singapore, Singapore

Santi Prasad Maity
Department of Information Technology
Indian Institute of Engineering Science
and Technology
Howrah, India

Jagannath Samanta
Department of Electronics
and Communication Engineering
Haldia Institute of Technology
Haldia, West Bengal, India

Avisankar Roy
Department of Electronics
and Communication Engineering
Haldia Institute of Technology
Haldia, West Bengal, India

ISSN 1876-1100 ISSN 1876-1119 (electronic)
Lecture Notes in Electrical Engineering
ISBN 978-981-16-9153-9 ISBN 978-981-16-9154-6 (eBook)
https://doi.org/10.1007/978-981-16-9154-6

This Springer imprint is published by the registered company Springer Nature Singapore Pte Ltd.
The registered company address is: 152 Beach Road, #21-01/04 Gateway East, Singapore 189721, Singapore

Committee

Chief Patron

Lakshman Chandra Seth, Chairman, Haldia Institute of Technology, India

Mentor of Advisory Committee

Padma Shri. Sankar Kumar Pal, National Science Chair, Government of India. Emeritus Professor, Distinguished Scientist and former Director, Indian Statistical Institute, Kolkata, India

General Chair

Chanchal Kumar De, Haldia Institute of Technology, India
Biplab Sikdar, National University of Singapore, Singapore

Program Chair

Avisankar Roy, Haldia Institute of Technology, India
Tirthadip Sinha, Haldia Institute of Technology, India

Organizing Chair

Surajit Mukherjee, Haldia Institute of Technology, India
Kushal Roy, Haldia Institute of Technology, India

Publication Chair

Jagannath Samanta, Haldia Institute of Technology, India
Avishek Das, Haldia Institute of Technology, India

Finance Chair

Dibyendu Chowdhury, Haldia Institute of Technology, India

Online Activity Chair

Banibrata Bag, Haldia Institute of Technology, India

International Advisory Committee

Members, Organization

Matteo Gaeta, University of Salerno, Fisciano (Sa), Italy
Honkala Iiro, University of Turku, Finland
George A. Tsihrintzis, University of Piraeus, Greece
Dilip Sarkar, University of Miami, Florida, USA
Saifur Rahman, Virginia Tech College of Engineering, USA
Anand Nayyar, Duy Tan University, Vietnam
Raphael A Guerrero, Ateneo De Manila University, Philippines
Jan Kubicek, VSB-Technical University of Ostrava, Czech Republic
S. M. Abdur Razzak, Rajshahi University of Engineering and Technology, Bangladesh
Antonio Piratelli-Filho, Universidade de Brasilia, Brazil
Kamla Prasan Ray, DRDO, Government of India

Bikash Kumar Dey, IIT Bombay, India
Sukumar Nandi, Professor, IIT Guwahati, India
Animesh Maitra, University of Calcutta, India
Sunandan Bhunia, Central Institute of Technology, Kokrajhar, India
Ashutosh Kedar, DRDO, Government of India
Debashis De, MAKAUT, Kolkata, India
Jaydeb Bhaumik, Jadavpur University, Kolkata, India
Santi Prasad Maity, IIEST, Shibpur, India
Abhijit Biswas, University of Calcutta, Kolkata, India
Sanjay Dhar Roy, NIT Durgapur, India
Sourangshu Mukhopadhyay, University of Burdwan, India
C. K. Sarkar, Jadavpur University, Kolkata, India
J. P. Bandopadhyay, University of Calcutta, India
J. K. Mandal, Kalyani University, India
Malay Kumar Pandit, Haldia Institute of Technology, Haldia, India
Kisalaya Chakrabarti, Haldia Institute of Technology, Haldia, India
Manu Malek, Editor-in-Chief, *Journal of Computer and Electrical Engineering*, Elsevier
Abhijit Chandra, Jadavpur University, Kolkata, India

Technical Program Committee Members

TPC Members, Organization

Sudip Roy, IIT Roorkee, India
Gandeva Bayu Satrya, Telkom University Bandung, West Java, Indonesia
Huang Sunan, National University of Singapore, Singapore
Indranil Hatai, Myanmar Institute of Information Technology, Myanmar
Priyantha Wijayatunga, Umeå University, Sweden
Corneliu Doroftei, Alexandru Ioan Cuza University of Iasi, Romania
Arnab Nandi, NIT Silchar, Assam, India
Kaushik Mandal, University of Calcutta, India
Subhankar Joardar, Haldia Institute of Technology, India
Abhishek Sarkhel, NIT Meghalaya, India
Debashis Maji, Vellore Institute of Technology (VIT), India
Sanjeev Kumar Metya, NIT Arunachal Pradesh, India
Susanta Kumar Parui, IIEST, Shibpur, India
Sumit Kumar Jindal, Vellore Institute of Technology (VIT), India
Somnath Ghosh, IIT Jodhpur, India
Santigopal Pain, Haldia Institute of Technology, India
Arindam Biswas, Asansol Engineering College, India
Sudipta Das, IMPS College of Engineering and Technology, India

Sudipta Sahana, JIS College of Engineering, India
Bidhan Malakar, JIS College of Engineering, India
Soma Barman (Mandal), Calcutta University, Kolkata, India
Prasun Chowdhury, St. Thomas College of Engineering and Technology, India
Parthapratim Sarkar, UIT, University of Burdwan, India
Swarup Kumar Mitra, MCKV Institute of Engineering, India
Juin Acharjee, St. Thomas College of Engineering and Technology, India
Amol C. Adamuthe, Rajarambapu Institute of Technology, India
Sudip Kumar Adhikary, Coochbehar Government Engineering College, India
Rinkee Chopra, IIITDM Kancheepuram, India
Shamba Chatterjee, Haldia Institute of Technology, India
Khondekar Mofazzal Hossain, Dr. B. C. Roy College of Engineering, India
Samiran Chatterjee, Vignan's Institute of Management and Technology for Women, India
Wriddhi Bhowmik, KIIT, Bhubaneswar, India
Surjeet Dalal, SRM University, India
K. Vasu Babu, JNTUK, Kakinada, India
Chiranjib Goswami, Asansol Engineering College, India
Sunil Lavadiya, Marwadi University, India
Vishal Sorathiya, Marwadi University, India
Ritam Dutta, Siksha 'O' Anusandhan University, India
Mauparna Nandan, Brainware University, India
Dharmpal Singh, JIS College of Engineering, India
Amit Majumder, JIS College of Engineering, India
Debaprasad Das, Assam University, India
Aloke Saha, Dr. B. C. Roy Engineering College, India
Anirban Das, UEM University, Kolkata, India

Additional Reviewers

Reviewers, Organization

Mainak Saha, R. K. Mahato Government Engineering College, India
Bidyut Das, Haldia Institute of Technology, India
Kunal Chakraborty, North Eastern Hill University, India
Heranmoy Maity, NSHM Knowledge Campus Durgapur, India
Siddhartha Chatterjee, Gargi Memorial Institute of Technology, India
Mehaboob Mujawar, Goa College of Engineering, India
Ch. Murali Krishna, IIIT Design and Manufacturing, Jabalpur, India
Mrinmay Sen, Haldia Institute of Technology, India
Rajesh Mukherjee, Haldia Institute of Technology, India

Local Advisory Committee

Sayantan Seth, Vice Chairman, Haldia Institute of Technology
Asish Lahiri, Secretary, Haldia Institute of Technology
M. N. Bandyopadhyay, Director, Haldia Institute of Technology
A. K. Saha, Principal, Haldia Institute of Technology
A. Mishra, Registrar, Haldia Institute of Technology
A. B. Maity, Dean, SAS and H, Haldia Institute of Technology
T. K. Jana, Dean, SECI, Haldia Institute of Technology
S. K. Basu, Finance Manager, Haldia Institute of Technology
D. Das, Manager Administration, Haldia Institute of Technology

Local Organizing Committee

Asim Kumar Jana
Sudipta Bardhan
Amit Bhattacharyya
Raj Kumar Maity
Akinchan Das
Pinaki Satpathy
Santanu Maity
Dipak Samanta
Jayanta Kumar Bag
Tilak Mukherjee
Pallabi Pahari
Razia Sultana
Moumita Jana
Sayani Ghosh
Pulak Maity
Sourav Das
Sachindeb Jana
Shubhendu Barman
Atanu Pradhan
Tapan Maity
Ira Samanta
Asim Kuilya

Preface

The 3rd International Conference on Communication, Devices and Computing (ICCDC 2021) was held at Haldia Institute of Technology, Haldia, from August 16 to 18, 2021. Haldia is a city in Purba Medinipur district of Indian state West Bengal. Haldia institute of Technology is dedicated to the objectives of creating highly trained professional manpower in various disciplines of engineering. It has gained reputation through institutional dedication to teaching and research.

In response to call for papers of ICCDC 2021, a total 130 papers were submitted for presentation and inclusion in proceedings of conference. These papers were evaluated and ranked based on their novelty, significance and technical quality by at least two reviewers per paper. After a careful and blind refereeing process, 70 papers were selected for inclusion in the proceeding. These papers cover current research in communication, signal processing, image processing, wireless network, semiconductor devices, VLSI design, antenna design and machine learning. The conference hosted six virtual invited talks by Prof. Hiroshi Iwai, (International College of Semiconductor Technology, National Yang Ming Chiao Tung University, Taiwan), Prof. Mamun Bin Ibne Reaz, (Universiti Kebangsaan Malaysia, Malaysia), Prof. Sunandan Bhunia, (CIT Kokrajhar, Assam, India), Prof. Anand Nayyar, (Duy Tan University, Vietnam), Prof. Dilip Kumar Sarkar, (University of Quebec at Chicoutimi, Canada), and Prof. Bikash Kumar Dey, (IIT Bombay, India).

A conference of this kind would not be possible without the full support from different committee members. The organizational aspects were looked after by the organizing committee members who spent their time and energy in making the conference a reality. We also thank all the technical program committee members and additional reviewers for thoroughly reviewing the papers submitted to the conference and sending their constructive suggestions to improve the quality of papers. Our hearty thanks to Springer for agreeing to publish the conference proceedings.

We are indebted to Haldia Institute of Technology for sponsoring and supporting the event. Last but not least, our sincere thanks go to all speakers, participants, all authors who have submitted papers to ICCDC 2021. We sincerely hope that the readers will find the proceedings stimulating and inspiring.

Singapore — Biplab Sikdar
Howrah, India — Santi Prasad Maity
Haldia, India — Jagannath Samanta
Haldia, India — Avisankar Roy

Contents

About the Editors

Prof. Biplab Sikdar is an Associate Professor in the Department of Electrical and Computer Engineering at the National University of Singapore. He received the B.Tech. degree in electronics and communication engineering from North Eastern Hill University, Shillong, India, in 1996, the M.Tech. degree in electrical engineering from the Indian Institute of Technology, Kanpur, India, in 1998, and the Ph.D. degree in electrical engineering from the Rensselaer Polytechnic Institute, Troy, NY, USA, in 2001. He was an Assistant Professor from 2001 to 2007 and Associate Professor from 2007 to 2013 in the Department of Electrical, Computer, and Systems Engineering at Rensselaer Polytechnic Institute from 2001 to 2013. He is a recipient of the NSF CAREER award, the Tan Chin Tuan fellowship from NTU Singapore, the Japan Society for Promotion of Science fellowship, and the Leiv Eiriksson fellowship from the Research Council of Norway. His research interests include wireless wireless MAC protocols, network security, and network performance evaluation. Dr. Sikdar is a member of Eta Kappa Nu and Tau Beta Pi. He served as an Associate Editor for the IEEE Transactions on Communications from 2007 to 2012 and currently serves as an Associate Editor for the IEEE Transactions on Mobile Computing.

Prof. Santi Prasad Maity received his B.E. degree in Electronics and Communication Engineering from National Institute of Technology Durgapur and M.Tech. in Microwaves from the University of Burdwan, India in 1993 and 1997, respectively. He received his Ph.D. degree in Engineering from the Indian Institute of Engineering Science and Technology, Shibpur, India in 2008. He received a couple of post-doctoral research positions from the institutes like Nanyang Technological University, Singapore, University of Vigo, Spain and Supelec, France. He did Post Doctoral work from January 2009 to July 2009 and February 2011 to July 2011 at the Laboratoire des Signauxet Systems (CNRS–Supelec–Universite Paris-Sud 11) in France. He is having more than 23 years (since 1997) teaching experiences at different academic institutions and at present he is working at Indian Institute of Engineering Science and Technology, Shibpur, India since July 2000 as Professor in the Department of Information Technology. His research interests include Cognitive Radio-Cooperative Spectral Sensing, Joint Spectral Sensing and Secondary Transmission,

security, energy harvesting, relay-based routing in cognitive radio network, Machine Learning and Deep Learning in medical image processing. He has published more than 280 research papers in International journals that include IEEE Transactions, IEEE Journals, IEEE Letters, Elsevier, Springer, Wiley etc.

Dr. Jagannath Samanta is an Associate Professor in the Department of Electronics and Communication Engineering at the Haldia Institute of Technology, Haldia, West Bengal, India. He received the B.Tech. and M.Tech. degree in Electronics and Communication Engineering from West Bengal University of Technology, West Bengal, India, in 2005 and 2008, respectively. Dr. Samanta received Gold Medal during M.Tech. degree. He received his Ph.D. (Tech) degree in from the Institute of Radio Physics and Electronics in 2018. His research interests include Digital VLSI Design, Error Correcting Codes. He has published more than 47 research papers in International journals that include IEEE Transactions, Springer etc. He is the reviewers of referred journal like IEEE Transactions, Springer, Elsevier, etc.

Dr. Avisankar Roy was born in Malda, West Bengal, India on 1984. He was felicitated with a Ph.D. in Engineering from University of Kalyani, West Bengal, India in the year of 2018. He has obtained his M.Tech. degree in Mobile Communication and Network Technology and B.Tech. degree in electronics and communication engineering from West Bengal University of Technology (Presently known as Maulana Abul Kalam Azad University of Technology), West Bengal, India, in the year of 2009 and 2006 respectively.

He has almost 11 years of teaching experiences. He is currently working as Associate Professor at the Department of Electronics and Communication Engineering in Haldia Institute of Technology, Haldia, West Bengal, India. He has contributed to numerous research articles in various journals, book chapters and conferences of repute. He was appointed as reviewer of some SCI and SCOPUS indexed journals. His area of research interest includes microstrip antenna design and frequency selective surfaces.

Noise Suppressing Cascaded IIR Elliptic Filter Design for ECG Signals

Suman Saha and Soma Barman (Mandal)

Abstract Electrocardiogram (ECG) is the common clinical observation to detect heart abnormalities. ECG signal is often contaminated with noises during recording which leads to faulty interpretation of heart condition. Digital filters are efficient enough to clean such noisy recorded ECG signal. In this paper, we have designed and simulated three digital IIR elliptic filters in MATLAB environment to de-noise ECG signal. We compared our result with the existing works for ECG signal conditioning in terms of the SSNR and found our designed filter model performed 21% better than others.

Keywords ECG · IIR elliptical filter · SNR · SSNR

1 Introduction

In the present year, we are leaving in a pandemic situation, and due to lock down, our physical activities are confined within four walls. Not only that, the fear of COVID-19 drags us into stressful lives which impact on the cardiovascular system and apparently affects the heart [1]. The ECG or electrocardiogram is a graphical approach to capture the electrical activity of the heart which contains detailed information of heart condition. These signals are non-stationary and low power in nature. The frequency range of ECG signal is from 0.5 to 100 Hz [2] which makes it corrupted frequently by noise mostly from power line interference and its harmonics, electrode motion artifact [3] from the electrode skin contact point, muscle noise in higher-frequency range and baseline wander in very low-frequency range [4] during acquisition. Clean ECG signal acquisition is very important to extract significant features from it and makes decision about various types of heart diseases. The authors

S. Saha · S. Barman (Mandal) (✉)
Institute of Radio Physics and Electronics, University of Calcutta, 92, A.P.C. Road, Kolkata 700009, India
e-mail: sbrpe@caluniv.ac.in

B. Sikdar et al. (eds.), *Proceedings of the 3rd International Conference on Communication, Devices and Computing*, Lecture Notes in Electrical Engineering 851,
https://doi.org/10.1007/978-981-16-9154-6_1

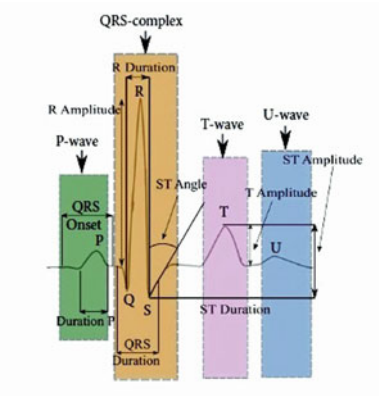

Fig. 1 Heartbeat pulse model represented with features (amplitudes and durations) of the P-wave, QRS complex, T-wave, U-wave and ST segment [5]

in this paper address the issue of de-noising ECG signal which prevent for wrong interpretation of heart condition.

Figure 1 shows a typical ECG signal of a healthy person. This signal contains two types of information: (i) morphological information and (ii) interval information. Morphological information is confined in P-wave, QRS complex, T-wave and U-wave, and interval information can be found in PR segment, ST segment, PR interval, ST interval and RR interval [6]. These information all together are used for diagnosis of heart disease.

A number of significant works have been carried out on digital filtering techniques to extract key features from noisy ECG signal with acceptable accuracy to diagnose heart disease. Sravan Kumar et al. [7] designed both IIR and FIR filters with various methods to remove noise from ECG signal and showed Kaiser Window of order 56 is best for this case. They have ignored the effect of phase delay introduced by high-order FIR filter in their model. Also they have compared the performance of first-, second- and third-order IIR filters with FIR filters of order 56th, 300th, 450th and 600th. Singh et al. [8] have designed a fifth-order IIR low-pass Butterworth filter with cutoff 20 Hz to remove high-frequency muscle noise. But their design not performed well for all ECG signals, especially for MIT-BIH Normal Sinus Rhythm Database where output is distorted due to the cutoff frequency of low-pass filter. A cascaded form of low pass – high pass – band stop IIR elliptic filters have applied by Chavan et al. [9] in their work to clean ECG signal. They proposed fourth-order 100 Hz, 0.5 Hz and fourth-order 50 Hz cutoff frequencies for low-pass, high-pass and band stop filter, respectively. The order of the high-pass filter has not been mentioned in their paper. The drawback of this de-noising model is its cutoff frequency of low-pass filter which is not able to remove high-frequency muscle noise, and also higher order of the filter may introduce extra impulses in filtered signal. According to Choudhary et al. [10], Butterworth is the best of the three IIR filters for ECG signal processing when compared to Chebyshev I and II. However, the low SNR value of the filtered signal indicates that the filter is unable to effectively attenuate the noise signal. Apart from these conventional filtering techniques, many researchers have worked

on algorithm-based filtering techniques like Sun et al. [11] developed morphological filtering algorithm for baseline correction and Lastre-Dominguez et al. [5] proposed an adaptive-horizon unbiased FIR smoothing algorithm for de-noising ECG signal. But these filters are complicated in design.

Effective de-noising of ECG signal helps in accurate interpretation of heart condition. In this paper, the authors proposed an elliptical approximation-based three types of IIR filters to de-noise ECG signal, and filter orders are considered from second to fifth. These filters are cascaded in such a fashion that can handle a wide range of noisy ECG signals. Signal-to-noise ratio (SNR) and signal-to-signal plus noise ratio (SSNR) metrics are used to evaluate the performance of the proposed ECG de-noising technique and compared the performance with other existing ECG de-noising IIR filtering techniques. This paper is organized as follows: Section 2—Material: Discuss about sample ECG databases and different noises associated with ECG signal. Section 3—Methods: Manifest the architecture of proposed system with design procedure of IIR filters. The experimental results of our proposed system and comparison with existing work are discussed in Sect. 4: Results and Discussion. Finally, the paper is concluded in Sect. 5.

2 Material

2.1 Database

In our work, we have used Physio Bank open-access database such as MIT-BIH Arrhythmia, MIT-BIH Normal Sinus Rhythm and ECG-ID [12–14]. ECG-ID database is treated as the benchmark for our work because this database provides recorded ECG signal of a particular person in noisy and clean both versions which enable us to compare our result with the standard one. These three databases contribute 376 ECG recordings with sampling frequencies of 360 Hz, 128 Hz and 500 Hz for MIT-BIH Arrhythmia, MIT-BIH Normal Sinus Rhythm and ECG-ID Database, respectively. To normalize the all databases frequency, a uniform sampling frequency 360 Hz is used for our work.

2.2 ECG Noises

An ECG signal is susceptible to noise because of its low amplitude, and ECG waveform gets distorted. Many cardiac diseases can be diagnosed by studying ECG waveforms. But distorted ECG waveform may mislead in interpretation of cardiac abnormalities. Thus, understanding the patterns of common ECG noises is very important to design a decent de-noising model. In the next section, brief description of different types of noises is discussed.

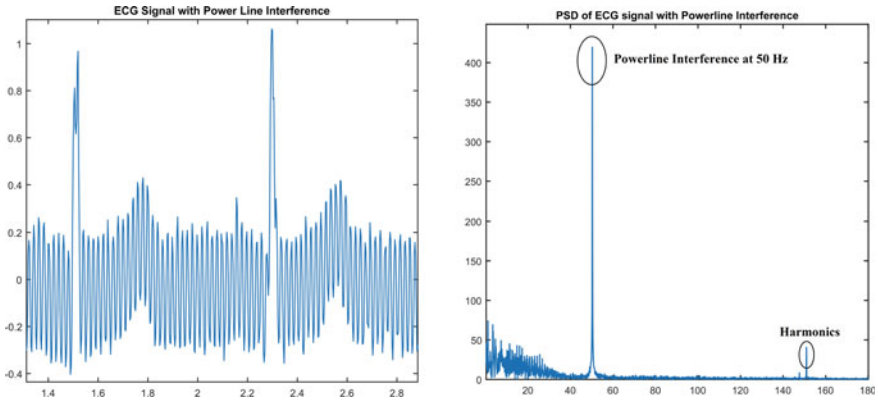

(a)ECG signal with Powerline Interference

(b) PSD of ECG signal with Powerline Interference

Fig. 2 Time domain and frequency domain plots of ECG signal with powerline interference

Powerline Interference Powerline interference is a stationary, narrow band noise that interfered at 50 Hz or 60 Hz depending on the country. Its bandwidth is less than 1 Hz and may have harmonics [15]. Figure 2a shows an ECG signal with powerline noise, and Fig. 2b is its PSD which shows clear peaks 50 Hz and harmonic 150 Hz. Powerline interference is a continuous electromagnetic interference caused by powerline frequency. Improper grounding of the ECG machine or cable loops may also contribute to this noise.

Baseline Wander Baseline wander is a very low-frequency noise possessing spectral content between 0.1 and 0.5 Hz. The primary source of this noise is due to the patient's respiration motion. Another source of this noise is due to mismatch of impedance between the electrode and the patient's skin. Figure 3 shows an ECG signal with baseline noise. It is clear from the picture that the DC level or baseline of the ECG signal is fluctuating in nature and makes it difficult to measure different interval information especially ST segment.

Electrode Motion Noise This type of noise is introduced due to the sudden body movement by the patient while recording ECG. Movement of the body results in a sharp change in electrode skin impedance which brings in great deflection in ECG signal which is displayed in Fig. 4.

Muscle Noise or Electromyography Noise This noise is generated by the contraction of muscles other than the heart. Figure 5 shows an ECG signal corrupted by muscle noise. The ECG electrical wave is the depolarization or repolarization contraction of the heart, and thus, the contraction of other muscles is also captured by the electrodes at the time of ECG recording. This noise is non-stationary, ranging from 5 Hz to 450 Hz [15] which is hard to remove since its frequency band is overlapped with the ECG signal.

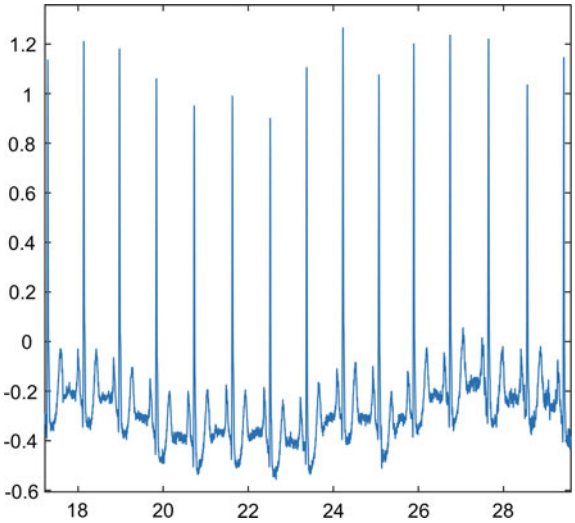

Fig. 3 ECG signal with baseline wandering

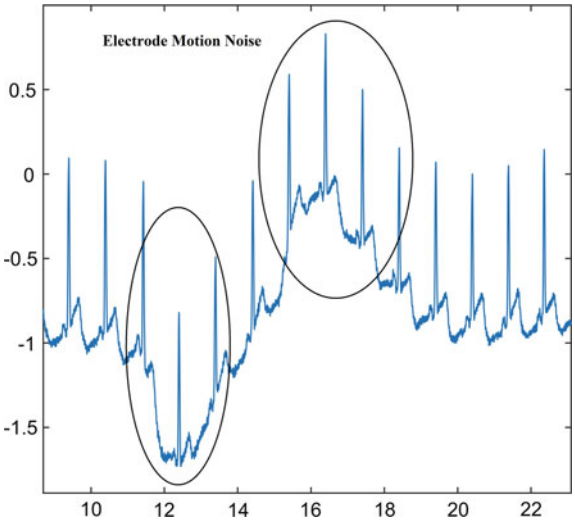

Fig. 4 ECG signal with electrode motion noise

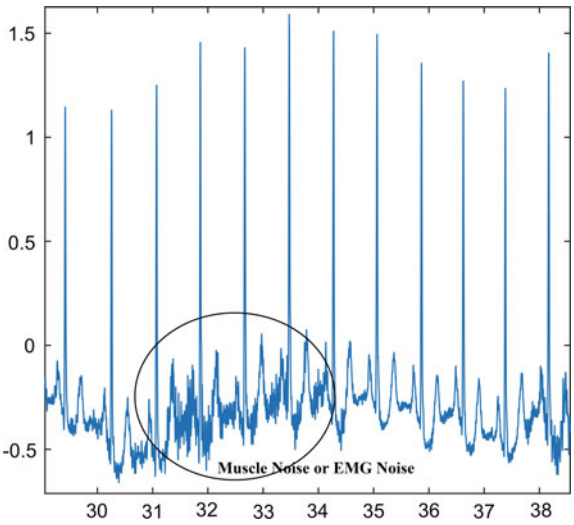

Fig. 5 ECG signal with muscle noise

3 Methods

3.1 System Architecture

Various types of de-noising models are available in the literatures to remove artifacts [3], which are noises caused by muscle twitching or wrong placement of electrodes, from ECG signals. Many of them are digital filters in their main module. In the present work, we propose elliptic IIR digital filters for the same. Figure 6 illustrates the block diagram of the proposed work.

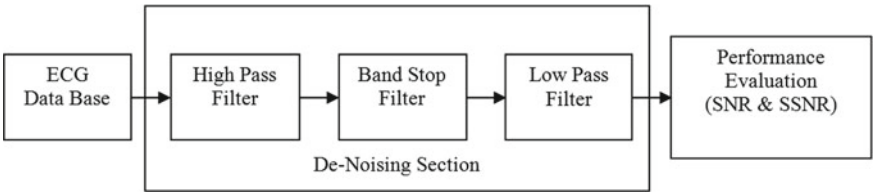

Fig. 6 Proposed de-noising mechanism

3.2 Digital Filter Design

Digital filters are classified into two types: finite impulse response (FIR) and infinite impulse response (IIR) filter. In the FIR system, the impulse response has a finite number of nonzero terms, whereas the IIR system has an infinite number of nonzero terms. Here for de-noising ECG signal, we prefer IIR filter because for low-order filter design, IIR performs better than FIR filter. FIR filter may work better at higher order [7], but introduces a large phase delay in the output. Also, the IIR filter is recursive in nature, i.e., it requires feedback, and its design procedure is simple compared to FIR filters.

Digital Elliptic Filter Design Elliptic filter is also called the Cauer filter. This filter has the equiripple property both at pass band and stop band as shown in Fig. 7. Among the other filter types, for a given filter order, an elliptic filter has the minimum transition bandwidth between the pass band and the stop band. The magnitude squared response of this filter is given in Eq. 1 [16].

$$| H_a = (j\Omega) |^2 = \frac{1}{1 + \epsilon^2 U_N(\frac{\Omega}{\Omega_c})} \tag{1}$$

where N = order of the filter
$U_N(\mathrm{x})$ = Nth order Jacobian elliptic function
ϵ = constant related to pass band ripple
Ω_c = cutoff frequency.
In z-domain, the transfer function is given by [16]

$$H(z) = \frac{Y(z)}{X(z)} = \frac{\sum_{k=0}^{M} b_k z^{-k}}{1 - \sum_{k=1}^{N} a_k z^{-k}} \tag{2}$$

where a_k = delay-dependent feedback coefficient
b_k = delay-dependent feed forward coefficient.

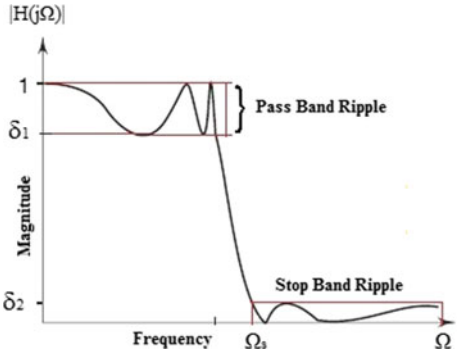

Fig. 7 Magnitude response of a low-pass elliptic filter [16]

Table 1 Filter information

Filter parameters	High-pass filter	Band stop filter		Low-pass filter
		For 60 Hz Powerline noise	For 50 Hz Powerline noise	
Order	5th	4th	4th	2nd
Stop band frequency	0.2 Hz	59.97 and 60.23 Hz	49.97 and 50.23 Hz	174.82 Hz
Pass band frequency	0.5 Hz	55.5 and 65 Hz	45.5 and 55 Hz	35 Hz
3 dB point frequency	0.48 Hz	56.35 and 63.81 Hz	46.35 and 53.81 Hz	42 Hz
Pass band ripple	1 dB	0.5 and 1 dB	0.5 and 1 dB	1 dB
Stop band attenuation	80 dB	80 dB	80 dB	80 dB

In our work, direct from II structure is used to realize the filters and simulated their responses in MATLAB (2015) platform. Filter parameters listed in Table 1 are used to calculate feedback and feed forward coefficients of Table 2 using MATLAB filter designer.

To remove the baseline wander, we proposed a high-pass fifth-order IIR filter. Figure 8a–c illustrates the direct from II structure, magnitude response and pole zero plot for high-pass filter, respectively. To attenuate powerline interference, we proposed a band stop fourth-order IIR filter. In Fig. 9a–c, the direct from II structure, magnitude response and pole zero plot for band stop filter of 50 Hz cutoff frequency are shown. The second-order low-pass filter, used to eliminate high-frequency noises, presents in ECG signal. Figure 10a–c shows, respectively, the filter structure, magnitude response and pole zero pattern of the said filter.

4 Result and Discussion

To test our proposed model, we select the ECG recording of three persons from the ECG-ID database and compare it with the clean ECG recording available on the same database. Results are depicted in Fig. 11a–e. Table 3 compares the SNR and SSNR values of clean and filtered signal. Method to calculate SNR and SSNR is given in Eqs. 3 and 4.

$$\text{SNR(in dB)} = 10\ \log_{10}\left(\frac{\text{Signal Power}}{\text{Noise Power}}\right) \tag{3}$$

$$\text{SSNR(in dB)} = 10\ \log_{10}\left(\frac{\text{Signal Power}}{\text{Signal Plus Noise Power}}\right) \tag{4}$$

Table 2 Filter coefficients for direct from II structure

Type of filter coefficient		High-pass filter	Band stop filter		Low-pass filter
			For 60 Hz Powerline noise	For 50 Hz Powerline noise	
b_n	b_0	0.9808445003005	0.8184225674041	0.8184225674041	0.0671769724046
	b_1	−4.9042072369386	−1.6300564230156	−2.1005380606757	0.1340791638009
	b_2	9.8083992093615	2.4484913383789	2.9846377941606	0.0671769724046
	b_3	−9.8083992093615	−1.6300564230156	−2.1005380606757	NA
	b_4	4.9042072369386	0.8184225674041	0.8184225674041	NA
	b_5	−0.9808445003005	NA	NA	NA
a_n	a_1	−4.9614059839484	−1.9046032765601	−2.4543271118803	−1.2233115911186
	a_2	9.8461787468218	2.7357527046114	3.3373189222071	0.5244984927249
	a_3	−9.7700922326241	−1.7533034997940	−2.2593578242032	NA
	a_4	4.8472721999557	0.8480702103376	0.8480702103376	NA
	a_5	−0.9619527298513	NA	NA	NA

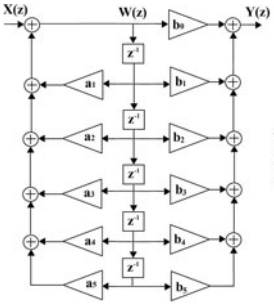

(a) Direct From II structure

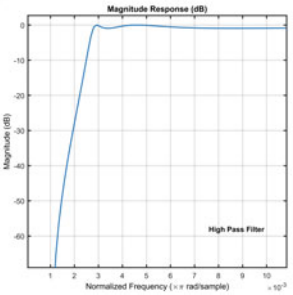

(b) Magnitude response

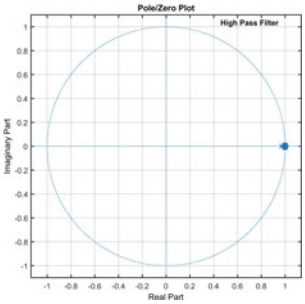

(c) Pole – Zero Plot

Fig. 8 High-pass elliptic filter parameters

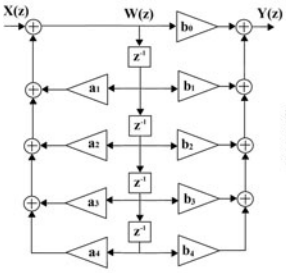

(a) Direct From II structure

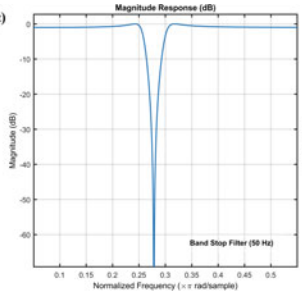

(b) Magnitude response

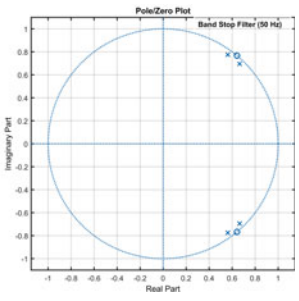

(c) Pole – Zero Plot

Fig. 9 Band stop elliptic filter parameters

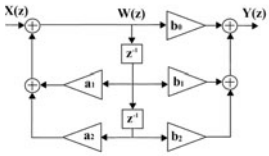

(a) Direct From II structure

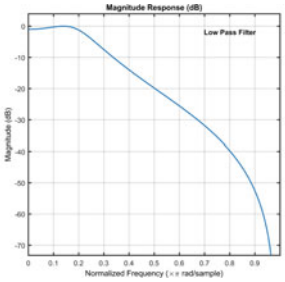

(b) Magnitude response

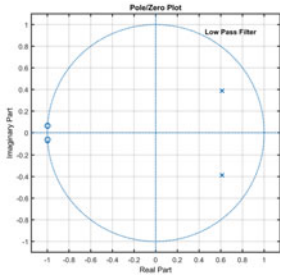

(c) Pole – Zero Plot

Fig. 10 Low-pass elliptic filter parameters

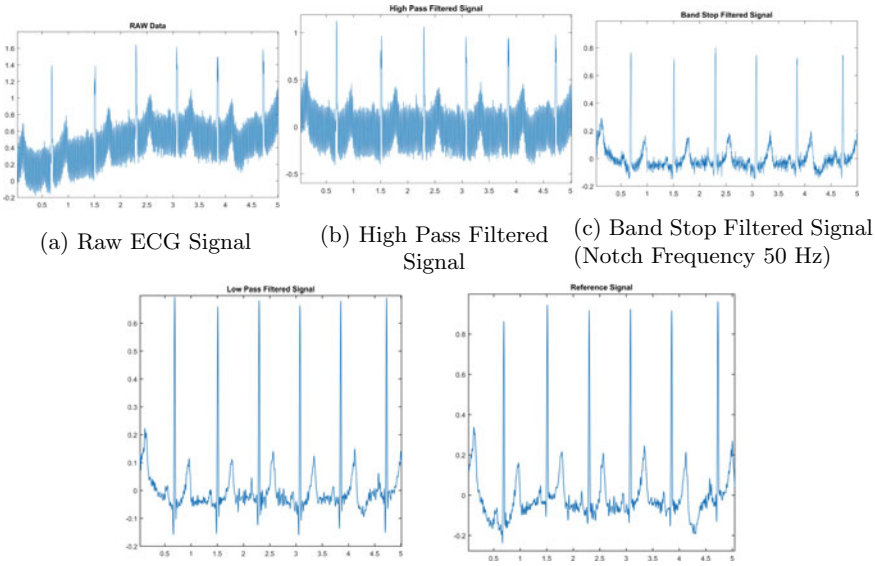

(a) Raw ECG Signal (b) High Pass Filtered Signal (c) Band Stop Filtered Signal (Notch Frequency 50 Hz)

(d) Low Pass Filtered Signal (e) Reference Signal

Fig. 11 Step-by-step events representing the strategy of the ECG signal de-noising

Table 3 SNR and SSNR values of clean signal and filtered signal

Clean signal		Filtered signal	
SNR (dB)	SSNR (dB)	SNR (dB)	SSNR (dB)
−12.0262	−12.2892	−15.3475	−15.6105

The SNR and SSNR values in Table 4 are obtained from our model (highlighted in gray color) and the existing model in [9] for the same input and compared it with each other. Here, we use the ECG recordings from all the three databases mentioned in Sect. 2.1.

5 Conclusion

The purpose of this study is to clean a noisy ECG signal using low-order digital IIR filters. The complexity of low-order design is less, and IIR filters can easily transform into analog domain. In [9], the authors used an elliptic low-pass filter of order 4, whereas we have used a second-order low-pass elliptic filter which performed better than them. In [8], the authors proposed 20 Hz cutoff frequency for low pass filter. But that design parameter is not working with many ECG recordings especially for MIT-BIH Normal Sinus Rhythm Database. In [10], the proposed model has a SNR

Table 4 SNR and SSNR comparison between existing model [9] and proposed model

S. No.	Name of database	Record no.	Existing model		Proposed model		Percentage increase in SSNR (%)
			SNR (dB)	SSNR(dB)	SNR (dB)	SSNR (dB)	
1	MIT-BIH	19830	−1.0267	−6.1461	0.8935	−4.2278	31.75%
2	Normal sinus	16272	1.2880	−5.5758	3.2516	−3.6330	34.84%
3	Rhythm database	16265	3.4534	−5.4211	5.2818	−3.5948	33.67%
4	ECG-ID Data base	Person 1 Record 2	0.4855	−5.9946	1.7609	−4.7235	21.20%
5		Person 2 Record 6	−6.0477	−8.3251	−5.4407	−7.7181	7.29%
6		Person 3 Record 1	−16.0458	−16.2950	−15.3475	−15.6105	4.20%
7	MIT-BIH	101	−9.7321	−10.8781	−8.1828	−9.3282	14.25%
8	Arrhythmia	103	−3.9670	−7.3397	−2.2397	−5.6118	23.54%
9	Database	105	−4.5111	−7.5615	−3.3195	−6.3724	15.72%

of −23.80 dB, which is much lower than ours. Data sets of Tables 3 and 4 and visual inspection of time domain output shown in Fig. 11 are the evidence that our proposed model is very much able to remove noise.

Acknowledgements The authors would like to thank UGC UPE, II 'Modern Biology Group B: Signal Processing Group,' University of Calcutta, for providing research facility and technical support.

References

1. Muhammad, D.G., Abubakar, I.A.: COVID-19 lockdown may increase cardiovascular disease risk factors. Egypt Heart J. **73**(1), 2
2. Velayudhan, A., Peter, S.: Noise analysis and different denoising techniques of ECG signal—a survey. IOSR J. Electron. Commun. Eng. pp. 40–44 e-ISSN: 2278-2834, p-ISSN: 2278-8735 (2016)
3. Pérez-Riera, A.R., Barbosa-Barros, R., Daminello-Raimundo, R., de Abreu, L.C.: Main artifacts in electrocardiography. Ann Noninvasive Electrocardiol. **23**(2), e12494 (2018)
4. Moody, G.B., Muldrow, W.K., Mark, R.G.: A noise stress test for arrhythmia detectors. Comput. Cardiol. **11**, 381–384 (1984)
5. Lastre-Domínguez, C., Shmaliy, Y.S., Ibarra-Manzano, O., Munoz-Minjares, J., Morales-Mendoza, L.J.: ECG signal denoising and features extraction using unbiased FIR smoothing. BioMed Res. Int. **2019**, Article ID 2608547 16 (2019)
6. Chatterjee, S., Thakur, R.S., Yadav, R.N., Gupta, L., Raghuvanshi, D.K.: Review of noise removal techniques in ECG signals. IET Signal Process **14**(9), 569–590 (2020)
7. Kumar, K.S., Yazdanpanah, B., Kumar, P.R.: Removal of noise from electrocardiogram using digital FIR and IIR filters with various methods. In: 2015 International Conference on Communications and Signal Processing, pp. 157–162 (2015)

8. Singh, N., Ayub, S., Saini, J.P.: Design of digital IIR filter for noise reduction in ECG signal. In: 2013 5th International Conference and Computational Intelligence and Communication Networks, pp. 171–176 (2013)
9. Chavan, M., Agarwala, R.A., Uplane, M.: Digital elliptic filter application for noise reduction in ECG signal. WSEAS Trans. Electron. **3**, 58–63 (2005)
10. Choudhary, M., Narwaria, R.P.: Suppression of noise in ECG signal using low pass IIR filters. In: IJECSE 2012, ISSN: 2277-1956
11. Sun, Y., Chan, K.L., Krishnan, S.M.: ECG signal conditioning by morphological filtering. Comput. Biol. Med. **32**(6), 465–479 ISSN: 0010-4825 (2002)
12. Moody, G.B., Mark, R.G.: The impact of the MIT-BIH arrhythmia database. IEEE Eng. Med. Biol. Magaz. **20**(3), 45–50 (2001)
13. Goldberger, A.L., Amaral, L.A., Glass, L., et al.: PhysioBank, PhysioToolkit, and PhysioNet: components of a new research resource for complex physiologic signals. Circulation **101**(23), E215–E220 (2000)
14. The MIT-BIH noise stress test database. Available: http://www.physionet.org/physiobank/database/nstdb/. Accessed 17 Aug 2020
15. Chieng, T.M., Hau, Y.W., Omar, Z.: The study and comparison between various digital filters for ECG de-noising. In: 2018 IEEE-EMBS Conference on Biomedical Engineering and Sciences, pp. 226–232 (2018)
16. Salivahanan, S.: Digital Signal Processing, 3rd edn. New Delhi, McGraw Hill Education (India) Private Limited (2015)

Performance Analysis of Berlekamp–Massey-Based KES Block for 3-Byte RS Decoder

Jagannath Samanta, Raj Kumar Maity, Debnath Ghosh, and Sudipta Bardhan

Abstract Reed–Solomon (RS) codes are mainly powerful subclass of cyclic non-binary BCH codes which are widely employed to detect and correct both the burst and random errors in different digital transmission systems and storage media. In RS codes, the most important and complex block is key equation solver (KES) which is responsible to compute the unknown error location polynomial and magnitude polynomial. The designers mostly prefer the Berlekamp–Massey (BM)-based algorithms for computation of this KES block. In this paper, we have analyzed and implemented Berlekamp–Massey algorithm-based three important algorithms, namely inversionless Berlekamp–Massey (iBM) algorithm, reformulated inversionless Berlekamp–Massey (riBM) algorithm and extended reformulated inversionless Berlekamp–Massey (RiBM) algorithm. These three algorithms have been simulated and evaluated using both FPGA and ASIC platforms. The KES blocks based on three algorithms are compared in terms of area occupied and propagation delay. It is observed that iBM algorithm-based KES block requires lesser area with higher delay. On the other way, the RiBM algorithm-based KES block has lowest delay with larger area. This analysis will help the design engineer to implement resource constraints application in digital communication systems and storage systems.

Keywords Galois field · Reed–Solomon codes · Berlekamp–Massey algorithm · Key equation solver block · FPGA and ASIC

1 Introduction

In 1960, two great researchers Irving S. Reed and Gustave Solomon invented Reed–Solomon (RS) codes at MIT Lincoln laboratory [1]. The RS codes are generally cyclic non-binary BCH codes. These codes have different properties such as (i) random and burst error correcting capability and (ii) erasure recovery capability. The RS codes have been widely employed in numerous commercial applications including

J. Samanta (✉) · R. K. Maity · D. Ghosh · S. Bardhan
Department of ECE, Haldia Institute of Technology, Haldia, India

B. Sikdar et al. (eds.), *Proceedings of the 3rd International Conference on Communication, Devices and Computing*, Lecture Notes in Electrical Engineering 851,
https://doi.org/10.1007/978-981-16-9154-6_2

satellite communication, mobile data communication, deep space communication, high-speed modems, optical and magnetic storage systems (CD, DVD, hard disk, Blu-ray disk, smart card), digital television/digital video broadcasting (DVB), etc. [1, 2].

The error magnitude polynomial $\Omega(x)$ and error locator polynomial $\Lambda(x)$ are computed from the syndrome polynomial $S(x)$ in KES block. The key equation is written as follows:

$$(S(x).\Lambda(x)) = (\Omega(x)\ mod\ x^{2t}) \tag{1}$$

Many researchers have concentrated to optimize the complexity of decoders without disturbing the decoder's performance. To accommodate the continuously increasing demands for higher-speed communication systems, RS decoders should be able to decode data at much higher rate.

Here, different algebraic or hard decoding algorithms of RS decoder are discussed. These hard decision decoding algorithms are still an open challenging issue to the researchers. In algebraic decoding or hard decision decoding, there exist three different algorithms: (i) Berlekamp–Massey (BM) algorithm, (ii) extended Euclidean algorithm and (iii) Peterson–Gorenstein–Zierler (PGZ) algorithm. But the BM algorithm is popular than other two algorithms.

In this paper, KES block based on iBM, riBM and RiBM algorithms has been designed and implemented. The KES blocks of 3-byte RS codes are simulated and synthesized by employing both FPGA and ASIC platforms. The performances of three KES blocks are also presented.

The remaining part of the paper is organized as follows. Overview of KES block is described briefly in Sect. 2. Different algorithms for KES block are presented in Sect. 3. In Sect. 4, FPGA and ASIC-based synthesis results are presented, and finally the paper is concluded in Sect. 5.

2 Overview of Key Equation Solver (KES) Block

The BM algorithm and Euclidean algorithm are the two most important techniques to solve the key equation in KES block. Both these algorithms can be employed to locate the error locator polynomial and magnitude polynomial. A practical technique for decoding the BCH codes over the different Galois fields (GF) or finite fields is used in hardware construction for a modified syndrome generator, graphical purpose units (GPUs) and an error corrector [3]. A low-complexity single byte error correction RS decoding algorithm is proposed to employ in majority logic techniques which get away from the needs of computing GF multiplication, GF divisions, GF inversions and GF logarithms [4].

The main advantage of Euclidean algorithm is very fast in computation, whereas the BM algorithm needed lesser area to implement. Compared to the modified Euclidean (ME) architectures [5–8], the BM architecture has irregular structure and extensive critical path delay. But BM generally employs simpler computation technique to search the error locator polynomial.

A ME decoding algorithm [9] is used to solve the key equation without performing the operations of field element inversion and polynomial division. The ME architecture requires huge number of clock cycles to compute the key equation [9]. Now, the enhanced degree computationless modified Euclidean (E-DCME) algorithm is introduced to minimize the hardware complexity [10, 11]. The simplified degree computationless modified Euclids (S-DCME) algorithm [12] reframes the existing ME algorithm. This algorithm introduces a new initial condition to minimize the hardware complexity. The critical path delay of S-DCME is $T_{\text{Mul}} + T_{\text{ADD}} + T_{\text{MUX}}$ which is equal to RiBM. Thus, S-DCME algorithm consumes the lower hardware complexity and the shorter critical path delay [13].

The concept of pipelining and folding is considered in RiBM algorithm which is named as pipelined reformulated inversionless Berlekamp–Massey (pRiBM) algorithm [14–16]. The pipelined RS decoder using a unique pipelined syndrome computation block based on RiBM algorithm block is introduced in [14]. The pRiBM architecture reduces the hardware complexity and improves the clock frequency of the RS decoders. The pRiBM-based architecture consists of pipelined GF multiplier which are used in syndrome block, KES block, Forney block and Chien search block. The overall design will enhance the clock frequency and need lower hardware complexity.

A truncated inversionless Berlekamp–Massey (TiBM) architecture [17] is introduced which notably reduced the hardware complexity and high speed in KES block of RS decoder. This area-efficient architecture is acquired by diminishing the unnecessary processing elements (PE) in the conventional RiBM [13] design. In TiBM, the number of PE for the KES block is decreased from $(3t + 1)$ to $(2t + 2)$. Efficient decoding techniques for RS codes based on iBM, riBM and RiBM algorithm are presented in the following.

3 Three Different Berlekamp–Massey-Based Algorithms

The three important RS decoding algorithms are discussed in the following.

3.1 inversionless Berlekamp–Massey (iBM) Algorithm

The iBM algorithm was introduced by Berlekamp and Massey in 1991 [18]. The iBM algorithm is the most suitable algorithm which is employed in KES block due to its smaller area [18–20]. A serial architecture is invented based on BM algorithm which intensely minimized the hardware complexity, maintaining the overall decoding speed [21].

We have considered the initial values of all parameters for the three algorithms (named as Algorithm 1, Algorithm 2 and Algorithm 3) are as follows: (i) The values of error location coefficients are $\lambda_0(0) = 1,\ \lambda_1(0) = 0,\ \lambda_2(0) = 0,\ \lambda_3(0) = 0$; (ii) the iterative coefficient values are $d_0(0) = 1,\ d_1(0) = 0,\ d_2(0) = 0,\ d_3(0) = 0,$

(iii) $p(0) = 0$ and (iv) $\gamma(0) = 1$. Syndromes values are also same for all three algorithms which are $s_0 = 186,\ s_1 = 219,\ s_2 = 191,\ s_3 = 13,\ s_4 = 172,\ s_5 = 222$. The pseudocode representation of iBM algorithm is presented in Algorithm 1.

Input: $s_j,\ j = 0, 1, 2, ..., (2t-2), (2t-1)$.
for $(r = 0;\ r \leq (2t-1);\ r++)$
begin
Step iBM1: $\delta(r) = s_r.\lambda_0(r) + s_{r-1}.\lambda_1(r) + ... + s_{r-t}.\lambda_t(r)$
Step iBM2: $\lambda_j(r+1) = \gamma(r).\lambda_j(r) - \delta(r)d_{j-1}(r)\ \ (j = 0, 1, 2, ..., t)$
  Step iBM3: $\delta(r) \neq 0$ **and** $p(r) \geq 0$
  then
  begin
   $d_j(r+1) = \lambda_j(r),\ \ (j = 0, 1, 2, ..., (t-1), t)$
   $\gamma(r+1) = \delta(r)$
   $p(r+1) = -p(r) - 1$
  end
  else
  begin
   $d_j(r+1) = d_{j-1}(r),\ \ (j = 0, 1, 2, ..., (t-1), t)$
   $\gamma(r+1) = \gamma(r)$
   $p(r+1) = p(r) + 1$
  end
end
for $(r = 0;\ r \leq (t-1);\ r++)$
Step iBM4: $\omega(2t) = s_j.\lambda_0(2t) + s_{j-1}.\lambda_1(2t) + ... + s_0.\lambda_j(2t)$
Output: $\lambda_j(2t),\ (j = 0, 1, 2, ..., t);\ \ \omega_j(2t),\ (j = 0, 1, 2, ..., (t-2), (t-1))$.

Algorithm 1: Pseudo code representation of iBM algorithm

Table 1 shows the values of error location polynomial and error magnitude polynomial based on iBM algorithm for 3-byte KES block.

3.2 reformulated inversionless Berlekamp–Massey (riBM) Algorithm

Sarwate et al. [13] have introduced a new decoding algorithm based on iBM algorithm. This is widely known as reformulated iBM algorithm (riBM). The riBM implements the KES block based on regular semi-systolic architecture with lesser critical path delay due to simple GF multiplier and GF adder. The riBM algorithm has minimized the irregular structure and larger delay of the BM architecture. The RiBM algorithm-based KES block removes the unnecessary components and makes the architecture simple and low latency compared to the conventional BM architectures. The pseudocode representation of riBM algorithm is presented in Algorithm 2. Table 2 shows the error location polynomial and error magnitude polynomial based on riBM algorithm in 3-byte KES block.

Table 1 Parameter calculation of 3-byte KES block based on iBM algorithm

Iteration	Values of δ	Values of λ	Values of d	Values of γ
0	$\delta(0) = 186$	$\lambda_0(1) = 1, \lambda_1(1) = 186$ $\lambda_2(1) = 0, \lambda_3(1) = 0$	$d_0(1) = 1, d_1(1) = 0$ $d_2(1) = 0, d_3(1) = 0$	$\gamma(1) = 186$
1	$\delta(1) = 229$	$\lambda_0(2) = 186, \lambda_1(2) = 219$ $\lambda_2(2) = 0, \lambda_3(2) = 0$	$d_0(2) = 0, d_1(2) = 1$ $d_2(2) = 0, d_3(2) = 0$	$\gamma(2) = 186$
2	$\delta(2) = 208$	$\lambda_0(3) = 62, \lambda_1(3) = 251$ $\lambda_2(3) = 208, \lambda_3(3) = 0$	$d_0(3) = 186, d_1(3) = 219$ $d_2(3) = 0, d_3(3) = 0$	$\gamma(3) = 208$
3	$\delta(3) = 94$	$\lambda_0(4) = 138, \lambda_1(4) = 179$ $\lambda_2(4) = 64, \lambda_3(4) = 0$	$d_0(4) = 0, d_1(4) = 186$ $d_2(4) = 219, d_3(4) = 0$	$\gamma(4) = 208$
4	$\delta(4) = 148$	$\lambda_0(5) = 15, \lambda_1(5) = 143$ $\lambda_2(5) = 220, \lambda_3(5) = 239$	$d_0(5) = 138, d_1(5) = 179$ $d_2(5) = 64, d_3(5) = 0$	$\gamma(5) = 148$
5	$\delta(5) = 173$	$\lambda_0(6) = 31, \lambda_1(6) = 136$ $\lambda_2(6) = 216, \lambda_3(6) = 79$	$d_0(6) = 0, d_1(6) = 138$ $d_2(6) = 179, d_3(6) = 64$	$\gamma(6) = 148$
	Output	Err. Loc. Coeff. $l_0 = 31, l_1 = 136$ $l_2 = 216, l_3 = 79$	Err. Mag. Coeff. $\omega_0 = 215, \omega_1 = 122$ $\omega_2 = 159$	

Input: $s_j,\ j = 0, 1, 2, ..., (2t-2), (2t-1)$
$\delta_j(0) = \theta_j(0) = s_j\ j = 0, 1, 2, ..., (2t-2), (2t-1)$
for $(r = 0;\ r \leq (2t-1);\ r++)$
begin
Step riBM1: $\lambda_j(r+1) = \gamma(r).\lambda_j(r) - \delta_0(r).d_{j-1}(r)\ \ (j = 0, 1, 2, ..., (t-1), t)$
$\delta_j(r+1) = \gamma(r).\delta_{j+1}(r) - \delta_0(r).\theta_j(r)\ \ (j = 0, 1, 2, ..., (2t-2), (2t-1))$
Step riBM2: $\delta_0(r) \neq 0$ **and** $p(r) \geq 0$
then
begin
$d_j(r+1) = \lambda_j(r),\ \ (j = 0, 1, 2, ..., (t-1), t)$
$\theta_j(r+1) = \delta_{j+1}(r),\ \ (j = 0, 1, 2, ..., (2t-2), (2t-1))$
$\gamma(r+1) = \delta_0(r)$
$p(r+1) = -p(r) - 1$
end
else
begin
$d_j(r+1) = d_{j-1}(r),\ \ (j = 0, 1, 2, ..., (t-1), t)$
$\theta_j(r+1) = \theta_j(r)(r),\ \ (j = 0, 1, 2, ..., (2t-2), (2t-1)$
$\gamma(r+1) = \gamma(r)$
$p(r+1) = p(r) + 1$
end
end
Output: $\lambda_j(2t),\ (j = 0, 1, 2, ..., (t-1), t);\quad \omega_j(2t),\ (j = 0, 1, 2, ..., (t-2), (t-1))$

Algorithm 2: Pseudo code representation of riBM algorithm

Table 2 Parameter calculation of 3-byte KES block based on riBM algorithm

Iteration	Values of δ and γ	Values of λ	Values of d	Values of θ
0	$\delta_0(1) = 229, \delta_1(1) = 68$	$\lambda_0(1) = 1$	$d_0(1) = 1$	$\theta_0(1) = 219, \theta_1(1) = 191$
	$\delta_2(1) = 91, \delta_3(1) = 125$	$\lambda_1(1) = 186$	$d_1(1) = 0$	$\theta_2(1) = 13, \theta_3(1) = 172$
	$\delta_4(1) = 52, \delta_5(1) = 147$	$\lambda_2(1) = 0$	$d_2(1) = 0$	$\theta_4(1) = 222, \theta_5(1) = 0$
	$\gamma(1) = 186$	$\lambda_3(1) = 0$	$d_3(1) = 0$	
1	$\delta_0(2) = 208, \delta_1(2) = 186$	$\lambda_0(2) = 186$	$d_0(2) = 0$	$\theta_0(2) = 219, \theta_1(2) = 191$
	$\delta_2(2) = 236, \delta_3(2) = 185$	$\lambda_1(2) = 219$	$d_1(2) = 1$	$\theta_2(2) = 13, \theta_3(2) = 172$
	$\delta_4(2) = 22, \delta_5(2) = 0$	$\lambda_2(2) = 0$	$d_2(2) = 0$	$\theta_4(2) = 222, \theta_5(2) = 0$
	$\gamma(2) = 186$	$\lambda_3(2) = 0$	$d_3(2) = 0$	
2	$\delta_0(3) = 94, \delta_1(3) = 109$	$\lambda_0(3) = 62$	$d_0(3) = 186$	$\theta_0(3) = 186, \theta_1(3) = 236$
	$\delta_2(3) = 148, \delta_3(3) = 30$	$\lambda_1(3) = 251$	$d_1(3) = 219$	$\theta_2(3) = 185, \theta_3(3) = 22$
	$\delta_4(3) = 215, \delta_5(3) = 0$	$\lambda_2(3) = 208$	$d_2(3) = 0$	$\theta_4(3) = 0, \theta_5(3) = 0$
	$\gamma(3) = 208$	$\lambda_3(3) = 0$	$d_3(3) = 0$	
3	$\delta_0(4) = 148, \delta_1(4) = 24$	$\lambda_0(4) = 138$	$d_0(4) = 0$	$\theta_0(4) = 186, \theta_1(4) = 236$
	$\delta_2(4) = 187, \delta_3(4) = 153$	$\lambda_1(4) = 179$	$d_1(4) = 186$	$\theta_2(4) = 185, \theta_3(4) = 22$
	$\delta_4(4) = 0, \delta_5(4) = 0$	$\lambda_2(4) = 64$	$d_2(4) = 219$	$\theta_4(4) = 0, \theta_5(4) = 0$
	$\gamma(4) = 208$	$\lambda_3(4) = 0$	$d_3(4) = 0$	
4	$\delta_0(5) = 173, \delta_1(5) = 167$	$\lambda_0(5) = 15$	$d_0(5) = 138$	$\theta_0(5) = 24, \theta_1(5) = 187$
	$\delta_2(5) = 160, \delta_3(5) = 234$	$\lambda_1(5) = 143$	$d_1(5) = 179$	$\theta_2(5) = 153, \theta_3(5) = 0$
	$\delta_4(5) = 0, \delta_5(5) = 0$	$\lambda_2(5) = 220$	$d_2(5) = 64$	$\theta_4(5) = 0, \theta_5(5) = 0$
	$\gamma(5) = 148$	$\lambda_3(5) = 239$	$d_3(5) = 0$	
5	$\delta_0(6) = 126, \delta_1(6) = 75$	$\lambda_0(6) = 31$	$d_0(6) = 0$	$\theta_0(6) = 24, \theta_1(6) = 187$
	$\delta_2(6) = 7, \delta_3(6) = 0$	$\lambda_1(6) = 136$	$d_1(6) = 138$	$\theta_2(6) = 153, \theta_3(6) = 0$
	$\delta_4(6) = 0, \delta_5(6) = 0$	$\lambda_2(6) = 216$	$d_2(6) = 179$	$\theta_4(6) = 0, \theta_5(6) = 0$
	$\gamma(1) = 148$	$\lambda_3(6) = 79$	$d_3(6) = 64$	
	Output:$l_0 = 31, l_1 = 136$	$l_2 = 216, l_3 = 79$	$\omega_0 = 126$	$\omega_1 = 75, \omega_2 = 7$

3.3 Reformulated inversionless Berlekamp–Massey (RiBM) Algorithm

The authors in [13] have also introduced another decoding algorithm based on riBM which is known as reformulated iBM algorithm (RiBM). The RiBM algorithm is the extended version of riBM algorithm. This RiBM algorithm further removes the unnecessary components of the KES block than riBM algorithm. Pseudocode representation of RiBM algorithm is presented in Algorithm 3. Table 3 shows the error location polynomial and error magnitude polynomial based on RiBM algorithm of 3-byte KES block.

Input: $s_j,\ j = 0, 1, 2, ..., (2t-2), (2t-1)$
$\delta_j(0) = \theta_j(0) = s_j\ j = 0, 1, 2, ..., (2t-2), (2t-1)$
for $(r = 0;\ r \leq (2t-1);\ r++)$
begin
Step RiBM1: $\delta_j(r+1) = \gamma(r).\delta_{j+1}(r) - \delta_0(r).\theta_j(r)\ \ (j = 0, 1, 2, ..., (3t-1), 3t)$
Step RiBM2 $\delta_0(r) \neq 0$ **and** $p(r) \geq 0$
then
begin
$\theta_j(r+1) = \delta_{j+1}(r),\ \ (j = 0, 1, 2, ..., (3t-1), 3t)$
$\gamma(r+1) = \delta_0(r)$
$p(r+1) = -p(r) - 1$
end
else
begin
$\theta_j(r+1) = \theta_j(r),\ \ (j = 0, 1, 2, ..., (3t-1), 3t)$
$\gamma(r+1) = \gamma(r)$
$p(r+1) = p(r) + 1$
end
end
Output:
$\lambda_j(2t) = \delta_{t+j}(2t),\ (j = 0, 1, 2, ..., t);\ \ \omega_j(2t) = \delta_j(2t),\ (j = 0, 1, 2, ..., (t-2), (t-1))$

Algorithm 3: Pseudo code representation of RiBM algorithm

Table 3 Parameter calculation of 3-byte KES block based on RiBM algorithm

Iteration	Values of δ	Values of γ	Values of θ
0	$\delta_0(1) = 229, \delta_1(1) = 68$ $\delta_2(1) = 91, \delta_3(1) = 125$ $\delta_4(1) = 52, \delta_5(1) = 147, \delta_6(1) = 0$ $\delta_7(1) = 0, \delta_8(1) = 219, \delta_9(1) = 186$	$\gamma(1) = 186$	$\theta_0(1) = 219, \theta_1(1) = 191$ $\theta_2(1) = 13, \theta_3(1) = 172$ $\theta_4(1) = 222, \theta_5(1) = 0, \theta_6(1) = 0$ $\theta_7(1) = 0, \theta_8(1) = 1, \theta_9(1) = 0$
1	$\delta_0(2) = 208, \delta_1(2) = 186$ $\delta_2(2) = 236, \delta_3(2) = 185$ $\delta_4(2) = 22, \delta_5(2) = 0, \delta_6(2) = 0$ $\delta_7(2) = 251, \delta_8(2) = 219, \delta_9(2) = 0$	$\gamma(2) = 186$	$\theta_0(2) = 219, \theta_1(2) = 191$ $\theta_2(2) = 13, \theta_3(2) = 172$ $\theta_4(2) = 222, \theta_5(2) = 0, \theta_6(2) = 0$ $\theta_7(2) = 0, \theta_8(2) = 1, \theta_9(2) = 0$
2	$\delta_0(3) = 94, \delta_1(3) = 109$ $\delta_2(3) = 148, \delta_3(3) = 30$ $\delta_4(3) = 215, \delta_5(3) = 0, \delta_6(3) = 37$ $\delta_7(3) = 251, \delta_8(3) = 208, \delta_9(3) = 0$	$\gamma(3) = 208$	$\theta_0(3) = 186, \theta_1(3) = 236$ $\theta_2(3) = 185, \theta_3(3) = 22$ $\theta_4(3) = 0, \theta_5(3) = 0, \theta_6(3) = 251$ $\theta_7(3) = 219, \theta_8(3) = 0, \theta_9(3) = 0$
3	$\delta_0(4) = 148, \delta_1(4) = 24$ $\delta_2(4) = 187, \delta_3(4) = 153$ $\delta_4(4) = 0, \delta_5(4) = 168, \delta_6(4) = 243$ $\delta_7(4) = 64, \delta_8(4) = 0, \delta_9(4) = 0$	$\gamma(4) = 208$	$\theta_0(4) = 186, \theta_1(4) = 236$ $\theta_2(4) = 185, \theta_3(4) = 22$ $\theta_4(4) = 0, \theta_5(4) = 0, \theta_6(4) = 251$ $\theta_7(4) = 219, \theta_8(4) = 0, \theta_9(4) = 0$
4	$\delta_0(5) = 173, \delta_1(5) = 167$ $\delta_2(5) = 160, \delta_3(5) = 234$ $\delta_4(5) = 173, \delta_5(5) = 177, \delta_6(5) = 166$ $\delta_7(5) = 239, \delta_8(5) = 0, \delta_9(5) = 0$	$\gamma(5) = 148$	$\theta_0(5) = 24, \theta_1(5) = 187$ $\theta_2(5) = 153, \theta_3(5) = 0$ $\theta_4(5) = 168, \theta_5(5) = 243, \theta_6(5) = 64$ $\theta_7(5) = 0, \theta_8(5) = 0, \theta_9(5) = 0$
5	$\delta_0(6) = 126, \delta_1(6) = 75$ $\delta_2(6) = 7, \delta_3(6) = 31$ $\delta_4(6) = 136, \delta_5(6) = 216, \delta_6(6) = 79$ $\delta_7(6) = 0, \delta_8(6) = 0, \delta_9(6) = 0$	$\gamma(6) = 148$	$\theta_0(6) = 24, \theta_1(6) = 187$ $\theta_2(6) = 153, \theta_3(6) = 0$ $\theta_4(6) = 168, \theta_5(6) = 243, \theta_6(6) = 64$ $\theta_7(6) = 0, \theta_8(6) = 0, \theta_9(6) = 0$
	Output:$l_0 = 31,\ l_1 = 136,\ l_2 = 216$	$l_3 = 79$	$\omega_0 = 126,\ \omega_1 = 75,\ \omega_2 = 7$

4 Implementation of KES Blocks

The KES block of 3-byte RS codes based on three different decoding algorithms is synthesized using both FPGA and ASIC platforms.

4.1 FPGA-Based Synthesis Results

The KES block of 3-byte RS decoder has been simulated and synthesized using Vertex 4 (4vfx12ff668-10) FPGA device family. The input and output simulation waveforms based on iBM algorithm are shown in Fig. 1. All the input and output parameters are shown in Fig. 1. All the input and output values are matched with Table 1.

FPGA-based synthesis results are presented in Table 4. In iBM algorithm, it is observed that least area (in terms of look-up tables (LUTs)) consumes but critical path delay is more. On the other hand, RiBM-based KES block requires maximum area but least critical path delay. Average area and delay are obtained in riBM algorithm-based KES block.

4.2 ASIC-Based Synthesis Results

All three algorithms are also synthesized in Leonardo Spectrum tool of Mentor Graphics. The ASIC-based synthesis results are given in Table 5. Area in terms of universal NAND/NOR gates and number of instances are given in Table 5. It is observed that the iBM algorithm-based KES block requires least area but more delay. But the RiBM-based KES block consumes maximum area. Data arrival time and path slack information are also presented in Table 5. Path slack is showing a negative value which indicates that there is not much time to schedule for a particular task.

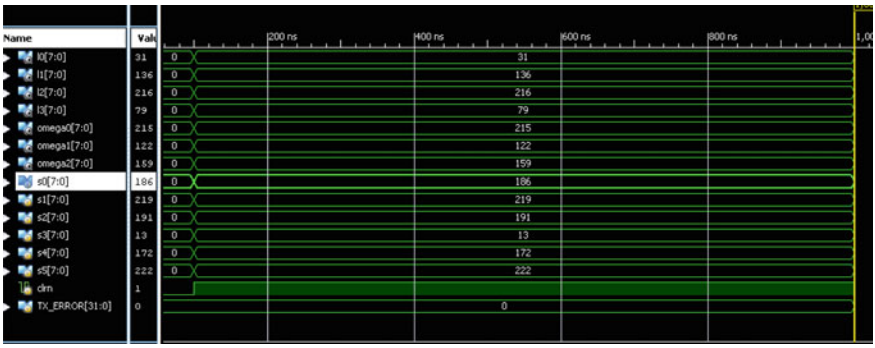

Fig. 1 Simulation waveforms based on iBM algorithm

Table 4 FPGA-based synthesis results of 3-byte KES block using three algorithms

	iBM based (Algorithm 1)	riBM based (Algorithm 2)	RiBM based (Algorithm 3)
Number of LUTs	2002	2480	3813
Max. Combinational path delay	27.849	21.001	19.921

Table 5 ASIC-based synthesis results of of 3-byte KES block using three algorithms

Parameters	iBM based (Algorithm 1)	riBM based (Algorithm 2)	RiBM based (Algorithm 3)
Number of gates	9370	16965	17192
Number of accumulated instances	6799	12951	13045
Data arrival time	28.81	25.4	27.81
Path slack	−18.81	−15.4	−17.81

5 Conclusion

In this paper, Berlekamp–Massey algorithm-based three algorithms, namely iBM algorithm, riBM algorithm and RiBM algorithm, have been analyzed and implemented for 3-byte RS decoder. Three algorithms have been simulated and implemented using both FPGA and ASIC platforms. It has been observed that iBM algorithm-based KES block requires lesser area with higher delay, and RiBM algorithm-based KES block has lowest delay with larger area. As KES block is simplified using these algorithms, so overall performance of the RS decoder is also modified. This work improves the confidence of design engineer to implement resource constraints application in digital transmission systems and storage systems. We will implement these algorithms for higher-order error correcting RS codes.

References

1. Wicker, S.B., Bhargava, V.K.: Bhargava: Reed-Solomon Codes and Their Applications. IEEE Press, Piscataway, NJ (1994)
2. Yuan, B., Wang, Z., Li, L., Gao, M., Sha, J., Zhang, C.: Area efficient Reed-Solomon decoder design for optical communications. IEEE Trans. Circuits Syst.-II, Express Briefs **56**(6), 469–473 (2009)
3. Subbiah, A., Ogunfunmi, T.: A flexible hybrid BCH decoder for modern NAND flash memories using general purpose graphical processing units (GPGPUs). Micromachines **10**(6), 365 (2019)
4. Garcia-Herrero, F., Sánchez-Macián, A., San-Isidro, M., Aranda, L.A., Maestro, J.A.: Efficient majority-logic Reed-Solomon decoders for single symbol correction. IEEE Trans. Device Mater. Reliab. **20**(2), 390–394 (2020)

5. Chang, Y.W., Truong, T.K., Jeng, J.H.: VLSI architecture of modified Euclidean algorithm for reed-Solomon code. Inf. Sci. **155**(1), 139–150 (2003)
6. Lee, H.H.: Modified Euclidean algorithm block for high-speed Reed-Solomon decoder. IEE Electron. Lett. **37**(14), 903–904 (2001)
7. Lee, S., Lee, H.: A high-speed pipelined degree-computationless modified Euclidean algorithm architecture for Reed-Solomon decoders. IEICE Trans. Fund. Electron. Commun. Comput. Sci. **E91-A**(3), 830–835 (2008)
8. Sarwate, D.V., Yan, Z.: Modified Euclidean algorithms for decoding Reed-Solomon codes. In: Proceedings in IEEE International Symposium Information Theory, pp. 1398–1402 (2009)
9. Lee, H.: High-speed VLSI architecture for parallel Reed-Solomon decoder. IEEE Trans. Very Large Scale Integrat. (VLSI) Syst. **11**(2), 288–294 (2003)
10. Baek, J.H., Sunwoo, M.H.: New degree computationless modified Euclid algorithm and architecture for Reed-Solomon decoder. IEEE Trans. Very Large Scale Integrat. (VLSI) Syst. **14**(8), 915–920 (2006)
11. Baek, J.H., Sunwoo, M.H.: Enhanced degree computationless modified Euclid's algorithm for Reed-Solomon decoders. IEE Electron. Lett. **43**(3), 175–176 (2007)
12. Baek, J., Sunwoo, J.: Simplified degree computationless modified Euclids algorithm and its architecture. In: Proceedings in IEEE International Symposium on Circuits and Systems, pp. 905–908 (2007)
13. Sarwate, D.V., Shanbhag, N.R.: High-speed architectures for Reed-Solomon decoder. Trans. Very Large Scale Integrat. (VLSI) Syst. **9**(5), 641–655 (2001)
14. Park, J.I., Lee, K., Choi, C.S., Lee, H.: High-speed low-complexity Reed-Solomon decoder using pipelined Berlekamp-Massey algorithm and its folded architecture. J. Semiconductor Technol. Sci. **10**(3), 193–202 (2010)
15. Kavian, Y.S., Falahati, A., Khayatzadeh, A., Naderi, M.: High speed Reed-Solomon decoder with pipeline architecture. In: Proceedings in WOCN2005, pp. 414–419 (2005)
16. Duan, Y., Li, Y.: An improved decoding algorithm to decode quadratic residue codes based on the difference of syndromes. IEEE Trans. Inf. Theory **66**(10), 5995–6000 (2020)
17. Park, J.I., Lee, H.: Area-efficient truncated Berlekamp-Massey architecture for Reed-Solomon decoder. Elec. Lett. **47**(4), 241–243 (2011)
18. Reed, I.S., Shih, M.T., Truong, T.K.: VLSI design of inverse-free Berlekamp Massey algorithm. Proc. Inst. Elect. Eng. **138**, 295–298 (1991)
19. Jeng, J.H., Truong, T.K.: On decoding of both errors and erasures of a Reed-Solomon code using an inverse-free Berlekamp-Massey algorithm. IEEE Trans. Commun. **47**(10), 1488–1494 (1999)
20. Hazem, A., Hamed, S., Tallal, E., Fahmy, A.H.: A low energy high speed Reed-Solomon decoder using decomposed inversionless Berlekamp-Massey algorithm. In: Proceedings in 44th Conference on Signals, Systems and Computers (ASILOMAR), pp. 406–409 (2010)
21. Chang, H.C., Shung, C.B.: New serial architecture for the Berlekamp Massey algorithm. IEEE Trans. Commun. **47**(4), 441–443 (1999)

Compact Broadband Antenna Using Modified Ground Plane

Smarajit Maity, Tapas Tewary, Surajit Mukherjee, Avisankar Roy, and Sunandan Bhunia

Abstract A compact broadband rectangular patch antenna is designed, simulated, and analyzed. This antenna is designed and simulated by RT/Duroid 5880 with relative permittivity of 2.2, thickness of 1.588 mm, and loss tangent of 0.0009. Before modification, the reference structure resonates at 10.17 GHz with 5.21% fractional bandwidth. The ground plane of the reference structure is modified to achieve the compactness as well as broadband nature. The proposed antenna exhibits an impedance bandwidth of 1 GHz (3.4–4.4 GHz) with two resonating frequencies at 3.6 and 4.3 GHz. Compactness of 85% with percentage bandwidth of 25.31% has been achieved in the proposed antenna. Stable radiation patterns with sufficient isolation between co-pol and cross-pol in both E plane and H plane with peak gain of 6.3 dBi are achieved. All the simulation results are obtained by CST Microwave Studio. The designed compact microstrip patch antenna is suitable for S band and C band applications.

Keywords Compact · Broadband · Modified ground plane · Microstrip patch antenna

1 Introduction

Microstrip patch antenna is now the indispensable component of wireless transmission network. For many years, the trend of the antenna design has been in the direction of achieving compactness while preserving the required characteristic features intact. In the process of compactness, it must be ensured that shape, size, gain, and other

S. Maity (✉) · T. Tewary
Academy of Technology, Bandel, Hooghly, West Bengal, India
e-mail: smarajit.maity@aot.edu.in

S. Mukherjee · A. Roy
Haldia Institute of Technology, Haldia, West Bengal, India

S. Bhunia
Central of Technology, Kokrajhar, Assam, India

B. Sikdar et al. (eds.), *Proceedings of the 3rd International Conference on Communication, Devices and Computing*, Lecture Notes in Electrical Engineering 851,
https://doi.org/10.1007/978-981-16-9154-6_3

characteristics of the antenna are such that it can be easily integrated and packaged in a product.

Immense numbers of ways are there to realize compact size. Each and every compact antenna design customizes the traditional architecture or follows an appropriate miniaturization approach, but every technique has its own advantages and disadvantages. An elementary antenna design along with inset fed can lead to a compact size antenna. Because of the inset fed, architecture impedance of the radiating plane design equals with the feed impedance and the needed outcome can be obtained with minimum dimensions with respect to the design dimensions before modification [1, 2]. Defective ground structure modifies the current distribution which in turn raises effective capacitance and inductance. As a consequence, it reduces the reflection coefficient and desired result is attained in conjunction with the compact size [3]. Alternative approaches like meander lines, which are basically random fold of lines depicted in the radiating plane that changes the current distribution to a great extent, are also taken up. Total length covered by the current increases by these arbitrary horizontal and vertical folded lines. The increased length helps the antenna to operate in C band, L band, etc., minimizing the overall desired dimensions [4, 5]. However, a very much well accepted approach involves etching slots in the radiating plane and/or redesigning the ground plane with DGS. This greatly helps in achieving a compact size [6–13].

The proposed article proposes inset fed thin compact microstrip patch antenna that modifies ground plane of the reference structure by incorporating slots in appropriate position and appropriate dimension. High peak gain of 6.3 dBi at 4.7 GHz is achieved. The size of 4.32 GHz conventional microstrip patch antenna has been reduced to a percentage minimization of patch area above 85%.

2 Antenna Configuration and Optimized Dimension

Initially, the reference structure is designed which resonates at 10.17 GHz with 5.21% fractional bandwidth. The reference patch antenna dimensions (length, width, etc.) were calculated for 10 GHz by using conventional antenna design equation [14]. The antenna is designed by using CST Microwave Studio, and then, the best favorable dimensions were decided from experimental modification. The dimension of the designed antenna, along with the substrate, is 21.208×11.588 mm. A 50 Ω microstrip feed line, with 3.2 mm width and 7.49 mm length, is used for feeding the antenna. The dimension of rectangular patch is 11.86×9.06 mm.

Only the ground plane of the reference structure, discussed in the previous section, is modified to obtain the compact structure and broadband nature. Figure 1 shows the ground plane of the proposed antenna with modified ground plane. Figure 2 shows the structure of the radiating plane of the proposed antenna. The initial modification (design 1 in Fig. 3b) shows multiband characteristics (3.6–3.7 GHz and 4.6–4.7 GHz). Without modifying the radiating patch, only the slots are incorporated in the ground plane to achieve broadband nature (design 2 in Fig. 3b). The proposed antenna

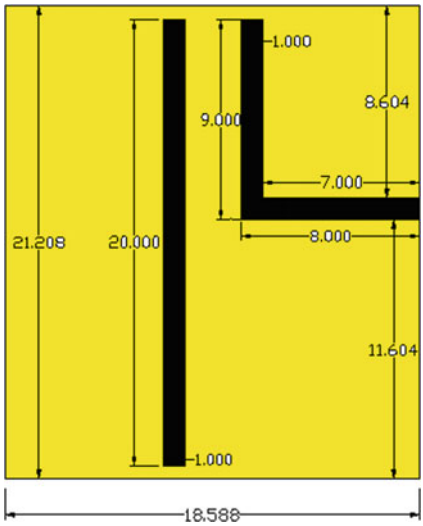

Fig. 1 Structure of ground plane

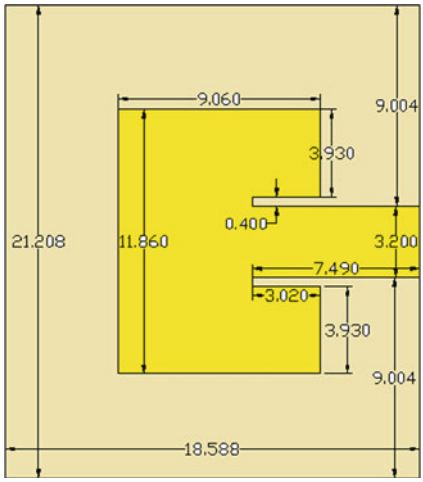

Fig. 2 Structure of radiating plane

shows broadband (3.4–4.4 GHz) characteristics with resonance frequencies at 3.6 and 4.3 GHz. Table 1 shows the details design summary of reference antenna and proposed antenna.

3 Antenna Results and Discussion

Figure 3a represents simulated reflection coefficient of the reference antenna structure, and Fig. 3b exhibits reflection coefficient of initially modified antenna (design

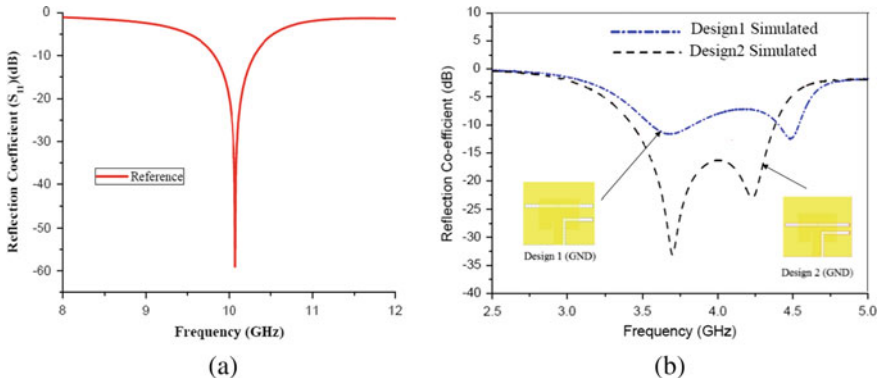

Fig. 3 Reflection coefficient of **a** reference structure, **b** proposed antenna

Table 1 Design summary of the proposed antenna (all dimensions are in mm)

Parameters	Reference antenna	Proposed antenna
Material	RT/Duroid 5880	RT/Duroid 5880
Thickness	1.588	1.588
Resonance frequency	10.17 GHz	3.6 GHz and 4.3 GHz
Impedance bandwidth (%)	5.21%	25.31%
Patch	11.86 × 9.06	11.86 × 9.06
Ground	21.208 × 18.588	21.208 × 18.588
Substrate	21.208 × 18.588	21.208 × 18.588
Feed	3.2 × 7.49	3.2 × 7.49
Slit on patch		3.02 × 0.4
Slot1 on ground		20 × 1
Slot2 on ground		9 × 1
Slot3 on ground		7 × 1

1) and proposed (design 2) compact antenna. It can be observed that the proposed antenna resonates at 3.6 GHz and 4.3 GHz with reflection coefficient of −33.14 dB and −22.10 dB, respectively. It also shows that due to this modification bandwidth of 1 GHz (3.4–4.4 GHz) with fractional bandwidth of 25.31% is also achieved. Figure 4 exhibits simulated peak gain of the proposed (design 2) antenna, initially modified antenna (design 1). Simulated peak gain of 5.4 dBi at 4.3 GHz is achieved for the proposed antenna.

Figure 5 shows the surface current distribution of the proposed antenna at resonant frequencies. It can also be observed that current intensity in the 2nd resonant

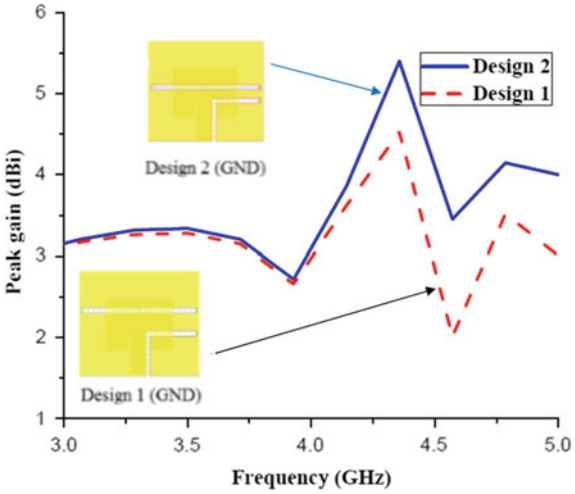

Fig. 4 Peak gain

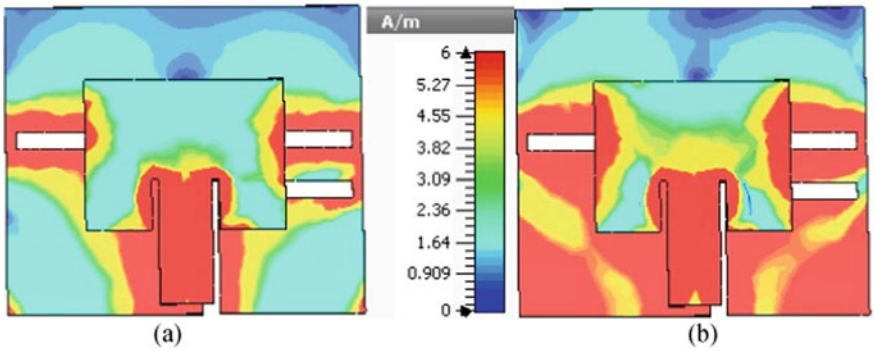

Fig. 5 Surface current distribution of the proposed antenna at **a** 3.6 GHz, **b** 4.3 GHz

frequency is higher than the 1st one so the effective gain is higher for the 2nd resonant frequency. Figure 6 shows that efficiency of the proposed antenna at resonant frequencies (3.6 and 4.3 GHz) is more than 90%. VSWR of nearly 1.2 over the entire bandwidth (3.4–4.4 GHz) has been achieved, shown in Fig. 7, in the proposed antenna.

The E plane and H plane co-polarization and cross-polarization radiation pattern are shown in Figs. 8 and 9, respectively. Maximum isolation between co-pol and cross-pol at the frequencies 3.6 GHz and 4.3 GHz in E plane is 33 dB and 32 dB, respectively. Similarly, in H plane, maximum isolation between co-pol and cross-pol at the frequencies 3.6 GHz and 4.3 GHz is 20 dB and 19 dB, respectively.

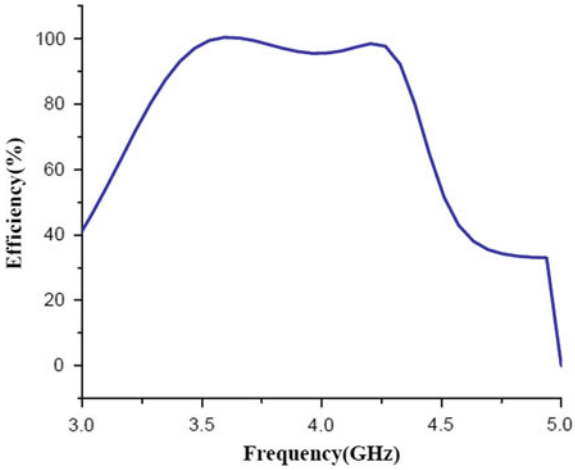

Fig. 6 Simulated efficiency

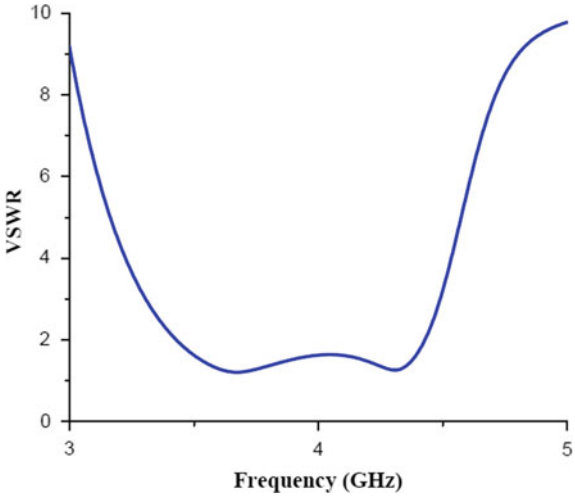

Fig. 7 Simulated VSWR

4 Conclusion

A thin (1.588 mm) compact broadband inset fed microstrip patch antenna is designed, simulated, and investigated. The proposed antenna exhibits a wide bandwidth of 1 GHz (3.4–4.4 GHz) with 25.31% bandwidth and peak gain of 6.3 dBi at 4.3 GHz along with stable radiation pattern. The achieved average compactness is about 85%. Therefore, this antenna can be considered as a good candidate for WiMAX technology, mobile broadband application, and wireless local area network (WLAN).

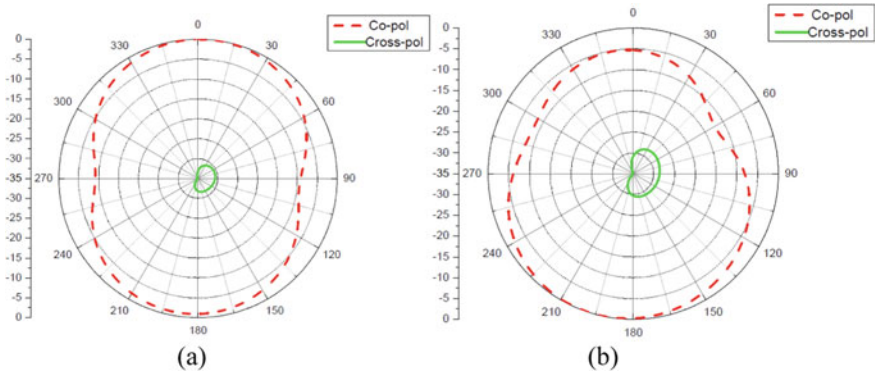

Fig. 8 Radiation patterns of the proposed antenna: E plane **a** at 3.6 GHz, **b** at 4.3 GHz

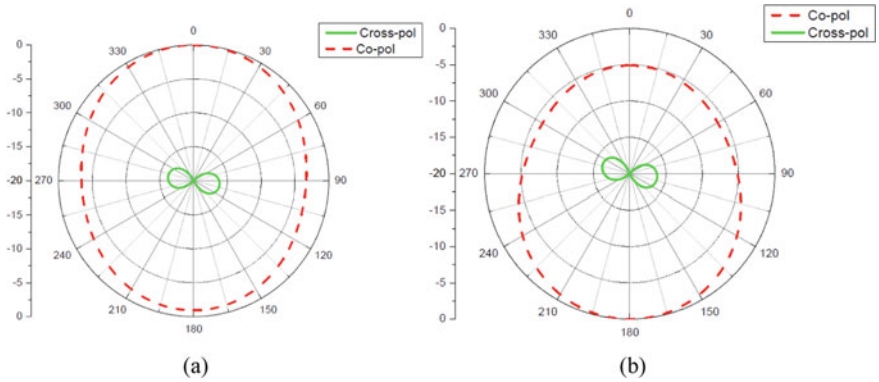

Fig. 9 Radiation patterns of the proposed antenna: H plane **a** at 3.6 GHz, **b** at 4.3 GHz

Acknowledgements The authors would like to express a sincere appreciation and thankfulness to DETS, University of Kalyani, West Bengal, India, and Central Institute of Technology, Kokrajhar, B.T.A.D. Assam for providing great facilities such IEEE Xplore digital library and research laboratory facility that made this research able to complete.

References

1. Patil, S.B., Kanphade, R.D., Vivek, V.R.: Design and performance analysis of inset feed microstrip square patch antenna for 2.4 GHz wireless applications. In: 2nd International Conference on Electronics and Communication System, pp. 51–54 (2015)
2. Karthick, M.: Design of 2.4 GHz patch antennae for WLAN applications. In: IEEE Seventh National Conference on Computing, Communication and Information Systems, pp. 7–11 (2015)

3. Deb, P., Moyra, T., Bhowmik, P.: Return loss and bandwidth enhancement of Microstrip antenna using Defected Ground Structure. In: 2nd International Conference on Signal Processing and Integrated Networks, pp. 25–29 (2015)
4. Muktii, P.H., Setijadi, E., Ardelina, N.: A compact dual-band antenna design using meander-line slots for WiMAX application in Indonesia. In: The 1st International Conference on Information Technology, Computer and Electrical Engineering, pp. 447–450 (2014)
5. Wang, X-Y., Fu, Y., Wang, H., Gui, G., Yang, G. M.:A compact 433 MHz antenna with enhanced performance by using multi-resonant meander line structure. Asia–Pacific Microwave Conf (APMC) **2**, 1–3 (2015)
6. Rosaline, S.I., Raghavan, S.:Compact dual band antenna for GSM/WiMAX applications. In: 3rd International Conference on Signal Processing, Communication and Networking, pp. 1–3 (2015)
7. Singh, B., Rana, H., Verma, A., Duhan, A., Zayed, M.: SRR loaded microstrip patch antenna for Bluetooth, HIPERLAN/WLAN and WIMAX. In: 3rd International Conference on Signal Processing and Integrated Networks, pp. 34–37 (2016)
8. Sharma, S., Sombanshi, D.: Annular-Ring Slotted Microstrip Patch Antenna for ISM Band Applications. International conference on Computer, Communication and Control, pp. 1–4 (2015)
9. Guo, X., Liao, W., Zhang, Q., Chen, Y.:A dual-band embedded inverted T-slot circular microstrip Patch Antenna. In: IEEE 5th Asia-Pacific Conference on Antennas and Propagation, pp. 151–152 (2016)
10. Rama, R.S., Vakula, D.: Triangular patch antenna with asymmetric V-slots for Tri-band wireless applications. In: IEEE International Microwave and RF Conference, pp. 293–296 (2014)
11. Mondal, K., Sarkar, P., Samadder, P., De, S., Sarkar, P.P.: Broadband microstrip patch antenna of reduced sized for multiband application. Indian J. Pure Appl. Phys. **53**, 555–556 (2015)
12. Mondal, K., Sarkar, P.P.: A compact broadband microstrip patch antenna for WiMAX/LAN/Wi-Fi/WLAN application. Indian J. Pure Appl. Phys. **54**, 727–732 (2016)
13. Samal, P., Soh, P., Zakaria, Z.: Compact microstrip-based textile antenna for 802.15.6 WBAN-UWB with full ground plane. Int. J. Antennas Propag. (2019)
14. Balanis, A.: Antenna theory, analysis and design. Wiley

A Highly Sensitive and Ultra-Low Loss Photonic Crystal Fiber-Based Gas and Chemical Sensor

M. Hussayeen Khan Anik, Sakib Mahmud, Pratyayee Chakma, Hriteshwar Talukder, Kisalaya Chakrabarti, and Shovasis Kumar Biswas

Abstract A Hexagonal-shaped photonic crystal fiber (PCF) with a circular analyte core bordered by six elliptical-shaped analyte channels is exemplified in this paper for gas and chemical sensing purposes. Fused silica is used as the pedestal fiber background of the sensor. The finite element method (FEM) is applied for numerical inspections. The sensor reveals maximum relative sensitivity of 85.55% for Benzene at 1.3 μm wavelength. The sensor displays ultra-low confinement loss of 1.309×10^{-11} dB/m for Benzene at 1.3 μm with a sensing range of 0.8–1.5 μm. The maximum V parameter value is of 2.235 for this sensor which secures single-mode propagation of light. This work also focuses on other vital properties just as, nonlinearity, effective area, mode field radius, and beam divergence for the usefulness of the sensor. Considering this sensor's relative sensitivity, confinement loss, and other properties, this PCF can be a very favorable candidate in the field of gas and chemical sensing.

Keywords Photonics · Relative sensitivity · Confinement loss · V parameter · Mode field radius · Nonlinearity · Beam divergence · Fiber optic transmission

M. Hussayeen Khan Anik · S. Mahmud · P. Chakma · H. Talukder
Department of Electrical and Electronic Engineering, Shahjalal University of Science & Technology, Sylhet, Bangladesh
e-mail: sakib40@student.sust.edu

P. Chakma
e-mail: pratyayee52@student.sust.edu

H. Talukder
e-mail: hriteshwar-eee@sust.edu

K. Chakrabarti
Department of Electronics and Communication Engineering, Haldia Institute of Technology, Haldia, West Bengal 721657, India

S. K. Biswas (✉)
Department of Electrical and Electronic Engineering, Independent University Bangladesh, Dhaka 1229, Bangladesh
e-mail: biswassk@iub.edu.bd

B. Sikdar et al. (eds.), *Proceedings of the 3rd International Conference on Communication, Devices and Computing*, Lecture Notes in Electrical Engineering 851,
https://doi.org/10.1007/978-981-16-9154-6_4

1 Introduction

Photonic crystal fiber (PCF) is comprised of a repeated pattern of the dielectric material that creates an alternation to the propagation property of the optical modes. It is the latest type of optical fiber which procures its waveguide properties from an arrangement variation of the tiny spaced small air holes. In the 1990s, a group of researchers first introduced and fabricated a silica-based hexagonal-shaped photonic crystal fiber [1]. After that, PCF attracts many researchers to explore and develop this field as this fiber offers more facilities than conventional fiber. PCF has the ability to confine an electric field in a small area which is impractical in a normal optical fiber. It gives us the liberty of designing and adjusting the fiber. Moreover, PCF responds faster and has very lightweight. Variously shaped and numerous structures of fibers are developed over the past few years just as hexagonal [2], elliptical [3], rectangular-hollow core [4]. Advanced fabrication technologies have given us more freedom in designing the PCF. Nowadays, PCF has many important and noteworthy applications in optical communication [5], temperature sensing [6], pressure sensing [7], chemical sensing [8].

PCF has tremendous facilities for various chemical and gas sensing purposes as it directly helps the propagated light to interact with the chemical by confining the light in the analyte core. This reciprocity between light and the targeted chemical is known as relative sensitivity (RS). A higher value of RS is desirable as it confirms elevated reciprocity between light and the chemical. When the light confines in a small core in a PCF, there occurs an exposure loss due to the outflowing nature of the fiber which is noted as loss of confinement. This loss should be minimized as much as possible for securing sensing accuracy, over the past few years, researchers worked hard to develop and contribute in the field of chemical and gas sensing using PCF. Kawsar et al. suggested a hexagonal PCF for environmental pollutants for detecting purposes. Maximum RS of 62.24% with a maximum nonlinearity of 18.4 W^{-1} $km^{-1}$was reported in the paper [9]. Maximum papers that have been previously reported do not focus on gases and chemicals that have low RIs. On the contrary, these works did not discuss about beam divergence, splice loss, and mode filed radius (MFR).

Our proposed PCF comes forward with a modified hexagonal-shaped air cladding with newly approached circular and elliptical-shaped analyte core in the center region of the fiber for gas and chemical sensing purposes. This sensor delivers high relative sensitivity of 85.55% and an ultra-low confinement loss of 1.309×10^{-11} dB/m for benzene in 1.30 μm wavelength which is better than all the previously mentioned PCF sensors. We have selected five different chemicals including methane gas. This work tries to discuss about splice loss by delivering information about the MFR of the sensor for different chemicals and gases. We have also concentrated on other optical properties such as V parameter, nonlinearity, effective area, and beam divergence which ensures greater serviceability of the sensor. Thus, this sensor holds a promising position in developing the sensing performance of different liquids, chemicals, and gases using a PCF.

2 Modelling and Design

Here in Fig. 1, the 2D cross-sectional perspective of our suggested PCF-based sensor is shown through a colored illustration to vividly portray its geometrical structure. The core region of the sensor consists of multiple analyte channels congested together which will carry the sensing chemical. There is a circular channel in the center which has the largest radius marked as d_c. Six elliptical channels surround the center channel maintaining a circular pattern and 60° spacing between each pair. In the region between the center channel and the elliptical channels, six small circular channels (d_2) and six slightly larger circular channels (d_1) coincide in a circular and periodic pattern. In the cladding region, uniform circular airhole rings form a hexagonal pattern surrounding the core. We took fused silica as the foundation material for its superior optical properties. There is a Perfectly matched layer (PML) surrounding the cladding region to absorb radiations and eliminate environmental effects. Ideal design parameters found after watchful observation are $d_1 = 0.55$ μm, $d_2 = 0.30$ μm, and $d_c = 1.22$ μm. The diameter of cladding airholes is kept at 0.90 μm. The total radius of the sensor is maintained at 6.2 μm with a computational PML layer having a thickness of 0.7 μm. Distance between two cladding airholes is set at 1 μm.

In the experimental arrangement, we see an optical tunable source (OTS) is present that generates the light required to pass through the waveguide. For linear polarization, we have a polarizer in the arrangement as well as a setup to control the polarization. The linearly polarized light is guided into the PCF waveguide via an SMF. The analyte chemicals are passed through a mass flow controller (MFC) which secures the proper flow of these analytes into the inlet. An outlet draws out the analytes from the PCF. The light that traveled through the PCF waveguide is further guided by another SMF into an optical spectrum analyzer (OSA) which is maneuvered to sense the waveforms via a computer. The stack-and-draw method's primary principle is

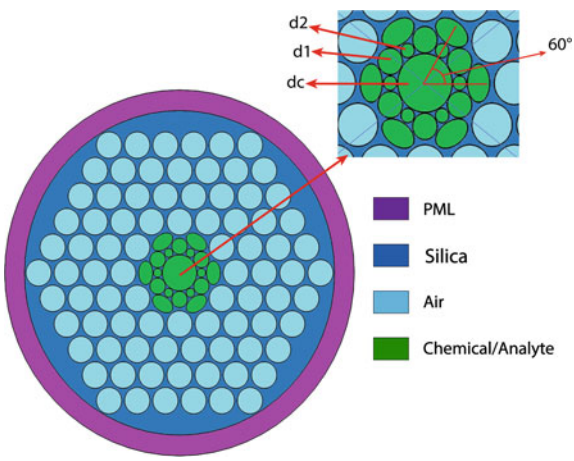

Fig. 1 2D representation of the suggested sensor

to stack glass rods (of various forms like square, rectangular, circular, etc.), tubes, capillaries.

As we have mentioned earlier that we have used fused silica as our background material for its superior optical properties, popularity, and availability. Its refractive index is not steady and depends on operating wavelength λ. This shift in refractive index follows Sellmeier equation and can be derived directly from it. The equation is as follows [10]:

$$n^2(\lambda) = 1 + \sum_{i=1}^{3} \frac{B_i \times \lambda^2}{\lambda^2 - C_i} \tag{1}$$

Here B_i and C_i, where $i = 1, 2, 3$, are fused silica's Sellmeier coefficients and λ is the operating wavelength in μm.

Loss for confinement is one of the vital limiting parameters of a PCF sensor regarding sensing efficiency. No matter how well confining a design is, it is not possible to completely confine light in the core. Owing to the outflowing nature of the mode and finite amount of possible airholes in the cladding region, some leakage is bound to happen to clad region from the core area. Taking the unreal part of the effective mode index, loss of con is measured via the following equation [11]:

$$L_c = 8.686 \times \frac{2\pi}{\lambda} \mathrm{Im}[n_{\mathrm{eff}}] \left(\frac{\mathrm{dB}}{\mathrm{m}} \right) \tag{2}$$

In this equation, $\mathrm{Im}[n_{\mathrm{eff}}]$ denotes the imaginary part of the effective mode index and λ is the operating wavelength. The term $\frac{2\pi}{\lambda}$ is also called the propagation constant and is often denoted by k_0.

Relative sensitivity is one of the most important of all properties because it generates a relative and vivid perspective of the reciprocity between propagated light and the sensing chemical. Relative sensitivity is generally denoted by r and can be measured by the following equation [8]:

$$r = \frac{n_s}{R_e(n_{\mathrm{eff}})} f \tag{3}$$

Here, n_s is the refractive index of the analyte chemical and $R_e(n_{\mathrm{eff}})$ is the real part of the effective mode index. f denotes power fraction which is calculated as follows [8]:

$$f = \frac{\int_{\mathrm{analyte}} R_e(E_x H_y - E_y H_x)\, \mathrm{d}x\mathrm{d}y}{\int_{\mathrm{total}} R_e(E_x H_y - E_y H_x)\, \mathrm{d}x\mathrm{d}y} \times 100 \tag{4}$$

Here E_x, E_y and H_y, H_x are respectively the transverse electric and magnetic field of the guided mode.

Another essential parameter that needs to be discussed for any photonic crystal fiber-based sensor is the numerical aperture (NA) as it calculates the acceptance angle

of incoming light into the fiber. Numerical aperture is measured using the following equation [12]:

$$\mathrm{NA} = \frac{1}{\sqrt{1 + \frac{\pi A_{\mathrm{eff}}}{\lambda^2}}} \tag{5}$$

Here A_{eff} denotes an effective area, which is another very essential sensing parameter. Effective area is a quantification of the area covered in the fiber for sensing purpose by the propagated light in the crosswise plane. It is measured by the following equation [8]:

$$A_{\mathrm{eff}} = \frac{(\iint |\mathrm{E(x, y)}|^2 \, \mathrm{dxdy})^2}{\iint |\mathrm{E(x, y)}|^4 \, \mathrm{dxdy}} \tag{6}$$

E denotes the electric field distribution.

It is important to confirm if a fiber is working in single-mode or multi-mode and both can be desirable in different situations. V parameter, denoted by V, is a dimensionless frequency parameter that distinguishes between single-mode and multi-mode PCF by providing an idea on the number of operating modes. It is calculated by the following equation [12]:

$$V = \frac{2\pi a}{\lambda} \times \mathrm{NA} \tag{7}$$

λ here denotes the operating wavelength. We can see that numerical aperture (NA) is necessary to calculate V parameter and the relation is directly proportional. a here denotes the radius of the core region of the fiber. It is to be noted that if V parameter value is less than 2.405, it indicates the fiber is single-mode and multi-mode when the value is higher than 2.405.

For observing the sensing operation, it is necessary to attach the sensor with a single-mode fiber (SMF) with a splicer. At this joint between PCF and SMF, which is specifically called splicing point, optical power loss occurs. This loss hinders sensing performance and needs to be reduced to achieve better sensing. The mode field radius (MFR) difference of the PCF and the SMF vivifies the amount of splice loss, the higher the difference greater the loss and vice versa. MFR can be defined by the transverse leakage of the mode's electric field distribution. So, to reduce splice loss we need to reduce the MFR difference of PCF and SPR. MFR, denoted by W_{eff} can be measured via the following equation [12]:

$$W_{\mathrm{eff}} = a\left(0.65 + \frac{1.619}{V^{3/2}} + \frac{2.879}{V^6}\right) \tag{8}$$

Here, a is the radius of the core. This equation is appropriate for values of V greater than 1.

Beam divergence is an important optical parameter that is computed using mode field radius (MFR). Beam divergence is mainly defined by the measurement of the beam expansion speed from its beam waist. A high beam divergence value indicates that the beam's ability to focus on a small point is low. Beam divergence is calculated by the following equation [12]:

$$\text{Beam divergence}\left(\theta_{\text{degree}}\right) = \tan^{-1}\left(\frac{\lambda}{\pi W_{\text{eff}}}\right) \times \left(\frac{180^{\circ}}{\pi}\right) \tag{9}$$

Here W_{eff} denotes the mode field radius and λ denotes the operating wavelength.

To control how much light intensity will be confined in the fiber core, the PCF's nonlinear coefficient must be realized. The amount of intensity of light greatly relies on the coefficient. The coefficient is designated by γ and is deliberated by the following equation [12]:

$$\gamma = \frac{2\pi}{\lambda} \times \frac{n_2}{A_{\text{eff}}} \tag{10}$$

Here n_2 is silicon's nonlinear coefficient of the background material, which is fused silica in our case.

3 Simulation Outcomes and Discussion

Figure 2a, b portrays the electric field allocation of our proposed sensor respectively in x-polarization and y-polarization for ethanol analyte. It is evident that light is

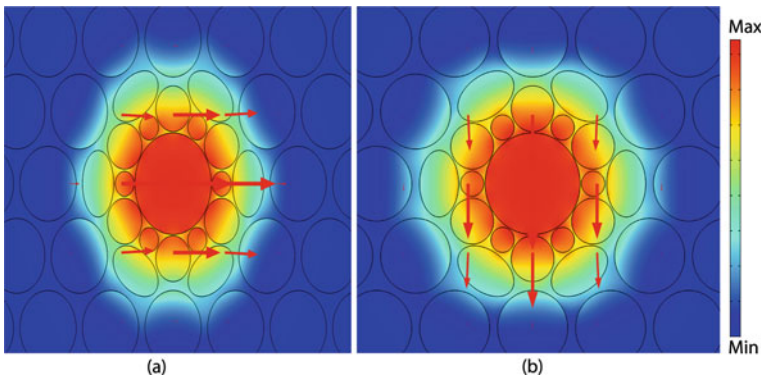

Fig. 2 Electric field profiles in x (**a**) and y (**b**) polarizations for ethanol at 1.30 μm

effectively constructed in the core region which means propagating light and the analyte liquid carried by the channels in the core are interacting very strongly.

3.1 Discussion of Sensing Properties

We have performed simulations and analyses via COMSOL Multiphysics to verify the sensing capabilities of our proposed sensor. In Fig. 3 we can see the relative sensitivity plots against operating wavelength ranging in between 0.8 and 1.5 μm for multiple analytes. We have used 5 different kinds of chemicals including a gas for all analyses. They are methane gas (na = 1.244), liquid freon-12 (na = 1.285), water (na = 1.33), ethanol (na = 1.354) and benzene (na = 1.366). Benzene among all the analytes has the highest refractive index of 1.366 and its relative sensitivity is the highest of 85.55% at 1.30 μm. We have found RS of 79.63% for methane gas, 82.20% for liquid freon-12, 84.26% for water, and 85.15% for ethanol at 1.30 μm.

In Fig. 4, plots of confinement loss against operating wavelength are shown for five of our chosen analytes. It is desirable that the propagated light mode will be completely confined in the core region. It is desirable that the confinement loss will

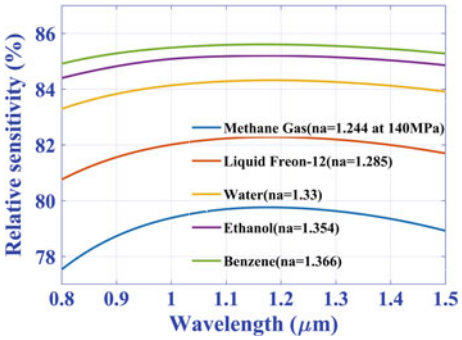

Fig. 3 Relative sensitivity versus wavelength for all the chemicals

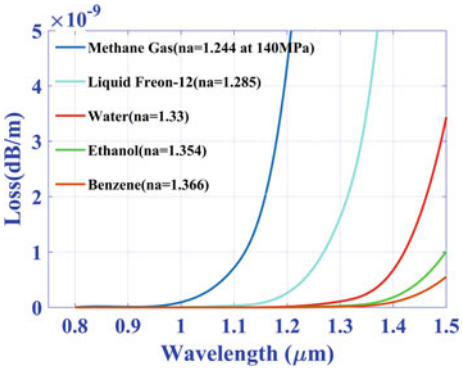

Fig. 4 Loss of confinement for all chemicals versus wavelength shifts

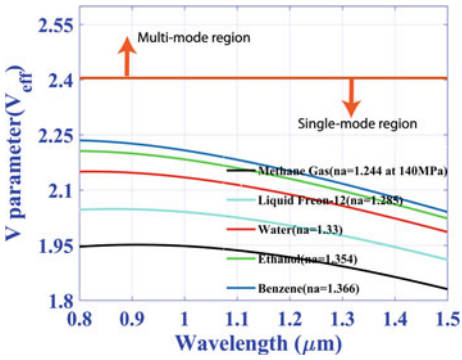

Fig. 5 V parameter curves for all chemicals versus wavelength shifts

be as low as possible. We see that the analyte having the highest refractive index which is benzene has the lowest loss. The analyte with the lowest refractive index which is methane gas has a negligible amount of loss from 0.8 to 1.1 μm.

Lower refractive indexed chemicals are usually less active in interacting with the propagated light. So, it becomes difficult to keep the light in the core region for lower refractive indexed chemicals. Confinement losses of 1.648×10^{-9} dB/m, 1.094×10^{-10} dB/m, 2.582×10^{-11} dB/m and 1.309×10^{-11} dB/m is found for freon-12, water, ethanol and benzene respectively.

Figure 5 portrays V parameter relation of our proposed sensor with respect to operating wavelength. The operating wavelength range is taken from 0.8 to 1.5 μm. V parameter ensures a clear idea about the mode number in a fiber. If the V parameter value is below 2.405, the fiber is operating in single-mode and if the value is more than 2.405 it is in multi-mode. From the graph, we can see that the lower the index of refraction of the analyte the lower its curve takes place. The highest point of benzene's curve is 2.235 at 0.8 μm, which is still less than 2.405. And benzene having the highest V parameter curve among all the analytes clearly indicates that for all our analytes, the fiber operates in a single-mode. It is convenient from the illustration that higher indexed chemicals have higher V parameter values.

In Fig. 6a, we have plotted mode field radius with respect to wavelength. MFR is an important optical property because the MFR difference of the PCF and the SMF provides the idea of splice loss. We have found the MFR value of 1.801 μm, 1.729 μm, 1.669 μm, 1.642 μm, and 1.631 μm respectively for methane, liquid freon, water, ethanol, and benzene at 1.30 μm wavelength. Figure 6b contains the plots of beam divergence against operating wavelength. Beam divergence has a proportional relation with the wavelength. This property is computed using mode field radius (MFR) value. The figure shows that benzene has the highest refractive index and the highest beam divergence curve, which is opposite of the MFR curve. We found beam divergence values of 14.25° and 12.94° for benzene and methane respectively at 1.30 μm.

Figure 7a shows the effective area of Methane has the highest effective area curve with the highest point of 6.115 μm^2 at 1.5 μm and benzene has the lowest effective area curve with the highest point of 4.782 μm^2 at 1.5 μm.

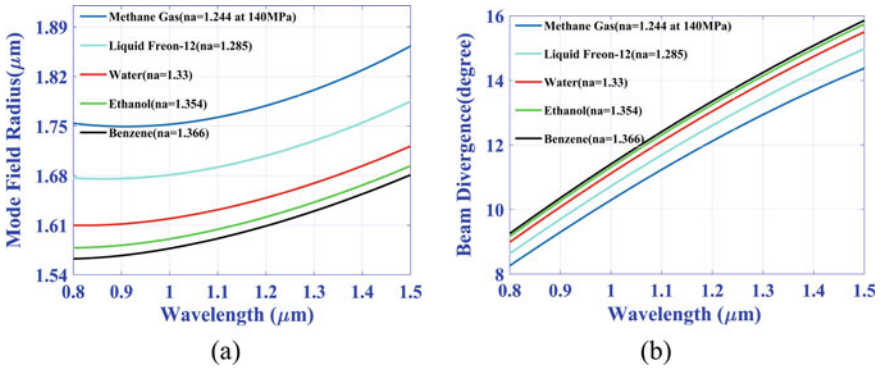

Fig. 6 Mode field radius (**a**) and beam divergence (**b**) versus wavelength for all chemicals

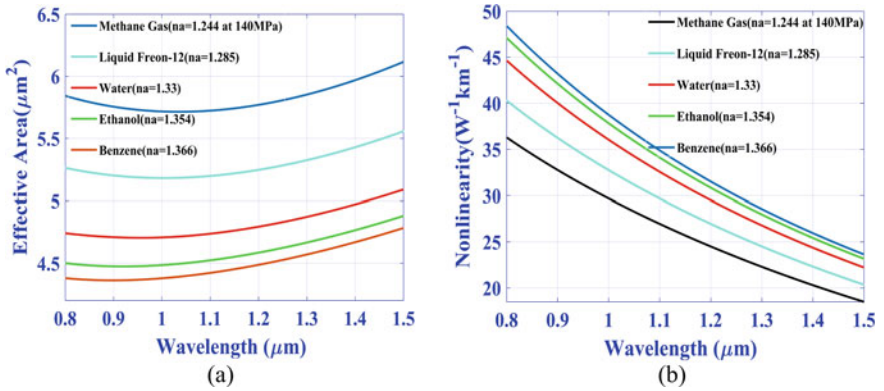

Fig. 7 Variations of effective area (**a**) and nonlinearity (**b**) for all chemicals

Figure 7b illustrates the relation between the nonlinearity coefficient and operating wavelength. Nonlinearity coefficients of 22.3 W^{-1} km^{-1} and 28.94 W^{-1} km^{-1} are found for methane gas and benzene respectively at 1.30 μm.

3.2 Design Parameter Variation

Figure 8a contains the relative sensitivity shift owing to variation of diameter of d_1 channels for freon-12. The optimum value of d_1 is 0.55 μm and from its relative sensitivity curve, we find that the highest value is 82.29%. Because of increasing the value of d_1 by 0.02 μm, we see that the relative sensitivity curve has shifted upwards. For 0.57 μm, the highest relative sensitivity value is 84.2%. Figure 8b, c respectively portray the shifts in relative sensitivity due to diameter variation by 0.02 μm for d_2 channels and dc channels. It is evident that when channel diameters are increased,

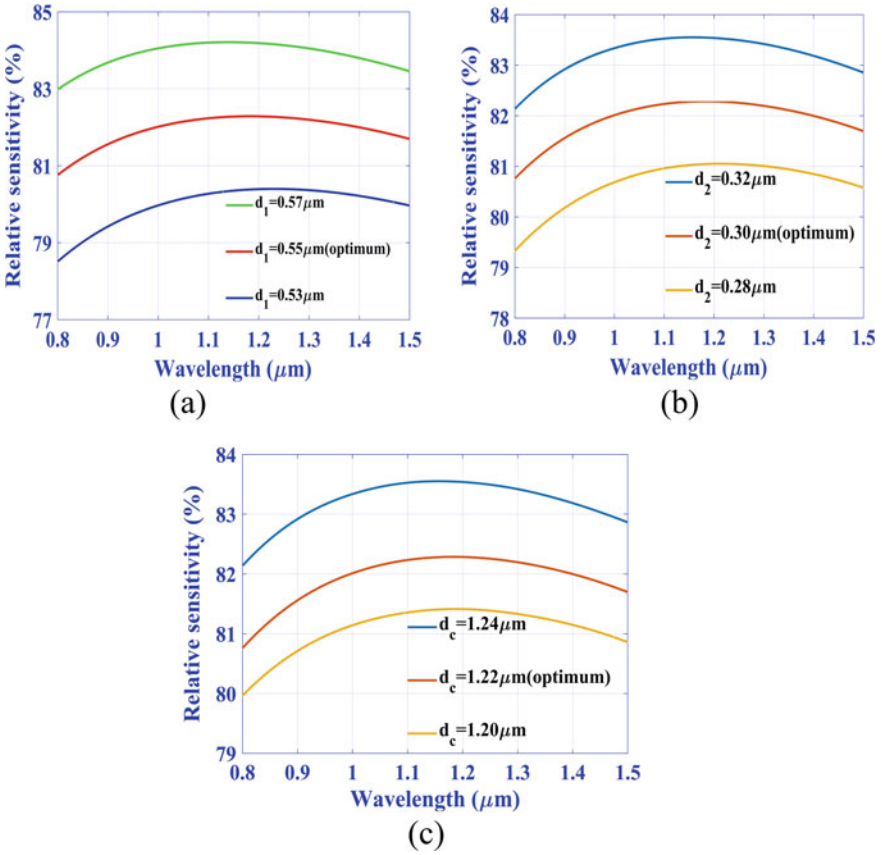

Fig. 8 Relative sensitivity curves with variation of airholes d_1 (**a**), d_2 (**b**), and d_c (**c**) for freon-12

light confinement improves resulting in higher relative sensitivity. Opposite case occurs when channel diameters are decreased.83.55% and 81.05% are respectively the highest relative sensitivity values for increasing and decreasing the value of d_2 by 0.02 μm. And 83.55% and 81.41% are respectively the highest relative sensitivity values for increasing and decreasing the value of dc by 0.02 μm.

3.3 Comparative Analysis

Table 1 comes forward to show a comparison among our proposed PCF-based sensor with newly printed PCF sensors. From the table, it is confirmed that our PCF sensor has the highest RS among all the mentioned references. Our paper has evinced a very high RS and very low confinement loss as well as provided valuable information about

Table 1 Comparison among our suggested sensors with newly published PCF sensors

References	Operating wavelength (μm)	Concerned chemical	Relative sensitivity (%)	Confinement loss (dB/cm)	Nonlinearity (W^{-1} km^{-1})
[9]	1.40	Ethanol	62.24	5.56×10^{-11}	18.40
[12]	1.33	Ethanol	53.22	–	41.46
[13]	1.33	Ethanol	74.55	4.63×10^{-11}	22.53
[14]	1.30	Water	49.13	5.583×10^{-5}	-
Proposed	1.30	Ethanol	85.15	2.635×10^{-11}	28.64

sensor's mode field radius, beam divergence and V parameter. This makes our work more unique than most of the previously reported PCF sensors.

4 Conclusion

We proposed a hexagonal-shaped air cladding with circular and elliptical-shaped analyte core photonic crystal fiber-based gas and chemical sensor in this paper. The sensor displayed the highest relative sensitivity of 85.55% and minimum loss of confinement of 1.309×10^{-11} dB/m for benzene in 1.30 μm. This sensor exhibited a relatively high sensitivity of 79.63% for methane gas which has a low RI. The paper also discussed about nonlinearity and effective area for the usefulness of the sensor as well as nonlinearity is an essential property for fiber optic transmission systems. This PCF-based sensor can be an excellent contender in the field of gas and chemical sensing.

References

1. Knight, J.C., Birks, T.A., Russell, P.S.J., Atkin, D.M.: All-silica single-mode optical fiber with photonic crystal cladding: errata. Opt. Lett. **22**(7), 484 (1997)
2. Wu, T., Shao, Y., Wang, Y., Cao, S., Cao, W., Zhang, F., Liao, C., He, J., Huang, Y., Hou, M.: Surface plasmon resonance biosensor based on gold-coated side-polished hexagonal structure photonic crystal fiber. Opt. Express **25**(17), 20313 (2017)
3. Kim, S.E., Kim, B.H., Lee, C.G., Lee, S., Oh, K., Kee, C.-S.: Elliptical defected core photonic crystal fiber with high birefringence and negative flattened dispersion. Opt. Express **20**(2), 1385 (2012)
4. Islam, M.S., Sultana, J., Rifat, A.A., Dinovitser, A., Wai-Him Ng, B., Abbott, D.: Terahertz sensing in a hollow core photonic crystal fiber. IEEE Sens. J. **18**(10), 4073–4080 (2018)
5. Kaijage, S.F., Namihira, Y., Hai, N.H., Begum, F., Razzak, S.A., Kinjo, T., Miyagi, K., Zou, N.: Broadband dispersion compensating octagonal photonic crystal fiber for optical communication applications. Jpn. J. Appl. Phys. **48**(5), 0524011–0524018 (2009)

6. Mollah, M.A., Islam, S.M.R., Yousufali, M., Abdulrazak, L.F., Hossain, M.B., Amiri, I.S.: Plasmonic temperature sensor using D-shaped photonic crystal fiber. Res. Phys. **16**, 102966 (2020)
7. Bock, W.J., Jiahua, C., Eftimov, T., Urbanczyk, W.: A photonic crystal fiber sensor for pressure measurements. Conf. Rec. IEEE Instrum Meas Technol Conf. **2**(4), 1177–1181 (2005)
8. Anik, M.H.K., Mahmud, S., Isti, M.I.A., Nuzhat, S., Biswas, S.K., Talukder, H.: A novel highly sensitive photonic crystal fiber sensor for detecting ph levels of acetic acid aqueous solution based on surface plasmon resonance. In: 2020 11th International Conference on Computing, Communication and Networking Technologies (ICCCNT) , pp.1–5. IEEE (2020)
9. Ahmed, K., Islam, S., Kumar, B.: ScienceDirect design and numerical analysis: effect of core and cladding area on hybrid hexagonal microstructure optical fiber in environment pollution sensing applications. Karbala Int. J. Mod. Sci. **3**(1), 29–38 (2017)
10. Anik, M.H.K., Islam, S.R., Talukder, H., Mahmud, S., Isti, M.I.A., Sadeghi-niaraki, A., Kwak, K.-S., Biswas, S.K.: A highly sensitive quadruple d shaped open channel photonic crystal fiber plasmonic sensor: a comparative study on materials effect. Res. Phys. 104050 (2021)
11. Anik, M.H.K., Isti, M.I.A., Islam, S.M.R., Mahmud, S., Talukder, H., Piran, M.J., Biswas, S.K., Kwak, K.S.: Milled microchannel-assisted open d-channel photonic crystal fiber plasmonic biosensor. IEEE Access **9**, 2924–2933 (2021)
12. Islam, S., Kumar, B., Ahmed, K.: Liquid-infiltrated photonic crystal fiber for sensing purpose: design and analysis. Alexandria Eng. J. **57**(3), 1459–1466 (2018)
13. Islam, I., Ahmed, K., Islam, S., Kumar, B.: ScienceDirect single-mode spiral shape fiber based liquid sensor with ultra-high sensitivity and ultra-low loss: design and analysis. Karbala Int. J. Mod. Sci. **3**(3), 131–142 (2017)
14. Leon, M.J.B.M., Kabir, M.A.: Design of a liquid sensing photonic crystal fiber with high sensitivity, bireferingence & low confinement loss. Sens. Bio-Sensing Res. **28**, 100335 (2020)

Raspberry Pi Controlled Home Security and Defense Robot with Visual and Audio Recognition with Android Application Control

Palak Tripathi, Aakansha Mishra, Aniket Agrawal, and Sumit Kumar Jindal

Abstract In this fast-pacing world, security threats are increasing with growing technologies. Science and innovation in this particular area has grown exponentially and is still on its way to discover more. In recent years, security solutions are getting merged with fields like Artificial Intelligence, network computing, and automation. This work is designed to develop an application-controlled robot for remote operation. It comes with a wireless camera and microphone for surveillance purposes. The application is developed to control the motion, to transmit real time video and audio input from the surroundings. The output can be managed by the users accordingly. A robot is a pre-programmed electronic tool capable of performing meaningful tasks without any external support. This work suggests applications based on remote operation due to which wireless communication, automation and the user interface becomes an integral part of disc.

Keywords Raspberry Pi · Pi camera · Android studio

1 Introduction

The advent of high-speed technologies and increased data storage has set forth realistic and logical robot control and its theory [1–3]. Periphery in this field shifts continuously as robots are evolving along with our ideas. This evolution together with the present demands for high technical performance has created more accurate, sensitive and intelligent robot control devices. Electro-mechanical tools like BOTs for industrial purposes and various other services are always required to cater the perpetual needs of managing various assets like power lines, communication lines, and water pipes. These assets require regular inspection and its quality maintenance task is labor intensive. This new technology serves as a replacement for humans, performs risky and repetitive tasks that eventually promote a safer work environment. This work mainly focuses on its application in extreme workplace conditions

P. Tripathi · A. Mishra · A. Agrawal · S. K. Jindal (✉)
School of Electronics Engineering, Vellore Institute of Technology, Vellore, Tamil Nadu, India

B. Sikdar et al. (eds.), *Proceedings of the 3rd International Conference on Communication, Devices and Computing*, Lecture Notes in Electrical Engineering 851,
https://doi.org/10.1007/978-981-16-9154-6_5

like war fields and nuclear power plants [4]. There are life threatening risks while spying or in nuclear plants. The proposed robot examines its environment using a wireless camera and microphone attached to it. Discussed work is an economical alternative of heavy robots and machinery used. Generally, the circuitry used is wired Reprogramming if any change occurs takes time. In order to make it user-friendly, steps are made to have user commanded work. To fulfill the needs an android application is being developed. This application uses Wi-Fi to interface with the bot. In these modern times, android Smartphones have become an integral part of our day-to-day lifestyle. Hence, an application is designed to control embedded hardware. The hardware is developed using raspberry pi and controlled by the android smartphone using an application as a medium. Raspberry pi receives command from the app and sends it to the motor driver in order to control the wheels, Camera, and microphone. An in-built WI-FI module [5] in r-pi provides necessary support in interfacing the device with the smartphone. The main motivation behind the work is to provide a great user-friendly experience. Major purpose is easy-to-use and pocket friendly robots by making it easy circuitry and simplified architecture design.

2 Proposed System

A 5 V 2A power is supplied to the raspberry pi through a power bank. The Raspberry pi is connected to the android application for taking the user input as shown in Fig. 1.

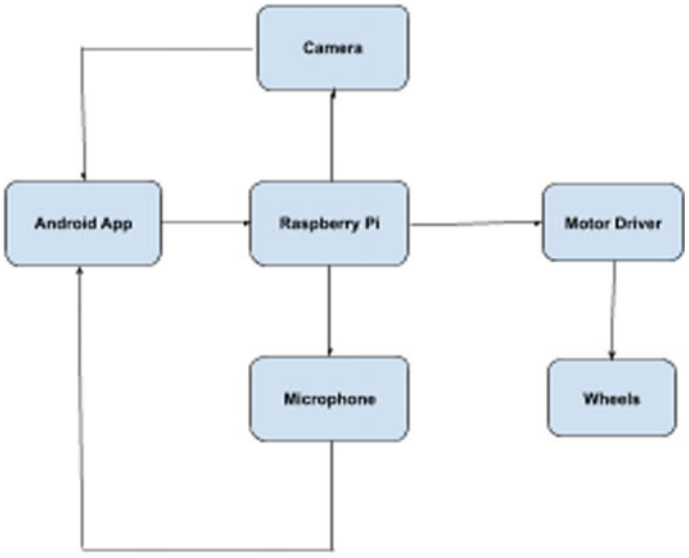

Fig. 1 Block diagram of proposed system

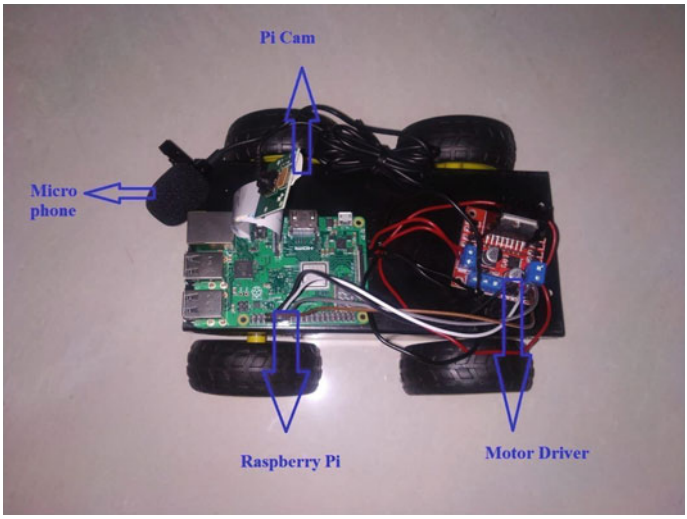

Fig. 2 Experimental setup of proposed model

The Pi cam and microphone are connected to Raspberry Pi for surveillance of the environment.

3 Experimental Setup

A Raspberry Pi is used to control the motor driver as well as Pi cam and Microphone as shown in Fig. 2. Raspberry Pi receives commands from the user through an Android-based app as shown in Fig. 3. Microphone and Pi Cam take care of the surveillance of the system. While developing the application, the features of UI design were incorporated.

4 Hardware Used

An Android App [6] is used for communication between the user and the robot. A Raspberry pi is used to control the robot according to the commands given by the user. The reason behind choosing a Raspberry Pi [7] is due to its huge processing power in a small board also it has many interfaces (HDMI [8], multiple USB etc.) with many GPIo's. A pi cam is used for surveillance and used to capture the pic. A dedicated mic is used to record the audio when commanded to do so.

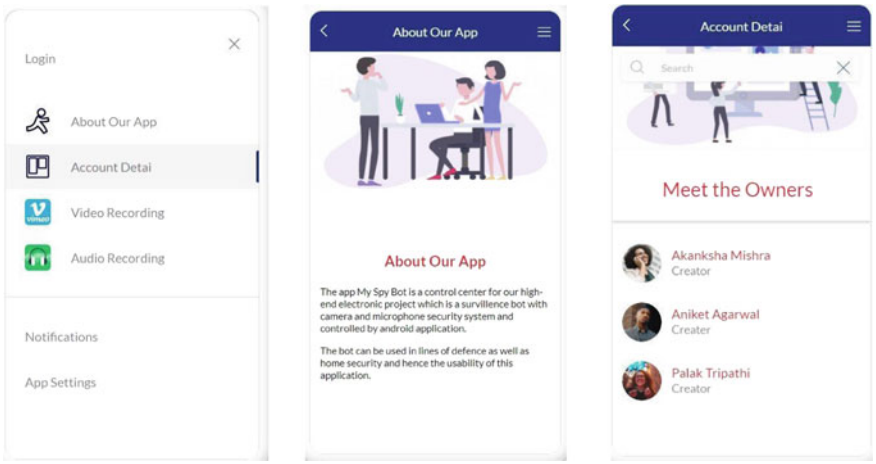

Fig. 3 App UI which will be used to control the proposed model

5 Result and Discussion

To implement this, software and a hardware tool (Robot) is used. An android application is used to control the robot. The whole system will be powered by a portable power bank which makes the entire robot self-sufficient, which can work in hostile environments without the need of an external power source. This makes it a robust and reliable product to be used in the environment. The mobile application developed is for the ease of the user to control the bot from anywhere and anytime. For its development fully-customizable widgets are used to build native interfaces. Easy to use UI interface makes the user experience great. The user gives command to the Raspberry pi through the application which in turn, commands the motor driver to move in the specified direction. Using the app, the robot can capture the picture or can live stream the conditions of the hostile environment if needed, through the pi camera installed in the robot. Also, audio can be recorded through a dedicated microphone mounted on the robot which will furthermore help for the better understanding of the environment. It will provide much more comprehensive data to act on. The command control facility provided by the application will enable it to move from one location to another.

The image is sent from the site to the developed application. This could be life-saving intelligence in the field of war. We record the video with the help of a camera mounted on the robot and hence the site's activities get recorded as shown in Figs. 4 and 5.

The audio signals from the site are recorded by the robot as shown in Fig. 6. This could be used for spying and getting a better idea of the area. The audio recorded is felicitated by the microphone mounted on the robot. The robot is minimally equipped for its mobility and is mobile.

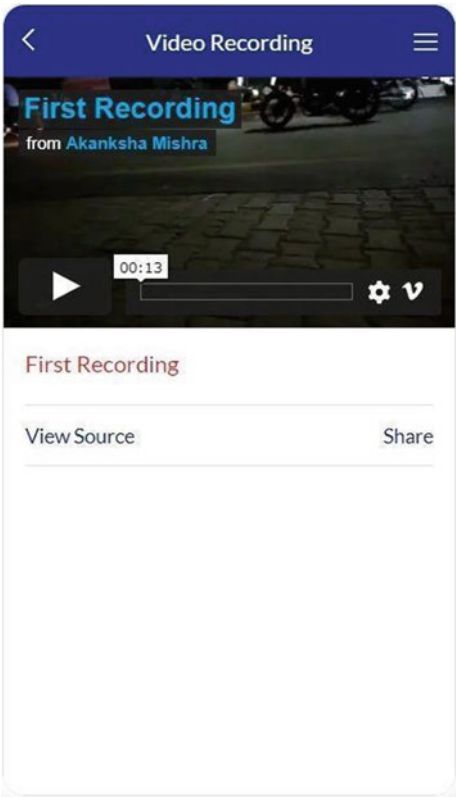

Fig. 4 Shows the proposed prototype of a complete robot which will be used for surveillance

Fig. 5 Video sent by the robot

6 Comparative Study with Existing Literature

See Table 1.

Fig. 6 Audio recorded by the robot

Table 1 Comparative study

S. No.	Title	Result	Comparison
1	Surveillance robot for military application [9]	Implementation of surveillance using video streaming	Security provided using video as well as audio surveillance
2	Arduino controlled war field spy robot using night vision wireless camera and Android [10]	Arduino controlled implementation with video surveillance	Proposed work utilizes latest technology by using R Pi along with two factor security coverage
3	Spy robot with wireless camera using GSM [11]	Key feature is usage of GSM sensor for the wireless camera operation	Proposed work does not include GSM instead an android app approach has been made

7 Extension and Future Scope

The extension to this work could be making the robot an obstacle avoiding autonomous vehicles using Model Predictive Control (MPC) [12] which can be used to move the robot in a specified path. Using this, the robot can move on its own avoiding the obstacles in the path and acquiring the data of the hostile environment. Also, a battery pack could be used with a buck converter to power the Raspberry pi which could be recharged with a solar panel. That would make the robot more self-sufficient in terms of power management.

8 Conclusion

The audio-visual security Bot is an excellent way to have a secure line of defense at places where humans should not be present or a remote surveillance is required. This ensures minimum human life involvement and endangerment with 360° surveillance. The camera becomes the human eye in the security set-up with a maximum of 5 MP visibility capacity. The Microphone attached is the human ear in the whole security set-up. The system acts as eyes and ears in any and all situations. The proposed model can be enhanced with cameras with more megapixels' capacity and using a microphone with the feature to adjust the coverage distance. It can be more enhanced if the data collected by the equipment is stored on an occasional basis so as to provide ideas to the security authorities of any red flags in the future. Application of Machine learning can be more viable in this situation. The application of proposed work has several extensions. It can be upgraded by extending the coverage area and with the use of night vision cameras. With the growing technology, new upgraded sensors and modules can significantly improve the performance of the BOT. The usage of mobile applications brings out the uniqueness of the work as it has made the BOT, easy to use and easy to control. The low-cost, reliable, and efficient designing and working of the BOT has been tested in different conditions. This work puts forward multifunctional, multi-purpose opportunities and usage in the field of engineering. In the field of electronics, device set-up used by demonstrated work is much needed in real life scenarios as compactness, efficiency, and utility as worldwide demand.

References

1. Colby, C.L., Mithas, S., Parasuraman, A.: Service robots: how ready are consumers to adopt and what drives acceptance? In: Frontiers in Service Conference, pp. 4–16. Bergen, Norway (2016)
2. Huang, M.H., Rust, R.T.: Artificial intelligence in service. J. Service Res. 21(2), 155–172 (2018)
3. Jörling, M., Böhm, R., Paluch, S.: Service robots: drivers of perceived responsibility for service outcomes. J. Serv. Res. **22**(4), 404–420 (2019)

4. Priyanka, K., Barani Krishnan, G.V.: Robotics for nuclear power plant. Int. J. Eng. Res. Technol. (2018)
5. Harshitha, H.S., Kruthika, M., Mithun, P., Khanm, S., Geetha, M.N., Zaidi, S.: Patient monitoring system using Wi-Fi technology. Int. J. Recent Trends Eng. Res. 23–30 (2018)
6. Pahuja, R., Kumar, N.: Android mobile phone controlled Bluetooth robot using 8051 microcontroller. Int. J. Sci. Eng. Res. 2347–3878 (2014)
7. Ehsan Irshad, M., Feroz, M.: Scope of IoT: performance and hardware analysis between raspberry pi-3 and arduino uno. Int. J. Comput. Sci. Mobile Comput. (IJCSMC) **5**(6), 580–588 (2016)
8. Xiong, J., Yi, Q., Shi, M., Li, T.: Research and design of data transmission system based on HDMI actions. In: International Conference on Computer Science and Electronics Engineering (ICCSEE) (2013)
9. Joshi, S.A., Tondarkar, A., Solanke, K., Jagtap, R.: Surveillance robot for military application. Int. J. Eng. Comput. Sci. **7**(5), 23939–23944 (2018). ISSN: 2319-7242
10. Patoliya, J., Mehta, H., Patel, H.: Arduino controlled war field spy robot using night vision wireless camera and Android application. In: 5th Nirma University International Conference on Engineering (NUiCONE) (2015)
11. Shakya, D., Jyoti, S.G., Rajput, S.: Spy robot with wireless camera using GSM. Int. Res. J. Eng. Technol. **04**(**03**) (2017)
12. Park, J.M., Kim, D.W., Yoon, Y.S., Kim, H.J., Yo, K.-S.: Obstacle avoidance of autonomous vehicles based on model predictive control. Proc. Inst. Mech. Eng. Part D J. Automob. Eng. **223**(12), 1499–1516 (2009)

A Simple but Accurate Method for Prediction of Reflected Intensity Noise for Single-Mode Circular Core Triangular Index Fiber Excitation via Upside Down Tapered Hemispherical Microlens on the Tip of Fiber

Shubhendu Maiti and Sankar Gangopadhyay

Abstract In optical communication system, the coupling efficiency relating to laser to fiber coupling emerges as an important topic. But it is found that misalignment in the context of fiber to lens coupling reduces the coupling efficiency. The lateral mismatch leads to generation of unwanted noise owing to back-reflection from fiber end to laser diode. Here, we report a simplified theoretical method for estimating the reflected intensity noise (RIN) in case of a laser diode to triangular type index fiber coupling via upside down tapered hemispherical microlens on the corresponding fiber tip. We present RIN values as a function of possible lateral misalignments. The concerned coupling efficiency under the presence of lateral mismatch case has been formulated by applying relevant ABCD matrix. The results found shall prove to be beneficial to the system designers and engineers in the context of minimizing such noise in this coupler.

Keywords Single-mode triangular index fiber · Upside down tapered hemispherical microlens · Misalignment · Reflected intensity noise

1 Introduction

Proper fabrication of a suitable microlens on the fiber tip has certainly emerged as an important practice for increasing the coupling efficiency in the context of laser diode to optical fiber coupling [1–3]. Different kinds of appropriate microlensing

S. Maiti
Department of Physics, Murshidabad College of Engineering & Technology, Berhampore, Murshidabad, West Bengal 742102, India

Department of Physics, University College of Science and Technology, University of Calcutta, Rajabazar, Kolkata, West Bengal 700009, India

S. Gangopadhyay (✉)
Department of Electronics and Communication Engineering, Brainware University, Barasat, Kolkata, West Bengal 700125, India

B. Sikdar et al. (eds.), *Proceedings of the 3rd International Conference on Communication, Devices and Computing*, Lecture Notes in Electrical Engineering 851,
https://doi.org/10.1007/978-981-16-9154-6_6

techniques are being used on the fiber tip in order to maximize the coupling efficiency of the said fiber [4–12]. Fabrication of various kinds of "upside-down-taper lens (UDTL)" on the tips of different kinds of fiber tip has been also shown to be a very efficient coupling technique [13–18]. Comprehensive theoretical analysis of "upside-down-taper hemispherical microlens (UDTHML)" at the end of mono-mode circular shaped core triangular type index fiber using the ABCD matrix formalism, has already been reported and it has been shown that execution of the mentioned theoretical formalism is quite convenient in its approach yet it provides accurate outcomes in the form of results [17]. Further, accurate estimation of coupling losses in the presence of possible mismatches for the case of laser diode to mono-mode circular core triangular index fiber excitation via UDTHML by ABCD matrix method has also contributed to the enrichment of literature [18]. But, the said kinds of couplers involve optical back-reflection from the fiber to the laser. This results in increase of optical noise on the signal in the case of concerned laser diode to single-mode circular core triangular index kind of fiber excitation via UDTHML and degradation of the performance and lifetime of the semiconductor laser diode [19–32]. This necessitates the use of optical isolators for preventing reflection from fiber to laser diode. But, use of such isolator is not cost effective and it makes the alignment procedure quite complicated. Accordingly, the design of the coupling scheme demands that it should not only be optimized with respect to the coupling efficiency as well as alignment tolerance but at the same time it should minimize RIN.

This present paper reports study of RIN in terms of lateral mismatch between microlens and the fiber for the case of laser diode to single-mode circular shaped core triangular index fiber excitation via UDTHML. The results obtained are extremely important from the standpoint of design of this coupling device so that maximum coupling efficiency with minimum RIN is achieved in this respect.

As far our knowledge is concerned in the contemporary field of fiber optics, no such estimation of RIN for this particular coupling device on the basis of evaluation of coupling losses owing to lateral mismatches by the implementation of ABCD matrix formalism has been added to the literature of fiber optics till date. Thus, our study can be regarded as a novel one.

2 Theory

The appropriate schematic representation of the "single-mode circular core triangular index fiber" coupled by an "upside down tapered hemispherical microlens (UDTHML)" on the fiber tip is presented below in Fig. 1. The ray direction of reverse-reflection is also shown in figure. This back-reflection generates three kinds of reflected intensity noise (RIN) in fiber-laser coupling system. These are intrinsic noise (RIN_{int}), noise because of re-coupling effect of input light coming from fiber input end (RIN_{input}) and noise owing to reflection of light at junction point between two fibers (RIN_{fib}). Thus, effective RIN in the system can be simply written as [30–32],

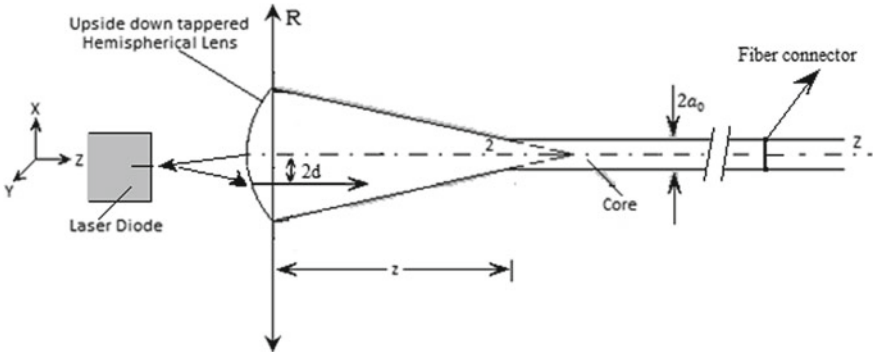

Fig. 1 Schematic representation of coupling of "upside down tapered hemispherical microlens" on a "triangular index fiber" tip with back-reflections

$$\mathrm{RIN} = \mathrm{RIN}_{\mathrm{int}} + \mathrm{RIN}_{\mathrm{input}} + \mathrm{RIN}_{\mathrm{fib}} \tag{1}$$

The noise due to fiber dispersion is not considered here, since the operation can be implemented in the dispersion less window. The expression of $\mathrm{RIN}_{\mathrm{input}}$ and $\mathrm{RIN}_{\mathrm{fib}}$ can be written using the limiting condition $2\pi\tau\Delta\nu \gg 1$ [30, 31] as,

$$\mathrm{RIN}_{\mathrm{input}} = \frac{4RR_{LD}}{\pi}\frac{\Delta\nu}{\Delta\nu^2 + f^2} \tag{2}$$

$$\mathrm{RIN}_{\mathrm{fib}} = \frac{4R^2}{\pi}\frac{\Delta\nu}{\Delta\nu^2 + f^2}\frac{N(1-\alpha) - 1 + \alpha^N}{(1-\alpha)^2} \tag{3}$$

here, R, α and N denote the reflection co-efficient, attenuation constant parameter of the fiber material and the total number of optical connectors respectively. In addition $\Delta\nu$ and f are spectral width and frequency considered in the radio-frequency region respectively. R_{LD} includes re-coupling efficiency of the unwanted light (η_r) and the reflection co-efficient of the output light of laser diode at output face (R_{sof}) and it can be expressed as follows [30],

$$R_{LD} = \eta_r R_{\mathrm{sof}} \tag{4}$$

Using Gaussian kind field approximation in case of laser as well as fiber field, we can estimate expression of coupling efficiency (η) of an UDTHML fitted on the triangular index profile fiber tip as written below [17, 18, 33],

$$\eta = \frac{4w_{2x}w_{2y}w_f^2}{\left[\left(w_f^2 + w_{2x}^2\right)^2 + \frac{k_2^2 w_f^4 w_{2x}^4}{4R_{2x}^2}\right]^{1/2} \times \left[\left(w_f^2 + w_{2y}^2\right)^2 + \frac{k_2^2 w_f^4 w_{2y}^4}{4R_{2y}^2}\right]^{1/2}} \tag{5}$$

where, w_f and k_2 are defining fiber "spot-size" and "wave number" of laser light wave in lens medium respectively. The "spot sizes" of transformed light ($w_{2x,2y}$) and the "radii of curvature" of transformed light ($R_{2x,2y}$) are related with spot sizes of laser source along X and Y axes as [17, 18, 33],

$$w_{2x,2y}^2 = \frac{A_2^2 w_{1x,1y}^2 + \left(\lambda_1 B^2\right)/\left(\pi^2 w_{1x,1y}^2\right)}{n(A_2 D - BC_2)}$$

and

$$\frac{1}{R_{2x,2y}} = \frac{A_2 C_2 w_{1x,1y}^2 + \left(\lambda_1^2 BD\right)/\left(\pi^2 w_{1x,1y}^2\right)}{A_2^2 w_{1x,1y}^2 + \left(\lambda_1^2 B^2\right)/\left(\pi^2 w_{1x,1y}^2\right)} \tag{6}$$

where, "$\lambda_1 (= \lambda_0/n_1)$" is wavelength in the medium of incidence and the constants A_2, C_2 are particularly related with concerned transformation matrix elements (A, B, C, D) and radius of curvature (R_1) of incident wavefront as "$A_2 = (A + B/R_1)$; $C_2 = (C + D/R_1)$". Since the wavefront of incident light can be considered as a plane wavefront to get sufficiently accurate results, we use here $R_1 = \infty$ [1, 7–9, 11, 13, 15, 17, 18, 33]. In above expression, the refractive index is the ratio of the refractive-index of lens medium (n_2) and that of air medium (n_1). The output parameter "q_2" of laser beam can be expressed in terms of matrix elements (A, B, C, D) and input parameter "q_1" as [17, 18, 33],

$$q_2 = \frac{Aq_1 + B}{Cq_1 + D} \tag{7}$$

The "q_1" and "q_2" can also be written in terms of refractive index (n), wavelength of light in free space (λ_0), radius of curvature of wavefront (R) and its spot size (w) as below,

$$\frac{1}{q_{1,2}} = \frac{1}{R_{1,2}} - \frac{j\lambda_0}{\pi w_{1,2}^2 n_{1,2}^2} \tag{8}$$

Relevant transformation matrix for UDTHML on tip of triangular type index profile fiber can be explicitly expressed as follows [17, 18, 33],

$$\begin{pmatrix} A & B \\ C & D \end{pmatrix} = \begin{pmatrix} A_1 & B_1 \\ C_1 & D_1 \end{pmatrix} \begin{pmatrix} 1 & u \\ 0 & 1 \end{pmatrix} \tag{9}$$

where, A_1, B_1, C_1 and D_1 are individual matrix elements [17, 18]. For UDTHML on triangular profile fiber tip the matrix elements have values as mentioned below,

$$A_1 = r_2(z) + \frac{n_{co} - 1}{n_{co} R_0} r_1(z)$$
$$B_1 = \frac{r_1(z)}{n_1}$$
$$C_1 = \frac{dr_2(z)}{dz} + \frac{n_{co} - 1}{n_{co} R_0} \frac{dr_1(z)}{dz}$$
$$D_1 = \frac{1}{n_{co}} \frac{dr_1(z)}{dz} \tag{10}$$

The variables "$r_1(z)$, $\frac{dr_1(z)}{dz}$, $r_2(z)$ and $\frac{dr_2(z)}{dz}$" are given by [18],

$$r_1(z) = -\frac{L}{\alpha}\left(1 - \frac{z}{L}\right)^{1/2} \sin\delta(z),$$
$$\frac{dr_1(z)}{dz} = \frac{1}{\left(1 - \frac{z}{L}\right)^{1/2}}\left[\cos\delta(z) + \frac{1}{2\alpha}\sin\delta(z)\right]$$
$$r_2(z) = \left(1 - \frac{z}{L}\right)^{1/2}\left[\cos\delta(z) - \frac{1}{2\alpha}\sin\delta(z)\right]$$
$$\frac{dr_2(z)}{dz} = \frac{C'^2 L}{\alpha\left(1 - \frac{z}{L}\right)^{1/2}} \sin\delta(z) \tag{11.1}$$

Moreover, parameters $\delta(z)$, α, C' and z are given by [17, 18],

$$\delta(z) = \alpha \ln\left(1 - \frac{z}{L}\right)$$
$$\alpha = \left(C'^2 L^2 - \frac{1}{4}\right)^{1/2}$$
$$C' = \frac{1}{D}\left[\ln\left(\frac{1}{1 - C_0^2 a_0}\right)\right]^{1/2}$$

where [18],

$$C_0^2 = \frac{1}{a_0}\left[1 - \exp\left\{-\frac{2D^2\left(1 - \frac{z}{L}\right)^2 \ln\left(\frac{n_{co}}{n_{cl}}\right)}{a_0^2}\right\}\right] \tag{11.2}$$

In the coupling system the axis fiber can shift from its actual coordinate position (0, 0) in "X–Y plane" to a new coordinate position (d, d) which causes the lateral offset in coupling system. Now the position of the axis can be expressed by the relations [18, 33]

$$x = x' + d \quad \text{and} \quad y = y' + d \tag{12}$$

Finally, expression of efficiency (η_r) for the fiber coupling system when the lateral mismatch occurred is suitably written as follows [17, 18, 33],

$$\eta_r = \eta \exp\left[\frac{2d^2}{w_f^2}\left\{\frac{w_{2x}^2\left(w_{2x}^2+w_f^2\right)}{\left(w_f^2+w_{2x}^2\right)^2+\left(k_2^2 w_{2x}^4 w_f^4\right)/4R_{2x}^2}-1\right\}\right] \times \exp\left[\frac{2d^2}{w_f^2}\left\{\frac{w_{2y}^2\left(w_{2y}^2+w_f^2\right)}{\left(w_f^2+w_{2y}^2\right)^2+\left(k_2^2 w_{2y}^4 w_f^4\right)/4R_{2y}^2}-1\right\}\right] \tag{13}$$

3 Results and Discussions

In case of optical fiber coupling, the lateral mismatch is an important factor which decreases efficiency and increases the noise in signal as well because of back-reflection of light at the mismatch region. So, study of reflected intensity noise (RIN) is very much desirable and important so as to manage the noise factor for coupling system of a particular fiber optical device. Here, in this paper we estimate RIN of triangular profile optical fiber coupled via an UDTHML for different values of normalized frequency (V) of the fiber and also observe the variation of RIN value with lateral offset.

Here, we take three triangular type index fiber profiles of typical "V" values as "4.380, 3.511and 1.924 having w_f values 2.676 μm, 3.238 μm and 9.901 μm" [17, 18] respectively for studying the RIN characteristics. We also use two laser diodes of wavelengths "1.5 μm (w_{1x} = 0.843 μm, w_{1y} = 0.857 μm) and 1.3 μm (w_{1x} = 1.081 μm, w_{1y} = 1.161 μm)" as sources [17, 18]. We first calculate value of coupling efficiency (η) using Eq. 5 and then the re-coupling efficiency (η_r) from Eq. 13 in case of lateral offset between taper lens and laser source for said optical fibers corresponding to two wavelengths and then estimate the RIN for each case. Finally, Eqs. 1–4 are used to find out RIN value. The other relevant parameters of interest for calculating RIN value are considered as: "radius of spherical surface of lens (R_0) is 90 μm, attenuation constant is 0.5 dB/km" [17, 18], "optical reflection coefficient of fiber is − 32 dB with $N = 1$" (in absence of connector); "spectral width of source is 50 MHz" [30, 31]. Here, we consider carrier frequency in radio-frequency range [25, 28] such as 2 GHz and 200 MHz specifically.

We plotted the graph of variation RIN with the change of lateral offset (d, d) in absence of connector for three fibers corresponding to source wavelengths "λ = 1.5 μm and λ = 1.3 μm" [17, 18] that are presented in Figs. 2, 3, 4, 5, 6 and 7. It is found from the graphs that for both frequencies f = 200 MHz and f = 2 GHz the RIN value decreases gradually with increase of lateral mismatch. The graphical presentations show rate of changes of RIN for the specified wavelength

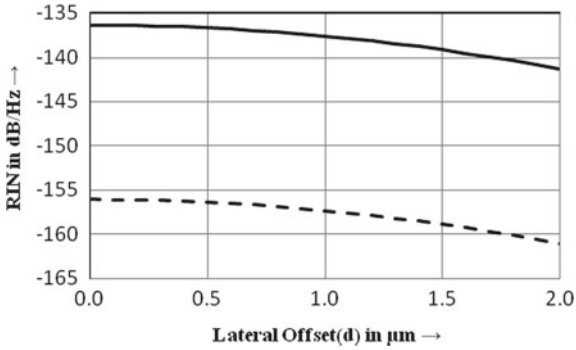

Fig. 2 RIN value versus lateral mismatch (d, d) graph in absence of connector of UDTHML on tip of triangular profile fiber having "$V = 4.380$" [17, 18] and excited wavelength $\lambda = 1.5\ \mu$m for $\nabla v = 50$ MHz with $f = 200$ MHz (—) and $f = 2$ GHz (- - -)

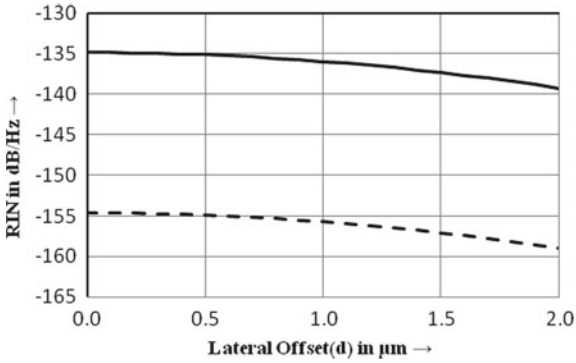

Fig. 3 RIN value versus lateral mismatch (d, d) graph in absence of connector of UDTHML on tip of triangular profile fiber having "$V = 3.511$" [17, 18] and excited wavelength $\lambda = 1.5\ \mu$m for $\nabla v = 50$ MHz with $f = 200$ MHz (—) and $f = 2$ GHz (- - -)

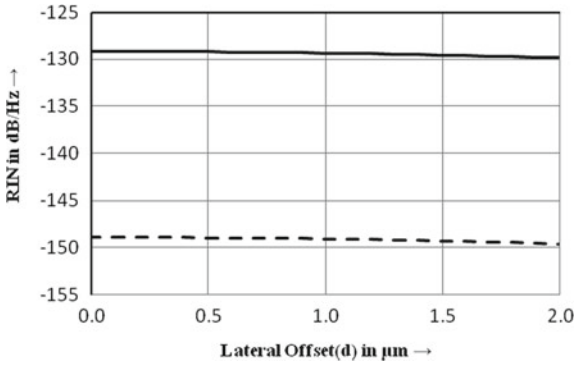

Fig. 4 RIN value versus lateral mismatch (d, d) graph in absence of connector of UDTHML on tip of triangular profile fiber having "$V = 1.924$" [17, 18] and excited wavelength $\lambda = 1.5\ \mu$m for $\nabla v = 50$ MHz with $f = 200$ MHz (—) and $f = 2$ GHz (- - -)

"$\lambda = 1.5\ \mu$m and $\lambda = 1.3\ \mu$m" [17, 19] for each triangular index fiber used here. Thus the observations lead us to the suitable choice of triangular index fiber profile and operating wavelength for minimization of RIN with less sacrifice of coupling efficiency.

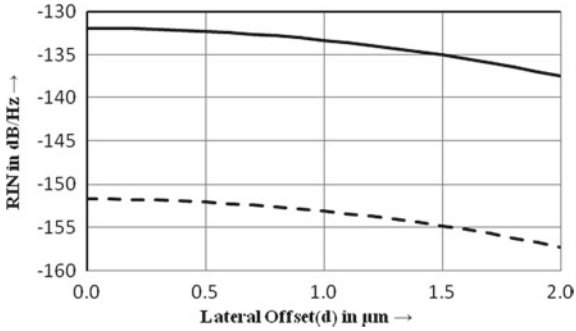

Fig. 5 RIN value versus lateral mismatch (*d, d*) graph in absence of connector of UDTHML on tip of triangular profile fiber having "$V = 4.380$" [17, 18] and excited wavelength $\lambda = 1.3\ \mu m$ for $\nabla v = 50$ MHz with $f = 200$ MHz (—) and $f = 2$ GHz (- - -)

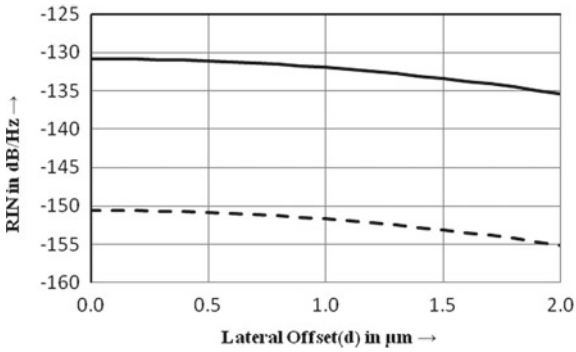

Fig. 6 RIN value versus lateral mismatch (*d, d*) graph in absence of connector of UDTHML on tip of triangular profile fiber having "$V = 3.511$" [17, 18] and excited wavelength $\lambda = 1.3\ \mu m$ for $\nabla v = 50$ MHz with $f = 200$ MHz (—) and $f = 2$ GHz (- - -)

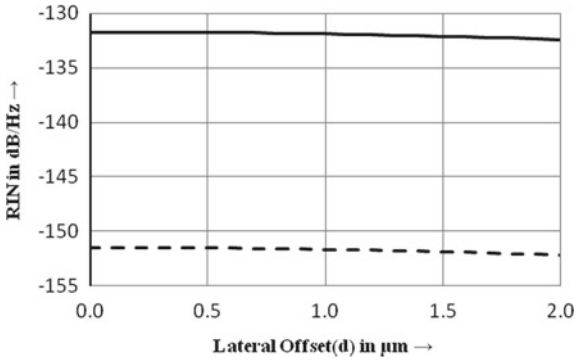

Fig. 7 RIN value versus lateral mismatch (*d, d*) graph in absence of connector of UDTHML on tip of triangular profile fiber having "$V = 1.924$" [17, 18] and excited wavelength $\lambda = 1.3\ \mu m$ for $\nabla v = 50$ MHz with $f = 200$ MHz (—) and $f = 2$ GHz (- - -)

4 Conclusion

The coupling efficiency of an optical coupler is reduced due to lateral mismatch. Side by side, the lateral mismatch causes back reflection from fiber to laser and this results in the production of noise in the communication system. The present study involves development of a simplified theoretical formalism for estimating the

reflected intensity noise (RIN) in case of a laser diode to a triangular refractive index profile typed optical fiber coupling via upside down tapered hemispherical microlens (UDTHML) on the concerned fiber tip. In long haul communication system, the present investigation leads to optimization of coupling efficiency and carrier to noise ratio so as to ensure an efficient communication system. Keeping in mind that in case of short haul communication, noise is comparatively more important than the coupling efficiency, it can be inferred that it is desirable to minimize RIN at the cost of sacrifice of a few dB units of coupling efficiency. The present analysis leads to judicious choice of the fiber, operating wavelength, frequency and later mismatch so as to reduce reflected intensity noise at the cost of minimum sacrifice of coupling efficiency. Thus, the results projected in the present work will definitely benefit communication technologists and researchers involved in the broad field of optical engineering.

References

1. John, J., Mclean, T.S.M., Ghagouri-Shiraz, H., Niblett, J.: Matching of single-mode fiber to laser diode by microlenses at 1.5–1.3 μm wavelength. IEE Proc. Optoelectron. **141**, 178–184 (1994)
2. Presby, H.M., Edwards, C.A.: Near 100% efficiency fibre mircolenses. Electron. Lett. **28**, 582–584 (1992)
3. Edwards, C., Presby, A.H.M., Dragone, C.: Ideal microlenses for laser to fiber coupling. J. Lightwave Technol. **11**, 252–257 (1993)
4. Presby, H.M., Edwards, C.A.: Efficient coupling of polarization maintaining fiber to laser diodes. IEEE Photon. Techn. Lett. **4**, 897–899 (1991)
5. Edwards, C.A., Presby, H.M.: Coupling-sensitivity comparison of hemispherical and hyperbolic microlens. App. Opt. **32**, 1573–1577 (1993)
6. Kurokawa, K., Becker, E.E.: Laser fiber coupling with a hyperbolic lens. IEE Trans. Microwave Theory Techn. **23**, 309–311 (1975)
7. Mondal, S.K., Gangopadhyay, S., Sarkar, S.N.: Analysis of an upside-down taper lens end from a step-index fiber. Appl. Opt. **37**, 1006–1009 (1998)
8. Roy, K., Majumdar, A., Maiti, S., Gangopadhyay, S.: Laser diode to single-mode graded index fiber coupling via cylindrical microlens on the fiber tip: evaluation of coupling efficiency by ABCD matrix formalism. J. Opt. Commun. (2020). https://doi.org/10.1515/joc-2020-0234
9. Mukhopadhyay, S.: Coupling of a laser diode to single mode circular core graded index fiber via parabolic microlens on the fiber tip and identification of the suitable refractive index profile with consideration for possible misalignments. J. Opts. **45**, 312–323 (2016)
10. Sankar, S.P., Hariharan, N., Varatharajan, R.: A novel method to increase the coupling efficiency of laser to single mode fibre. Wirel. Pers. Commun. **87**, 419–430 (2016)
11. Rakshit, R., Majumdar, A., Gangopadhyay, S.: Misalignment considerations in laser diode to single-mode graded index fiber coupling via upside down tapered parabolic microlens on the circular core fiber. Opt. Fiber Technol. **61,** 102448 (2021)
12. Selvanandan, S., Anbarasan, P.M.: Power coupling efficiency enhancement in multimode step-index fiber using refractive and diffractive microlenses. Int. J. Opt. 601675 (2010)
13. Maiti, S., Biswas, S.K., Gangopadhyay, S.: Study of coupling optics involving graded index fiber excitation via upside down tapered parabolic microlens on the fiber tip. Optik **199**, 163318 (2019)
14. Yuan, L., Qui, A.: Analysis of a Single-mode fiber with taper lens end. J. Opt. Soc. Am. A **9**, 950–952 (1992)

15. Mondal, S.K., Sarkar, S.N.: Coupling of a laser diode to single-mode fiber with an up-side down tapered lens end. Appl. Opt. **38**, 6272–6277 (1999)
16. Libo, Y., Reilan, S.: Formation of power properties an upside down taper lens at the end of an optical fiber. Sens. Actuat. A **23**, 1158–1161 (1990)
17. Maiti, S., Maiti, A.K., Gangopadhyay, S.: Laser diode to single-mode triangular-index fiber excitation via upside down hemispherical microlens on fiber tip: Prescription of ABCD matrix of transmission and estimation of coupling efficiency. Optik **144**, 481–489 (2017)
18. Mandal, H., Maiti, S., Chiu, T.L., Gangopadhyay, S.: Mismatch considerations in laser diode to single-mode circular core triangular index fiber excitation via upside down tapered hemispherical microlens on the fiber tip. Optik **168**, 533–540 (2018)
19. Ho., K.P., Khan, J.M.: Methods of cross talk measurement and reduction in dense WDM systems. J. Lightwave Technol. **14**, 1127–1135 (1996)
20. Kallimari, K.I., O'Mahony, M.J.: Relative intensity noise for laser diodes with arbitrary amounts of optical feedback. IEEE J. Quant. Electron. **34**, 1438–1446 (1998)
21. Way, W.I., Lin, C., et al.: Multiple-reflection-induced intensity noise studies in a lightwave system for multichannel AM-VSB television signal distribution. IEEE Photon. Technol. Lett. **2**, 360–362 (1990)
22. Yoshinaga, H., Kikushima, K., et al.: Influence of reflected light on erbium-doped fiber amplifiers for optical AM video signal transmission systems. J. Lightwave Technol. **10**, 1132–1136 (1992)
23. Langley, L.N., Shore, K.A.: Effect of the optical feedback on the noise properties of vertical cavity surface emitting laser. IEE Proc. Optoelectron. **144**, 34–38 (1997)
24. Woodward, S.L., Koch, T.L., Koren, U.: RIN in multisection MQW-DBR laser. IEEE Photon. Technol. Lett. **2**, 104–108 (1990)
25. Tkach, R.W., Chraplyvy, A.R.: Phase noise and linewidth in an InGaAsP DFB laser. J. Lightwave Technol. **LT-4**, 1711–1716 (1986)
26. Elwan, H.H., Khayatzadeh, R., Poette, J., Cabon, B.: Relative intensity noise in optical heterodyning applied to millimeter-wave systems. Microwave Photon. Paphos Cyprus. Hal. 01958040 (2015)
27. Khayatzadeh, R., Rzaigui, H., Poette, J., Cabon, B.: Accurate millimeter-wave laser phase noise measurement technique. IEEE Photon. Technol. Lett. **25**(13) (2013)
28. Shin, S., Sharma, U., Tu, H., Jung, W., Boppart, S.A.: Characterization and analysis of relative intensity noise in broadband optical sources for optical coherence tomography. IEEE Photon. Technol. Lett. **22**(14), 1057–1059 (2010)
29. Gimlett, J.L., Cheung, N.K.: Effects of phase-intensity noise conversion by multiple reflections on gigabit-per-second DFB laser transmission systems. J. Lightwave Technol. **7**, 888–895 (1989)
30. Mondal, S.K., Shi, F.G.: Novel lensed-fiber offset coupling scheme to reduce reflected intensity noise in optimizing carrier-to-noise ratio. Opt. Commun. **199**, 399–405 (2001)
31. Keiser, G.: Optical Fiber Communication. McGraw-Hill, New York (2000)
32. Aburakwa, Y., Ohtsuka, H., Araki, K.: An inclined coupling between laser and fiber scheme to reduce optical reflection with a spot-size converter integrated laser diode. J. Lightwave. Thechnol. **17**, 2342–2348 (1999)
33. Gangopadhyay, S., Sarkar, S.N.: Misalignment considerations in laser diode to single-mode fiber excitation via hemispherical lens on the fiber tip. J. Opt. Commun. **19,** 217–221 (1998)

A Brief Review on the Performances of Two-Bladed and Three-Bladed H-Darrieus Rotors

R. Medda, D. Gope, A. Chakraborty, N. Debnath, S. Das, and A. R. Sengupta

Abstract In recent times, the demand for renewable energy has increased very rapidly. Among all the renewable energy sources, wind energy is one of the most reliable options due to its high energy generation and zero CO_2 outflows to the climate. Wind turbines are a type of device which produces energy from the wind. Wind turbines are primarily categorized into two types, horizontal axis wind turbines (HAWTs) and vertical axis wind turbines (VAWTs). HAWTs are popular to use commercially, but the development and research on the VAWTs are increasing gradually nowadays. In this present work, a brief review of the performances of two-bladed and three-bladed H-Darrieus rotors has been done considering different performance parameters like tip speed ratio, solidity, and power coefficient. It is seen that a two-bladed H-Darrieus rotor having a NACA0018 profile with a solidity of 0.12, tip speed ratio (TSR) of 4.5 showed the optimum power coefficient compared to the other investigations of similar rotors. Again, for the three-bladed H-Darrieus rotor, the highest power coefficient is achieved by the LS-0413 blade at a TSR of four which is higher than the NACA0018 blade for the same rotor. This study deals with the research progress of two-bladed rotor and three-bladed H-Darrieus rotor which can be helpful for future researchers to further improve the designs and performances of the same.

Keywords H-Darrieus rotor · Power coefficient · Tip speed ratio · Solidity · Wind turbine

1 Introduction

Energy has a significant role in the social and economic evolution and prosperity of humanity. The energy demands every year are growing exponentially all over the globe. Mostly, the demand for the energy required is, as electricity, to make this up: addressing renewable energy is one of the vital approaches for the development and

R. Medda · D. Gope · A. Chakraborty · N. Debnath · S. Das · A. R. Sengupta (✉)
Department of Mechanical Engineering, JIS College of Engineering, Kalyani, WB 741235, India

B. Sikdar et al. (eds.), *Proceedings of the 3rd International Conference on Communication, Devices and Computing*, Lecture Notes in Electrical Engineering 851,
https://doi.org/10.1007/978-981-16-9154-6_7

the environment. We have been using conventional resources of energy since finding their application of these resources. As these resources have a limited amount in nature, so it's exhausting rapidly day by day. Also, it creates an excessive amount of greenhouse gases which caused global warming. Because of these issues, the uses and applications of renewable energy are extensively grown. It has increased the research and development activities in the field in the past few years. In a comparison of fossil fuels to renewable energy resources, renewable resources do not emit any harmful greenhouse gases into the atmosphere. There are several renewable sources are available for instance solar, wind, wave, biofuels, geothermal, and others. Among these renewable resources, wind is available abundantly in nature, even harvesting wind energy from the wind is easy to compare with others; the wind energy is economically suitable to generate and supply. A wind turbine is a kind of device which transforms kinetic energy into mechanical energy. Wind turbines could be installed in both distant areas and urban areas as well. Wind energy accomplished one-fourth of the total produced renewable energy every year, and it is growing over time. So, renewable is the future of the energy system, and wind energy is a part of it [1].

Wind energy is pretty convenient in terms of power generation, which is increasing over time. In 2020, the total electricity generation from renewable energy has raised by approximately 6.6% following the completion of approximately 462 TWh than the previous year. The electricity generated by wind in 2020 is around 12%, which is 177.8 TWh greater than the last year following. It is visible from the data that almost 40% of total renewable energy is generated from wind only [2].

1.1 Classification of Wind Turbines

Wind turbine extracts the power from wind and converts mechanical energy into electrical energy; wind turbines are primarily characterized into two classes: Horizontal axis wind turbine (HAWT) and vertical axis wind turbine (VAWT) can be seen in Fig. 1. HAWT is the most common type of wind turbine (shown in Fig. 1a) which generates power by aerodynamic lift. The main advantage of HAWT is, it provides high power output as compare to others, and they are more likely to operate at higher wind speed.

On the other hand, VAWT can be easily mounted as compared to other wind turbines. It is portable, can run at low wind speed, is less expensive, creates less noise, and most importantly, it is omnidirectional. It can run in extreme weather, with variable wind speed. VAWTs can be divided into two categories: (a) Savonius rotor and (b) Darrieus rotor. The drag-type Savonius turbines (shown in Fig. 1b) rotate relatively slowly but yields a high torque compared to Darrieus turbines. On the contrary, in the lift-type Darrieus turbine, multiple blades are attached to a shaft that rotates, which is also categorized by its blade shapes, like Troposkien and H-Darrieus rotor. Several other kinds of VAWTs can be seen out there such as hybrid

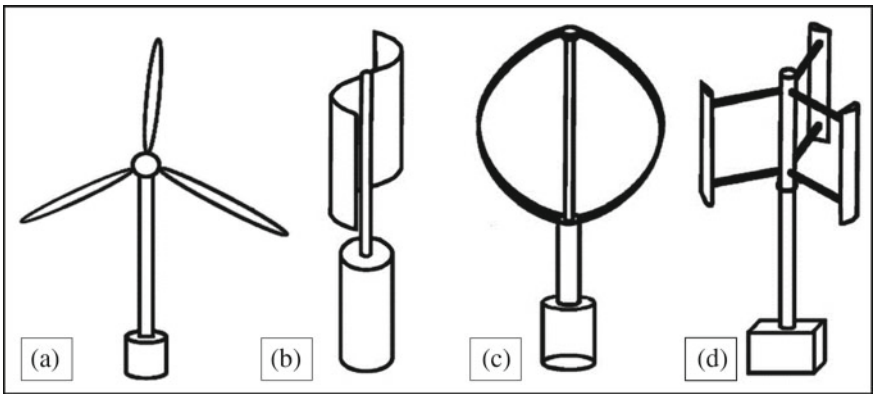

Fig. 1 **a** Horizontal axis wind turbine, **b** Savonius turbine, **c** Darrieus turbine, **d** H-Darrieus turbine [3]

Darrieus-Savonius, multistage rotor, augmented rotor, helical rotor, multi-bladed rotor, and V-type rotor [4].

2 Purpose of the Present Study

VAWT research has been accelerated over, past few decades both through experimental and numerical simulation. However, our awareness of certain key factors influencing their performance is still lacking. An enormous amount of work has been done on the three-bladed H-Darrieus rotor, but very less work has been done on the two-bladed H-Darrieus rotor in terms of their improvement of performance. The objective of this present investigation is to review the effects on the performance by the number of blades, different shaped airfoils, solidity, turbulence models, TSR range, wind velocity.

3 Comparative Study on the VAWTs

3.1 On Two-Bladed H-Darrieus Rotors

Over the years, various researches have been performed on the improvement of the performance of two-bladed H-Darrieus rotor in terms of modifying the design, the number of blades, types of airfoils, augmentation, dimension, etc. Some of the important researches are summarized below.

Lei et al. [5] have performed a computational study over the IDDES turbulence model, and compared the results with the experimental and validated data of the SST

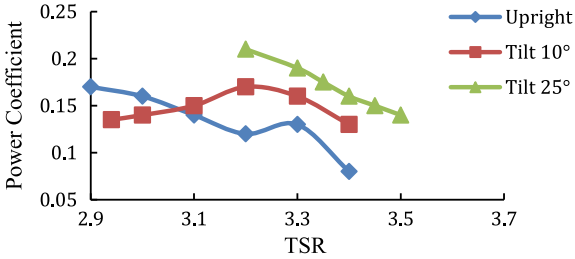

Fig. 2 *Cp* versus TSR graph in upright, 10° tilted, and 25° tilted position [7]

$k-\omega$ turbulence model at TSR range between 1.450 and 2.478. In the IDDES model, the power coefficient value is near around to the experimental data than the SST $k-\omega$ model. The optimum C_P is about 0.18 at a TSR of 2.23. Buchner et al. [6] have studied the dynamic stall of the two-bladed H-Darrieus VAWT; a 2D URANS model was used followed by a wind tunnel test to validate the simulation performance. Chowdhury et al. [7] have carried out a CFD study based on the inclination of the rotor shaft; three cases are carried out through the study, upright, 10° tilted and 25° tilted with the Y-axis. They have also concluded that the SST $k-\omega$ model shows better performance compared to other turbulence models. The VAWT, with a 25° tilted rotor axis, has produced a maximum C_P of 0.21 at TSR 3.2 which is shown in Fig. 2.

Bedon et al. [8] have investigated the aerodynamic characteristics of the H-Darrieus rotor with the newly developed WUP1615-shaped airfoil and compared it with NACA 0018 airfoil. The CFD study revealed that at a positive angle of attack, the lift coefficient (C_L) of the WUP1615 rotor is increased, but at a negative angle of attack, the values of the lift coefficient (C_L) are similar to the NACA 0018 bladed rotor. Biswas and Gupta [9] studied the effect of the different blade profiles, aspect ratios, and the twist at the trailing edge to improve the unsteadiness of the rotor at a low Reynolds number. They noticed that a 30% blade twist at the trailing edge of an airfoil helps to enhance the performance of a two-bladed rotor at a low Reynolds number. The velocity contour plot is shown in Fig. 3 where the wake structures past

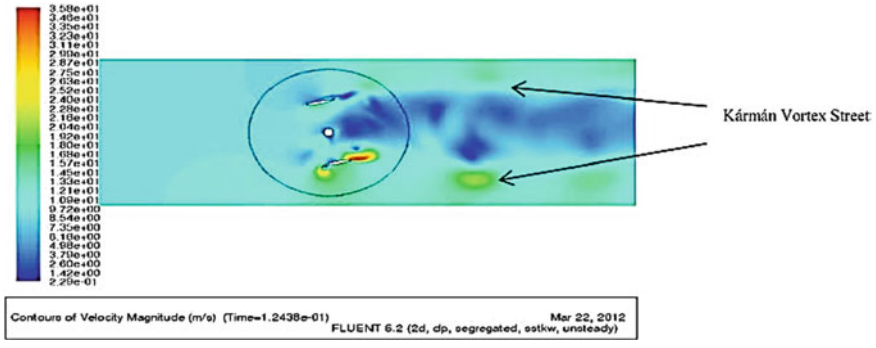

Fig. 3 Velocity contour in a quasi-periodic period [9]

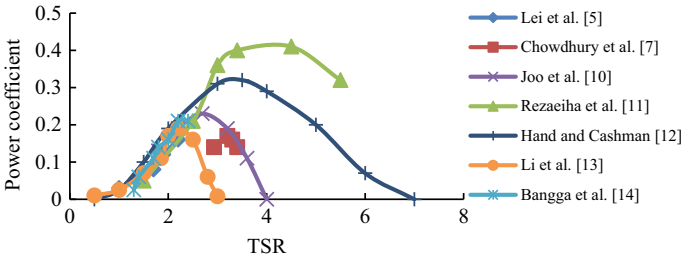

Fig. 4 Power coefficient (C_p) versus TSR of two-bladed literature

the rotor along with the Karman vortex street layers can be seen. The difference of velocity between the upstream and downstream sides of the rotor helps to determine the lift generated by the rotor blades. Joo et al. [10] have performed a computational study on the aerodynamic characteristics of two-bladed H-Darrieus rotors at several rotating speeds and solidities, with a moving framework. They have found that the maximum efficiency (C_p) of 0.23 at a solidity of 0.5 and TSR of 2.69. Rezaeiha et al. [11] in their numerical studies found that NACA0018 two-bladed H-Darrieus turbine having a solidity value of 0.12 and 4.5, TSR was able to display the highest power coefficient of 0.41.

Hand and Cashman [12] have investigated different parameters like solidity, aspect ratio, blade number, and TSR. They also found that the two-bladed turbine has shown a maximum C_p of 0.32 with the corresponding TSR of 3.14 at a wind velocity of 13 m/s. Li et al. [13] have experimented on the two-bladed H-Darrieus rotor having NACA0021 airfoils. It was noticed that the optimum performance of the rotor was achieved at a TSR 2, and the speed of wind ranges between 6 and 7 m/s. Bangga et al. [14] have carried out a 2D CFD analysis on a two-bladed H-Darrieus turbine at a wind velocity of 8 m/s having NACA0021 airfoils and found an optimum C_P of 0.2 at TSR 2.6 for the same. A comparative analysis of power coefficient values for the two-bladed H-Darrieus rotor obtained by various researchers is shown in Fig. 4.

The above literature covered up the effect of different geometrical and aerodynamic parameters like solidity, TSR, the angle of attack, aspect ratio, wind speed, turbulence model, blade shape in CFD, and many others. The important findings are mentioned in the conclusion section.

3.2 On Three-Bladed H-Darrieus Rotors.

In the recent past, researchers have performed various investigations on several parameters of three-bladed H-Darrieus rotors to improve their performance; among which, some important findings are discussed below.

Sengupta et al. [15] have investigated three blade profiles; among them, one is symmetrical (NACA0018) blade, and the other two chambered (EN0005 and S815)

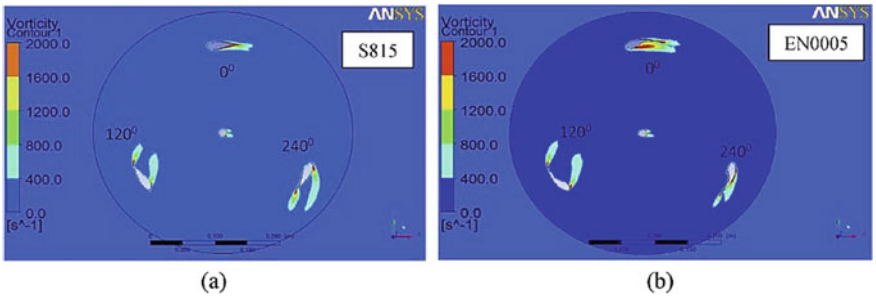

Fig. 5 Generation of vortices at wind velocity 6 m/s for unsymmetrical blade H-Darrieus rotors [16]

blades. They found that the maximum C_p of 0.19 for S815 and 0.17 for NACA 0018 airfoils at a flow velocity of 6 m/s. Again, Sengupta et al. [16] have emphasized the effect of the curvature and camber of the unsymmetrical airfoils to improve the performance of the turbine at low wind speeds. Result showed that in the power stroke, due to higher curvature in the suction side of the S815 airfoil, better performance is achieved. But, in the return stroke, the EN0005 airfoil with higher camber and lesser curvature shows better performance. The vorticity formation contour plots for these two blades are reproduced in Fig. 5 where the comparison has been done of rotor performances for different azimuthal angle positions in terms of vorticity generation.

Mohamed et al. [17] have investigated 25 different airfoil shapes in a broad TSR range with rotor solidity of 0.1. They found that LS-0413 airfoil delivered the highest power coefficient (C_P) of 0.415 at TSR 4, with an expansion of 10% compared to NACA 0018. They have also noticed that NACA 63-415 has the widest operating speed ratio range, and the maximum power coefficient (C_P) is 0.40 at TSR 4. The C_p versus TSR plot is shown in Fig. 6. Rezaeiha et al. [18] have attempted a computational study, which is based on the three different sets of VAWTs with different characteristics and extended range of operational conditions in seven different turbulence models, namely the Spalart–Allmaras (S–A), RNG $k-\varepsilon$, realizable $k-\varepsilon$, SST $k-\omega$, intermittency transition model (SSTI), $k-k_l-\omega$ transition model, and transition SST $k-\omega$ (TSST). The results showed only three turbulence models (TSST, SST $k-\omega$, and SSTI); out of those, seven can be used to achieve approximately accurate

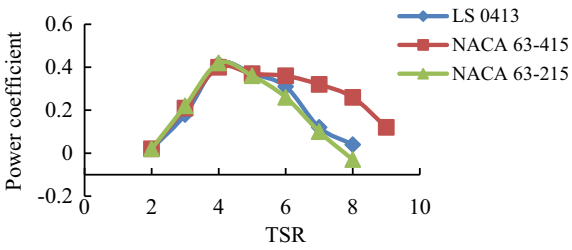

Fig. 6 Power coefficient (C_P) versus TSR for the best three blade sections in Mohamed et al. [17]

aerodynamic performance. The highest C_p of 0.369 at TSR of 3.29 in TSST among the accurate turbulence model and TSST turbulence has the minimum overall deviation of 18.6% from the experimental data of Castelli et al. [19]. Balduzzi et al. [20] have performed CFD analysis with the H-Darrieus VAWT to find the most precise simulation setup and found that the best turbulence model is SST $k-\omega$ for simulating Darrieus rotors. Their study revealed that the highest power coefficient (C_P) of 0.31 was found at a TSR of 2.25 for the considered operating conditions.

Mohamed [21] again investigated the major problem of being able to self-start Darrieus turbines, to improve this downside. The impact of solidity and the utilization of a hybrid system which is a combination of both Savonius and H-Darrieus turbines have been investigated numerically and experimentally. It was found that enhancing the solidity of the turbine does improve its self-starting ability at low TSR. The hybrid system shows a better static torque coefficient which configures the self-starting ability, but the performance of the turbine is decreased in exchange. The rotor obtained the highest static torque at a solidity of 0.25, in which case the maximum (C_P) of 0.38 is produced by the rotor at TSR 4. Kumar et al. [22] have performed a CFD analysis on the performance improvement of the H-Darrieus rotor with cavities on the pressure side of the airfoils. The result has shown that the overall performance has been increased due to the suppression of the free stream boundary layer around the airfoil surface near the cavities. There is a significant improvement in self-starting capability; the optimum power coefficient (C_P) of 0.16 is achieved at TSR 1.3. Two unsymmetrical (S815 and EN0005) and one symmetrical (NACA 0018) blades are considered by Sengupta et al. [23, 24] to compare the performance of these three rotors by experimental analysis. The rotors have shown their optimum performance at the solidity of 0.51 and aspect ratio (H/D) of 1. The maximum power coefficient (C_P) is found at 0.19 for the S815 bladed rotor. It was concluded that high solidity unsymmetrical-bladed rotor has better dynamic and static torque coefficient and power coefficient values compared to the low-solidity blade rotors. Subramanian et al. [25] have attempted to find the performance of AIR 001, NACA 0015, NACA 0012, and NACA 0030 for H-Darrieus turbines. The TSR (λ) range was considered in between 1 and 2.5 with an incoming wind speed of 10 m/s. They concluded that the NACA0030 blade shape showed the optimum power coefficient at a low TSR of 1.8 considering the wind speed of 10 m/s. In Table 1, some important results of three-bladed H-Darrieus turbines for different parameters are mentioned.

Martinez et al. [26] performed the CFD simulation over four various thicknesses of NREL S815 airfoils to increase the performance of VAWT at wind speed conditions

Table 1 Results of the three-bladed H-Darrieus turbines

Literature	TSR	Solidity	Flow velocity (m/s)	Aspect ratio	Maximum Cp
Mohamed et al. [17]	1.0	0.1	5	1.0	0.41
Rezaeiha et al. [18]	3.29	0.25	9	1.0	0.36
Sengupta et al. [24]	1.43	0.24	8	1.4	0.19
Martinez et al. [26]	1.7	0.51	8	1.0	0.32

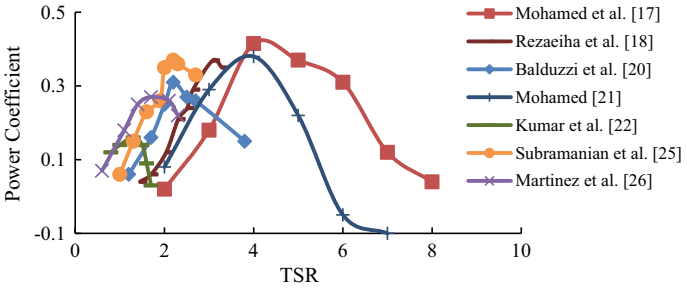

Fig. 7 Power coefficient versus TSR

of 6 and 8 m/s. The range of the TSR in this study was considered from 0.6 to 2.25. It was noticed that along with the increment of the thickness and TSR values, the performance of the rotor also increased until it has reached the optimum point (19.2% thickness). The highest C_P of 0.32 is achieved at a TSR of 1.725 in 8 m/s which is higher as compared to C_P of 0.28 at the same TSR in 6 m/s wind speed. In Fig. 7, C_p versus TSR graph for two-bladed H-Darrieus rotors obtained by various researchers is plotted.

On three-bladed H-Darrieus rotors, a lot of research works have been done and are being continued. Among those studies, some of the important literature on three-bladed H-Darrieus rotors have been presented here considering several performance parameters.

4 Conclusion

This review shows a brief overview of the performance of two and three-bladed H-Darrieus rotors considering several performance parameters. From this present study, some vital outcomes are listed below:

- Two-bladed H-Darrieus rotor having NACA0018 profile with a solidity of 0.12, TSR of 4.5, and an angular time step of 0.1° to 0.5° showed the optimum power coefficient of 0.41 for the considered operating conditions.
- The most accurate turbulence model is SST k-ω for the two-bladed rotor, and in the three-bladed rotor, the TSST $k-\omega$ shows the most accurate result compared to the SST $k-\omega$ and SSTI $k-\omega$ turbulence model. TSST $k-\omega$ turbulence model is able to capture the stall vortices around the blade surface in low Reynolds number.
- From the literature, optimal C_P is obtained for both two-bladed and three-bladed rotors at low solidity of around 0.1 in the moderate TSR range. If the solidity is increased at low TSR, the three-bladed rotor exhibits more power coefficient than the two-bladed rotor. But, in a high TSR range, a two-bladed rotor needs low solidity to display higher performance.

- For the three-bladed H-Darrieus rotor, the highest C_P of 0.415 is acquired by LS-0413 blade at TSR of four with a rise of 10% compared to NACA 0018 for the considered operating conditions.
- With an increase of the airfoil thickness, the performance is increased for the unsymmetrical S815 three-blade H-Darrieus rotor, but after the optimal thickness percentage (19.2% of the chord length), the performance is dropped down.

This investigation has gathered some valuable information regarding the performance of the two-bladed and three-bladed H-Darrieus rotor systems. This current study can be referred by future researchers to work in this field for comparative analysis in between two and three-bladed H-Darrieus rotors.

References

1. Nehrenheim, E.: Introduction to renewable energy. Ref. Module Earth. Syst. Environ. Sci. (2018)
2. IEA: Renewables 2020 Data Explorer, IEA, Paris (2020). https://www.iea.org/articles/renewables-2020-data-explorer. Accessed on 21 Jul 2021
3. https://www.researchgate.net/figure/The-major-wind-turbine-types-including-the-propeller-type-horizontalaxis-wind-turbine_fig3_263161316. Accessed 01 Mar 2021
4. https://www.engineeringenotes.com/electrical-engineering/turbines/classification-of-wind-turbines-electrical-engineering/29504. Accessed on 02 Mar 2021
5. Lei, H., Zhou, D., Bao, Y., Li, Y., Han, Z.: Three-dimensional improved delayed detached eddy simulation of a two-bladed vertical axis wind turbine. Energy Conv. Manag. **133**, 235–248 (2017)
6. Bunchner, A-J., Lohry, M.W., Martinelli, L., Soria, J., Smits, A.J.: Three-dimensional improved delayed detached eddy simulation of a two-bladed vertical axis wind turbine. J. Wind Eng. Ind. Aerodyn. **146**, 163–171 (2015)
7. Chowdhury, A.M., Akimoto, H., Har, Y.: Comparative CFD analysis of vertical axis wind turbine in upright and tilted configuration. Renew. Energy **85**, 327–337 (2016)
8. Bedon, G., Betta, S.D., Benini, E.: Performance-optimized airfoil for Darrieus wind turbines. Renew. Energy. **94**, 328–340 (2016)
9. Biswas, A., Gupta, R.: Unsteady aerodynamics of a twist bladed H-Darrieus rotor in low Reynolds number flow. J. Renew. Sustain. Energy **6**, 033108 (2014)
10. Joo, S., Choi, H., Lee, J.: Aerodynamic characteristics of two-bladed H-Darrieus at various solidities and rotating speeds. Energy **90**, 439–451 (2015)
11. Rezaeiha, A., Montazer, H., Blocken, B.: Towards accurate CFD simulations of vertical axis wind turbines at different tip speed ratios and solidities: guidelines for azimuthal increment, domain size and convergence. Conv. Manag. **156**, 301–316 (2018)
12. Hand, B., Chashman, A.: Conceptual design of a large-scale floating offshore vertical axis wind turbine. Energy Procedia. **142**, 83–88 (2017)
13. Li, Q., Maeda, T., Kamada, Y., Murata, J., Yamamot, M., Ogasawara, T., Shimizu, K., Kogak, T.: Study on power performance for straight-bladed vertical axis wind turbine by field and wind tunnel test. Renew. Energy. **90**, 291–300 (2016)
14. Bangga, G., Lutz, T., Dessoky, A,. Kramer, E.: Unsteady Navier-Stokes studies on loads, wake, and dynamic stall characteristics of a two-bladed vertical-axis wind turbine. Renew. Sustain. Energy **9**, 053303 (2017)
15. Sengupta, A.R., Biswas, A., Gupta, R.: The aerodynamics of high solidity unsymmetrical and symmetrical blade H-Darrieus rotors in low wind speed. J. Renew. Sustain. Energy **9**, 043307 (2017)

16. Sengupta, A.R., Biswas, A., Gupta, R.: Comparison of low wind speed aerodynamics of unsymmetrical blade H-Darrieus rotors-blade camber and curvature signatures for performance improvement. Renew. Energy 1412–1427 (2019)
17. Mohamed, M.H., Ali, A.M., Hafiz, A.A.: CFD analysis for H-rotor Darrieus turbine as a low speed wind energy converter. Eng. Sci. Technol. Int. J. **18**, 1–13 (2015)
18. Rezaeiha, A., Montazeri, H., Blocken, B.: On the accuracy of turbulence models for CFD simulations of vertical axis wind turbines. Energy. **180**, 838–857 (2019)
19. Castelli, M.R., Englaro, A., Benini, E.: The Darrieus wind turbine: proposal for a new performance prediction model based on CFD. Energy **36**, 4919–34 (2011)
20. Balduzzi, F., Bianchini, A., Maleci, R., Ferrara, G., Ferrari, L.: Critical issues in the CFD simulation of Darrieus wind turbines. Renew. Energy. **859**, 419–435 (2016)
21. Mohamed, M.H.: Impacts of solidity and hybrid system in small wind turbines performance. Energy **57**, 495–504 (2013)
22. Kumar, Y., Sengupta, A.R., Biswas, A., Mazarbhuiya, H.M.S.M., Gupta, R.: CFD analysis of the performance of an H-Darrieus wind turbine having cavity blades. Recent Advances in Mechanical Engineering. (2021) 711–719.
23. Sengupta, A.R., Biswas, A., Gupta, R.: Studies of some high solidity symmetrical and unsymmetrical blade H-Darrieus rotors with respect to starting characteristics, dynamic performances and flow physics in low wind streams. Renew. Energy 536–547 (2016)
24. Sengupta, A.R., Biswas, A., Gupta, R.: Investigations of H Darrieus rotors for different blade parameters at low wind speeds. Wind Struct. **25**, 551–567 (2017)
25. Subramanian, A., Yogesh, S.A., Sivanandan, H., Giri, A., Vasudevan, M., Mugundhan, V., Velamati, R.K.: Effect of airfoil and solidity on performance of small scale vertical axis wind turbine using three dimensional CFD model. Energy **133**, 179–190 (2017)
26. Martinez, R., Urquiza, G., Castro, L., Garcia, J.C., Rodríguez, A.,. Pirin, O.T., Dávalos, J.O., Errera, U.C.: Shape effect of thickness of the NREL S815 profile on the performance of the H-rotor Darrieus turbine. J. Renew. Sustain. Energy **13**, 013301 (2021)

MUX-Based Novel 9-trit CMOS Ternary Barrel Shifter

Somashree Chakraborty, Sonali Priya, Tripti Kumari, Saloni Thakur, and Aloke Saha

Abstract Barrel shifter is one of the key data-path elements to offer block of data-transfer in single clock cycle. Ternary barrel shifter (T-barrel shifter) is the center of attraction among circuit/system community due to reduced interconnect complexity and the associated drawbacks as compared to binary-based counterpart. This present study explores new 9-trit ternary barrel shifter using 3:1 ternary multiplexer on 32 nm CMOS technology. This proposed T-barrel shifter for shift and rotate operation is discussed. Ternary digit values "0", "1", and "2" are considered as 0, 0.5, and 1.0 V, respectively. This proposed circuit is designed and optimized using enhancement-type metal oxide semiconductor (E-MOS) transistor with 1.0 V supply rail at 27 °C temperature on 32 nm standard CMOS technology using Tanner EDA. The validation of proposed design is carried-out by performing extensive T-Spice transient simulations with piecewise linear (PWL) ternary input. Characteristics of proposed barrel shifter for shift and rotate operation are evaluated and recorded.

Keywords Interconnect complexity · Power-delay-product (PDP) · Ternary barrel shifter · Ternary number system · Ternary multiplexer

1 Introduction

Barrel shifter [1–5] is a critical circuit element that can shift and/or rotate multiple digits in a single clock cycle and hence forms the essence for most digital processing/computing systems. Binary is the well acceptable number system among digital designer due to natural ON–OFF characteristics of practical solid state devices that are suitable to represent bit values "1" and "0", respectively [6–9]. However, steady increase in input bit-length calls for large interconnect complexity for binary-based barrel shifter circuit. As an obvious outcome, the circuit reliability suffers due to generation of localized heat or hotspot. The increased interconnect complexity also increases spurious circuit activity and hence the spurious power as well. As per

S. Chakraborty · S. Priya · T. Kumari · S. Thakur · A. Saha (✉)
Department of Electronics and Communication Engineering, Dr. B. C. Roy Engineering College, Durgapur, India

B. Sikdar et al. (eds.), *Proceedings of the 3rd International Conference on Communication, Devices and Computing*, Lecture Notes in Electrical Engineering 851,
https://doi.org/10.1007/978-981-16-9154-6_8

study [10–12], ternary (base-3) can offer reduced interconnect complexity for equal data processing due to less number of circuit elements in the system. The reduction in fan-in/out for ternary system also offers better delay characteristics as compared to binary counterpart for identical amount of data processing.

Ternary barrel shifter [13–15] available in open literature utilizes unreliable CNTFET or complex variable threshold strategy. This work proposes new 9-trit ternary barrel shifter based-on 3:1 ternary multiplexer using conventional enhancement-type metal oxide semiconductor (E-MOS) transistor that can reduce interconnect complexity with improved speed-power and reliability. The circuit configuration for shift and rotate operation with proposed T-barrel shifter is pictorially presented and explained. The complete circuit is designed and optimized on 32 nm standard CMOS technology with 1.0 V supply rail at 27 °C temperature. In this proposed work, the ternary digits "0", "1", and "2" are denoted with 0, 0.5, and 1.0 V, respectively. Extensive T-Spice simulations with piecewise linear (PWL) ternary-input validate the working of designed T-barrel shifter circuit. Evaluated speed-power characteristic of proposed T-barrel shifter is presented.

The rest of this paper is organized as follows: The circuit configuration and working principle of proposed T-barrel shifter are explored in Sect. 2. Section 3 presents the design and T-Spice simulation results for proposed circuit. This paper is concluded in Sect. 4.

2 Proposed 9-trit T-Barrel Shifter: Circuit and Working Principle

The circuit structure along with operating principle of proposed 9-trit T-barrel shifter for shift and rotate operation is disclosed in this section.

Table 1 presents the I/O relation for proposed 9-trit right-shift T-barrel shifter circuit. 9-ternary inputs are denoted by D0–D8 in Table 1, whereas Y0–Y8 represent the 9-outputs from the circuit. Two ternary selection inputs are S0 and S1 here. The corresponding circuit diagram for proposed 9-trit right-shift T-barrel shifter (Table 1) is shown in Fig. 1. The specified number of shifting occurs as per selection input status as listed in Table 1.

Here in Fig. 1, each 3:1 ternary multiplexer selects one out of three inputs based on its selection input status. With selection inputs "0", "1", and "2", the corresponding 3:1 T-MUX output selects input at terminal "0", "1", and "2", respectively. Detail on 3:1 T-multiplexer is out of scope for present study and hence is omitted for brevity. Inputs D0–D8 are applied suitably to properly arrange 3:1 T-multiplexer circuits in order to achieve the right shift operation as per Table 1. Following same principle the left-shift T-barrel shifter is also constructed (not shown).

Table 1 Right shift 9-trit T-barrel shifter I/O relation

Selection I/P		Input								
		D0	D1	D2	D3	D4	D5	D6	D7	D8
		Output								
S1	S0	Y0	Y1	Y2	Y3	Y4	Y5	Y6	Y7	Y8
0	0	D0	D1	D2	D3	D4	D5	D6	D7	D8
0	1	0	D0	D1	D2	D3	D4	D5	D6	D7
0	2	0	0	D0	D1	D2	D3	D4	D5	D6
1	0	0	0	0	D0	D1	D2	D3	D4	D5
1	1	0	0	0	0	D0	D1	D2	D3	D4
1	2	0	0	0	0	0	D0	D1	D2	D3
2	0	0	0	0	0	0	0	D0	D1	D2
2	1	0	0	0	0	0	0	0	D0	D1
2	2	0	0	0	0	0	0	0	0	D0

Table 2 summarizes the I/O relation for proposed right rotate 9-trit T-barrel shifter circuit. The corresponding circuit diagram is shown in Fig. 2. Here, again the 3:1 T-multiplexers are suitably arranged with proper input in order to achieve the desired output. The design and simulation result of proposed T-barrel shifter are explored in Sect. 3.

3 Front-End Circuit Design and Evaluation

The proposed 9-trit T-barrel shifter is designed and optimized using BSIM4 device parameter on 32 nm standard CMOS technology with 1.0 V supply rail at 27 °C temperature. Ternary digit values “0”, “1”, and “2” are represented with 0 V, 0.5 V, and 1.0 V, respectively. The T-Spice simulation of proposed circuit is carried out by applying ternary input using PWL input source. Input rise/fall time is set to 10 ps for the simulation purpose. The schematic diagram of proposed T-barrel shifter with right-shift and right-rotate operation is shown in Fig. 3a and in Fig. 3b, respectively.

The T-Spice transient response of proposed right-shift and right-rotate 9-trit T-barrel shifter with selection input as per Fig. 4a is shown in Fig. 4b and in Fig. 4c, respectively. The applied 9-trit inputs D0, D1, D2, D3, D4, D5, D6, D7, and D8 are considered as “2”, “1”, “0”, “2”, “1”, “0”, “2”, “1”, and “0”, respectively. The evaluated speed-power performance of proposed T-barrel shifter is summarized in Table 3.

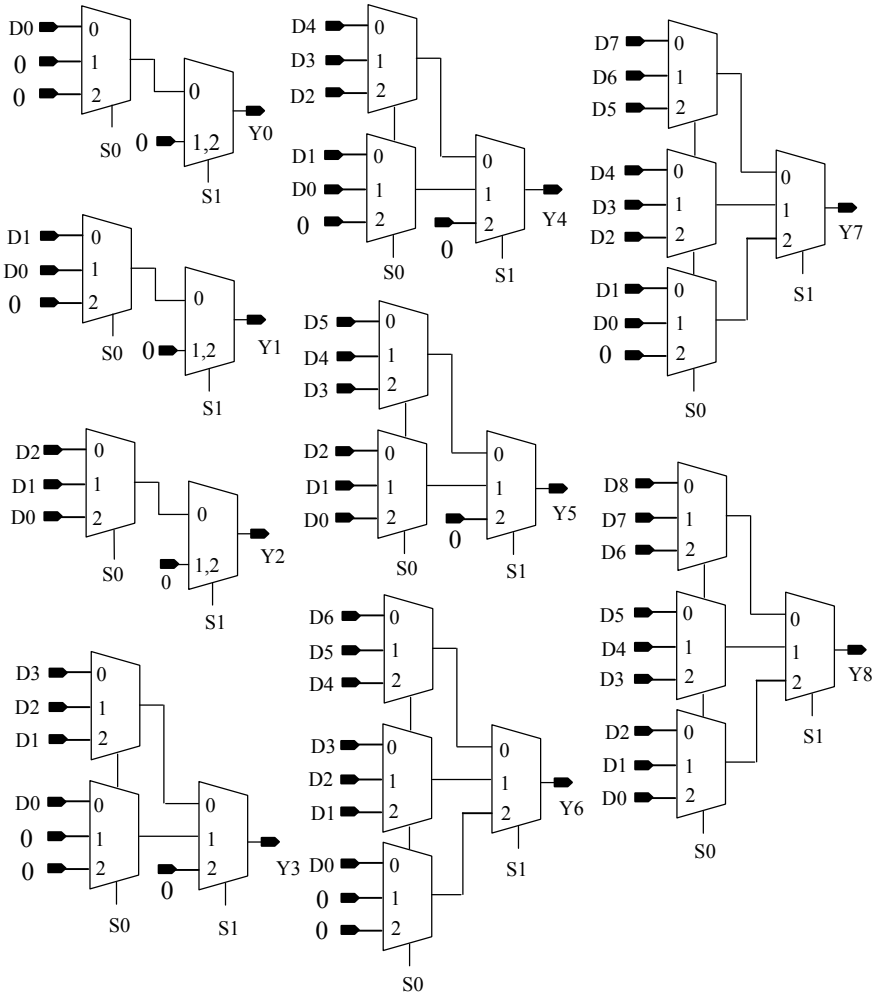

Fig. 1 Proposed 9-trit right shift T-barrel shifter

As presented in Table 3, the proposed 9-trit T-barrel shifter dissipates 172.57 and 174.06 μW average-power with 43.08 and 50.07 ps propagation-delay for right-shift and right-rotate operation, respectively. The total node-count, active devices, and power-delay-product (PDP) for right-shift T-barrel shifter become 2497, 558, and 7.43×10^{-3} pJ, respectively and for right-rotate T-barrel shifter becomes 2731, 612, and 8.72×10^{-3} pJ, respectively. The comparative study with other competitive

Table 2 Right rotate 9-trit T-barrel shifter I/O relation

Selection I/P		Input								
		D0	D1	D2	D3	D4	D5	D6	D7	D8
		Output								
S1	S0	Y0	Y1	Y2	Y3	Y4	Y5	Y6	Y7	Y8
0	0	D0	D1	D2	D3	D4	D5	D6	D7	D8
0	1	D8	D0	D1	D2	D3	D4	D5	D6	D7
0	2	D7	D8	D0	D1	D2	D3	D4	D5	D6
1	0	D6	D7	D8	D0	D1	D2	D3	D4	D5
1	1	D5	D6	D7	D8	D0	D1	D2	D3	D4
1	2	D4	D5	D6	D7	D8	D0	D1	D2	D3
2	0	D3	D4	D5	D6	D7	D8	D0	D1	D2
2	1	D2	D3	D4	D5	D6	D7	D8	D0	D1
2	2	D1	D2	D3	D4	D5	D6	D7	D8	D0

T-barrel shifter design could not be performed due to lack of information in open literature. However, the use of normal process E-MOS transistor for proposed work resolves the reliability issues associated with CNFET-based design of open literature. Again, the available multi threshold-MOS-based T-barrel shifter suffers from large fabrication complexity and that can also be eliminated with proposed idea.

4 Conclusion

This work proposes new 9-trit T-barrel shifter using conventional enhancement-type MOS transistor. The circuit structure of proposed T-barrel shifter is constructed with 3:1 T-multiplexer and is explained for right-shift and right-rotate operation. All the circuits are designed and optimized on 32 nm standard CMOS technology with 1.0 V supply rail at 27 °C temperature. Trit values “0”, “1”, and “2” are denoted with 0, 0.5, and 1.0 V, respectively. T-Spice transient simulation is performed with PWL input-data to validate the proposed design. The evaluated characteristic of designed circuit both for right-shift and right-rotate operation is recorded. This proposed T-barrel shifter can be applied to design efficient floating point ternary multiplier next.

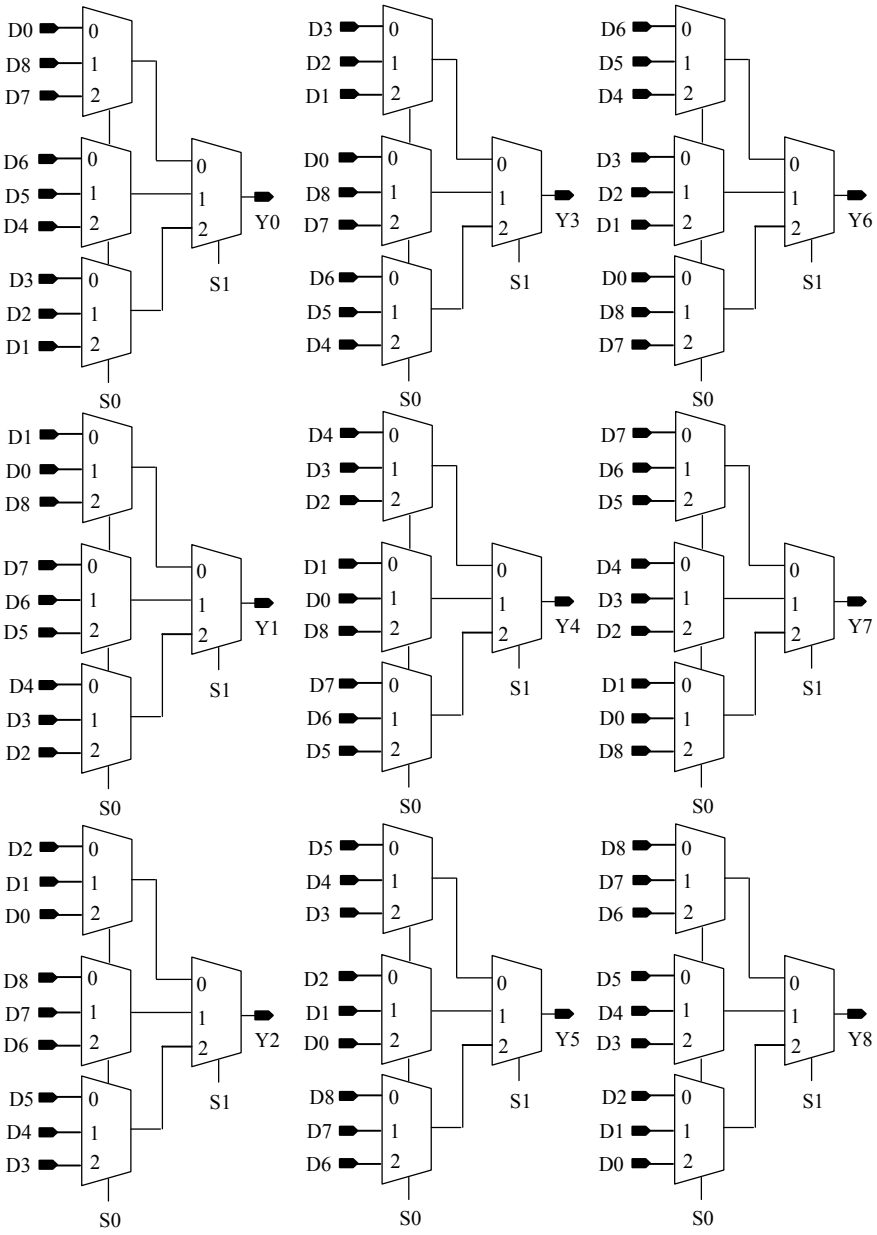

Fig. 2 Proposed 9-trit right rotate ternary barrel shifter

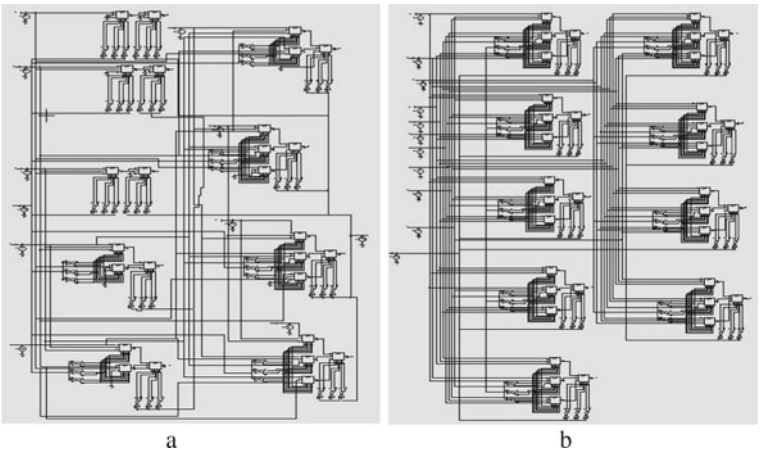

Fig. 3 Proposed 9-trit **a** right-shift, **b** right rotate ternary barrel shifter

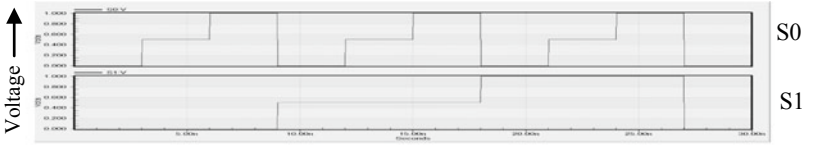

(a)

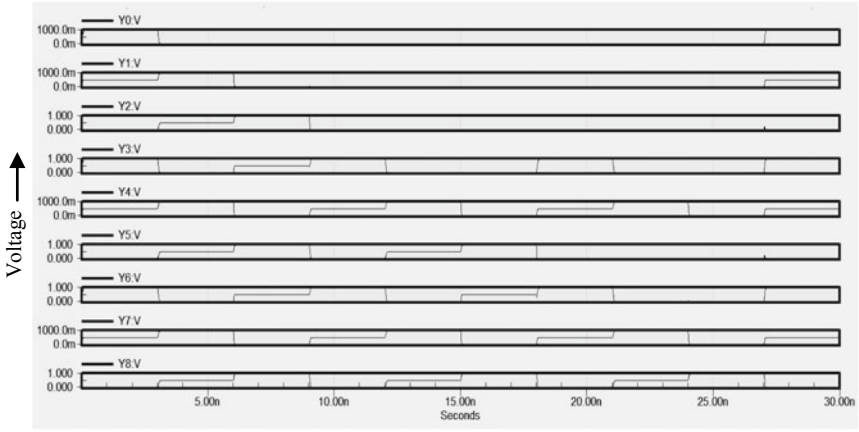

(b)

Fig. 4 **a** Selection input. **b** Right shift 9-trit T-Barrel shifter output. **c** Right rotate 9-trit T-Barrel shifter output

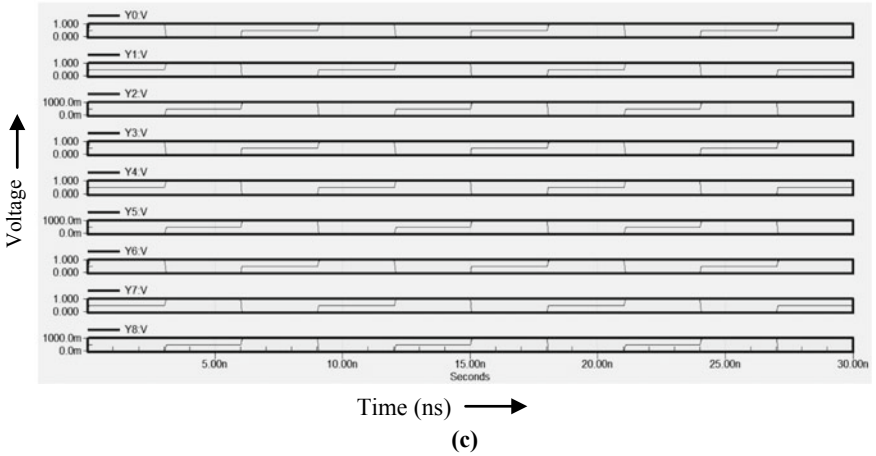

(c)

Fig. 4 (continued)

Table 3 Evaluated result of proposed T-barrel shifter for shift and rotate operation

Barrel shifter operation	Total nodes	Active device	Avg. power (μW)	Delay (ps)	PDP (PJ)
Right-shift	2497	558	172.57	43.08	7.43×10^{-3}
Right-rotate	2731	612	174.06	50.07	8.72×10^{-3}

References

1. Neerja, B., Ramya, K.: Design and analysis of an energy efficient 4-bit Barrel Shifter circuits in 45nm technology. Int. J. Eng. Adv. Technol. (IJEAT) **9**(4), 885–890 (2020)
2. S. Kotiyal and H. Thaliyal, "Design Methodologies for Reversible Logic Based Barrel Shifters," *Journal of Circuits, Systems and Computers, World Scientific,* vol. 25, no. 2, pp. 1650003(1–34), 2016.
3. Nowrin, S., Jamal, L., Babu, H.M.H.: Design of an optimized reversible bidirectional barrel shifter. In: IEEE International Symposium on Circuits and Systems (ISCAS), pp. 730–733 (2016)
4. Pradeep, T.: Logarithmic reversible barrel shifter. In: IEEE International Conference on Advanced Communication Control and Computing Technologies (ICACCCT), pp. 153–156 (2012)
5. Das, S., Khatri, S.P.: A timing-driven approach to synthesize fast barrel shifters. IEEE Trans. Circuits Syst. II Express Briefs **55**(1), 31–35 (2008)
6. Saha, A., Pal, D.: DPL-based novel binary-to-ternary converter on CMOS technology. In: AEU-International Journal of Electronics and Communications (IJEC), vol. 92, pp. 69–73. Elsevier (2018)
7. Saha, A., Pal, D.: DPL-based novel time equalized CMOS ternary-to-binary converter. In: International Journal of Electronics (IJE), vol. 107, no. 3, pp. 431–443. Taylor & Francis
8. Saha, A., Singh, R.K., Gupta, P., Pal, D.: DPL-based novel CMOS 1-trit ternary full-adder. In: International Journal of Electronics (IJE), vol. 108, no. 2, pp. 218–236. Taylor & Francis (2020)

9. Saha, A., Singh, N.D.: Systematic design strategy for DPL-based ternary logic circuit. In: Special Issue on: 2018 IEEE EDKCON Recent Advances in Nano-Electronic Devices and Technology, International Journal of Nanoparticles (IJNP), Inderscience, vol. 12, no. 1–2 (2019)
10. Saha, A., Singh, N.D., Pal, D.: Efficient ternary comparator on CMOS technology. In: Microelectronics Journal, vol. 109. Elsevier (2021)
11. Wu, X.W.: CMOS ternary logic circuits. In: IEEE Proceedings, vol. 137, Pt. G, no. 1, pp. 21–27 (1990)
12. S. L. Hurst, "Multiple-valued logic: Its status and its future," *IEEE Transactions on Computers*, vol. C-33, no. 12, pp. 1160–1179, Dec. 1984.
13. Srinivasu, B., Sridharan, K.: A synthesis methodology for ternary logic circuits in emerging device technologies. In: IEEE Transactions on Circuits and Systems–I: Regular Papers, Vol. 64, no. 8, pp. 2146–2159 (2017)
14. Lisa, N.J., Md., H., Babu, H.: A compact representation of a quantum controlled ternary barrel shifter. In: IEEE International Symposium on Circuits and Systems (ISCAS) 2015, pp. 2145–2148, 24–27. Lisbon, Portugal (2015)
15. Kotiyal, S., Thapliyal, H., Ranganathan, N.: Design of a ternary barrel shifter using multiple-valued reversible logic. In: Proceedings of 10th IEEE International Conference on Nanotechnology, pp. 1104–1108, 17–20 August. Korea (2010)

Design and Analysis of Quaternary to Binary Radix Converter Using SOA-PRS

Ashif Raja, Kousik Mukherjee, and Jitendra Nath Roy

Abstract This paper reports a new design of a quaternary to binary radix converter. Semiconductor optical amplifier-based polarization rotation switches (SOA-PRS) have been used for the basic switching element in the design. A dual-SOA structure is utilized to design the circuit. The design is simple, made off only two SOAs. The circuit performance has been analyzed with a Gaussian pulse train, and the extinction ratio has been calculated. The simulation work is done at an ultra-high data rate (100 Gb/s). SOA-based design is simple and compact than other switching structures. The SOA-PRS works on the principle of the cross-polarization modulation (XpolM) effect.

Keywords Semiconductor optical amplifier · Cross-polarization modulation · Radix converter

1 Introduction

Multivalued logic-based circuit design is the most interesting and practically important field of research. Some multivalued electronic [1, 2] and optical [3–12] circuits have been designed in the last decade. The performance of optical circuits is always better than electronic circuits in all aspects [3]. Whether in the case of power consumption, noise, thermal fluctuation, longevity, speed of operation, etc., optical technology establishes its superiority over electrical and electronic technology. Lots of arithmetic logical units have been designed using all-optical switches (active and passive). Lots of switching structures have been implemented for this purpose.

A. Raja (✉) · J. N. Roy
Kazi Nazrul University, Asansol, West Bengal, India

K. Mukherjee
B. B. College, Asansol, West Bengal, India

K. Mukherjee · J. N. Roy
Centre for Organic Spintronics and Optoelectronics Devices (COSOD), Kazi Nazrul University, Asansol, West Bengal, India

B. Sikdar et al. (eds.), *Proceedings of the 3rd International Conference on Communication, Devices and Computing*, Lecture Notes in Electrical Engineering 851,
https://doi.org/10.1007/978-981-16-9154-6_9

Design of binary to decimal and decimal to binary number converter is proposed in [4] using surface stimulated ferro-electric liquid crystal (SSFLC). But the triggering voltage is high, and the switching speed is limited in SSFLC. All-optical conversion scheme from binary to modified trinary number (MTN) is proposed in [5] using nonlinear materials (NLM). But the use of high-power laser sources (~MW) makes the designs expensive for practical use. Designs of all-optical radix converters have been reported in [6, 7] using passive elements. But the circuits using passive elements are not suitable for modern optical integrated circuits. Alignment and fitting of passive optical elements in a particular design are very difficult and mainly for the higher-order circuits. These passive circuits also need high-power optical sources. Terahertz optical asymmetric demultiplexer (TOAD) based binary to its 2^n radix converter has been proposed in [8]. But TOAD is an asymmetric interferometric structure, where the signals move in a different path of unequal length and combine in an external coupler to interfere. Then, the structure deals with phase handling problems and noise. A common problem in these circuits is the output power fluctuation due to polarization-dependent loss.

In this communication, we have designed a quaternary to binary radix converter using the dual-SOA structure [13] with SOA-PRS switches [14–18]. The SOA-PRS switch works on the principle of cross-polarization modulation (XpolM) or nonlinear polarization rotation (NPR) effect in SOA. In this switch, the SOA is biased with low-power electrical (~160 mA) and optical (<1mW) sources. In most of the switching structures (TOAD, MZI) and designs, a common problem is handling the phase and polarization of signals. But in the nonlinear polarization rotation or cross-polarization modulation effects of SOA, we have utilized the polarization-sensitive property as the main tool of switching. The phase change happens internally within the cavity of SOA. So we have to choose only some suitable parameters of the switch [9]. The operation of the radix converter is expressed in terms of polarization encoding scheme utilizing quaternary (4) states of polarization of optical signal (where 0, 1, 2, and 3 represent no light, horizontally polarized light, vertically polarized light, and mixed polarized light, respectively) [18]. We have designed an SOA-PRS based binary to quaternary radix converter reported in [19]. The SOA-based switches are always preferable for compactness (<1 mm in length), variety of nonlinear effects, fast gain recovery, and wide gain bandwidth [20–22].

2 Operation of the SOA-PRS

The basic theory of operation of SOA-PRS based switches is based on nonlinear polarization rotation in SOA. The parameters and mathematical models are described in [14, 15]. We have also implemented the theory in our previous communications to design some binary and multivalued operational circuits [13, 17–19]. Our simulation work is based on the time-dependent solutions of the “rate equations” of SOA. Most

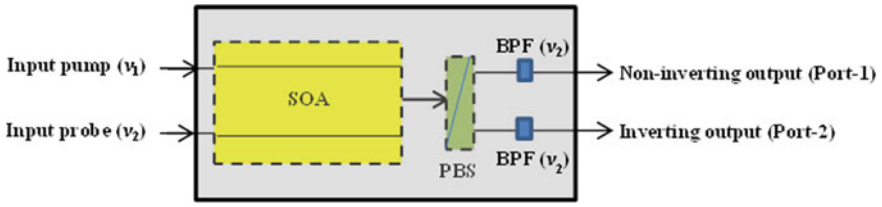

Fig. 1 Design of the SOA-PRS

of the simulation work is done with MATLAB computational program. The time-dependent solutions will lead to the real change in the transfer functions, the pulse shape, and the extinction ratio.

The switch has two input and two output ports. In the input ports, we can apply a high-intensity pump ($\leq$0.5 mW) and a low-intensity probe signal (~0.023 mW). The output port-1 is known as the non-inverting port where the polarization rotated probe signal will emit in presence of the pump signal. The second output port is known as the inverting port. In this port, the output signal intensity decreases with the increase in the intensity of the pump signal and vice versa. At the high intensity of the pump signal (0.5 mW), the output probe power will be zero. The plot of variation in the output power with input pump power for both ports 1 and 2 has already been shown in our papers related to cross-polarization modulation in SOA [17–19].

The effect of amplified spontaneous emission (ASE) [21] noise is present when the intensity is considered for high and low state pulses of the output signal in both of the ports. When the pump and probe both are present, we get a high state in port-1 and a low state in port-2. When the probe is absent, we get nothing at the output ports no matter whether the pump is present or not. When the pump is absent and the probe is present, we get a low state in port-1 and a high state in port-2. If the input probe signal is horizontal and the pump is present, then we get a vertical signal at port-1 and vice versa. A polarity of mixed polarized probe signal will remain unchanged after rotation by 90 degrees in presence of a pump signal. The block diagram of the SOA-PRS switch is shown in Fig. 1. The circuit needs one polarization-sensitive bulk-strained SOA, one polarization beam splitter (PBS), and two band-pass filters (BPF). The truth table of the SOA-PRS is given in Table 1.

3 Design and Operation of a Quaternary to Binary Converter

A quaternary to binary converter converts each quaternary number to its equivalent binary number. The device converts quaternary 0, 1, 2, and 3 to their binary numbers $< 00 >$, $< 01 >$, $< 10 >$, and $< 11 >$, respectively. Our all-optical quaternary to binary radix converter does the same thing. The output signals corresponding to the most significant bit (MSB) and least significant bit (LSB) can also be used as the

Table 1 Truth table of SOA-PRS

Pump	Probe	Port-1	Port-2
Present (1, 2, 3)	0	0	0
Present (1, 2, 3)	1	2	0
Present (1, 2, 3)	2	1	0
Present (1, 2, 3)	3	3	0
Absent (0)	0	0	0
Absent (0)	1	0	1
Absent (0)	2	0	2
Absent (0)	3	0	3

Table 2 Truth table for quaternary to binary radix converter

Quaternary input	Binary output	
Pump (Y)	MSB (A)	LSB (B)
0	0	0
1	0	1
2	1	0

two inputs of a binary optical logic gate. So we get the benefit of two optical sources utilizing only one optical source. So, this radix converter is useful to design complex circuits. The truth table of the quaternary to binary radix converter circuit is given in Table 2.

The design of the radix converter is shown in Fig. 2. The circuit needs two SOA-PRS, two polarization analyzers (PA), and few polarization controllers (PC) to perform the desired operation. The quaternary numbers enter the input port Y of

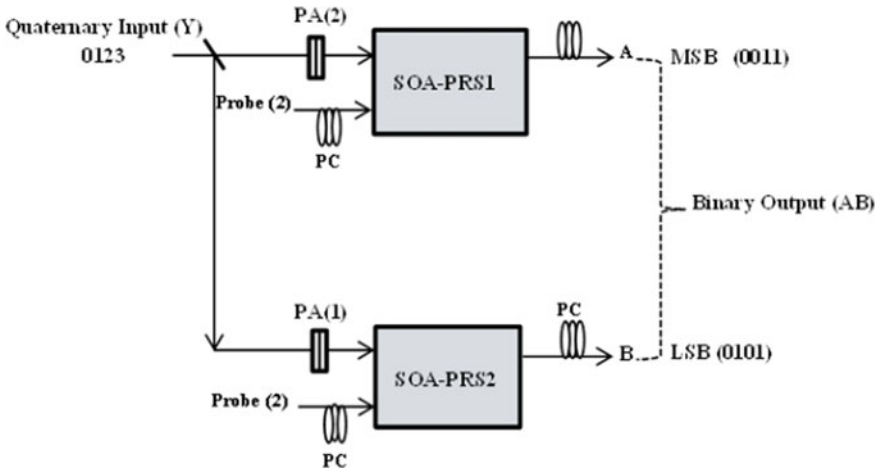

Fig. 2 Design of quaternary to binary radix converter

the design as a control signal for SOA-PRS 1 and SOA-PRS2. Probe (2) represents a vertically polarized probe signal. A and B outputs represent the MSB and LSB of binary numbers, respectively. PA (2) and PA (1) are the polarization analyzers passing vertically (2) and horizontally (1) polarized light, respectively.

Case 1 When $Y = 0$, both the pump signal for SOA-PRS 1 and SOA-PRS 2 are absent. So, both of the switches emit 0 from their non-inverting ports. Then, we have $A = B = 0$. The combination of AB represents binary 0 (00).

Case 2 When $Y = 1$, only SOA-PRS 2 receives a control signal. Then, the vertically polarized probe signal of SOA-PRS 2 will be converted to a horizontally polarized (1) signal due to NPR. In absence of the pump signal, SOA-PRS 1 emits no signal. Then, the final outputs $A = 0$ and $B = 1$. The combination of AB gives binary 1 (01).

Case 3 When $Y = 2$, only SOA-PRS 1 receives a vertically polarized control signal. Then, the vertically polarized probe signal of SOA-PRS 1 will be converted to a horizontally polarized (1) signal due to the NPR effect. In absence of the pump signal, SOA-PRS 2 emits 0. Then, the final outputs $A = 1$ and $B = 0$. The combination of AB will give binary 2 (10).

Case 4 When $Y = 3$, both of the SOA-PRS will have their control signals. In that case, both of the switches emit a polarization rotated signal at their output. So we get $A = B = 1$. The combination of AB gives binary 3 (11).

4 Results and Discussion

For a better understanding of the operational efficiency of the radix converter circuit, we have mathematically generated a Gaussian pulse train using Eq. 1 and, as shown in Fig. 3. After passing through the SOA-PRS, the output signals are still Gaussian and are shown in Figs. 4 and 5. The mathematical equations used in the simulation work are mentioned in the "Appendix" section.

4.1 Extinction Ratio of the Design

We have shown the variation of extinction ratio (ER) with pump power at different probe power and the different noise factor in Figs. 6 and 7, respectively.

4.2 The Pseudo Eye Diagram of the Design

We have shown the pseudo-eye diagram of the design in Fig. 8. We can see distinct high (Blue colored) and low states (Yellow colored) in the diagram. The high states

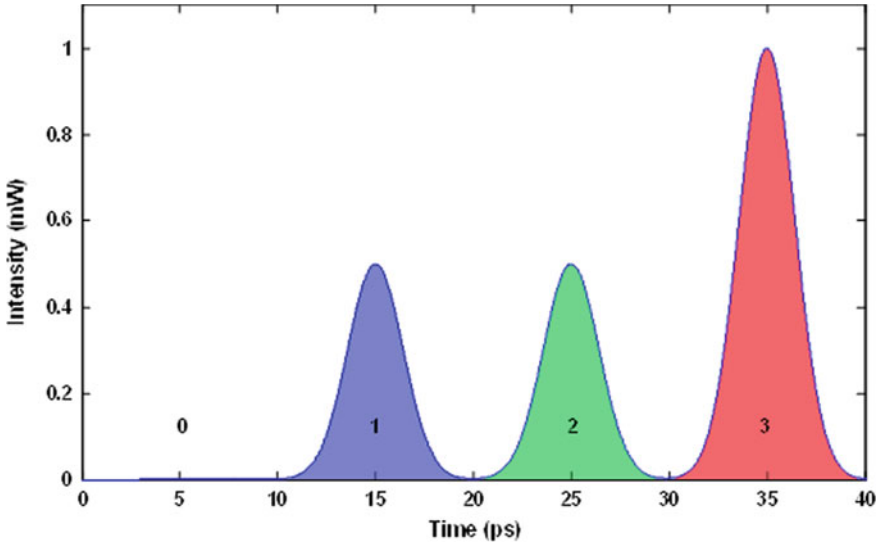

Fig. 3 Signal Y representing quaternary input

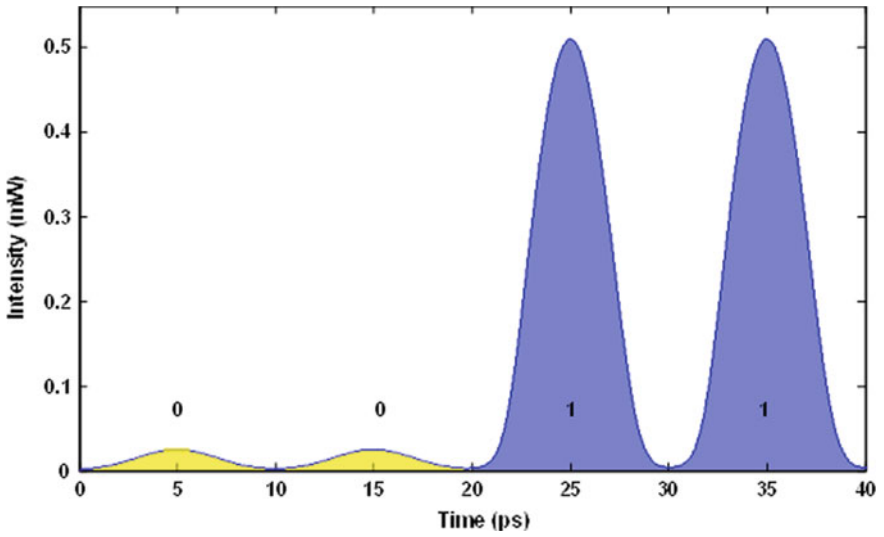

Fig. 4 Signal A representing MSB of binary output

only differ by the additive ASE noise. The noise factor is very small in presence of the pump signal. We get a very sharp "relative eye-opening" (~90%) from the diagram.

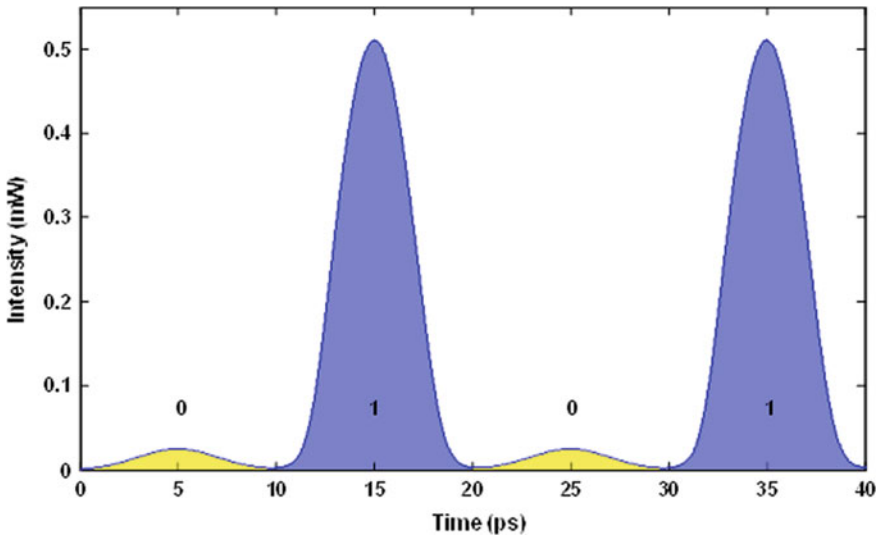

Fig. 5 Signal B representing LSB of binary output

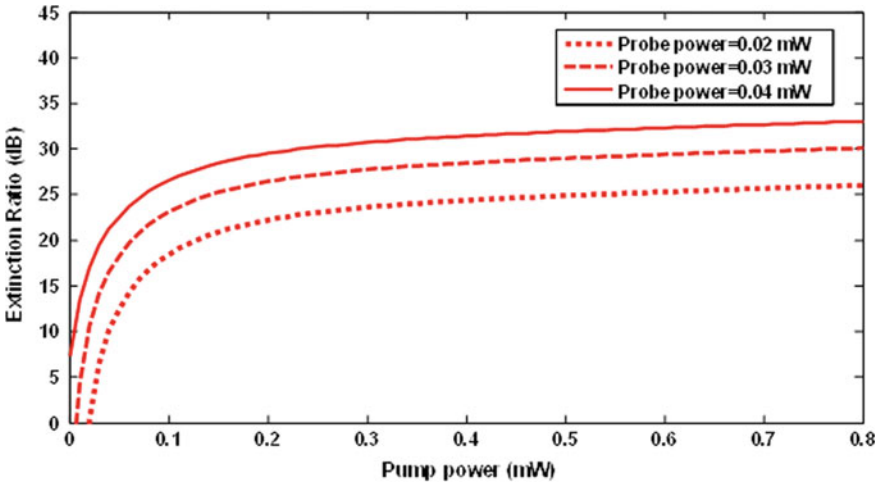

Fig. 6 ER versus pump power at different probe power

5 Conclusion

The design is simple and compact. The SOA-PRS based switches have the advantage of using two output ports with a very simple setup. The switch is free from the outer phase handling problem of interfering signals, which occurs in interferometric switching structures like TOAD and SOA-MZI. The simulation work is performed

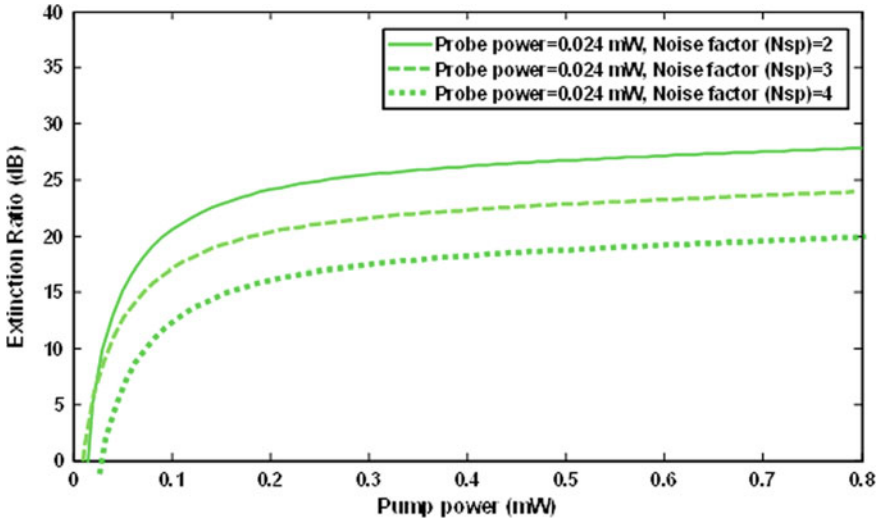

Fig. 7 ER versus pump power at different noise factor

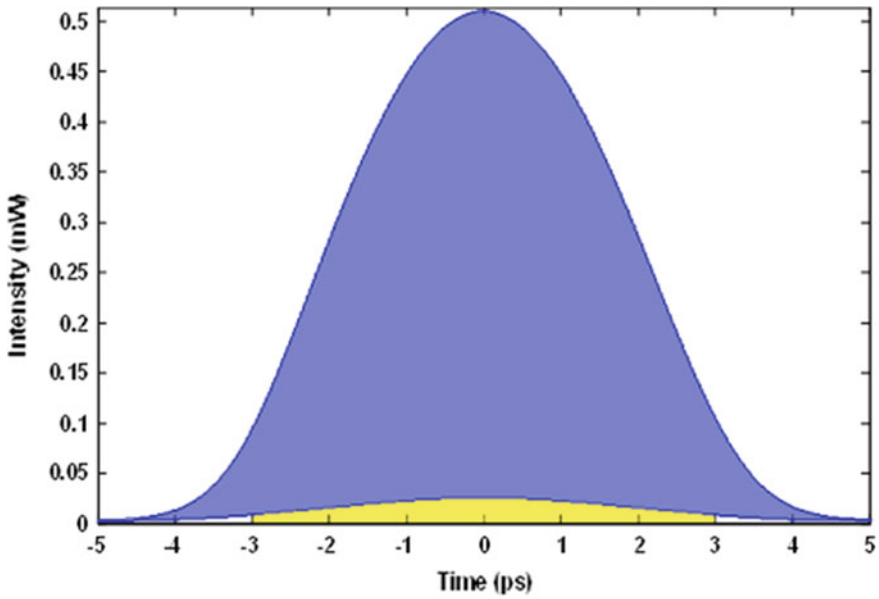

Fig. 8 Pseudo eye diagram of the circuit

with a high-speed data signal (~100 Gb/s), and we get a less distorted output signal. We get a practically acceptable value of extinction ratio (>10 dB). The binary to quaternary and quaternary to binary radix converter can be used as the encoder–decoder device in quaternary logic-based designs (adder, multiplier, etc.) made of binary units (logic gates) [23]. The quaternary to binary radix converter also reduces the number of light sources because it generates two different signals at the output from a single input. The polarity of the signals is sometimes affected by the heating effect and can be adjusted using polarization controllers (PC). The circuit can also be implemented in other multi-bit radix converters and higher-order complex designs.

Appendix

The Gaussian-shaped output pulses used in each of the input signals of the circuit can be expressed in Eq. 1 as,

$$P = P_0 \sum_i \exp\left(\frac{t_i^2}{\sigma^2}\right)$$
$$\text{where, } P_0 = \frac{1}{\sigma\sqrt{\pi}} \text{ and } \sigma = \frac{T}{1.665}. \tag{1}$$

where, P_0, T and t represent "maximum power", "full width at half maximum (FWHM)" and the "bit-period" respectively.

A time-dependent solution of the rate equation is utilized. The output power of the polarization rotation switch from Port-1 is given by [14, 15]

$$P_{\text{out}} = P^{\text{TE}} + P^{\text{TM}} - 2\sqrt{P^{\text{TE}} P^{\text{TM}}}\cos(\theta) \tag{2}$$

where, P^{TE} and P^{TM} are the respective intensities of TE and TM components of the output probe signal. θ, is the phase difference between TE and TM components.

The small peaks arise due to the noise effects produced by the SOA's and mainly the Amplified Spontaneous Emission effect [17, 21] expressed as (Eq. 3),

$$P_{\text{ASE}} = N_{\text{SP}}.h.(G-1)B \tag{3}$$

where, G is the gain, h Planck's constant, B optical bandwidth of a filter within which P_{ASE} is determined, $N_{\text{sp}}$is the spontaneous emission factor or noise factor (~1 for ideal amplifier).

The Extinction Ratio [17] of the design can be calculated using Eq. 4,

$$\text{ER} = 10.\log_{10}\left(\frac{P_1^{\min}}{P_0^{\max}}\right) \tag{4}$$

where P_1^{min} represents the minimum power in high state 1 and P_0^{max} represents the maximum power in low state 0. The plots of the ER versus pump power at different probe power and noise factor are shown in Figs. 6 and 7 respectively in the "Results and Discussion" section.

References

1. Hurst, S.L.: Multiple-valued logic—it's status and its future. IEEE Trans. Comput. C-33, 1160–1179 (1984)
2. Park, S.J., Yoon, B.H., Yoon, K.S., Kim, H.S.: Design of quaternary logic gate using double pass-transistor logic with neuron MOS down literal circuit. In: 34th International Symposium on Multiple-valued logic, pp. 198-203, Toronto (2004), https://doi.org/10.1109/ISMVL.2004.1319941
4. Roy, J.N., Chattopadhyay, T.: All-Optical quaternary logic-based information processing: challenges and opportunities. Des. Archit. Digital Signal Proc. **04**, 81–109 (2013). https://doi.org/10.5772/51559
5. Mukhopadhyay, S.: An optical conversion system: from binary to decimal and decimal to binary. Optics Commun. **76**, 309–312 (1990)
6. Maity, A.K., Roy, J.N., Mukhopadhyay, S.: All-optical conversion scheme from binary to its MTN from with the help of non-linear material based tree-net architecture. Chin. Opt. Lett. **05**, 480–483 (2007)
7. Chattopadhyay, T., Roy, J.N.: All-optical conversion scheme: binary to quaternary and quaternary to binary number. Opt. Laser Technol. **41**, 289–294 (2009)
8. Chattopadhyay, T., Roy, J.N.: An all-optical technique for a binary-to-quaternary encoder and a quaternary-to-binary decoder. J. Opt. A: Pure Appl. Opt. **11**, 1–8 (2009)
9. Roy, J.N., Maity, G.K., Gayen, D.K., Chattopadhyay, T.: Terahertz optical asymmetric demultiplexer based tree-net architecture for all-optical conversion scheme from binary to its other 2^n radix based form. Chin. Opt. Lett. **6**, 536–540 (2008)
10. Chattopadhyay, T., Taraphdar, C., Roy, J.N.: Quaternary Galois field adder based all-optical multivalued logic circuits. Appl. Opt. **48**, E35–E44 (2009)
11. Mandal, S., Maity, G.K., Bhattacharya, A., Taslim, A.K.A.H.: All-optical quaternary MIN gate and quaternary delta literals using MZI.: In: International Conference on Inventive Communication and Computational Technologies, pp. 313–317, Coimbatore (2017)
12. Gorai, S.K.: Method of developing all-optical trinary JK, D-type and T-type flip-flops using semiconductor optical amplifiers. Appl. Opt. **51**, 1757–1764 (2012)
13. Ghosh, P., Mukhopadhyay, S.: Implementation of tristate logic-based all-optical flip-flop with nonlinear material. Chin. Opt. Lett. **3**, 478–479 (2005)
14. Raja, A., Mukherjee, K., Roy, J.N.: Analysis of new all-optical polarization-encoded Dual SOA-based ternary NOT and XOR gate with simulation. Photon Netw. Commun. **41**, 242–251 (2021)
15. Dorren, H.J.S., Lenstra, D., Liu, Y., Hill, M.T., Khoe, G.D.: Nonlinear polarization rotation in semiconductor optical amplifiers: theory and applications to all-optical flip flop memories. IEEE. J. Quant. Elect. **39**, 141–148 (2003)
16. Zhang, S., Liu, Y., Zhang, Q., Li, H., Liu, Y.: All-optical sampling based on nonlinear polarization rotation in semiconductor optical amplifiers. J. Optoelectron. Biomed. Mater. **1**, 383–388 (2009). https://doi.org/10.1007/s10825-019-01393-5
17. Guo, L.Q., Connelly, M.J.: Signal induced birefringence and dichorism in a tensile-strained bulk semiconductor optical amplifier and its application to wavelength conversion. J. Lightwave Technol. **23**, 4037–4045 (2005)

18. Raja, A., Mukherjee, K., Roy, J.N.: Design, analysis, and application of all-optical multi-functional logic using semiconductor optical amplifier-based polarization rotation switch. J. Comput. Electron. (2020). https://doi.org/10.1007/s10825-020-01607-1
19. Raja, A., Mukherjee, K., Roy, J.N., Maji, K.: Analysis of all-optical polarization-encoded quaternary Galois field adder processing soliton pulses. J. Opt. (2020). https://doi.org/10.1007/s12596-020-00594-7
20. Raja, A., Mukherjee, K., Roy, J. N.: All-optical Binary to Quaternary Radix Converter using SOA-PRS.: In: International Conference on Evolving Materials and Nanotechnology for Sustainable Development, Kokrajhar (2020)
21. Zoiros, K.E.: Special issue on applications of semiconductor optical amplifiers. Appl. Sci. **8**, 1185 (2018)
22. Said, Y., Rezig, H.: SOAs nonlinearities and their applications for next generation of optical networks. Adv. Opt. Amplifiers **2**, 27–52 (2011)
23. Cleary, C.S., Power, M.J., Schneider, S., Webb, R.P., Manning, R.J.: Fast gain recovery rates with strong wavelength dependence in a non-linear SOA. Opt. Express **18**, 25726 (2010)
24. Roy, J.N., Chattopadhyay, T.: All-optical quaternary computing and information processing: a promising path. J. Optics **42** (2013). https://doi.org/10.1007/s12596-013-0126-0

Stock Price Prediction Using Deep Learning-Based Univariate and Multivariate LSTM and RNN

Akash Ranjan and Asim Kumar Mahadani

Abstract Stock market has always been uncertain in terms of prediction, and it attracts the attention of all the stakeholders to predict the stock price. We have used different deep learning techniques, namely recurrent neural network (RNN) and long short-term memory (LSTM) to model our problem. The models or approaches which have been used yet are mainly build on simple linear regression like ARIMA that does not make use of full dataset and only keep one aspect in consideration for predicting the stock price, i.e., nonlinear univariate models like TAR, ARCH, etc. The prime objective of this paper is to predict the best fit machine learning model for predicting stock price. In this paper, we have compared LSTM, bi-directional LSTM, and RNN models with univariate and multivariate features. For all the models, we have set same training parameters like epochs, timesteps, neurons in each layer, learning rate and batch size. We have estimated the effectiveness of our study by using the following performance criteria: the root mean square error (RMSE) and the mean square error (MSE). As per our analysis, it has been found that recurrent neural network approach having high accuracy either with univariate or multivariate to solve the problem of prediction of stock prices.

Keywords LSTM · RNN · Stock price prediction · Deep learning

1 Introduction

It has always been a challenging task for market experts to predict a stock price. This prediction mainly comes before buying the stocks which is supposed to increase in term of price, and latter stocks are sold before the fall. Stock market prediction is mainly done in two ways. Firstly, fundamental analysis as in fundamental analysis mainly concentrates over the market, growth rate, expenditures, etc. information of some particular companies and mainly dependent on company's policies. Second is the technical analysis method, which mainly focuses on the earlier chats and pattern

A. Ranjan · A. K. Mahadani (✉)
Department of Computer Science and Engineering, Bankura Unnayani Institute Engineering, Bankura, India

B. Sikdar et al. (eds.), *Proceedings of the 3rd International Conference on Communication, Devices and Computing*, Lecture Notes in Electrical Engineering 851,
https://doi.org/10.1007/978-981-16-9154-6_10

to predict the growth of stocks. A few years back, this method was quite common in financial experts for grasping the nerves of stock market [1, 2]. But today with the progress of time, we have developed more efficient ways even in predicting the stock market likewise analysis of data by data scientists and involvement of computer scientists over these data using their machine learning methods. These methods improve the performance and accuracy of predictions. Moreover, deep learning would be an upgrade in predicting stock prices [3, 4]. Prediction in stock market can be a hard nut to crack, but with the support of data scientist, it can be eased up. It can be said, with data science beside stock market, prediction will just become a calculative move for the financial experts.

We have explored different kinds of deep learning techniques which result in improving the performance, reliability in prediction, and reduce the complexities of algorithms. The techniques are RNN and LSTM.

Gao et al. [5] has studied three different kind of machine learning models, namely convolutional neural network (CNN), multilayer perception (MLP), and long short-term memory (LSTM) and one attention-based neural network. In this paper, the focus is on predicting the next day stock price as per the historical dataset. There are seven variables that are taken into consideration as per input involves daily data, macroeconomic variables, and technical indicators. This paper showed that attention-based model has better performance compared to other alternative models, and it is able to explain the relationship among nonlinear time series which is a tough task due to low signal–noise ratio and huge noise in nonlinear series [5]. This paper did not explore combination of linear and nonlinear model using an exponential smoothing method to predict stock price.

Ghosh et al. [6] have studied the model that depends on long short-term memory (LSTM) that would be used to calculate the company's net growth and helped to predict the future growth of the company. To train the model from the past data and to take futuristic decision on prediction, artificial neural network (ANN) played a vital role and used deep learning networks like recurrent neural network (RNN), convolutional neural network (CNN), etc., which works well with multivariate time series data. The main advantage in this paper is that long short-term memory (LSTM) which is particular type of recurrent neural network (RNN) is based fit for predicting future company's growth of different sector as per the past stock prices [6]. The weakness in this paper is that it has taken only one factor from dataset into consideration while predicting future stock price.

Khaled et al. [7] have studied the models that depend on deep recurrent neural network, i.e., GRU and LSTM. This paper uses deep recurrent neural network focused on GRU and LSTM which compared and evaluated a number of variants while training the models. It considered both unidirectional and bi-directional stacked architectures with multi-variate inputs while performing long-term and short-term forecasting, and stacked LSTM architecture is showing better forecasting performance for both long and short term [7]. The article did not explore other deep recurrent neural networks models like bi-directional LSTM, simple RNN, CNN, etc.

Menon et al. [8] have studied the Indian National Stock Exchange dataset for the financial domain problem, and he has done predictions for many companies

with accurate estimation which is used in algorithmic trading. In this paper, a few discussions on these primitive classy models like GARCH, ARMA, ARIMA, and ARCH are been implemented through spark jobs for processing huge amount of data and forecast the result in faster and efficient way [8]. This paper did not explore deep recurrent neural network models and only focused on univariate models.

It is been proved that deep learning algorithms are able to recognize the existing patterns in the data and utilizing them with the use of soft computing process. Like other machine learning and statistical algorithms, deep learning architectures are efficient to find dependencies for both long and short term in the data and provide better predictions by linking those hidden relationships [9].

There are lot of opportunities to compare more variety of deep learning algorithms like different variant of LSTM and RNN model. Above all studies focused on specific type of use cases like linear or nonlinear. They have to try some new features of LSTM like bi-directional learning of neurons. They have not considered different variate of parameters like open, close, high, low, volume, etc., in their prediction approach. There is a huge gap in prediction result, depending on the features we choice for our training model process [10, 11].

2 Purpose of Our Study

We want to explore more on the variant side along with different -deep learning models. Most of the studies are more focused on long short-term memory (LSTM) and gated recurrent unit (GRU). Simple LSTM may not perform better alone because it is one-directional training model having forget gate, input gate, and output gate, and GRU is also a LSTM without any output gate. So, we tried bi-directional LSTM that has high accuracy as compared with simple one-directional LSTM. Next level, we tried with simple RNN model which has again higher accuracy as compared with bi-directional LSTM [12–14].

After the model selection, we trained our model on two different types of dataset, first on dataset with close price series; thus, it is a univariate model and secondly dataset having series of high, volume and close price of the stock, thus it is a multivariate model.

For each model, i.e., LSTM, bi-directional LSTM, and RNN, we have studied with univariate and multivariate features with same set of training parameters like epochs, timesteps, neurons in each layer, learning rate and batch size. Finally, we found univariate RNN having highest accuracy followed by multivariate RNN.

3 Methodology

For our study, we have collected the historical dataset of Google.com, Inc. (GOOG) stock obtained from Kaggle. It has 5982 records of daily stock prices of the stock.

Every record is having details of low, high, closing, and opening value of stocks along with the precise amount of stock sold on that particular day.

Before training the model, first we clean our dataset before processing by removing the noisy data and some redundant data like the records which are identical to previous record and records having volume 0. Then, we use Min–Max normalization that will convert the values into the range of 0–1.

After preprocessing the dataset, we will train our model using three different deep learning architectures such as LSTM, bi-directional LSTM, and RNN for our research. Finally, each model has been evaluated based on the test dataset and their respective R2 score, MSE (Mean Squared Error) and RMSE (Root Mean Squared Error) have been calculated.

4 Result and Discussion

Google dataset from Kaggle has been used for this analysis.

All models have been trained with the below parameters:

(i) Batch size: 32,
(ii) Time steps: 30,
(iii) Neurons in each layer: 50 and 45, and
(iv) Learning rate: 0.001.

As per the above parameters, the model is trained using the training dataset for 200 epochs and validation dataset is used to validate the model.

First of all, model has been divided into two categories based on number of fields taken into consideration for stock market analysis:

1. Univariate - > has “CLOSE” attribute
2. Multivariate - > has “CLOSE,” “HIGH,” and “VOLUME” attributes.

Then, for each variate, we have done analysis on three models:

1. LSTM, 2. bi-directional LSTM, 3. RNN.

Amazon (AMZN) dataset from Kaggle has been used for the comparison for the same parameters and models where RNN again proves to be better model compared to LSTM and bi-directional LSTM.

As per the above result, it is clear that univariate having higher R-squared scores when compare to multivariate and univariate RNN has highest R-squared score even multivariate RNN has better R-squared score as compared with others multivariate models. So, as per our analysis, we can conclude that RNN model is the better model for stock market analysis (Figs. 1, 2, 3, 4, 5 and 6).

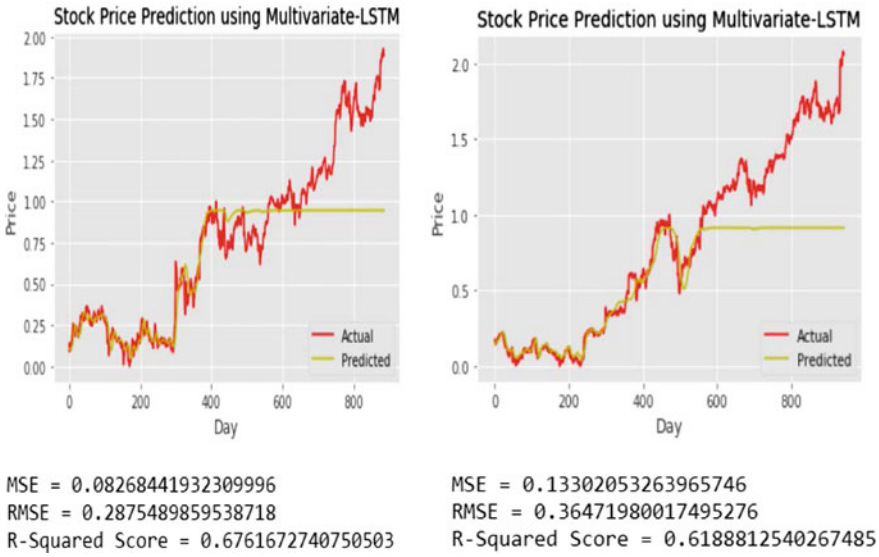

Fig. 1 Multivariate LSTM for google (*left side*) and Amazon (*right side*)

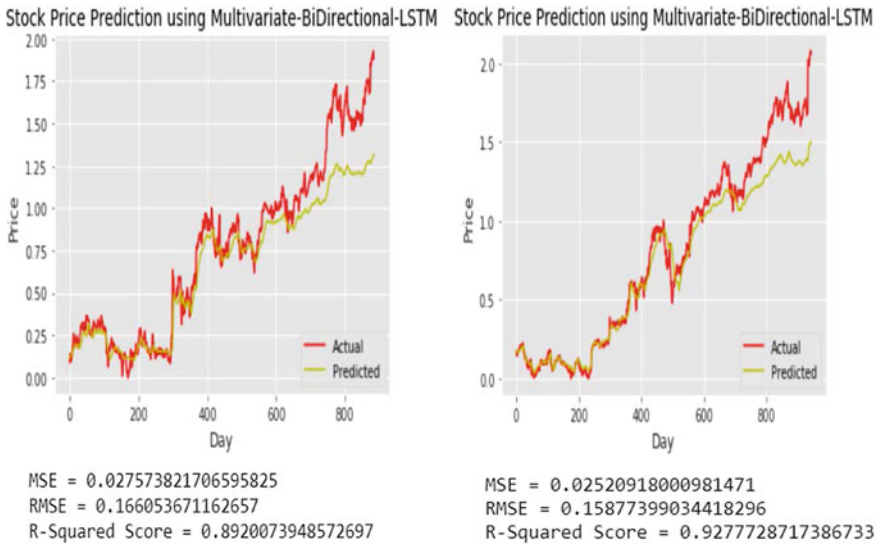

Fig. 2 Multivariate bi-directional LSTM for google (*left side*) and Amazon (*right side*)

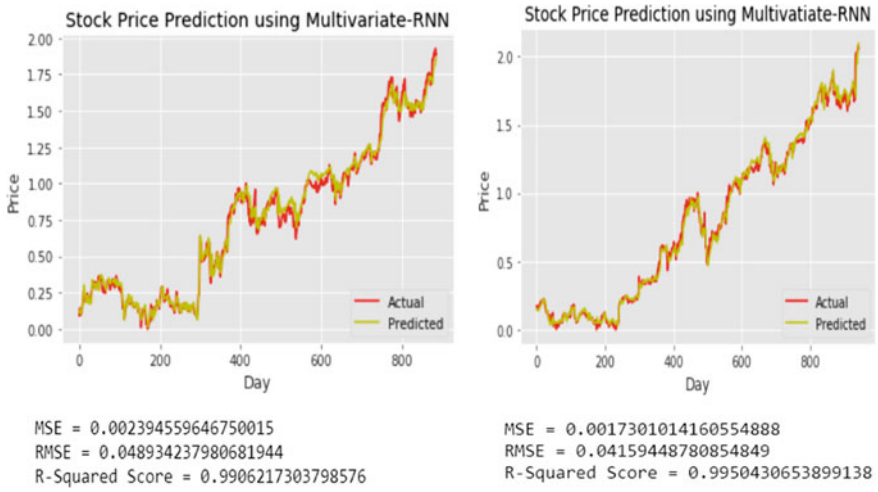

Fig. 3 Multivariate RNN for google (*left side*) and amazon (*right side*)

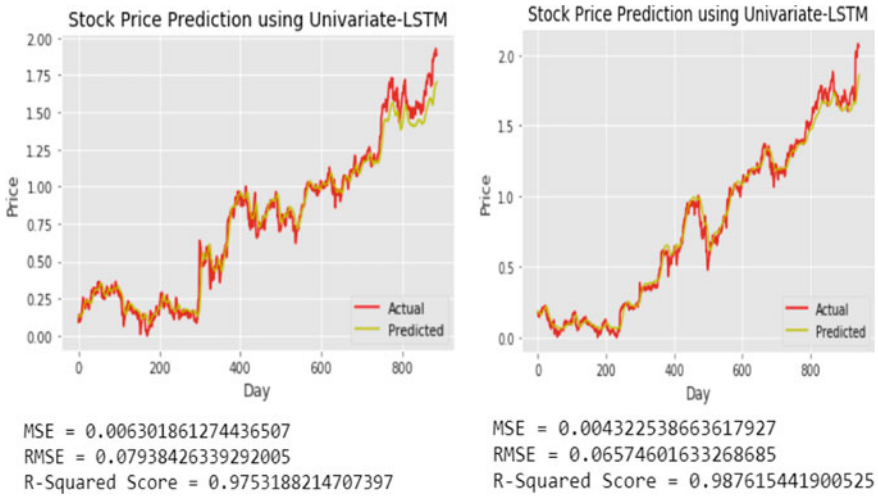

Fig. 4 Univariate LSTM for google (*left side*) and amazon (*right side*)

5 Conclusions and Future Scope

We have proposed a recurrent neural network approach is the best fit to solve the stock price prediction problem. We have concluded that RNN model is the better model for stock market analysis either with univariate or multivariate and improves both efficiency and performance of the prediction of stock price. We proposed a

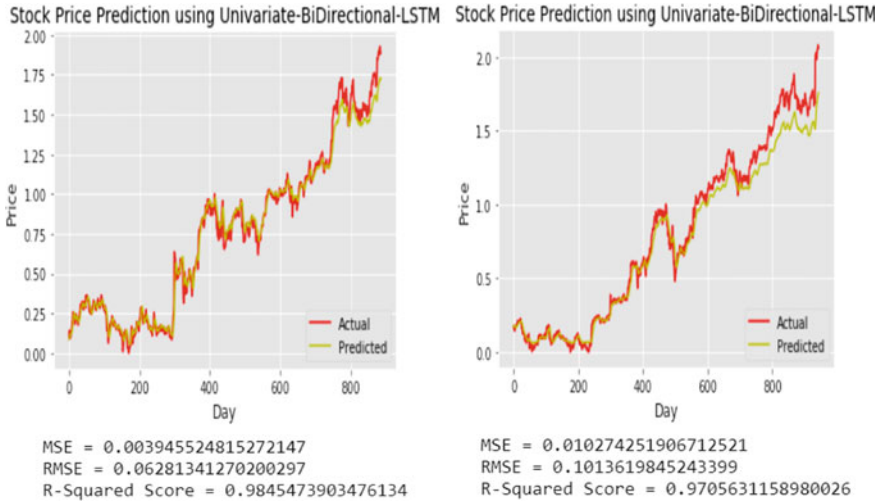

Fig. 5 Univariate bi-directional LSTM for Google (*left side*) and Amazon (*right side*)

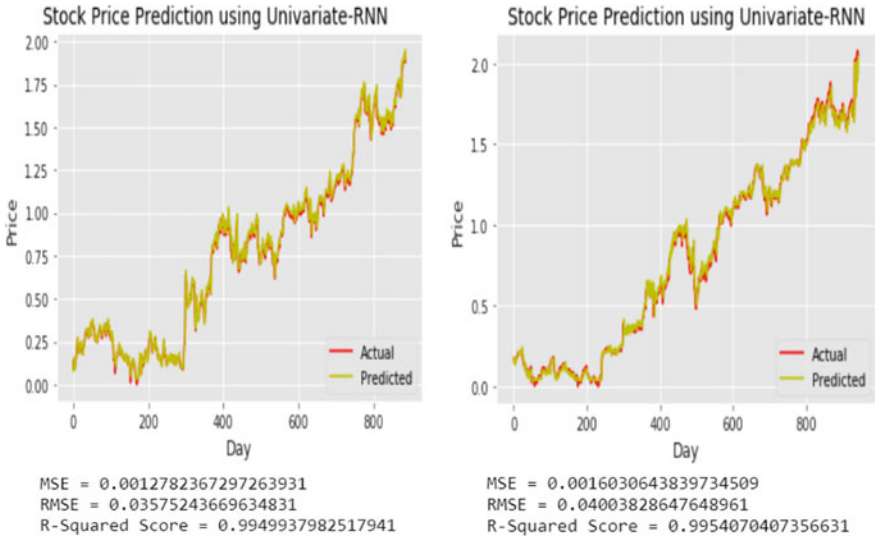

Fig. 6 Univariate RNN for google (*left side*) and Amazon (*right side*)

multivariate deep learning-based method for the stock prices prediction (Tables 1 and 2).

The approaches we have used are consolidated after comparison with other models of stock price analysis. As a future scope, we can compare the predicted results with existing state-of-the-art methods, and also, we can figure it out the reason of the

Table 1 Result of all the models is mentioned below for Google dataset

Models	MSE	RMSE	R-squared score
Univariate LSTM	0.006301861	0.079384263	0.975318821
Univariate bi-directional LSTM	0.003945525	0.062813413	0.984547390
Univariate RNN	0.001278237	0.035752437	0.994993798
Multivariate LSTM	0.082684419	0.287548986	0.676167274
Multivariate bi-directional LSTM	0.027573822	0.166053671	0.892007395
Multivariate RNN	0.002394559	0.048934237	0.990621730

Table 2 Result of all the models is mentioned below for Amazon dataset

Models	MSE	RMSE	R-squared score
Univariate LSTM	0.004322538	0.065746016	0.987615441
Univariate bi-directional LSTM	0.010274251	0.101361984	0.970563115
Univariate RNN	0.001603064	0.040038286	0.995407040
Multivariate LSTM	0.133020532	0.364719800	0.618881254
Multivariate bi-directional LSTM	0.025209180	0.158773990	0.927772871
Multivariate RNN	0.001730101	0.041594487	0.995043065

underperformance of simple unidirectional LSTM and bi-directional LSTM models of multivariate analysis.

References

1. Murphy, J.J.: Technical Analysis of the Financial Markets: A Comprehensive Guide to Trading Methods and Applications. Penguin (1999)
2. Turner, T.: A Beginner's Guide To Day Trading Online, 2nd edn. Simon and Schuster (2007)
3. Maqsood, H. et al.: A local and global event sentiment based efficient stock exchange forecasting using deep learning. Int. J. Inform. Manage. **50**, 432–451 (2020)
4. Long, W., Zhichen, L., Lingxiao, C.: Deep learning-based feature engineering for stock price movement prediction. Knowl. Based Syst. **164**, 163–173 (2018)
5. Penglei Gao, P. Zhang, R., Yang, X.: The Application of Stock Index Price Prediction with Neural Network, pp. 5–13. Springer (2020).
6. Ghosh, A. Bose, S. Maji, G. Debnath N.C., Sen, S.: Stock Price Prediction Using LSTM on Indian Share Market, pp. 103–109. Springer (2019)
7. Althelaya, K.A., El-Alfy, E.S.M., Mohammed, S.: Stock market forecast using multivariate analysis with bidirectional and stacked (LSTM, GRU). In: 21st Saudi Computer Society National Computer Conference (NCC), pp. 2–5. Springer (2018)
8. Menon, V.K.S., Sureshkumar, K.V., Pedamallu, V.T.N., Jami, S.A., Vasireddy, N.C.: Bulk price forecasting using spark over NSE data set. In: International Conference on Data Mining and Big Data, pp. 137–146. Springer (2016)
9. Bengio, Y., Goodfellow, I. J., Courville, A.: Deep learning. Nature **521**, 436–444 (2015)
10. Zhang, Z.P., Liu, G.Z., Yang, Y.W.: Stock market trend prediction based on neural networks, multiresolution analysis and dynamical reconstruction. IEEE/IAFE Proc. CIFE 155–56 (2000)

11. Pascanu, R., Mikolov, T., Bengio, Y.: On the Difficulty of Training Recurrent Neural Networks, pp. 1–9. arXiv:1211.5063 (2013)
12. Hochreiter, S., Schmidhuber, J.: Long short-term memory. Neural Comput, 1735–1780 (1997). doi:https://doi.org/10.1162/neco.1997.9.8.1735
13. Cho, K.: Learning Phrase Representations using RNN Encoder-Decoder for Statistical Machine Translation, 1–11 (2014). arXiv:1406.1078
14. Lin, C.S., Khan, H.A., Huang, C.C.: Can the neuro fuzzy model predict stock indexes better than its rivals?. Proc. CIRJE **165** (2002)

Accurate Prediction of Petermann I and II Spot Sizes of First Higher Order Mode for Kerr Type Nonlinear Graded Index Fiber by a Simple Method

Jayanta Aich, Angshuman Majumdar, and Sankar Gangopadhyay

Abstract We develop an easy but error-free way of evaluation of the spot sizes, namely Petermann I and II, corresponding to first larger order mode in case of fiber having Kerr nonlinearity and graded index profile. Here, we use the field expression of the first larger order mode of the said fiber, which is obtained by using Chebyshev method. Analytical expressions for the aforementioned spot sizes are derived and presented here. In the absence of nonlinearity, these are used to estimate the spot sizes. When the said kind of nonlinearity is present, the iteration approach is applied on the analytical expression in order to get the concerned spot sizes. Very less use of computer is required for evaluation by our proposed method. We have demonstrated that our values and the numerically exact values, arrived at with the help of finite element technique, are virtually identical. In our research, we have restricted ourselves to some fibers having step and parabolic refractive index profiles. Thus, our method will be useful for the analysis of Kerr type dual mode fiber.

Keywords Spot sizes-Petermann I and II · Chebyshev formalism · First larger order modal field · Kerr type nonlinearity

1 Introduction

In optical fiber technology, the domination of various kinds of nonlinear terms on the properties of graded index fiber has attracted attention in the domain of research [1–7]. The intensity of the beam of light and the type of channel are two very important candidates for the creation of different types of nonlinear terms [5, 6]. Third order nonlinear term actually corresponds to Kerr type nonlinear term.

J. Aich
Department of Computer Science and Engineering, Brainware University, Barasat, Kolkata, West Bengal 700125, India

A. Majumdar · S. Gangopadhyay (✉)
Department of Electronics and Communication Engineering, Brainware University, Barasat, Kolkata, West Bengal 700125, India

B. Sikdar et al. (eds.), *Proceedings of the 3rd International Conference on Communication, Devices and Computing*, Lecture Notes in Electrical Engineering 851,
https://doi.org/10.1007/978-981-16-9154-6_11

The presence of nonlinearity property not only adversely affects the information volume by restricting channel bit rate, channel spacing, bandwidth etc., but also it produces pulse compression. The dispersion expands the pulse and nonlinearity causes compression of pulse and thus, if the compression is balanced by expansion, the pulse propagates retaining its form. This phenomenon is known as generation of soliton optically [5, 6] and this has produced huge interest in the domain of nonlinear optical technology.

Chebyshev series expression accurately predicts the first larger order mode cut-off V number in presence of Kerr nonlinearity [8]. On the other hand, different characteristics related to propagation in mono-mode optical fiber having third order nonlinearity have also been assessed accurately by applying the said series expression [9]. This simple technique has also been shown to estimate accurately the fields corresponding to the fundamental as well as the first higher order modes, when Kerr nonlinearity exists [10, 11]. Again, Refs. [12–17] report accurate prediction of different types of communication characteristics of third order nonlinear single-mode optical fibers by application of Chebyshev formalism. The correctness of the aforementioned technique has inspired us to use this for evaluation of the spot sizes under study for such fibers in both cases having nonlinearity and no nonlinearity at all. It is very essential to surface that spot size (W_e), namely Petermann I, is related to micro-bending loss and also the losses on account of minor mismatch of angular type at the joint ends while spot size (W_d), namely Petermann II, estimates the modal dispersion, group delay and splice losses. Further, the importance of dual-mode fiber has been reported in connection with optical network system [18–20]. This has led us to study the above mentioned spot sizes for first higher order modal field. The finite element solution [21] for nonlinear graded index slab waveguides involves lengthy computation. Thus, an easy but correct approach for estimation of such kinds of spot sizes for third order nonlinear graded index fiber is the most challenging topic presently.

We present here the estimation of Petermann spot sizes for first larger order mode in case of fiber of graded index profile in both cases of nonlinearity and no nonlinearity at all. The evaluation for the said communication parameters by our proposed technique needs less involvement in computation but our values and the exact values are more or less the same. Further, necessary survey has led us to infer that no such simple but correct approach for estimating the spot sizes under study has been contributed to literature. Accordingly, the contribution in this paper can be regarded as a novel one.

2 Theory

In case of cylindrical fiber, radial distribution of refractive index is represented as [10]

$$n^2(R) = \begin{cases} n_1^2(1 - 2\delta f(R)), & R \leq 1 \\ n_2^2, & R > 1 \end{cases} \tag{1}$$

Here, normalized radial distance 'R' $= [r/a]$, 'δ' represents the relative refractive index difference, 'a' represents the radius of core. Further, 'n_1', 'n_2' carry their usual meanings. For graded type optical fiber we can write [10]

$$f(R) = (R)^q \quad \text{for} \quad R \leq 1 \tag{2}$$

where the values of 'q' are ∞, 1 and 2 for step, triangular and parabolic profile respectively. The third order nonlinear refractive index is related to linear refractive index by the following relation [11, 22]

$$n^2(R) = n_L^2(R) + \frac{n_2^2 n_{\mathrm{NL}}(R)}{\eta_0} \psi^2(R) \tag{3}$$

where, n_L and n_{NL} are respectively representing the refractive index in the linear case and the Kerr coefficient in the nonlinear case with [22]

$$\eta_0 = \sqrt{\frac{\mu_0}{\varepsilon_0}}$$

Here, permeability and permittivity of vacuum are represented by 'μ_0' and 'ε_0' respectively. The field of first larger order mode of a third order nonlinear fiber satisfies the following scalar wave equation [11, 22],

$$\begin{aligned} &\frac{d^2\psi(R)}{\mathrm{d}R^2} + \frac{1}{R}\frac{\mathrm{d}\psi(R)}{\mathrm{d}R} \\ &+ \left[V^2\{1 - f(R)\} - W^2\right]\psi(R) - \frac{\psi(R)}{R^2} \\ &+ V^2 g(R)\psi^3(R) = 0 \end{aligned} \tag{4}$$

The term g is given by [22]

$$g(R) = \frac{n_2 n_{NL} P}{\pi\, a^2 (n_1^2 - n_2^2)}$$

The optical power is represented by 'P', cross sectional area by 'a' and Kerr coefficient by 'n_{NL}'.

In this context, the equation of continuity at $R = 1$ gives [22]

$$\left[\frac{1}{\psi}\frac{\mathrm{d}\psi}{\mathrm{d}R}\right]_{R=1} = -\left[1 + \frac{W K_0(W)}{K_1(W)}\right] \tag{5}$$

Here, K_1 and K_0 denote Bessel function of modified type, representing first order and zero order respectively. Again, W represents the cladding decay parameter for the fiber.

Employing Chebyshev formalism based on simple power series expansion form considering graded index fiber, LP_{11} modal field expression within core as well as cladding can be shown to be [11, 23–25],

$$\begin{aligned}\Psi(R) &= \left(a_1 R + a_3 R^3 + a_5 R^5\right) \quad \text{for } R < 1 \\ &= (a_1 + a_3 + a_5) K_1(WR)/K_1(W) \quad \text{for } R > 1\end{aligned} \tag{6}$$

Using Eqs. (6) and (4), we obtain [23]

$$\begin{aligned}&a_1\left\{V^2(1 - f(R)) - W^2 + V^2 g\psi^2(R)\right\} \\ &\quad + a_3\left\{8 + R^2[V^2(1 - f(R)) - W^2 + V^2 g\psi^2(R)]\right\} \\ &\quad + a_5\left\{24R^2 + R^4[V^2(1 - f(R)) - W^2 + V^2 g\psi^2(R)]\right\} = 0\end{aligned} \tag{7}$$

Only two distinct Chebyshev points R_m are chosen taking $m = 1, 2$ for the purpose of computation of a_3, a_5 that are expressed in terms of a_1. Chebyshev points under consideration are expressed by [11, 24]

$$R_m = \cos\left(\frac{2m - 1}{2M - 1}\frac{\pi}{2}\right), \text{ for } m = \{1, 2 \ldots (M - 1)\} \tag{8}$$

In this connection, we choose value of M to be 3 depending on power series terms and, obtain R_1 with specific value 0.9511 and R_2 having value 0.5878. Using these relevant Chebyshev points R_m for $m = 1, 2$ in Eq. (7), we obtain the pair of equations with R_1 and R_2 terms and the same is given by [20]

$$\begin{aligned}&a_1\left\{V^2(1 - f(R_1)) - W^2 + V^2 g\Psi^2(R_1)\right\} \\ &\quad + a_3\left\{8 + R_1^2\left[V^2(1 - f(R_1)) - W^2 + V^2 g\Psi^2(R_1)\right]\right\} \\ &\quad + a_5\left\{24R_1^2 + R_1^4\left[V^2(1 - f(R_1)) - W^2 + V^2 g\Psi^2(R_1)\right]\right\} = 0\end{aligned} \tag{9}$$

$$\begin{aligned}&a_1\left\{V^2(1 - f(R_2)) - W^2 + V^2 g\Psi^2(R_2)\right\} \\ &\quad + a^3\left\{8 + R_2^2\left[V^2(1 - f(R_2)) - W^2 + V^2 g\Psi^2(R_2)\right]\right\} \\ &\quad + a_5\left\{24R_2^2 + R_2^4\left[V^2(1 - f(R_2)) - W^2 + V^2 g\Psi^2(R_3)\right]\right\} = 0\end{aligned} \tag{10}$$

$K_1(W)/K_0(W)$ is seen to vary with reciprocal of W almost linearly for the values of W starting from 0.60 to 2.50 [26]. Therefore, we resort to the technique of least square fitting in the aforesaid interval range and thereafter arrive at the below mentioned linear relationship as [11, 26, 27]

$$\frac{K_1(W)}{K_0(W)} = \alpha + \frac{\beta}{W} \tag{11}$$

with '$\alpha = 1.034623$ and $\beta = 0.389032$'.

Further, applying Eqs. (6), (11) and (5), one gets [26]

$$\begin{aligned} &a_1[2(\alpha W + \beta) + W^2] + a_3[4(\alpha W + \beta) + W^2] \\ &+ a_5[6(\alpha W + \beta) + W^2] = 0 \end{aligned} \tag{12}$$

Here, Eqs. (9), (10) and (12) shall finally give solution for the coefficients a_1, a_3 and a_5 if the below mentioned (3×3) determinant vanishes [23]

$$\begin{vmatrix} A_1 & B_1 & C_1 \\ A_2 & B_2 & C_2 \\ A_3 & B_3 & C_3 \end{vmatrix} = 0 \tag{13}$$

where [27],

$$\begin{aligned} A_1 &= \left\{V^2(1 - f(R_1)) - W^2 + V^2 g\psi^2(\mathrm{R}_1)\right\} \\ A_2 &= \left\{V^2(1 - f(R_2)) - W^2 + V^2 g\psi^2(R_2)\right\} \\ A_3 &= 2(\alpha W + \beta) + W^2 \\ B_1 &= \left\{8 + R_1^2[V^2(1 - f(R_1)) - W^2 + V^2 g\psi^2(R_1)]\right\} \\ B_2 &= \left\{8 + R_2^2[V^2(1 - f(R_2)) - W^2 + V^2 g\psi^2(R_2)]\right\} \\ B_3 &= 4(\alpha W + \beta) + W^2 \\ C_1 &= \{24R_1^2 + R_1^4[V^2(1 - f(R_1)) - W^2 + V^2 g\psi^2(R_1)]\} \\ C_2 &= \{24R_2^2 + R_2^4[V^2(1 - f(R_2)) - W^2 + V^2 g\psi^2(R_2)]\} \\ C_3 &= 6(\alpha W + \beta) + W^2 \end{aligned} \tag{14}$$

It has been observed that existence of terms like Ψ^2 (R) make the solution of Eq. (13) extensively tedious and complicated. So to simplify it, we first consider 'g' $= 0$ in Eq. (13) in order to find W value with respect to any specific V in the linear region. The cladding decay parameter 'W' value for any specific 'V' corresponding to a particular fiber is estimated for the linear region. In the succeeding step, taking this calculated W and corresponding V the coefficient terms a_3, a_5 that are in terms of a_1 are computed under the absence of nonlinearity. This involves calculation for the linear fiber case. Proceeding with this technique, in the presence of nonlinearity for any particular value of $g(R)$ and V number, the process of iteration is performed till we obtain convergent W values and the relevant field coefficients. This suitably illustrates our computation for the nonlinear fiber case. Accordingly, A_3 and A_5 are

the normalized values of a_3 and a_5 in terms of a_1 and can simply be expressed as $A_3 = (a_3/a_1)$ and $A_5 = (a_5/a_1)$.

Spot sizes—Petermann I (W_e) and II (W_d), normalized with respect to the radius of the fiber, are given as follows [27–32]

$$W_e^2 = 2\frac{\int_0^\infty \psi^2(R)R^3\mathrm{d}R}{\int_0^\infty (\psi(R))^2 R\mathrm{d}R} \tag{15}$$

$$W_d^2 = 2\ \frac{\int_0^\infty \psi^2(R)\ R\,\mathrm{d}R}{\int_0^\infty (\psi/(R))^2\ R\,\mathrm{d}R} \tag{16}$$

Using Eqs. (15), (16) and (6), we get [27]

$$W_e^2 = \frac{S_5 - (1/3)S_4^2(1 - (K_2^2(W)/K_1^2(W)))}{S_2 - S_1(1 - (K_0(W)K_2(W)/K_1^2(W)))} \tag{17}$$

$$W_d^2 = \frac{2[S_2 - S_1(1 - (K_0(W)K_2(W)/K_1^2(W)))]}{S_6 - S_4^2[-(W^6/6)(10K_0^2(W) - 4K_2^2(W) - K_3^2(W))/10K_1^2(W)) - 1/2) \\ -(1/2)(K_0^2(W)/K_1^2(W)) - 1 - (W^3/3)((K_0(W) - K_2(W))/K_1(W))]} \tag{18}$$

where [27],

$$\begin{aligned}
S_1 &= (a_1 + a_3 + a_5)^2/2 \\
S_2 &= (a_1^2/4) + (1/3)a_1a_3 + (1/8)(a_3^2 + 2a_1a_5) \\
&\quad + (1/5)a_3a_5 + (a_5^2/12) \\
S_3 &= \frac{a_1}{3} + \frac{a_3}{5} + \frac{a_5}{7} \\
S_4 &= a_1 + a_3 + a_5 \\
S_5 &= (a_1^2/3) + (1/2)a_1a_3 + (1/5)(a_3^2 + 2a_1a_5) \\
&\quad + (1/3)a_3a_5 + (1/7)a_5^2 \\
S_6 &= (a_1^2/2) + (3/2)a_3^2 + (5/2)a_5^2 + (3/2)a_1a_3 \\
&\quad + (5/3)a_1a_5 + (15/4)a_3a_5
\end{aligned}$$

3 Results and Discussion

Using the method given in Sect. 2, W corresponding to a specific V value for a specific linear fiber as stated by $f(R_i)$ and hence field coefficients are evaluated. Next, using this W and the value of the field in Eqs. (17) and (18), the given spot sizes are evaluated for the linear fiber. This W value and the field coefficients for the linear fiber along with any specific value of $g(R)$ as well as V number are used and as mentioned in Sect. 2, we apply iterative technique to evaluate respective W and the field coefficients. The normalized values of field coefficients and W are used in Eqs. (17) and (18) for estimation of the said spot sizes for the particular fiber corresponding to the specific g value characterizing Kerr nonlinearity.

Using Table 1, we present LP_{11} mode normalized Petermann I spot sizes (W_e) for various V number related to step index profile, when there is nonlinearity and no nonlinearity as well. Figure 1a gives the graphical presentation of variation of W_e with V, using the observations given in Table 1. In Table 2, we present LP_{11} mode normalized spot sizes—Petermann II (W_d) for dissimilar values of V for step profile in attendance and non-attendance of nonlinearity. Figure 1b gives the graphical presentation of variation of W_d with V number, using the observations shown in Table 2.

Similarly, when parabolic index fiber is taken for investigation, Tables 3 and 4 contain found first higher order mode W_e and W_d values for different V numbers both, when chosen kinds of nonlinearity are attending or non-attending while Fig. 2a, b give the graphical presentation using the observation in Tables 3 and 4 respectively. The simulated exact results presented in the Figs. are indicated. Our results and the exact ones are observed to be effectively same. This verifies the correctness of our simple formalism.

It is also found that the value of each kind of spot size decreases with the increase of V number. Further, it is observed that lower V value produces larger spot size leading to more leaking of field in the cladding. Thus the proposed formulation can be successfully employed for fibers of low V number in the context of evanescent field coupling in switches, directional couplers etc. This motivates one to apply such simple and accurate formalism in other branches of linear and nonlinear photonics.

Table 1 LP_{11} mode normalized spot sizes, Petermann I type (W_e) relating to fiber with step profile

V	$n_{NL}P = +1.5 \times 10^{-14}$	$n_{NL}P = 0$	$n_{NL}P = -1.5 \times 10^{-14}$
2.6	2.003253338233090	2.125995150329880	2.301078156766480
2.8	1.597608949234710	1.647765118272620	1.699290065069160
3	1.417193800390050	1.443008332529810	1.471285174591560
3.2	1.310221632141690	1.327242312068400	1.345598329715730

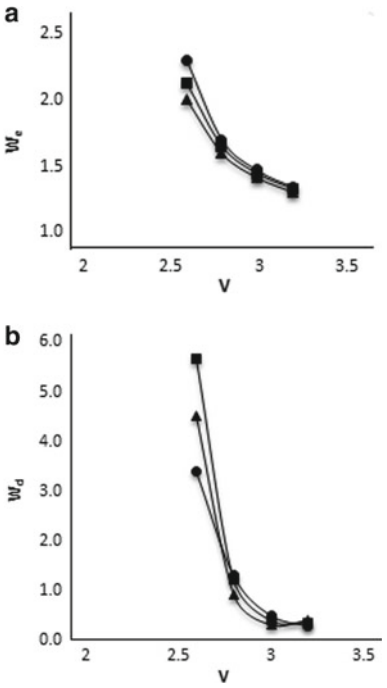

Fig. 1 **a** LP_{11} mode normalized spot size, Petermann I type (W_e) versus V for fiber with step profile for different values of $n_{NL}P$ (found results: ▲ for $n_{NL}P = +\ 1.5 \times 10^{-14}$ m^2, • for $n_{NL}P = -\ 1.5 \times 10^{-14}$ m^2, · for $n_{NL}P = 0$ and numerical exact results: —). **b** LP_{11} mode normalized spot size, Petermann II type (W_d) versus V for fiber with step profile for different values of $n_{NL}P$ (found results: ▲ for $n_{NL}P = +\ 1.5 \times 10^{-14}$ m^2, • for $n_{NL}P = -\ 1.5 \times 10^{-14}$ m^2, • for $n_{NL}P = 0$ and numerical exact results: —)

Table 2 LP_{11} mode normalized spot sizes, Petermann II type (W_d) relating to fiber with step profile

V	$n_{NL}P = +\ 1.5 \times 10^{-14}$	$n_{NL}P = 0$	$n_{NL}P = -\ 1.5 \times 10^{-14}$
2.6	4.522907224814730	5.651095662484580	3.398774078703740
2.8	0.925088267582994	1.225488450698730	1.306586222637530
3	0.312222910066291	0.411687014246066	0.507984325541085
3.2	0.405333398140624	0.356497853282117	0.293859160739515

Table 3 LP_{11} mode normalized spot sizes, Petermann I type (W_e) relating to fiber with parabolic profile

V	$n_{NL}P = +\ 1.5 \times 10^{-14}$	$n_{NL}P = 0$	$n_{NL}P = -\ 1.5 \times 10^{-14}$
3.7	1.807178673027730	2.013562059484420	2.375504822893690
3.9	1.493342284788270	1.572203926602330	1.675284708192760
4.1	1.333238927039730	1.375954322818110	1.428203237710270
4.3	1.232667254035940	1.260751372250670	1.293259800204580

Table 4 LP_{11} mode normalized spot sizes, Petermann II type (W_d) relating to fiber with parabolic profile

V	$n_{NL}P = +1.5 \times 10^{-14}$	$n_{NL}P = 0$	$n_{NL}P = -1.5 \times 10^{-14}$
3.7	3.065601456393350	2.232476776681430	2.038597629477230
3.9	1.268372736177620	1.964210595332410	1.678003929850090
4.1	0.481868567313219	0.683940728772566	0.938660486646043
4.3	0.347556326700778	0.186103956407668	0.283388778221445

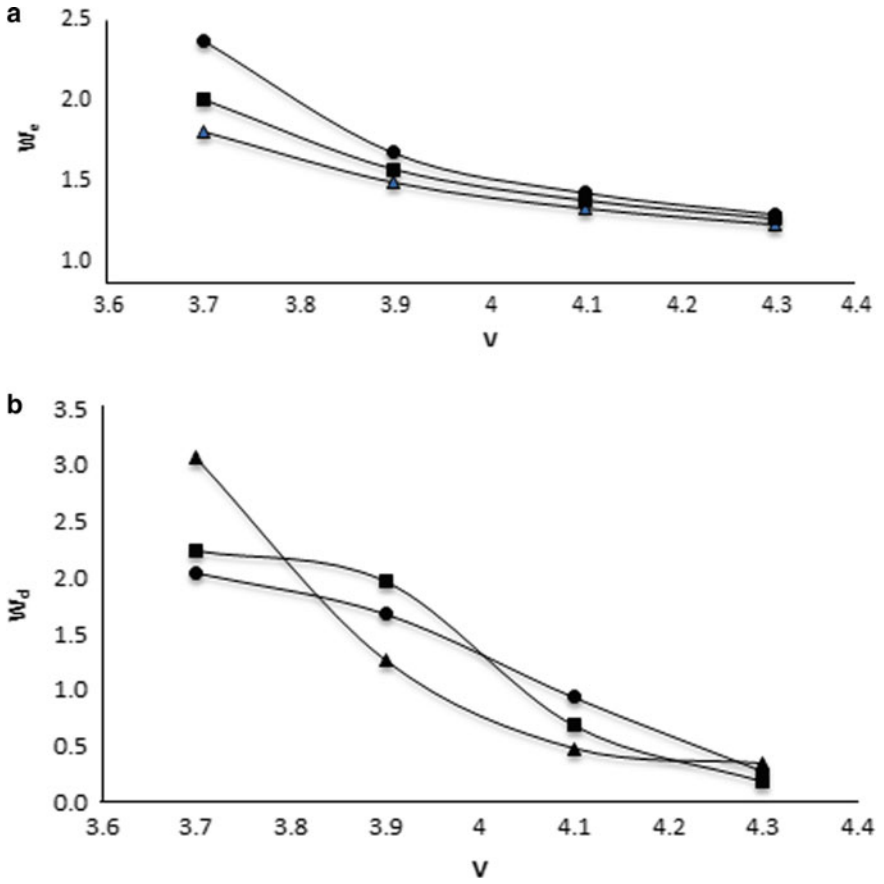

Fig. 2 **a** LP_{11} mode normalized spot size, Petermann I type (W_e) versus V for fiber with parabolic profile for different values of $n_{NL}P$ (found results: ▲ for $n_{NL}P = +1.5 \times 10^{-14}$ m^2, • for $n_{NL}P = -1.5 \times 10^{-14}$ m^2, • for $n_{NL}P = 0$ and numerical exact results: —). **b** LP_{11} mode normalized spot size, Petermann II type (W_d) versus V for fiber with parabolic profile for different values of $n_{NL}P$ (found results: ▲ for $n_{NL}P = +1.5 \times 10^{-14}$ m^2, • for $n_{NL}P = -1.5 \times 10^{-14}$ m^2, • for $n_{NL}P = 0$ and numerical exact results: —)

4 Conclusion

We report a novel approach for calculation of spot sizes namely Petermann I and II types relating to fibers having graded profile and third order nonlinearity. Our method involves use of Chebyshev formalism and the method of iteration. The execution of our technique needs very small use of computer. The accuracy or correctness of our simple formalism has been checked and verified. In this way this straightforward strategy will be of immense importance to the researchers working with third order nonlinearity of different kinds of fibers.

References

1. Tomlinson, W.J., Stolen, R.H., Chank, C.V.: Compression of optical pulses chirped by self-phase modulation in fibers. J. Opt. Soc. **1**, 139–149 (1984)
2. Tai, K., Tomita, A., Jewell, J.L., Hasegawa, A.: Generation of subpicosecond soliton like optical pulses at 0.3 THz repetition rate by induced modulational instability. Appl. Phys. Lett. **49**, 236–238 (1986)
3. Snyder, A.W., Chen, Y., Poladian, L., Mitchel, D.J.: Fundamental mode of highly nonlinear fibres. Electron. Lett. **26**, 643–644 (1990)
4. Goncharenko, I.A.: Influence of nonlinearity on mode parameters of anisotropic optical fibres. J. Mod. Opt. **37**, 1673–1684 (1990)
5. Agrawal, G.P., Boyd, R.W.: Contemporary Nonlinear Optics. Academic Press, Boston (1992)
6. Agrawal, G.P.: Nonlinear Fiber Optics. Academic Press, Cambridge, Massachusetts (2013)
7. Antonelli, C., Golani, O., Shtaif, M., Mecozzi, A.: Nonlinear interference noise in space-division multiplexed transmission through optical fibers. Opt. Express **25**, 13055–13078 (2017)
8. Roy, D., Sarkar, S.N.: Simple but accurate method to compute LP11 mode cut off frequency of nonlinear optical fibers by Chebyshev technique. Opt. Commun. **55**, 0841051–0841054 (2016)
9. Sadhu, A., Karak, A., Sarkar, S.N.: A simple and effective method to analyze the propagation characteristics of nonlinear single mode fiber using Chebyshev method. Microw. Opt. Technol. Lett. **56**, 787–790 (2013)
10. Chakraborty, S., Mandal, C.K., Gangopadhyay, S.: Prediction of fundamental modal field for graded index fiber in the presence of Kerr nonlinearity. J. Opt. Commun. https://doi.org/10.1515/joc-2017-0126
11. Chakraborty, S., Mandal, C.K., Gangopadhyay, S.: Prediction of first higher order modal field for graded index fiber in the presence of Kerr nonlinearity. J. Opt. Commun. https://doi.org/10.1515/joc-2017-0206
12. Mukherjee, T., Maiti, S., Majumdar, A., Gangopadhyay, S.: A simple but accurate formalism for study of single-mode graded index fiber directional coupler in presence of Kerr nonlinearity. Optik **213**, 164772 (2020)
13. Maiti, S., Majumdar, A., Biswas, S.K., Gangopadhyay, S.: Evaluation of splice loss of single-mode graded index fiber in presence of Kerr nonlinearity. Optik **203**, 163962 (2020). https://doi.org/10.1016/j.ijleo.2019.163962
14. Aich, J., Maiti, A.K., Majumdar, A., Gangopadhyay, S.: A novel and simple formalism for study of effect of Kerr nonlinearity on Petermann I and II spot sizes of single-mode graded index fiber. J. Opt. Commun. https://doi.org/10.1515/JOC-2019-0167
15. Roy, K., Majumdar, A., Gangopadhyay, S.: Simple but accurate method for estimation of the effect of Kerr nonlinearity on confinement and excitation of the fundamental mode in single mode graded index fiber. Optik **216**, 164939 (2020)

16. Mukherjee, T., Majumdar, A., Gangopadhyay, S.: Influence of Kerr nonlinearity on group delay and modal dispersion parameters of single-mode graded index fibers: evaluation by a simple but accurate method. J. Opt. Commun. https://doi.org/10.1515/joc-2020-0192
17. Rakshit, R., Majumdar, A., Gangopadhyay, S.: A simple but accurate method for prediction of splice loss in mono-mode dispersion shifted and dispersion flattened fibers in presence of Kerr nonlinearity. J. Opt. Commun. https://doi.org/10.1515/joc-2020-0259
18. Spajer, M., Charquille, B.: Application of intermodal interference to fiber sensors. Opt. Commun. **60**, 261–264 (1986)
19. Eguchi, M.: Dispersion-compensating dual-mode optical fibers desirable for erbium-doped-fiber-amplified systems. J. Opt. Soc. Am. B. **18**, 737–741 (2001)
20. Eguchi, M., Koshiba, M., Tsuji, Y.: Dispersion compensation based on dual-mode optical fiber with inhomogeneous profile core. J. Lightwave Technol. **14**, 2387–2394 (2002)
21. Hayata, K., Koshiba, M., Suzuki, M.: Finite-element solution of arbitrarily nonlinear, graded-index slab waveguides. Electron. Lett. **23**, 429–431 (1987)
22. Mondal, S.K., Sarkar, S.N.: Effect of optical Kerr effect nonlinearity on LP11 mode cutoff frequency of single-mode dispersion shifted and dispersion flattened fibers. Opt. Commun. **127**, 25–30 (1996)
23. Patra, P., Gangopadhyay, S., Goswami, K.: A simple method for prediction of first-order modal field and cladding decay parameter in graded index fiber. Optik **119**, 209–212 (2008)
24. Chen, P.Y.P.: Fast method for calculating cut-off frequencies in single-mode fibers with arbitrary index profile. Electron Lett. **18**, 1048–1049 (1982)
25. Shijun, J.: Simple explicit formula for calculating LP11 mode cut off frequency. Electron Lett. **23**, 534–536 (1987)
26. Abramowitz, M., Stegun, I.A.: Handbook of Mathematical Functions. Dover Publications, New York (2012)
27. Gangopadhyay, S., Sarkar, S.N.: Evaluation of modal spot size in single-mode graded index fibers by a simple technique. J. Opt. Commun. **19**, 173–175 (1998)
28. Neumann, G.E.: Single-Mode Fibers Fundamentals. Springer-Verlag, Berlin (1998)
29. Sansonetti, P.: Modal dispertion in single mode fiber, simple approximation issued from mode spot size spectral behaviour. Electron. Lett. **18**, 647 (1982)
30. Sansonetti, P.: Prediction of modal dispertion in single mode fiber from spectral behaviour of mode spot size. Electron. Lett. **18**, 136 (1982)
31. Pask, C.: Physical interpretation of Petermann's strange spot size for single mode fibers. Electron. Lett. **20**, 144 (1984)
32. Povlsen, J.H.: Characterisation of graded single mode fiber by fundamental spot size variation. Electron. Lett. **20**, 1543 (1984)

Analysis of All-Optical XNOR Gate Using Quantum Dot Semiconductor Optical Amplifier (QDSOA)

Siddhartha Dutta, Kousik Mukherjee, and Subhasish Roy

Abstract In this paper all-optical logic XNOR Gate by using Quantum Dot Semiconductor Optical Amplifier (QDSOA) is designed and analyzed. The Extinction Ratio (ER), Contrast Ratio (CR), Quality factor and the Amplitude Modulation (AM) variation with the control input power are studied. Also, the variation of ER, CR, AM and Relative Eye Opening (REO) with the Amplified Spontaneous Emission (ASE) noise factor (Nsp) are analyzed. The input and output bit patterns are shown in this paper.

Keywords The extinction ratio (ER) · Contrast ratio (CR) · Amplified spontaneous emission (ASE)

1 Introduction

For high-speed data processing some basic special types of switching devices are useful nowadays. These include Mach–Zehnder interferometer (MZI), Semiconductor Laser Amplifier (SLA), Four Wave Mixing (FWM) based wavelength conversion, Tera-hertz Optical Asymmetric Demultiplexer (TOAD), Cross Gain Modulation (XGM) in Quantum Dot Semiconductor Optical Amplifier (QDSOA), Cross Phase Modulation (XPM). Among them QDSOA is most attractive because of its high saturated output gain and low noise figure. It has ultra-fast carrier relaxation between energy states. QDSOA has the advantages of strong nonlinearities and small size and ultrahigh speed operation [1] and finds application in designing interferometric switches also [1–3]. Recently QDSOA based logic gates and processors have been implemented by different researchers [3–9]. The work [2] reports a NOR gate

S. Dutta · S. Roy
Physics Department, Visva-Bharati University, Shantiniketan, India

K. Mukherjee (✉)
Physics Department, B B College, Asansol, India

Centre of Organic Spintronics and Optoelectronic Devices (COSOD), Kazi Nazrul University, Asansol, India

B. Sikdar et al. (eds.), *Proceedings of the 3rd International Conference on Communication, Devices and Computing*, Lecture Notes in Electrical Engineering 851,
https://doi.org/10.1007/978-981-16-9154-6_12

using Mach Zehnder Interferometer based on QDSOA. The performance of all-optical logic XNOR gate was reported at a speed of 250 Gb/s by using QDSOA Mach–Zehnder interferometer [1]. The work [3] makes use of QDSOA in Tera Hertz Optical Asymmetric Demultiplexer (TOAD) and applies to design ultra-fast digital to analog converter at 1 Tb/s. In the work [10] the performance of XNOR gate is analyzed with the help of Two Photon Absorption (TPA) and Mach–Zehnder interferometer (MZI). Most of these works use interferometric switches for its design [1–3, 5–7]. However, the work [4] proposes a digital to analog converter without using any interferometer structure and is very efficient. The NOR gate using QDSOA in non-interferometric structure [8] shows efficient performance. However, interferometric structures require perfect balance of gain and phase which is very difficult to maintain. The present paper analyzes the performance of all-optical logic XNOR by numerical simulation. The differential equations are solved and simulated in 4th order Runge–Kutta method in Scilab.

The rest of the paper is organized as below.

2 Design of XNOR Gate

Figure 1 shows the XNOR gate using QDSOA. A and B are two inputs and clock are the data signal. The QDSOA2 uses attenuated version of input signal B as data input. The control signals and data or clock signals are Gaussian pulse train. The control signals modulate the gains of the QDSOAs. Data or clocks have very low intensity not sufficient to produce gain modulation. Variable Optical Attenuator (VOA) is used to reduce the intensity of the QDSOA1 before cascading. The cross-gain effect in the QDSOAs in the Fig. 1 produces XNOR operation as follows:

Case 1 When both the inputs A and B are zero ('0'), QDSOA1 and QDSOA2 have no gain saturation. They produce high outputs. Output from QDSOA1 saturates

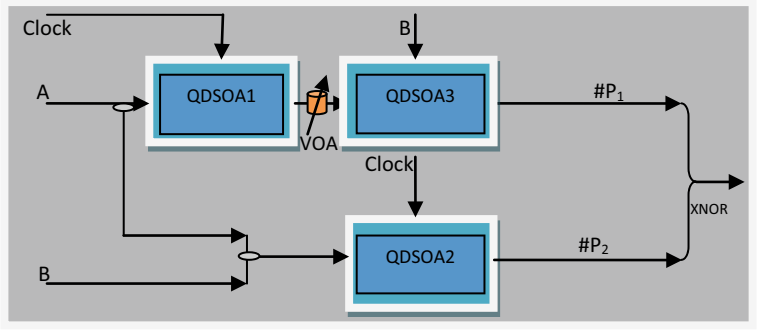

Fig. 1 QDSOA based XNOR gate

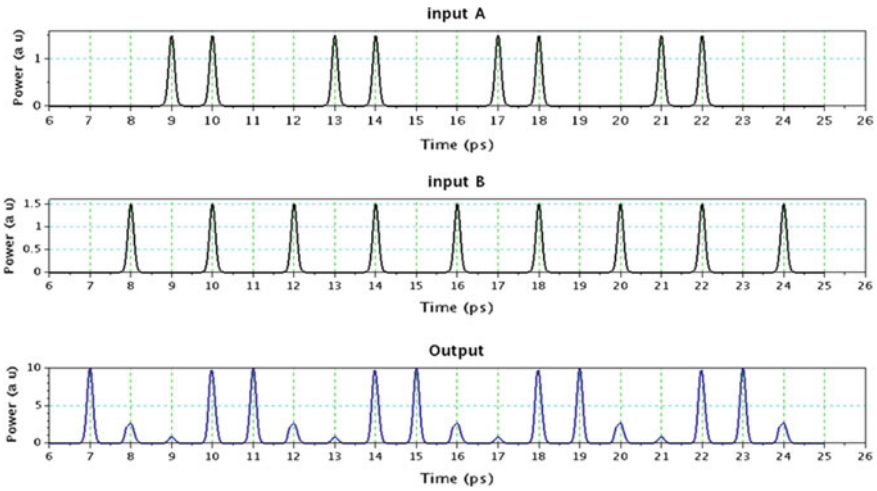

Fig. 2 Input output bit patterns

QDSOA3, and output from upper path #P_1 is low. However, output from lower path #P_2 makes final output high (‘1’).

Case 2 When either A is low (‘0’) and B is high (‘1’), high output from QDSOA1 makes QDSOA3 saturated, and high input B saturates QDSOA2. This corresponds to low (‘0’) final output.

Case 3 When A is high (‘1’) and B is low (‘0’), QDSOA2 becomes gain saturated and output #P_2 remains low. Since data or clock B in this condition to the QDSOA3 is low, output #P_1 is also low. Therefore, final output is low.

Case 4 When A and B both are high (‘1’), QDSOA1 and QDSOA3 have low saturated gain. This makes lower path output #P_2 low. However, low output from QDSOA1 does not lower the gain of the QDSOA3 significantly. This results in high output in upper path #P_1 and hence the final output high (‘1’).

Figure 2 shows the input output bit patterns of the XNOR gate.

3 Theoretical Analysis

The basic equations governing dynamics of QDSOA are [9]

$$\frac{\partial W}{\partial t} = \frac{I}{eVN_{\mathrm{WM}}} - \frac{W}{\tau_{\mathrm{WR}}} - \frac{W(1-h)}{\tau_{\mathrm{WE}}} + \frac{N_{\mathrm{ESM}}}{N_{\mathrm{WM}}}\frac{h(1-W)}{\tau_{\mathrm{EW}}} \tag{1}$$

$$\frac{\partial h}{\partial t} = \frac{-h}{\tau_{\mathrm{ESR}}} + \frac{N_{\mathrm{WM}}}{N_{\mathrm{ESM}}}\frac{W(1-h)}{\tau_{\mathrm{WE}}} - \frac{h(1-W)}{\tau_{\mathrm{EW}}} + \frac{N_{\mathrm{GSM}}}{N_{\mathrm{ESM}}}\frac{f(1-h)}{\tau_{\mathrm{GE}}} - \frac{h(1-f)}{\tau_{\mathrm{EG}}} \tag{2}$$

$$\frac{\partial f}{\partial t} = \frac{-f}{\tau_{\mathrm{GSR}}} - \frac{f(1-h)}{\tau_{\mathrm{GE}}} + \frac{N_{\mathrm{ESM}}}{N_{\mathrm{GSM}}}\frac{h(1-f)}{\tau_{\mathrm{EG}}} - \frac{\Gamma_{\mathrm{d}}}{A_{\mathrm{d}}}.a.(2f-1).\frac{S_{\mathrm{c}}}{N_{\mathrm{GSM}}.\hbar\omega} \tag{3}$$

$$\frac{\partial S_{\mathrm{c}}}{\partial z} = [g_{\max}(2f-1) - \alpha_{\mathrm{int}}].S_{\mathrm{c}} \tag{4}$$

where w, h, f are population probability of wetting layer, GS and ES. S_{c} is the input control signal. Equations (1)–(4) are numerically solved using 4th order Runge–Kutta method in Scilab. Table 1 describes the parameters used for simulation.

S_{c} is the input control signal. The gain is defined by $G(t) = \frac{S_{\mathrm{c}}(L,t)}{S_{\mathrm{c}}(0,t)}$ [8]. Basically, the profile of S_{c} is a Gaussian function.

Table 1 Parameters used for simulations

Parameters	Values
Spontaneous lifetime (radiative) in the WL (τ_{wR})	0.2 ns
Relaxation time of electron from the WL to ES (τ_{w2})	3 ps
Relaxation time of electron from ES to GS (τ_{21})	0.16 ps
Group velocity (V_{g})	8.3×10^7 m/s
Escape time of electron from ES to WL ($\tau_{2\mathrm{w}}$)	1 ns
Escape time of electron from GS to ES (τ_{12})	1.2 ps
Radiative lifetime (spontaneous) in Quantum dot ($\tau_{1\mathrm{R}}$)	0.4 ns
Material gain coefficient, $g_{\max}$	14 cm^{-1}
internal loss α_{int}	1 cm^{-1}
Injection current density (J)	1.33 kA/cm^2
L_{w}, effective thickness of the active layer	250 nm
Energy levels' density of state, N_{w}	5.4×10^{17} cm^{-1}
Effective area, A_{eff}	0.75 $\mu\mathrm{m}^2$
$\mathbf{N_w}$:$\mathbf{N_e}$:$\mathbf{N_g}$	15:2:1

4 Results and Discussions

Figures 3, 4 and 5 show the variations of ER, AM and Q factor with control power. ER, AM and Q values show optimized performance at control power 1.5 mW. Q factor nearly 9 dB and AM below 0.2 dB imply efficient performance of the logic gate. The relatively low ER value is possibly due to cascading effect. The values of the ER can be improved by selecting QDSOAs with higher gains. A low value of AM implies that the high state intensities have low fluctuations. This is also confirmed by high value of Q factor. A high value of Q factor signifies low value of bit error rate (BER).

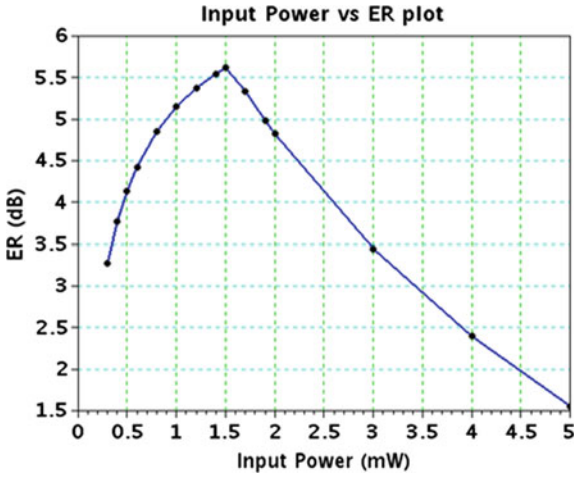

Fig. 3 Variation of ER with input control power

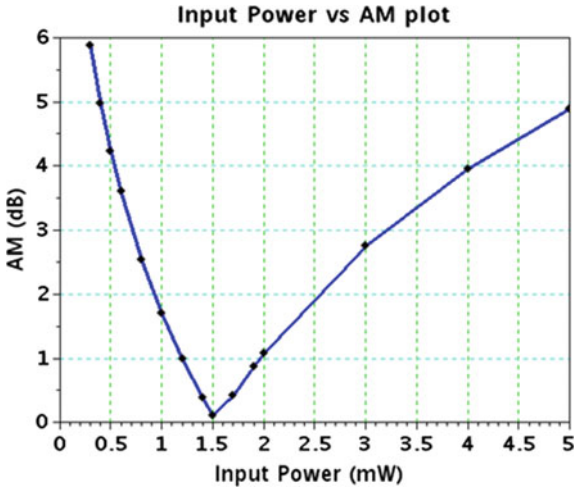

Fig. 4 Variations of AM with control power

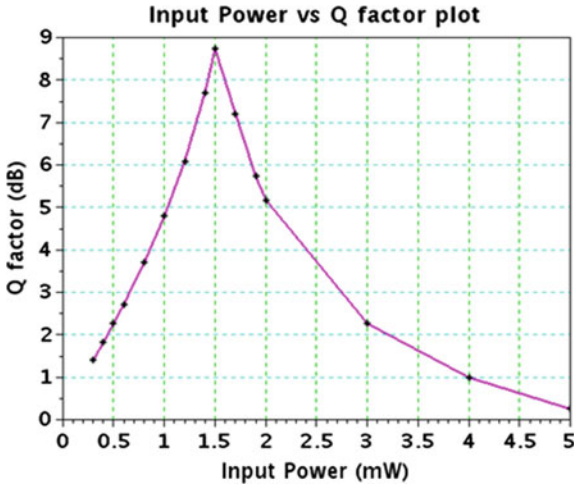

Fig. 5 Variations of Q with control power

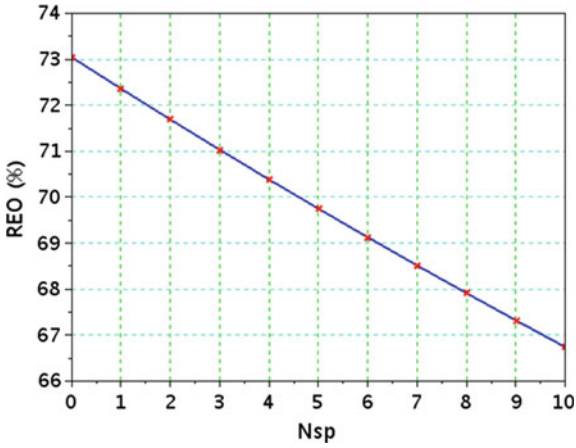

Fig. 6 Variation of relative eye opening with spontaneous noise factor

Figure 6 shows the variation of Relative Eye Opening (REO) with spontaneous noise factor (N_{sp}). It is obvious that REO will decrease with the increase of (N_{sp}) and the figure manifests the theory.

5 Conclusions

Simple design of XNOR gate using only three QDSOAs has been analyzed and optimized for control power. The simulation results show acceptable values for Q factor and AM. Betterment of ER value can be made by increasing the gain of

the QDSOAs used. The XNOR gate finds applications to design comparator, parity checker etc. which may be our future communications.

References

1. Kotb, A., Zoiros, K.E.: Simulation of all-optical logic XNOR gate based on quantum-dot semiconductor optical amplifiers with amplified spontaneous emission. Opt. Quant. Electron. **45**, 1213–1221 (2013). https://doi.org/10.1007/s11082-013-9742-9
2. Kotb, A.: Theoretical analysis of soliton NOR gate with semiconductor optical amplifier-assisted Mach-Zehnder interferometer. Opt. Quant. Electron. **49**, 180 (2017)
3. Mukherjee, K., Dutta, S., Roy, S. et al.: All-Optical digital to analog converter using Tera Hertz Optical Asymmetric Demultiplexer based on quantum dot semiconductor optical amplifier. Opt. Quant. Electron. **53**, 242 (2021). https://doi.org/10.1007/s11082-021-02900-4
4. Mukherjee, K.: A terabit-per-second all-optical four-bit digital-to-analog converter using quantum dot semiconductor optical amplifiers. J. Compute. Electron. (2021). https://doi.org/10.1007/s10825-021-01675-x
5. Mukherjee, K.: Design and analysis of all optical frequency encoded X-OR and X-NOR gate using Quantum Dot Semiconductor Optical amplifier-Mach Zehnder Interferometer. Accepted for publication, Optics and Laser Technology, Elsevier (2021)
6. Sun, H., Wang, Q., Dong, H., Dutta, N.K.: All-optical logic performance of quantum dot semiconductoramplifier- based devices. Microw. Opt. Technol. Lett. **48**, 29 (2006)
7. Hu, H., Zhang, X., Zhao, S.: High-speed all- optical logic gate using QD-SOA and its application. Cogent Phys. **4**, 1388156 (2017)
8. Komatsu, K., Hosoya, G., Yashima, H.: All-optical logic NOR gate using a single quantum-dot SOA- assisted an optical filter. Opt. Quant. Electron. **50**, 131 (2018)
9. Lin, W., Shaozhen, M., Hu, H., Dutta, N.K.: All optical latches using quantum-dot semiconductor optical amplifier. Opt. Commun. **285**, 5138–5143 (2012)
10. Kotb, A., Guo, C.: All-optical NOR and XNOR logic gates at 2 Tb/s based on two-photon absorption in quantum-dot semiconductor optical amplifiers. Opt. Quant. Electron. **52**, 30 (2020). https://doi.org/10.1007/s11082-019-2142-z

New COVID-19 Normal: An Experimental Prototype of Smart Face Mask Vending Machine—An Indispensable Kiosk

Surya Chappidi, Kunal Nag, Devansh Shukla, and Sumit Kumar Jindal

Abstract In the ongoing COVID19 situation, one of the most basic yet necessary supplies for any human being is the face mask. Medical stores are facing shortage of face masks and it is also leading to crowding in confined spaces like medical stores hence aggravating the situation. The only solution to this is increasing the sources from where the citizens can get face masks and at the same time avoiding crowding and contact with any other human. The proposed Mask Vending Machine will make this happen. The physical machine that will store and vend the masks will have the Raspberry Pi as the central processing unit and the additional components like the steppers motors and monitor for display will be controlled by the Raspberry Pi. For payment and choice of quantity, an app has been designed. A QR code will be displayed on the monitor of the vending machine which has to be scanned with the app. Once scanned, it will ask the user for the number of masks needed and also facilitate the transaction process. Once successful, the masks will be vended.

Keywords COVID19 · Mask vending machine · Raspberry Pi · QR code · Transaction

1 Introduction

A conventional vending machine is an automatic machine that one can find at airports and metro stations typically in India. They provide items like bottled water, cold beverages, snacks, tickets, and many other days to day items [1]. Vending machines are accepted worldwide for dispensing daily or less common items without going to actual shops. The items are vended only after a successful and valid transaction [2].

The orthodox transaction options with a vending machine are putting coins and notes of the liable amount in return for the items selected by the consumer [3]. This method has worked fine for years but it has two major issues with it. Firstly, people have found techniques to defy the transaction mechanism by using tapes and fake

S. Chappidi · K. Nag · D. Shukla · S. K. Jindal (✉)
School of Electronics Engineering, Vellore Institute of Technology, Vellore, Tamil Nadu, India

B. Sikdar et al. (eds.), *Proceedings of the 3rd International Conference on Communication, Devices and Computing*, Lecture Notes in Electrical Engineering 851,
https://doi.org/10.1007/978-981-16-9154-6_13

currencies, therefore incurring losses to the vending company. Secondly, it involves a lot of physical contact with the vending machine which is the last thing anybody wants at the moment with a roadside parked object [4].

The modern transaction approaches include swiping credit cards, debit cards, or pre-loaded balance cards [5]. They have helped in putting an end to the invalid yet successful transaction and have also managed to decrease the physical contact amount and period to a certain extent but not fully [6]. The most effective transaction method which checks all the boxes is QR code-based payment [7]. The consumer only scans the QR code displayed on the machine and pays the liable amount using a payment method or gateway as per his/her convenience [8].

Keeping in mind all these factors, this work aims to revamp the conventional vending machine and bring it to the best use of the consumers in the current pandemic situation. At present, the need of the hour is face masks [9]. People are standing in queues to buy masks and even the medical stores are facing a shortage in supply of masks. In the proposed model, an attempt has been made to solve three problems simultaneously such as crowding of confined spaces like medical stores, economic losses due to unethical practices while transaction and short supply of masks in rural as well as urban locations [10].

This prototype centrally uses a Raspberry Pi 3 model B as its central processing unit. It coordinates with the hardware peripherals like the display and the servo motor as well as the software's for the proper working of the model. The interaction of the users with the vending machine will be through a python-based Graphical User Interface (GUI) and a minimalistic mobile application which has been developed primarily. The user will be scanning the QR code on the display using the QR code scanner of the app and will proceed with the transaction process. Once the transaction is complete, the corresponding number of masks will be vended.

With the abundant use of smartphones and internet all over the country including the rural section, deploying this machine in rural isolated areas would also be feasible [11, 12]. It will act as relief for places where less or no medical stores are present. Alongside, it will also benefit the urban parts too if positioned strategically across the city.

2 Proposed System

Figure 1 is the block diagram that briefly chalks out the proposed system of the advanced vending machine. A python-based GUI will be employed on the LCD screen of the vending machine which will help the user to interact with the machine with minimal physical contact. The user will enter the number of masks it requires and the entered data will be sent to the real-time database running on firebase. The availability of the masks is checked and then the user is prompted to proceed with the payment process. The payment is facilitated by a mobile app developed specifically for the purpose of paying for the masks bought through the vending machine. A QR code is displayed on the GUI screen placed on the vending machine which will

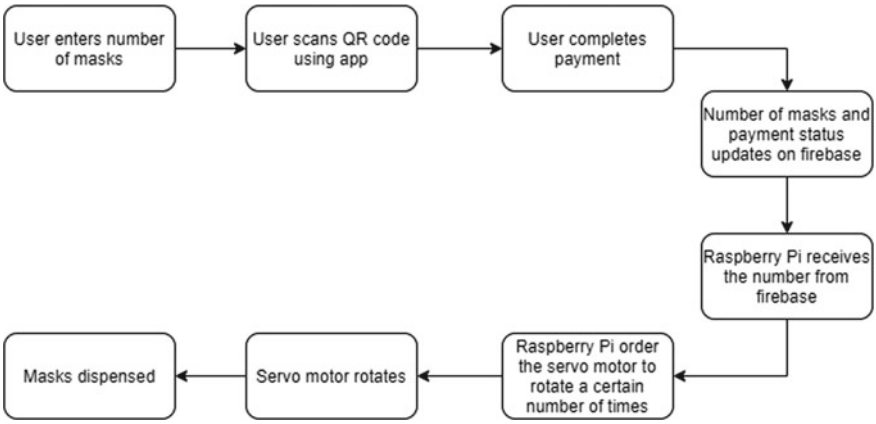

Fig. 1 Block diagram of proposed system

be scanned by the user. Once the payment is complete and the status of payment is changed on the firebase, the Raspberry Pi instructs the servo motor to rotate in order to vend the masks. The number of rotations depends on the masks requested by the user.

3 Experimental Setup

In Fig. 2, the LCD display is showing the python rendered GUI which is the user interface for inputting the number of masks and contains the pay button with an input box. The servo motors are connected to the Raspberry Pi and are ready to work on receiving the command.

Fig. 2 Experimental setup of proposed model

Raspberry Pi is used for communication between the vending machine and user. Servo motor is used for the mask dispensing mechanism and a Raspberry Pi touch LCD display is used as GUI for the user to enter the required type and number of masks present in the vending machine.

4 Results and Discussion

Figure 3 shows the first page which will be displayed on the monitor of the vending machine with which the users will interact with the vending machine to enter the number of masks it requires. The GUI can be used to display other additional information based on requirements and situations.

Figure 4 shows that the user has entered the number of masks it requires i.e. three. Once the user clicks on the pay button, a QR code is an auto-generated on the GUI which will be scanned by the user with the app that will help the user proceed with the transaction process. The required information is also updated in the firebase.

In Fig. 5, once the user enters his mask request, the database automatically receives and records the number in the "Masks" key of the firebase. This will be used for checking the availability of masks in the vending machine.

As shown in Fig. 6, the user can open the vending machine Application for making the Contactless Payment in an easy method using QR code. The User Interface of the Application is well designed for any user to be able to make the payment smoothly without any hassle.

Figure 7 shows when the user clicks on the "Pay" button it will be redirected to the next screen where the user needs to scan the QR code generated from the Mask Vending Machine Graphical User Interface as shown in Fig. 4 for a payment method.

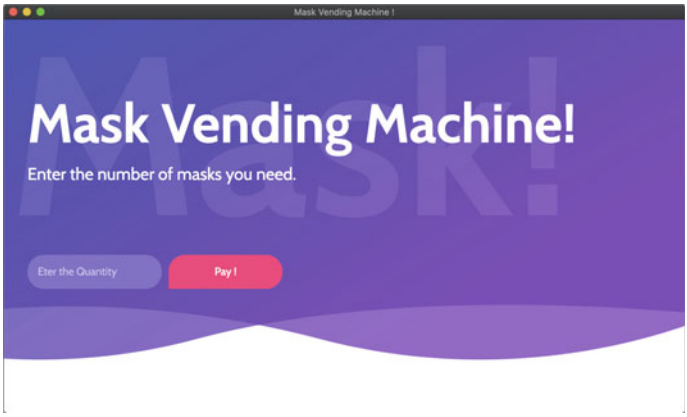

Fig. 3 Display GUI of the machine

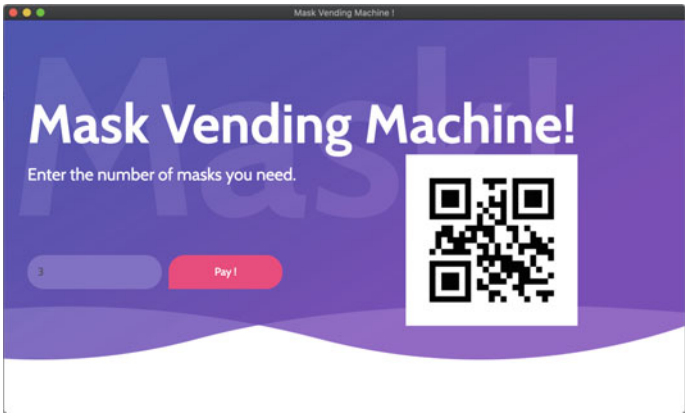

Fig. 4 User entered mask requirement

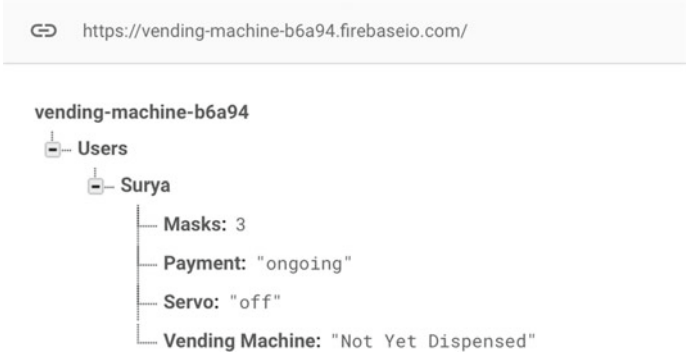

Fig. 5 Firebase before successful payment

Figure 8 shows after successful payment of the liable amount through any of the Payment Gateway present in the app, it updates the vending machine Database and displays the number of masks user has requested along with the payment confirmation on the app itself.

Figure 9 shows the database after the payment is completed. The payment status, servo motor status, and vending machine status are updated on the firebase automatically in the "Payment", "Servo", and "vending machine" keys of the firebase respectively.

In Fig. 10, The Raspberry Pi will communicate with the database which requests conditions such as number of masks, payment status, and servo motor status. Upon successful payment, the servo motors will be triggered by the Raspberry Pi and they will rotate a certain amount of times to dispense the appropriate number of masks requested by the user.

Fig. 6 Landing page of the App

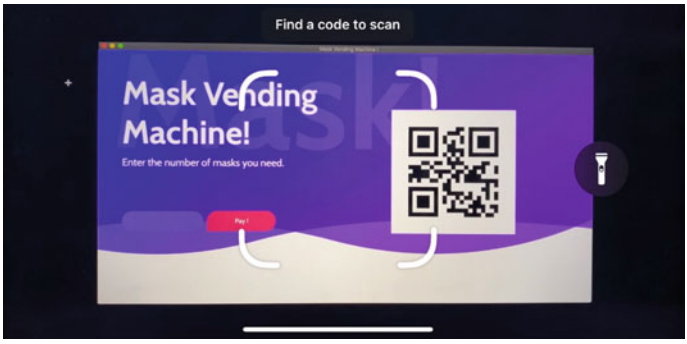

Fig. 7 QR scanning app window

Fig. 8 Entering recipient through serial monitor

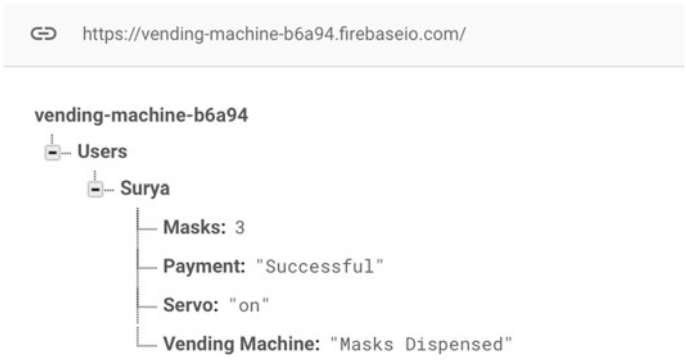

Fig. 9 Database after successful payment

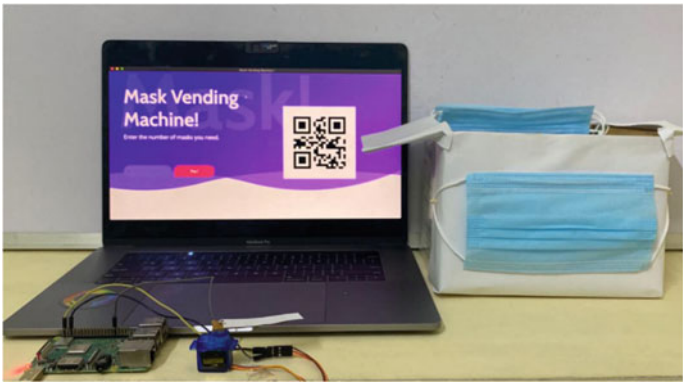

Fig. 10 Vending machine dispensing the masks

Table 1 Comparative study of the proposed model with existing literature

Sr. no.	Title	Result	Improvement
1	Coin acceptor based vending machine using microcontroller [3]	Implementation of coin acceptor vending machine using microcontroller system	QR code-based vending machine is implemented using microcontroller
2	Secure quick response-payment (QR-Pay) system using mobile device [8]	It provides non-repudiation and confidentiality of payment information	Basic payment process is achieved with real-time firebase database
3	Beverages in dispenser machine according to capsule identification with barcode [13]	It presented the basic idea of different kinds of vending machines and the products it vends	Basic Mask vending machine is implemented which also has a monitor for displaying information

5 Comparative Study of the Proposed Model with Existing Literature

See Table 1.

6 Conclusions

- The process of vending the desired number of masks by the user once it has given the input to the python-based GUI has been implemented successfully. This process was facilitated using the Raspberry Pi 3 and peripheral components like the servo motor and the display monitor.

- The Raspberry Pi acted as the central processing unit for the hardware system and the servo rotated to dispatch the mask. The monitor was used to display necessary information. The payment process was completely cashless and was done using a QR code scanning app developed for this purpose.
- Many future implementations can be made in the proposed system, such as displaying the locations of masks vending machines on a map. Whenever a user opens the app, user will get the information regarding the nearest located machine. This feature can provide the user the flexibility of tracking the machine, making masks easily accessible.

References

1. Baum, D.: Vending machine. In: Dave Baum's Definitive Guide to LEGO MINDSTORMS, vol. 10, issue no. 1, pp. 32–42. Apress, Berkeley, CA (2017)
2. Naeini, H.S., Mostowfi, S.: Using QUIS as a measurement tool for user satisfaction evaluation (case study: vending machine). Int. J. Inform. Sci. **5**(1), 14–23 (2015)
3. Oo1, H.M., Tun1, K.T., Aung2, S.M.: Coin acceptor based vending machine using microcontroller. Int. J. Trend Sci. Res. Dev. (IJTSRD) **3**(5) (2019)
4. Masood, M., Masood, Y., Newton, J.T.: Vending machine threat. Brit. Dent. J. **215**, 60 (2013)
5. Dua, A., Rustagi, C., Bhardawaj, A.: A novel approach to designing intelligent vending machines. IJITE**2**(12) (December 2014)
6. Gan, Z.X., Ng, W.S., Lee, B.H., Gwee, J.J., Jauw, V.L.: Vending machine transaction mechanism. Res. Develop. Mach. Des. **2**(2) (2018)
7. Surekha, A., Rubesh Anand, P.M., Indu, I.: E-payment transactions using encrypted QR codes. Int. J. Appl. Eng. Res. **10**(77) (2015). ISSN 0973-4562
8. Lee, J., Cho, C.H., Jun, M.S.: Secure quick response-payment (QR-Pay) system using mobile device. In: 13th International Conference on Advanced Communication Technology (ICACT) (2011)
9. Howard, J., Huang, A.: Face masks against COVID-19: an evidence review (2020)
10. Maharaj, S., Kleczkowski, A.: Controlling epidemic spread by social distancing: do it well or not at all. Maharaj and Kleczkowski BMC Public Health **12**, 679 (2012)
11. Watkins, J., Kitner, K.R., Mehta, D.: Mobile and smartphone use in urban and rural India. J. Media Cult. Stud. 26 (2012)
12. Singh, A., Banerjee, S.: A comparative study of consumer involvement amongst ruraland Urban consumers of smart phone. Int. J. Recent Sci. Res. **8**(9), 19692–19695 (2017)
13. Bodhale, A.P., Kulkarni, J.S.: Beverages in dispenser machine according to capsule identification with barcode. In: International Conference on Computing, Communication, Control and Automation (ICCUBEA) (2017)

Arduino and ESP32-CAM-Based Automatic Touchless Attendance System

Sumit Kumar, Kajal Sharma, Gaurav Raj, Dishani Datta, and Arpita Ghosh

Abstract Attendance is a compulsory requirement of every organization. Maintaining attendance register manually on a regular basis is a tough and laborious task. Some of the available solution to the same are biometric, RFID, eye detection, voice recognition, and many more. This paper delivers an effective and smart process for detecting the presence and marking attendance. This system uses motion detection and capture images and send those captured images to the respective mail id with the confirmation that the attendance has been received. The detailed explanation of the image capturing while motion is detected, and saving the images in a micro SD card is elaborated along with email sending procedure.

Keywords Arduino · PIR sensor · Motion detection · ESP32 camera

1 Introduction

Each and every organization either it is an educational institution or business organization, it has to maintain a proper record of attendance of students or employees for the effective functioning of organization. Designing an efficient attendance management system for students to maintain the records with ease and accuracy is the main purpose of the present work is to develop an automated touchless attendance system. Still today, the attendance is noted on paper as a record, and further, the related calculations are carried out at the end of the month. It causes unnecessary delay in the entire procedure starting from the recording to calculation to inform the students about their attendance status. There are several types of attendance reported some uses of RFID tags [1–3], QR codes [4, 5], biometric based [6], finger print based [7], face recognition [8–13], reported earlier. For the RFID tag-based system, each and every individual of the organization must be provided RFID tag-based identity cards, but in case of any intruder, there is no provision to keep a record of his or her presence. For fingerprint-based or biometric-based attendance system as well matches,

S. Kumar · K. Sharma · G. Raj · D. Datta · A. Ghosh (✉)
RCC Institute of Information Technology, Kolkata 700015, India

B. Sikdar et al. (eds.), *Proceedings of the 3rd International Conference on Communication, Devices and Computing*, Lecture Notes in Electrical Engineering 851,
https://doi.org/10.1007/978-981-16-9154-6_14

the entered finger print or biometric details through some card are matched with the database; if match is found accordingly, attendance is made. In this case also, only recognition of intruder is possible when data does not match with the saved database, but no provision is there to keep the details of the intruder or visitor so that afterward he/she can be identified. Same thing happens for the QR code-based systems also. The different face recognition systems, mainly algorithms, are there through which the person can be matched with the stored database. The visual recognition part can be implemented by training the system with a set of available data.

This presented work mainly focuses on the image acquisition and saving it in the SD card by detecting any motion. Afterward, the captured and stored image is sent to the predefined email address of the concerned authority. The images further can be matched with database available to the authority and using any face recognition algorithm [14–16]. In this way, the attendance can be marked for the particular person. The system can also detect the visitors/intruders as well as take and save their images for future reference. The present work mainly focuses on the first part, i.e., motion detection, image capturing, storing in SD card, and emailing the image. Here, a simple and portable approach to attendance with the help of ARDUINO Uno and ESP32-CAM module has been implemented. This system would improve accuracy of attendance records because it will remove all the hassles of roll calling (in case of classroom attendance of students) and will save valuable time of the teachers as well as students. This will also prevent proxy attendance, thus increasing the reliability of attendance records. The records are securely stored and can be reliably retrieved whenever required by the authority.

The overall method is explained in Sect. 3. Block diagram, circuit diagram and associated flowchart are elaborated in Sects. 4, 5, and 6, respectively. The hardware implementation and the result discussions are included in Sects. 7 and 8, respectively.

2 Method

This ongoing pandemic situation has forced us to choose several touchless systems to be chosen over the biometric or finger print-based systems which need direct contact with the surface. The presented work is also one of such systems which reduces the chance of any kind of direct contact while getting the information or images of the person entering an organization or classroom. For attendance record generally manual, fingerprint based, biometric based, QR code system, or RFID tag-based systems are used. Among these, most of them require direct contact with the scanning system or close proximity with that. Our aim is to mainly remove the direct contact or touch. The system is implemented with ARDUINO Uno, ESP32CAM module, and PIR sensor. The ARDUINO is a known efficient platform for implementing different applications [17–19]. The PIR sensors can be placed near the entrance or the gate or the door (for a specific room). If any kind of motion is detected, the rest of the part gets activated, and automatically, the images are being taken. Those images are first stored inside the SD card placed within the system to keep a track on the details with

time stamp for future reference. Then, the images are directly send to the email id of the corresponding authority. Those images further can be accessed and matched with the stored database using any face recognition system.

3 Block Diagram

The main objective of this work is the design and implementation of a touchless automated attendance management system. The work proposed to integrate both motion detection, capturing image, and sending to the appropriate authority for attendance management as well as intruder/visitor detection.

The block diagram of the complete system is portrayed in Fig. 1. The integral part of the block diagram is mainly Arduino Uno, PIR sensor, ESP32-CAM, power supply module, storage device(SD card), Internet.

3.1 Arduino Uno

The ARDUINO Uno is an open-source microcontroller board based on the microchip ATmega328P microcontroller, developed by Arduino.cc. The board is equipped with a set of analog and digital input/output (I/O) pins for enabling the interfacing to various expansion boards (shields) and other circuits. It has 14 digital input/output pins (of which six can be used as PWM outputs), six analog inputs, a 16 MHz ceramic resonator, a power jack, a USB connection, an ICSP header, and a reset button. The power supply connection for the board can be done with a USB cable connected to a computer or through battery or an AC-to-DC adapter (Fig. 2).

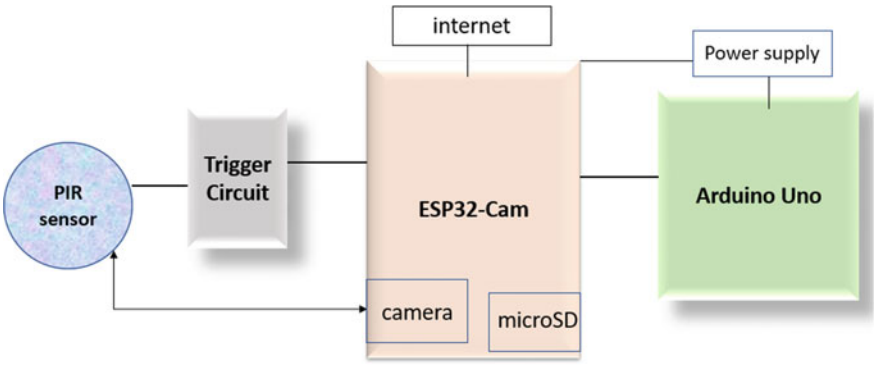

Fig. 1 Block diagram of the attendance system

Fig. 2 Arduino Uno board

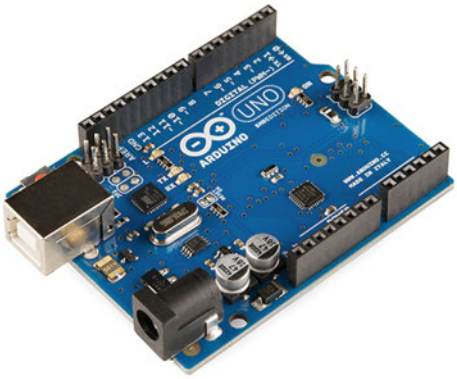

3.2 ESP 32 Camera

The ESP32-CAM is a development board with an ESP32 camera, microSD card slot for storing images taken with the camera or to store files and several GPIOs to connect peripherals. The ESP32-CAM board has two pins power (either 3.3 V or 5 V) and three for ground connection (GND). The GPIO 1 and GPIO 3 act as the serial pins and are required for uploading the code. The function of GPIO 0 pin is to identify whether the ESP32 is in flashing mode or not. Thus, the role of GPIO 0 pin is very important (Fig. 3).

Fig. 3 ESP 32 camera

4 Circuit Diagram

The connections for interfacing the Arduino with ESP32 CAM shown in Fig. 4 are explained below. Mainly, it consists of total six connections.

i. Arduino 5 V pin is connected to ESP 32 CAM 5 V.
ii. Arduino GND is connected to GND of ESP32.
iii. Arduino RX (receive pin) to CAM board RX and TX (transfer) pin of Arduino to TX of ESP32 CAM.
iv. Arduino reset pin is connected to GND.
v. ESP 32 CAM D0 is connected to GND.
vi. CAM board DO is connected to GND. The connection between CAM board and GND is essential to enable ESP 32 flash mode for programming. But, after completion of the programming, D0-GND and IO0-GND pins are disconnected.

Figure 5 shows the circuit diagram for ESP32-CAM-based motion triggered image capturing system. The trigger circuit which lies between the motion sensor and ESP32-CAM board generates an interrupt to wake up the ESP32-CAM module when the motion is detected by PIR motion sensor. The ESP32-CAMm board does not contain any onboard USB connector. Here, to solve this problem mainly, the Arduino Uno has been used, to upload the code through the serial pins known as U0T and U0R pins. For keeping the ESP32-CAM in the flashing mode pin, GPIO 0 (IO0) is connected to GND. In this way, the code uploading feature is enabled.

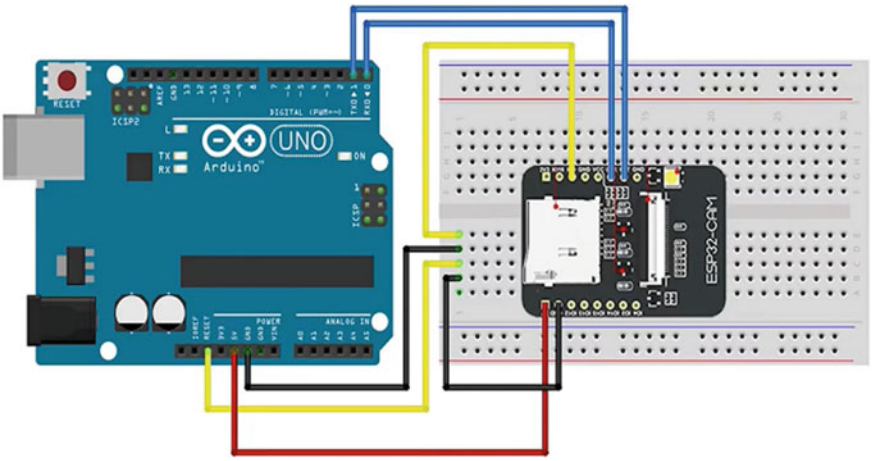

Fig. 4 Interfacing of ESP32-CAM with ARDUINO

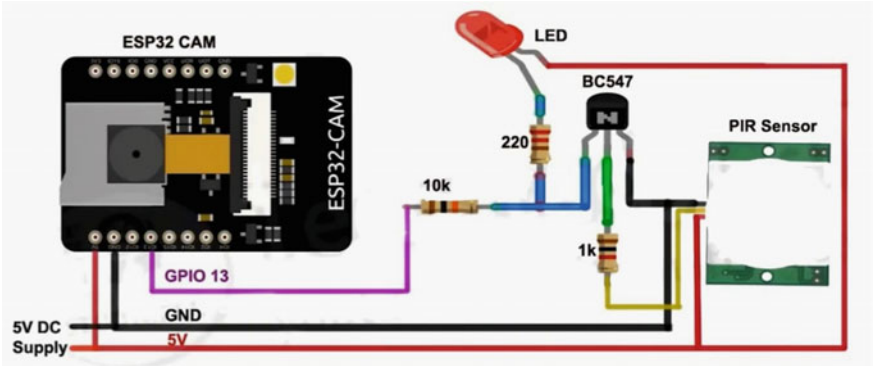

Fig. 5 Circuit diagram of automatic image capturing part

5 Flowchart

The flowchart of the automatic touchless attendance system with Arduino and ESP32-CAM is depicted in Fig. 6. Here, any kind of direct contact between the system and the human being can be totally avoided while recording/capturing the images as attendance data. The flow of work for the system first starts with the process in which at first motion is detected with the help of PIR sensor. After that image is captured with the help of ESP32 camera and that captured image is saved to the micro SD card. All the captured photos are emailed to the previously stored mail id of the admin or authority. For enabling the system to store as much as data or image,

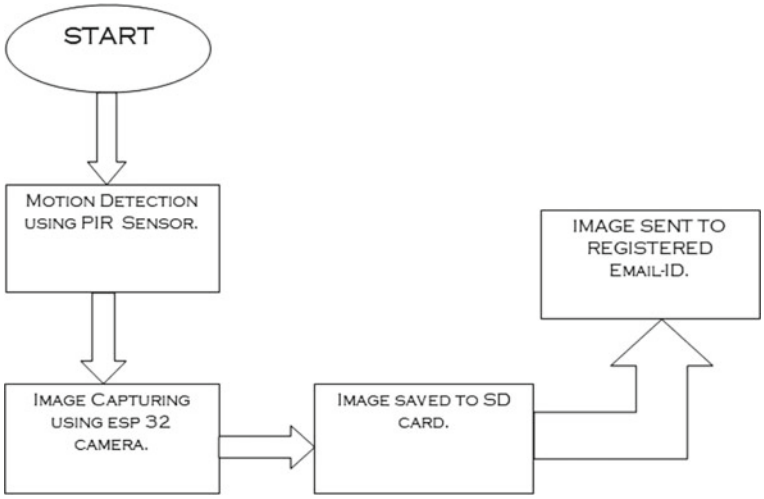

Fig. 6 Flowchart of the image acquisition and mail transfer system for the automatic attendance system with Arduino and ESP32-CAM

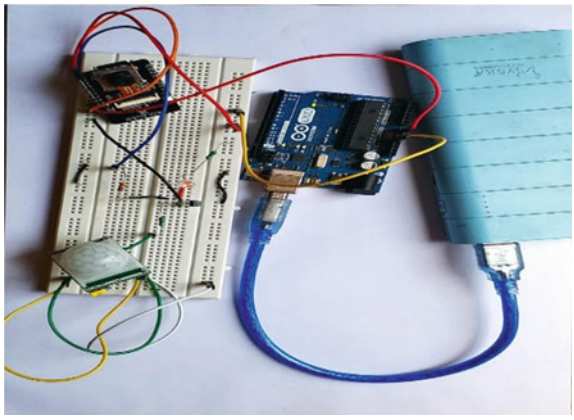

Fig. 7 Hardware implementation of the complete circuit

only, the memory card size needs to be increased. The steps for sending email to the corresponding authority starting from motion detection can be divided into five blocks. The motion sensing part, image capturing unit, image storing unit, and finally, the images sending as attachments to the authorized mail id for further processing or verification.

6 Hardware Implementation

The entire hardware part of the system is shown in the schematic below in Fig. 7. It includes the motion detection part designed with the PIR sensor and ESP32-CAM through a BJT (BC547). The transistor is working here as a switch, whenever any motion is detected; accordingly, the associated pin of ESP32-CAM gets the proper activation to start operating. Second part of the schematic includes interfacing of the ESP32-CAM module with Arduino Uno. For powering up the Uno board, a power bank has been used. All the interfacing and the circuit implementation have been done in the bread board.

7 Result and Discussion

On the serial monitor log, ESP32-CAM is successfully connected to the Wi-Fi network. The mounted microSD card successfully captures the images and then goes to deep-sleep mode. The ESP32-CAM remains in deep-sleep mode with external wake up enables at pin 13. Whenever the PIR sensor senses any movement within the range, the output pin of the PIR sensor becomes high. In this way, the ESP32-CAM gets the wake-up signal. After waking up, it captures the pictures. Then, flow of work is followed by storing the picture in the microSD card connected with ESP32-CAM.

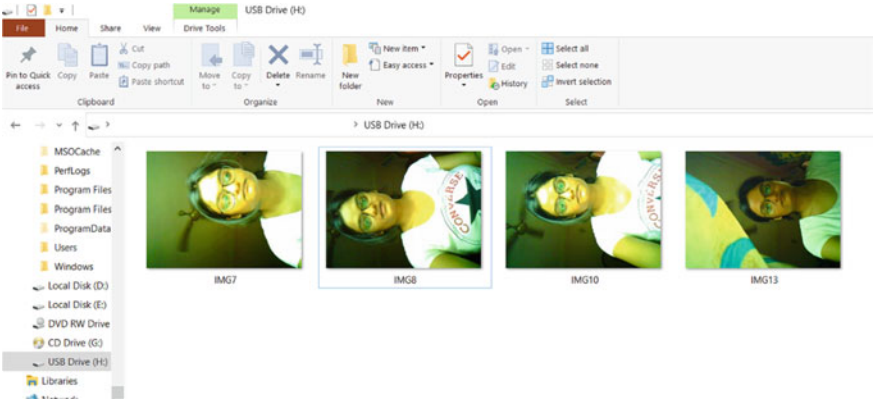

Fig. 8 Images captured and stored in the SD card

After some millisecond delay, the ESP32-CAM again goes to the deep-sleep mode until it gets the next wake-up signal at pin 13. The switching between sleep modes and waking up reduces the power consumption of the circuit and allows to take the pictures only when any motion is detected by the PIR sensor. Images captured and stored in the microSD card with the help of the PIR motion sensor, and ESP32-CAM is shown below in Fig. 8.

The number of images captured can be improved by increasing the storage capacity of the microSD card. Figure 9 shows one of the stored images after being captured and mailed as an attachment to the authorized mail id (here dishanidutta1500@gmail.com). The authorized person will get the email notification, whenever any movement is detected along with the captured and stored image as an attachment.

8 Conclusion

The attendance system presented in this work is automatic system implemented with Arduino Uno, PIR sensor, and ESP32-CAM. The main advantage of this system is contact less. By using the Arduino platform, system becomes more faster in response, and while burning the code, it is just like plug and play device. User can change the application accordingly by using Arduino. It is very easy to use and simple to implement. Whenever any motion near the PIR sensor is detected, the ESP32-CAM starts taking images and saves them in the microSD card attached. The images are then sent to the concerned authority for tracking or matching the images with the database for attendance purpose. For intruder/visitor detection, the images can be accessed in future also with proper timestamp.

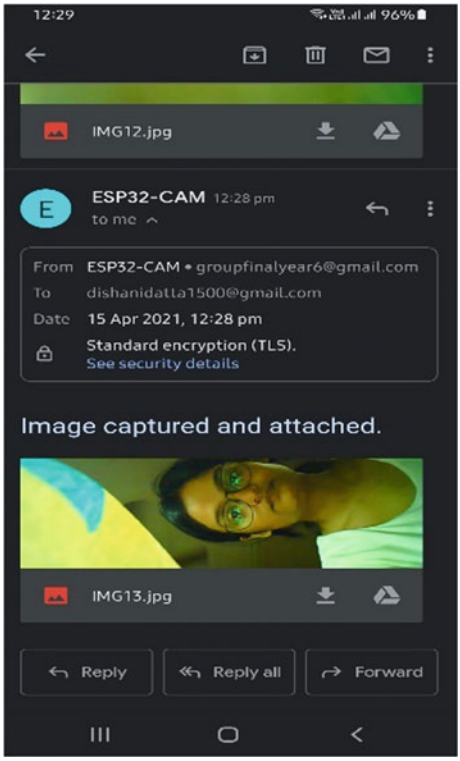

Fig. 9 Attachment of captured image in the mail id of the authority

References

1. Joshi, A.: RFID based attendance system. Int. J. Modern Trends Sci. Tech. **7**, 40–43 (2021)
2. Arulogun, O., et al.: RFID-Based Students Attendance Management System. Int. J. of Eng. Sci. Res. **4**(2), 1–9 (2013)
3. Kariapper, R.K.A.R., Razeeth, S.: RFID based (IoT) automatic attendance system: a survey analysis. SSRN Electr. J. (2019) https://doi.org/10.2139/ssrn.3372734
4. Zailani, F.: QR Code Attendance System (2020). https://doi.org/10.5281/zenodo.4310523
5. Manori, A., Devnath, N., Pasi, N.: QR code based smart attendance system. Int. J. Smart Bus. Technol. **5,** 1–10 (2017). https://doi.org/10.21742/ijsbt.2017.5.1.01
6. Imran, E., Ujan, I.A., Ismaili, I.A.: Biometric attendance system. In: The 2011 IEEE/ICME International Conference on Complex Medical Engineering, pp. 499–501 (2011). https://doi.org/10.1109/ICCME.2011.5876792
7. Ezema, L., et.al.: Fingerprint Based Attendance Management System. Int. J. Sci. Eng. Res. **6**(7), 1623–1628 (2015). ISSN 2229–5518
8. Kar, N., Barma, D.M.K.D.: Study of implementing automated attendance system using face recognition technique. Int. J. Comput. Comm. Eng. **1**(2), 100–103 (2012). ISSN: 2010-3743
9. Bradski,T., Kaehle,A.: Opencv ml algorithms, in Learning OpenCV. O'Reilly Media, Inc, p. 580 (2008)
10. Kanti, J., Papola, J.: Smart attendance using face recognition with percentage analyzer. Int. J. Adv. Res. Comput. Comm. Eng. **3** (2014)
11. Joseph, J., Zacharia, K.: Automated attendance management system using face recognition. Int. J. Sci. Res. **2** (2013)

12. Sawhney, S., et.al.: Real-Time Smart Attendance System using Face Recognition Techniques. In: International Conference on Cloud Computing, Data Science and Engineering (Confluence), pp. 522–525 (2019). doi:https://doi.org/10.1109/CONFLUENCE.2019.8776934
13. Selvi, K., Chitrakala, P., Jenitha, A.: Face recognition based attendance marking system. IJCSMC **3**(2), 337–342 (2014)
14. Wei, Y.: Review of face recognition algorithms. In: International Conference on Biomedical Imaging, Signal Processing, Kitakyushu Japan, pp. 28–31 (2020). https://doi.org/10.1145/3436349.3436367
15. Alghamdi, J., et.al.: A survey on face recognition algorithms. In: International Conference on Computer Application and Information Security (ICCAIS), Riyadh, Saudi Arabia, pp. 1–5 (2020). https://doi.org/10.1109/ICCAIS48893.2020.9096726
16. Tao, Y., He, Y.: Improved PCA face recognition algorithm, In: Zeng, J., Jing, W., Song, X., Lu, Z. (eds.) Data Science, ICPCSEE 2020. Communications in Computer and Information Science, vol. 1257. Springer, Singapore (2020). https://doi.org/10.1007/978-981-15-7981-3_44
17. Mukherjee, S., Dhar, M., Ghosh, A.: Accelerometer based wireless gesture controlled robot for medical assistance using Arduino Lilypad. Int. J. Eng. Technol. Sci. Res. **5**(3), 155–161. ISSN: 2394–3386(2018)
18. Mukherjee, S., Ghosh, A., Sarkar, S.K.: Arduino based wireless heart-rate monitoring system with automatic SOS message and/or call facility using SIM900A GSM module. In: International Conference on Vision Towards Emerging Trends in Communication and Networking (ViTECoN), pp. 1–5 (2019). doi:https://doi.org/10.1109/ViTECoN.2019.8899504.
19. Datta, S., et. al.: ARDUINO based Water Level Detector for Visually Impaired people**,** Computational Science and Engineering, pp. 137–140. CRC Press, Taylor & Francis (2016). ISBN: 978-1-138-02983-5

Speech Emotion Recognition of Tamil Language: An Implementation with Linear and Nonlinear Feature

S. Prayla Shyry, A. Christy, and Y. Bevish Jinila

Abstract In the past decades, speech emotion recognition has made remarkable footprints in human–computer interaction and affective computing. Conventional techniques use acoustic, prosodic, lexical, and paralinguistic features and proved the importance and accuracy rate. Also, K-nearest neighbor, support vector machine, other standard classifiers are used to classify the different emotions. In this paper, video and audio signals are fetched from the Tamil speaking people, and the emotions of the people are recognized with good recognition rates. Both video and audio signals are preprocessed to remove the noise using the bandpass filter. Temporal feature extraction is used to improve the recognition rate. Remarkable comparison is made with nonlinear (Hurst parameter) and linear feature parameters (wavelet packet cepstral coefficient). To avoid false classification, operational, and computational cost, the dimensionality of the feature set is reduced with principal component analysis. The selected features are classified with KNN, GMM for five emotion classes, namely happy, sad, angry, fear, and disgust. The proposed mixed/hybrid model of KNN, HMM, and GMM is implemented to recognize the emotions, and the results are compared with traditional KNN and GMM. Also, our present database is compared with different standard databases like Tamil Speech Data-ASR, CMU-INDIC, and LDC-IL.

Keywords Dimensionality reduction · Linear feature · Nonlinear feature · Speech recognition · Emotion recognition

1 Introduction

Even though the research focus in artificial intelligence has made tremendous outcomes, there is a gap and large thirst for speech emotion recognition in affective computing. Since machines do not understand human emotions, natural human–computer interaction is struggling a lot to strive and compete with today's market.

S. Prayla Shyry (✉) · A. Christy · Y. Bevish Jinila
Sathyabama Institute of Technology, Chennai, Tamil Nadu, India

B. Sikdar et al. (eds.), *Proceedings of the 3rd International Conference on Communication, Devices and Computing*, Lecture Notes in Electrical Engineering 851,
https://doi.org/10.1007/978-981-16-9154-6_15

Day-to-day physical and psychological behavior of human is influenced by emotions. Other than behavioral expressions, emotion recognition from speech signal is the challenging modality. Many researchers have proved that the selection of appropriate features and suitable classifiers marks accurate recognition of emotion. Rajisha et al. [4] used Mel frequency cepstral coefficients, pitch and short time energy for feature extraction and artificial neural network (ANN), and support vector machine (SVM) for classification. Kun Han et al. have used segmentation-level and utterance-level features for classification of emotion classes. Muzaffar et al. used rank-ordered formant frequency and log entropy feature for the emotion classification and SVM, KNN for pattern classification. Yi Lin et al. [31] used sequential forward selection (SFS) to determine the best feature subset and have made a classical comparison with Mel frequency cepstral coefficients and classified the emotion states using HMM and SVM. Chandra et al. [26] analyzed the speech signal through prosodic features like energy and pitch. Sanchez et al. [32] studied a long memory process through Hurst exponent by R/S analysis. Tomasso et al. [33] have compared subjective valence and arousal features and proved Hurst exponent as a suitable indicator of subjective valence. Numerous researches focus in emotion recognition for French, English, and Spanish, but very less attention has been taken for the Tamil language. So a novel approach for speech emotion recognition is proposed for Tamil, the south Indian Dravidian language, native language of Tamil people. Hence, the main objective of this paper is to come with a more accurate recognition rate of emotion states by extracting both linear and nonlinear features. Also both the features are compared and the feature set is reduced by vector quantization and principal component analysis. The selected and reduced feature set is classified by KNN, GMM and mixed model of KNN, GMM, and HMM, and comparative study of these results are made with three different databases, namely Tamil Speech Data-ASR, CMU-INDIC, and LDC-IL which has beautiful Tamil audio files.

2 Preliminaries

Reliable speech emotion recognition ensures quality interaction between the human and the computer. Nanavare and Jagtap [1] have proposed Mel frequency cepstral coefficient (MFCC) to extract the features and hidden Markov model to classify the emotion dataset created by their style by retrieving the utterances from various speakers. They have also studied the similarities between two sequences with dynamic time warping. Their results revealed that the accuracy rate of HMM is better when compared to the dynamic time warping.

Ling et al. [2] experimented speech emotion recognition with a prerecorded dataset and real-time recording with four different emotion scenarios. They have achieved remarkable accuracy rate, and they have tested the speech emotion Recognition model in online learning. They have analyzed the student's emotions for their courses, and such type of model helps the online courses to be customized to satisfy the students. Jianfeng et al. [3] recognized emotion features from speech with long

short-term memory (CNN LSTM) networks, two convolutional neural networks, and one 2D CNN LSTM network and one 1D CNN LSTM network. Their experiments revealed that two CNN with LSTM networks have noticeable overall performance than traditional methods and can learn discern various features, model high level of from the emotional information.

Rajisha et al. [4] have developed speech emotional retrieve model for one specific Malayalam language with short time energy (STE), Mel frequency cepstral coefficients (MFCCs) and pitch to extract the features. They have classified the patterns by SVM and ANN and determined the accurate recognition rate and concluded that ANN has much better accuracy compared to SVM. Such a remarkable accuracy is achieved by ANN because of its resistance to the insufficient amount of data. Turgut [5] developed new methodology to extract the acoustic features for speech emotion recognition. Experimental tests are carried with four different datasets with eight different emotions, and they have achieved a 71.66% accuracy rate compared to PCA, SFS, and FCBS feature selection methods.

Assel et al. [6] studied the speech emotional distinguishability for the prerecorded dataset with the peak to peak distance from the graphical representation of speech signals for 30 different subjects. Results show that data collected from a single person yields better accuracy than the features retrieved from a group of people. Rupayan et al. [7] proposed a novel emotion recognition for acted and spontaneous speech for call centers, IVR, and EModatabase. The lapse time of the utterances in the linguistic contents and the audio call is validated, and they tested the framework with matched and unmatched train-test conditions.

3 Materials and Methods

3.1 Preprocessing

The system accepts both video and audio signals, and the video signals are converted to .wav files using video signal and share audio converter. Usually, the target signal gets mixed with additive noise due to bad weather, background noise, and also may be due to a transmission channel. Many researchers have struggled to reduce additive noises using better quality microphones and machine learning algorithms. Also, they have focused on speech intelligibility of the speaker and insisted to use exact and appropriate phonetics. To improve the quality of the voice, unwanted noise is removed from the audio files. Figure 3 gives the general block diagram of the proposed work. In this work, the second-order bandpass filter is used to filter the additive noise to reach the clarity of the voice. A second-order bandpass filter is used to preserve cut-off frequencies within the selective band and attenuates all that falls outside the specified range. Advantage of bandpass over other filters is that it never adds extra noise while computation. Figure 1 shows the frequency preserve using a filter.

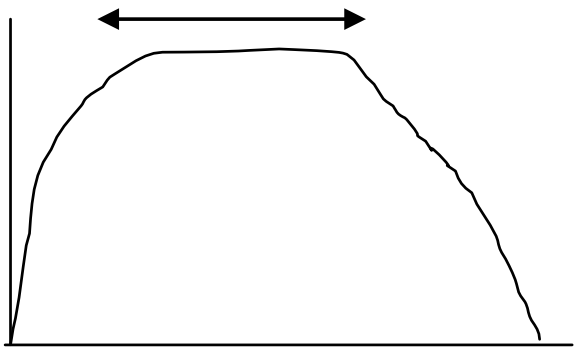

Fig. 1 Preserve frequency using bandpass filter

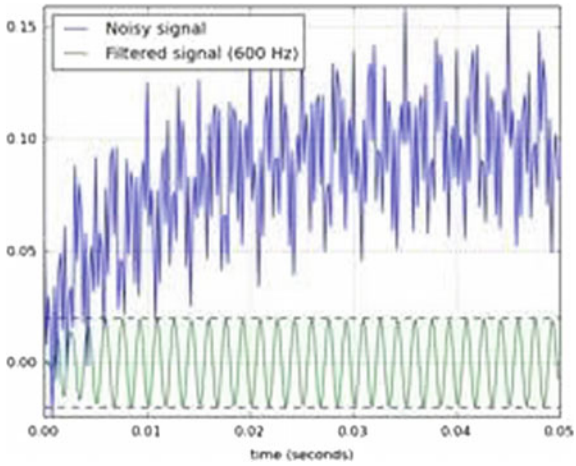

Fig. 2 Filtered signal using bandpass filter

Figure 2 shows the removal of noise from the audio signal, blue wave is noisy signal, and the green signal indicates the preprocessed filtered signal.

Figure 3 receives the .wav files, and the input signal is preprocessed to remove the unwanted background noise by a bandpass filter to get the exact attenuation. The features in the preprocessed signal are extracted using both nonlinear and linear parameters. The feature set is then reduced for simplicity using principal component analysis. The selected features are classified with three different classifiers to classify the emotion class.

3.2 Nonlinear and Linear Feature Extraction

The Hurst parameter is derived by rescaled range statistics, and the smoothness of a fractal time series is analyzed that is based on the asymptotic pattern of the rescaled

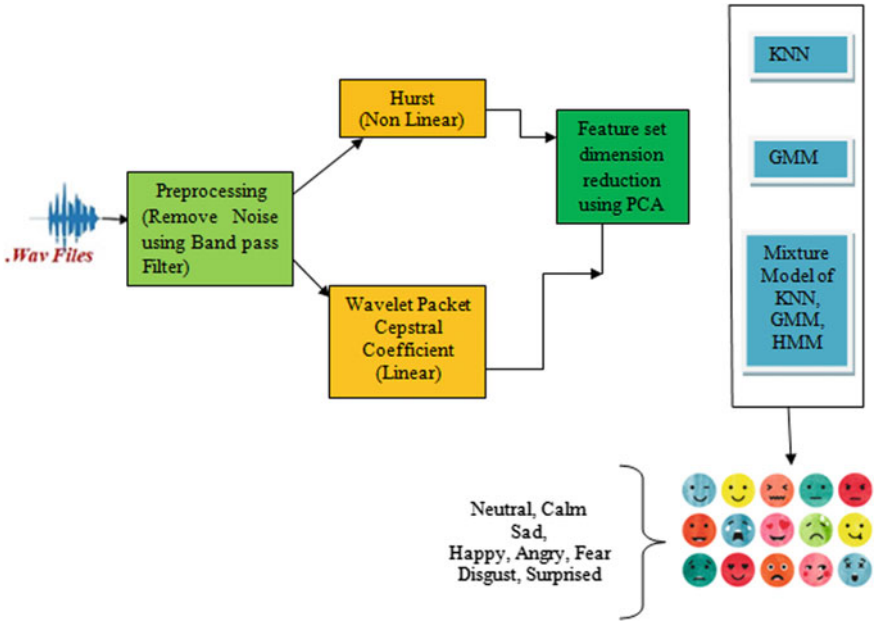

Fig. 3 Block diagram of the speech emotion recognition

range of the process. The total accumulated deviation of the mean of time series overtime is computed.

3.2.1 Determination of Hurst Parameter by R/S Method

1. The audio clip concerning time series is divided into multiple subseries, each with length T.
2. Find the mean and standard deviation of all the subseries.
3. Normalize the data of the subseries and create the cumulative time series.
4. Find the difference between maximum and minimum of cumulative time series.
5. Apply linear regression over a sample increasing time horizons.
6. The rescaled range *R*/*S* with time Ti as,

$$R/S \sim T_1^H \tag{1}$$

where, R = (maximum deviation-minimum deviation of mean), S = Standard deviation.

From the above Eq. 1, Hurst Parameter is derived as below

$$H = \log(R/S)/\log(T_i) \tag{2}$$

where, *R*/*S*—Rescaled Range, T is the length of sample data.

The other feature I have used for classification is wavelet packet cepstral coefficient (linear feature). Conventional methods take fixed frames of speech and transform it into the corresponding frequency domain. Since it uses fixed frames, the localized events and abrupt changes in the present speech signal are poorly analyzed, and it eventually leads to pitiful recognition rate. So many researches are already in the race to overcome this issue, and they have landed with the idea of wavelets.

3.2.2 Determination of Wavelet Packet Cepstral Coefficient

The input audio signal is decomposed by the repetition of low-pass and high-pass filters. This decomposed signal is again decomposed to second-order decomposition. At the end of each decomposition, filtering and subsampling results in the number of samples and frequency resolutions doubling

1. The input audio signal is pre-emphasized using filters that does enhancement of the signal's high frequencies in the spectrum.
2. The whole signal is divided into small frames (windows) using windowing operation, in which the whole speech signal is greater than the size of the duration of the signal. Here, the shift duration for two consecutive windows and the width of the window is calculated.
3. For each window, [2] decompose the signal using discrete wavelet transform to get the cepstral coefficient for each level.
4. The detail coefficient of all the levels is passed through the log energy calculation.
5. The log energy of the wavelet coefficients at a particular level j is (from [2])

$$c_s[m, 2^j] = \frac{1}{\sqrt{2^j}} \sum_{n=0} s[n] \Psi\left(\frac{n-m}{2j}\right) \tag{3}$$

6. All the wavelet coefficients of the levels are concatenated together to form the single vector cepstrals.

The size of the feature set is reduced by the principal component analysis, and finally, pitch, speaking rate, intensity, jitter, shimmer, and frequency are selected.

3.3 Emotion Classification

In the speech emotion recognition system after calculation of the features, the selected features are provided to the classifier. The classifiers recognize the emotion in the speaker's speech utterance. Various types of classifier have been proposed for the task of speech emotion recognition. Gaussian mixed model (GMM), K-nearest neighbors

Table 1 Recognition rate for KNN classifier (68.36)

Emotions	Happy	Fear	Angry	Sad	Disgust
Happy	78.8	10.9	7	0	13
Fear	10.6	64.3	6.6	2.2	2.8
Angry	7.3	10.3	79.3	2.6	6.9
Sad	0	2.3	0	65.8	6.4
Disgust	2	8.4	3.7	7.9	53.6

Table 2 Recognition rate for GMM classifier (62.46)

Emotions	Happy	Sad	Fear	Angry	Disgust
Happy	**74.1**	0	13.3	0	9.7
Sad	0	**71.3**	1.7	10.8	12
Fear	9.7	3.5	**53.5**	2.1	0.7
Angry	0	11.4	1.9	**61.9**	9.7
Disgust	4.5	1.6	11.9	6.2	**51.5**

Table 3 Recognition rate of mixed model of HMM/KNN/GMM classifier (70.54)

Emotions	Sad	Happy	Fear	Angry	Disgust
Sad	**73.7**	0	6.7	0	5.8
Happy	2	**81.7**	0	9.8	9.5
Fear	7.7	2.9	**66.3**	1.2	7.3
Angry	0	1.3	0	**77**	9.9
Disgust	4.9	4.2	11.9	5.5	**54**

(KNN), and hidden Markov model (HMM) are the classifiers used in the speech emotion recognition system (Tables 1, 2 and 3).

4 Results and Discussion

It is revealed from Fig. 5 that the recognition rate of emotion classification is 70.54 with mixed model of HMM/KNN/GMM classifier which is much better when compared to KNN and GMM classifiers (Fig. 4 and Table 4).

Nonlinear and linear features are compared with different classifiers, and the accuracy of recognition rate for nonlinear features varies with an average of 2% from linear features (Table 5).

Both audio and video signals are acceptable as the input, and the accuracy of recognition rates of emotion classification is calculated.

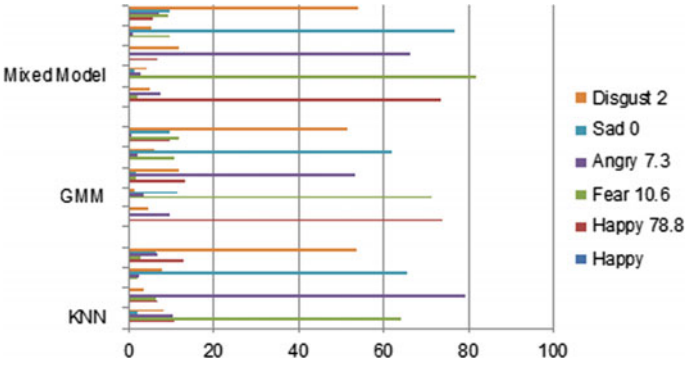

Fig. 4 Comparison of the recognition rates of KNN, GMM, and mixed model of HMM, KNN, and GMM

Fig. 5 Percentage of dataset for training and testing

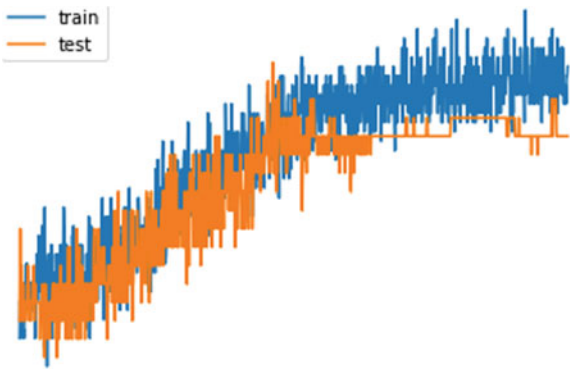

Table 4 Comparison of the Hurst parameter and wavelet packet cepstral coefficient with classifiers

Model	Accuracy with nonlinear feature (%)	Accuracy with linear feature (%)
GMM	62	61
KNN	68.36	67
Mixed model of HMM + KNN + GMM	70.57	68.45

Table 5 Comparison of accuracy rate for two input signals

Models	Audio	Video
GMM	55.23	60.9
KNN	63.12	67
Mixture model of HMM, SVM, and KNN	65.9	70.17

Table 6 Comparison of jitter (angry emotion) with Hurst parameter (H) and wavelet packet cepstral coefficient (WPCC)

Jitter	Models	Hurst	WPCC
	KNN	1.2	1.8
	GMM	0.8	1.1
	Mixed model of HMM, GMM, KNN	0.5	0.8

The above Table 6 shows the values of jitter (angry emotion) for linear and nonlinear features for different classifiers, and the results show that WPCC shows marvelous outcome for mixed model of HMM, GMM, and KNN.

5 Conclusion and Future Scope

Automated speech emotion recognition plays a remarkable role in the field of human–computer interaction and affective computing. The quality of human speech recognition relies on the set of features selected and the type of classifiers used for recognition. This work depicts the speech emotion recognition in the Tamil language for both audio and video signals. Great research is delivered in this paper with the comparison of linear and nonlinear features with three different classifiers. Husk values and the wavelet packet cepstral coefficient features are extracted, and the dimensionality of the feature set is reduced by the principal component analysis. The algorithms are implemented with three Tamil datasets Data-ASR, CMU-INDIC and LDC-IL, and the qualitative values are calculated to determine the accuracy rate of the speech emotion recognition. In a practical view, it is found that the nonlinear feature selection outperforms well than linear features both for audio and video input signals. Also, the proposed mixed model of HMM, GMM, and KNN yields better accuracy rate of recognition for the classes of emotions.

6 Availability of Data and Material

Generated real database and compared with traditional database Tamil Speech Data-ASR, CMU-INDIC, and LDC-IL.

Funding: The research has not received any funding from agencies. Conflicts of interest/Competing interests: There is no conflict of Interest.

Availability of data and material: Generated real database and compared with traditional database Tamil Speech Data-ASR, CMU-INDIC, and LDC-IL.

Authors' contributions: The authors have equal contributions in the implementation and draft preparation ethics approval.

References

1. Nanavarea, V.V., Jagtap, S.K.: Recognition of Human Emotions from Speech Processing. Procedia Comp. Sci. **49**, 24–32 (2015)
2. Cen, L., Wu, F., Yu, Z.L., Hu, F.: A real-time speech emotion recognition system and its application in online learning. Emotions Technol. Des. Learn. 27–46 (2016)
3. Zhaoa, J., Maoa, X., Chena, L.: Speech emotion recognition using deep 1D & 2D CNN LSTM networks. Biomed. Signal Process. Control **47**, 312–323 (2019)
4. Rajisha, T., Sunija, M., Riyas, A.: Performance analysis of malayalam language speech emotion recognition system using ANN/SVM. Procedia Technol. **24**, 1097–1104 (2016)
5. Ozseven, T.: A novel feature selection method for speech emotion recognition. Appl. Acoust. **146**, 320–326 (2019)
6. Davletcharovaa, A., Sugathan, S., Abraham, B., James, A.P.: Detection and analysis of emotion from speech signals. Procedia Comput. Sci. 91–96 (2015)
7. Chakraborty, R., Pandharipande, M., Kopparap, S.K.: Knowledge- based framework for intelligent emotion recognition in spontaneous speech. Procedia Comput. Sci. **96**, 587–596 (2016)
8. Khan, M., Goskula, T., Nasiruddin, M., Quazi, R.: Comparison between k-nn and svm method for speech emotion recognition. Int. J. Comput. Sci. Eng. 3(2), 607–611 (2011)
9. Khan et al.: KNN and SVM for speech recognition and their results shows average accuracy 91.71% for KNN and 76.57% for SVM classifier (2011)

Radiation-Resilient GaN/$In_xGa_{1-x}N$ Multi-junction Solar Cells with Varying in Contents

Nath Pramita and Biswas Abhijit

Abstract This present work reports development of an analytical model for InGaN/GaN multi-junction solar cells having to vary in contents validated with numerical simulation results using Sentaurus TCAD. The performance of the solar cells is optimized with reference to various Mg doping concentrations in the cap layer and in the content of the two layers acting as the active region of the solar cell. Results obtained from our model show an excellent concordance with the simulation data and also limited experimental data reported elsewhere. The simulation study reveals that the optimum Mg doping density is 10^{19} cm^{-3} which balances between the front surface recombination phenomena and the extraction of electron–hole pair at the two ends. The obtained results show that the proposed solar cell yields a peak power conversion efficiency of 2.87%, a fill-factor of 64%, a short-circuit current density of 6.60 mA-cm^{-2}, and an open-circuit voltage of 0.68 V. Most importantly, our optimized solar cell yields 70% improvement in power conversion efficiency in comparison with the conventional structure at AM1.5 solar irradiance.

Keywords InGaN/GaN multi-junction solar cell · Open-circuit voltage · Power conversion efficiency · Short-circuit current density

1 Introduction

In recent years III-V nitride-based materials have shown promise for processing electronic and opto-electronic devices including power transistors, LASERs, blue LEDs, and many more [1–9]. To date, particularly ternary InGaN alloys have attracted much interest as an excellent candidate in photo-voltaic applications such as high-temperature PV modules, terrestrial photo-voltaic thermal solar light collector suitable for space applications and top cells in multi-junction (MJ) solar cells [2]. The demand for these nitride materials is ever-increasing due to their unique properties which include direct bandgap ranging from 0.64 to 3.4 eV covering the entire visible

N. Pramita (✉) · B. Abhijit
Institute of Radio Physics and Electronics, University of Calcutta, 92, Acharya Prafulla Chandra Road, Kolkata 700091, India

B. Sikdar et al. (eds.), *Proceedings of the 3rd International Conference on Communication, Devices and Computing*, Lecture Notes in Electrical Engineering 851,
https://doi.org/10.1007/978-981-16-9154-6_16

solar spectrum, high absorption coefficient, thermal stability, high carrier mobility, and outbreaking irradiance resistance [2]. Among these properties, the high tolerance capability of InGaN alloy to large energy (2 meV) photon irradiance than other conventional photo-voltaic materials like GaAs, GaInP, silicon, and organics [6, 7], has captivated the attention of the scientific community. This special property enables applications of nitride-based modules in harsh environmental conditions. The processing of InGaN alloys was initially started by Anderson's group at the Florida University (2003) [3] and subsequently, extensive research works have been conducted toward the fabrication of nitride materials [3] in order to produce good quality materials and reduce polarization induced effects [2]. Moreover, various schemes were reported, for instance, incorporation of strained InGaN/GaN multiple quanta well in the active region of solar cells [10], use of free-standing GaN substrate to overcome the dislocation densities [2], and adoption of different fabrication methodologies [11]. To alleviate polarization-related issues the semi-polar and non-polar structures have been developed [6, 12, 13]. Screening the earlier literature, it turns out that the researchers have mainly focused on mitigation of the material ailments, control polarization issues using back surface field (BSF), front surface field (FSF), alongside a window layer in the architectures [6] with a view to obtaining the power conversion efficiency. However, the least attention was paid to the impact of varying in content on the performance of radiation-resilient GaN/InGaN multiple quanta well solar cells.

In this present work, we investigate GaN/InGaN MJ solar cell architecture employing a band gap tailoring scheme using analytical approach supported by numerical simulation. We develop a model for non-polar GaN/InGaN-based multi-junction solar cells employing different layers of InGaN materials containing indium mole fractions of 0.2 and 0.3 in the active region. In addition, the impact of Mg doping of the cap layer on PV performances is studied using numerical analysis. Furthermore, the photo-voltaic performance of our optimized solar cell is compared with earlier reported results published elsewhere.

2 Structure of the Solar Cell

The cross-sectional view of our proposed GaN/InGaN multi-junction solar cell is illustrated in Fig. 1. The entire multilayer structure may be grown using (0001) GaN substrate by dint of Metal Oxide Chemical Vapor Deposition (MOCVD) technique [10]. In order to reduce lattice strain between InGaN and GaN, a 150 nm thick GaN layer followed by a 5-nm thick Si-doped n-GaN matching layer is used. Next, two active layers-one 15-nm thick p-$In_{0.3}Ga_{0.7}N$ and the other 15-nm thick n-$In_{0.3}Ga_{0.7}N$ layers are deposited. Subsequent to that a 5-nm thick p-GaN film having an acceptor doping concentration of $1.2 \times 10^{18} cm^{-3}$ the cap layer is grown on top of the n-InGaN active layer [14]. Contacts are placed on the top and bottom of the solar cell accordingly [14]. Indium tin oxide (ITO) is used as the top anode contact. The device

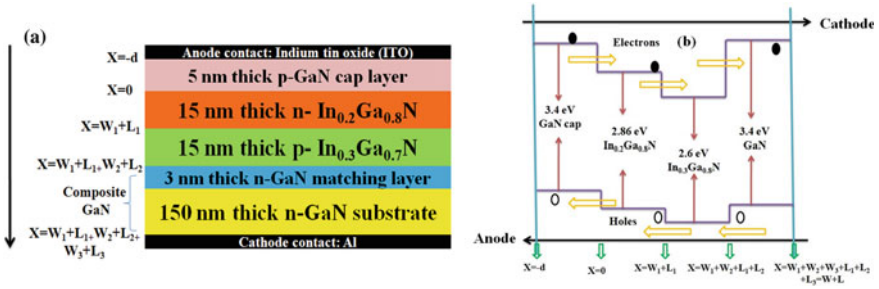

Fig. 1 **a** Schematic cross-sectional view of the GaN/InGaN solar cell and **b** its band-diagram

geometry is designed in the rectangular shape having a cross-sectional area of 200 $\times$ 50 nm^2.

3 Material, Transport and Optical Parameter

The device under study comprises GaN layers, InGaN layers having In contents 20 and 30%, and also GaN/InGaN hetero-interfaces (Fig. 1a). The molar content x of indium in InGaN influences various material parameters such as bandgap, electron affinity, and also conduction and valence band offsets at the GaN/InGaN hetero-interfaces [13]. The energy band gaps of $In_xGa_{1-x}N$ for 0.2 and 0.3 indium content, working as active region material is 2.86 eV and 2.59 eV respectively and the band-diagram of various materials is depicted in Fig. 1b. It has been validated from the spectral response, depicted in Fig. 2b, where the absorption spectra show the maximum limit in the 433–478 nm wavelength range which is the evidence of using active layer in the proposed device structure and falls monotonically outside of the range. The

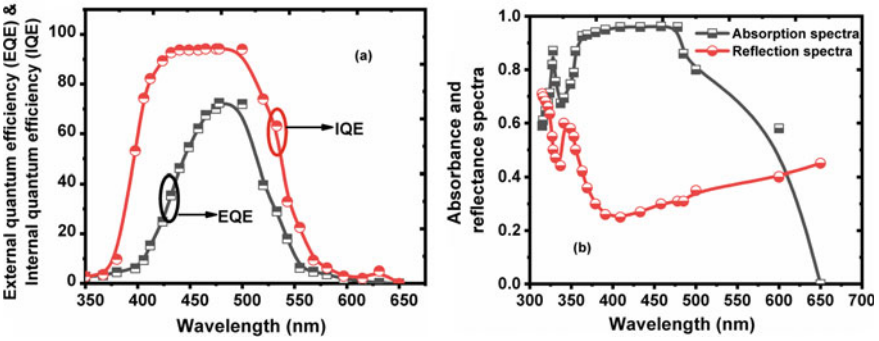

Fig. 2 Spectral response of the proposed device: **a** internal quantum efficiency (IQE) and external quantum efficiency (EQE), and **b** absorption and reflection spectra

simulated internal quantum efficiency (IQE) and external quantum efficiency (EQE) profile, shown in Fig. 2a hold the same agreement with the previous one.

4 Analytical Modeling of Multi-Junction (MJ) Solar Cells

We intend to model the current density versus voltage characteristics of a double junction GaN/InGaN solar cell portrayed in Fig. 1 under illumination conditions. Under short-circuit conditions, the value of J is designated as J_{sc}. As the structure consists of multiple semiconductor–semiconductor interfaces, the photo-generated carriers encounter the following loss mechanisms:

a. Bulk recombination
b. Recombination in the barrier region
c. Recombination at the top contact and back contact
d. Interface recombination through localized states situated in the metallurgical junction.

The net current density J crossing at $x = L_1 + L_2 + L_3 + W_1 + W_2 + W_3$ under illumination condition may be written as,

$$J = q\int_{-d}^{L_1+L_2+L_3W_1+W_2+W_3} G_L(x)\mathrm{d}x - q\int_{-d}^{L_1+L_2+L_3W_1+W_2+W_3} R(x)\mathrm{d}x - J_{sr}(-d) - J_{sr}(L_1 + L_2 + L_3W_1 + W_2 + W_3) - J_{ir}, \quad (1)$$

where W_1, W_2, and W_3 are the depletion widths of three junctions from right to left respectively, L_1, L_2, and L_3 the lengths of the remaining portions for three junctions along the x-axis. $J_{sr}(-d)$, $J_{sr}(L_1 + L_2 + L_3W_1 + W_2 + W_3)$and J_{ir} [3] denote top surface loss due to recombination, back surface loss due to recombination, and interface recombination loss, respectively. Thus,

$$J_{sr}(-d) = qn_{po}S_n\left(e^{\frac{E_{fn}}{K_BT}} - 1\right), \quad (2)$$

where S_n is the surface recombination velocity of electrons in p-type and E_{fn} is the quasi Fermi energy level of electrons. K_B is the Boltzmann constant and T is the temperature in the absolute scale.

And

$$J_{ir} = \frac{qV_{th}\sigma_n N_t[n_0p_0 - {n_i}^2]}{\sigma_p[p_0 + \Delta p] + \sigma_n[n_0 + \Delta n]}$$

where V_{th} = thermal velocity of carriers, σ_n and σ_p are the capture cross-section of electrons and holes, N_t is the interface trapped charge density of energy state E_t [15]. In this work the term; J_{ir} is neglected because of low $D_{it} < 3 \times 10^9 \text{cm}^{-2}\text{eV}^{-1}$[10, 16]. The important parameters, i.e., carrier mobility, carrier lifetime, absorption coefficient etc. required for the modeling are being taken from the respective literatures [3, 15].

$G_L(x)$ and $R(x)$ denote the net generation rate and net recombination rate, respectively and can be expressed as

$$G_L(x) = \frac{8\pi v^2 K_B{}^4 T^4}{h^4} \int_0^\infty \frac{\alpha[\eta(x)^2]}{e^x - 1} x^3 \mathrm{d}x, \text{[18]} \tag{3}$$

where v is the velocity of light in the material, h the Planck constant and $\eta(x)$ is the refractive index of the material and,

$$R(x) = \frac{n_{po}\left(e^{\frac{E_{fn}(x)}{K_B T}} - 1\right)}{\tau_n}, \tag{4}$$

τ_n is the minority electron life time and n_{p0} the equilibrium minority electron concentration.

The open-circuit voltage, V_{oc}, of the device under illumination condition can be expressed as [15],

$$V_{OC} = \int_0^{W+L} (\xi - \xi_o)\mathrm{d}x \tag{5}$$

Under illumination condition, the thermodynamic equilibrium is no longer maintained, the electric field changes from the electrostatic field ξ_o at equilibrium to a new value $\xi(x)$ which can be expressed as,

$$\xi(x) = \frac{\mathrm{d}}{\mathrm{d}x}\left(E_{fn} + E_n + \chi\right) - \left(\frac{\mathrm{d}}{\mathrm{d}x}\left(E_{fp} - E_p + E_g + \chi\right)\right)\text{[18]} \tag{6}$$

Where $E_n = E_c - E_{fn}$, $E_p = E_{fp} - E_v$ and χ is the electron affinity.
Under equilibrium,

$$J_n = \sigma\xi(n) = e\mu_n n_0\left(\frac{\mathrm{d}E_{fn}}{\mathrm{d}x}\right) = 0 \text{and} J_p = \sigma\xi(p) = e\mu_n p_0\left(\frac{\mathrm{d}E_{fp}}{\mathrm{d}x}\right) = 0 \tag{7}$$

It is well known that at thermodynamic equilibrium, $n_0 = N_c e^{\frac{-E_{n0}}{K_B T}}$ and $p_0 = N_v e^{\frac{-E_{p0}}{K_B T}}$, and under illumination, $n = N_c e^{\frac{-E_n}{K_B T}}$ and $p = N_v e^{\frac{-E_p}{K_B T}}$, with $n = n_0 + \Delta n$, $p = p_0 + \Delta p$, and $\sigma = \sigma_0 + \Delta\sigma$ [15]. n and p denote the total concentration of electrons and holes, where Δn and Δp are the excess carrier concentrations generated

due to illumination. σ is the total conductivity of the material in the presence of sunlight, which is larger than the thermodynamicequilibriumconductivityσ_0 by an amount of $\Delta\sigma$.

The built-in electrostatic field (ξ_0) was computed using Poisson's equation subject to boundary conditions as indicated at the interface and thus the Eq. (7) can be rewritten as

$$\begin{aligned} V_{\text{oc}} = &-\int_0^{W+L} \xi_o \mathrm{d}x + \int_0^{W+L} \frac{\mathrm{d}\chi}{\mathrm{d}x}\mathrm{d}x + \int_0^{W+L} \left(\frac{\mathrm{d}\chi}{\mathrm{d}x} + \frac{\mathrm{d}E_g}{\mathrm{d}x}\right)\mathrm{d}x \\ &- K_B T \int_0^{W+L} (q\mu_p \Delta p \frac{dlnN_v}{dx} - q\mu_n \Delta n \frac{\mathrm{d}lnN_c}{\mathrm{d}x})\mathrm{d}x \\ &+ K_B T \int_0^{W+L} \left(q\mu_p \frac{\mathrm{d}\Delta p}{\mathrm{d}x}\Delta p - q\mu_n \frac{\mathrm{d}\Delta n}{\mathrm{d}x}\Delta n\right)\mathrm{d}x \end{aligned} \tag{8}$$

The first term of the above equation represents the voltage due to the built-in electrostatic field. The second and third terms represent the variation of conduction and valence band edge with position due to the electron affinity alteration, this term emphasizes that the photo-conductivity varies with material property variations. The fourth term arises due to the band density of state variations with positions. Apart from the first term, the other terms arise due to the effective force fields and hence as a function of material property. The fifth term is the Dember potential. For this work, the last term has been ignored. From the knowledge of open-circuit voltage and short-circuit current, we can evaluate fill-factor and power conversion efficiency using respective formulas, taken from respective literature [15].

5 Simulation Framework and Model Calibration

We employ the numerical device simulator SENTAURUS TCAD to simulate our device. To capture the effect of carrier recombination, the radiative recombination model is considered, AMI.5G solar spectrum text file is incorporated, and the transfer matrix method (TMM) is used as optical solver, and to estimate the carrier distribution Fermi–Dirac statistics is activated. Finally, the drift–diffusion transport model is invoked to capture transport of carriers. The thin-film single-junction InGaN/GaN solar cell as reported in Matioli et al. [10] is simulated in the Sentaurus TCAD platform. Figure 3 compares TCAD simulated J–V characteristics with the corresponding experimental results as demonstrated in [10]. An excellent concordance between the reported and simulated results ensures the validity of our simulation deck. We also present a comparison between our analytical model and simulation results in Fig. 4. A pretty good agreement between them verifies our modeling framework.

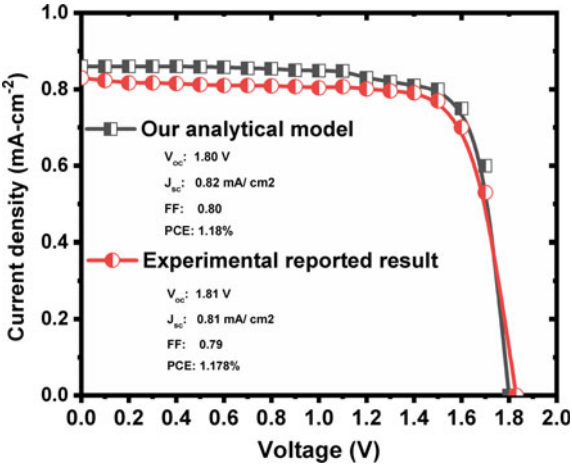

Fig. 3 Comparison of our analytical data with experimental results for conventional GaN/InGaN solar cell [10]

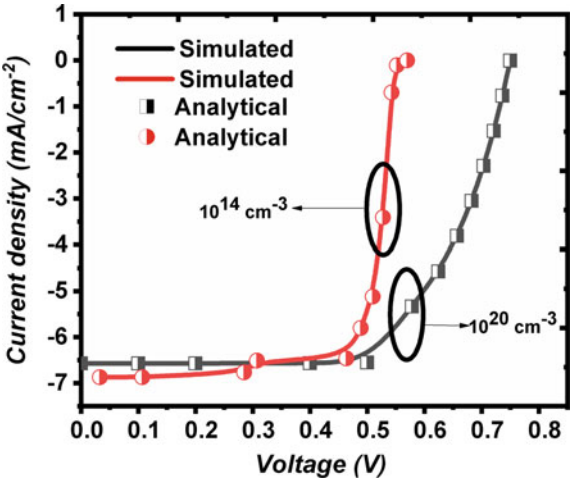

Fig. 4 Comparison of analytical and simulated current density as a function of voltage for two sets of Mg doping density of cap layer

6 Results and Discussion

Having calibrated our analytical setup, we simulate our proposed non-polar GaN/InGaN multi-junction solar cell structure with different indium contents in the active region as demonstrated in Fig. 1a. We numerically determine the current density–voltage (J–V) characteristics for various doping concentration of Mg as p-type dopant at the cap region and obtain the opto-electronic characteristics from our proposed device.

6.1 Optical Response

Optical response ensures the evidence of the production of the photo-generated current in the solar cell. The optical response that includes the variation of the internal quantum efficiency, external quantum efficiency, reflectance, and absorbance spectra with optical wavelength, provides information regarding the optical characteristics of solar cells. In this study, we insert two thin layers of $In_{0.2}Ga_{0.8}N$ and $In_{0.3}Ga_{0.7}N$ one after another (Fig. 1a) to capture the solar energy efficiently by tailoring their energy gap so as to enable them to absorb solar energy from different regions of solar spectra. Figure 2a represents the internal quantum efficiency (IQE) and external quantum efficiency (EQE) respectively which are regarded as the most important parameters to analyze the optical behavior of the solar cell. IQE is the ratio of generated electron–hole pairs (EHPs) to the number of absorbed photons in the active region of the material whereas the EQE is the ratio of the converted EHPs producing photo-current to the number of incident photons. In Fig. 2a, a close examination of IQE and EQE suggests that the maximum limit of the proposed cell has been set to 94% and 74% respectively. Both the quantum efficiencies do not show the sharp cut-off at 478 nm rather gradually decay to zero with increasing optical wavelength. This interesting observation is mainly attributed due to phase separation in InGaN alloy and recombination in the front and back surfaces. As the optical path length increases in the active region at larger wavelengths (>362 nm), absorption within the active region also increases as a result of more confinement of light [17]. This improvement of photo-voltaic performance has been further examined from the reflectance and absorbance spectra shown in Fig. 2b. Reflectance and absorbance provide insight into how the proposed device is responding at different optical wavelengths. From Fig. 2b, it is observed that for wavelength $\lambda > 365$ nm, the absorbance starts to increase while the reflectance starts to decrease. Initially, at $\lambda <= 365$ nm, the photon absorbance is minimum due to the top GaN layer which does not contribute to the carrier generation, instead, it allows sunlight to pass through the layer and contribute to front surface recombination due to the presence of dangling bonds at the surfaces and short carrier diffusion length [17]. Within the active region for wavelengths ranging from 365 to 478 nm corresponding to band gap energies 2.86–2.59 eV, the photon absorption rises to 0.96 and beyond 478 nm the absorption begins to dropdown.

6.2 Impact of Mg Doping Concentration of Cap Layer on PV

Importantly, it is very crucial to choose the proper dimension and doping concentration of p-GaN cap layer to obtain the optimized device performance. In this work, we focus on the p-type (Mg) doping concentrations in the cap layer and investigate their effect on the proposed device structure. Figure 5 demonstrates current

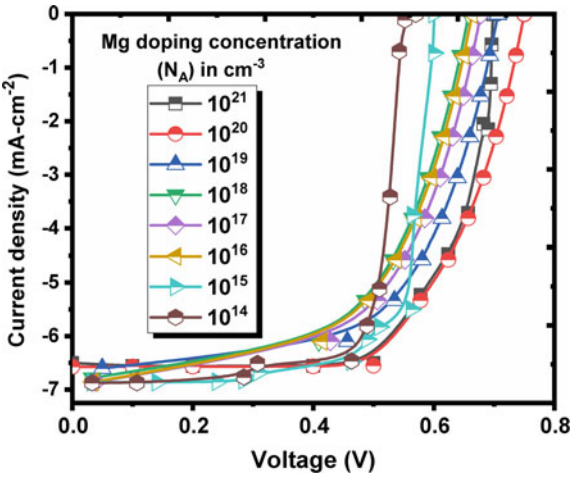

Fig. 5 J–V characteristics for various Mg doping concentration from 10^{14} to 10^{21} cm^{-3} in cap layer

density–voltage (J–V) characteristics of the proposed solar cell (Fig. 1a). The presence of unintentional deep donor (or acceptor) impurity, carbon, during the MOCVD growth of GaN materials results in higher resistivity of p-GaN cap layer. The light hole concentration and high resistivity of p-GaN cap region are the bottlenecks to limit the effective absorption of solar spectrum [3] since the short-circuit current density J_{sc} depends on the incident light absorption and the EHP extraction rate [3]. Hence, higher acceptor doping concentration in p-GaN cap layer would compensate for the effect of carbon impurity-related ailments. It is evident from Fig. 6 that an inverse relationship exists between V_{oc} and J_{sc}. As the doping concentration of the cap layer increases from 10^{14} to 10^{20} cm^{-3}, V_{oc} increases from 0.57, attains its peak value of 0.75 V for doping concentration 2×10^{19} cm^{-3} and thereafter decreases monotonically to 0.70 V for 10^{20} cm^{-3}. Since V_{oc} increases with decreasing reverse saturation current which drops as the minority carrier concentration reduces.

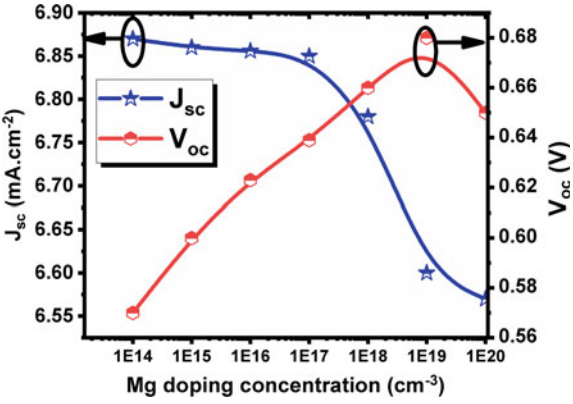

Fig. 6 Variation of J_{sc} (mA/cm^2) and V_{oc} (V) with Mg doping concentration of the cap layer

A higher cap doping concentration effectively lowers the minority carrier concentration thereby resulting in a larger V_{oc}. However, degradation of V_{oc} beyond doping of 2×10^{19} cm^{-3} may primarily be attributed to the lattice relaxation and defects that occur during processing of nitride layers [16]. In fact, the growth of p-GaN cap layer with hole concentration higher than 10^{19} cm^3 using MOCVD is hard to execute [16] and the coherency strain gets accumulated which finally leads to lattice relaxation and generation of defects in the grown layer. As a result the crystal quality deteriorates with heavy p-doping and directly degrades V_{oc} [16]. These defects include the non-radiative recombination center, V-shaped pits, phase separation which increases leakage currents within the GaN material and also weakens the electrostatic field which causes separation of carriers. Due to these combined effects V_{oc} starts to decrease. Simultaneously, with increasing acceptor doping density, the mobility of carriers degrades due to electron–phonon scattering within the material [3]. As a result, the diffusion length of minority carriers and minority carrier lifetimes are also reduced, resulting in the recombination of photo-generated carriers before they are collected. Hence the photo-current J_{ph} goes down following the relationship, $J_{ph} = qG(L_n + L_p + w)$, where L_n and L_p are the minority carrier diffusion length due to electrons and holes, G is the generation rate of EHP from absorbed photons [3]. On the basis of our in-depth analysis considering processing aspects, the optimum doping concentration of the cap layer is chosen as 10^{19} cm^{-3}.

6.3 Impact of Inserting Multiple Layers with Varying Indium Composition in the Active Layer

The lattice mismatch between InN and GaN and low-temperature growth of InGaN material by MOCVD method result in impurity incorporation, formation of V-defects, etc. which are responsible for generating non-radiative recombination centers (NRCs) within the material. Hence the maximum amount of In is restricted to 30% in order to have acceptable crystal quality while exploiting the benefits of In incorporation [3]. As indium composition increases, the critical thickness of InGaN layer decreases and so does its bandgap. Figure 7a, b nicely demonstrate the comparison of the current density–voltage and power density–voltage characteristics respectively for different molar contents of indium in InGaN alloy used in the active layer of the proposed device. It has been observed from the figures that, as the indium content is increased from 20 to 30% all figures of merit of solar cell i.e. J_{sc}, V_{oc}, fill-factor, and most importantly the power conversion efficiency (PCE) show an excellent improvement. However, the most striking observation has been found when two InGaN layers of different indium contents i.e., 20 and 30% are inserted successively in the active region. This inclusion has set a benchmark in the performance parameters for the solar cell device. The derived parameters e. g., J_{sc}, V_{oc}, fill-factor, and PCE are found to improve by 14.57%, 34%, 16.36%, and 70%, respectively over the corresponding value obtained from the conventional structure. The variation of molar content of

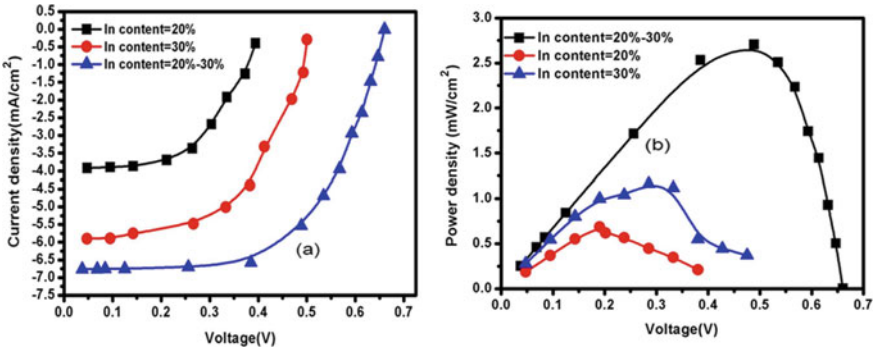

Fig. 7 **a** J–V characteristics and **b** P–V characteristics for different molar contents of indium

indium in InGaN alloy essentially causes modulation of bandgap of the alloy. Due to this reason, the confinement of photons having different energies corresponding to different band gaps i.e., 2.86 eV for 20% and 2.59 eV for 30% has facilitated enhancing both short-circuit current density and power density as shown in Fig. 7a, b. A higher photo-absorption leads to an increase in the number of electron–hole pair generation which upon separation by the built-in field contributes to augmenting the open-circuit voltage. These combined effects are observed in terms of enhanced power conversion efficiency. Such a nice technique not only eliminates the critical layer thickness constraint but also broadens the photo-absorption effectively by enhancing the active region thickness. Hence, it can be suggested that this technique would reduce the future fabrication complexity to some extent.

Table 1 compares various performance matrices of solar cells obtained from our proposed solar cell with the corresponding reported parameters of four different experimental research findings. It is evident from Table 1 that our optimized device yields an improvement of 385%, 721.9%, 214%, and 478.9% in J_{sc} and 62.14%, 173%, 20%, and 173% respectively in PCE compared to the reported experimental results for device 1, 2, 3 and 4, respectively [16, 18–20]. Our structural and compositional design of solar cell turns out to be promise for the next generation radiation-resilient solar cell fabrication.

Table 1 Comparative study of our proposed device with the experimental reported results

S. No.	Device	V_{oc} (V)	J_{sc} (mA cm^{-2})	FF	Efficiency (%)
1	Device 1 [16]	2.18	1.360	0.59	1.77
2	Device 2 [18]	2.32	0.803	0.55	1.05
3	Device 3 [19]	2.26	2.100	0.70	2.4
4	Device 4 [20]	1.94	1.140	0.45	1.05
6	Our device	0.68	6.600	0.64	2.87

7 Conclusion

We have developed an analytical model for InGaN/GaN multi-junction solar cells supported by numerical simulation data and investigated their electrical performance with various doping concentrations in the cap region alongside two InGaN alloy layers with indium percentages of 20 and 30% in the active region. Also, a comparison has been presented between important photo-voltaic parameters such as short-circuit current density, open-circuit voltage, fill-factor, and power conversion efficiency of our optimized solar cell and earlier reported data. Our findings reveal that the proposer device outperforms other earlier nitride-based solar cells in terms of many photovoltaics parameters. Hence, our device concept and design may be considered for the next generation of radiation resilient solar cells with a view to their applications in space.

Acknowledgements The first author acknowledges the "UNIVERSITY RESEARCH FELLOWSHIP" program under the University of Calcutta for providing financial support for University Research Fellow (URF) vide Ref. No. DPO/44/Fellow (University) dtd. 12.02.2021.

References

1. Deldago, R.-L., Valenzuela, Raynaud, A.-Z., Carraczco, A.-R., Pelayo, J.-E., Mendoza, D.-B., Ramos, M.-E.-A., Ayon, A.: Solar cell efficiency improvement employing down-shifting silicon quantum dots. Microsyst. Technol. **24**, 495 (2017)
2. Nath, P., Biswas, A., Nath, V.: Performance optimization of solar cells using non-polar, semi-polar and polar InGaN/GaN multiple quantum wells alongside AlGaN blocking layers. Microsyst. Technol. 301–306 (2020)
3. Bhuiyan, A.-G., Sugita, K., Hashimoto, A., Yamamoto, A.: InGaN solar cells: present state of the art and important challenges. IEEE J. Photovolt. 276–293 (2012)
4. Tsai, C.-T., Muna, Y.-B., Kuo, C.-C.: Optimal design and performance analysis of solar microsystem for mini-grid applications. Microsyst. Technol. **69** (2018)
5. Deldago, R.-L., Valenzuela, R.-A.-Z., Carraczco, A.-R., Pelayo, J.-E., Mendoza, D.-B., Ramos, M.-E.-A., Ayon, A.: Solar cell efficiency improvement employing down-shifting silicon quantum dots. Microsyst. Technol. **24**, 495 (2017)
6. Kirubaray, A.-A., Moni, D.-J., Devaprakasam, D.: Large scale fabrication of asymmetric 2D and 3D micro/nano array pattern structures using multi-beam interference lithography technique for solar cell texturing application. Microsyst. Technol. **24**, 2569 (2018)
7. Sayed, I., Bedair, S.-M.: Quantum well solar cells: principles, recent progress, and potential. IEEE J. Photovolt. 402–423 (2019)
8. Siddharth, G., Garg, V., Sengar, B.-S., Bhardwaj, R., Kumar, P., Mukherjee, S.: Analytical study of performance parameters of InGaN/GaN multiple quantum well solar cell. IEEE Trans. Electron Devices. 3399–3404 (2019)
9. Kotamraju, S., Sukeerthi, M., Puthanveettil, S.-E.: Modeling of InGaP/InGaAs-GaAsP/Ge multiple quantum well solar cell to improve efficiency for space applications. Sol. Energy. 328–334 (2019)
10. Kucukgok, B., Wu, X., Wang, X., Liu, Z., Ferguson, I.-T., Lu, N.: The structural properties of InGaN alloys and the interdependence on the thermoelectric behaviour. Appl. Phys. Lett. **6**, 025305 (2016)

11. Wang, J., Higashihara, C.-L., Chen, W.-C.: All-conjugated donor-acceptor graft/block copolymers as single active components and surfactants in all-polymer solar cells. Microsyst. Technol. **23**, 1183 (2017)
12. Chen, X., Matthews, K.-D., Hao, D., Schaff, W.-J., Eastman, L.-F.: Growth, fabrication, and characterization of InGaN solar cells. Phys. Stat. Sol. (A) 1103–1105 (2008)
13. Bandic, Z.-Z., Bridger, P.-M. , Piquette, E.-C., McGillb, T.C.: Electron diffusion length and lifetime in p-type GaN. Appl. Phys. Lett. **73**, 3276 (1998)
14. Kuwahara, Y., Fujii, T., Sugiyama, T., Iida, D., Isobe, Y., Fujiyama, Y., Morita, Y., Iwaya, M., Takeuchi, T., Kamiyama, S., Akasaki, I., Amano, H.: GaInN-based solar cells using strained-layer GaInN/GaInN superlattice active layer on a freestanding GaN substrate. Appl. Phys. Exp. **4**, 021001 (2011)
15. Fonash, S.J.: Solar cell device physics, 2nd ed. Anderson, L.L., Tillman, D.A. (eds.) Academic Press, New York, London, Toronto, Sydney, San Francisco (2009)
16. Matioli, E., Neufeld, C., Iza, M., Cruz, S.-C., Heji, A.-A., Chen, X., Farrell, R.-M., Keller, S., DenBaars, S., Mishra, U., Nakamura, S., Speck, J., Weisbuch, C.: High internal and external quantum efficiency InGaN/GaN solar cells. Appl. Phys. Lett. **98**, 021102 (2011)
17. Muth, J.-F., Lee, J.-H., Shmagin, I.-K. Kolbas, R.-M., Casey, H.-C. , Keller, B.-P., Mishra, U.-K., DenBaars, S.-P.: Absorption coefficient, energy gap, exciton binding energy, and recombination lifetime of GaN obtained from transmission measurements. Appl. Phys. Lett. **71**, 2572 (1997)
18. Huang, X., Chen, H., Fu, H., Baranowski, I., Montes, J., Yang, T.-H, Fu, K., Gunning, B., Koleske, P.-D., Zhao, Y.: Reliability analysis of InGaN/GaN multi-quantum-well solar cells under thermal stress. Appl. Phys. Lett. **111**, 233511 (2017)
19. Young, N.-G., Farrell, R-.M., Hu, Y.-L., Terao, Y., Iza, M., Keller, S., DenBaars, S.-P., Nakamura, S., Speck, J.-S.: High performance thin quantum barrier InGaN/GaN solar cells on sapphire and bulk (0001) GaN substrates. Appl. Phys. Lett. **103**, 173903 (2013)
20. Bi, Z., Zhang, J., Zheng, Q., Zhiyu, L., Lin, L., Shan, H., Peixian, L., Xiaohua, M., Yiping, H., Hao, Y.: An InGaN based solar cell including dual InGaN/GaN multiple quantum wells. IEEE J. Photovolt. 2117–2120 (2016)
21. Huang, X., Chen, H., Fu, H., Baranowski, I., Montes, J., Yang, T.-H, Fu, K., Gunning, B.P.-D., Koleske, Zhao, Y. : Energy band engineering of InGaN/GaN multi-quantum-well solar cells via AlGaN electron- and hole-blocking layers. Appl. Phys. Lett. **113**, 043501 (2018)

A Simple but Accurate Mathematical Formalism for Prediction of the Far Field Pattern of First Higher Order (LP_{11}) Mode in Kerr Type Nonlinear Step Index Optical Fiber

Kushal Roy, Angshuman Majumdar, and Sankar Gangopadhyay

Abstract We present in our paper, the first higher order mode far field pattern in Kerr type nonlinear fibers having step index profile. Simultaneously we compare our result with the linear case. We utilize a simple method to formulate power series structured on Chebyshev technique to formulate the mathematical equations for far field intensity in linear fibers and then apply the iterative method for the given kind of nonlinearity until convergent values of concerned parameters are obtained. The results obtained show excellent match with the one obtained using finite element method which we establish, using optical fiber having step type refractive index profile as example. This endorses the accuracy of our formalism. Therefore the proposed formalism shall prove beneficial for system engineers and researchers involved with integrated nonlinear optics.

Keywords Step index optical fiber · LP_{11} mode · Far field profile · Chebyshev technique · Kerr type nonlinearity

1 Introduction

Precise determination of various propagation parameters in optical fiber under nonlinear condition is of utmost importance since most of the practical fibers tend to behave differently under the influence of nonlinearity. This is because of the dependent nature of light intensity and refractive index profile of the fiber. The propagation parameters tend to vary from those in the linear region, particularly when high intensity lasers are used as source of optical power [1–3].

Optical communication is highly influenced by Kerr type nonlinearity which is also known as third order nonlinearity. Various phenomena which deeply impact the

K. Roy
Department of Electronics and Communication Engineering, Haldia Institute of Technology, Haldia, West Bengal 721657, India

A. Majumdar · S. Gangopadhyay (✉)
Departments of Electronics and Communication Engineering, Brainware University, Barasat, West Bengal 700125, India

B. Sikdar et al. (eds.), *Proceedings of the 3rd International Conference on Communication, Devices and Computing*, Lecture Notes in Electrical Engineering 851,
https://doi.org/10.1007/978-981-16-9154-6_17

propagation characteristics of the optical fiber are self and cross-phase modulation along with four wave mixing [4–6]. Moreover, it has been reported that integrated optics is based on strong Kerr nonlinearity micro resonator [7].

In optical communication system, dual-mode fibers find a distinctive place of great importance [8, 9]. As reported, they are of particular importance in designing dispersion compensated dual mode fibers [10]. Moreover, the dual mode double layer fibers tend to exhibit less transmission and bending losses compared to simple dispersion shifted fibers [10, 11]. The far field pattern, which is one of the most important propagation parameters in graded index fiber; has been formulated mathematically and likewise predicted for the fundamental (LP_{01}) mode considering linear case [12]. Recently, the effect of Kerr type nonlinearity on far field pattern in LP_{01} has also been analyzed and reported for graded index fibers [13]. But the same in presence of nonlinearity for the first higher order mode in graded index fibers still remains of high interest among the researchers and thereby requires in depth investigation. For accurate determination of the modal field, numerical or variational techniques are applied [14]. However, these techniques require rigorous computations. Many efforts are being made by the researchers over the years to develop a simple yet accurate technique to estimate various important fiber characteristics of the fiber in both linear and nonlinear regions [15–18]. Chebyshev method, for estimation of first higher order mode cut off frequency is already available in the literature [19]; and is reported to have considerable accuracy in determining various parameters of graded index fibers [17, 19–22]. Recently the propagation constants for nonlinear single mode fibers have also been accurately predicted by Chebyshev technique [23]. Detailed analysis of graded index Kerr type nonlinear fiber directional coupler using the said simple technique has also been added to literature [24].

In this presented work we have utilized a simple expansion of power series for the obtaining the nature of far field profile with $k_0 a \sin\theta$ for LP_{11} mode in absence of Kerr type nonlinearity. Then we resort to the application of 'method of iteration' and extend the same for nonlinear optical fiber. We have illustrated our findings taking some examples of fibers with step type refractive index profile. Any attempt for the prediction of first higher order field's far field profile has not been presented in the literature as and when considering the effect of Kerr type nonlinearity using such simple formalism. Therefore the presented work inherits a certain degree of novelty.

2 Theory

In weakly guided fiber with circular core, the refractive index profile is given by the expression

$$n^2(R) = \begin{cases} n_1^2(1 - 2\delta f(R)), & R \leq 1 \\ n_2^2\ , & R > 1 \end{cases} \tag{1}$$

Here R is the ratio (r/a), δ is defined as the relative difference of the refractive index, further 'core radius' and 'refractive indices' are denoted by 'a' and 'n_1, n_2' respectively. The function $f(R)$, represented as R^q; gives the 'profile of the refractive index'; where q can have values ∞, 1 and 2 for step, triangular and parabolic type profile fiber.

In the present work, we have considered step index fibers with different V numbers corresponding to LP_{11} mode; therefore $f(R) = 0$.

For fibers with Kerr nonlinear effect; refractive index is formulated as

$$"n^2(R) = n_L^2(R) + \{\frac{n_2^2}{\eta_0} n_{NL}(R)\psi^2(R)\}" \text{ [15]} \tag{2}$$

where $n_L(R)$ is the linear value of the refractive index and $n_{NL}(R)$ represent the nonlinear Kerr coefficient having the unit (m^2/W) and $\eta_0 = (\mu_0/\varepsilon_0)^{1/2}$. It is known from the available literature that, for weakly guided fibers the complex vector and scalar wave equation are the same and the solution of which forms linearly polarized (LP) modes. For the first higher order LP_{11} mode the modal field satisfies the scalar wave equation represented as

$$\begin{aligned} &"\frac{d^2\psi(R)}{dR^2} + \frac{1}{R}\frac{d\psi(R)}{dR} + \left[V^2\{1 - f(R)\} - W^2\right]\psi(R) - \frac{\psi(R)}{R^2} \\ &+ V^2 g(R)\psi^3(R) = 0" \text{ [15, 16]} \end{aligned} \tag{3}$$

In the above equation $g(R) = \frac{n_2 n_{NL} P}{\pi a^2 (n_1^2 - n_2^2)}$; where the optical power is represented by 'P', cross-sectional area by 'a' and Kerr coefficient by 'n_{NL}'. The boundary condition at core cladding interface (for $R = 1$) can be expressed as

$$"\frac{1}{\psi}\frac{d\psi}{dR} = -\left\{1 + \left(\frac{WK_0(W)}{K_1(W)}\right)\right\} at\, R = 1" \text{ [16]} \tag{4}$$

The above equation utilizes modified Bessel's function of first and second order represented by K_i. Furthermore 'V' represents the normalized frequency and 'W' represents the cladding decay parameter [17].

Within the core and cladding of a graded index fiber, the LP_{11} modal field can be expressed using Chebyshev formalism based power series expression as [17–20],

$$\begin{aligned} \psi(R) &= \left\{(a_1 R) + \left(a_3 R^3\right) + \left(a_5 R^5\right)\right\} \text{for all} R \le 1 \\ &= \{a_1 + a_3 + a_5\}\frac{K_1(WR)}{K_1(W)} \text{for} R > 1 \end{aligned} \tag{5}$$

Using Eq. (5) in Eq. (3), we get the expression

$$a_1\left\{V^2(1 - f(R)) - W^2 + V^2 g\psi^2(R)\right\}$$

$$+ a_3\{8 + R^2[V^2(1 - f(R)) - W^2 + V^2 g\psi^2(R)]\}$$
$$+ a_5\{24(R^2) + (R^4)[(V^2)(1 - f(R)) - W^2 + V^2 g\psi^2(R)]\} = 0 \quad (6)$$

Using Eq. (7); we have considered the two Chebyshev points corresponding to 'R' and thereby express 'a_3, a_5' in terms of a_1

$$R_m = \cos\left(\left(\frac{2m-1}{2M-1}\right)\frac{\pi}{2}\right) \quad \text{for } m = (1, \ldots (M-1)) \quad (7)$$

Taking $M = 3$, R_i values are obtained for $i = 1, 2$ as 0.9511 and 0.5878. These Chebyshev points are used in Eq. (6), to obtain the two separate equations in terms of R_i as mentioned in the literature [21].

As previously established, the ratio of $K_1(W)$ to $K_0(W)$ varies linearly with W^{-1} within the interval (0.6, 2.5) [21], so least square fitting technique is applicable within the said interval and the values of α and β are found to be 1.034623 and 0.3890323 [21, 22]

$$\frac{K_1(W)}{K_0(W)} = [\alpha + \left\{\frac{\beta}{W}\right\}] \quad (8)$$

Furthermore, we apply Eq. (5) and Eq. (8) in Eq. (4) and get

$$a_1\{2(\alpha W + \beta) + W^2\} + a_3\{4(\alpha W + \beta) + W^2\} + a_5\{6(\alpha W + \beta) + W^2\} = 0 \quad (9)$$

The coefficients; a_1, a_3 and a_5 as given in Eqs. (6) and (9) will have a nontrivial solution only if

$$\begin{vmatrix} B_1 & C_1 & D_1 \\ B_2 & C_2 & D_2 \\ B_3 & C_3 & D_3 \end{vmatrix} = 0 \quad (10)$$

where, for $i = 1, 2$.

$$"B_i = \{V^2(1 - f(R_i)) - W^2 + V^2 g\varphi^2(R_i)\}$$

$$C_i = [8 + R_i^2\{V^2(1 - f(R_i)) - W^2 + V^2 g\Psi^2(R_i)\}]$$

$$D_i = [24R_i^2 + R_i^4\{V^2(1 - f(R_i)) - W^2 + V^2 g\Psi^2(R_i)\}]$$

$$B_3 = \{2(\alpha W + \beta) + W^2\}; C_3 = \{4(\alpha W + \beta) + W^2\};$$
$$D_3 = \{6(\alpha W + \beta) + W^2\}" [17, 19 - 21]$$

The determinant shown in Eq. (10) is quite complicated for its solution because of the term $\Psi^2(R_i)$. Therefore to ease the computation we first consider the linear case taking $g(R) = 0$ and obtain the W values for each V number, taking $f(R_i) = 0$ for step index fiber. In the next step we compute the values of a_3 and a_5 with the help of W values obtained previously for the linear case. To consider the presence of Kerr nonlinearity; for any value of $g(R)$ and V, the iteration technique is used till convergent W values are obtained and subsequently the values of a_3 and a_5 are obtained in terms of a_1. Also to mention, A_3 and A_5 represent the normalized of a_3 and a_5 and can be represented as $A_3 = a_3/a_1$ and $A_5 = a_5/a_1$.

Thus the core and cladding field is given by

$$\begin{aligned}\psi(R) &= a_1\left\{R + \left(A_3R^3\right) + \left(A_5R^5\right)\right\}\text{for all}R \le 1\\ &= a_1(1 + A_3 + A_5)\frac{K_1(WR)}{K_1(W)}\text{for}R > 1\end{aligned} \tag{11}$$

Considering the cylindrically symmetric structure of the optical fiber, the corresponding far field is given by

$$u(\theta) = 2\pi C\int_0^\infty \psi(R)J_0(K_0a\ R\sin\theta)R\mathrm{d}R \tag{12}$$

where, the core axis and measurement direction is separated by an angle 'θ'; 'C' represents a constant and 'k_0' is used to represent the free space wave number [22, 25].

$$\begin{aligned}\frac{u(\theta)}{2\pi C} &= \frac{A_1}{B^3}\left[2BJ_0(B) + \left(4 - B^2\right)J_1(B) - 2BJ_2(B)\right)\right]\\ &+ \frac{A_3}{B^5}\left[2B^3J_0(B) + \left(12B^2 - \frac{B^4}{3} - 32\right)J_1(B) + 2B^3J_2(B)\right]\\ &+ \frac{A_5}{B^7}\left[\left(2B^5 - 8B^3\right)J_0(B) + \left(\frac{2}{15}B^6 + \frac{16}{3}B^4 + 8B^2 + 128\right)\right.\\ &\left.J_1(B) + \left(2B^5 + 8B^3\right)J_2(B)\right]\\ &- \frac{(A_1 + A_3 + A_5)}{\left(B^2 + W^2\right)K_1(W)}[BK_1(W)J_1(B) - W\{(K_2(W)J_0(B))\}]\end{aligned} \tag{13}$$

$$"Bk_0a\sin\theta",\ A_1 = a_1/a_1 = 1 \tag{14}$$

By substituting $\theta = 0$ we get $u(0)$ from Eq. (15) as [22, 25, 26]

$$u(0) = 2\pi C\left[-2\frac{A_1}{3} - 4\frac{A_3}{5} - 6\frac{A_5}{7}\right] \tag{15}$$

The above expression given in Eq. (13) utilizes Bessel function 'J_i' and modified Bessel function 'K_i' respectively [22, 27].

Hence the normalized values of intensity for the 'far field' is given by

$$I(\theta) = \left|\frac{u(\theta)}{u(0)}\right|^2 \tag{16}$$

3 Results and Discussions

The accuracy of our formalism is verified by plotting $I(\theta)$ versus B (=$K_0 a\text{Sin}\theta$) for different V numbers in case of step type RI profile fiber considering both linear and nonlinear cases. In order to incorporate the Kerr nonlinearity effect in our paper, we have taken the positive and negative nonlinearity values ($n_{NL}P$) as " $+1.5 \times 10^{-14}$ m^2 and $-1.5 \times 10^{-14} m^2$" respectively [17]. Furthermore, following our prescribed formalism, the far-field pattern is plotted for step type refractive index profile fibers with 2.5, 3.0 and 3.5 'V' numbers as shown in Figs. 1, 2 and 3.

For better understanding, the relevant values corresponding Figs. 1, 2 and 3 are provided in Tables 1, 2 and 3 considering the same optical fiber parameters.

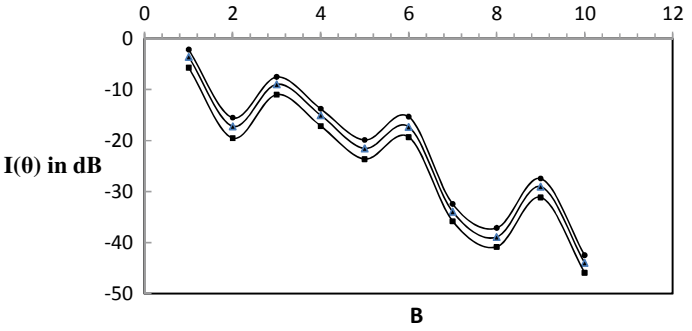

Fig. 1 Showing variation in normalized "*far field intensity with B (=$k_0 a\text{Sin}\theta$)*" for step type refractive index profile fiber with V no as 2.5. (Our results are depicted by: ▲ ***for linear case,*** ■ ***for "n_{NL} $P = +1.5 \times 10^{-14} m^2$"*** ● ***for "$n_{NL}$ $P = -1.5 \times 10^{-14} m^2$"*** and the exact results from simulations are shown with solid lines)

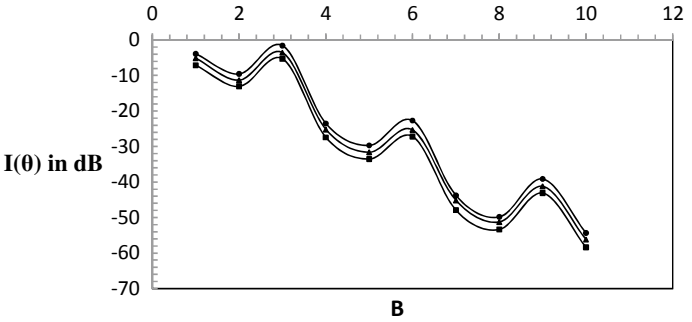

Fig. 2 Sowing variation in normalized "*far field intensity with B (=$k_0 a Sin\theta$)*" for step type refractive index profile fiber with V no as 3.0. (Our results are depicted by: ▲ ***for linear case,*** ■ ***for "n_{NL} P = +1.5 × 10^{-14} m^2",*** ● ***for "n_{NL} P = −1.5 × 10^{-14} m^2"*** and the exact results from simulations are shown with solid lines)

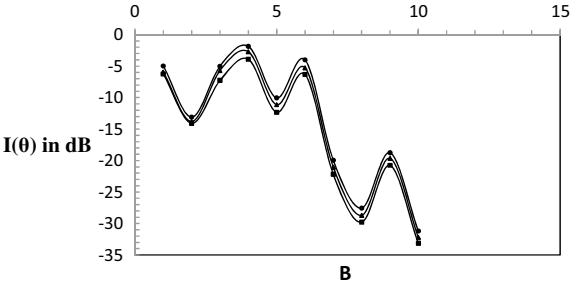

Fig. 3 Sowing variation in normalized "*far field intensity with B (= $k_0 a Sin\theta$)*" for step type refractive index profile fiber with V no as 3.5. (Our results are depicted by: ▲ ***for linear case,*** ■ ***for "n_{NL} P = +1.5 × 10^{-14} m^2",*** ● ***for " n_{NL} P = −1.5 × 10^{-14} m^2"*** and the exact results from simulations are shown with solid lines)

Table 1 Relevant data corresponding to Fig. 1 correlating 'B ($k_0 a \sin\theta$)', 'θ' and $I(\theta)$ (in dB scale both with and without nonlinearity) for $V = 2.5$

B	θ	$I(\theta)$ '$n_{NL}P = 0$'	$I(\theta)$ '$n_{NL}P = +1.5 \times 10^{-14}$ m^2'	$I(\theta)$ '$n_{NL}P = -1.5 \times 10^{-14}$ m^2'
1	3.2416	−3.5621	−5.6715	−2.1512
2	6.8555	−17.1879	−19.5214	−15.5091
3	10.3144	−8.9565	−10.9778	−7.5152
4	13.8117	−15.0215	−17.1358	−13.7545
5	17.3625	−21.5298	−23.6125	−19.8672
6	20.9835	−17.2986	−19.3128	−15.3251
7	24.6946	−33.9367	−35.7932	−32.4142
8	28.5199	−38.9125	−40.8298	−37.1251
9	32.4897	−29.0159	−31.1154	−27.4245
10	36.6433	−43.9735	−45.8975	−42.4751

Table 2 Relevant data corresponding to Fig. 2 correlating '$B(k_0 a\sin\theta)$', 'θ' and $I(\theta)$ (in dB scale for both with and without nonlinearity) for $V = 3.0$

B	θ	$I(\theta)$ '$n_{NL}P = 0$'	$I(\theta)$ '$n_{NL}P = +1.5 \times 10^{-14}$ m^2'	$I(\theta)$ '$n_{NL}P = -1.5 \times 10^{-14}$ m^2'
1	3.2416	−5.1329	−7.1159	−3.8947
2	6.8555	−11.2981	−13.0558	−9.5478
3	10.3144	−3.5613	−5.2759	−1.5691
4	13.8117	−25.1927	−27.4312	−23.5173
5	17.3625	−31.6111	−33.5137	−29.6815
6	20.9835	−25.3341	−27.1679	−22.6987
7	24.6946	−45.1998	−47.9216	−43.8119
8	28.5199	−51.2719	−53.3479	−49.8366
9	32.4897	−41.2238	−43.1121	−39.1359
10	36.6433	−56.1977	−58.3929	−54.3761

Table 3 Relevant data corresponding to Fig. 3 correlating 'B $(k_0 a\sin\theta)$', 'θ' and $I(\theta)$ (in dB scale for both with and without nonlinearity) for $V = 3.5$

B	θ	$I(\theta)$ '$n_{NL}P = 0$'	$I(\theta)$ '$n_{NL}P = +1.5 \times 10^{-14}$ m^2'	$I(\theta)$ '$n_{NL}P = -1.5 \times 10^{-14}$ m^2'
1	3.2416	−5.9412	−6.2411	−4.9857
2	6.8555	−13.8094	−14.0769	−13.1116
3	10.3144	−5.7120	−7.2679	−5.0268
4	13.8117	−2.7153	−3.9111	−1.8647
5	17.3625	−11.1279	−12.3342	−10.0624
6	20.9835	−5.2678	−6.3191	−4.0101
7	24.6946	−21.0619	−22.1979	−19.9742
8	28.5199	−28.7110	−29.7986	−27.5614
9	32.4897	−19.6479	−20.7715	−18.7763
10	36.6433	−32.2196	−33.1587	−31.2146

As the value of 'B' is dependent on the product '$k_0 a$', we have taken the practical value of $a = 4$ μm and $\lambda = 1.5$ μm. Also it is worth mentioning here that $n_{NL}(R)$ is the refractive index of the nonlinear fiber medium and is dependent on the product of n_{NL} (m^2/watt) and optical power P (watt). We present our results in three different notations to distinguish between the linear far field pattern for LP_{11} mode (n_{NL} $P = 0$), positive and negative Kerr nonlinearity (n_{NL} P) as " $+1.5 \times 10^{-14}$ m^2 and -1.5×10^{-14}m^2" respectively. The exact simulated result in each case is shown by solid line. The normalized frequency corresponding to 'cut off' in case of the fundamental mode is for V number of value 2.405, hence to investigate the variation of far-field intensity with and without Kerr type nonlinearity near the cut off frequency, we have selected the lowest V number as 2.5 and is incremented by 0.5 in each case. It is

observed from Figs. 1, 2 and 3 that the pattern for positive and negative values of nonlinearity come out to be equally spaced being nearly symmetrical about the linear values.

4 Conclusion

Here we conclude that the formalism presented by us in this paper provides the variation pattern of the far-field intensity of the LP_{11} mode in step type RI profile fiber with excellent accuracy. Furthermore the Kerr type nonlinearity effect on the intensity variation of far field is also presented. The technique is simple and it reduces the computation complexity involved with the various techniques available in the literature. The simplicity of the formalism will be of great help to researchers and engineers in determining the far field pattern of Kerr type nonlinear step index fibers accurately using lesser computations and thereby avoiding mathematical complexities.

References

1. Snyder, A.W., Chen, Y., Poladian, L., Mitchel, D.J.: Fundamental mode of highly nonlinear fibres. Electron Lett. **26**, 643–644 (1990)
2. Goncharenko, I.A.: Influence of nonlinearity on mode parameters of anisotropic optical fibres. J. Mod. Opt. **37**, 1673–1684 (1990)
3. Agrawal, G.P., Boyd, R.W.: Contemporary nonlinear optics. Boston Academic Press (1992)
4. Agrawal, G.P.: Nonlinear fiber optics. Academic Press, Cambridge, MA (2013)
5. Saitoh, K., Fujisawa, T., Kirihara, T., Koshiba, M.: Approximate empirical relations for nonlinear photonic crystal fibers. Opt. Express. **14**, 6572–6582 (2006)
6. Tomlinson, W.J., Stolen, R.H., Chank, C.V.: Compression of optical pulses chirped by self-phase modulation in fibers. J. Opt. Soc. **1**, 139–149 (1984)
7. Xiyuan, L., Lee, J.Y., Rogers, S., Lin, Q.: Optical Kerr nonlinearity in a high-Q silicon carbide microresonator. Opt Express. 30826–30832 (2014)
8. Spajer, M., Charquille, B.: Application of intermodal interference to fiber sensors. Opt. Commun. **60**, 261–264 (1986)
9. Eguchi, M., Koshiba, M., Tsuji, Y.: Dispersion compensation based on dual-mode optical fiber with inhomogeneous profile core. J. Lightwave Technol. **14**, 2387–2394 (2002)
10. Pederson, B.: Small-single erbium-doped fiber amplifiers pumped at 980 nm: a design study. Opt. Quantum Electron. **26**, S237–S244 (1994)
11. Monerie, M.: Propagation in doubly clad single mode fibers. IEEE J. Quant. Electron. QE **18**, 534–535 (1982)
12. Majumdar, A., Chakraborty, S., Gangopaghyay, S.: A simple method for prediction of far-field pattern of mono-modegraded index fibers in the low V region **127**, 5295–5300 (2016)
13. Roy, K., Majumdar, A., Gangopadhyay, S.: Far field profile estimation in mono mode step index optical fiber with kerr type nonlinearity by a simple technique: IEEE VLSI-DCS Kolkata India, pp. 248–252 (2020)
14. Ghatak, A.K., Thyagarajan, K.: Introduction to fiber optics, 2nd edn. Cambridge University Press, UK (2002)
15. Sharma, A.K., Goyal, I.C., Ghatak, A.K.: Calculation of cutoff frequencies in single mode fibers for arbitrary profiles using the matrix method. IEEE J. Quant. Electron. **16**, 2317–2320 (1981)

16. Shijun, J.: Simple explicit formula for calculating LP11 mode cutoff frequency. Electron Lett. **23**, 534–536 (1987)
17. Mondal, S.K., Sarkar, S.N.: Effect of optical Kerr effect nonlinearity on LP11 mode cutoff frequency of single-mode dispersion shifted and dispersion flattened fibers. Opt. Commun. **127**, 25–30 (1996)
18. Chakraborty, S., Mandal, C.K., Gangopadhyay, S.: Prediction of first higher order modal field for graded index fiber in presence of Kerr nonlinearity. J. Opt. Commun. (2018). https://doi.org/10.1515/joc-20170206
19. Patra, P., Gangopadhyay, S., Goswami, K.: A simple method for prediction of first-order modal field and cladding decay parameter in graded index fiber. Optik **119**, 209–212 (2008)
20. Chakraborty, S., Mandal, C.K., Gangopadhyay, S.: Prediction of fundamental modal field for graded index fiber in presence of Kerr nonlinearity. J. Opt. Commun. (2017) https://doi.org/10.1515/joc-2017-0126
21. Chakraborty, S., Mandal, C.K., Gangopadhyay, S.: Prediction of first higher order modal field for graded index fiber in presence of Kerr Nonlinearity. J. Opt. Commun. (2018). https://doi.org/10.1515/joc-20170206
22. Gangopadhyay, S., Sarkar, S.N.: Evaluation of modal spot size in single-mode graded index fibers by a simple technique. J. Opt. Commun. **19**, 173–175 (1998)
23. Mukherjee, T., Majumdar, A., Gangopadhyay, S.: Kerr nonlinearity effect on dimensionless scalar and vector propagation constants of single-mode graded index fiber: estimation by a simple but accurate method. In: IEEE International Conference on VLSI DCS, pp. 253–257. MSIT Kolkata, India (2020)
24. Mukhejee, T., Maity, S., Majumdar, A., Gangopadhyay, S.: A simple but accurate formalism for study of single-mode graded index fiber directional coupler in presence of Kerr nonlinearity. Optik (213), 64772 (2020)
25. Abramowitz, M., Stegun, I.A.: Handbook of Mathematical Functions, Dover Publications, New York (1981)
26. Gradshteyn, I.S., Ryzhik, I.M.: Table of Integrals, Series and Products, Academic Press, London (1980)
27. Watson, G.N.: A treatise on the theory of Bessel functions. Cambridge University Press, U.K. (1944)

A Priority Based Routing Protocol to Improve Quality of Service (QoS) in Wireless Body Area Network for COVID and Diabetic Patients

Koushik Karmakar, Sohail Saif, Suparna Biswas, and Sarmistha Neogy

Abstract Use of electronic devices has increased many times in our daily life. It is used for many purposes including healthcare. Small sensor devices on patients' body that reads patients' physiological data and send those data to a remote server. Doctors and other healthcare professionals can view this data sitting at their home. Thus remote health monitoring is possible known as Wireless Body Area Networks (WBAN). Routing and providing seamless connectivity is a big challenge and a topic of research. In this work, a priority based routing protocol designed for WBAN has been developed where data has been classified into normal and emergency data. This routing protocol is especially applicable for COVID and diabetic patients. Normal data will be processed in cloud server but emergency data will be processed locally. Results obtained prove that our protocol is faster and also gives minimum delay.

Keywords Sensor-based health monitoring system · WBAN · Emergency data · Edge computing

1 Introduction

Research works has increased in emerging fields like sensors, networks and other smart devices, Internet of Things (IoT) and various related areas. They have huge applications in different fields including healthcare. Our current research is based on sensor-based remote healthcare monitoring system. Sensor-based remote health monitoring system is gaining popularity worldwide [1–4]. Small sensor devices can be used to collect physiological data from the patient. They are sent to a remote server for details study. Proper routing technique is required which will provide seamless

K. Karmakar (✉)
Narula Institute of Technology, Kolkata, India

S. Saif · S. Biswas
Maulana Abul Kalam Azad University of Technology, Haringhata, Nadia, West Bengal, India

S. Neogy
Jadavpur University, Kolkata, India

B. Sikdar et al. (eds.), *Proceedings of the 3rd International Conference on Communication, Devices and Computing*, Lecture Notes in Electrical Engineering 851,
https://doi.org/10.1007/978-981-16-9154-6_18

data connectivity. In this paper, a priority based routing protocol has been proposed which is especially useful for COVID as well as diabetic patients. We classify sensor data into normal data type and priority data type. Normal data is processed in the cloud server but priority data is processed locally, often in the sink node of the WBAN. It uses the concept of edge computing technique [5]. Our protocol ensures less delay and faster data delivery, which are basic criterion for a healthcare monitoring system. Structure of this paper is described as follows. In Sects. 2 and 3, WBAN architecture, literature survey and sensor node placement technique is described. Two possible cases have been described in Sect. 5. Proposed solution has been described in Sect. 6 followed by result calculation in Sect. 7. Performance analysis and brief comparison of the proposed work has been explained in Sect. 8. Section 9 concludes this work.

2 WBAN Architecture

A standard WBAN architecture is shown in Fig. 1 [1–3]. There are three layers in WBAN called tier-I, tier-II and tier-III. Each layer has many small components. Sensor nodes can be implanted as well as wearable on human body. In the first layer sensor nodes are attached with the body which reads information and send to sink node. Then data is communicated between the sink node and the external Access point (AP). At last data is communicated between the AP and the portable Personal Server (PS).

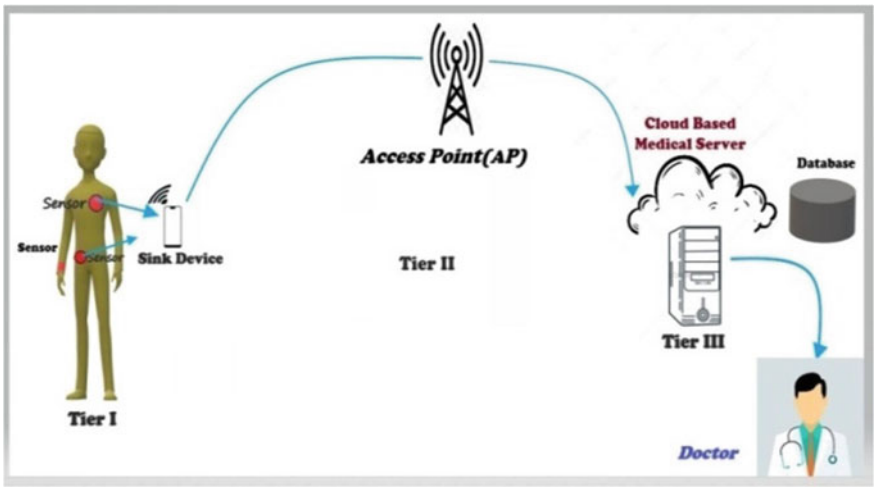

Fig. 1 WBAN communication architecture

3 Literature Survey

Research works focused on sensor networks and smart devices has been carried out for many years. In this section we describe a brief summary of them. In this work [6], a routing algorithm (PERA) was suggested based on priority. Emergency data has been assigned highest priority, on demand has been assigned second level priority and regular data is assigned third highest priority. In another work [7], a routing protocol (MHRP) was suggested that can handle different types of user mobility. Analytically it was proved that this protocol performs in a much better way than other similar protocols existed at that time. In M-SIMPLE [8], a better approach was suggested whose parameters are throughput, residual energy level, and factors like path loss. In another similar work [9], a routing method has been suggested based on nodes' thermal energy and energy efficiency level. In this work, a weighted average of the three factors are considered for selection of the routing path. In this work [10], a thermal aware routing algorithm has been proposed. This is also a priority based work and considers node temperature limit for assigning priority. In this work, an MAC protocol based algorithm has been developed for data classification that classifies data into three different categories. In another work [11], a data priority based method has been described. Classification of the sensor data is based on weighted energy and QoS (WEQ) based algorithm which selects the optimal path for data transmission. Another protocol [12] is also developed which is based on the quality of the link routing on demand (LATOR). It is used to improve rate of the delivery of the data packets (PDR). In another significant work [13] critical data routing code is used for data transmission. This is called Critical Data Routing (CDR) technique. In this paper [14] a block chain based routing protocol (ATEAR) has been suggested [14]. In another work [15] a protocol was designed considering different factors like latency, temperature and energy. It finds the optimum routing path by sensor nodes temperature. For that purpose two threshold limits have been set. In case sensor node temperature crosses its maximum limit, emergency signals will be sent. Another routing method [16] was suggested where a routing protocol called ERRS was proposed. It was designed based on forwarder node selection method and forwarder node rotation method. A comparative study of the above routing methods is shown in Table 1.

4 Sensor Node Position in WBAN

The different types of nodes are used to collect physiological data. Sensor nodes considered in this work are ECG sensor node, body temperature node, pulse sensor node. They collect information and then transferred to the relay node which is then sent to the sink node. From sink node it goes to the Access Point (AP). These sensor nodes and the relay node form a cluster. One such node placement arrangement is shown in Fig. 2.

Table 1 Comparison of different routing techniques in WBAN

Authors, year	Technology used and application	Simulation environment	Results
Ahmed et al. [6]	Protocol (PERA) is developed based on sensor data priority. Emergency data has been given highest priority	MATLAB is used for experiment	Give better output with respect to throughput, path loss
Karmakar et al. [7]	Protocol (MHRP) was designed based on handling user mobility. It can handle user mobility in WBAN	Analytical comparison was given	Better output in terms of delay, mobility handling
Khanna et al. [8]	Protocol (ERRS) was designed which works on forwarder node selection and rotation method	MATLAB based experiment was done	Achieves longer stability period and network lifetime
Ahmed et al. [9]	Weighted average of the three factors was considered at the time of routing path selection	MATLAB based experiment was done	Gives better output
Kathe and Deshpande [10]	An MAC-based algorithm was developed considering temperature and other factors for data priority	Discrete event based simulation was done	Gives better performance in various respect
Ibrahim et al. [11]	An algorithm called weighted energy and QoS (WEQ) has been designed for selection of the best path	OMNET++ was used for simulation	Better performance
Caballero et al. [12]	A new protocol called Link aware and thermal aware on-demand routing (LATOR) protocol has been developed. It was designed considering node temperature and overheating problem	OMNET++ based simulation was done	Gives better packet delivery rate

(continued)

Table 1 (continued)

Authors, year	Technology used and application	Simulation environment	Results
Sagar et al. [13]	A critical data routing technique (CDR) was developed. It can transmit data between inner body nodes and on body medical super sensor nodes	MATLAB based experiment was done	Better avg. packet delivery ration was found
Shahbazi and Byun [14]	A block chain based routing protocol called ATEAR was developed	OMNET++ based simulation was done	Better performance with respect to factors like energy, latency and node temperature
Banuselvasaswathy and Rathinasabapathy [15]	Determines optimal path by measuring sensor node temperature and defining two threshold limits	MATLAB based simulation was done	Better performance with respect to network lifetime, delay, power and energy
Ullah et al. [16]	One routing protocol called an energy-efficient and reliable routing scheme (ERRS) was proposed	MATLAB based experiment was done	Gives better throughput, residual energy and lower path loss

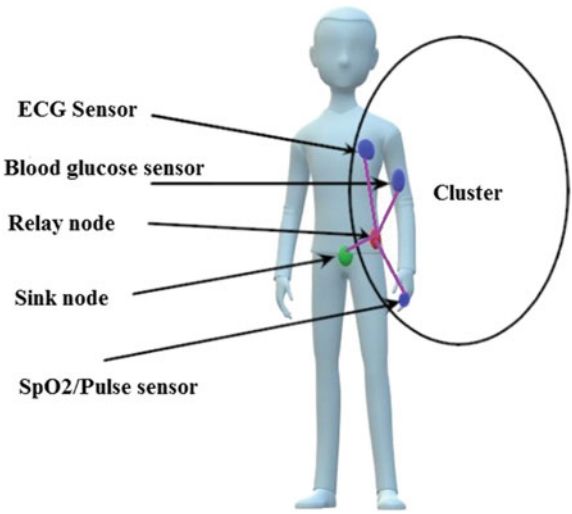

Fig. 2 WBAN sensor node placement

5 Problem Description

5.1 Case1

We consider the following two different cases. In the first case SpO2 sensor attached to the body (which senses oxygen level in the blood) senses oxygen saturation level. If oxygen level in the body is measured to be lower than the required oxygen level, patient needs immediate attention. In such a condition, patient will suffer from breathing problem. This is also one of the symptoms of COVID affected patients. In that case, procedures within WBAN should take extra care and should seek immediate attention. It may generate warning also.

5.2 Case2

We consider the second case when sensor on the patient's body detects lower blood glucose level. As this is regarding diabetic patient, this patient also needs immediate attention. Here also WBAN must take extra care and should be active immediately. It should ask the actuator device (insulin pump) to inject extra insulin in the patient's body without any delay.

6 Proposed Solution

In our work sensor data is classified and their priority is set. If the data lies in the normal range then it is called normal data. If it lies outside the normal range then it is called critical data. Based on the sensed data, it is classified into two different types:

1. Normal data (data lies within the normal range)
2. Critical data (data lies outside its normal range and tolerable limit).

Important health issues and different medical information are required to be followed in a health monitoring system. Normal range for blood oxygen saturation level is 95–100%. Blood oxygen value below this level is considered to be critical. And blood sugar level value up to 140 mg/dl is considered to be normal. But, a larger value than that of this is considered to be beyond normal range. Sensor reading outside of this range is considered to be abnormal for a patient. Such a patient is considered to be a sick patient and his physiological data is considered to be an emergency data. If an emergency data is detected, it needs to be attended as soon as possible. Such data is therefore processed locally often in the 'sink' node instead of the remote cloud server computer. This follows the idea of edge computing [5].

6.1 Case 1

We detailed problem description that is given in Sect. 5 part 1. As soon as emergency data is detected, 'sink' node will process this data locally. As soon as the SpO2 device detects less oxygen concentration level in blood, 'sink' node will instruct the oxygen supply unit (actuator) to increase oxygen level in the patient's body. This will help in solving the breathing problem of the patient.

Routing path:

1. 'Sensor node' collects data.
2. 'SpO2 node' detects less oxygen.
3. 'Emergency condition' is detected.
4. Local processing by 'sink' node.
5. 'Sink node' instructs oxygen supply unit (actuator).
6. Actuator will increase blood oxygen level.

6.2 Case2

Another problem description is given in Sect. 5 part 2. Like the previous case, here too data processing will be done by the sink node locally as soon as emergency is detected. If a lower blood glucose level is detected in the body, insulin pump will inject more insulin to the patient's body. This will increase insulin level and will reduce blood glucose level. Routing path will be similar to that of the previous one. It is described below. Entire process is described in a flowchart in Fig. 3.

Routing path:

1. 'Sensor node' collects data.
2. 'Blood sugar sensor' detects blood glucose level.
3. 'Emergency condition' is detected.
4. Local processing by 'sink' node.
5. 'Sink node' instructs insulin supply unit (actuator).
6. Actuator will increase blood oxygen level.

7 Delay Calculation

Delay in the link from node i to node j can be calculated as follows [17]. Delay in the link $D_{(i,j)}$ means sum of queuing delay, transmission delay and propagation delay which can be calculated using Eq. 1.

$$D_{(i,j)} = (d_q + d_T + d_P) \tag{1}$$

In this equation different values have following meanings,

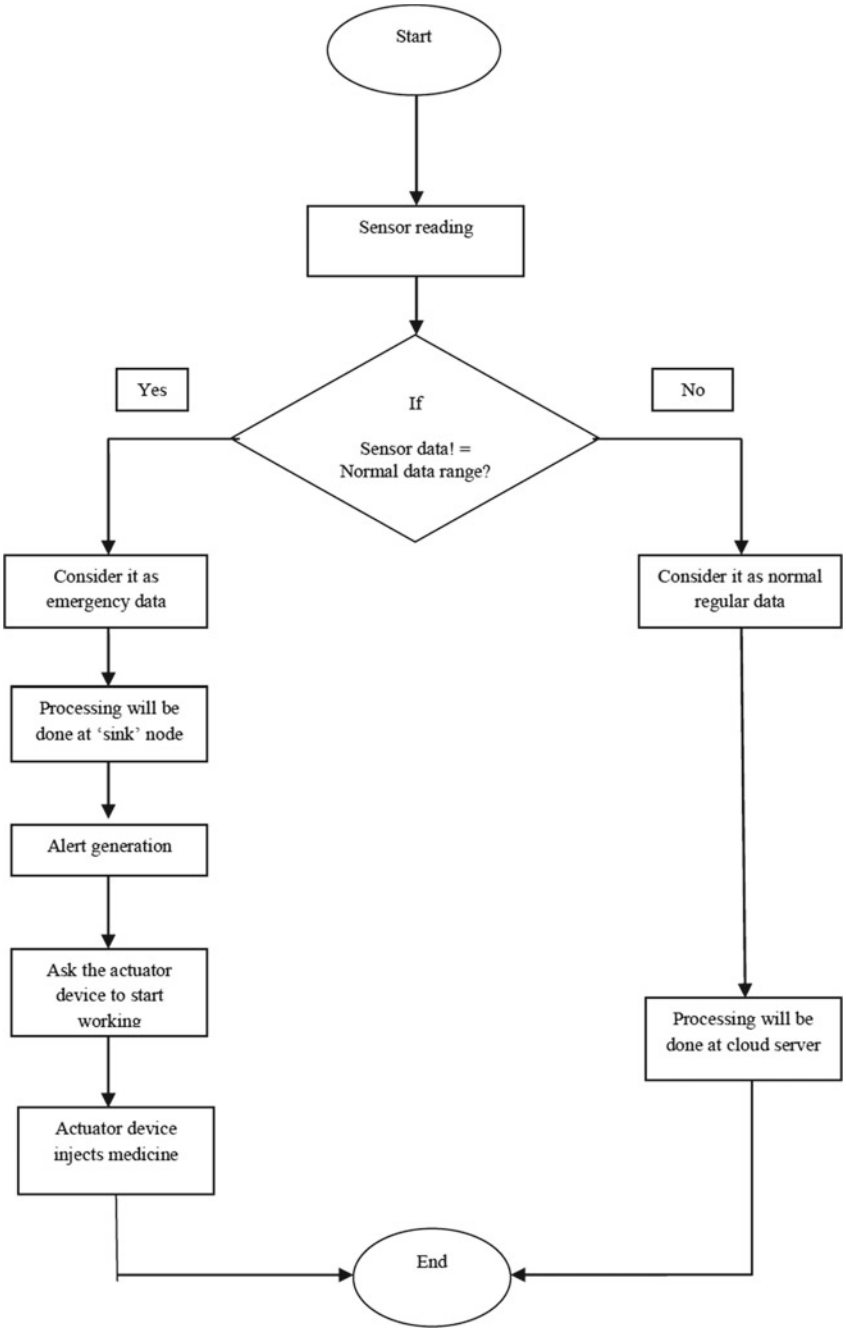

Fig. 3 Flowchart of the proposed system

d_q: Refers to Queuing delay in each node,
d_T: Refers to delay during transmission and.
d_P: Refers to delay during propagation.

where $d_T = L/B$; L indicates packet size in bits, B indicates link bandwidth (bps).

$d_P = d_{ij}/S$; where d_{ij} indicates length of the physical link between i and j.

S refers to the propagation speed of the medium (m/s).

$d_q = 1/(a - b)$; a refers to the service rate and b represents new packet entry rate.

An end to end delay $D_{x,s}$ from x to s can be calculated using Eq. 2.

$$D_{(x,s)} = \sum D_{(i,j)} = \sum (d_q + d_T + d_P) = \sum 1/(a - b) + \frac{L}{B} + \frac{d_{ij}}{S} \quad (2)$$

7.1 Design and Result Calculation

We have performed the design for simulation in GNS3 version 2.2.20. Node placement is shown in Fig. 4. Three sensor nodes have been placed in different positions of a patient. They are respectively ECG sensor, temperature sensor and pulse oximeter sensor (SpO2). They collect and send physiological information to the sink node.

In this diagram node1, node2 and node3 respectively represents ECG sensor, temp sensor and SpO2 sensor.

Node1 to sink node distance ($d1$) = 1.5 m.
Node2 to sink node distance ($d2$) = 2 m.
Node3 to sink node distance ($d3$) = 1.5 m.
Sink node to Access Point (AP) distance ($d4$) = 10 m.

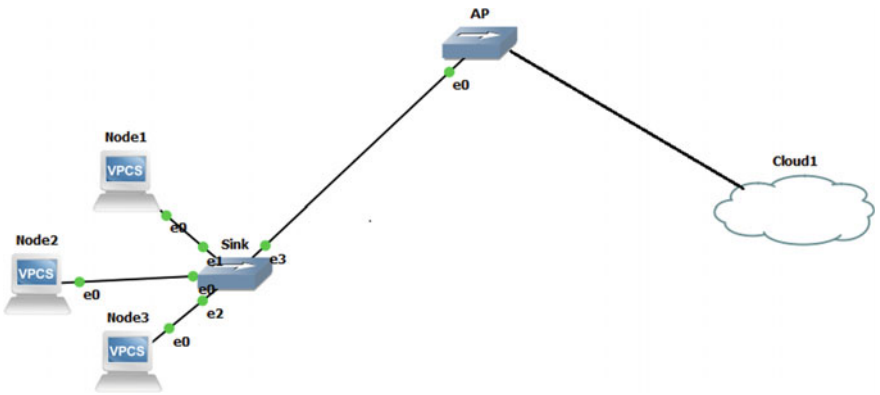

Fig. 4 Node placement and simulation

AP to cloud server distance ($d5$) = 10 km meters = 10^4 m.

Therefore, if emergency is detected in the SpO2 sensor itself, it will traverse only ($d3$) 0.5 m as the same will be processed locally in the sink node. But, if it reaches to the cloud server, then it will traverse a total distance of

$$(D) = (d3 + d4 + d5) = (1.5 + 10 + 10^4) = 10011.5\text{m}$$

As, ($d5$) >> ($d3$, $d4$)

$d5$ is almost equivalent to D.

So, $d5 >> d3$

Therefore, data will have to travel much shorter distance if it is processed locally. Also, delay will be much less in such a situation.

We consider a data of message size (L) = 40 bytes. Initial energy is 1 J. B is the link bandwidth = 25 kHz.

So, $d_T = (L/B) = (40 \times 8)/(25 \times 103 \times 2) = 0.0064$ s.

Again, d_P is calculated as $d_P = \frac{d_{ij}}{S}$; where d_{ij} means the distance between one sensor node and another node and S means the speed of the signal through the air which is (3×108) (m/s). Value of d_Q is constant value and often negligible. Putting 10 different values of d_{ij} in Eq. (1) we calculate the sum of the end to end delay in seconds and get the following Fig. 5. From this graph it is clear that the delay is significantly low when distances between the sensor nodes are very less. It proves that local processing is always better as the delay will be lower.

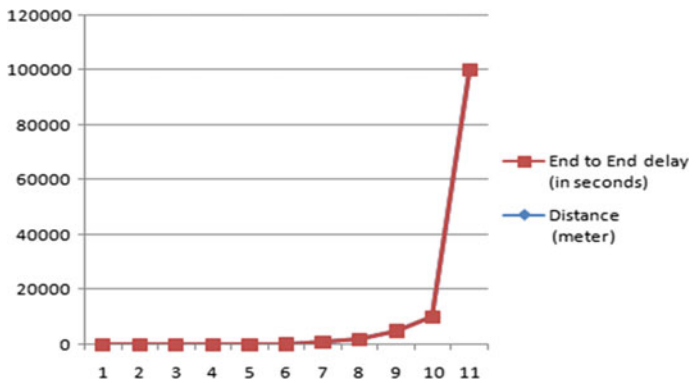

Fig. 5 End to end delay versus distance graph

Table 2 Comparison table

	Banuselvasaswathy and Rathinasabapathy [15]	Proposed work
Data priority	Data priority is decided on sensor node temperature	Data priority is decided on sensor node data
Optimal path selection	Through sensor node temperature and through two threshold limits	Local processing is done once emergency data is detected
Edge computing	No local processing/edge computing concept is used	Used the concept of local processing/edge computing
Delay analysis	Data delivery delay is calculated	Delay is much lower as local processing is done
Energy consumption	Energy consumption is calculated from the given equation	Energy consumption is not considered in our work

8 Performance Analysis

We compare our work with the work described in paper [15]. In their paper, Banuselvasaswathy and Rathinasabapathy [15] have proposed a method of choosing optimal path through routing algorithm in WBAN using sensor node temperature and two thresholds definition. However, we have proposed a concept of local processing of the emergency data i.e. we have used the 'edge' computing concept. In Table 2, we have a made a brief comparison of our work with [15].

9 Conclusion

In this work we have proposed a priority based routing protocol on WBAN for COVID and diabetic patients. We have considered two cases here. As soon as an emergency data is detected, it will be processed locally in the 'sink' to save time and delay instead of remote processing in the cloud server. Our protocol ensures faster service as well as seamless data processing. It improves Quality of Service (QoS). This gives better output with respect to end to end delay.

References

1. Chen, M., Gonzalez, S., Vasilakhos, A., Cao, H., Leung, V.C.M.: Body area networks: a survey, in Springer. Mobile Netw. Appl. **16**(2), 171–193 (2011)
2. Ullah, S., Hignis, H., Braem, B., Latre, B., Blondia, C., et al.: A: a comprehensive survey of wireless body area networks, in 2012 Springer. J. Med. Syst. **36**(3), 1065–1094 (2012)
3. Latre, B., Braem, B., Moerman, I., Blondia, C., Demeester, P.: A survey of wireless body area network, in Springer. J. Wireless Netw. **17**(1), 1–18 (2011)

4. Afridi, N.J., Jamil, S., Akbar, M., Khan, Z.A., Qasim, U.: HEAT: horizontal moveable energy-efficient adaptive threshold based routing protocol for WBAN. In: Proceedings of 28th IEEE International Conference on Advanced Networking and Applications Workshops (WAINA), 13–16 May (2014)
5. Shi, W., Cao, J., Zhang, Q., Li, Y., Xu, L.: Edge computing: vision and challenges. IEEE IoT J. **3**(5), 637–646 (2016)
6. Ahmed, G., Jianhua, Z., Sadiq Fareed, M.M.: PERA: priority based energy efficient routing algorithm for WBANs. Springer Wireless Personal Commun. (2017)
7. Karmakar, K., Biswas, S., Neogy, S.: MHRP: a novel mobility handling routing protocol in wireless body area network. In: Proceedings of the 2017 International Conference on Wireless Communications, Signal Processing and Networking (WISPNET), Chennai, India, 22–24 March (2017), pp. 1939–1945 (2017)
8. Khanna, A., Chaudhary, V., Gupta, S.H.: Design and analysis of energy efficient wireless body area network (WBAN) for health monitoring. Springer (2018)
9. Ahmed, G., Mahmood, D., Islam, S.: Thermal and energy aware routing in wireless body are networks. Int. J. Distrib. Sensor Netw. **15**(6) (2019)
10. Kathe, K.S., Deshpande, U.A.: A thermal aware routing algorithm for a wireless body area network. Springer Wireless Personal Commun. (2019)
11. Ibrahim, A., Bayat, O., Ucan, O.N., Salisu, S.: Weighted energy and QoS based multi-hop transmission routing algorithm for WBAN. In: 6th International Engineering Conference "Sustainable Technology and Development". Erbil, Iraq IEC (2020)
12. Caballero, E., Ferreira, V.C., Lima, R.A., Albuqerque, C., Muchaluat-Saade, D.C.: LATOR; link-quality aware and thermal aware on-demand routing protocol for WBAN. In: Proceedings of the IWSSIP (2020)
13. Sagar, A.K., Singh, S., Kumar, A.: Energy-aware health monitoring using critical data routing (CDR). Springer Wireless Personal Commun (2020)
14. Shahbazi, Z., Byun, Y.C.: Towards a secure thermal energy aware routing protocol in wireless body area network based on block chain technology. MDPI Sensor (2020)
15. Banuselvasaswathy, B., Rathinasabapathy, V.: Self-heat controlling energy efficient OPOT routing protocol for WBAN. Springer Wireless Netw. (2020)
16. Ullah, F., Khan, M.Z., Faisal, M., Rehman H.U., Abbas, S., Mubarek, F.S.: An energy efficient and reliable routing scheme to enhance the stability period in wireless body area networks. Elsevier Comput. Commun. **165**, 20–32 (2021)
17. Huynh, T.T., Dinh-Duc, A.V., Tran, C.H.: Delay-constrained energy-efficient cluster-based multihop routing in wireless sensor networks. J. Commun. Netw. **18**(4) (2016)

Accurate Estimation of Dimensionless Vector and Scalar Propagation Constants for First Higher Order Mode of Kerr Type Nonlinear Graded Index Fiber by Simple Mathematical Formalism

Tilak Mukherjee, Angshuman Majumdar, and Sankar Gangopadhyay

Abstract A simplified yet accurate method based on Chebyshev formalism is employed for the estimation of dimensionless vector and scalar propagation constants of first higher order mode of graded index kind fiber. The method involves application of series expression of first higher order modal field of graded index fiber for the relevant analysis, considering the absence as well as the presence of the Kerr type nonlinearity effect. In this context, we restrict our investigation on a typical parabolic index fiber as an example of graded index fiber. Our mathematical formalism includes considerably less calculations and still our outcomes match excellently with exact results obtainable by the variational method incorporating Gaussian-exponential-Hankel function in the linear case and rigorous finite element computation technique for the Kerr type nonlinear case. The said conventional methods of exact analysis require lengthy and cumbersome computations involving longer time. Thus, our simple but accurate formalism definitely generates adequate scope for its successful application in the analysis of dual mode fibers considering the extensive domain of contemporary nonlinear optics and devices.

Keywords First higher order mode · Chebyshev formalism · Dimensionless vector and scalar propagation constants · Kerr nonlinearity

1 Introduction

The estimation and performance evaluation of the optical fiber propagation parameters both in the absence and presence of nonlinear effects is of extreme importance in communication engineering. The nonlinearity is produced because of the dependence of such optical fiber refractive index profile function particularly on the strength of

T. Mukherjee
Department of Electronics & Communication Engineering, Haldia Institute of Technology, Haldia and Brainware University, Kolkata, West Bengal, India

A. Majumdar · S. Gangopadhyay (✉)
Department of Electronics & Communication Engineering, Brainware University, Kolkata, West Bengal, India

B. Sikdar et al. (eds.), *Proceedings of the 3rd International Conference on Communication, Devices and Computing*, Lecture Notes in Electrical Engineering 851,
https://doi.org/10.1007/978-981-16-9154-6_19

electric field related to optical beam with high intensity. Consequently, such nonlinear kind of fibers when subjected to intense light source exhibit propagation attributes that do differ from those fibers in linear condition [1–5]. Nonlinearity is broadly categorized as third order or fifth order etc. according to the nature of harmonics generation as the case may be. The formation of any particular kind of nonlinearity is essentially dependent on optical beam intensity, as well as doping nature of the concerned optical fiber medium. Dispersion phenomenon is mainly responsible for pulse broadening while nonlinearity causes pulse compression, and this interesting interplay between dispersion along with nonlinearity phenomena is the primary cause for optical beam propagation in the fiber popularly termed as soliton propagation. Such soliton pulses do not possess any distinct variation in amplitude, velocity or shape and are described by large information capacity. Optical communication is extremely influenced by Kerr type nonlinearity which is also called third order nonlinearity. It generates undesirable prominent effects in the form of "self phase modulation, cross phase modulation and four wave mixing" [5–7]. These effects are non scattering in nature. Proper analysis and study of nonlinear fibers and their propagation attributes is of paramount importance in optical fiber communication technology and allied high performance systems and devices. Accordingly, these nonlinearities largely affect the information capacity by their adverse impact on launched power, channel spacing and bit rate, bit error rate and also bandwidth of any fiber optic communication system. Noticeable consequences in the form of optical beam defocusing or self focusing occurs mainly because of the dependence of refractive index profile on the optical beam intensity in a nonlinear manner [5–7]. The impact of Kerr nonlinearity with its repercussions has sparked adequate interest in the potential area of emerging nonlinear photonics involving devices photonic crystal fibers, opto-mechanical ring resonator and its modeling with respect to mode division multiplexing and the same have been reported in literature [6–9].

In this context, it is relevant to note that dual mode optical fiber has gained prominent importance in optical communication area. The scalar type wave equation solution particularly leads to scalar mode electric fields which are termed to be linearly polarized (LP) modes. These LP modes have fields that are transverse in nature. First higher order (LP_{11}) mode for a dual type mode fiber has the significant potential to nullify positive dispersion by large negative waveguide dispersion and thereby the fiber acts as a dispersion compensating fiber, thus making it quite acceptable for doped fiber amplifier operation. Moreover, in comparison to the conventional core-cladding dispersion shifted type fibers, such dual mode double layer profile dispersion shifted kind fibers have much lower transmission losses as well as bending losses which makes it reasonably suitable for broadband transmission of communication at a particular wavelength [10, 11]. The amount of group delay prevalent between the fundamental mode (LP_{01}), and (LP_{11}) is continuously being exploited and implemented in sensor devices as example of extended applications in the promising field of interconnecting optics [10, 11].

The study of polarization and birefringence is largely facilitated with the help of knowledge of vector mode propagation characteristics for a fiber. Using scalar mode propagation constant, one can evaluate vector mode propagation constant employing

Snyder-Young perturbative formulation [12]. For the particular case of the typical step type index fiber without the Kerr nonlinear effect, we have analytical form for the relevant modal field expression, but considering graded index fibers like parabolic index or triangular index profile nature, one needs to resort to approximation procedures or numerical methods to predict respective modal field and other propagation parameters of interest. Typical cases of parabolic index fiber with V number greater than 3.5 has been considered in this paper as an example of graded index fiber, particularly involving first higher order mode only. Variational computational technique employing Gaussian-exponential-Hankel function provides reasonably good accuracy for linear condition so as to estimate the fiber propagation parameters [13]. In presence of Kerr nonlinearity rigorous finite element approach consisting of several partial differential equations has been used to predict the modal field and appropriate propagation parameters [14]. However, all these existing methods are quite cumbersome involving computational complexity. Here lies the research gap which is suitably addressed by the simplified power series mathematical computation method in the evaluation of fiber parameters and associated devices. Literature still requires efficient modeling for study, assessment and exploring applications of different kinds of optical devices and verification of the results with the available exact ones so as to lead to justification of the accuracy and simplicity of the proposed model.

In this purview, a simplified but accurate formalism that is based on Chebyshev power series expression is applied to predict the dimensionless vector as well as scalar propagation constants related to first higher order mode considering parabolic index fiber. Chebyshev formalism has proved to be extremely effective in the performance analysis of linear fibers. Accordingly, one can appreciably extend it for the Kerr type nonlinearity domain by using iterative technique in the formalism for linear case and this leads to accurate prediction of the concerned propagation parameters under the presence of Kerr nonlinearity also [15–21]. Therefore, the mathematical formalism is extremely user friendly in its approach and leaves ample scope for parameter evaluation in the area pertaining to nonlinear optical technology as illustration of broadened applications.

2 Theory

For the case of a circularly shaped core optical fiber under weakly guiding approximation, expression for refractive index profile is,

$$n^2(R) = \begin{cases} n_1^2(1 - 2\delta f(R)), & R \leq 1 \\ n_2^2\ , & R > 1 \end{cases} \tag{1}$$

Here, normalized radial distance 'R' = [r/a], 'δ' represents relative refractive index difference, 'a' is the radius of core. Further, 'n_1', 'n_2' are the corresponding

refractive indices of the core, and also cladding. Term *f(R)* is profile function of optical fiber under consideration, and for graded type index fiber case that has been aptly expressed below,

$$f(R) \text{ equals to } (R)^q, \text{ for} R \leq 1 \tag{2}$$

where, 'q stands for profile exponent term, and whose respective values for step, triangular and parabolic index fibers are ∞, 1 and 2' [18–20]. For the present work, parabolic graded index fibers with different V numbers have been considered with $f(R) = (R^2)$ for $R \leq 1$. Refractive index profile distribution of any optical fiber in the presence of Kerr nonlinearity is mathematically expressed to be [19, 20],

$$n^2(R) = n_L^2(R) + \frac{n_2^2 n_{NL}(R)}{\eta_0}\psi^2(R) \tag{3}$$

where, terms '$n_L(R)$' and '$n_{NL}(R)$' signify radial distribution of the refractive index under linearity and Kerr type nonlinearity effect of the concerned fiber respectively with, $\eta_0 = \sqrt{\frac{\mu_0}{\varepsilon_0}}$. Terms '$\mu_0$', '$\varepsilon_0$' signify permeability and permittivity for the free space medium respectively. For the case of any weakly guiding approximation fiber (n_1 almost near to n_2), the complex vector mode wave equation gets merely reduced to a simplified form of scalar wave equation and the solution of such equation generates linearly polarized (LP) modes. For the first higher mode (denoted as LP_{11}), the modal field that aptly satisfies the following scalar mode wave equation is mathematically expressed below as,

$$\begin{aligned} &"\frac{d^2\psi(R)}{dR^2} + \frac{1}{R}\frac{d\psi(R)}{dR} + \left[V^2\{1 - f(R)\} - W^2\right]\psi(R) - \left(\frac{\psi(R)}{R^2}\right) \\ &+ [V^2 g(R)\psi^3(R)] = 0"[19,\ 20] \end{aligned} \tag{4}$$

In this context $g(R) = \frac{n_2 n_{NL} P}{\pi\, a^2 (n_1^2 - n_2^2)}$, and it essentially accounts for the nonlinear kind of Kerr coefficient, NA, cross sectional area as well as power (P). Applying proper boundary value condition at the interface of core and cladding [19, 20];

$$\left[\frac{1}{\psi}\frac{d\psi}{dR}\right]_{at\, R=1} = -\left[1 + \frac{\{W K_0(W)\}}{\{K_1(W)\}}\right] \tag{5}$$

Here, K_1 along with K_0 represent modified Bessel function terms for first order kind and that of zero order respectively with appropriate subscripts. Term '$V = \{k_0 a (n_1{}^2 - n_2{}^2)^{1/2}\}$ is the normalised frequency, and $W = \{a(\beta^2 - n_2{}^2 k_0{}^2)^{1/2}\}$ represents cladding decay parameter' for the fiber [17–20]. Also, 'k_0' represents wave number in free space medium whereas 'β' indicates the propagation constant in the expression for V and W [17–20].

Employing Chebyshev formalism based on simple power series expansion form considering graded index fiber, LP_{11} modal field expression within core as well as cladding can be shown to be [17, 20],

$$\begin{aligned}\Psi(R) &= \left[(a_1 R) + \left(a_3 R^3\right) + \left(a_5 R^5\right)\right], \text{for} R < 1 \\ &= [(a_1 + a_3 + a_5)]\frac{K_1(WR)}{K_1(W)}, \text{for} R > 1\end{aligned} \tag{6}$$

Using Eq. (6) in the above mentioned Eq. (4), so we attain the following expression;

$$\begin{aligned}&"a_1\left\{V^2(1 - f(R)) - W^2 + V^2 g\psi^2(R)\right\} \\ &+a_3\{8 + R^2\left\{[V^2(1 - f(R)) - W^2 + V^2 g\psi^2(R)]\right\} \\ &+a_5\{24R^2 + R^4\left\{[V^2(1 - f(R)) - W^2 + V^2 g\psi^2(R)]\right\} = 0" \text{ [19, 20]}\end{aligned} \tag{7}$$

Only two distinct Chebyshev points R_m are chosen taking $m = 1, 2$ for the purpose of computation of a_3, a_5 that are expressed in terms of a_1. Appropriate Chebyshev points under consideration are expressed by [15, 20–23],

$$R_m = \cos\left(\frac{(2m - 1)}{(2M - 1)}\frac{\pi}{2}\right) \quad \text{for} m = 1, 2, 3, \ldots, (M - 1) \tag{8}$$

In this connection, we choose value of M to be 3 depending on power series terms and, obtain R_1 with specific value 0.9511 and R_2 having value 0.5878. Using these relevant Chebyshev points R_m for $m = 1, 2$ in Eq. (7), we obtain the pair of equations with R_1 and R_2 terms and the same has been mentioned in literature [20].

Ratio of the Bessel functions in the modified form is $\frac{K_1(W)}{K_0(W)}$, and its variation nature with $(1/W)$ over the defined interval [0.60, 2.50] for W is observed to be practically linear [24]. Therefore, we resort to the technique of least square fitting in the aforesaid interval range and thereafter arrive at the below mentioned linear relationship as [20, 23, 24],

$$\frac{K_1(W)}{K_0(W)} = \left(\alpha + \frac{\beta}{W}\right) \tag{9}$$

where terms 'α' equals 1.034623 and 'β' equals 0.3890323 [20, 23, 24].

Furthermore, we apply Eq. (6) as well as Eq. (9) in the above Eq. (5) and derive,

$$"a_1 2(\alpha W + \beta) + W^2 + a_3 4(\alpha W + \beta) + W^2 + a_5 6(\alpha W + \beta) + W^2 = 0" \text{ [20]} \tag{10}$$

Here terms a_1, a_3, a_5 as mentioned in Eq. (7) and also Eq. (10) shall finally lead to the definite nontrivial type solution provided the following mentioned condition is strictly satisfied for the (3×3) determinant [20],

$$\begin{vmatrix} A_1 & B_1 & C_1 \\ A_2 & B_2 & C_2 \\ A_3 & B_3 & C_3 \end{vmatrix} = 0 \tag{11}$$

Individual determinant elements (A_i, B_i, C_i) with subscript 'i' = 1, 2 are [20]:

$$"A_i = \left[\left\{V^2(1 - f(R_i)) - -W^2 + V^2 g\Psi^2(R_i)\right\}\right]";$$
$$"B_i = \left\{8 + R_i^2\left[V^2(1 - f(R_i)) - -W^2 + V^2 g\Psi^2(R_i)\right]\right\}"$$
$$"C_i = \left\{24R_i^2 + R_i^4\left[V^2(1 - f(R_i)) - -W^2 + V^2 g\Psi^2(R_i)\right]\right\}"$$

and

$$"A_3 = \left\{2(\alpha W + \beta) + W^2\right\}"; "B_3 = \left\{4(\alpha W + \beta) + W^2\right\}"; "C_3 = \left\{6(\alpha W + \beta) + W^2\right\}"$$

It has been observed that existence of terms like $\psi^2(R_i)$ make the solution of above determinant extensively tedious and complicated in calculation. So to simplify it, we first consider for $g(R) = 0$ in order to solve Eq. (11) for the linear fiber condition. The cladding decay parameter (W) value for any specific V number corresponding to a particular fiber is estimated for the linear region. In the succeeding step, taking this calculated W and corresponding V the coefficient terms a_3, a_5 that are in terms of a_1 are computed under the absence of nonlinearity. This involves calculation for the linear fiber case. Proceeding with this technique, in the presence of nonlinearity for any particular value of *g(R)* and V number, we subsequently adopt iterative technique and the process of iteration is performed till we obtain convergent W values; and corresponding values of a_3, a_5 that are in terms of a_1. This suitably illustrates our computation for the nonlinear fiber case. Accordingly, A_3 and A_5 are the normalized values of a_3 and a_5 in terms of a_1 and can simply be expressed as $A_3 = (a_3/a_1)$ and $A_5 = (a_5/a_1)$. The calculated values of W, A_3 and A_5 are further used for determination of the dimensionless vector propagation constants (U) as well as dimensionless scalar propagation constants ($\hat{U}$) for the LP_{11} mode of a parabolic index fiber profile having V number value greater than 3.5 for linearity as well as Kerr type nonlinearity influence respectively.

Furthermore in this respect, this is noteworthy that for the typical case of refractive index with power law profile (where q represents power exponent), the mathematical relationship between (U) and ($\hat{U}$) is expressed by the following relationship [25, 26],

$$U^2 = \hat{U}^2 - (q\delta)\frac{\int_0^1 \psi \frac{d\psi}{dR}\left(R^q + \delta R^{2q} + \delta^2 R^{3q}\right)dR}{\int_0^\infty |\psi|^2 R dR} \tag{12}$$

where, $U^2 = a^2(k_0{}^2\, n_1{}^2 - \beta^2)$ and $\hat{U}^2 = a^2(k_0{}^2\, n_1{}^2 - \hat{\beta}^2)$. Also, $k_0 = (2\pi/\lambda)$, and 'β', '$\hat{\beta}$'are the propagation constants for the case of vector mode along with scalar mode respectively with their usual notations.

Substituting Eq. (6) in the above Eq. (12) and performing sufficient mathematical integration within defined limits for corresponding core and cladding region, the dimensionless vector propagation constant (U) is obtained for the typical case of parabolic graded type index fiber having q whose value is numerically equal to 2 [22, 24, 27],

$$U^2 = \hat{U}^2 - 2\delta\left(\frac{N}{D_1 + D_2}\right) \tag{13}$$

The numerator part is $N = (0.25 + \delta/6 + \delta^2/8 + 2A_3/3 + \delta A_3/2 + 2A_3\,\delta^2/5 + 3A_5/4 + 3A_5\delta/5 + \delta^2\,A_5/5 + 3A_3{}^2/8 + 3A_3{}^2\,\delta/8 + \delta^2 A_3{}^2/4 + 4A_3A_5/5 + 2\delta\,A_3A_5/3 + 4A_3A_5\,\delta^2/7 + 5\,A_5{}^2/12 + 5\delta\,A_5{}^2/14 + 5\,A_5{}^2\delta^2/16)$.

Denominator component $D_1 = \left(\frac{1}{3} + \frac{A_3}{5} + \frac{A_5}{7}\right)$, and other component D_2 is expressed as:

$$D2 = (1 + A_3 + A_5)^2\left[\left\{\frac{K_0(W)K_2(W)}{2K_1^2(W)}\right\} - \frac{1}{2}\right] \tag{14}$$

$\hat{U}$ for any specific V value is easily evaluated using the following relationship [28],

$$\hat{U}^2 = (\mathrm{V}^2 - \mathrm{W}^2) \tag{15}$$

The cladding decay parameter (denoted by W) for any particular V number is computed with the extensive aid of Chebyshev formalism [17, 20]. Therefore, with prior adequate knowledge of V, and also W in this respect as from Eq. (15), one is capable to readily calculate the parameter $\hat{U}$. Consequently, U can be evaluated successfully using Eqs. (13) and (14).

3 Results with Discussions

The present paper exclusively deals with the estimation of dimensionless scalar mode propagation constant ($\hat{U}$), and dimensionless vector mode propagation constant (U) pertaining to graded index fiber. First higher order (LP_{11}) mode for a parabolic type index fiber ($q = 2$) with typical V number values of 3.7, 3.9 and 4.1 are considered in the work. The cut-off V number for LP_{11} for parabolic index type fiber is around 3.518 and so, V values greater than this specific cut-off value are selected for our investigation [16, 20]. The results are calculated considering absence and presence of typical Kerr type nonlinearity effect, eventually leading to the verification of

Table 1 Calculated dimensionless vector propagation constants (U) and scalar propagation constants ($\hat{U}$) for the first higher mode (LP_{11}) of a parabolic index fiber ($q = 2$) in the absence and presence of Kerr type Nonlinearity with different δ values

V	Nonlinearity parameter values '$n_{NL}P$' (in m^2)	$\hat{U}$	U ($\delta = 0.0025$)	U ($\delta = 0.005$)	U ($\delta = 0.01$)
3.7	0	3.6530	3.6531	3.6531	3.6532
	$+1.5 \times 10^{-14}$	3.6325	3.6326	3.6326	3.6328
	-1.5×10^{-14}	3.6715	3.6716	3.6716	3.6717
3.9	0	3.7933	3.7934	3.7934	3.7936
	$+1.5 \times 10^{-14}$	3.7684	3.7685	3.7686	3.7687
	-1.5×10^{-14}	3.8168	3.8169	3.8169	3.8171
4.1	0	3.9237	3.9238	3.9239	3.9240
	$+1.5 \times 10^{-14}$	3.8955	3.8956	3.8957	3.8959
	-1.5×10^{-14}	3.9509	3.9510	3.9511	3.9512

the prescribed mathematical formalism. It should be referenced here that we have particularly chosen the cladding refractive index (denoted by n_2) having numerical value of 1.47. The value of fiber parameter $a\sqrt{\left(n_1^2 - n_2^2\right)} = 0.22$ μm in our current work. The combined multiplicative term of the nonlinear refractive index as denoted by '$n_{NL}(R)$' (m^2/W units) along with power represented by 'P' (W units) is suitably represented to be '$(n_{NL}P)$'.

In this connection, the typical value of $n_{NL}P$ in our present study has been considered to be ' $+(1.5 \times 10^{-14})$ m^2 and $-(1.5 \times 10^{-14})$ m^2 for the positive type and negative type Kerr nonlinearity parameters respectively' [19, 20]. Here, $n_{NL}P = 0$ simply signifies the absence of nonlinearity and certainly implies for the linear condition [19, 20]. MATLAB is the tool for simulation in the process of parameter estimation and evaluation.

Table 1 shows the calculated values of $\hat{U}$ and U under linear and nonlinear condition for different δ values, namely 0.0025, 0.005 and 0.01 for the first higher mode (LP_{11}) of a parabolic graded index fiber.

$\hat{U}$ depends only on V and W values as it can be observed and also supported by Eq. (15). U depends on δ and there is slight increase of U value as δ increases from 0.0025 to 0.01. It has been observed that with increase in V number the propagation constants also tend to increase and this behavioral trend bears strong consistency with the fact that modal spot size decreases with increase in V number for any fiber. The propagation constants decrease for positive nonlinearity parameter while on the contrary increase for negative nonlinearity parameter. For step index fibers the vector mode and scalar mode propagation parameters are identical. These investigations are immensely beneficial related to the studies of birefringence attributes and devices that are polarization dependent.

Our results based on simple Chebyshev power series formalism are in good coherence with the computed exact results that are obtained by the application of rigorous

finite element computation method for the case of nonlinear fibers [14]. Furthermore, it is relevant to state that in absence of nonlinearity also, the agreement has been considerably excellent [25–28]. Thus, our formalism based on iteration procedure stands the excellence of being considered as a suitable yet simple mathematical alternative in contrast to the conventional cumbersome existing computational methods in the evaluation of propagation constants without much compromise on accuracy. Here lies the novelty of our prescribed formalism that incorporates simple mathematical computation consisting of determinant solution, coefficient evaluation and iteration as integral part of its execution. The adopted methodology is convenient and at the same time correct.

4 Conclusion

This paper reports the applicability of a simplified but also accurate mathematical formalism for the estimation of dimensionless vector mode and scalar mode propagation constants for the case of first higher mode of a parabolic graded index type profile fiber. Evaluation has been successfully carried out under the presence and absence of Kerr type nonlinearity effect. Our predicted results have been found to match quite excellently with the numerical exact results obtainable with the help of rigorous methods as available in literature. The execution of our power term series formalism is reasonably simplified in its approach and can be broadly extended for other kinds of fibers as well. This shall contribute to the estimation of various propagation parameters related to first higher mode and their performance assessment. The analysis also leads to proper selection and estimation of V number for minimizing the influence of nonlinearity in respect of modal noise associated with different graded index fibers. Taking into consideration that dual mode fibers are extremely promising in the vast field of optical communication and sensor applications, our method generates feasible and user friendly yet considerably accurate formalism for the system technologists and researchers dealing with the emerging area of nonlinear optics and associated devices.

References

1. Tomlinson, W.J., Stolen, R.H., Shank, C.V.: Compression of optical pulses chirped by self-phase modulation in fibers. J. Opt. Soc. **1**, 139–149 (1984)
2. Synder, A.W., Chen, Y., Poladian, L., Mitchel, D.J.: Fundamental mode of highly nonlinear fibres. Electron. Lett. **26**, 643–644 (1990)
3. Goncharenko, I.A.: Influence of nonlinearity on mode parameters of anisotropic optical fibres. J. Mod. Opt. **37**, 1673–1684 (1990)
4. Sammut, R.A., Pask, C.: Variational approach to nonlinear waveguides-Gaussian aproximations. Electron. Lett. **26**, 1131–1132 (1990)
5. Agrawal, G.P., Boyd, R.W.: Contemporary nonlinear optics. Academic Press, Boston (1992)

6. Saitoh, K., Fujisawa, T., Kirihara, T., Koshiba, M.: Approximate empirical relations for nonlinear photonic crystal fibers. Opt. Express. **14**, 6572–6582 (2006)
7. Agrawal, G.P.: Nonlinear fiber optics. Academic Press, Cambridge, MA (2013)
8. Antonelli, C., Golani, O., Shtaif, M., Mecozzi, A.: Nonlinear interference noise in space-division multiplexed transmission through optical fibers. Opt. Express. **25**, 13055–13078 (2017)
9. Yu, Y.F., et al.: Force-induced optical nonlinearity and Kerr-like coefficient in opto-mechanical ring resonators. Opt. Express. **20**, 18005–18015 (2012)
10. Eguchi, M., Koshiba, M., Tsuji, Y.: Dispersion compensation based on dual-mode optical fiber with inhomogeneous profile core. J. Lightwave. Technol. **14**, 2387–2394 (2002)
11. Monerie, M.: Propagation in doubly clad single mode fibers. IEEE J. Quant. Electron. QE **18**, 534–535 (1982)
12. Snyder, A.W., Young, W.R.: Modes of optical waveguides. J. Opt. Soc. Am. **68**, 297–309 (1978)
13. Hosain, S.I., Sharma, A., Ghatak, A.K.: Splice loss evaluation for single-mode graded index fibers. Appl. Opt. **21**, 2716–2721 (1982)
14. Hayata, K., Koshiba, M., Suzuki, M.: Finite element solution of arbitrary nonlinear, graded-index slab waveguides. Electron. Lett. **23**, 429–431 (1987)
15. Chen, P.Y.P.: Fast method for calculating cut-off frequencies in single-mode fibers with arbitrary index profile. Electron. Lett. **18**, 1048–1049 (1982)
16. Shijun, J.: Simple explicit formula for calculating LP_{11} mode cutoff frequency. Electron. Lett. **23**, 534–535 (1987)
17. Patra, P., Gangopadhyay, S., Goswami, K.: A simple method for prediction of first-order modal field and cladding decay parameter in graded index fiber. Optik **119**, 209–212 (2008)
18. Chakraborty, S., Mandal, C.K., Gangopadhyay, S.: Prediction of fundamental modal field for graded index fiber in presence of Kerr nonlinearity. J. Opt. Commun. https://doi.org/10.1515/joc-2017-0126 (2017)
19. Mondal, S.K., Sarkar, S.N.: Effect of optical Kerr effect nonlinearity on LP11 mode cutoff frequency of single-mode dispersion shifted and dispersion flattened fibers. Opt. Commun. **127**, 25–30 (1996)
20. Chakraborty, S., Mandal, C.K., Gangopadhyay, S.: Prediction of first higher order modal field for graded index fiber in presence of Kerr nonlinearity. J. Opt. Commun. https://doi.org/10.1515/joc-20170206 (2018)
21. Shibata, N., Tateda, M., Seikai, S., Uchida, N.: Spatial technique for measuring modal delay differences in a dual-mode optical fiber. Appl. Opt. **19**, 1489–1492 (1980)
22. Watson, G.N.: A treatise on the theory of Bessel functions. Cambridge Univ Press, U.K (1995)
23. Gangopadhyay, S., Sarkar, S.N.: Evaluation of modal spot size in single-mode graded index fibers by a simple technique. J. Opt. Commun. **19**, 173–175 (1998)
24. Abramowitz, M., Stegun, I.A.: Handbook of Mathematical Functions. Dover Publications, New York (2012)
25. Kundu, M.C., Gangopadhyay, S., Basu, T., Sarkar, S.N.: Evaluation of dimensionless vector and scalar propagation constants for single-mode graded index fibers by a simple technique. Optik **116**, 511–514 (2005)
26. Meher, H., Hossain, S.I.: Variational approximation for single-mode graded-index fibers: some interesting applications. J. Opt. Commun. **24**, 25–30 (2003)
27. Gradshteyn, I.S., Ryzhik, I.M.: Table of Integrals. Academic Press, London, Series and Products (2014)
28. Ghatak, A., Thyagarajan, K.: Introduction to fiber optics.Cambridge University Press, UK (2002)

A Simple Method for Accurate Prediction of Splice Loss for First Higher-Order Mode of Step-Index Fiber in Presence of Kerr Nonlinearity

Ramkrishna Rakshit, Angshuman Majumdar, and Sankar Gangopadhyay

Abstract In this paper, we prescribe mathematical expressions for the estimation of transmission coefficient at the splice when mismatches of both angular and transverse kinds corresponding to the first higher-order mode (LP11) for step-index fiber are present. Here, we apply Chebyshev formalism-based simple series expression for LP11 mode for step-index profile for the purpose of evaluation of the parameters under study. The iteration method is applied to the analytical mathematical expressions for finding out the said characteristics when Kerr type nonlinearity is present. It has been shown that our predicted outcomes match well with the correct values, that are determined by simulation technique involving finite element method. Thus, the prescribed method generates sufficient potential for studies related to other propagation parameters in dual-mode kind of optical fiber.

Keywords Splice loss · First higher-order mode · Transverse offset · Angular offset · Kerr nonlinearity

1 Introduction

The goal of a splice is to join two fiber terminals precisely so as to provide negligible interruption to the flow of optical energy. Currently, a two-mode kind of fiber is an important optical device in the case of fiber optic communication. Splice losses involving the "fundamental modal field in case of single-mode dispersion-shifted, dispersion-flattened and graded-index fibers" in the linear region have already been reported [1–4]. At the same time, knowledge of the first higher-order modal field is essential for the calculation of the required transmission coefficient at the joint

R. Rakshit
Department of Electronics and Communication Engineering, Dr. B. C. Roy Engineering College, Durgapur, West Bengal, India
e-mail: ramkrishna.rakshit@bcrec.ac.in

R. Rakshit · A. Majumdar · S. Gangopadhyay (✉)
Department of Electronics and Communication Engineering, Brainware University, Barasat, Kolkata, West Bengal 700125, India

B. Sikdar et al. (eds.), *Proceedings of the 3rd International Conference on Communication, Devices and Computing*, Lecture Notes in Electrical Engineering 851,
https://doi.org/10.1007/978-981-16-9154-6_20

for LP11 mode propagation. The cut-off frequency for LP11 mode in case of fiber having graded-index profile, as found by Chebyshev formalism, is already available in literature [5, 6] and based on Refs. 5 and 6, an "approximate power series based mathematical expression of first higher-order modal field (LP11) for graded-index fiber" profile has also been developed [7]. There are different categories of nonlinearity such as saturable, third-order as well as fifth-order, etc. and those are generated "depending on the intensity of optical beam and the nature of the medium as well" [8]. Kerr nonlinearity is known as third-order nonlinearity. Kerr nonlinearity effect on various propagation characteristics of photonic crystal fibers and graded-index fibers are very important and interesting additions in the domain of nonlinear optical technology [9–12]. The influence of third-order nonlinearity on the cut-off frequency of first higher-order mode in respect of "mono-mode dispersion-shifted type as well as dispersion-flattened type fibers" is a significant contribution to the literature [13]. It has been found that Refs. [10–13] involve huge computations for the concerned estimation. A simple series expression based on Chebyshev method can easily provide simple yet accurate prediction of various "propagation characteristics of single-mode graded-index fibers in the linear region" [14–18]. Use of the said formalism along with method of iteration has also been reported for estimating correctly several propagation characteristics concerned with third-order nonlinear mono-mode graded kind index as well as fiber involving dispersion compensation [19–23]. Moreover, by applying Chebyshev formalism, LP11 field of graded profile fiber has also been reported accurately under the presence of Kerr type of nonlinearity [24]. In addition, the new contribution related to the evaluation of splice losses for third-order nonlinear mono-mode graded-index fiber as well as dispersion managed fibers by applying the Chebyshev formalism has also enriched the literature recently [25, 26].

This striking simplicity clubbed with the accuracy of said Chebyshev formalism dealing with the above-mentioned cases have further motivated us to use the prescribed formalism in the estimation of splice losses of LP11 mode in step-index fiber both in the existence of third-order nonlinearity as well as in its absence. We have used iteration method in case of investigations associated with nonlinearity. The concerning execution of our formalism needs simple computational procedures but our results justify good coherence with the accurate results achieved by simulation using finite element method.

Further, as per our knowledge, this kind of convenient yet exact method for evaluation of splice losses of LP11 mode for step-index profile having third order nonlinearity has enriched the literature of fiber optics till date. Thus, our method can certainly be considered as a novel approach in this connection.

2 Theoretical Analysis

Refractive index distribution nature for fiber having very small refractive index difference between core and cladding, is expressed as

$$n^2(R) = \begin{cases} n_1^2(1 - 2\delta f(R)), & R \leq 1 \\ n_2^2\ , & R > 1 \end{cases} \tag{1}$$

incidentally, "$\delta = ({n_1}^2 - {n_2}^2)/2{n_1}^2$, $R = (r/a)$ with n_1, n_2 and a are the refractive indices of the axis of the core, the cladding and core radius and *f(R)* define the shape of the refractive index profile of the fiber" respectively. For fiber having reflective index profile of graded nature, we have

$$f(R) = R^q, \quad R \leq 1 \tag{2}$$

where 'q' represents the power of the profile; and 'q' values are different according to fiber kinds. In our present investigation, we have considered step-index fiber for the first higher mode with different V. For this type of fiber $q = \infty$ and therefore *f(R)* $= 0$.

Following Ref. [13], R.I. profile of a Kerr type nonlinear optical fiber on LP11 mode is taken as

$$n^2(R) = n_L^2(R) + \frac{n_2^2 n_{NL}(R)}{\eta_0}\psi^2(R) \tag{3}$$

where, $\eta_0 = (\mu_0/\varepsilon_0)^{1/2}$. Here, ε_0 is the "permittivity of free space and μ_0 is the permeability of free space" [13].

Further, $n_L(R)$ defines the "refractive index profile in absence of Kerr nonlinearity while the radial distribution of nonlinear Kerr coefficient (m^2/W) is denoted by *nNL(R)*. The first higher-order modal field under the influence of Kerr nonlinearity satisfies the following wave equation" [13, 24],

$$\frac{\mathrm{d}^2\psi(R)}{\mathrm{d}R^2} + \frac{1}{R}\frac{\mathrm{d}\psi(R)}{\mathrm{d}R} + \left[V^2\{1 - f(R)\} - W^2\right]\psi(R) - \frac{\psi(R)}{R^2} + V^2 g\psi^3(R) = 0 \tag{4}$$

In the above equation, $g(R)$ term is expressed as follows,

$$g(R) = \frac{n_2 n_{NL} P}{\pi\, a^2(n_1^2 - n_2^2)}$$

Further "$V\left[= k_0 a(n_1^2 - n_2^2)^{1/2}\right]$ and $W\left[= a(\beta^2 - n_2^2 k_0^2)^{1/2}\right]$ represent the normalized frequency and cladding parameter respectively".

Again, the boundary condition at $R = 1$ is given by

$$\left[\frac{1}{R}\frac{\mathrm{d}\psi}{\mathrm{d}R}\right]_{R=1} = -\left[1 + \frac{W K_0(W)}{K_1(W)}\right] \tag{5}$$

Here, "$K0\ (W)$ and $K1\ (W)$ are the modified Bessel functions of zero and first order respectively" [27–29]. The cladding field is given by

$$\psi(R) \sim K_1(WR) \text{for} R > 1$$

The "modal field $\psi(R)$ expression for LP11 mode in step-index fiber is given by" [5–7, 24]

$$\begin{aligned} \psi(R) &= a_1 R + a_3 R^3 + a_5 R^5, \quad R \leq 1 \\ &= (a_1 + a_3 + a_5)\frac{K_1(WR)}{K_1(W)}, \quad R > 1 \end{aligned} \tag{6}$$

Here, terms 'a_1', 'a_3' with 'a_5' being the constants.
Chebyshev points are [5, 24],

$$R_m = \cos\left(\frac{2m-1}{2M-1}\frac{\pi}{2}\right) m = 1, 2, \ldots, (M-1) \tag{7}$$

Here, M is 3 corresponding to Eq. (6). Thus, we get relevant values of R as $R_1 = 0.9511$ (for $m = 1$) and $R_2 = 0.5878$ (for $m = 2$).
Using these two Chebyshev points and Eq. (6) with Eq. (4), we derive the following dual equations:-

$$\begin{aligned} &"a_1\left\{V^2(1 - f(R_1)) - W^2 + V^2 g\,\Psi^2(R_1)\right\} \\ &+ a_3\left\{8 + R_1^2\left[V^2(1 - f(R_1)) - W^2 + V^2 g\,\Psi^2(R_1)\right]\right\} \\ &+ a_5\left\{24\,R_1^2 + R_1^4\left[V^2(1 - f(R_1)) - W^2 + V^2 g\,\Psi^2(R_1)\right]\right\} = 0" \end{aligned} \tag{8}$$

$$\begin{aligned} &"a_1\left\{V^2(1 - f(R_2)) -\!- W^2 + V^2 g\,\Psi^2(R_2)\right\} \\ &+ a_3\left\{8 + R_2^2\left[V^2(1 - f(R_2)) -\!- W^2 + V^2 g\,\Psi^2(R_2)\right]\right\} \\ &+ a_5\left\{24\,R_2^2 + R_2^4\left[V^2(1 - f(R_2)) -\!- W^2 + V^2 g\,\Psi^2(R_2)\right]\right\} = 0" \end{aligned} \tag{9}$$

Linear characteristic of plot of $K_1(W)/K_0(W)$ versus $1/W$ is observed in the range "$0.6 \leq W \leq 2.5$" [29]. Therefore, we use linear fitting technique for developing the relation given below

$$\frac{K_1(W)}{K_0(W)} = \alpha + \frac{\beta}{W} \text{with} \alpha = 1.034623 \text{and} \beta = 0.3890323 \tag{10}$$

Using Eqs. (6), (10), and (5), we get

$$a_1\left[2(\alpha W + \beta) + W^2\right] + a_3\left[4(\alpha W + \beta) + W^2\right] + a_5\left[6(\alpha W + \beta) + W^2\right] = 0 \tag{11}$$

Equations (8), (9), and (11) can generate nontrivial solutions for the normalized coefficients a_1, a_3, and a_5, if Eq. (12) satisfies the following condition

$$\begin{vmatrix} A_1 & B_1 & C_1 \\ A_2 & B_2 & C_2 \\ A_3 & B_3 & C_3 \end{vmatrix} = 0 \tag{12}$$

where,

$$\begin{aligned} A_1 &= V^2\{1 - f(R_1)\} - W^2 + V^2 g\psi^2(R_1) \\ A_2 &= V^2\{1 - f(R_2)\} - W^2 + V^2 g\psi^2(R_2) \\ A_3 &= 2(\alpha W + \beta) + W^2 \\ B_1 &= 8 + R_1^2\left[V^2\{1 - f(R_1)\} - W^2 + V^2 g\psi^2(R_1)\right] \\ B_2 &= 8 + R_2^2\left[V^2\{1 - f(R_2)\} - W^2 + V^2 g\psi^2(R_2)\right] \\ B_3 &= 4(\alpha W + \beta) + W^2 \\ C_1 &= 24R_1^2 + R_1^4\left[V^2\{1 - f(R_1)\} - W^2 + V^2 g\psi^2(R_1)\right] \\ C_2 &= 24R_2^2 + R_2^4\left[V^2\{1 - f(R_2)\} - W^2 + V^2 g\psi^2(R_2)\right] \\ C_3 &= 6(\alpha W + \beta) + W^2 \end{aligned} \tag{13}$$

Since there is presence of term in the form of $\Psi^2(R_i)$, solution of Eq. (12) is very difficult. So, at first, we consider $g(R) = 0$ in this equation in order to find W for a specific V. Using this found value of W with the corresponding V value, we evaluate a_3, a_5 in terms of a1 for the linear region. Further, in case of nonlinearity for any $g(R)$ value and the said V value, we apply the iteration method in order to obtain W and normalized values of a_3 and a_5 after convergent is reached. Those normalized values of a_3 as well as a_5, which are in terms of a_1, shall be used to calculate splice losses. This process is repeated for all V numbers relating to step-index fibers used in our study.

Considering small amount of angular mismatch (θ), the overlap integral is [1–4]

$$C_a(p) = \int_0^{\infty}\int_0^{2\pi} \psi^2(R)\exp(ipR\cos\phi)RdRd\phi \tag{14}$$

Here, $p = ak0n2\theta$ while a, $k0$ and $n2$ are representing "core radius, free space wavenumber and refractive index of index matching fluid respectively".

For angular mismatch, we can write [1–4]

$$T_a(p) = \left|\frac{C_a(p)}{C_a(0)}\right|^2 \tag{15}$$

Expanding exponential term of Eq. (14) first, one gets

$$C_a(p) = 2\pi \sum_{n=0}^{n=\infty} \frac{(-p^2/4)^n}{(n!)^2} \int_0^\infty |\psi(R)|^2 R^{2n+1} \mathrm{d}R \tag{16}$$

Further, sufficient accuracy is obtained if we consider only the first four terms in Eq. (16). This relates to angular mismatch up to 1° ($p = 0.8$ approximately) in case of a typical optical fiber with $n_2 = 1.5$, λ (operating wavelength) $= 0.8$ μm and $a =$ 4 μm.

Using $\psi(R)$ expression given by Eq. (6) in Eqs. (15) and (16), one obtains [27–29]

$$Ta(p) = \left| \frac{(S_1(1/2)S_2S_3) - P^2(S_4(1/24)S_2S_5) + p^4(S_4 - (1/2560)S_2S_7) - p^6(S_8 - S_2S_9)}{(S_1 - (1/2)S_2S_3)} \right|^2 \tag{17}$$

where,

$S_1 = \frac{1}{4}a_1^2 + \frac{1}{8}a_2^2 + \frac{1}{12}a_5^2 + \frac{1}{3}a_1a_3 + \frac{1}{4}a_1a_5 + \frac{1}{5}a_3a_5$

$S_2 = \left(\frac{a_1+a_3+a_5}{K1(W)}\right)^2$

$S_3 = K1^2\,(W) - K0\,(W)\,K2\,(W)$

$S_4 = \frac{1}{24}a_1^2 + \frac{1}{16}a_1a_2 + \frac{1}{40}a_2^2 + \frac{1}{20}a_1a_5 + \frac{1}{24}a_3a_5 + \frac{1}{56}a_5^2$

$S_5 = K^2\,(W) - K^2\,(W)$

$S_6 = \frac{1}{512}a_1^2 + \frac{1}{320}a_1a_2 + \frac{1}{768}a2^2 + \frac{1}{384}a_1a_5 + \frac{1}{448}a_3a_5 + \frac{1}{1024}a_5^2$

$S_7 = 5K^2\,(W) - 4K^2(W) - K^2(W)$

$S_8 = \frac{1}{23040}a_1^2 + \frac{1}{13828}a_1a_2 + \frac{1}{32256}a_2^2 + \frac{1}{16128}a_1a_5 + \frac{1}{18432}a_2a_5 + \frac{1}{41472}a_5^2$

$S_9 = \left(\frac{S_7}{13440W^2}\right) - \frac{1}{32256W^2}[W^2K^2\,(W) + (12 - W^2)\,K^2(W) + 4W\,K1(W)\,K2(W)]$

Moreover, in this regard, the transmission coefficient $T_t(\Delta)$ at the splice for very small mismatch (d), can simply be expressed as

$$T_t(\Delta) = \left| \frac{C_t(\Delta)}{C_t(0)} \right|^2 \tag{18}$$

Here, $\Delta = d/a$ and taking $\Delta \leq 0.8$, the transverse coefficient $T_t(\Delta)$ can be expressed as [3, 4]

$$\frac{Ct(\Delta)}{Ct(0)} = 1 - \frac{B_1}{B_0}\left(\frac{\Delta}{2}\right)^2 + \frac{B_2}{B_0}\left(\frac{\Delta}{2}\right)^4 - \frac{B_2}{B_0}\left(\frac{\Delta}{2}\right)^6 \tag{19}$$

where,

$B_0 = \int_0^\infty R dR |\Psi(R)|^2$

$B1 = \int_0^\infty R dR |\frac{d\Psi}{dR}|^2$

$B2 = \frac{1}{4}\left(\int_0^\infty R dR \left|\frac{d^2\Psi}{dR^2}\right|^2 + \int_0^\infty \frac{dR}{R}\left|\frac{d\Psi}{dR}\right|^2\right)$:

$B3 = \frac{1}{36}\int_0^\infty R dR \left|\frac{d^2\Psi}{dR^2}\right|^2 - \frac{1}{12}\int_0^\infty \frac{dR}{R}\frac{d\Psi}{dR}\frac{d^3\Psi}{dR^3} - \frac{1}{24}\left(\frac{d^2\Psi}{dR^2}\right) R = 0$

The above integrals can readily be solved utilizing the $\Psi(R)$ expression and the results are presented below:

$B_0 = S_1 - \frac{1}{2}S_2 S_3$

$B_1 = S_{10} - S_2\,[\frac{W^2}{2}S_3 - W^2 S^2 + \frac{1}{2}\,S_{11} - WS_{12}].$

$B_2 = S_{13} - S_2\,W^2\,[\frac{1}{8}S_5 - \frac{1}{8}\,S_{11} + \frac{W^2}{8}\,S_3 + \frac{1}{4}(W - \frac{3}{8W})\,S_{12}]$

$B_3 = S_{14} - S_2 W^4\,[(\frac{1}{48W^2} + \frac{W}{72} + \frac{1}{48})S_5 - \frac{1}{48}\,S_{11} - \frac{W^2}{36}\,S_3 - \frac{1}{128W}\,S_{15} + \frac{1}{48W}\,S_{12}].$

Where,

$S_{10} = \frac{a_1^2}{2} + \frac{3}{2}{a_2}^2 + \frac{5}{2}a^{52} + \frac{3}{2}a_1a_2 + \frac{5}{3}a_1a_5 + \frac{15}{4}a_2a_5$

$S_{11} = {K_0}^2\,(W) - {K_1}^2\,(W)$

$S_{12} = K_0\,(W)\,K1\,(W) - K_1\,(W)\,K_2\,(W)$

$S_{13} = \frac{45}{16}{a_3}^2 + \frac{425}{32}{a_5}^2 + \frac{3}{4}a_1a_3 + \frac{5}{8}a_1a_5 + \frac{45}{4}a_3a_5$

$S_{14} = -\frac{1}{4}{a_3}^2 + \frac{75}{6}{a_5}^2 - \frac{5}{2}a_1a_5 + \frac{5}{8}a_2a_5$

$S_{15} = K_1\,(W)\,K_2\,(W) - K_0\,(W)\,K_3\,(W)$

Using the evaluated values of a_1, a_3, a_5 and W for a particular V value both under the presence as well as absence of particular Kerr nonlinear effect, one can compute the transmission coefficient for angular and transverse mismatches by employing Eq. (17) along with Eq. (18) respectively.

3 Results and Discussions

For our investigation relating to the splice loss for LP11 mode of step kind index fiber under the domination of Kerr effect, we have taken up typically two cases by choosing V numbers 2.6 and 3.4. In each case of a particular V number, we consider two identical step-index profile fibers. Following Refs. [13, 25] we carry on our investigation for two nonlinear parameters like $n_{NL}(R)P = 1.5 \times 10^{-14}$ m2, $n_{NL}(R)P = -1.5 \times 10^{-14}$ m2, and another corresponding to $n_{NL}(R)P = 0$. Variation of *Ta* (p) parameter with (p) relating to the step-index fiber of V number

2.6 "both in existence as well as in absence of nonlinearity" is presented graphically in Fig. 1. Again, Fig. 2 represents the plot of $Tt(\Delta)$ parameter at the splice versus Δ for the above-mentioned kind of fiber having V value 2.6 both in the presence and absence of the said kinds of nonlinearity. Further, in Figs. 3 and 4, we show the variations of $Ta(p)$ with p and $Tt(\Delta)$ with Δ respectively for step-index fiber of V number 3.4 for the said values of $[n_{NL}(R)P]$. It is relevant to mention that our observations are made for LP11 mode only. We have shown our results by the symbols ■, ▲ and • corresponding to $n_{NL}P$ being equal to $+1.5 \times 10^{-14}$, -1.5×10^{-14} and 0 in all the figures.

The solid lines as depicted in Figs. 1, 2, 3 and 4, indicate the exact or specific numeric outcomes. Without nonlinearity impact, our computed results were compared with Refs. [3, 4] and in presence of nonlinearity, our results have been compared and verified with that of the accurate results calculated by finite element calculation methodology [10]. In both cases, it is found that outstanding meet occurs between our estimated outcomes and the accurate values. Thus, the accuracy of our convenient formalism is verified. It is highly relevant to point out here that the "cut-off V value for first higher-order mode of step-index fiber is 2.405" [6]. Accordingly, we have selected V values of step-index fiber as 2.6 and 3.4 for the study of splice loss relating to LP11 mode. Here, the V value 2.6 happens to be closer to the LP11 mode cut-off V value. The results found reflect the degree of tolerance of the splices with respect to both transverse as well as angular mismatches when third-order nonlinearity is either present or absent. Therefore, the results are extremely important and

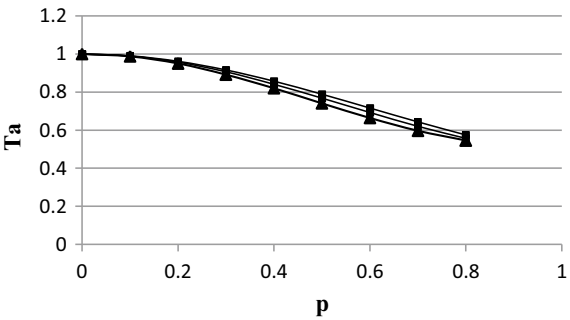

Fig. 1 Graph of *Ta*—*p* for step-index fiber with $V = 2.6$ for different nonlinearity parameters *nNLP* (Our results: ■ for $n_{NL}P = 1.5 \times 10^{-14}$, • for $n_{NL}P = 0$, ▲ for $n_{NL}P = -1.5 \times 10^{-14}$ and _____ for simulated exact results)

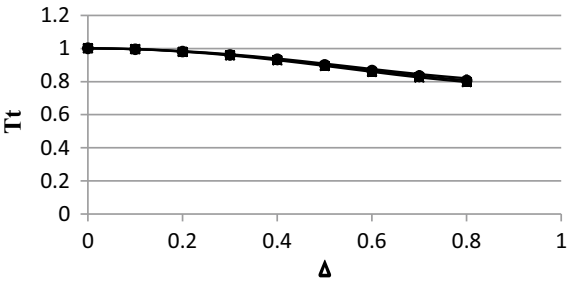

Fig. 2 Graph of *Tt*—Δ for step-index fiber with $V = 2.6$ for different nonlinearity parameters *nNLP* (Our results: ■ for $n_{NL}P = 1.5 \times 10^{-14}$, • for $n_{NL}P = 0$, ▲ for $n_{NL}P = -1.5 \times 10^{-14}$ and _____ for simulated exact results)

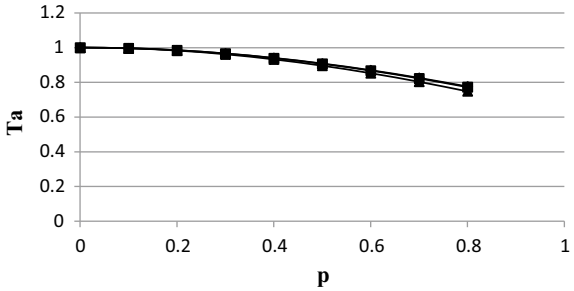

Fig. 3 Graph of *Ta*—*p* for step-index fiber with $V = 3.4$ for different nonlinearity parameters *nNLP* (Our results: ■ for $n_{NL}P = 1.5 \times 10^{-14}$, ● for $n_{NL}P = 0$, ▲ for $n_{NL}P = -1.5 \times 10^{-14}$ and _____ for simulated exact results)

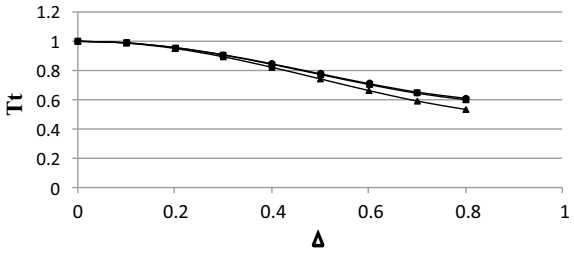

Fig. 4 Graph of *Tt*—Δ for step-index fiber with $V = 3.4$ for different nonlinearity parameters *nNLP* (Our results: ■ for $n_{NL}P = 1.5 \times 10^{-14}$, ● for $n_{NL}P = 0$ ▲ for $n_{NL}P = -1.5 \times 10^{-14}$ and _____ for simulated exact results)

relevant from the judicious point of view of long haul communication system design comprising of a dual-mode step-index fiber.

4 Conclusion

Here, we have applied a simple series-based approximate expression for the modal field of step-index fiber corresponding to the first higher-order mode in order to predict splice loss due to both transverse and angular offsets, when Kerr nonlinearity is present or absent. For the specific purpose of prediction of the said fiber propagation characteristics and parameters under the presence of Kerr kind of nonlinearity, we apply iteration method on the concerned analytical expressions formulated in the absence of nonlinearity. Our execution process is simple but the results found are very accurate. The prescribed formalism has proved its merit in being considerably user-friendly in its execution, and therefore it will be very much advantageous to the system designers and engineers associated with the applications of dual-mode fiber.

References

1. Chakraborty, S., Majumdar, A., Gangopadhyay, S.: A simple but accurate method for prediction of splice loss in single-mode dispersion shifted trapezoidal as well as dispersion flattened graded and step W fibers. Optik **124**, 6752–6756 (2013)
2. Debnath, R., Gangopadhyay, S.: A simple but accurate method for analytical estimation of splice loss in single-mode triangular index fibers for different V numbers including the low ones. J. Opt. Commun. **37**, 321–327 (2016)
3. Gangopadhyay, S., Choudhury, S., Sarkar, S.N.: Evaluation of splice loss in single-mode graded index fibres by a simple technique. Opt. Quant. Electron. **31**, 1247–1256 (1999)
4. Hossain, S.I., Sharma, A., Ghatak, A.: Splice loss evaluation for single mode graded index fibres. Appl. Opt. **21**, 2716–2723 (1982)
5. Chen, P.Y.P.: Fast method for calculating cut-off frequencies in single-mode fibers with arbitrary index profile. Electron. Lett. **18**, 1048–1049 (1982)
6. Shijun, J.: Simple explicit formula for calculating LP11 mode cut-off frequency. Electron. Lett. **23**, 534–536 (1987)
7. Patra, P., Gangopadhyay, S., Goswami, K.: A simple method for prediction of first-order modal field and cladding decay parameter in graded index fiber. Optik **119**, 209–212 (2008)
8. Agrawal, G.P.: Nonlinear fiber optics, Cambridge. Academic Press, Massachusetts (2013)
9. Saitoh, K., Fujisawa, T., Kirihara, T., Koshiba, M.: Approximate empirical relations for nonlinear photonic crystal fibers. Opt. Express. **14**, 6572–6582 (2006)
10. Hayata, K., Koshiba, M., Suzuki, M.: Finite-element solution of arbitrarily nonlinear, graded-index slab waveguides. Electron Lett. **23**, 429–431 (1987)
11. Okamoto, K., Marcayili, E.A.J.: Chromatic dispersion characteristics of fibers with optical Kerr-types nonlinearity. J. Lightwave Technol. **7**, 1988–1989 (1994)
12. Khijwania, S.K., Nair, V.M., Sarkar, S.N.: Propagation characteristics of single-mode graded-index elliptical core linear and nonlinear fiber using super-Gaussian approximation. Appl. Opt. **48**, G156–G162 (2009)
13. Mondal, S.K., Sarkar, S.N.: Effect of optical Kerr effect nonlinearity on LP11 mode cutoff frequency of single-mode dispersion shifted and dispersion flattened fibers. Opt. Commun. **127**, 25–30 (1996)
14. Gangopadhyay, S., Sarkar, S.N.: Confinement and excitation of the fundamental mode in single-mode graded index fibers: computation by a simple technique. Int. J. Opt. Electron. **11**, 285–289 (1997)
15. Patra, P., Gangopadhyay, S., Sarkar, S.N.: Confinement and excitation of the fundamental mode in single-mode graded index fibers of low V number: estimation by a simple technique. J. Opt. Commun. **22**, 166–170 (2001)
16. Gangopadhyay, S., Sengupta, M., Mondal, S.K., Das, G., Sarkar, S.N.: Novel method for studying single-mode fibers involving Chebyshev technique. J Opt Commun. **18**, 75–78 (1997)
17. Patra, P., Gangopadhyay, S., Sarkar, S.N.: A simple method for studying single-mode graded index fibers in the low V region. J. Opt. Commun. **21**, 225–228 (2000)
18. Gangopadhyay, S., Sarkar, S.N.: Prediction of modal dispersion in single-mode graded index fibers by Chebyshev technique. J. Opt. Commun. **19**, 145–148 (1998)
19. Sadhu, A., Karak, A., Sarkar, S.N.: A simple and effective method to analyze the propagation characteristics of nonlinear single mode fiber using Chebyshev method. Microw. Opt. Technol. Lett. **56**, 787–790 (2013)
20. Chakraborty, S., Mandal, C.K., Gangopadhyay, S.: Prediction of fundamental modal field for graded index fiber in the presence of Kerr nonlinearity. J. Opt. Commun. https://doi.org/10.1515/joc-2017-0126
21. Aich, J., Maiti, A. K., Majumdar, A., Gangopadhyay, S.: A novel and simple formalism for study of effect of Kerr nonlinearity on Petermann I and II spot sizes of single-mode graded index fiber. J. Opt. Commun. https://doi.org/10.1515/JOC-2019-0167

22. Roy, K., Majumdar, A., Gangopadhyay, S.: Simple but accurate method for estimation of the effect of Kerr nonlinearity on confinement and excitation of the fundamental mode in single mode graded index fiber. Optik **216**, 164939 (2020)
23. Mukherjee, T., Majumdar, A., Gangopadhyay, S.: Influence of Kerr nonlinearity on group delay and modal dispersion parameters of single-mode graded index fibers: evaluation by a simple but accurate method. J. Opt. Commun. https://doi.org/10.1515/joc-2020-0192
24. Chakraborty, S., Mandal, C.K., Gangopadhyay, S.: Prediction of first higher order modal field for graded index fiber in the presence of Kerr nonlinearity. J. Opt. Commun. https://doi.org/10.1515/joc-2017-0206
25. Maiti, S., Majumdar, A., Biswas, S.K., Gangopadhyay, S.: Evaluation of splice loss of single-mode graded index fiber in presence of kerr nonlinearity. Optik **203**, 163962 (2020). https://doi.org/10.1016/j.ijleo.2019.163962
26. Rakshit, R., Majumdar, A., Gangopadhyay, S.: A simple but accurate method for prediction of splice loss in mono-mode dispersion shifted and dispersion flattened fibers in presence of Kerr nonlinearity. J. Opt. Commun. https://doi.org/10.1515/joc-2020-0259
27. Watson, G.N.: A treatise on the Theory of Bessel Functions. Cambridge University Press, U.K. (1944)
28. Gradshteyn, I.S., Ryzhik, I.M.: Table of Integrals. Academic Press, London, Series and Products (1980)
29. Abramowitz, M., Stegun, I.A.: Handbook of Mathematical Functions. Dover Publications, New York (1981)

Issues of Knowledge Management in Deep Web and Its Graph-Based Analysis

Subrata Paul, Chandan Koner, Robiul Islam Kabir, and Anirban Mitra

Abstract There has been an enormous evolution of the Internet and network technologies since the past few decades, alongside the increase in the count of users and their ever increasing demand for preservation of identity and privacy. In order to meet the demand of the users, scientists have come up with the novel thoughts, thereby leading to the evolution of the large portion of the Internet, i.e., the deep Web. Although the demand of the privacy preservation has been solved by the deep Web for some gentle users, but alongside, it has opened up the arena for the accommodation of several unlawful activities, leading to the generation of dark Web. This necessitates in the search of automatic solutions in support of the law and parallel assisting the security agencies for collection of information from dark Web in order to disclose similar activities. In this paper, the authors will present a brief overview of the deep Web and present its features. The main point of focus shall be the issue of knowledge management and how it will be utilized for making a graph-based analysis. The paper concludes with an example of a proposed system for extraction of knowledge.

Keywords Identity · Privacy · Deep Web · Dark Web · Knowledge management · Graph analysis

1 Introduction

Internet has been a widespread achievement by humans that has viewed a quick evolution thereby has been drawing the attention by the researchers from various dissimilar areas for addition of extensive amenities and conveniences and making

S. Paul (✉)
MAKAUT, Kolkata, Kalyani, India

C. Koner
Department of CSE, BCREC, Durgapur, India

R. I. Kabir · A. Mitra
Department of CSE, ASET, Amity University, Newtown, Kolkata, India

B. Sikdar et al. (eds.), *Proceedings of the 3rd International Conference on Communication, Devices and Computing*, Lecture Notes in Electrical Engineering 851,
https://doi.org/10.1007/978-981-16-9154-6_21

it accessible to various users for various purposes. The users can range from an individual entity to a society and institution where there are many users accessing the Internet at the same time for different purposes. Although Internet assures privacy and security for all its users at the same time, but there exists some specific portion of Internet where users accomplishes their actions being devoid of any kind tracking and monitoring. For such an activity, geographical location from where such an activity is being hosted remains unidentified. Although in such a circumstances, numerous users whose main concerns have been the privacy preservation in the Internet connectivity alongside the aspiration for the usage of information resources on Web with the preservation of confidentiality for such accomplishments. This is achievable with the usage of certain distinct technologies which encrypts connections with redirection of traffics through quite a few nodes within the network [1]. Nevertheless, numerous malicious happenings overpower with the usefulness of technologies that include trading drugs, weapons, pornography, child abuse, malware and hacking software, fraud, forgery, identity theft, and many others.

Since the coining of the word dark Web at the inception of 2000s [2], it has been studied by numerous researches, where they have focused on the area of terrorism and extremism, with a special emphasis on the determination of the identity of terrorist organizations and outlining their philosophies.

Knowledge management endorses the procedure in dealing with the hurdles which is related to the cybercrime investigations concerning the various resources at the human and technical level, alongside the knowledge, skills, and abilities (KSAs) desirable for the smooth and efficient conduction of such an investigation. Knowledge management (KM) pursues "in creation, protection, and usage of an extensive variety of knowledge resources that include people and information" for the improvement of a procedure or a consequence [3–5].

2 Web Types and Their Definition

The classification of Internet can be done under three extensive categories:

The preliminary category is referred to as surface Web which focuses on those portions of Internet which was deliberated as being public and accountable. The consideration of being public comes to the fact that any kind of access has no restriction over any kind of authentication or payment, identified and cataloged by all search engines, further has the accountability in the form of stakeholders (ranging from host to user) remain distinguishable and therefore are subjected to the law of enforcement. For searching any content in surface Web, the user needs to enter any query. Accordingly, the search engine will return all the documents satisfying the query [6].

Further, deep Web emphasizes on those portions of Web which are not accessed by general public which means they are private besides not being indexed by any kind of search engines although are being further subjected to the concern of accountability.

Table 1 Classification of different Web

Type of Web	Example	Access options
Surface Web	Search engines like Google and Yahoo Social networking sites like Facebook and Twitter E-Commerce Web sites like Amazon and Flipkart News Web sites like Times of India and Zee News	Accessible publicly
Deep Web	Financial record of an individual in Bank Portal Legal record of an individual in portal of court Subscription information of an individual Medical record of an individual in associated portal of Web site	Accessed privately with authentication details
Dark Web	Onion sites Drug trafficking Political protests Several other illegal activities	Requires distinct software for access, not accountable

Due to the fact that such a network functions as a component of an internal network, access restrictions often prevail within it.

In conclusion, we have the dark Web forming such a subset of network which are not cataloged by search engines since it entails the usage of distinct software for its access. It comprises of such constituents that are public and private in cooperation, which means either they are publicly accessible or being accessible with the usage of proper credentials—on condition that accurate software are being used for the purpose. The basic differentiation among three different Webs is of the fact that there exists the absence of accountability among the dark Web. The user within such networks or to those persons involved in the task of monitoring cannot be identified. Therefore, there is an efficient anonymity of the activities performed on these networks. Table 1 presented beneath overviews on the classification of different Web, and some examples that have been discussed in this section [7].

3 Dark Web Features

Dark Web maintains the purpose of remaining unidentifiable and bear the potential not to be caught within the grasp of anyone, especially by law enforcement (LE).

3.1 The Onion Routing (TOR) Protocol and Hidden Services

The feature of anonymity is dark Web that depends upon the Onion routing (TOR or Tor) protocol that can be accessed through Tor browser [8]. This browser is capable of accessing the Web sites which are generally accessed on surface Web with addition of the feature of privacy since the source IP is cannot be identified in practical sense. These relays embrace the entry (guard) node, middle relay, and an exit node. This selection of node is done from a wide range of Tor relays and bridges which frames the network besides being handled by individuals and organizations. This system, on combination with the scheme of public-key cryptography and traffic layers in a method where every connected node, is solely responsive to its adjacent nodes. In cases where there exist multiple users, the basic factor for the usage of overlay network similar to Tor is that besides having anonymous admittance to regular Web sites, a wide variety of Web sites are accessible which cannot be accessed on surface Web, with the exception of being accessed solely by the Tor network [7, 9].

3.2 Dark Web as a Distributed System

Similar to the Internet and being an overlay, dark Web occurs on such systems whose nature is decentralized besides being distributed without any presence of central servers or control point. This hint on an inability of prompt shut down of the system [10] besides enabling the associations among individuals that could else be controlled by legal authorities.

Such distributed systems are devoid of any governing or functioning authority, therefore its extension or lessening is solely dependent on the hosts who voluntarily become a part of the network. Various activist groups promoting human right causes or university that endorses the availability of open access to knowledge resources have dynamically donated bandwidth so that their agendas are being met [7, 11, 12].

3.3 Accessing the Dark Web

The available dark Web networks that include I2P, Freenet, and Tor have individual mechanisms for their operation. Tor network, the popularized dark Web network might be accessed by downloading Tor browser. After installation, Tor browser repossess Tor nodes list from the directory server, and proceeds by choosing three (or more) nodes among them and recovers every cryptographic keys necessitated for the encryption of packets and thereafter establishes a virtual circuit throughout the chosen network [8]. For all the packets that are directed from browser, encryption is carried out by the keys for every node throughout the circuit and finally being handed over to the first node, which in turn performs the process of decryption from 1st layer

with cryptographic key and forward encrypted packet to next node which repeats the decryption process in the same way. The penultimate or the exit node bears the ability in viewing the original packet and thereafter forward it to destination [7].

3.4 Using Tor Versus a VPN Service

The basic dissimilarity among VPN service and Tor are as follows:

(a) VPN proceeds with a single hop/node over which the encryption and routing of traffic takes place; on the other hand, the same hop is made over three or more nodes in case of Tor.
(b) Since the VPN provider is a third party, therefore it might account for the connections that are made through them, thereby forming a link from source to destination for every packets by deanonymization of the user; on the other hand, Tor is assembled with a protocol that safeguards to the fact that solitarily none of the nodes bear adequate information for being able to accomplish the property of deanonymization. Additionally, only hidden or onion services might only be retrieved through the Tor network [7, 12].

3.5 Online Privacy in the Dark Web

TOR has been used in empowering private, unidentified, and protected transportation of network packets and performs certain precise activity that includes [13, 14]:

- Anti-censorship and political activities. For avoidance of censorship, reaching specific endpoints or substances which are blocked, TOR empowers individuals in accessing the blocked contents in specific regions. TOR has also been used by some political protesters for securing and maintaining the unidentified communications and positions [13].
- Sensitive communications. Certain delicate communications for personal and business purposes through certain chat rooms or forums are also made accessible by the usage of TOR. Such a tool can be used for protecting children from using abusive contents and even by companies to protect their project from the competitor spies [13, 15, 16].
- Leaked information. TOR might also be used to establish secure communication between journalists with their informers and dissidents [13, 16]. It might also be used by security agencies to gather some secret information about the rival country and help the defense ministry [17].

3.6 Advantages and Disadvantages of Dark Web

Advantages of the dark Web include the fact that the dark Web has assisted numerous people in expressing their thoughts with maintaining privacy that would not be possible on the surface Web with the threat of certain stalkers or criminals. Certain open discussion on social media which is not possible because of the tracking of posts has been made possible by TOR. Lastly, communications among undercover police officers have been possible due to increasing acceptance of dark Web among criminals.

Disadvantages of the dark Web include that the dark Web has been used abusively by certain people for commitment of nastiest crimes like the amalgamation of dark Web with cryptocurrencies has made possible for hiring someone and commits a crime through him. Additionally, in certain areas, privacies are also violated such as private photos, medical records, and even financial information might be stolen from someone and shared all through the dark Web [18].

4 Issue of Knowledge Management in Context of Dark Web

The foremost application of knowledge management is cybercrime investigations [3] where it encompasses the identity as well as assessment of the required knowledge in general as well as to some specific cybercrime investigations, after which the required as well as available knowledge are compared for identification of knowledge gaps. Upon identification, several methods are projected for filling these gaps which also includes some KM practices [4].

Knowledge management contains persons who are involved in the task of obtaining, using, creation, management, as well as communication of the knowledge gained through the available procedures, and technology which would facilitate such a process [19]. Knowledge sharing (KS) has been an essential portion of knowledge management which is applied in law enforcement [20] including external services which thrusts knowledge to others (like, education and awareness campaigns) and internal influences which efforts someone for seeking knowledge (such as pull factors) for pursuing his proficiency or aid on the area concerned [21]. Europol's Dark Web Team purposes in enhancement of technical and investigative actions mutually for conduction of training and creativities for capacity-building, alongside the inhibition and consciousness-raising campaigning on dark Web [4, 22].

KS pursues in making knowledge along with its sources (e.g., people) accessible for the required users. There exist two wide-ranging types of manageable and communal knowledge: explicit knowledge and tacit knowledge [23]. As an illustration UNODC's Sharing Electronic Resources and Laws on Crime (SHERLOC) knowledge management portal may be cited that comprises of directories of competent national authorities (CNA directory) which might acquire, react to besides the development of mutual legal assistance treaties (MLATs) as well as repatriation

demands through countries, case law, legislation, and a bibliographic database [24]. These national and international databases repositories have empowered individuals in searching and retrieval of explicit knowledge contained within such databases, thus simplifying the share of explicit knowledge [4].

Surrounded by knowledge management, unstructured database has found its existence. Researches have shown that users working with knowledge management have expended more than 30% of their time in search of information. Since Diffbot bears the potential in automating data searching, this is quite different from the working of Google. The outcomes Google displays are actually a pointer or URL to Webpage where the keyword can be found. Entity graph databases have been used by a few bigger organizations for building personal knowledge bases for categorization of internal information besides restructuring the admittance to valuable data [25].

Representing the content of dark Web (which consist of structured and unstructured knowledge) can be done and visualized using knowledge graph. Individual versions of knowledge graphs are created by company/group/individual for bounding complexity and organizing the information into data and knowledge like, Google's knowledge graph, Microsoft's Satori. Within a wider perception, Knowledge graph is defined as an alternative of semantic network with additional constrictions whose possibility, structure, characteristics with some uses are not totally understood within the enhancement procedure. Machine learning is used to perform a variety of tasks such as classification, etc., accurately within a variety of datasets. In contrast, knowledge representation conveys the capability in representation of variety of entities alongside their associations and relationships with greater reliability, explainability, and reusability. Latest advancements in knowledge representation learning include mining of logical rules from the graph [26].

The methodology of knowledge management associates knowledge node and relation node with the corresponding graphic nodes. Visualized directed acyclic graph G composes a series of limited node N and directed edge E. A knowledge node k is connected to another node j; if (i, j) is a previous edge of G, then edge (i, j) reports the relevant event between node i and node j.

Generally, ontology-dependent visualization procedure is composed of four steps namely data analysis, data comparison, data retrieval [27], and data evaluation.

Visual knowledge management. Concerning the application of instance visualization management, a decision is made for increment of view scene related to RDF (S) data. Initially, user selects an equivalent illustration of fragmented pattern for visualization. Further, it customs certain self-definition interactive script for separation of unconventional instances of visualization. GViz tool is used where the pop window demonstrates the perceptions alongside their associations. Such as, for categorizing an art item as true of false, visualization technology can be used for finding knowledge in connection to it [28, 29].

Analysis of such knowledge management visualization graphs can be done easily. Graph theory has been extensively used as a preferred tool for analysis of social associations for the dark Web in addition to enumeration of engineering properties like search ability [30–32]. SNA [33] has been a graph-based technique for analysis of social associations besides their influence on individual behavior and organizational

structure. Subsequent to the classification and clustering of the apprehended data, certain features of special contestants might be extracted. SNA has facilitated social interactions with other cybercrime for gathering sufficient knowledge in connection to the kind of publication content alongside the regularity of discussion on certain participating topics [34]. After the analysis has been done, such a kind of graph can be easily stored in graph database, which provides an efficient storage medium for structured and unstructured data and has been proved to be much efficient than the traditional database [35] in some respect.

5 An Example Based on the Proposed System

Figure 1 presents a proposed system by the authors. In the first step of the figure, a Web crawler is used to extract the hyperlinks available in the two different Web sites in different Web in a single crawl. One of the Web site provides security to personal information on the surface Web, while other sells credit card information present on dark Web. Hybrid-focused Web crawler has been used for this specified purpose as it works efficiently in both the Webs. In the next step, the hyperlinks fetched using the crawler are saved in the repository and are fetched one by one for content link extraction. These content links extract the URLs, or surrounding texts of these hyperlinks and passes on extracted link and context information to LARS generator and ontology-based score generator. LARS generator generates a decision tree on the relevant and irrelevant pages that can be reached from the hyperlinks, while OBRS generator generates the relevance of these hyperlinks on the basis of the importance table generated by any search query entered by the user. The nodes of the relevant hyperlinks within the decision tree can be used in creating a directed graph. Further, the nodes of the directed graph are analyzed on the basis of the in-degree, out-degree, and the relevance scores. On successful completion of the analysis, sufficient knowledge can be gained on whether the security techniques used by security Web site can be used in securing credit card information to prevent its theft by mapping of parameters of both Web sites. If during a single crawl sufficient results are not generated, the multiple security Web sites on surface Webs may be explored using this technique and can be figured out of which security technique will be best suited for preserving credit card information. Although this system has not been validated with the real-time data inputs, but it is hoped that the extracted knowledge obtained within the proposed system can be utilized in gathering information about the cybercriminal activities.

6 Conclusion

Throughout the paper, the authors have discussed various aspects of deep Web. It has also been illustrated that from technical perspective, dark Web might be defined as

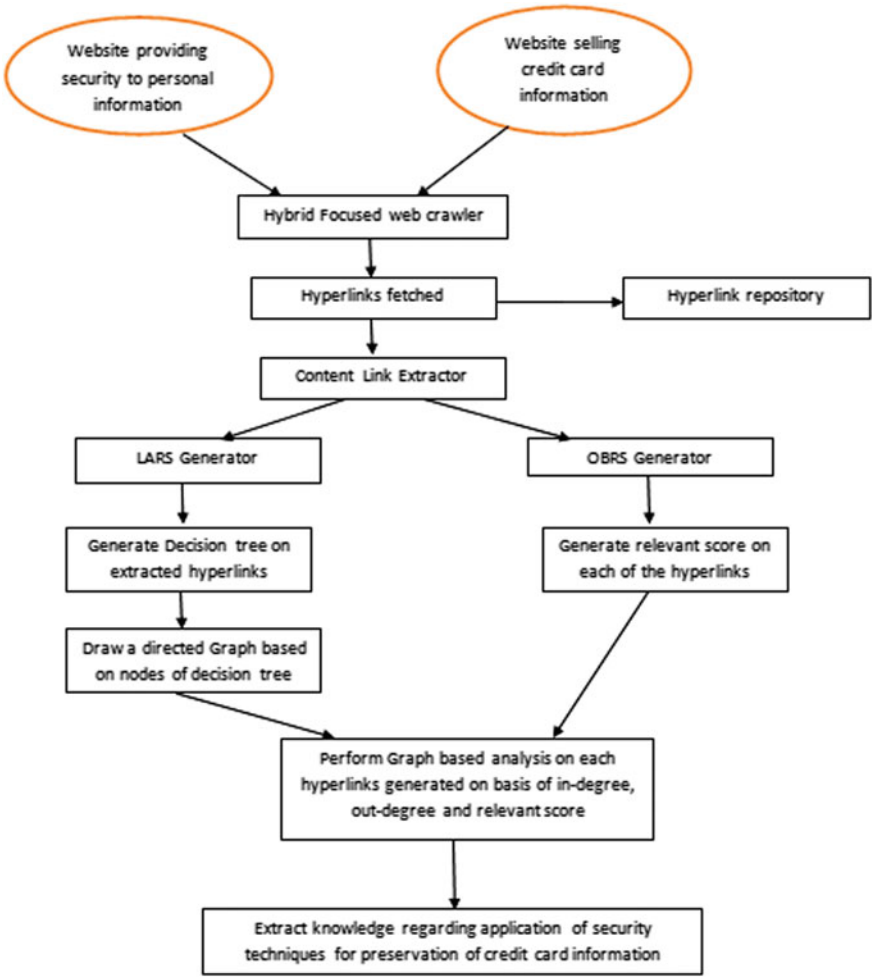

Fig. 1 Example of proposed system for knowledge extraction

a distributed system besides being an overlay network that is accessible through the usage of special software. It has also been demonstrated that knowledge management visualization of deep Web is a creative process although difficult in formalization. It has been widely applied in various areas, and its analysis is made possible by graph theory. In the final section of the paper, an example of the proposed system has been illustrated that will extract knowledge efficiently from both the Web sites of surface and dark Web. The authors plan to use this system further in taking some important decisions based on the extracted knowledge so as to mitigate the cybercriminal activities.

References

1. Zulkarnine, A.T., Frank, R., Monk, B., Mitchell, J., Davies, G.: Surfacing collaborated networks in dark web to find illicit and criminal content. In: 2016 IEEE Conference on Intelligence and Security Informatics (ISI), pp. 109–114 (2016)
2. Baravalle, A., Lopez, M.S., Lee, S.W.: Mining the dark web: drugs and fake Ids. In: 2016 IEEE 16th International Conference on Data Mining Workshops (ICDMW), pp. 350–356 (2016)
3. Chang W., Chung P.: Knowledge management in cybercrime investigation—a case study of identifying cybercrime investigation knowledge in Taiwan. In: Chau, M., Chen, H., Wang G.A., Wang, J.H. (eds.) Intelligence and Security Informatics. PAISI 2014. Lecture Notes in Computer Science, vol. 8440. Springer, Cham, 8–17 (2014)
4. E4J university module series: cybercrime: cybercrime module 5 key issues: knowledge management. https://www.unodc.org/e4j/en/cybercrime/module-5/key-issues/knowledge-management.html (2019). Accessed 17 May 2021
5. Alkhatib, B., Basheer, R.: Crawling the dark web: a conceptual perspective, challenges and implementation. J. Digital Inf. Manag. **17**(2), 51–60 (2019)
6. Paul, S., Mitra, A., Dey, S.: Implementation and application of Bio inspired computing techniques based web crawlers for data retrieval and information extractions, bio-inspired computing for information retrieval applications. IGI-Global, USA, ISBN: 9781522523758 (2017)
7. Gupta, A., Maynard, S.B., Ahmad, A.: The dark web phenomenon: a review and research agenda, arXiv e-prints (2021)
8. The Tor Project. Tor Project. https://www.torproject.org/. (2018)
9. Broadhurst, R., Woodford-Smith, H., Maxim, D., Sabol, B., Orlando, S., Chapman-Schmidt, B., Alazab, M.: Cyber terrorism: research review: research report of the Australian National University Cybercrime Observatory for the Korean Institute of Criminology (2017)
10. Tanenbaum, A.S., Van Steen, M.: Distributed systems: principles and paradigms. Prentice- Hall (2007)
11. Owen, G., Savage, N.: Empirical analysis of Tor hidden services. IET Inf. Secur. **10**(3), 113–118 (2016)
12. Hotspot Shield: Tor vs VPN. https://www.hotspotshield.com/resources/tor-vs-vpn/ (2018). Accessed 20 May 2018
13. Finklea, K.: Dark Web. Congressional Research Service, Washington DC, pp. 1–19 (2017)
14. Jardine, E.: The dark web dilemma: tor, anonymity and online policing. Centre for International Governance Innovation and Chatham House, **20**, 1–24 (2015)
15. Yang, L., Liu, F., Kizza, J., Ege, R.: Discovering topics from dark websites. In: Proceedings of the IEEE Symposium on Computational Intelligence in Cyber Security, Nashville, pp. 1–5 (2009)
16. Zhang, Y., Zeng, S., Huang, C.N., Fan, L., Yu, X., Dang, Y., Larson, C., Denning, D., Roberts, N., Chen, H.: Developing a dark web collection and infrastructure for computational and social sciences. In: Proceedings of the IEEE International Conference on Intelligence and Security Informatics, Vancouver, pp. 1–6 (2010)
17. Beshiri, A.S., Susuri, A.: Dark web and its impact in online anonymity and privacy: a critical analysis and review. J. Comput. Commun. **7**(3), 30–43 (2019)
18. Bloomenthal, A.: Dark Web. Laws & Regulations: Cyber security. https://www.investopedia.com/terms/d/dark-web.asp (2021). Accessed 16 Mar 2021
19. Acharyulu, G.V.R.K.: Information management in a health care system: knowledge management perspective. Int. J. Innov. Manag. Technol. **2**(6), 534–537 (2011)
20. Hunton, P.: Managing the technical resource capability of cybercrime investigation: a UK law enforcement perspective. Public Money Manag. **32**(3), 225–232 (2011)
21. Dixon, N.M.: Common knowledge. Harvard Business School Press, How companies thrive by sharing what they know (2000)

22. Press release Europol: crime on the dark web: law enforcement coordination is the only cure. https://www.europol.europa.eu/newsroom/news/crime-dark-web-law-enforcement-coordination-only-cure (2018). Accessed 17 May 2021
23. Dean, G., Cathrine, F., Petter, G.: Knowledge sharing in criminal investigations: an empirical study of Norwegian police as value shop. Crim. Justice Stud. **19**(4), 423–437 (2006)
24. Global Cyber Security Capacity Centre.: Cybersecurity capacity review: republic of Lithuania (2017)
25. Woodie, A.: The graph that knows the World. Datanami. https://www.datanami.com/2018/10/02/the-graph-that-knows-the-world/ (2018). Accessed 2 Oct 2018
26. Chowdhury, S.: Knowledge graph: the perfect complement to machine learning, towards data science. https://towardsdatascience.com/knowledge-graph-bb78055a7884 (2019). Accessed 18 July 2019
27. Fluit, C., Sabou, M., van Harmelen F.: Ontology-based information visualization: toward semantic web applications. In: Geroimenko, V., Chen, C. (eds.) Visualizing the Semantic Web. Springer, London (2001)
28. Frasincar, F., Telea, A., Houben, G-Jan.: Adapting graph visualization techniques for the visualization of RDF data. Visualizing the Semantic Web, 2nd edn. Springer (2005)
29. Wei, F., Zhiming, C.: Research on knowledge management visualization of deep web. Key Eng Mater **439–440** Online: 2010–06–07. Trans Tech Publications, Switzerland, pp. 189–194 (2010)
30. Griffith, V., Xu, Y., Ratti, C.: Graph Theoretic Properties of the Darkweb, arXiv, (2017)
31. Borgatti, S.P, Jones, C., Everett, M.G.: Network measures of social capital. Connections **21**, 27–36 (1998)
32. Wu, P, Wen, J.R, Liu, H, Ma, W.Y.: Query selection techniques for efficient crawling of structured web sources. In: Proceedings of the 22nd international conference on data engineering, IEEE (2006)
33. Yang, D., Yang, H-M., Wang, P, Li, S-J.: Design and implement of large-scale social network analysis platform based on Hadoop. J Inf Hiding Multimedia Signal Process ISSN 2073–4212, Ubiquitous International Volume **8**(2), 300–309 (2017)
34. Yang, Y et al.: Hadoop-based dark web threat intelligence analysis framework. In: 2019 IEEE 3rd Advanced Information Management, Communicates, Electronic and Automation Control Conference (IMCEC), Chongqing, China, 1088–1091 (2019)
35. Paul, S., Mitra, A., Koner, C.: A review on graph database and its representation. In: 2019 International Conference on Recent Advances in Energy-efficient Computing and Communication (ICRAECC), pp. 1–5 (2019)

A Generic Approach for Interpolation and Image Fusion to Obtain Pan-Sharpening

Aindrila Das, Amartya Bhattacharjee, Bivas Ranjan Dutta, Souvik Masanta, Sudipta Sahana, and Dharampal Singh

Abstract An image that holds both high spatial and spectral information is the most preferred one. A panchromatic (PAN) image contains high spatial resolution, whereas a multispectral (MS) image contains high spectral information. Pan-sharpening is a technique that combines more than one image into a single image that has been used after extracting the spatial information from panchromatic image and spectral information from multispectral image. The pixel resolution of the PAN image is greater than that of the MS image, and before image fusion, both should be on the same scale. We have solved this by an innovative interpolation approach in this paper. We have done a detailed study on several fusion algorithms, but wavelet and Brovey transforms are the most frequently used methods in the current scenario. We have also introduced a new image fusion technique that takes complete information from both images. Wavelet transform preserves spectral information, whereas Brovey transform holds the spatial information. A combination of these two methods is applied after the interpolation, and it results well. This paper presents a combination of wavelet and Brovey Transformation fusion algorithm, and a new fusion technique followed by an innovative interpolation approach.

Keywords Panchromatic image · Multispectral image · Spatial resolution · Spectral resolution · Pan-sharpening · Interpolation · Wavelet transform · Brovey transform

1 Introduction

Remote sensing is a process through which we can collect images of an object or surface area from satellites, planes, drones, and many more. It has vast practical applications in remote sensing such as natural hazards, disaster management, environmental monitoring, oceanography, forestry, map updating, medical science, and many more [1]. Due to some limitations of technologies, remote sensing does not

A. Das · A. Bhattacharjee · B. R. Dutta (✉) · S. Masanta · S. Sahana · D. Singh
Department of Computer Science and Engineering, JIS College of Engineering, Kalyani, Nadia 741235, India

B. Sikdar et al. (eds.), *Proceedings of the 3rd International Conference on Communication, Devices and Computing*, Lecture Notes in Electrical Engineering 851,
https://doi.org/10.1007/978-981-16-9154-6_22

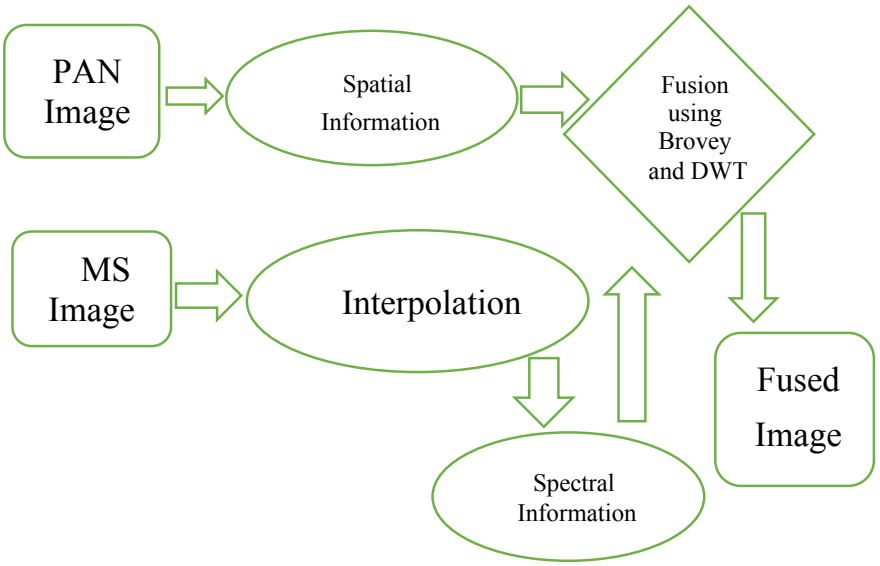

Fig. 1 General flow diagram

provide both spatial and spectral information together within a single dataset. It gathers spatial information that helps in earth observation in PAN images, while the MS image contains high spectral information. Here comes the idea of image fusion. Pan-sharpening has become an effective way to produce a high-resolution multispectral (HR-MS) image by fusing PAN and MS images [2].

As the spatial resolution of PAN image is so high, the number of pixels of PAN image is more than the number of pixels of MS image. An interpolation on MS has been introduced, so that both the image remains in the same scale. This interpolation results in equal pixel resolution for both the images and makes it possible for Pan-sharpening. We have also introduced a new fusion technique and then performed quantitative analysis of our proposed fusion technique with novel interpolation technique and some commonly known image fusion algorithms like DWT, Brovey, and fusion of Brovey and wavelet (Fig. 1).

2 Literature Survey

The popular interpolation techniques are nearest neighbor interpolation [3], bicubic [4] interpolation, and bilinear [5] interpolation. Nearest neighbor interpolation is a simple approach that takes the nearest pixel value for interpolation instead of calculating some average values. Although bicubic takes more time than bilinear, it gives a smoother result. In comparison with these techniques, our model shows better results for interpolation.

Although various fusion techniques are available, most of these techniques have some advantages and disadvantages. A fused image should have specific characteristics such as relevant information from all input images, minimum noise, consistency, and many more. These fusion techniques are broadly divided into two classes, spatial and frequency. We obtain the result in the spatial class. All methods deal with pixel values of input images and operating these pixels. Brovey [6], principal component analysis (PCA) [7, 8], and intensity hue saturation (IHS) [9–11] are the most common spatial fusion techniques. HIS shows the best results to preserve spatial quality, but it works on only three bands. PCA has a significant drawback in the form of spectral degradation and color distortion. On the other hand, Brovey overcomes three-band problems, helpful for visual interpretation, and preserve spatial information but creates spectral distortion.

Discrete wavelet transform (DWT) [12] is a powerful method in frequency class that decomposes input images into several low- and high-frequency bands. It provides a better compression ratio and minimizes spectral distortion in the fused image. Although it gives good spectral information, it fails to deliver good directionality and spatial information.

To overcome the above problems, a combination of Brovey and DWT shows a more effective result. This technique unites the benefits of both Brovey and DWT. As a result, the fused image will contain spatial information from the PAN image and spectral information from the MS image.

3 Methodology

In Pan-sharpening, interpolation is a crucial part. In order to fuse the images, the images should be in the exact sizes. As we know, the resolution of MS image is less than PAN image, so it is evident that the number of pixels representing the MS image is less than PAN image. In this paper, we tried to implement a novel approach to implement interpolation technique which is very simple and effective for any dataset. Then, to validate our interpolation approach, we have used image fusion methods like wavelet and Brovey transform.

We have divided our whole task into two steps:

1. Interpolation of MS image
2. Fusion of interpolated MS image with PAN image.

3.1 Interpolation of MS Image

Image interpolation means converting the image from one size to another. Image interpolation is needed when we want to decrease or increase the total numbers of pixels. This is a necessary step to do image fusion. We get the MS and PAN image of the same size or the same number of pixels in this step. For doing this step, at

first, we need to find the interpolation factor (λ). The interpolation factor indicates the number of times the PAN image is larger than the MS image. For example, if λ = 2, the PAN image is two times larger than the MS image. The formula for finding λ is:

$$\lambda = \frac{\text{Resolution of PAN}}{\text{Resolution of MS}} \tag{1}$$

After finding the λ, we have to distribute the MS pixels in the whole interpolated image. So, in our algorithm, we have interpolated with the help of λ. If the $\lambda = K$, then one pixel of MS will represent $(K \times K)$ grid of pixels. By doing this, the information of the MS image is distributed among the interpolated image without any distortion or artifacts. Since we are using the actual MS pixels as our interpolated image pixels, there is no chance of spurious entries in the interpolated image that leads to image distortion.

3.2 Fusion of Interpolated MS Image with PAN Image

3.2.1 Fusion of Interpolated MS Image with PAN Image Using Brovey

This famous fusion technique was proposed by an American scientist named Bob Brovey. It incorporates a Red–Green–Blue (R, G, B) color transform method. It was developed to overcome the disadvantages of the multiplicative method. A part of the high-resolution PAN image reconstructs every MS band in addition to MS bands. The special information is maintained, but this generally triggers spectral distortion.

$$\text{MS}_\text{i} = \frac{\text{MS}_i}{\frac{1}{n}\sum_{i=0}^{n} \text{MS}_i} * \text{PAN} \tag{2}$$

where $i = 1, 2\ldots. n$, MS_i is the ith band and n is the number of bands of MS image. This injects the special information into the low-resolution multispectral image.

3.2.2 Fusion of Interpolated MS Image with PAN Image Using Discrete Wavelet

The discrete wavelet transform, an effective and popular image fusion technique, was introduced by Daubechies, Mallet, and others. It divides the signal based on the primary function: wavelets. In this method, a high-resolution PAN image is divided into four components named diagonal, horizontal, vertical, and approximation. The special information of both the MS band and approximation component is the same, but the spectral information of the MS band is much more. Now, the approximation component is replaced by that MS band. Finally, a reverse wavelet transform is done

to rebuild the original high resolution. This process is applied for each band of MS images. However, the fused image contains high spectral information but lacks spatial information.

3.2.3 Proposed Method of Image Fusion

This algorithm compares the pixel value of the PAN image with the interpolated MS image. The comparison is done to get the higher spectral and the spatial resolution in an image. In this algorithm, a new image is formed by taking the color information from the MS image and the resolution from the pan image. This is done by taking the higher pixel information from two images. The MS image is first divided according to its bands. A new matrix is made having the same size that of PAN image. Each pixel values of each band of MS image and the PAN image are compared. The pixel having higher value is stored in the new matrix. The process is repeated till all the bands are compared. Then, the new matrices obtained using the above process are merged to get a new Pan-sharpened image of high spectral and spatial information.

4 Results and Discussion

This section depicts the analytical and visual analysis of the output generated by the different algorithms and the concept applied on the dataset in the entire paper. The following concept has been processed and collated with different quantitative approaches or methods.

For the analysis, and output generation, certain setup, and requirements are required. The following are the requirements for the same:

(1) Editor: Spyder (Anaconda-3)
(2) Operating system: Windows (Version: 10)
(3) Coding language: Python 3.9.0
(4) RAM: 16 GB
(5) Processor: Intel(R)-CoreTM-i5-L16G7-3.0 GHz.

4.1 Quantitative Assesment Functions

This section depicts the analytical results generated by the quantitative methods applied on the different approaches used in the paper. A qualitative assessment focuses more on intuition than on hard facts and data. This analysis determines the quality and justifies the desired result. For this analysis, we consider some quantitative methods that helps to validate the algorithms used in the paper. The following are the selected methods that have been considered for the same:

1. Correlation coefficient (CC)
2. Universal image quality index (UIQI)
3. Peak signal-to-noise ratio (PSNR)
4. Root mean square error (RMSE)
5. Structural similarity index measure (SSIM)
6. Relative dimensionless global error (ERGAS).

Correlation coefficient is the statistical term that is used to describe the degree in which the two coordinate moves with one-another. If each coordinate moves in the same direction, then it is said to have a positive correlation [13].

$$\mathrm{CC} = \frac{\sum_i (r_i - r_m)(f_i - f_m)}{\sqrt{\sum_i (r_i - r_m)^2 (f_i - f_m)^2}} \tag{3}$$

In the above formula, r_i and f_i symbolize the intensity information of ith pixel in the referenced (R) and fused image (F), respectively. r_m and f_m symbolize the mean intensity values of the referenced and fused image, respectively. The more the value of the cc factor, the better the result would be.

Universal image quality index mainly considers CC, luminance distance, and contrast distortion of the R and F into consideration

$$\mathrm{UIQI}(R, F) = \frac{\sigma_{RF}}{\sigma_R \sigma_F} * \frac{2\mu_R \mu_F}{\mu_R^2 + \mu_F^2} * \frac{2\sigma_R \sigma_F}{\sigma_R^2 + \sigma_F^2} \tag{4}$$

In the above formula μ_R and μ_F symbolize the mean information of R and F, respectively. σ_R and σ_F depict the standard deviation of R and F, respectively. ${\sigma^2}_R$ and ${\sigma^2}_F$ symbolize the variance of R and F, respectively. σ_{RF} is the covariance of R and F.

PSNR ratio between the largest and smallest possible values of a changeable quantity the PSNR is usually expressed in terms of the logarithmic decibel scale [14].

$$\mathrm{PSNR} = 10 * \log_{10}\left(\frac{P^2}{\frac{\sum_{i,j=1}^{mn}\left(R_{ij} - F_{ij}\right)^2}{mn}}\right) \tag{5}$$

In the above formula, P will be equal to $(2b) - 1$. And b is the absolute number of bits that are utilized to represent a single pixel of the R. Higher the value of PSNR is better for the quality check.

RMSE is the basic difference between the predicted output and the actual input or the referenced input

$$\mathrm{RMSE} = \sqrt{\frac{\sum_{i,j=1}^{mn}\left(R_{ij} - F_{ij}\right)^2}{mn}} \tag{6}$$

In the above formula, R_{ij} and F_{ij} depict the intensity information of the (i, j)th pixel of the R and F, respectively. m and n symbolize the total number of the rows and columns of F. If the RMSE value less, then better will be the result. Less the error, better will be the quality of images.

The SSIM is an improvement over UIQI. It quantifies the similarity between intensity in the local pattern of R and F. It varies within -1 to $+1$.

$$\mathrm{SSIM}(R, F) = \left(\frac{2\mu_R\mu_F + C_1}{\mu_R^2 + \mu_F^2 + C_1}\right)\left(\frac{2\sigma_{RF} + C_2}{\sigma_R^2 + \sigma_F^2 + C_2}\right) \tag{7}$$

In the above equation K1 and K2 are the two constants. L depicts the maximum intensity value, and C_1 and C_2 are the two constants given by $(K_1L)^2$ and (K_2L), respectively. The higher the value, the better the result. The relative dimensionless global error offers the global view for the quality of the output image.

4.2 Quantitative and Qualitative Evaluation and Validation

The total paper mainly focuses on the new approach of interpolation and fusion of the MS image with the PAN image to get a Pan-sharpened image. This portion depicts the analytical results of comparing the described approach and the other different approaches for the interpolation purpose. The paper also focuses on improving the image quality after interpolation. Here, we depict the comparison factors after implementing the fusion algorithm on the interpolated image with the four different interpolation techniques and three different fusion algorithms. This analysis is helpful for the justification of the stated conclusion. The different approaches used for the interpolation purpose are as follows:

1. Proposed algorithm
2. Bilinear interpolation
3. Bicubic interpolation
4. Nearest neighbor interpolation.

And the different fusion algorithm used for the comparison factor are:

1. Discrete wavelet transformation (DWT) fusion algorithm
2. Brovey fusion algorithm
3. Both Brovey and discrete wavelet transformation (DWT) fusion algorithm.

All the images are radiometrically corrected and geo-referenced. Figure 2 is the dataset that we have used in our paper. The figure contains an MS image and a PAN image. The MS image compromises of 256×256 number of pixels, and the PAN image contains 1024×1024 number of pixels.

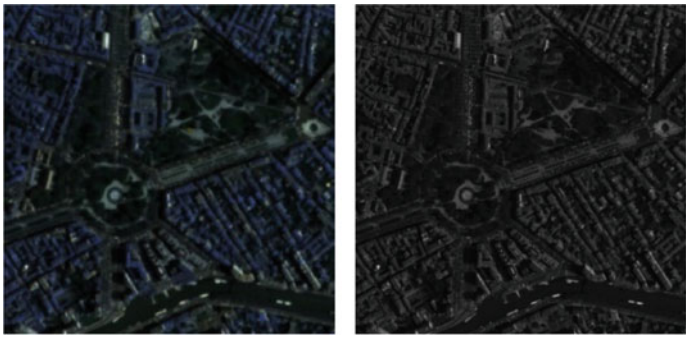

a b

Fig. 2 **a** MS image of 256 × 256 pixels and **b** PAN image of 1024 × 1024 pixels

The proposed algorithm that has been stated in the paper is implemented on these datasets. The MS image of 256 × 256 pixels has been first interpolated to the same scale of the PAN image. With the interpolation factor of 4, the interpolation of the MS image has been implemented by the proposed algorithm. For the comparison purpose, the dataset has been interpolated by the three different types of techniques: bilinear interpolation, bicubic interpolation, and nearest neighbor interpolation. The following results of the interpolated images by the different techniques are shown in Fig. 3. The figure contains the interpolated MS image of 1024 × 1024 number of pixels using the proposed method, bilinear interpolation, bicubic interpolation, and nearest neighbor interpolation.

These are the following outputs with the various types of interpolation methods. Now, these all serves as the datasets for the upcoming techniques for the fusion algorithm. Our paper focuses on the fusion of interpolated MS image and PAN image to get a Pan-sharpened image. So, the above-interpolated images undergo three different types of fusion algorithms. These algorithms are then compared to the referenced image with the quantitative methods, and the analysis leads to the final conclusion.

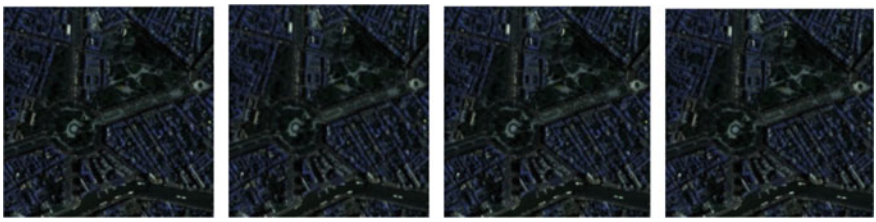

a. b. c. d.

Fig. 3 **a** UP-SCALED_BICUBIC, **b** UP-SCALED_BILINEAR, **c** UP-SCALED_NEAREST_NEIGHBOUR, **d** UP-SCALED_PROPOSED METHOD

The three different types of fusion algorithms mentioned above are:

Brovey fusion algorithm—In this method, the MS image has split into the number of comprising bands, and the mean value of the band has been taken. After that, each band is divided by the mean value and then multiplied with the intensity value PAN image. And at last, all the bands have been merged to get a pan-sharpened image.

Discrete Wavelet Transformation fusion algorithm—The MS image has been divided into four coefficient values in this method, and the PAN image has also been divided into four different coefficient values. Then, the intensity values of the two images are replaced, and then with the help of the inverse wavelet algorithm, we have got a pan-sharpened image.

Mixture of Brovey and Wavelet fusion algorithm—The above algorithms are efficient, and in the Brovey fusion algorithm, the color information is satisfactory. However, the image quality is not up to the mark. In the discrete wavelet transformation fusion algorithm, it is the opposite. To have a solution, we implemented this method where first Brovey fusion algorithm is implemented and then with the output result in the discrete wavelet transformation fusion algorithm is applied to get a better Pan-sharpened image.

The above is the brief concepts of the fusion algorithms used on the interpolated image. Figure 4 depicts the output that is given after the implementation of the following fusion algorithm on the interpolation algorithm:

The following figure depicts the output results of the fused images. Now, we have analyzed the values after comparing the output images with the different types of quantitative methods. In this part, we have separately analyzed the comparison value of the fused images with the proposed algorithm stated in the paper. This analysis helps for the justification of the stated conclusion. The following three tables depict the comparison values of the proposed interpolation algorithm stated in our paper with the algorithms stated in other research paper.

There are altogether three different tables, and each gives a different conclusion.

Tables 1, 2, and 3 depict the analytical values of the proposed interpolation method and the bilinear, bicubic, and nearest neighbor interpolation method after fusion. If we take a closer look at the table, we can notice that our proposed method is better than that of the other method used in case of most of the factors.

In the next part, we have depicted the analytical and the visual outputs of the Pan-sharpened images generated by the proposed fusion algorithm. Here, we have done the comparison between our fusion algorithm and available existing fusion algorithms.

Figure 5 depicts the visual output of the different pan-sharpened images.

The following figure depicts the output results of the fused images. Now, we have analyzed the values after the comparison of the output images with the different type of quantitative methods. In this part, we have separately analyzed the comparison values of the different Pan-sharpened images (Tables 4, 5 and 6).

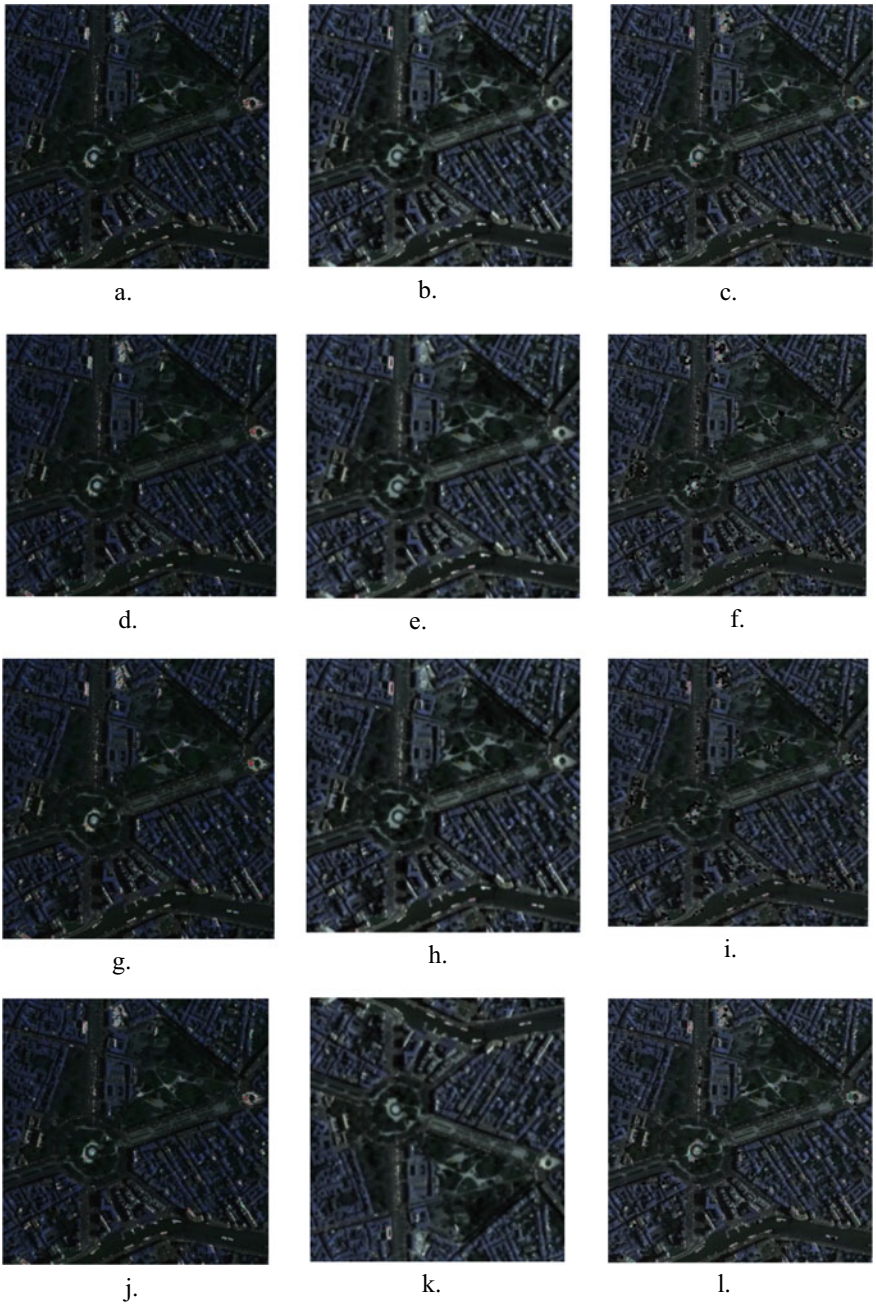

Fig. 4 **a** Proposed Brovey algorithm, **b** Proposed wavelet algorithm, **c** Proposed both algorithms, **d** Bilinear Brovey algorithm, **e** Bilinear wavelet algorithm, **f** Bilinear both algorithms, **g** Bicubic Brovey algorithm, **h** Bicubic wavelet algorithm, **i** Bicubic both algorithms, **j** Nearest neigh. Brovey algorithm, **k** nearest Neigh. Wavelet algorithm, **l** nearest neigh. both algorithms

Table 1 Comparison between proposed method and bilinear method

	Proposed method and fused			Bilinear method and fused		
Quantitative parameter	Brovey	Wavelet	Brovey and wavelet	Brovey	Wavelet	Brovey and wavelet
Correlation coefficient (Red)	0.888	0.985	0.921	0.925	0.991	0.948
Correlation coefficient (Green)	0.712	0.985	0.848	0.989	0.991	0.943
Correlation coefficient (Blue)	0.938	0.983	0.893	0.907	0.991	0.941
Average correlation coefficient	0.846	0.984	0.887	0.910	0.991	0.944
RMSE	0.053	0.062	0.075	0.067	0.073	0.090
PSNR	32.72	28.37	28.47	30.82	28.961	28.938
ERGAS	0.047	0.036	0.040	0.064	0.041	0.055
UIQI	0.947	0.852	0.820	0.861	0.807	0.775
SSIM	0.847	0.874	0.739	0.796	0.824	0.708

Table 2 Comparison between proposed method and bicubic method

	Proposed method and fused			Bicubic method and fused		
Quantitative parameter	Brovey	Wavelet	Brovey and wavelet	Brovey	Wavelet	Brovey and wavelet
Correlation coefficient (Red)	0.888	0.985	0.921	0.905	0.987	0.903
Correlation coefficient (Green)	0.712	0.985	0.848	0.925	0.986	0.850
Correlation coefficient (Blue)	0.938	0.983	0.893	0.890	0.986	0.923
Average correlation coefficient	0.846	0.984	0.887	0.907	0.896	0.892
RMSE	0.053	0.062	0.075	0.064	0.072	0.091
PSNR	32.727	28.371	28.476	30.821	29.118	28.992
ERGAS	0.047	0.036	0.040	0.065	0.042	0.056
UIQI	0.947	0.852	0.820	0.860	0.820	0.772
SSIM	0.847	0.874	0.739	0.794	0.847	0.704

Table 3 Comparison between proposed method and nearest neighbor method

	Proposed method and fused			Nearest Neighbor method and fused		
Quantitative parameter	Brovey	Wavelet	Brovey and Wavlet	Brovey	Wavelet	Brovey and Wavlet
Correlation coefficient (Red)	0.888	0.985	0.921	0.921	0.981	0.889
Correlation coefficient (Green)	0.712	0.985	0.848	0.720	0.983	0.844
Correlation coefficient (Blue)	0.938	0.983	0.893	0.876	0.983	0.925
Average correlation coefficient	0.846	0.984	0.887	0.839	0.982	0.886
RMSE	0.053	0.062	0.075	0069	0.072	0.804
PSNR	32.727	28.371	28.476	30.820	29.063	28.952
ERGAS	0.047	0.036	0.040	0.065	0.041	0.049
UIQI	0.947	0.852	0.820	0.860	0.816	0.788
SSIM	0.847	0.874	0.739	0.794	0.842	0.719

The above tables depict three different sets of quantitative values. In all the three above tables, it has been observed that the Pan-sharpened image produced by the proposed interpolation and fusion algorithm gives the best results as compared to the other existing interpolation and the fusion algorithms.

5 Conclusions

This study proposed new approaches for interpolating the MS image and image fusion. In this study, we have two input images: PAN image and MS image with 1024×1024 and 256×256 pixels, respectively. The MS image has been interpolated with three existing interpolation algorithms and fused with three different fusion algorithms to have a comparative study. All the acquired outputs, comparative results, and the related theory are presented in the study. Taking an average analysis of the report and having all the scopes for future improvements, we can conclude that the proposed algorithm stated in the study gives a better result than other existing methods.

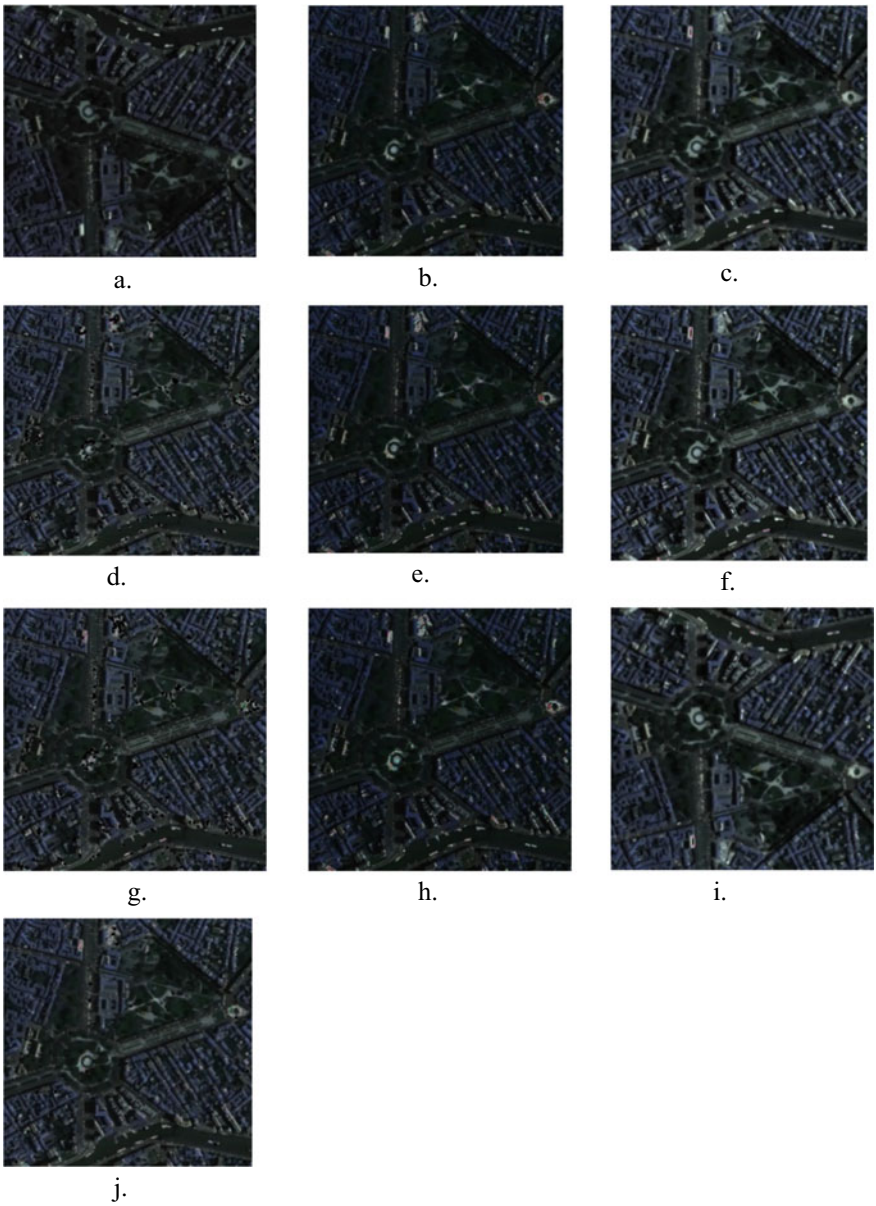

Fig. 5 **a** Proposed Brovey algorithm, **b** Bilinear Brovey algorithm, **c** Bilinear wavelet algorithm, **d** Bilinear both algorithms, **e** Bicubic Brovey algorithm, **f** Bicubic wavelet algorithm, **g** Bicubic both algorithms, **h** Nearest neighbor with Brovey algorithm, **i** Nearest neigh. wavelet algorithm, **j** nearest neigh. both algorithms

Table 4 Comparison with our proposed method with bilinear interpolation technique and fusion algorithm

	Bilinear method and fused			
Quantitative parameter	Proposed	Brovey	Wavelet	Brovey and wavelet
Correlation coefficient (Red)	0.996	0.925	0.991	0.948
Correlation coefficient (Green)	0.997	0.989	0.991	0.943
Correlation coefficient (Blue)	0.997	0.907	0.991	0.941
Average correlation coefficient	0.997	0.910	0.991	0.944
RMSE	0.027	0.067	0.073	0.090
PSNR	33.235	30.827	28.961	28.938
ERGAS	0.021	0.064	0.041	0.055
UIQI	0.947	0.861	0.807	0.775
SSIM	0.878	0.796	0.824	0.708

Table 5 Comparison with our proposed method with bicubic interpolation technique and fusion algorithms

	Bicubic method and fused			
Quantitative parameter	Proposed	Brovey	Wavelet	Brovey and wavelet
Correlation coefficient (Red)	0.996	0.905	0.987	0.903
Correlation coefficient (Green)	0.997	0.925	0.986	0.850
Correlation coefficient (Blue)	0.997	0.890	0.986	0.923
Average correlation coefficient	0.997	0.907	0.896	0.892
RMSE	0.027	0.064	0.072	0.091
PSNR	33.235	30.821	29.118	28.992
ERGAS	0.021	0.065	0.042	0.056
UIQI	0.947	0.860	0.820	0.772
SSIM	0.878	0.794	0.847	0.704

Table 6 Comparison with our proposed method with nearest neighbor interpolation technique and fusion algorithms

	Nearest neighbor and fused			
Quantitative parameter	Proposed	Brovey	Wavelet	Brovey and wavelet
Correlation coefficient (Red)	0.996	0.921	0.981	0.889
Correlation coefficient (Green)	0.997	0.720	0.983	0.844
Correlation coefficient (Blue)	0.997	0.876	0.983	0.925
Average correlation coefficient	0.997	0.839	0.982	0.886
RMSE	0.027	0069	0.072	0.804

(continued)

Table 6 (continued)

	Nearest neighbor and fused			
Quantitative parameter	Proposed	Brovey	Wavelet	Brovey and wavelet
PSNR	33.235	30.820	29.063	28.952
ERGAS	0.021	0.065	0.041	0.049
UIQI	0.947	0.860	0.816	0.788
SSIM	0.878	0.794	0.842	0.719

References

1. Ghassemian, H.: A Review of remote sensing image fusion methods, information fusion, pp. 1566–2535 (2016)
2. Fu, X., Lin, Z., Huang, Y., Ding, X.: A variational pan-sharpening with local gradient constraints, computer vision foundation, pp. 10265–10274 (2015)
3. Angelos, A., Ioannis, A.: A survey on evaluation methods for image interpolation. Measur. Sci. Technol. **20**(10), 104015 (2009)
4. Hwang, J.W., Lee, H.S., Adaptive image interpolation based on local gradient features. IEEE Signal Process. Lett. **11**(3), 359–362 (2004)
5. Dahiya, S., Garg, P.K., Jat, M.K. A comparative study of various pixel-based image fusion techniques as applied to an urban environment. Int. J. Image Data Fusion **4**(3), 197–213 (2013)
6. Mandhare, R.A., Upadhyay, P., Gupta, S.: Pixel-level image fusion using brovey transforme and wavelet transform. Int. J. Adv. Res. Electr. Electr. Instrum. Eng. 2278–8875
7. Kwarteng, P., Chavez, A.: Extracting spectral contrast in landsat thematic mapper image data using selective principal component analysis. Photogramm. Eng. Remote Sens **55**, 339–348 (1989)
8. Chavez, P.S., Sides, S.C., Anderson, J.A.: Comparison of three different methods to merge multiresolution and multispectral data: TM & Spot Pan. Photogramm. Eng. Remote. Sens. **57**, 295–303 (1991)
9. Carper, W.J.: The use of intensity-hue-saturation transformations for merging spot panchromatic and multispectral image data. Photogramm. Eng. Remote Sens. **56**(4), 457–467 (1990)
10. Haydn, R., Dalke, G.W., Henkel, J., Bare, J.E.: Application of HIS color transform to the processing of multisensor data and image enhancement. In: Proceeding of International Symposium Remote Sensing Arid Semi-Arid Lands. Cairo, Egypt, pp. 599–616 (1982)
11. Chu, H., Zhu, W.: Fusion of IKONOS satellite imagery using IHS transform and local variation. IEEE Geosci. Remote Sens. Lett. **5**(4), 653–657 (2008)
12. Temizel, A.: Image resolution enhancement using wavelet domain hidden Markov tree and coefficient sign estimation. In: 2007 IEEE International Conference on Image Processing, vol. 5. IEEE, pp. V-381 (2007)
13. Wang, Z., Bovik, A., Sheikh, H., Simoncelli, E.: Image quality assessment: from error visibility to structural similarity. Image Process. IEEE Trans. **13**, 600–612 (2004)
14. Sarp, G., Spectral and spatial quality analysis of pan-sharpening algorithms: a case study in Istanbul. Eur. J. Remote Sens. **47**(1), 19–28

FastResponse—A Smart Ambulatory System for Monitoring Accident/Disaster Victims Along with Live Tracking Facility

Mahasweta Ghosh and Soma Barman (Mandal)

Abstract Delay in delivering healthcare facilities to a disaster/accident victim would be fatal. Thus, our proposed FastResponse—a smart ambulatory system for monitoring accident/disaster victims with a live-tracking facility is essential to save lives when many people are injured in a disaster/accident. The proposed system can monitor the heart rate and body temperature of a patient non-invasively, either at the accident site or in ambulances and has provision to incorporate other sensors. It is also equipped with facilities for emergency notifications and remote communication to hospitals/paramedics. The monitoring system's performance is judged by the Receiver Operating Characteristics curve and is found to be more than 80% accurate for both sensors. The proposed system can additionally track the ambulance in real-time both at the ambulance-end and at a remote-end. The system helps in identifying critical patients at the accident site and provide faster medical facilities on reaching the hospitals.

Keywords Ambulatory monitoring · Live tracking · Receiver operating characteristics curve · Remote communication

1 Introduction

An immense challenge of the Indian healthcare system is to deliver uninterrupted service to everyone and everywhere, especially in case of emergencies. By using state-of-the-art technology, an emergency patient physiological parameter (PPP) monitoring system can affordably reach these people and save lives during any catastrophe. According to the Ministry of Health and Family Welfare (MoHFW), Government of India, there are 11090 government-run ambulances all over India as of 30 Sept 2020 [1]. But all of these ambulances do not even have a facility of basic

M. Ghosh · S. Barman (Mandal) (✉)
Institute of Radio Physics and Electronics, Uniersity of Calcutta, 92, APC Road, Kolkata 700009, India
e-mail: sbrpe@caluniv.ac.in

B. Sikdar et al. (eds.), *Proceedings of the 3rd International Conference on Communication, Devices and Computing*, Lecture Notes in Electrical Engineering 851,
https://doi.org/10.1007/978-981-16-9154-6_23

health monitoring and support systems. Most of the old models do not even have a Global Positioning System (GPS) hardware or any other vehicle tracking facility. As a result, a large number of people in India, even in urban areas, lose their lives at various stages before their treatment starts, like, at the accident/disaster site, on their way to the hospital or even just after reaching the hospital. Thus, FastResponse—a combination of a smart pre-hospital and ambulatory monitoring system (SPHAMS) in association with a good and reliable ambulance live tracking and management system (ALTMS) is of utmost necessity in India's current healthcare scenario.

Previously, Rajya Laxmi et al. proposed a potential smartwatch for dementia patients [2] using market available sensors ICs like MLX90614 for body temperature measurement and MAX30100 for heart rate measurement. But these sensors will not be suitable for low-cost system design and their sensitivity and specificity are not mentioned in the datasheets. Munem and Croock have developed a health monitoring system using Wireless Sensor Network (WSN) that can be used in ambulances as a part of an emergency system [3]. They have used commercial Arduino-compatible sensors to build their WSN but have mainly focused on building an emergency database and webpage that records the vital data feed from various ambulances. They were unable to track their ambulances in real-time and hence, unable to estimate the time of arrival of the ambulances at the hospitals leading to unnecessary delay in the patient's treatment. An IoT-based ambulance service that can remotely monitor patient's health parameters like heart rate, body temperature, blood pressure and blood sugar is proposed by Lolita et al. [4]. However, an Arduino board has a very small memory and it crashes when multiple operations are performed simultaneously. So, in their system, the sensors must be manually disconnected and reconnected continuously to get all these data to the paramedic/doctor, making it unsuitable for an emergency. They too have not focused on tracking the ambulance. Most of the other works mainly discuss more efficient vehicle tracking techniques or ambulance fleet management or deployment and not on developing an efficient smart ambulance management system.

Pre-hospital patient monitoring becomes very important to identify the patients who require the most urgent treatment from a large number of victims of a disaster/accident, where the availability of ambulances is very few. Such people require immediate medical care, like constant health monitoring, regular contact with doctors and live ambulance tracking, even during the journey to the hospital. Our designed ARM Cortex based SPHAMS of FastResponse fulfils such desired need. This user-friendly low-power system will monitor the vital signs of a person accurately. For designing the system, most importance is given on measurement accuracy, the top-most priority of any medical device. To reduce the financial burden on government-run medical centres, we also considered a cost-effective way of measurement during the system's inception. Another important aspect of both the SPHAMS and ALTMS is the error-free remote transmission of PPP and ambulance location to doctor/traffic guard in real-time. The system has been equipped with a remote Zigbee communication link for PPP data transmission. Our designed system is validated by a registered medical practitioner measuring the PPP of the volunteers and its performance has been judged by Receiver Operating Characteristics (ROC) analysis with more than

80% accuracy in both cases. The ALTMS helps in tracking the real-time location of any ambulance registered with our system and thus help in estimating the time of reaching a hospital.

The rest of the paper is organized as follows: Sect. 2 presents the overview of the proposed system. Its experimental set-up and methodology is elaborated in Sect. 3. Section 4 describes the performance analysis of the SPHAMS based on the measured vital signs and shows the real-time output of the ALTMS. Finally, Sect. 5 presents the concluding remarks and novelty of our work.

2 System Architecture

The generalized layout of our proposed FastResponse is given in Fig. 1.

The proposed system FastResponse has two major parts—the SPHAMS, an embedded portable, low power, remote, vital sign monitoring system and the ALTMS, a web-based real-time ambulance tracking and management system.

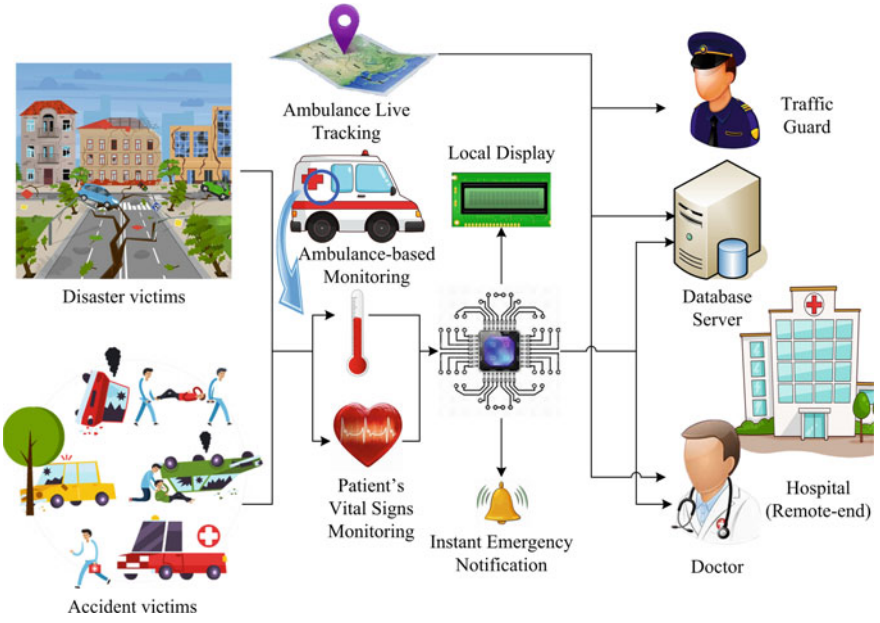

Fig. 1 The overall layout of the proposed FastResponse system

2.1 Smart Pre-hospital and Ambulatory Monitoring System (SPHAMS)

The SPHAMS can collect the vital signs of the disaster/accident victims from the accident sites or in ambulances and the LPC1768, ARM Cortex M3 architecture-based microcontroller displays the measured vital signs to the paramedic. It also has instant notification facilities to warn the doctors/nursing staff in the hospitals/ambulance, whenever the patient's vitals show any abnormality or deterioration in the patient's health [5]. A Zigbee communication link is also attached to the system which collects vital signs data from the Zigbee transmitter of the SPHAMS and remotely sends this data to a Zigbee receiver hub. Such a hub can be connected to approximately 6500 individual nodes. This feature makes our system extremely useful in disaster sites or accident cases with a large number of victims, especially in case of shortage of ambulance. In such a situation, these systems can be used to primarily identify the victims who need immediate medical attention, if it is not apparent from their external injuries.

2.2 Ambulance Live Tracking and Management System (ALTMS)

The proposed ALTMS has a real-time ambulance tracker, trackable both at the ambulance-end and at the hospital/traffic guard-end (remote-end). The system can be used by any ambulance registered with our system. This enables the hospitals/ambulance agencies to manage their ambulances and track their current location/patient carrying status. The traffic guards can also track any registered ambulance for transferring the victims to the nearest hospital through "green corridors", increasing their chances of survival. The live location is tracked using the free **HTML5 geolocation API** (Application Programming Interface). These location data for each ambulance are then uploaded to the real-time database, Firebase, from where the data is read by the tracker at the remote-end. Location can also be displayed on a map (Google map) for better visualization.

3 Methodology

The flowchart for the entire ALTMS and the experimental setup of the SPHAMS of the FastResponse are shown in Fig. 2 and Fig. 3 respectively.

All the important components and their purpose of use in the FastResponse system are summarized in Table 1.

The heart rate and body temperature of 65 volunteers are tested by using our designed SPHAMS whose demographics are listed in Table 2.

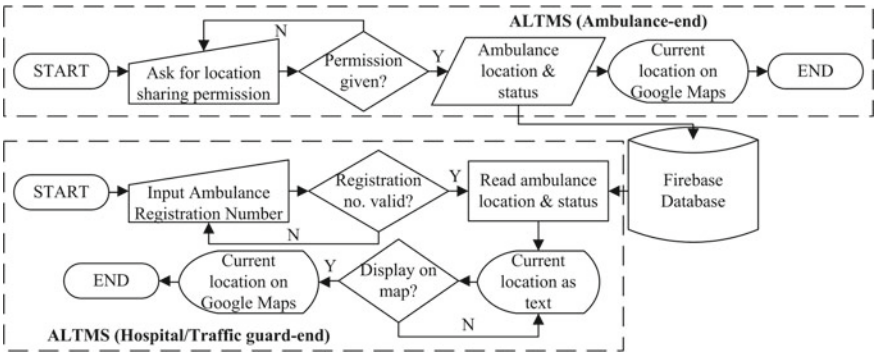

Fig. 2 Flowchart for the working of the ALTMS of the proposed FastResponse system

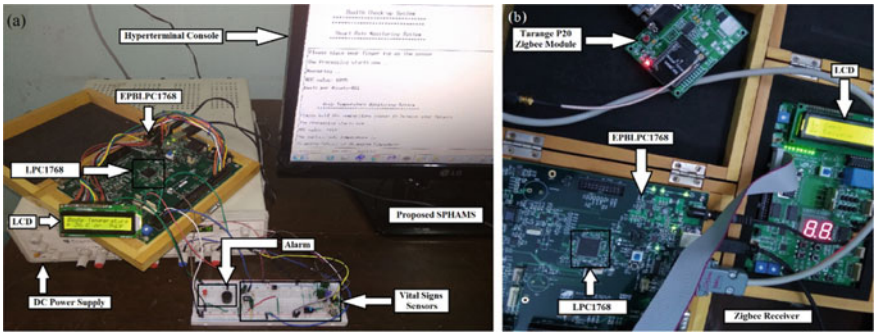

Fig. 3 The experimental set-up of the **a** proposed SPHAMS and **b** Zigbee receiver for remote monitoring

4 Results and Discussion

The performance of the SPHAMS is analyzed by comparing it with the data validated by a registered medical practitioner [heart rate (HR) measured from the radial artery and body temperature (BT) measured using a digital thermometer]. Both the PPP were measured after resting in a sitting position for 10 min in a room of ambient temperature of 32–34 °C.

4.1 Smart Pre-hospital and Ambulatory Monitoring System (SPHAMS)

The performance of the SPHAMS is analyzed based on the ROC curves both for the HR and BT measurements. The threshold values for "Healthy"and "Unhealthy"data of both HR and BT measurements are portrayed in Fig. 4.

Table 1 Hardware and software tools used in the proposed FastResponse system

Tools used	Type	Purpose of use
TCRT5000 IR optical sensor [6]	Hardware	Senses the heartbeats using rPPG
LM35 temperature sensor [7]	Hardware	Senses the body temperature
LPC1768 [8]	Hardware	ARM Cortex M3 architecture-based embedded processor chip
Educational practice board EPBLPC1768	Hardware	EPB with the embedded processor chip LPC1768 used during the experimental study
Eclipse Kepler 4.3 IDE (Integrated Development Environment)	Software	Compiles and executes codes written in embedded C
Flash Magic	Software	Downloads code in the EPB for working in the stand-alone mode
16 × 2 LCD	Hardware	Locally displays vital signs' data
Hyperterminal console	Software	Locally displays vital signs' data on the computer's console (used only for experimental purposes)
Red LED & Piezo Buzzer	Hardware	Warning for abnormal vital signs
Tarang P20 Zigbee module [9]	Hardware	Modules that transmit or receive the vital signs' data using the Zigbee communication link
Visual Studio Code	Software	Open-source editor for the code of ALTMS in HTML5
Firebase	Software	Online real-time database for a live location update
An internet-enabled device with compatible browser, like, Chrome, Mozilla, Safari, Edge, etc.	Embedded system	ALTMS, both at ambulance-end and remote-end, is accessed from and displayed here

Table 2 Demographics of volunteers whose data were measured for validating the SPHAMS

Vital parameter measured	Age group	Sex [number of volunteers]
Heart rate (HR)	20–52 years	Male [35] and female [20]
Body temperature (BT)	20–48 years	Male [7] and female [3]

According to the American Heart Association (AHA), a person's resting heart rate is almost unaffected by age though it varies with the sex of a person [12]. The heart rate depicting "Below Average"and "Poor"heart conditions are considered as "Unhealthy". The body temperature measured from the wrist of the hand is 35.5 °C at 34 °C ambient temperature. However, the effect of the ambient temperature will be more prominent and surface body temperature will be lower when the measurement is taken from a body part far away from the core of the body. Since SPHAMS takes the measurements from the fingertip, the maximum normal body temperature is 36.2 °C at 34 °C ambient temperature. This threshold temperature has been stated in

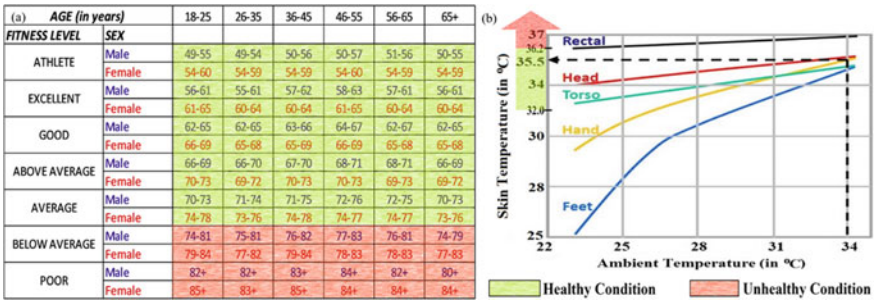

(a) AGE (in years)		18-25	26-35	36-45	46-55	56-65	65+
FITNESS LEVEL	SEX						
ATHLETE	Male	49-55	49-54	50-56	50-57	51-56	50-55
	Female	54-60	54-59	54-59	54-60	54-59	54-59
EXCELLENT	Male	56-61	55-61	57-62	58-63	57-61	56-61
	Female	61-65	60-64	60-64	61-65	60-64	60-64
GOOD	Male	62-65	62-65	63-66	64-67	62-67	62-65
	Female	66-69	65-68	65-69	66-69	65-68	65-68
ABOVE AVERAGE	Male	66-69	66-70	67-70	68-71	68-71	66-69
	Female	70-73	69-72	70-73	70-73	69-73	69-72
AVERAGE	Male	70-73	71-74	71-75	72-76	72-75	70-73
	Female	74-78	73-76	74-78	74-77	74-77	73-76
BELOW AVERAGE	Male	74-81	75-81	76-82	77-83	76-81	74-79
	Female	79-84	77-82	79-84	78-83	78-83	77-83
POOR	Male	82+	82+	83+	84+	82+	80+
	Female	85+	83+	85+	84+	84+	84+

Fig. 4 Analysis and decision data (with threshold values) for **a** heart rate (HR) [10] and **b** body temperature (BT) [11] measurement

many previous works of literature including a study by Chen et al. [13]. In case, the recorded temperature is higher than 36.2 °C at 34 °C ambient temperature, the person may be suffering from fever, and hence classified as "Unhealthy".

Using Fig. 4, the decision matrices for both the HR and BT are determined (Fig. 5) and used to plot their respective ROC curves (Fig. 6). The decision matrices have manually measured data (by registered medical practitioner) along the horizontal row and the SPHAPMS measured data along the vertical column.

The performance of the SPHAMS is judged by using different metrics given in Table 3. The area under the curve (AUC) for the given ROC plots give the respective PPP's error-free measurement percentages, when measured by our proposed system.

(a)

	$(\text{Unhealthy})_M$	$(\text{Healthy})_M$
$(\text{Unhealthy})_S$	True Positive (TP) [34]	False Positive (FP) [4]
$(\text{Healthy})_S$	False Negative (FN) [1]	True Negative (TN) [16]

(b)

	$(\text{Unhealthy})_M$	$(\text{Healthy})_M$
$(\text{Unhealthy})_S$	True Positive (TP) [2]	False Positive (FP) [0]
$(\text{Healthy})_S$	False Negative (FN) [1]	True Negative (TN) [7]

Fig. 5 Decision matrices for the ROC plot of **a** HR sensor and **b** BT sensor of SPHAMS

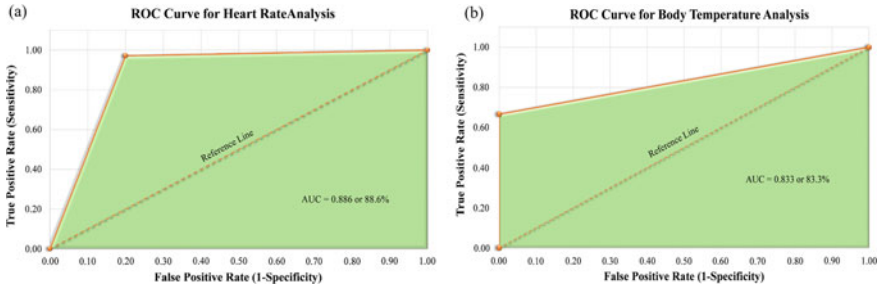

Fig. 6 ROC plots for the vital signs data collected by the **a** HR sensor and **b** BT sensor of the SPHAMS

Table 3 The performance analysis of the SPHAMS

Performance metrics	HR monitoring system	BT monitoring system
Sensitivity or true positive rate or recall	0.971	0.667
Specificity or true negative rate	0.800	1.000
False positive rate or (1—specificity)	0.200	0.000
Positive likelihood ratio	4.857	∞
Negative likelihood ratio	0.036	0.333
Positive predictive value or precision	0.895	1.000
Negative predictive value	0.800	0.875
F1 score	0.932	0.800
Kappa (κ)	0.797	0.737
Area under the curve (AUC) (from the ROC curve of Fig. 6)	0.886	0.833
Overall accuracy (at the optimal cut-off point of the ROC curve)	0.909	0.900

The cutoff point on the ROC plots is obtained at a point where both sensitivity and specificity are maximum after a trade-off between them. This point helps us to determine the accuracy of our system's measurement.

4.2 Ambulance Live Tracking and Management System (ALTMS)

The output of the ALTMS program when displayed in a web browser is depicted in Fig. 7. Figure 7a–c shows the various stages of tracking of a registered ambulance from the remote-end (hospital, traffic guard, etc.) while Fig. 7d shows the live location of the ambulance from its end.

5 Conclusion

In this paper, we present FastResponse, a cost-effective embedded system, with low power consumption, which accurately measures two vital signs of a person and also tracks an ambulance continuously. FastResponse provides an easy and accurate way for pre-hospital monitoring of a person's vital signs at the disaster/accident site or inside an ambulance on his/her way to the hospital. It can monitor, update and warn a paramedic/doctor. It will be highly beneficial for the local paramedics to identify the most critical victims, who must be hospitalized immediately. The live update of the patient's vital signs and location, journeying towards the hospital, help in the

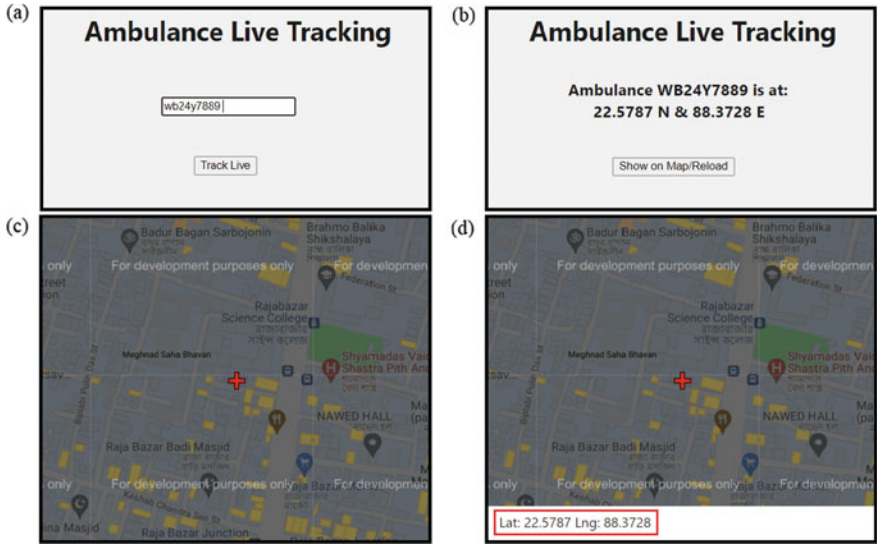

Fig. 7 ALTMS's live ambulance tracking from **a**–**c** Remote-end and **d** Ambulance-end (In **c** and **d**, the ambulance location is marked by the red plus symbol)

preparation for his/her treatment at the hospital. The proposed system can thus reduce the pressure on the ambulance services since there is a shortage of ambulances in India, especially in rural areas. The ROC plots in both these cases imply the SPHAMS can predict both the vital signs of a person accurately in more than 80% of cases. The statistical analysis of the collected data shows that the system has sufficient sensitivity, specificity, precision and accuracy to be appropriately used as a medical device.

The system is flexible enough to incorporate other vital sign monitoring sensors like blood pressure, blood oxygen saturation, respiration rate, etc. along with existing sensors for a complete health check-up. The ALTMS can further be extended in finding the nearest hospital, setting up a "green corridor", etc. for faster transport of the victims to the nearest hospital. This can increase the chances of the victims' survival by about 50%.

5.1 Novelty of the Proposed Work

The proposed work brings together remote patient health monitoring and ambulance live tracking and fleet management to provide a complete self-sufficient environment for ambulatory patient monitoring. The proposed work aims to have the fastest response to any accident or disaster victim and save lives by providing medical care at the earliest. The novelties of this work include:

Table 4 The comparative performance analysis of the proposed SPHAMS with commercially available monitors (MAE = Maximum average Error; MAPE = Maximum Average Percentage Error)

Health monitors	MAE	MAPE	Sensitivity	Specificity	AUC
HR of SPHAMS	2.57 bpm	3.26%	0.971	0.800	0.886
BT of SPHAMS	0.25 °C	0.70%	0.667	1.000	0.833
Non-contact IR thermometer (measurement from wrist) [13]	–	–	0.864	0.67	0.790
Apple Watch Sport 42 mm [14]	6.34 bpm	10.69%	–	–	–

- The HTML5 API tracks the live location using any means available, including GPS, wifi network, cell tower, etc., which gives a better prospect of accurate tracking under a variety of circumstances.
- It gives a location accuracy up to the street level at least and in case of availability of GPS, it can track up to the closest landmark/building.
- The delay in tracking the ambulance's location at the remote-end is less than 5 ms, which includes the delay in locating the vehicle at the ambulance-end, uploading this location along with the patient status in the ambulance (with or without patient) to the Firebase database, downloading this information at the remote-end and displaying the ambulance's marker on the map.
- The highly secure location sharing in ALTMS made it dependent on the ambulance's discretion to allow the API to check and update its location.
- Extensive information about hospitals, rigorous database management and association with the local traffic authorities to set up a "green corridor".
- The statistical performance comparison of the SPHAMS with previous works of literature is given in Table 4.

Acknowledgements The authors would like to thank UGC UPE II, "Modern Biology Group B: Signal Processing Group", University of Calcutta for providing research facility and technical support.

References

1. MoHFW: Quarterly NHM MIS Report: National Overview (2020). https://nhm.gov.in/index4.php. Accessed 31 Oct 2020
2. Rajya Lakshmi, P.N., Venkatesan, P., Prasad, R.G.: Smart watch for healthcare monitoring. Int. J. Eng. Technol. Sci. Res. **5**, 1107–1111 (2018)
3. Munem, A.S.A., Croock, M.S.: Health monitoring system for ambulance emergency system using wireless sensor network. Eng. Technol. J. **34**, 2877–2890 (2016)
4. Lolita, C.M., Roopalakshmi, R., Pais, S.L., Ashmitha, S., Banu, M., Akhila: IoT-based patient remote health monitoring in ambulance services. In: Smys, S., Bestak, R., Chen, J.Z., Kotuliak, I. (eds.), International Conference on Computer Networks and Communication

Technologies. Lecture Notes on Data Engineering and Communications Technologies, vol. 15 (2019). Springer, Singapore, pp. 421–429
5. Ghosh, M., Basu, S., Pandit, S., Barman (Mandal), S.: Design of a health monitoring system for heart rate and body temperature sensing including embedded processing using ARM Cortex M3. In: Das, A., Nayak, J., Naik, B., Pati, S., Pelusi, D. (eds.), Computational Intelligence in Pattern Recognition. Advances in Intelligent Systems and Computing, vol. 999 (2020). Springer, Singapore, pp. 93–103
6. Vishay Semiconductors: Reflective optical sensor with transistor output (2009). https://www.vishay.com/docs/83760/tcrt5000.pdf. Accessed 12 Sept 2018
7. Texas Instruments: LM35 precision centigrade temperature sensors. http://www.ti.com/lit/ds/symlink/lm35.pdf (2017). Accessed 16 Sept 2018
8. Nxp Semiconductors: UM10360 LPC176x/5x User manual Rev. 4 (2016). https://www.nxp.com/docs/en/user-guide/UM10360.pdf. Accessed 30 Nov 2018
9. Melange Systems Pvt. Ltd.: Tarang PTM product manual (2011). https://fccid.io/N3Y-TARANG-P20/User-Manual/Manual-1723546.pdf. Accessed 10 Jan 2020
10. Wood, R.: Resting heart rate measurement (2008). https://www.topendsports.com/testing/heart-rate-resting.htm. Accessed 13 June 2019
11. Denton, E.: Learn how to measure body temperature accurately and cost effectively (2015). http://www.ti.com/lit/ml/slyw051/slyw051.pdf. Accessed 6 Dec 2020
12. American Heart Association: All about heart rate (Pulse) (2015). https://www.heart.org/en/health-topics/high-blood-pressure/the-facts-about-high-blood-pressure/all-about-heart-rate-pulse. Accessed 21 May 2018
13. Chen, G., Xie, J., Dai, G., Zheng, P., Hu, X., Lu, H., et al.: Validity of wrist and forehead temperature in temperature screening in the general population during the outbreak of 2019 novel coronavirus: a prospective real-world study. MedRxiv (in press) (2020)
14. Falter, M., Budts, W., Goetschalckx, K., Cornelissen, V., Buys, R.: Accuracy of Apple Watch measurements for heart rate and energy expenditure in patients with cardiovascular disease: cross-sectional study. J. Med. Internet Res. **7**(3), e11889 (2019)

A Performance Analysis of a Photo Voltaic Array Under Different Temperature Conditions and Semiconductor Materials

Arpan Ghatak and Bidhan Malakar

Abstract This paper presents a comparative analysis on the effect of different environmental temperature conditions to study the relationship between the generation of output power and voltage of a Photo Voltaic (PV) array. This work also discusses some important parameters like open-circuit voltage (VOC), short-circuit current (ISC) that can affect the output power of PV cells. Apart from this, the paper considers most importantly the bandgap of semiconductor material used in a PV cell, which also affects the performance of PV cells. The results of this study show that the performance of the PV cell depends on the proper adjustment of these parameters and should be considered carefully.

Keywords Photo voltaic (PV) array · Short-circuit current · Bandgap · Temperature

1 Introduction

Various types of renewable energy sources are available on this earth like wind energy, biomass energy, tidal energy, geothermal energy, solar energy, etc. Above all of these energy resources, solar energy has gained its reputation because it is easily available, requires low maintenance cost and most importantly it is totally eco-friendly as the power source of this energy is the sunlight [1, 2]. However, this solar energy comprises a PV cell, which is a current source and this PV cell produces electricity which is the powerhouse for driving various electrical equipment [2]. To get continuous power, which is the most essential requirement in these recent days, solar energy might be the solution for the world. There are several factors that can affect the performance of a PV cell. The generated electrical power, by the PV cell is dependent upon various factors like solar irradiance, environmental temperature, series and shunt resistance, etc. [3].

A. Ghatak (✉) · B. Malakar
Department of Electrical Engineering, JIS College of Engineering, Kalyani, Nadia, West Bengal 741235, India

B. Sikdar et al. (eds.), *Proceedings of the 3rd International Conference on Communication, Devices and Computing*, Lecture Notes in Electrical Engineering 851,
https://doi.org/10.1007/978-981-16-9154-6_24

There are basically two types of PV cell models available in the market, they are single—diode and two–diode models. There is another type of PV cell is used by some researchers, which is Dye-Sensitized Solar Cell (DSSC), and this type of cell generally uses chlorophyll A and chlorophyll B for casing the semiconductor, but these pigments are not so correct to convert solar energy to electricity [4]. Out of these models, the most preferred model is the single–diode model. It includes a series resistance and a shunt resistance, a diode, and most importantly a power source [5]. The series resistance is introduced in order to produce a perfect shape in between MPP (Maximum PowerPoint) and the open-circuit voltage (V_{OC}) [6] and the shunt resistance to improve the temperature sensitivity of that PV module [7–9]. In every PV cell, there is always an MPP, in which the maximum power for that particular PV cell is formed [10].

Basically, the PV cell is a p–n junction made of different semiconductor materials like silicon, selenium, etc. and each of them has a different bandgap. This bandgap plays a very important role in determining the efficiency of PV cells [11]. This Section analyses the effect of band gap for different semiconductor materials under different environmental temperature conditions.

After the introduction, Sect. 2 provides the Modelling of PV cells under different temperature conditions with a block diagram and after that, we can find the Results and Discussions part to analyze the effect of different temperature conditions of PV cells in Sect. 3. The conclusion part is added in Sect. 4.

2 Modelling of PV Cell Model Under Different Temperature Conditions

A mathematical model based on the below-mentioned equations [12, 13] is done in this Section to model the PV cell in SIMULINK.

We know that,

$$I_D = I_S - \left\{\exp\hat{}[(q(V + I_T * R_{Se})/BK\alpha] - 1\right\} \tag{1}$$

$$I_{sh} = (V + I_T * R_{se})/R_{sh}, \tag{2}$$

$$I_T = I_{Ph} - I_S\{\exp[q(V + I_T * R_{se})/BK\alpha] - 1\} - (V + IT * Rse)/Rsh \tag{3}$$

In this section, a SIMULINK model for a 72 solar cell connected in series is developed. Here, solar irradiance of 1000 W/sq.m is considered as PS constant and different values of temperature are considered here to obtain different values of voltage, current, and output power from the PV cell. The block diagram of the model is shown in Fig. 1 which shows the relationship between the output power of a solar cell with environmental temperature conditions.

This block diagram is used to obtain the simulation model and is further used to plot various characteristics. These are related to the output current, voltage, and generated power. It is mainly done to investigate the effect of temperature and bandgap of different semiconductor materials used in PV cells. The detailed analysis is discussed in the next section.

3 Results and Discussions

3.1 Results

It can be seen from the above Section that environmental temperature plays an important role in the generation of the power of a PV module. But there is another vital parameter that can also affect the output of a PV cell, which is the bandgap of the semiconductor material. In this section, the effect of bandgap and temperature on the output parameters like maximum voltage, current, and power of a PV cell is studied and is arranged in Table 1.

From this previously mentioned Table, it can be clearly observed that the different temperature conditions and different band gaps affect the performance of a PV cell.

It can also be observed from this Section that, environmental temperature is an influential factor in the output power of a PV module. Now a comparative study is conducted on the effect of temperature which also affects the output parameters like V_{OC}, I_{SC}, maximum power (Pmax) of a solar cell. From the below-mentioned Table 2, it is clearly visible that, the output power of the proposed model is far better

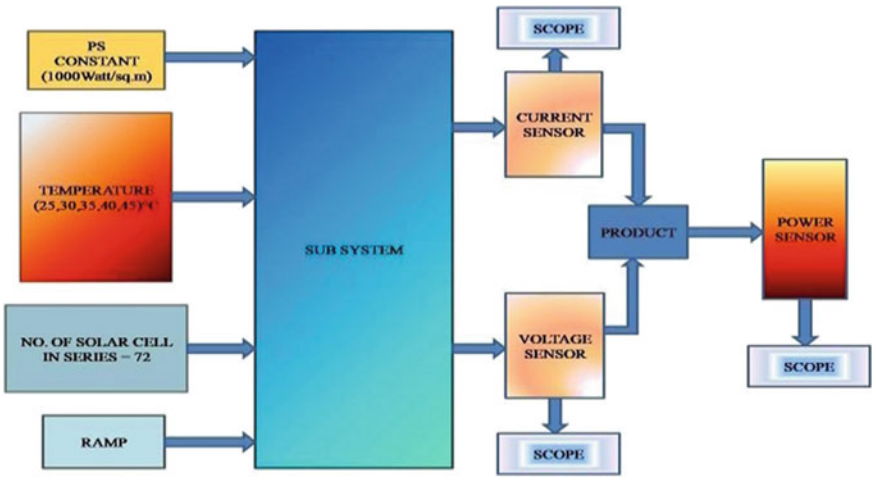

Fig. 1 Block diagram of solar array simulation model

Table 1 Maximum power (Pmax), average Pmax for different temperatures and bandgap of different semiconductor

Sl. No.	Semiconductor	Band gap (ev)	Temperature (°C)	Maximum power (P_{max}) (W)	Average Pmax
1	Silicon (Si)	1.11	25 30 35 40 45	244.73 239.47 234.21 226.31 221	233.145 W
2	Copper oxide (CuO)	1.20	25 30 35 40 45	242.85 238.09 230.95 226.19 219.04	231.424 W
3	Indium Phosphide (InP)	1.35	25 30 35 40 45	244.73 236.84 228.94 221.05 213.15	228.942 W
4	Gallium Arsenide (GaAs)	1.43	25 30 35 40 45	245 237.5 227.5 220 212.5	228.5 W
5	Cadmium Telluride (CdTe)	1.49	25 30 35 40 45	245 235 227.5 217.5 210	227 W
6	Cadmium Selenide (CdSe)	1.73	25 30 35 40 45	242.5 232.5 222.5 212.5 202.5	222.5 W
7	Selenium (Se)	1.74	25 30 35 40 45	242.85 233.33 223.80 211.90 202.38	222.852 W

than the previous work [14], even in the same short-circuit current and for the same semiconductor material also.

From this above-mentioned Table 2, it is clearly visible that how different temperatures and short-circuit current can affect the output voltage and power of a PV cell.

Table 2 Maximum power (Pmax) for different temperatures and short-circuit current

Sl. No.	Semiconductor material	Band gap (ev)	Short-circuit current (Isc) (amp)	Temperature compared (°C)	Maximum power (Pmax) (watt)	Remarks
1	Silicon (Si)	1.11	4.75	30	147.12	Output power of proposed work is greater
Reference						
[14]				40	141.39	
2 Proposed work	Silicon (Si)	1.11	4.75	30	155	
				40	147.5	
			7.34	30	239.47	
				40	226.31	

In the below-mentioned figures, we can easily understand the variation of current, voltage, and power for different temperatures of different semiconductors. From the below-mentioned Fig. 2, the comparative analysis can be clearly observed by the plotted graph, which is below mentioned.

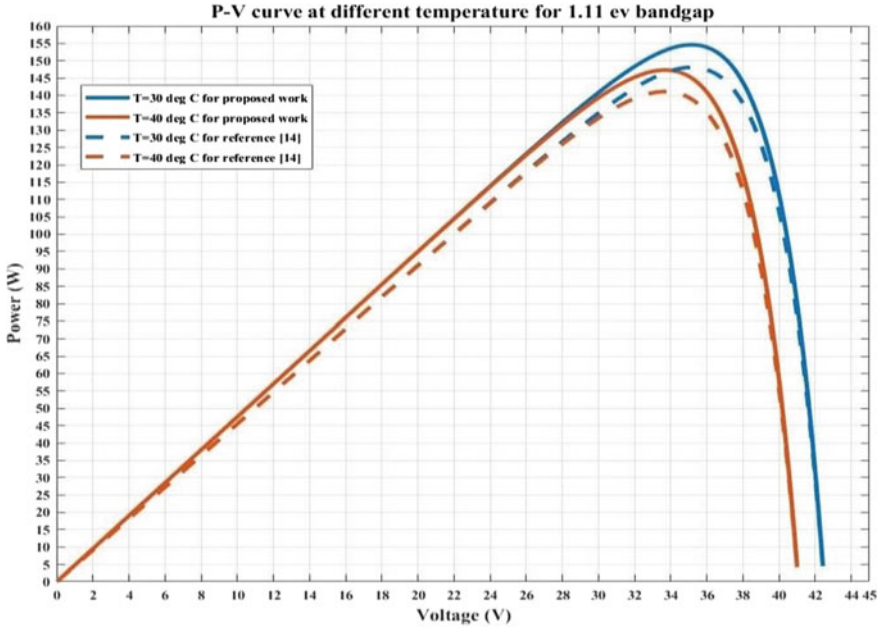

Fig. 2 P–V curve of a comparative analysis with the reference [14] at different temperature

3.2 Discussions

So, from the above-mentioned Table 1 and Figs. 3 and 4, it can be easily understandable that:

Silicon semiconductor with a bandgap of 1.11 eV, generate the maximum power (Pmax) of 244.73 W, maximum voltage (Vmp) of 36.66 V at STC (25 °C) and maximum current (Imp) of 7.05 amp and average Pmax of 233.145 W.

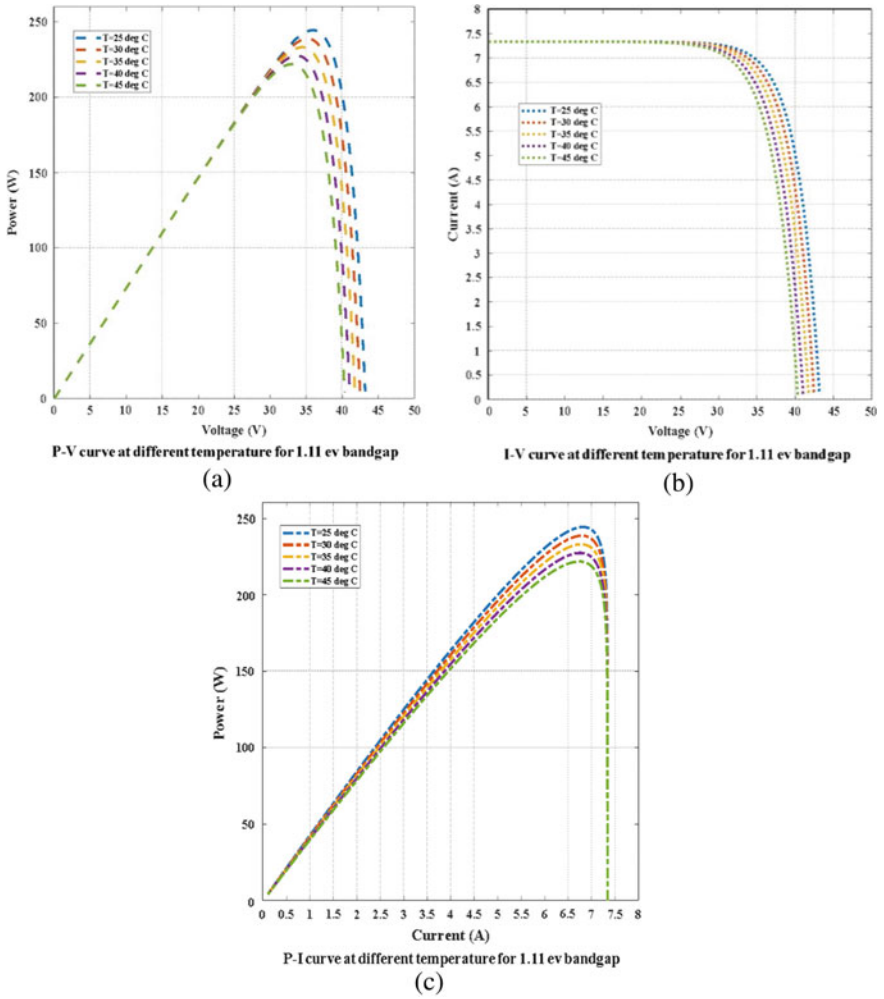

Fig. 3 **a** P–V curve, **b** I-V curve **c** P-I curve of proposed work at 7.34 amp short-circuit current for 1.11 eV bandgap

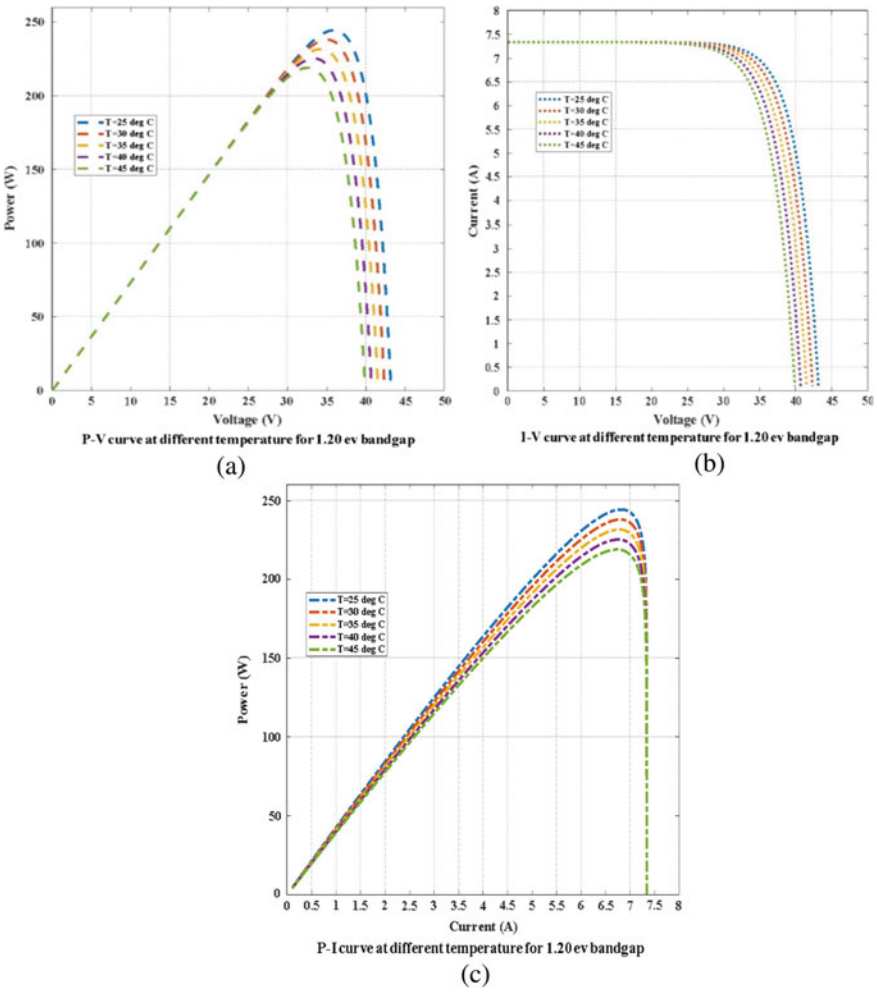

Fig. 4 **a** P–V curve **b** I-V curve, **c** P-I curve of proposed work at 7.34 amp short-circuit current for 1.20 eV band gap

Copper oxide with the bandgap of 1.20 eV, produces the Pmax of 242.85 W and Vmp of 36.38 V at STC and maximum current (Imp) of 6.74 amp. It will produce an average Pmax of 231.424 W.

Indium phosphide with the bandgap of 1.35 eV can produce the Pmax of 244.73 W, Vmp of 36.38 V at STC, and maximum current (Imp) of 6.73 amp and average Pmax of 228.942 W.

From the above-mentioned Table 2 with Fig. 2 it can be easily understandable that:

Silicon semiconductor with a bandgap of 1.11 eV can produce the maximum power (Pmax) of 155 W and 147.5 W, at 30 °C and 40 °C temperatures respectively at 4.75 amp short-circuit current.

This comparative analysis is based on the work reported by F.E. Tahiri et aI. [14], and also the results are compared with [14].

It is observed that there is an improvement of [(155–147.12)/147.12] × 100 = 5.35% in the parameter Pmax at 30 °C temperature, and [(147.5–141.39)/141.39] × 100 = 4.32% at 40 °C temperature when compared with the earlier reported work [14].

4 Conclusions

A brief parametric study and a comparative analysis is done for a PV array of 72 cells connected in series on different temperature and various semiconductor materials and simulated in MATLAB/SIMULINK by varying different parameters. It can also be observed that an improvement of 5.35% and 4.32% in the parameter Pmax at 30 °C and 40 °C temperature respectively when compared with the earlier reported work [14].

References

1. Jiang, J., Huang, T., Hsiao, Y., Chen, C.: Maximum power tracking for photovoltaic power systems. Tamkang J. Sci. Eng. **8**(2), 147–153 (2005)
2. Abderezak, L., Aissa, B., Hamza, S.: Comparative study of three MPPT algorithms for a photovoltaic system control. IEEE (2015)
3. Dera, D., Kerekes, T., Teodorescu, R., Blaadjerg, F.: Improved MPPT algorithms for rapidly changing environmental conditions. Power Electronics and Motion Control Conference 2006. EPE-PEMC (2006)
4. Ali Zakar, A.M., Naman, S.A., Ahmed, S.M.: Improvement of the efficiency of dyed mono crystalline silicon solar cell by covering it with natural plants pigments. 2019 International Conference on Advanced Science and Engineering (ICOASE), pp. 230–235. Zakho, Duhok, Iraq, (2019)
5. Abdelsalam, A.K., Massoud, A.M., Ahmed, S., Enjeti, P.N.: High performance adaptive perturb and observe MPPT technique for photovoltaic-based microgrids. IEEE Trans. Power Electron. **26**(4), 1010–1021 (2011)
6. Tan, Y.T., Kirschen, D.S., Jenkins, N.: A model of PV generation suitable for stability analysis. IEEE Trans. Energy Convers. **19**(4), 748–755 (2004)
7. Tian, H., Mancilla-David, F., Ellis, K., Muljadi, E., Jenkins, P.: Detailed Performance Model for Photovoltaic Systems: Preprint, p. United States, N. (2012) Web
8. Krishan, R., Sood, Y.R., Kumar, B.U.: The simulation and design for analysis of photovoltaic system based on MATLAB. 2013 International Conference on Energy Efficient Technologies for Sustainability, pp. 647–651. Nagercoil, (2013)
9. Busacca, A.C., et al.: Parametrical study of multilayer structures for CIGS solar cells. 2014 International Conference on Renewable Energy Research and Application (ICRERA), pp. 964–968. Milwaukee, WI (2014). https://doi.org/10.1109/ICRERA.2014.7016528

10. Wasynczuk, O.: Dynamic behavior of a class of photovoltaic power systems. IEEE Trans. Power Apparatus Syst. **PAS-102**(9), 3031–3037 (1983)
11. http://solarcellcentral.com/junction_page.html
12. Rai, A., Awasthi, B., Dixit, A., Dwivedi, C.K.: Modeling of solar photovoltaic module and study parameter variation effect using MATLAB/Simulink. In Proceeding International Conference IEEE Control, Computer Communication Materiaux, pp. 1–6 (2016)
13. Rezk, H., Hasaneen, E.-S.: A new MATLAB/Simulink model of triple- junction solar cell and MPPT based on artificial neural networks for photovoltaic energy systems. AIN Shams Eng. J. **6**(3), 873–881 (2015)
14. Tahiri, F.E., Chikh, K., Khafallah, M., Saad, A., Breuil, D.: Modeling and performance analysis of a solar PV power system under irradiation and load variations. 2017 14th International multi-conference on systems, signals & devices (SSD), pp. 234–238. Marrakech, (2017)

COVID-19 Data Forecasting Using Soft Computing Technique

Arindam Roy, Dharmpal Singh, and Sudipta Sahana

Abstract Corona viruses are large family of viruses that may affect human and animals. Middle East respiratory syndrome (MERS) and severe acute respiratory syndrome (SARS) are the respiratory infections caused by several corona viruses in human. COVID-19 is an infectious disease due to most recently discovered Corona virus. This Corona Virus Disease (COVID-19)'s outbreak was started from Wuhan, China in December 2019. The disease can spread from one person who has the virus to another person who is not infected. This is how the outbreak began and became a pandemic. This pandemic has become the biggest problem in the world. Number of infected and deaths are gradually increasing throughout the world. This effort is to analysis the graph and determine that when the graph will go down. Basically, we will make the prediction using some a time series forecasting techniques based on neural network.

Keywords COVID-19 · Time series forecasting · Neural network · NAR · Soft computing

1 Introduction

Corona viruses or we can say a RNA viruses are of family Coronaviridae. Among four genera of corona virus, beta corona virus can be further divided into two groups. Severe acute respiratory syndrome corona virus (SARS-CoV) and Middle East respiratory syndrome corona virus (MERS-CoV) are the types of beta corona. Among these two, SARS-CoV is the currently affected virus [1, 2]. WHO named this disease 2019-n CoV originated from Wuhan, China. However outbreak of corona virus disease or COVID-19 has tilted the normality of the whole world. Not only people

A. Roy (✉)
Department of Computer Science and Engineering, Surendra Institute of Engineering and Management, Siliguri, Darjeeling 734009, India

D. Singh · S. Sahana
Department of Computer Science and Engineering, JIS College of Engineering, Kalyani, Nadia 741235, India

B. Sikdar et al. (eds.), *Proceedings of the 3rd International Conference on Communication, Devices and Computing*, Lecture Notes in Electrical Engineering 851,
https://doi.org/10.1007/978-981-16-9154-6_25

were killed in COVID-19 virus incursion, the disease broke the economy of the world. Developing countries suffered due to hunger and unemployment. Our country becomes second affected country in the world. It became very important to analyse the cases and the graph to predict the future of the country. These are the reason behind the selection of this work. It was Kerala; the state was reported first COVID-19 case as per the government data. Victim disclosed that she returned from Wuhan, China. Two more cases were reported in next two days and 14 cases in a month. Overtime, the states like Telengana, Delhi, Rajasthan were reported with COVID-19-affected patients. Day by day, the graph of COVID-19 cases were increasing throughout the country. However, the graph takes a high peak at June–August 2020. The effort is to analyse the COVID-19 cases of India based on the records of daily cases. Analysing all reports, we made a graph. Along with the graph, a forecasted result was made using multiple soft computing techniques. The paper will represent the techniques that are quite easy but effective in the field of prediction and analysis.

2 Literature Review

Nowadays, forecasting using several soft computing modes is widely used by the scientists in many areas. Lots of soft computing models are present in the market. Among all, fuzzy logic and artificial neural network are most popular in the field of predictions.

Dharmpal Singh et al. published a study on exported mangoes quantity, where it has been clearly stated that the performance of fuzzy logic for the purpose of assessment is undoubtedly good [2]. This model is treated as a simple soft computing model also. In another report, Arindam Roy et al. had mentioned that neural network performs slightly better for an assessment or for prediction [3]. These two papers left a scope for doing further analysis on forecasting. They have predicted on a topic of their preference. The techniques can be further implemented in medical field and in many other purposes. That is why the effort was to make this prediction using artificial neural network to get an idea of the COVID-19 cases rise and fall.

It is seen in literature that the time series has a wide application in scientific area. Meanwhile, time series forecasting using ANN becomes a hot topic nowadays. Luis Gonzaga emulated multiple neural network time series forecasting techniques with basic differentiation between NAR and NARX [4]. The paper addresses the problems of neural network over the prediction of energy consumption. Author introduces nonlinear autoregressive techniques to deliver good result. In another research, Caswell proposed a NAR approach for statistical prediction of storm using solar data [5]. Kirbas mentioned in his publication that nonlinear autoregressive NN forecasts a time series using past values [6]. As per the author, advanced study in artificial intelligence shows that artificial neural networks may be more successful than well-known statistical approaches in pattern recognition and forecasting. The motivations and the knowledge gathered from this research work made our project and the study successful.

3 Methodology

There are lots of soft computing techniques available in market for forecasting. We are basically focusing on artificial neural network to make this prediction-based analysis. The methods that has been used for the project, is listed here.

3.1 Artificial Neural Network (ANN)

A neural network is inspired by biological nervous systems; it is a combination of multiple processing layers, using simple elements operating in parallel. ANN basically works with one or more hidden layers, where it takes input using an input layer and result is generated from output layer. These layers are consists of several nodes, known as neurons. Neurons interconnect the different layers, connecting the each layers output with next layer Input. There is another factor called weight of neurons. Each neuron typically has weights. These weights are adjusted during the learning process. Weight decrease or increase changes the strength of the signal of that particular neuron. ANN has a number of effective applications; it includes the use of neural network on disease, GDP, weather prediction, image processing etc. As ANN works creating knowledge base based on past data to build new decision and predict with more accuracy that is why it is suitable on such applications.

3.2 Time Series Forecasting

Forecasting is a process of taking historical data to predict future observations. A time series is a series of data points that is listed or graphed in time order, which is most commonly a sequence with successive equally spaced points in time. Thus, it is widely used for economic data, weather data, stock-price data and other non-stationary data. In health science, this technique is also very popular.

If we look for time series forecasting, then artificial neural network is definitely one of the most successful techniques. It has been used into major investigative works. As a simple search in SCOPUS chains with “Time Series Forecasting” or “Time Series” or “Neural Network,” we can find more than 4000 reported documents, some of among them are irrelevant, but most are the appropriate [7]. For the application of time series forecasting, some popular techniques are nonlinear autoregressive neural network (NAR), nonlinear autoregressive exogenous neural network (NARX), recurrent neural network (RNN), autoregressive integrated moving average (ARIMA) etc. For forecast, RNN model does not need past time series values and delays, NAR and NARX model use these parameters though [8, 9]. The section below contains a discussion on NARNN as the technique plays major role in this project.

3.2.1 Nonlinear Autoregressive (NAR) Neural Network

Artificial neural network (ANN) simulates the human that gains knowledge from the past experiences. It is examined that the time series has a wide application area. For this reason, it has a great influence on researches. Nonlinear autoregressive neural networks (NARNN) are one of the simplest techniques which is designed to forecast a time series from past values [10]. NAR-based networks can be used to train and predict future values. Each network model has their own benefits and costs, where NARNN methods are simpler than NARXNN and also the cost-efficient model. It uses only time series past values as inputs and trains the network without emulating any target values. This is why the method is being selected for our desired project. However, this requires MATLAB programming language skills. This technique can accept dynamic inputs represented by time series sets, which is again a major benefit where less number of parameters are present in the dataset [11].

A NAR neural network, when it is applied to time series forecasting, describes a discrete, non-linear, autoregressive model [12, 13].

$$Y(t) = h(y(t-1), y(t-2), \cdots, y(t-p)) + \varepsilon(t)$$

The formula describes the use of nonlinear autoregressive neural network, where, the NAR network is used to predict the value of data series Y at t time. $h(.)$ is a function to train the network that aims to approximate the function by optimizing the weights and bias. $y(t)$ is for p numbers of past values of the time series. Last but not the least, $\varepsilon(t)$ is used for error of the approximation at time t [14].

In this study, NARNN is being used to model COVID-19 total cases and to predict the future graphical analysis. The network structure contains total cases as input at a certain time period, and the output is the predicted next day value, i.e., $Y(t)$. The working of the network has been in Fig. 1.

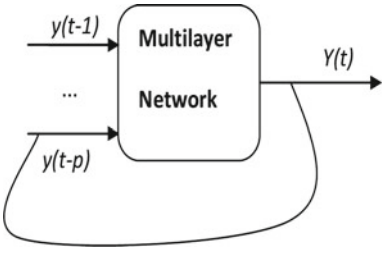

Fig. 1 Non-linear autoregressive neural network

Table 1 Dataset of total confirmed cases in India

Date	Total confirmed cases	Date	Total confirmed cases
30–01–2020	1	30–08–2020	3,542,733
31–01–2020	1	31–08–2020	3,621,245
01–02–2020	2	01–09–2020	3,691,166
02–02–2020	3	02–09–2020	3,769,523

4 Implementation

In this paper, NARNN has been used with the advantage of its simplicity for COVID-19 data forecasting for India. Since, our main study objective is the NAR-based interface, we have to clarify the application introduction first. NAR was developed for MATLAB using the app designer programming environment. MATLAB provides time series neural network inbuilt interface, which has been used for this project reference. The analysis was made with day-wise confirmed cases up to 31 August 2020. As per the dataset, the counting of total daily confirmed cases began from 30 January 2020. The time when the country was mostly having highest number of cases and deaths, it was June–August 2020. It was 19 May 2020, India reached a value of 1 lakh total COVID-19 cases and within 15 days, the count reached 2 lakhs. At the end of August, it reached more than 3.5 lakhs confirmed cases in India, Table 1 shows the corresponding data.

At first glance, these are just some numbers, but it is the main object for this effort. The knowledge base is created where the number of daily cases from the beginning to the end of August has been treated as the input of NAR neural network. The network is trained with Levenberg–Marquardt (trainlm) function and 10 hidden layers for open loop. Best fed result has been taken for more accuracy. The network is shown in Fig. 2.

Now the aim is to forecast the future data. On account of this, closed loop is used for multi-step ahead performance. For the initial test, the network was trained using a closed loop for 1 day ahead prediction. Now, the forecasted result is being checked with the original data for the corresponding day. The result shows the accuracy of the experiment. It satisfies and encourages to do further prediction work. Here, a half monthly assessment is targeted, looking forward to that forecasting. The network was trained again for 2 step ahead result; it was trained repeatedly for the best result up to 15 steps ahead. As a result, we get forecasted data of next 15 days confirmed COVID-19 daily cases, which is up to 15 September 2020.

5 Result Analysis

When working with neural network, best feed with best training and validation returns highest accuracy in result. Figures 3 and 4 show best validation performance of the

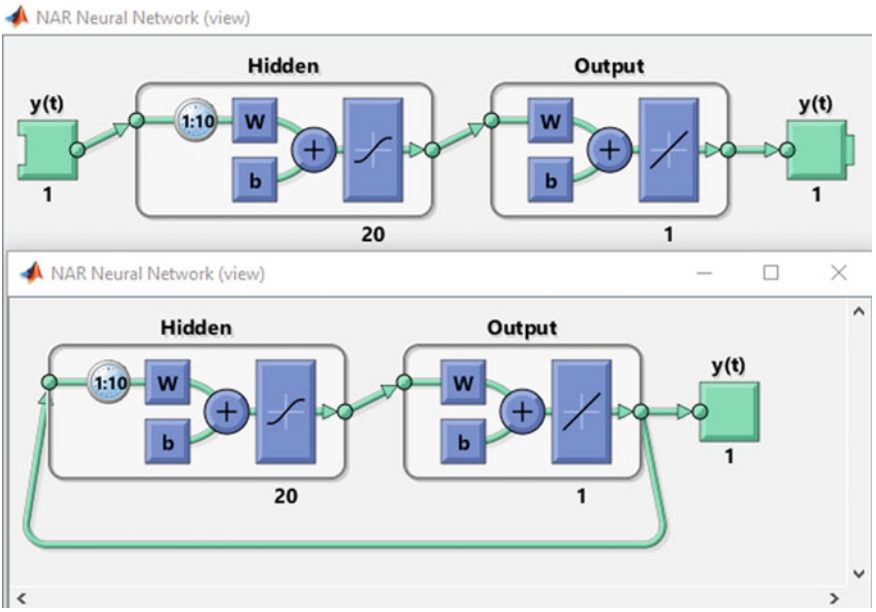

Fig. 2 Network view of open loop and closed loop

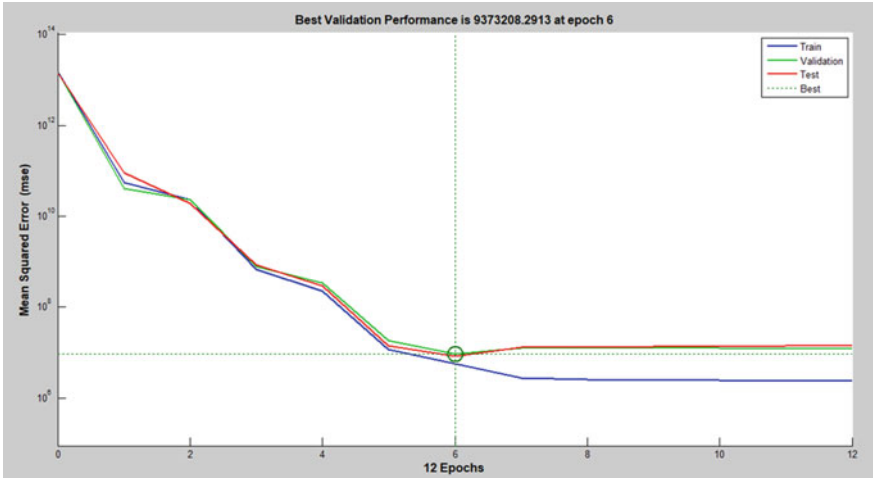

Fig. 3 Best validation performance

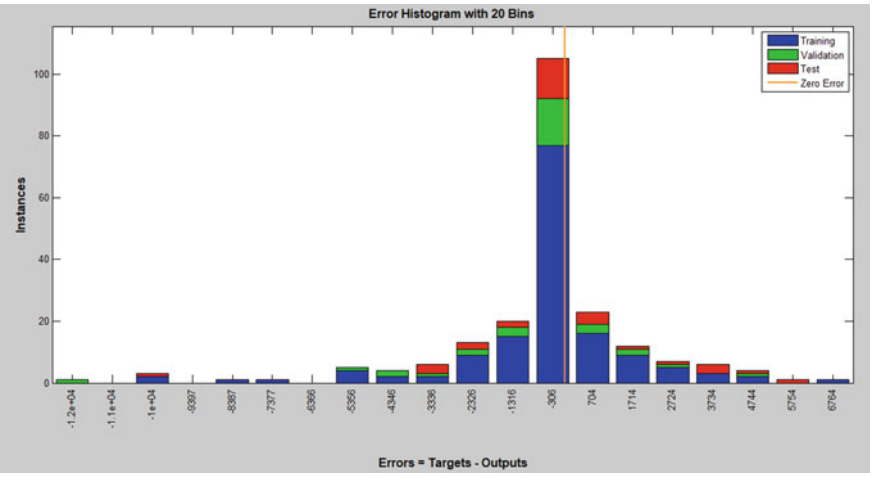

Fig. 4 Error histogram

network for the tested data and error histogram for the first predicted value (i.e., data for 1 September 2020) accordingly.

Figures 5 and 6 show MATLAB-generated graph based on the NARNN forecasted data, where Fig. 5 shows 1 day ahead prediction graph and Fig. 6 shows next 15 days peak. Here, the daily confirmed cases are shown in Y axis with respect to dates.

The table below shows the actual and corresponding forecasted daily confirmed cases, which in turn to an error of 2.036% on average (Table 2).

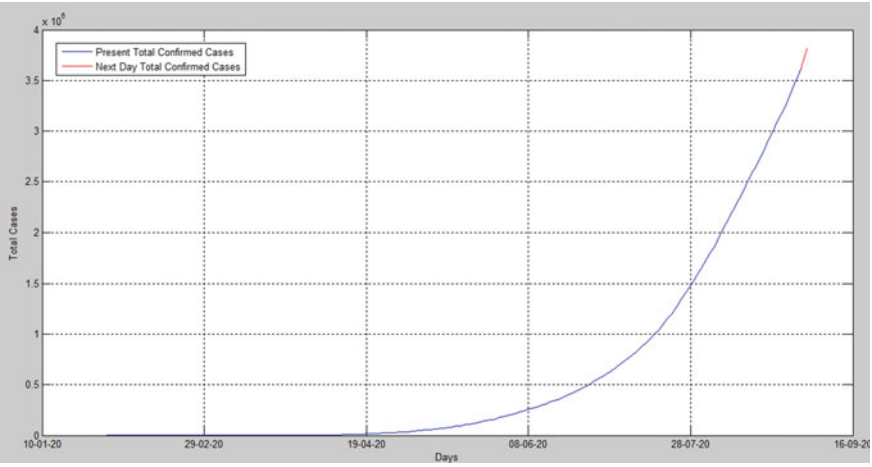

Fig. 5 Daily cases up to 31st August 2020

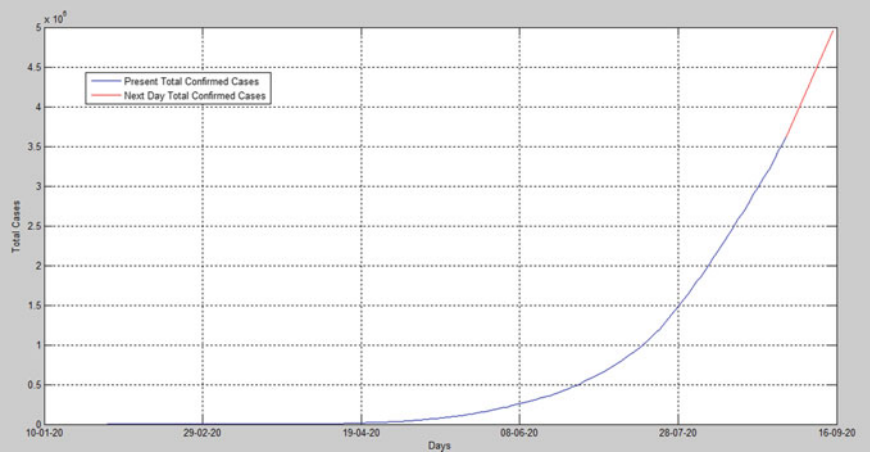

Fig. 6 Forecasted data up to 15th September 2020

Table 2 Error analysis

Date	01–09–2020	02–09–2020	03–09–2020	–	14–09–2020	15–09–2020
Actual data	3,691,166	3,769,523	3,853,406	–	4,846,427	4,930,236
Forecasted data	3,708,082	3,824,931	4,180,283	–	4,597,039	4,830,758
Avg. error (in %)	2.0358					

6 Conclusion

In the current scenario, the pandemic brought social as well as economic life to a standstill. It affected the manufacturing and the service sectors that causes many workers and employees became jobless. More than 45% of households have reported an income drop than previous year. However, the analysis over COVID-19 cases in India has become much significant, that is why researchers are giving their efforts for various types of analysis and graphical analysis for different prospective. In this similar way, we can conclude that using several types of soft computing techniques prediction can be made, the effort of this project also shows some acceptable results though and can be used for further analysis.

References

1. Li, Q., Guan, X., Wu, P., Wang, X., Zhou, L., Tong, Y. et al.: Early transmission dynamics in Wuhan, China, of novel coronavirus-infected pneumonia. N. Engl. J. Med. (2020). https://doi.org/10.1056/NEJMoa2001316
2. Singh, D., Jena, A.R., Choudhary, J.P.: Assessment of exported mango quantity by soft computing model. Int. J. Inf. Technol. Knowl. Manag. **2**(2), 393–395 (July–December 2009)
3. Roy, A., Singh, D., Sahana, S., Nath, I., Rakshit, P.: Assessment of exported tea quantity using fuzzy neural model. Int. J. Comput. Sci. Eng. **08**(01), 59–63 (2020)
4. Ruiz, L.G.B., Cuéllar, M.P., Calvo-Flores, M.D., Jiménez, M.D.C.P.: An application of non-linear autoregressive neural networks to predict energy consumption in public buildings. Energies **9**, 684 (2016). https://doi.org/10.3390/en9090684
5. Caswell, J.M.: A nonlinear autoregressive approach to statistical prediction of disturbance storm time geomagnetic fluctuations using solar data. J. Signal Inf. Process. **05**(02), 42–53 (2014)
6. Kirbas, I.: NAR based forecasting interface for time series analysis: T-seer. ICENS Int. Conf. Eng. Nat. Sci. (2018)
7. Ahmed, T.: Time series forecasting using artificial neural networks methodologies: a systematic review. Future Comput. Inf. J. https://doi.org/10.1016/j.fcij.2018.10.003
8. Ghiormez, L. et al.: Time series prediction in the case of nonlinear loads by using ADALINE and NAR neural networks. International Conference on Applied Sciences (ICAS2017). IOP Conference Series: Materials Science Engineering, vol. 294, p. 012026. (2018)
9. Cao, Q., Ewing, B.T., Thompson, M.A.: Forecasting wind speed with recurrent neural networks. Eur. J. Oper. Res. **221**(1), 148–154 (2012)
10. Hagan, M.T., Demuth, H.B., Beale, M.H.: Neural Network Design, 1st edn. PWS Pub, Boston (1996)
11. Ruiz, L.G. et al.: An application of non-linear autoregressive neural networks to predict energy consumption in public buildings. http://creativecommons.org/licenses/by/4.0/
12. Nyanteh, Y.D., Srivastava, S.K., Edrington, C.S., Cartes, D.A.: Application of artificial intelligence to stator winding fault diagnosis in permanent magnet synchronous machines. Electr. Power Syst. Res. **103**, 201–213 (2013)
13. López, M.: Application of SOM neural networks to short-term load forecasting: the Spanish electricity market case study. Electr. Power Syst. Res. **91**, 18–27 (2012)
14. Ibrahim, M., Jemei, S., Wimmer, G., Hissel, D.: Nonlinear autoregressive neural network in an energy management strategy for battery/ultra-capacitor hybrid electrical vehicles. Electr. Power Syst. Res. **136**, 262–269 (2016)

Lossless Grounded Resistorless Active Inductor Using FTFNTA

Yumnam Shantikumar Singh, Ashish Ranjan, Shuma Adhikari, and Benjamin A. Shimray

Abstract This paper introduced a lossless resistorless active inductor using ICs-based four terminal floating nullor transconductance amplifier (FTFNTA). The proposed active inductor employs one FTFNTA active block and a grounded capacitor. The simulated inductor is electronically tunable and free from matching conditions. The active inductor simulation results are obtained using 0.18 μm TSMC CMOS technology parameters and ±1.25 V supply voltage. For validation, the simulator is tested in the second order current mode multifunction and voltage mode band pass filters. The proposed simulator is simple and utilized four ICs (two ICs AD844 and two ICs LM13700) in the experimental setup/behavioral model.

Keywords Four terminal floating nullor transconductance amplifier (FTFNTA) · Current feedback operational amplifier (CFOA) · Filter

1 Introduction

A physical inductor plays a vital role in the analog signal processing circuit applications. However, it has many problems in electronic circuit and systems such as radiation of magnetic energy, occupied large area, includes more parasitic effects, bulky size, more expensive, lack of tunability, and difficult to fabricate [1–14]. From these reasons, many researchers are motivated to develop an alternative inductance circuit work as physical inductor. Therefore, active inductance simulator is substituted instead of physical inductor in the application of high frequencies filter circuit design, oscillator, and eliminating electromagnetic effects.

Over the past few decades, various literatures have been introduced different topologies of active inductor simulator realization using high operating frequency

Y. S. Singh (✉) · A. Ranjan
Department of Electronics and Communication Engineering, National Institute of Technology, Imphal, Manipur, India

S. Adhikari · B. A. Shimray
Department of Electrical Engineering, National Institute of Technology, Imphal, Manipur, India

B. Sikdar et al. (eds.), *Proceedings of the 3rd International Conference on Communication, Devices and Computing*, Lecture Notes in Electrical Engineering 851,
https://doi.org/10.1007/978-981-16-9154-6_26

active building blocks such as CCII [2], CFOA [3], FTFN [4], PFTFN [5], OTRA [6], DXCCII [7], DXCCTA [8], MO-DXCCTA [9], VDCC [10], CDTA [11], VDIBA [12], FTFNTA [13], VCII [14], and few more. In addition, current mode active building block such as FTFN [4, 5, 15] can be developed using two commercially available IC AD844. Moreover, current mode active device an interesting advantages such as large bandwidth, large dynamic range, high linearity, high slew rate, and few more. Among the versatile ABBs, FTFN is also one of them which offers many advantages over traditional operational amplifier (OA) and CCII in several signal processing circuit design. Due these advantages, a new active element, namely FTFNTA, is introduced and reported as CM in [13] with an application of active inductor simulator. The proposed in [13] uses single FTFNTA active element and two grounded passive elements. However, in [4] used two FTFN active elements and five passive elements whereas in [5] used one PFTFN and five passive elements. Another merits of FTFNTA is reported in [16] with an application of single resistance controlled oscillator (SRCO) using single FTFNTA active element and four grounded passive elements. Moreover, in [17] proposed lossy inductance simulator using single FTFNTA active element and three passive elements. However, till now, no resistorless grounded active inductor using single FTFNTA active element and a grounded capacitor is reported in the literature.

Therefore, in this manuscript, proposed a lossless grounded resistorless active inductor using single FTFNTA and a grounded capacitor. The proposed active inductor is quite simple and easy to IC implementation. A physical study of active inductor design with existing literature is given in Table 1. From the Table 1, the following characteristics study are found as.

1. Matching component constraint is required in [2, 6, 7].
2. Excessive passive component is used in [2–7, 17] and in [8, 10, 12, 13] used more than one passive component.
3. More than one active building blocks are used in [2, 4, 11, 14].
4. One active building block is used in [3, 5–8, 10, 12, 13] similar to propose one but they used more than one passive components.
5. All passive components are grounded in [2, 8, 10, 11, 13, 17] similar to proposed active inductor.
6. Electronically tunable property is found in [6, 8, 10–12, 17] similar to proposed one, but lack of tunability is found in [2–5, 7, 14].

2 FTFNTA and Proposed Inductance Simulator

The FTFNTA is a CM ABB which is reported in [13] with the combination of FTFN as input stage and OTA as output stage. The schematic structure and internal CMOS implementation of FTFNTA are depicted in Fig. 1. The FTFNTA is a six terminal active element in which the X and Y are act as input terminals, and Z, W, $O+$, and $O-$ are act as output terminals. Among these terminals, X and Y are voltage buffer and W is low impedance terminal while other are high impedance. The transconductance

Table 1 A physical comparative study of proposed circuit design with open literature

Reference No.	Name of ABB	No. of ABBs	No. of (R + C)	Tunability feature	All passive element grounded	Technology	Free from matching	Type of *L*	Power supply (V)
[2]	CCII	3	4	No	Yes	AD844	No	*G*	±12
[3]	CFOA	1	3	No	No	0.13 μm	Yes	*G*	±0.75
[4]	FTFN	2	5	No	No	3 μm	Yes	*G*	±5
[5]	PFTFN	1	5	No	No	0.35 μm	Yes	*G*	±5
[6]	OTRA	1	4	Yes	No	1.2 μm	No	*G*	±5
[7]	DXCCII	1	4	No	No	0.35 μm	No	*G*	±2.5
[8]	DXCCTA	1	2	Yes	Yes	0.18 μm	Yes	*G*/F	±1.25
[10]	VDCC	1	2	Yes	Yes	0.18 μm	Yes	*G*	±0.9
[11]	CDTA	2(G), 3(F)	1	Yes	Yes	0.5 μm	Yes	*G*/*F*	±2.5
[12]	VDIBA	1	2	Yes	No	0.25 μm	Yes	*G*	±0.75
[13]	FTFNTA	1	2	Yes	Yes	0.18 μm	Yes	*G*	±1.65
[14]	VCII	2	3	No	No	0.18 μm	Yes	*G*	±0.9
[17]	FTFNTA	1	3	Yes	Yes	0.18 μm	Yes	*G*	±1.65
Prop	FTFNTA	1	1	Yes	Yes	0.18 μm	Yes	*G*	±1.65

Notes *G* = Grounded, *F* = Floating, *L* = Inductor

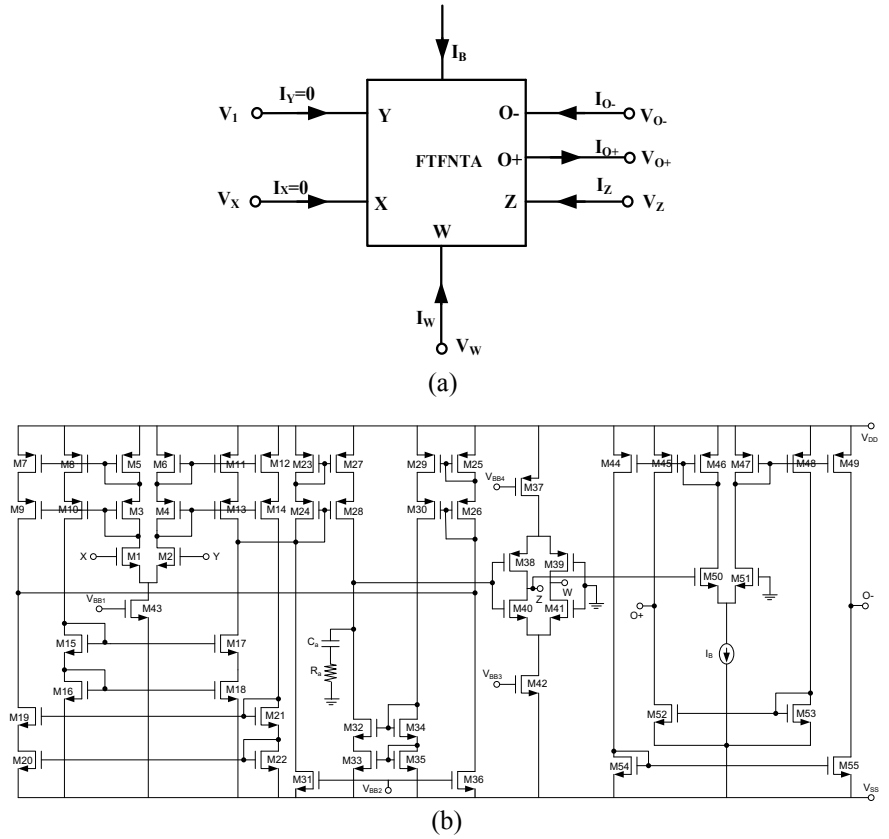

Fig. 1 FTFNTA: **a** Schematic structure, **b** internal CMOS implementation [13]

gain is available at the I_{O+} and I_{O-} output current terminals. The characteristic equation of FTFNTA in matrix form is given as

$$\begin{bmatrix} I_X \\ I_Y \\ V_X \\ I_Z \\ I_{O+} \\ I_{O-} \end{bmatrix} = \begin{bmatrix} 0 & 0 & 0 \\ 0 & 0 & 0 \\ 1 & 0 & 0 \\ 0 & -1 & 0 \\ 0 & 0 & g_m \\ 0 & 0 & g_m \end{bmatrix} \begin{bmatrix} V_Y \\ I_W \\ V_Z \end{bmatrix} \tag{1}$$

In Eq. (1), g_m is the transconductance term which offers an electronically tunable property in the entire circuit. It is obtained as

$$g_m = \sqrt{\mu C_{ox} I_B \frac{W}{L}} \tag{2}$$

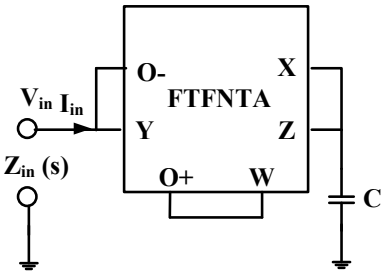

Fig. 2 Proposed lossless grounded active inductor

where μ, C_{ox}, I_B, W, and L are stated as mobility charge carrier available in the channel, gate-oxide capacitance, bias current, channel width, and channel length, respectively.

The proposed lossless grounded resistorless active inductor using single FTFNTA active element and a grounded capacitor is shown in Fig. 2. By circuit routine analysis, the transfer function of input impedance is obtained as

$$Z_{\text{in}}(S) = \frac{V_{\text{in}}(s)}{I_{\text{in}}(s)} = \frac{sC}{g_m^2} = sL_{eq} \tag{3}$$

From Eq. (3), the equivalent inductance simulator is obtained as

$$L_{\text{eq}} = \frac{C}{g_m^2}$$

In addition, the sensitivity of the proposed active inductor can be easily obtained as

$$S_{g_m}^L = -2,\ S_C^L = 1 \tag{4}$$

From Eq. (4), a low sensitivities are observed.

3 Nonideality Analysis

Due to the present of nonidealities in the ABBs, the terminal relationship of these ABBs is deviated from ideal one [13]. In FTFNTA active element, the deviation is due to α, β, and γ nonideality present in it. The modified characteristic equation with the effects of α, β, and γ will be

$$\begin{aligned} &I_X = I_Y = 0,\ V_X = \alpha V_Y, \\ &I_Z = -\beta I_W,\ I_{O+} = I_{O-} = \gamma g_m V_Z \end{aligned} \tag{5}$$

By considering these effects, the new transfer function of input impedance is obtained as

$$Z_{\text{in}}(s) = \frac{V_{\text{in}}(s)}{I_{\text{in}}(s)} = \frac{sC}{\alpha\beta\gamma^2 g_m^2} \tag{6}$$

In addition, another nonideality effect is due to parasitic elements that are parasitic resistor and parasitic capacitor which are connected in parallel with each terminals. A general schematic structure of FTFNTA along with parasitic elements is well discuss in [13, 16]. Figure 3 shows the proposed grounded active inductor with parasitic elements. The equivalent parasitic resistance and capacitance at Y and $O-$, X and Z, W, and $O+$ connections are found as $\{R_{\text{eq1}} = R_Y \| R_{O-},\ C_{\text{eq1}} = C_Y + C_{O-}\}$, $\{R_{\text{eq2}} = R_X \| R_Z,\ C_{\text{eq2}} = C + C_X + C_Z\}$, and $\{R_{\text{eq3}} = R_W \| R_{O+},\ C_{\text{eq3}} = C_W + C_{O+}\}$, respectively.

The input admittance of the active inductor with parasitic effects is given as

$$Y_{\text{in}}(s) = \frac{I_{\text{in}}(s)}{V_{\text{in}}(s)} = g_m^2 Z_2 - \left(Z_3 g_m + \frac{Z_3}{Z_2} + \frac{1}{Z_1}\right) \tag{7}$$

where

$$Z_1 = R_{\text{eq1}} \| C_{\text{eq1}}$$
$$Z_2 = R_{\text{eq2}} \| C_{\text{eq2}}$$
$$Z_3 = R_{\text{eq3}} \| C_{\text{eq3}}$$

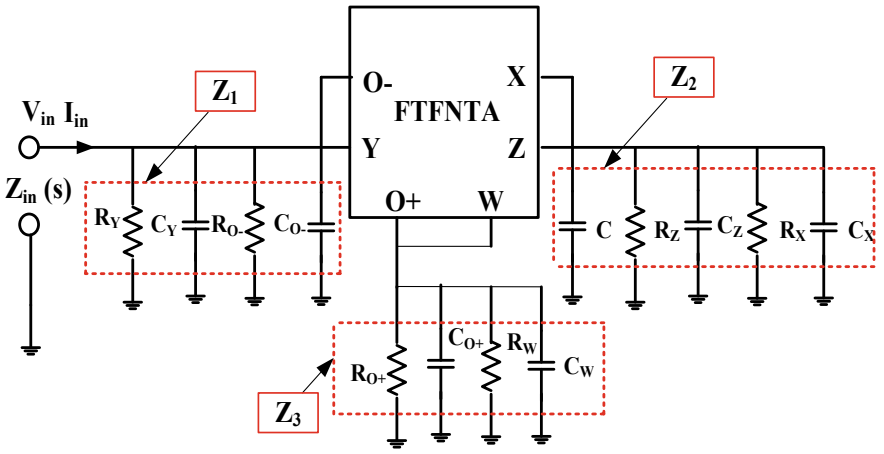

Fig. 3 Proposed lossless grounded active inductor with parasitic elements

4 Simulation Results

To judge the response of the proposed lossless grounded active inductor, PSPICE simulation is carried out using 0.18 μm TSMC CMOS technology parameter with aspect ratio of [13]. The DC power supply and bias voltages are chosen as ±1.65 V, VBB1 = VBB2 = −1 V, VBB3 = −0.8 V, and VBB4 = 0.5 V, respectively. The proposed active inductor of Fig. 2 is simulated with C = 100 pF and bias current I_B = 500 μA (g_m = 0.19564 mS). With these passive elements, the equivalent simulated inductor is obtained as 0.511 mH. The simulated frequency response of magnitude and phase is shown in Fig. 4.

For testing the proposed grounded active inductor, it is employed in current mode multifunction filter with passive components R = 7kΩ, C = 100 pF, and Leq = 15.24 mH for 400 kHz cutoff frequency. The basic cell is an inductor simulator with a parallel capacitor (C_L) and resistor (R_L) to form parallel resonant circuit as shown in Fig. 5.

$$\frac{I_{LP}}{I_{IN}} = \frac{\frac{1}{LC}}{s^2 + \frac{s}{RC} + \frac{1}{LC}} \tag{8}$$

$$\frac{I_{BP}}{I_{IN}} = \frac{\frac{s}{RC}}{s^2 + \frac{s}{RC} + \frac{1}{LC}} \tag{9}$$

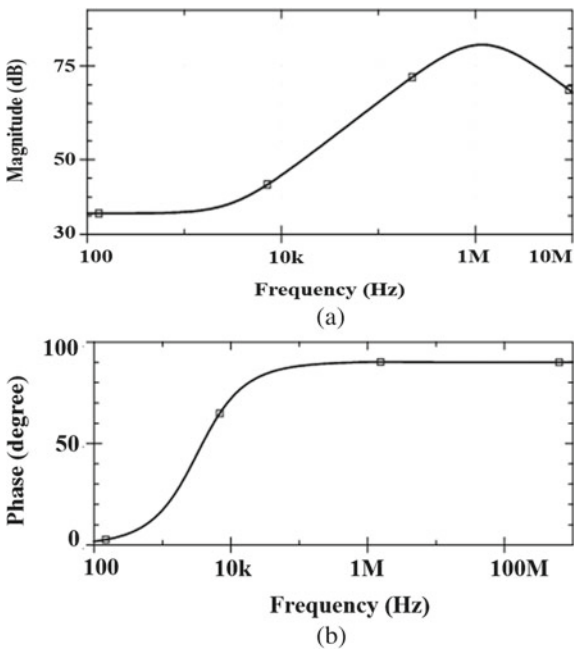

Fig. 4 Frequency response of proposed active inductor: **a** magnitude, **b** phase

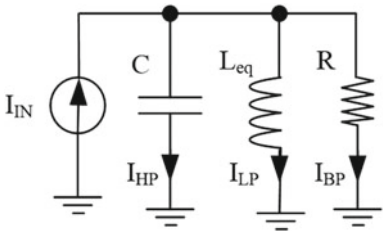

Fig. 5 Parallel resonant filter circuit

$$\frac{I_{HP}}{I_{IN}} = \frac{s^2}{s^2 + \frac{s}{RC} + \frac{1}{LC}} \tag{10}$$

From Eq. (8–10), it is observed that the sensitivity value is found below unity and suitable for active filter circuit design. Simulated frequency response of CMOS-based FTFNTA active inductor for multifunction current mode filter is shown in Fig. 6.

For testing the tunability of the proposed lossless grounded active inductor, different frequency response of LP filter using Fig. 5 for different bias currents $I_B = 500\ \mu A$, $600\ \mu A$, $700\ \mu A$ is shown in Fig. 7.

Moreover, an experimental verification for proposed lossless grounded active inductor is carried out with FTFNTA realization using CFOA (ICAD844) and OTA (CA3080) of [13]. An experimental time domain verification is done by selecting passive component as $C = 100$ pF, $I_B = 800\ \mu A$, and its transient response is shown

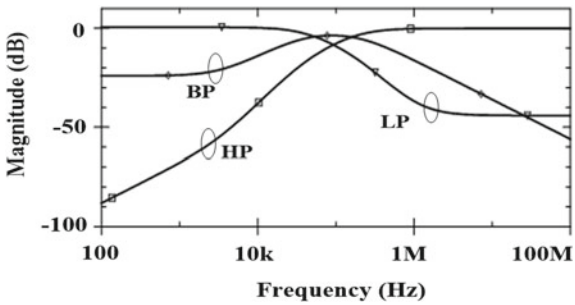

Fig. 6 Multifunction filter response using proposed active inductor

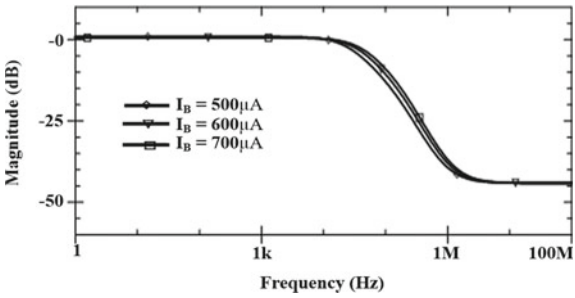

Fig. 7 Tunable LPF using Fig. 5 for different bias currents

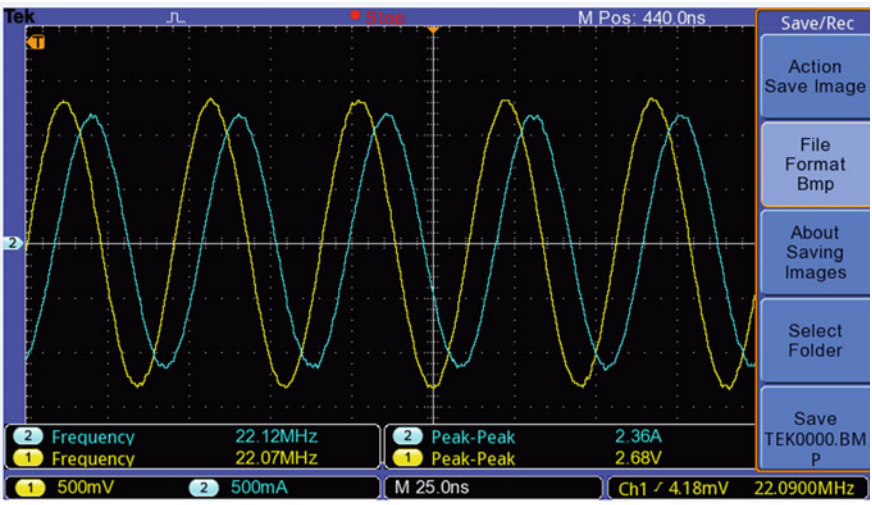

Fig. 8 Experimental transient response of proposed lossless active inductor

in Fig. 8. From Fig. 8, it is observed that the current is lack approach 89° with the voltage.

5 Conclusion

In this manuscript, a compact configuration of lossless grounded resistorless active inductor employing single FTFNTA active element and an external grounded capacitor is introduced with an application of second order CM multifunction filter. The proposed simulated inductor has various advantages such as (1) used single active element, (2) used only one grounded capacitor as passive element, (3) free from matching condition, (4) fully controllable using bias current, (5) low sensitivity, and (6) easy to IC fabricate. The simulated frequency responses are well supported the theoretical approach.

References

1. Senani, R., Bhaskar, D.R.: A simple configuaration for realizing voltage controlled impedances. IEEE Trans. Circ. Syst. I, Fund Theor. Appl. **39**(1), 52–59 (1992)
2. Cicekoglu, M.O.: Active simulation of grounded inductors with CCII+s and grounded passive elements. Int. J. Electron. **85**, 455–462 (1998)
3. Alpaslan, H., Yuce, E.: Inverting CFOA based lossless and lossy grounded inductor simulators. Circ. Syst. Sig. Process. **34**(10), 3081–3100 (2015)

4. Kiliç, R., Çam, U., Alçi, M., Kuntman, H., Uzunhisarcikli, E.: Realization of inductorless Chua's circuit using {FTFN}-based nonlinear resistor and inductance simulator. Frequenz **58**, 1–4 (2004)
5. Kumar, P., Senani, R.: New grounded simulated inductance circuit using a single PFTFN. Analog Integr. Circ. Sig. Process. **62**, 105–112 (2010)
6. Çam, U., Kaçar, F., Cicekoglu, O., Kuntman, H., Kuntman, A.: Novel grounded parallel immittance simulator topologies employing single OTRA. AEU-Int. J. Electr. Commun. **57**(4), 287–290 (2003)
7. Metin, B.: Supplementary inductance simulator topologies employing single DXCCII. Radioengineering **2011**(20), 614–618 (1996)
8. Navnit, K., Vista, J., Ranjan, A.: A Tuneable active inductor employing DXCCTA: grounded and floating operation. Microelectron. J. **90**, 1–11 (2019)
9. Singh, Y.S., Ranjan, A., Adhikari, S., Shimray, B.A.: Dual mode grounded active inductor employing MO-DXCCTA. 4th International Conference on Electronics, Communication and Aerospace Technology (ICECA), pp. 368–373. (2020)
10. Kaçar, F., Yesil, A., Minaei, S., Kuntman, H.: Positive/negative lossy/lossless grounded inductance simulators employing single VDCC and only two passive elements. AEU—Int. J. Electr. Commun. **68**, 73–78 (2014)
11. Prasad, D., Bhaskar, D.R., Singh, A.K.: New grounded and floating simulated inductance circuits using current differencing transconductance amplifiers. Radioengineering **19**, 194–198 (2010)
12. Tangsrirat, W.: Synthetic grounded lossy inductance simulators using single VDIBA. IETE J. Res. **63**, 134–141 (2017)
13. Tarunkumar, H., Singh, Y.S., Ranjan, A.: An active inductor employing a new four terminal floating transconductance amplifier (FTFNTA). Int. J. Electr. 2–21 (2019)
14. Safari, L., Yuce, E., Minaei, S., Ferri, G., Stornelli, V.: A second-generation voltage conveyor (VCII)-based simulated grounded inductor. Int. J. Circ. Theor. Appl. 1–4 (2020)
15. Ranjan, A., Perumalla, S., Kumar, R., Vista, J., Yumnam, S.: Second order universal filter using four terminal floating nullor (FTFN). J. Circ., Syst. Comput. **28**, 1950091 (2019)
16. Prasad, D., Singh, R., Ranjan, A., Tarunkumar, H.: Grounded capacitors single resistance controlled oscillator using single FTFNTA. Indian J. Pure Appl. Phys. **58**, 525–530 (2020)
17. Prasad, D., Singh, R.: Grounded lossy inductance simulator using single FTFNTA. IEEE 17th India Council International Conference (INDICON), pp. 1–6 (2021)

Partial Reversible Data Hiding Scheme Using Graphical Code

Debajit Sensarma and Samar Sen Sarma

Abstract Nowadays, data hiding has been received much attention for information security due to the rapid growth of the Internet and multimedia technologies. Good steganography techniques can be used to achieve a high level of security. In this paper, a new image steganography technique, namely partial reversible data hiding using graphical code (PRDHGC), has been proposed taking the advantage of graphical error-correcting codes and a secret shared key. It is mainly a partial reversible data hiding scheme, and comparison with various methods has been shown that the proposed scheme performs better than the existing schemes in terms of PSNR, embedding efficiency and embedding payload.

Keywords Data hiding · Graphical code · Steganography · Fundamental circuit matrix · Fundamental cut-set matrix

1 Introduction

The protection of digital confidential data becomes more important. To cope with this, digital steganography has been developed rapidly and it is an attractive research topic in both the field of academia and industry. The word "steganography" comes from the Greek words "steganos" meaning covered, concealed, or protected and "graphein" meaning writing [1]. So, this is the art of concealing a file, message, image, or video within another file. Good steganography schemes required high embedding efficiency, security, and a large embedding payload. According to [2], "the goal of steganography is to avoid drawing suspicion on the transmission of a hidden message. If suspicion is raised, then the goal is defeated." The steganography techniques, based on the cover medium, are mainly of four categories such as (i)

D. Sensarma (✉)
Department of Computer Science, Vivekananda Mission Mahavidyalaya, affiliated to Vidyasagar University, Haldia, India

S. S. Sarma
Department of Computer Science and Engineering, University of Calcutta Kolkata, Kolkata, India

B. Sikdar et al. (eds.), *Proceedings of the 3rd International Conference on Communication, Devices and Computing*, Lecture Notes in Electrical Engineering 851,
https://doi.org/10.1007/978-981-16-9154-6_27

image steganography, (ii) steganography in audio, (iii) video steganography, and (iv) text steganography [3]. Image steganography is the most popular among them. Besides this, there are three types of steganography techniques, they are (i) pure steganography, (ii) secret key steganography, (iii) public key steganography [4].

In image steganography, the main is to hide the image into the cover image for secret transmission. In the image steganography technique, the sender hides message "m" into the cover image (CI) using the message embedding algorithm and a stego image (SI) is generated which is passed to the receiver. Then, by applying, the message extraction algorithm receiver can extract the original image. Here, the cover image is the original image (i.e., without hiding the data) and the stego image is the image with hiding secret data. The aim is to embed a large amount of data while minimizing the sum of the cost of all changed pixels.

Set of all even sub-graphs of connected graph G of n vertices with e edges forms a binary linear code C, with parameters $[n, e-n+1, g]$, where g is the girth of the graph G [5–7]. The concepts of graph-theoretic codes like cut-set codes, circuit codes, and augmented circuit codes are given and the decoding procedure (i.e., majority logic decoding) along with the efficiency of this graph-theoretic block codes has been described in [5, 7–9].

In this article, we mainly considered the image steganography technique based on graphical code and a shared secret key. We also have compared the performance of the PRDHGC method with other existing methods.

The main contribution of this work is to (i) send a secured message with an arbitrary length by embedding it in an image, (ii) take the advantage of graphical codes as it purely depends on the types of graphs, they can be dynamically generated according to the requirement [5, 7, 10], (iii) use the concept of partial reversible data hiding using error-correcting code [11], and (iv) enhance the security using a secret shared key, i.e., if the receiver does not know the secret key, the secret message extraction is not possible.

This paper is organized as follows: In Sect. 2, some related works are given. The proposed PRDHGC method of data hiding is given in Sect. 3. Section 4 contains an illustrative example. Experimental results related to the proposed method are given in Sects. 5, and 6 concludes the article by giving future scopes.

2 Related Works

Recently, data hiding schemes are drastically used in the field of military and commercial communications. Firstly, in [12], author devised a method of parity checking that could correct a single error and detect the double error. So, in [13], author proposed a data hiding scheme called matrix encoding and pointed out that embedding efficiency could be improved by using the coding method. In [14], author proposed a data hiding scheme, namely the Hamming $+1$ scheme. It uses one moreover pixel than the matrix encoding scheme while the cost remains unchanged but the embedding capacity increased. Also, the authors of [15] proposed a scheme using the nearest

covering code. The marked image quality is superior in comparison with the previous two methods. In [16], author proposed a steganography technique F_5, based on the matrix encoding idea which has improved embedding efficiency. Here, m bit data can be embedded in 2 m−1 cover symbols by changing at most one symbol. The concept of Hamming code is used in this scheme. Next, the authors of [17] proposed a data hiding scheme that considers the quality of the image after data hiding. Authors in [18] take advantage of Reed Solomon codes (RS codes) which according to [19] is a good tool for steganography technique. They have proposed a matrix embedding technique based on RS codes which allow an easy way to solve the bounded syndrome problem. In [20], authors proposed a method based on the ternary Hamming code and ternary Golay code and suggested that they are optimum in the sense that they achieve the smallest possible distortion. Random linear code of small dimension based data hiding scheme has been proposed in [21] which provides good embedding efficiency. Next, in [22], authors proposed a data hiding scheme (DHHC) based on (15, 11) Hamming code to hide the secret data into a halftone image. Authors of [23] proposed a dispersed data hiding scheme (DDHHC) based on Hamming code. Next, in [24], authors have proposed a secure partially reversible data hiding scheme using hamming error-correcting code (PRDHHC). In [25], authors proposed a steganography technique using BCH [2 m−1, 2 m−2 m−1] code $\{m = 3,\ldots,7\}$ and majority logic decoding. Next, the authors of [26] proposed a new technique called product perfect code and its steganography application. In [27], a robust (non-fragile) steganography technique has been introduced based on matrix encoding using self-synchronizing variable-length T-codes and RS codes for obtaining a compressed image from the original image and robustness against transmission error.

3 Proposed Data Hiding Technique

Let, $t(X) \in {F_2}^n$ be the polynomial representation of the extracted vector from the cover image. $V(X) \in {F_2}^n$ be the polynomial representation of vector of stego image, and $m(X) \in {F_2}^{n-k}$ is the polynomial representation of vector of the message to be embedded. The aim is to change $t(X)$ to $V(X)$ such that $m(X)$ is embedded in $V(X)$ and the least number of bit positions are flipped.

Suppose, $e(X)$ be the flip pattern representing the number of bit positions flipped. So, the stego-data

$$V(x) = t(X) + e(X). \tag{1}$$

From the relationship between m and v, it can be seen that

$$v.H^T = m. \tag{2}$$

[H = Parity check matrix].
So, from Eq. (1) and Eq. (2), we can get

$$v.H^T = m.$$

or

$$(t + e)H^T = m$$

or

$$t.H^T + e.H^T = m$$

or

$$e.H^T = m - t.H^T$$

So, a vector e has to be found whose syndrome is

$$s = m - t.H^T. \tag{3}$$

First of all, from the original image pixel, a cover image pixel has been generated using graphical error-correcting code. Then, secret data have been embedded using syndrome computed in Eq. (3) above. Lastly, a bit is flipped based on the shared secret key and this produces the final pixel of the stego image. This process continues for each pixel depending on the length of the secret message.

At the time of data extraction, the stego image pixel bit is flipped depending on the shared secret key and the secret message is extracted using syndrome decoding. Then, the bit/bits of the syndrome have been flipped and we get the cover image pixel but not the original image pixel as this is a partial reversible data hiding scheme. This process continues for each pixel depending on the length of the secret message. The algorithm for data embedding and extraction has been given below:

Algorithm 1: Data Embedding of PRDHGC

Inputs: Original image *OI* (*HxW*) (*H* = Height, *W* = Width), secret message *M*.

Output: Stego image *SI* (*HxW*).

Step 1: Initialize $H = 512$, $W = 512$, $C = L/4$ (where L = secret message length), $i = 1$, flag $= 0$, $g = 1$ and break the message M into C sub-messages $m_1, m_2, \ldots, m_C$ and also the shared secret key n (between 1 to 8). For each i-th pixel, key $k_i = (n \times i)\ \%8 + 1$.

Step 2: If ($i <= C$), then take i-th pixel of the original greyscale image, covert pixel value into 8-bit binary form, and go to step 3 else go to step 10.

Step 3: Compute syndrome "s" from Eq. (3).

Table 1 Leader syndrome table

Syndrome	Coset leader
0001	e_5
0010	e_7
0011	$e_5 + e_7$
0100	e_6
0101	$e_5 + e_6$
0110	$e_6 + e_7$
0111	$e_5 + e_6 + e_7$
1000	e_8
1001	$e_5 + e_8$
1010	$e_7 + e_8$
1011	$e_5 + e_7 + e_8$
1100	$e_6 + e_8$
1101	$e_5 + e_6 + e_8$
1110	$e_6 + e_7 + e_8$
1111	$e_5 + e_6 + e_7 + e_8$

Step 4: If $s = 0$, then data are already hidden in the pixel and go to step 7, else go to step 5.

Step 5: Find vector e from leader-syndrome (Table 1).

Step 6: Modify the cover image pixel $p[i] = p[i] + e$ [Here, $p[i]$ represents i-th pixel of the cover image and generate vector v which is the modified pixel after secret message embedding].

Step 7: If $i <= 8 \times g$, then go to step 8 else $g = g + 1$ and go to step 8.

Step 8: If $k_i <= 4$ and flag $!= 1$, then set flag $= 1$ else $k_i = k_i + 4$;

Step 9: Flip bit $p[k_i]$ of the modified pixel. Set $i = i + 1$ and go to step 2.

Step 10: Stop.

Algorithm 2: Data Extraction of PRDHGC

Input: Stego image SI (HxW).

Output: Secret data M.

Step 1: Initialize $H = 512$, $W = 512$, $C = \text{L}/4$ (where $L =$ secret message length), $M =$ NULL, $i = 1$;

Step 2: If ($i <= C$), then take i-th pixel of the original greyscale image, covert pixel value into 8-bit binary form, and go to step 3 else go to step 7.

Step 3: Flip bit $p[k_i]$ of the received pixel.

Step 4: Calculate data m_i from Eq. 2.
Step 5: Compute $M = M + m_i$ (Here "+" represents concatenation).
Step 6: Set $i = i + 1$ and go to step 2.
Step 7: Stop.

4 Illustration with an Example

We have to take an arbitrary graph G which gives rise to a binary linear code with parameters [3, 4, 9], where the number of edges = 8, number of vertices = 5, and girth = 3 [6] (Figs. 1, 2 and 3).

Example: Suppose, we want to hide the 4-bit data $(1100)_2$ in a greyscale image using minimal bit flip.

Solution:
Data embedding from Algorithm 1.

Suppose, any arbitrary pixel value original image is **203**. After conversion from decimal to binary, the 8-bit binary number is given below:

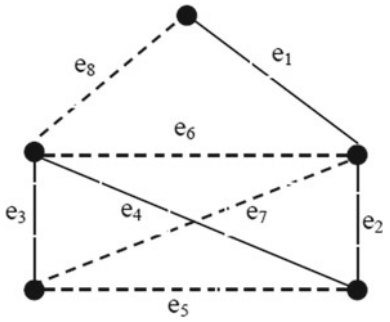

Fig. 1 Arbitrary graph with 5 vertices and 8 edges

e_1	e_2	e_3	e_4	e_5	e_6	e_7	e_8
1	0	0	0	0	1	0	1
0	1	0	0	1	0	1	0
0	0	1	0	0	1	1	0
0	0	0	1	1	1	1	0

Fig. 2 Fundamental circuit matrix of the graph in Fig. 1

Fig. 3 Fundamental cut-set matrix of the graph in Fig. 1

e_1	e_2	e_3	e_4	e_5	e_6	e_7	e_8
1	0	0	0	0	0	0	1
1	0	1	1	0	1	0	0
0	1	1	1	0	0	1	0
0	1	0	1	1	0	0	0

$$\begin{array}{cccccccc} e_1 & e_2 & e_3 & e_4 & e_5 & e_6 & e_7 & e_8 \\ 1 & 1 & 0 & 0 & 1 & 0 & 1 & 1 \end{array}$$

Now,

$$\begin{aligned} s_1 &= e_1 + e_8 = 0 \\ s_2 &= e_1 + e_3 + e_4 + e_6 = 1 \\ s_3 &= e_2 + e_3 + e_4 + e_7 = 0 \\ s_4 &= e_2 + e_4 + e_5 = 0 \end{aligned}$$

So, after error correction, the cover pixel value will be $(11001111)_2$ or $(207)_{10}$.
If we consider the original pixel value, then from Eq. (3), we get

$$\text{Syndrome } s = (1100 - 0100) = (1000)_2.$$

So, from Table 1:

$$\begin{array}{c} \text{Vector } e = e_1\ e_2\ e_3\ e_4\ e_5\ e_6\ e_7\ e_8 \\ 0\ 0\ 0\ 0\ 0\ 0\ 0\ 1 \end{array}$$

So, modified vector $v = (11001011 + 00000001) = (11001010)_2$.
Suppose, shared secret key = 3.
So, $k_1 = (3 \times 1)\%8 + 1 = 4$.
Now, flip the 4th bit of the modified pixel and the final pixel becomes $= (11011010)_2$.
After decimal conversion, the pixel value of the final modified pixel becomes **218**.

Data extraction from Algorithm 2.

After conversion from decimal to the binary of pixel value **218** and flipping the 4th bit of the pixel, the 8-bit binary number is given below:

$$\begin{array}{cccccccc} e_1 & e_2 & e_3 & e_4 & e_5 & e_6 & e_7 & e_8 \\ 1 & 1 & 0 & 0 & 1 & 0 & 1 & 0 \end{array}$$

Now,

$$s_1 = e_1 + e_8 = 1$$
$$s_2 = e_1 + e_3 + e_4 + e_6 = 1$$
$$s_3 = e_2 + e_3 + e_4 + e_7 = 0$$
$$s_4 = e_2 + e_4 + e_5 = 0$$

So, the required hidden message is $(1100)_2$.

Now, by taking 1100 as a syndrome and flipping the bit position 6 and 8, respectively (from Table 1), the pixel becomes $(11001111)_2$ or $(207)_{10}$. It is the cover pixel. So, this provides partial data hiding.

5 Experimental Results

High embedding efficiency and high embedding payload are the main primary objective of a good steganography technique. For embedding efficiency which is also called embedding quality of the setgo image, a well-known measurement called peak-to-signal-noise rate (*PSNR* in short) is used to evaluate the degree of similarity between the stego image and the original image to avoid evaluation by human necked eyes. So, *PSNR* is defined by the following Eq. (4):

$$PSNR = 10 \log \log_{10} \frac{255^2}{MSE} dB \tag{4}$$

Here, *MSE* is the mean square error. It represents the difference between the stego image and the original image with size *HxW* pixels. The *MSE* is defined using the following formula (5):

$$MSE = \frac{1}{HxW} \sum_{i=1}^{H} \sum_{j=1}^{W} \left(I_{ij} - I_{ij}{}'\right) \tag{5}$$

The high value of *PSNR* means that the stego image is very similar to the original image according to visual quality evaluation and also the embedding efficiency of the steganography scheme is high. Here, low *PSNR* means there is very much distortion in the stego image concerning the original image and also low embedding efficiency. In general, if the *PSNR* value is greater than 30 dB, then it is very hard to find the distortion by human eyes.

Besides this, there are various types of human visual system (*HVS*)-based measurement which is used to measure the similarity between the stego image and the original image. Structural similarity index (*SSIM*) is one of them. It is a full reference metric. The measurement depends on the initial uncompressed or distortion-free

image as a reference. It is a slightly improved measurement than *MSE* and *PSNR*. The resultant *SSIM* is the value between −1 and 1, where value 1 depicts two identical data. For image size *HxW*, *SSIM* is calculated as follows:

$$SSIM(x, y) = \frac{(2\mu_x\mu_y + C_1)(2\sigma_{xy} + C_2)}{(\mu_x^2 + \mu_y^2 + C_1)(\sigma_x^2 + \sigma_y^2 + C_2)} \tag{6}$$

Here, $\mu_x, \mu_y, \sigma_x, \sigma_{xy}$ are the local means, standard deviation, and cross-covariance for the image x, y. Here, $C_1 = (K_1L)^2$ and $C_2 = (K_2L)^2$ are two variables to stabilize the division with a weak denominator. L has the dynamic range of pixel values and $K_1 = 0.01$ and $K_2 = 0.03$ by default.

Table 2 shows the *PSNR* and *SSIM* of five popular 512 × 512 greyscale images of Fig. 4 after embedding 4096 bits and 16384 bits, respectively. Also in Table 2, *PSNR* and *SSIM* of images Lena, Barbara, Tiffany are given after embedding of 20000, 50000, 100000, and 200000 bits, respectively. It can be shown the quality of the image of the stage is not much degraded after embedding secret data, and the average PSNR value is greater than 30. Data embedding and data extraction of the proposed method have been implemented in GNU OCTAVE Version 5.2.0 [28] (Table 3 and Fig. 5).

Tables 4 and 5 show the comparison of our proposed scheme PRDHGC using two existing steganography techniques DHHC [22], DDHHC [23], and PRDHHC [24]. It can be seen that there is much improvement in PSNR value concerning the existing methods. Like, the PSNR value for the DHHC scheme is 38.12 dB when embedding 4096 bits and 32.03 dB when embedding 16384 bits. For the DDHHC scheme, it is 44.71 dB when embedding 4096 bits and 38.60 dB when embedding 16,384 bits, 53.52 dB when embedding 4096 bits and 46.89 dB when embedding 16,384 bits. But for the proposed scheme PRDHGC, the PSNR is 54.14 dB (for 4096 bits) and 47.54 (for 16384 bits), respectively which is improved than the existing methods.

Furthermore, embedding payload can be measured using the following equation:

$$B\frac{|\delta|}{HxW} \tag{7}$$

Table 2 *PSNR* and *SSIM* of stego images

	4096 bits		16384 bits	
Image	*PSNR*	*SSIM*	*PSNR*	*SSIM*
Lena	54.14	0.999	47.54	0.998
Barbara	53.08	1.0	47.22	0.999
Tiffany	53.63	1.0	47.55	0.999
Goldhill	54.08	0.999	47.99	0.999
Peppers	53.18	1.0	47.67	0.999
Average	53.62	0.999	47.59	0.998

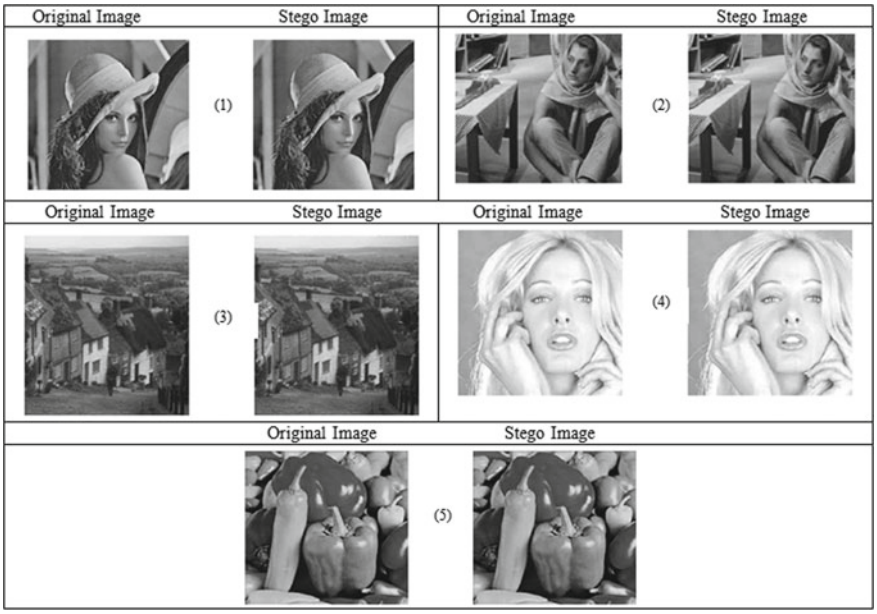

Fig. 4 Original images and their corresponding stego images, namely (1) Lena (2) Barbara (3) Goldhill (4) Tiffany (5) Peppers

Table 3 *PSNR* and *SSIM* of stego images

	20000 bits		50000 bits		100000 bits		200000 bits	
Image	*PSNR*	*SSIM*	*PSNR*	*SSIM*	*PSNR*	*SSIM*	*PSNR*	*SSIM*
Lena	46.66	0.999	42.27	0.993	39.80	0.986	36.80	0.965
Barbara	46.35	0.999	42.35	0.996	39.40	0.991	36.49	0.982
Tiffany	46.66	0.999	42.64	0.994	39.70	0.986	36.72	0.972
Average	46.55	0.999	42.42	0.994	39.63	0.987	36.67	0.973

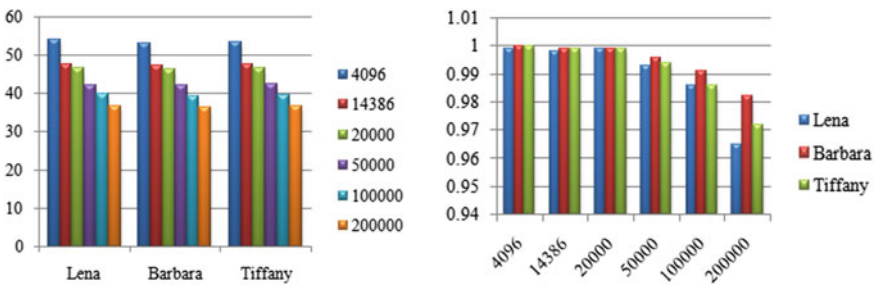

Fig. 5 *PSNR* (left image) and SSIM (right image) of stego images

Table 4 Comparison in terms of *PSNR* values

		4096 bits		
Image	DHHC	DDHHC	PRDHHC	PRDHGC
Lena	38.12	44.71	53.52	54.14
Barbara	38.14	44.77	51.67	53.08
Tiffany	38.04	42.91	53.29	53.63
Peppers	38.10	44.19	52.31	53.18
Goldhill	38.11	44.96	52.11	54.08

Table 5 Comparison in terms of *PSNR* values

		16384 bits		
Image	DHHC	DDHHC	PRDHHC	PRDHGC
Lena	32.03	38.6	46.89	47.54
Barbara	32.03	38.57	44.88	47.22
Tiffany	31.72	36.24	46.87	47.55
Peppers	31.98	38.02	45.85	47.67
Goldhill	32.02	38.66	45.89	47.99

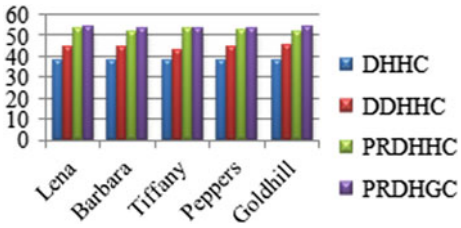

Fig. 6 Comparison in terms of *PSNR* (4096 bits)

So, here, δ represents the number of bits in the secret message and B represents bits per pixel (bpp) which is the payload. In the proposed method, PRDHGC embedding capacity in a (512×512) greyscale image is 1048576 bits. So, $B = 4$ bpp which is improved than some existing methods (Figs. 6 and 7).

6 Conclusion

In this paper, a novel data hiding scheme PRDHGC has been proposed taking the advantage of graphical codes and a shared secret key. As graphical codes purely depend on the types of graphs, they can be dynamically generated according to the requirement. Also, this scheme is partially reversible as we can construct the cover image from the stego image. In this hiding scheme, an $(8, 4, 3)$ graphical code has been

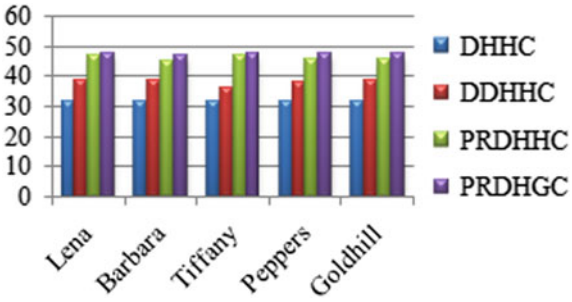

Fig. 7 Comparison in terms of *PSNR* (16384 bits)

generated which only modifies the maximum four least significant bits of the pixel of the original image to embed the secret data. Comparison with other methods has shown that the proposed method gains good *PSNR*, high payload, and high efficiency. In future, this method can be applied to design in reversible steganography scheme design and also in other real-life problem solving depending on further research.

Acknowledgements The authors would like to thank the University of Calcutta, West Bengal, India, Vivekanda Mission Mahavidyalaya, Vidyasagar University for supporting the work and the reviewers for their constructive and helpful comments and especially the computer without which no work was possible.

References

1. Shih, F.Y.: *Digital watermarking and steganography: fundamentals and techniques*. CRC Press, (2007)
2. Johnson, N.F., Sushil, J.: Steganalysis: the investigation of hidden information. In 1998 IEEE Information Technology Conference, Information Environment for the Future (Cat. No. 98EX228), pp. 113–116. IEEE, (1998)
3. Swain, G., Saroj, K.L.: Classification of image steganography techniques in spatial domain: a study. J. Comput. Sci. Eng. Technol. (IJCSET) **5**(03), 219–232 (2014)
4. Al-Ani, Z.K., Zaidan, A.A., Zaidan, B.B., Hamdan, A.: Overview: main fundamentals for steganography. arXiv preprint arXiv:1003.4086 (2010)
5. Hakimi, S., Bredeson, J.: Graph theoretic error-correcting codes. IEEE Trans. Inf. Theory **14**(4), 584–591 (1968)
6. Jungnickel, D.: Graphs, Networks and Algorithms. Springer, Berlin (2005)
7. Sensarma, D., Samar, S.S.: Data Hiding using Graphical Code based Steganography Technique. arXiv preprint arXiv:1509.08743 (2015)
8. Hakimi, S., Frank, H.: Cut-set matrices and linear codes (Corresp.). IEEE Trans. Inf. Theory **11**(3), 457–458 (1965)
9. Bredeson, J., Hakimi, S.: Decoding of graph theoretic codes (Corresp.). IEEE Trans. Inf. Theory **13**(2), 348–349 (1967)
10. Jungnickel, D., Vanstone, S.A.: Graphical codes revisited. IEEE Trans. Inf. Theory **43**(1), 136–146 (1997)
11. Wu, X., Yang, C.-N., Liu, Y.-W.: A general framework for partial reversible data hiding using hamming code. Sig. Process. **175**, 107657 (2020)

12. Hamming, R.W.: Error detecting and error correcting codes. Bell Syst. Tech. J. **29**(2), 147–160 (1950)
13. Crandall, R.: Some notes on steganography. Posted Steganography Mailing List. 1–6 (1998)
14. Zhang, W., Wang, S., Zhang, X.: Improving embedding efficiency of covering codes for applications in steganography. IEEE Commun. Lett. **11**(8), 680–682 (2007)
15. Chang, C.-C., Duc, K., Chou, Y.-C.: Using nearest covering codes to embed secret information in grayscale images. In Proceedings of the 2nd International Conference on Ubiquitous Information Management and Communication, pp. 315–320. (2008)
16. Westfeld, A.: F5—a steganographic algorithm. In International Workshop on Information Hiding, pp. 289–302. Springer, Berlin, Heidelberg, (2001)
17. Tseng, Y.-C., Chen, Y.-Y., Pan, H.-K.: A secure data hiding scheme for binary images. IEEE Trans. Commun. **50**(8), 1227–1231 (2002)
18. Diop, I., Farssi, S.M., Khouma, O., Diouf, H.B., Tall, K., Sylla, K.: New steganographic scheme based of reed-solomon codes. Int. J. Distrib. Parallel Syst. **3**(2), 81 (2012)
19. Fontaine, C., Fabien, G.: How reed-solomon codes can improve steganographic schemes. EURASIP J. Inf. Secur. **2009**(1), 274845 (2009)
20. Willems, F.M.J., van Dijk, M.: Capacity and codes for embedding information in gray-scale signals. IEEE Trans. Inf. Theor. **51**(3), 1209–1214 (2005)
21. Fridrich, J., Petr, L., David, S.: On steganographic embedding efficiency. In International Workshop on Information Hiding, pp. 282–296. Springer, Berlin, Heidelberg, (2006)
22. Kim, C., Dongkyoo, S., Dongil, S.: Data hiding in a halftone image using hamming code (15, 11). In Asian Conference on Intelligent Information and Database Systems, pp. 372–381. Springer, Berlin, Heidelberg, (2011)
23. Lien, B.K., Chen, S.-K., Wang, W.-S., King, K.-P.: Dispersed data hiding using hamming code with recovery capability. In Genetic and Evolutionary Computing, pp. 179–187. Springer, Cham, (2015)
24. Jana, B., Giri, D., Mondal, S.K.: An efficient data hiding scheme using hamming error correcting code. Proceedings of the Sixth International Conference on Computer and Communication Technology 2015. (2015)
25. Medeni, M.B., Souidi, E.M.: A novel steganographic protocol from error-correcting codes. J. Inf. Hiding Multimedia Sig. Process. **1**(4), 337–343 (2010)
26. Rifà-Pous, H., Rifà, J.: Product perfect codes and steganography. Digit. Sig. Process. **19**(4), 764–769 (2009)
27. Kumar, S., Muttoo, S.K.: Robust and secure image steganographic algorithm based on matrix embedding. Int. J. Electr. Secur. Digit. Forensics **6**(3), 219–240 (2014)
28. Eaton, J.W., Bateman, D., Hauberg, S., Wehbring, R.: GNU Octave version 5.2. 0 manual: a high-level interactive language for numerical computations. (2020). https://www.gnu.org/software/octave/doc/v5.2
29. Michaels, J.G., Rosen, K.H. (eds.): Applications of Discrete Mathematics, vol. 267. McGraw-Hill, New York (1991)
30. Deo, N.: Graph Theory with Applications to Engineering and Computer Science. Courier Dover Publications, (2017)
31. Solé, P., Zaslavsky, T.: The covering radius of the cycle code of a graph. Discret. Appl. Math. **45**(1), 63–70 (1993)
32. Stremler, F.G.: Introduction to communication systems. In ics. (1990)

Productivity Enhancement in Clock Domain Crossings Verification

Mangal Das, Niharika, and Amit Kumar Singh

Abstract A rapid rise in the complexity of designs and shrinking device dimensions has recently led to multimillion gate systems run with numerous asynchronous clocks. Traditional digital design testing and verification methods in many cases are unable to detect clock domain crossing (CDC) issues. At structural and functional level, existing methods provide an ad hoc partial verification which are erroneous and take huge time to analyze. If these source of potential error are not addressed and verified early in the design cycle, then the designs may go to silicon with functional errors. Detection of these errors in post-silicon verification is very costly in terms of time and money. Automatic tools can warrant that these multi-clock designs are corrected prior to final tape out of design. But, these tools give errors in the range of thousands if not used properly. Analysis of these reports can be very time-consuming as the number of false errors and warnings (noise) is generally huge. Manual CDC verification techniques only work well for verification but not for detection of issues. In this paper, the key optimization techniques have been reviewed which when used with the automatic tools will reduce the no of noise in analysis report. Reduction in false issues speed up verification cycle thus saving the overall cost.

Keywords Multi-clock design · CDC analysis tool · Asynchronous design · SoC · Missing clock information · Real CDC issue

M. Das
Department of Mechatronics Engineering, Manipal University Jaipur, Jaipur, Rajasthan, India

Niharika
Hindu College, University of Delhi, New Delhi, India

A. K. Singh (✉)
Department of Electronics and Communication Engineering, Manipal University Jaipur, Jaipur, Rajasthan, India

B. Sikdar et al. (eds.), *Proceedings of the 3rd International Conference on Communication, Devices and Computing*, Lecture Notes in Electrical Engineering 851,
https://doi.org/10.1007/978-981-16-9154-6_28

1 Introduction

Power-efficiency is one of the major concerns in the present day SOCs; higher number of clocks are required to fulfill the need of low-power design. Multiple clocks give rise to clock domain crossings between the signals of different domains. These clock domain crossings (CDCs) give rise to problems like metastability and hold violation. This makes CDC analysis mandatory for multimillion gate designs. Again, one of the biggest challenges in the analysis of clock domain crossing (CDC) is huge number of false error, tricky setup, total generated IPs, harden macros, legacy IPs, etc. The number of errors and warnings during CDC analysis could reach in the range of millions (100,000–1000) which makes analysis a time-consuming job. Automatic tools like SPYGLASS from Atrenta and Cadence CDC solution can ensure that the multi-clock designs are correct before the final tape out of design. But, these tools give errors in the range of thousands if not used properly. Analysis of these reports can be very time-consuming as number of false errors and warnings (noise) is generally huge. There are a number of papers [1–4] which discuss this issues from automatic tool usage. Techniques discussed in papers [5–8] are very good for manual CDC verification. These techniques only work well for verification but not for detection of issues.

Enhanced techniques related to synchronous and asynchronous reset design with Verilog-2001 ANSI-style have been discussed [1]. A detailed study on false errors after CDC analysis and solutions with cases studies has been presented [2]. The design issues and major challenges in treatment of CDC has been discussed along with the fundamentals of CDC [3]. Various methods have been discussed to enable robust development and verification of multi-asynchronous-clock designs [4]. Coding guidelines for nonblocking assignments and nonblocking assignments with delays have been discussed in detail [5]. Techniques to design and synthesize a safe FIFO between different clock domains have been presented for a range of asynchronous clocks speeds [6, 7]. Clock domain crossing (CDC) errors can be avoided by following certain guidelines and by utilizing well recognized verification practices [8]. A number of synchronization design errors have been presented, and several synchronizers have been discussed [9]. An approach for verifying clock-domain crossings in SoC hardware designs has been presented [10].

In this paper, various approaches to reduce number of false errors (noise) which come in to effect due to different reasons have been discussed. In Sect. 2, effects of wrong setup on CDC tool have been discussed. Issues related to asynchronous design are discussed in Sect. 3. Effects of glitches on valid acknowledgment-based synchronizer, reset issues are discussed in Sect. 4.

2 Setting-UP Environment for CDC Analysis Tools

Tools which are used in CDC verification are very sensitive to input given in form of RTL and setup. Wrong setup will result either in huge numbers of false errors or no errors at all. Some typical mistakes and their effect on the result are discussed in this section.

(i) Wrong or missing clocks and test clock.
(ii) Missing clock domain information for primary inputs and outputs.

CDC analysis tools divide the input and output on the basis of clock domains which are defined in the setup file. Spyglass design constraints (SGDC) is an example of such a setup file used by SPYGLASS. Generally, default clock is the first clock defined in the setup file. All unconstrained input and output are by default is in this clock domain. Missing test clock constraints will give rise to false errors in shift and capture mode. Missing clock information may hide real CDC issues as show in Fig. 1. In Fig. 1, groups A, B, C, and D come under clock domain 1 (A, C) and 2 (B, D). Let us consider clock domain 1 (group A) is default clock domain. Any unconstrained input or output pin will be considered in clock domain 1; in our case that will be a pin (THICK GRAY) of group B. Ideally, any convergence between signals of different clock domains should be reported as glitch in CDC analysis. But here, we will not get any warning or error form tool because it considers this pin by default in group A.

(iii) Quasi Static Signal

Quasi static signal is those register bits or primary inputs which shows no change in the value of long time of operation except while changing modes or enabling, disabling a portion of the design. Not defining quasi static (stable) signal will produce a large no. of false errors.

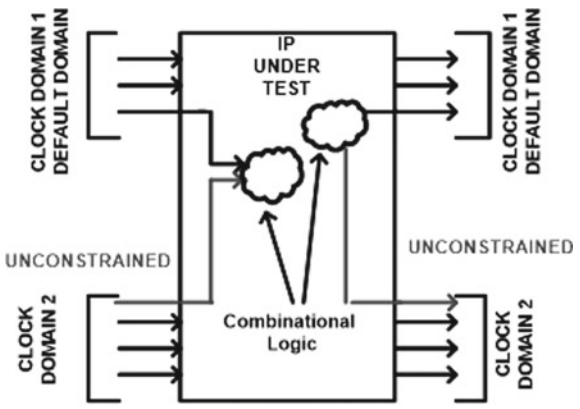

Fig. 1 Real CDC issues (between two clock domains) hidden due to missing clock information

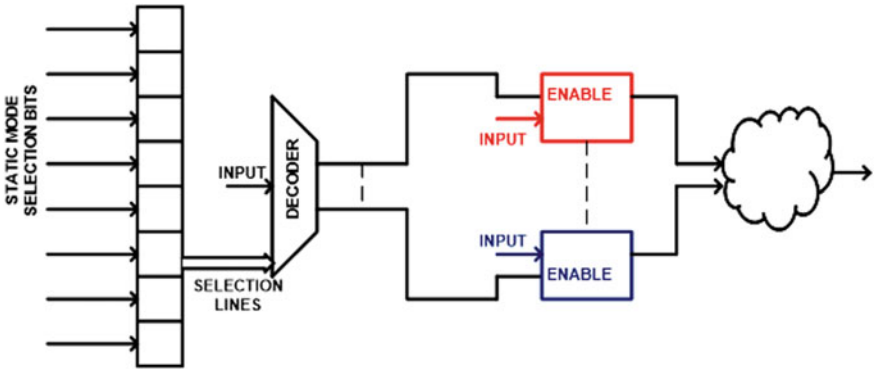

Fig. 2 Real CDC issues (quasi-static signal) hidden due to missing clock information

The case shown in Fig. 2 may give rise to a false error of glitch, but if the designer confirms that both sections of the design will not come into operation simultaneously, then there will be no glitch.

3 Customized Structures

Designers tend to use some special synchronization techniques which may in general give rise to clock domain crossing problems but work well with specific designs. Such errors can be waived, if the designer confirms no harm to the design. Single input multiple output (SIMO), FIFO, customized valid—acknowledgment synchronization technique will give rise to false errors.

Sometime companies use their own customized libraries for synthesis, hard macros in RTL or silicon verified legacy IPs. These structures cannot be understood by CDC analysis tools which cause noise in the results. It is good to verify these customized structures according to the given specification and if possible replace them by synopsis design ware library equivalents.

4 Real Issues

In this section, real CDC issues are discussed which can be easily overlooked due to noise present in the report.

(i) Reset errors: Asynchronous reset is advantageous but a risky affair. Even experienced designers may face problems with recovery and removal of time issues. Reset assertion may be done asynchronously, but reset removal should always be done in a synchronous manner.

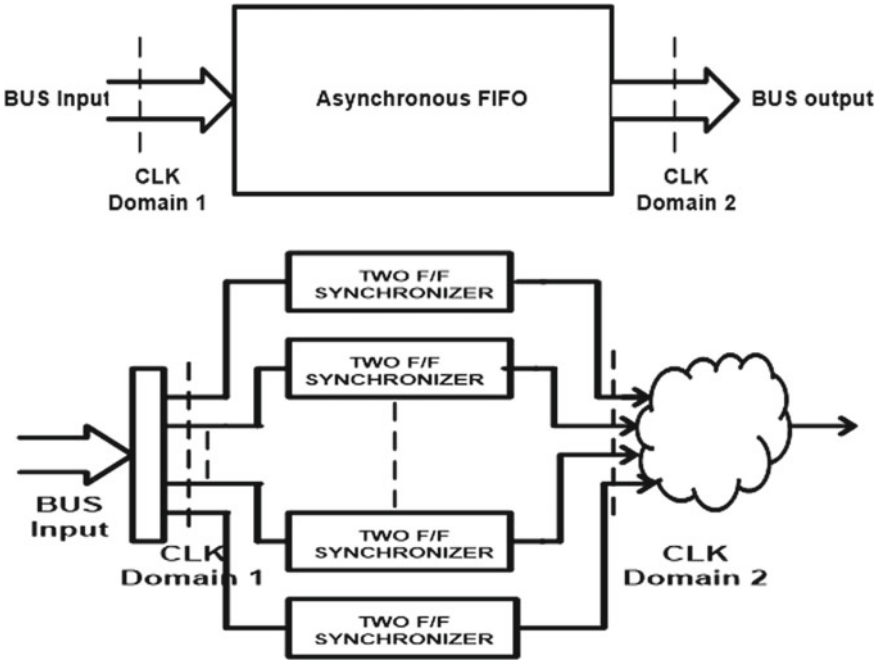

Fig. 3 Wrong way of multiple bit synchronization of the same bus

(ii) Multiple bit synchronization for same bus vector signals: Fig. 3 shows a wrong way of multiple bit synchronization of the same bus. In this scheme, bits of same bus are synchronized by two flip-flop synchronizers. Inherent latency present in the synchronizer can cause glitches on the convergence point of these signals. Standard way to handle multiple bit synchronization is to use asynchronous FIFO.

(iii) Valid acknowledgment structure: Valid acknowledgment structure shown in Fig. 4 is very effective single bit synchronization technique. But, this synchronization technique is also susceptible to glitch because glitch produced in clock domain 1 can be easily captured by first flop of synchronizer present in clock domain 2. This causes generation of false acknowledge signal in clock domain 2 which is sent back to domain 1 via the synchronizer. One possible solution of this problem is to use one more flops in clock domain1 just before the flop already present.

(iv) Problem of jitter in slow domain to fast domain crossing: one of the rarely seen problems in slow to fast domain crossing is jitter. Whenever low-frequency digital signal is derived from analog to digital convertor, it has an inherent jitter associated with it. Figure 5 shows the solution of this typical problem. These low-frequency digital signals should be fed to a Schmitt trigger. Output of this trigger can be fed to high frequency clock domain directly. This minimizes the noise at the clock domain crossing.

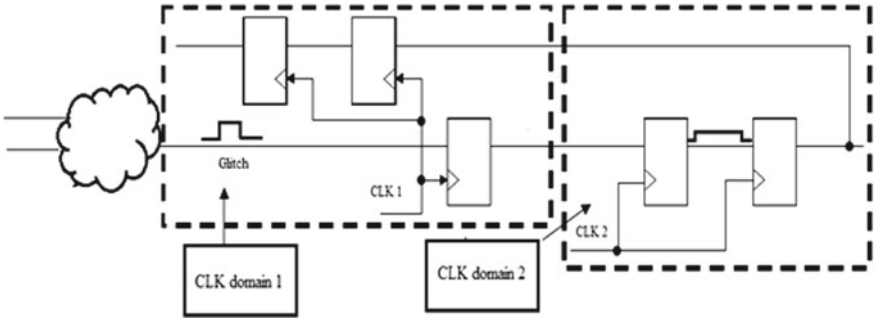

Fig. 4 Valid acknowledgment structure

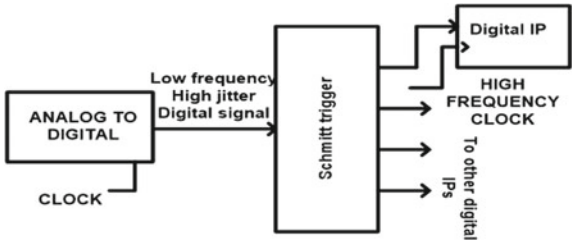

Fig. 5 Solution to the problem of jitter in slow domain to fast domain crossing

5 Conclusion

Automatic tools can ensure that the multi-clock designs are work correctly prior to final tape out of design. The errors given by these tools lie in the range of thousands if not used properly. Analysis of these reports can be very time-consuming as a number of false errors and warnings (noise) is generally huge. CDC verification techniques do not work for detection of issues. Optimization techniques have been discussed which when used with automatic tools will reduce the noise in the analysis report. It has been observed that clock domain crossing verification can done in much less time with much less noisy result through acknowledgment-based approach.

References

1. Cummings, C.E., Mills, D., Golson, S.: Asynchronous and Synchronous Reset Design Techniques. Part Deux. SNUG Bost. 9 (2003)
2. Lee, Y., Kim, N., Kim, J.B., Min, B.: Millions to thousands issues through knowledge based SoC CDC verification. In: ISOCC 2012–2012 International SoC Design Conference (2012). https://doi.org/10.1109/ISOCC.2012.6407123
3. Inc. www.cadence.com: Clock Domain Crossing: Closing the Loop on Clock Domain Functional Implementation Problems, Cadence Design Systems

4. Cummings, C.E.: Synthesis and Scripting Techniques for Designing Multi- Asynchronous Clock Designs. SNUG San Jose 2001. 26 (2001)
5. Cummings, C.: Verilog Nonblocking Assignments With Delays, Myths and Mysteries. Synopsys User Gr. Meet. (SNUG), Bost. (2002)
6. Clifford E.C.: Simulation and Synthesis Techniques for Asynchronous FIFO Design, Sunburst Design, Inc. (2002)
7. Cummings, C.E., Alfke, P.: Simulation and synthesis techniques for asynchronous FIFO design with asynchronous pointer comparisons post-SNUG editorial comment (by Cliff Cummings). In: SNUG (2002)
8. Cummings, C.E.: Clock domain crossing (CDC) Design and verification techniques using system verilog. Techniques (2008)
9. Ginosar, R.: Fourteen ways to fool your synchronizer. In: Proceedings—International Symposium on Asynchronous Circuits and Systems (2003) https://doi.org/10.1109/ASYNC.2003.1199169
10. Plassan, G., Peter, H.J., Morin-Allory, K., Sarwary, S., Borrione, D.: Improving the efficiency of formal verification: the case of clock-domain crossings. In: IFIP Advances in Information and Communication Technology (2017). https://doi.org/10.1007/978-3-319-67104-8_6

ABID: Attention-Based Bengali Image Description

Bidyut Das, Arif Ahmed Sekh, Mukta Majumder, and Santanu Phadikar

Abstract Image caption or description generation is a fundamental problem of artificial intelligence. It requires both knowledge, natural language processing, and computer vision together. It automatically produces description(s) from an image. The Bengali language is the fifth language spoken widely in the world. It is considered in many areas of research and development. Various established datasets are available in the literature for image caption generation in English since no such standard dataset exists for Bengali. This paper proposes a model for automatic image captioning in the Bengali language. This study uses a Bengali dataset to train the encoder–decoder neural network model. The proposed model trained with two descriptions per image and achieved a 0.67 BLEU-1 score. We expect that a far better result is obtained with a larger and more diverse dataset.

Keywords Bengali image caption · Image description · Bengali NLP · Deep learning · Attention mechanism

1 Introduction

Over the past few years, the automatic image description generation has taken a lot of attention. Numerous researchers worked in the area of image captioning and showed a notable improvement using the encoder–decoder framework [31]. The encoder–decoder framework involves convolutional and recurrent neural network (CNN +

B. Das (✉)
Department of Information Technology, Haldia Institute of Technology, Haldia, India

A. A. Sekh
School of Computer Science and Engineering, XIM University, Bhubaneswar, India

M. Majumder
Department of Computer Science and Application, University of North Bengal, Darjeeling, India

S. Phadikar
Department of Computer Science and Engineering, Maulana Abul Kalam Azad University of Technology, West Bengal, India

B. Sikdar et al. (eds.), *Proceedings of the 3rd International Conference on Communication, Devices and Computing*, Lecture Notes in Electrical Engineering 851,
https://doi.org/10.1007/978-981-16-9154-6_29

Fig. 1 Attention-based image caption

RNN). The CNN is used as an encoder to encode the image. The RNN is used as the decoder to predict the sequence of words [12, 14, 34].

In the literature, several datasets are available freely for English captioning, such as Flickr8K [10], Flickr30K [35], MS COCO [19], and many more. But we have found few works of image captioning in regional language due to the lack of datasets. The possible application of image captioning in the regional language is image searching, image description for social media, news, e-commerce Web sites, and audio of image descriptions for visually challenged people. The three most popular languages of image captioning research in the world are English, Chinese, and Spanish [8]. However, there is very limited research on image captioning in the Bengali language, but the Bengali language is the world's fifth most spoken language. It is also a widely spoken Indian language, and some people living here do not know English. Therefore, image captioning in Bengali can be useful for those people who do not understand any language other than Bengali.

The paper is organized into six sections. Section 2 describes the previous works on image captioning in English and other regional languages. Section 3 explains the proposed method. Next, Sect. 4 exhibits the used dataset and how the model is trained for generating Bengali image captions. The results of the experiment and discussion are depicted in Sect. 5. In the end, Sect. 6 concludes the work.

2 Related Work

We present here the state of the art and the various strategies employed in the literature of image captioning. Several researchers worked in this research area and proposed different methods to describe the image [3]. Previous works are illustrated into two subsections based on the description language of the image: (2.1) image captioning in

English and (2.2) image captioning in regional languages. At last, we have included our observation from previous literature in subsection (2.3).

2.1 Image Captioning in English

Fundamental work on image captioning was focused mainly on two types of research methods: retrieval-oriented method and template-oriented method [3]. The disadvantage was that the methods were not described enough [3] and used a hardcoded language structure. For this reason, these methods become no longer extant, and the neural network arrived into play [11]. The attention-based encoder–decoder is the next advanced encoder–decoder framework. Xu et al. [32] introduced the first attention mechanism in the image caption generation. This attention framework was adding random weights to an image. Hence, some essential parts of the image are getting missed for generating captions. You et al. [34] proposed a semantic attention framework to overwhelm this limitation. It focused on linguistically significant objects/actions in the image. Next, Lu et al. [20] developed an adaptive attention mechanism. It is a more advanced version than the attention model. It decides automatically to use the visual signal or the language model. If it decides to use visual signal, then it chooses which portion of the image to use. Chen et al. [4] employed a semantic attention model and compared it with pre-trained CNN, e.g., VGG16 or ResNet50. Their experiments showed that ResNet50 gave better results than VGG16. Anderson et al. [1] proposed a visual attention model that combined bottom-up and top-down model for image captioning. This advanced method generates natural captions and got the highest accuracy on the MS COCO dataset.

2.2 Image Captioning in Regional Languages

Miyazaki and Shimizu (2016) [22] developed an image captioning dataset '*YJ captions 26k*' in Japanese. They analyzed three learning techniques in their research and observed that the best technique is transfer learning to generate Japanese image captions. Yoshikawa et al. (2017) [33] formed *STAIR Caption*, a Japanese caption dataset from the images of the MS COCO dataset. Usually, researchers collected image descriptions from two sources for captioning research in Japanese: crowdsource and machine translator [25]. In Chinese, Li et al. (2016) [17] obtained image description from three sources for Flicker-8k images to generate captions: crowdsource, machine translator, and human translator. Li et al. (2019) [18] developed caption datasets from crowdsource. Besides crowdsourcing caption, Lan et al. (2017) [16] utilized human resources to translate and modify the image description. Zeng et al. (2017) [36] trained their model with machine-translated captions for generating image captions. Apart from Japanese image captioning, little research on image description generation has been conducted in German, Dutch, French, and Spanish languages. Elliott

et al. (2015) [6] developed an image captioning model. It is a multilingual model where German and English descriptions are grounded parallelly against image features. Miltenburg et al. (2017) [30] present their work in the image captioning area to generate Dutch image descriptions. They had collected Dutch image descriptions from crowdsourcing and combined them with the Multi30k dataset. They analyzed the Dutch image descriptions with the English and French image descriptions using the Multi30k dataset. They found separate image descriptions for different languages because of their cultural differences. Gomez-Garay et al. (2018) [8] proposed a system for generating and verbalizing Spanish image descriptions for visually impaired people. Elliott et al. (2016) [7] stated the best evaluation method is human evaluation for generating image descriptions. Therefore, their research considered the manual evaluation for evaluating the correctness of generated captions. But their research used only high BLEU-scored captions for the human evaluation due to the limitation of time. Kama et al. [13] proposed an automated image captioning system, TextMage, that generates image descriptions in Bengali with a south Asian bias. Khan et al. [15] developed a Bengali image captioning system. It used a one-dimensional convolutional neural network with a pre-trained model ResNet50 for extracting visual features.

2.3 Observation from Previous Literature

Numerous approaches are applied to the image captioning literature in English and other non-English languages. But we did not find any research that achieved satisfactory results in Bengali for generating captions. After investigating the past methods, our work decided to consider the attention-based encoder–decoder framework for generating captions in Bengali. For training purposes, the neural network model requires a Bengali dataset. In the experiment, we trained our model using the publicly available dataset '*BanglaLekhaImageCaptions*' [21].

3 Proposed Method

The proposed method is an encoder–decoder-based deep learning framework. It consists of (1) a CNN-based encoder and attention module and (2) an RNN-based decoder. The method is depicted in Fig. 2.

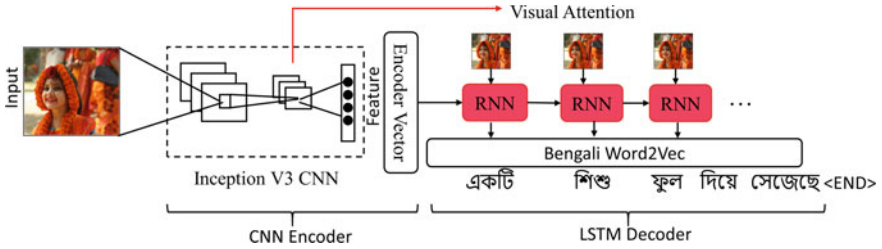

Fig. 2 Modules of the proposed system. The caption একটি শিশু ফুল দিয়ে সেজেছে (A child is dressed with flowers)

CNN-based Encoder and Attention: The main role of the CNN-based encoder is to extract the visual feature and provide suitable attention to the image. We have used the Inception V3 [28] architecture, pre-trained on ImageNet [26], for feature extraction and attention generation. The method takes 299 × 299 image as input and provides 2048 feature vectors. We have used neural translation attention proposed by Bahdanau et al. [2]. The attention is defined by a context vector (κ_i) defined by the sum of sequence annotation (h_i). The vector is defined by equation (1), where L_x is the length of the input sequence (x) and α_{ij} is the weight of each input annotation h_t. α is estimated during training.

$$\kappa_i = \sum_{j=1}^{L_x} \alpha_{ij} h_j \tag{1}$$

RNN-based Decoder: The RNN-based decoder consists of gated recurrent units (GRUs) [5]. It takes 256 dimension word embedding of the caption. It consists of two fully connected layers that combine the attention. The decoder combines the previous state with the context vector (κ). The role of the RNN is to map the captions with attention. Let the temporal attention at time (t) be defined by the feature f_t, and the description is defined by the word (w_i). We define a relation between f_t and (w_i). The loss is defined by the recurrent loss of a description with the attention as follows:

$$L = 1 - \sum_{j=1} N(match(w_i, f_t)) \tag{2}$$

Network and Training Parameters: The method uses 299 × 299 RGB image as input. Next, the image is converted into 2048 dimension feature vector extracted from the last fully connected Inception V3 layer. We have used 64 × 1 attention extracted from the skip connections of different convolution layers of the Inception module. In the RNN, we have used 512 hidden units that combine 64 × 1 attention map and 256 dimension word embedding from caption. We have used sparse categorical cross-entropy loss. The model is trained using Adam optimizer over 120 epochs.

4 Dataset

A dataset is required to train the model of image captioning in Bengali. We used *BanglaLekhaImageCaptions* [21] dataset to train our model. It includes 9154 images with two captions for every image. Two Bengali native speakers generated the captions for this dataset. This dataset is small in volume than the available datasets in English. The dataset keeps some relevance to Bengali culture. But it has a large amount of human bias. The bias prevents the ability of any model to generate caption on non-human subjects. In some cases, the captions are also not detailed. So, the training of any model and its evaluation accuracy using this dataset is not achieved as expected. We have divided the total dataset into three parts: 80% images are used for training, 10% are used for validating, and the rest 10% are used for testing.

5 Results and Discussion

The captions generated from our proposed method were analyzed using the popular evaluation measure *Bilingual Evaluation Understudy (BLEU)* [23]. Table 1 includes a comparison between our model with other existing models. We tested our method with VGG16 [27], ResNet50 [9], and Inception V3 [28] model and found Inception V3 outperforms than others. Figure 3 shows the loss curve over epochs during training. Figure 4 displays the attention regions of an image to generate captions. Figure 5 visualizes some results of our model.

Table 1 Performance of our model with other models on BanglaLekhaImageCaptions dataset

Method	Accuracy	
	BLEU-1	**BLEU-4**
Mixture model [29]	0.63	0.16
Injection model [24]	0.61	0.16
Encoder–decoder [15]	0.58	0.17
Proposed + VGG16 [27]	0.52	0.16
Proposed + ResNet50 [9]	0.58	0.18
Proposed + Inception [28]	0.67	0.26

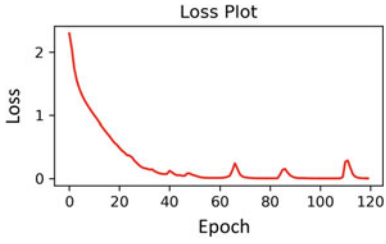

Fig. 3 Loss over epochs during training

Real Caption: 'একটি শিশু হাসি মুখে তাকিয়ে আছে।' 'একজন বাচ্চা দাঁত বের করে চেয়ে আছেন।'
(A child is looking with a smile on his face. A child looking with showing his teeth.)

Prediction Caption: 'একটি শিশু তাকিয়ে আছে।' 'একজন ছোট মেয়ে হাঁসি দিয়ে দাঁত বের করে চেয়ে আছে।'
(A child is looking. A little girl is laughing and gritting her teeth.)

Fig. 4 Example of different attention regions generated by the proposed method and corresponding caption

455.png

R: একটি শিশু ফুল দিয়ে সেজেছে।, একটি বাচ্চা মেয়ে ফুল মাথাই দিয়ে হাসছে।
A child is dressed with flowers, A baby girl is smiling with a flower head.

P: একটি শিশু তাকিয়ে আছে।, একজন ছোট মেয়ে হাঁসি দিয়ে দাঁত বের করে চেয়ে আছে।
A child is looking. A little girl is laughing with gritting her teeth.

3511.png

R: নৌকায় দুইজন মানুষ আছে।, ১ টি নৌকায় বসে আছে মাঝি এবং আরেকজন পুরুষ নৌকা থেকে জাল ফেলছে পানিতে।
There are two people in the boat, A boatman is sitting in one boat and another man is throwing nets from the boat into the water.

P: দুইজন মানুষ একটি নৌকা চালাচ্ছে।, নদীর উপর দিয়ে মাছ ধরছে।
Two people are driving a boat, Fishing on the river.

3346.png

R: সরিষা ক্ষেতের মাঝ দিয়ে দুইজন মানুষ হেঁটে যাচ্ছে।, অনেকগুলো সরিষা ক্ষেত যার মাঝ দিয়ে একটি রাস্তা দিয়ে হেটে যাচ্ছে ৩ জন মানুষ।
Two people are walking through the middle of a mustard field. There are many mustard fields through which 3 people are walking along a road.

P: সরিষা ক্ষেতের মাঝ দিয়ে দুইজন মানুষ হেঁটে যাচ্ছে।, সরিষার ক্ষেত দিয়ে তিন জন যাচ্ছে।
Two people are walking through the mustard field. Three people are walking through the mustard field.

4808.png

R: এটি একটি মন্দির।, পুরাতন একটি মসজিদ।
It is a temple, An old mosque.

P: একটি মসজিদ আছে।, একটি পুরাতন মন্দির।
There is a mosque, An old temple.

Fig. 5 Random images are taken from the dataset to visualize the result of our proposed model. The R indicates the real captions, and the P indicates the predicted captions in the figure

This research gives a concept of generating image captions in Bengali using the visual attention model. Our model has trained using 9154 images where each image contains two captions. We observed that the accuracy of our attention model beats other models in Bengali. It achieved the highest accuracy 0.67 and 0.26 in BLUE-1 and BLUE-4, respectively. We tested our model with 120 epoch and showed as low as 0.002 loss at the end. It indicates the model stability of our model.

6 Conclusion

This paper presents an image captioning system in the Bengali language. The proposed method generates Bengali image captions using the visual attention mechanism. The model is trained with the *BanglaLekhaImageCaptions* dataset. The dataset consists of two descriptions for each image. The model achieved high BLEU-1 score than other models. In the future, we will train our model with more descriptions per image to improve the BLEU score. The model suffers from the recognition of non-human subjects because the dataset is biased toward human subjects. Therefore, there is a need to develop a well-varied and detailed captioning dataset in Bengali to improve accuracy. However, the experimental results show that the model can contribute to Bengali image captioning research, and it can be a useful model in the future.

References

1. Anderson, P., He, X., Buehler, C., Teney, D., Johnson, M., Gould, S., Zhang, L.: Bottom-up and top-down attention for image captioning and visual question answering. In: Proceedings of the IEEE Conference on Computer Vision and Pattern Recognition, pp. 6077–6086 (2018)
2. Bahdanau, D., Cho, K., Bengio, Y.: Neural machine translation by jointly learning to align and translate. arXiv preprint arXiv:1409.0473 (2014)
3. Bai, S., An, S.: A survey on automatic image caption generation. Neurocomputing **311**, 291–304 (2018)
4. Chen, Q., Li, W., Lei, Y., Liu, X., He, Y.: Learning to adapt credible knowledge in cross-lingual sentiment analysis. In: Proceedings of the 53rd Annual Meeting of the ACL and the 7th International Joint Conference on NLP (Volume 1: Long Papers), pp. 419–429
5. Cho, K., van Merriënboer, B., Gulcehre, C., Bahdanau, D., Bougares, F., Schwenk, H., Bengio, Y.: Learning phrase representations using rnn encoder–decoder for statistical machine translation. In: Proceedings of the 2014 Conference on Empirical Methods in Natural Language Processing (EMNLP), pp. 1724–1734 (2014)
6. Elliott, D., Frank, S., Hasler, E.: Multilingual image description with neural sequence models. arXiv preprint arXiv:1510.04709 (2015)
7. Elliott, D., Frank, S., Sima'an, K., Specia, L.: Multi30k: Multilingual English-German Image Descriptions. arXiv preprint arXiv:1605.00459 (2016)
8. Gomez-Garay, A., Raducanu, B., Salas, J.: Dense captioning of natural scenes in Spanish. In: Mexican Conference on Pattern Recognition, pp. 145–154. Springer (2018)

9. He, K., Zhang, X., Ren, S., Sun, J.: Deep residual learning for image recognition. In: Proceedings of the IEEE Conference on Computer Vision and Pattern Recognition, pp. 770–778 (2016)
10. Hodosh, M., Young, P., Hockenmaier, J.: Framing image description as a ranking task: Data, models and evaluation metrics. J. Artif. Intell. Res. **47**, 853–899 (2013)
11. Hossain, M.Z., Sohel, F., Shiratuddin, M.F., Laga, H.: A comprehensive survey of deep learning for image captioning. ACM Comput. Surv. (CsUR) **51**(6), 1–36 (2019)
12. Johnson, J., Karpathy, A., Fei-Fei, L.: Densecap: fully convolutional localization networks for dense captioning. In: Proceedings of the IEEE Conference on Computer Vision and Pattern Recognition, pp. 4565–4574 (2016)
13. Kamal, A.H., Jishan, M.A., Mansoor, N.: Textmage: the automated Bangla caption generator based on deep learning. In: 2020 International Conference on Decision Aid Sciences and Application (DASA), pp. 822–826. IEEE (2020)
14. Karpathy, A., Fei-Fei, L.: Deep visual-semantic alignments for generating image descriptions. In: Proceedings of the IEEE Conference on Computer Vision and Pattern Recognition, pp. 3128–3137 (2015)
15. Khan, M.F., Shifath, S., Islam, M., et al.: Improved bengali image captioning via deep convolutional neural network based encoder-decoder model. arXiv preprint arXiv:2102.07192 (2021)
16. Lan, W., Li, X., Dong, J.: Fluency-guided cross-lingual image captioning. In: Proceedings of the 25th ACM International Conference on Multimedia, pp. 1549–1557 (2017)
17. Li, X., Lan, W., Dong, J., Liu, H..: Adding Chinese captions to images. In: Proceedings of the 2016 ACM on International Conference on Multimedia Retrieval, pp. 271–275 (2016)
18. Li, X., Xu, C., Wang, X., Lan, W., Jia, Z., Yang, G., Xu, J.: COCO-CN for cross-lingual image tagging, captioning, and retrieval. IEEE Trans. Multimedia **21**(9), 2347–2360 (2019)
19. Lin, T.-Y., Maire, M., Belongie, S., Hays, J., Perona, P., Ramanan, D., Dollár, P., Zitnick, C.L.: Microsoft coco: common objects in context. In: European Conference on Computer Vision, pp. 740–755. Springer (2014)
20. Lu, J., Xiong, C., Parikh, D., Socher, R.: Knowing when to look: Adaptive attention via a visual sentinel for image captioning. In: Proceedings of the IEEE Conference on Computer Vision and Pattern Recognition, pp. 375–383 (2017)
21. Mansoor, N., Kamal, A.H., Mohammed, N., Momen, S., Rahman, M.M.: Banglalekhaimage-captions, mendeley data (2019). Date last accessed 15 July 2014
22. Miyazaki, T., Shimizu, N.: Cross-lingual image caption generation. In: Proceedings of the 54th Annual Meeting of the Association for Computational Linguistics (Volume 1: Long Papers), pp. 1780–1790 (2016)
23. Papineni, K., Roukos, S., Ward, T., Zhu, W.-J.: Bleu: a method for automatic evaluation of machine translation. In: Proceedings of the 40th Annual Meeting of the Association for Computational Linguistics, pp. 311–318 (2002)
24. Rahman, M., Mohammed, N., Mansoor, N., Momen, S.: Chittron: an automatic Bangla image captioning system. Procedia Comput. Sci. **154**, 636–642 (2019)
25. Rathi, A.: Deep learning apporach for image captioning in Hindi language. In: 2020 International Conference on Computer, Electrical & Communication Engineering (ICCECE), pp. 1–8. IEEE (2020)
26. Russakovsky, O., Deng, J., Su, H., Krause, J., Satheesh, S., Ma, S., Huang, Z., Karpathy, A., Khosla, A., Bernstein, M., et al.: Imagenet large scale visual recognition challenge. Int. J. Comput. Vis. **115**(3), 211–252 (2015)
27. Simonyan, K., Zisserman, A.: Very deep convolutional networks for large-scale image recognition. arXiv preprint arXiv:1409.1556 (2014)
28. Szegedy, C., Vanhoucke, V., Ioffe, S., Shlens, J., Wojna, Z.: Rethinking the inception architecture for computer vision. In: Proceedings of the IEEE Conference on Computer Vision and Pattern Recognition, pp. 2818–2826 (2016)
29. Tanti, M., Gatt, A., Camilleri, K.: What is the role of recurrent neural networks (rnns) in an image caption generator? In: Proceedings of the 10th International Conference on Natural Language Generation, pp. 51–60 (2017)

30. van Miltenburg, E., Elliott, D., Vossen, P.: Cross-linguistic differences and similarities in image descriptions. arXiv preprint arXiv:1707.01736 (2017)
31. Vinyals, O., Toshev, A., Bengio, S., Erhan, D.: Show and tell: a neural image caption generator. In: Proceedings of the IEEE Conference on Computer Vision and Pattern Recognition, pp. 3156–3164 (2015)
32. Xu, K., Ba, J., Kiros, R., Cho, K., Courville, A., Salakhudinov, R., Zemel, R., Bengio, Y.: Show, attend and tell: Neural image caption generation with visual attention. In: International Conference on Machine Learning, pp. 2048–2057. PMLR (2015)
33. Yoshikawa, Y., Shigeto, Y., Takeuchi, A.: Stair captions: constructing a large-scale japanese image caption dataset. arXiv preprint arXiv:1705.00823 (2017)
34. You, Q., Jin, H., Wang, Z., Fang, C., Luo, J.: Image captioning with semantic attention. In: Proceedings of the IEEE Conference on Computer Vision and Pattern Recognition, pp. 4651–4659 (2016)
35. Young, P., Lai, A., Hodosh, M., Hockenmaier, J.: From image descriptions to visual denotations: new similarity metrics for semantic inference over event descriptions. Trans. Assoc. Comput. Linguist. **2**, 67–78 (2014)
36. Zeng, X., Wang, X.: Add English to image Chinese captioning. In: 2017 IEEE 2nd International Conference on Cloud Computing and Big Data Analysis (ICCCBDA), pp. 333–338. IEEE (2017)

Performance Study of a Cambered Blade H-Rotor by CFD Analysis

Dipankar Sarkar and Anal Ranjan Sengupta

Abstract Vertical axis wind turbines (VAWTs) have performed well and delivered a prominent fortitude to harvest the energy from the complex wind condition; as because of it, the application and development are increased in the past few decades. This present study is conducted to analyze the performance of an unsymmetrical LS-0421 profile three-bladed H-rotor and then compared with a symmetrical S-1046 profile three-bladed H-rotor. At the solidity of 0.42, and at the low TSR range of 2.0–4.0, the LS-0421 rotor shows better performance. Between two different computational wind speeds (6 and 8 m/s) conditions, in 8 m/s condition, the H-rotor has obtained the highest C_P of 0.41 at TSR 3.5. Additionally, this study has covered only the 2-dimensional computational simulation; there will be a bit different result in 3-dimensional simulation than this study result.

Keywords Power coefficient · Lift coefficient · TSR · LS-0421 · H-rotor

1 Introduction

Nowadays, human being is more dependent upon renewable energy resources due to the increased emission of greenhouse gases, global warming, and the exponential reduction of the fossil's fuels. In the past few decades, the demand and uses of renewable energy have been growing rapidly. In the 1970s, the energy crisis occurred when petroleum production declined worldwide [1], then alternative to fossils fuels the uses of renewable resources such as solar, hydro, wind, biomass, geothermal, biofuels have been increasing because of the depletion of conventional fuels. Among the several renewable energy sources, wind energy is a highly prominent and abundantly available source. The wind turbine is such a device that extracts the energy from the wind and converts it into the desired form of energy. Vertical axis wind turbines (VAWTs) are familiar with their simple structure and independent of the direction of the wind. Precise designed VAWTs can produce wind energy in both

D. Sarkar (✉) · A. R. Sengupta
Department of Mechanical Engineering, JIS College of Engineering, Kalyani, West Bengal, India

B. Sikdar et al. (eds.), *Proceedings of the 3rd International Conference on Communication, Devices and Computing*, Lecture Notes in Electrical Engineering 851,
https://doi.org/10.1007/978-981-16-9154-6_30

cases at lower and higher wind speeds. VAWTs can be installed in remote places as well as in urban areas for their compact design. Because of these above advantages of the VAWTs, beyond the 1980s, research, development, and its application in this field have emerged highly. In terms of small wind power generation, VAWTs have great future forecasts among the allover wind technologies, especially in the built environment. The wind turbines are majorly categorized into two systems according to their rotation of the axis. These are (a) horizontal axis wind turbine or HAWT and (b) vertical axis wind turbine or VAWT. There are main classifications of the VAWT exists, (a) Darrieus rotor, (b) Savonius rotor and (c) hybrid Darrieus-Savonius rotor (in Fig. 1). In this study, we are especially looking forward to the three-bladed H-Darrieus rotor or H-rotor. In the wide application of the VAWTs, the excellent harvests of energy are the most important part of the investigation. The VAWTs system depends upon various factors such as the definite environment, wind speed, blade design, weight, a system of energy conversion components [2]. The primary concern of the investigation on the VAWTs is improving the performance of the system. Darrieus rotor has a greater power coefficient (C_P) than the conventional Savonius rotor and lesser sensitivity to the turbulent wind condition [3]. Alternative structure of the Darrieus, straight blade except curved blade known as H-rotor, which is a simpler design and easy to construct. Though the H-rotor harvests more power than the Savonius rotor, it is poor in self-starting nature.

Other accesses were anticipated to improving the self-starting characteristics by optimizing the configuration and parameters such as turbine solidity, the thickness of blades, pitch angle, tilted blades [5], variable pitch [6], flexible sails.

Baker [7] has theoretically compared symmetrical NACA 0012 with the asymmetrical NACA 0012 airfoil, and stated that the cambered airfoil would exhibit higher tangential force across a broad range of the angle of attack (AOA) causing self-starting ability of this rotor. In the event of high solidity and low-wind speed at TSR range from 0.5 to 2.4 Sengupta et al. [8] worked on a symmetrical (NACA 0018) and an unsymmetrical (S815) blade H-rotor to compare the performance of these. The results have resolute that in 6 m/s as the optimum wind speed the S815 blade rotor has produced maximum power coefficient (C_P), at 270° of azimuthal position

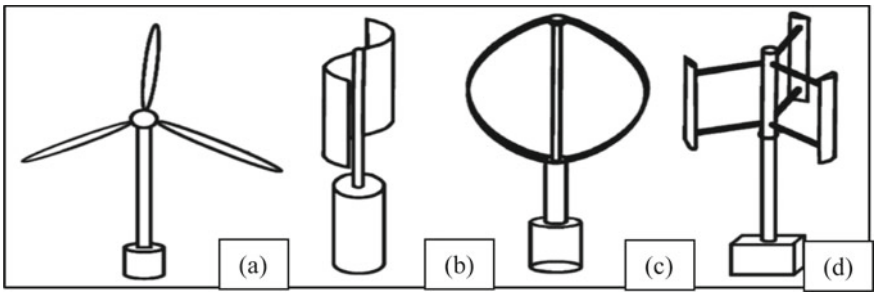

Fig. 1 Different types of wind turbines, **a** HAWT, **b** Savonius turbine, **c** Darrieus turbine, **d** H-Darrieus turbine [4]

makes higher lift coefficient. Deshpande et al. [9] have performed a numerical study over three selected symmetrical (NACA 0018 and NACA 0015) and unsymmetrical (S1210) blade profiles; the highest C_P is 0.4 for NACA0018 at a solidity of 0.2 and TSR 3 in wind speed of 5 m/s. The maximum C_P for NACA0015 is 0.42 at TSR 2 with a solidity of 0.4 in the same wind speed; the S1210 airfoil produces a quite lower, but closer power output to others. Sengupta et al. [10] have found that the cambered S815-bladed rotor has exhibited higher dynamic torque and C_P than cambered EN0005 and symmetrical NACA 0018-bladed H-Darrieus rotors. The optimum C_P value is 0.19.

Mohamed [11] found that the increment of the C_P by 26.83% for the experimental model is better than the traditional Darrieus turbine. Danao et al. [12] confirmed in an experiment that a little cambered airfoil such as the LS-0421 can enhance the performance of the VAWT. LS-0421 has carried out the best performance with a C_P of 0.40 at TSR 3.5. A downward cambered along with the blade path is the reason; the blade generates a higher value of torque correspondingly in the upwind and the downwind areas, but an upward inverted cambered blade produces power generally in the upwind area. In another study, Sengupta et al. [13] have performed on the impact of the blade camber and the curvature to the performance ofVAWT inwind speed from 4 to 8 m/s. Authors have been determined that in advancing stroke higher curvature blade (S815) displays a better result. On the other hand, in returning stroke, lower curvature blade has shown a better result.

Ramkissoon et al. [14] worked on the turbine is being made up of three NACA 0018 blades. They concluded that the varying of the angle of attack (AOA) from 10° to −10° hasn't indicated any substantial effects on improving the output power from the turbine. Sayed et al. [15] have performed the 2D CFD study over a set of airfoil profiles and examined that at the lower angle of attack (AOA), lift coefficient (C_L) has increased, and drag coefficient (C_D) has decreased. Mohamed [16] performed both numerical and experimental analysis to check the self-starting ability. The result indicates that the drag type blade has a static torque higher than the lift type. In an experimental study, Bhuyanand Biswas [17] has found that the regular H-rotor at a TSR of 2.29 and R_e is 1.92×10^5, generates optimum C_P is of 0.28. Sengupta et al. [18] have experimentally performed with three unique blade profiles to investigate the threshold staring time of the H-rotor, discovered that EN0005 profile H-rotor has taken the lowest time to start. Moreover, in 0.51 optimum solidity, the S815-bladed H-rotor exhibits the maximum of C_P of 0.19 at TSR 1.43. Gupta et al. [19] tested a rotor, and it is found that the maximum power coefficient of 0.46 was obtained at an optimum H/D ratio of 1.54. Islam et al. [20] have observed that in smaller-scaled SB-VAWT, the conventional NACA symmetrical airfoils are not suitable to use. Rather, it is useful to operate in low-speed conditions for the unsymmetrical thick airfoils which have a higher lift and lower drag characteristics.

2 Objectives of the Present Study

The comparative study has an overview of several parameters of the H-rotor, which have been set to realize the intended goal is to investigate the performance of the H-rotor in the low TSR range. From the existing literature, it is found that the unsymmetrical LS-0421 profile-bladed H-rotor would show significant results in low TSR and low wind speed. Hence, 2D CFD simulation of the H-rotor with different dimensions has been conducted at different wind speeds. Furthermore, the aerodynamics performance of the unsymmetrical-bladed H-rotor [11] to the existing symmetrical-bladed H-rotor is also carried out.

3 CFD Simulation

3.1 Geometrical Model

For this study, the selected unsymmetrical airfoil profile LS-0421 is equipped with a rotor. The rotor is made up of three LS-0421 blades with a diameter of 3 m. The struts of the rotor are connected at the ¼th of the length from the leading edge to the airfoils. The chord length of the LS-0421 is 0.18 m. The domain has mainly two regions: the rotating domain which has represented the rotor and the fixed domain the rest of the domain, as the wind tunnel (Fig. 2). These two regions are tangentially contracted by two adjacent circles, which helps the rotating region as well as the rotor to rotate gradually, this technique is known as the sliding-mesh method (SMM). The free stream air is coming from the inlet velocity section to strike the rotor and then goes through the pressure outlet section. All the meshing has been conducted by the ANSYS Mesh® component. Because of the uneven layout of the blade profile, an unstructured triangular mesh in the rotating domain and an unstructured quad mesh method in the fixed domain are used with resolution factor 2, which implies that the

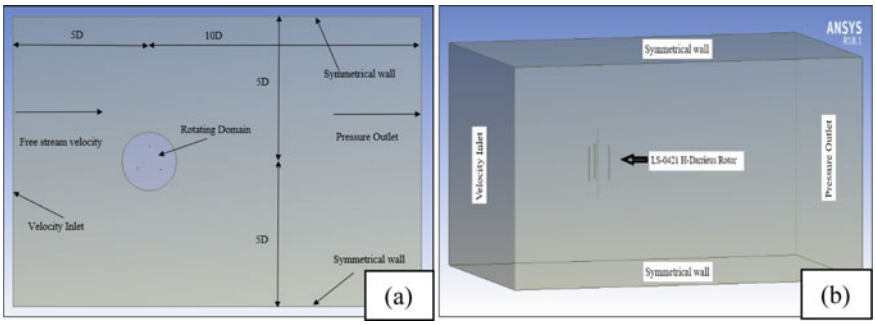

Fig. 2 **a** 2D view and **b** 3D view of the computational domain

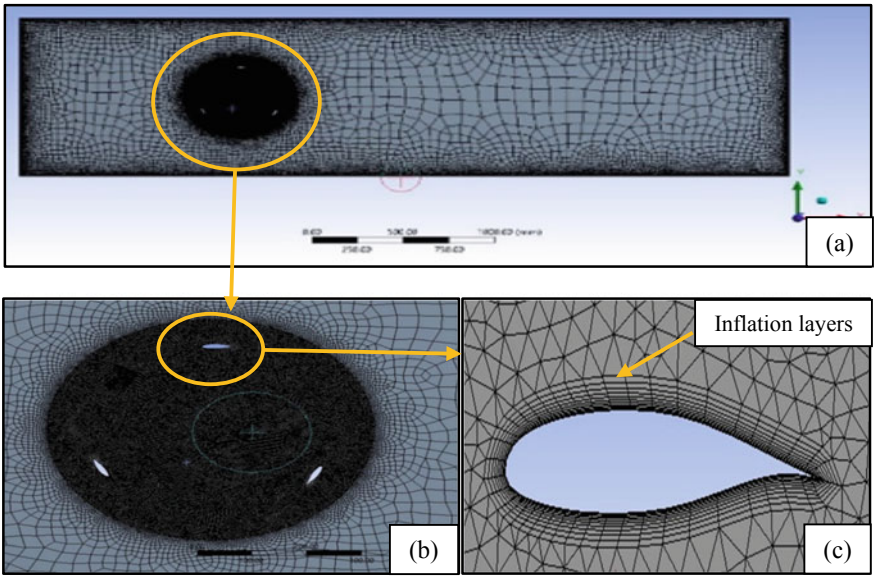

Fig. 3 **a** Mesh of the computational domain, **b** Mesh of the rotating domain (H-Rotor), **c** Mesh of the airfoils

mesh is finer. The meshing of the computational domain and one of the airfoils of the rotor is illustrated in Fig. 3.

The grid independence study (GIS) is performed to achieve the accurate aerodynamics forces by changing the quality of the mesh number of times. The lift coefficient (C_L) is considered as that GIS parameter. The number of elements all over the computational domain in the final refinement level is around 150,000. It is seen that the mesh is much denser at the rotating domain as compared to the remaining of the domain. Even the inflation layers adjacent to the surface of the airfoils are formed finely. Inflation has been done around every boundary surface of the airfoils, with 20 layers in total and a growth rate of 1.2.

3.2 Numerical Setup

Present numerical simulations are accomplished in the ANSYS Fluent® software package. In the present study, the whole simulation is performed to simulate the turbulent flow in the transient state. The simulation is conducted at two different wind speeds, at 6 and 8 m/s. Simulations have been done in the TSR range of 2.0–4.0. There are few turbulence models are available, which have unique conditions, formulas and approaches to solve the specific problem. From the comparative study, it has been found that the effects of selection of the accurate turbulence models in numerical simulations of the VAWTs are important to get the result precisely, and

stated that the realizable k-ε model is the proper one, having lower computational cost as well. The 'Near-wall treatment' function is selected as 'Standard wall functions'. Properties of fluid (air) are measured at a normal room temperature of 25 °C. At the velocity-inlet, the magnitude of inflow wind is 6 and 8 m/s differently with the turbulence intensity of 0.1%. Two horizontal walls are in no-slip condition. The present model setup or problem solved by the pressure–velocity coupling method under the SIMPLEC algorithm solver with the skewness correction is 3. Spatial discretization of pressure is in second-order, momentum; turbulent kinetic-energy and turbulent dissipation-rate are in second-order; transient formulation is in second-order implicit. The 'Initialization' method is standard, and calculation is computed from the inlet and reference zone as the rotating domain. Time step size is the most important component to get the simulation converged. Monitoring the forces is easy and can be calculated for the specific displacement of the rotor by precisely sizing the time step. The optimum time step size has found that it is equivalent to the ½° rotation of the rotor.

4 Results and Discussion

Under two wind speed conditions, the moment produced by the rotor is collected against the azimuthal angle (θ) in a series of simulations. Despite using standard aerodynamic forms of the forces, dimensionless coefficients are further suitable terms were adopted for lift, power, and moment coefficients are followed by, C_L, C_P, and C_M. After the simulation, the power coefficient (C_P) has been captured in a lower TSR range.

4.1 Flow Physics Analysis of Contour Plots

Simulation has been done under the TSR range of 2.0–4.0 for two different wind speed conditions and the optimum value located at TSR 3.5 for both wind speed conditions. In Fig. 4a, b, the contour plots of the static pressure and in Fig. 5a, b contour plots of velocity profiles have been graphed to comprehend the flow physics of the present H-rotor. The plots are shown that the decreases of the static pressure and velocity from the suction side (convex side) to the pressure side (concave side) of the airfoil, from Figs. 4a, b and 5a, b the airfoil, airfoil 1 at 9 o'clock position is assuming as the advancing blade.

A higher velocity and pressure difference specify the higher lift generation; thus, it is also ensuring the overall higher performance of the rotor at this azimuthal angle. From Tables 1 and 2, it is found that the rotor shows higher performance in 8 m/s wind speed condition.

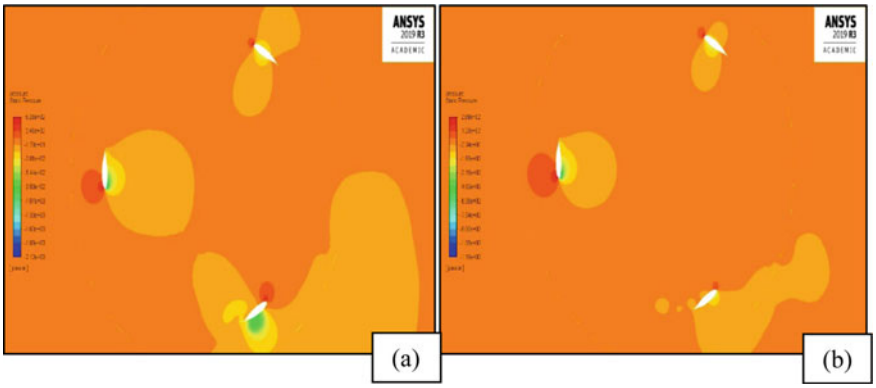

Fig. 4 Static-pressure contour plots of the rotor in **a** 6 m/s and **b** 8 m/s wind speed at TSR 3.5

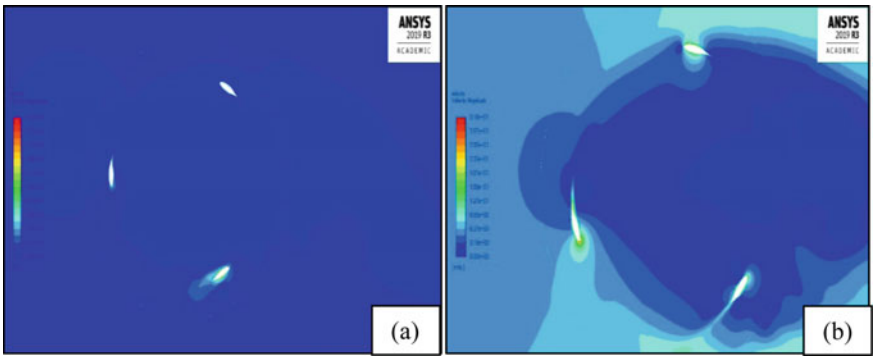

Fig. 5 Velocity contour plots of the rotor in **a** 6 m/s and **b** 8 m/s wind speed at TSR 3.5

Table 1 Static-pressure around the airfoil 1 in various wind speed

Contours of static pressure	Wind condition (m/s)	Pressure at suction-side of the airfoil	Pressure at pressure-side of the airfoil
	6	1.23×10^2 Pa	-2.01×10^2 Pa
	8	2.46×10^2 Pa	-2.29×10^2 Pa

Table 2 Velocity around the airfoil 1 in various wind speed

Contours of velocity profile	Wind condition (m/s)	Velocity at suction-side of the airfoil (m/s)	Velocity at pressure-side of the airfoil (m/s)
	6	12.7	6.37
	8	22.8	15.2

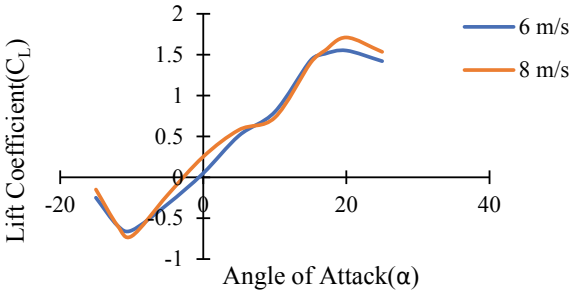

Fig. 6 The lift coefficient (C_L) versus angle of attack (α) in 6 m/s and 8 m/s at TSR 3.5

4.2 Analysis of Aerodynamics Parameters

As per the flow physics ethics, the lift force generation by the rotor is greater at 8 m/s wind speed condition than the 6 m/s wind speed condition in Fig. 6 for different AOA.

Here is the simulation result of lift coefficient (C_L) against the azimuthal angle only for the final revolution of the rotor and the result can be seen from the curve that at 8 m/s wind speed condition the value of lift coefficient (C_L) is improved than the value at 6 m/s wind speed condition. The higher lift force will generate a higher moment for the rotor, which is illustrated in Fig. 7.

In this portrayal of the calculation of the power coefficient, the value of C_p is being greater at 8 m/s wind speed condition (in Fig. 8) in the same TSR value due to changes of the Cm magnitude. The produced C_p of 0.41 at TSR 3.5, which is a 2% greater value than the C_p value of 5 m/s wind speed condition of Danao et al. [12] result. And the C_p value of 0.41 is also greater than the validation result of Mohamed [11], which is the optimum C_p value of 0.405 in 6 m/s wind speed at TSR 4.0. The performance is 1.21% gained in experimented 8 m/s wind speed of LS-0421 blade.

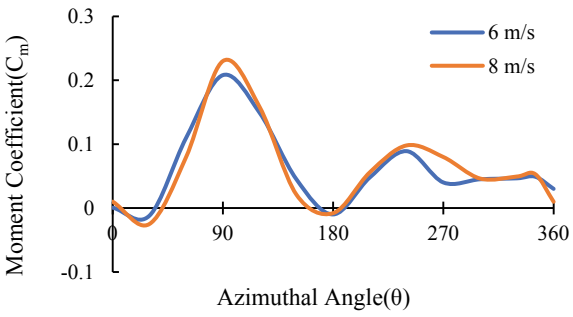

Fig. 7 Moment coefficient (C_M) versus azimuthal angle (θ) in 6 m/s and 8 m/s at TSR 3.5

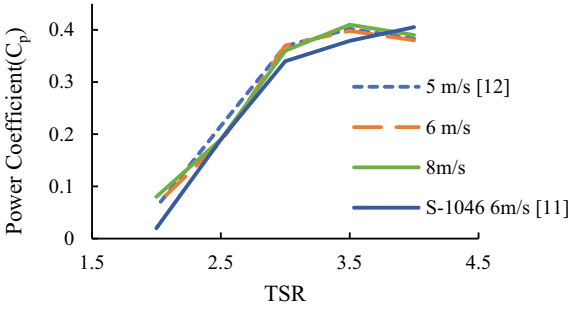

Fig. 8 C_P versus TSR curve in 5 m/s [12], 6 m/s [11] 6 m/s, 8 m/s of LS-0421

5 Conclusions

The performance of the H-rotor depends on the various parameters; with low solidity and low TSR, the rotor gives a prominent performance. The experimental result may have different from this result.

- The present study has been done in a two-dimensional simulation; however, the aerodynamics performance such as different parameters like drag coefficient, lift coefficient, moment coefficient of the rotor may be different in the three-dimensional simulation.
- Unsymmetrical blade has shown better results at lower TSR than the symmetrical blade.
- The lift coefficient (C_L) value in 8 m/s wind speed is 6.95% higher at 8 m/s wind speed condition than 6 m/s wind speed condition.
- The maximum C_p of 0.41 is produced in 8 m/s wind speed conditions which is a 1.2% greater value than the validation result of the S-1046 symmetrical airfoil which has a C_p of 0.405 at TSR 4.0.

6 Scope of the Future Works

Present project work has shown that the H-rotor has progressive aerodynamic performance under the development of different parameters and designs. Further, study on this specific area might direct future research toward on,

- This study can be done experimentally and compare the performance of the rotor with the numerical data.
- The three-dimensional study with the rotor shaft and the struts would give precise results.

References

1. https://en.wikipedia.org/wiki/1970s_energy_crisis. Accessed 28 May 2020
2. Bansal, R.C., Bhatti, T.S., Kothari, D.P.: On some of the design aspects of wind energy conversion systems. Energy Convers. Manag. **43**(16), 2175–2187 (2003)
3. https://www.researchgate.net/figure/The-major-wind-turbine-types-including-the-propeller-type-horizontalaxis-wind-turbine_fig3_263161316. Accessed on 17 July 2021
4. Balduzzi, F., Bianchini, A., Carnevale, E.A., Ferrari, L., Magnani, S.: Feasibility analysis of a Darrieus vertical-axis wind turbine installation in the rooftop of a building. Appl. Energy. **97**, 921–929 (2012)
5. Drees, H.M.: Self-starting windmill energy conversion system. United States patent 4180367, Available at: https://www.google.com/patents/US7686583. Accessed 28 May 2020
6. Hurley, B.: A novel vertical axis sail rotor. In: Proceedings of Wind Energy Workshop, pp. 40–47, 19–20 Apr 1979
7. Barker, J.R.: Features to aid or enable self-starting of fixed pitch low solidity vertical axis wind turbines. J. Wind Eng. Ind. Aerodyn. **15**, 369–380 (1983)
8. Sengupta, A.R., Biswas, A., Gupta, R.: The aerodynamics of high solidity unsymmetrical and symmetrical blade H-Darrieus rotors in low wind speed conditions. J. Renew. Sustain. Energ. **9**(4), 043307 (2017)
9. Deshpandae, P., Li, X.: Numerical study of Giromill-wind turbine with symmetrical and non-symmetrical airfoils. Eur. Int. J. Sci. Technol. **2**(8), 195–208
10. Sengupta, A.R., Biswas, A., Gupta, R.: Studies of some high solidity symmetrical and unsymmetrical H-Darrieus rotor with respect to staring characteristics, dynamic performances and flow in low wind stream. Renew. Energy. **93**, 536–547 (2016)
11. Mohamed, M.H.: Performance investigation of H-rotor Darrieus turbine with new airfoil shapes. Energy **47**(1), 522–530 (2012)
12. Danao, L.A., Qin, N., Howell, R.: A numerical study of blade thickness and camber effects on vertical axis wind turbine. Proc. I. Mech. Eng. Part A: J. Power and Energy **226**(7), 867–881 (2012)
13. Sengupta, A.R., Biswas, A., Gupta, R.: Comparison of low wind speed aerodynamics of unsymmetrical blade H-Darrieus rotors-blade camber and curvature signatures for performance improvement. Renew. Energy. **139**, 1412–1427 (2019)
14. Ramkissoon, R., Manohar, K.: Increasing the power output of the Darrieus vertical axis wind turbine. Curr. J. Appl. Sci. Technol. **3**(1), 77–90 (2013)
15. Sayed, M.A., Kandil, H.A., Shaltot, A.: Aerodynamic analysis of different wind turbine blade profiles using finite-volume method. Energy Convers. Manag. **64**, 541–550 (2012)
16. Mohamed, M.H.: Impacts of solidity and hybrid system in small wind turbines performance. Energy **57**, 495–504 (2013)
17. Bhuyan, S., Biswas, A.: Investigation on self-starting and performance characteristics of simple H and Hybrid H-Savonius vertical axial wind rotors. Energy Convers. Manag. **87**, 859–867 (2014)
18. Sengupta, A.R., Biswas, A., Gupta, R.: Investigations of H-Darrieus rotors for different blade parameters at low wind speeds. Wind. Struct. An Int. J. **25**(6), 551–567 (2017)
19. Gupta, R., Roy, S., Biswas, A.: Computational fluid dynamics analysis of a twisted airfoil shaped two-bladed H-Darrieus rotor made from fiberglass reinforced plastic (FRP). Int. J. Energy. Environ. **1**(6), 953–968 (2010)
20. Islam, M., Ting, D.S-K., Fartaj, A.: Desirable airfoil features for smaller-capacity straight-bladed VAWT. Wind Eng. **31**(3), 165–196 (2007)

Exploring the Campus of a University—An AR-Based Application—"Drishti"

Dipali Basumatary, Swapna Rawat, and Ranjan Maity

Abstract Recently, with the advancement in technology and rapid development of modern electronic devices, the use of mobile-based applications has increased immensely in the past few years. New techniques in mobile devices like—GPS, sensors, built-in camera, compass, accelerometer, and an Internet connection are used by augmented reality applications. In this paper, we introduce an Augmented Reality-based application "Drishti" for exploring a university. It shows the University's environment, facilities, and provides required important information to the visitors to engage them in new and more intuitive ways. The proposed work was developed using VUFORIA, a toolkit for making an Augmented Reality application that runs on UNITY GAME ENGINE.

Keywords Augmented Reality · Mobile Augmented Reality · Marker-based · Campus Navigation · Android mobile Application

1 Introduction

In Augmented Reality (AR) technology, virtual objects are added to the real world. An Augmented Reality system provides an efficient way for a user to interact with the real and virtual environment. Typically, AR technology displays virtual information and also determines the user's position and orientation. AR augments reality, instead of completely replacing it [1]. Augmented Reality applications are currently seen in various fields including medical, military, advertising, entertainment, education, maintenance and repair, geographical information systems, and many more [2]. With the recent development of high-power mobile devices, AR has become mobile. It has extended from personal computers (PCs) to mobile devices platforms such as tablets, smartphones, and other wearable devices.

With the availability of internet access, high processing power, better resolution display, and many additional features of mobile devices, Mobile Augmented Reality

D. Basumatary (✉) · S. Rawat · R. Maity
Central Institute of Technology, Kokrajhar, Assam, India

B. Sikdar et al. (eds.), *Proceedings of the 3rd International Conference on Communication, Devices and Computing*, Lecture Notes in Electrical Engineering 851,
https://doi.org/10.1007/978-981-16-9154-6_31

(MAR) has become feasible that integrates virtual content with the real world. MAR provides easy access to information about their surroundings always and everywhere. AR has emerged as a subset of mobile media since the first mobile AR browser was made publicly available in 2008 [3]. Various Mobile AR applications have been developed like games, navigation, and many more. Using Augmented Reality Applications in educational institutions for campus guides or learning new experiences, has been widely used and acknowledged. Navigation-based applications can help and guide users on reaching a target location spot [4].

The goal of this paper is to discuss our system architecture of "Drishti", a Mobile-based AR application for campus exploration. Each year millions of students enroll in new Universities all over the world. The Structure of Universities is expanding worldwide as the number of students is increasing year by year. Due to the large structural size of the campus, there is a high chance that newly enrolled students along with parents would not find their way on campus [5]. Generally, freshers require a couple of weeks to become familiar with the new College or University campuses. The large area of campus sometimes makes new students or visitors get lost easily among several buildings [6]. So, this kind of Augmented Reality application helps students or visitors to guide themselves around the campus as a companion. Our application provides the inside knowledge of the Central Institute of Technology Campus, which is located in Kokrajhar, Assam. Students from all over the country enrolled in this University every year. Our university has quite a big area and has several buildings for various departments, which creates confusion for the visitors. There have been many AR-based works done to date. However, there is no generalized work that can be used for our university. The AR application that has been developed can work as a solution for newly admitted students as well as their guardians. It will give all the relevant information regarding buildings and other infrastructures of the Institute. The application not only provides static information but also gives an interactive visual view and knowledge to users on mobile devices [7].

The remaining paper is arranged as follows: Sect. 2 provides a brief historical background of Augmented Reality. Section 3 presents the related work; Sect. 4 shows an implementation overview of our proposed system "Drishti". Section 5 shows the experimental setup. Section 6 shows our observation and discussion and lastly, in Sect. 7 we have concluded by stating our future work.

2 The Genesis of Augmented Reality

In 1957, to some extend Augmented Reality was first developed by Morton Heilig, a cinematographer. It was known as Sensorama, which delivered sounds, visuals, vibration, and smell to the viewer [8]. Some have stated this as the first sample of augmented reality but it was more of virtual reality. In 1968, American Computer scientist Ivan Sutherland's developed the first Head-Mounted Display (HMD). HMDs are used for viewing the merged virtual and real environments [8]. The nickname of the world's first head-mounted display was Sword of Damocles. It was primitive and

bulky and made impractical for mass use. Myron Krueger, an American Computer artist built the "artificial reality" or "virtual reality" interface called the Video place, in 1974. Virtual reality or augmented reality existed as a separate concept when in 1989 virtual reality (VR) was first coined by Jaron Lainer and it was Professor Thomas P. Caudell, of Boeing, who first coined the term augmented reality in 1990. The HMD (head-mounted display), which he referred was used in aircraft to direct the workers to assemble electrical wires. In 1992, there was the first properly functioning AR system developed by Louis Rosenberg at USAF Armstrong's Research Lab. It was an incredibly complex robotic system called "Virtual Fixtures" [8]. The system improves human productivity by overlaying sensory information on a workspace.

Augmented Reality was defined by Azuma in 1997 [1]. He defined AR as a combination of real and virtual objects which runs in real-time and is registered in three-dimensional (3D). "AR supplements reality, rather than completely replacing it" [1]. Milgram and Kishino defined the continuum of reality-virtuality. "AR acts as a middle ground between VE (completely synthetic) and telepresence (completely real)" [9].

3 Related Works

The implementation of AR campus navigation development was initiated at Columbia University by Feiner et al. [10] for outdoor navigation and information seeking on campus. Chou and ChanLin [6] developed a system for campus touring system at Fu-Jen Catholic University. It was designed to make visitors familiar with the campus environment. The result of the research unveiled that the smartphone campus touring AR system is a good assistance mobile tool as it gives freshmen companions if they get lost. Pawade et al. [7] introduced an application, "ARCampusGo". It is a Mobile Augmented Reality-based system. The system provides a campus visual understanding of the Somaiya Vidyavihar. It requires scanning the structures like buildings, monuments and landmarks then the application will provide static information on mobile devices. Usability testing was evaluated with different users for the application during different day time and night time. The application is usable even during low light intensity.

Alqahtani and Kavakli [11] developed an application, "iMAP-CampUS", which is another example of locating places of interest (POIs) at Macquarie University that provides the students with rich information about the buildings nearby. The iMAP-CampUS has been developed for both Android and iOS platforms and run-on tablets and smartphones. Chao et al. [12] developed a MAR application -the Campus Event App. The goal of the application was to guide users to find daily campus events. The application shows event information by showing the map and route in real-time. Delail et al. [13] developed CAViAR, a mobile system for indoor environments. It effectively allows campus members to find places easily and be aware of their location. The application provides indoor maps inside the building, supports voice-command search, shows the shortest path and POIs (places of interest), inertial

navigation that helps to track user indoor location and location sharing. Ramsugeerthi et al. [14] proposed AR system to identify the Mahendra Institute of Engineering and Technology (MIET) campus. Several other colleges are located within the institutional campus and one of them is Mahendra Engineering College (MEC). The entrance gate for both the campuses is the same. Therefore, their application helps the users to find out the direction as well as the distance of campuses to reach their target destination. Romli et al. [15] develop AR Applications for smart campuses using the library as the environment. They aimed to design an AR-based Android Mobile Application to improve the user experience inside the library and provide them the right direction.

COVID-19 has spread in many countries. The government of India announced a lockdown in March 2020 and has tried to fight the disease. India was having a high rate of infected patients; Universities were not open even after the unlock phase started. Millions of students across India could not attend colleges or Universities and that may affect their learning. In this kind of situation, where most of the Universities are closed, it came out as a helpful system. Since Universities campuses are quite big and have many buildings, it is quite difficult to find the required POI (Point of Interest). Right now, it is quite difficult for the students to choose and decide which colleges they should take admission to. In this situation, students can visit our university and use this application and see the inside of the classrooms, library, laboratories virtually using the DRISHTI application even if it is closed from inside. It can help students decide the best college for them. This application requires scanning the markers then the videos with a detailed description of that place will be played. Since now University has operated with minimal staff and allowed the minimum number of persons to visit for necessary purposes, it will help students or family members who visit the university for the first time for admission or other purposes when there is no one to guide them.

Augmented Reality increases a user's perception by overlaying virtual objects in the real world that a user cannot visualize with his senses. It provides static important information and allows interaction in real-time. Traditionally, campuses are explored via signposts, campus guides, or through asking around people on campus. Even so, these sorts of methods cannot give them the full visual experience of learning the campus environment. Fred Brooks said that Intelligence Amplification (IA) is using the computer as a tool for humans to perform tasks easier, and so, AR is a perfect example of that.

4 Proposed System—Drishti

In this section, we discuss our proposed system—"DRISHTI", a Mobile Augmented Reality application that can help effectively in our University Campus exploration. It is an android based application and can be used offline. Since most people nowadays have smartphones so they can use them in a go. Our university has quite a big area and has lots of buildings, and each building has different classrooms, laboratories, a

cafeteria, hostels, auditorium, offices and many more. THE "DRISHTI" AR application helps to learn everything about the campus. Whenever a new person comes to visit and is unaware of the surroundings as to which place is for which purpose, this application can help to figure out places for them. It uses markers for the recognition of places that are stored in a database. It requires running the AR application camera over the target image of that place, if the image is detected then the video will be played with the required information. Building names, classroom numbers, department names, etc. are used as markers. This system allows the student to easily locate their classrooms, laboratories, library, etc.

Our goal is to provide visual information and experience of the University on mobile devices. Being university students, we have the best knowledge of our campus and also, we have done a survey. Drishti is a marker-based tracking system where we have to use target images to be detected. We have collected information and stored the target image in a database. If someone scans an image that is not in the database, then a message "not match" is displayed. The application is created in VUFORIA, a toolkit for making an application in Augmented Reality that runs on UNITY GAME ENGINE. To develop this application, we surveyed the different AR-based applications and found Vuforia and Unity as suitable candidates. Unity is a game engine and helps for implementing cost-free augmented reality applications. Our application was developed in free version Unity Software without any cost. On the other hand, Unity integrates the Vuforia Engine, to create advanced innovative augmented reality applications for both handheld and head-worn devices.

Figure 1 shows the flowchart description of the project. In which we capture the images from a smartphone. And then stored the captured image in the Vuforia database. For storing the image, we must log in to the Vuforia account that was already created. Then download the images from the Vuforia to Unity. Go to Unity and set the required settings such as angle, rotation, scaling, etc. Under each image, we can select any figure for the video to be played but here we have selected quadrilateral, basically called quad for a 3D object. After that go to the File and click on "build the project". After building the project an apk file will be created, install the .apk file in android mobile. After receiving the .apk file, an android app will be created on the phone, and on placing the camera anywhere above the image that has been selected, the respective video (giving the information of the image) will be played. If the image is matched video will be played, otherwise it will not run the video.

The implementation of the Drishti application is shown in Fig. 2. Figure 2a, shows the front panel of Unity, where the images shown are stored in the Vuforia database. Now, the various processing and testing are done on these images. We have done the processing in such a way that whenever the Android application that we developed opens, it detects only these stored images. The videos that are stored in the Assets of the Unity give information about the classroom, library, etc.

The image shown in Fig. 2b, shows a target image that has been chosen for detection. Whenever the AR application is ON, on the detection of this target classroom image the stored video will be played for the classroom. The image is already stored in the Vuforia database and has been retrieved from it into Unity. When selecting the

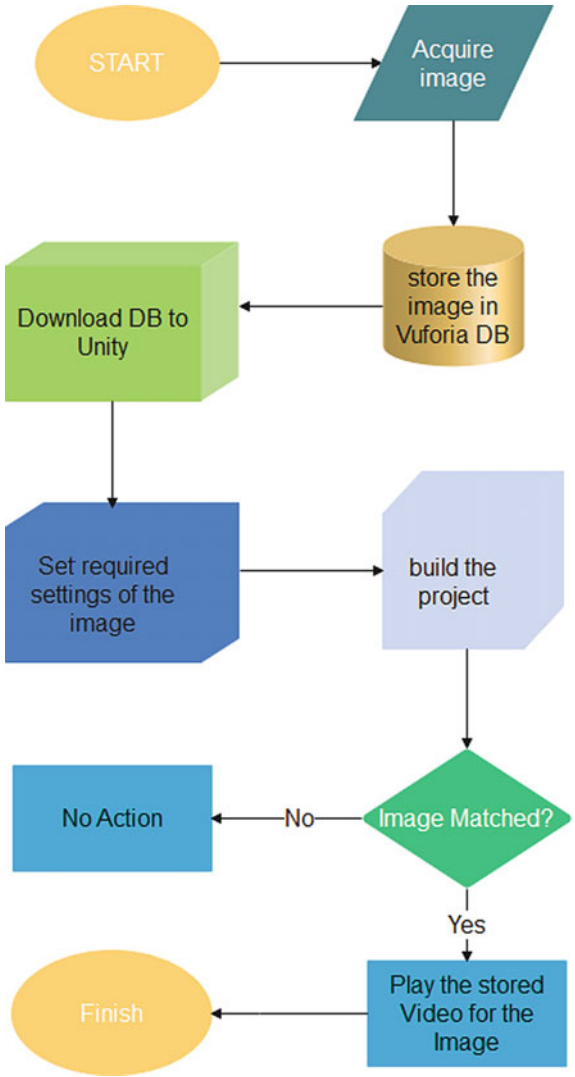

Fig. 1 Flowchart of Drishti application

target location for the image in Unity, we are required to select the database of the specified name which has been created.

Figure 2c shows the output of the video being played on the android device when the marker is detected. On detection of classroom image as a marker, the saved video for the image is played. Figure 2d shows the result of the video being played after detection of the library target image.

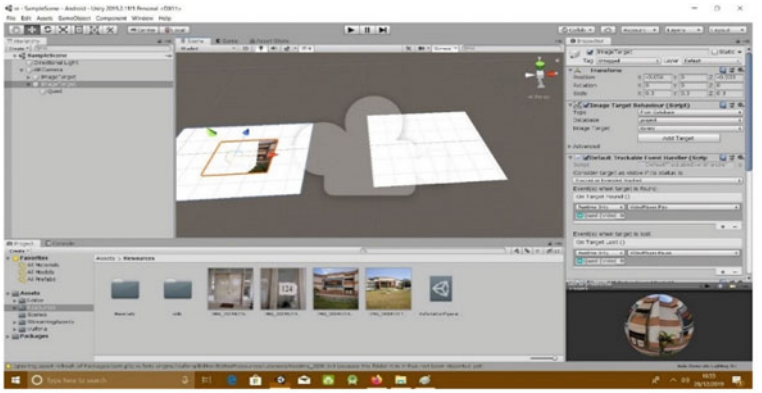

(a)

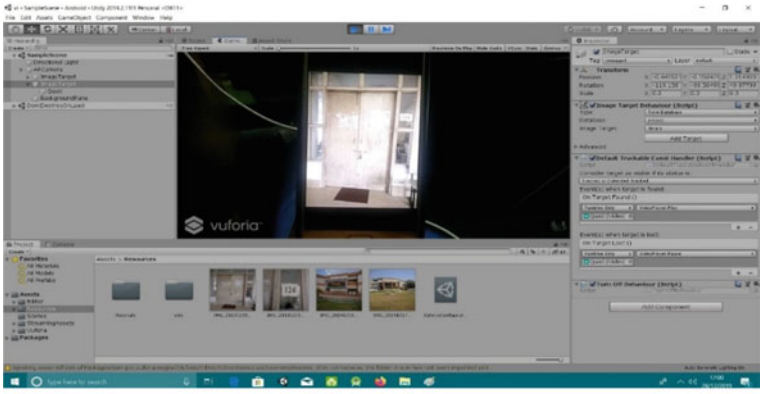

(b)

(c)

Fig. 2 **a** Front panel of Unity, **b** Picture of a classroom as target image and **c** Video played after detecting the marker of classroom, **d** Video played after detecting the marker of library

(d)

Fig. 2 (continued)

5 Experimental Setup

In this Section, the experimental setup used for the implementation of DRISHTI is discussed. As mentioned earlier, we have used UNITY and VUFORIA for the implementation of DHISHTI. We have briefly discussed them in the following two subsections, and subsequently, the procedure followed by us.

5.1 Unity Game Engine

The Unity game engine is a cross-platform and real-time engine designed by Unity Technologies. It was launched at Apple Inc.'s Worldwide Developers Conference, in 2005. Earlier it supported only the Mac OS game engine but now the engine has expanded to support above 25 platforms. It can create 2-Dimensional, 3-Dimensional, virtual reality (VR), and augmented reality (AR) games using the Unity game engine [16, 17]. The Unity Editor is a helpful and low-cost platform to developed augmented reality applications with many asset components for mobile devices. Unity also allows free version software development and supports the Vuforia SDK.

5.2 Vuforia

Vuforia software is an AR Software Development Kit (SDK). It allows building Augmented Reality software for mobile devices [18]. Vuforia provides a free license key for learning purposes [19]. It is easy to use and robust. It allows to recognize

objects and images and communicate with them in real-time [20]. Vuforia SDK uses advanced computer vision-based AR technology to detect features of 2-Dimensional and 3-Dimensional planes in real-time camera images [21].

5.3 Procedure

The various steps followed in the process are listed below:

i. Install Unity.
ii. Go to the Vuforia Developer Portal and login to the account if we already have it, or else register as a new user and create an account.
iii. Then go to the Get Development Key and give a license name of our own. Click on the terms and conditions checkbox and confirm.
iv. Go to Target Manager and Add Database and create a database of our own.
v. Select the database that we have created and go to the Add Target, Choose the file which we want to add to the database, give the width of the image and then name it. And lastly, click on Add.
vi. After adding all the files in the database, go to Download Database and select Developer Portal, then select the Unity Editor option and download it.
vii. In Unity, go to the menu, select the Vuforia Configuration and in the App License key add the license key from the Get Development Key from Vuforia Developer Portal.
viii. Delete the main camera from the Hierarchy window and add AR Camera.
ix. Inside the AR Camera, go to the Vuforia Engine and select the image option.
x. This way we can select as many images as we want to add to the AR Camera.
xi. Under each image, select any 3D object but here, we have selected the Quad as the object for playing the videos.
xii. The videos that need to be played inside each image are dragged inside the Resources in the Project window.
xiii. In the Hierarchy window click on the Image target, and on the right side in the Inspector window, select the Type in the Image Target Behaviour. Here we have selected from the Database since our images are present in the Database.
xiv. Again, in the Image Target Behaviour, go to the Database and select the name of the database we have created. In the Image, Target selects the required image.
xv. Again, in the Inspector window, there are two functions namely “On Target found” and “On Target lost”. Under the on Target found function, select on the Add to list option, and in the None Object option drag and drop the quad where we are trying to play the video. In the no function option, right-click and go to the Video player and select the play option and for the “On Target lost” option, select the pause option.
xvi. Now save the settings by pressing Ctrl + S in the Inspector window.

xvii. In the Hierarchy window go to the quad option, and on the right-hand side in the Inspector window, go to add a component.
xviii. After adding the component, we need to drag and drop the video that we have already saved in the Resources of the Project window.
xix. After dragging and dropping we need to uncheck the Play on awake option.
xx. After all these, we need to again save the settings.
xxi. In the scene, we can select the image or video and change the orientation and perform scaling and rotation of the objects.
xxii. After that, go to the File and then go to the Build settings option, here we need to select Android as we are developing an android application.
xxiii. Under the Build settings, go to the Player settings and inside the XR settings check on the Vuforia Augmented Reality support.
xxiv. Then finally build and run the project, which will be saved in the .apk file format, and finally, an android application will be created in the phone which will be connected to the system throughout the whole process.

6 Discussion

It has been observed that this application can help those people who are new to the Campus and have no idea about its whereabouts. This kind of application is required on every campus because google maps can only show direction and cannot give the complete direction and information of the inside campus. The DRISHTI application provides unknown hidden information that cannot be visualized with the normal view. The benefit of using our app is that users can find places easily instead of wandering around for required places. Our AR application requires visitors to place the phone's camera in front of the marker/landmark then automatically the dedicated video of that place will be played without the need to search. But if the videos were traditionally recorded and stored in a file then the user might require time to search the required video manually and become confused among several videos.

Since our application is cost-free software, users are not required to log in, and also their verifications are not required. Users just need to download and install it on android mobile phones. The application will only work inside the campus since all the markers are situated inside the campus. Later we are planning to upload the application to the Play store with some improvements. The application will allow users to understand and interact using text information, video, and sound. The traditional method of asking location will be replaced. And during this COVID-19 situation, it is not safe as well.

Augmented Reality and Virtual Reality are two emerging technologies for application development but we have selected Augmented Reality as a suitable tool because Virtual Reality requires a VR headset and it is not environmentally friendly for users to walk around with the headset on their face. Virtual Reality fully immersed the user into the virtual world without the view from the real-world environment which we did not want. Augmented Reality adds digital content and information to the real

world. We want visitors to have views of the real world of the campus along with the dedicated videos just by placing the mobile device camera in front of the marker which Augmented Reality supports. Since nowadays everybody owns smartphones so no additional display device or HMD (Head-Mounted Display) should be bought.

Usability Challenges have been considered and this application has been made easy and simple for easy and better navigation. Most of the parents have a generation gap with students and face challenges handling mobile devices therefore it has considered the older generation as well.

Due to the COVID-19 situation, we could not collect all the building's information and place it in the database and so we have very few images stored in the database.

7 Conclusion

The system or the Android application developed gives relevant information about particular places of our Institute. The use of Unity for the development of AR applications along with the Vuforia is that Unity is used mainly to create games and it has an awesome editor, API, platform, and tools to come up with one. Vuforia Unity is a set of scripts made to work with. The AR application we developed guides a person traveling to our university giving them information related to that place. Whenever a new person comes for a visit and is unaware of the surroundings as which place is for which purpose then they can just use the AR application and run the AR application camera over the image of that place then they will get the information of that place playing the stored video for that particular place. For now, we have just focused only on some of the buildings of the Institute and gave related information only of those particular buildings.

Due to the COVID-19 outbreak, it was also not possible to do usability testing to find out the efficiency of the DRISHTI Application. Therefore, in the future, we will do the testing and focus on providing more information on the whole Institute buildings. And also make the AR application more user-friendly and more interactive.

Acknowledgements We would like to thank the Authorities and the faculty and staff members of the Central Institute of Technology, Kokrajhar for supporting this work.

References

1. Azuma, R.: A survey of augmented reality. Presence Teleoperators Virtual Environ. **6**(4), 355–385 (1997)
2. Azuma, R., Baillot, Y., Behringer, R., Feiner, S., Julier, S., MacIntyre, B.: Recent advances in augmented reality. IEEE Comput. Graph. Appl. **21**(6), 34–47 (2001)
3. Liao, T.: Future directions for mobile augmented reality research: understanding relationships between augmented reality users, nonusers, content, devices, and industry. Mob. Media Commun. **7**(1), 131–149 (2019)

4. Rocha, S., Lopes, A.: Navigation based application with augmented reality and accessibility. In: Extended Abstracts of the 2020 CHI Conference on Human Factors in Computing Systems, pp. 1–9 (2020)
5. Biemba, A., Nyirenda, M.: Augmented Reality Aided Navigation System Model for Support of Student Registration Process (ICICT 2019)
6. Chou, T.L., ChanLin, L.J.: Augmented reality smartphone environment orientation application: a case study of the Fu-Jen University mobile campus touring system. Procedia-Soc. Behav. Sci. **46**, 410–416 (2012)
7. Pawade, D., Sakhapara, A., Mundhe, M., Kamath, A., Dave, D.: Augmented reality based campus guide application using feature points object detection. Int. J. Inf. Technol. Comput. Sci. (IJITCS) **10**(5), 76–85 (2018)
8. Augmented Reality: The past, the present and the future, [online] Available: https://www.interaction-design.org/literature/article/augmented-reality-the-past-the-present-and-the-future/
9. Milgram, P., Kishino, F.: A Taxonomy of mixed reality visual displays. IECE Trans. Inf. Syst. (Special Issue on Networked Reality) **77**(12), 1321–1329 (1994)
10. Feiner, S., MacIntyre, B., Hollerer, T., Webster, A.: A touring machine: prototyping 3D mobile augmented reality systems for exploring the urban environment. Pers. Technol. **1**, 208–217 (1997)
11. Alqahtani, H., Kavakli, M.: iMAP-CampUS: developing an intelligent mobile augmented reality program on campus as a ubiquitous system. In: Proceedings of the 9th International Conference on Computer and Automation Engineering, pp. 1–5 (2017)
12. Chao, J.T., Pan, L., Parker, K.R.: Campus event app—new exploration for mobile augmented reality. Issues Inf. Sci. Inf. Technol. **11**, 1–11 (2014)
13. Delail, B. A., Weruaga, L., Zemerly, M. J.: CAViAR: Context aware visual indoor augmented reality for a university campus. In: 2012 IEEE/WIC/ACM International Conferences on Web Intelligence and Intelligent Agent Technology, Macau, pp. 286–290 (2012)
14. Ramsugeerthi, A., Umamaheswari, A., Prassana, D.: Location Navigation Assistance for Educational Institutions using Augmented Reality (2020)
15. Romli, R., Razali, A. F., Ghazali, N. H., Hanin, N. A., Ibrahim, S. Z.: Mobile augmented reality (AR) marker-based for indoor library navigation. In: IOP Conference Series: Materials Science and Engineering, vol. 767, no. 1, p. 012062. IOP Publishing (2020)
16. Wang, S., Mao, Z., Zeng, C., Gong, H., Li, S., Chen, B.: A new method of virtual reality based on Unity3D. In: 2010 18th International Conference on Geoinformatics, pp. 1–5 (2010)
17. Kim, S. L., Suk, H. J., Kang, J. H., Jung, J. M., Laine, T. H., Westlin, J.: Using Unity 3D to facilitate mobile augmented reality game development. In: 2014 IEEE World Forum on Internet of Things (WF-IoT), pp. 21–26 (2014)
18. Vuforia Augmented Reality SDK, [online] Available: https://en.wikipedia.org/wiki/Vuforia$/_$Augmented$/_$Reality$/_$SDK/
19. Vuforia, [online] Available: https://docs.unity3d.com/Manual/vuforia-sdkoverview.html/
20. Vuforia Developer Library, [online] Available: https://library.vuforia.com/articles/Training/gettingstarted-with-vuforia-in-unity.html/
21. Amin, J., Govilkar, S.: Comparative study of augmented reality SDKs, 3rd ed. Int. J. Comput. Sci. Appl. **5**(1), 11–26 (2015)

Overview the Design Challenges of Phase-Frequency Detector for Clock and Data Recovery Circuit

Madhusudan Maiti, Sayan Jana, Shuvoshree Patra, and Subhas Chandra Saha

Abstract In modern communication systems phase-frequency detector plays an important role. An overview of design challenges for clock and data recovery circuits of phase-frequency detectors is presented here. Investigations are made keeping our focus on critical design issues of different phase-frequency detectors with advantages and limitations.

Keywords Phase detector · Clock and data recovery · Voltage control oscillator · SerDes · Phase-lock loop

1 Introduction

The network for clock and data recovery (CDR) is a key building circuit for high-speed telecommunication systems, digital circuits, and serializer/deserializer (SerDes) systems. An essential unit of CDR or phase-lock loop (PLL) circuit is the linear or non-linear phase detector (PD) or phase-frequency detector (PFD), which is displayed in Fig. 1 [1]. The primary function of PFD is to identify the error in phase for input data and output of the voltage control oscillator (VCO) employed in the CDR for recovering data & clock. The efficiency of a CDR circuit relies upon the performance of PFD. The major design challenge of PD or PFD in the CDR system is to recover the missing data transition in non-return to zero data (NRZ) in a high-speed signal. Several novel configurations and design techniques have been reported dealing with issues on missing data transition but they have some drawbacks

M. Maiti (✉)
Department of Electronics and Communication Engineering, C.V. Raman Global University, Bidyanagar, Mahura, Janla Bhubaneswar, Odisha 752054, India

S. Jana · S. Patra
Department of Pure and Applied Science, Midnapore City College, Midnapore, West Bengal 721129, India

S. C. Saha
Departments of Electronics, Vidyasagar University, Midnapore, West Bengal 721102, India

B. Sikdar et al. (eds.), *Proceedings of the 3rd International Conference on Communication, Devices and Computing*, Lecture Notes in Electrical Engineering 851,
https://doi.org/10.1007/978-981-16-9154-6_32

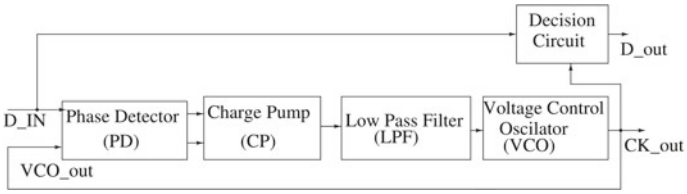

Fig. 1 The basic CDR circuit

also. In this paper, we have investigated different critical design issues, advantages, and drawbacks for both linear and non-linear CMOS PFDs. The different types of phase detectors are XOR PD, two-state phase detector, dynamic phase detector, etc. which are also called the PFDs [2–4].

In this paper the presentation is made as: techniques for designing of PD/PFDs and their advantages and limitations are explored briefly in Sect. 2. The design issues of PFDs and comparison table of past proposed phase detector circuits are described in Sects. 3 and 4, respectively. Finally in Sect. 5, concludes our works.

2 Design Techniques of Phase Detector

The PD/PFD circuit can be implemented generally category based on behavior characteristics: (i) Ex-OR PD, (ii) Edge-trigger PD, and (iii) Bang-bang phase detector [4]. In the following, we investigate different design techniques and examine the advantages and limitations of each PD/PFD.

2.1 XOR Phase Detector

One of the simplest phase detectors is an XOR phase detector Fig. 2a and its output response timing diagram as shown in Fig. 2b [5] which detects the phase between input signals. Originally an XOR gate was used as a phase detector module in the CDR circuit. It helps only for the detection of phase but fails to detect the frequency difference between the input signals. Its advantage is phase acquisition range 0° to 180° [2]. The main problem of the XOR phase detector is that it cannot detect the frequency difference. Moreover, it locks on the reference clock harmonics.

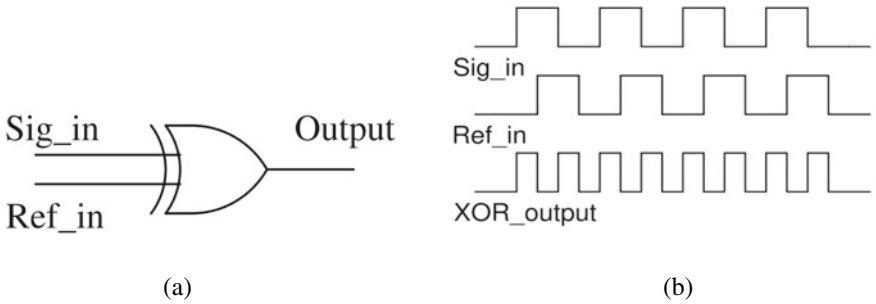

Fig. 2 **a** An XOR phase detector and **b** Timing diagram of the XOR phase detector

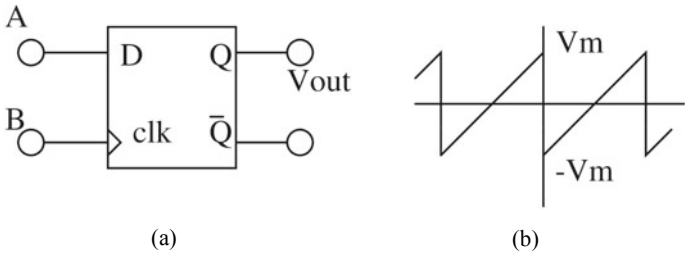

Fig. 3 **a** Latch based edge-triggered PD, **b** Output timing diagram

2.2 Edge-Triggered Latch-Based PD

An S-R latch-based edge-triggered flip flop is shown in Fig. 3a [6] and its inputs and output timing diagram are shown in Fig. 3b. The merits of this PD are self-determination of the average value of its outputs and an enhancement of the acquisition range 0°–360°. The drawbacks of this circuit are: (1) it does not suitable for frequency synthesis due to the presence of similar frequency both in input and output and (2) in lock condition output jitter creates because of metastability [2, 6–10].

2.3 D Flip-Flop Based PFD

A conventional PFD circuit is represented in Fig. 4a having two D flip-flops and an ANDgate [6]. The D flip flop is edge-triggered and resettable, and its input is at a logic high state. The Fref and Fvco signals are employed as the inputs in the circuit of PFD which generates the two outputs Up and Dn. Figure 4b represents the D flip-flop-based PFD circuit performance by timing diagram. This PFD has number of advantages: (1) it can ascertain phase and frequency difference both; (2) it improves the frequency acquisition range $\pm 2\pi$. The limitations of this PFD are:

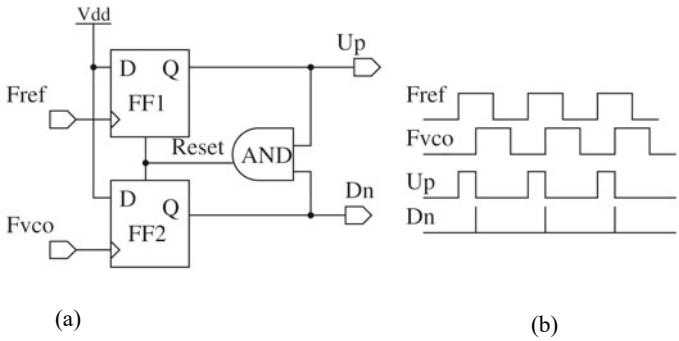

Fig. 4 **a** D flip-flop-based PFD, **b** timing diagram

(1) it possesses a large dead zone for a switching delay, (2) it creates output jitter in lock condition due to metastability, and (3) input data pattern is very sensitive in this design.

2.4 Two-XOR-Based PFD

Figure 5a depicts the block diagram of two-XOR-based PFD for the CDR circuit [2]. The charge pump input is connected to the output of XOR-based PFD. The charge pump output connects to VCOwhich generates the differential clock signals clk1 to clk4 each differenced by 45°. The output of VCOand input data connected to XOR, clk1 and clk3 are inputs of one XOR, and clk3 and input data are inputs of another XOR. The input and output waveforms of XOR-based PFD are shown in Fig. 5b [2]. The merits of this circuit are simple to design, large acquisition range, and detection of both phase and frequency errors [1–4].

2.5 Bang-Bang Phase Detector

A block diagram of a bang-bang phase detector for CDR is presented in Fig. 6a and the corresponding logic diagram is shown in Fig. 6b [7]. The edge-triggered D flip-flops are used sampling data as input in the bang-bang phase detector. A clock input of PD comes from the output of the VCO circuit. This VCO produces five clock pulses each phase shifted by 45° which are employed in the bang-bang phase detector as inputs. The PD produces two "up" signals Pu2 and Pu1 and two "down" signals Pd2 and Pd1 which are in digitized form. The input and output waveforms of the bang-bang are sketched in Fig. 6c. An abridge activity on VCO control line may

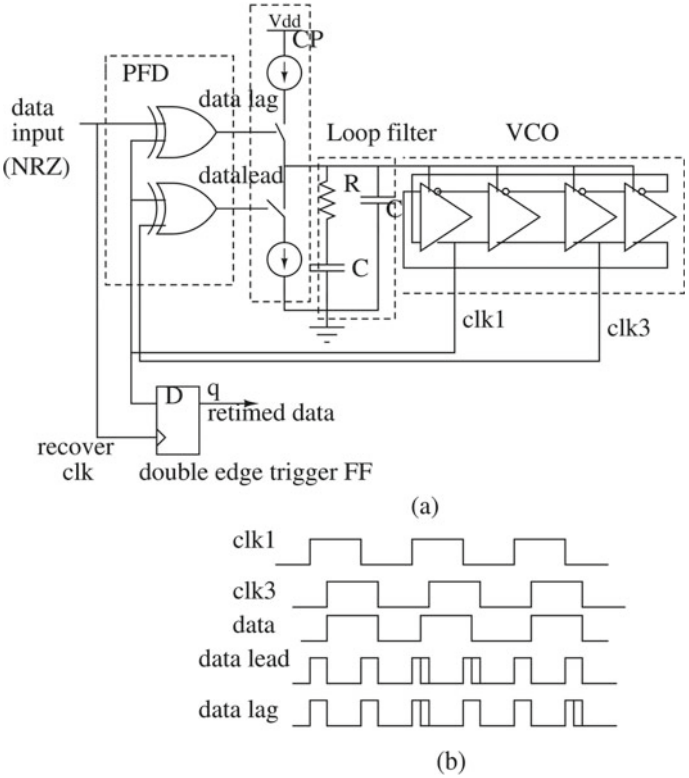

Fig. 5 Two-XOR-Based PFD: **a** block diagram, **b** inputs and output waveforms

be marked as the advantage but it has a negative aspect in the metastability, which creates in the lock condition.

2.6 Half-Rate Phase Detector

The half-rate (HR) PD circuit is drawn in Fig. 7a [8, 9]. Four latches and two XORs are required to build the circuit. The circuit operates as a timing diagram is shown in Fig. 7b [9]. It creates a systematic phase error if the two-XOR logic circuits are not symmetric with respect to their differential inputs. It has the advantages: (1) working at a high speed, (2) performing dead zone free operation as well as low jitter. Its main disadvantage is that circuit is complex [8, 9].

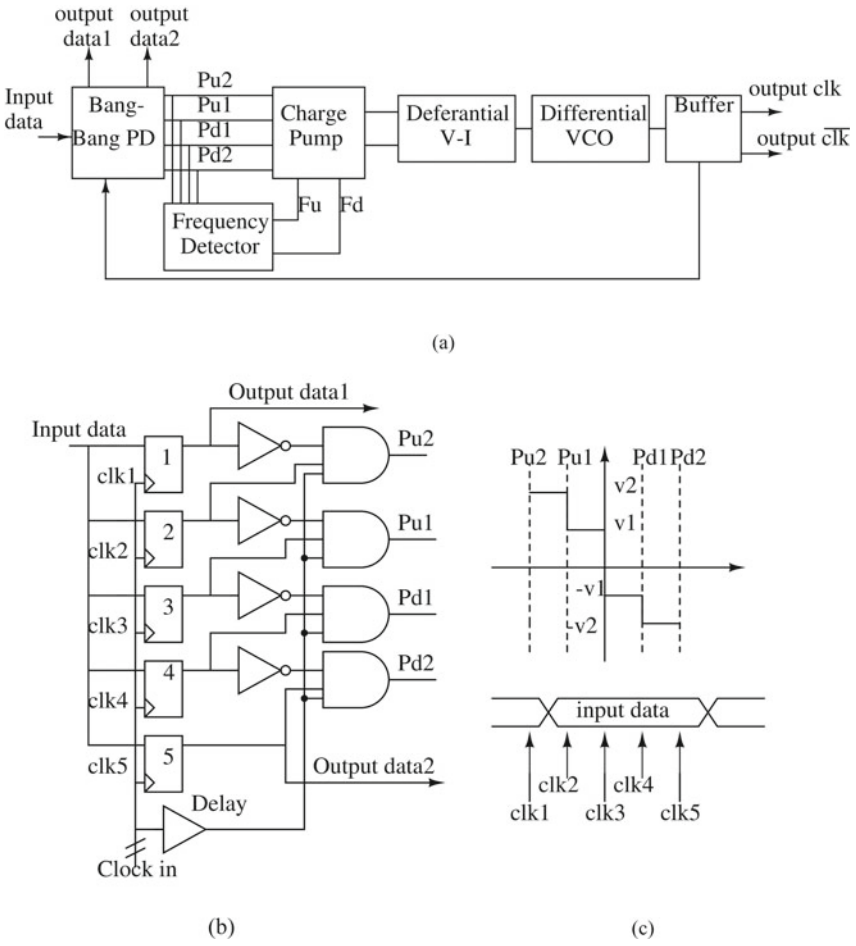

Fig. 6 Bang-Bang phase detector: **a** block diagram, **b** logic diagram, and **c** waveform

3 Design Issues

In high-speed communication, the PFD has many design issues which are discussed below.

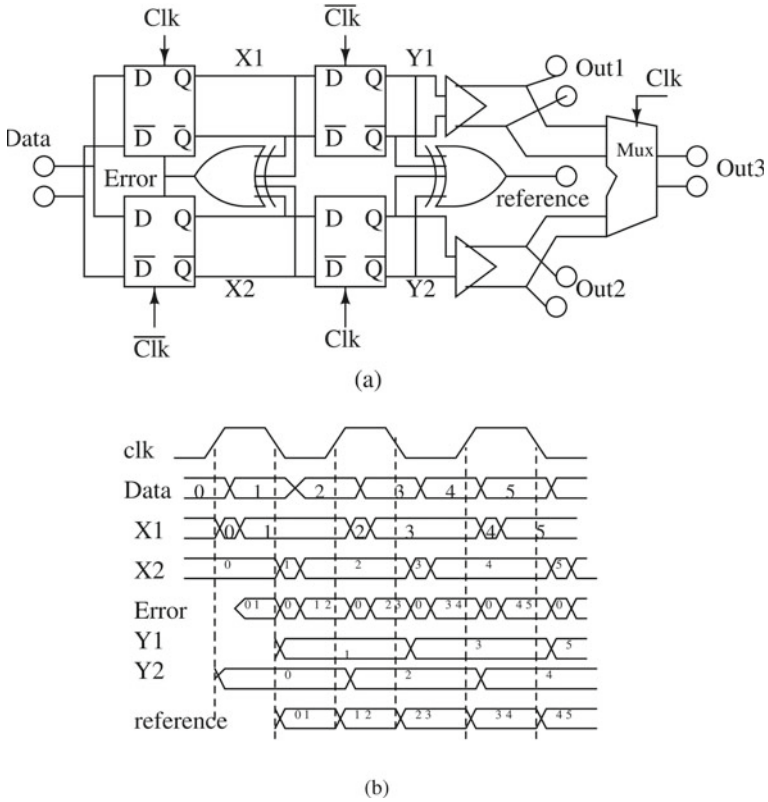

Fig. 7 Half-rate phase detector in CDR: **a** Logic diagram, **b** Input and output response in timing diagram [9]

3.1 Mechanism of Sampling

The output of PD is a distinction between input data and output of a VCO as a sampling or vice versa. If the input signal varies due to the duty cycle, the input of the PD creates a high ripple for the control line of the VCO and the system generates a high jitter [1, 4–7].

3.2 Dead Zone

Dead zone forms, when two inputs phase difference is very close to each other and PD cannot detect the phase error. The dead zone of a phase detector depends on the design techniques. If we use the reset path in the phase detector circuit, it creates a

large dead zone resulting in a missing of data. Therefore, in PD design avoiding the reset path use of the variable delay element also creates a problem [1, 2].

3.3 Analog Versus Digital PD

We have observed the digital phase detector uses one or more flip-flops which activated any one of them at a time. Digital phase detector has a large lock-in time due to substantial latch activated time and it is not appropriate for high-speed operation. An analog phase detector is more appropriate in high-speed operation but it is more complex in circuit designing. Both analog and digital PDs consume static power [4, 6].

3.4 Pattern Sensitivity on Input

The data configuration of input is a serious concern in the PFD circuit due to sensitivity. Maximum phase detector designs need that input data to have the smallest amount of phase difference [1, 4–7].

4 Comparisons of Recent PFDs

This section is a comparative study of several recent phase detectors carried out for performances like maximum operating frequency, dead zone, merit, and demerits as shown in Table 1.

5 Conclusions

In this paper, an overview of design techniques of both linear and non-linear phase detectors and various critical issues for a proper circuit design is discussed. It is found that a reset path is an important design issue for controlling dead zone and blind zone. For high-speed operation pre-charged-based PFD, current mode logic (CML) would be a better form of CMOS phase detector. The Comparison table is signified to understand different PFD circuits based on design techniques, operation speed, merit, and demerit.

Table 1 Comparison of past proposed phase detectors

Type of phase detector	Highest operating frequency (GHz)	Merits	Demerits	References with year
Falling edge PFD	2.5	Dead zone free, low power consumption, high speed, single-ended switch of the charge pump	The feedback path involved creates the dead zone	Ismail et al. (2009) [10]
Minimal blind zone PFD	2.94	Blind zone reduced	Reset time is large and missing data	Chen et al. (2010) [11]
GDI PFD	5.0	The dead zone around zero, low jitter	This PFD cannot detect the leading and lagging. Only detects the phase	Rasmi et al. (2012) [12]
Pre-charge based pass transistor PFD	3.72	Dead zone free, eliminates the blind zone and enhances the acquisition process	At high-frequency output signal is very noisy	Majid et al. (2013) [13]
Fast acquisition PFD	1.0	Removes a glitch, no blind zone, and no static power dissipation	The frequency range is low. Large chip area	Yi et al. (2014) [14]
PFD using tri-state DFF	2.5	Minimizes dead zone, suppresses unwanted glitches. It can drive a high capacitive load	Large chip area. The circuit is complex and sensitive	Strzelecki et al. (2015) [15]
Dynamic PFD	0.650	Low power, low glitches, and no dead zone	The operating frequency is low	Garg et al. (2016) [16]
Pass transistor logic-based PFD	3.0	Small reset path delay, high operating frequency, and minimal blind zone	Uses a reset path Present a dead zone	Gholami (2017) [17]
Pre-charge logic PFD	1.0	Almost removed the blind zone	Large power consumption and low operating frequency	Kuncham et al. (2018) [18]

(continued)

Table 1 (continued)

Type of phase detector	Highest operating frequency (GHz)	Merits	Demerits	References with year
Latch-based architecture	1.0	Low power consumption	Low operating frequency, dead zone present, and large chip area	Fathi et al. (2019) [19]
Differential and pseudo-differential mode PFD	1.0	Low power dissipation Very low area dead zone	Low operating frequency	Abolhasani et al. (2020) [20]

References

1. Razavi, B.: Challenges in the design high-speed clock and data recovery circuits. IEEE Commun. Mag. **40**(8), 94–101 (2002)
2. Kang, J.-K, Kim, D.-H.: A CMOS clock and data recovery with two-XOR phase-frequency detector circuit. In: The 2001 IEEE International Symposium on Circuits and Systems, 2001. ISCAS 2001, vol. 4. IEEE (2001)
3. Hogge, C.: A self correcting clock recovery circuit. J. Lightw. Technol **3**(6), 1312–1314 (1985)
4. Soliman, S., Yuan, F., Raahemifar, K.: An overview of design techniques for CMOS phase detectors. In: IEEE International Symposium on Circuits and Systems, 2002. ISCAS 2002, vol. 5. IEEE (2002)
5. Buchanan, S., Bonello, J.: Phase Locked Loop Integrated Circuit (2015)
6. Razavi, B.: Monolithic phase-locked loops and clock recovery circuits. In: Theory and Design. John Wiley & Sons (1996)
7. Ramezani, M., Salama, C.A.T.: An improved bang-bang phase detector for clock and data recovery applications. In: The 2001 IEEE International Symposium on Circuits and Systems, 2001. ISCAS 2001, vol. 1. IEEE (2001)
8. Savoj, J., Razavi, B.: A 10-Gb/s CMOS clock and data recovery circuit with a half-rate linear phase detector. IEEE J. Solid-State Circ. **36**(5), 761–768 (2001)
9. Cheng, Y.-P., et al.: A 7 Gb/s half-rate clock and data recovery circuit with compact control loop. In: 2016 International Symposium on VLSI Design, Automation and Test (VLSI-DAT). IEEE (2016)
10. Smail, N.M.H., Othman, M.: CMOS phase frequency detector for high speed application. In: International Conference on Microelectronics, Marrakech, Morocco, pp. 201–204 (2009)
11. Chen, W.-H., Inerowicz, M.E., Jung B.: Phase frequency detector with minimal blind zone for fast frequency acquisition. IEEE Trans. Circ. Syst. II Express Briefs **57**(12), 936–940 (2010)
12. Rashmi, S.B., Yellampalli, S.S.: Design of phase frequency detector and charge pump for high frequency PLL. Int. J. Soft Comput. Eng. 2, 88–92 (2012)
13. Majeed, K.A., Kailath, B.J.: A novel phase frequency detector for a high frequency PLL design. Procedia Eng. **64**, 377–384 (2013)
14. He, Y., et al.: An improved fast acquisition PFD with zero blind zone for the PLL application. 2014 IEEE International Conference on Electron Devices and Solid-State Circuits (EDSSC). IEEE (2014)
15. Strzelecki, J., Ren, S.: Near-zero dead zone phase frequency detector with wide input frequency difference. Electron. Lett. **51**(14), 1059–1061 (2015)
16. Garg, S.K, Singh, B.: A novel design of an efficient low power phase frequency detector for delay locked loop. In: IEEE International Conference on Power Electronics, Intelligent Control and Energy Systems (ICPEICES). IEEE (2016)

17. Gholami, M.: Phase detector with minimal blind zone and reset time for GSamples/s DLLs. Circ. Syst. Sig. Process. **36**(9), 3549–3563 (2017)
18. Kuncham, S.S. et al.: A novel zero blind zone phase frequency detector for fast acquisition in phase locked loops. In: 2018 31st International Conference on VLSI Design and 2018 17th International Conference on Embedded Systems (VLSID). IEEE (2018)
19. Fathi, A., Mousazadeh, M., Khoei, A..: High-speed, low power, and dead zone improved phase frequency detector. IET Circ. Dev. Syst. **13**(7), 1056–1062
20. Abolhasani, A., Mousazadeh, M., Khoei, A.: A high-speed, power efficient, dead-zone-less phase frequency detector with differential structure. Microelectron. J. **97**, 104719 (2020)

Multi-object Tracking over Fiber-Wireless Networks for Better Wild Life Protection

Deepa Naik and Tanmay De

Abstract A warning system based on sensor networks and hybrid networks (passive optical integration with a wireless network) is proposed here to identify wild animals near the road/speeding trains and strange activities in the forest region. These early warnings help relevant local authorities to handle the evolving situations. Further, these early warnings can alert passing vehicles about potential animal crossings/face-off with animals. Sensors integrated with a built-in camera to capture the images and estimate the distance of the captured images. The sensor has low processing capabilities. Hence, data from sensor networks are sent to base stations to identify the image and send alert messages. The relevant information is transferred to the base station. This decreases energy consumption for image transfer and latency in the whole process. The proposed system reduces animal deaths due to accidents and poaching and loss of human and animal lives due to conflicts and improves man and wild animal cohabitation.

Keywords Hybrid networks · Base station · Edge computing devices · Global Positioning System (GPS) · Machine learning · Wireless sensor networks (WSN) · Convolution neural network (CNN)

1 Introduction

Wild animals regularly frequent near villages, roads, train tracks and water bodies. This leads to human and animal conflict resulting in loss of human lives and accidental collisions between animals and vehicles/trains [1]. Although to build smart cities, technological advances in computing and networking are being used today. These rail/road networks, etc., were not considered for cohabitation between animals

D. Naik (✉) · T. De
National Institute of Technology, Durgapur, India
e-mail: dn.12cse1103@phd.nitdgp.ac.in

T. De
e-mail: tanmay.de@cse.nitdgp.ac.in

B. Sikdar et al. (eds.), *Proceedings of the 3rd International Conference on Communication, Devices and Computing*, Lecture Notes in Electrical Engineering 851,
https://doi.org/10.1007/978-981-16-9154-6_33

and humans [2]. Very few studies have been carried out on human cohabitation with animals. A smart fault detection system in Sri Lanka has electrical controlled fences [3]. In India, a wireless sensor network (WSN) consisting of passive nodes is used to prevent elephant crossovers on railway tracks.[4]. In [5], infrared and seismic sensors are used for spotting wild elephants approaching the villages. WSN system proposed by [6, 7] alerts drivers about wildlife crossing. WSN in [8] gathers information, and a neural network-based classification algorithm there detects animals. This paper discusses usage of a hybrid network integrated with machine learning algorithms (convolution neural network and long short-term memory) to solve the challenges in animal–human cohabitation.

We propose a hybrid network-based early warning system based on cloud service integration. This hybrid network is made up of sensors, optical fiber and AI-enabled base stations (BSs). Distributed cloud computing, artificial intelligence methods and fiber-wireless networks are among the technologies used. The hybrid network can complement each other. The passive optical networks provide high bandwidth but restricted by the distance. The wireless network is capable of providing the higher coverage but have limited by the bandwidth. In order to provide coverage and higher bandwidth, the hybrid network plays an important role. Hybrid networks are used for providing low-cost connectivity for rugged geographical terrains. PON is used as back haul and WiMAX as front-end networks along with the cloud services. The capacity of edge devices (base station) to compute and process data locally, which is latency-sensitive, is the major goal of employing hybrid networks to develop a smart system for early object detection. The end devices are paired with the a Raspberry Pi, a GPS and other sensors. When they are enabled with AI, they could send only important data to base stations. This reduces network congestion and energy consumption in image formation process. We have used hybrid network consisting of optical and wireless network. This is for providing low-cost broad band connectivity. Animal movements are detected at the sensor nodes, the AI-enabled CNN algorithm at the end devices detects if some objects are detected, and then only forward sensor data is then passed on to the base station over wireless sensor aggregation networks. The AI-enabled base station processes the critical data and requests optical line terminal (OLT) to grant the bandwidth depending on the traffic demands. The base station is unable to process the huge data. The critical traffic demands are locally handled by the base station. The non-critical data is sent to OLT which has cloud computing and MI capability. Here in OLT huge data is processed. The important factor is latency in early object detection and passing out alert signals. For latency-sensitive early warning systems, hybrid systems play an important role. The contributions of this paper are as follows.

- A traffic management system with an early warning system for approaching objects/animals.
- We use a hybrid networks with a convolution neural network to predict objects/animals presence.
- The sensor nodes are also AI enabled in order to process the data locally and transfer only relevant information to base station. This leads to minimize the energy

requirements for data transfer. The OLT enabled the cloud services and machine learning infrastructure to predict the traffic demands ahead from each base station. This leads to minimize the time delay in serving the requests.

The remainder of this paper has Sect. 2 defining the problem statement. Section 3 briefly introduces hybrid networks and machine learning. Section 3.1 illustrates the proposed machine learning algorithms as applied to human–animal cohabitation. In Sect. 4, implementation specifics of an early warning system and performance through simulation in Sect. 5 are explained. Finally, in Section 6, we draw conclusions.

2 Problem Definition

The traditional methods to save animals from pouching and accidents and human–animal conflicts are based on conservation, natural balance, ecology and habitat preservation oriented. There are very few schemes based on early warning type that too within the stipulated time. Here we have proposed the hybrid network integrated with the cloud devices. The passive optical network devices and base station are enabled with the built-in machine learning algorithms. These machine learning algorithms are helpful in the early identification of objects and also predict the traffic demands ahead in order to allocate the resource. Hybrid networks usage minimizes the need of fiber connectivity to cover the entire geographical areas. Due to the geographical restriction, it is not possible to lay the optical fiber to customer premises.

3 Hybrid Network

The term 'hybrid network' refers to a network that combines optical and wireless networks. This network provides universal Internet access at a low cost, with comparable higher capacity. A base station connects wireless nodes to an optical network unit (ONU). Sensors, smart phones, handheld computers and computing machines are examples of nodes. Optical line terminals (OLT) are located at the service provider's central office. ONUs are integrated with the base station and connect end users via wireless links. Heterogeneous traffic is handled by ONUs. This is where wireless traffic between base stations and subscribers is done. The orthogonal frequency-division multiplexing (OFDM) technique is used to serve the traffic demands. OLT creates an OFDM spectrum and assigns a portion of it to each ONU. As a result, latency time is reduced, and synchronization time for optical and wireless network is improved [9].

Figure 1 shows the wireless sensor nodes that have been mounted along the road/train tracks. Wireless links bind these sensors to the base station. When they sense an animal, they send the captured image picture and position to the base station.

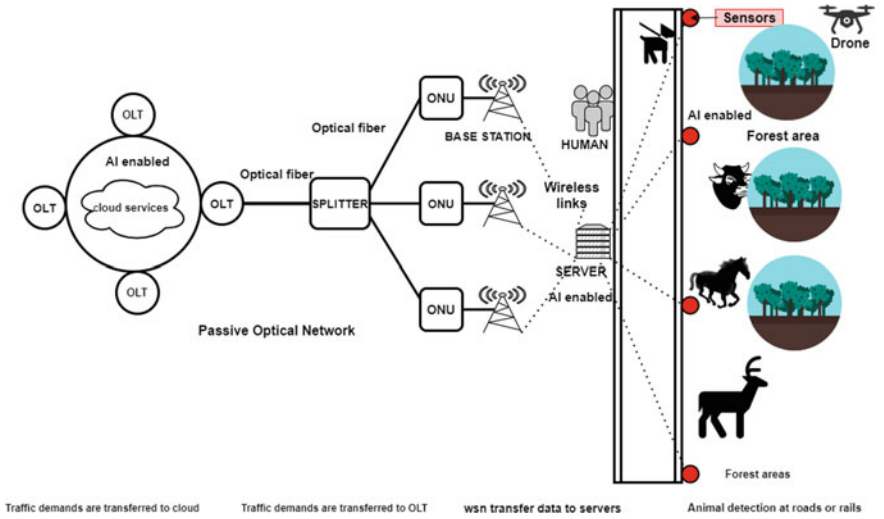

Fig. 1 Object detection using hybrid network

3.1 The Role of Machine Learning for Traffic Prediction

The performance of optical networks has been improved by the usage of machine learning techniques. In our work, machine learning is used for allocating bandwidth. Allocation is based on traffic prediction for heterogeneous services. In PON, data rates are low in an upstream flow (e.g., 2.5 Gb/s) and high in downstream (e.g., 10 Gb/s). Hence, upstream data is critical. Allocation of OFDM subcarriers at ONU and time slots are very complex as traffic patterns vary during a day.

The OLT consists of AI-enabled cloud services to predict traffic demands. The long short-term memory (LSTM) network model minimizes latency. It learns long-term dependencies and avoids vanishing gradients. LSTM networks mine out future traffic predictions using historical traffic patterns. Once bandwidth allocation from OLT to ONU is done, base station sends an early alert signal to passing vehicular and humans under the coverage area of the base station. In the traditional scenario, ONU requests for the bandwidth and then OLT assigns the bandwidth depending on the network status. The machine learning-based bandwidth assignment scheme can reduce the latency time by pre-computing the required bandwidth and assigning to the ONUs. The OFDM-PON technology is used for bandwidth assignment scheme. This technology is flexible to assign the required frequency slots depending on the traffic demands.

3.2 ML for Predicting the Animals

Animal identification here is using passive infrared (PIR) sensor [1]. ML algorithms are used for classifying images locally. Images may be captured and transferred instantaneously, or it will be captured, processed and then transferred to base stations. The base station has a pre-trained model based on a convolution neural network (CNN) algorithm to classify the images. These images when processed give an idea of about animal's size, position, speed, numbers and direction. If the object detected is a pet animal (cat, dog), then alarm signals are not generated. If the object detected is space object or vehicle inside the forest area, alert messages are sent to the respective authority to take action.

The model can recognize all ten image classes after training. These image classes may be the presence or the absence of an object inside the captured image; if present, then what type of animal is found and the location of the animal and the average walking or running speed of the animals are computed.

3.3 Deep Learning for Image Detection

Deep learning is used to predict the location and behaviors of wild animals in this study. This paper looks at the ability to gather camera trap image data involuntarily and reliably, as well as a motion sensor for tracking wildlife movements. However, extracting data from these images is still a time-consuming, physically demanding process, and hence, deep learning is used for automatic extraction. A comparison of the artificial neural network (ANN) and the convolution neural network (CNN) shows that the CNN model can accurately identify objects. The implementation of a hybrid network to handle real-time collected photos helps lower the important application's latency time. This technique can offer a low-cost, high-impact way to manage real-time collected images and correctly classify them so that the decision can be taken to transmit alert signals or not to the respective authority.

CNN is a deep learning tool consisting input and output layers and many layers which are hidden. Only a few of these layers are convoluted, and the results are carried on to subsequent layers via mathematical models. The convolution layers are the most significant of these layers. These convolution layers are constructed from a fundamental building block known as a convolution, as the name implies. A convolution is used to sample the values of pixels in a small region of an image and transform it to a single pixel. To create a new image, it is added to each region of pixels in the image.

The building block of CNN model is explained below.

3.4 Pooling

When the images are too large, pooling layers reduce the number of parameters. In the max pooling layer, pixel number is reduced in the output from the previous convolution layer when it is added to the model. This results in reduction of image dimensions. Figure 2 illustrates how the max pooling layer works.

3.5 Flattening

In flattening, a two-dimensional array is converted into a single, long continuous linear vector. It flattens the output of the convolution layers to create a single, long feature vector, which is then passed to the next layer below for image classification. Flattening is depicted in Fig. 3.

3.6 Fully Connected Layers

Fully connected layers are shown in Fig. 4 as hidden layers within a convolution neural network. These are a special type of hidden layer that must be used in conjunction with the CNN. This is used to combine the features into more attributes in order to more accurately predict the outputs. The problem statements determine the output layers. If there are two objects to classify, there will be two outputs.

3.7 Energy Reduction Using AI-Enabled Hybrid Networks

Raspberry Pi3 is used as an end device with a passive infrared (PIR) sensor that detects object movement in human–animal cohabitation regions. It turns on a 5-megapixel (MP) infrared camera that records photos of objects. The lower-powered Zigbee communication protocol is used to communicate between the end devices and the base station. Here for effective communication, two Zigbee transceivers are

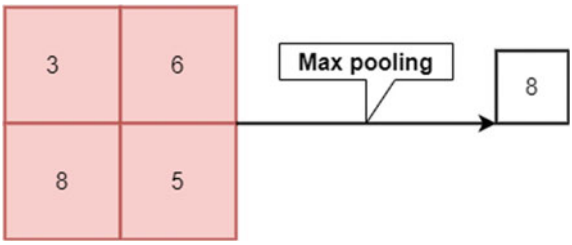

Fig. 2 Max pooling

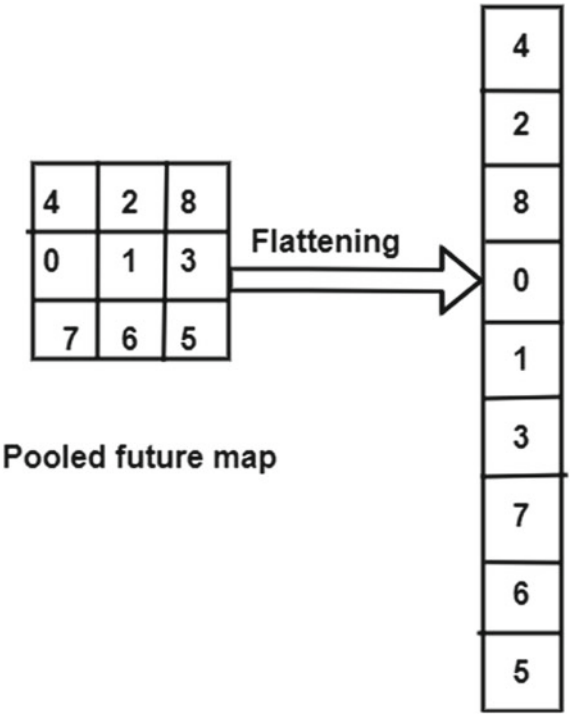

Fig. 3 Flattening

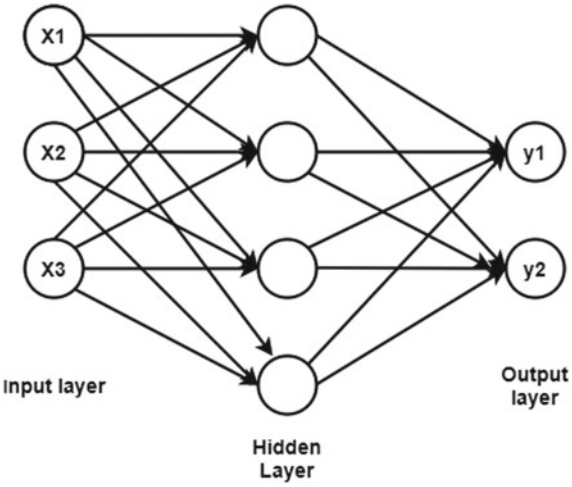

Fig. 4 Fully connected network

conceived. One is connected to the Raspberry Pi, and the other is configured as the coordinator, collecting data from all of the sensor devices. The Raspberry Pi uses a minimal amount of computational capacity to process data locally and only send pertinent data to the coordinator.

If the Raspberry PI was not AI enabled, then it transferred the captured images to the coordinator Zigbee device and the processing of the image is done at the base station with are AI-enabled machine learning algorithms to detect the animal and classify. In this scenario, huge energy is consumed to transfer the image. In order to avoid this energy consumption, the end devices are also provided the small amount of computing power in order to detect the animal present and then to transfer the relevant information to the base station. Thus, we can conclude that this method reduces the energy consumption of the end devices, by transferring relevant and critical information to the server. Use of Ml algorithms by sensor nodes in image processing reduces energy consumption. However, these devices are provided with a small processing capacity, and the classification accuracy would be reduced, in order to make it more energy efficient.

3.8 Latency Time Reduction Using Machine Learning

To address the issue of latency time in predicting the traffic demands in each base station, we use machine learning-based traffic prediction to allocate bandwidth as per traffic demands of each base station. Long short-term memory (LSTM) learns long-term dependencies. Hence, for predicting time series traffic, we have used LSTM network model [10]. In machine learning, error function gradient decreases; hence, learning process is not improved. This is called vanishing gradient. LSTM eliminates vanishing gradients. Further training machine learning algorithm by different traffic patterns makes prediction accurate. The network resources are assigned before hand to each base station, so the time required for traffic request and grant get reduced. In our approach, we first generate a time-varying traffic (real data). In order to predict the bandwidth demands of the future for one hour, the previous seven hours traffic demands are learnt by the LSTM algorithm. The 'ADAM' optimizers are used for all the models. The data set is split into 80:20 ratio for training and testing. The accuracy around 70 percent of accuracy was achieved in this model.

3.9 Data Set

This project was created in a real-world setting. However, utilizing sensors to capture such a large number of data sets was impossible. The data set used here is a collection of image data libraries (CIFAR-10 data set) that includes a variety of animal and other images from this class. The data set is divided into two parts: train and test, with a 75:25 split.

4 Early Waring System for Animal Detection

4.1 Animal Detection Simulation

The flowchart of the proposed animal detection algorithm is illustrated in Figure. 5. We use the low-powered Zigbee communication protocol to transfer data between sensor nodes and the base station. The maximum data date assumes to be 250 kb/s data rate over unlicensed spectrum of 2.4 GHz. The shortest path is used to transfer the data between the sensor and base station. The distance between base station and sensor nodes is set to be within one kilometer range. We assume that the fiber capacity as 4 THz in OFDM-PON, which is divided into 320 spectrum slice. Each slice is 12.5 GHz in capacity.

- Sensors nodes detect the animals movements.
- The sensed critical information is sent to the base station.
- The bandwidth allocation decisions are done at the OLT side for the PON network. The OLT is located between base station and the cloud.
- Alert signals are sent to the human and passing vehicles and relevant local authorities
- Non-critical images identification is done at the clouds.

5 Analysis of Results

In the CNN model, the accuracy 79% and ANN model model around 59% after running the simulation for 10 Epoc are depicted in Figs. 6 and 7.

6 Conclusion

Thus, this project makes the comparative study of ANN with convolution neural network (CNN) algorithm to detect objects animals. The CNN algorithm is able to classify objects efficiently with a good number of accuracy compared to ANN algorithm. Detecting wild animals with a good accuracy reduces the animal–human conflicts by sending alert message to passing vehicles and humans. And also this project will help to minimize the animal pouching and illegal activities inside the forest area. Functionality of this system can be further enhanced so as to detect wild fire and unusual activities at forest premises.

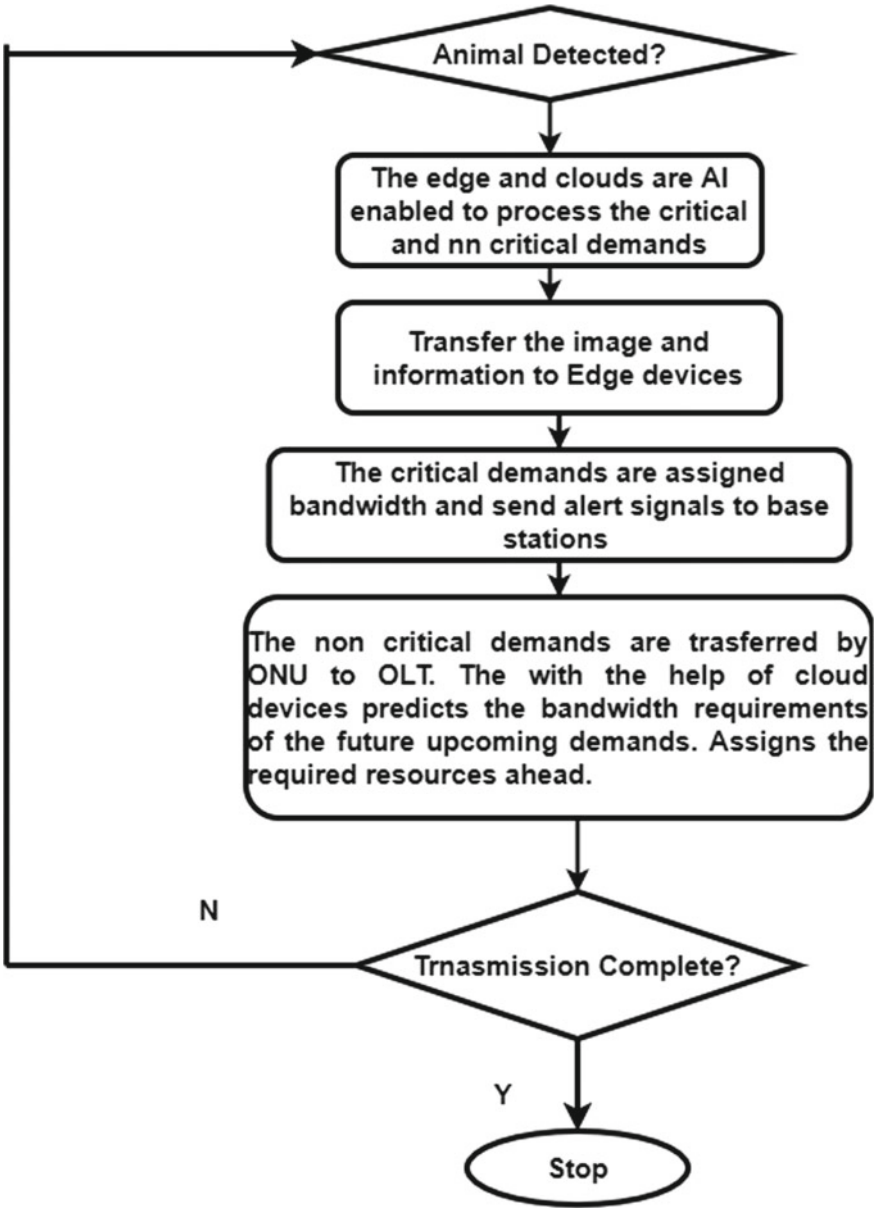

Fig. 5 Flow of algorithm

```
Epoch 1/10
1563/1563 [==============================] - 126s 81ms/step - loss: 1.9256 - accuracy: 0.3129
Epoch 2/10
1563/1563 [==============================] - 138s 88ms/step - loss: 1.6496 - accuracy: 0.4167
Epoch 3/10
1563/1563 [==============================] - 134s 86ms/step - loss: 1.5550 - accuracy: 0.4529
Epoch 4/10
1563/1563 [==============================] - 123s 79ms/step - loss: 1.4834 - accuracy: 0.4802
Epoch 5/10
1563/1563 [==============================] - 127s 81ms/step - loss: 1.4462 - accuracy: 0.4951
Epoch 6/10
1563/1563 [==============================] - 121s 78ms/step - loss: 1.3911 - accuracy: 0.5106
Epoch 7/10
1563/1563 [==============================] - 117s 75ms/step - loss: 1.3570 - accuracy: 0.5217
Epoch 8/10
1563/1563 [==============================] - 115s 74ms/step - loss: 1.3130 - accuracy: 0.5393
Epoch 9/10
1563/1563 [==============================] - 115s 74ms/step - loss: 1.2764 - accuracy: 0.5578
Epoch 10/10
1563/1563 [==============================] - 113s 72ms/step - loss: 1.2471 - accuracy: 0.5638
<tensorflow.python.keras.callbacks.History at 0x7ffb3d6a3210>
```

Fig. 6 ANN model

```
Epoch 1/10
1563/1563 [==============================] - 54s 34ms/step - loss: 1.6585 - accuracy: 0.3979
Epoch 2/10
1563/1563 [==============================] - 54s 34ms/step - loss: 1.1324 - accuracy: 0.6039
Epoch 3/10
1563/1563 [==============================] - 53s 34ms/step - loss: 0.9838 - accuracy: 0.6567
Epoch 4/10
1563/1563 [==============================] - 54s 34ms/step - loss: 0.8929 - accuracy: 0.6870
Epoch 5/10
1563/1563 [==============================] - 54s 34ms/step - loss: 0.8260 - accuracy: 0.7149
Epoch 6/10
1563/1563 [==============================] - 54s 34ms/step - loss: 0.7705 - accuracy: 0.7328
Epoch 7/10
1563/1563 [==============================] - 54s 35ms/step - loss: 0.7229 - accuracy: 0.7493
Epoch 8/10
1563/1563 [==============================] - 53s 34ms/step - loss: 0.6713 - accuracy: 0.7671
Epoch 9/10
1563/1563 [==============================] - 53s 34ms/step - loss: 0.6281 - accuracy: 0.7789
Epoch 10/10
1563/1563 [==============================] - 52s 33ms/step - loss: 0.5868 - accuracy: 0.7956
```

Fig. 7 CNN model

References

1. Suman, P., Gupta, P., Kassey, P.B., Saxena, N., Choudhary, Y., Singh, V., Radhakrishna, M.: Identification of trespasser from the signatures of buried single mode fiber optic sensor cable. In: Annual IEEE India Conference (INDICON). IEEE, vol. 2015, pp. 1–6 (2015)
2. Jukan, A., Masip-Bruin, X., Amla, N.: Smart computing and sensing technologies for animal welfare: a systematic review. ACM Comput. Surv. (CSUR) **50**(1), 1–27 (2017)
3. Tennakoon, E., Madusanka, C., De Zoysa, K., Keppitiyagama, C., Iyer, V., Hewage, K., Voigt, T.: Sensor-based breakage detection for electric fences. In: IEEE Sensors Applications Symposium (SAS). IEEE, vol. 2015, pp. 1–4 (2015)
4. Mathur, P., Nielsen, R.H., Prasad, N.R., Prasad, R.: Wildlife conservation and rail track monitoring using wireless sensor networks. In: 4th International Conference on Wireless Communications, Vehicular Technology, Information Theory and Aerospace & Electronic Systems (VITAE). IEEE, vol. 2014, pp. 1–4 (2014)

5. Nakandala, M., Namasivayam, S., Chandima, D., Udawatta, L.: Detecting wild elephants via wsn for early warning system. In: 7th International Conference on Information and Automation for Sustainability. IEEE, pp. 1–6 (2014)
6. Viani, F., Rocca, P., Lizzi, L., Rocca, M., Benedetti, G., Massa, A.: Wsn-based early alert system for preventing wildlife-vehicle collisions in alps regions. In: 2011 IEEE-APS Topical Conference on Antennas and Propagation in Wireless Communications. IEEE, pp. 106–109 (2011)
7. Viani, F., Polo, A., Giarola, E., Robol, F., Benedetti, G., Zanetti, S.: Performance assessment of a smart road management system for the wireless detection of wildlife road-crossing. In: IEEE International Smart Cities Conference (ISC2). IEEE, vol. 2016, pp. 1–6 (2016)
8. Dominguez-Morales, J.P., Rios-Navarro, A., Dominguez-Morales, M., Tapiador-Morales, R., Gutierrez-Galan, D., Cascado-Caballero, D., Jimenez-Fernandez, A., Linares-Barranco, A.: Wireless sensor network for wildlife tracking and behavior classification of animals in doñana. IEEE Commun. Lett. **20**(12), 2534–2537 (2016)
9. Habel, K., Koepp, M., Weide, S., Fernandez, L., Kottke, C., Jungnickel, V.: 100g ofdm-pon for converged 5g networks: from concept to real-time prototype. In: Optical Fiber Communication Conference, Optical Society of America, W1K–4 (2017)
10. Hochreiter, S., Schmidhuber, J.: Long short-term memory. Neural Comput. **9**(8), 1735–1780 (1997)

All Optical Photonic Switch Based on Semi Reflective Quantum Dot Semiconductor Optical Amplifier

Kousik Mukherjee

Abstract Semi reflective quantum dot semiconductor optical amplifier (SRQDSOA) is used to design a simple interferometer switch for all optical application. The operation speed is ultrafast (1 Tb/s). The switch works on the principle of cross-gain and cross-phase modulation between two signals in SRQDSOA. The switch shows high extinction ratio between low and high states. The relative eye opening is also high is clear from the pseudo eye diagram. The amplitude modulation (AM) of the switch is also analyzed. These features of the switch are numerically analyzed with ASE noise taken into account.

Keywords All optical switch · Quantum dot SOA · ASE noise · Interferometer

1 Introduction

Optical communication system needs all types of node functionalities to be implemented in optical domain [1, 2]. This boosted up research of all optical logic gates and processors with capabilities of handling data at ultra high speed. All optical devices have enhanced the efficiency of data communication system. Semiconductor optical amplifier (SOA) is a versatile gain medium having controllable optical nonlinearities [3]. These nonlinearities find applications in implementing different optical logic processors at high speed [4–10]. A varieties of optical switch based on interferometer structure using SOA or reflective SOA (RSOA) with bulk, quantum well or quantum dot active medium have been implemented and successfully demonstrated [11]. These interferometric switches include Mach Zehnder Interferometer (MZI), tera hertz optical asymmetric Demultiplexer (TOAD), dual-control dual-SOA TOAD (DCDSTOAD), Michelson interferometer etc. These nonlinear optical switches have been utilized to design different all optical logic gates and processors [12–17]. A

K. Mukherjee (✉)
Physics department, Banwarilal Bhalotia College, Asansol, India

Centre of Organic Spintronics and Optoelectronic Devices(COSOD), Kazi Nazrul University, Asansol, India

B. Sikdar et al. (eds.), *Proceedings of the 3rd International Conference on Communication, Devices and Computing*, Lecture Notes in Electrical Engineering 851,
https://doi.org/10.1007/978-981-16-9154-6_34

semi reflective SOA is a variant of SOA not extensively used for all optical logic gate and processor design and in [18], it is utilized to design a regenerator. Recently, RSOA based on quantum dot devices in MZI configuration have attracted attention of researchers [16, 19]. However, semi reflective QDSOA (SRQDSOA)-based interferometer switches are not used to design optical logic gates to best of the author's knowledge. Using SOA or RSOA, an MZI configuration requires two identical active elements; however, in this communication, it is shown that the interferometer designed uses a single active element (SRQDSOA). This reduces the circuit complexities and enhances operating speed. The switch is analyzed in terms of extinction ratio and contrast ratio. The results of operation show that it has potentiality to be an important part of all optical signal processing system.

2 Mathematical Modeling and Design of the Switch

Figure 1 shows the design of the interferometer switch based on SRQDSOA.

A single SRQDSOA is used to design the switch. An SRQDSOA consists of an active layer of quantum dots deposited between p and n type semiconductor layers. It has one facet partially reflecting and another facet has antireflection coating. Basic principle of operation of the switch is cross-phase modulation (XPM) between a weak probe signal (P_r) and the strong pump signal (P_c). When the pump signal is absent or zero, the unsaturated single pass gain, G_u of the SRQDSOA is high. Therefore, the probe signal gets amplified and one part exits through the path T and another reflected part exits through the path R after double passing. Therefore, these two signals have different intensities and phase difference. These two signals T and R should be of equal intensity for proper interferometer operation and should have phase difference zero or $\pm 2n\pi$, $n = 1, 2, 3 \ldots$etc., in the absence of pump signal. The phase shifter adjusts the phase of the signal R for this purpose. The reflectivity of the coating is adjusted to make the intensities of these two signals to be equal. When the pump is made on, SRQDSOA gain begins to saturate, and the pump power can be

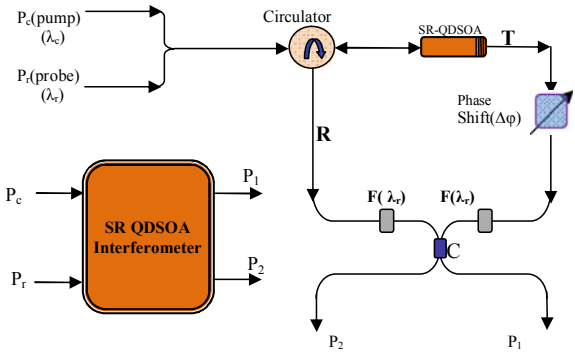

Fig. 1 SRQDSOA-based interferometer switch

adjusted to give a phase difference of π between the signals T and R. These signals interfere at the coupler C and the probe signal is selected by the filters F to exit from the constructive and destructive ports P1 and P_2, respectively.

The outputs of the constructive ('+' sign in Eq. (1)) and destructive port ('−' sign in Eq. (1)) at probe wavelength are given by

$$P_{1,2} = (rG_t^2 + (1-r).G_t \pm 2\sqrt{r(1-r)G_t^3}\cos(\Delta\phi).P_{\text{probe}} \quad (1)$$

where r is the reflectivity of QDSOA facet, G_t is the time dependent gain calculated using rate equation model [15, 16, 19], and P_{probe} is the input probe power. Both pump and probe signals are taken Gaussian pulses of the form:

$$p_{\text{peak}} \exp(-4\ln(2)t^2/\tau_{fwhm}^2)$$

P_{peak} and τ_{fwhm} are the maximum power and full with at half maxima of the pulses, respectively. With output in Eq. (1), the amplified spontaneous emission noise is numerically added.

3 Simulation Results and Performance

Figure 2 shows the input control bit pattern and corresponding output bit patters of the signals R and T. From the Fig. 2, it is clear that R and T are almost equal for facet reflectivity, $r = 0.91$ for unsaturated single pass gain of 10 dB.

The corresponding pseudo eye diagram (PED) is shown in Fig. 3. The eye diagram shows clear eye opening for both the T and R outputs. The relative eye opening for the signals in R port is more than 90% and that of T port is nearly 99% shows efficient performance (Fig. 3).

Numerical simulations reveal that the switch gives optimum performance at control power of 8 mW. Figure 4 shows the PED for constructive and destructive port. The pseudo eye diagram shows relative eye opening of 75% for constructive port and 98.5% for destructive port. This implies that destructive port is better than constructive port as par as the optical switching is concerned. This difference is due to the dynamics of the SRQDSOA since the SRQDSOA does not always recover its gain uniformly. This also introduces phase fluctuations, and SRQDSOA does not satisfy exact zero or π phase difference condition. However, the overall performance of both the ports is more than satisfactory. The amplitude modulation of the constructive port output bits is 0.0043 dB which is more than satisfactory. The corresponding AM of destructive port is 0.074 dB. All these parameters are calculated in presence of control power. In the absence of control power, the extinction ratio between the constructive and destructive port is 18.36 dB is quite high. This value reduces to 5.89 dB in the presence of control power. This also establishes clear distinction between states with control on and control off.

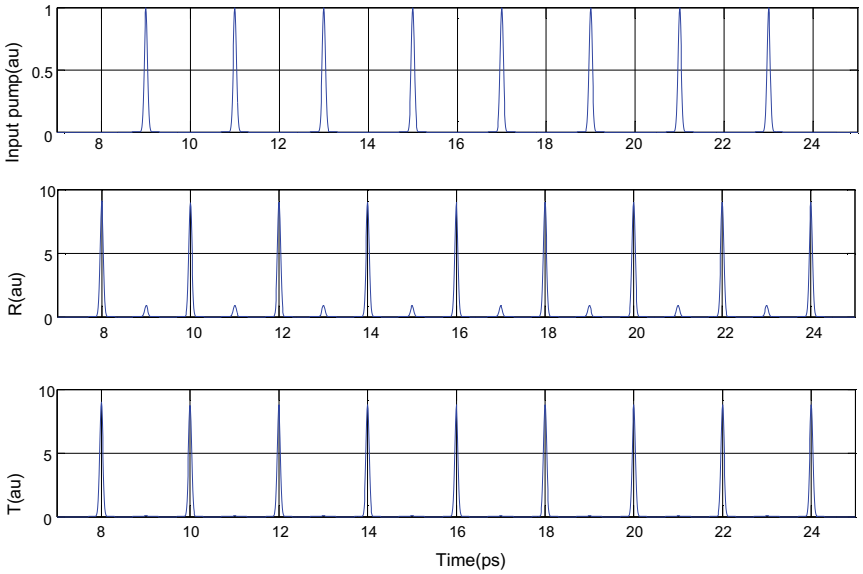

Fig. 2 Simulated output signals R and T

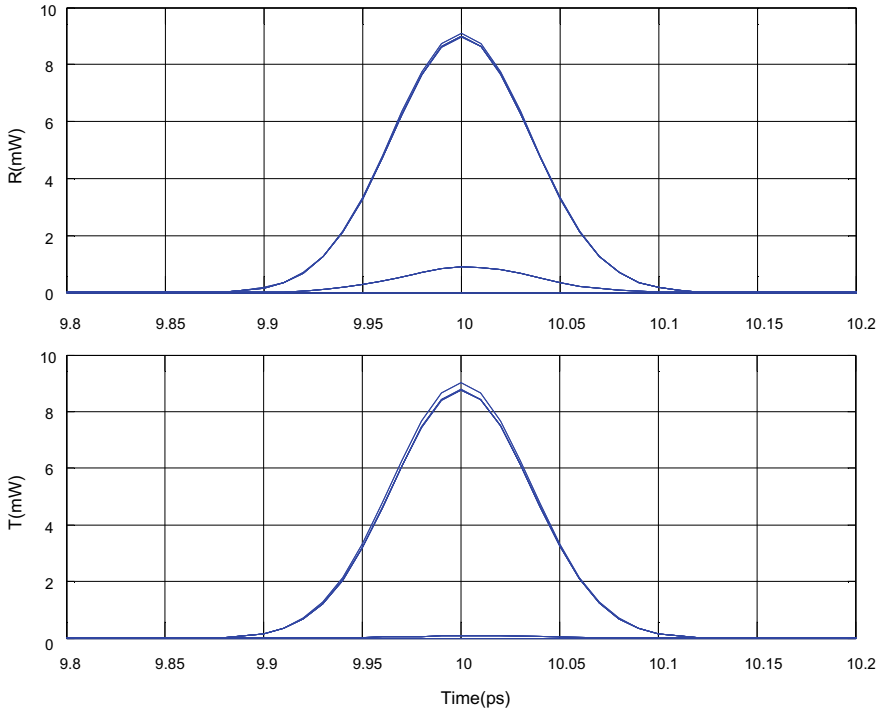

Fig. 3 PED of R and T outputs

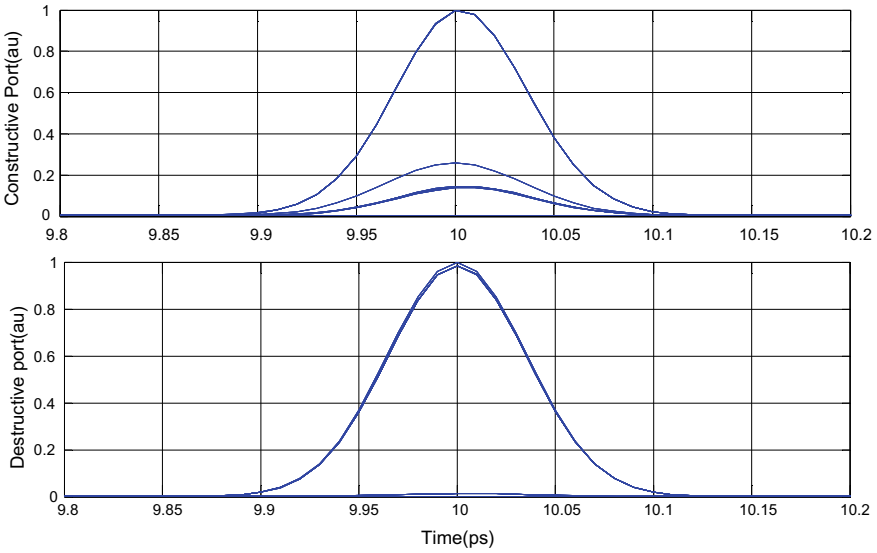

Fig. 4 PED of constructive and destructive port outputs

4 Conclusions

SRQDSOA-based interferometer switch is designed and numerically analyzed its performance for the first time to the best of author's knowledge. PED, AM, REO, and AM of the proposed switch shows efficient performance and practical feasibility of the switch. Therefore, in future, this switch can be an important part of all optical logic gates and processors for photonic applications.

References

1. Kumar, A., Kumar, M., Jindal, S.K., et al.: Implementation of all-optical active low/high tri-state buffer logic using the micro-ring resonator structures. Opt. Quant. Electron. **51**, 191 (2019). https://doi.org/10.1007/s11082-019-1898-5
2. Ali, F., Muhammad, F., Habib, U., et al.: Modeling and minimization of FWM effects in DWDM-based long-haul optical communication systems. Photon Netw. Commun. **41**, 36–46 (2021). https://doi.org/10.1007/s11107-020-00913-9
3. Stubkjaer, K.: Semiconductor optical amplifier-based all-optical gates for high-speed optical processing. IEEE J. Sel. Top. Quant. Electron. **6**(6), 1428–1435 (2000). https://doi.org/10.1109/2944.902198
4. Raja, A., Mukherjee, K., Roy, J.N.: Design analysis and applications of all-optical multi-functional logic using a semiconductor optical amplifier-based polarization rotation switch. J. Comput. Electron. **20**, 387–396 (2021). https://doi.org/10.1007/s10825-020-01607-1
5. Mukherjee, K., Raja, A.: Three input NAND gate using semiconductor optical amplifier. IEEE VLSI Dev. Circ. Syst. (VLSI DCS) **2020**, 142–145 (2020). https://doi.org/10.1109/VLSIDC

S47293.2020.9179931
6. Mukherjee, K., Raja, A., Maji, K.: All-optical logic gate NAND using semiconductor optical amplifiers with simulation. J. Opt. **48**, 357–364 (2019). https://doi.org/10.1007/s12596-019-00555-9
7. Raja, A., Mukherjee, K., Roy, J.N.: Analysis of new all optical polarization-encoded dual SOA-based ternary NOT & XOR gate with simulation. Photon Netw. Commun. (2021). https://doi.org/10.1007/s11107-021-00932-0
8. Raja, A., Mukherjee, K., Roy, J.N.: Polarization rotation-based all-optical AND gate using single semiconductor optical amplifier and implementation of a majority gate. J. Opt. Commun. online first 2021, pp. 000010151520200303. https://doi.org/10.1515/joc-2020-0303
9. Mukherjee, K.: All optical read only memory with frequency encoded addressing technique. Optik **122**(16), 1437–1440 (2011). https://doi.org/10.1016/j.ijleo.2010.09.024
10. Maji, K., Mukherjee, K., Raja, A.: An alternative method for implementation of frequency-encoded logic gates using a terahertz optical asymmetric demultiplexer (TOAD). J. Comput. Electron. **18**, 1423–1434 (2019). https://doi.org/10.1007/s10825-019-01393-5
11. Singh, P., Tripathi, D.K., Jaiswal, S, Dixit, H.K.: All-optical logic gates: designs, classification, and comparison. Adv. Opt. Technol. 2014, Article ID 275083, 13 pages (2014). https://doi.org/10.1155/2014/275083
12. Maji, K., Mukherjee, K.: Performance analysis of optical logic XOR gate using dual-control Tera Hertz Optical Asymmetric Demultiplexer (DCTOAD). Dev. Integr. Circ. (DevIC) **2019**, 58–60 (2019). https://doi.org/10.1109/DEVIC.2019.8783496
13. Sharma, S., Roy, S.: Design of all-optical parallel multipliers using semiconductor optical amplifier-based Mach-Zehnder interferometers. J. Supercomput. (2021). https://doi.org/10.1007/s11227-020-03543-0
14. Hakimian, F., Shayesteh, M.R., Moslemi, M.R.: Optimization of four-wave mixing wavelength conversion in a quantum-dot semiconductor optical amplifier based on the genetic algorithm. Opt. Quant. Electron. **53**, 140 (2021). https://doi.org/10.1007/s11082-021-02763-9
15. Mukherjee, K., Dutta, S., Roy, S., et al.: All-Optical digital to analog converter using Tera Hertz Optical Asymmetric Demultiplexer based on quantum dot semiconductor optical amplifier. Opt. Quant. Electron. **53**, 242 (2021). https://doi.org/10.1007/s11082-021-02900-4
16. Anzabi, K.S., Sharif, A.H., et al.: Performance enhancement of an all-optical XOR gate using quantum-dot based reflective semiconductor optical amplifiers in a folded Mach-Zehnder interferometer. Opt. Laser Technol. **135**, 106628 (2021)
17. Rendón-Salgado, I., Gutiérrez-Castrejón, R.: 160Gb/s all-optical AND gate using bulk SOA turbo–switched Mach–Zehnder interferometer. Opt. Commun. **399**, 77–86 (2017). https://doi.org/10.1016/j.optcom.2017.04.054
18. Kim, T.Y., Kim, J.Y., Han, S.K.: All-optical regenerator using semi-reflective semiconductor optical amplifier. J. Opt. Soc. Korea **10**(1), 11–15 (2006). https://doi.org/10.3807/JOSK.2006.10.1.011
19. Anzabi, K.S., Habibzadeh-Sharif, A., Connelly, M.J., Rostami, A.: Wideband steady-state and pulse propagation modeling of a reflective quantum-dot semiconductor optical amplifier. J. Lightw. Technol. **38**, 797–803 (2020)

LORANEX: A New Paradigm for Multimodal Approach to Forecast Weather

Dwaipayan Saha, Indrani Mukherjee, Jesmin Roy, Sudipta Sahana, and Dharmpal Singh

Abstract Weather forecasting is the solicitation of science and technology which in together predicts the state of the atmosphere for a given location. It has always been an important application in meteorological field, and it is one of the most scientifically and technologically challenging problem around the world. Various predictions and work have been done in this weather field, but still researches are going on to achieve better accuracies in the field of weather forecasting. In our work, we have analyzed the dataset of Australia's weather record and have considered the attributes which are present in the dataset and accordingly made our prediction model. Trained and tested the dataset and accordingly observations are made. The dataset is then classified using several classifiers, and the accuracies are compared. After classifying, we created our own ensemble model and have compared the accuracies and found that our proposed ensemble model resulted in higher accuracies.

Keywords Weather forecasting · Ensemble learning · LORANEX · Extra trees · Random forest · Logistic regression

1 Introduction

Weather forecasting is a vast area and has become an important field of research in the last few decades [1]. For centuries, people have tried to forecast weather informally and officially weather was forecasted during nineteenth century. In early years, weather forecasting used to be done by manually mostly focusing on barometric pressure, studying the existing weather pattern and looking the sky and cloud pattern [2]. But as the years passed, new techniques are introduced and implemented and everything became computer based.

Weather plays an important role in our daily chores. The ultimate goal of weather forecasting is to provide information and accordingly people, and various organizations can use this forecasting to solve weather-related issues and enhance societal

D. Saha · I. Mukherjee · J. Roy (✉) · S. Sahana · D. Singh
Department of Computer Science and Engineering, JIS College of Engineering, Kalyani, Nadia, West Bengal, India

B. Sikdar et al. (eds.), *Proceedings of the 3rd International Conference on Communication, Devices and Computing*, Lecture Notes in Electrical Engineering 851,
https://doi.org/10.1007/978-981-16-9154-6_35

accompanies, which includes protection of life and property, public health and safety, and support of economic prosperity and quality of life [1]. In the field of fields of agriculture and farming, weather plays an integral role. Temperature is the determining factor for farming of various fruits and vegetables. If crops get proper temperature, then it will grow nicely. Forecast based on temperature, rainfall, [3] and humidity will prepare farmers beforehand to make plans regarding crop irrigations, harvesting, and fertilizing time and many more [1, 4]. This in turn will save them from losses which will cause due to unpredictable weather change. As we already know, that the earth is almost 3/4th covered by the water bodies and the areas surrounding those water bodies get highly affected by the weather change, there is a high chance of changing pressure above the water bodies due to which the coastal areas can experience heavy rainfall, sometime can experience cyclone also, and if cyclone hits the coastal areas, the people will have to face serious issues [1, 5]. In this purpose, weather forecasting helps a lot, and the forecast saves a lot of lives by warning the people living in the coastal areas, so that they can be prepared beforehand. Weather forecasting too helps people regarding planning for trips to various adventurous places, in transportation of heavy goods and materials and helps in business especially in power plant areas.

The range of weather forecasting is divided into three divisions, short-range weather forecasting last for one or two days, medium-range weather forecasting last for three to four days up to two weeks, and long-range forecasting lasts for times longer than four weeks [6]. According to newest technology, there are various methods for forecasting the weather:

- Synoptic method of forecasting: In synoptic method, a systematic study of recent weather condition is being prepared and the present scenario of the area is compared [6]. Predictions are made based on the ground that current scenery will behave analogous with the past behaviors.
- Statistical method of forecasting: In statistical method, regressions and other related equations are made between various weather elements and climatic conditions.
- Numerical weather prediction technique of forecasting: This numerical method is optimal for medium-ranged forecasting, and the weather is forecasted by using various statistical models of atmosphere and water bodies, depending on the current situations [6].

In the course of this paper, we will be coming across a few more literature related to weather forecasting under Sect. 2 (Literature Review). After which we have mentioned a methodology under Sect. 3 which has been further divided into a number of subsections. Here, we have also mentioned about the dataset that we have used. In Sect. 4, we have shown the results obtained and have complimented them with a few screenshots that were obtained during the execution of the work. Lastly in Sect. 5, we have drawn a conclusion regarding our work.

2 Literature Review

Yuan [7] along with other authors stated in their work that after researching on weather forecast through historical database they found that traditional method is not an effective method as the atmosphere pattern is complex and nonlinear in nature as it changes every then and now. They introduced a potential method to forecast weather properly by the help of multilayer neural network. The atmosphere is divided into five regions based on rainfall with help of back propagation neural networks and accordingly observations are being made.

Kumar [8] in their work highlighted that nowadays weather datasets are nonlinear in nature, and hence, the approaches should shift toward nonlinearity predictions. The paper shows the application of artificial neural network and approach made by developing effective and reliable nonlinear predictive models for weather analysis and also compared and evaluated the performance of the developed nonlinear models using different transfer functions, hidden layers, and neurons to forecast maximum, temperature for 365 days of the year.

Ali [5] developed an artificial neural network (ANN) technique to estimate tropical cyclone heat potential (TCHP) for estimating the cyclone and predicting the intensity. They estimated TCHP by the help of an ANN technique, a two-layer reduced gravity model, and a multiple regression technique and compared the estimations with the observations. Out of the three methods, they found that ANN approach has given the best and the highest results. The results suggested the importance of the ANN technique in estimating TCHP with better accuracy in the North Indian Ocean that certainly, in turn, helps in improving the cyclone track and intensity predictions.

Gupta [3] in their paper tested and trained dataset of 2245 samples of New Delhi recorded rainfall period from June to September from 1996 to 2014. Then, they used various classification and regression algorithms on the dataset and tested their accuracies accordingly. After comparing all the accuracies, it was concluded that 5–10-1 pattern recognition neural network gave the highest accuracy comparing to K-nearest neighbor, regression tree (CART), and Naïve Bayes algorithm.

Sawaitul [9] along with other authors in their work depicted that they prepared their own prediction model and have divided the predictions into three regions. First region of the proposed model describes about the different models used in the weather forecasting. The second part introduces a wireless network kit for weather forecasting, and the third part highlighted about the back propagation algorithm used in the approach. They just made a rough idea sketch about the artificial neural network and showed some possibilities that the forecasting can be done.

Prasetya [10] in their research paper showed that data mining approaches can be applied to forecast the weather of a given place. Along with data mining approaches, classification was done on the dataset, and different classifiers were applied such as classification tree algorithm, Naïve Bayes, and K-nearest neighbor algorithm. In the work, three algorithms were used to predict rain with validation parameters of Brier score, confusion matrix, and ROC curves. After the analysis was done, it was

concluded that Naïve Bayes gave the highest accuracy among the three classifiers around 77.01% accuracy.

Rivero [11] in their paper dealt with an algorithm to fit with attributes using a Bayesian method for calculating cumulative rainfall time series forecasting. The forecasting will be implemented by an artificial neural network filter. Their proposed technique is based on the preceding delivery assumptions, and predictions are obtained by weighting up all probable models and restriction values according to their posterior distribution. If the time series is soft or rough, the fitting algorithm can be transformed accordingly to be in utility. And accordingly, predictions are being made.

Gad [12] in their work they explored and examined set of the common machine learning techniques to generate robust weather forecasting model for long periods of time. The combinations of all the model parameters are considered for simulations and the performance and accuracy results of each method using tenfold cross-validation procedures are presented in the paper. The experimental results of the classifiers show that the decision tree CART, XGBoost, and AdaBoost models exhibit better classification and gives better accuracy when compared with the other methods and for regression task, the linear regression method performs better in terms of R2 metric.

Gupta [13], their work shows that during this research process they have used some parameters to predict weather and the parameters are temperature, rainfall, evaporation, sunshine, wind speed, wind direction, cloud, humidity, and total size of dataset. Their research aims to compare the performance of machine learning algorithms for predicting weather using weather dataset which they collected. From the collected weather dataset which contains some weather attributes, which are most relevant to weather prediction. In their paper, various machine learning techniques have been examined and explored which includes Naive Bayes Bernoulli, logistic regression, Naive Bayes Gaussian, and KNN. The examined result shows that Naive Bayes Bernoulli algorithm has good level and highest of accuracy compared other algorithms as used by the authors.

The work described by Mathur [14] focused on maximum and minimum temperature forecasting and relative humidity prediction using time series analysis method. Their proposed networking model used a multilayer feedforward artificial neural network with back propagation learning method. The direct and statistical input parameters and the period are compared. For minimum/maximum temperature forecasting, the optimal time seems to be a 15 week period of input data values. Input features were features of maximum and minimum, respectively, and these features are moving average, exponential moving average, oscillator, rate of change, and the third moment. For the 15 week period, the error calculated was less than 3%. The result they concluded was that in general statistical parameters can be used to extract trends.

3 Methodology

Weather forecasting is such an important aspect in an individual's everyday life that it at times is capable of taking away one's life, if forecasted in an incorrect way. For instance, a weather forecast is done stating that the sky will be clear, and there will be no rain or storm. Believing this forecast, hundreds and thousands of fishermen sail in the mid sea to catch fishes. And now, there is tempest, as a result, the boats and ships get wrecked and the unfortunate innocent fishermen drown. Can we imagine how a false prediction is capable of taking away lives? Not only lives of fishermen, but the family members of the fishermen are in complete distress, they have lost their near and dear ones, may be they have lost the only earning member of their family. This fatal can be an incorrect prediction.

Several work and researches have already been done, and a lot of them are still in progress, in the field of weather forecasting and prediction. Here, in this work, we have worked with the dataset of Australia, done classification, and made a model which is capable of predicting whether there will be a rainfall or not. In this work, we have also done a comparative study of the accuracies of several classification techniques and have also proposed a new ensemble model, which yields a better accuracy when compared to the existing ones.

3.1 Dataset Description

The data used in this study is the weather condition recorded for Australia. The data was recorded from 01.12.2008 to 25.06.2017, and a total of 145,461 days of data were taken for the study. The dataset holds variation of weather recorded for all the cities of Australia. This dataset contains in total 22 attributes over which the variations are recorded. The attributes are like rainfall, sunshine, evaporation, minimum temperature, maximum temperature, and wind direction, cloud, wind gust, wind speed, humidity, pressure, and temperature recorded at 9 am and 3 pm, respectively.

3.2 Data Preprocessing

We have worked with a dataset in which daily observations from the 1st of December 2008 to the 25th of June 2017 have been mentioned for all the cities of Australia. Several attributes like date, location, maximum temperature, minimum temperature, evaporation, rainfall, sunshine, humidity, wind direction, and pressure are observed and recorded. Since the size of the dataset is pretty descent, data preprocessing is one of the most essential and initial task that requires attention and needs to be executed prior to the training and testing of data from the dataset, to avoid errors and minimize them if any to a great extent.

Here, in our work, firstly, we have checked for the null values. On checking for the same, we found a number of features contained approximated 40% to 50% null values. Since the percentage of the missing values was almost half of the total percentage, we could not neglect and ignore those attributes. Had we done so, there would have been a huge impact on our modeling. So we created a heat-map among the features whose values were missing. And this gave such a correlation value among the attributes, which made it possible for us to delete the columns which were not relevant to us.

Next we checked the number of columns that have a numeric value, and the number of columns that does not contain numeric values. After this, we had split the date in year, month, and day, and this is done with a purpose that in the later section of the work, we can delete or omit a part of the date which is not relevant to us. Outliers were another challenge in the data. Hence, the outliers were first identified, and then, they were replaced by the mean of the observations. After this, we split the data into the training and testing data.

3.3 Data Visualization

It becomes very easy to interpret the data once the data is presented in any pictorial or graphical format. The statistical data is always represented in various forms of graphs. Here, we have depicted some of the data in a graphical format, from which we have drawn a few conclusions. These conclusions have been very useful in the course of our work.

Firstly, we have plotted the total amount of rainfall with respect to all the years. Next we have plotted and observed how temperature and pressure change with respect to time and have drawn inference from the plots in the later section of this work.

3.4 Classification

For the purpose of classification, we have used a number of classification techniques, and after using these classification techniques, we have made a comparison on the basis of the accuracies received from each. Then, we have proposed a novel ensemble model, compared its accuracy, and also presented a confusion matrix for the same.

3.4.1 LORANEX Classifier (A Novel Ensemble Model)

There are many ensemble algorithms, and bagging is one of the approaches, in which this algorithm will fit a number of models on various subsets of the given training dataset, after which all the predictions are combined.

This novel ensemble model is a collection of several models of random forest classifier, which is itself an extension of bagging approach of an ensemble algorithm. This new ensemble model also consists of models of extra trees classifier and logistic classifiers, respectively. Hence, we have named this model LORANEX model, abbreviated from logistic regression (LO), random forest classifier (RAN), and extra trees classifier (EX), respectively.

This model is capable of giving better result when compared to the other existing standard models and have been tested with the data from the used dataset in this work. In the later section of this work, we have shown the output received from this novel model and have also compared its better performance with some of the present finest techniques which have given good results as well.

3.5 Our Work

Figure 1 as mentioned earlier, the initial part of the work involved data preprocessing, during which the raw data was first collected, followed by cleaning of the dataset to achieve better accuracy. After the data was cleaned, some parts of the data were omitted due to their irrelevance and owing to the fact that they have no significant impact on the target objective of the work and rainfall. After which the rest of the significant impactful data was selected. From the selected data, some of the data was transformed as required for the data usage and need (Figs. 2 and 3).

After the data was cleaned and processed, it was then split into two halves. The first half contained 80% of the data, for the purpose of training the models, and the other half contained the rest of the 20% data for the purpose of testing and validation. We have used multimodal approach to classify the data. We have used a number of existing classifiers, namely KNN classifier, Gaussian Naïve Bayes classifier, Bernoulli Naïve Bayes classifier, logistic regression classifier, random Forest classifier, linear SVC classifier, and extra trees classifier. After this, we have used our own novel LORANEX ensemble model classifier, which is a collection of various models of logistic regression classifier, random forest classifier, and extra trees classifier (Fig. 4).

After the training and testing of data using different classification techniques, we have found the accuracy obtained from each classifier along with respective confusion

Fig. 1 Data preprocessing

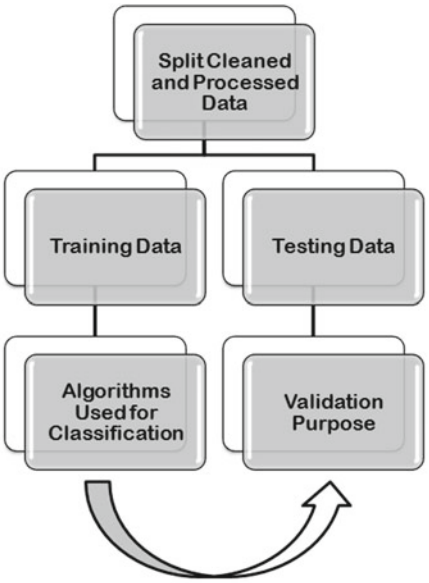

Fig. 2 Work flow diagram of data processing

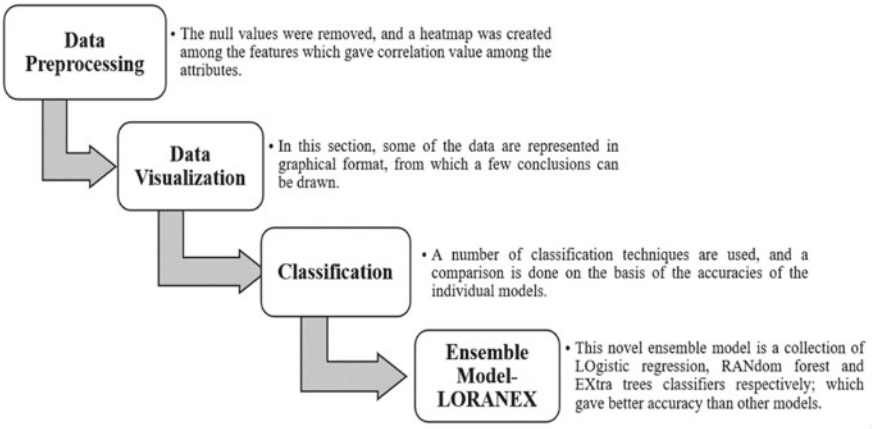

Fig. 3 Flow diagram of the entire working procedure

matrix. And after this, we have made a comparison among the pre-existing techniques and our proposed and devised novel technique. We have discussed about the results in the later section of this work.

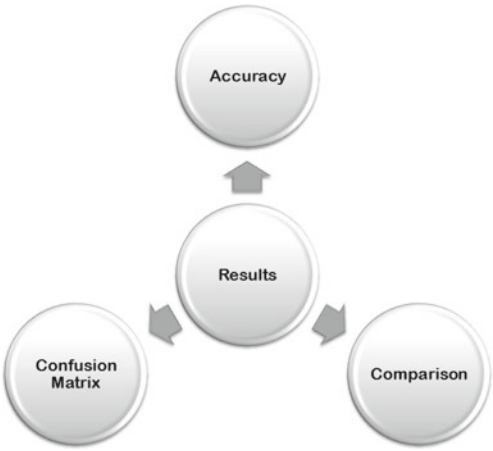

Fig. 4 Flow diagram of work after obtaining results

4 Results

As mentioned above, under Sect. 3.3, the data has been visualized using bar graphs. Here below, some of the graphs obtained as output have been mentioned, and a detailed explanation of the graphs has been presented (Fig. 5).

It is seen from the above graph that there has been a periodic rainfall visible over the years starting from 2009 and 2016. We can see that there is a certain drop in the amount of rainfall in the year 2017. And the amount of rainfall in the year 2009 has taken a quantum jump when compared to the amount of rainfall in 2008 (Fig. 6).

It is observed from the above graph that temperature at the starting and end of the year varies between 20 and 45 ℃, and in the middle of the year, it varies between 10 and 30 ℃. So, it is evident that there is a drop in the temperature in the middle of the year, and then, again the temperature increases in the later part of the year. It is clear

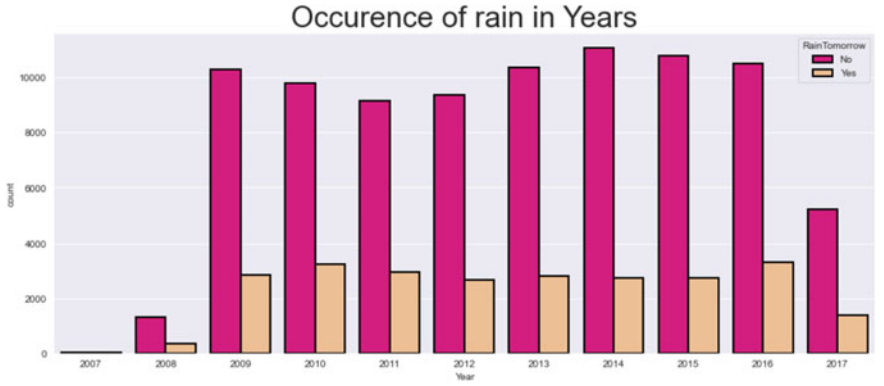

Fig. 5 Occurrence of rainfall with respect to year

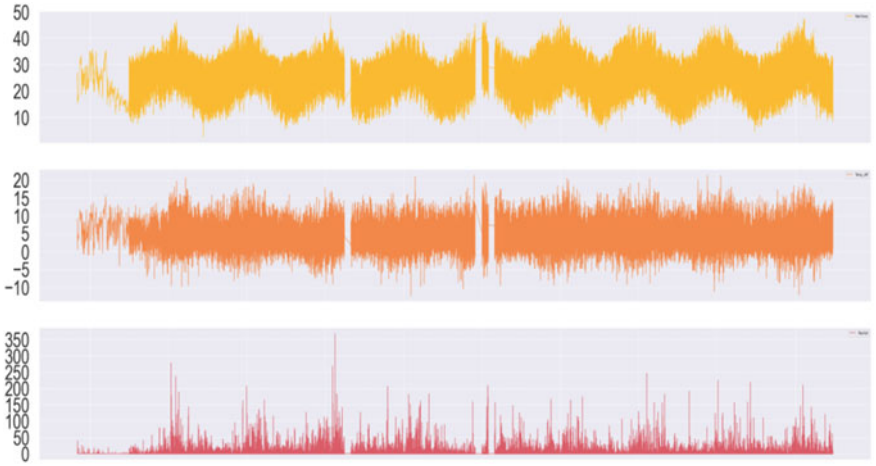

Fig. 6 Temperature plotted with respect to time, along with rainfall

that there is almost 90% temperature difference between 9AM and 3PM. Thus, it signifies that the in the latter half of the day, the temperature starts increasing. Hence, it is expected to have frequent rain at the starting of the day and more heavy rainfall at the end of the day (Fig. 7).

It is evident from the above graph that amount of rainfall is much more in January and February, but rainfall is more frequent in the middle of the year. Thus, it is concluded from the visualization of data that Australia suffers rainfall throughout the year (Table 1; Fig. 8).

It was observed that Gaussian Naïve Bayes has given the least accuracy (63.83%) among all the classifiers that have been used. Bernoulli Naïve Bayes was somewhat better that Gaussian Naïve Bayes in terms of accuracy with a percentage of 78.55.

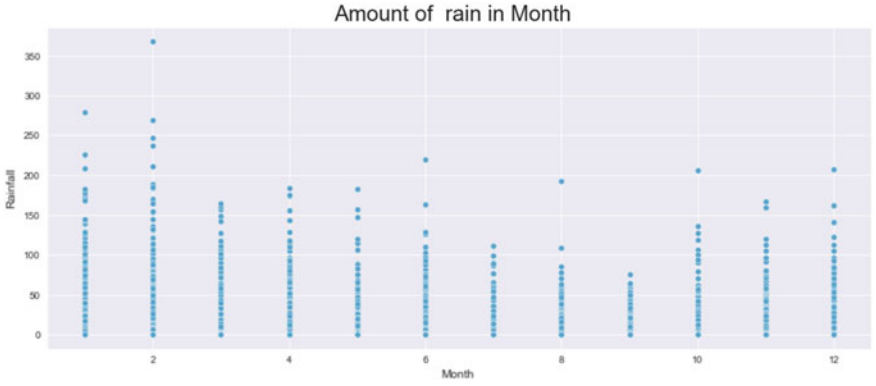

Fig. 7 Occurrence of rain according to months of a year

Table 1 Accuracy of various classifiers used

Classifier used	Accuracy (%)
K-nearest neighbor	85.04
Logistic regression	84.99
Gaussian Naïve Bayes	63.83
Bernoulli Naïve Bayes	78.55
Linear SVM	84.29
AdaBoost	85.24
Extra trees	85.92
Random forest	85.71
LORANEX	85.98

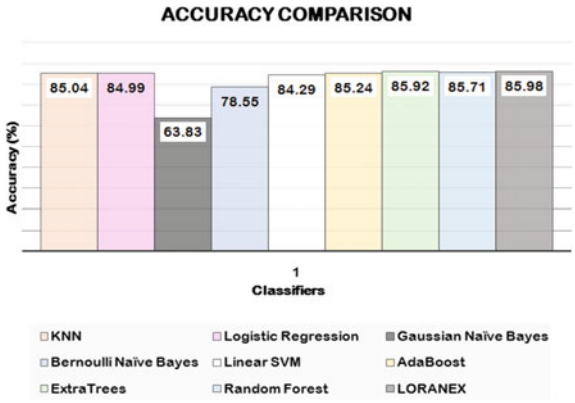

Fig. 8 Accuracy comparison of different classifiers

Linear SVM has given a better output when compared to the previously mentioned classifiers and has given a percentage of 84.29 in terms of accuracy. Logistic regression, KNN, and AdaBoost have been neck to neck with each other in terms of accuracy. Extra trees classifier has just passed random forest classifier by a small margin to yield the highest accuracy among the pre-existing classifiers with a percentage of 85.92, whereas the latter could only attain 85.71%. The novel LORANEX classifier that we have designed exclusively has given the highest accuracy among all the classifiers, almost 86% accuracy which has been achieved (85.98 precisely) (Fig. 9).

Our study area was Australia, where we studied every attribute related to weather and tried to accurately determine the conditions of weather prevailing over the region over the years. Overall the accuracy of all the other classifiers when considered individually was less than the ensemble model that has been proposed by us. Generally, existing ensemble models are also designed with the objective to hike the accuracy as compared to other individual models. But the ensemble model proposed by us, LORANEX, has been solely designed for the purpose of weather forecasting. Hence, it gives better and precise accuracy when compared to existing ensemble models.

```
seed = 7
kfold = model_selection.KFold(n_splits=10, random_state=seed, shuffle=True)
results = model_selection.cross_val_score(ensemble, X_train, y_train, cv=kfold)
print(results)
```

```
[0.85875581 0.86473323 0.85410671 0.85377463 0.86960372 0.85986274
 0.85598849 0.85344255 0.85964135 0.86429046]
```

Fig. 9 Cross-validation score

5 Conclusion

Weather forecasting when done accurately can be of great help to the society. Weather is that element of nature that keeps on changing from time to time, over a very short period of time. And also the weather of two different regions separated by a very small distance can also have different weather at same interval of time. Thus, the prediction of weather can be very abrupt and inconclusive if not done correctly or not give proper importance to the changing elements of weather. Elements of weather, like, temperature, rainfall, pressure, wind speed, etc., may often changes within short span of time, and hence, determining them for a future reference can be a very tedious one. But by using proper technology and correctly implementing those, it is possible to determine the weather for a region.

There are many organizations who are currently working upon this, and they are day-to-day updating their techniques so as to make this more precise and accurate. This approach proposed by us will result in accurate determination of weather or the elements of weather. The novel ensemble model implemented in this can reduce the risks of inappropriately forecasting of weather. The forecasting of weather is not only an important area of study for the present, but also it can be further improved with new emerging technologies in the near future.

Weather forecasting has a long path ahead. It can be modified to work with artificial intelligence to reduce the human effort.

References

1. Wiston, M., Mphale, K.M.: Weather forecasting: from the early weather wizards to modern-day weather predictions. J Climatol Weather Forecasting (2018). https://doi.org/10.4172/2332-2594.1000229
2. Iseh, A. J., Woma, T.Y.: Weather forecasting models, methods and applications. Int J Eng Res Technol (IJERT) **2**(12) (2013). ISSN: 2278-0181
3. Gupta, D., Ghose, U.: A comparative study of classification algorithms for forecasting rainfall. In: Published in: 2015 4th International Conference on Reliability, Infocom Technologies and Optimization (ICRITO) (Trends and Future Directions) (2015). Electronic ISBN: 978-1-4673-7231-2. https://doi.org/10.1109/ICRITO.2015.7359273

4. Garcia, A., Hansen, J.W., Mariani, L., Nain, A.S.: Weather and climate forecasts for agriculture (2010). https://www.researchgate.net/publication/255651193_Weather_and_Climate_Forecasts_for_Agriculture
5. Ali, M.M., Jagadeesh, P.S.V., Lin, I.-I., Hsu, J.-Y.: A neural network approach to estimate tropical cyclone heat potential in the Indian Ocean. IEEE Geosci. Rem. Sens. Lett. **9**(6), 1114–1117 (2012)
6. Balasubramanian, A.: Weather forecasting (2016). https://doi.org/10.13140/RG.2.2.20270.51522
7. Yuan, Q., Lu, Y.: Research on weather forecast based on neural networks. In: Proceedings of the 3rd world congress on intelligent control and automation (Cat. No.00EX393) (2000). https://doi.org/10.1109/WCICA.2000.863402. ISBN: 0-7803-5995-X
8. Abhishek, K., Singh, M.P., Ghosh, S., Anand, A.: Weather forecasting model using artificial neural network. (2012). https://doi.org/10.1016/j.protcy.2012.05.047
9. Sawaitul, S.D., Wagh, K.P., Chatur, P.N.: Classification and prediction of future weather by using back propagation algorithm-an approach. **2**(1). ISSN 2250-2459
10. Prasetya, R., Ridwan, A.: Data mining application on weather prediction using classification tree, Naïve Bayes and K-Nearest neighbour algorithm with model testing of supervised learning probabilistic brier score, confusion matrix and ROC. JAICT **4**(2) (2019)
11. Rivero, C.R., Pucheta, J., Laboret, S., Herrera, M., Sauchelli, V.: Time Series forecasting using bayesian method: application to cumulative rainfall. IEEE Latinamerica Trans. **11**(1), 359–364 (2013)
12. Gad, I.: A comparative study of prediction and classification models on NCDC weather data (2020). https://doi.org/10.1080/1206212X.2020.1766769
13. Gupta, R.: Review on weather prediction using machine learning. Int. J. Eng. Dev. Res. **8** (2020). ISSN: 2321-9939
14. Mathur, S., Kumar, A., Chandra, M.: A feature based neural network model for weather forecasting. World Acad. Sci. Eng. Technol. **34** (2007)

Improvement of Efficiency and Uniformity of Dual Wavelength Emission for GaN/InGaN Multiple Quantum Well LEDs Through Triangular Electron Blocking Layer

Mainak Saha and Abhijit Biswas

Abstract Dual wavelength GaN-based light emitting diodes (LEDs) are extensively used in various fields ranging from energy efficient solid-state lightning to medical diagnosis. In this work the effect of a triangular shaped Electron Blocking Layer (EBL) on the emission of such dual wavelength has been studied. The simulation results show that the proposed structure gives an efficient dual wavelength emission with improved wavelength uniformity. This improvement is obtained due to suppression of the piezoelectric polarization at the active region and EBL boundary which results in enhancement of the barrier height for the electrons to confine them in the active region and the reduction of the potential barrier height for the hole injection into the active region.

Keywords Dual broadband LED · Efficiency droop · Electron blocking layer · GaN/InGaN multiple quantum well · TCAD

1 Introduction

The InGaN/GaN multiple-quantum well (MQW) light emitting diodes (LEDs) have shown immense potential in solid state lighting due to their direct bandgaps supporting emissions covering the range from near-ultraviolet to near-infrared [1, 2]. In addition these structures have shown ability of multicolor emission which has also gained popularity in the field of micro-displays [3], visible light communication [4], solid state white light sources [5] and medical diagnosis [6]. A common need in all these applications has always been an efficient emission of dual wavelength from a monolithic structure. One of the most straight forward methods to meet this requirement is to realize the quantum wells in the active region of the LED with different In

M. Saha (✉)
Ramkrishna Mahato Government Engineering College, Vill: Agharpur, P.O.- Ramamoti, P.S.- Joypur, Dist.- Purulia 723103, India

A. Biswas
Institute of Radio Physics and Electronics, University of Calcutta, 92, Acharya Prafulla Chandra Road, Kolkata 700009, India

B. Sikdar et al. (eds.), *Proceedings of the 3rd International Conference on Communication, Devices and Computing*, Lecture Notes in Electrical Engineering 851,
https://doi.org/10.1007/978-981-16-9154-6_36

components so that they can emit light of different wavelengths [7]. However, this capability is greatly obstructed by the abrupt drop in emission efficiency at high injection currents. This phenomenon, termed as efficiency droop [8, 9], puts limitations in using these LEDs for applications that demands high power. Many suggestions for its contributing factors have been reported, such as the Auger recombination [10], Electron leakage [11], carrier injection efficiency [12], Polarization field [13] and filling of localized states [14]. Nevertheless, the cause and exact physical explanation for efficiency droop is yet to be addressed and hence a complete description is still to be investigated. On the other hand a good uniformity in the intensity of the dual wavelength emission requires fabrication processes that are complex and challenging when considered for large scale production. Therefore, cost-effective and highly-efficient alternatives are in great demand for dual wavelength emission.

In this paper, a dual wavelength emitting LED with triangular shaped EBL is proposed in Sect. 2. Section 3 discusses the calibration of the different simulation parameters by comparing the simulated result with the reported ones. The optical and electrical properties of this proposed structure has been numerically obtained through TCAD [15] simulation using parameter values obtained in Sect. 3. Thereafter, these performances are compared with other reported dual wavelength broadband LEDs in Sect. 4 and finally in conclusion (Sect. 5) the proposed structure has been found to provide an optimized performance.

2 Device Structure

The conventional blue InGaN LED used as a reference is a real device grown by Kuo et al. [16]. The redesigned structure as reported by Wang et al. [17] is considered for broadband dual wavelength emission. Finally the proposed structure has a triangular EBL instead of a constant composition EBL as shown in Fig. 1. In the proposed structure the Al composition in the EBL is linearly graded up from 0 at the boundary of the last barrier to 0.15 at the middle of the layer and then linearly graded down to zero at the boundary with the p-GaN layer.

3 Simulation Set-Up

The SILVACO ATLAS is a two-dimensional (2-D) self-consistent simulation program that incorporates the solution of the carrier transport equations, Poisson's equation, photon rate equation, quantum mechanical wave equations, current continuity equations, and heat transfer equations.

The temperature-dependent bandgap energies of alloys have been calculated with Varshni formula [18] and found to be $E_g(GaN) = 3.435$, $E_g(InN) = 0.711$, and $E_g(AlN) = 6.138$ eV for GaN, InN, and AlN (at temperature of 300 K).

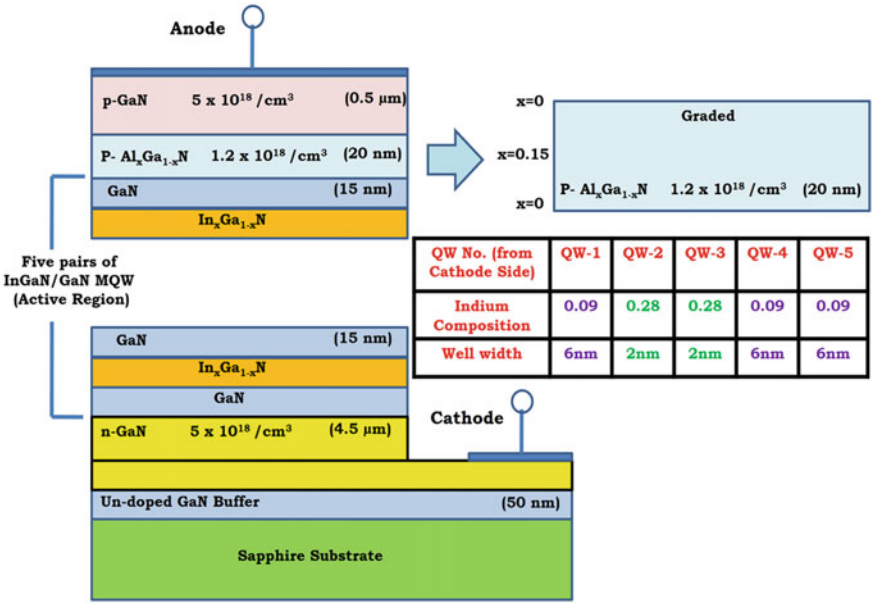

Fig. 1 Schematic diagram of the proposed LED with triangular EBL

For InGaN and AlGaN ternary alloys, the bandgap energies can be described as a linear interpolation of binary alloys

$$E_g(In_xGa_{1-x}N) = x \cdot E_g(InN) + (1-x) \cdot E_g(GaN) - x \cdot (1-x) \cdot B_{EG}(InGaN)$$

$$E_g(Al_xGa_{1-x}N) = x \cdot E_g(AlN) + (1-x) \cdot E_g(GaN) - x \cdot (1-x) \cdot B_{EG}(AlGaN),$$

where $B_{EG}(InGaN)$ and $B_{EG}(AlGaN)$ are bowing parameters of bandgap energies of ternary nitrides and are taken to be 1.43 and 0.7 [19] respectively. The band offset ratio is selected to be $\Delta E_C/\Delta E_V = 0.66/0.34$. The method suggested by Fiorentini et al. [20] has been followed to calculate the piezoelectric and spontaneous polarization of GaN, AlGaN, and InGaN. Screened percentages of polarization charges due to defects are set to be 40%. The Caughey-Thomas approximation [20] is employed to determine the electron mobility as a function of doping density where different parameters are selected as per Ref. [22]. The low-field hole mobility values are taken to be 2 cm^2/Vs for the InGaN [23], and 10 cm^2/Vs for the AlGaN [24].

4 Results and Discussion

The reported and obtained normalized internal quantum efficiency (IQE) vs. current curves for the conventional blue LED structure are plotted in Fig. 2. Figure 3 depicts the reported and obtained spontaneous emission rates at a current of 100 mA as a function of wavelength for the reported dual wavelength broadband LED. These figures show a good agreement of the obtained data with the reported results, and hence validity of the present simulation framework is established.

Figure 4 compares the spontaneous emission rates of the reported and the proposed dual wavelength emitting structures at 100 mA. Clearly the proposed structure exhibits a higher emission rate for green and violet QWs and most importantly the ratio of the peak spontaneous emission rate of violet QW to that of the green QW is found to be 0.80 for the proposed structure instead of 0.70 for the reported structure

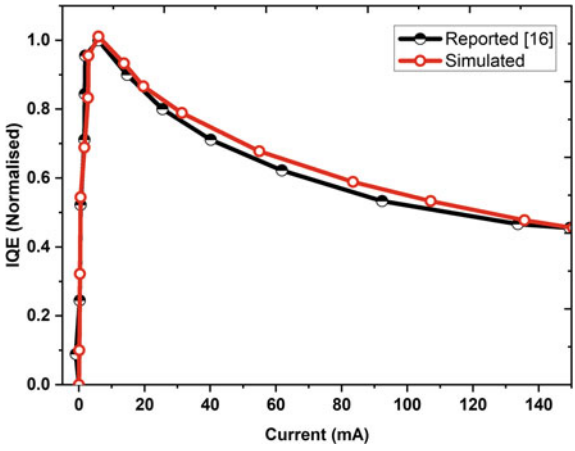

Fig. 2 Reported and obtained variation of IQE as a function of injection current for the conventional blue LED

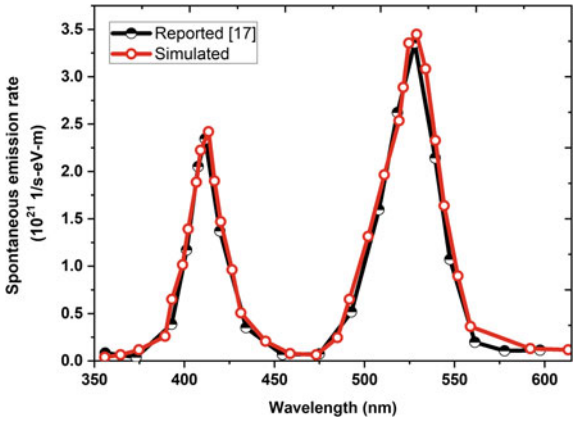

Fig. 3 Reported and obtained spontaneous emission rates at 100 mA as a function of wavelength for the broadband LED

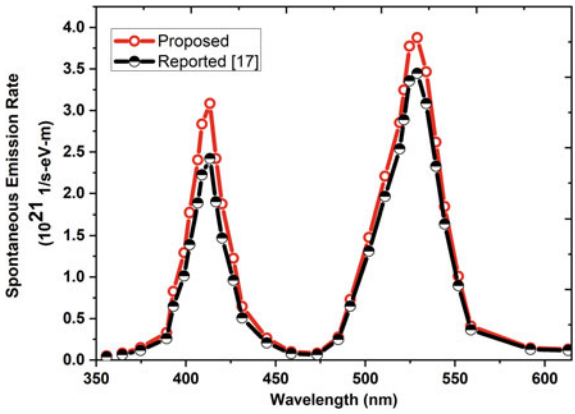

Fig. 4 Spontaneous emission rate as function of wavelength for the reported and proposed structure at 100 mA

(where the ratio of 1 indicates the peak emission for both wavelengths are equal). This indicates that the proposed structure emits dual wavelength more uniformly.

The light output power as a function of injection current for the reported and proposed dual wavelength emitting structures is also derived and depicted in Fig. 5 it shows that a better linearity in the variation of the output power with input current is obtained for the proposed structure than the reported structure, and notably, at an injection current of 260 mA the proposed structure offers 46% higher power output compared to the reported structure.

Figure 6 shows the plot of the normalized internal quantum efficiency (η) as a function of injection current for the reported and proposed dual wavelength emitting structures. The efficiency droop calculated as $\left(\eta_{\text{peak}} - \eta_{260\text{mA}}\right)/\eta_{\text{peak}}$ has been found to be only 8% for the proposed structure compared to 25% for the reported structure.

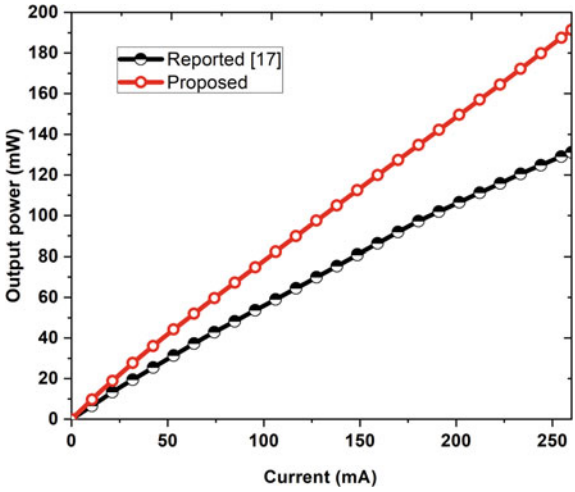

Fig. 5 Light output power as a function of injection current for the reported and proposed structure

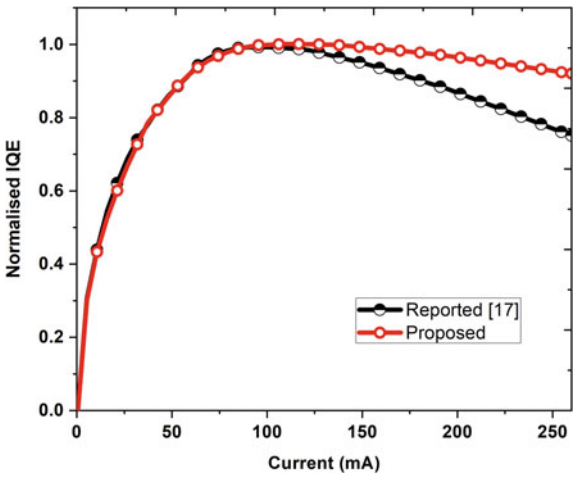

Fig. 6 Normalized IQE as a function of injection current for the reported and proposed structure

To investigate the contributing factors toward this improved performance, the energy band diagram and both electron and hole concentrations for reported and proposed dual wavelength emitting structures are obtained and analyzed.

Figure 7 shows the energy band diagrams of the reported and proposed dual wavelength emitting LEDs at an injection current of 100 mA. From Fig. 7b one can easily visualize that the band diagram for the proposed structure takes a triangular shape in the EBL region. The deviation from a perfect triangular shape can be attributed to the presence of polarization field in this region. Notably the potential barrier for electrons at the interface of the last barrier and EBL is increased to 379 meV in the proposed structure compared to 330 meV as observed in reported dual wavelength emitting LED. On the other hand, the potential barrier for the hole injection at the p-GaN and EBL junction is reduced to 257 meV compared to 281 meV which is obtained for the reported structure. These two facts contribute to better electron confinement and enhanced hole injection into the active region respectively for the proposed structure. The alteration in barrier heights occurs as the peak electric field in the EBL region for the proposed structure is lowered due to the triangular barrier caused by the reduction in the polarization field at the EBL. This phenomenon takes place due to a gradual change from GaN barrier to AlGaN EBL and then again gradual change from AlGaN EBL to p-GaN by using triangular EBL.

Figure 8 depicts the electron concentration for the reported and proposed structure at 100 mA. The electron concentration in the green quantum wells is observed to be higher in both the structures compared to violet quantum wells due to its higher depth arising from high in content there. For the proposed structure the density of electrons in quantum wells increases because of better electron confinement. For example, the electron concentration in the third (green) and fifth (violet) quantum wells (calculated from cathode side) of proposed structure is 20% and 40% higher respectively, compared to the corresponding values in the reported structure. On the other hand, due to less electron overflow, the concentration of electrons in the EBL

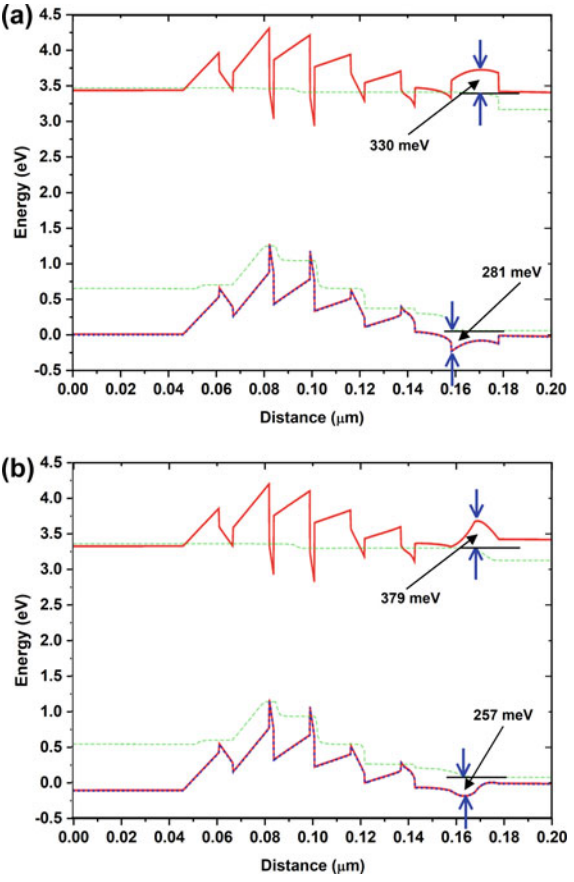

Fig. 7 Energy band diagram of the **a** reported LED [17] and **b** proposed LED at 100 mA

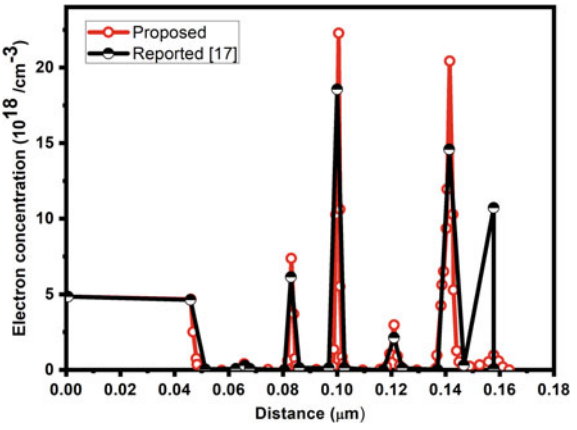

Fig. 8 Electron concentration in the quantum wells for the reported and proposed structure at 100 mA

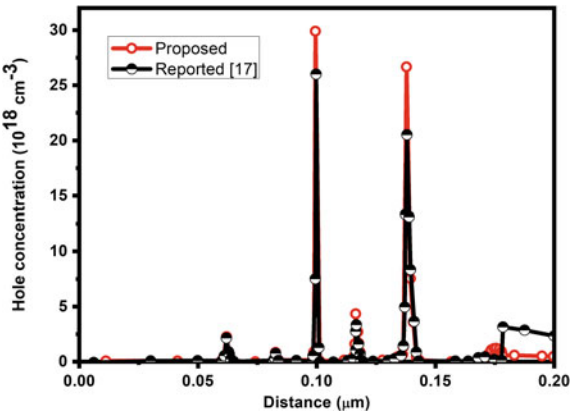

Fig. 9 Hole concentration in the quantum wells for the reported and proposed structure at 100 mA

of proposed structure is found to reduce by 90% compared to that in the reported structure.

The obtained hole concentrations at 100 mA for the reported and the proposed structures are shown in Fig. 9. Like electron concentration the hole concentration is also found to be higher in green quantum wells compared to violet quantum wells due to higher In content in the green wells. From the figure, it is clearly evident that the hole concentration for all the quantum wells increases in the proposed structure. For example this increment is found to be 15% and 29% in the third (green) and fifth (violet) quantum wells, respectively.

The improvement in electron and hole concentrations is more in fifth (violet) quantum well compared to third (green) quantum well due to the nearer location of the former to the EBL that plays the major role in contributing to these phenomena. As a result of these enhanced carrier concentrations the radiative recombination in the violet quantum wells of proposed structure increases, and a better uniformity in emission is achieved compared to the reported structure. Moreover the overall increase in carrier concentration in the quantum wells results in improving the optical performance of the proposed structure.

Additionally, the performance of the proposed structure is compared with other similar dual wavelength emitting LEDs [25–27]. The results of such comparison are shown in Table 1.

From Table 1, it is evident that the proposed dual wavelength LED offers much lower droop in quantum efficiency and provides better linearity in the variation of output power with input current. Such properties are beneficial for optical communication oriented applications. Thus the proposed structure turns out to be the optimized structure since it offers higher optical power output with emission of improved uniformity as well as lower efficiency droop at a higher injection current.

Table 1 Comparison of electro-optical performance of the proposed LED structure with other reported LEDs with dual emission

Quantity	Jahangir et al. [25]	Ooi et al. [26]	Li et al. [27]	Proposed
1. Quantum Efficiency Droop	18% at 105 A/cm^2	56% at 250 A/cm^2	Not reported	0.36% at 105 A/cm^2 and 8% at 250 A/cm^2
2. Variation of power with input current	Linear with R^2 value of 0.98813	Linear with R^2 value of 0.97431	Linear with R^2 value of 0.99613	Linear with R^2 value of 0.99947

5 Conclusion

We have studied the performance of the InGaN/GaN dual wavelength broadband LEDs with a triangular graded composition AlGaN EBL. The reduced polarization field due to the triangular EBL causes a better electron confinement and hole injection into the active region resulting in an efficient distribution of the carrier producing more output power while reducing non-uniformity in emission of two wavelengths. Moreover the proposed structure enhances the electron and hole concentrations in the wells which attributes to 17% reduction in efficiency droop compared to the reported broadband dual wavelength LED in Ref. [17].

References

1. Gong, Y., Jiu, L., Bruckbauer, J., Bai, J., Martin, R.W., Wang, T.: Monolithic multiple colour emission from InGaN grown on patterned non-polar GaN. Sci. Rep. **9**(1), 986–986 (2019)
2. Ruterana, P., Morales, M., Chery, N., Ngo, T.H., Chauvat, M.-P., Lekhal, K., et al.: Effect of AlGaN interlayer on the GaN/InGaN/GaN/AlGaN multi-quantum wells structural properties toward red light emission. J. Appl. Phys. **128**(22), 223102–223102 (2020)
3. Liu, Y., Zhang, K., Hyun, B.-R., Kwok, H.S., Liu, Z.: High-brightness InGaN/GaN micro-LEDs with secondary peak effect for displays. IEEE Electron. Device Lett. **41**(9), 1380–1383 (2020)
4. Huang, Y., Guo, Z., Wang, X., Li, H., Xiang, D.: GaN-Based high-response frequency and high-optical power matrix micro-LED for visible light communication. IEEE Electron. Device Lett. **41**(10), 1536–1539 (2020)
5. Jain, B., Velpula, R.T., Thang Bui, H.Q., Nguyen, H.-D., Lenka, T.R., Nguyen, T.K., Nguyen, H.P.T.: High performance electron blocking layer-free InGaN/GaN nanowire white-light-emitting diodes. Opt. Express **28**(1), 665–675 (2020)
6. Piprek, J.: Efficiency models for GaN-based light-emitting diodes: status and challenges. Materials (Basel, Switzerland) 13(22) (2020)
7. El-Ghoroury, H.S., Nakajima, Y., Yeh, M., Liang, E., Chuang, C.-L., Chen, J.C.: Color temperature tunable white light based on monolithic color-tunable light emitting diodes. Opt. Express **28**(2), 1206–1215 (2020)
8. Meng, X., Wang, L., Hao, Z., Luo, Y., Sun, C., Han, Y., et al.: Study on efficiency droop in InGaN/GaN light-emitting diodes based on differential carrier lifetime analysis. Appl. Phys. Lett. **108**(1), 13501–13501 (2016)

9. Kim, M.-H., Schubert, M.F., Dai, Q., Kim, J.K., Schubert, E.F., Piprek, J., Park, Y.: Origin of efficiency droop in GaN-based light-emitting diodes. Appl. Phys. Lett. **91**(18), 183507–183507 (2007)
10. Bertazzi, F., Goano, M., Zhou, X., Calciati, M., Ghione, G., Matsubara, M., Bellotti, E.: Looking for Auger signatures in III-nitride light emitters. Appl. Phys. Lett. **106**(6), 61112–61112 (2015)
11. Wang, C.K., Chiou, Y.Z., Chuang, S.B.: Enhancement in output power of blue nitride-based light-emitting diodes with an electron retarded layer. J. Display Technol. **11**(12), 1005–1009 (2015)
12. Kuo, Y.-K., Tsai, M.-C., Yen, S.-H., Hsu, T.-C., Shen, Y.-J.: Effect of P-Type last barrier on efficiency droop of blue InGaN light-emitting diodes. IEEE J. Quantum Electron. **46**(8), 1214–1220 (2010)
13. Bai, J., Xu, B., Guzman, F.G., Xing, K., Gong, Y., Hou, Y., Wang, T.: (11–22) semipolar InGaN emitters from green to amber on overgrown GaN on micro-rod templates. Appl. Phys. Lett. **107**(26), 261103–261103 (2015)
14. Chang, S.-P., Lu, T.-C., Zhuo, L.-F., Jang, C.-Y., Lin, D.-W., Yang, H.-C., et al.: Low droop nonpolar GaN/InGaN light emitting diode grown on m-Plane GaN substrate. J. Electrochem. Soc. **157**(5), H501 (2010)
15. ATLAS User's Manual, software version 5.18.3.R, Silvaco International, Santa Clara, CA (2012)
16. Kuo, Y.-K., Chang, J.-Y., Tsai, M.-C., Yen, S.-H.: Advantages of blue InGaN multiple-quantum well light-emitting diodes with InGaN barriers. Appl. Phys. Lett. **95**(1), 11116–11116 (2009)
17. Wang, T.-H., Kuo, Y.-K.: Spectral competition of chirped dual-wavelength emission in monolithic InGaN multiple-quantum well light-emitting diodes. Appl. Phys. Lett. **102**(17), 171112–171112 (2013)
18. Varshni, Y.P.: Temperature dependence of the energy gap in semiconductors. Physica **34**(1), 149–154 (1967)
19. Piprek, J.: Semiconductor Optoelectronic Devices. Academic Press, Amsterdam (2003)
20. Fiorentini, V., Bernardini, F., Ambacher, O.: Evidence for nonlinear macroscopic polarization in III–V nitride alloy heterostructures. Appl. Phys. Lett. **80**(7), 1204–1206 (2002)
21. Caughey, D.M., Thomas, R.E.: Carrier mobilities in silicon empirically related to doping and field. Proc. IEEE **55**(12), 2192–2193 (1967)
22. Maziar, C.M., Lundstrom, M.S.: Caughey-Thomas parameters for electron mobility calculations in GaAs. Electron. Lett. **22**(11), 565–566 (1986)
23. Kumakura, K., Makimoto, T., Kobayashi, N.: Mg-acceptor activation mechanism and transport characteristics in p-type InGaN grown by metalorganic vapor phase epitaxy. J. Appl. Phys. **93**(6), 3370–3375 (2003)
24. Jiang, H.X., Jin, S.X., Li, J., Shakya, J., Lin, J.Y.: III-nitride blue microdisplays. Appl. Phys. Lett. **78**(9), 1303–1305 (2001)
25. Jahangir, S., Pietzonka, I., Strassburg, M., Bhattacharya, P.: Monolithic phosphor-free InGaN/GaN quantum dot wavelength converter white light emitting diodes. Appl. Phys. Lett. **105**, 1111171–1111174 (2014)
26. Ooi, Y.K., Zhang, J.: Design analysis of phosphor-free monolithic white light-emitting-diodes with InGaN/ InGaN multiple quantum wells on ternary InGaN substrates. AIP Adv. **5**, 571681–571687 (2015)
27. Li, H., Li, P., Kang, J., Li, Z., Li, Z., Li, J., Yi, X., Wang, G.: Phosphor-free, color-tunable monolithic InGaN light-emitting diodes. Appl. Phys. Express **6**, 1021031–1021034 (2013)

Generalized Multi-server Platform-Based Remote User Authentication

Rohit Kesarwani and Prerna Mohit

Abstract The user authentication scheme based on the multi-server environment approach provides an additional facility over the traditional single server environment. The proposed method uses a combination of a user's random string and password to design a remote user authentication scheme over a multi-server environment. The involvement of a smart card provides the user's access to different servers after registering once with the registration center and uses the same identity and password to access the several. This phenomenon resolved the problem of users managing and memorizing the different credentials that enhance the security level compared to the traditional single server model. In addition, the proposed scheme contains all the goals and security requirements. The corresponding simulation is performed using the extensively used automated validation application tool AVISPA, and the derived simulation will indicate that the proposed scheme is secure and lightweight.

Keywords Authentication · Hash function · Session key agreement · AVISPA · Multi-server · Smart card

1 Introduction

In the last few years, the rapid development of Internet technologies helps users get different services via the Internet, such as multimedia applications, automated teller machines (ATM) and remote login systems. However, using these services over the Internet would require an authentication server, the legitimate user against the different kinds of attacks, i.e., denial of service attack (Dos), password guessing attack, replay attack, stolen-verifier attack, insider attack and others.

This development of Internet has revolutionized the lifestyle of the people because it provides a reliable, portable and scalable platform for several services over the public network such as e-commerce, e-learning, e-medicine, e-governance, access to information, entertainment and financial service. So, to protect the users access-

R. Kesarwani · P. Mohit (✉)
Indian Institute of Information Technology Senapati Manipur, Imphal, India

B. Sikdar et al. (eds.), *Proceedings of the 3rd International Conference on Communication, Devices and Computing*, Lecture Notes in Electrical Engineering 851,
https://doi.org/10.1007/978-981-16-9154-6_37

ing these services from the adversary, several authentication techniques have been proposed. Authentication of any remote user is defined as the integrity of the user or proving the identity. The authentication process is categorized based on server, i.e., single server environment or multi-server environment (the remote user has access to several servers distributed over the Internet). Based on the users present in mutual authentication, multi-server authentication protocols [1] have two broader categories. The first category consists of user and server, and the second category consists of user, server, and registration center. A multi-server (MS) scheme is far better than a single server scheme. Here, the MS system is implemented with three constituents: the remote user, registration center, and server. A trusted third party named as registration center (RC) administers all the users and registered servers. Multi-server authentication scheme provides the user with the ease of login into distinct servers with a single registration and reduces the problem of memorizing and storing a lot of credentials.

The rest of the paper is organized as follows: Sect. 2 comes with the existing work. Section 3 brings the proposed user authentication scheme for multi-server environment. The security analysis of the proposed scheme is presented in Sect. 4. Then the computation cost comparison is presented in Sect. 5. Finally, Sect. 6 ends with conclusion.

2 Related Work

There are a number of research work done in the field of remote user authentication in various domains such as health care [2], multi-server [3], and WSN [4, 5]. In 2000, a password-based verifier-free authentication scheme was proposed by Hwang and Li [6], which uses the smart card and is based on the public key method. However, this scheme does not permit the users to choose and alter their passwords voluntarily. Also, the scheme was vulnerable to impersonation attack (the kind of attack in which an adversary successfully assumes one of the legitimate parties or a communications protocol, e.g., fake social media profile). Furthermore, to improve Hwang and Li et al. scheme efficiency, a no-verifier password authentication scheme was proposed by Sun et al. [7]. To design a new scheme, Sun et al. [7] use the smart cards and cryptographic hash functions, but some major pitfalls have been found in terms of password change.

In 2002, Chien et al. [8] proposed a scheme to achieve mutual authentication. In his scheme, users can voluntarily choose their password and the smart card (SC), where the SC does not contain the user's ID_i, so it avoids the risk of IDi-theft or impersonation. Chien et al. [8] also pointed out to Sun et al.'s [7] system that this scheme achieves unilateral user authentication. Unfortunately, Chien et al.'s [8] scheme cannot withstand the parallel session attack. Further, Chien et al. [8] method pointed out by Ku et al.'s [9] that the scheme is vulnerable to an insider attack, password guessing attack, and reflection attack. However, Yoon et al. [10] presented that Ku et al. [9] scheme was insecure for changing the user's password and easily

susceptible to parallel session attack. Yoon et al. [11] also proposed an enhancement version of Ku et al.'s [9] scheme to overcome the problems. Ku et al. [9] and Yoon et al.'s [11] scheme exhibits great application potentiality in smart cards based on the smart card schemes. Instead of using costly modular exponentiation, we used several hash operations.

Das et al. [12] in 2004 had presented a dynamic ID-based remote user authentication scheme that uses smart cards. Das et al. [12] strategy permitted the users to choose and change their passwords voluntarily. The scheme was also not maintaining any verifier table and securing against the ID theft. In 2014, Chuang et al. [13] had given multi-server scheme based on smart cards and biometrics in which the normal validation of user's identity had been performed. Later in 2017, Jangirala et al. [14] had first inspected that the Shunmuganathan et al. [15] remote user authentication scheme for the multi-server platform is vulnerable to stolen smart card's attack, user impersonation attack, password guessing, forgery attack and replay attack. Also, the scheme fails to provide two-factor authority and forward secrecy. To overcome the shortcomings of these security weaknesses, Jangirala [14] proposed a multi-server authentication system using dynamic ID that can resist and sustain all the requirements of a multi-server environment. In our proposed scheme, users can freely choose their credentials such as user identification ID_i and password Pw_i for login and have to register with register center R_C only once. Moreover, our proposed schemes provide more functionality and security features such as a no verification table, mutual authentication and session key agreement.

3 The Proposed Scheme

This section presents a string-based remote user authentication scheme for remote access. In our proposed scheme, a trusted third- party authoritative known as registration center R_C will be invoked/implored only during the registration phase. A presented authentication scheme can be defined as a message M, the pre-shared key P_K, the identities ID_i, a family $h()$ of hash function from $\{0, 1\}^*$ to $\{0, 1\}^l$ and a related family of message authentication code(MAC) from $\{0, 1\}^k \times \{0, 1\}^*$ to $\{0, 1\}^l$. We denote the string as STR_i and secret value of R_C as X. The used notations are described as follows:

Notations Used:

U_i = the ith user X = registration center's secret value

R_C = registration center
ID_i = public identity of remote user U_i
SID_j = public identity of server S_j
PW_i = user $U_i's$ password
STR_i = random string data of U_i
AID_i = anonymous identity of U_i
$h()$ = one-way hash function

N_i = arbitrary nonce
SC = smart card P_K = master key shared among authorized registration center R_C & servers S_j
$\oplus$ = bitwise exclusive-or (XOR) operator
$\|$ = message concatenation operator.

Our proposed remote user authentication scheme has four stages: (1) initialization phase (IP); (2) user registration phase (URP); (3) user login phase (ULP) and (4) authentication phase (AP). The detailed description of these four phases is described as follows.

3.1 IP

An IP consists of two steps: (1) the system setup step and (2) the server enrollment step. The system will be implemented in system setup only once to the R_C to set up the overall control environment. In the second step, i.e., server enrollment, a legitimate server S_j is provided with pre-shared key $P_K \epsilon P$ by registration center R_C, where P_K is shared between R_C and the server S_j.

3.2 URP

The URP is initialized only once and will be invoked whenever a new user U_i wants to register itself to the remote system. During the registration phase, the U_i selects his IDi, h($PW_i \oplus STR_i$) and submits it to the R_C via a secure communication channel. On obtaining a registration request from user U_i, the R_C performs the following calculations:

(i) $IDX_i = h(ID_i \| X)$
(ii) $hIDX_i = h(IDX_i)$
(iii) $C_i = h(PW_i \oplus STR_i) \oplus hIDX_i$
(iv) $D_i = P_K \oplus IDX_i$
(v) $E_i = h(PW_i \oplus STR_i) \oplus ID_i$.

Now these parameters will be generated by user U_i's smart card and will send it to U_i via a secure channel (Fig. 1).

3.3 ULP

Now, the user U_i intrigued to login on server S_j with identifier SID_j, and then user U_i must perform the following steps:

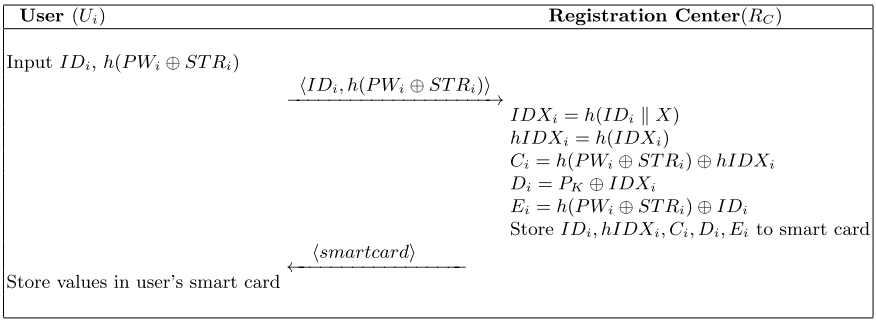

Fig. 1 URP structure

(i) The user U_i places his/her smart card into a card reader and also inputs his/her ID_i, PW_i and random string STR_i at the input side.
(ii) Now, smart card validates the entered user's identity ID_i with the stored value of E_i, i.e., $ID_i = h(PW_i \oplus STR_i) \oplus E_i$ and also performs h$(PW_i \oplus STR_i) \oplus C_i$. If the $hIDX_i$ matches with the h$(PW_i \oplus STR_i) \oplus C_i$, then it generates a random number Num_1.
(iii) U_i inputs ID_i now, and smart card performs following messages:

$$Msg_1 = h(hIDX_i) \oplus Num_1$$
$$AID_i = h(Num_1) \oplus ID_i,$$
$$Msg_2 = h(Num_1 \parallel AID_i \parallel D_i).$$

3.4 AP

In user will be authenticated in the authentication phase based on the message generated in login step for authentication. U_i and server S_j execute the following actions to carry out the mutual authentication and session establishment key.
(i) An authentication message (AID_i, Msg_1, Msg_2, D_i) will be transmitted by smart card to server S_j
(ii) On getting the authentication request (AID_i, Msg_1, Msg_2, D_i), the S_j validates the U_i, the S_j uses P_K to obtain ($IDX_i = D_i \oplus P_K$). S_j yields the value of Num_1, i.e., ($Num_1 = Msg_1 \oplus h(h(IDX_i))$) and verifies whether h$(Num_1 \parallel AID_i \parallel D_i)$ matches with Msg_2. The server S_j rejects the authentication request and terminates the session if the result does not match because the authentication message has been modified. Now S_j generates the arbitrary number Num_2 and calculates the session key SK_{ij} which is h$(Num_1 \parallel Num_2)$. At last, S_j computes the authentication reply message Msg_3 and Msg_4, where Msg_3 as $Num_2 \oplus h(h(Num_1))$ and Msg_4 as h$(SID_j \parallel Num_2)$.

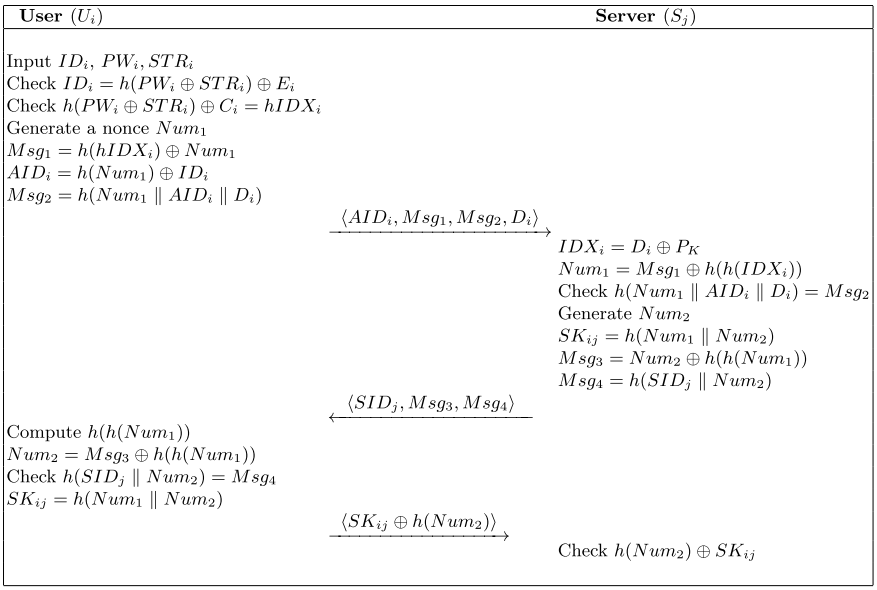

Fig. 2 ULP, AP structure

(iii) Server S_j sends the authentication reply message (SID_j, Msg_3, Msg_4) to the SC.
(iv) Now, the SC validates S_j, then SC retrieves the random number $Num_2 = Msg_3 \oplus h(h(Num_1))$ and verifies whether h($SID_j \parallel Num_2$) matches with Msg_4. If the values are matched, then the session key SK_{ij} = h($Num_1 \parallel Num_2$)) will be computed by SC.
(v) The SC transmits the (i.e., $SK_{ij} \oplus h(Num_2)$) message to S_j.
(vi) The S_j retrieves the value $h(Num_2)$ using the session key SK_{ij}. Then it validates the value, i.e., ($SK_{ij} \oplus h(Num_2)$) to prevent an illegitimate user from executing the replay attack (Fig. 2).

3.5 Simulation Based on AVISPA

The workability of the proposed scheme is validated using "Automated Validation of Internet Security Protocols and Applications (AVISPA)" tool [16]. An implementing of the protocol using AVISPA can be reached and executed through role-oriented language, called high-level protocol specification language (HLPSL) [17]. The primary roles for the entities (Patient, health care, doctor) are involved in the communication with mandatory session key and instanced with concrete arguments. The four backends, specifically (1) OFMC, (2) CL-AtSe, (3) SATMC and (4) TA4SP, are integrated in the proposed protocol using AVISPA. The simulation results in Table 1 inform the safety feature of the proposed design against the active and passive attack. In the OFMC, the depth for the search is 6, with 132 nodes and searching time is only

Table 1 Simulation results under OFMC and CL-AtSe

% OFMC	SUMMARY
% Version of 2006/02/13	SAFE
SUMMARY	
SAFE	DETAILS
DETAILS	BOUNDED_NUMBER_OF_SESSIONS
BOUNDED_NUMBER_OF_SESSIONS	TYPED_MODEL
PROTOCOL	
/home/span/span/testsuite/results/user.if	PROTOCOL
GOAL	/home/span/span/testsuite/results/user.if
as_specified	GOAL
BACKEND	As_specified
OFMC	BACKEND
COMMENTS	CL-AtSe
STATISTICS	STATISTICS
parseTime: 0.00s	Analyzed: 0 states
searchTime: 0.63s	Reachable: 0 states
visitedNodes: 132 nodes	Translation: 32.88 s
depth: 6 plies	Computation: 0.00 s

0.63 s. The CL-AtSe states that all the states are also reachable. The translation and computation taken for this backend are 32.88 s and 0.0 s, respectively. The simulation results assure that the proposed scheme satisfies the design properties, and it is secure against both active and passive attacks.

4 Security Analysis

In this section, we will perform the security analysis for proposed scheme to validate the suitability of several known attacks.

4.1 Resist Against Insider Attack

User U_i sends registration center and R_C a registration request in the registration phase, i.e., ID_i and $h(PW_i \oplus STR_i)$. Moreover, R_C will not retrieve the value of PW_i and STR_i due to the involvement of one-way hash function. Hence, the proposed scheme is free from insider attacks.

4.2 No Verification Table

Password PW_i and string STR_i are not stored in database by registration center R_C and server S_j. Therefore, even if somehow adversary attacks on the R_C, the adversary will not be able to obtain the authentication information of user U_i.

4.3 Resist Against Guessing Attack

Password PW_i, pre-shared key P_K, string STR_i and R_C's secret value, i.e., X, are unknown to the adversary. If, somehow, the stored information, $hIDX_i$, C_i, D_i and E_i, has been disclosed, the system will also be secure. The one-way cryptographic hash function is used to protect password PW_i and the random string STR_i of the user, which means that the adversary will not be able to check whether his guessed password PW_i, i.e., $h(PW_i \oplus STR_i) = C_i \oplus hIDX_i$ is correct or not.

4.4 Resist Against Replay Attack

If, somehow, adversary eavesdrops on the communication between user U_i and server S_j, in future, it may attempt to use this message for opening the connection to a server. However, to protect from such eavesdropping, our proposed scheme uses a random number $Num1$ and adds this random number Num_1 to the message so that, if adversary tried to replaying the message by getting the authentication message AID_i, Msg_1, Msg_2, D_i, the server will identify the invalid random number Num_1, i.e., $Num_1 = Msg_1 \oplus h^2(IDX_i)$, and the server will reject the replay request.

4.5 Mutual Authentication

A mutual authentication can be defined as the process in which both the server and the user need to prove their legitimacy with each other. In the authentication phase, with the value $Num_1 = Msg_1 \oplus h^2(IDX_i)$, the server authenticates the user, and with $Num_2 = Msg_3 \oplus h^2(Num_1)$, the server is authenticated by the user. If the attacker somehow catches the messages and acts as a legitimate server or user, then attacker has to generate a valid reply message to the user/server. However, the attacker does not know the pre-shared key P_K and the random numbers Num_1 and Num_2. So he will be incapable of computing a valid reply message.

4.6 Session Key Agreement

A temporary key that is only used once for short period is encrypting or decrypting the data and ensures that the communications are confidential. Moreover, the arbitrary number and a cryptographic one-way hash function are to generate the session key $SK_{ij} = h(Num_1||Num_2))$. Hence, in this session, the key is like a one-time password that resets the user login and is generated for each login. Obtain the session key SK_{ij} from the intercepted messages which will be challenging for the adversary.

5 Computation Cost Comparison

In this section, we have compared the computation cost and performance among several schemes with our proposed scheme. It shows that our proposed scheme tries to recover some flaws that are found in old schemes. As we have previously observed that Shunmuganathan et al.'s scheme, Jangirala et al.'s scheme and Das et al.'s scheme were vulnerable to several attacks such as Shunmuganathan et al.'s scheme does not prevent the user impersonation, password guessing, etc., and also, we have seen that its computation cost is bit higher, i.e., $7C_h + 3C_x$ for the login phase and $13C_h + 7C_x$ for the authentication phase.
The performance metrics that we have used in our scheme is

C_h: Computation cost of hash function
C_x: Computation cost of XOR function (Fig. 3).

In our proposed scheme, we have tried to reduce the computation cost as well as vulnerabilities. We have tested our scheme using AVISPA simulation in which we got search time of nearly 0.63 s with 132 nodes under the OFMC model. The computation cost that our proposed scheme incurs for both the user login and authentication phase is $19C_h + 11C_x$ which represents that our scheme is efficient in communication against the relevant old schemes.

Scheme	ULP	AP	Total Cost
Das et al. [12]	$5C_h + 7C_x$	$5C_h + 7C_x$	$10C_h + 14C_x$
Shunmuganathan et al. [15]	$7C_h + 3C_x$	$13C_h + 7C_x$	$20C_h + 10C_x$
Jangirala et al. [14]	$8C_h + 6C_x$	$17C_h + 6C_x$	$25C_h + 12C_x$
Prosposed	$5C_h + 6C_x$	$14C_h + 5C_x$	$19C_h + 11C_x$

Fig. 3 Computation cost comparison

6 Conclusions

In this paper, a simple, secure and lightweight remote user authentication scheme is presented which can assist multi-server environment that uses registration center R_C to save the users to unnecessarily memorize the credentials. As the scheme uses only the cryptographic hash function, it corresponds to lightweight authentication scheme. Moreover, informal security analysis ensures the following security properties: resistance from an insider attack, no verification tables, resistance against guessing attack, user anonymity and resistance against replay attacks mutual authentication. Furthermore, the proposed scheme has been simulated under the extensively accepted and used tool AVISPA for security verification, the simulation results indicate that our proposed method is secure.

References

1. Baruah, K.C., Banerjee, S., Dutta, M.P., Bhunia, C.T.: An improved biometric-based multi-server authentication scheme using smart card. Int. J. Secur. Appl. **9**(1), 397–408 (2015)
2. Mohit, P., Amin, R., Biswas, G.: An e-healthcare authentication protocol employing cloud computing. Int. J. Ad Hoc Ubiquitous Comput. **36**(3), 155–168 (2021)
3. Zhang, Y., Li, B., Liu, B., Hu ,Y., Zheng, H.: A privacy-aware pufs-based multi- server authentication protocol in cloud-edge iot systems using blockchain. IEEE Internet Things J. (2021)
4. Mohit, P., Amin, R., Biswas, G.: Design of authentication protocol for wireless sensor network-based smart vehicular system. Veh. Commun. **9**, 64–71 (2017)
5. Mohit, P., Amin, R., Biswas, G., Khan, M.K.: A standard mutual authentication protocol for cloud computing based health care system. J. Med. Syst. **41**(4), 50 (2017)
6. Hwang, L.M.S., Li, L.H.: A new remote user authentication scheme using smart card (2004)
7. Sun, H.-M.: An efficient remote use authentication scheme using smart cards. IEEE Trans. Consum. Electron. **46**(4), 958–961 (2000)
8. Chien, H.Y., Jan, J.K., Tseng, Y.M.: An efficient and practical solution to remote authentication: smart cards
9. Ku, W.C., Chen, S.N.: Weakness and improvement of an efficient password based remote user authentication scheme using smart cards (2004)
10. Yoon, E.J., Ryu, E.K., Yoo, K.Y.: Further improvement of an efficient password based remote user authentication scheme using smart cards (2004)
11. Yoon, E.-J., Ryu, E.-K., Yoo, K.-Y.: An improvement of Hwang-Lee-Tang's simple remote user authentication scheme. Comput. Secur. **24**(1), 50–56 (2005)
12. Das, M.L., Saxena, A., Gulati, V.P.: A dynamic id-based remote user authentication scheme. Ph.D. dissertation, Indian Institute of Technology, Bombay, India (2004)
13. Chuang, M.C., Chen, M.C.: An anonymous multi-server authenticated key agreement scheme based on trust computing using smart cards and biometrics. Expert Syst. Appl. **41**(4), 1411–1418 (2014)
14. Jangirala, S., Mukhopadhyay, S., Das, A.K.: A multi-server environment with secure and efficient remote user authentication scheme based on dynamic id using smart cards. Wireless Pers. Commun. **95**(3), 2735–2767 (2017)
15. Shunmuganathan, S., Saravanan, R.D., Palanichamy, Y.: Secure and efficient smart-card-based remote user authentication scheme for multiserver environment. Can. J. Electr. Comput. Eng. **38**(1), 20–30 (2015)

16. Armando, A., Basin, D., Boichut, Y., Chevalier, Y., Compagna, L., Cuellar, J., Drielsma, P.H., Héam, P.-C., Kouchnarenko, O., Mantovani, J., et al.: The avispa tool for the automated validation of internet security protocols and applications. In: International Conference on Computer Aided Verification, pp. 281–285. Springer (2005)
17. AVISPA, Team, Automated validation of internet security protocols and applications (2015)

Simulation and Fabrication of High Gain Diffracted Ground-Based Metamaterial Microstrip Patch Antenna for C Band

Sunil Lavadiya, Vishal Sorathiya, and Sudipta Das

Abstract A novel structure of microstrip patch antenna is presented for high gain enhancement and broadband wireless applications. The manuscript describes a comparative analysis of the patch antenna with the multiple split-ring resonators loaded patch antenna. The design performance was examined using different parameters like return loss, frequency resonance, voltage standing wave ratio, gain, and directivity. Gain enhancement is possible by enabling diffracted ground in the ground layer. The metamaterial behavior of the antenna is observed by a negative refractive index for complementary split-ring resonators (CSRR) structure. The coaxial feed is given to the antenna for excitation. The proposed design provides the return loss of −29 dB, voltage standing wave ratio (VSWR) of 1.08, and total gain of 8.34 dB. Results are authenticated by physical designing of the antenna and measuring results using a vector network analyzer. The proposed antenna structure will be used for a satellite TV network, weather radar station, Terrestrial microwave links under C band applications.

Keywords Gain · Metamaterial · Complimentary split-ring resonator · Microstrip patch antenna

S. Lavadiya (✉) · V. Sorathiya
Department of Information and Communication Technology, Marwadi University, Rajkot, Gujarat, India
e-mail: sunil.lavadiya@marwadieducation.edu.in

V. Sorathiya
e-mail: vishal.sorathiya@marwadieducation.edu.in

S. Das
Department of Electronics and Communication Engineering, IMPS College of Engineering and Technology, Malda, West Bengal, India

B. Sikdar et al. (eds.), *Proceedings of the 3rd International Conference on Communication, Devices and Computing*, Lecture Notes in Electrical Engineering 851,
https://doi.org/10.1007/978-981-16-9154-6_38

1 Introduction

The patch antenna has been used by a plethora of researchers for various purposes like a miniaturized design, ease of fabrication, frequency operation, etc. In the current scenario, a microstrip patch antenna has certain drawbacks like power handling capacity, bandwidth, and less control on magnetic nature. Power handling capacity can be improved by cavity-backed microstrip radiators, waveguide-fed microstrip patch antenna, etc. Numerous scientists have proposed various architectures for gain and bandwidth enhancement [1]. It can be improved by stacking phenomena, implementation of "shi" shaped patch, surface mounted horn antenna feed by patch antenna, rotation of upper microstrip patch radiators concerning the lower patch, etc. This report presents the work on gaining improvement by implementing split-ring resonators concepts [2]. With the help of split-ring resonators (SRR), the magnetic nature can be optimized for a specific frequency. Microstrip resonators size reduction can be possible using SRR. A unit cell split-ring resonator has multiple pairs of loops which split into opposite sides. It can be fabricated by metal like copper and it is available in different shapes like square, circular, etc., [3]. The split-ring resonator structure (SRR) demonstrates that it has narrow gaps between the two opposite ends and hence generates a large number of capacitive values [4]. This phenomenon will lower the resonating frequency. The dimensions of the SRR structure are very small in contrast to the desired wavelength. This structure will enhance the gain, lower the radiating losses henceforth improving the quality factor. Novel design of the patch antenna will increase the gain and broadband behavior is possible by the implementation of multiple CSRR into the microstrip structure [5, 6]. Effects of multiple CSRR (one, two, three, and eight) have been compared and their effects have been observed.

2 Design and Modelling Introduction

Design parameters of the presented microstrip patch antenna have been specified in Fig. 1. The size of the substrate layer and patch are the same. Figure 1 represents the three-dimensional view of a proposed patch antenna. Ground layer and patch are made of copper material. The dimensions of substrate and ground are 103 mm by 103 mm. The substrate is made of FR4 material has a dielectric constant of 4.4. The patch is made of copper material and its dimensions are 60 mm by 60 mm. The height of the ground and patch is 0.35 mm and the height of the substrate is 1.5 mm.

A patch antenna is designed by mentioned equations [7]. The width and length of the proposed design are calculated by Eq. (1) and Eq. (2). The effective permittivity $\left(\varepsilon_{eff}\right)$ is found using the Eq. (4).

$$W = \frac{C_0}{2fr}\sqrt{\frac{2}{_r + 1}} \tag{1}$$

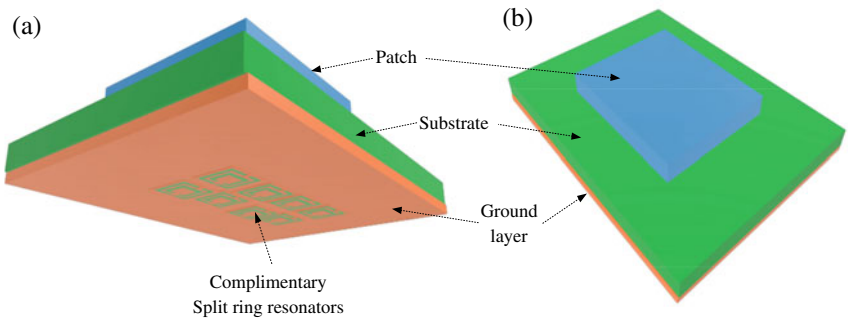

Fig. 1 Prototype of the proposed microstrip patch antenna. **a** three-dimensional view. **b** Top view of design

$$L = \frac{C}{2f_r\sqrt{e}} - 2l \tag{2}$$

$$\frac{\Delta l}{h} = 0.412\frac{(\varepsilon_e + 0.300)\left(\frac{w}{h} + 0.264\right)}{(\varepsilon_e - 0.258)\left(\frac{w}{h} + 0.8\right)} \tag{3}$$

$$\varepsilon_{eff} = \frac{\varepsilon_r + 1}{2} + \frac{\varepsilon_r - 1}{2}\left(1 + \frac{12h}{w}\right)^{-\frac{1}{2}} \tag{4}$$

$$W_0 = \sqrt{\frac{2}{Ls.Co}} \tag{5}$$

$$N = \pm\frac{Cos^{-1}\left(1 - S_{11}^2 + S_{21}^2\right)}{kd * S_{21}} \tag{6}$$

$$Z = \sqrt{\frac{(1 + S_{11})^2 - S_{21}^2}{(1 - S_{11})^2 - S_{21}^2}} \tag{7}$$

$$\varepsilon_e = \frac{n}{z} \tag{8}$$

$$\mu = n.z \tag{9}$$

where W is the width of the patch, f_0 is the resonance frequency, h is the height of substrate, L is the length of the patch, ε_r is the relative permittivity of the dielectric substrate, C is the speed of light: 3×10^8 (m/s), ε_{ef} is effective dielectric constant [8]. The scattering parameters are required for the analysis at high-frequency analysis. Two complementary split-ring resonators perform as L–C has driven resonating structure. By changing the dimension and spacing between two rings, the resonance frequency is changed. The resonance frequency of the split-ring resonator is found by self-inductance(L) and capacitance/unit length (C_{pul}) is calculated by following

equations [9–11].

$$f_0 = \frac{1}{2\pi\sqrt{L_{\text{net}} * C_{\text{net}}}} \tag{10}$$

$$C_{\text{net}} = \frac{(Cs + Cg)}{2} \tag{11}$$

$$Cs = (4a_e - g)C_{\text{pul}} \tag{12}$$

$$Cg = \frac{\varepsilon_0 wt}{g} \tag{13}$$

$$C_{\text{pul}} = \frac{\sqrt{\varepsilon_r}}{CZ_0} \tag{14}$$

$$C_{\text{net}} = \left(2a_e - \frac{g}{2}\right)C_{\text{pul}} + \left(\frac{\varepsilon_o wt}{g}\right) \tag{15}$$

$$L_{\text{net}} = (0.0002)l\left(2.303 * \log_{10}\frac{4l}{w} - \gamma\right) \tag{16}$$

$$l = 8a_e - g \tag{17}$$

where L_{net} is the total inductance and C_{net} is the total capacitance of the structure. Cs is series capacitance and Cg is the gap capacitance, W is the width of metal split rings and t is the thickness of the metal rings, a_e is the ring dimension, Cs is distributed capacitance, ε_o is free space permittivity, g is the split gap dimension and C_{pul} is the capacitance per unit length, Z_0 the characteristic impedance of the line, l is the wire length, and square-shaped wire loop has a constant parameter of $\gamma = 2.853$ [12]. The dimensions of the split-ring are shown in Fig. 2.

The meshing of the prototype model demonstrates the complexity of structure at the micro-level and therefore there is always a tradeoff between computation time and accuracy of results concerning the size of the structure [13]. The meshing of CSRR structure is more complex than normal microstrip patch antenna (MPA) is shown in Fig. 3.

Four CSRR structures have been implemented. The first structure has one CSRR, the Second has two CSRR, the third has three CSRR and the fourth have eight CSRR is illustrated in Fig. 4.

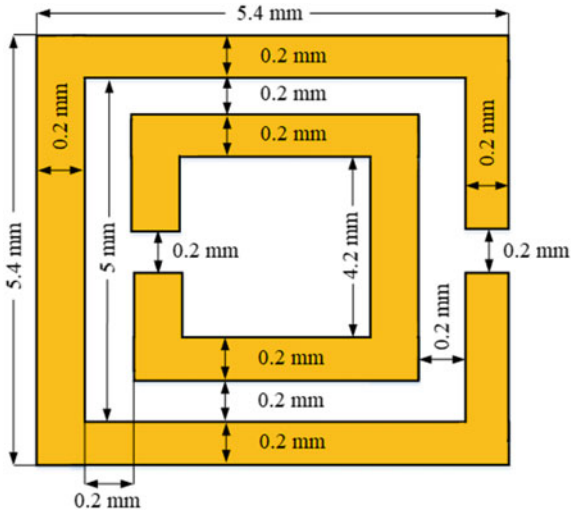

Fig. 2 Outer split-ring resonator has dimension 5.4 mm by 5.4 mm, Inner split-ring resonator has dimension 4.2 mm by 4.2 mm. The thickness of both SRR is 0.2 mm, Inner and outer SRR rings are separated by 0.2 mm

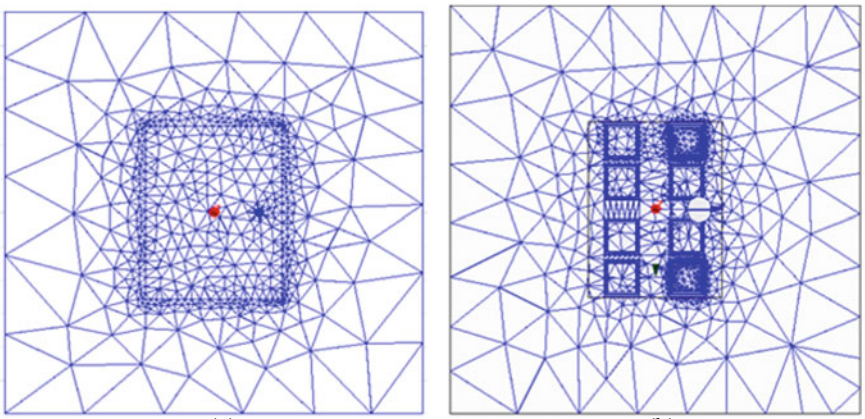

Fig. 3 **a** Meshing of the simple microstrip patch antenna. **b** The meshing of eight-cell SRR, Tetrahedral meshes are implemented by a high-frequency structure simulator. Meshes are very much complex at the feed

3 Design and Modelling

The antenna must have a maximum amount of absorption for applied signal and this thing is observed by return loss. The required value should be more than −10 dB indicates proper design [14]. Normal patch antenna gives reflectance response of −

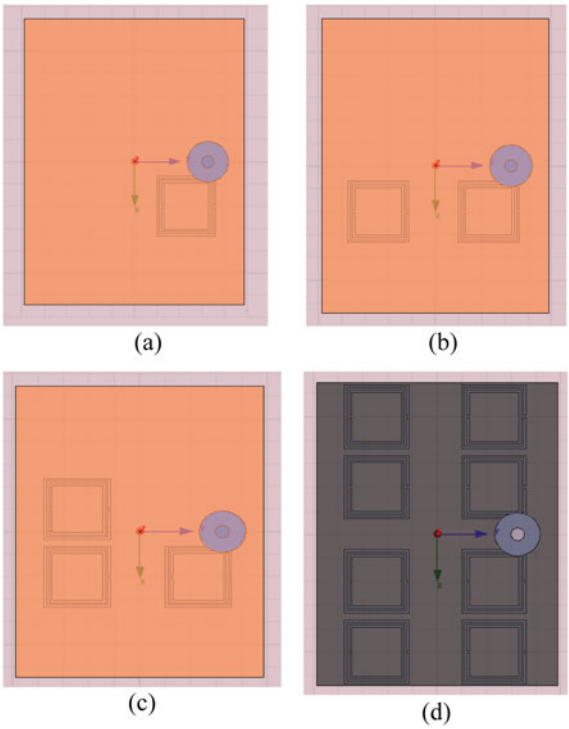

Fig. 4 CSRR loaded ground layer of proposed patch antenna **a** Single SRR, **b** Double SRR, **c** Triple SRR, **d** Eight SRR cell

29 dB with a bandwidth of 360 MHz (4.82 GHz – 4.46 GHz) and Patch antenna with CSRR provides two bands, first band with S_{11} of −26 dB and bandwidth of 440 MHz (4.55 GHz – 4.11 GHz), Second band with S_{11} of −17 dB gain and bandwidth of 520 MHz (4.90 GHz – 4.38 GHz) is reflected in Fig. 5.

Figure 6 represents the gain plot represents the amount of power distribution for specific theta. More gain represents more power is radiated from the antenna. Figure 7 represents for Microstrip patch antenna the gain value is more than 5 dB for the range −30° to +40° and for MPA with CSRR gain value is more than 5 dB for the range −40° to +40°. Gain plot spread over a wider range and uniform in nature. Gainplot represents the percentage of power is radiating from an antenna and it is observed from Fig. 7 that 8.1895 dB power is radiated by normal MPA and MPA with the usage of eight complementary split-ring resonators gives 8.3503 dB gain.

Antenna with metamaterial property provides a negative refractive index. This characteristic is observed by the Real and Imaginary impedance value [15] (Table 1 and Fig. 8).

As per the above table, a structure without SRR has a resonating frequency at 4.63, and further implementation of the unit SRR structure deviates from the actual frequency. The behavior of directivity is slightly changing in each model although the final model suggests the maximum resonating frequency.

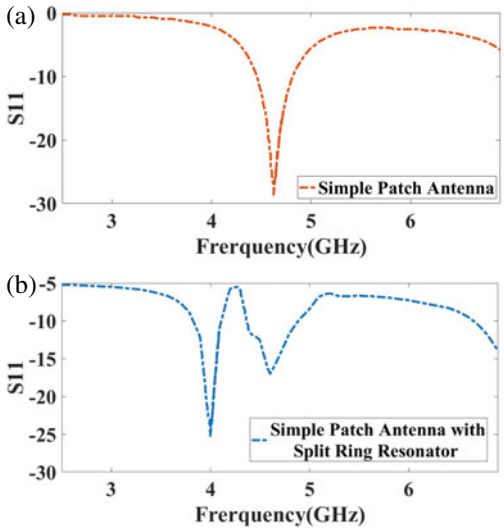

Fig. 5 **a** The Return loss of −29 dB at Resonant Frequency 4.63 GHz for a simple microstrip patch antenna without SRR. **b** First Return loss of −26 dB at 4 GHz and Second return loss at −17 dB at 4.6 GHz for Microstrip patch antenna with eight SRR

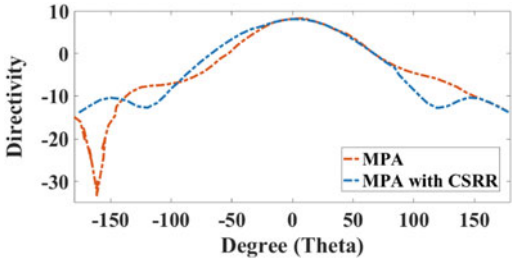

Fig. 6 Gain value of normal MPA is 8.1895 dB and 8.3403 dB for MPA with CSRR

4 Fabrication and Measurement

To verify the proposed design measurement of the fabricated model has been done. Fabrication of metamaterial property-based patch antenna is presented. The back view of fabricated geometry with a coaxial probe has been presented in Fig. 9. Reflectance response has been measured with the help of a vector network analyzer is shown in Fig. 10. Measured results show a good agreement with the simulated one.

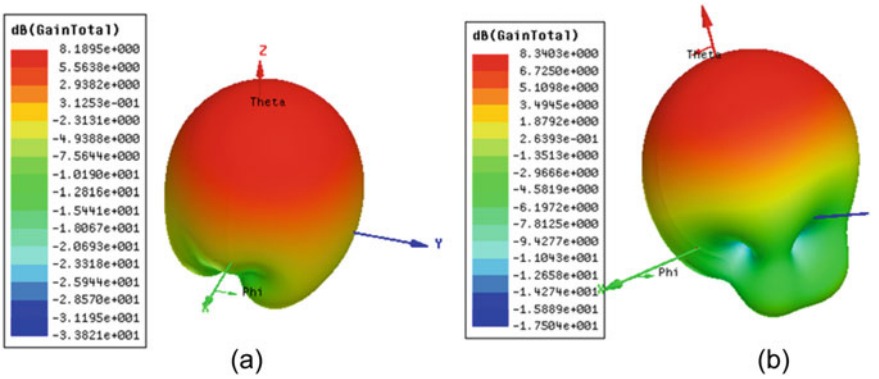

Fig. 7 Three-dimensional gain plot of the normal Microstrip patch antenna and another using eight CSRR. **a** 8.1895 dB gain for normal Patch antenna. **b** 8.3403 dB gain for Patch antenna with CSRR

Table 1 Comparison of various models

Sr. No.	Model name	S11 (dB)	Resonant frequency (GHz)	VSWR	Gain (dB)
1	Without SRR	−29	4.63	1.08	8.18
2	One SRR	−28	4.58	1.12	8.19
3	Two SRR	−28	4.23	1.14	8.21
4	Three SRR	−27	4.23	1.17	8.25
5	Eight SRR	−26	4.00	1.19	8.34

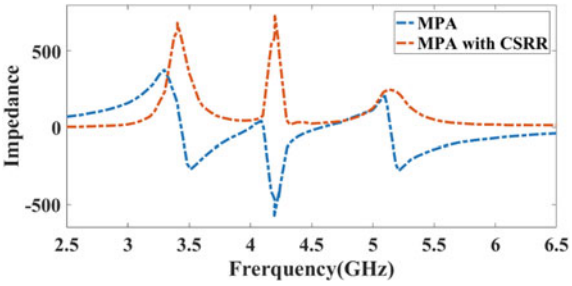

Fig. 8 Real and imaginary components of the simulated patch antenna with CSRR

5 Conclusion

The novel microstrip patch antenna with diffracted ground antenna is proposed using a split-Ring Resonator in the ground layer. Design is numerically investigated and different parameters like reflectance response, voltage standing wave ratio, gain, and resonance frequency are compared for the different numbers of CSRR. It has been observed that by adding split-ring resonators the gain is improved and broadband behavior is achieved. The design provides the minimum reflectance response

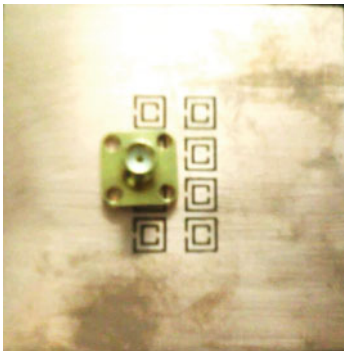

Fig. 9 Top view of fabricated microstrip patch antenna with eight split-ring resonators

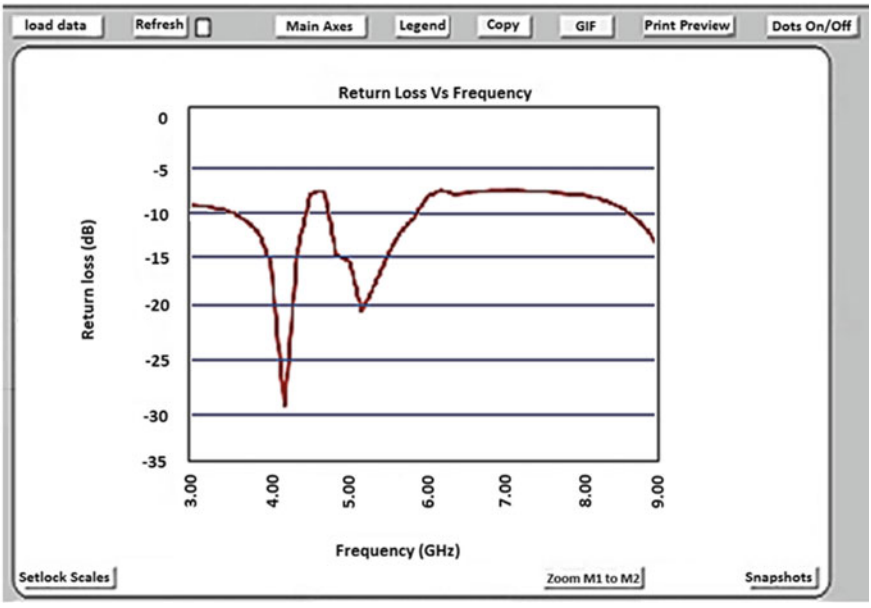

Fig. 10 Vector network analyzer represents −28 dB return loss at 4.05 GHz for CSRR based microstrip patch antenna

of −29 dB. The maximum gain of 8.34 dB is achieved by adding eight split-ring resonators is achieved for eight split-ring resonators. Physical designing of microstrip patch antenna with eight split-ring resonators has been done and results are observed by using a vector network analyzer. The proposed design is used for satellite communication and Wi-Fi devices.

References

1. Asaadi, M., Afifi, I., Sebak, A.R.: High gain and wideband high dense dielectric patch antenna using FSS superstrate for millimeter-wave applications. IEEE Access **6**, 38243–38250 (2018). https://doi.org/10.1109/ACCESS.2018.2854225
2. Lavadiya, S.P., Patel, S.K., Rayisyan, M.: High gain and frequency reconfigurable copper and liquid metamaterial tooth based microstrip patch antenna. AEU—Int. J. Electron. Commun. **137**, 153799 (2021). https://doi.org/10.1016/j.aeue.2021.153799
3. Sumathi, K., Lavadiya, S., Yin, P.Z., Parmar, J., Patel, S.K.: High gain multiband and frequency reconfigurable metamaterial superstrate microstrip patch antenna for C/X/Ku-band wireless network applications. Wirel. Networks **27**(3), 2131–2146 (2021). https://doi.org/10.1007/s11276-021-02567-5
4. Aydin, K., Bulu, I., Guven, K., Kafesaki, M., Soukoulis, C.M., Ozbay, E.: Investigation of magnetic resonances for different split-ring resonator parameters and designs. New J. Phys. **7**(1), 168 (2005). https://doi.org/10.1088/1367-2630/7/1/168
5. Li, L.W., Li, Y.N., Yeo, T.S., Mosig, J.R., Martin, O.J.F.: A broadband and high-gain metamaterial microstrip antenna. Appl. Phys. Lett. **96**(16), 3–5 (2010). https://doi.org/10.1063/1.3396984
6. Lavadiya, S.P., et al.: Design and verification of novel low-profile miniaturized pattern and frequency tunable microstrip patch antenna using two PIN diodes. Brazilian J. Phys. (Aug. 2021). https://doi.org/10.1007/s13538-021-00951-2
7. Wong, K.-L.: Compact and Broadband Microstrip Antennas. (2002)
8. Zhou, H., et al.: A novel high-directivity microstrip patch antenna based on zero-index metamaterial. IEEE Antennas Wirel. Propag. Lett. **8**, 538–541 (2009). https://doi.org/10.1109/LAWP.2009.2018710
9. Jaydeep, S., Sunil, L.: An investigation on recent trends in metamaterial types and its applications. i-manager's J. Mater. Sci. **5**(4), 55 (2018). https://doi.org/10.26634/jms.5.4.13974
10. Wevers, J.W.: Chapter 14. (2019)
11. Patel, S.K., Lavadiya, S., Kosta, Y.P., Kosta, M., Nguyen, T.K., Dhasarathan, V.: Numerical investigation of liquid metamaterial-based superstrate microstrip radiating structure. Phys. B Condens. Matter **585**, 412095 (2020). https://doi.org/10.1016/j.physb.2020.412095
12. Roy, S., Chakraborty, U.: Metamaterial based dual wideband wearable antenna for wireless applications. Wirel. Pers. Commun. **106**(3), 1117–1133 (2019). https://doi.org/10.1007/s11277-019-06206-3
13. Vidhi, P., Ramesh, J.D., Sunil, L.: New approach of high power testing of spacecraft passive components using diplexer. i-manager's J. Commun. Eng. Syst. **9**(1), 1 (2020). https://doi.org/10.26634/jcs.9.1.17395
14. Jain, K., Gupta, K.: Different substrates use in microstrip patch antenna-A survey. (2014). Accessed: Feb. 27, 2021. [Online]. Available: https://www.ijsr.net/archive/v3i5/MDIwMTMyMTQw.pdf
15. Yilmaz, H.O., Yaman, F.: Metamaterial antenna designs for a 5.8-GHz doppler radar. IEEE Trans. Instrum. Meas. **69**(4), 1775–1782 (2020). https://doi.org/10.1109/TIM.2019.2914131

A Novel Hybrid DNA Cryptographic System Using Symmetric Algorithm and Dynamic DNA Sequence Generator

Animesh Hazra and Ishani Roy

Abstract By the end of the twentieth century, an innovative technique for securing data was introduced called DNA Cryptography setting a new horizon in the security domain based on the concepts of DNA computing. In this paper, an enhanced version of the Blowfish algorithm combined with the Base64 encoding system and dynamic DNA sequence generator is proposed. Blowfish's versatile usability along with the incorporation of the Sequence generator's dynamicity introduces randomness in the whole security system making it intrusion-free. The proposed system's lower computation time and less complicated approach make it almost an ideal procedure for incorporating in security fields.

Keywords Base64 · Blowfish · DNA · Dynamic · OTP · Sequence generator

1 Introduction

In the field of cryptography, apart from the implementation of various symmetric algorithms, cryptographers realized the requirement of building asymmetric algorithms. Asymmetric algorithms are believed to be secure than most symmetric algorithms but in the case of speed, they are much slower. As conclusion, it can be said that cryptographers are constantly working on inventing new techniques. In the year 1994 Leonard Max Adleman one of the persons behind the invention of the RSA algorithm [1] invented the foundation concepts of DNA Cryptography. Since then, this technique is considered very promising in the domain of security for its numerous attractive features. So, in this paper, an innovative and simple cryptographic system has been proposed. The suggested system is unique because no matter how much security other systems can provide, only a very few numbers of them can be able to

A. Hazra
Jalpaiguri Government Engineering College, Jalpaiguri, West Bengal, India
e-mail: animesh.hazra@cse.jgec.ac.in

I. Roy (✉)
Cooch Behar Government Engineering College, Cooch Behar, West Bengal, India

B. Sikdar et al. (eds.), *Proceedings of the 3rd International Conference on Communication, Devices and Computing*, Lecture Notes in Electrical Engineering 851,
https://doi.org/10.1007/978-981-16-9154-6_39

do that in a very less time-consuming manner. It is needless to say in the case of a double layer security system, robustness will be provided very well. Blowfish is an algorithm which is known for its strong security incorporation power and with this, our special dynamic sequence generator makes the message decryption work for any intruder impossible. Last but not least this security system is able to deliver another added advantage that can be seen in very few cryptographic systems, convenient to use. Not all security systems are able to come up with such praiseworthy qualities all encapsulated together in a single system. At the end of the paper, in the security analysis of the proposed algorithm section, a brief analysis of its performance is presented. Before proceeding to the discussion of the proposed method, in the technical background section, a thorough review of the used techniques is done in a systematic manner.

2 Technical Background

The encryption mechanisms are mainly divided into two categories that are symmetric algorithm and asymmetric algorithm [2]. Symmetric algorithms use an identical key for encryption and decryption purposes whereas asymmetric algorithms use different keys for encryption and decryption purposes (public key for the encryption at sender end and private key for the decryption at the receiver end). All the basic concepts on which the proposed algorithm depends on are discussed below in detail as follows.

2.1 Blowfish Algorithm

It is one of the famous symmetric algorithms [3] invented by Bruce Schneier and block cipher as well as a Feistel cipher of 16 rounds. Unlike other algorithms, it has a variable key size ranging from 32 to 448 bits. It works on a 64-bit block size. The algorithm works in two stages. In the first stage, from the key bits, several sub-keys are generated. P-arrays consist of 18 entries each, having 32-bit sub-keys and four 32-bit S-boxes having 256 entries each, are initialized with a fixed string of hexadecimal digits of pi (mathematical constant π). After initialization, p1 is bitwise XOR-ed with the first 32 key bits, p2 is bitwise XOR-ed with the second 32 key bits and so on until all the key bits are XOR-ed successfully (possible up to p14). For p15 to p18, first to fourth key bits are reused for bitwise XOR operation. Next, the sub-keys (p-arrays and S-boxes are referred to as sub-keys) are used on a 64-bit block initialized with every bit value 0 to run the Blowfish encryption process. The resultant 64 bit is halved and each 32-bit replaces the prior 32-bit values of p1 and p2 respectively. The resultant values are again encrypted with modified sub-keys. Now, the resulting 64 bit is halved and replaces the prior values of p3 and p4 respectively. In this fashion up to p18 and after p-arrays, all previous values of S-boxes are changed.

2.2 Base64 Encoding Scheme

Base64 is prevalent among many binaries to text encoding schemes in the cyber world. Here, binary data is converted into ASCII string format. A specific MIME (Multipurpose Internet Mail Extension) content transfer encoding is the origin of the term "Base64". It translates the binary data into a radix 64 representation. Each Base64 digit represents the 6-bit binary data. It is used to embed binary data like image files into text formats like HTML and CSS files.

2.3 One-Time Pad (OTP)

One-time pad, also known as Vernam cipher or the perfect cipher is one of the renowned cryptographic methods where a random secret key (referred to as one-time pad) of at least the same size or longer in length than the message to be sent is generated. Once generated key cannot be reused. The plaintext is paired by having bitwise or character-wise modular operation to the corresponding each bit or character of the generated key. There are only two copies of the generated key, one for the sender and another for the receiver. It can be presented with the help of a simple equation as follows:

$$C_p = B_p \odot O_p (p = 0, 1, 2, 4 \cdots n). \tag{1}$$

Here, C_p is the resultant ciphertext, B_p is the bitwise binary value, O_p is the bitwise one-time pad (OTP) value, and $\odot$ is the XNOR operation. Infinite time as well as infinite computations cannot break this encryption mechanism, as it is mathematically impossible.

2.4 DNA Computing

It is a branch of computing that uses DNA molecules, biochemistry, and other biological background-based hardware. Leonard Adleman in 1994 invented the DNA computing concept [4]. From that time this approach has been implemented in various applications, i.e., developing GPS systems, recognition systems combined with artificial intelligence (AI), etc. Therefore, it can be concluded that DNA is well suited for data processing. Some of its numerous features are listed below as follows:

(a) 1 g DNA can hold 10^8 TB of data.
(b) As specified by Adleman DNA strand combined computations made the calculations speed far better than the fastest computers (nearly 100 times faster).
(c) There is no requirement of external power sources as chemical bonds are the basis of DNA formation.

DNA molecules process different types of combinations at once and as a result, developing various characteristics from it is the basic point of its parallel form of computing.

3 Literature Survey

It is recommended to discuss about some previously suggested security systems by other authors to develop a concept regarding the presented work approach as well as the pros and cons of those suggested methodologies which is also shown in Table 4.

Raj et al. [5] developed an innovative DNA cryptographic procedure based on a symmetric algorithm where the input plain text is converted into ASCII values followed by binary values and then DNA base sequences. A modular cyclic operation is done using that private key on them producing the final encrypted text. Shanmugasundaram et al. [6] introduced a new DNA encryption procedure based on cellular automata where input plain text is converted into DNA base sequences followed by binary bitstream generation. Hassan Al-Mahdi et al. [7] developed a unique DNA security system. The input plain text is converted into ASCII values followed by binary bits. Finally, binary groups are converted to hexadecimal values to represent the final ciphertext. In the paper of Kamaraj et al. [8], the authors developed a DNA cryptographic algorithm based on the FPGA and Vigenere cipher concept. The input plain text is given through FPGA to convert the text into triplet codons as per the table recommended by the authors. Finally, the codons are encrypted by XOR operation with generated key followed by Vigenere cipher.

4 Proposed Methodology

An ideal security system consists of three major constituents, i.e., speed, security, and key generation. To ensure security it is recommended to work on versatile key generations. To increase feasibility, the whole security system should respond quickly. To overcome the shortcomings mentioned earlier in the literature survey section, in this paper Blowfish algorithm has been implemented to introduce a more convenient way than the past security schemes along with a unique dynamic sequence generator to create randomness in the entire system. This enhanced, highly secured, and ideal procedure is discussed in depth further below.

4.1 Proposed Encryption Procedure

Step 1. A plain text (P) is taken as input.

Step 2. The text is encoded using the Blowfish algorithm in CFB (Cipher Feed-Back) mode. In this mode, each ciphertext block gets fed back into the encryption process in order to encrypt the next plain text block.
Step 3. The encrypted text (C_k) is now encoded using the Base64 encoding scheme which is discussed earlier in sub-Sect. 2.2.
Step 4. Now, the encoded string obtained previously is converted to ASCII values.
Step 5. Each digit of the ASCII value string obtained is now transformed into 4-bit binary values.
Step 6. Now, a complement operation on each bit of binary bitstream is made.
Step 7. Complemented binary bitstream obtained in the previous step is now converted to hexadecimal values.
Step 8. Each hexadecimal value produces different DNA base sequences from the list at a different time as recommended in the sequence generator table illustrated in Table 1. Suppose, the hexadecimal digit is 6, then the sequencer can generate CATA or CATG or any other base sequences for the value 6 shown in Table 1.
Step 9. At present, the DNA base sequences are converted to binary bitstreams (B_p) as per the scheme described in Table 2 as follows.
Step 10. Now, the previously obtained binary bit stream is XNOR-ed with another random generated binary bit stream of same length (O_p) or OTP.
Step 11. The resultant binary bit stream (C_p) is finally converted into the DNA base sequences (cipher-text) as per the scheme described in Table 2.

4.2 Flowchart of Proposed Algorithm

To make the whole decryption procedure handy, it can be easily done only in reverse order. In Fig. 1 below, a flowchart of encryption as well as decryption procedure is presented in detail.

5 Discussion

The setup requirements as well as the security analysis of the algorithm proposed are illustrated below in detail.

5.1 Specifications of Computing Processor and Software Used

The proposed security system is built using the Python 3.7 programming language on Spyder 3.3.2 IDE. The device used for developing this security scheme consists of an Intel Core i5 7th Generation processor with 2.71 GHz speed, 1 TB of Hard

Table 1 Illustration of the hexadecimal digit to random DNA base sequence generation

Hexadecimal digit	Possible 16 DNA sequences corresponding to each hexadecimal digit							
0	GCTA GCCA	GCAA GCGA	GCTT GCCT	GCAT GCGT	GCTC GCCC	GCAC GCGC	GCTG GCCG	GCAG GCGG
1	CGTA CGCA	CGAA CGGA	CGTT CGCT	CGAT CGGT	CGTC CGCC	CGAC CGGC	CGTG CGCG	CGAG CGGG
2	AGAA AGGA	AATA AACA	AGAT AGGT	AATT AACT	AGAC AGGC	AATC AACC	AGAG AGGG	AATG AACG
3	GATA GACA	TGTA TGCA	GATT GACT	TGTT TGCT	GATC GACC	TGTC TGCC	GATG GACG	TGTG TGCG
4	CAAA CAGA	GAAA GAGA	CAAT CAGT	GAAT GAGT	CAAC CAGC	GAAC GAGC	CAAG CAGG	GAAG GAGG
5	GGTA GGCA	GGAA GGGA	GGTT GGCT	GGAT GGGT	GGTC GGCC	GGAC GGGC	GGTG GGCG	GGAG GGGG
6	CATA CACA	ATTA ATCA	CATT CACT	ATTT ATCT	CATC CACC	ATTC ATCC	CATG CACG	ATTG ATCG
7	ATAA ATGA	TTAA TTGA	ATAT ATGT	TTAT TTGT	ATAC ATGC	TTAC TTGC	ATAG ATGG	TTAG TTGG
8	CTTA CTCA	CTAA CTGA	CTTT CTCT	CTAT CTGT	CTTC CTCC	CTAC CTGC	CTTG CTCG	CTAG CTGG
9	AAAA AAGA	ATGA TTTA	AAAT AAGT	ATGT TTTT	AAAC AAGC	ATGC TTTC	AAAG AAGG	ATGG TTTG
a	TTCA CCTA	CCCA CCAA	TTCT CCTT	CCCT CCAT	TTCC CCTC	CCCC CCAC	TTCG CCTG	CCCG CCAG
b	CCGA TCTA	TCCA TCAA	CCGT TCTT	TCCT TCAT	CCGC TCTC	TCCC TCAC	CCGG TCTG	TCCG TCAG
c	TCGA AGTA	AGCA ACTA	TCGT AGTT	AGCT ACTT	TCGC AGTC	AGCC ACTC	TCGG AGTG	AGCG ACTG
d	ACCA ACAA	ACGA TGGA	ACCT ACAT	ACGT TGGT	ACCC ACAC	ACGC TGGC	ACCG ACAG	ACGG TGGG
e	TATA TACA	GTTA GTCA	TATT TACT	GTTT GTCT	TATC TACC	GTTC GTCC	TATG TACG	GTTG GTCG
f	GTAA GTGA	TAAA TGAA	GTAT GTGT	TAAT TGAT	GTAC GTGC	TAAC TGAC	GTAG GTGG	TAAG TGAG

Table 2 DNA base to binary bit conversion scheme

DNA base	Binary value
A	00
T	01
C	10
G	11

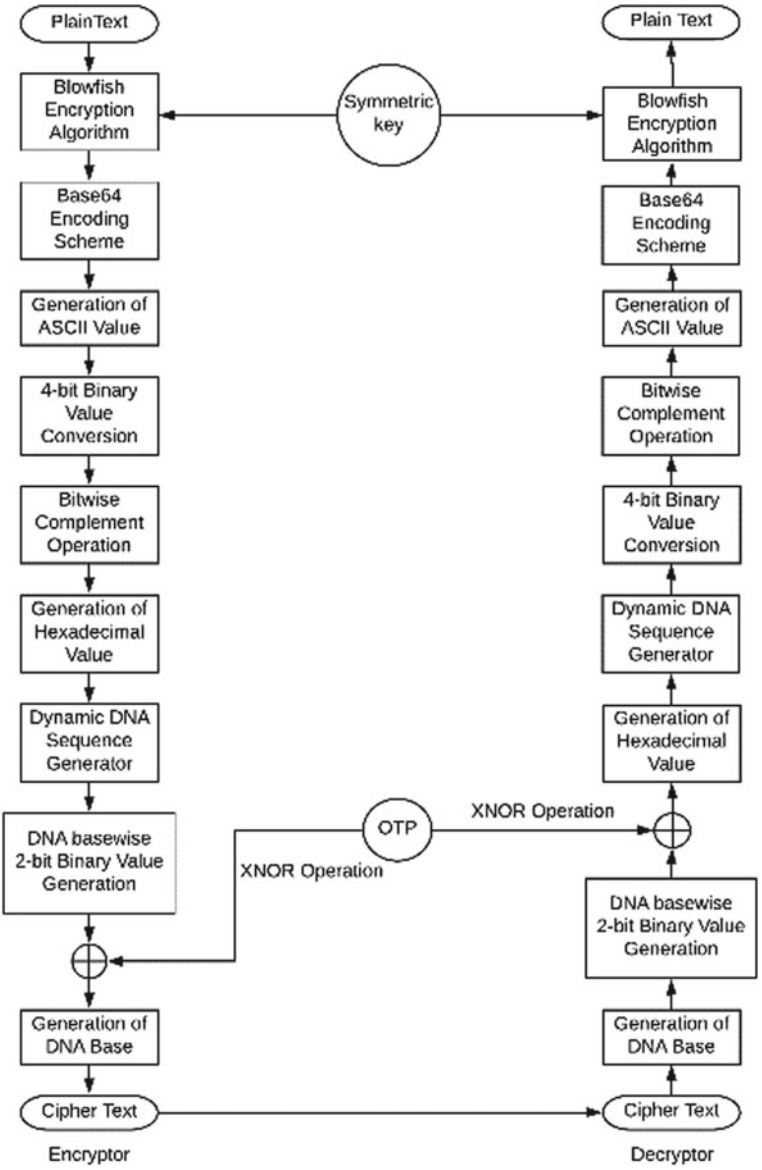

Fig. 1 Flowchart of the proposed encryption and decryption procedure

Disk Drive, and 8 GB RAM. The entire development was done on the Windows 10 (64-bit) Professional platform.

5.2 Security Analysis of the Proposed Algorithm

On examining the proposed methodology, complexities of the suggested algorithm as well as some salient security features are presented in this section as follows.

(a) Double layer security is incorporated in the presented algorithm. Plain text is encrypted using two keys, i.e., first time by symmetric key and the second time by a one-time pad.
(b) The time complexity of every step of the algorithm along with the proposed method is explained and shown in Table 3 where n is the length of the input string.
(c) Longer key length (up to 448 bits) in the Blowfish encryption procedure ensures stronger security but increases the computational complexity. It is the users choice so that they can generate how much longer the key length they want to use as per their requirements. Enabling users to generate different lengths of keys makes the entire algorithm highly flexible.
(d) One-time pad generation of n-bit long string has $O(2^n)$ computational complexity. Suppose there is an OTP, which is 4-bit long. To guess the correct OTP, at first 16 OTPs (0000, 0001, 0010, 0011, 0100, 0101, 0110, 0111, 1000, 1001, 1010, 1011, 1100, 1101, 1110, 1111) needs to be generated, and then only they can be applied one by one to evaluate the correct one. With increasing the length of OTP, it becomes more difficult to assume the correct bit sequence without having any prior knowledge. Therefore, it is extremely difficult for cryptanalysts as well as supercomputers to successfully break the correct OTP.
(e) In this proposed algorithm, a dynamic DNA sequence generator incorporates another degree of security. For one hexadecimal value, there are 16 possible values available. Suppose four hexadecimal digits are taken, then the total possibility of DNA sequence generation is $16 \times 16 \times 16 \times 16$, i.e., 16^4. Therefore, if n digits are taken, then the total number of permutations will be 16^n. So, the overall permutation complexity will be $O(16^n)$, i.e., $O(2^{4n})$. It is an exponential time complexity algorithm and for a modest value of n it produces a huge value. Hence, we can say that the algorithm proposed here is highly secured and almost impossible to crack for the intruder.

5.3 Comparative Study

In this section, a comparative study is done based on the advantages and disadvantages of various encryption and decryption systems suggested by the researchers [9] Table 4.

Table 3 Time complexity evaluation of each step of the proposed algorithm

Name of the algorithm	Step no.	Steps of the proposed algorithm	Time Complexity of the associated step	The overall time complexity of the algorithm
Proposed encryption procedure	1	Blowfish encryption	O(n)	**O(n)**
	2	Base64 encoding	O(n)	
	3	Base64 to ASCII conversion	O(n)	
	4	ASCII to binary conversion	O(log n)	
	5	Complement operation	O(n)	
	6	The complement to hexadecimal conversion	O(n)	
	7	Dynamic DNA sequence generation	O(n)	
	8	OTP generation	O(n)	
	9	XNOR operation	O(n)	
	10	DNA base generation	O(n)	
Proposed decryption procedure	1	DNA base to 2-bit binary value generation	O(n)	**O(n)**
	2	XNOR operation	O(n)	
	3	Dynamic DNA sequence generation	O(n)	
	4	DNA sequence to hexadecimal conversion	O(n)	
	5	Hexadecimal to binary value conversion	O(n)	
	6	Complement operation	O(n)	
	7	Binary to ASCII value conversion	O(log n)	
	8	ASCII to Base64 encoding	O(n)	
	9	Base64 decoding	O(n)	
	10	Blowfish decryption	O(n)	

Table 4 Summary of some existing cryptographic techniques with the proposed methodology

Serial No.	Authors	Used methods	Advantages	Disadvantages
1	Babu et al. [10]	(a) Variable random length key (b) XOR operation	(a) Less storage space needed (b) Improved energy efficiency	(a) Distribution of key is really hectic
2	Kamaraj et al. [8]	(a) Vignere cipher (b) XOR operation	(a) Double layered security	(a) Security is too much dependent on the private key
3	Biswas et al. [11]	(a) Generation of the dynamic sequence table (b) RSA, ElGamal, and Paillier asymmetric encryption and decryption systems used	(a) Triple-layered security (b) Generation of the dynamic sequence table is mathematically impossible for the intruder	(a) Introducing different asymmetric cryptosystems increase the time complexity
4	Akkasaligar and Biradar [12]	(a) Pixel selection algorithm (b) Conversion to DNA encoded matrix as per the DNA base encoding rules	(a) Less time complexity (b) The security key is vast enough to resist the exhaustive attack	(a) Complex enough to implement in reality
5	Rahman et al. [13]	(a) Intron sequence generation (b) XNOR operation (c) Matrix manipulation	(a) Different cipher text is generated in each session (b) Can be adapted to the digital computing environment	(a) Requires to establish mutual authentication (b) Each time new encoding table generation is very hectic
6	Proposed Methodology	(a) Symmetric key (b) Dynamic DNA sequencer (c) XNOR operation	(a) Double layered security (b) User friendly for providing the scope of changing security key length according to user preference (c) Impossible to crack for its unique random nature	(a) Consumes more memory space in spite of small plain text

6 Conclusion and Future Scope

In this paper, one methodology is recommended where symmetric key exchange, OTP scheme, and dynamic DNA sequence generator give birth to a distinct hybrid cryptographic system. Cryptanalysts are unable to decipher the Blowfish encryption

procedure until date. Dynamic DNA sequencer makes the whole system so random that it is impossible for the intruder to break the cipher text without prior knowledge. Changing the key length in the Blowfish encryption algorithm as per the security requirements of the user as well as less complicated methods make this algorithm convenient to use in overall. By analyzing the whole encryption and decryption procedure, it can be concluded that it is theoretically as well as practically impossible to decrypt the cipher text hence ensuring the highest security possible in reality. In near future, implementing this algorithm in different applications and analyzing its complexity as well as feasibility is the utmost objective. Developing the proposed methodology accordingly on different mediums of data is another important agenda in the future. In case of smaller plain texts, the suggested algorithm generates much longer cipher texts that can be a setback in case of storage space utilization. Overcoming this hitch can also be considered as another future work for the existing methodology.

References

1. Pandey, M.K.: Implementation of DNA cryptosystem using hybrid approach. Res. J. Comput. Inf. Technol. Sci. **6**, 1–7 (2018)
2. Kahate, A.: Cryptography and Network Security, 3rd edn. New Delhi (2016)
3. Vadaviya, D.O., Tandel, P.H.: Secure encryption techniques using DNA computation. Int. J. Mod. Trends Eng. Res. **2**, 176–182 (2015)
4. Adleman, L.M.: Molecular computation of solutions to combinatorial problems. Science **266**, 1021–1024 (1994)
5. Raj, B.B., Vijay, J.F., Mahalakshmi, T.: Secure data transfer through DNA cryptography using symmetric algorithm. Int. J. Comput. Appl. **133**, 19–23 (2016)
6. Shanmugasundaram, G., Thiyagarajan, P., Pavithra, S.: A novel DNA encryption system using cellular automata. Int. J. Secur., Priv. Trust Manage. **4**, 39–49 (2015)
7. Al-Mahdi, H., Shahin, O.R., Fouad, Y., Alkhaldi, K.: Design and analysis of DNA binary cryptography algorithm for plaintext. Int. J. Eng. Technol. **10**, 699–706 (2018)
8. Kamaraj, A., Bhrintha, A.P., Bhavithara, M.: DNA-based encryption and decryption using FPGA. Int. J. Curr. Res. Mod. Educ. 89–94 (2016)
9. Hazra, A., Ghosh, S., Jash, S.: A review on DNA based cryptographic techniques. Int. J. Netw. Secur. **20**, 1093–1104 (2018)
10. Babu, E.S., Raju, C.N., Prasad, M.HM.K.: Inspired pseudo biotic DNA based cryptographic mechanism against adaptive cryptographic attacks. Int. J. Netw. Secur. **18**, 291–303 (2016)
11. Biswas, M.R., Alam, K.M.R., Tamura, S., Morimoto, Y.: A technique for DNA cryptography based on dynamic mechanisms. J. Inf. Sec. Appl. **48**, 1–8 (2019)
12. Akkasaligar, P.T., Biradar, S.: Selective medical image encryption using DNA cryptography. Inf. Secur. J.: Glob. Perspect. **29**, 91–101 (2020)
13. Rahman, N.H.U., Balamurugan, C., Mariappan, R.: A novel DNA computing based encryption and decryption algorithm. Int. Conf. Inf. Commun. Technol. **46**, 463–475 (2015)

High Gain 3-D Printed 2 × 2 Trapezoidal Planar Antenna Array for X-band Wireless Applications

Ashraf E. Ahmed, Wael A. E. Ali, and Sudipta Das

Abstract In this work, a high gain 3-D printed 2 × 2 trapezoidal planar antenna array is designed for RF systems. An innovative manner for printing the substrate using PLA dielectric material is implemented. The designed planar antenna array consists of four trapezoidal antenna elements combined with a modified Wilkinson power divider network on the top layer of substrate with an overall size of 52.28 × 55.21 × 3 mm^3, and all parts of the antenna are fixed by screw nails. The planar array simulated results such as S_{11} is reached −15.54 dB at 10 GHz and a gain of 11.35 dBi is obtained at the achieved band which makes the suggested array suitable for various X-band wireless applications. Modeling and simulation of the proposed planar array are performed by Ansoft High Frequency Structure Simulator (HFSS 13).

Keywords 3-D printing · PLA · Trapezoidal · Planar antenna array

1 Introduction

Usually, the planar antenna array systems are used in the design of radar and satellite wireless applications to achieve high gain, narrow beamwidth, and multi-band operations. The traditional fabrication method for antenna array structure is

A. E. Ahmed
Department of Electronics and Communication Engineering, Higher Institute of Engineering and Technology, King Marriott, Alexandria, Egypt

W. A. E. Ali
Department of Electronics and Communication Engineering, College of Engineering and Technology, Arab Academy for Science, Technology and Maritime Transport (AASTMT), Alexandria, Egypt
e-mail: wael.ali@aast.edu

S. Das (✉)
Department of Electronics and Communication Engineering, IMPS College of Engineering and Technology, Malda, West Bengal, India

B. Sikdar et al. (eds.), *Proceedings of the 3rd International Conference on Communication, Devices and Computing*, Lecture Notes in Electrical Engineering 851,
https://doi.org/10.1007/978-981-16-9154-6_40

usually complex, and it needs high-cost, non-smaller weight and profile with high-temperature welding that causes a loss in the substrate material [1]. The individual antennas in a planar antenna array system are usually connected to a single receiver or transmitter by different feed lines that feed the power by a specific phase relationship. The radio waves radiated by each antenna are combined together to enhance the power radiated in desired directions, and to suppress the power radiated in other directions [2]. A 3-D printing, or additive manufacturing, is the construction of a three-dimensional object from a digital 3-D model. The term "3D printing" can refer to a variety of processes in which material is deposited, joined, or solidified under computer control to create a 3-D object, with the material being added together (such as plastics, liquids or powder grains being fused together), typically layer by layer. In the 1980s, 3-D printing techniques were considered suitable only for the production of functional prototypes, and a more appropriate term for it at the time was rapid prototyping. As of 2019, the accuracy, repeatability, and material range of 3-D printing have increased to the point that some 3-D printing processes are considered applicable as an industrial production technology, whereby the term additive manufacturing can be used suitably with 3-D printing. One of the key advantages of 3-D printing is the ability to produce very complex shapes or geometries that would be otherwise impossible to construct by hand, including hollow parts structures to reduce weight and profile. Fused deposition modeling (FDM), which uses a continuous string of a thermoplastic material like PLA, is the most common 3-D printing process in use [3, 4]. The advantages of using the 3D printing structure are controlling of the entire compact size of the substrate with less shape, profile and low cost.

A 3-D printed 2 × 2 antenna array is used to achieve the main aims as the high gain and directivity desired for radiation pattern which cannot be achieved by a single element [5–12]. In this paper, we used a trapezoidal planar antenna array connected together with a Wilkinson network power divider to improve the overall performance. The patch antenna and ground plane are made from red copper with a thickness of 1 mm, and the dielectric part is printed by 3DP machine using PLA thermoplastic material of thickness 1 mm to enhance the gain and performance of antenna array [13, 14], then all parts are fixed by PLA screw nails using holes to adjust resonant frequency accurately. This search is arranged as follows: In part II, design and fabrication procedures based on 3-D printing technique for substrate part of the antenna array. In part III, the simulation results of the 3-D printed antenna array system are presented. In part IV, the conclusion is presented.

2 Design and Fabrication Procedure

The 3-D printed 2 × 2 trapezoidal planar array antenna operates at 10 GHz, fed through an SMA connector which is welded to input feeding T. L. (transmission line) which is united with the Wilkinson power divider network. The 3DP antenna array consisting of four trapezoidal antenna elements is connected with the multiple

Wilkinson power divider and the substrate is made from PLA material with relative permittivity 3.1 and loss tangent 0.001 [15, 16] to achieve a high gain performance.

2.1 Trapezoidal Antenna Element

A trapezoidal antenna is used to achieve the desired operation in the X-band. As shown in Fig. 1, it can be observed that the trapezoidal antenna achieved the value of reflection coefficient S_{11} of −21.67 dB at 10.1 GHz [17]. The parametric analysis for trapezoidal antenna element with and without stub discussed in ref. [17].

2.2 First Wilkinson Power Divider Network

The power divider as shown in Fig. 2 consists of a standard Wilkinson power divider made of a copper patch and ground plane with a thickness of 1 mm, the divider split the input power by equal halves, and it is confirmed from the S-parameters results in Fig. 2 that the S_{21} and S_{31} are at the same level of approximately −3 dB over the achieved band (1 GHz −12 GHz) and S_{11} is −13.23 dB at 10 GHz.

2.3 Second Wilkinson Power Divider Network

As shown in Fig. 3, the Wilkinson power divider network was designed to divide the input power to equal four portions and to feed the trapezoidal planar array with one input feeding. It can be noticed from Fig. 3 that the input power is equally divided to the four ports with the same level of insertion loss and S_{11} is −14.22 dB at 10 GHz.

3 Simulation Results of the 3-D Printed 2 × 2 Trapezoidal Planar Antenna Array

A 3DP 2 × 2 trapezoidal planar antenna array consists of four trapezoidal antenna elements united with the final Wilkinson power divider and the simulated S_{11} results are shown in Fig. 4. The simulations are carried out using (HFSS) software v.13 with a patch and ground plane of thickness 1 mm which are made from red copper and substrate from PLA of 1 mm thickness. The four outputs of the final Wilkinson network power divider connected to four different lengths of T. L as 6, 9.75, 13.5, 17.27 mm before the input of antenna elements to change the phase of the RF signal.

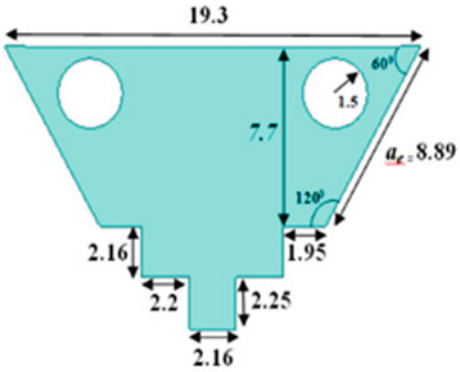

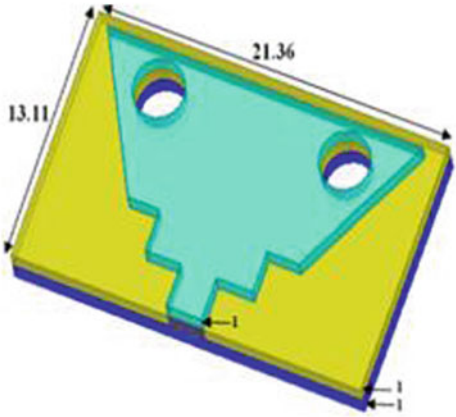

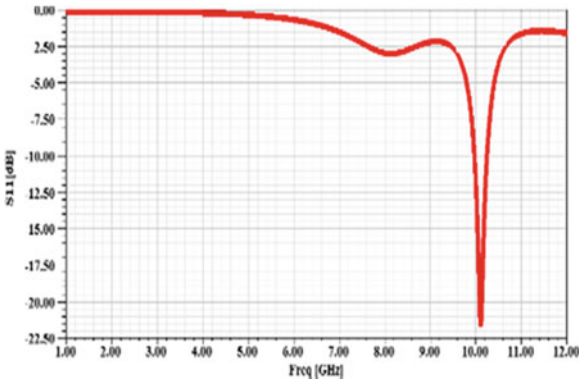

Fig. 1 The 2D, 3D views and simulated S_{11} result of trapezoidal antenna element (all dimensions in mm)

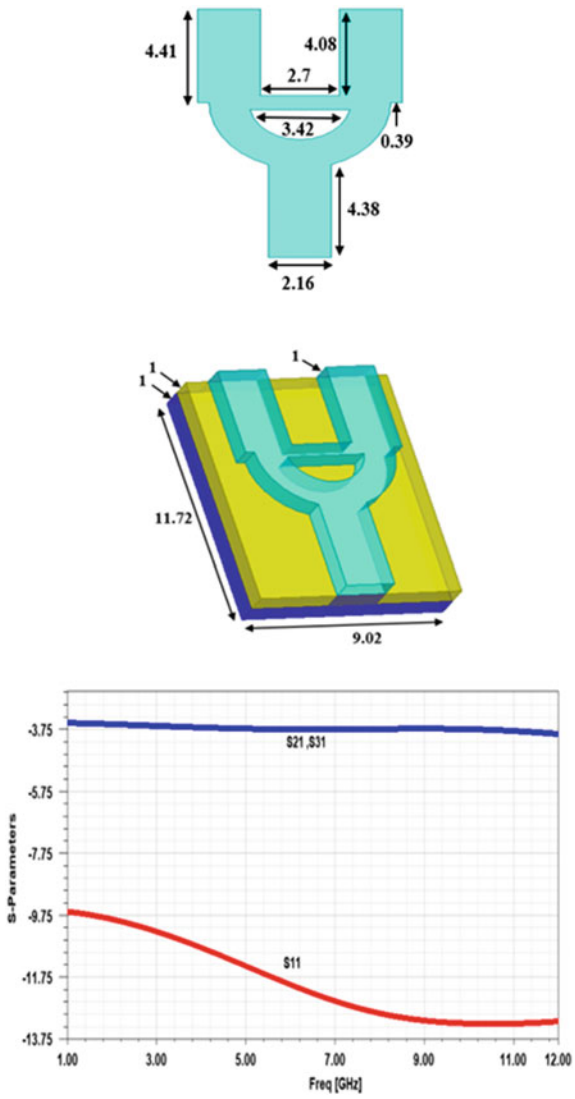

Fig. 2 The 2-D, 3-D views, simulated S-parameters result for 1st Wilkinson power divider

The simulation result is indicated in Fig. 4, and it can be demonstrated that the proposed 3DP trapezoidal planar antenna array achieved S_{11} with various levels of −10.08, −17.86, −33.09, −16.97, −22.18 dB at 4.8, 6.6, 8.9, 10, 11.04 GHz, respectively. The multiband behavior of the proposed planar array antenna makes it suitable for X-band wireless applications [18]. The final proposed array design can also operate in five multiband frequencies.

Figure 5 depicts a uniform current distribution for the proposed array antenna at X-band and introduces a uniform medium surface current density at four trapezoidal

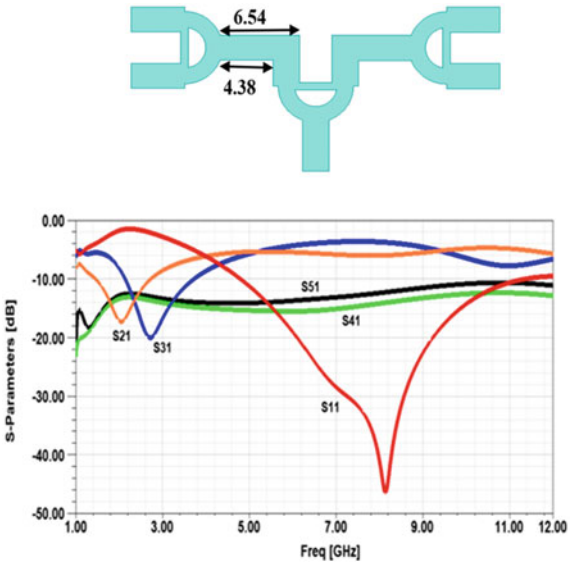

Fig. 3 The 2-D view, simulated S-parameters result for 2nd Wilkinson network power divider

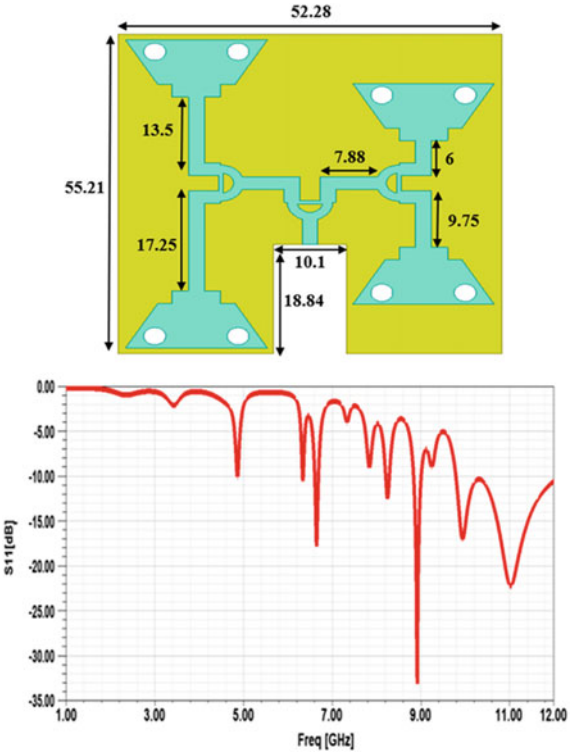

Fig. 4 The 2-D view, simulated S_{11} parameter result for final 3DP 2 × 2 trapezoidal planar antenna array

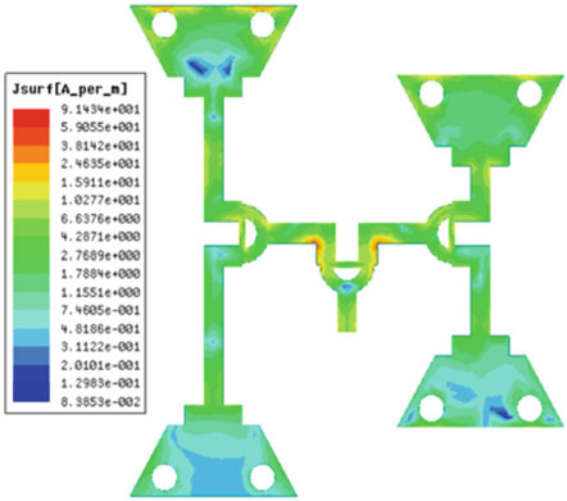

Fig. 5 Current density for final 3DP 2 × 2 Trapezoidal planar antenna array at 10 GHz

antenna elements and high distribution at arms of Wilkinson power divider. Figure 6 indicates the 3D pattern of the total gain at the same band for 3DP 2 × 2 trapezoidal antenna array, and it can be noticed that it achieved a higher gain of 11.35 dBi with a nearly directional pattern along the z-axis. It is worth noting that the antenna array was constructed in the x–y plane, and the total gain and current distribution are simulated at 10 GHz.

In order to investigate the availability of the proposed array antenna for various wireless applications, the radiation pattern is presented. The required performance of the planar array operating for different wireless applications is the omni–directional

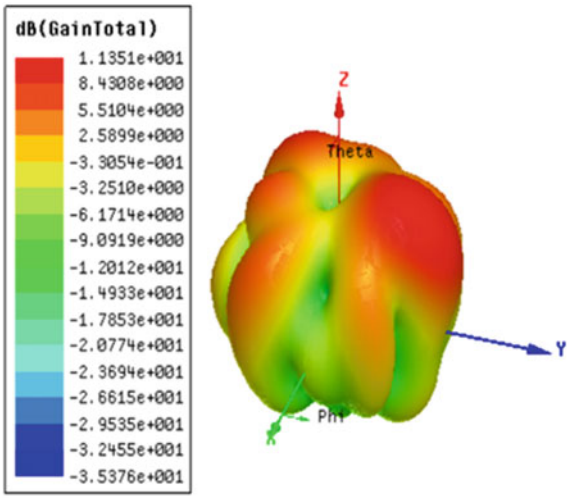

Fig. 6 The simulated total gain for 3D Printed 2 × 2 trapezoidal planar antenna array at 10 GHz

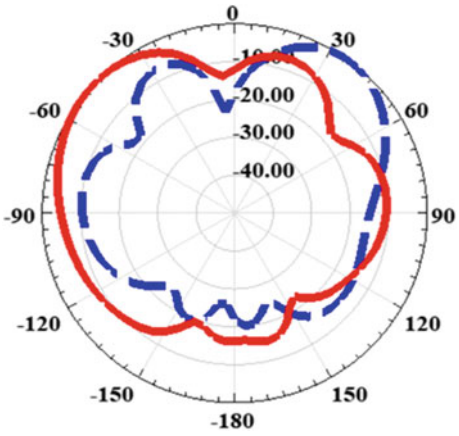

Fig. 7 Simulated radiated electric field in E–plane (solid) and H–plane (dashed) for the proposed array at 10 GHz

with stable radiation pattern, and this requirement was achieved in our array as shown in Fig. 7. The patterns are nearly omnidirectional in both planes (E and H planes) at the resonance frequency of the final planar array. In the radiation pattern of the proposed array, a deep null −22 dBi is observed at the broadside direction at angle −5° and can use it to overcome the jamming in this direction. It is clearly noticed that from the show results that the 3–DP 2 × 2 trapezoidal planar antenna array is capable of achieving the required radiation characteristics for X-band wireless applications.

The comparison of 3D printing structure and conventional structure is shown in Table 1. It can be clearly observed that the proposed antenna offers the highest amount of peak gain taking less antenna dimension.

Table 1 Comparison between the suggested array antenna and recently reported array antennas

References	Dimensions (mm)	Operating frequencies (GHz)	Peak gain (dBi)	Characteristics
[19]	80 × 80 × 3.04	3.8	9.2	4-feed/2square-loop
[20]	70 × 30 × 0.8	1.56	2.1	Folded slot with a branch edge
[21]	68 × 39 FR4 (4.3)	2.3	5.7	Planar dipole antenna
[22]	50 × 69 FR4 (4.4)	2.08	1.38	Planar monopole antenna
[23]	227 × 95.9 FR4 (4.4)	2.45	7.75	Slot and DGS loaded structure
[24]	110.5 × 83 FR4 (4.4)	2.40	9.22	Slot incorporated patch array
This work	52.28 × 55.21 × 3 PLA(3.1)	10	11.35	1-feed/trapezoidal array structure

4 Conclusion

In this paper, a four-element trapezoidal antenna array printed on PLA substrate was designed and simulated for wireless applications. The most important parameters of the proposed 3-DP 2 × 2 trapezoidal antenna array, which are mainly reflection coefficient S_{11} and high gain, have been carried out to confirm the required performance. The proposed antenna array is achieved a return loss of −15.54 dB at 10 GHz with a high gain reached 11.35 dBi. The entire size of the final design of the 3DP antenna array was 52.28 × 55.21 × 1 mm^3. Consequently, the suggested antenna array could be used for various wireless application systems.

References

1. Ullah, U., Mahyuddin, N., Arifin, Z.: Antenna in LTCC technologies: a review and the current state of the art. IEEE Antennas Propag. Mag. **57**(2), 241–260 (2015)
2. Bevelacqua, P.: Array Antennas. Antenna-theory.com. Retrieved 23, Feb. 2017. (2016)
3. Most used 3D printing technologies 2017–2018, Statistic. Statista. Retrieved 2, Dec. 2018
4. Liang, M., Yu, X., Shemelya, C., MacDonald, E., Xin, H.: 3D printed multilayer microstrip line structure with vertical transition toward integrated systems. IEEE MTT-S Intl. Microw. Symp. (IMS) (May 2015)
5. Ali, W.A., Hamad, E.K., Hamdalla, M.Z.: High gain triple band microstrip antenna based on metamaterial super lens for wireless communication applications. IEEE International conference on innovative trends in computer engineering (ITCE'2018). At Aswan, Egypt, pp. 197–204
6. Ali, W.A.E., Mohamed, H.A., Ibrahim, A.A., Hamdalla, M.Z.M.: Gain improvement of tunable band-notched UWB antenna using metamaterial lens for high speed wireless communications. Microsyst Technol **25**(11), 4111–4117 (2019)
7. Lakrit, S., Medkour, H., Das, S., Madhav, B.T.P., Ali, W.A.E., Dwivedi, R.P.: Design and analysis of integrated Wilkinson power divider-fed conformal high-gain UWB array antenna with band rejection characteristics for WLAN applications. J. Circ., Syst. Comput. 1–13 (2020). https://doi.org/10.1142/S0218126621501334
8. Das, S., Sarkar, P.P., Chowdhury, S.K.: Design and analysis of a compact monitor-shaped multifrequency microstrip patch antenna. J. Electromagnet. Waves Appl. **28**(7), 827–837 (2014)
9. Das, S., Sarkar, P.P., Chowdhury, S.K.: Modified π-shaped slot loaded multifrequency microstrip antenna. Prog. Electromagnet. Res. B. **64**(1), 103–117 (2015)
10. Das, S., Sarkar, P.P., Chowdhury, S.K.: Design and analysis of a novel open ended T-shaped slot loaded compact multifrequency microstrip patch antenna. Microw. Opt. Technol. Lett. **56**(2), 316–322 (2014)
11. Boutejdar, A., Salamin, M.A., Challal, M., Das, S., El Hani, S., Bennani, S.S., Sarkar, P.P.: A compact wideband monopole antenna using single open loop resonator for wireless communication applications. Telkomnika (Telecommun. Comput. Electron. Control). **16**(5), 2023–2031 (2018)
12. Das, S., Sarkar, P.P., Chowdhury, S.K.: Investigations on miniaturized multifrequency microstrip patch antennas for wireless communication applications. J. Electromagnet. Waves Appl. **27**(9), 1145–1162 (2013)
13. Ketterl, T.P., Vega, Y., Arnal, N.C., et al.: (2015) A 2.45 GHz phased array antenna unit cell fabricated using 3-D multi-layer direct digital manufacturing. IEEE Trans. Microw. Theory Tech. **63**(12), 4382–4394

14. Yu, X., et al.: 3D printed parts for a multilayer phased array antenna system. IEEE Antennas Wirel. Propag. Lett. **17**(11), 2150–2154 (2018)
15. Ahmed, A.E., Ali, W.A.E.: A novel multiband antenna with 3D-printed multicircular substrate for wireless applications. 2020 International Conference on Electrical, Communication, and Computer Engineering (ICECCE), pp. 1–5. Istanbul, Turkey
16. Ahmed, A.E., Ali, W.A.E.: Analysis and design of 3-D printed fractal triangular antenna for wireless communications applications. 2020 International Conference on Electrical, Communication, and Computer Engineering (ICECCE), pp. 1–5. Istanbul, Turkey, (Jan 2020)
17. Ahmed, A.E., Ali, W.A.E., Chowdhury, A., Das, S.: A 3-D printed trapezoidal antenna for X–band wireless communications applications. VICFCNT, India, (2020)
18. Fang-Yao, K., Hwang, R.B.: High-isolation X-band marine radar antenna design. IEEE Trans. Antennas Propag. **62**(5), 2331–2337 (2014)
19. Pal, A., Mehta, A., Deo, P.: Dual-band low-profile capacitively coupled beam-steerable square-loop antenna. IEEE Trans. Antennas Propag. **62**(3), 1204–1211 (March 2014)
20. Hung, C., Chiu, T.: Dual-band reconfigurable antenna design using slot-line with branch edge. IEEE Trans. Antennas Propag. **63**(2), 508–516 (2015)
21. Terhzaz, J., Tribak, A., Riouch, F.: Novel miniaturized multiband antenna and applications for smart navigation media. Int. J. RF Microw. Comput. Aided Eng. (Sep 2019)
22. Brar, R.S., Saurav, K., Sarkar, D., Srivastava, K.V.: A quad-band dual-polarized monopole antenna for GNSS/UMTS/WLAN/WiMAX applications. Microw. Opt. Technol. Lett. **60**, 538–545 (2018)
23. Tabakh, I., Das, S., Jorio, M., El Idrissi, N.E.A., Mohapatra, S., Barad, D.: Defected ground structure (DGS) incorporated RFID reader antenna array for indoor positioning systems at 2.45 GHz. Int. J. Microw. Opt. Technol. **15**(6), 517–524 (Nov 2020)
24. El Alami, A., Ghazaoui, Y., Das, S., Bennani, S.D., El Ghzaoui, M.: Design and simulation of RFID array antenna 2×1 for detection system of objects or living things in motion. Procedia Comput. Sci. **151**, 1010–1015 (2019)

A Survey on the Applications and Advancements in Smart Water Meter

Deb Sekhar Roy, Debajyoti Sengupta, Debraj Paul, Aftab Khan, Ankush Das, Debjit Pal, and Bidhan Malakar

Abstract This paper reviews on some of the recent methodologies of intelligent water metering system used in the smart water meter (SWM) to overcome the problem of water crises. The conservation of water is one of the vital problems in worldwide that needs proper attention. Due to the unpredictable rise in water consumption, the entire fresh water sources are diminishing day by day. At present, there is a gradual advancement in the technologies used for the purpose of monitoring of the proper utilization of water sources. This resulted into better functioning and solving various water loss issues in broad spectrum. The different frameworks available for SWM including the advanced communication protocols are also being discussed in this paper that could help for further advancement in the SWM.

Keywords Smart water meter (SWM) · Frameworks · Protocols · Intelligent water metering system

1 Introduction

One of the most important living resources for every living being on this earth for its survival is "water." The purpose of our living to fulfill our requirements of freshwater is mainly served by the groundwater, not the seawater or brackish water. As a matter of fact, the freshwater makes up a very small fraction of all water available on this earth [1]. It is an interesting fact among us that nearly 70% of the world is covered by water; out of which, 2.5% is only fresh, and the rest is saline or ocean based [2]. Even then, just 1% of our freshwater is easily accessible, with much of it trapped in glaciers and snowfields.

D. S. Roy (✉) · D. Sengupta · D. Paul · A. Khan · A. Das · D. Pal · B. Malakar
Department of Electrical Engineering, JIS College of Engineering, Kalyani, West Bengal, India

B. Malakar
e-mail: bidhan.malakar@jiscollege.ac.in

B. Sikdar et al. (eds.), *Proceedings of the 3rd International Conference on Communication, Devices and Computing*, Lecture Notes in Electrical Engineering 851,
https://doi.org/10.1007/978-981-16-9154-6_41

Focusing on the ground water, a vital source for obtaining every single drop of freshwater is now becoming limited. This freshwater is used to quench our requirements which indicates that this matter is of great significance and also of serious concern. This is not only a concern for now, but for the future of every living being to exist that there will be run-down due to the crises of water on this earth [3]. In this context, the misuse of water should be restricted completely, or else it will end us by taking the life of every living being.

From the countries which are dealing with acute water deficiency, India ranks the 13th with 600 million people dealing with extreme water scarcity [4]. On a percentage of one billion people residing in water deficient regions, about 0.2% million people dies due to insufficient water in every year. Water crisis in India, itself will result into loss of 6% of GDP by 2050 [5]. On behalf of increasing population in corporate privatization, industrialization, excessive wastage in household use and lack of government planning, irregular maintenance of water pipelines has resulted into severe water crisis in India.

With the introduction of hi-tech era, the usage of Internet technologies to connect the world wide has increased within a decade. Now, with the advancement in embedded system (microprocessor/microcontroller), wireless sensing mechanism radio-frequency identification {(RFID)/sensors}, data management software (big data/cloud computing) have made human life much easier. The advancement in wireless sensor networks (WSN), Internet, other communication technologies {GSM (Global System for Mobile Communications)/GPRS (general packet radio service)} and with machine-to-machine communication (i.e., wire/wireless communication) has taken the world to adopt Industry 4.0 [6–9].

Nowadays, smart technologies are implemented to solve any real-time problems with great accuracy without human interference using Internet of Things (IOT). Application of IOT devices in different sectors which include healthcare, agriculture, education system, industrialization has resulted into implementing ideas of smart cities, smart agricultural system, smart healthcare system, smart waste management system, and also smart meter reading system [10–13].

The reduction of water resources due to climate change and the increasing demand associated with population growth is a renewed concern. Water distribution monitoring and smart metering are essential tools to improve distribution efficiency. Also, the problem of over use of water in household, public, and private sectors can be solved by checking and monitoring the usage. But, for a man himself or an agency to track, detect and monitor the water usage of a society on daily basis are a cumbersome process.

Water meter has become a notable topic in today's technological discussion, as our resources of drinking water are decreasing day by day. In this fast-paced life, water suppliers and consumers need to introduce a new water system which is more efficient and comparatively quicker. Digital water meters are used to measure the volume of water used by residential and commercial buildings that are supplied with water by a public water supply system. Thus, by using this, we can keep monitoring on the usage of water by different consumers. The main objective is to make water supply more

accountable and transparent which reduces the manual assistance, deliver secure and time-efficient solution for the complex water system.

This problem leads to a solution named SWM consisting of different embedded systems, sensors, and data monitoring devices to detect water usage of a whole municipality. Researchers from all over the world over an era utilized their ideas and came up with existing technologies to make SWM more and more efficient. This paper presents a detailed and comprehensive survey of some works done within a decade on SWM utilizing past and present technologies.

The researchers from different countries of the world are now united to develop an effective technique to solve the problem of water crisis. One of the solutions to solve and optimize the upcoming crisis of water is to use SWM [14].

Therefore, this paper provides a detailed survey on the recent advancements in SWM. After the Introduction, Sect. 2 provides a detailed description on the water leakage problem with its available solution till now. Section 3 discusses about the recent technological advancement in SWM. Section 4 presents a proposal on an advanced SWM in author's perspective. Section 5 provides the conclusions of the work.

2 Problem from Water Leakage and Its Available Solution

According to the present scenario, the problem of water leakage results for the majority of the overall crisis and depletion of the level of ground water. To restrict the misuse of water dispersion universally, various consumer friendly networks had been proposed, which would help to overcome the crises as discussed in [15–18].

In 2016, researchers from University of Johannesburg, South Africa had proposed about a system known as smart water leakage detection and metering (SWLDM). Its main operation is to deliver the amount of water consumption level to the consumer and also detect the possibilities of any unknown leakages. Also, the data of consumption will be sent to the water supply office for any billing purposes, which would further assist in the knowledge of the overall usage of the water supply in a local area. In SWLDM, external power supply is not required as it will be working from solar modules [15]. In the year 2017, a methodology was proposed in [16] known as automatic water distribution and leakage detection system. The system has the ability to control the water supply distribution and leakage network by the application of programmable logic controller (PLC). Within that year, researchers from Palestine Technical University, Palestine had shown their contribution by proposing and developing a prototype of a wireless network system known as smart water leakage detection (SWLD). Its main operation is to deliver the knowledge of water leakage to the consumer as well as to restrict the water facility from that consumer, by the help of GSM technology and microcontrollers [17]. In [18], a research was published in 2018 about a self-learning SWM module. Its operation is to set the limit of water

supply with previous supply usage data and restrict the main water supply distribution during an emergency leakage. This module is readily applicable for buildings with complex water distribution systems.

Therefore, this section provides a brief survey on the available solution of water leakage problems, in domestic as well as locality.

3 Development in Design and Networks of Smart Water Meter

Before developing any unique models or hardware, the priority retains in the current developments in the twenty-first century models [19–30]. In 2010, researchers from China, proposed a smart metering design frame work based on wireless Zigbee technology. The framework overcomes the hectic problem of manual way as well as cable connected meter reading. They resolved the problem by updating the meter-reading data from consumer's end to data processing center through general packet radio service (GPRS) network. A smart metering design framework based on wireless Zigbee technology proposed in [19] to overcome the hectic problem of manual way as well as cable connected meter reading. There are some limitations in this model related to power consumption, cost management, and theft control misuse that cannot be managed. In 2011, researchers from Latvia, Europe proposed a solution of monitoring the water distribution network in Talsi city (City in Latvia) through automatic wireless meter-reading technology. The automatic meter reading (AMR) framework includes water flow and water pressure meters that provides data to sensors and transmitters, short-range devices (SRD) that transmits data from sensors to concentrators. The concentrators that make use of Atmel's microcontroller to store data, Telit's GSM modem used to transmit data through GPRS network, MYSQL database to store data. This AMR framework faced some challenges including system's operating lifetime without replacement of batteries and reading, transmitting rate of metering data through sensor nodes. The researchers resolved the problem of battery replacement by using 7500–8000 (mAh) battery having estimated lifetime of 10 years. Hence, this model effectively resolved the area of cost-effectiveness and robustness [20].

In 2012, researchers from Brussel, Belgium proposed a methodology that overcome the major issue of usage of batteries, disposal of which causes environmental pollution by using self-powered wireless sensor over embedded systems and sensors that were energized by batteries or electric sources. The proposed model makes use of the kinetic energy within the fluid stream to rotate a turbine converting it to mechanical energy which is again converted into electrical energy by alternator. Hence, the smart meter device gives energy to itself using self-powered WSN and rotating turbine reducing human interference [21]. In 2013, a research paper was published that discussed about an intelligent metering system for the urban water distribution. This paper reviews about the current development of water meters and its process networks to enhance the sustainability of future urban water supply management

[22]. In 2014, researchers from Spain proposed smart water management model with the help of IoT for decision systems and to monitor the business procedures. The final model as discussed consists of three main elements: water management model, common communication interface, and coordination subsystems (C-S) interface [23]. In 2015, researchers from Council for Scientific and Industrial Research (CSIR), Pretoria, South Africa, which introduces the water management system on wireless network system known as WSN. On a contrary, the system uses as an open-source application to create a sturdy and smart system [24]. In 2016, researchers from University of Pretoria, South Africa in collaboration with Nanjing University of Posts and Telecommunications, China reviewed about the various proposed and existing topologies used in the SWM, like ZigBee network topologies and wireless communication options. This paper also highlighted the challenges of scalable smart water meter networks [25].

In 2017, researchers from Kerala, India proposed a methodology that uses low-cost IoT devices and smart phone application for smart metering. This proposed technology allows both the consumers as well as meter readers to get information of meter reading, updating data to database and bill payment. This easy to access metering device uses customer relation and billing management (CRBM) system to store, access, and analyze the data from multiple meters specified with data time [26]. In 2018, researchers from Tamil Nadu, India proposed a framework that works on water theft control in government pipelines and efficient water distribution using IOT devices. The proposed model works on Arduino as microcontroller and uses solenoid valve, relay circuit, water flow sensor, hall effect flow meter to calibrate the water consumption by the consumers. The Blynk cloud application is used to store and record the data of daily water usage by the consumers. This cloud application can also be used to control (ON/OFF) water supply line through phone [27]. In 2019, a review paper was published by Auckland University of Technology that not only provides the review of design about an existing water meter, but also proposed about a self-powered smart utility water meter and its application in various other fields [28]. In 2020, researchers from University of Calcutta, Kolkata, India proposed a smart water meter framework which is based on Internet of Things (IOT) and cloud computing. This proposed model makes use of machine learning algorithms which detects excessive usage of water at domestic, industrial, and other sectors. The data acquisition units of previously proposed modules lag the factor of cloud computing, malfunctioning of which may lead to failure of data recording by servers and even users get no information of unit failure until physically checked. Although some drawbacks of the model have been depicted, one of which is burring the water pipelines deep within the building design causes difficulty in connecting with the water meter; another is the disruption of Internet connectivity may cause interruption of data storage in cloud [29].

Henceforth, this section describes about the existing technologies of the smart water meters in the recent decade. The specification of technologies used in SWM has been discussed in Table 1.

Table 1 The specification of technologies used in SWM

Sl. No.	Year of publication	Adapted technologies for SWM				References
		Technologies used in SWM	Hardware		Software	
			Embedded system	Sensors or actuators	Data analyzing system	
1	2010	General packet radio service (GPRS) network, Zigbee wireless technology (IEEE 802.15.4)	PIC16F946 (microcontroller)	Not specified by author	Database management system	[19]
2	2011	GSM network (GPRS), Short-range devices (SRD) (unlicensed telemetry band, 868 to 870 Megahertz)	ATMEGA48/88 (microprocessor)	Water flow and water pressure meters	MySQL	[20]
3	2012	Wireless M-bus (868 MHz frequency band), mobile network data link (UMTS, 3G, LTE, etc.)	MSP430L092 (microcontroller)	Not specified by author	Not specified by author	[21]
4	2013	GPRS, CDMA, GSM, private radio transmission	Not specified by author	Not specified by author	Not specified by author	[22]
5	2014	Water management model, common communication interface, coordination subsystems (C-S) interface	Not specified by author	Not specified by author	Not specified by author	[23]
6	2015	Wireless sensor networks (WSN)	STM32W_108, MSP430G2231 (microprocessors)	Not specified by author	Pandora FMS, web-based monitoring application, CoAP web-based application	[24]

(continued)

Table 1 (continued)

Sl. No.	Year of publication	Adapted technologies for SWM				References
		Technologies used in SWM	Hardware		Software	
			Embedded system	Sensors or actuators	Data analyzing system	
7	2016	Provides a review on SWM using magnetic sensing, capacitive Sensing, Image processing	Provides a review on SWM using wire based and wireless systems, network topologies, ZigBee smart energy, ZigBee network topologies, wireless communication options, existing and proposed smart water meter networks, network simulation			[25]
8	2017	Ethernet, TCP/IP network	Electronic interface module (EIM)	Hall-effect-based sensor, Tamper-flag sensors	Customer relations and billing management (CRBM) system	[26]
9	2018	Ethernet shield W5100, internet of things (IOT) networking	Arduino UNO (microcontroller)	YS-S20 flow sensor, hall effect sensor, Solenoid values	Blynk cloud application	[27]
10	2019	Universal asynchronous receiver transmitter (UART) protocol, bluetooth transceiver (HC-06 bluetooth module)	Atmega16L-SAU (microcontroller)	Water turbine generator, flow measurement sensor, hall-effect sensor	An application based on MIT app inventor	[28]
11	2020	Internet of things (IOT) networking, ESP8266 Wi-Fi system, data collection using thingspeak cloud platform	NodeMCU	YF-S201 water flow sensor, magnetic hall-effect sensor	ThingSpeak cloud platform, data collection using machine learning tools	[29]

4 Proposal for an Advanced Smart Water Metering System

There is an extensive research work carried out in the past decade as mentioned in the earlier sections in this paper. So, we propose a SWM named as "A2BD4-SWM," which is to be installed in the supplied water line as well as in groundwater pumpers. This will put a limit on the use of amount of water for each subject ("subject" refers to the users of domestic houses and organizations).

The meter will have the capability to calculate the amount of water needed on a daily basis for every domestic house or organization. Once the daily limit is crossed, there will be a provision for the supply of emergency extra water, but there will be an additional payment, after the emergency water supply is covered. So, this will generate consciousness of overuse of water, and water loss can be eliminated from their mindsets.

This meter will also be installed while pumping the water from the groundwater to regulate the water supply from ground water. The total amount of water requirements will be calculated as from the supplied water as well as ground water, i.e., (Total water used in the subject = Amount of supplied water used in the subject + Amount of extracted ground water used in the subject).

Thus, we can regulate the amount of water in each subject and place a payment setup, which would activate after certain limits of water supply and sufficient water will be supplied to that subject for that particular day which would also save that day's water. Figure 1 shows the block diagram of the proposal of A2BD4-SWM.

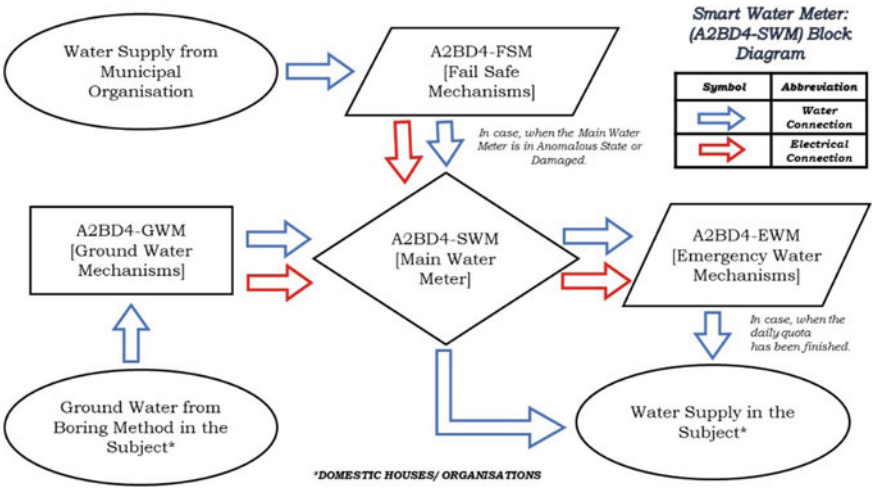

Fig. 1 Block diagram of proposed A2BD4-SWM

5 Conclusions

The scarcity of water at present has been a threat over worldwide mankind. There are different technologies developed and used currently as discussed in this paper to overcome the problem of water crisis. In this paper, the current as well as past research works on SWM system are carefully reviewed. More specifically, the paper presents and assess previous published works based on the technologies implemented, smart consumption, leaks, theft detection techniques, modes of communication protocols, data storing software and power harvesting.

Furthermore, the challenges and disadvantages of the models are discussed accordingly. This paper not only provides a survey on SWM but also highlights the major problem of water crisis as well as discusses on the way to restore the level of the ground water with a proposal of a SWM.

References

1. Hossain, M.Z.: Water: the most precious resource of our life. Glob. J. Adv. Res. **2**(9), 1–11 (2015)
2. Mankar, G.U., Satpute, M.S.: Experimental investigation with software validation for exergy analysis of solar still by reticular porous media with glass cover of (IAO) coating–a review. **09**, 43–46 (2019)
3. Chakkaravarthy, D.N., Balakrishnan, T.: Water scarcity-challenging the future. Int. J. Agric., Environ. Biotechnol. **12**(3), 187–193 (2019)
4. Ghosh, P.: Water stress and water crisis in large cities of India. Sustain. Clim. Action Water Manage. 131 (2021)
5. Shah, S.H., Narain, V.: Re-framing India's "water crisis": an institutions and entitlements perspective. Geoforum **101**, 76–79 (2019)
6. López, T.S., Ranasinghe, D.C., Harrison, M., McFarlane, D.: Adding sense to the internet of things. Pers. Ubiquit. Comput. **16**(3), 291–308 (2012)
7. Sliwa, J.: A generalized framework for multi-party data exchange for IoT systems. 30th International Conference on Advanced Information Networking and Applications Workshops (WAINA). IEEE, pp. 193–198 (2016)
8. Mankad, U., Arolkar, H.A.: Survey of IoT frameworks for smart water metering. Management **24**, 26 (2018)
9. Kandris, D., Nakas, C., Vomvas, D., Koulouras, G.: Applications of wireless sensor networks: an up-to-date survey. Appl. Syst. Innov. **3**(1), 14 (2020)
10. Dlodlo, N., Foko, T.E., Mvelase, P., Mathaba, S.: The state of affairs in internet of things research. Academic Conferences International Ltd, pp. 224–258. (2012)
11. Agrawal, S., Vieira, D.: A survey on internet of things. Abakós **1**(2), 78–95 (2013)
12. Zanella, A., Bui, N., Castellani, A., Vangelista, L., Zorzi, M.: Internet of things for smart cities. IEEE Internet Things J. **1**(1), 22–32 (2014)
13. Perwej, Y., Haq, K., Parwej, F., Mumdouh, M., Hassan, M.: The internet of things (IoT) and its application domains. Int. J. Comput. Appl. **975**(8887), 182 (2019)
14. Dogo, E.M., Salami, A.F., Nwulu, N.I., Aigbavboa, C.O.: Blockchain and internet of things-based technologies for intelligent water management system. In Artificial Intelligence in IoT, pp. 129–150. Springer, Cham (2019)
15. Sithole, B., Rimer, S., Ouahada, K., Mikeka, C., Pinifolo, J.: Smart water leakage detection and metering device. IST-Africa Week Conference, pp. 1–9. IEEE, (2016)

16. Rao, N., Waghmode, R., Gaikwad, D., Tupe, A.: Automatic water distribution and leakage detection using PLC and SCADA. Technology 2.1 (2014)
17. Daadoo, M., Daraghmi, Y.A.: Smart Water Leakage Detect. Using Wirel. Sens. Netw. (SWLD) **7**(1), 1–16 (2017)
18. Fikejz, J., Roleček, J.: Proposal of a smart water meter for detecting sudden water leakage, pp. 1–4. ELEKTRO. IEEE (2018)
19. Zhang, B., Liu, J.: A kind of design schema of wireless smart water meter reading system based on ZigBee technology. International Conference on E-Product E-Service and E-Entertainment, pp. 1–4. IEEE, (2010)
20. Zabasta, A., Kunicina, N., Chaiko, Y., Ribickis, L.: Automatic wireless meters reading for water distribution network in Talsi city. EUROCON-International Conference on Computer as a Tool, pp. 1–4. IEEE, (2011)
21. Di Zenobio, D., Steenhaut, K., Celidonio, M., Sergio, E., Verbelen, Y.: A self-powered wireless sensor for water/gas metering systems. International Conference on Communications (ICC), pp. 5772–5776. IEEE, (2012)
22. Boyle, T., Giurco, D., Mukheibir, P., Liu, A., Moy, C., White, S., Stewart, R.: Intelligent metering for urban water: a review. Water **5**(3), 1052–1081 (2013)
23. Robles, T., Alcarria, R., Martín, D., Morales, A., Navarro, M., Calero, R., López, M.: An internet of things-based model for smart water management. 28th International Conference on Advanced Information Networking and Applications Workshops, pp. 821–826. IEEE, (2014)
24. Mudumbe, M.J., Abu-Mahfouz, A.M.: Smart water meter system for user-centric consumption measurement.13th International Conference on Industrial Informatics (INDIN), pp. 993–998. IEEE, (2015)
25. Marais, J., Malekian, R., Ye, N., Wang, R.: A review of the topologies used in smart water meter networks: a wireless sensor network application. J. Sens. **2016**, 12 (2016)
26. Suresh, M., Muthukumar, U., Chandapillai, J.: A novel smart water-meter based on IoT and smartphone app for city distribution management. 2017 IEEE Region 10 Symposium (TENSYMP), pp. 1–5. IEEE, (2017)
27. Tamilselvan, G.M., Ashishkumar, V., Prasath, S.J., Yusuff, S.M.: IOT based automated water distribution system with water theft control and water purchasing system. Int. J. Recent Technol. Eng. (IJRTE) **7**(4S) (2018)
28. Li, X.J., Chong, P.H.J.: Design and Implementation of a self-powered smart water meter. Sensors **19**(19), 4177 (2019)
29. Ray, A., Goswami, S.: IoT and cloud computing based smart water metering system. In 2020 International Conference on Power Electronics & IoT Applications in Renewable Energy and its Control (PARC), pp. 308–313. IEEE, (2020)
30. Alvisi, S., Luciani, C., Franchini, M.: Using water consumption smart metering for water loss assessment in a DMA: a case study. Urban Water J. **16**(1), 77–83 (2019)

Development of a Programmable Logic Controller-Based Advance Control Strategy for the Multiple Boiler System

Kunal Chakraborty, Sanchita Mukherjee, Urmi Mukherjee, Sudipta Das, and Samrat Paul

Abstract This technical article outlines the eight steps of operation associated with the conversion of a manually operated multiple boilers station towards a semi-automated multiple boilers station with the help of Programmable logic controller (PLC). This report focuses on the passing of only one input from PLC control room to the four boilers at a particular temperature and this process continued until the operating temperature reached 900 °C. Although the four boilers are not working at the same time, each boiler has required a continuous inspection at frequent intervals. In our method, each boiler is operated for 10 min interval with every power setting. Through the RSLOGIX 5000 ladder diagram, the PLC sends a single input to the system and the four boilers started to operate simultaneously with the possible eight outputs with two power settings.

Keywords Control system · Instrumentation · Ladder logic

1 Introduction

A PLC-based control system is a well-adapted controlling method to perform various industrial works namely, manufacturing, capping-filling of a bottle, oil refining and storage for the industry where the cost maintenance and operation are relatively

K. Chakraborty · S. Paul
Advanced Materials Research and Energy Application Laboratory, Department of Energy Engineering, North Eastern Hill University, Shillong, Meghalaya 793022, India

S. Mukherjee
Electrical Engineering Department, Madhav Institute of Technology and Science, Gwalior, Madhya Pradesh, India

U. Mukherjee
Life Science Department, Vidyasagar Teachers' Training College, Midnapore, West Bengal, India

S. Das (✉)
Electronics and Communication Engineering Department, IMPS College of Engineering and Technology, Malda, West Bengal, India

B. Sikdar et al. (eds.), *Proceedings of the 3rd International Conference on Communication, Devices and Computing*, Lecture Notes in Electrical Engineering 851,
https://doi.org/10.1007/978-981-16-9154-6_42

higher [1, 2]. On the other side, a process industry requires continuous observation when it is operated manually. Such a manual system increases the possibilities of system errors. Thus Scientists and Engineers have developed the automation technology which is gradually replacing the manual system with HMI (human–machine interface)-based industrial automation control system. The K-type thermocouple plays an important role to find the temperature of the boilers in terms of the raw value. The master control PLC converts that raw data as per its required value. This conversion process is invisible for the operator as it is embedded in the processor of the master control system. Chakraborty et al. (2015) shows a PLC-SCADA-based automation system for a mass production bottling plant in which at a particular time interval the bottles of soft drink are capping and filling automatically without a failure [3]. Kumar et al. (2016) developed a simple automatic liquid filled control system with higher system reliability [4].

The main objective of our study is to build a single power setting start-up control among the multiple boiler system (In this case, it is a four-boiler system) via a PLC-based master control system. The entire control system will be controlled and manipulated by an RSLOGIX 5000 software Ladder diagram, which is made by Rockwell Automation Inc [3, 5]. This unique control system ensures that the above four-boilers are not run at a time in the system.

2 Development of the Proposed System

The construction of proposed multiple boiler system consists of four-boilers, two power setting heater (power setting-1 and power setting-2), 4-K-type (Chromel Alumel) digital thermocouple which has a range of 95–1260 °C, master programming monitor (LG Electronics India Pvt. Ltd.) with other boiler auxiliaries inlet valve, pipes. The proposed system view is shown in Fig. 1. The above figure shows that boiler-1, boiler-2 has a single power setting, boiler-3, boiler-4 has another single

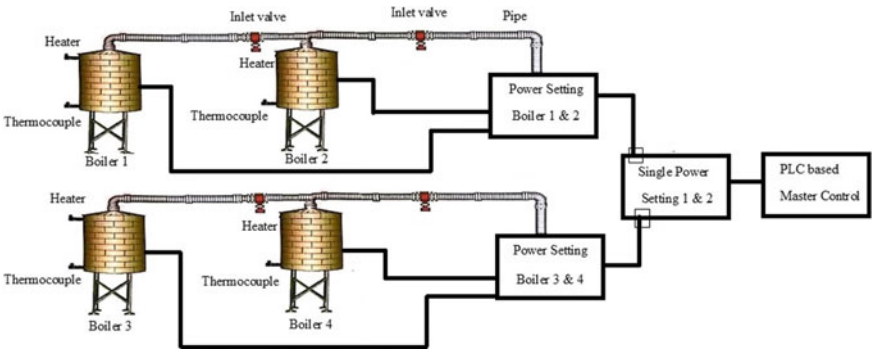

Fig. 1 Schematic view of the single power proposed control system

power setting. Our proposed control system proposes a single power setting for all the four boilers and that power setting will be controlled automatically by a PLC-based system. Each boiler is internally attached with thermocouple and the output of the thermocouple is connected to the PLC input box [6, 7]. Thermocouple sets the temperature of the boilers in such a way that if the temperature falls below 800 °C, the boiler-1 of power setting-1 gets started automatically. After 10 min, power setting-2 of boiler-1 is starting to reheat the boiler-1 for the next 10 min and then again, power setting-1 heat boiler-2 for the next 10 min, the process is repeated until it reached to 900 °C. When the final temperature of the system is reached to the desired value (900 °C), all the four-boilers are automatically turned off sequentially. Then, when the temperature of the system reached below the value of 800 °C, boiler-1 will start again by the power setting heater 1 and 2. This approach will be very useful for the batch production industry where turn on and turn off of the boiler is required continuously [8–10].

3 Outcome and Discussion

3.1 Ladder Logic Diagram and Automatic Control System

PLC has so many input and output terminals where inputs are directly connected with the sensors, switches and output terminals are connected with loads like motors, lights [11, 12]. In an effort to make programming part of PLCs easier, ladder logic diagram is the most commonly used programming method. In this study, we have performed the PLC programming in RSLOGIX 5000 PLC software. Figure 2 shows the ladder logic diagram for the proposed control system. The programming part of RSLOGIX 5000 software is directly transferred to the virtual emulator through the data cable within the same local station [13, 14]. But, before sending the data through a virtual emulator, the operator must check the correctness of the programming part.

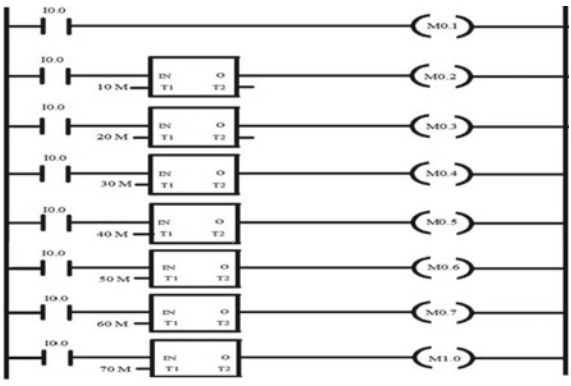

Fig. 2 Ladder logic diagram for the proposed control system

Table 1 The description of all the outputs of RSLOGIX 5000

Outputs	Power setting	Boiler No.	Scan time (Minutes)
M0.1	1	1	–
M0.2	2	1	10
M0.3	1	2	20
M0.4	2	2	30
M0.5	1	3	40
M0.6	2	3	50
M0.7	1	4	60
M1.0	2	4	70

The above ladder logic diagram consists of one input signal (I0.0) which is coming from PLC-based master control system and eight output signals (M0.1, M0.2, M0.3, M0.4, M0.5, M0.6, M0.7, M1.0) which are coming from four different boilers within the same local station. The lists of the outputs are shown in Table 1 (Fig. 3).

3.2 Efficiency Analysis of the Proposed System

Efficiency and optimization of cost are the prime concern to improve the productivity of any project. Here, Tables 2 and 3 shows the potential cost reduction analysis of the proposed system with manual and proposed automatic control system respectively. The data highlighted in Tables 2 and 3 are based on the data received from the annual report of Greenwave Solutions Pvt. Ltd for the FY-2014–15.

From both the tables, it is clear that with the proposed automatic control system, the main essential contents of a plant, like the labour cost can be reduced up to 50% from the manual data value. Similarly, other contents like electricity, repairing costs also may be reduced up to a significant level.

4 Future Outlook

This technical work is an example of a multiple boiler control system where all the essential parameters can be covered using the single input control system. In this present study, we have only covered the temperature parameter. With that recommended control system, all the field interlocks like the boiler pressure, operation of the boiler feed-pump can be controlled and manipulated by this RSLOGIX-5000 software.

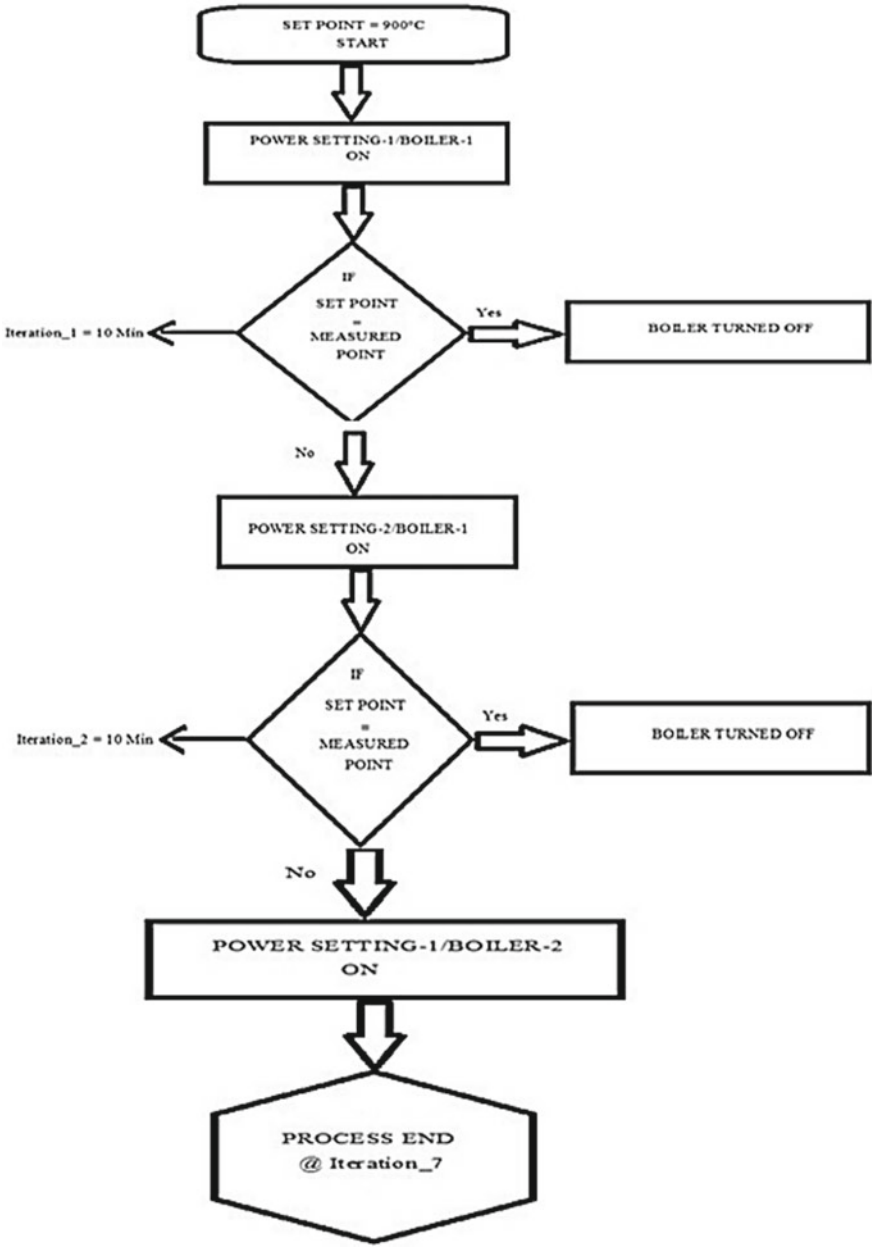

Fig. 3 Flow chart of the operation of the proposed control system

Table 2 Manual data value of various essential contents

Contents	Quantity (3 Shift)	Cost/Month (Lac)	Annual Cost (Lac)
Labour/Technician	12	5	60
Electricity	12	1	12
Maintenance	12	–	5
Miscellaneous	12	–	0.5

Table 3 Automatic system data value of various essential contents

Contents	Quantity (3 Shift)	Cost/Month (Lac)	Annual Cost (Lac)
Labour/Technician	6	5	30
Electricity	12	0.85	10
Maintenance	12	–	3
Miscellaneous	12	–	0.2

Acknowledgements The authors are thankful to Mrs. Swapnila Chakraborty, Director, Greenwave Solutions Pvt. Ltd., Kolkata, West Bengal, India for providing the experimental set up and proper training on Automation technology (Registration No.- R/4913/14-15) for our studies.

References

1. Thanupillai, K., Praveena, R.: PLC based automatic bottle filling and capping system with user defined volume selection. Int. J. Emerg. Tech. Adv. Eng. **2**, 134–137 (2012)
2. Wiliem, L., Hargreaves, D.J., Stapelberg, R.F., Yarlagadda, P.K.D.V. : Development of real-time data filtering for SCADA system. J. Achievements Math. Manage. Eng. **21**, 89–92 (2007)
3. Chakraborty, K., Roy, I., De, P., Das, S.: Controlling process of a bottling plant using PLC and SCADA. Indonesian J. Electron. Eng. Inf. **3**, 39–44 (2015)
4. Kumar, G.S., Suhail, A.M., Naveen, R.S., Rajavikram, R.: Real time liquid level control system using PLC and SCADA. Int. J. Prog. Device Circuits Syst. **8**, 233–235 (2016)
5. Xibin, W.: PLC-based SCADA system for oil storage and application. In: International Conference on Electric Information and Control Engineering, Vol 1, pp 1–3 (2011)
6. Ioannides, M.G.: Design and implementation of PLC-based monitoring control system for induction motor. IEEE Trans. Energy Conv. **19**, 469–476 (2004)
7. Shankar, K.G.: Control of boiler operation using PLC-SCADA. In: Proceedings of the International MultiConference of Engineers and Computer Scientists, Vol. II, pp. 19–21 (2008)
8. Dong-Il: Dependence of machining accuracy on acceleration/deceleration and interpolation methods in CNC machine tools. In: IEEE Industry Applications Society Annual Meeting, Vol. 3, pp. 1898–1905 (1994)
9. Pradhan, G.: Automation of tank level by using PLC and SCADA/HMI. Int. J. Adv. Res., Ideas Innov. Tech. **4**, 1935–1943 (2018)
10. Vosough, S.: PLC and its applications. Int. J. Multidisc. Sci. Eng. **2**, 41–46 (2011)
11. Wagner, V.E.: Power quality and factory automation. IEEE Trans. Ind. Appl. **26**, 620–626 (1990)

12. Saeed, A.U.A.: Industrial applications of PLCs in Bangladesh. Int. J. Sci. Eng. Res. **3**, 1–4 (2012)
13. Erickson, K.T.: Programmable logic controllers. IEEE Potent. **15**, 14–17 (1996)
14. Rao, B.K.N.: Handbook of Condition Monitoring, 1st edn. Elsevier Adv. Tech., Oxford (1996)

A Study of Localization in 5G Green Network (5G-GN) for Futuristic Cellular Communication

Devasis Pradhan, P. K. Sahu, Rajeswari, and Hla Myo Tun

Abstract The fifth-generation (5G) remote environment will be fundamental for a horde of new applications dependent on precise area mindfulness and other logical data. Such a remote environment will be empowered by cutting-edge 5G remote innovations coordinated with existing advancements for the Internet-of-things (IoT) and the worldwide route satellite framework. With immense mm-Wave range and tight shaft reception apparatus innovation, exact position area is currently conceivable in 5G and future portable correspondence frameworks. As yet being a field being developed, a restriction is relied upon to be completely unavoidable in the following not many years. Albeit the improvement of such strategies is driven by the commercialization of area-based administrations (e.g., route), its application to help cell the executives are considered to be a vital methodology for improving its flexibility and execution. This paper gives a depth of the concept, requirements, and signal processing advancement in localization for accurate positioning.

Keywords 5G · Green network · Distributed localization · Location-awareness · Strategies · Positioning · Global transformation

D. Pradhan (✉) · Rajeswari
Department of Electronics & Communication Engineering, Acharya Institute of Technology, Bengaluru, Karnataka, India
e-mail: devasispradhan@acharya.ac.in

Rajeswari
e-mail: rajeswari@acharya.ac.in

P. K. Sahu
National Institute of Technology, Rourkela, Odisha, India
e-mail: pksahu@nitrkl.ac.in

H. M. Tun
Department of Electronic Engineering, Faculty of Electrical and Computer Engineering, Yangon Technological University, Yangon, Myanmar
e-mail: hlamyotun@ytu.edu.mm

B. Sikdar et al. (eds.), *Proceedings of the 3rd International Conference on Communication, Devices and Computing*, Lecture Notes in Electrical Engineering 851,
https://doi.org/10.1007/978-981-16-9154-6_43

1 Introduction

For cell organizations, area administration, otherwise called cell phone following, is upheld in 2G and 3G organizations through radio asset control (RRC), radio asset area administrations convention (RRLP), and IS-801 to meet the prerequisites of crisis administrations and business applications [1]. In the current 4G long haul advancement (LTE) norms, three autonomous handset-based situating strategies, i.e., helped GNSS, noticed time difference of arrival (TDOA), and upgraded cell-ID (UCID), are upheld [2], where LTE Positioning Protocol (LPP) is executed to empower situating over LTE. The observing of these networks, progressively normal and one of the normal key situations in 5G, infers significant difficulties [3] because of the exceptionally powerful nature of their client circulations, their quick evolving execution, inclusion covering, and truly factor traffic interest. Thusly, the viability of components that are simply founded on network execution, similar to the ones followed by past approaches, is exceptionally reduced.

Five problematic advancements would be embraced in 5G, i.e., gadget-driven designs, millimeter wave, massive—MIMO, more brilliant gadgets, and local help for machine-to-machine (M2M) correspondences. The vast majority of them would be helpful for limitations. The 5G will bring high exactness situating to indoor situations while additionally giving preferred situating precision outside over conceivable with LTE or GNSS alone [4]. It is normal that numerous highlights valuable for situating can be separated from the predetermined components than just the proposed highlights during the normalization. For example, fingerprinting, radio organization streamlining, delicate data extraction, and so on [1, 2]. It is likewise conceivable to utilize signs and estimations characterized for versatility and radio asset the executives for situating. Such empowering influences can be appropriate for situating with regard to 5G-Green Network (5G-GN).

2 5G-Green Network

The 5G Green Network (5G-GN) is a key empowering innovation to full the necessity of information transmission. With the limited expansion in the number of clients and their requests for quality assistance, energy utilization is relied upon to very increment. Driving cell networks with environmentally friendly power sources is an idea of green correspondence. This energy effectiveness can be conceivable through the energy reaping strategies as referenced like, range sharing, millimeter wave, D2D correspondence, super thick organization, network-driven methods, huge MIMO, IoT empower network, femtocells, and like Cloud RAN. Figure 1 shows an ecosystem of the 5G Green Network.

An extra truth of green correspondence is energy collecting which upholds energy transmission at far-off access. The energy gathering arrangements the utilization of sunlight-based energy, wind energy, and other ecological fuel hotspots for charging

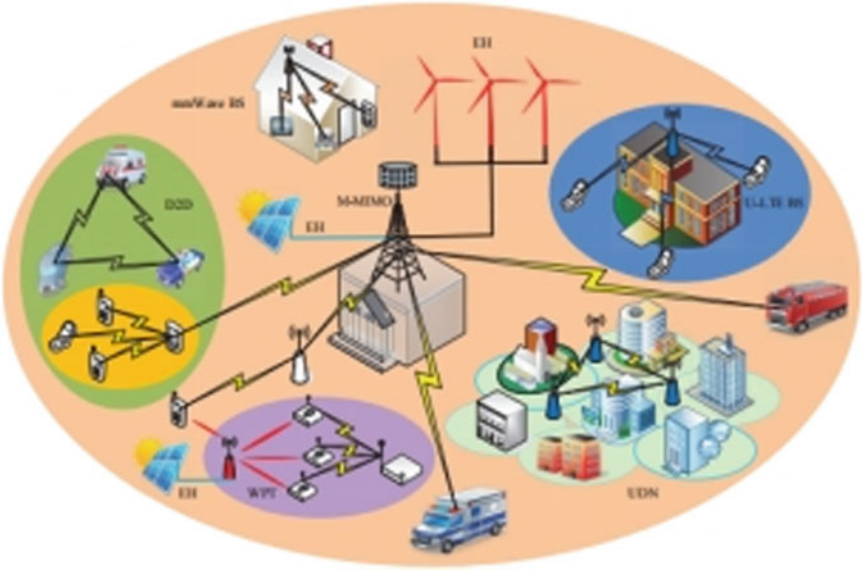

Fig. 1 An ecosystem of 5G-Green network for futuristic uninterrupted communication

the force station. In another manner, the radio recurrence signals obstruction which is an ominous marvel, likewise the previously mentioned complex impedance in the phone area is considered as a wellspring of environmentally friendly power energy. It tends to be utilized as energy collecting gadgets to improve the lifetime of the force source and productivity of the network. Figure 2 shows the classification of Green Network.

Fig. 2 Classification of 5G-Green Network (5G-GN)

2.1 On-Grid Base Station (ON-GBS)

In the on-grid network, the base stations are associated with the matrix. The base station is associated with the force lattice and those associated with the savvy network.

2.2 Off-Grid Base Station (OFF-GBS)

In the off-grid network, the base stations are not associated with the framework. The other sustainable assets are utilized to give capacity to the base station. They are not prepared to grant fuel sources to one another, and the possible coordinated effort incorporates supporting each other distantly by changing their sent force or conceivably offloading customers. The objective of the green organization is improving the energy asset thusly which can support the administrations to the end-clients.

3 Localization Techniques

On a fundamental level, any sign spreading in a remote climate characteristically passes on position-subordinate data that can be abused for limitation. Such position-subordinate data can be separated from estimations of sign measurements like got signal strength, Time of Arrival (TOA), Angle of Arrival (AOA), stage, or mixes of them, contingent upon the radio innovation. One or then again numerous collectors process signal estimations as for one or different reference transmitters and afterward construe the situation through a limitation calculation.

3.1 Trilateration

The positioning gauge is acquired by converging mathematical structures, for example, circles or hyperbolas, made by distance or point estimations between the terminal and the reference transmitters or collectors. A few sorts of estimations can be utilized, like time of arrival (ToA), time distinction of arrival (TDoA), direction or angle of arrival (DoA or AoA), and received signal strength.

3.2 Fingerprinting

The calculation depends on tracking down the best counterpart for a specific sign estimation, like RSS, time postponement, or channel defer spread, from an information base of fingerprints. Each unique mark is related to a particular area.

3.3 Proximity

The realized transmitter position is doled out to be the situation of the terminal. A model is a cell-ID strategy, where the position given is one of the serving base stations.

3.4 Dead Reckoning (DR)

DR procedure depends on inertial estimation unit sensors; the sensor can follow target development by the prepared accelerometer, gyrators, and magnetometers. Knowing the objective's speed at a known area, the position is refreshed by adding the assessed uprooting to the recently assessed area. Be that as it may, it requires an exact introductory situation to stay away from mistakes, despite the fact that, since there are no outer reference signals is utilized for amendment, blunders are aggregated after some time. Half breed methods are utilized to have more precise outcomes (Table 1).

4 Localization in 5G-Green Network (5G-GN)

5G is showing up around 2022. Contrasted with current portable correspondence frameworks, new advancements would be received. These advancements may give 10–100× higher client information rate, 1000× higher portable information volume per region, 10–100× higher number of associated gadgets, 10× longer battery lifetime, and 5× decreased start to finish inertness [5]. Aside from these accomplishments identified with interchanges, it has been accounted for that network-based restriction in three-dimensional space would be upheld in 5G, with precision from 10 m to under 1 m on 80% of events, and better than 1 m for inside [1, 2, 4]. Utilizing such precise area data, 5G would be the original to profit by restriction in remote organization plan and improvement. The principle leaps forward in 5G is because of the work of huge different info various yield (MIMO) beamforming and millimeter wave (mm-Wave) signals.

Table 1 Techniques and technology used in localization for 5G Green Network

Technique	Technology	Cost	Coverage	Method	Accuracy (m)
Trilateration	Satellite	High	Floor level	TOA & TDOA	3–5
	Magnetic based	Low	Floor level	–	2
	Acoustic	Low	Room level	TOA	1–2
	Infrared	Medium	Room level	TOA	1–2
	Wi-Fi	Low	Floor level	RSS	1–5
	ZigBee	Medium	Floor level	RSS	3–5
	Bluetooth	Low-medium	Around 10 m	RSS	2–5
	Ultra-wideband	High	Few meters	TOA, TDOA, RSS	0.01–1.0
	RFID	Low	Room level	RSS	1–5
	Cellular network	Low	80 km	RSS, TOA	2.5–25
Fingerprinting	Magnetic based	Low	Floor level	-	2
	Wi-Fi	Low	Floor level	TDOA	1–5
	ZigBee	Medium	Floor level	AP ID, RSS	3–5
	Bluetooth	Low-medium	Around 10 m	TOA	2–5
	RFID	Low	Room level	AP ID, RSS	1–5
	Cellular network	Low	80 km	RSS, TOA	2.5–25
Proximity	Infrared	Medium	Room level	TOA	1–2
	Wi-Fi	Low	Floor level	AP ID, TDOA	1–5
	Bluetooth	Low-Medium	Around 10 m	AP ID, TOA	2–5
	RFID	Low	Room level	AP ID, RSS	1–5
	Cellular network	Low	80 km	TOA	2.5–25
Dead reckoning	Inertial	Low	Floor level	–	2

The utilization of mm-Wave brings a two-overlap advantage: enormous accessible data transfer capacity and the likelihood to pack countless reception apparatus components even in little spaces (e.g., in a cell phone). An enormous number of radio wire components empowers monstrous MIMO and extremely exact beamforming. This will make conceivable the presentation of single-anchor approaches giving

cm-level and degree-level precision in 6D situating (3D position and 3D direction) [2], consequently conquering the issue of conveying a repetitive specially appointed foundation which is, these days, a significant bottleneck for the far reaching selection of indoor confinement frameworks.

5 Enabling Technologies Helps in Localization

5.1 Small Cell

Cell size has contracted from many square kilometers in original (1G) cell organizations to parts of a square kilometer in metropolitan zones to date. In 5G, there would be settled little cells, for example, picocells (range under 100 m) and femtocells (WiFi-like reach), as well as appropriated receiving wire frameworks (comparable inclusion to picocells) [5–10]. In little cells, radio channels are overwhelmed by the LOS-way.

5.2 Higher Frequencies and Signal Bandwidths—MIMO

For a sign with data transfer capacity B (Hz) which is a lot slower than the middle recurrence Fc (Hz) and claims a consistent sign to-clamor proportion (SNR) over the sign data transfer capacity, where Ts is the term of the sign. This demonstrates that higher frequencies, what is more, signal data transfer capacity improve the TOA estimation precision. Additionally, higher sign data transmissions permit a superior goal of multi-path segments, which builds the likelihood to discover LOS way and hence diminishes the blunder brought about by multi-path inclinations [8, 9]. Higher transporter frequencies, specifically in the mm-wave range, are overwhelmed by the LOS gatherings since any NLOS way is inclined to be obstructed. This diminishes the inclination brought about by abusing NLOS ways. Moreover, higher frequencies empower monstrous MIMO plans, which could give additional heading estimations by setting different reception apparatuses on singular terminals.

5.3 D2D Communication

Mobile terminals with D2D correspondence ability recognize 5G from the past cellular networks in encouraging high-precision limitation. Through synchronization or channel assessment between MTs, inter-node estimations can be separated to infer area data comparative with one another. As the quantity of associated MTs builds,

the inter-node estimation number increments with the square of the MT number [11–13]. Since associated MTs are close, more LOS ways with adequate SNR could be seen to substitute the weak NLOS estimation from inaccessible BSs. Moreover, D2D interchanges permit the trading of fundamental information, which can be utilized to circulate the limitation task, share channel data, move area data, and set up secures (terminal with known areas). Basically, a helpful limitation would be a credulous decision in 5G- Green Network (5G-GN).

6 Strategy for 5G-Green Network Operation

The exhibition of restriction in 5G relies upon the communicating energy, signal transmission capacity, network math, and channel conditions. Such factors are driven by the organization activity methodology, which decides the portion of assets, the organization hubs from which the estimations are taken, and the sending of versatile hubs and base stations [13, 14]. Organization activity systems for effective limitation and the route can be sorted into a few functionalities, including hub prioritization (for example prioritization systems for dispensing communicating assets like force, transmission capacity, and time to accomplish the best compromise between asset utilization and confinement exactness), hub actuation (for example initiation techniques for deciding the hubs that are permitted to make between hub estimations so the restriction precision of the whole organization is expanded), and hub sending (arrangement systems for deciding the places of new hubs in the organization so the confinement exactness of certain current hubs can be maximally improved).

7 Technical Challenges

As per the requirement of the end-user of any technical system number of challenging demands need to be identified. Some technical challenges were discussed as follows.

7.1 Heterogeneous Network

Emerging from the wide assortment of likely applications, the test of heterogeneity must be examined. In contrast to GNSS and cell organizations, where a solitary innovation stage is equipped for supporting a very wide scope of utilization situations, a variety of (remote) advances will be expected to help area mindful electronic frameworks with the presentation necessities laid out above [15, 16]. Cell phones are a drastically more remarkable stage that as of now offers a scope of remote interfaces and other sensors supporting restriction. Future remote standards, which

are at present being created under the mark of 5G frameworks will at last offer a limitlessly upgraded restriction exactness and dependability.

7.2 Multi-path Propagation

For radio-based situating frameworks, multi-path engendering is viewed as the key actual test blocking the execution of 10 cm-level position exactness. This applies likewise to indoor frameworks and to worldwide route satellite frameworks (GNSS)–based vehicular applications [16].

7.3 LOS Availability

The coherence of administration is emphatically identified with the accessibility/permeability of the foundation, for example, reference point radio signs. On account of radio frameworks focusing at the 10 cm-precision levels, even one hindered view of the association might be adequate to intrude on rightness. Optical frameworks depend on the accessibility of guide data to encourage total situating. Changes in the climate may essentially affect guide (and fingerprinting) based methods, bringing about helpless vigor [17–19].

7.4 Synchronization of Time

Radio handsets determine their inward planning reference from free neighborhood oscillators, and as a result of assembling resiliences and temperature varieties, these oscillators go through an arbitrary stage and recurrence float after some time [20]. Synchronizing the circumstance reference of free radio handsets is along these lines a significant essential for frameworks that utilization spread defer assessment. The least difficult strategy is to share a typical nearby oscillator through a committed spine network, yet this arrangement is frequently costly and ailing in sending adaptability.

7.5 Power Consumption

It is one of the principal specialized difficulties in cell phones for IoT applications. These sensors are relied upon to have a long battery life (for example a long time long battery life), in this manner their operational undertakings have a restricted computational weight. Besides, their expense must be low to permit the arrangement of thousands of these gadgets. Given the high sum and low-intricacy of IoT

gadgets, the organization assets designated for these gadgets are likewise exceptionally restricted, like the sign transmission capacity. This diminishes the quantity of relevant area techniques [20, 21].

7.6 Hardware Implementation of Antenna Array

Huge radio wire exhibit frameworks can essentially improve the accuracy of point-of-appearance-based confinement frameworks. Be that as it may, various moves should be handled both at the equipment space and at the sign preparing area. Right off the bat, completely advanced designs require the acknowledgment of a restrictively high number of RF-to-Base-Band chains. In this manner, novel blended simple advanced structures should be conceived, for example, misusing RF exchanged receiving wire plans or stage shifter procedures in the simple area [18–20]. Additionally, higher quantization commotion levels are seen by utilizing minimal effort A/D converters. Energy utilization is additionally an issue that is exacerbated in enormous reception apparatus exhibits where a monstrous measure of information should be prepared. Besides, suitable radio wire setups must be concentrated to meet tough actual space constraints. Denser radio wire clusters present shared coupling, inconsistent gains, and stage reaction impacts that require an improved plan and adjustment procedures.

8 Signal Processing Advancement (SPA)

Limitation precision got by SVE-put together techniques depends vigorously with respect to the nature of such SVEs, which corrupts in remote conditions, for example within the sight of multi-path and NLOS that lead to estimation predispositions [22]. To adapt to remote proliferation weaknesses, ordinary limitation approaches center around improving the assessment of single qualities. Strategies to refine the SVE have been misused by depending on models for SVEs mistakes (e.g., the predisposition initiated by NLOS conditions) recently, new limitation methods have been built up that depends on a bunch of potential qualities instead of on a solitary distance gauge (DE), alluded to as delicate reach data [23]. To improve the confinement execution it is vital for plan restriction networks that abuse delicate data, like SRI or delicate point data (SAI), along with natural data, for example, context-oriented information including an advanced guide, dynamic model, and client's profiles [24].

The 5G and IoT situations offer the likelihood to abuse various sensors in conditions with tough impediments as far as energy and force utilization. Indeed, the dependability of multi-sensor IoT lies in combining information and estimations

gathered from heterogeneous sensors with low calculation and correspondence abilities [16], and in planning productive organization activity methodologies [25]. Circulated limitation calculations require the correspondence of messages [24–26], which includes high dimensional relying upon the sort of SI. Hence, it is of most extreme significance to create SI dimensional decrease procedures for message passing [27].

9 Positioning Technologies

Lately, the acquaintance of remote advancements focused on various application fields going from cell organizations, IoT, and vehicular interchanges. Simultaneously, new advances like monstrous reception apparatus clusters, mm-Wave, Tera-Hertz, and noticeable light correspondences will be presented in an inescapable way. Every one of them offers various types of estimations and consequently various freedoms for misuse for situating. Particularly IoT networks are asset restricted, implying that energy-effective situating arrangements, even battery-less or latent, are of incredible interest [28].

9.1 mm-Wave and Antenna Array

This ability is getting increasingly significant, particularly for indoor conditions. Indeed, the utilization of just one anchor will permit the misuse of a similar framework utilized for correspondences likewise for situating purposes. This defeats the issue of sending a repetitive specially appointed framework which is, these days, the bottleneck easing back the broad dissemination of indoor restriction frameworks [6–8]. Additionally, it opens new points of view in framework-less IoT situations where the client terminal straightforwardly communicates with objects (labels) sent in the climate by, conceivably, driving up by means of remote force move, imparting, and limiting them moderately to its own position [29–31].

9.2 VLC and mm-Wave Positioning

Blend of visual light correspondence (VLC) and radio correspondence in the unlicensed THz range and mm-Wave up/downlink diverts in unlicensed 30–300 GHz range is a promising arrangement that permits remote correspondence organizations to be sent in structures that can give bit rates more prominent than 10 Gbits/sec, latencies under 1 ms, area exactness under 10 cm, while decreasing EMF levels and obstruction, bringing down energy utilization at transmitter/recipient and expanding User Equipment (UE) energy battery lifetime [5–9]. The principal advantage of such heterogeneous mm-Wave and VLC correspondence frameworks is the accessibility

of broadband communications administrations and indoor confinement of UEs with an exactness better than 10 cm. High situating precision is to be accomplished by joining mm-Wave and VLC innovations in area assessment.

10 Conclusion

Limitation advancements are called to assume a focal part in the plan of 5G correspondence frameworks and IoT remote advancements. Additionally, productive strategies to alleviate/abuse multi-path spread, the identification of view accessibility, or time synchronization plans for independent radio handsets should be created. Notwithstanding that huge reception apparatus exhibit frameworks (liable to be utilized in future 5G frameworks) can fundamentally improve the exactness of point of-appearance based limitation frameworks, specific consideration must be paid to equipment intricacy and cost intricacy contemplation; while power utilization and computational weight end up being key difficulties for IoT -based restriction.

References

1. Witrisal, K., Meissner, P., Leitinger, E., Shen, Y., Gustafson, C., Tufvesson, F., Haneda, K., Dardari, D., Molisch, A.F., Conti, A., Win, M.Z.: High-accuracy localization for assisted living: 5G systems will turn multipath channels from foe to friend. IEEE Signal Process. Mag. **33**(2), 59–70 (2016)
2. Guerra, A., Guidi, F., Dardari, D.: Single-anchor localization and orientation performance limits using massive arrays: MIMO vs. beamforming. IEEE Trans. Wireless Commun. **17**(8), 5241–5255 (2018)
3. del Peral-Rosado, J.A., Raulefs, R., López-Salcedo, J.A., Seco-Granados, G.: Survey of cellular mobile radio localization methods: From 1G to 5G. IEEE Commun. Surv. Tutorials **20**(2), 1124–1148 (2018)
4. Liu, Y., Shi, X., He, S., Shi, Z.: Prospective positioning architecture and technologies in 5G networks. IEEE Network **31**(6), 115–121 (2017)
5. Skolnik, M.I.: Radar Handbook, 2nd ed. McGraw-Hill Professional (1990)
6. Win, M.Z., Meyer, F., Liu, Z., Dai, W., Bartoletti, S., Conti, A.: Efficient multi-sensor localization for the internet-of-things. IEEE Signal Process. Mag. **35**(5), 153–167 (2018)
7. Fargas, B.C., Petersen, M.N.: GPS-free geolocation using LoRa in low-power WANs. In: 2017 Global Internet of Things Summit (GIoTS), June 2017, pp. 1–6
8. del Peral-Rosado, J.A., Lûpez-Salcedo, J.A., Seco-Granados, G.: Impact of frequency hopping NB-IoT positioning in 4G and future 5G networks. In: 2017 IEEE International Conference on Communications Workshops (ICC Workshops), May 2017, pp. 815–820
9. Lin, X., Bergman, J., Gunnarsson, F., Liberg, O., Razavi, S.M., Razaghi, H.S., Rydn, H., Sui, Y.: Positioning for the internet of things: a 3GPP perspective. IEEE Commun. Mag. **55**(12), 179–185 (2017)
10. Colone, F., Pastina, D., Falcone, P., Lombardo, P.: WiFi-based passive ISAR for high resolution cross-range profiling of moving targets. IEEE Trans. Geosci. Remote Sens. **52**(6), 3486–3501 (2014)
11. Bartoletti, S., Conti, A., Giorgetti, A., Win, M.Z.: Sensor radar networks for indoor tracking. IEEE Wireless Commun. Lett. **3**(2), 157–160 (2014)

12. Bartoletti, S., Giorgetti, A., Win, M.Z., Conti, A.: Blind selection of representative observations for sensor radar networks. IEEE Trans. Veh. Technol. **64**(4), 1388–1400 (2015)
13. Bekir, E.: Introduction to Modern Navigation Systems. World Scientific (2007)
14. Hu, G., Zhang, W., Wan, H., Li, X.: Improving the heading accuracy in indoor pedestrian navigation based on a decision tree and Kalman filter. Sensors **20**(6), 1578 (2020)
15. Jung, S.-Y., Hann, S., Park, C.-S.: TDOA-based optical wireless indoor localization using LED ceiling lamps. IEEE Trans. Consum. Electron. **57**(4), 1592–1597 (2011)
16. Chen, Z., Zhu, Q., Soh, Y.C.: Smartphone inertial sensor-based indoor localization and tracking with iBeacon corrections. IEEE Trans. Industr. Inf. **12**(4), 1540–1549 (2016)
17. Wu, X., Shen, R., Fu, L., Tian, X., Liu, P., Wang, X.: iBILL: using iBeacon and inertial sensors for accurate indoor localization in large open areas. IEEE Access **5**, 14589–14599 (2017)
18. Yang, H., et al.: Smartphone-based indoor localization system using inertial sensor and acoustic transmitter/receiver. IEEE Sens. J. **16**(22), 8051–8061 (2016)
19. Vy, T.D., Nguyen, T.L.N., Shin, Y.: A smartphone indoor localization using inertial sensors and single Wi-Fi access point. In: International Conference on Indoor Positioning and Indoor Navigation (IPIN), 2019, 1–7 (2019)
20. Diaz, E.M., Ahmed, D.B., Kaiser, S.: A review of indoor localization methods based on inertial sensors. In: Geographical and Fingerprinting Data to Create Systems for Indoor Positioning and Indoor/Outdoor Navigation, pp. 311–333. Elsevier, Amsterdam (2019)
21. Shu, Y., Bo, C., Shen, G., Zhao, C., Li, L., Zhao, F.: Magicol: Indoor localization using pervasive magnetic field and opportunistic WiFi sensing. IEEE J. Sel. Areas Commun. **33**(7), 1443–1457 (2015)
22. 3GPP, 3GPP TR-2 2.872 : Study on positioning use cases. In: ETSI, Tech. Report 16, 2018. Available: http://www.3gpp.org/
23. Mazuelas, S., Conti, A., Allen, J.C., Win, M.Z.: Soft range information for network localization. IEEE Trans. Signal Process **66**(12), 3155–3168 (2018)
24. Davidson, P., Piché, R.: A survey of selected indoor positioning methods for smart phones. IEEE Commun. Surveys Tutorials **19**(2), 1347–1370 (2016)
25. Subbu, K.P., Gozick, B., Dantu, R.: LocateMe: Magnetic-fields-based indoor localization using smartphones. ACM Trans. Intell. Syst. Technol. **4**(4), 1–27 (2013)
26. Gozick, B., Subbu, K.P., Dantu, R., Maeshiro, T.: Magnetic maps for indoor navigation. IEEE Trans. Instrum. Meas. **60**(12), 3883–3891 (2011)
27. The 3rd generation partnership project (3GPP). Available: http://www.3gpp.org/
28. Savazzi, S., Sigg, S., Nicoli, M., Rampa, V., Kianoush, S., Spagnolini, U.: Device-free radio vision for assisted living: leveraging wireless channel quality information for human sensing. IEEE Signal Process. Mag. **33**(2), 45–58 (2016)
29. Cherian, S.S., Rudrapatna, A.N.: LTE location technologies and delivery solutions. Bell Labs Tech. J. **18**(2), 175–194 (2013)
30. Chiani, M., Giorgetti, A., Paolini, E.: Sensor radar for object tracking. In: Proceedings of IEEE, vol. 106, no. 6, pp. 1022–1041 (2018) (Special Issue on Foundations and Trends in Localization Technologies).
31. 3GPP, 3GPP RP-172795: Handling new SI/WI proposals in RAN. In: ETSI, Tech. Report 12, 2017. Available: http://www.3gpp.org/

Modeling of Apoptotic p53 Protein Pathway for Damaged DNA

Trisha Patra, Sanghamitra Chatterjee, and Soma Barman (Mandal)

Abstract Apoptosis is an organised cell death procedure, necessary for healthy survival of cells in living organisms. p53 protein plays the dominant role in deciding the cell fate once the DNA is damaged. Apoptosis is the last option if the cell is beyond repair. In the present work, dynamics of apoptosis process is studied by formulating mathematical model of the pathway. The behaviour of participating proteins involved in the pathway are converted into ordinary differential equations (ODE) using law of mass action and simulated. The complete apoptotic pathway is transformed into a system model and simulated in order to study the behaviour of apoptosis. The simulation of protein's ODE and system model is performed using MATLAB 2014A platform. The simulated behaviour of proteins is validated with existing literature.

Keywords p53 · Apoptosis · ODE · System model · DNA

1 Introduction

Apoptosis is a highly programmed and regulated cell death process, initiated by tumour suppressor protein, p53 [1]. This process is responsible for organ and body part formation in foetus [2]. It also eliminates cancerous or infected cells and performs essential function in the immune system [3].

The tumour suppressor protein, p53, is responsible for taking necessary steps for healthy existence of cells. It includes DNA damage repair, cell cycle arrest, apoptosis etc. Under normal DNA condition, p53 is present in inactive state. Its activation occurs in response to DNA damage and other cellular stresses [4]. ATM

T. Patra · S. Barman (Mandal) (✉)
Institute of Radio Physics Electronics, University of Calcutta, 92 APC Road, Kolkata 700009, India
e-mail: sbrpe@caluniv.ac.in

S. Chatterjee
Camellia Institute of Technology, Kolkata 700129, India

B. Sikdar et al. (eds.), *Proceedings of the 3rd International Conference on Communication, Devices and Computing*, Lecture Notes in Electrical Engineering 851,
https://doi.org/10.1007/978-981-16-9154-6_44

(ataxia telangiectasia mutated) phosphorylates (activates) the p53 and guides it to take action for damage under stress condition [5]. Once the damage is taken care of, p53 needs to be deactivated to avoid unnecessary death of healthy cells. It is done by Wip1 (Wild-type p53-induced phosphatase 1) protein. Wip1 is a direct transcription target of p53 as well as a deactivator of p53, thus creating a negative regulatory feedback loop [6]. Once the p53 is inactivated, it is degraded by its primary negative regulator, Mdm2 protein which is transcripted from Mdm2-mRNA by p53. This forms second negative feedback pathway.

If the damage is repairable, p53 recruit proteins as applicable. But if it is beyond repair, apoptosis or cell death is the only option. Active p53 protein activates proapoptotic protein (apoptosis activator) BAX and Apaf-1 (Apoptotic protease activating factor-1). BAX works at the cell membrane of mitochondria and forms an opening for the release of Cytochrome C protein into cytoplasm [7, 8]. Apaf-1 combines with Cytochrome C to form a complex called Apoptosome. This structure activates enzyme called Caspase-9. Caspase-9 activates the main eliminator protein Caspase-3 [9]. Caspase-3 acts as a scissor and splits the damaged cells into pieces for elimination [2, 10, 11]. Since the initiation of apoptotic process takes place inside the cell membrane, this type of pathway is called intrinsic pathway [2].

An adult human loses 7000 crore cells everyday due to apoptosis which is a normal phenomenon for existence of human being [1]. Most pharmacological processes, like chemotherapy, proceeds through intrinsic apoptotic pathway [12]. So, the study of apoptosis pathway is very important in cancer research. Stefan Kallenberger and Stefan Legewie mathematically modeled the extrinsic apoptosis pathway induced by death ligands [12]. ODE model for apoptosis was developed by William E, Schiesser where hypoxia or deprivation of oxygen in cells is considered as a stress condition [13].

Understanding the importance of apoptosis process, in this paper, authors have considered the intrinsic pathway. Natural behaviour of each protein and enzyme involved in the process is studied minutely and transformed mathematically into ODEs using law of mass action. A system model is thereby derived for the complete pathway based on Michealis–Menten kinetics and biochemical reactions within the pathway. The ODEs and system model outputs are simulated using MATLAB 2014a platform.

The novelty of the work is two fold; first: we have taken into account each participating protein in the apoptosis pathway to understand their contributions. Second: the pathway is converted into a system model. This approach will help to understand the biological phenomenon and its stages. The contribution of each protein in the pathway and considering pathway as a system might not have been considered by previous researchers.

This paper is organised as follows: In Sect. 2, p53 protein-based apoptosis pathway is briefly discussed and contribution of each protein is highlighted. The mathematical model formulation for each participating protein is elaborated in Sect. 3. Here, ODEs are discussed along with the parameters for calculations. In Sect. 4, system model representation of the pathway is discussed, including its mathematical formulation. In Sect. 5, simulation results are presented and validated. It is followed by conclusion and future scopes of our work.

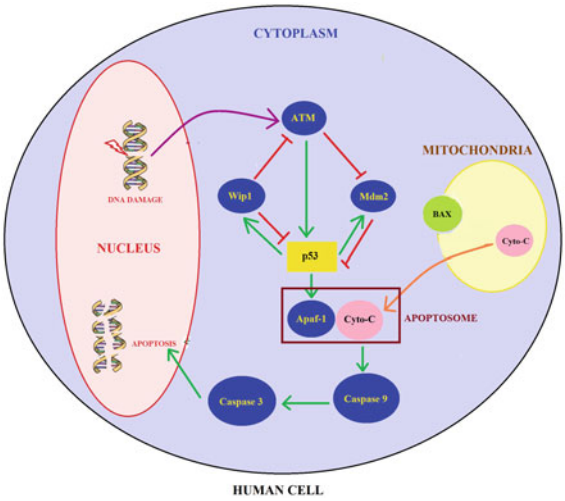

Fig. 1 Apoptosis pathway

2 p53 Protein-Based Intrinsic Apoptosis Pathway

During inactivation of p53, tumour cells resist the treatment [14]. So, activation of p53 is necessary for cancer treatment. Phosphorylation, guided by ATM kinase, activates p53 and prevent it from degradation by Mdm2 [15]. Activated p53 protein acts as a transcriptional agent for Wip1 and takes the decision of damage repair or apoptosis based on level of damage.

The active p53 gains ability to regulate transcription of proapoptotic Bcl2 family members, like BAX [16] as well as proteases like Apaf-1 [8]. BAX protein activation leads to release of Cytochrome C into cytoplasm [7, 8, 16]. Once the BAX protein is free, it blocks the action of anti-apoptotic proteins (IAP), like BCL-XL that tries to prevent apoptosis [17]. Cytochrome C now binds with Apaf-1 and forms a complex called apoptosome that activates Caspase-9 enzyme. Caspase-9 acts as a activating agent for Caspase-3 which is the main agent for fragmentation of DNA [18]. Once the 'problem' (DNA damage) in cells is resolved, p53 needs to be inactivated to avoid undesirable cell deaths. It is done by Wip1 protein by the process called dephosphorylation [19]. Mdm2 protein is a primary negative regulator of p53 and is activated by it. Mdm2 degrades inactive p53 by the process of Ubiquitination [20]. The complete pathway is shown in Fig. 1.

3 Mathematical Representation Of Apoptosis Pathway

In this paper, the representation of ordinary differential equations (ODE) of individual protein involved in the pathway is based on the assumption that the process is dynamic in nature. Equation 1 represents the basic form of rate of concentration change of

reactant X. Each term in the right hand side of the equation represents individual reactions. The rate of each reaction is based on rate law and has appropriate rate constants associated with them [21].

$$\mathrm{d}X/\mathrm{d}t = \text{Synthesis} - \text{Degradation} - \text{Phosphorylation} + \text{Dephosphorylation} \quad (1)$$

3.1 Formulation Of ODE For Proteins

The formulation of mathematical model represents each biochemical reaction in the pathway is based on nature of each participating protein and its role in the process that is discussed elaborately in Sect. 2. Rate of change of concentrations of each protein are given by Eqs. 2–11. Here, W, A, P, M, B, F, C, I, $C9$ and $C3$ stand for Wip1, ATM, active p53, Mdm2, BAX, Apaf-1, Cytochrome C, anti-apoptotic protein, Caspase-9 and Caspase-3, respectively.

$$\mathrm{d}W/\mathrm{d}t = a_1.P - a_2.W \quad (2)$$

$$\mathrm{d}A/\mathrm{d}t = a_3 - a_4.A.W^N/(W^N + T) - a_5.A \quad (3)$$

$$\mathrm{d}P/\mathrm{d}t = k_1.p_i.A^N/(j^n + A^N) - k_2.P - (k_3.M.P)/(j + p_i) \quad (4)$$

$$\mathrm{d}M/\mathrm{d}t = k_4.M_0 - k_5.M - k_6.M \quad (5)$$

$$\mathrm{d}B/\mathrm{d}t = b_1.[B][P] - b_2.[B] \quad (6)$$

$$\mathrm{d}F/\mathrm{d}t = b_3.[P] - b_4.[F] \quad (7)$$

$$\mathrm{d}C/\mathrm{d}t = b_5.[B] - b_6.[C] \quad (8)$$

$$\mathrm{d}I/\mathrm{d}t = -b_7.B \quad (9)$$

$$\mathrm{d}C9/\mathrm{d}t = b_8.([F] + [C])[C9] - (k_7 + k_8.[I]).C9 + b_8.C3 \quad (10)$$

$$\mathrm{d}C3/\mathrm{d}t = b_9.C9.C3 - (k_9 + k_8.[I]).C3 \quad (11)$$

3.2 Parameters and Their Values

The constant terms and their values are presented in Table 1. The values of b_3, b_4, b_5 and b_6 are assumed within the range of other parameter values. Rest of the parameter values were taken from the works of [17, 22, 23].

Table 1 Parameters and their values[17, 22, 23]

Parameter	Description	Value
a_1	p53-induced Wip1 production	$0.0041\,\text{min}^{-1}$
a_2	Wip1 degradation	$0.012\,\text{min}^{-1}$
a_3	ATM production	$0.83\,\text{min}^{-1}$
a_4	Wip1-induced inactivation of ATM	$0.167\,\text{min}^{-1}$
a_5	ATM degradation	$0.125\,\text{min}^{-1}$
N	Hill Coefficient	4
T	ATM inhibition threshold	0.2
p_i	Initial concentration of active p53	0.48 M
k_1	ATM-dependent activation rate of p53	$0.2\,\text{min}^{-1}$
k_2	Dephosphorylation rate of p53	$0.1\,\text{min}^{-1}$
k_3	Basal degradation rate of p53	$0.05\,\text{min}^{-1}$
k_4	Nuclear import rate of Mdm2cp	$0.06\,\text{min}^{-1}$
k_5	Nuclear export rate of Mdm2n	$0.09\,\text{min}^{-1}$
k_6	ATM-dependent degradation rate of Mdm2	$0.05\,\text{min}^{-1}$
M_0	Initial concentration of cytoplasmic Mdm2	$0.4\,\text{min}^{-1}$
j	Michaelis constant of Mdm2-dependent p53 degradation	$0.1\,\text{min}^{-1}$
b_1	Rate of BAX releasing due to p53 activity	$0.1\ \text{uM}^{-1}\ \text{s}^{-1}$
b_2	Basal degradation of BAX	$0.1\ \text{s}^{-1}$
b_3	Rate of Apaf-1 releasing due to p53 activity	$0.1\ \text{uM}^{-1}\ \text{s}^{-1}$
b_4	Basal degradation of Apaf-1	$0.1\ \text{s}^{-1}$
b_5	Rate of Cytochrome C releasing due to BAX activity	$0.1\ \text{uM}^{-1}\ \text{s}^{-1}$
b_6	Basal degradation of Cytochrome C	$0.1\ \text{s}^{-1}$
b_7	IAP inhibition due to Bax activity	$0.02\ \text{s}^{-1}$
b_8	Rate of procaspase-9 activation	$0.01\ \text{uM}^{-1}\ \text{s}^{-1}$
b_9	Rate of procaspase-3 activation	$0.1\ \text{uM}^{-1}\ \text{s}^{-1}$
k_7	Basal degradation of Caspase-9	$0.1\,\text{s}^{-1}$
k_8	Caspase-9 inhibition due to IAP	$1\ \text{uM}^{-1}\ \text{s}^{-1}$
k_9	Basal degradation of caspase-3	$0.1\,\text{s}^{-1}$

3.3 Formulation of System Model

In order to convert a chemical reaction into mathematical form, Michealis–Menten kinetics and steady state assumptions are considered. It is based on association and dissociation reactions and its constants. The apoptosis pathway can be represented by the following reaction

$$\mathrm{C}_9 \underset{\mathrm{I}}{\overset{\mathrm{F{\cdot}C}}{\rightleftharpoons}} \mathrm{C}_3 \tag{12}$$

Here, forward reaction represents the activation process of $C3$ by $C9$ using the apoptosome structure formed by Apaf-1 and Cytochrome C, depicted by $F * C$. The backward reaction explains the negative impact of IAPs in preventing apoptosis process by inhibiting Caspases. Using Michealis–Menten kinetics, the above reaction can be mathematically represented by Eq. 13.

$$\mathrm{d}C3/\mathrm{d}t = [F * C] * C9 - [I] * C3 \tag{13}$$

Using steady-state approximation, we assume change in $C3$ concentration is constant, i.e., $\mathrm{d}[C3]/\mathrm{d}t = 0$. So, Eq. 13 becomes

$$C3 = ([F * C] * C9)/[I] \tag{14}$$

Considering total Caspases, $T = C3 + C9$, Eq. 14 becomes

$$[C3]/[T] = [F * C]/([F * C] + [I]) \tag{15}$$

This is the mathematical form of $C3$, and it resembles the final form of enzyme concentration in Michaelis–Menten kinetics of enzyme–substrate saturation.

3.4 System Model Realisation of Complete Apoptotic Pathway

Figure 2 represents system model realisation of apoptosis pathway, based on Eq. 15. In Eq. 15, total caspase, T is considered as input and Caspase-3 as output of our system model since it acts as a scissor in DNA fragmentation. Two subtractors are used for representing two feedback loops. Feedback loop, $F1$ represents independent degradation pathway of Caspase-3. Loop $F2$ represents inhibition of action of caspases due to IAPs. Integrator block is used for obtaining solution since proteins are considered in their ODE forms in the model. Here, the block representing apoptosome formation, i.e., $[F * C]$, where p53 protein factor involved for initial stages of activation of Apaf-1 and Cytochrome C from BAX. The protein p53 is involved in every step of apoptotic pathway.

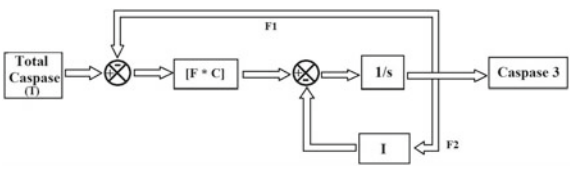

Fig. 2 System model of apoptosis pathway

4 Results and Discussion

The ODEs of individual proteins involved in the pathway are simulated using MATLAB 2014A software. The concentration variation of ATM protein, in Fig. 3a, shows degrading trend. Initially, its concentration rises since it senses the presence of DNA damage. The degradation is due to two factors, first: it is spent during activation of p53. Second: Wip1 protein degrades it once the damage condition is over [24]. In Fig. 3b, the concentration of Wip1 is initially high due to transcription by p53 protein. During cell division, the phosphatase part of Wip1 degrades [25]. Figure 3c shows

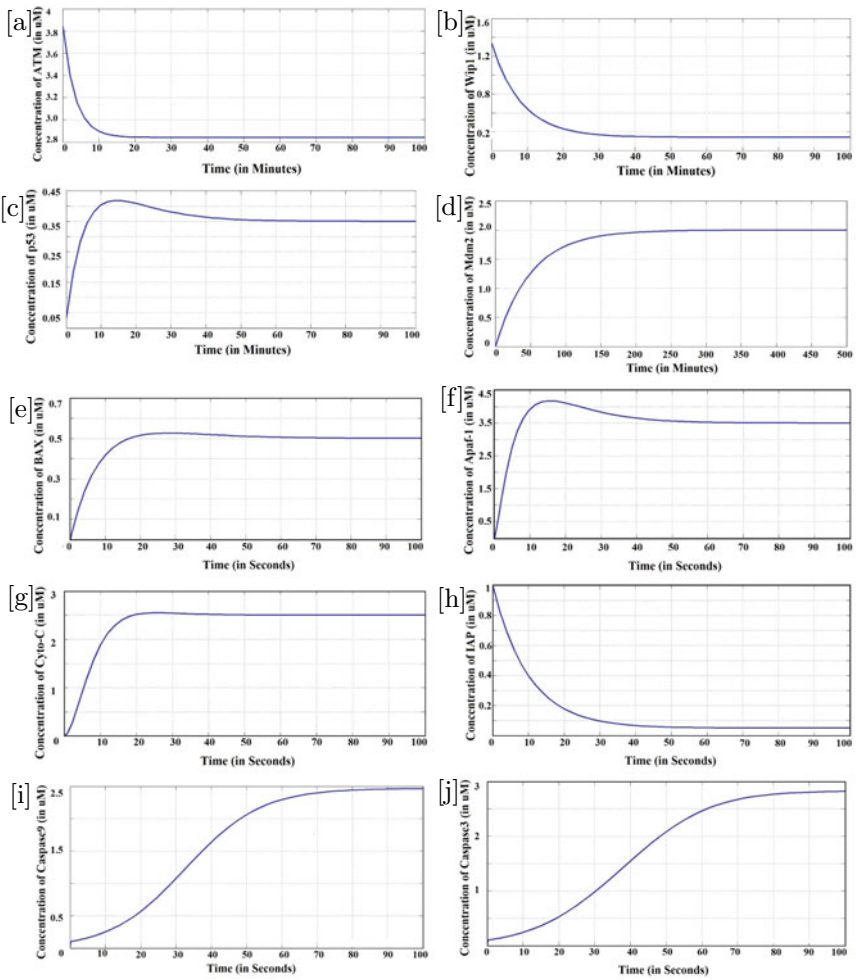

Fig. 3 MATLAB Simulation output rate of change of concentration of **a** ATM, **b** Wip1, **c** p53 and **d** Mdm2, **e** BAX, **f** Apaf-1, **g** Cytochrome C **h** IAP, **i** Caspase-9 and **j** Caspase-3 with time

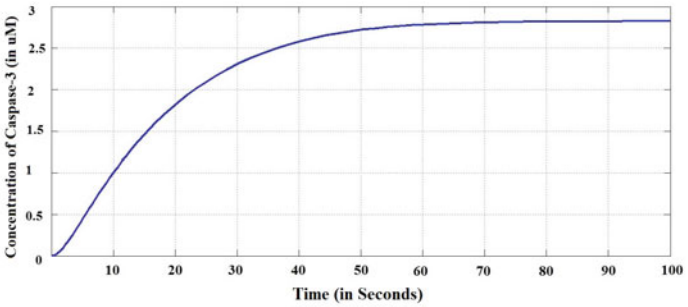

Fig. 4 Simulation result for system model of apoptosis pathway

rate of concentration change of p53 protein. Initial rise represents its activation by ATM protein. After it reaches its peak, it gradually gets involved in DNA damage repair process and hence degrades in small amount before attaining stability [21]. In Fig. 3d, Mdm2 concentration stabilises at a particular value after initial degradation. It points out the fact that once the job is done as a negative regulator for one p53 molecule, it tends to reside in the cell in order to combine with other p53 molecules.

In Fig. 3e, f, rate of concentration change of BAX and Apaf-1 shows stability after initial rise due to activation by p53. Its stable level is very necessary for apoptosis process [7]. Concentration change of Cytochrome C shows stabilisation after its rise due to the action of BAX. Both, Apaf-1 and Cytochrome C, shown in Fig. 3g, need to maintain stable level in order to produce apoptosomes. Anti-apoptotic protein (IAP) needs to be degraded in order to carry out effective apoptosis process. Figure 3h shows necessary degradation of concentration of IAPs due to BAX [17]. In Fig. 3i, the concentration of Caspase-9 shows favourable rise after its activation due to apoptosomes. It validates the works of [9]. Once active, it goes on activating Caspase-3 that executes the apoptosis process. The Caspase-3 particles activates other fellow Caspase-3 particles by the process called Caspase-Cascade [2]. This further increases its concentration. Its output plot, shown in Fig. 3j, verifies the work of Kallenberger and Legewie [12]. So, the ODEs rightfully represents the biological nature of proteins.

The system model, shown in Fig. 2 is simulated using MATLAB 2014A software. The output of the model is Caspase-3, whose presence ensure apoptosis process. The simulation result is shown in Fig. 4. The nature of concentration change resembles the ODE output for Caspase-3, shown in Fig. 3j. Hence, the system model rightfully represents the apoptosis pathway.

5 Conclusion and Future Scope

In this paper, modeling and simulation of p53 protein-based apoptosis pathway is proposed. Apoptosis is an inevitable part of our cell survival. p53, also known as the 'Guardian of Genome', triggers necessary signals and takes appropriate steps for healthy living. So, it becomes very important in cancer research. In our work, each and every important protein involved in the pathway has been taken into account for better understanding of this important phenomenon. Each protein is represented as ODE to highlight its contribution with p53 in the process. The ODE outputs validates the biological nature of the respective proteins and results of previous works by [9, 12, 20, 21]. The system model response of the pathway will help in understanding the biological pathway dynamics without using wet laboratory experiments. The simulated output of protein Caspase-3 resembles its biological nature and works of [12]. Apoptosis process occurs in both plants and animals but follows different pathways [26]. In the present work, apoptosis in human cells is considered.

For real-time biological investigation, animal tissue or cells are used for clinical studies and different chemicals are directly applied on it for experimentation. This is cumbersome as well as costly method and produce toxicity effect on samples. These disadvantages can be overcome by equivalently modeling the pathway and study its dynamics from the response of the model without using wet laboratory experimentation. In future, each block of the system model will be converted into its equivalent electrical circuit model. This will help in validating our results using hardware implementation.

Acknowledgements The authors would like to thank West Bengal Higher Education, Science and Technology and Biotechnology (Science and Technology) funded project "Cytomorphic Circuit Modeling of p53 Protein Pathway for Synthetic Biology Applications" for funding support of the research work.

References

1. Renehan, A.G., Booth, C., Potten, C.S.: What is apoptosis, and why is it important? BMJ (Clinical research ed.) **322**(7301), 1536–1538 (2001). https://doi.org/10.1136/bmj.322.7301.1536
2. Elvire Thouvenot-Nitzan (2016, Oct 18) What is apoptosis? The apoptosis pathways Caspase Cascade [video file]. Youtube. https://youtu.be/vmtk-bAC5E
3. Ekert, P.G., Vaux, D.L.: Apoptosis and the immune system. Br Med Bull. **53**(3), 591–603 (1997). https://doi.org/10.1093/oxfordjournals.bmb.a011632
4. Lakin, N., Jackson, S.: Regulation of p53 in response to DNA damage. Oncogene **18**, 7644–7655 (1999). https://doi.org/10.1038/sj.onc.1203015
5. Jiang, H., Reinhardt, H.C., Bartkova, J., Tommiska, J., Blomqvist, C., Nevanlinna, H., Bartek, J., Yaffe, M.B., Hemann, M.T.: The combined status of Atm and p53 link tumor development with therapeutic response. Genes Development pp. 1895–1909 (2009)
6. Crescenzi, E., Raia, Z., Pacifico, F., Mellone, S., Moscato, F., Palumbo, G., Leonardi, A.: Down-regulation of wild-type p53-induced phosphatase (wip1) plays a critical role in regulating several p53-dependent Functions in premature senescent tumor cells. J. Biol. Chem. **288**, 16212–16224 (2013)

7. Pawlowski, J., Kraft, A.S.: Bax-induced apoptotic cell death. Proc. Natl. Acad. Sci. **97**(2), 529–531 (2000). https://doi.org/10.1073/pnas.97.2.529
8. Robles, A.I., Bemmels, N.A., Foraker, A.B., Harris, C.C.: APAF-1 is a transcriptional target of p53 in DNA damage-induced apoptosis. Cancer Res. **61**(18), 6660–4 (2001)
9. Fussenegger, M., Bailey, J.E., Varner, J.: A mathematical model of caspase function in apoptosis. Nat Biotechnol. **18**(7), 768–74 (2000). https://doi.org/10.1038/77589. Erratum. Nat. Biotechnol. 19(2), 173 (2001)
10. Porter, A.G., Jänicke, R.U.: Emerging roles of caspase-3 in apoptosis. Cell Death Differ. **6**(2), 99–104 (1999). https://doi.org/10.1038/sj.cdd.4400476
11. Caspase 3, the executioner of apoptosis. https://www.novusbio.com/antibody-news/antibodies/caspase-3-the-executioner-of-apoptosis::text=Caspase
12. Kallenberger, S., Legewie, S.: Systems Biology of Apoptosis. Springer, New York (2013). https://doi.org/10.1007/978-1-4614-4009-3
13. Schiesser, W.E.: Differential Equation Analysis in Biomedical Science and Engineering: Ordinary Differential Equation Applications with R. Wiley (2014). https://doi.org/10.1002/9781118705070
14. Symonds, H., Krall, L., Remington, L., Saenz-Robles, M., Lowe, S., Jacks, T., Van Dyke, T.: p53-dependent apoptosis suppresses tumor growth and progression in vivo. Cell. **78**(4), 703–11 (1994). https://doi.org/10.1016/0092-8674(94)90534-7
15. Jiang, H., Reinhardt, H.C., Bartkova, J., Tommiska, J., Blomqvist, C., Nevanlinna, H., Bartek, J., Yaffe, M.B., Hemann, M.T.: The combined status of ATM and p53 link tumor development with therapeutic response. Genes Development **23**(16), 1895–1909 (2009). https://doi.org/10.1101/gad.1815309
16. Hainaut, P., Wiman, K.G. (Eds.): 25 Years of p53 Research. (2005) https://doi.org/10.1007/978-1-4020-2922-6
17. Bensussen, A., Díaz, J.: Dynamics of p53 and Cancer. Evolution of Ionizing Radiation Research (2015). https://doi.org/10.5772/60916
18. Wikipedia contributors. (2021, April 6). Caspase 3. In Wikipedia, The Free Encyclopedia. Retrieved 13:01, June 5, 2021, from https://en.wikipedia.org/w/index.php?title=Caspase3oldid=1016385675
19. Crescenzi, E., Raia, Z., Pacifico, F., Mellone, S., Moscato, F., Palumbo, G., Leonardi, A.: Down-regulation of wild-type p53-induced phosphatase 1 (Wip1) plays a critical role in regulating several p53-dependent functions in premature senescent tumor cells. J. Biol. Chem. **288**(23), 16212–16224 (2013). https://doi.org/10.1074/jbc.M112.435149
20. Shi, X., Qin, K., Liu, Z., Zheng, Y.: A simplified dynamic model for the p53-Mdm2 feedback loop. In: 2013 10th IEEE International Conference on Control and Automation (ICCA), 2013, pp. 264–267. https://doi.org/10.1109/ICCA.2013.6565180.
21. Conrad, E., Tyson, J.: Modeling molecular interactions and non-linear odes, system modeling in cellular biology. In: Szallasi, J.S.Z., Periwal, V. (eds.) System Modeling in Cellular Biology, pp. 97–124
22. Sun, T., Chen, C., Wu, Y., Zhang, S., Cui, J., Shen, P.: Modeling the role of p53 pulses in DNA damage-induced cell death decision. BMC Bioinform. **22**(10), 190 (2009). https://doi.org/10.1186/1471-2105-10-190
23. Zhang, X.P., Liu, F., Wang, W.: Two-phase dynamics of p53 in the DNA damage response. Proc. Natl. Acad. Sci. U S A. **108**(22), 8990-5. https://doi.org/10.1073/pnas.1100600108
24. Eliaš, J., Dimitrio, L., Clairambault, J., Natalini, R.: The p53 protein and its molecular network: modelling a missing link between DNA damage and cell fate. Biochim. Biophys. Acta. **1844**(1 Pt B), 232–47. https://doi.org/10.1016/j.bbapap.2013.09.019
25. Jeong, H.C., Gil, N.Y., Lee, H.S., Cho, S.J., Kim, K., Chun, K.H., Cho, H., Cha, H.J.: Timely degradation of Wip1 phosphatase by APC/C activator protein Cdh1 is necessary for normal mitotic progression. J. Cell Biochem. **116**(8), 1602–12 (2015). https://doi.org/10.1002/jcb.25114
26. Mea, M.D., Serafini-Fracassini, D., Duca, S.D.: Programmed cell death: similarities and differences in animals and plants. A flower paradigm. Amino Acids. **33**(2), 395–404 (2007). https://doi.org/10.1007/s00726-007-0530-3

Design of Dual Band Rejected Square UWB Microstrip Antenna

Surajit Mukherjee, Avisankar Roy, Smarajit Maity, Tapas Tewary, and Sunandan Bhunia

Abstract In this article, a square-shaped dual-band rejected microstrip monopole ultra-wideband (UWB) antenna has been reported. The antenna has been designed with a U-shaped slot on the patch, and a U-shaped metallic parasitic element in the ground plane. The regularly used WLAN band (5.2–5.8 GHz) has been eliminated due to incorporating a U-shaped slot on the radiating patch. Simultaneously the presence of the U-shaped parasitic strip in the ground plane eliminates the X-band downlink frequency (7.25–7.75 GHz). The total dimension of the proposed design is only 24×26 mm^2, which makes the antenna very compact. The operating frequency range has been found as 3–10.7 GHz (VSWR < 2), which signifies that the −10 dB impedance bandwidth of 110% of its center frequency has been obtained. The designed antenna has been simulated in commercially available full-wave electromagnetic solver Ansys HFSS. A bidirectional radiation pattern and very good gain characteristics have been observed for the proposed antenna.

Keywords Ultra-wideband · Dual-notched band · Microstrip antenna · U-shaped slot · Parasitic element

1 Introduction

Trends in wireless communication have created a demand for a wideband system where multiple communication channels can be accommodated. Also, the data rate can be enhanced using a wideband system. The application of an ultra-wideband

S. Mukherjee (✉) · A. Roy
ECE Department, Haldia Institute of Technology, Haldia, West Bengal, India

S. Maity
AEIE Department, Academy of Technology, Haldia, West Bengal, India

T. Tewary
ECE Department, Academy of Technology, Haldia, West Bengal, India

S. Bhunia
ECE Department, Central Institute of Technology, Kokrajhar, Assam, India

B. Sikdar et al. (eds.), *Proceedings of the 3rd International Conference on Communication, Devices and Computing*, Lecture Notes in Electrical Engineering 851,
https://doi.org/10.1007/978-981-16-9154-6_45

(UWB) system is the primary focus of the research community to mitigate the demand. Microstrip antenna with UWB frequency response is highly beneficial in terms of cost and the weight of modern communication devices. Interference with narrowband wireless networks is a significant concern during the practical implementation of the UWB system. The filtering effect on the frequency response of the UWB antenna can eliminate the interference issues.

Researchers have proposed various articles to articulate the band-notch effect over UWB antennas. Microstrip radiating elements of different shapes such as rectangular, circular, hexagonal, square, scarecrow, fractal [1–9] nature have been designed to achieve radiation characteristics over the entire UWB band, which is 3.1–10.6 GHz, as defined by the FCC (Federal Communications Commission). The band notch effects have been obtained by introducing different techniques such as cutting the slots [1–4] on the radiating element, which is the most common method. Other methods like cutting slots in the ground plane [5–7], introducing parasitic elements at the ground layer [8, 9], using shorted stepped impedance resonator (SIR) filter [10], multi-mode resonator (MMR) filter [11] etc. have also been reported. The primary objectives of these proposals were to eliminate the regularly used narrowband applications such as WiMAX (3.2–3.7 GHz), WLAN (5.15–5.85 GHz), downlink frequency for X-band satellite communication (7.25–7.75 GHz) bands etc.

The proposed square-shaped, U-shaped slotted microstrip antenna with added parasitic element on the ground depicts dual-band rejection characteristics. The WLAN frequency band has been eliminated by using a U-shaped slot on the metallic radiating patch. Furthermore, by the inclusion of a U-shaped metallic parasitic strip in the ground plane a band rejection for the downlink frequency X-band satellite communication has been achieved. As a result, the proposed design exhibits bidirectional radiation characteristics with suitable gain.

2 Antenna Design Concept and Analysis

A square-shaped microstrip patch antenna with microstrip line feeding has been taken as the reference antenna for the proposed work. A minimized ground plane with a square notch has been used for this reference monopole antenna shown in Fig. 1. The reference and modified proposed antenna have been designed on a 1.6 mm thick FR4 epoxy substrate having dielectric constant $\varepsilon_r = 4.4$, and loss tangent 0.02. Initially, a U-shaped slot has been etched out from the radiating patch to construct the proposed design. Along with this modification, a U shaped metallic parasitic element has been placed on the ground plane and beneath the patch symmetrically. Several parametric studies have been carried out to determine the dimension of slots and parasitic elements such that the desired result can be obtained. The proposed antenna structure after applied modification has been shown in Fig. 2. The optimum design parameters of the reference and proposed antenna are shown in Table 1. The design steps toward the proposed antenna from the reference antenna have been demonstrated in Fig. 3.

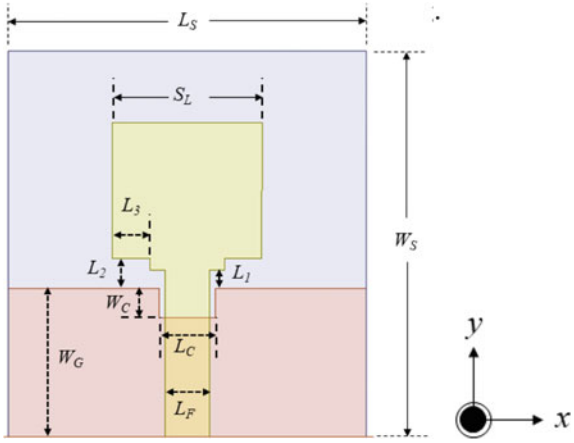

Fig. 1 Structure of the reference antenna

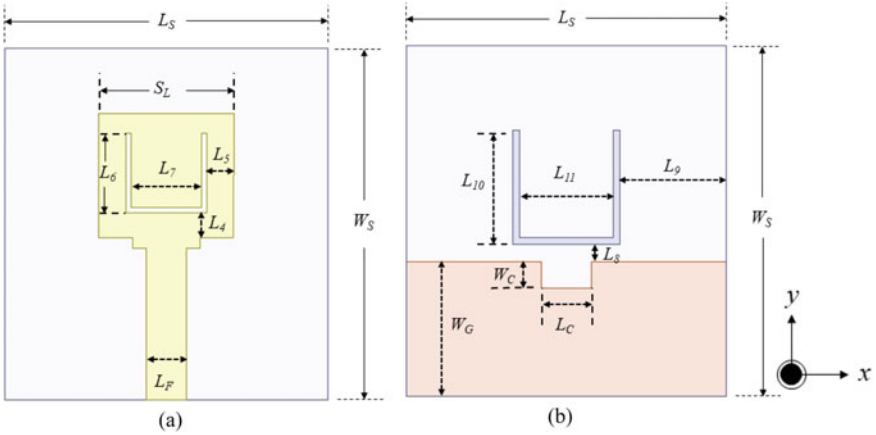

Fig. 2 Structure of the proposed antenna **a** radiating plane **b** ground plane

Table 1 Design parameters of the proposed antenna (units are in mm)

Parameters	Values	Parameters	Values
L_S	24	L_3	2.5
W_S	26	L_4	1.8
W_G	10	L_5	2
L_C	3.8	L_6	5.5
W_C	2	L_7	5.2
L_F	*3*	L_8	1.3
S_L	*10.6*	L_9	8
L_1	*1.2*	L_{10}	8.4
L_2	*0.8*	L_{11}	7

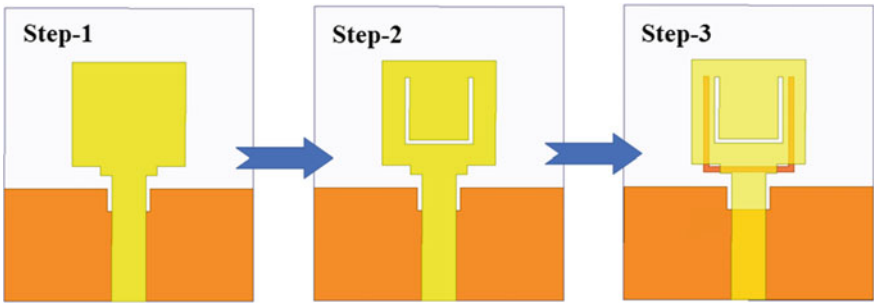

Fig. 3 Design steps for the proposed Antenna

The length of the square patch is 10.6 mm. The overall size of the antenna is compact in nature with having dimension of 24 × 26 mm^2. A 50 Ω microstrip feed line has been considered to excite the radiating element. A rectangular notch in the ground plane under the feedline has been etched out to improve impedance matching of the antenna. Multiple resonant modes are generated in monopole structure having a finite ground plane, and UWB characteristics are achieved due to the overlapping resonant modes. A small gap between the ground plane and the patch along with the staircase feedline has been used for proper input impedance matching.

A U-shaped slot has been etched out from radiating patch to eliminate the WLAN applications for the 5.1–5.85 GHz frequency band. The slots on the patch are behaving like the slot lines. Again, the slot on the patch also behaves like shorted resonant slot line when the guided wavelength at a particular frequency is twice to the total length of the slot. And most of the energies concentrate around the slot at the frequency for which the resonant modes are hampered. As a result, the band-notched characteristics of the antenna appear. In this designed antenna, proposed in this article, a U-shaped metallic parasitic element has been placed at the ground plane under the patch to reject the X-band downlink frequency for the 6.85–7.9 GHz frequency band. It has been observed from the surface current distribution of the designed antenna that the surface currents are mostly accumulated around the metallic strip at the notch frequency, and their directions are opposite among the strip and the radiating patch. So that the resultant radiation fields have cancelled each other, and highly attenuated notch frequency has been produced.

3 Results and Discussion

The reference and proposed antenna have been designed by simulating using commercially available full-wave electromagnetic solver Ansys HFSS. The variation of the S_{11} parameter with respect to frequency for the effects of slot on the patch and parasitic strip in the ground plane separately has been depicted in Fig. 4. Initially, for

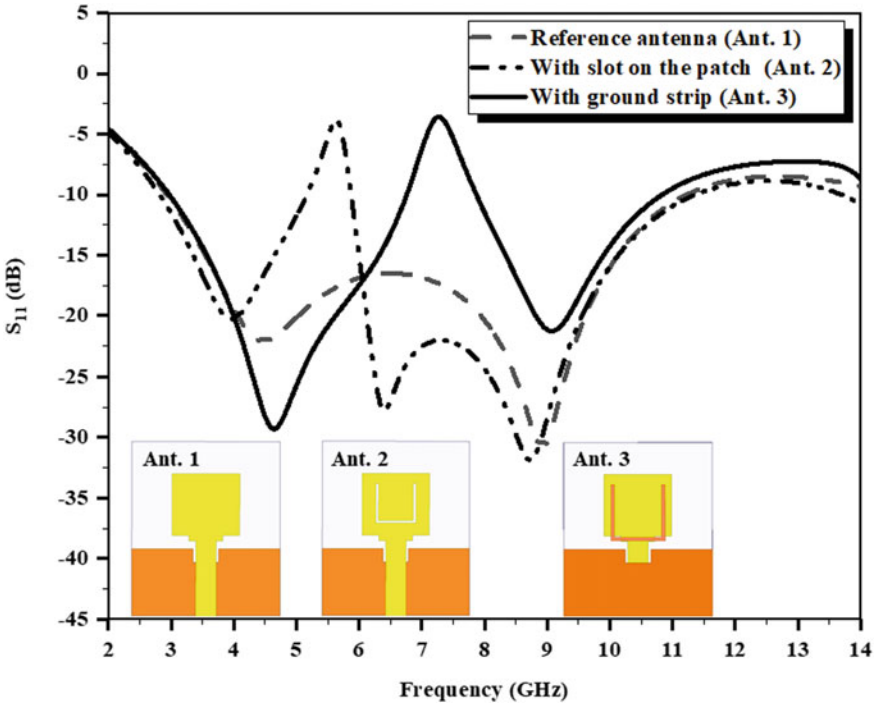

Fig. 4 Reflection coefficient response comparison for applied different modifications

the reference antenna (referred to as Ant. 1 in the figure), a wide impedance bandwidth from 2.95 to 11.15 GHz (VSWR < 2) has been achieved, which covers the UWB frequency spectrum. Next, a band elimination characteristic for the frequency ranges from 5.1 to 5.85 GHz has been observed by only the inclusion of a U-shaped slot on the radiating patch. Reflection coefficient response with the slot has been depicted in Fig. 4 (mentioned as Ant. 2). By calculating the total length of the slot an approximate value of the center notch frequency can be determined. Further, due to the inclusion of the metallic strip in the ground plane, a notch over the frequency range from 6.85 to 7.9 GHz has been realized (mentioned as Ant. 3 in Fig. 3). The center frequency of the notch due to the parasitic element depends upon half of the total length of the element. The mentioned notch bands will able to eliminate the WLAN band and X-band downlink frequency band, respectively. The reflection coefficient response of the proposed antenna has been depicted in Fig. 5. Both reference and proposed antennas have a wide impedance bandwidth of 116%. The simulated results of both reference and proposed antennas are shown in Table 2. The realized gain at the center frequencies of the two band-notches has been noted as −8 dBi and −3.5 dBi for WLAN and X-band downlink bands, respectively. The variation of gain and VSWR of the proposed design is shown in Fig. 6. The simulated surface current distribution for the notch-bands center frequencies (5.5 GHz and 7.5 GHz)

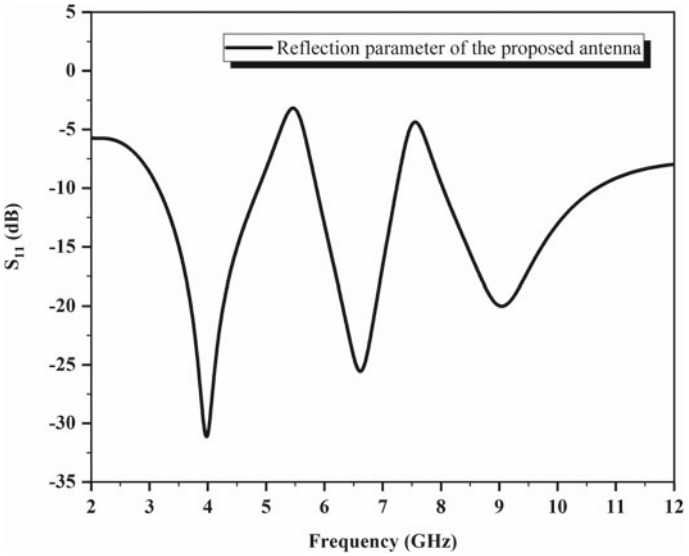

Fig. 5 Reflection coefficient response of the proposed antenna

Table 2 Simulated results of the reference and proposed antenna

	Bandwidth (GHz), %	Rejection band at lower band (GHz)	Rejection band at higher band (GHz)
Ref. antenna	2.95–11.15, 116%	–	–
Proposed antenna	2.9–10.95, 116%	4.95–5.9	7.2–7.95

has been depicted in Fig. 7. It can be witnessed that the modifications applied over the reference antenna are responsible for the notch effects. The simulated E-plane radiation patterns for the proposed antenna at 4 GHz, 6.6 GHz, and 9.2 GHz are shown in Fig. 8a–c with both co-polarization and cross-polarization characteristics. The proposed antenna possesses a good bidirectional radiation pattern.

The total length of the slots may be approximately calculated as half guided wavelength at the center notch frequency. From the simulated current distribution of the designed antenna shown in Fig. 7, the center notch frequency for the slots may be predicted by the equation [4],

$$f_{\text{Notch}} = \frac{c}{2L_s\sqrt{\frac{\varepsilon_r+1}{2}}} \tag{1}$$

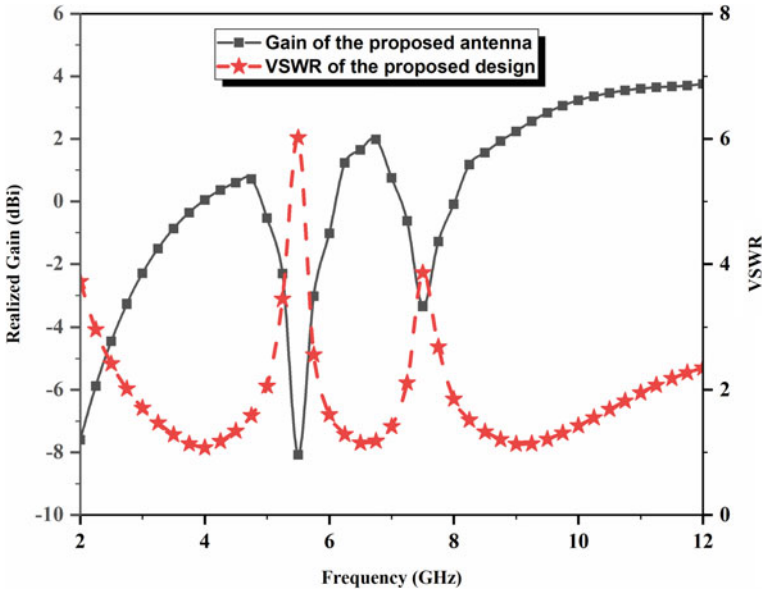

Fig. 6 Simulated realized gain and VSWR of the antenna

where c is the speed of light in free space, ε_r is the dielectric constant of the substrate, and L_s is the total calculated slot length.

4 Conclusion

The design of an ultra-wideband square-shaped microstrip antenna with dual-band rejection properties has been presented in this literature. The proposed antenna has been designed by simulating using electromagnetic solver Ansys HFSS. The antenna poses a wide −10 dB impedance bandwidth from 2.9 to 10.95 GHz (VSWR $\leq$ 2) which covers the entire UWB range. The elimination characteristics for the two narrow bands namely WLAN (5.15–5.85 GHz) and ITU-defined downlink frequency for X-band (7.25–7.75 GHz) have been achieved by implementing the slot on the patch and addition of parasitic element in the ground plane. The antenna may be used for wideband wireless communication systems.

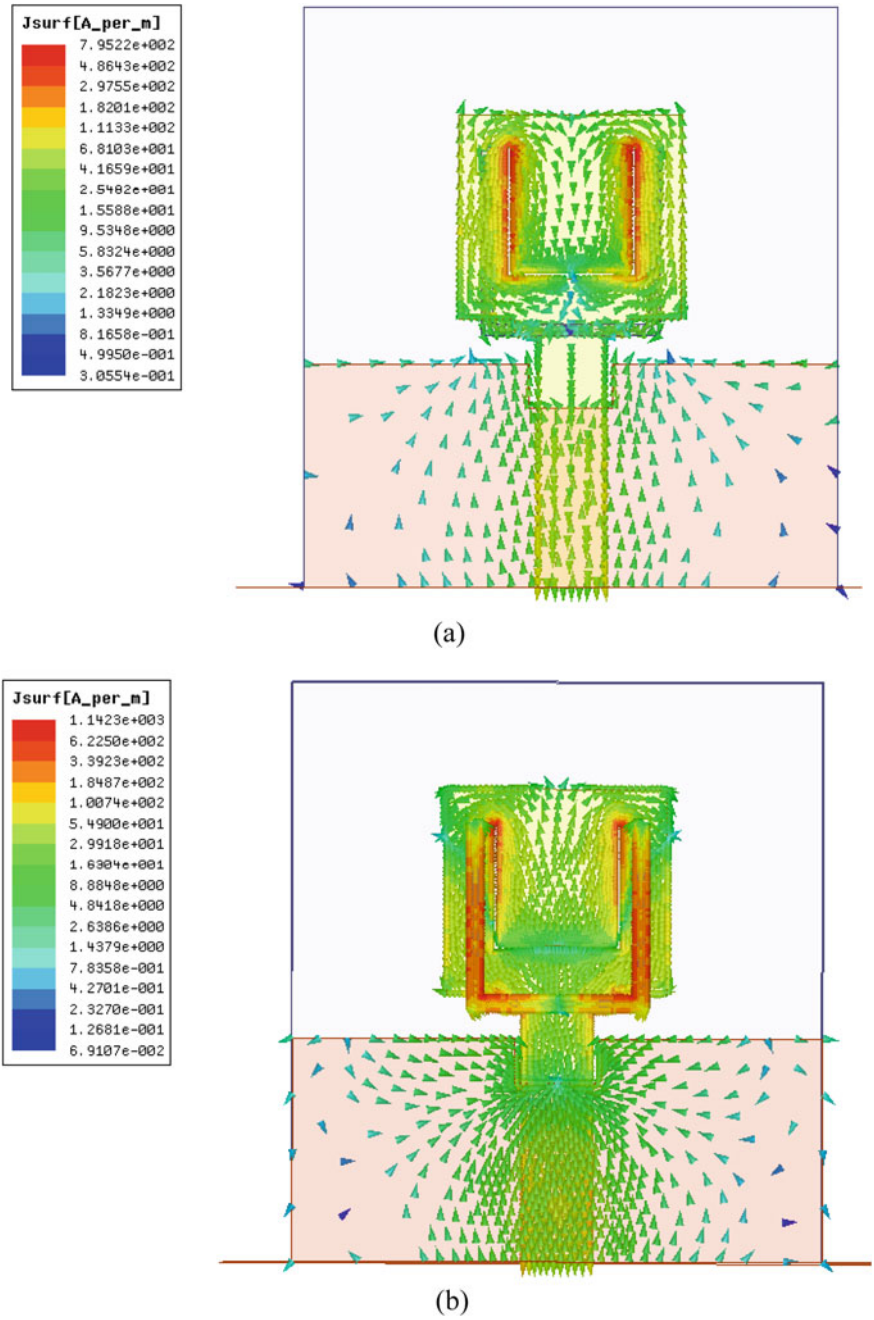

Fig. 7 Simulated vector current distribution at **a** 5.5 GHz, and **b** 7.5 GHz of the proposed antenna

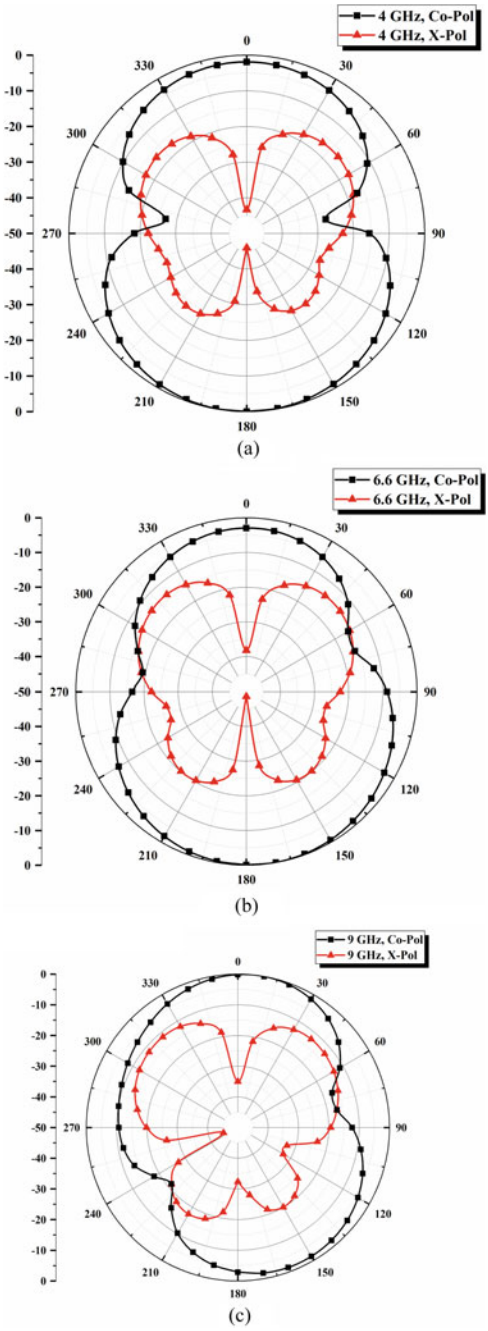

Fig. 8 Radiation pattern of the proposed antenna at **a** 4 GHz, **b** 6.6 GHz, **c** 9 GHz

References

1. Chu, Q.X., Yang, Y.Y.: A compact ultrawideband antenna with 3.4/5.5 GHz dual band-notched characteristics. IEEE Trans. Antennas Propag. **56**(12), 3637–3644 (2008)
2. Zhou, Z.L., Li, L., Hong, J.S.: Compact UWB printed monopole antenna with dual narrow band notches for WiMAX/WLAN bands. Electron. Lett. **47**(20), 1111–1112 (2011)
3. Yadav, A., Sethi, D., Khanna, R.K.: Slot loaded UWB antenna: dual band notched characteristics. AEU - Int. J. Electron. Commun. **70**(3), 331–335 (2016)
4. Hu, Z., Hu, Y., Luo, Y., Xin, W.: A novel rectangle tree fractal UWB antenna with dual band-notched characteristics. Prog. Electromagn. Res. C **68**(September), 21–30 (2016)
5. Ojaroudi, N., Ojaroudi, M., Ghadimi, N.: Dual band-notched small monopole antenna with novel coupled inverted U-ring strip and novel fork-shaped slit for UWB applications. IEEE Antennas Wirel. Propag. Lett. **12**, 182–185 (2013)
6. Zhang, Y., Li, C.: Design of small dual band-notched UWB slot antenna **51**(22), 1727–1728 (2015)
7. Tiwari, R.N., Singh, P., Kanaujia, B.K.: Small-size scarecrow-shaped CPW and microstrip-line-fed UWB antennas. J. Comput. Electron. **17**(3), 1047–1055 (2018)
8. Liu, X., Yin, Y., Liu, P., Wang, J., Xu, B.: A CPW-fed dual band-notched UWB antenna with a pair of bended dual-l-shape parasitic branches. Prog. Electromagn. Res. **136**(January), 623–634 (2013)
9. Azim, R., Islam, M.T., Mobashsher, A.T.: Dual band-notch UWB antenna with single tri-arm resonator. IEEE Antennas Wirel. Propag. Lett. **13**, 670–673 (2014)
10. Sung, Y.: UWB monopole antenna with two notched bands based on the folded stepped impedance resonator. IEEE Antennas Wirel. Propag. Lett. **11**, 500–502 (2012)
11. Gorai, A., Ghatak, R.: Multimode resonator-assisted dual band notch UWB antenna with additional bluetooth resonance characteristics. IET Microwaves, Antennas Propag. **13**(11), 1854–1859 (2019)

Modeling of p53 Protein Pathway Using Markov Chain Based Probabilistic Boolean Network

Mala Sau Giri, Sanghamitra Chatterjee, and Soma Barman Mandal

Abstract The complexity of the gene regulatory network (GRN) depends on the total number of genes involved in a network to regulate a specific cell function. Understanding the regulation of gene functions, a synthetic model of GRN is realized by using Probabilistic Boolean Network (PBN). The deterministic Boolean Network is failed to model correctly the stochastic behavior of the gene network. To overcome such limitations, a Markov Chain Concept-based PBN model is considered in this paper to realize the gene regulatory network synthetically. The biological pathway of the tumor suppressor protein p53 is used as a sample gene regulatory network to develop its synthetic model. The dynamic behavior of genes is investigated by simulating the PBN model in MATLAB 2014 platform.

Keywords Gene · p53 protein · Gene regulatory network · Boolean functions · Synthetic biology · Markov chain

1 Introduction

Genes are basic physical and functional units of heredity, made of the chemical DNA (deoxyribonucleic acid) that codes for specific proteins of the living organisms. Inside a cell, two or more genes form a network for interaction among themselves to control a specific cell function which is commonly known as gene regulatory network (GRN) [1]. Gene regulatory network modeling has played a major role to understand biological systems [2]. Gene regulatory networks are composed of nodes, which mainly target genes or proteins, their regulators, and edges, which control the regulation between genes or proteins [3]. The network is directional because regulatory genes control target genes and, in some cases, target genes themselves act as regulators of other genes inside the network [4]. The molecular activity and

M. S. Giri · S. B. Mandal
Institute of Radiophysics and Electronics, University of Calcutta, Kolkata, India

S. Chatterjee (✉)
Camellia Institute of Technology, Kolkata, India

B. Sikdar et al. (eds.), *Proceedings of the 3rd International Conference on Communication, Devices and Computing*, Lecture Notes in Electrical Engineering 851,
https://doi.org/10.1007/978-981-16-9154-6_46

cellular pathways of living organisms are based on gene–gene interaction [5]. To study the cellular mechanism of biological systems, decipher all hidden information of GRN, and develop a synthetic model of GRN is a new research horizon of system biologists [6]. Gene regulatory network is used to realize the holistic nature of genetic interactions and their role in the presence of different stress functions which also helps to understand the malfunctioning of cellular activity [7]. The disease is nothing but when a normal cell function is disturbed by some external or internal stress. To control disease, one must first be able to understand the natural dynamic of the network and then how the nature of the network is changed under stress. Researchers have developed various mathematical models of GRN using Ordinary differential equations (ODE), Bayesian network, Gillespie algorithm, Markov chain, etc. to study the genetic network behavior [8]. In this paper, the authors have used Probabilistic Boolean Network (PBN) to develop a synthetic model of the p53 protein pathway which plays a significant role in cancer progression. The simulated response of the synthetic model is used to study the behavior of the p53 protein pathway. In the past few decades research has focused on p53 because it acts as a tumor suppressor [9, 10] gene and plays a significant role in cancer therapy. The most frequent genetic changes observed in cancer cells when there is a mutation in the p53 gene lead to uncontrolled cell proliferation and malignancy. Mdm2 protein plays a pivotal role in the regulation of p53 also its excess activity promotes several types of human cancer. The relationship between Mdm2 and p53 is very interesting inside the regulatory pathway and both of them have a decisive role in the case of controlling malignancy [11]. Mdm2 has a significant effect on the p53-Mdm2 regulatory network creating a negative feedback loop to control the activity of p53 since it becomes highly unregulated in absence of Mdm2. Excessive production of Mdm2 may promote cancer in humans without any alteration in p53. So, the combination of p53 and Mdm2 is a very promising domain for the research interest of system biologists [12]. In GRN, the genes are either expressed (1) or not expressed (0) depending on the stress signal. This condition is similar to the two conditions (ON or OFF) of Boolean Network (BN) [11]. In BN gene expression is quantized to only two states: logical ON and OFF, when the gene is expressed, then that state is called "ON" state and when it is not expressed, then it is called "OFF" state, and gene–gene interactions are expressed by different logic functions which are commonly known as Boolean functions in BN. But the stochastic behaviors of the biological network cannot be truly represented by deterministic BN [13]. So, researchers have introduced PBN where probability has been incorporated along with the rule-based structure of GRN to study the dynamic behavior of complex biological systems [14]. PBN helps to interpret the long-term dynamic behavior of any complex biological network. The modeling of BN has been modified using probability to realize the long-term influence (steady-state) of the target gene on other genes in the context of the Markov Chain. The research on PBNs for clinical application is just developing and may be a useful tool for the first-hand diagnosis of disease soon [15, 16]. Since PBN is gaining popularity in GRN and realizing the significance of p53 in cancer research, we have used PBN to realize the synthetic model of the p53 protein pathway.

The paper is organized as follows: Sect. 2 Modeling of p53 pathway using PBN: describe the structure and design methodology of the proposed model of the p53 pathway using PBN. Section 3 Implementation of p53 pathway dynamics using Markov Chain: describes the realization of PBN using Markov Chain Concept. Section 4 Results and Analysis: displays the simulated result of PBN. Finally, the conclusion is drawn in Sect. 5 based on the simulated results in Sect. 4.

2 Modeling of p53 Pathway Using PBN

In Boolean Network, genes are represented by a set of binary-valued nodes, and the state transition of genes is described by a list of Boolean functions. Boolean Network is defined by $G(V, F)$ where $V = \{x1, x2,\ldots, xn\}$, a set of binary-valued nodes, $F = \{F1, F2, \ldots, Fn\}$, a list of sets of Boolean function: $Fi = \{f_1{}^{(i)}, f_2{}^{(i)}, \ldots, f_{l(i)}{}^{(i)}\}$ and $l(i)$ is the number of possible Boolean functions for ith gene, $i \in [1, n]$ [17]. (Each $x_i(t)$ represents the present state of ith gene, where $x_i(t) = 1$ (or 0) indicates that ith gene is expressed (or not). State transition matrix shows the change of state of genes (Present state $x_i(t) \rightarrow$ Next state $x_i(t + 1)) \rightarrow$ Steady-state based on the selection of Boolean functions during state transition. The stochastic behavior of the p53 pathway is represented by PBN where gene interactions are associated with certain probabilities and those interactions are predictor functions. The state transition, i.e., $x_i(t)$ to $x_i(t + 1)$ of target gene is determined by predictor functions with varying probabilities [14]. The tumor suppressor protein p53 pathway can disrupt the fidelity of DNA due to different stress signals, i.e., Gamma or UV radiation, alkylation of bases, depurination of DNA, or reaction with oxidative free radicals [18]. Different feedback mechanisms are actively involved to regulate p53 which in turn controls DNA damage. Therefore, the p53 is considered as the target gene inside the p53 regulatory pathway and others genes that are associated with p53 basically control the expressions of target gene p53, termed as regulatory genes. The p53 pathway is composed of a network of genes, and the interaction of genes within the pathway is significant to understand the behavior of cancer. In this paper, a synthetic model of the p53 pathway is developed using Probabilistic Boolean Network (PBN) and for simplicity, we choose the p53 pathway composed of p53-Mdm2-p14ARF-E2F1 genes.

Figure 1 depicts the p53 pathway and its equivalent diagram where genes are represented by binary-valued variables. The arrowhead indicates activation (stimulation) and the bar head indicates repression/ (inhibition). From Fig. 1, it is clear that p53 activates MDM2, and E2F-1 stimulates p14ARF whereas p14ARF inhibits MDM2, and E2F1 both. Again, p53 inhibits p14ARF. The concentration level of p53 increases the level of MDM2 which in turn decreases the concentration level of p53 and ultimately leads to the destruction of p53. To develop a synthetic model of the p53 pathway some transition rules have been established based on gene–gene interactions (p53-Mdm2-p14ARF-E2F1 interactions). Boolean network $\{G(V, F)\}$ for this selected pathway is designed by assigning $V = \{x1, x2, x3, x4\}$, a set of

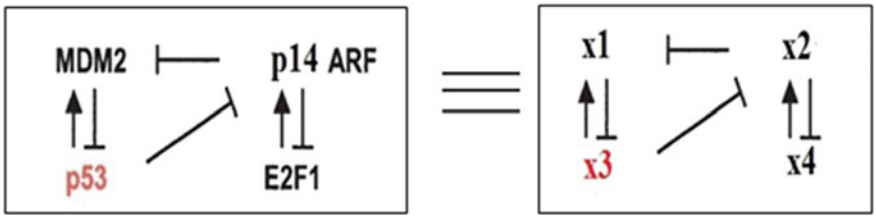

Fig. 1 Schematic diagram of p53GRN with assigned variables

binary-valued nodes and $F = \{F1, F2, F3, F4\}$ a list of sets of Boolean functions. The set $F1$ determines the next state of gene "$x1$" and "$f_j{}^i$" is the Boolean function associated with $x1$ where "j" gives the total number of functions. Boolean network maps the inter-relation between genes which determines the next state of a target gene and its regulators. In our synthetic model, the four genes are represented by four variables as MDM2 $\rightarrow$ $x1$, p14ARF $\rightarrow$ $x2$, p53 $\rightarrow$ $x3$, and E2F-1 $\rightarrow x4$. The prior knowledge of interactions between genes is used here to establish function classes, i.e., $F1$, $F2$, $F3$ and $F4$ where, $F1 = ({f_1}^1, {f_2}^1)$ and $F2 = ({f_1}^2, {f_2}^2)$ and $F3 = {f_1}^3$, $F4 = {f_1}^4$. In the expression, superscripts denote gene numbers and subscripts show gene functions. The next state of gene–gene interaction is controlled by the status of the present state and Boolean functions associated with the selected genes. The present state of $x1$ is represented by $x1(t)$ and the next state by $x1(t + 1)$. From Fig. 1, it is observed that the next state $x1(t + 1)$ depends on the present state $x2(t)$ and $x3(t)$. The next state $x2(t + 1)$ depends on the present state $x3(t)$ and $x4$(t). The next state $x3(t + 1)$ depends on the present state $x1(t)$. The next state $x4(t + 1)$ depends only on the present state $x2(t)$. The following logic expressions are derived based on these relations.

$$x1(t+1) = \overline{x}2(t).x3(t) \tag{1}$$

$$x1(t+1) = \overline{x}3(t) \tag{2}$$

$$x2(t+1) = \overline{x}3(t).x4(t) \tag{3}$$

$$x2(t+1) = \overline{x}4(t) \tag{4}$$

$$x3(t+1) = \overline{x}1(t) \tag{5}$$

$$x4(t+1) = \overline{x}2(t) \tag{6}$$

Boolean functions of different genes are formed by using the above logic expressions. The truth table of GRN is constructed from the above Boolean functions and the present states of four genes respectively.

A 4-bits truth table is constructed assigning $x1(t)$ as first bit, $x2(t)$ as second bit, $x3(t)$ as third bit, and $x4(t)$ as the fourth bit. So total 16 (2^4) combinations (1, 0) are possible to get the values (0,1) of Boolean functions. It has been observed from the above logic expressions that the value of ${f_1}^{(1)}$ depends on $x2(t)$ and $x3(t)$, ${f_2}^{(1)}$ depends on $x3(t)$, ${f_1}^{(2)}$ depends on $x3(t)$ and $x4(t)$, ${f_2}^{(2)}$ depends on $x4(t)$ and so on. In Table 1, columns no. 2 to 5 indicate the present state of genes MDM2, p14ARF, p53, and E2F1, respectively and columns no. 6 to 11 indicate the states of the Boolean functions.

To overcome the deterministic rigidity of Boolean algebra, BN is modified to PBN by introducing a probability factor in each Boolean function. The modified Boolean functions are called predictor functions. The next state of i^{th} gene is determined by all possible predictor functions in F_i, i.e., ${f_1}^{(i)}, {f_2}^{(i)}, \ldots, {f_{l(i)}}^{(i)}$ with probability values ${c_1}^{(i)}, {c_2}^{(i)}, \ldots, {c_{l(i)}}^{(i)}$,where $l(i)$ is the total no. of possible predictor functions associated with the ith gene. The predictor functions and the condition of the present state of the system mainly regulate the p53 pathway which ultimately leads to a steady-state. The block diagram of PBN is shown in Fig. 2.

Where ${c_{l(i)}}^{(i)}$ is the probability that the Boolean function (BF) ${f_{l(i)}}^{(i)}$ is selected for gene i. In the selected pathway, there are total of six Boolean functions (BF) ${f_1}^{(1)}$, ${f_2}^{(1)}, {f_1}^{(2)}, {f_2}^{(2)}, {f_1}^{(3)}, {f_1}^{(4)}$, and the associated probabilities are ${c_1}^{(1)}, {c_2}^{(1)}, {c_1}^{(2)}, {c_2}^{(2)}$,

Table 1 The truth table of p53 pathway showing initial states and associated Boolean functions

Serial No.	$x1(t)$	$x2(t)$	$x3(t)$	$x4(t)$	$f1^{(1)}$	$f2^{(2)}$	$f1^{(2)}$	$f2^{(2)}$	$f1^{(3)}$	$f1^{(4)}$
1	0	0	0	0	0	1	0	1	1	1
2	0	0	0	1	0	1	1	0	1	1
3	0	0	1	0	1	0	0	1	1	1
4	0	0	1	1	1	0	0	0	1	1
5	0	1	0	0	0	1	0	1	1	0
6	0	1	0	1	0	1	1	0	1	0
7	0	1	1	0	0	0	0	1	1	0
8	0	1	1	1	0	0	0	0	1	0
9	1	0	0	0	0	1	0	1	0	0
10	1	0	0	1	0	1	1	0	0	1
11	1	0	1	0	1	0	0	1	0	1
12	1	0	1	1	1	0	0	0	0	1
13	1	1	0	0	0	1	0	1	0	1
14	1	1	0	1	0	1	1	0	0	0
15	1	1	1	0	0	0	0	1	0	0
16	1	1	1	1	0	0	0	0	0	0

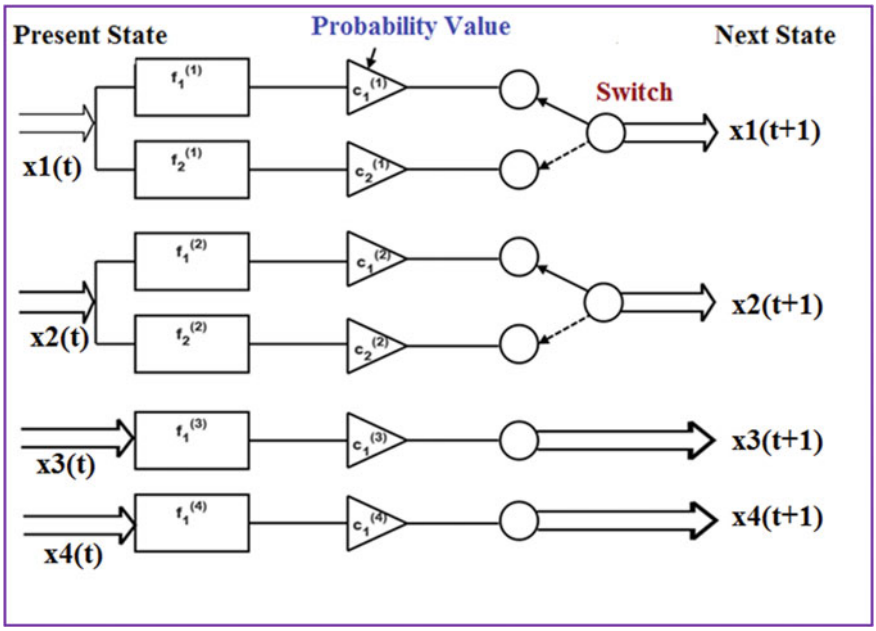

Fig. 2 Block representation of PBN of p53 pathway

$c_1{}^{(3)}$, $c_1{}^{(4)}$, respectively. When the BF is multiplied by the associated probability value, it becomes predictor function $f_1{}^{(x1)}$.

For example, gene $x1$ has two BF $f_1{}^1$ and $f_1{}^2$ and their associated probabilities are $c_1{}^1$and $c_1{}^2$. The predictor function associated with $x1$ is $f_1{}^{x1}, f_2{}^{x2}$ where $f_1{}^{x1} = f_1{}^1.c_1{}^1$ and $f_2{}^{x1} = f_2{}^{(1)}.c_2{}^1$. In GRN during a state transition, the pathway can reach any of the available states from their present state.

The Markov Chain Concept is introduced in BN to convert it into PBN. The derived state transitions matrix of the pathway is used here to implement PBN and using its dynamic behavior of the p53 pathway is modeled [19]. The concept of Markov chain is applied in our application described into some steps as follows:

Step 1: a state set $S = \{s1, s2, \ldots, sr\}$ and the process starts in any one of these states and moves successively from one state to another and each move is called a step.

In our sample p53 network: No. of genes = 4, the total number of states = $16(2^4)$.

A step is a movement from any one of the 16 states to another state at any instant of time.

Step 2: Suppose, the current state of the chain is $\rightarrow s_i$, state $s_j \rightarrow$ the next step of the process or chain moves with a probability P_{ij}, the probabilities P_{ij} are called transition probabilities for movement from i to j states.

Step 3: A transition matrix P is formed based on transition probability, where the entries in the first row of the matrix P (Table 2) represent the transition probabilities for the change of states from 00 to {00, 01, 10, 11}. For, two gene networks, the

Table 2 State transition matrix (P)

Time (t)	Time ($t+1$)			
State	00	01	10	11
00	P_{11}	P_{12}	P_{13}	P_{14}
01	P_{21}	P_{22}	P_{23}	P_{24}
10	P_{31}	P_{32}	P_{33}	P_{34}
11	P_{41}	P_{42}	P_{43}	P_{44}

possible total number of states $= 4(4 = 2^2)$. Where P_{11} represents the probabilities from state 1 to state 1, i.e., state 00 to 00. P_{12} represents the probability value from state 1 to 2 means 00 to 01. Similarly, a matrix of transition probabilities or the transition matrix is formed.

Step 4: A steady-state response is obtained based on the matrix P, where P_{mn} is the state transition probability from state m to state n at time t to $t+1$. As an example, in Table 2, P32 ($m = 3, n = 2$) is the probability of occurrence of changing state from "10" to "01" at a time "t" to "$t+1$".

3 Implementation of p53 Pathway Dynamics Using Markov Chain

A Probabilistic Boolean Network is based on the number of constituent Boolean functions and a probability factor governing the BN which determines the next state. The truth table of BN of p53 regulatory network is modified for PBN by introducing probability values $c_{l(i)}{}^{(i)}$ of the six Boolean functions $f_1{}^{(1)}, f_2{}^{(1)}, f_1{}^{(2)}, f_2{}^{(2)}, f_1{}^{(3)}, f_1{}^{(4)}$ where set of Boolean function is given by $F1 = \{f_1{}^{(1)}, f_2{}^{(1)}\}$, $F2 = \{f_1{}^{(2)}, f_2{}^{(2)}\}$, $F3 = \{f_1{}^{(3)}\}$ and $F4 = \{f_1{}^{(4)}\}$. The probability value of each Boolean function is calculated by considering the total number of "ON" states associated with it.

Transition from $x1(t)$ to $x1(t+1)$ of gene $x1$ depends on Boolean functions $f_1{}^{(1)}$ or $f_2{}^{(1)}$. Here, the probability value of BF $f_1{}^{(1)}$ is determined by total number of "1" present in that particular column under $f_1{}^{(1)}$ divided by "total number of 1" associated with gene $x1$ considering both functions (Table 3). So, the probability of occurrence of $f_1{}^{(1)}$ is controlled by $c_1{}^{(1)} = 0.33(4/12 = 0.33)$. Similarly, the probabilities of occurrence of rest of the Boolean functions are calculated. The Boolean function ($f_1{}^{(1)}$) is multiplied by its probability value ($c_1{}^{(1)}$) and transforms to predictor function $f_1{}^{(x1)}$. State transition matrix of the p53 pathway consisting of four genes is formed using the predictor functions $f_1{}^{(x1)}, f_2{}^{(x1)}, f_1{}^{(x2)}, f_2{}^{(x2)}, f_1{}^{(x3)}$ and $f_1{}^{(x4)}$.Since, there are two predictor functions for each node $x1$ and $x2$, and one predictor function for each node $x3$ and $x4$, there are $2 \times 2 \times 1 \times 1 = 4$ set of PBN given by four network transition functions $f1 = \{f_1{}^{(1)}, f_1{}^{(2)}, f_1{}^{(3)}, f_1{}^{(4)}\}, f2 = \{f_1{}^{(1)}, f_2{}^{(2)}, f_1{}^{(3)}, f_1{}^{(4)}\}, f3 = \{f_2{}^{(1)}, f_1{}^{(2)}, f_1{}^{(3)}, f_1{}^{(4)}\}$ and $f4 = \{f_2{}^{(1)}, f_2{}^{(2)}, f_1{}^{(3)}, f_1{}^{(4)}\}$ with associated probabilities $C1 = c_1{}^{(1)}.c_1{}^{(2)}.c_1{}^{(3)}.c_1{}^{(4)} = (0.33).(0.33).(1).(1) = 0.11$; $C2 = (0.33).(0.67).(1).(1)$

$= 0.22$; $C3 = (0.67).(0.33).(1).(1) = 0.22$ and $C4 = (0.67).(0.67).(1).(1) = 0.45$ respectively are formed. Total probability value is always $1(C1 + C2 + C3 + C4 = 1)$.

As an example, it is observed from the state transition diagram (Fig. 3) that the transition probability from the initial state of the p53 pathway, 0000 to 0011 is $C1$, 0000 to 0111 is $C2$, 0000 to 1011 is $C3$, and 0000 to 1111 is $C4$. Also, from the

Table 3 Truth table of p53 pathway showing initial states and associated Predictor functions with their probabilities

Serial No.	Input states				Output states					
	$xl(t)$	$x2(t)$	$x3(t)$	$x4(t)$	$f_1^{(x1)}$	$f_2^{(x1)}$	$f_1^{(x2)}$	$f_2^{(x2)}$	$f_1^{(x3)}$	$f_1^{(x4)}$
1	0	0	0	0	0	1	0	1	1	1
2	0	0	0	1	0	1	1	0	1	1
3	0	0	1	0	1	0	0	1	1	1
4	0	0	1	1	1	0	0	0	1	1
5	0	1	0	0	0	1	0	1	1	0
6	0	1	0	1	0	1	1	0	1	0
7	0	1	1	0	0	0	0	1	1	0
8	0	1	1	1	0	0	0	0	1	0
9	1	0	0	0	0	1	0	1	0	1
10	1	0	0	1	0	1	1	0	0	1
11	1	0	1	0	1	0	0	1	0	1
12	1	0	1	1	1	0	0	0	0	1
13	1	1	0	0	0	1	0	1	0	0
14	1	1	0	1	0	1	1	0	0	0
15	1	1	1	0	0	0	0	1	0	0
16	1	1	1	1	0	0	0	0	0	0
$C_j^{(i)}$					0.33	0.67	0.33	0.67	1	1

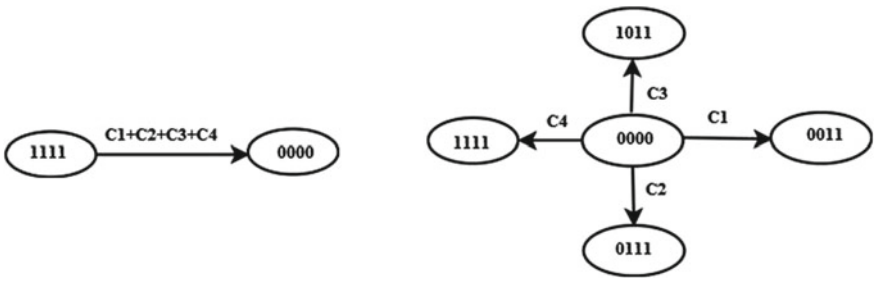

Fig. 3 Transition Probability of state 1111 to 0000 with probability $C1 + C2 + C3 + C4$ and from state 0000 to different states with probability $C1$, $C2$, $C3$, $C4$, where $C1 + C2 + C3 + C4 = 1$

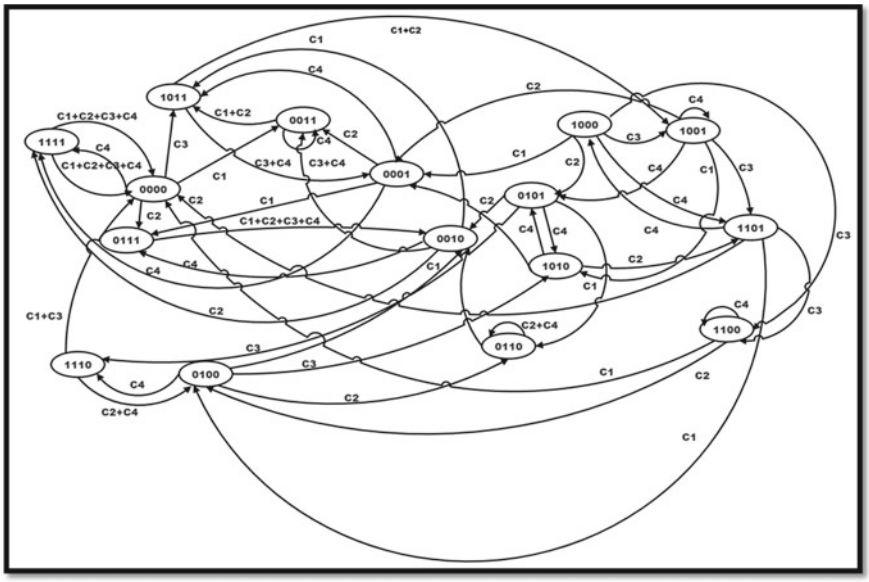

Fig. 4 Graphical Representation of Table 3 of p53 pathway using PBN

initial state 1111 to 0000, the transition probability is $C1 + C2 + C3 + C4$ which are illustrated in Fig. 3.

The state transition diagram of the regulatory network is shown in Fig. 4 where the significance of the number assigned inside each circle are states of network and $C1$, $C2$, $C3$, or $C4$ assigned to each arc shows transition probability.

4 Results and Analysis

The analysis of BN is controlled by the selection of gene functions that is deterministic which is the main limitation of BN. But the natural biological system is stochastic, so a synthetic model of a biological system cannot be perfectly realized using BN because of its deterministic nature. The stochastic behavior of the p53 pathway is modeled by introducing probability in BN which is called PBN. State transition of the p53 pathway from the current state to the next state is regulated by probability. The state transitions of genes involved in the p53 pathway are simulated using Matlab-2014. The probability of occurrence of any state and time taken to reach a steady-state is visualized from Fig. 5. Different states take different times to reach a steady-state which verifies the kinematics of the p53 pathway.

The dynamic characteristics of an individual state of the pathway and the dynamic characteristics of the complete pathway are plotted in Fig. 5a, b respectively.

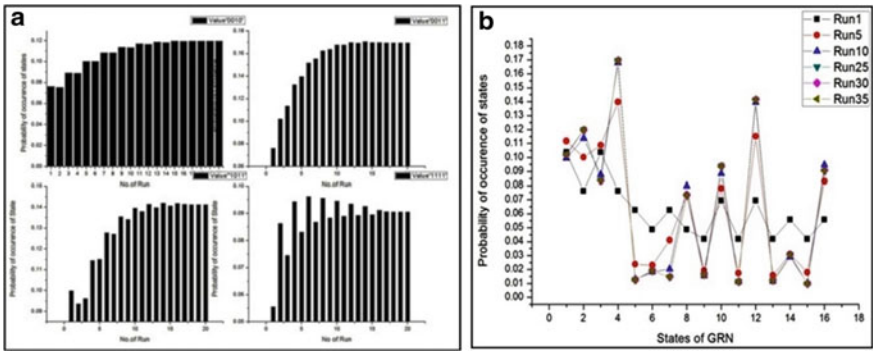

Fig. 5 **a**, **b** Dynamic characteristics of an individual state and Dynamic characteristic of p53 regulatory pathway

The Boolean Network is converted into a Probabilistic Boolean Network (PBN) which is capable to describe the dynamism of the p53 pathway. Here, the p53 pathway is an example of GRN which involves the interaction of four genes.

By using the Markov concept in PBN, the transition matrix for the pathway (GRN) is derived. Initially, it is assumed that all the 16 states of the GRN which is shown in Table 3 have equal probability. The state changes follow the rule: $u(n) = u.\ P^n$ and steady-state response of the GRN is obtained. The result shows that though the initial probability of all the states was 6.25%(1/16 = 0.0625) but after several runs ($n = 35$), the probabilities of the states vary randomly. After several runs, the GRN is reached to a steady-state, i.e., "0011" which indicates the genes $x1$(MDM2), $x2$(p14ARF) attain the highest probability of not to expressed (OFF) whereas the probability of $x3$ (p53) and $x4$ (E2F-1) genes expressed (ON) is 17%. This implies that when p53 is on MDM2 is off and also E2F-1 is on while p14ARF is off in the synthetic p53 pathway which validates the autoregulatory feedback loop between p53 and MDM2 gene in the biological p53 pathway.

Similarly, p14ARF has also deactivated the function of E2F-1 while it is expressed ON. The obtained simulated result of PBN also reflects the same biological phenomena of the p53 pathway. Therefore, a synthetic model of the p53 protein pathway is successfully implemented by using PBN and validates the biological pathway.

When the GRN is disturbed by any internal or external stress, there is a possibility of changing states of the pathway which may be varied from this steady-state probability occurrence. Change in steady-state probability value indicates the presence of stress signal inside the GRN which leads to abnormal gene expressions. The PBN analysis using the Markov concept is a good indicator to detect stress signals in the gene network.

5 Conclusion

This limitation of BN is overcome by Probabilistic Boolean Network. Markov chain's concept is used to describe the stochastic behavior of gene expression. The Markov Chain Concept in PBN is used to derive the state transition matrix of the p53 pathway. To find out the steady-state gene expressions, the dynamic behavior of the p53 pathway is simulated in the Matlab-2014 environment. To test this model, a simple pathway of p53 protein is chosen where only the interaction of four genes is considered. In the future, this concept may further be extended to realize the synthetic model of other biological pathways. This study has potential applications, e.g., p53-based targeted therapies, designing of a protein-based drug, and controlling drug dosages.

Acknowledgements The authors would like to thank West Bengal Higher Education, Science and Technology and Biotech (Science and Tech.) funded project "Cytomorphic Circuit Modeling of p53 Protein Pathway for Synthetic Biology Applications" for partial support of infrastructure.

References

1. Liang, J., Han, J.: Stochastic Boolean networks: an efficient approach to modeling gene regulatory networks. BMC Syst. Biol. **12**(6), 113. http://www.biomedcentral.com/1752-0509/6/113.
2. Rothenberg, E.V.: Causal gene regulatory network modeling and genomics: second-generation challenges. J. Comput. Biol. **26**, 703–718 (2019)
3. Murrugurra, D., Dimitrova, E.S.: Molecular network control through Boolean canalization. J. Bioinform. Syst. Biol. **9** (2015). https://doi.org/10.1186/s13637-015-0029-2
4. Murrugarra, D., Veliz-Cuba, A., Aguilar, B., Laubenbacher: Identification of control targets in Boolean molecular network models via computational algebra. BMC Syst. Biol. **10,** 94 (2016). https://doi.org/10.1186/s12198-016-0332-x
5. Flores, M., Hsiao, T., Chiu, Y., Chuang, E., Huang, Y., Chen, Y.: Gene regulation, modulation, and their applications in gene expression data analysis. Adv. Bioinform. **2013**, Article ID 360678
6. De Jong, H.: Modeling and simulation of genetic regulatory system: a literature review. J. Comput. Biol. **9**(1), 67–103 (2002). https://doi.org/10.1089/1066527025233208
7. Layek, R., Datta, A., Doughrty, E.R.: From biological pathways to regulatory networks. Mol. Biosyst. **7**, 843–851 (2011)
8. Lahdesmaki, H., et al.: Relationships between probabilistic Boolean networks and dynamic Bayesian networks as models of gene regulatory networks. Sign. Process. **86**(4), 814–834 (2006). https://doi.org/10.1016/j.sigpro.(2005).06.008
9. George, P.: p53 how crucial is its role in cancer. Int. J. Curr. Pharm. Res. **3**, 19–25 (2011)
10. Jain, A.K., Barton, M.C.: p53: emerging roles in stem cells, development and beyond. Development **145**, dev158360 (2018)
11. Gasco, M., Shami, S., Crook, T.: The p53 pathway in breast cancer. Breast Cancer Res. **4**, 70 (2002)
12. Zhao, Y., Yu, H., Hu, W.: The regulation of mdm2 oncogene and its impact on human cancers. Acta Biochem. Biophys. Sin. **46**, 180–189 (2014)
13. Xiao, Y.: A tutorial on analysis and simulation of Boolean gene regulatory network models. Curr. Genomics **10**, 511–525 (2009)

14. Shmulevich, I., Gluhovsky, I., Hashimoto, R.F., Dougherty, E.R., Zhang, W.: Steady-state analysis of genetic regulatory networks modelled by probabilistic Boolean networks. Comparat. Funct. Genomics **4**, 601–608 (2003)
15. Kauffman, S.: Homeostasis and differentiation in random genetic control networks. Nature **224**, 177–178 (1969)
16. Tay, J.C., Tan, P.: Finding intervention points in the pathogenesis of dengue viral infection. In: 2006 International Conference of the IEEE Engineering in Medicine and Biology Society, pp. 5315–5321. IEEE, New York (2006)
17. Shmulevich, I., Dougherty, E.R., Zhang, W.: From Boolean to probabilistic Boolean networks as models of genetic regulatory networks. Proc. IEEE **90**, 1778–1792 (2002)
18. Harris, S.L., Levine, A.J.: The p53 pathway: positive and negative feedback loops. Oncogene **24**, 2899–2908 (2005)
19. Layek, R.K., Datta, A., Dougherty, E.R.: From biological pathways to regulatory networks. Mol. BioSyst. **7**, 843–851 (2011)

Design of an Energy-Efficient Probabilistic Algorithm for a Hybrid Healthcare Network

Pratik Bhattacharjee, Sandip Roy, Suparna Biswas, and Rajesh Bose

Abstract Smart parks are almost an integral part of any smart city. People of varied age groups usually gather in the smart park and performs different activities of daily living (ADL). People in a smart park may be sedentary (sitting/standing) or mobile. The mobility is low for the persons who are walking and moderate for those performing jogging/running. Often these activities are monitored via individual smart devices that are connected to a smart healthcare network. Such kind of health network must be extremely robust and hybrid in nature. Data generated through various individuals are synced to a remote server for further clinical processing. The present work proposes an intelligent methodology to minimize the transmission overhead by dynamically selecting the optimal nodes for data transmission. It takes care of both the stationary and the moving objects inside a smart park using a two-state Markov model. Additionally, it is also observed that the overall packet delivery ratio(PDR)is increased and energy consumption is reduced compared to popular LEACH-Mobile (LEECH-M) and LEACH-Mobile-Enhanced (LEACH-ME)protocols, using the proposed methodology.

Keywords Smart park · Group monitoring · Self servicing · Routing · Mobility · Healthcare · Two-state Markov chain

1 Introduction

Modern healthcare systems and devices extend their capabilities beyond the indoor monitoring. The IoT-based ambulatory and non-ambulatory devices are often used to monitor the activity of daily living (ADL) of the people belonging to different

P. Bhattacharjee (✉) · S. Biswas
Department of CSE, MAKAUT, Kolkata, WB, India
e-mail: pratikb@ieee.org

S. Roy · R. Bose
Department of Computational Science, Brainware University, Kolkata, WB, India
e-mail: dr.rb@brainwareuniversity.ac.in

B. Sikdar et al. (eds.), *Proceedings of the 3rd International Conference on Communication, Devices and Computing*, Lecture Notes in Electrical Engineering 851,
https://doi.org/10.1007/978-981-16-9154-6_47

age group and gender. The subjects are often monitored in a group by the remote server. The unattended outdoor group monitoring is slowly becoming popular in the smart parks of the modern cities. The city dwellers often enjoy the monitoring of their body vitals during the outdoor exercises. The remote outdoor monitoring is also appreciated by the family members of the elderly people, during their solo morning/evening walk. It is more convenient for the healthcare service providers to monitor the activities in a group through a remote server connected via Wi-Fi or cellular network.

1.1 The Possible Deployment Options

There may be several alternatives through which such smart park can be deployed. The ADL of the smart park users may be monitored by installing camera at different points in the park. Although camera-based monitoring has some serious privacy issues in case of an indoor monitoring, but there is no such issue for the outdoor monitoring in an open park.

However, camera-based monitoring requires substantial initial investment and a high recurring maintenance cost. Additionally, the image data requires substantial bandwidth to be transferred to the remote monitoring server. The analysis of the image is also costly in terms of processing and memory requirement. These problems multiplies for a group-based monitoring. Furthermore, in a wide area such as a park, the possibility of having multiple blind spots and dead zones is quite high that may affect the overall accuracy of the system. The response time of such a system is expected to be slow which may decrease its usability in case of an emergency health situation in the park.

The popularity of the IoT sensor-based ADL monitoring is on rise due to its low cost and low infrastructure requirement. The quality of service parameters such as frequency of failure, security, response time and accuracy are quite satisfactory for sensor-based monitoring. A wide range of personal monitoring systems (both ambulatory and non-ambulatory) are available now from different vendors. These types of monitoring is done via the popular sensors such as accelerometer, gyroscope, magnetometer and GPS. Such monitoring devices usually have either cellular or Wi-Fi network connectivity feature (or both) along with Bluetooth connectivity for long- and short-range communications.

However, as the IoT devices and sensors have some serious resource and energy limitations, an optimized routing algorithm is required that can minimize the communication cost as well as have the capability of self-servicing to support unattended operation of the system.

1.2 Amalgamation of Static and Mobile Wireless Sensor Networks

The wireless sensor networks (WSN) enhances the idea of funnelling the data to a receiving node via intermediate node/s. The wireless network boosts the tracking from a mere human-monitoring to a broader healthcare management. The present work is based on an amalgamation of stationary and mobile networks. The system must pass the data to the user, utilizing both the stationary and semi-mobile nodes (roaming subjects under monitoring) at the same time.

1.3 Sensor Nodes Power Sources

Sensor nodes, when deployed in a remote location, are often equipped with batteries of their own. The replacement of the batteries is not only onerous, but also causes a disruption in the existing WSN functionality. This may cause the loss of data, which may detoriate quality and accuracy of the system beyond the acceptable limit. So the target is to minimize the number of hops required from a sensor to the sink. This requires designing an optimum path that requires minimum energy consumption, using the intermediate neighbouring nodes, from the source to the destination.

1.4 The Cloud Integration

One of the design goals of the proposed system is to collect the raw sensor data and stream them to a cloud-based system. So a green cloud-based solution will enhance the proposed design.

The rest of the paper is organized as follows: Sect. 2 discussed about the relevant state-of-the-art works performed by other researchers. Section 3 addresses few drawbacks from some state-of-the-art methods and our approach to resolve them. The design and simulation result is shown in Sect. 4 and the PDR and energy efficiency comparison with LEACH-M and LEACH-ME is shown in Sect. 5. Finally, the entire work is concluded in Sect. 6.

2 Earlier Works

A smart park may consists of three types of subjects: subjects with no mobility (sitting on bench or performing Yoga like stationary activities), subjects with low mobility(walking) and subjects with moderate mobility (jogging) as shown in Fig. 1. Subjects with low mobility may further use smart assisting devices [1]. A suitable healthcare network is needed to monitor these subjects and send the data to a remote server for processing.

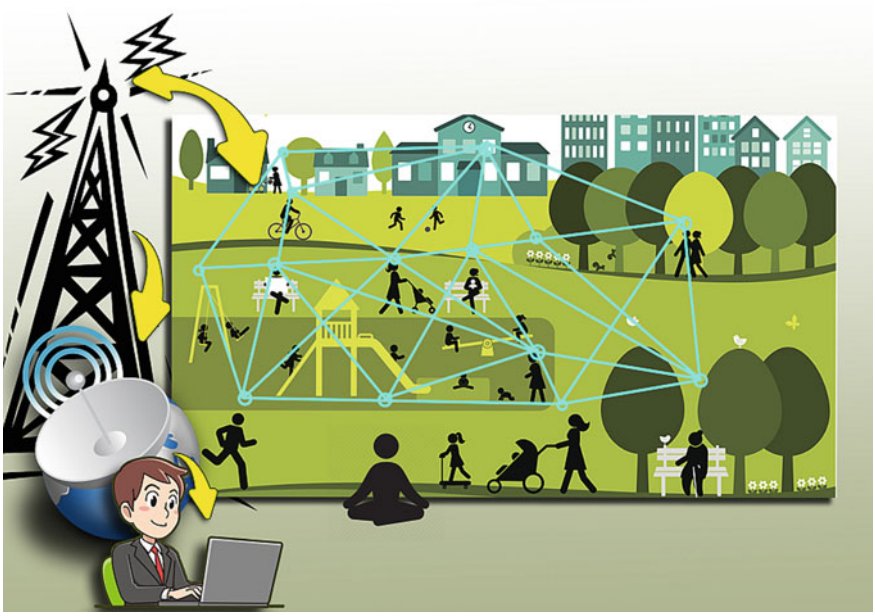

Fig. 1 The smart park in a smart city

The authors [2] have designed an optimum network that has the self-healing capacity and can be installed in a remote forest for monitoring the animals fitted with intelligent collar bands. In another work [3], researchers have proposed a method to minimize the transportation cost using optimal routing paths for multiple delivery vehicles, operating simultaneously using multi-chromosome genetic algorithm. The work is successfully implemented in 26 suburb locations in Canberra, Australia. Another approach is a new Energy-Aware Cluster Based Multi-hop (EACBM) routing algorithm [4] for hybrid networks that uses both clustering and multi-hop communications to reduce the energy consumption. However, the algorithm was tested under the simulation environment only.

A few energy-efficient algorithms [5, 6] using multi-modal sensor networks were developed for forest fire detection. They formulated path optimization and path selection algorithm that has some fail-safe mechanism. An energy-efficient and reliable M2M communication routing methodology is proposed by [7] that is based on cluster–parent relationship.

Optimize routing techniques were also developed based on fuzzy clustering [8] that proved to be useful. Some researchers also implemented dynamic cluster-based routing [9].

Energy-efficient routing algorithms for smart cities [10–13] have considered several optimization factors such as energy efficiency, optimum path selection and minimum packet drop ratio. It is also possible to connect the smart homes [14] with such healthcare networks.

Gaussian Markov model [15] and compressing sense-based data aggregation [16] are two popular approaches for designing optimal routing strategies on WSN. Some other algorithms and methods worth mentioned here are [17–19].

3 Problem Formulation

The difficulties faced by some researchers [10, 12, 17] in designing a mobile adhoc network is primarily maintaining a stable network with the mobile nodes. Quick selection of cluster head also is a problem as the head tends to loose energy quickly due to large amount of data exchange. The aspect of premature death of a sensor is not considered in few cases [8].

3.1 Contribution of the Proposed Work

The present work proposes a system that accommodates the following features

1. Energy-efficient stable path selection from source to sink.
2. To select a stable node, the residual energy, the mobility and the premature death of the sensor node is considered.
3. The system supports mobility upto 15 km/h which is slightly comparable with the two established algorithms [LEACH-M and LEACH-ME].

The proposed design targets to reduce the data loss and improve robustness. This method improves quality of data transmission and also felicitate the energy conservation to the maximum possible extent. Although shortest path is a popular approach to transmit end-to-end data, it suffers from packet loss resulting a decline in quality of service.

3.2 Calculating the Best Path

A *path score* is used to compute the optimum path. The path score is the best-fit path among the available paths from one node to another. So, we define a path as follows:

$$\begin{aligned} \text{Path} = \{\text{Path}_i\}, \ \text{where } 1 \leqslant i \leqslant k, \\ \text{and } k = \text{ Total available paths} \end{aligned} \tag{1}$$

where, i is the individual path from the set of paths.

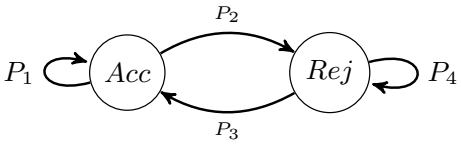

Fig. 2 Accept-reject using 2-state Markov chain

3.3 Representation of the Links for a Path

One sensor link is joined with another to form a single continuous chain. $Link_{ij}$ is the link joining two sensor nodes A_i & A_j, in a path. So, the total links, n, for Path$_i$, Link$_{ij}$ will be $\{(A_i, A_j)\}$ where $1 \leqslant i, \ j \leqslant n$.

3.4 The Two State Markov Model

The two-state Markov model indicates if a state of acceptance is possible by inspecting the energy level of the target sensor. If we define a state of acceptance as Acc, and a state of rejection as Rej, then the probabilities following the two-state Markov model, is represented by Eq. 2, and the corresponding diagram in Fig. 2.

$$\begin{pmatrix} P_1 & P_2 \\ P_3 & P_4 \end{pmatrix} \tag{2}$$

Let the following are the probabilities that—

- P_1: the next state is Acc if the current state is Acc.
- P_2: the next state is Rej if the current state is Acc.
- P_3: the next state is Acc if the current state is Rej.
- P_4: the next state is Rej if the current state is Rej.

The sum of each row in Eq. 2 is 1.

3.5 Computation of the Node Stability

The stability of each node need to be calculated to determine the possibility of establishing a path. Node stability may be found out by the sum of

1. The node's energy level.
2. mobility index of the node.
3. possibility of premature death the sensor.

If the weighted priority of the above 1,2,3 be wp_1, wp_2, and wp_3, respectively, considering $wp_1 > wp_2 > wp_3$ and $wp_1 + wp_2 + wp_3 = 1$.

Then, the node stability may be calculated by Eq. 3

$$\text{node\_stability}(N) = X + Y + Z \tag{3}$$

where

- $X = wp_1 \times \text{probability(accept\_state)} = w_1 \times \text{Maximum}(P_1, P_3)$.
- $Y = (-wp_2) \times \text{probability(mobility\_chance)} = (-wp_2) \times \frac{V_P}{V_{MAX}}$
- $Z = (-wp_3) \times \text{probability(premature\_death)}$.

where V_P is the velocity of the node at present and V_{MAX} is the maximum velocity of the node. Y and Z are shown as negative due to two reasons. A node moving towards its *maximum velocity* will be losing its capacity to communicate the data. Similarly, a high possibility of *premature death* will lead to transmission failure.

The probability of the premature death of a node may be calculated using the Poisson probability distribution. Equation 4 represents the probability mass function(PMF), using Poisson distribution.

$$P(X = k) = \frac{e^{-\mu}\mu^k}{k!} \text{ where } k = 0, 1, 2, 3... \text{ and } \mu \text{is the expected value of } X. \tag{4}$$

Thus, link stability is represented by Eq. 5

$$\text{link\_stability}(A_i, A_j) = \frac{\text{node\_stability}(A_i) + \text{node\_stability}(A_j)}{2} \tag{5}$$

We calculate the total number of nodes that are in mobile state, for a path as

$$L\text{score}(\text{Path}_i) = \text{count}(NM) \text{ where } NM \text{ represents mobile nodes} \in \text{Path}_i$$

Path stability ($PP(\text{Path}_i)$) of each path will be

$$PP(\text{Path}_i) = \prod_{L_k \in (\text{Path}_j)} \text{probability}(L_k)$$

Now, we maximize the objective function using Eq. 6 to calculate the Path score.

$$f(.) = k_1 \times \left(\frac{\text{Path}_i\text{\_stability}}{\max(\text{Path\_stability})}\right) + k_2 \times \left(\frac{\text{hop\_count}_i}{\max(\text{hop\_count})}\right) + k_3 \times \left(\frac{L\text{score}}{\max(L\text{score})}\right) \tag{6}$$

where and $k_1 > k_2 > k_3$ and $| k_1 | + | k_2 | + | k_3 | = 1$. The maximum path score is now calculated from all the available path score values. The path with the maximum

score will have the maximum stability during transmission between a node and the sink as shown in Eq. 7

$$\text{Path\_score} = \max_{\forall \text{Path}_i} f(\text{Path}_i) \tag{7}$$

4 Design and Implementation

4.1 Calculation of Stable Path

We have taken a sample network consisting of ten nodes as shown in Fig. 3. The following three properties are considered while selecting the nodes in order of their importance are-

1. Energy level or charge (Higher is better).
2. Mobility of the subject/node (Lower is better).
3. Possibility of premature death (Lower is better).

Assumptions and Initializations

1. The Activeness of a node may be calculated from Eq. 2 as

$$\text{Activeness} = \begin{cases} 0.9 & \text{Energy} \geq 75\% \\ 0.7 & 50\% \leq \text{Energy} < 75\% \\ 0.3 & \text{Otherwise} \end{cases}$$

2. Set $wp_1 = 0.5$, $wp_2 = -0.3$ and $wp_3 = -0.2$. Since more mobility or premature death implies less likely to be selected, so wp_2 and wp_3 are considered as negative contribution to the result.

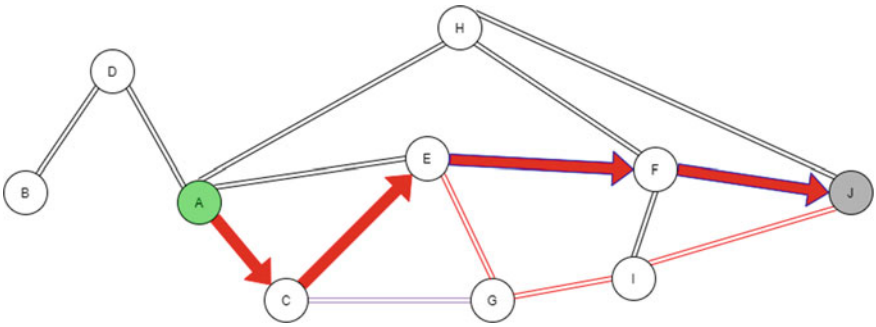

Fig. 3 The maximum stable path from *A* to *J* in the example network

3. Selection of node based on link stability is considered as-

$$\text{Link stability} = \begin{cases} 0.35\text{–}0.45 & \text{select single node} \\ 0.15\text{–}0.34 & \text{select two nodes} \\ \text{otherwise} & \text{select every adjacent node} \end{cases}$$

4. The average premature death probability is considered as 10% for every node. So, from Eq. 4, $P(X = 1) = e^{0.1} \times (0.1)^1 = 0.09$
5. For calculation of path score using Eq. 6, set $k_1 = 0.5$, $k_2 = 0.3$ and $k_3 = 0.2$
6. The mobility is calculated based on average mobility of the Indian male and female during activity of daily living inside a park as shown by [20]. The highest mobility is considered as 20 km/h and compared against each individual mobility of the node. The stationary node (person sitting on the bench) or a node with lower mobility is preferable for stable path selection.

An example of calculating node stability from Table 1 for node $A = (0.5 \times 0.9) - (0.3 \times 0.01) - (0.2 \times 0.09) = 0.429$

The example network with three alternative paths from source A to destination J are calculated from Tables 2 and 3 as

1. (A, C, E, G, I, J)
2. (A, C, E, F, J)
3. $(A, C, G, I.J)$.

Now, using Eq. 7, the maximum path stability is found for path $[A, C, E, F, J]$.

Table 1 Calculation of individual node stability

Node	% of energy	Activeness	Mobility	Stability
A	95	0.9	0.01	0.429
B	58	0.7	0.05	0.317
C	66	0.7	0.03	0.323
D	72	0.7	0.25	0.257
E	65	0.7	0.40	0.212
F	86	0.9	0.02	0.426
G	55	0.7	0.03	0.323
H	62	0.7	0.05	0.317
I	73	0.7	0.02	0.326
J	90	0.9	0.01	0.429

Table 2 Determination of immediate neighbours

Node	Immediate neighbours			
A	*C*	*D*	*E*	*H*
B	*D*			
C	*A*	*E*	*G*	
D	*A*	*B*		
E	*A*	*C*	*F*	*G*
F	*E*	*H*	*I*	*J*
G	*C*	*E*	*I*	
H	*A*	*F*	*J*	
I	*F*	*G*	*J*	
J	*F*	*H*	*I*	

Table 3 Determination of link stability

Node pair	(A, H)	(A, E)	(A, D)	(A, C)	(B, D)	(C, G)	(C, E)	(E, F)
Calculated stability	0.37	0.32	0.34	0.38	0.29	0.32	0.27	0.32
Node pair	(E, G)	(F, H)	(F, I)	(F, J)	(G, I)	(H, J)	(I, J)	
Calculated stability	0.27	0.37	0.38	0.43	0.32	0.37	0.38	

5 PDR and Energy Efficiency

We have proposed a hybrid design consisting of both stationary and mobile nodes. Stationary sensors are deployed on trees, towers or other stationary objects in the park. Persons who are roaming in the smart park are equipped with devices consisting of mobile sensors.

For the energy and packet delivery calculation purpose, it is assumed that 15 mobile and 30 static nodes are deployed arbitrarily over 2500 m^2 area. The maximum communication range per sensor was fixed at 100 m. Each sensor node can recharge their batteries automatically via solar panels, when the energy level drops below the threshold limit. Each sensor node can communicate with each other freely within their transmission range. The initial energy for each sensor is considered to be 10 J. A MICA2 energy model [21] was adopted for communication. It is computed that 2.34 μJ/bit is required for receive and 4.602 μJ/bit for transmission of signals. Furthermore, we defined the size of

- data packets = 512 bytes
- ENQUIRY packet = 5 bytes
- ENQUIRY_ACK = 5 bytes
- ROUTE_REQUEST = 16 bytes
- ROUTE_REPLY = 16 bytes.

The sensor density is varied between 50 and 70 for good simulation result while the average mobility is fixed at 0.5.

The value of 0.4 is fixed for premature death of up to 5% per round. The simulation was done over 5–50 rounds for any arbitrary network setting.

The simulation result is compared against the LEACH-M [22, 23] and LEACH-ME [24, 25] protocols for energy efficiency and packet delivery ratio.

5.1 Packet Delivery Ratio (PDR)

A PDR may be defined as per Eq. 8

$$\text{PDR} = \left(\frac{R}{S}\right) \times 100 \tag{8}$$

where S and R are the total number of packets send and received by the source and destination nodes respectively.

Figure 4 shows that the proposed method gives better PDR value compared to LEACH-M and LEACH-ME in terms of number of rounds. This is due to the fact that in both the methods, the elected cluster head dies before all the round finishes and as a result, nodes in this cluster lose their data.

5.2 Average Energy Consumption Rate

Average energy consumption is important and it varies depending on the number of nodes. The average energy consumption rate is calculated by Eq. 9

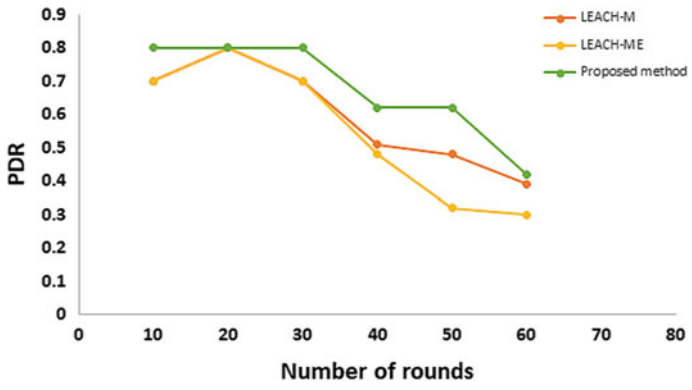

Fig. 4 Packet delivery ratio versus number of rounds

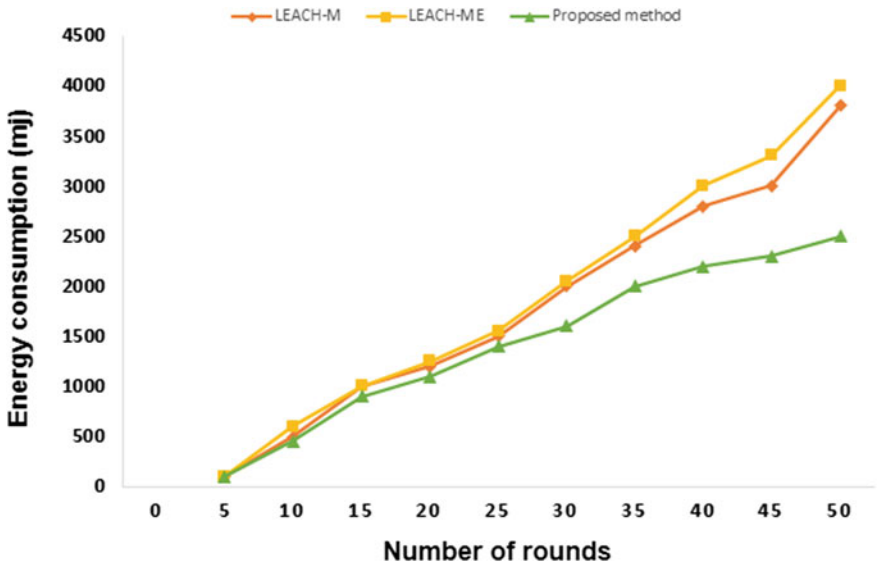

Fig. 5 Average energy consumption rate

$$\text{Average Energy Consumption Rate} = \frac{E_i - E_c}{E_i} \times 100 \tag{9}$$

where E_i is the initial energy and E_c is the energy consumed after n rounds.

Figure 5 shows a clear improvement over the two LEACH-based methods since election of cluster head does not require any additional energy.

6 Conclusion

As the smart healthcare is becoming more and more IoT dependent, the healthcare network is growing leaps and bounds. People are becoming more interested in constant monitoring and analysis of health data even for normal ADLs. The smart health devices are becoming increasingly popular and the healthcare networks are becoming more and more crowded. The complex nature of such network that has different types of nodes (mobile, semi-mobile and stationary) requires efficient and economic routing. Our proposed routing method proved to be optimal and energy-efficient compared to traditional cluster-based algorithms. The proposed methodology removes the requirement of selecting a cluster head and thereby reduces the overhead and energy consumption. If properly implemented, the method will be very useful for any unattended mobile hybrid network, such as in several components of a smart city.

References

1. Bhattacharjee, P., Biswas, S.: Smart walking assistant (SWA) for elderly care using an intelligent realtime hybrid model. In: Evolving Systems (2021), pp. 1–15. https://doi.org/10.1007/s12530-021-09382-5
2. Roy, S., Bose, R., Sarddar, D.: Self-servicing energy efficient routing strategy for smart forest. Brazilian J. Sci. Technol. (2016). https://doi.org/10.1186/s40552-016-0026-3
3. Nguyen, L.: An Efficient Multi-Vehicle Routing Strategy for Goods Delivery Services. TechRxiv (2021). https://doi.org/10.36227/techrxiv.14481702.v1
4. Toor, A.S., Jain, A.K.: A new energy aware cluster based multi-hop energy efficient routing protocol for wireless sensor networks. In: 2018 IEEE International Conference on Smart Energy Grid Engineering (SEGE) (2018). https://doi.org/10.1109/sege.2018.8499464
5. Moussa, N., El Belrhiti El Alaoui, A., Chaudet, C.: A novel approach of WSN routing protocols comparison for forest fire detection. In: Wireless Networks (2020). https://doi.org/10.1007/s11276-018-1872-3
6. Noureddine, H., Bouabdellah, K.: Field experiment testbed for forest fire detection using wireless multimedia sensor network. Int. J. Sens. Wireless Commun. Control (2020). https://doi.org/10.2174/2210327909666190219120432
7. Zhao, M.: Energy-efficient and reliable routing techniques for machine-to-machine communications (2019). https://doi.org/10.32657/10356/69202
8. Pattnaik, S., Sahu, P.K.: Assimilation of fuzzy clustering approach and EHO-Greedy algorithm for efficient routing in WSN. Int. J. Commun. Syst. (2020). https://doi.org/10.1002/dac.4354
9. Jain, J.K.: A coherent approach for dynamic cluster-based routing and coverage hole detection and recovery in Bi-layered WSN-IoT. Wireless Personal Commun. (2020). https://doi.org/10.1007/s11277-020-07377-0
10. Wala, T., Chand, N., Sharma, A.K.: Energy efficient data collection in smart cities using IoT. In: Handbook of Wireless Sensor Networks: Issues and Challenges in Current Scenario's, pp. 632–654 . Springer, Berlin (2020)
11. Rabelo, R., Silva, J., Ferreira, C.: Low-energy smart cities network with LoRa and bluetooth (2019). https://doi.org/10.1109/MobileCloud.2019.00011
12. Almeida, R., et al.: Forwarding strategies for future mobile smart city networks, pp. 1–7 (2018). https://doi.org/10.1109/VTCSpring.2018
13. Quijano-S'anchez, L., et al.: Recommender systems for smart cities. Inf. Syst. (2020), p. 101545
14. Wang, J., et al.: Unobtrusive health monitoring in private spaces: the smart home. Sensors **21**(3), 864 (2021)
15. Nguyen, L., et al.: Mobile robotic sensors for environmental monitoring using Gaussian Markov random field. Robotica **39**(5), 862–884 (2021)
16. Puneeth, D., Kulkarni, M.: Data aggregation using compressive sensing for energy efficient routing strategy. Proc. Comput. Sci. **171**, 2242–2251 (2020). https://doi.org/10.1016/j.procs.2020.04.242
17. Binu, G., Shajimohan, B.: A novel heuristic based energy efficient routing strategy in wireless sensor network. In: Peer-to-Peer Networking and Applications 13 (Nov. 2020). https://doi.org/10.1007/s12083-020-00939-w
18. Sampath, O., Babu, P.S.: Energy efficient routing strategies for large scale wireless sensor in heterogeneous networks. Int. J. Trend Sci. Res. Dev. **3**, 80–85 (2019). https://doi.org/10.31142/ijtsrd20281
19. Khalifeh, A., et al.: Wireless sensor networks for smart cities: network design, implementation and performance evaluation. Electronics **10**, 218 (2021). https://doi.org/10.3390/electronics10020218
20. Gore, N., et al.: Comparative analysis of pedestrian walking speed on sidewalk and carriageway. In: Transportation Research, pp. 65–76. Springer, Berlin (2020). https://doi.org/10.1007/978-981-32-9042-6_6

21. de Azevedo, L.P., da Silva, M.V.L.: Formal methods to analyze energy efficiency and security for IoT: a systematic review. In: Advanced Information Networking and Applications. AINA 2021. Lecture Notes in Networks and Systems, p. 227. Springer, Berlin (2021). https://doi.org/10.1007/978-3-030-75078-7_28
22. Tan, L., et al.: Improved LEACH-M protocol for processing outlier nodes in aerial sensor networks. IEICE Trans. Commun. **E104.B** (2020). https://doi.org/10.1587/transcom.2020EBP3060
23. Santhosh Kumar, G., Vinu, P.M.V., Jacob, K.P.: Mobility metric based leach-mobile protocol. In: 16th International Conference on Advanced Computing and Communications, Vol. 2008, pp. 248–253. IEEE, New York (2008)
24. Qubbaj, N., Taleb, A.A., Salameh Walid, A.: LEACH based protocols: a survey. Adv. Sci. Technol. Eng. Syst. J. **5**, 1258–1266 (2020)
25. Mahapatra, R.P., Yadav, R.K.: Descendant of LEACH based routing protocols in wireless sensor networks. Proc. Comput. Sci. **57**, 1005–1014 (2015)

Smart Environmental Monitoring Using LoraWAN

G. Kannayeram, M. Madhumitha, S. Mahalakshmi, P. Menaga Devi, K. Monika, and N. B. Prakash

Abstract The motive of this paper is to monitor the environmental parameters using LoRaWAN technology. The main objective of this device is to establish an intelligent monitoring system and a system that covers an entire city using a long-range wireless network. LORAWAN technology is a wireless network that transfers data from one point to another point, and these points can be tens to hundreds of kilometers apart from the transmitter section. In the receiver section, the LoRa gateway allows sensing devices to transmit data to the cloud. In this paper, monitorization of all sensor data by accessing the webserver. The advantages that LoRaWAN possesses are it is a low-cost product, needs only a little maintenance which means low maintenance offers a very low cost of deployment. It consumes low power while transmitting and receiving the data. Here the mobile based monitoring is used to study the characteristics of the environment at various locations. The mobile app is developed through which the parameters can be easily viewed through mobile phone. Sensors are used to sense the characteristics of temperature, humidity, pressure, CO_2, Ammonia, etc. This system also holds applications in LoRaWAN security, smart agriculture, smart logistics, smart homes, and smart cities for monitoring the environmental parameters. Arduino open-source platform is used to integrate all the sensors.

Keywords Arduino UNO · LoRaWAN · Sensors

G. Kannayeram · M. Madhumitha · S. Mahalakshmi · P. Menaga Devi · K. Monika · N. B. Prakash (✉)
Department of Electrical and Electronics Engineering, National Engineering College, K.R Nagar, Kovilpatti, India

M. Madhumitha
e-mail: 173071@nec.edu.in

S. Mahalakshmi
e-mail: 173068@nec.edu.in

P. Menaga Devi
e-mail: 173013@nec.edu.in

K. Monika
e-mail: 183412@nec.edu.in

B. Sikdar et al. (eds.), *Proceedings of the 3rd International Conference on Communication, Devices and Computing*, Lecture Notes in Electrical Engineering 851,
https://doi.org/10.1007/978-981-16-9154-6_48

1 Introduction

India is a developing country with top-level technologies. Globally, it is also a country with numerous resources, and our ancestors are very cautious in safeguarding it. But due to the evolution in industry and automation, that degrades the sanctity of the pleasant atmosphere through carbon compounds. Our country stays at the top in most polluted cities like Kanpur, Faridabad, Varanasi, and Gaya by a particulate matter of which is involved in shoe production that resulted in particulate matter of 173, 172, 149, 146, and 144, respectively, which should not exceed by 100 micros per meter cube that are referred in statistics in pollution. Air pollution has resulted in 9% of deaths. In the last three years, it has shown a low percentage of 2 in highly developed countries to 15% in countries like South East Asia. India contributes to the top in highly polluted cities that is 21 of 30 regarding 2019 statistics. The percentage of pollution caused is distributed like 51 from industries, 27 from vehicles, 17 from crop burning, and 5 from fireworks. This is also resulting in early deaths of nearly 2 to 3 million people each year in India because of lung, skin, breast, bladder cancer, cardiovascular diseases, shortened life span, sped up maturing of the lungs, loss of lung limit, and diminished lung work, improvement of illnesses like asthma, bronchitis, and emphysema. So, people are in much need of a device that detects, monitors, and analysis the environmental parameters that make us pre-ready for any sort of catastrophic issues and that should be an updated technology that should knock out all the issues that we people are facing with. Figure 1 shows the impact of pollution in Delhi city.

In [1], portrays that with expanding populace, urbanization, energy, transportation, and horticultural turns of events, contamination is debasing the environmental factors with always expanding pace. The debasement inside the environmental factors on account of contamination will just influence the norm of human existence by expanding medical conditions. Thusly, to stay away from wellbeing hazards due to the defiled environmental factors, it is crucial for watch its state. Nonetheless, as of now, recognition of information on the condition of the environmental factors is certifiably not a well-informed field. In this manner, it is expected to foster a framework that may quickly gather and break down data on the environmental factors to stay away from any likely dangers. The net is one among the compulsory and fundamental devices five which might be wont to foster a framework equipped for recognition and sharing information on ecological contamination.

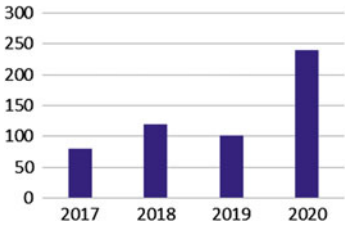

Fig. 1 Impact of pollution in Delhi city

Table 1 The characteristics of existing wireless network

Long range, low data rate (LPWAN)	Short range, high data rate (WIFI)	Short range, low data rate (ZigBee)
Large	Small	Small
Long	Short	Short
500 kHz–900 MHz	2.4, 3.6, 5, and 60 GHz	<2.4 GHz
Low	High	Low
Low	High	Low

In the past few years, radio communication with wireless networks becomes one of the most widely used technologies in the world. The most wireless network conventional cellular network and Wi-Fi that offer high data rate and it provide the needs of heavy-bandwidth application such as video streaming and cloud computing. Without main power, these networks cannot be operated and due to the high cost of maintenance and installation, these are difficult to deploy in remote and underground areas. Due to several issues such as low coverage range and rate of power consumption and data rate, we come with the new invention of low-power wide area network (LPWAN) technology without any human intervention to create a communication of information transmission triggered from machine-to-machine (M2M) communication [2, 3]. LPWAN is suitable for a monitoring system in a remote area. It does not require high data rates and has minimal power consumption. Table 1 shows the characteristics of the existing wireless network.

Four types of sensors like DHT11, BMP180, MQ135, and rainfall detection sensors are used that are used to measure the parameters like pressure, temperature, humidity, rainfall, and gas level. [4–10] Here, there are two sections, namely the transmitter and receiver section with transmits and receives data. In the transmitter section, sensors were embedded and the data which is collected is serially transmitted to Arduino UNO.

The manuscript is organized as follows. Existing of top-level technology and other basic has been discussed in Sect. 1 as introduction. Various components and modules have been explained in Sect. 2. The proposed methodology is narrated in Sect. 3. The output results and discussion are explained in Sect. 4 and concluded with outcomes of project in Sect. 5.

2 Description of Components

2.1 Arduino Uno

Arduino is an open-source board-based microcontroller on the ATmega328P. It allows you to upload a code to it using a USB connection. It has 14 digital input–output pins, and 6 pins are capable of pulse width modulation outputs and 6 analog input–output pins. It operates at a voltage of 5 V. Analog pins provide 10 bits resolution. It has an internal pull-up resistor of 20–50 K ohm which is disconnected by default. Arduino board supports TWI and SPI communication. For serial communication, a software serial library allows any of the digital pins of the Uno. Each of the pins can be used as an input or output which can be controlled by Arduino software (IDE) using analogRead (), digitalRead (), digitalWrite (), and pinMode () function.

2.2 LoraWAN Module (Sx1278 with Esp32)

For the past few years ago, communication technology plays a major role to interact between IOT devices. Bluetooth module and Wi-Fi also more popular, but these have some limitations like high power consumption, limited range, etc. To solve these issues, LoRa technology was introduced. This technology was first introduced by Semtech with a single battery for more than one year. In this, LoRa module, SX1278 will be interfaced with the ESP32 board, which is used for transmitting and receiving the data. The received data will be displayed in a 0.96-inch I2C OLED display. Figure 2 presents the Heltec sx1278 Lora with an OLED display.

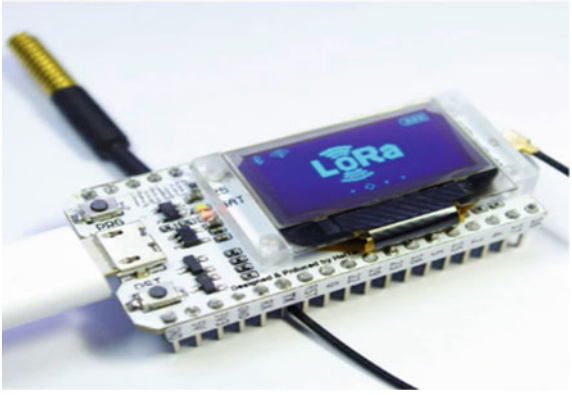

Fig. 2 LoRaWAN module

2.2.1 Sx1278 Module

This module features like LoRa. SX1278 module could achieve sensitivity over − 148 dbm. The main advantage of LoRa SX1278 is blocking and selectivity, wireless alarm, solving traditional design, and energy consumption.

2.2.2 OLED Display (Organic Light Emitting Diode)

0.96 inch is the size of the OLED display module, and it will be in blue color. This display module interfaced with the microcontroller by SPI/IIC protocols. The resolution of this module is 128 * 64. It is a self-light-emitting technology. The display is made up of multi-layered organic film between anode and cathode. It is the ultimate technology for the future generation.

3 Methodology

LoRa is a long-range network, which is a spread spectrum modulation. It is a technique derived from chirp spread spectrum (CSS) technology. Long-range and low-power wireless platforms like Semtech's LoRa devices and wireless radio frequency have become the de facto technology for IoT worldwide. These devices enable smart IoT applications that solve the biggest challenges that people face like management of energy, control of pollution, the efficiency of infrastructure, prevention of disaster, and many other issues. These technologies will amaze the people turning the regular structure into smart cities, smart homes, smart buildings, renovating agriculture metering, supply chain, and logistics into innovative which will result in a smarter geoid. LoRaWAN owns specifications of wide-area networking protocol with low power mode [11]. It is designed with a wirelessly connected battery both at the regional and global level and has a protocol and provides seamless interoperability within the devices. Here, the Semtech issues the LoRa radio chips which is a non-profit association and which is also the fastest technology alliance that drives standardization and global harmonization.

LoRa is a strategy that utilizes a trilled and a multi-image arrangement to encode the data which is utilized for communicating radio while LoRaWAN is a highlight multipoint organizing convention that utilizes Semtech's LoRa regulation plan. Semtech which is a chip maker made this restrictive framework which is likewise authorized with different makers too which has a standard ISM that can utilize LoRa or FSK to change over the radio recurrence into bits with no utilization of composed code to run the radio framework while LoRaWAN is not just about the radio waves yet in addition about the correspondence of radio waves with the LoRaWAN entryways to perform capacities like encryption and ID. This framework additionally incorporates a cloud segment that is associated with numerous doors. Because of LoRaWAN's limits, this is once in a while utilized for modern applications; however, LoRa can

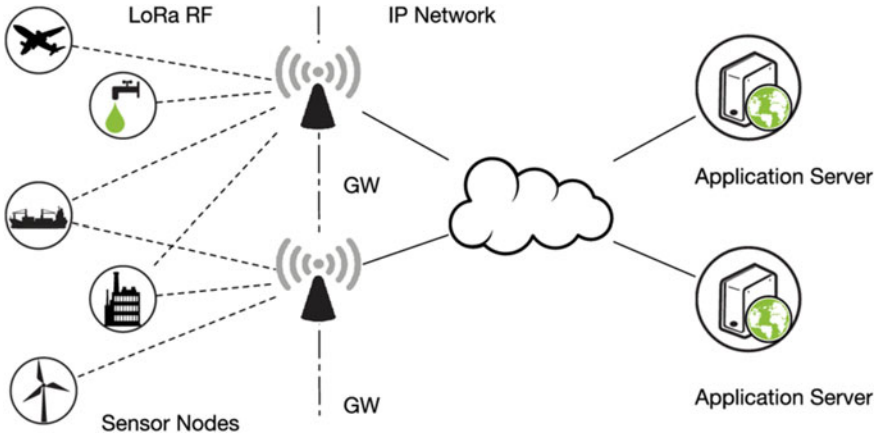

Fig. 3 Architecture of LoRaWAN

be utilized in a wide range of utilizations in a wide region because of its lower-level actual layer innovation.

LoRa devices with a Semtech innovation offer IoT applications such as long-range, secured data transmission, and low power consumption. This can be applied in a wide range of organizations like public, private, or half and half organizations which give a more noteworthy reach than regular cell organizations. This innovation of LoRa can be handily connected to current foundation and will empower us minimal expense battery-worked IoT applications. These chipsets can be installed into gadgets that were fabricated by an enormous environment of IoT arrangement suppliers and were associated with LoRaWAN-based organizations around the whole world encasing that it interfaces all gadgets to the cloud. Figure 3 shows the design of LoRaWAN.

It is designed for LoRaWAN protocol, LoRa devices, and IoT communications which will enable the connections between the point-of-use devices and LPWANs for delivery in terms of analytic applications. Silicon is used for the making of LoRa modulation's layer which is a wireless module that is used to create a long-range communication link. Transceivers that are designed for a multitude of industry applications are embedded into sensor devices or end-nodes configured with LoRa devices. Gateways capture data that are transmitted and captured by sensors over long and short and also for indoor and outdoor with minimal requirement. For network management functions like data de-duplication, adaptive rate control, traffic management gateways send information through Ethernet, cellular to the network server, or Wi-Fi. LoRaWAN is a device with 3 types of classes that operate at the same time. Class A is called a pure ALOHA system which is asynchronous which does not wait for a particular time to speak to the gateway and is dormant whenever they transmit. Messages are sent down to battery-powered nodes but class B. Beacon is transmitted by the gateway every 128 s. Download messages can be sent by Class C at any time which allows nodes to listen constantly. This is utilized for AC-powered applications.

Fig. 4 Esp32 LoRa sensor monitoring with webserver

4 Result and Discussion

A few examinations have been led to recognize the better arrangement which will upgrade the nature of the sign of LoRa and furthermore expanding the bundle proportion. The estimations were conveyed in a few ecological spots. They are planted in an inclination way course to lessen the interferences or aggravations from the deterrents that get through the hardware's which may utilize the very kind of channels that matches with the checking framework that we use and the geographical obstructions (Fig. 4).

5 Conclusion

The system that performed real-time monitoring to detect various types of data like atmospheric pollutant concentrations has used LoRa communications. Power consumption and the cost of the device both can be reduced efficiently by the LoRa module. This covering a range of tens of kilometers and capable to serve up thousands of devices. The function of low power function will allow the system to have a sleep function by combining the sensors and processors which are used to collect the data for relatively long periods at high frequency. The robustness of the system is proved by empirical tests. As some claim that the data can be lost in the cases such as the increased distance between the LoRa substations and nodes and the availability of obstructions between them, so the stability and LoRaWAN technology cannot be denied. In increasing the range of the device and in penetration capability, further improvement is required and also researches on the compatible wireless sensors to monitor the environmental parameters both on land and water. For example, an air quality monitoring system for measuring contaminant tools which is a viable tool

for air. By all these long-term planning can be taken for strategic decisions and the impact of industrial emissions.

Acknowledgements The authors would like to thank the project coordinators and the Head of Department (EEE) for having given suggestions and review comments towards the success of the project.

References

1. Alam, S.S., Islam, A.J., Hasan, M.M., Rafid, M.N.M., Chakma, N., Imtiaz, M.N.: Design and development of a low-cost IoT based environmental pollution monitoring system. In: 4th International Conference on Electrical Engineering and Information & Communication Technology (iCEEiCT) (2018)
2. Vilajosana, X., Adelantado, F., Vilajosana, X., Tuset-peiro, P., Martinez, B., Melia, J.: Understanding the limits of LoRaWAN. IEEE Commun. Maga. (2017)
3. Ismail, I.S.: Performance analysis of data recovery via application layer for LPWAN. In: IEEE 89th Vehicular Technology Conference, pp. 1–5 (2019)
4. Srivastava, D., Kesarwani, A., Dubey, S.: Measurement of temperature and humidity by using Arduino Tool and DHT 11. Int. Res. J. Eng. Technol. **5**(12), 876–878 (2018)
5. Wang, Y., Chi, Z.: System of wireless temperature and humidity monitoring based on Arduino uno Platform. In: 2016 Sixth International Conference on Instrumentation & Measurement, Computer, Communication and Control (IMCCC) (2016)
6. Kwon, S.-H., Kim, W.K.: Rain drop counting measurement sensor with energy harvesting technology of water motion. In: Proceedings 2018, vol. 2, 1393; https://doi.org/10.3390/proceedings2131393(2019)
7. Kalbande, A.G.: Smart automation system using Arduino and rain drop sensor. Int. J. Curr. Eng. Sci. Res. (IJCESR) **4**(6), 82–86 (2017)
8. Kanti, A., Jagadish, P.M., Soumya, P.: Air pollution monitoring system using Arduino with MQ135 sensor. Int. Res. J. Modern. Eng. Technol. Sci. **2**(8), 412–421 (2020)
9. Abbas, F.N., Saadoon, M.I.M., Abdalrdha, Z.K., Abud, E.N.: Capable of gas sensor MQ-135 to monitor the air quality with Arduino UNO. Int. J. Eng. Res. Technol. **13**(10), 2955–2959 (2020)
10. Mungekar, A.A., Sadnki, Y.K., Swarnalatha, R.: Real time weather surveillance via lab view interfaced Arduino. Int. J. Eng. Technol. **7**(4), 2715–2717 (2018)
11. Tzortzakis, K., Papafotis, K., Sotiriadis, P.P.: Wireless self powered environmental monitoring system for smart cities based on LoRa. In: 2017 Panhellenic Conference on Electronics and Telecommunications (PACET) (2017)

A Video-Based Uncertainty Technique for Human Action Recognition—A Deep Learning Approach

Moloy Dhar, Subhajit Sanyal, and Bidesh Chakraborty

Abstract The Human action recognition (HAR) has diverse application in many research areas and also a great challenge in the ground of computer perception and deep learning. Deep learning is a method which uses complex models to solve tasks difficult to implement by hand, like in computer vision. The purpose of this research work is to design deep learning-based uncertainty techniques that recognize various action recognitions (running, walking) of different human in videos with better accuracy. Bayesian method used here to maintain a general structure to evaluate unpredictability of human actions. A well-calibrated prediction in regression tasks is our ultimate desire (provide a credible interval of 95%). A simple procedure has been suggested for that, when applied to Bayesian models. This model produces accuracy of 92% for running and 96% for walking.

Keywords Deep learning · ABC method · IID data · HAR · Uncertainty quantification

1 Introduction

In normal life, we deal with unpredictability in various areas related to human actions. The goal is to generate outcome which is based on assembled view and unclear sector familiarity. At present, we could depend on machine learning and deep learning models, that can evaluate the unpredictability to achieve statistical inference [1, 2]. Assumptions built by these types of models are unpredictable as they are accustomed to noises and inaccurate model assumption likewise the preparatory guesses which are built-in in case of unpredictability. Hence, this is extremely covetable to serve unpredictability in an accurate way in several AI-related schemes. This type

M. Dhar (✉) · S. Sanyal
Guru Nanak Institute of Technology, Sodepur, Panihati 700114, India
e-mail: moloy.dhar@gnit.ac.in

B. Chakraborty
Haldia Institute of Technology, ICARE Complex, Medinipur (Purba), W.B. 721657, India

B. Sikdar et al. (eds.), *Proceedings of the 3rd International Conference on Communication, Devices and Computing*, Lecture Notes in Electrical Engineering 851,
https://doi.org/10.1007/978-981-16-9154-6_49

of computerized schemes be going capable to execute exactly by conduct unpredictability adequately. Uncertainty quantification (UQ) is the science of quantitative description and devaluation of unpredictability's in both real world and computational applications. This competes to resolve how likely specific outcomes we get, if some characters of the system are unknown. Principle of uncertainty performs a major part in AI contexts such as detailed learning algorithms [3], and active learning (AL) [4].

Origin of unpredictability happens when the training and test data are unsuited and data unpredictability appears as a result of class superimpose or due to the existence of cacophony in the data [5]. Predicting knowledge unpredictability is also challenging related to data unpredictability that normally calculates it as an outcome of maximum likelihood training. Origins of unpredictability in forecasting are necessary to handle the unpredictability assessment issues [6]. Two main sources of unpredictability are there, said Epistemic and Aleatoric unpredictability [7]. Epistemic unpredictability is associated to missing messages or skills whereas Aleatory unpredictability is associated to conclusions that for practicable goals cannot be assumed and so dealt with as stochastic. Here, we have to use Epistemic unpredictability with ABC method that gave us better accuracy for 2 classes (running, walking) compared to other methods used in different papers [1, 4, 5]. The detail of the approach is described in methodology section.

Lakshminarayanan et al. [8] and Gal et al. [6] suggested unpredictability assessment methods for deep neural networks, that incorporate ensemble processes, concrete dropout, and heteroscedastic regression. These methods desire reshaping the model and might not always produce completely calibrated assessments. In weather forecasting article, calibration has been broadly considered [5]; after all these methods promote to be specialized and tough to generalize apart from utilizations in the climate science. In some cases, it is the Contact Volume Editor that checks all the pdfs. In such cases, the authors are not involved in the checking phase.

The alternative idea is to calibrate models using Platt scaling which recalibrates the assumptions of a pre-trained classifier in a post-transforming step. The models have been tested by support vector classifier.

The rest of this paper is formed as follows: Bayesian method is defined in Sect. 2. Methodology is specified in Sect. 3. Discussion of the proposed model accomplished Human action recognition and details of the Algorithms and Techniques are discussed in Sect. 4. Results and Conclusions, including potential improvements, are discussed in Sect. 5.

2 Bayesian Method

The *Bayesian* Method describes by a prior and likelihood function which gives us to predict model framework to handle model analogy and build model projections. As, Bayesian estimation is carried out by econometrician's inference for the full information of the structural model which is to be predicted.

The prior function $p(\mu)$ with the parameter μ is available in the econometrician which is not depend on the sample of data inspections. Therefore, Eq. (4) may be considered as revise rule which uses data inspections to restore the econometrician's prior faith related with the model parameters. Bayesian Method assumes the parameters as arbitrary variables. Suppose z be a sample of data inspections which is defined by model M and μ serve as model parameters. The conditional joint probability of (z, μ) on model M is denoted by

$$p(z, \mu|M) = L(z|\mu, M)p(\mu|M) \tag{1}$$

which can be further represented as,

$$p(z, \mu|M) = p(\mu|z, M)p(z|M) \tag{2}$$

$L(z|\mu, M)$ in Eq. (1) represents likelihood function. Now, associating Eqs. (1) and (2) in order to eliminate the joint probability, we get

$$p(\mu|z) = L(z|\mu)p(\mu)/p(z) \tag{3}$$

This expression refers to a specific model M. Here, $p(\mu)$ states prior distribution and $p(\mu \mid z)$ states the posterior distribution and Posterior kernel is denoted by

$$p(\mu|z) \propto (z|\mu)p(\mu) \tag{4}$$

3 Methodology

At first, we have extracted and pre-processed a video dataset and then, divide the dataset into 2 categories i.e. training data and testing data. A neural network model has been created and trained it with the training data. Further testing is performed using test data for test the model. Then, we have compared the performance of the model with some pre-existing models. A deep learning-based UQ method has been used for reasoning under unpredictability. This model is our main architecture for appropriate and predictable machine learning schemes.

The dataset can be obtained from *HAR dataset*. The video dataset contains 6 types of human actions (jogging, running, walking, boxing, hand clapping, hand waving). Here, we use only running and walking class that executed many times by 25 persons with 5 distinct schemes i.e. outdoors $s1$, outdoors with scale variation $s2$, outdoors with different clothes $s3$, and indoors $s4$ and $s5$ as demonstrated in Fig. 1. We have considered the dataset consists of 2391 sequences under the identical environment with a fixed camera with *25* fps frame rate. All the sequences were down sampled to the spatial resolution of 160×120 pixels and have a length of 4 s on average with a sampling frequency of 463 images. The dataset contains 300 videos–150 videos

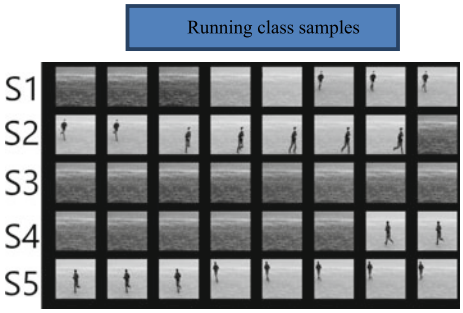

Fig. 1 Training sample RE-LU matrix

for each of the 2 categories. The model will be constructed irrespective of these scenarios. This paper suggests methods for accustom with Bayesian models in such a way that matches appropriate experimental frequencies.

All the sequences were distributed corresponding to the subjects into the training set (8 persons/Activity), validation set (8 persons/Activity), and the test set (9 persons/Activity). Here, the classifiers are trained on a training set. The validation set was used to optimize the parameters of every process. Recognition results are gained on the test set of 463 frames/person. All the sequences are collected using the AVI file format and are accessible on-line (DIVX-compressed version). Next, there are some sample frames for some videos from the HAR dataset. In Fig. 1, there is a total of 2 categories–running and walking. While loading the data, we convert these text labels into integers according to the following mapping: Running as 1 and Walking as 2.

Figures 2 and 3 state the running and walking classes respectively.

Fig. 2 Running detection

Fig. 3 Walking detection

3.1 Convolutional Neural Networks (CNN)

The CNN is used to implement the model. Figure 4 is detached into domains, and each domain is then appointed to distinct unseen nodes. Each unseen node discovers arrangement in one and only of the domains in the Fig. 4. This domain is resolute by the help of kernel i.e. window/filter. The filter is convoluted in addition to the pair of x and y-axis [9]. Output of 1 filter when convoluted during the whole of the unified image produces a 2-D zone of neurons i.e. denoted as feature map. Every filter is accountable for one feature map [1, 2].

These feature maps pushed into a 3-D array, that can be used as the input to the zones. It is accomplished by convolutional layer in a CNN. These zones are pursued by the Pooling layers, which decrease the spatial aspects of the turnout (gained from the convolution layers) i.e. a window is drifted in both the axes and the maximum value in that filter/window is taken (Max-Pooling layer). Repeatedly, average pooling layer is also used where the only dissimilarity is to ensure the average value inside the window alternatively of the maximum value. Therefore, the convolutional layers

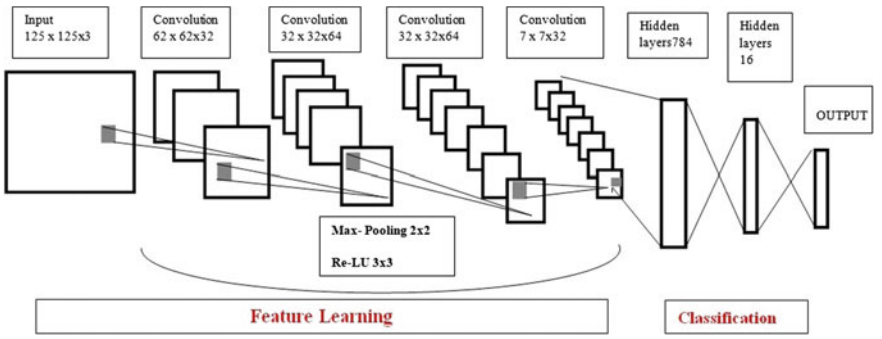

Fig. 4 Analyzing image in forms of matrix

boost the depth of the input image, when in fact the pooling layers decline the spatial aspects (peak and span). Such type of design encrypts the ease of an image that can be leveled into a 1-D array.

Here, we have used pooling layers and 2-d convolutional layers. It is 2-D, because the filter is wrap around onward the x-axis and y-axis of the image. However, in video, we have added temporal z-axis. Therefore, a 3-d convolutional layer is recycled, where the filter (also 3-D) is convoluted beyond all the 3 axes.

3.2 Model Parameters

In each convolutional layer, (Fig. 4) we have configured the following parameters:

Filters—Total number of feature maps i.e. needed as the outcome of the convolutional layer.
kernel size—Window size which will get convoluted on entirely the axes of the input data to produce a single feature map.
strides—Total number of pixels by which the convolutional window will drift by.
padding—To determine what appears on regression models.

Appropriate UQ is decisive for real-world utilizations of machine learning. After all, current deep neural networks result unpredictable uncertainty which often yields over-confident assumptions. Bayesian Method contributes a general framework i.e. used to quantify unpredictability using Eqs. 1–4 (Sect. 2) in our work. Because of model wrongly specified and the adopt of approximate inference [10], Bayesian unpredictability predicts are regularly erroneous [11]—for e.g. 90% credible interval may not consist of the true issue 90% of the time.

In this paper, we propose ABC (Approximate Bayesian Computation) Method to provide a credible interval of 95%. The ABC method is used for accomplish Bayesian posterior inference, over the lens of density prediction. Visualization approach of 450 samples is used to allow plots of calibration factor, confidence band (representing uncertainty of every data points) of our model. We have given a labeled dataset x_t, $y_t \in X \times Y$ for $t = 1, 2, \ldots, T$ of i.i.d. recognition of arbitrary variables X, $Y \sim P$. Here, P is the data distribution. Given x_t, a forecaster H: $X \to (Y \to [0, 1])$ results a probability distribution $F_t(y)$ targeting the label y_t. When Y is continuous, F_t is a cumulative probability distribution (CDF). Here, we estimate $Y = \{0, 1\}$ for simplicity purpose in binary classification.

Generally, calibration signifies that when the forecaster assigns a possibility of 0.9 to an activity, then that activity should occur about 90% of the time. We say that H is calibrated if

$$\frac{\sum_{t=1}^{T} y_t I\{H(x_t)=p\}}{\sum_{t=1}^{T} y_t I\{H(x_t)=p\}} \xrightarrow{} p, \quad \text{for all} \quad p\,\varepsilon\,[0,1] \tag{5}$$

as $T \to \infty$. Here, for clarity, we utilize $H(x_t)$ to represent the possibility of the activity $y_t = 1$. When the x_t, y_t are i.i.d. realizations of arbitrary variables X, $Y \sim P$, a sufficient condition for calibration is:

$$P(Y = 1|H(x) = p) = p, \quad \text{for all} \quad p\varepsilon[0,1] \tag{6}$$

Calibration is not sufficient to assure a fruitful forecast. A forecaster that every time assumes $E[Y]$ is calibrated, but not very fruitful. As good assumptions also require to be acute, which intuitively state that probabilities should be close to 0 or 1. The classic forecaster predicts outcomes with 100% confidence and calibrated. A base BABC classifier H: $X \to \Phi$ may also output features $\varphi \in \Phi \subseteq R^d$ which do not correspond to probabilities. For e.g. this sequential CNN outputs the margin between the splitting hyperplane and xt. To achieve further instinct, H can be demonstrated as projecting the x_t into a low-dimensional space Φ (CNN margin), such that the data is detached in Φ. Then the recalibrator R: $\Phi \to [0, 1]$ executes density prediction to learn the Bayesian ABC optimal classifier $P(Y = 1 \mid H\ (X) = \varphi)$. This is tractable, when φ is low-dimensional; additionally $R \circ H$ is appropriate as the classes Y are disconnected in φ. $R \circ H$ is also calibrated as $P(Y = 1 \mid H(X) = \varphi$ is Bayes-optimal.

4 Proposed Model

Till now, 154 frames for each video were extracted and given as the input to the models. Compare to [1–4], in this paper, from each video, 154 contiguous frames (8 s) were being extracted. As, we know that the human body performs these activities (running, walking) with a certain speed. Within one second, the human body does not make much of a movement. Therefore, we do not need to collect every frame for each second of video that we are capturing.

Now, we have extracted only 5 frames/ second. There is also a maximum limit on the number of frames that have to be extracted from each video. We have set this value to 40. So, these 40 frames will be selected from the front of the extracted frames.

The range of normalized pixels has also been changed from [0, 1] to [−1, 1]. This is because the mean of the pixels would then be 0, which would help the model converge faster.

The model (Fig. 5.) was learned on the training data for 40 epochs. The weights of the model that gave the finest achievement on the validation data were weighted. Then the model was tested on the test data.

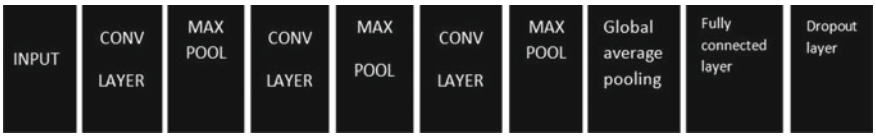

Fig. 5 Model architecture

The model provides an accuracy of 96% (walking) and 92% (running) on the test data. So, our model provides a higher accuracy than the previous models. Further we have added another pair of max pooling and convolutional layer was added. This made the output of the final convolutional layer to have a depth of 1024. We have selected NADAM as the optimizer. For NADAM, the default value of learning rate is 0.02 and there is a scheduled decay of learning rate. NADAM gave better results than ADAM. Also, at the end of 40 epochs, the model did not overfit, but in case of ADAM, the model showed some signs of over fitting.

4.1 Algorithms and Techniques

Algorithm 1: UET

Input: Set of Video Frames containing n image instances ans PS with m_f class Indentifiers.
Output: N mini batches MB = $\{mb_i \mid i = 1,2,...N\}$ for CNNs
Segregate n instances into N subsets X = $\{x_i \mid i = 1,2,...,N\}$, each with $S(d_n)$ negative instances.

```
Assign Temp = PS                          //save a copy of all positive instances
 for i = 1 : N
    pos = omega                           // pos: positive subset in the mini-batch
            if (length(Temp) < Sm):
               Temp = random(PS);
            for 1 : Sn
                randomly pick an instance t
                pos = pos U t;
               Temp = Temp-t;
            end for
               mbi = xi U pos;
end for
return MB to train CNNs
```

Algorithm 2: BABC Uncertainity

Input: encoder g(.),data x*, dropout probability p ,prediction network h(.), number of iterations B
Output: uncertainity n_1 , Prediction y'*mc
for b = 1 to B do
e*(b) <-- VariationalDropout(g(x*),p)
z*(b) <-- Concatenate(e*(b), extFeatures)
y*(b) <-- Dropout (h(z*(b)),p)
end for
y'*mc <-- dot(1/B, summation(y'*(b))) // prediction
$(n_1)^2$ <-- dot(1/B, sum(y'*(b) – y'*)**2) // Model uncertainty and confidence
return y'*mc, n_1

We have selected the videos of 9 persons (randomly) performing each of these actions and predict the outcomes of those frames by our model.

5 Results

Model Layer:

Model: "sequential_3".
See Table 1.

Figure 6 depicts the predicted actions based on different intervals. Above the observed values lines (yellow lines), it indicates running class, whereas the below region indicates walking class.

Steel blue shaded region in Fig. 7 specifies uncertain prediction zone of our classifier. Most of the prediction points are falling under the prediction zone after final epoch.

Figure 8 specifies our prediction by probability values of every classes (classes as 1–0). The dotted lines specify for perfect model. 0 indicates walking and 1 indicates running class. The progress over the experience of a definite metric associated to learn during the training of a machine learning model, is shown in Fig. 9. It simply shows the model performance is rising over time, that means the model is developing with skill (it's learning). The training loss shows how well the model is adjusting the training data, and the validation loss shows how well the model competent new data.

5.1 Analysis

Once the model has been trained on the training data, it's performance evaluated using the test data. Confusion matrix is used to determine accuracy. Since our data

Table 1 Sequential CNN

Layer (type)	Output shape	Parameter
conv3d_3 (Conv3D)	(−, 40, 128, 128, 16)	736
max_pooling3d_3 (MaxPooling3)	(−, 20, 64, 64, 16)	0
global_average_pooling3d_1	(−, 1024)	0
dense_2 (Dense)	(−, 32)	32,800
dropout_1 (Dropout)	(−, 32)	0
dense_3 (Dense)	(−, 2)	66
Total params: 5,066,882		
Trainable params: 5,066,882		
Results matrix		
Accuracy on test data: 94.44%		
Accuracy metrics		
MAE	0.335	
RMSE	0.453	
MDAE	0.274	
MARPD	61.649	
R^2	0.853	
Correlation	0.944	
Average calibration metrics		
Root-mean-squared calibration error	0.043	
Mean-absolute calibration error	0.035	
Miscalibration area	0.035	
Adversarial group calibration metrics		
Mean-absolute Adversarial Group Calibration Error		
Group Size: 0.11	Calibration Error: 0.149	
Group Size: 0.56	Calibration Error: 0.061	
Root-mean-squared Adversarial Group Calibration Error		
Group Size: 0.11	Calibration Error: 0.178	
Group Size: 0.56 –	Calibration Error: 0.074	
Sharpness Metrics		
Sharpness	0.512	
Scoring rule metrics		
Negative-log-likelihood	0.202	
CRPS	0.227	
Check score	0.115	
Interval score	1.081	

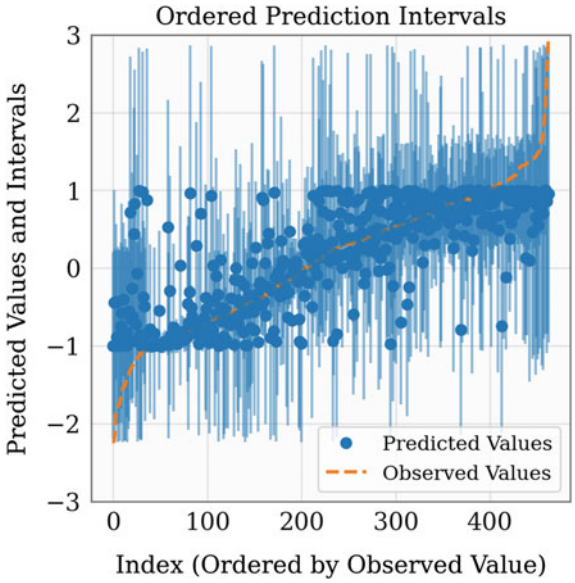

Fig. 6 True versus predicted visualization

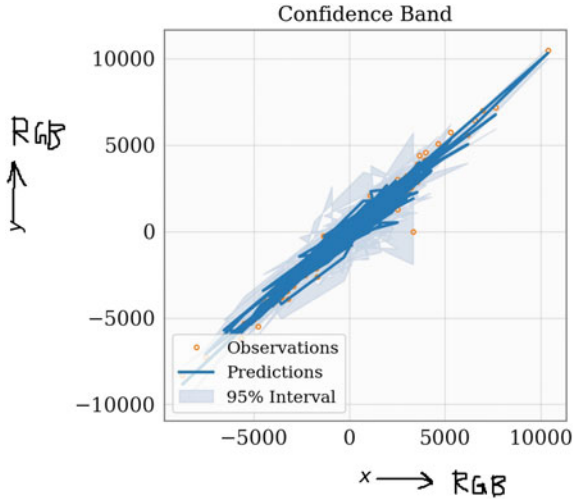

Fig. 7 RGB amplitude

sets have similar characteristics, accuracy would be a suitable metric to evaluate the model.

Comparison

According to Fig. 10 and Table 2, recommend that the suggested design was exceed (or at part) at assuming these activities than the benchmark model.

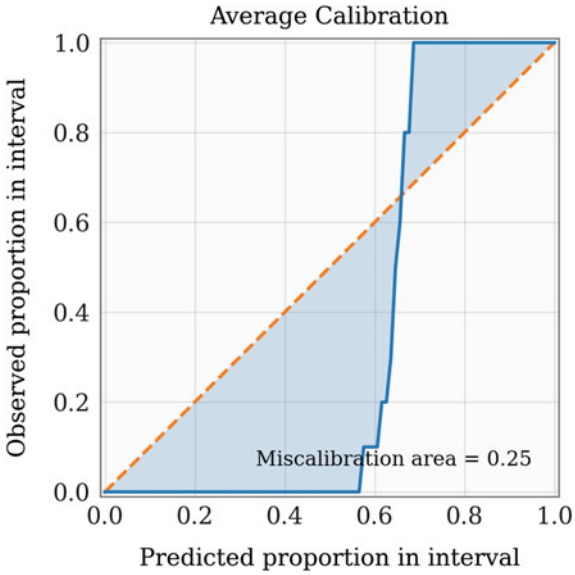

Fig. 8 Calibration plot

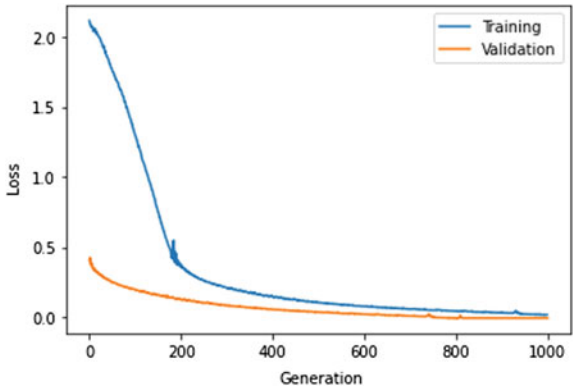

Fig. 9 Training-validation loss curve

Benchmark Model

Here we select [1, 3]. Benchmark model (Fig. 11.) was able to achieve an overall recognition rate of 80–85%. In order to compare the benchmark model with the suggested layout, confusion matrix of the benchmark model analyzed with the confusion matrix of the suggested layout and we get the better accuracy.

The dataset used to get the results of the benchmark model was HAR. According [1–3], the test data contains 9 persons. So, we randomly selected 9 different persons, processed all the videos of these 9 persons (i.e. $9 \times 24 = 216$ videos) and constructed the confusion matrix with using this proposed model.

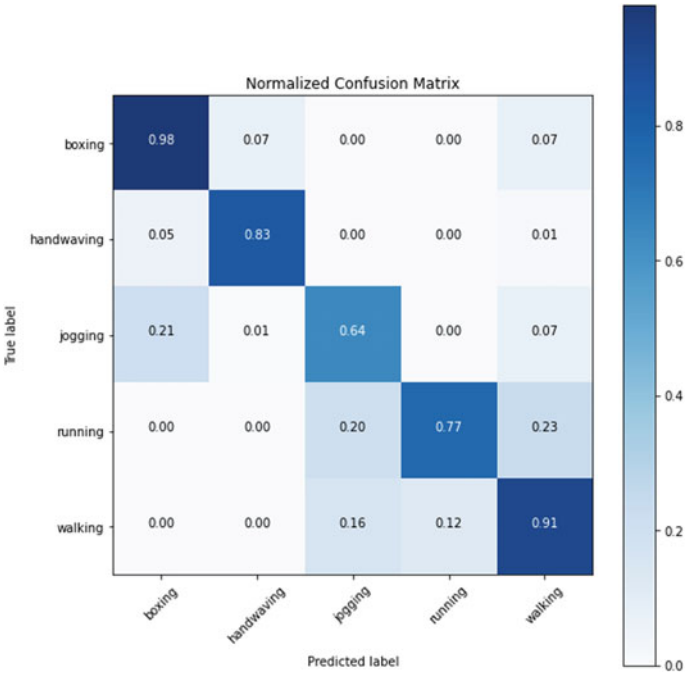

Fig. 10 Confusion matrix

Table 2 Accuracy table

Activity class	Benchmark accuracy	Proposed accuracy
Running	0.55	0.92
Walking	0.84	0.96

The confusion matrix of the benchmark model [1], as well as the proposed model have been converted in the same format. Also, the confusion matrix has been normalized.

6 Conclusions

We suggest a method for HAR which assigned an approach of calibration for continuous variables, drawing close connections to work in calibrated classification. Our method consistently produces well-calibrated unpredictability assessment, which is fruitful in reinforcement learning, time series forecasting, along with more commonly to develop interpretable, reliable, and interactive machine learning systems. Using this model, we have got accuracy of 92% for running and 96% for walking. In future, we will use an ordinary recalibration method which produces calibrated probabilistic

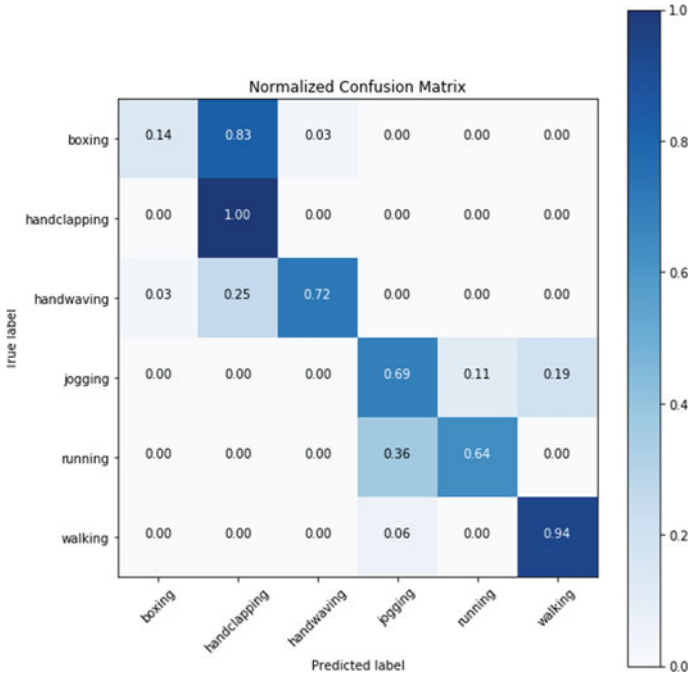

Fig. 11 Benchmark model (Confusion matrix) [1]

forecasts accustomed sufficient i.i.d. (Independent and Identically Distributed Data) data and consider rest 4 types of human actions (jogging, boxing, hand clapping, hand waving).

References

1. Malinin, A.: Uncertainty Estimation in Deep Learning with Application to Spoken Language Assessment, Ph.D. dissertation. University of Cambridge (2019)
2. Jiang, H., Kim, B., Guan, M., Gupta, M.: To trust or not to trust a classifier. In: Advances in Neural Information Processing Systems, pp 5541–5552 (2018)
3. Mitchell, T.M.: The Need for Biases in Learning Generalizations. Department of Computer Science, Laboratory for Computer Science Research (1980)
4. Nguyen, V.L., Destercke, S., Ullermeier, E.H.: Epistemic uncertainty sampling. In: International Conference on Discovery Science, pp. 72–86. Springer, Berlin (2019)
5. Phan, B.T.: Bayesian Deep Learning and Uncertainty in Computer Vision. Master's thesis, University of Waterloo (2019)
6. Gal, Y.: Uncertainty in Deep Learning. Ph.D. dissertation, University of Cambridge (2016)
7. Platt, J.C.: Probabilistic outputs for support vector machines and comparisons to regularized likelihood methods
8. Sharma, S., Lakshminarayanan, A.S., Ravindran, B: Learning to Repeat: Fine Grained Action Repetition for Deep Reinforcement Learning, Published as a conference paper at ICLR (2017)

9. Sen, S., Dhar, M., Banerjee, S.: Implementation of human action recognition using image parsing techniques. In: 2018 Emerging Trends in Electronic Devices and Computational Techniques, EDCT 2018, pp. 1–6 (2018)
10. Cooke, R.: Parameter fitting for uncertain models: modeling uncertainty in small models. Reliab. Eng. Syst. Saf. **44**, 89–102 (1994)
11. Fienberg, S.E.: An iterative procedure for estimation in contingency tables. Ann. Math. Stat. **41**, 907–917 (1970)

Outage Analysis of Joint Underlay/Overlay CR Network

Jayanta Kumar Bag, Dipak Samanta, Chanchal Kumar De, and Abhijit Chandra

Abstract In the presented paper, we propose a joint underlay/overlay cognitive radio (CR) network model assisted by adaptive hybrid relays (AHR) which are incorporated with multiple antennas. According to our proposed model, out of all primary users (PUs) band if certain number of PU bands are sensed empty, then overlay mode is used and if the PUs are communicating, then underlay mode is used. The source and relays are equipped with adaptive dual power switches, i.e., underlay and overlay mode power is selected on the basis of sensing the activity of primary users. The outage probability is calculated at the selection combined (SC)-based secondary destination. The outage performance of the system model under consideration is compared for varying number of underlay and overlay PUs. AF (amplify and forward relay), DF (decode and forward) and AHR forwarding protocols have been compared on the basis of outage performance. The influence of increasing number of relays on the overall system outage is also shown. The mathematical equation of the outage probability in different protocol has been shown in this paper.

Keywords Primary users · Secondary users · Underlay CR · Overlay CR · Adaptive hybrid relay · Selection combining

1 Introduction

Cognitive radio is a leading technology for the enhancement of efficient spectrum usage in wireless communication [1, 2]. Research on CR is based on two main paradigms: underlay [3] and overlay [4]. Each of these techniques needs different levels of knowledge about its complex working situation, which leads to various challenges. In underlay CR systems [5], the secondary user is granted to acquire

J. K. Bag (✉) · D. Samanta · C. K. De
Haldia Institute of Technology, Haldia, India

A. Chandra
Jadavpur University, Kolkata, India

B. Sikdar et al. (eds.), *Proceedings of the 3rd International Conference on Communication, Devices and Computing*, Lecture Notes in Electrical Engineering 851,
https://doi.org/10.1007/978-981-16-9154-6_50

the primary or licensed band only if an interference threshold is maintained at each primary receiver. In overlay CR systems [6], the secondary network first senses the primary band and checks if it is occupied or empty—if it is empty, then the secondary network operates at full power, otherwise it waits till the band is empty. In underlay mode communication, an interference threshold is maintained for all primary receivers even if they are not communicating. The secondary user can not access the active primary user band in overlay mode. To overcome the above-mentioned problems, a combination of underlay/overlay is proposed [7]. There have been many studies on the mixed of underlay and overlay mode in CR networks [8–13]. For a soft-decision CR, a proposed framework of adaptive modulation in [8] uses multiple-carrier-assisted signals to achieve hybrid overlay/ underlay waveform. In [9], Oh and Choi illustrated a hybrid CR system, where a probabilistically controlled overlay mode is transferred to an underlay mode to increase the data communication rate of the secondary user (SU). In Bao et al. [10], proposed a hybrid type CR network, where the transmission capacity measurement of the SUs is high under the primary and secondary outage limits. In [11], authors discussed an optimization model for energy-efficient hybrid spectrum sharing CR networks to maximize capacity. Authors in [12] have compared the system throughput using a learning phase in secondary network for both underlay and overlay models. Optimal power allocation algorithm has been developed for a hybrid underlay/overlay OFDM-based CR network in [13]. In the present work, we propose a joint underlay/overlay model, according to which, the secondary network senses the primary band and if the band is found to be empty, then the secondary network transmits at full available power. But if the primary bands are occupied, then the secondary network will communicate with each other by taking into account of interference threshold for the active primary receivers. Therefore, using this model, the secondary user can access all PU bands simultaneously using adaptive underlay/overlay switching. Multiple adaptive hybrid relays (AHR) deployed with multiple antennas are considered which can adaptively switch between AF and DF schemes depending on the channel conditions. Our key contributions are briefly discussed as follows: (i) Comparison of outage performance for underlay, overlay and joint underlay/overlay mode. (ii) Evaluation and comparison of joint underlay/overlay network using AF, DF as well as AHR forwarding protocols. (iii) Exploring the effect on the system for increasing relay numbers and antenna numbers at the respective relay. (iv) Analysis of the trade-off for the variation in the number of the antenna in relay to obtain the required outage performance. (v) Simulation of the analytical framework of our proposed model on the MATLAB platform.

The rest of the paper is organized as follows: Sect. 2 describes the proposed system model, while relaying protocols have been illustrated in Sect. 3. Simulation model and results have been presented in Sect. 4 followed by conclusive remarks in Sect. 5.

2 System Architecture

The network configuration shown in Fig. 1 comprises of single secondary source (S) and secondary destination (D) including multiple primary transceivers (PU_m; $m = 1, 2 \ldots M$) and multiple relays (R_k; $k = 1, 2 \ldots K$). At any given instant, it is known that N out of M number of users are communicating with its corresponding pair, i.e., they are operating in underlay paradigm ($\mathrm{PU}_{\mathrm{under}}$) and remaining $(M - N)$ number of users are idle, i.e., they are in overlay mode ($\mathrm{PU}_{\mathrm{over}}$). If the operating bandwidth of each PU is B, then the total bandwidth becomes MB. Now, according to our proposed system, N number of PUs operate in underlay mode which corresponds to a bandwidth of NB with channel rate $\frac{N}{M}R$. The remaining $(M - N)$ number of PUs operating in overlay mode uses a bandwidth of $(M - N)B$ with channel rate $\frac{M-N}{M}R$, where R is the total secondary network channel rate. This information is available to the secondary source S and the relays R_k utilizing various spectrum sensing methods as proposed in [14, 15]. It has been assumed that the secondary source, secondary destination as well as primary users are very well equipped par-

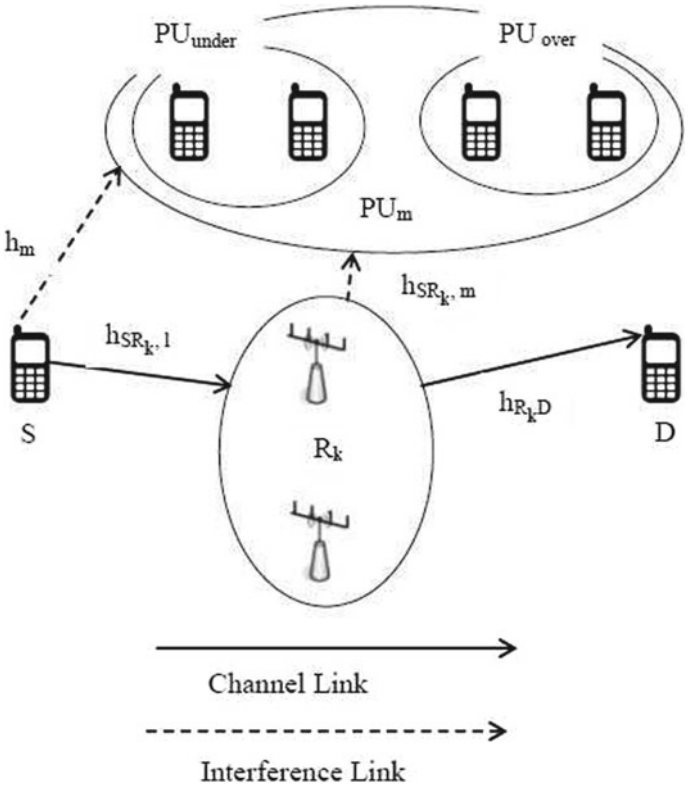

Fig. 1 System model of Joint underlay/overlay CR network

ticularly with single antenna whereas, on the contrary multiple receiving antennas ($l = 1, 2 \ldots, L$) and single transmitting antenna are provided at the secondary relays. It is also presumed that direct link existing between secondary source (S) and secondary destination (D) is unavailable due to extreme shadowing along with multipath propagation loss. Interference on secondary destination (D) due to primary users ($PU_m; m = 1, 2, \ldots, M$) has been neglected in the proposed system. In this model, all channel links are assumed to experience independent non-identical zero mean and unit variance Rayleigh fading plus additive white gaussian noise (AWGN) with N_0 variance. Channel coefficients are defined as follows: h_m represents for secondary source (S) to mth primary user (PU_m); $h_{SR_k,l}$ denotes for secondary source (S) to lth antenna of kth Relay (R_k); $h_{\mathrm{SR}_k} = \max_{l=1,2\ldots L} \{h_{\mathrm{SR}_k,l}\}$ denotes for secondary source (S) to kth relay; $h_{R_k,m}$ denotes for the channel between kth relay and mth primary user and finally, $h_{R_k,D}$ used for kth relay R_k to D. The existing secondary source S and relay R_k have the capability of transmitting a signal using two different powers in different time frames, i.e., in first period of time frames, the power allocated for underlay mode is used and in the second duration of time frame, the power is used for the overlay mode. The adaptive dual power allocation at source and relays are explained in the following section.

2.1 Power Management Policy

In this section, we have discussed a dual power management policy scheme at secondary source and secondary relays for operating in both underlay and overlay mode. The source and the relays can adaptively switch between the two power modes in two subsequent time slots. The algorithm of proposed system has been precisely illustrated by the flowchart shown in Fig. 2.

Power Management policy at Source In underlay mode, the secondary network communicates using the primary user's band by maintaining an interference constraint I_p of the primary network. Thus, the underlay mode transmit power is given by

$$P_S^{\text{under}} = \min(P_{S_1}, P_{S_2}, ..., P_{S_m}) \tag{1}$$

where $P_{S_m} = \frac{I_p}{|h_m|^2}$ and $m = 1, 2, \ldots, N$, since N is the total count of busy PUs.

In overlay mode, secondary source and destination communicates with each other by accessing unutilized primary band. For such a situation, the source can use the maximum available power for signal transmission. Therefore, the overlay mode power is given by

$$P_S^{\text{over}} = P_{S,\max} \tag{2}$$

where $P_{S,\max}$ represents the maximum secondary source power.

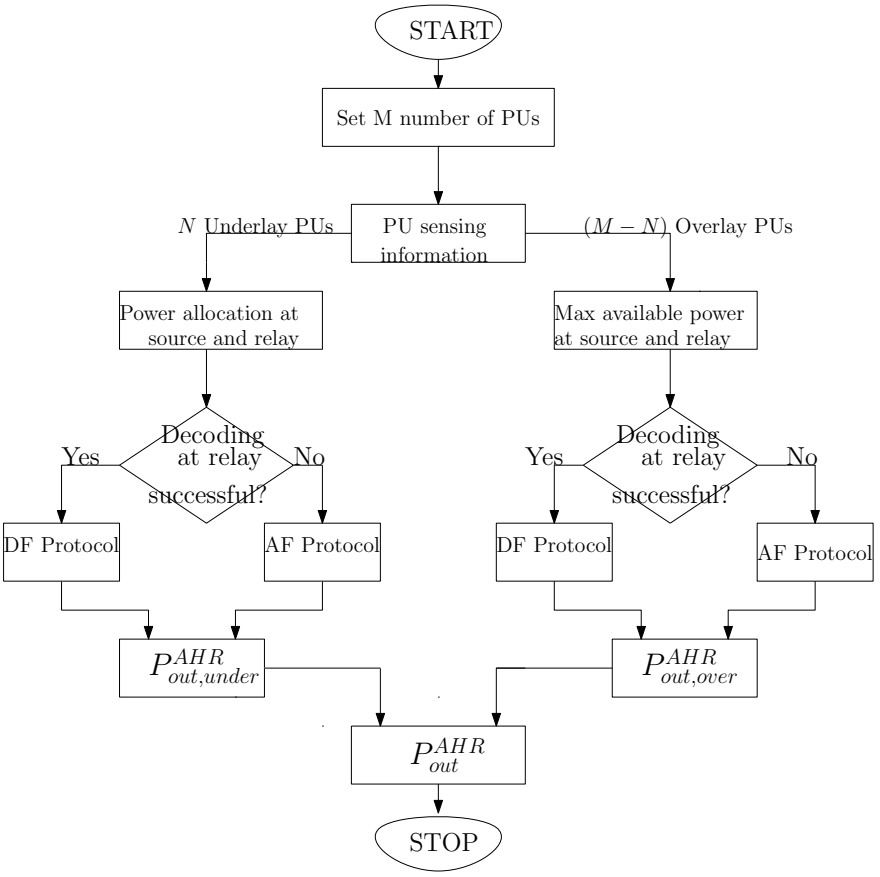

Fig. 2 Flowchart

Power Management policy at Relays The power management policy scheme at secondary relays is similar to source. After maintained an interference constraint I_p for all primary users, the transmitted power at relay in underlay mode is given by

$$P_{R_k}^{\text{under}} = \min_{m=1,2,\ldots,N} \{P_{R_k,m}^{\text{under}}\} \tag{3}$$

where $P_{R_k,m} = \frac{I_p}{|h_{R_k,m}|^2}$, $k = 1, 2 \ldots, K$ and N is the count of busy PUs.

Similarly, for overlay mode the transmitted power at kth, relay is expressed as

$$P_{R_k}^{\text{over}} = P_{R_k,\max} \tag{4}$$

where $P_{R_k,\max}$ denotes the maximum transmitted power capacity of the corresponding relay.

3 Relaying Protocols

In this section, we have discussed AF, DF and AHR protocols and evaluated their respective outage probabilities for joint underlay/overlay mode.

3.1 Amplify and Forward Type Relay Protocol

According to amplify and forward relay (AF) protocol, relay amplifies incoming source signal and transferred it to the respective destination [16]. As a result, which leads to hard error propagation but reduces the decoding complexity at the relays.

For underlay mode, the corresponding end-to-end received SNR through kth relay is expressed as [17]

$$\gamma_{k,\text{under}}^{\text{AF}} = \frac{\gamma_{\text{SR}_k}^{\text{under}} \gamma_{R_k D}^{\text{under}}}{\gamma_{\text{SR}_k}^{\text{under}} + \gamma_{R_k D}^{\text{under}} + 1} \tag{5}$$

where $\gamma_{\text{SR}_k}^{\text{under}} = \frac{P_S^{\text{under}}}{N_o} \mid h_{\text{SR}_k} \mid^2$ and $\gamma_{R_k D}^{\text{under}} = \frac{P_{R_k}^{\text{under}}}{N_o} \mid h_{R_k D} \mid^2$. Therefore, the SNR for underlay mode is

$$\gamma_{D,\text{under}} = \max_{k=1,2,\ldots,K} \left\{ \gamma_{k,\text{under}}^{\text{AF}} \right\} \tag{6}$$

The outage probability for underlay AF protocol is evaluated as

$$P_{\text{out,under}}^{\text{AF}} = \Pr\left(\gamma_{D,\text{under}} \leq \gamma_{\text{th,under}} \right) \tag{7}$$

where $\gamma_{\text{th,under}} = 2^{\frac{2R}{\text{MB}}} - 1$ and R is the channel rate.

For overlay operating mode, the corresponding end-to-end SNR is denoted as [17]

$$\gamma_{k,\text{over}}^{\text{AF}} = \frac{\gamma_{\text{SR}_k}^{\text{over}} \gamma_{R_k D}^{\text{over}}}{\gamma_{\text{SR}_k}^{\text{over}} + \gamma_{R_k D}^{\text{over}} + 1} \tag{8}$$

where $\gamma_{\text{SR}_k}^{\text{over}} = \frac{P_{S,\max}}{N_o} \mid h_{\text{SR}_k} \mid^2$ and $\gamma_{R_k D}^{\text{over}} = \frac{P_{R_k,\max}}{N_o} \mid h_{R_k D} \mid^2$. Thus, for overlay mode the SNR at destination is given by

$$\gamma_{D,\text{over}} = \max_{k=1,2,\ldots,K} \left\{ \gamma_{k,\text{over}}^{\text{AF}} \right\} \tag{9}$$

The corresponding outage probability for overlay AF protocol is evaluated as

$$P_{\text{out,over}}^{\text{AF}} = \Pr\left(\gamma_{D,\text{over}} \leq \gamma_{\text{th,over}} \right) \tag{10}$$

where $\gamma_{\text{th,over}} = 2^{\frac{2R}{\text{MB}}} - 1$ and R is the channel rate.

Therefore, combining underlay and overlay mode the outage probability for AF protocol in our system model is obtained as

$$P_{\text{out}}^{\text{AF}} = \frac{N}{M} P_{\text{out,under}}^{\text{AF}} + \frac{M-N}{M} P_{\text{out,over}}^{\text{AF}} \tag{11}$$

3.2 *Decode and Forward Type Relay Protocol*

In decode and forward (DF) relay protocol, initially relays decode the arriving source signal [18]. After this, relays re-encode successfully decoded signal and finally transfer it to the desired destination. If the decoding is unsuccessful, then transmission is aborted. Decoding capability at relays increases the computational complexity, but there is no hard error propagation. For underlay mode, a set of relays ξ_{under} depending on the successfully decoded incoming source signal is chosen. A threshold SNR μ_{th} is considered to compare with the received SNR at relay for deciding successful decoding. So, $\xi_{\text{under}} = \{\gamma_{\text{SR}_k}^{\text{under}} \geq \mu_{\text{th}}\}$. The corresponding end-to-end SNR for DF protocol is represented as [18]

$$\gamma_{k,\text{under}}^{\text{DF}} = \frac{P_{R_k}^{\text{under}}}{N_o} \mid h_{R_k D} \mid^2 \tag{12}$$

One relay is selected out of ξ_{under} set as [19]

$$\gamma_{D,\text{under}}^{\text{DF}} = \max_{k \in \xi_{\text{under}}} \left\{\gamma_{k,\text{under}}^{\text{DF}}\right\} \tag{13}$$

Therefore, outage probability for underlay is aptly given as

$$P_{\text{Out,under}}^{\text{DF}} = \Pr\{\gamma_{D,\text{under}}^{\text{DF}} \leq \gamma_{\text{th,under}}\} \tag{14}$$

where $\gamma_{\text{th,under}}^{\text{DF}} = 2^{\frac{2R}{\text{MB}}} - 1$ Similarly for overlay operating mode ξ_{over} set is chosen for all relays which can decode incoming signal. So, $\xi_{\text{over}} = \{\gamma_{\text{SR}_k}^{\text{over}} \geq \mu_{\text{th}}\}$ where μ_{th} stands for threshold SNR for determining the signal decoding process at the respective relay. The corresponding end-to-end SNR is mathematically expressed as

$$\gamma_{k,\text{over}}^{\text{DF}} = \frac{P_{R_k,\max}}{N_o} \mid h_{R_k D} \mid^2 \tag{15}$$

From set ξ_{over}, one particular relay is chosen to be [19]

$$\gamma_{D,\text{over}}^{\text{DF}} = \max_{k \in \xi_{\text{over}}} \left\{\gamma_{k,\text{over}}^{DF}\right\} \tag{16}$$

Thus, the outage probability is obtained as

$$P_{\text{Out,over}}^{\text{DF}} = \Pr\{\gamma_{D,\text{over}}^{\text{DF}} \leq \gamma_{\text{th,over}}\} \tag{17}$$

where $\gamma_{\text{th,over}} = 2^{\frac{2R}{\text{MB}}} - 1$ The outage probability by combining overlay and underlay mode is given by

$$P_{\text{out}}^{\text{DF}} = \frac{N}{M} P_{\text{out,under}}^{\text{DF}} + \frac{M-N}{M} P_{\text{out,over}}^{DF} \tag{18}$$

3.3 Adaptive Hybrid Type Relay Protocol

According to adaptive hybrid relay (AHR) type protocol, if incoming signal is unable to be decoded by relay, it is straight away amplified and forwarded to the terminus by the same relay [20]. The relay re-encodes the successfully decoded incoming signal and finally sends to the respective destination. This leads to reduced hard error propagation and low computing complexity at the relays. Thus, AHR type protocol is combined of AF along with DF protocol. When underlay mode is considered, the probability of operating using AF protocol is

$$P_{\text{under}}^{\text{AF}} = \Pr\{\gamma_{\text{SR}_k}^{\text{under}} < \mu_{\text{th}}\} \tag{19}$$

Therefore, the probability of following DF scheme is

$$P_{\text{under}}^{\text{DF}} = 1 - P_{\text{under}}^{\text{AF}} \tag{20}$$

The instantaneous SNR for underlay mode can be expressed as

$$\gamma_{k,\text{under}}^{\text{AHR}} = P_{\text{under}}^{\text{AF}} \gamma_{k,\text{under}}^{\text{AF}} + P_{\text{under}}^{\text{DF}} \gamma_{k,\text{under}}^{\text{DF}} \tag{21}$$

where $\gamma_{k,\text{under}}^{\text{AF}}$, $P_{\text{under}}^{\text{AF}}$, $\gamma_{k,\text{under}}^{\text{DF}}$ and $P_{\text{under}}^{\text{DF}}$ are obtained from Eqs. (5), (19), (12) and (20), respectively.

Using selection combining (SC) at the relay network, one relay is chosen as [21]

$$\gamma_{D,\text{under}}^{\text{AHR}} = \max_{k=1,2,\ldots,K} \left\{\gamma_{k,\text{under}}^{\text{AHR}}\right\} \tag{22}$$

Thus, the equation of outage probability for underlay mode using AHR protocol is

$$P_{\text{Out,under}}^{\text{AHR}} = \{\gamma_{D,\text{under}}^{\text{AHR}} < \gamma_{\text{th,under}}\} \tag{23}$$

where the outage threshold $\gamma_{\text{th,under}} = 2^{\frac{2R}{\text{MB}}} - 1$.

Similarly for overlay mode, the probability for following AF protocol is

$$P_{\text{over}}^{\text{AF}} = \Pr\{\gamma_{\text{SR}_k}^{\text{over}} < \mu_{\text{th}}\} \tag{24}$$

Thus, the probability for following DF protocol is

$$P_{\text{over}}^{\text{DF}} = 1 - P_{\text{over}}^{\text{DF}} \tag{25}$$

The instantaneous SNR is given by

$$\gamma_{k,\text{over}}^{\text{AHR}} = P_{\text{over}}^{\text{AF}} \gamma_{k,\text{over}}^{\text{AF}} + P_{\text{over}}^{\text{DF}} \gamma_{k,\text{over}}^{\text{DF}} \tag{26}$$

where $\gamma_{k,\text{over}}^{\text{AF}}$, $P_{\text{over}}^{\text{AF}}$, $\gamma_{k,\text{over}}^{\text{DF}}$ and $P_{\text{over}}^{\text{DF}}$ are obtained from Eqs. (8), (24), (15) and (25), respectively.

Using SC at relay network, one relay is chosen as [21]

$$\gamma_{D,\text{over}}^{\text{AHR}} = \max_{k=1,2,\ldots,K} \left\{\gamma_{k,\text{over}}^{\text{AHR}}\right\} \tag{27}$$

Thus, the outage probability for overlay mode using AHR protocol is

$$P_{\text{Out,over}}^{\text{AHR}} = \{\gamma_{D,\text{over}}^{\text{AHR}} < \gamma_{\text{th,over}}\} \tag{28}$$

where the outage threshold $\gamma_{\text{th,over}} = 2^{\frac{2R}{MB}} - 1$.

Thus, the outage probability combining both underlay and overlay mode for AHR protocol is

$$P_{\text{out}}^{\text{AHR}} = \frac{N}{M} P_{\text{out,under}}^{\text{AHR}} + \frac{M-N}{M} P_{\text{out,over}}^{\text{AHR}} \tag{29}$$

4 Results with Discussions

In this present section, we have discussed the outcomes obtained from performing simulations in MATLAB. We have considered similar value of maximum transmit power at relay as well as at source. The concerned system parameters are varied and corresponding outage performances are obtained.

Figure 3 explains outage probability for different combinations of PU_{under}, and PU_{over} is a mathematical function of $\frac{I_p}{N_0}$. The relays number(K), as well as antenna number (L), channel rate (R) and interference threshold (I_p) are all kept constant at 4, 4, 5 bits/s and 3 dB, respectively. The total number of PUs considered is 20 and number of underlay and overlay PUs are varied from 1 to 20 to obtain the results. It is seen that when all the 19 PUs are idle, then the outage probability is minimum. On the other hand, when all the 19 PUs are busy-the outage is maximum. This is because in overlay mode, there is no power constraint for signal transmission in secondary network which enables the secondary source to transmit using its full

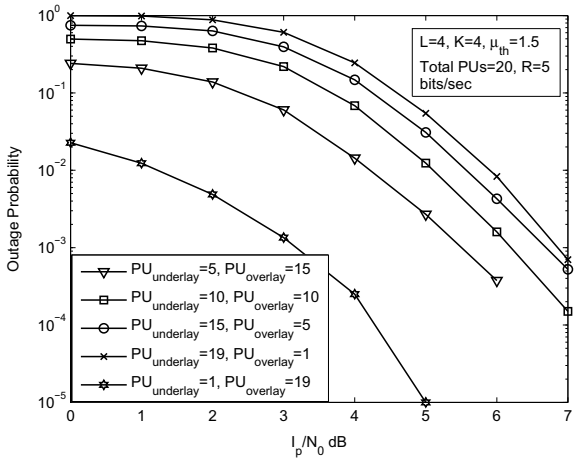

Fig. 3 Outage probability versus $\frac{I_p}{N_0}$ for underlay-overlay combination of PU

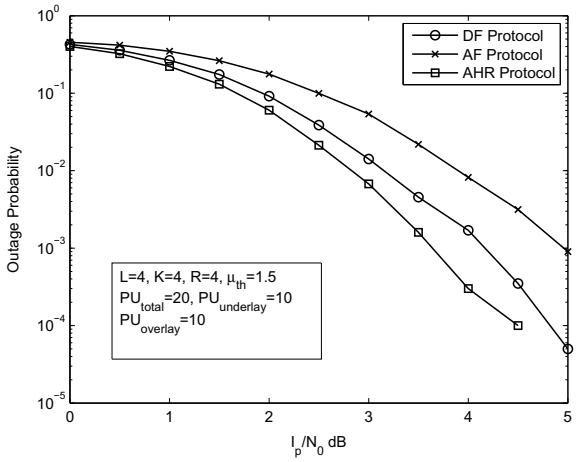

Fig. 4 Outage probability versus $\frac{I_p}{N_0}$ comparison of AF, DF and AHR protocol

available power. But in underlay mode, the signal transmission is handicapped by an interference constraint I_p which must be maintained for all PUs so as to avoid interference from secondary network. That is why we see an increased number of busy PUs gradually increase outage probability.

The graph shown in Fig. 4 is the respective outage performance comparison analysis for AF, DF and AHR protocol. The relays number (K), as well as antenna number (L), channel rate (R), interference threshold (I_p) and threshold SNR for determining successful decoding at relay (μ_{th}) are all kept constant at 4, 4, 4 bits/s, 5 dB and 1.5 dB, respectively. The total number of PUs is taken to be 20 equal number of busy and idle PUs. It is observed that outage analysis performance for AHR protocol is considerably better than individual AF as well as DF protocol. Because of an AHR protocol, the successfully decoded relays follow the DF protocol else AF protocol is followed. In our model, we have set the threshold SNR at 1.5 dB for determining suc-

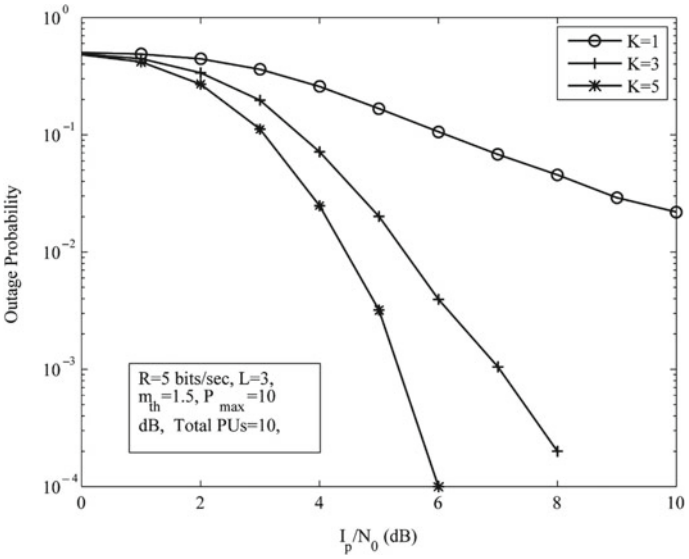

Fig. 5 Outage performance for increasing count of relays

cessful decoding of source signal at relay. Thus, all relays work together to make an enormous set of instantaneous SNR, which increases the diversity and consequently the outage probability decreases.

Figure 5 represents outage probability for increasing relay numbers. The specific system parameters are kept fixed—channel rate $R = 5$ bits/s, total number of primary users are 10 with 5 overlay PUs and 5 underlay PUs, maximum available power at secondary network for signal transmission $P_{\max} = 10$ dB, antenna number at individual relay $L = 3$, $\mu_{\text{th}} = 1.5$ dB. It is noticed that outage probability declines accordingly with the rise in relays number from 1 to 5 as $K = 1, 3, 5$. This is due to the fact, relays number improves high decoding as well as relay selection chances. This results in significant increase in SNR diversity. As a result, outage performance increases as the growing relay number.

In Fig. 6, we plot corresponding outage probability against $\frac{I_p}{N_0}$ for increasing antennas number at the individual relay. We keep the other system parameters constant, i.e., interference threshold $I_p = 5$ dB, number of relays $K = 5$, threshold SNR for determining successful decoding at the particular relay $\mu_{\text{th}} = 1.5$ dB, Total number of PUs =20 out of which $\text{PU}_{\text{under}} = 10$ and $\text{PU}_{\text{over}} = 10$. It is observed that as the number of antenna on each relay L is increased from 1 to 5 there is considerable decrease in outage probability. Here Increased antenna numbers enhance the count of similar copies of a signal at the relay, and thus increased SNR diversity improves the system outage performance.

Figure 7 depicts corresponding outage probability as a mathematical function of $\frac{I_p}{N_0}$ for different combination of relays number (K) as well as antennas number (L) at

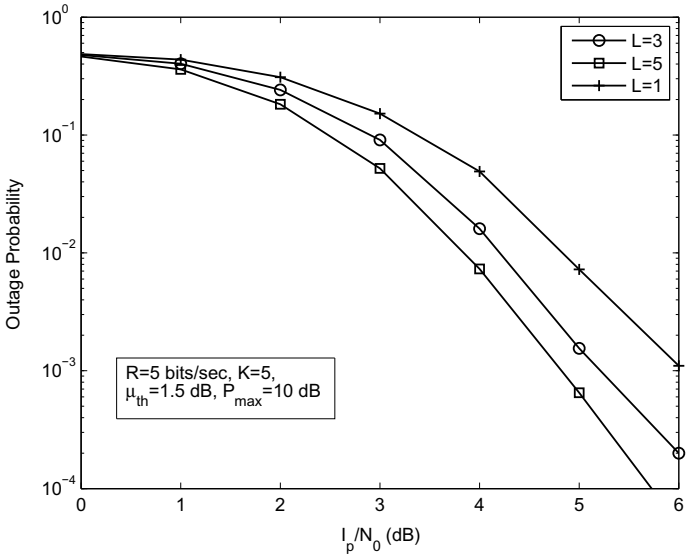

Fig. 6 Outage performance for increasing count of antenna at each relay

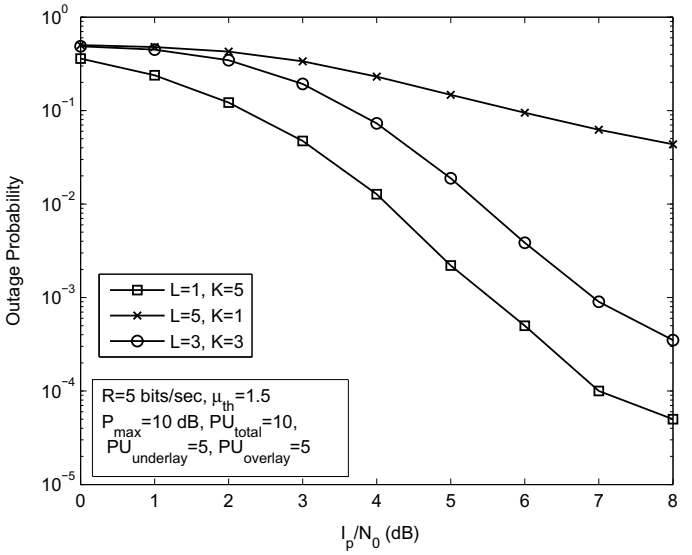

Fig. 7 Outage probability versus $\frac{I_p}{N_0}$ for different relays number and antenna number at respective relay

the individual relay. The threshold SNR μ_{th} is taken as 1.5 dB, maximum available transmit power at source $P_{\max}$ as 10 dB, channel rate R as 5 bits/s and total 10 number of PUs out of which 5 PUs are busy and 5 PUs are idle. The figure shows that for $K = 5$, $L = 1$, there is a significant performance improvement compared to the other two cases. So, the increased number of fixed antenna-based relays improves performance considerably, but when relays increase the number of antennas, then noticeable difference is not observed. Therefore, it can be said that number of relays has a greater impact on outage probability compared to antennas number at respective relay. Thus, there can be a trade-off between two parameters that are K as well as L for achieving a certain desired level of outage.

5 Conclusion

In the present paper, we have successfully analyzed outage performance assessment of our proposed joint underlay/overlay model under varying parameters. The AHR protocol-based relays transfer the source message to the respective destination. The outage performance is compared for varying number of busy PUs and idle PUs, and it is noticed that outage probability parameter increases with the busy PUs number, which exceeds the number of idle PUs. It is observed that AHR protocol performs better in terms of outage probability than AF and DF protocol. It is also seen that performance enhances as count of relays as well as antennas increases. Significant performance increase is seen in case of increasing relays than increasing antennas. Finally, a trade-off point has arrived where relays change their respective antennas number to obtain the required outage performance with in desired limit.

References

1. Mitola, J., Maguire, G.Q.: Cognitive radio: making software radios more personal. IEEE Personal Commun. **6**(4), 13–18 (1999)
2. Tanab, M.E., Hamouda, W.: Resource allocation for underlay cognitive radio networks: a survey. IEEE Commun. Surveys Tutorials **19**(2), 1249–1276 (2017)
3. Daoud, S., Haccoun, D., Cardinal, C.: On the achievable rate and average sum capacity of spread spectrum underlay CR networks. In: 2016 IEEE 84th Vehicular Technology Conference (VTC-Fall), pp. 1–5 (Sept. 2016)
4. Abdou, A., Ferré, G., Grivel, E., Najim, M.: Interference cancellation in multiuser hybrid overlay cognitive radio. In: 21st European Signal Processing Conference (EUSIPCO 2013), pp. 1–5 (Sept. 2013)
5. Saha, A., De, C.K., Nandi, A., De, D.: Cooperative spectrum sharing with multi antenna based amplify-and-forward and decode-and-forward relay. In: 2016 IEEE Uttar Pradesh Section International Conference on Electrical, Computer and Electronics Engineering (UPCON), pp. 224–228 (Dec. 2016)
6. Alhamad, R., Wang, H., Yao, Y.D.: Cooperative spectrum sensing with random access reporting channels in cognitive radio networks. IEEE Trans. Veh. Technol. **66**(8), 7249–7261 (2017)

7. Le, L.B., Hossain, E.: Resource allocation for spectrum underlay in cognitive radio networks. IEEE Trans. Wireless Commun. **7**(12), 5306–5315 (2008)
8. Chakravarthy, V., Li, X., Zhou, R., Wu, Z., Temple, M.: A novel hybrid over-lay/underlay cognitive radio waveform in frequency selective fading channels. In: 2009 4th International Conference on Cognitive Radio Oriented Wireless Networks and Communications, pp. 1–6 (June 2009)
9. Oh, J., Choi, W.: A hybrid cognitive radio system: a combination of underlay and overlay approaches. In: 2010 IEEE 72nd Vehicular Technology Conference - Fall, pp. 1–5 (Sept. 2010)
10. Bao, X., Martins, P., Song, T., Shen, L.: Capacity of hybrid cognitive network with outage constraints. IET Commun. **5**(18), 2712–2720 (2011)
11. Zuo, J., Zhao, L., Bao, Y., Zou, C.: Energy-efficient power allocation for cognitive radio networks with joint overlay and underlay spectrum access mechanism. ETRI J. **37**(3), 471–479 (2015)
12. Blasco-Serrano, R., Lv, J., Thobaben, R., Jorswieck, E., Kliks, A., Skoglund, M.: Comparison of underlay and overlay spectrum sharing strategies in miso cognitive channels. In: 2012 7th International ICST Conference on Cognitive Radio Oriented Wireless Networks and Communications (CROWNCOM), pp. 224–229 (June 2012)
13. Arpanaei, F., Navaie, K., Esfahani, S.N.: A hybrid overlay-underlay strategy for ofdm-based cognitive radio systems and its maximum achievable capacity. In: 2011 19th Iranian Conference on Electrical Engineering, pp. 1–6 (May 2011)
14. Arianandа, D., Lakshmanan, M., Nikookar, H.: A survey on spectrum sensing techniques for cognitive radio. In: Second International Workshop on Cognitive Radio and Advanced Spectrum Management (CogART) 2009, pp. 74–79. IEEE, New York(2009)
15. Yucek, T., Arslan, H.: A survey of spectrum sensing algorithms for cognitive radio applications. IEEE Commun. Surveys Tutorials **11**(1), 116–130 (2009)
16. Peer, M., Kalluri, T., Bohara, V.A., da Costa, D.B., Dias, U.S.: A time-splitting cooperative spectrum sharing amplify-and-forward relaying protocol with energy harvesting cognitive user. In: 2017 IEEE 18th Wireless and Microwave Technology Conference (WAMICON), pp. 1–6 (April 2017)
17. Duong, T.Q., Bao, V.N.Q., Zepernick, H.J.: Exact outage probability of cognitive af relaying with underlay spectrum sharing. Electron. Lett. **47**(17), 1001–1002 (2011)
18. Vashistha, A., Sharma, S., Bohara, V.A.: Outage analysis of a multiple-antenna cognitive radio system with cooperative decode-and-forward relaying. IEEE Wireless Commun. Lett. **4**(2), 125–128 (2015)
19. Khuong, H.V., Sofotasios, P.C., Son, V.Q., Tra, L.T., Lien, P.H.: Analysis of cognitive cooperative networks with best relay selection and diversity reception. In: 2015 International Conference on Advanced Technologies for Communications (ATC), pp. 651–656 (Oct. 2015)
20. Bhattacherjee, S.S., Saha, A., De, C.K., De, D.: Cooperative spectrum sharing using multi-antenna based adaptive hybrid relay. In: 2017 IEEE International Conference on Wireless Communications, Signal Processing and Networking (WispNet) (March 2017)
21. Al-Juboori, S., Fernando, X.: Correlated multichannel spectrum sensing cognitive radio system with selection combining. In: 2016 IEEE Global Communications Conference (GLOBECOM), pp. 1–6 (Dec 2016)

Capacitive Touch Sensor to Control Home Appliances Using PIC16 Microcontroller

Mehaboob Mujawar, Aiyas Rashid, and Jannisar Akhter Shah

Abstract Touch sensing technology has become very popular in today's world. It has become almost impossible to imagine the world of electronics without touch sensitive devices. Touch sensors are used in many applications in place of the primitive push buttons due to their ease of operation by just a touch. No additional force is required, as in the case of push buttons. Touch sensors come in two main variants—resistive and capacitive. In this paper we will be designing a circuit for touch sensors using capacitive touch sensing technology for operating home appliances. Here we will be using the PIC16 microcontroller. Four touch inputs are designed which will sense touch and operate the particular appliance connected to that input.

Keywords Touch sensors · Capacitive sensing · Proximity sensing · Touch panel · Bluetooth module · PIC16 microcontroller

1 Introduction

Touch sensors are circuits which operate similar to a switch when subjected to a touch. There are two types of touch sensors namely, Resistive sensors and Capacitive sensors. In this paper, we have designed a capacitive touch sensor to control home appliances. The primitive touch buttons which were employed till date, need force to be exerted in order to control connected devices. Capacitors can be thought of as two parallel conductors with an insulator or dielectric between them. Whenever our finger interacts with these conductor plates there is a change in capacitance which is measured by a measuring circuit thereby generating a signal. This change is due to the difference in the dielectric constant of our fingers in comparison to that of the capacitor. Capacitive touch sensors employ capacitors to form the touch sensing circuit. Here, four capacitive touch panels are used to control four home appliances

M. Mujawar (✉)
Goa College of Engineering, Goa, India

A. Rashid · J. A. Shah
Swami Devi Dayal Institute of Engineering and Technology, Barwala, Haryana, India

B. Sikdar et al. (eds.), *Proceedings of the 3rd International Conference on Communication, Devices and Computing*, Lecture Notes in Electrical Engineering 851,
https://doi.org/10.1007/978-981-16-9154-6_51

respectively. The construction of this circuit involves the following steps: (1) The touch on the capacitive touch panels determine which of the appliances will function. (2) As soon as the human finger touches the touch panel, the circuit is complete and there is a change in capacitance on account of the change in the dielectric constant. (3) These touch panels are connected to the input pins of a PIC microcontroller via a charge-sensing circuit. The microcontroller is programmed to determine whether a pin was touched or not. (4) Depending upon the inputs, the microcontroller then triggers the relay circuits which in turn drives the load i.e. the appliances.

2 Organization

The paper is as structured. In Sect. 3, we have discussed existing work with the support of literature survey and also comparison between different existing techniques has been listed. In Sect. 4, we have discussed in detail regarding the different components that have been used to build the circuit and also software PCB model along with the prototype has been described. Sections 5 and 6, state conclusion and future scope of the proposed system respectively.

3 Literature Survey

In paper [1], they have developed a home automation system using a capacitive touch screen. The touch screen is interfaced to a PIC microcontroller which is further programmed to control the home appliances connected to it. They used the PIC microcontroller because of its following advantages: (i) Cost Effective (ii) Easy Availability (iii) High Quality (iv) It also has an internal A/D convertor which converts analog coordinates from the touchscreen to digital coordinates which is then processed. Paper [2] deals with the basic concept of touch panels and the way it functions. How the sensor detects the moment a finger touches the surface and at which location of the panel. It discusses the various methods of detecting inputs. It also focuses on measurement methods, more specifically digital methods of calculating physical attributes such as pressure, liquid level, distance, etc. This concept is the main driving factor of this circuitry. In paper [3], they have used the concept of capacitive sensing technology in the production of new age devices, which use human body capacitance as their input and accordingly provide output as per received sensory feedback. They have used this technology to design a helmet which uses the capacitance of the human ear as input and the vehicle is activated only when the rider wears the helmet. This concept has been utilized in the making of this project. Paper [4] deals with Single-layer Multi-touch projective capacitance. It utilizes the technology of projective capacitance to develop a touch panel capable of detecting multiple touches. This technology is widely being used for touch sensitive devices as of today. A simple and cost effective device has been developed to counter the previously existing model of

resistive touch sensors. The novel touch panel structure comprises a touch panel over an LCD. ITO electrodes patterned by standard Photolithography separate the glass and LCD layer. The operating principle of the sensor is discussed which has been applied in this project. This involves change in capacitance due to the different dielectric constant of the human finger. Thus touch is detected. The touch sensing circuitry mentioned in this paper has been used in this project to sense touch inputs. Paper [5] discusses Fast Sample and Hold Charge-Sensing circuit with improvised speed of charge transfer due to the incorporation of a feedback loop. This circuit is useful for OCR applications and low cost data capturing devices. The circuitry mentioned in this paper has been used in the project for implementing charge sensing.

4 Circuit Design

As briefly mentioned in the introduction, the overall system consists of four touch inputs which control four output appliances respectively interfaced by the PIC16 microcontroller (Table 1).

Input section: The input section comprises two main sections i.e. power supply unit and touch sensors. The main elements of the Power Supply Unit are the TSR_1-24120 step down regulator module and the L7805 linear regulator. This unit provides the power to drive the entire circuitry. The TSR_1-24120 converts the incoming input voltage to a fixed 12 V output and L7805 gives a fixed output of 5 V DC which powers the PIC16 microcontroller. This entire setup has been connected to pin 11 of the PIC16 microcontroller. The touch sensing circuitry mainly constitutes capacitors, since capacitive touch has been incorporated. We have used the circuitry for mutual capacitive touch sensing from paper [4]. This setup is capable of detecting multiple touches and thus utilizing the projective capacitance technology. The sensor circuit works on the basic principle that any object when in close proximity to the sensor, causes a disruption in the existing electric field. This causes the field to shunt to the ground, thus reducing the capacitance Cds. Thus when a finger is placed on the

Table 1 Components used to build the circuit

Name of the component	Specification
Capacitors	100, 0.1 μ
Diode	IN4004
Relay	DPDT_FRT5
DC convertor	TSR_1-24120
Microcontroller	PIC16F877-XXIP
Transistor	BD139
Voltage regulator	L7805

sensor, a change in Cds occurs and a touch is detected, without having to apply any additional force. We have four touch sensor circuits connected to pins 2, 3, 4 and 5 of the PIC16 microcontroller. These are further connected to a charge-sensing circuit. This circuit monitors the mutual capacitance sensing and driving nodes.

Output section: The output section consists of the relay circuits which are switched through the transistor. We have used the BD139 transistor in our circuit. These relays are connected to pins 7, 8, 9 and 10 of the PIC16 microcontroller. There is a resistor connected to the base of each transistor to limit the flow of current. Then, we have our appliances which are connected as the loads. IN4004 diodes are connected across the relays to protect the circuit from any transient voltage that might be generated when the relay toggles (Figs. 1, 2 and 3).

5 Conclusion

A cost effective touch sensing device was thus developed using the widely used projective capacitance technology along with supporting multi-touch. The PIC16 microcontroller helped interface the touch inputs to output devices. Hence, output devices could be controlled by touch rather than conventional push buttons.

6 Future Scope

Their use is expected to increase in the future as they are highly durable, accurate, sensitive and easy to operate. The coming years can witness improvements in their build quality, accuracy and sensitivity. This can lead to a wide number of sectors adopting this technology thus increasing their demand over the coming years apart from domestic and personal usage. Advancement in this technology can help to overcome its existing limitations like inadaptability of the thin ITO sensors with thicker glass, the need of higher durability in industries and compatibility across different screen variants. Multi-user multi-touch experience is expected to rise in popularity. Advancements are expected to detect touch through cloth and also need for reduced power usage.

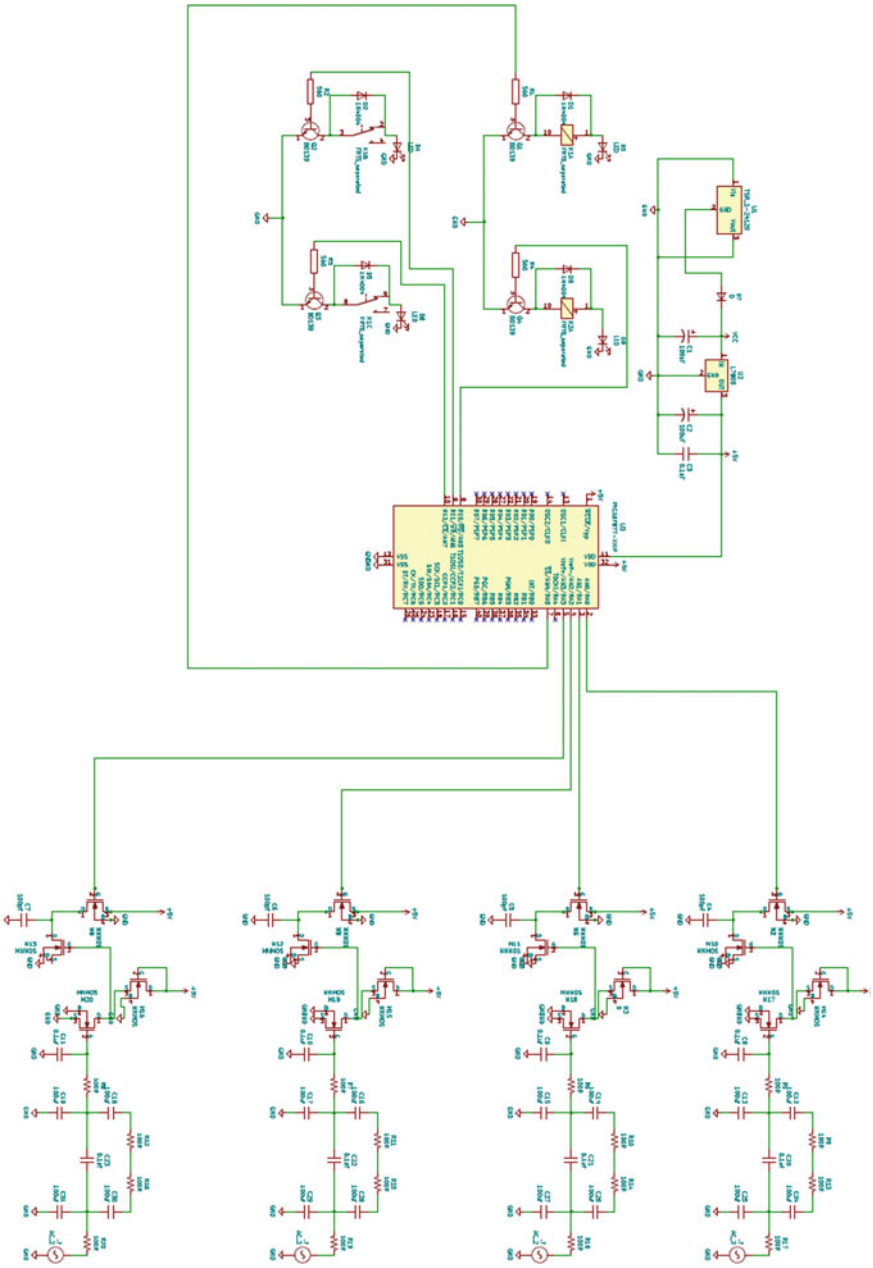

Fig. 1 Schematic diagram of the circuit in Ki-CAD software

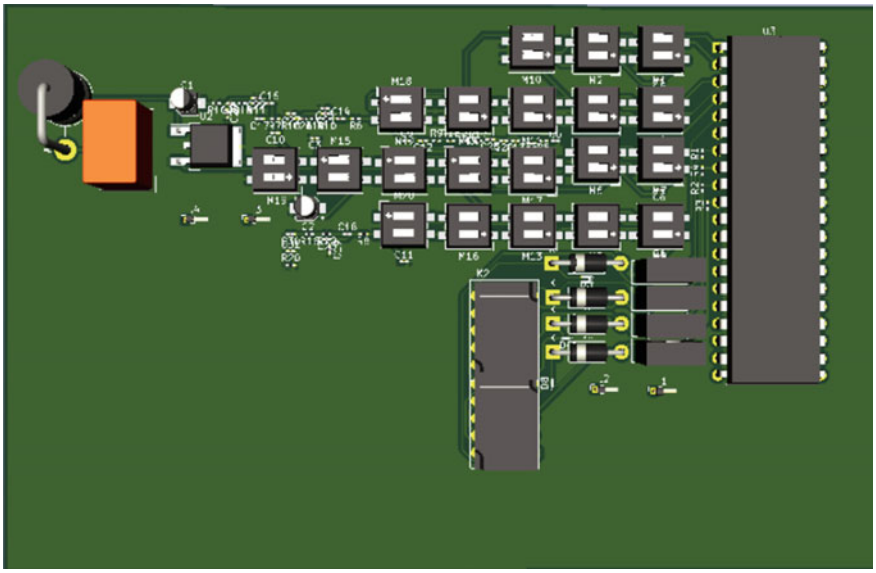

Fig. 2 PCB model of capacitive touch sensor

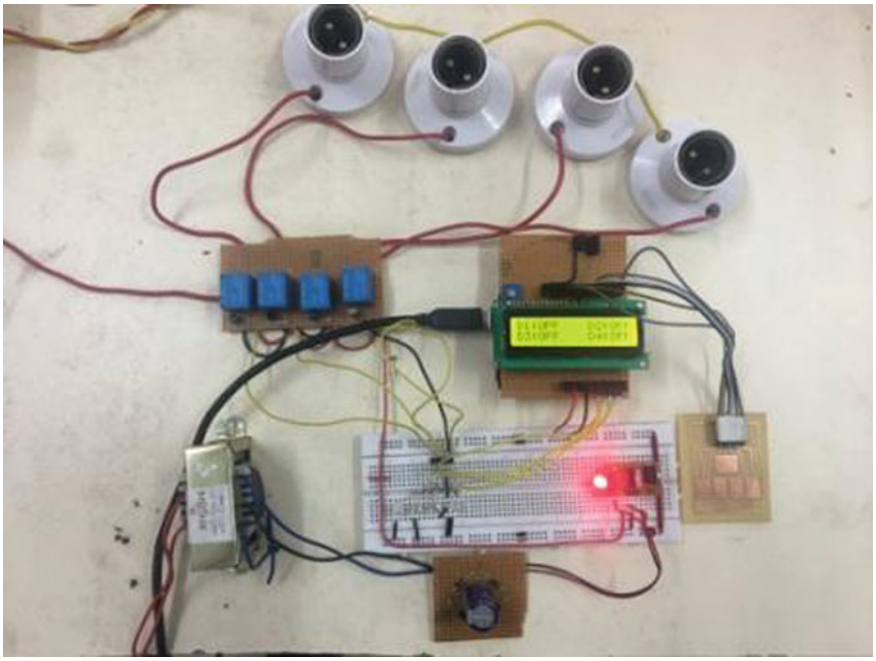

Fig. 3 Prototype of the capacitive touch sensor used in home automation system

References

1. Inaniya, Y., Kumari, N., Inaniya, Y.L.Y., et al.: Home automation system using capacitive touchscreen. Int. J. Eng. Res. Appl. **4**(6) (Version 2), 101–103. ISSN:2248-9622
2. Fischer, D.: Capacitive touch sensors application fields, technology overview and implementation example. Fujitsu Microelectron. Europe GmbH Pittlerstrasse **47**, 63225
3. Shadwani, M., Sachan, S., Sachan, P.: Capacitive sensing and its applications. Int. J. Eng. Res. General Sci. **4**(3) (2016). ISSN 2091-2730
4. Paul, G., Jespers, A.: A fast sample and hold charge-sensing circuit for photodiode arrays. IEEE J. Solid-State Dev. **SC-12**(3) (1997)
5. Sherif, M.H.: Intelligent homes: a new challenge in telecommunications standardization. Commun. Mag. **40**(1), 8 (2002)

Android Application for Effective Timing Management of Classes

Jayant Kr Shaw, Nayan Ghosh, Abhishek Srivastava, Sahil Singh, Sushri Mukherjee, Dharmbir Prasad, and Rudra Pratap Singh

Abstract Since mobile phones are popular among us and used in our day-to-day life very frequently, we have attempted to create a timetable management Android application that the students can easily access through their smart phones. Although there are many mobile platforms available in the market these days, Android OS is the most user friendly and programmerfriendly platform. This application will make more comfortable students' study life. This application that we are discussing here is the Semester Scheduler. Using this app, student will be able to maintain their class timetable and make changes in their plan according to that. Using this Android app, students as well as faculty members will be able to know their scheduled class time whenever they are in need. To make this table more informative, all the information's has been represented in an understandable manner.

Keywords Android app · Mobile application · Sustainable software · Classes time management

1 Introduction

Timetable management is an Android application developed to help the educational institutes to plan, schedule, and maintain regular classes following a specific schedule. The application aims to inform students about their schedule class timing and their semester subjects' details and its syllabus and their faculties' details like email ID, phone number, and their digital classroom meeting ID [1]. Using this app, a user can check the list of available classes and timings and does not need to visit their

J. K. Shaw · N. Ghosh · A. Srivastava · D. Prasad (✉) · R. P. Singh
Asansol Engineering College, Asansol, West Bengal 713305, India

S. Singh
Asansol Institute of Engineering and Management Polytechnic, Asansol, West Bengal 713339, India

S. Mukherjee
Indian Institute of Technology Delhi, New Delhi 110016, India

B. Sikdar et al. (eds.), *Proceedings of the 3rd International Conference on Communication, Devices and Computing*, Lecture Notes in Electrical Engineering 851,
https://doi.org/10.1007/978-981-16-9154-6_52

college Web site or make calls to respective faculty of subject for getting updated with his/her classes.

1.1 Related Works Review

Recently, many applications are emerging for various tasks with ease out our daily life. In 2015, authors have presented a traffic-sign-related Android system to learn and test those signs for safe and effective driving [1]. In the same year, Mirzaei and Heydarnoori [2] have worked on android fault localization through test smart mobile application [2]. A study on the threat and vulnerability of android app has been carried out by Schmeelk and Aho [3]. Vince et al. [4] have tested the Android system with a Web application-based JSON test protocol approach [4]. In this works, Sahar et al. [5] have tried to reduce energy consumption on a device using object-oriented simplified metric suites [5]. Yuan et al. [6] have proposed an API approach (e.g., '<Description, API>' and Callback) for a library (i.e., LibraryGuru) [6]. However, Rajkumar et al. [7] have presented an application for home automation. It will intimate users about various parameters for improved security measures [7].

Sarkar et al. [8] have proposed a layered technique (e.g., Application Layer, App Framework Layer, Android Runtime Layer, and Linux Kernel) for an Android system independent of platform applications such as compiling features of both existing java IDEs and Google Android SDK [8]. Cui et al. [9] have studied vulnerability aspects of Android applications to reduce security risks [9]. Xiao et al. have evaluated the risks MPDroid using associated with Android application [10]. Zhao et al. [11] have applied a double-layer packer approach, namely Dex2VM to deal with infringing issues of Android applications. Their security enhancing concept was virtualization from DEX to native level [11]. In 2020, Rajeswari and Anbalagan have designed and evaluated multiple parameters (for various shapes, viz triangular, square, rectangular, and circular) for an Android application for the micro-strip antenna [12]. Wongwiwatchai et al. [13] have made a lightweight static analysis for checking pilferage of personal information [13].

1.2 Proposed Applications Uniqueness

In the traditional way to check class routine, a student has to go to the college Web site and log in with his/her credentials which requires an internet connection and this process about takes 2 or 3 min. In some cases, educational body like schools and colleges which does not have their Web sites, they use a social platform like WhatsApp, Facebook, and Telegram App to share their respective class timetable, faculty details, and syllabus. But as time passes especially in this COVID phase when all communication is done with the help of social media platform due to a number of messages, this valuable information is lost in the heap of messages and student

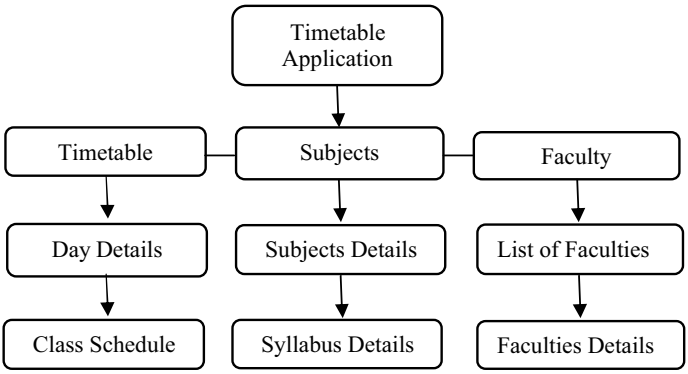

Fig. 1 Architecture of Android application

has to scroll up and down to get this information, as well as it is very difficult for the sender end to send this information to the targeted social media group. Its design architecture is presented as in Fig. 1. Most times, the students have to physically visit the notice boards in order to access their lectures and take a photograph of the timetable with their smartphones and save it to their gallery. Students usually end up losing track of the image on their phones thereby making it difficult for them to remember their lecture schedules.

Sometimes we the face problem that our departmental syllabus consisting details from the first year to the final year and also contains a syllabus of every elective subject which creates a headache for the student to find the specific syllabus of a particular subject in a specific semester. Therefore, there is a need for the development of an Android application timetable system that can fix the glitches of the current manual system. The specific features are as follows:

- This timetable application provides class timing, subjects details, and faculty details in a single place.
- It provides the facility to see the list of subjects and their syllabus.
- With the help of this application, contact details of the faculties, and their digital classroom meeting ID will be available in one place.
- It is a very compatible software, simple interface, and is easy to use.
- Being an Android applications, it is more flexible than currently in use the college Web site or Web application.
- All these features can be accessed anytime without the need for an Internet connection anywhere with users' smartphones.

Table 1 Requirements for proposed Android system

(a) Software requirements	(b) Hardware requirements:
• Mobile operating system: Android • Tools (IDE): Android Studio 4.2.1 • Code behind: JAVA, XML • SDK version: minimum-16 API, maximum-30 API • Internet: yes	• Android smartphone with minimum OS version Lollipop 5.0 • The processor is not less than 1 GHz • RAM is not less than 2048 MB • Resolution is not less than 480 * 800pixel

1.3 System Requirements

This system is mobile phone-based. The various necessities (resources) needed for the proper functionality of the proposed system are software components resources and hardware requirements (refer to Table 1).

2 Interfacing Process

This is the homepage page of this application. From this screen, the user can choose further three options—Timetable, Subjects, and Faculty (refer to Fig. 2). The corresponding program code is shown in Fig. 3. The whole timetable management app starting from homepage activity has been classified under the following activities:

- *Timetable Activity*: After clicking the Timetable option, the user will enter in this screen, and a list of days of the week will appear. After clicking one of the days from the list, the respective schedule classes with faculties name will appear.
- *Subject Activity*: On clicking the Subject option, the user will see a list of subjects, and after clicking any of the subject names, the respective subject syllabus will be displayed.
- *Faculty Activity*: After clicking the Faculty option, the user will see in this screen a list of faculties name. On clicking any faculty name from the list of faculty, the user will see the details of respective faculty like their name, profile photograph, contacts number, email ID, and most important of them is digital classroom meeting ID.

3 Security State of the Proposed App

The factors which make this timetable application more secure against vulnerability and threats are:

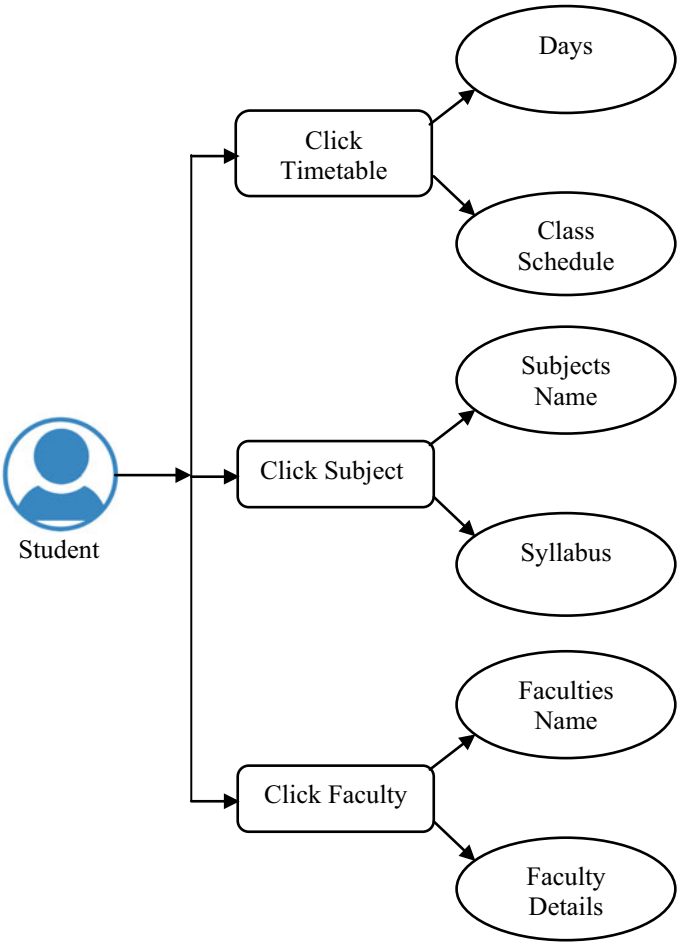

Fig. 2 Layout of user interfacing process

- The fundamental base of Android is the Linux kernel. This project prevents one app from accessing data stored by another app.
- This application also enforces the permission system that prevents accessing resources, such as files and databases, from other apps installed on the device.
- This app also does not require storage permission of the device. So, the stored data on the device cannot be breached from this application by using different methods hacking techniques.
- As mentioned, this app is a statics app, i.e., it does not require an internet connection for its operation, so it is free from remote hacking and the hacker cannot alter app data online (Fig. 4).

Programming Code: MainActivity.java

```
package com.example.timetabledemo;

import …

public class MainActivity extends AppCompatActivity {

private Toolbar toolbar;
private ListView listView;

@RequiresApi(api = Build.VERSION_CODES.LOLLIPOP)
@Override
protected void onCreate(Bundle savedInstanceState) {
super.onCreate(savedInstanceState);
        setContentView(R.layout.activity_main);

        setupUIViews();
        initToolbar();
        setupListView();
    }

@RequiresApi(api = Build.VERSION_CODES.LOLLIPOP)
private void setupUIViews(){
toolbar = (Toolbar)findViewById(R.id.ToolbarMain);
listView = (ListView)findViewById(R.id.lvMain);
    }

private void initToolbar(){
        setSupportActionBar(toolbar);
        getSupportActionBar().setTitle("Timetable App");
}
         .......
         .......
         .......
```

Fig. 3 Coding correlation of main activity

4 Conclusion

This Timetable Android app, being capable of providing a platform for planning and scheduling with a single application, can prove to be the most effective and reliable static Android smartphone application which does not require any Internet connectivity for its operation. As the application is designed in the Android platform, it can install all students' and facultys' cell phones. In this application, students cannot find the updated routine at the end of each semester or if there is an unavoidable change in the routine like faculty is replaced, etc. Because this application does not require an internet connection for its operation, so app's data cannot update or change on a real-time basis. To make any update in the routine or changes in faculties' details, once again there would be a requirement of the app developer. Thus, it is a user-friendly app for effective class timing management.

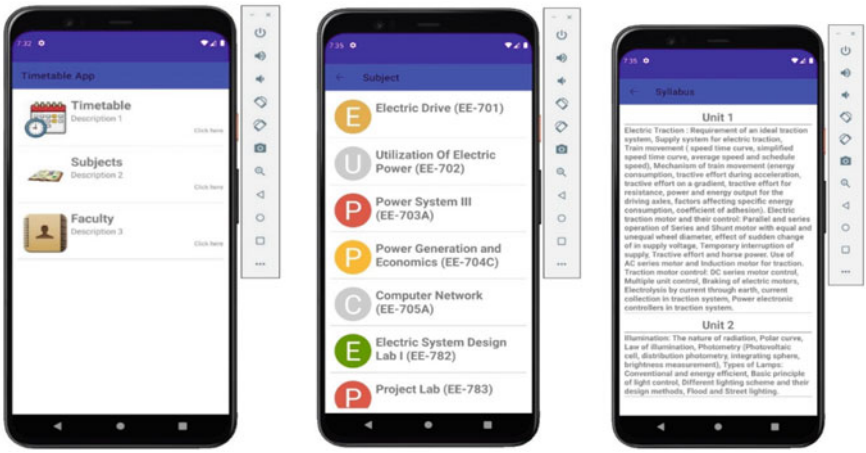

Fig. 4 Snapshot of testing pages of this android application

References

1. Janpla, S., Bumrugrad, P., Kularbphettong, K.: Developing a traffic-sign knowledge application on android system. Procedia Soc. Behav. Sci. **191**, 680–685 (2015)
2. Mirzaei, H., Heydarnoori, A.: Exception fault localization in Android applications. In: 2015 2nd ACM International Conference on Mobile Software Engineering and Systems, pp. 156–157. IEEE (2015)
3. Schmeelk, S., Aho, A.: Defending android applications availability. In: 2017 IEEE 28th Annual Software Technology Conference (STC), pp. 1–5. IEEE (2017)
4. [X9]. Vince, T., Lukáč, P., Schweiner, D., Tomčíková, I., Mamchur, D.: Android application supporting developed web applications testing. In: 2017 International Conference on Modern Electrical and Energy Systems (MEES), pp. 392–395. IEEE (2017)
5. Sahar, H., Bangash, A.A., Beg, M.O.: Towards energy aware object-oriented development of android applications. Sustain. Comput. Inform. Syst. **21**, 28–46 (2019)
6. Yuan, W., Nguyen, H.H., Jiang, L., Chen, Y., Zhao, J., Yu, H.: API recommendation for event-driven Android application development. Inf. Softw. Technol. **107**, 30–47 (2019)
7. Rajkumar, N., Rajendra, A.B., Vinod, V.: H2M communication for home appliances automation using android application. Proc. Comput. Sci. **167**, 2561–2569 (2020)
8. Sarkar, A., Goyal, A., Hicks, D., Sarkar, D., Hazra, S.: Android application development: a brief overview of android platforms and evolution of security systems. In: 2019 Third International conference on I-SMAC (IoT in Social, Mobile, Analytics and Cloud) (I-SMAC), pp. 73–79. IEEE (2019)
9. Cui, J., Wang, L., Zhao, X., Zhang, H.: Towards predictive analysis of android vulnerability using statistical codes and machine learning for IoT applications. Comput. Commun. **155**, 125–131 (2020)
10. Xiao, J., Chen, S., He, Q., Feng, Z., Xue, X.: An Android application risk evaluation framework based on minimum permission set identification. J. Syst. Softw. **163**, 110533 (2020)

11. Zhao, Y., Tang, Z., Ye, G., Peng, D., Fang, D., Chen, X., Wang, Z.: Compile-time code virtualization for android applications. Comput. Secur. **94**, 101821 (2020)
12. Rajeswari, P., Anbalagan, P.: Design and deployment of android based mobile application for performance analysis of micro strip patch antenna. Microprocess. Microsyst. **77**, 103111 (2020)
13. Wongwiwatchai, N., Pongkham, P., Sripanidkulchai, K.: Detecting personally identifiable information transmission in android applications using light-weight static analysis. Comput. Secur. **99**, 102011 (2020)

Analyze DGS Antenna Structure

Samiran Chatterjee, Uppuluri Shyamala Seshadri, R. Vani, and K. Pravallika

Abstract Here, we proposed the single feed, dual-layer DGS microstrip antenna for application of any microwave band frequency. In this proposed antenna, antenna consists of cutting two rectangular slots in addition with one circular slot from the patch and added some small rectangular slits with the slots and add two rectangular slits in top layer. Same as from bottom layer use *H*-shaped slots. The proposed antenna simulated with high return loss, increased frequency ratio and VSWR within 2:1 range. From the above-mentioned design of proposed antenna, we achieved a resonant frequency of about 4.23 GHz with − 12.75 dB return loss. For the above frequency, we also achieved a − 10 dB bandwidth of about 14.70 MHz. Also we achieved a resonant frequency of about 8.82 GHz with − 10.96 dB return loss. For the second resonant frequency, we got a bandwidth of about 26.86 MHz. Also, for first resonant frequency measure, the gain of about 2.04 dBi with 165.14° beamwidth (− 3db HPBW) and for second resonant frequency measure, the gain of about 1.53 dBi with 165.05° beamwidth (− 3db HPBW). The main achievement is that the proposed antenna has no intersymbol interference (ISI).

Keywords Beamwidth · DGS · Radiation pattern · Gain · VSWR

1 Introduction

In modern communication scenario, DGS antenna design creates a challenge with high bandwidth and gain with increasing frequency ratio [1–6] for young engineers. Microstrip antenna is essentially limited to some substrate [7]. Each substrate has two layers, i.e., the top layer and the bottom layer. For simple design of microstrip antennas, we use only the top layer, so it does not give off bandwidth. To get the

S. Chatterjee (✉)
Professor, ECE Department, Amrita Sai Institute of Science and Technology, Vijayawada, Paritala, India

U. S. Seshadri · R. Vani · K. Pravallika
Department of ECE, Vignan's Institute of Management and Technology for Women (Affiliated to JNTU, Hyderabad), Kondapur, Medchal, Malkagigiri, Telangana 501301, India

B. Sikdar et al. (eds.), *Proceedings of the 3rd International Conference on Communication, Devices and Computing*, Lecture Notes in Electrical Engineering 851,
https://doi.org/10.1007/978-981-16-9154-6_53

bandwidth, it requires cutting slots and cracks in the top layer as well as the bottom layer [8–11]. When we only cut some of the top and bottom layer, then we are not creating any disturbance to the ground layer [12]. This type of ground layer is called infinite earth layer, and it has some conductivity so that a ground layer behaves. But for the DGS structure, we need to make a disturbance in the ground layer in the form of cutting some holes and cracks. This type of ground plane is called the finite ground plane and has zero conductivity. We use IE3D [13] software for analysis of design antenna.

2 DGS Design

The DGS structure design with two unequal rectangular slots with one circular slot and some small rectangular slits, fitted with these slots which is shown in Fig. 1 with dimensions. The insulation material used is polytetrafluoroethylene-based substrate with FR_4. The upper layer uses 15 mm $\times$ 12 mm rectangular patch.

In the ground of patch, DGS uses vertical *H* slots shown in Fig. 2 designed. The bottom layer uses 16 mm $\times$ 14 mm rectangular patch.

3 Result Analysis

Here, we analyzed the various parameters, i.e., bandwidth, gain, half-power beamwidth, VSWR and return loss. Figure 3 illustrated return loss of the DGS structure.

As per the slots cutting technique, we achieved multiple resonant frequencies with deep return loss. All the resonant frequencies are summarized and placed in Table 1.

3.1 Electric and Magnetic Pattern

Figures 4, 5, 6 and 7 propose the electric and magnetic patterns of DGS structure for all resonances (Table 2).

4 Conclusion

The proposed compact DGS microstrip antenna uses two rectangular slots with one circular slot and added some small rectangular slits with the slots and adds two rectangular slits with the patch from the upper layer. Same as from bottom layer cutting *H*-shaped slots from the rectangular patch. In proposed design, antenna operate with

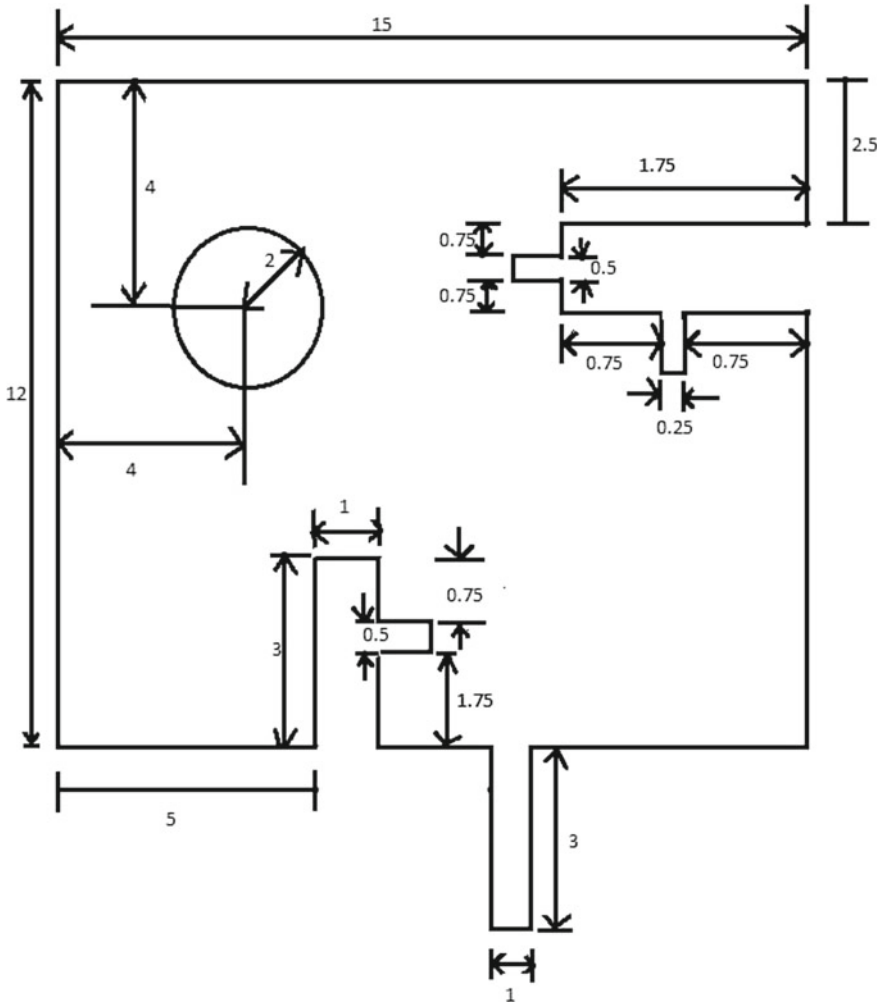

Fig. 1 DGS antenna (upper layer)

multiple resonant frequencies which belong to different microwave frequency bands application. Designing the proposed microstrip antenna using single transmission line feed at the ends of antenna structure in top layer shows that the antenna is working for the application for which it is intended. The proposed MSA achieved first resonant frequency at 4.23 GHz with − 12.75 dB return loss. For the above frequency also achieved a − 10 dB bandwidth of about 14.70 MHz. Also achieve a resonant frequency of about 8.82 GHz with − 10.96 dB return loss. For the second resonant frequency got a bandwidth of about 26.86 MHz. So it is concluded that there will be no ISI for the proposed antenna. The antenna achieved increased frequency ratio with 2:1 VSWR range and 165.14° of HPBW on an average on all resonant frequencies.

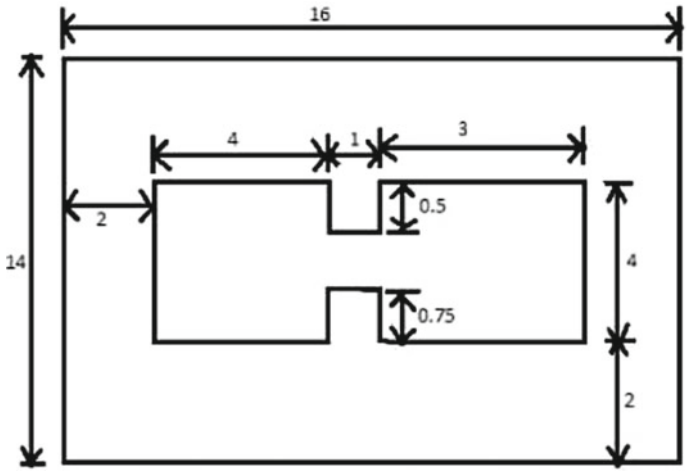

Fig. 2 DGS Antenna (bottom layer)

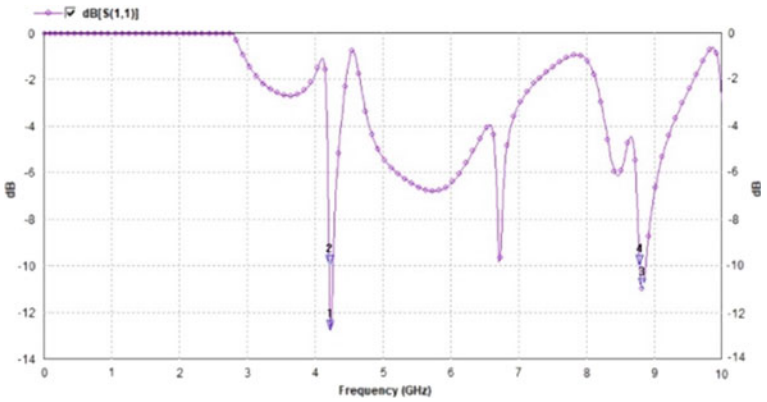

Fig. 3 Return loss

Table 1 Measurement of resonant frequency, bandwidth and VSWR

Frequencies (GHz)	Return loss	Bandwidth (MHz)	VSWR
$f_1 = 4.2293$	− 12.7539	14.7	1.60
$f_2 = 6.72$	− 9.7852	–	1.95
$f3 = 8.8165$	− 10.9581	26.86	1.79

The first resonant frequency is applicable for long-distance radio telecommunications, and second resonant frequency is applicable for satellite communications and space communications. The beamwidth is enough for the application for which it is intended.

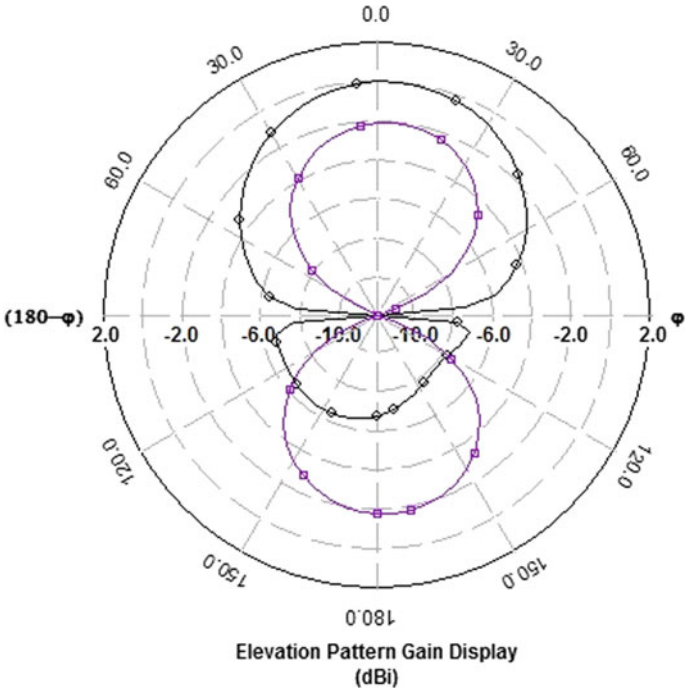

Fig. 4 Electric field pattern at 4.2293 GHz

Fig. 5 Magnetic field pattern at 4.2293 GHz

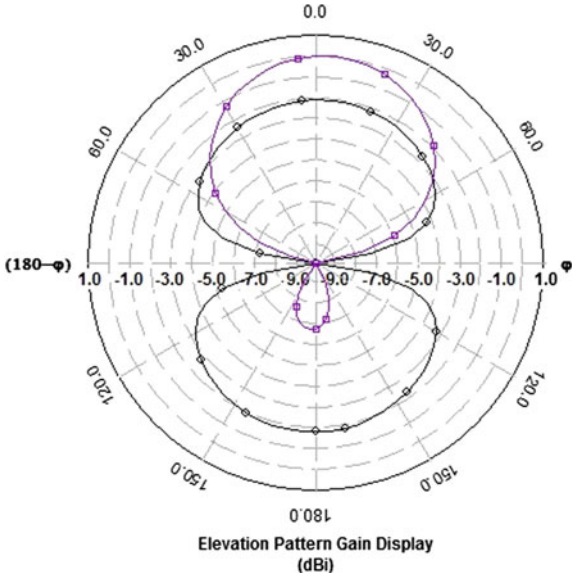

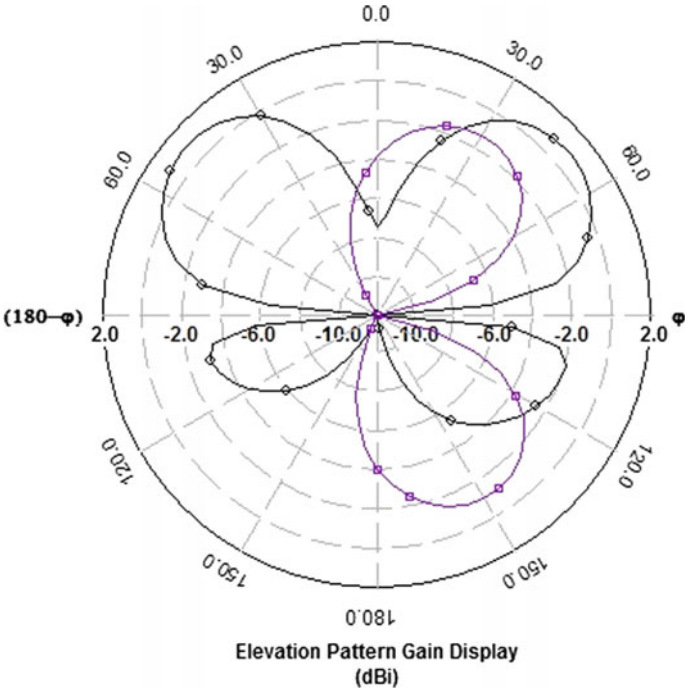

Fig. 6 Electric field pattern at 8.8165 GHz

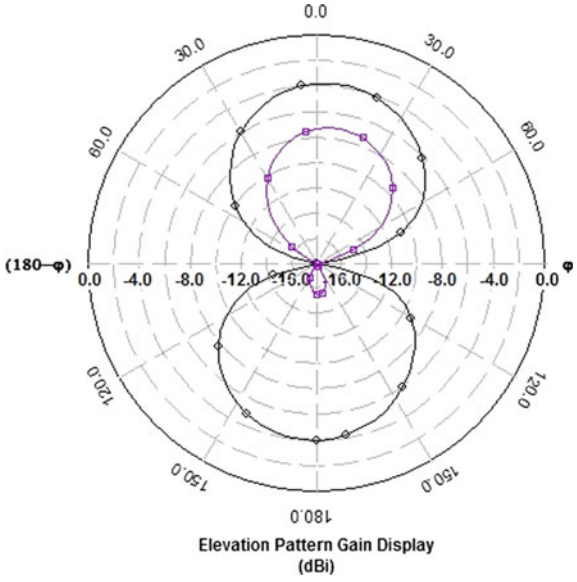

Fig. 7 Magnetic field pattern at 8.8165 GHz

Table 2 Measurement of gain and beamwidth

Frequencies (GHz)	Frequency ratio	Max. gain (dBi)	Beamwidth (°)
$f_1 = 4.2293$	1	2.04	165.141°
$f_2 = 6.72$	1.58	2.42	93.263°
$f3 = 8.8165$	2.08	1.53	5.053°

References

1. Sarkar, I., Sarkar, P.P., Chowdhury, S.K.: A new compact printed antenna for mobile communication. In: 2009 Loughborough Antennas & Propagation Conference, 16–17 Nov. 2009, Loughborough, UK
2. Chatterjee, S., Paul, J., Ghosh, K., Sarkar, P.P., Chanda (Sarkar), D., Chowdhury, S.K.: A compact microstrip antenna for WLAN communication. In: National Conference of Electronics, Communication and Signal Processing, 2011, Paper ID: 116
3. Chakraborty, U., Chatterjee, S., Chowdhury, S.K., Sarkar, P.P.: Triangular slot microstrip patch antenna for mobile communication. In: India Conference (INDICON), 2010 Annual IEEE, pp. 4–7, Paper ID: 511
4. Jan, J.-Y., Tseng, L.-C.: Small planar monopole antenna with a shorted parasitic inverted-L wire for wireless communications in the 2.4, 5.2 and 5.8 GHz bands. IEEE Trans. Antennas Propag. **52**(7), 1903–1905 (2004)
5. Chatterjee, S., Chakraborty, U., Sarkar, I., Chowdhury, S.K., Sarkar, P.P.: A compact microstrip antenna for mobile communication. In: India Conference (INDICON), 2010 Annual IEEE, pp. 1–3, Paper ID: 510
6. Danideh, A., Fakhr, R.S., Hassani, H.R.: Wideband coplanar microstrip patch antenna. Progr. Electromagn. Res. Lett. PIER **4**, 81–89 (2008)
7. Chatterjee, S., Paul, J., Ghosh, K., Sarkar, P.P., Chowdhury, S.K.: A printed patch antenna for mobile communication. In: Convergence of Optics and Electronics Conference, pp. 102–107, 2011, Paper ID: 15
8. Bahl, J., Bhartia, P.: Microstrip Antennas. Artech House, Dedham, MA (1980)
9. Chakraborty, U., Chatterjee, S., Chowdhury, S.K., Sarkar, P.P.: A compact microstrip patch antenna for wireless communication. Progr. Electromagn. Res. C **18**, 211–220 (2011)
10. Fallahi, R., Kalteh, A.-A., Golparvar Roozbahani, M.: A novel UWB elliptical slot antenna with band-notched characteristics. Progr. Electromagn. Res. C **18**, 211–220 (2011)
11. Chatterjee, S., Chowdhury, S.K., Sarkar, P.P., Sarkar, D.C.: Compact microstrip patch antenna for microwave communication. Indian J. Pure Appl. Phys. **51**, 800–807 (2013)
12. Balanis, C.A.: Advanced Engineering Electromagnetic. John Wiley & Sons, New York (1989)
13. Zeland Software Inc. IE3D: MOM-Based EM Simulator. http://www.zeland.com

Optimum Power Flow Scheduling with Valve-Point Effects Using Barnacles Mating Optimization

Sunil Kumar Choudhary, Kamalika Tiwari, and Santigopal Pain

Abstract This article proposes one novel method based on barnacles mating optimization (BMO) to achieve power flow scheduling (PFS) problems by considering non-linearities such as valve-point effects on a thermal power unit. The multi-objective function of the problem is to attain a reduced generation cost for a short-term period, maintaining the system constraints. The paper proposes a detailed framework of the power flow scheduling (PFS) problem. Numerical analysis of the test systems is discussed to explain the usefulness of the BMO approach to obtain an optimal solution of the PFS problem. The simulation results validate that BMO algorithm is well enough to provide lower economic cost than other meta-heuristic methods when various complex constraints in the problem of PFS are considered.

Keywords Power flow scheduling (PFS) · Barnacles mating optimization (BMO) · Valve-point effect

Nomenclature

i, j	Index of thermal, hydro power unit respectively
C_t, F_t	Total cost, fuel cost respectively
N_t, N_h	Total no. of thermal, hydro units respectively
τ, T	Time sub-interval and Scheduling period respectively
u_r	Index of upstream reservoir
$Q_{hj,\tau}$, $I_{hj,\tau}$	Discharge and inflow rate of jth hydro unit τ respectively
$P_{ti,\tau}$, $P_{hj,\tau}$	Thermal and hydro of ith and jth at τ

S. K. Choudhary (✉) · K. Tiwari
Department of E.E., Dr. B.C. Roy Engineering College, Durgapur, West Bengal, India

K. Tiwari
e-mail: kamalika.tiwari@bcrec.ac.in

S. Pain
Department of E.E., Haldia Institute of Technplogy, Haldia, West Bengal, India

B. Sikdar et al. (eds.), *Proceedings of the 3rd International Conference on Communication, Devices and Computing*, Lecture Notes in Electrical Engineering 851,
https://doi.org/10.1007/978-981-16-9154-6_54

$V_{hj,\tau}$, $S_{hj,\tau}$	Reservoir volume and spillage of jth hydro unit τ respectively
$P_{\mathrm{d},\tau}$, $P_{\mathrm{L},\tau}$	Total demand and transmission loss at τ
α_i, β_i, γ_i, δ_i, ε_i	Emission co-efficient of ith thermal unit
a_i, b_i, c_i, d_i	Fuel cost co-efficient of ith thermal unit
e_i, h_i	Co-efficient of the valve-point effect of ith thermal unit
$C_{(1-6)j}$	Hydro power output co-efficient of jth hydro unit
$P_{ti}^{\min}$, $P_{ti}^{\max}$	Minimum and maximum power limit of ith thermal unit
$P_{hj}^{\min}$, $P_{hj}^{\max}$	Minimum and maximum power limit of jth hydro unit
$Q_{hj}^{\min}$, $Q_{hj}^{\max}$	Minimum and maximum discharge limit of jth hydro reservoir
$V_{hj}^{\min}$, $V_{hj}^{\max}$	Minimum and maximum volume limit of jth hydro reservoir
$V_{hj}^{\min}$, $V_{hj}^{\max}$	Minimum and maximum volume limit of jth hydro reservoir
V_{hj}^{begin}, V_{hj}^{end}	Initial and final storage volume of jth hydro reservoir

1 Introduction

Power flow scheduling is inherently a non-linear dynamic constrained optimization problem. This possesses a significant contribution in the power system economy. It is evident that hydro energy possesses huge potential from a generation point of view. Besides, it is environment-friendly and hence contributes in energy conversion without emission unlike fossil fuel-based extraction techniques. So, harnessing hydro energy is very significant in terms of sustainable development. The purpose of short-term hydrothermal scheduling is multifold. It helps in determining an optimal generating schedule of hydro and thermal power over a scheduled time interval meeting the load demand while considering the constraints associated with thermal as well as hydro systems. Optimal scheduling of a hydrothermal system is carried out by considering a non-linear objective function along with a mixture of linear as well as non-linear constraints. Particle Swarm Optimization (PSO) was successfully implied for a short-term scheduling problem [1]. According to Sinha et al. [2] Fast Evolutionary Programming (FEP) method can be used for short-term hydrothermal scheduling considering economic emission-based objective cost function. Orero and Irving [3] presented an optimal solution for power generation scheduling adopting Genetic Algorithm (GA). Hota et al. [4] proposed a valve-point loading for a multi-reservoir cascaded hydro-electric system using improved PSO. Various research works based on Gray Wolf Optimization, improved real coded Genetic Algorithm, coupled-based PSO etc. were utilized to implement short-term hydrothermal scheduling [5–7]. However, most of the methods adopted so far were very straight forward and hence they possess limited ability in tackling real time short-term hydrothermal scheduling problems such as discontinuity, multimodality, non-linearity management etc. In [8], the researchers proposed a simplifying assumption to a practical problem leading to suboptimal solution. A fuzzy logic-based EP technique was proposed in [9] for economic-environmental short-term hydrothermal scheduling problems. Simulated

Annealing (SA) is a promising tool but scheduling for annealing should be carefully tuned for better results. However, implementation of an appropriate schedule for annealing is very time-consuming. In the last few decades, the metaheuristic global search methods like adaptive-PSO, mixed binary PSO, dynamically controlled PSO etc. are greatly influenced by the physics of nature and hence paved a way to address hydrothermal scheduling problems [10–12].

This paper uses an optimized cost function based on Barnacles Mating Optimization (BMO) for power flow scheduling and establishes a dependency of it with economic operation.

The computational steps for BMO are analyzed in view of the contradiction between optimization and depth and velocity existing within the swarm intelligence evolutionary algorithm.

The proposed technique is applied over a system for testing in MATAB environment and the simulation results are discussed proving the superiority of the adopted technique over the existing ones.

2 Mathematical Formulation of Power Flow Scheduling

This article is dedicated to power scheduling formulation of hydrothermal generation by including economic as well as valve-point effects and environmental aspects. The generation scheduling problem is more multifaceted due to the introduction of hydro energy resources.

2.1 Formulation of Multi-objective Function

It is evident that the cost involved in hydro-electric generation depends on plant output and the total generating cost consists of the cost involved in coal in a thermal power station. The objective function in this case needs to be minimized which includes the generation cost and pollution of the thermal plant and erection and maintaining all the constraints considered for short-term scheduling [13]. To tackle the present problem a non-linear multi-objective function assumed as follows:

$$\text{Min} \quad C_t(F_t, E_t) \tag{1}$$

$$\text{Min} \quad C_t = \sum_{\tau=1}^{T} \left(\sum_{i=1}^{N_t} \left(P_{ti,\tau} + E_{i\tau} \right) \right) \tag{2}$$

Power output in a hydal unit is a function of the water head and reservoir volume as [14]:

$$P_{hj,\tau} = \left(c_{1j} V_{hj,\tau}^2 + c_{2j} Q_{hj,\tau}^2 + c_{3j} V_{hj,\tau} Q_{hj,\tau} + c_{4j} V_{hj,\tau} + c_{5j} Q_{hj,\tau} + c_{6j}\right) \quad (3)$$

So, the multi-objective function (1) can be modified as:

$$\text{Min} \quad C_t(F_t + h_i \times E_t) \quad (4)$$

The fuel cost function in a coal-based power station is a quadratic function of the real power output [9]. The concerned mathematical formulation can be written as:

$$F_t = \sum_{\tau=1}^{T} \left(\sum_{i=1}^{N_t} \left[a_i P_{ti,\tau}^2 + b_i P_{ti,\tau} + c_i + \left| e_i \sin\left(f_i \left(P_{ti}^{\min} - P_{ti,\tau} \right) \right) \right| \right] \right) \quad (5)$$

Emission from a thermal plant depends on the power output of the concerned generating plant. Overall emission thus can be expressed as:

$$E_t = \sum_{\tau=1}^{T} \left(\sum_{i=1}^{N_t} \left[\alpha_i P_{ti.\tau}^2 + \beta_i P_{ti,\tau} + \gamma_i + \varepsilon_i \exp\left(\delta_i P_{ti,\tau} \right) \right] \right) \text{lb/h} \quad (6)$$

2.2 Equality and Inequality Constraints

It is evident that hourly the overall generation by the thermal and hydro units must match the total demand and the transmission losses. This can be expressed mathematically as a power balance constraint as:

$$\sum_{i=1}^{N_t} P_{ti,\tau} + \sum_{j=1}^{N_h} P_{hj,\tau} = P_{D,\tau} + P_{L,\tau} \quad (7)$$

where $P_{hj,\tau}$ is a function of water storage volume as well as water discharge rate (3).

Initial and final storage reservoir volumes are estimated by midterm scheduling progression. Physically this equality constraint signifies that the available water is fully utilized. This can be expressed as follows:

$$V_{hj,0} = V_{hj,\text{begin}} \quad (8)$$

$$V_{hj,T} = V_{hj,\text{end}} \quad (9)$$

Generator limits, reservoir volume, water balance, discharge limits etc. are the major constraints in the concerned problem. The dynamic water balance in the reservoir is given below

$$V_{hj,\tau} = V_{hj,\tau-1} + I_{hj,\tau} - Q_{hj,\tau} - S_{hj,\tau} + \sum_{m}^{R_{uj}} Q_{hm(\tau-t_{mj})} + S_{hm(\tau-t_{mj})} \quad (10)$$

Hourly the total real power generated from each of the hydro and thermal plants is bounded by maximum and minimum limits as expressed below:

$$P_{hj}^{\min} \leq P_{hj} \leq P_{hj}^{\max} \quad (j = 1, 2, 3 \ldots N_{\mathrm{h}}) \quad (11)$$

$$P_{ti}^{\min} \leq P_{ti} \leq P_{ti}^{\max} \quad (i = 1, 2, 3 \ldots N_{\mathrm{t}}) \quad (12)$$

Reservoir storage volume limit is given below

$$V_{hj,\tau}^{\min} \leq V_{hj,\tau} \leq V_{hj,\tau}^{\max} \quad (13)$$

Reservoir storage discharge limit is given below

$$Q_{hj,\tau}^{\min} \leq Q_{hj,\tau} \leq Q_{hj,\tau}^{\max} \quad (14)$$

3 Barnacles Mating Optimization

Barnacles mating optimization (BMO) algorithm is a novel bio-inspired meta-heuristic algorithm to test a function which is a well-established, efficient method to tackle high-dimensional, non-convex optimization problems [15].

Figure 1 shows the life cycle of Barnacles [16]. The larva formation of Barnacles involves six naupliar instars and a non-feeding pre-settling cyprid instar. The metamorphosed cyprid after settling on a surface turns adult.

3.1 Initialization

In BMO method, barnacles are considered as the candidate solution where the population is expressed as follows:

$$X = \begin{bmatrix} X_1^1 \,..\, X_1^N \\ : \;\; .. \;\; : \\ X_n^1 \,..\, X_n^N \end{bmatrix} \quad (15)$$

where N is the control variables and n is the number of barnacles or population size. The control variables of the ith variables in (15) are bounded as per the following:

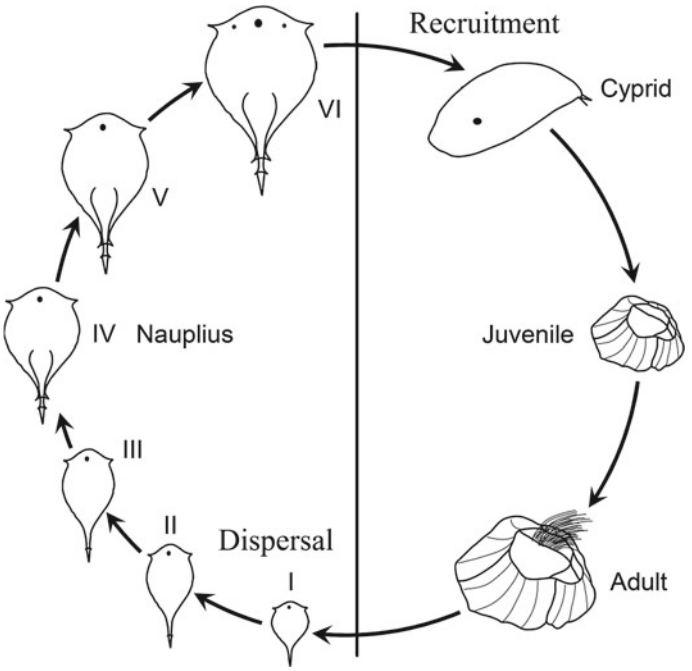

Fig. 1 The life cycle of barnacle

$$ub = [ub_1 \ldots ubi] \tag{16}$$

$$lb = [lb_1 \ldots lbi] \tag{17}$$

Initially the vector X is evaluated and then sorting is carried out in order to locate the best solution at the top of the vector.

The evaluation of the vector X is done initially, and the sorting process is performed to locate the best solution so far at the top of the vector.

3.2 Selection Process

The selection process mimics the behavior of barnacles which can be depicted mathematically as:

$$\text{barnacle\_ d} = \text{randperm}(n) \tag{18}$$

$$\text{barnacle\_ m} = \text{randperm}(n) \tag{19}$$

where barnacle_d and barnacle_m are the parents to be mated and n is the number of populations.

3.3 Reproduction

To show the BMO, following expressions produce new variables as offspring from existing barnacles' parents:

$$x_i^{N\_\text{new}} = p x_{\text{barnacle\_ d}}^N + q x_{\text{barnacle\_ m}}^N \tag{20}$$

where p is the normally distributed pseudo random numbers between [0, 1], $q = (1 - p)$, $x_{\text{barnacle\_ d}}^N$ and $x_{\text{barnacle\_ m}}^N$ are the variables of Dad and Mum of barnacles respectively which has been selected in (18) and (19). The sperm cast process is expressed as follows:

$$x_i^{n\_\text{new}} = \text{rand}() \times x_{\text{barnacle\_ m}}^n \tag{21}$$

where rand () is the random number between [0, 1].

The algorithm code regarding BMO is depicted in Fig. 2. BMO initiates the optimization by forming random solutions at first. After each iteration, the best solution obtained so far is updated to the top of the vector X (15). Each new off spring of barnacles is estimated and combined with parents in order to control the matrix expansion. Afterwards, half of the top solutions are sorted to fit the population size by eliminating the poor or dead results.

4 Computer Simulation and Test Results

This paper evaluates the daily performance of a BMO-based short-term power flow scheduling incorporated in two illustrative test systems and using MATLAB2020 code on personal computer. The effect of valve-point loading on fuel cost is included in the present analysis in order to establish the robustness of the proposed algorithm.

4.1 Test System

Test system consists of four coupled hydro plants along with an equivalent thermal plant. Transmission losses in the test system are neglected. Figure 3 diagrammatically represents the end conditions of each reservoir after adjustment of discharge from each one of them.

Fig. 2 The algorithm of barnacles mating optimization (BMO)

```
Initialize the population of barnacle Xi
Calculate the fitness of each barnacle
Sorting to locate the best result at the top
      of the population (T=the best solution)
while (l< Maximum iterations)
      set the value of pl
      selection using (18) and (19)
      if selection of Dad and Mum=pl
for each variable
      off spring generation using (20)
end for
else if selection of Dad and Mum>pl
  for each variable
      off spring generation using (21)
  end for
end if
Bring the current barnacle back if it goes outside
  the boundaries
Calculate the fitness of each barnacles
Sorting and update T if there is a better solution
Solution l=l+1
end while
Return T
```

Instance 1: Quadratic cost considering economic emission cost function without valve-point loading

Economic emission cost function is considered for the analysis in order to minimize fuel cost as well as emission level of a thermal power plant. Emission from each generator is expressed as a function of its output. Overall emission in the system is given by (6). Fuel as well as emission is linked together by a price penalty factor *h*. Emission effect function of thermal generator is considered to validate the feasibility of the proposed method. Table 1 shows the daily generation schedule of hydro and thermal power based on the proposed method. Optimized hydro reservoir storage volume and water discharge of 24 h for the test system are shown in Figs. 4 and 5 respectively. Convergence characteristic of fuel cost is shown in Fig. 6.

Table 2 shows a comparative analysis of optimal cost achieved by espousing diverse current techniques mentioned in the literature along with the proposed BMO method. It is imperative from the analysis that the projected method possesses both the high-quality result as well as the uppermost probability of concluding a better solution for the concerned problem.

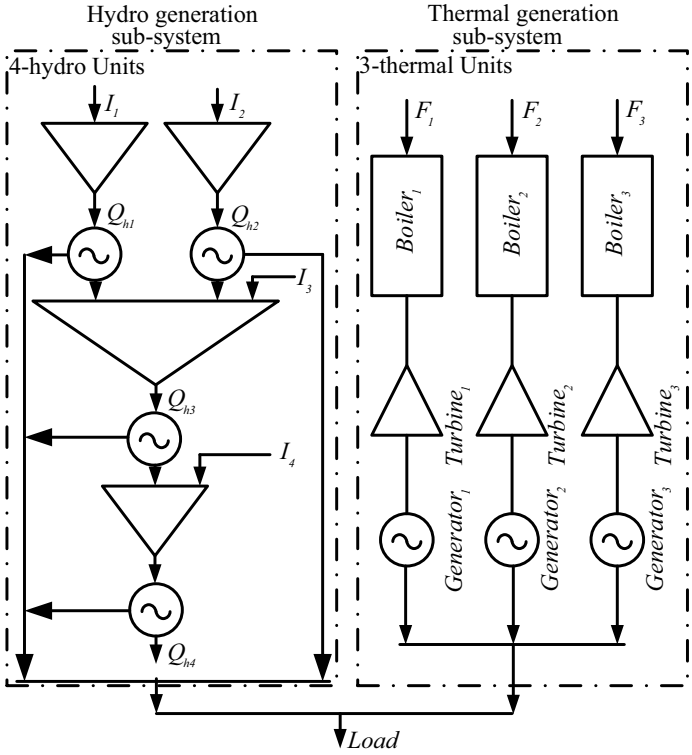

Fig. 3 Graphical illustration of the hydrothermal test system

Instance 2: Quadratic cost considering economic emission cost function with valve-point loading

Here both emission cost function as well as valve-point effect of generator is included to implement practical feasibility.

Table 3 lists hourly generating schedules of hydro as well as thermal power as assessed from the proposed method. Optimized water reservoir storage volume and hydro discharge of 24 h for the test system are shown in Figs. 7 and 8 respectively. Fuel cost convergence characteristic is depicted in Fig. 9.

A comparative analysis of optimal cost achieved by adopting different techniques available in the literature along with the proposed BMO method is shown in Table 4. It is flawless from the analysis that the projected method retains both the high-quality result as well as the uppermost probability of conclusion a better resolution for the concerned problem.

Table 1 Optimal power for test system instance 1

h	Hydro units (MW)				Thermal units (MW)
	Hydro1	Hydro2	Hydro3	Hydro4	
1	75.65284	50.27339	13.14998	159.8295	451.0943
2	77.18228	51.31588	38.70254	169.3951	443.4042
3	70.84255	52.92803	12.23750	115.2511	448.7409
4	64.16306	54.49660	31.02355	135.5294	364.7874
5	68.20014	55.53423	14.04445	171.2938	360.9274
6	76.56252	56.00392	10.01110	205.3390	462.0946
7	86.49101	64.47140	26.70710	158.3354	613.9951
8	82.57577	62.60345	22.90670	238.9859	602.9282
9	87.05689	71.05194	42.04998	241.1600	648.6812
10	88.01842	70.85728	27.40540	256.0422	637.6768
11	86.49417	67.71541	43.34571	297.1572	605.2876
12	89.57386	77.39280	26.98656	283.3159	672.7309
13	88.49333	75.58649	37.24234	264.8739	643.8039
14	66.64788	68.29001	46.66418	282.3862	566.0118
15	80.81378	68.69253	45.12017	265.1404	550.2331
16	73.03448	76.58578	39.56464	266.9451	603.8699
17	83.35660	72.11253	47.07622	291.6405	555.8142
18	88.18284	77.32009	51.22302	286.7611	616.5130
19	82.77466	74.76375	50.93883	287.6443	573.8785
20	72.04129	74.80364	49.27839	295.6009	558.2758
21	65.76737	69.63204	55.90518	283.7644	434.9310
22	56.63806	71.33203	57.57977	285.4814	388.9687
23	61.85357	72.34595	58.67360	284.1566	372.9703
24	55.07405	71.74891	58.99911	284.3968	329.7811

5 Conclusion

This article proposes Barnacles mating optimization (BMO) algorithm to address the PFS problem. The proposed method was proficiently and successfully applied on a hydrothermal system containing four hydro units and three thermal plant functioning on a daily basis. It was observed that the proposed method addressing a PFS problem involving quadratic cost functions produced a lower production cost than other existing methods over the specified time interval. Also, the proposed method gave better results than BBO for a PFS problem with prohibited discharge constraint. It was also observed that BMO finds better and cost-effective solutions than other existing methods even considering complex fuel characteristics by considering valve-point loading. Hence, considering all the concerned aspects as discussed above it can

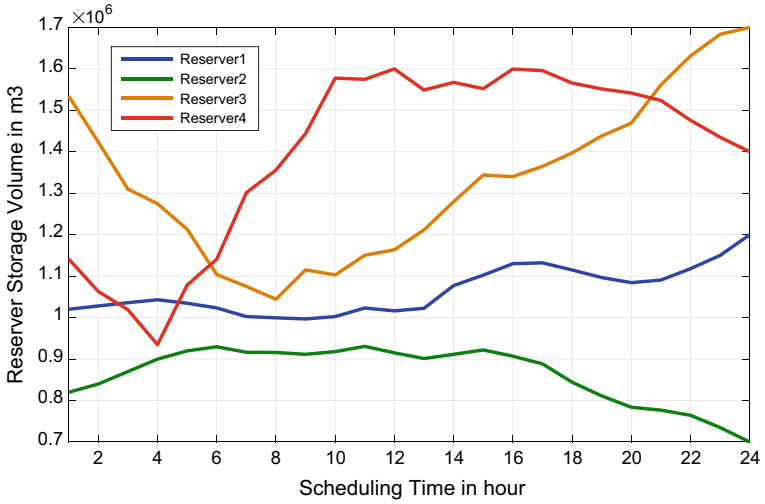

Fig. 4 Hydro reservoir storage volumes for test system case I

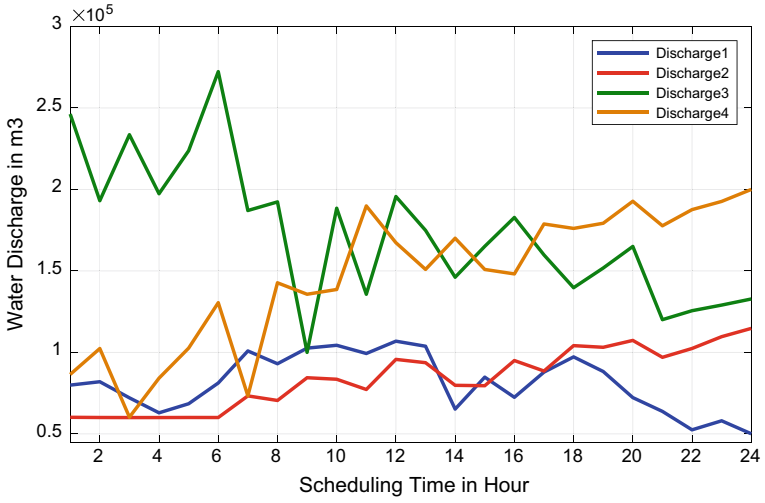

Fig. 5 Optimal water discharges with BMO for test system case I

be concluded that BMO outperforms previously proposed algorithms in case of PFS scenario.

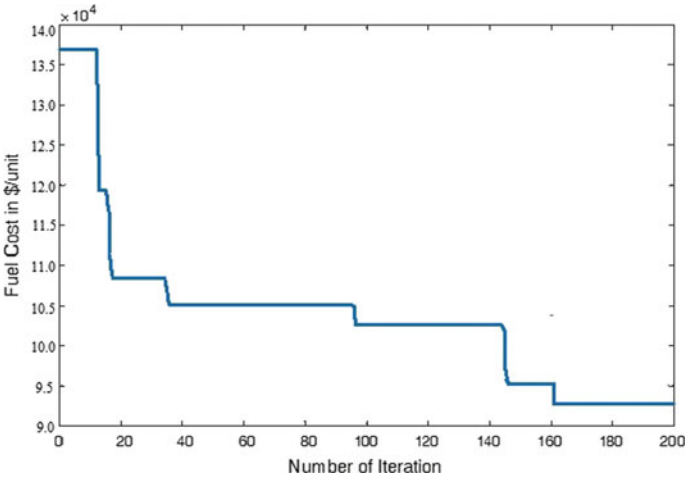

Fig. 6 Convergence characteristics of BMO test system case I

Table 2 Comparison of optimal costs for case 1

Optimization method	Minimum cost ($)	Maximum cost ($)	Average cost ($)
GA [3]	932,734.00	939,734.00	936,969.00
PSO [4]	928,878.00	938,012.00	933,085.00
EPSO [11]	922,904.00	924,808.00	923,527.00
Proposed BMO	922,301.16	922,843.10	922,436.70

Table 3 Optimal power for test system instance 2

h	Hydro units (MW)				Thermal units (MW)
	Hydro1	Hydro2	Hydro3	Hydro4	
1	69.61575	50.41403	47.61684	179.3826	402.9708
2	79.44064	61.65396	15.89608	128.223	494.7863
3	71.01504	53.0326	36.75861	171.9969	367.1969
4	67.02172	58.62645	32.10911	125.6979	366.5448
5	81.44839	62.25577	39.95256	157.825	328.5183
6	59.88178	54.25301	33.38401	204.5019	447.9793
7	72.6333	53.97011	45.43084	190.8725	587.0933
8	89.54992	62.09534	36.14884	200.5676	621.6383
9	86.83598	67.81283	28.15542	240.1821	667.0137
10	69.42535	64.00925	38.28329	224.5594	683.7228

(continued)

Table 3 (continued)

h	Hydro units (MW)				Thermal units (MW)
	Hydro1	Hydro2	Hydro3	Hydro4	
11	89.04011	67.38692	42.50843	240.228	660.8366
12	86.29472	67.64252	41.68654	270.2344	684.1418
13	63.95645	63.90278	50.37373	247.6776	684.0894
14	71.85681	78.43101	42.78483	220.4114	616.5159
15	94.59069	86.44693	41.49705	261.7333	525.7321
16	78.18501	76.28776	50.42753	241.1486	613.9511
17	75.94396	59.96487	52.60896	264.5913	596.8909
18	82.15429	75.00052	53.5014	295.0604	614.2834
19	81.15639	73.91659	49.67189	251.3857	613.8695
20	74.5687	68.04968	56.00922	269.7151	581.6573
21	77.7988	54.46126	56.62884	287.9517	433.1594
22	73.45909	74.65639	57.93013	263.5667	390.3877
23	79.17442	68.03831	56.01441	279.7229	367.0499
24	90.75516	80.82828	58.94997	284.3917	285.0748

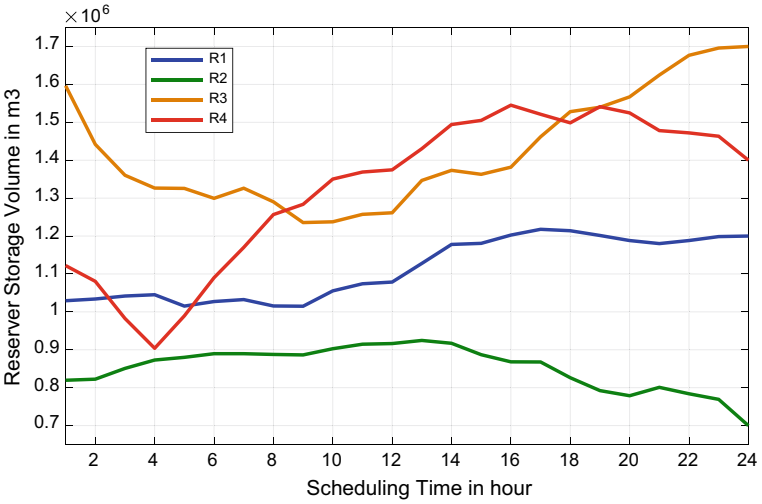

Fig. 7 Water reservoir storage volumes for test system instance 2

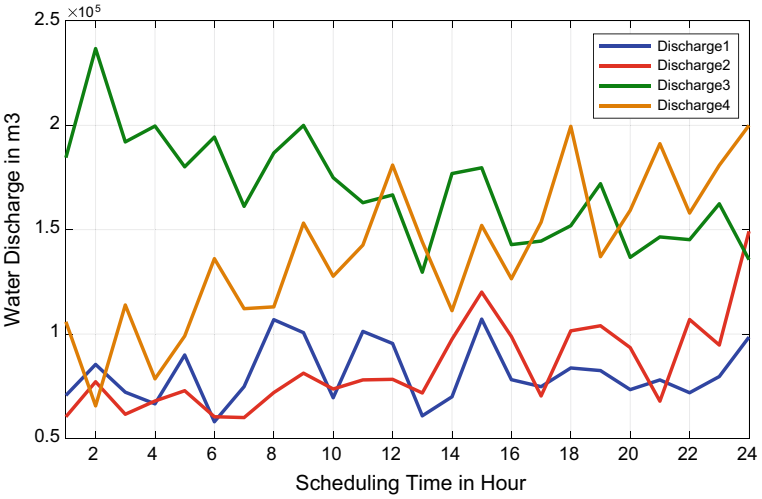

Fig. 8 Optimal water discharges with BMO for test system case II

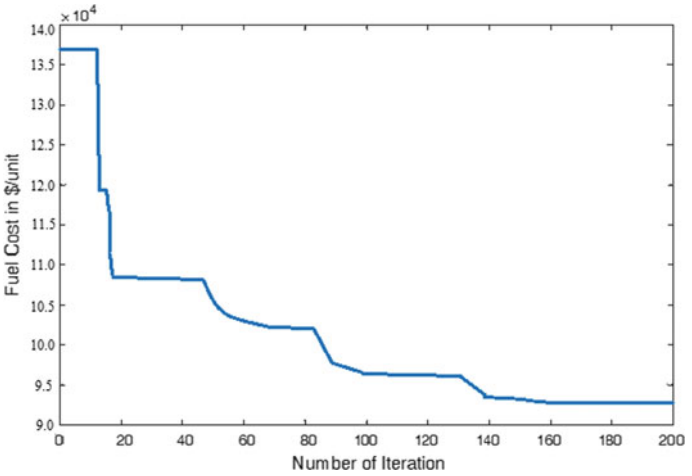

Fig. 9 Convergence characteristics of BMO test system case II

Table 4 Comparison of optimal costs for case II

Optimization method	Minimum cost ($)	Maximum cost ($)	Average cost ($)
IPSO [4]	925,978.00	–	–
APSO [10]	925,991.35	–	–
CPSO [10]	924,636.88	927,431.00	926,496.00
Proposed BMO	924,598.16	927,398.91	926,428.06

References

1. Mandal, K.K., Basu, M., Chakraborty, N.: Particle swarm optimization technique based short-term hydrothermal scheduling. Appl. Soft Comput. **8**(4), 1392–1399 (2008)
2. Sinha, N., Chakrabarti, R., Chattopadhyay, P.K.: Fast evolutionary programming techniques for short-term hydrothermal scheduling. IEEE Trans. Power Syst. **18**(1), 214–220 (2003)
3. Orero, S.O., Irving, M.R.: A genetic algorithm modelling framework and solution technique for short term optimal hydrothermal scheduling. IEEE Trans. Power Syst. **13**(2), 501–518 (1998)
4. Hota, P.K., Barisal, A.K., Chakrabarti, R.: An improved PSO technique for short-term optimal hydrothermal scheduling. Electric Power Systems Research **79**(7), 1047–1053 (2009)
5. Sharma, K., Dubey, H.M., Pandit, M.: Short-Term Hydrothermal Scheduling Using Gray Wolf Optimization. Advances in Computing and Intelligent Systems, pp. 253–269. Springer, Singapore (2020)
6. Ganguly, D., Das, S., Hazra, A., Laddha, A., Basu, M.: Improved real coded genetic algorithm-based short-term hydrothermal generation planning. Int. J. Hybrid Intell. **1**(2–3), 118–146 (2019)
7. Wu, Y., Wu, Y., Liu, X.: Couple-based particle swarm optimization for short-term hydrothermal scheduling. Appl. Soft Comput. **74**, 440–450 (2019)
8. Das, S., Bhattacharya, A.: Symbiotic organisms search algorithm for short-term hydrothermal scheduling. Ain Shams Eng. J. **9**(4), 499–516 (2018)
9. Basu, M.: An interactive fuzzy satisfying method based on evolutionary programming technique for multi-objective short-term hydrothermal scheduling. Electr. Power Syst. Res. **69**(2–3), 277–285 (2004)
10. Amjady, N., Soleymanpour, H.R.: Daily hydrothermal generation scheduling by a new modified adaptive particle swarm optimization technique. Electr. Power Syst. Res. **80**(6), 723–732 (2010)
11. Hinojosa, V.H., Leyton, C.: Short-term hydrothermal generation scheduling solved with a mixed-binary evolutionary particle swarm optimizer. Electr. Power Syst. Res. **92**, 162–170 (2012)
12. Adoun, V.K., Gupta, N., Niazi, K.R., Swarnkar, A.: Economic emission short-term hydrothermal scheduling using a dynamically controlled particle swarm optimization. Res. J. Appl. Sci. Eng. Technol. **8**(13), 1544–1557 (2014)
13. Choudhary, S.K., Pain, S.: Modified Particle Swarm Optimization (MPSO)-Based Short-Term Hydro-Thermal-Wind Generation Scheduling Considering Uncertainty of Wind Energy. Innovations in Sustainable Energy and Technology, pp. 195–205. Springer, Singapore (2021)
14. Choudhary, S., Ghoshal, S.: Crisscross Optimization (CSO) Based Short-Term Conventional Generation Scheduling Incorporating Renewable Energy, pp. 213–218. MFIIS-2020, Kolkata (2021)
15. Sulaiman, M.H., Mustaffa, Z., Saari, M.M., Daniyal, H: Barnacles mating optimizer: a new bio-inspired algorithm for solving engineering optimization problems. Eng. Appl. Artif. Intell. **87**, 103330 (2020)
16. Khandeparker, L., Anil, A.C.: Underwater adhesion: the barnacle way. Int. J. Adhesion Adhesives **27**(2), 165–172 (2007)

Sentiment Analysis of Twitter Classification by Applying Hybrid-Based Techniques

Mauparna Nandan, Siddhartha Chatterjee, Antara Parai, and Oindrila Bagchi

Abstract As technology advances, the world is rapidly transmuting as a result of current technologies, and specially, the Internet has grown ingrained in everyone's lives. The various social networking applications, namely Twitter, Facebook and Google+ are rapidly gaining huge popularity and most pertinently, Twitter has emerged to be the utmost popular platform for the individuals to coin their opinions and share their experiences with regard to various issues related to products and services. This harvesting of opinions by analysing the vast volume of unstructured information which are a result of social media sites is really a very tedious job. Sentiment analysis or opinion mining is a technique that aims to unveil the sentiments of the common people by analysing textual dissection and helps opinion formation regarding diversified areas. Sentiment analysis can assist researchers to gain insight with respect to numerous public issues specifically in marketing, business, products, services, politics, companies, governments etc. Sentiment analysis is a methodology of transforming unstructured data into structured data by classifying text attributes such as sentiment orientation and differentiate them into positive and negative sentiment category and has evolved in popularity as a subject of study in the modern era. The application of machine learning algorithms contribute significantly in the classification of sentiment analysis. This paper proposes both lexicon-based and machine learning techniques and aims to discuss about the current state-of-the-art of sentiment analysis techniques employed in the classification of tweet sentiment orientation and also addresses the challenges that can be employed to enhance the process of analysis, summarizing and classification of opinion mining.

M. Nandan
Brainware University, Kolkata 700125, India

S. Chatterjee (✉)
Gargi Memorial Institute of Technology, Kolkata 700144, India

A. Parai
Siliguri Institute of Technology, Siliguri 734009, India

O. Bagchi
Bengal Institute of Technology and Management, Santiniketan 731236, India

B. Sikdar et al. (eds.), *Proceedings of the 3rd International Conference on Communication, Devices and Computing*, Lecture Notes in Electrical Engineering 851,
https://doi.org/10.1007/978-981-16-9154-6_55

Keywords Sentiment analysis (SA) · Opinion mining (OM) · Natural language processing (NLP) · Machine learning · NLTK and lexicon

1 Introduction

The prominence rise of Web 2.0 applications, namely social networking, micro blogging, podcasting and content hosting services has hypnotized the people's mind in getting addicted to the world of social media. The numerous social media sites not only permits people to connect across the globe but can also transmit information, express their opinions and views and thus can be applied in various world events, healthcare, politics and business by improving their products and services. Since the social media acts as one of the largest free repository of open data-source, therefore, the data extracted from it is highly unstructured. In other words, we can say that social media has transformed into a pool of sentiments. As a result of these developments, sentiment analysis has emerged as the most challenging application of natural language processing (NLP) and opinion mining [1]. Text analysis and other computational methods are employed in natural language processing to automatically extract and identify sentiments from Internet reviews. Sentiment analysis, might be defined as the summary of opinions coined on the basis of analysis of colossal volumes of textual content produced by humans and machines.

Sentiment analysis is a method of extracting, converting and interpreting opinions from a text and segregating them as positive, negative or natural sentiments using natural language processing (NLP) [2]. The study of sentiment analysis started its journey during the early twentieth century but since the last decade, it has gained a significant importance and nowadays, ranks as one of the most pervasive tool to analyse human sentiments. Sentiment analysis is mainly categorized into five distinct types, namely document level, sentence level, phrase level, aspect level and emotion level. The primary objective behind this is to categorize the opinions obtained from these levels into positive and negative sentiments, respectively [3].

In the current scenario, as data is huge, selecting an acceptable approach for sentiment analysis is a mammoth task for the researchers. Sentimental analysis is primarily divided into three main categories—machine learning, lexicon-based and hybrid. Combining machine learning and lexicon-based learning, we get hybrid approach. Depending upon the data set, researchers select an appropriate method for data analysis purpose. Machine learning method is a supervised learning technique and in which the data is trained at first in order to be processed. SVM and naïve Bayes model are two popular machine learning methods for sentiment analysis. Selection of machine learning models also depends on the features of the data to be analysed. For well-formed text data, naïve Bayes algorithm has been successfully applied. Support vector machine (SVM), on the other hand, performs well with low-shape data sets. Lexicon-based approach is an unsupervised learning technique. It does not necessitate any data training and simply detects the polarity of each word by comparing with the dictionary and extracts out the positive and negative words. As no

training of data is required, it is suitable for analysing Facebook data [4] and Twitter [5, 6]. Hybrid approaches are also followed in many cases of sentiment analysis. Here, the combination of both machine learning and lexical analysis are used for good results [7, 8].

Researchers have been working on a novel sentiment analysis algorithm which is both effective and accurate. Other common names by which sentiment analysis is also identified are opinion mining, opinion extraction, sentiment mining, effect analysis, emotion analysis, review mining etc. [2]. Although, the intrinsic meanings of these terms are synonymous but may slightly vary depending upon the nature of their tasks and applications. Sentiment analysis is generally accomplished by supervised or unsupervised learning algorithms; the most prominent being the naïve Bayes, decision tree, random forest and support vector machine (SVM). The sentiment analysis has been used in the context of business and marketing, politics, public opinion, e-commerce and voting applications etc.

The structure of our paper is as follows. Section 1 highlights the introduction. Section 2 enumerates the literature review. Section 3 illustrates the classification levels of sentiment analysis. Section 4 defines the proposed architecture and its corresponding methodology of our research work. Section 5 depicts the conclusion part.

2 Related Work

The boom of Internet has revolutionized the entire world. For articulating one's opinion, a varieties of social networking sites such as Twitter, Facebook and Instagram; several review sites such as Mouthshut and Glassdoor; blogs and other competent channels are readily available. Opinion formation is basic to every human action. A number of literature-based ways to accessing sentiment analysis models using Twitter data have been proposed. The study of sentiment analysis can be traced back to the early twentieth century since the year 2004. During that time, data were collected from online documents, webpages and forum text and was used to analyse customer reviews on products, movies, shops and shoppers [9]. From that time, only about 101 articles on sentiment analysis were published in 2005, while it increased to about 5699 in 2015 over a decade. According to the recent data [10], more than 7000 papers have been published on sentiment analysis after 2004. So, it is quite obvious that sentiment analysis is gradually emerging as a rapidly expanding research field.

Nowadays, sentiment analysis is used in variety of fields such as stock markets [11], disaster management [7], politics [12], bitcoin price analysis [13], sports [14], impact of disease in social life [4] and also in various business activities [15]. Nowadays, mostly data are extracted from social media like Facebook, twitter, blogs etc. Social media is providing us millions and millions of data from online users of various parts of the world . A current study reveals that 88% of the data in modern days comes from Twitter [16]. Pak and Paroubek [17] suggested a technique for categorizing tweets into objective, positive and negative categories. They constructed a Twitter corpus by constructing the Twitter API to accumulate tweets and auto-

matically annotating them with emoticons. They used a training set comprising of only tweets having emoticons. Parikh and Movassate [18] utilized two models to classify tweets: a naïve Bayes bigram model and a maximum entropy model. The naïve Bayes classifiers outperformed the maximum entropy model. For categorizing tweets, Barbosa et al. [19] devised a two-phase automatic sentiment analysis technique. They classified tweets into objective or subjective, and then the subjective tweets were again categorized into positive or negative. Retweets, hashtags, links, punctuation and exclamation marks were utilized in combination with elements possessing polarity of words and POS.

Agarwal et al. [20] proposed a three-way model for categorizing sentiments into positive, negative and neutral categories. They explored models like the unigram, feature-based models and tree-kernel based models. They concluded that features that combine a word's prior polarity with its parts-of-speech (POS) tags are the most meaningful and hence play a substantial influence in classification. Davidov et al. [21] devised a method to leverage Twitter user-defined hashtags to categorize sentiment, which is then further integrated into a single feature vector to be implemented for sentiment classification, using punctuation, single words, n-grams and patterns as separate features. For recognizing polarity in English tweets, Pablo et al. [22] proposed variants of the naïve Bayes classifier. Baseline, which was trained to classify tweets as positive, negative or neutral, and Binary, which implements a polarity lexicon to classify them as positive or negative, were the two versions. Neutral tweets were neglected. Turney et al. [23] which employed the bag-of-words approach to sentiment analysis, which ignores word relationship and treats a document as a collection of words.

Machine learning algorithms such as naïve Bayes (NB), maximum entropy (ME) and support vector machine (SVM) have also been investigated for sentiment categorization [24]. The authors of [25] employed machine learning methodology to perform sentiment analysis. TextBlob, SentiWordNet and Word Sense Disambiguation (WSD) sentiment analysers were used to determine polarity. The basic elements of natural language processing are incorporated in TextBlob and they are employed to calculate the polarity and subjectivity of tweets. Machine learning approaches outperform traditional approaches when it comes to classification. On the other hand, machine learning algorithms employed for classification presume that the class values are not in any particular sequence, whereas in actual scenario, the class values possess a natural order. In our research work, we have implemented both lexicon-based approach and supervised machine learning algorithms.

3 Classification Levels of Sentiment Analysis

Sentiment analysis can be segregated as a five-layered approach [26]. The figure below illustrates the different sentiment classification techniques.

Sentence Level:

Sentence level analysis, which seeks to determine a sentence's polarity is extensively used in microblogging posts. This style of investigation distinguishes between objective sentences that include concrete information and subjective sentences that contain subjective ideas and opinions. Individual sentences are tagged with their respective polarities in sentence-level sentiment analysis. It divides sentences into three categories: positive, negative and neutral. Sentence level analysis, according to [27], primarily entails two tasks: subjectivity categorization and sentence classification.

Document Level:

Document-level analysis examines the entire "emotional" document and determines the document's overall polarity, viz. positive or negative. This analysis is inapplicable to documents that pertain thoughts regarding multiple entities as it strictly concentrates only on a single entity which is a severe drawback of real-world analysis since documents rarely focus on a single issue. However, recommender systems have found that this form of analysis is quite effective in acquiring a knowledge about public sentiments.

Phrase Level:

The contextual polarity of a text is the main focus of the phrase-level analysis. Even if the word has a positive connotation, the overall polarity of the phrase in which it appears can alter. As a result, the phrase's polarity is determined not only by the opinion words but also by the word's contextual polarity. A methodology for automatically accessing the contextual polarity of emotional expressions by first evaluating if the expression is polar or neutral and then removing the polar ones was established by.

Aspect Level:

In aspect-level analysis, the focus switches from linguistic constructions (documents, sentences, paragraphs and phrases) to unravel features of an entity in the so-called feature-based, topic-based, entity-based and target-based analysis. To identify the entity which is under observation is the first step in the analysis. The polarity is used to identify and categorize sentiment words associated with the entity into positive, negative and neutral. As a result, the entity's aspects are vividly found and scored according to polarity, thereby accomplishing fine-grained analysis.

Emotion Level:

Emotion level classifies the text according to the feelings that lie beneath such as happiness, sadness, anger or joy and is thus, more thorough and precise. At this level, sentiment analysis using emoticons (emojis) is effective. The emoticons (emojis) and hence the sentiments or emotions are easier to categorize. The lexicon-based technique is frequently used in emotion level analysis [26]. Furthermore, approaches for measuring sentiment strength can be classified based on the rating levels—one for

identifying characteristics of a product or service, and the other for rating a review on a global level, which solely considers the polarity of the review (positive/negative) (Anaiis Collomb).

4 Proposed Architecture and Methodology

In this section, we have investigated both lexicon-based approach and machine learning-based approach to implement sentiment analysis of Twitter data. In our present research study, we have implemented the combined or hybrid approach for Tweet classification in order to enhance the level of classification significantly. The approach and design methodology of our proposed research work is illustrated in Fig. 1.

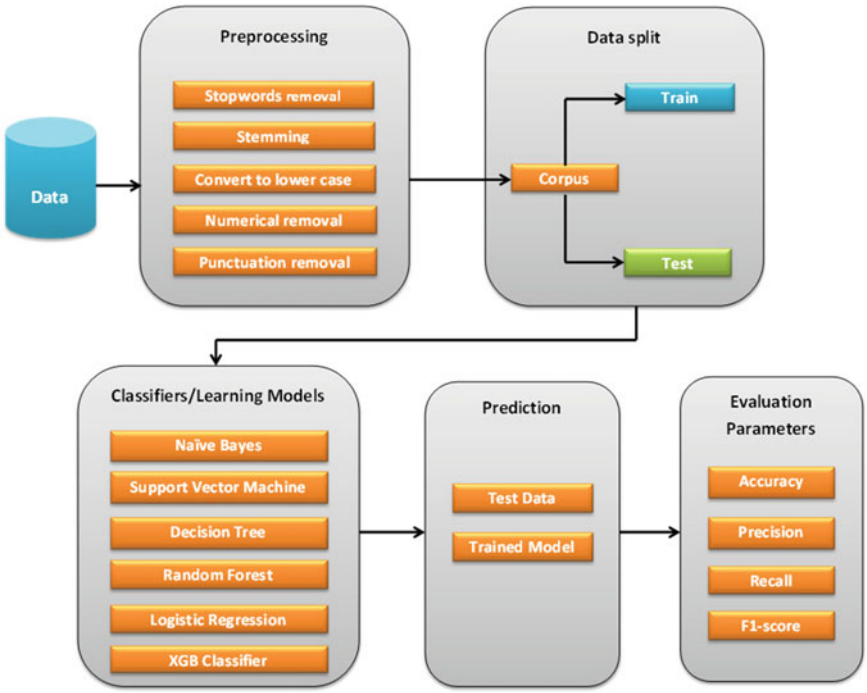

Fig. 1 The methodology adopted for Tweet classification

4.1 Tweet Classification Using Lexicon-Based Approach

The lexicon-based method is one of the methodologies or techniques used in semantic analysis. This methodology calculates the sentiment orientations of the entire document or group of phrases based on the semantic orientation of lexicons. Many sentiment analysis opinion texts are made up of a blend of positive phrases that convey desirable feelings and situations and negative words that convey unwanted feelings and situations. The lexicon-based technique is based on creating a dictionary that contains all positive and negative terms and then using it to assess the sentiments of a text based on the appearance of positive and negative words. The technique commences with tokenizing the input text, then scanning all tokens to determine whether any match the dictionary's lexicon, after which the emotion score is changed based on the type of word detected (negative or positive). Natural Language Toolkit (NLTK), Tweepy and TextBlob are the most significant tools used in the lexicon-based approach.

The lexicon-based approach can be further categorized into two different types:

1. **Dictionary-Based Approach**: In this method, a dictionary is built by starting with a few terms. Then, by including synonyms and antonyms of those terms, an online dictionary, thesaurus, or WordNet can be utilized to build that dictionary. The dictionary gets enlarged until there are no more terms that can be added to it. Manual inspection can help to improve the lexicon.
2. **Corpus-Based Approach**: The sentiment orientation of context-sensitive words is determined using this method. The two strategies used in this approach are as follows:

- **Statistical Approach**: Positive polarity is defined as phrases that demonstrate chaotic behaviour in positive activity. They have negative polarity if they display negative recurrence in negative text. The term has neutral polarity if the frequency is the same in both positive and negative text.
- **Semantic Approach**: This method maps sentiment values to words and words that are semantically similar to those words by locating synonyms and antonyms for the phrase in question.

  In our current research work, the methodology that was implemented for the lexicon-based approach is illustrated below:
- **Raw Data**: The first step was to comprehend the data, which entailed reviewing the data, which included data collection, description and exploration, and the most crucial stage was to validate the data's quality. Since the data is collected from an online source, it contains noise and thus, cannot be used directly for analysis; therefore, pre-processing is required.
- **Pre-processing**: In the second step, the data set is pre-processed as part of the methodology phase of this study. This step is implemented by using a variety of tools and libraries, such as the Natural Language Toolkit (NLTK) and Textblob. The Natural Language Toolkit, or NLTK, is a Python-based collection of tools

and applications for symbolic and statistical natural language processing (NLP) for English. Classification, tokenization, stemming, tagging, parsing and semantic reasoning are all supported by NLTK. The Textblob Library is typically used to process data in text format. TextBlob objects are handled as if they were Python strings that have learnt how to interpret natural language.

- **Tokenize Text**—Tokenization splits the sentences into words called tokens. This process helps in comprehending the context for the development of the model in NLP. Tokenization aids in interpreting the meaning of the text by analysing the sequence of words.
- **Data cleaning**—Data cleaning is done during pre-processing to boost the learning efficiency of machine learning models. Cleaning entails converting Twitter feeds to lowercase, removing English stop words, URLs, digits, punctuation marks, white spaces, alphanumeric characters and removal of sparse terms, etc. followed by stemming.
- **Remove Punctuation**—Punctuation is deleted from the data as it is irrelevant to the present text analysis work. Punctuation improves the readability of sentences but decreases the models' capacity to distinguish between punctuation and other letters.
- **Remove Numbers**—The numeric numbers from the tweets were then eliminated because they had no influence on text analysis and to reduce the training complexity.
- **Count Word Occurences**—The entire content in the tweets is transformed to lowercase after the numeric removal. This phase is crucial since text analysis is case sensitive. According to Yang and Zhang [28], probabilistic machine learning algorithms count the number of frequency each word appears.
- **Stemming**—Stemming is a significant pre-processing approach since the model's performance is improved by removing affixes from words and further reducing them to their basic form. The process of reducing these words to their base form is termed as stemming.
- **Remove Stop Words**—Stopwords are removed from tweets as the final step in the pre-processing phase. Stopwords have no analytic significance in text analysis; hence, they must be deleted to make the input feature less complex.

- **Polarity Tagging**: The lexicon is made up of positive, negative and neutral words. It implements a scoring mechanism to determine the sentiment polarity by scoring each sentence according to negative and positive words. Words are considered as numbers in this case. Positive numbers denote positive words (PW), whereas negative numbers denote negative words (NW). For positive, negative and neutral text, polarity is assigned as + 1, − 1, and 0.
- **Word Frequency**: This step computes the frequency of each word in each comment. Figure 2 depicts a bar chart of the most frequent words of the data set used for Tweet classification.
- **Word Cloud**: It is also crucial to learn about the most common occurrences of words in tweets. This will enable us to get an insight regarding the structure and the category of tweets. A word cloud is implemented to visualize this. The

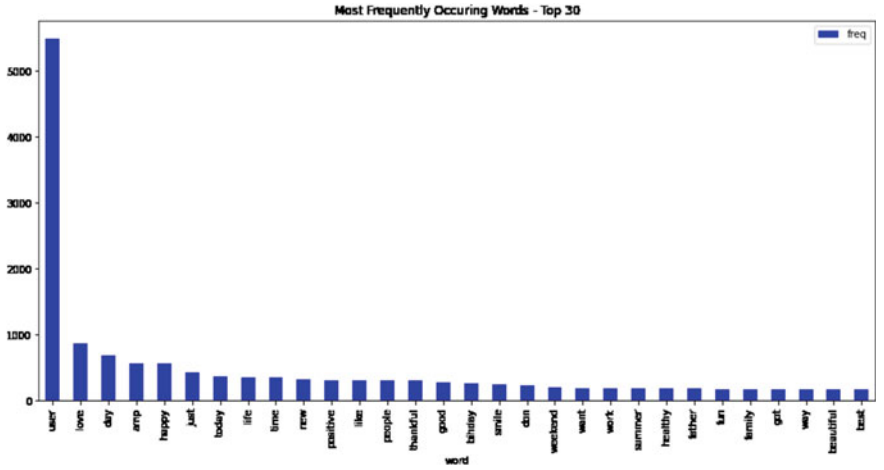

Fig. 2 Word frequency

Fig. 3 Negative word cloud

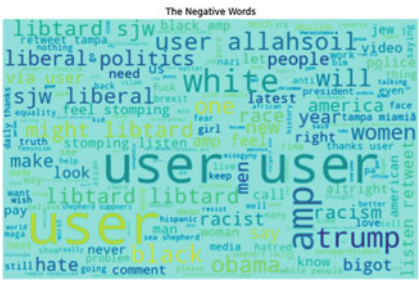

Fig. 4 Neutral word cloud

"wordcloud" programme is used to create the word cloud. The bigger the word in the word cloud, the frequency will be more in the corpus. Figures 3, 4 and 5 represents the word cloud visualization of negative, neutral and positive words, respectively.

- **Sentiment Score:** By subtracting the positive tweets from the negative tweets, the ultimate sentiment score of the tweets is determined. A zero score indicates that

Fig. 5 Positive word cloud

the text contains no opinion words, whereas a positive score indicates that the text is positive in polarity and a negative score indicates that the text is negative in polarity. This method yields good results opinion mining.

$$\text{Sentiment Score} = \sum_{i=1}^{n} PW(i) + NW(i) \tag{1}$$

4.2 Tweet Classification Using Machine Learning Classifiers

Machine learning is one of the most commonly used strategies for classification challenges due to its flexibility and high rate classification accuracy. It can be categorized into two categories: supervised learning, in which all input data is labelled so that algorithms may learn to predict the intended output from the input data; and unsupervised learning, in which all input data is left unlabeled so that algorithms can learn to predict the desired output from the given input data. Probability models and characteristics extracted from the input text are used in machine learning techniques. To examine the data, machine learning classifiers are implemented, which aids in the building of analytical models. These algorithms analyse and interpret data in real time in order to reveal hidden insights. Machine learning techniques are applied in diversified fields, including data analytics, IoT, and cyber security. Various performance assessment parameters, namely accuracy, precision, recall and $F1$-score are

evaluated and then compared with different machine learning classifiers employed in the present research work. The following are the relevant details of the machine learning classifiers employed in the current study for tweet classification.

1. **Naïve Bayes Classifier (NBC)**: Twitter sentiments are accessed based upon the feature selection of each score word. To select the best features, the naïve Bayes classifier (NBC) is used to train and test the features of a word, as well as to evaluate the sentiment polarity of each tweet. The main argument for utilizing NBC to design and perform sentiment analysis problems is that it is simple to develop, especially when working with large data sets. Naïve Bayes classifier is basically a classification technique that applies the Bayes algorithm by implementing the concept of conditional probability and possessing features that have a high level of independence. The sentiment analysis used in conjunction with the naïve Bayes classifier mainly determines the positive, neutral or negative sentiments extracted from Twitter data sets and serves as the most fundamental basic methods for text categorization.
2. **Support Vector Machine (SVM)**: Another machine learning classifier implemented in the current research work is the support vector machine, which is a linear model that can address both classification and regression issues. SVM analyse the data and identifies the significant data in the input space. The imperative data are arranged in two vectors called class. Each piece of information is organized into a class and expressed as a vector. The machine then determines the boundary between the two classes.
3. **Decision Tree Classifier**: The decision tree classifier differentiates those data that have numerous features. This type of classifier creates a hierarchical split in the training data space by separating data deploying attribute values. This method is repeated until a sufficient number of records have been registered with lead nodes for categorization, and it is predicated or dependent on the absence or presence of one or more words.
4. **Random Forest Classifier**: The random forest classifier is a classification learning method that creates a series of decision trees from a randomly selected subset of the training data. The output generated is in the form of several decision trees, with the ultimate forecast determined by combining the votes from different decision trees. The correlation between trees is randomly selected to increase efficiency and prediction power of the classifier.
5. **Logistic Regression Classifier**: Logistic regression is a discriminative classifier that is extensively used in applications of machine learning. Here, we have used this model to evaluate coefficients or weight for each input word in a Twitter sentence and then predicts the class of tweets as a word vector.
6. **XGB Classifier:** The XGBoost model is used as classifier for sentiment analysis and is also known as the XGB classifier. Grid Search method is used for each group of comment separately to achieve the highest level of precision in emotion classification.

4.3 Performance Evaluation Parameters

There are various performance evaluation parameters which can be evaluated to analyse the performance of the classifiers. Four basic notations, namely true positive (TP), true negative (TN), false positive (FP) and false negative (FN) are employed in these parameters which are used to calculate the accuracy, $F1$-score, recall and precision corresponding to each classifier to evaluate their performance.

Accuracy is defined as:

$$\text{Accuracy} = \frac{\text{TP} + \text{TN}}{\text{TP} + \text{TN} + \text{FP} + \text{FN}} * 100 \tag{2}$$

The completeness of a classifier is defined by recall, which is measured as:

$$\text{Recall} = \frac{\text{TP}}{\text{TP} + \text{FN}} \tag{3}$$

Precision refers to how accurate the classifiers are and is calculated as:

$$\text{Precision} = \frac{\text{TP}}{\text{TP} + \text{FP}} \tag{4}$$

The $F1$-score indicates how well the parameters, precision, and recall are balanced and is defined as:

$$F1 - score = 2 * \frac{\text{precision} * \text{recall}}{\text{precision} + \text{recall}} \tag{5}$$

The various performance evaluation parameters employed for the analysis of the machine learning classifiers in the current study are summarized in Table 1.

In our research work, the model performance was evaluated using confusion matrix with more than about 98% accuracy in all the models. The validation accuracy, precision score, recall score and $f1$-score was calculated for each model, respectively. We have also plotted the percentage and total no of tweets displaying true positive,

Table 1 Performance evaluation parameters of machine learning classifiers

	Training accuracy	Validation accuracy	Precision score	Recall score	$F1$-score
Naïve Bayes	0.9565	0.93	0.5562	0.4611	0.5042
SVM	0.9783	0.9364	0.9474	0.1865	0.3117
Decision tree	0.9997	0.9228	0.5	0.5078	0.5039
Random forest	0.9996	0.9428	0.75	0.3886	0.5119
Logistic regression	0.9995	0.9172	0.4657	0.4922	0.4786
XGB classifier	0.95	0.9324	0.8	0.1658	0.2747

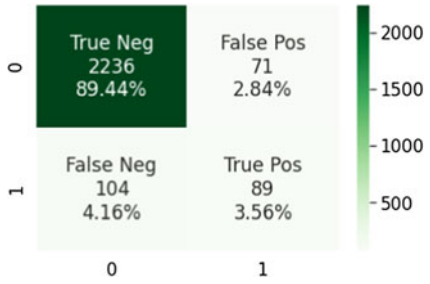

Fig. 6 Confusion matrix for Naïve Bayes classifier

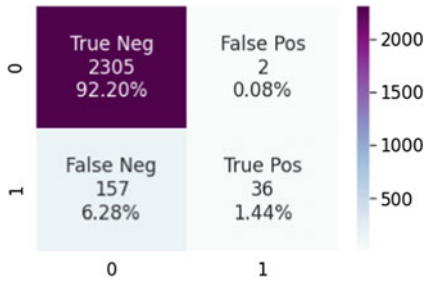

Fig. 7 Confusion matrix for SVM classifier

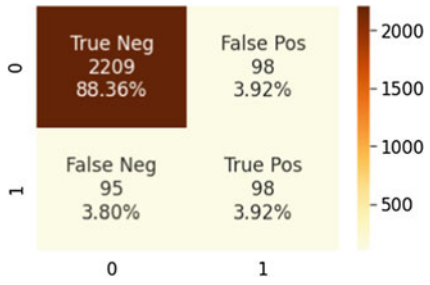

Fig. 8 Confusion matrix for decision tree classifier

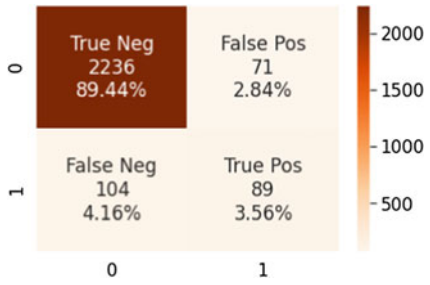

Fig. 9 Confusion matrix for random forest classifier

true negative, false positive and false negative for the machine learning which we have implemented in our study for classification of twitter data set which are depicted in Figs. 6, 7, 8, 9, 10 and 11.

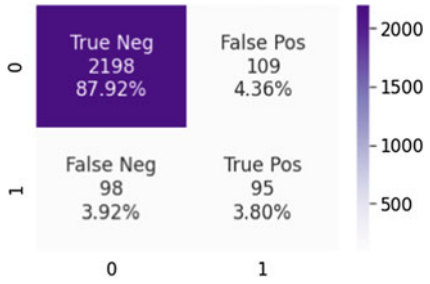

Fig. 10 Confusion matrix for logistic regression classifier

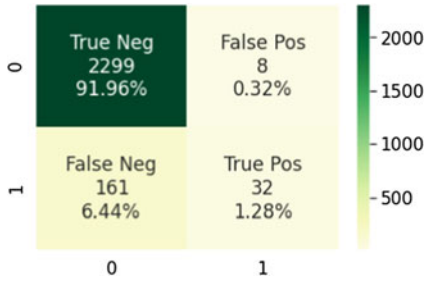

Fig. 11 Confusion matrix for XGB classifier

5 Conclusion

In this research article, various methodologies for Twitter sentiment analysis methods, such as lexicon (corpus)-based approaches and machine learning algorithms, commonly known as hybrid approach were explored. A new algorithm namely, XGB Classifier has been implemented which has not been studied earlier for sentiment classification. For sentiment analysis, lexicon analysis approach is used here followed by the machine learning approaches. At first, tokenization is performed on the data set, and then the data is categorized on the basis of their polarity. In the proposed approach, these steps have been followed respectively—pre-processing, tokenization, feature extraction and classification. For classification, machine learning classifiers like naïve Bayes, support vector machine (SVM), decision tree, random forest, logistic regression and XGB classifiers have been implemented. The proposed algorithm is very effective and the overall performance for all the classifiers is approximately 95–99%. This study also proposes a future scope where sentiment analysis may be done on new sensitive Twitter data set to get more accuracy using deep learning techniques.

References

1. Tang, H., Tan, S., Cheng, X.: A survey on sentiment detection of reviews. Expert Syst. Appl. **36**(7), 10760–10773 (2009)
2. Agarwal, B., Mittal, N., Bansal, P. Garg, S.: Sentiment analysis using common-sense and context information. J. Comput. Intell. Neurosci. **9** (2015)
3. Mishra, N., Jha, C.K.: Classification of opinion mining techniques. Int. J. Comput. Appl. **56**(13) (2015)
4. Isah, H., Neagu, D., Trundle, P.: Social media analysis for product safety using text mining and sentiment analysis. Works. Comput. Intell. UKCI Proc. **1**(1), 1–7 (2015). https://doi.org/10.1109/UKCI.2014.6930158
5. Singh, M., Jakhar, A.K., Pandey, S.: Sentiment analysis on the impact of coronavirus in social life using the BERT model. Soc. Netw. Anal. Min. **11**, 33 (2021)
6. Ravi, K., Ravi, V.: A survey on opinion mining and sentiment analysis: tasks, approaches and applications. Knowledge-Based Syst. **89**(1), 14–46 (2015). https://doi.org/10.1016/j.knosys.2015.06.015
7. Ragini, J., Rexiline, P.M., Anand, R., Vidhyacharan, B.: Big data analytics for disaster response and recovery through sentiment analysis. Int. J. Inf. Manage. **42**, 13–24 (2018)
8. Joyce, B., Jing, D.: Sentiment analysis of Tweets for the 2016 US presidential election. Proc. Comput. Sci. **117**, 129–136 (2017)
9. Boiy, E., Moens, M.-F.: A machine learning approach to sentiment analysis in multilingual Web texts. Inf. Retrieval **12**(5), 526–558 (2009). https://doi.org/10.1007/s10791-008-9070-z
10. Mäntylä, M.V., Graziotin, D., Kuutila, M.: The Evolution of Sentiment Analysis—A Review of Research Topics, Venues, and Top Cited Papers, Computer Science Review. https://doi.org/10.1016/j.cosrev.2017.10.002 (Dec 2016)
11. Suman, N., Gupta, P.K., Sharma, P.: Analysis of stock price flow based on social media sentiments. In: 2017 International Conference on Next Generation Computing and Information Systems (ICNGCIS) (Dec 11–12, 2017)
12. Joyce, B., Jing, D.: Sentiment analysis of Tweets for the 2016 US presidential election. In: IEEE MIT Undergraduate Research Technology Conference URTC, Cambridge, MA, USA, IEEE (2017)
13. Raju, S.M., Tarif, A.M.: Real-Time Prediction of BITCOIN Price using Machine Learning Techniques and Public Sentiment Analysis. Retrieved on May 2020 from http://arxiv.org/abs/2006.14473 (2020)
14. Gujar, M.A., Pardeshi, N.G.: Review on a sentiment analysis and predicting winner for Indian premier league using machine learning technique. Int. Res. J. Modern. Eng. Technol. Sci. **2**(6), 963–967 (2020)
15. Yi, S., Liu, X.: Machine learning based customer sentiment analysis for recommending shoppers, shops based on customers' review. Complex Intell. Syst. **1**(1). https://doi.org/10.1007/s40747-020-00155-2 (2020)
16. Shayaa, S., Phoong S.W., Chung, Y.W., Sulaiman, A., Jaafar N.I., Zakaria, S.B.: Social media sentiment analysis on employment in Malaysia. In: Proceedings of 8th Global Business and Finance Research Conference, Taipei, Taiwan (2017)
17. Pak, A., Paroubek P.: Twitter as a corpus for sentiment analysis and opinion mining. In: Proceedings of the Seventh Conference on International Language Resources and Evaluation, pp. 1320–1326 (2010)
18. Parikh, R., Movassate M.: Sentiment Analysis of User-Generated Twitter Updates using Various Classification Techniques. CS224N Final Report (2009)
19. Barbosa, L., Feng, J.: Robust Sentiment Detection on Twitter from Biased and Noisy Data. COLING, pp. 36–44 (2010)
20. Agarwal, X.B., Vovsha, I., Rambow, O., Passonneau R.: Sentiment analysis of Twitter data. In: Proceedings of the ACL 2011 Workshop on Languages in Social Media, pp. 30–38 (2011)
21. Davidov, D., Rappoport, A.: Enhanced Sentiment Learning Using Twitter Hashtags and Smileys. Coling, pp. 241–249. Beijing (Aug 2010)

22. Gamallo, P., Garcia M.: Citius: A Naive-Bayes strategy for sentiment analysis on English Tweets. In: 8th International Workshop on Semantic Evaluation (SemEval), pp. 171–175. Dublin, Ireland (Aug 2014)
23. Turney, P.D.: Thumbs up or thumbs down? Semantic orientation applied to unsupervised classification of reviews. In: Proceedings of the 40th Annual Meeting on Association for Computational Linguistics, pp. 417–424. Association for Computational Linguistics (2002)
24. Khairnar, J., Kinikar, M.: Machine learning algorithms for opinion mining and sentiment classification. Int. J. Sci. Res. Publ. **3**, 1–6 (2013)
25. Hasan, A., Moin, S., Karim, A., Shamshirband, S.: Machine learning-based sentiment analysis for twitter accounts. Math. Comput. Appl. **23**, 11 (2018)
26. Ge, J., Gretzel, Ulrike: Emoji rhetoric: a social media influencer perspective. J. Marketing Manage. (2018). https://doi.org/10.1080/0267257X.2018.1483960
27. Kolkur, S., Dantal, G., Mahe, R.: Study of different levels for sentiment analysis. Int. J. Current Eng. Technol. **5**(2) (2015)
28. Yang, S., Zhang, H.: Text mining of Twitter data using a latent Dirichlet allocation topic model and sentiment analysis. Int. J. Comput. Inf. Eng. **12**, 525–529 (2018)

Supervised Machine Learning Approach for the Prediction of COVID-19 Cases

Arjun Biswas and Pravin Kumar Samanta

Abstract COVID-19 was first discovered in the city of Wuhan. From then onward the virus has spread rapidly infecting thousands of people. The virus is still spreading and attempts are being made to predict and control the growth and spread of this virus. The trend of spread of this virus is highly unpredictable and normal statistical methods of predictions have not provided promising results, thus another approach of predicting the growth of this virus is required. This approach must be able to predict the nonlinear growth of the virus. Thus, an attempt is made to predict the growth of this virus and to show that the normal statistical methods are not able to predict the growth of the virus with high accuracy. The linear predicting algorithms used are Linear Regression, Support Vector Machine, Polynomial Regression and Auto Regressive Integrated Moving Average. The nonlinear predicting algorithm used is Prophet Algorithm for the prediction of exponential growth of spread of the virus. A comprehensive study is done to show how the spread of the virus takes place in different countries. A comparative study is also done to show the differences in performance parameters based on Absolute Mean Error, Mean Squared Error and *R*-squared (R^2) score among different types of predictors.

Keywords Machine learning · Supervised learning · Prediction · COVID-19 · Regression · ARIMA · Prophet · SVM

1 Introduction

COVID-19 is an infectious disease which is caused due to the virus SARS-COV2 [1]. The corona virus spreads in four stages. Only in the third stage does the virus get converted in the form of an epidemic. In the first stage the growth of the virus

A. Biswas (✉) · P. K. Samanta
School of Electronics Engineering, KIIT Deemed to be University, Bhubaneswar, India
e-mail: 1830082@kiit.ac.in

P. K. Samanta
e-mail: pravin.samantafet@kiit.ac.in

B. Sikdar et al. (eds.), *Proceedings of the 3rd International Conference on Communication, Devices and Computing*, Lecture Notes in Electrical Engineering 851,
https://doi.org/10.1007/978-981-16-9154-6_56

is negligible and the growth curve of the virus has just crossed the origin. In the second stage of the growth of the virus is the growth of local transmission in which the infected person or the patient zero transmits the virus to another person which in turn transmits the virus to another person and so on. Even in this case, the growth of the virus is localized and the growth of the virus is linear. In the third stage, the growth of the virus is uncontrollable and rapid transmission of the virus takes place. This stage is popularly called the stage of community transmission [2]. The source of the virus cannot be traced in this case. In this stage, the virus grows exponentially [3]. This stage is a particular case of concern for rapid transmission. In the fourth stage, the virus grows exponentially and is officially declared as an epidemic. It is accompanied by a large number of deaths and uncontrollable spread of the virus.

In this study, the data of the growth of the virus worldwide is taken and a visualization of the data is done to show the growth of the virus through all the four stages. After the visualization, the Machine Learning algorithms are used to predict the spread of the virus. Four machine learning algorithms are used. Out of the four algorithms three of the algorithms are linear statistical algorithms and the fourth one is a nonlinear classifier. An early analysis of growth dynamics for infectious diseases, like COVID-19, is needed to dissect the crucial driving factors that result in rapid disease transmission, refine the measures taken to control the pandemic and improve disease forecast [4].

Machine Learning (ML) based forecasting mechanisms have proved their significance to anticipate in preoperative outcomes to improve the decision making on the future course of actions [5–9]. This study demonstrates the capability of ML models to forecast the number of upcoming patients affected by COVID-19 which is presently considered as a potential threat to mankind. In particular, four standard forecasting models, such as Linear Regression, Polynomial Regression, Support Vector Machine (SVM) and Auto Regressive Integrated Moving Average (ARIMA) have been used in this study to forecast the threatening factors of COVID-19 [10]. The nonlinear predicting algorithm used is Facebook's algorithm Prophet [11, 12]. Several datasets are used for quality analysis. The first few datasets are based on the spread of the virus in India, Wuhan, Italy and visualization is done on this data. The second set of datasets is based on the spread of the virus in the world and the ML algorithms are used on this dataset [13]. Machine learning pipeline is followed before predicting the results. The evaluation parameters used are Absolute Mean Error (AME), Mean Squared Error (MSE) and Root Mean Squared Error (RMSE), *R*-squared (R^2) score [10].

2 Related Work

The corona virus spreads in four stages. Only in the third stage does the virus get converted in the form of an epidemic. In the first stage the growth of the virus is negligible and the growth curve of the virus has just crossed the origin. In the second COVID-19 has developed from an epidemic to a pandemic and its prediction

Fig. 1 Flow chart of the proposed work

has become important to track the growth of the virus. Rustam et al. [14] used the principle of machine learning to predict and track the growth of the virus. The algorithms used predicted to good accuracy of the spread of the virus. Jain et al. [15] applied logistic regression modelling to predict the growth of the virus. The technique of using logistic regression provides a better accuracy than normal models because the virus itself has shown a trend to grow in an exponential manner. Di Giamberardino et al. [16] proposed mathematical ordinary differential analysis to predict and track the growth of the virus. Mathematical modelling forms a basis of the most common machine learning models that we use today. Hence, mathematical modelling using Ordinary Differential Equations is an interesting and effective way to predict the growth of the virus, rather than using statistical methods. Sear et al. [17] used the principles of machine learning to predict the misinformation of the spread of COVID-19 that is most prevalent in the internet. Kang et al. [18] proposed Deep Learning methods [19–21] to predict and diagnose COVID-19 infections using the principles of medical imaging. In this proposed work various types of Supervised Machine Learning algorithms are used for better predictions.

3 Proposed Model

The basic ML pipeline is used to implement the model. The proposed research work takes place in two steps. In the first step, an initial study is conducted in which the spread of the virus is studied and an initial visualization is done. This initial study is made to prove that the spread of the virus is erratic.

The next step of the model is to predict the spread of the virus. The data is cleaned and augmented and then made to pass through different algorithms of SVM, Linear Regression, Polynomial Regression and ARIMA. The results obtained are compared with another algorithm called Prophet. The detailed flow chart of the proposed model is explained in Fig. 1.

4 Description of the Datasets

Different datasets are used for the proposed work which is publicly available. The first datasets are used for the visualization of the data and to show the growth of the virus in the country of India. The dataset contains the names of various states and the number of confirmed cases in the country along with the number of deaths. The

	S. No.	Name of State / UT	Total Confirmed cases (Indian National)	Total Confirmed cases (Foreign National)	Cured	Death
0	22	Maharashtra	23401	0	4786	868
1	12	Gujarat	8541	0	2780	513
2	10	Delhi	7233	0	2129	73
3	32	Tamil Nadu	8002	0	2051	53
4	30	Rajasthan	3988	0	2264	113
5	21	Madhya Pradesh	3785	0	1747	221

Fig. 2 A sample of the dataset which shows the spread of the virus in various states of India

dataset is obtained from the government of India website and the data is statistical data that contains the state-wise COVID-19 cases [13]. The dataset consists of five attributes. The various names of the states, the total number of confirmed COVID-19 cases among Indian nationals, the total number of confirmed cases among foreign nationals, the total number of cured cases and the total number of deaths. The second dataset is based on the spread of the virus throughout the world. It contains daily cases of the number of confirmed cases of the corona virus. On analysis of the data, it is seen that initially the numbers of cases are very less and the number of cases increases gradually. The data is then grouped by the date and the country and its province, thus on the basis of date the number of confirmed recovered and death cases of covid-19 can now be calculated. The data is used to calculate the total number of confirmed, recovered and dead patients. The obtained data is divided into 80% training, 10% testing and 10% validation. The data set is also cleaned by removing impurities and is normalized by Machine Learning algorithm. Different algorithms are used to analyze the data for future predictions and a comparative study is done on them (Fig. 2).

5 Proposed Models Used for the Predictions

5.1 Linear Regression

Linear Regression is a Regression problem that aims to establish a relation between two variables x and y, where x is the time given by the number of days and y is the number of confirmed cases. The model establishes a relation between y and x using the equation of a line. The linear regression model used is Stochastic Gradient Descent regressor.

5.2 Polynomial Regression

Polynomial Regression is an extension of Linear Regression in which a quadratic line is used to make the prediction line. The degree of the polynomial line has chosen to be of degree 5. The coefficients that are calculated are provided to the Linear Regression algorithm with the same hyper parameters.

5.3 Support Vector Machine (SVM)

The support vector machine (SVM) uses the principle of linear and Euclidean distance and Mean to predict a particular factor. It is popularly used in the classification problems but can be configured to use in the prediction problem. The gamma (γ) values are varied between 0.001 and 1 and the epsilon ($\acute{\epsilon}$) values are varied between 0.0001 and 0.001. The degree of the polynomial kernel is varied between 4 and 6; the number of iterations is kept at 40 iterations.

5.4 ARIMA (Auto Regressive Integrated Moving Average)

ARIMA is a time series analysis model which uses the concept of both time series and moving average to predict a future time series model. The model uses its own lags and lagged error as inputs and these are used to predict a future value.

5.5 Prophet

Prophet is a nonlinear predictor that takes everyday data and tries to predict based on particular intervals. The prophet algorithm takes everyday data and predicts the data based on the everyday data. The interval of taking the data can be changed to years or months even hours in this case the interval is changed to days since the data set takes everyday data.

5.6 Evaluation Parameters

(1) *R*-Squared (R^2) Value/Model Score: *R*-Squared (R^2) is an evaluation metric, it is also called confidence factor. It compares the Regression line with the Predicted values.

Table 1 The results of linear regression model

Model	Mean absolute error MAE (per 1000 cases)	Mean squared log error (MSE)	Latency	R^2 value (model score)
Linear regression	105.56	0.317	0.45	51.23%

$$R \text{ Squared } \left(R^2\right) = \frac{\text{Variance Explained by Model}}{\text{Total Variance}} \tag{1}$$

(2) Mean Absolute Error (MAE): It is the sum of difference between the predicted values and the actual values.

$$\text{MAE} = \frac{1}{n}\sum_{j=1}^{n}\left|\left(y_j - \widehat{y_j}\right)\right| \tag{2}$$

(3) Mean Squared Error (MSE): It is the mean of the square of the difference between predicted and actual values.

$$\text{MSE} = \frac{1}{n}\sum_{j=1}^{n}\left(y_j - \widehat{y_j}\right)^2$$

(4) Latency: It is the time required by an algorithm to give results.

6 Description of the Datasets

6.1 Results of Linear Regression

Table 1 shows that the model predicts the growth of the virus accurately to some extent; however it fails in to predict the growth of the virus in the later stages when the virus reaches the stage of community transmission. For this model the Mean Absolute Error (per 1000 cases) is 105.56 and the Mean Squared Log Error (MSE) is 0.317 and Model Score is quite low 51.23% with latency of 0.45. Figure 3 represents the COVID-19 actual occurrences versus the linear regression performance.

6.2 Results of Polynomial Regression

From the analysis of Table 2 it is clear that that the MAE is far less than the linear regression model. Thus, it is proving that the polynomial regression model is far more accurate than the linear regression model. The rate of the virus growth and

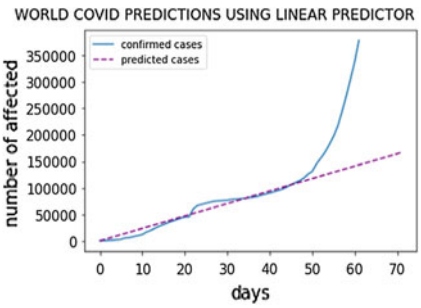

Fig. 3 Performance of the linear reg. model

Table 2 The results of polynomial regression model

Model	Mean absolute error MAE (per 1000 cases)	Mean squared log error (MSE)	Latency	R^2 value (model score)
Polynomial regression	22.606	0.0099	56.89	82.23%

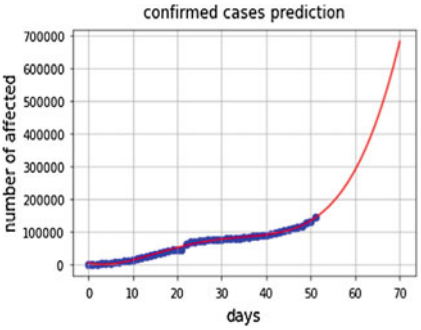

Fig. 4 Performance of the polynomial reg.

the regression line match to a good extent. Figure 4 is showing the performance of the polynomial Regression model. The Y axis represents the number of confirmed cases and the X axis represents the number of days. The graph depicts that the model performs very well in fitting the data.

6.3 Results of SVM

From Table 3 it is clear that the MAE for SVM is far less than the linear regression and Polynomial Regression model and model score is far better than these two models. This is proving that the SVM model is far more accurate than the linear regression model. Figure 5 shows that the rate of the virus growth and the regression line match to a great extent. The graph (Figure 5) shows the performance of the SVM model.

Table 3 The results of the SVM model

Model	Mean absolute error MAE (per 1000 cases)	Mean squared log error (MSE)	Latency	R^2 value (model score)
SVM	16.056	0.0069	42.106	94.01%

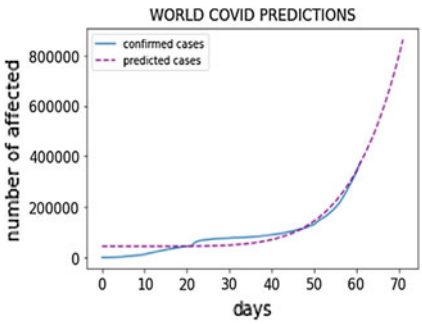

Fig. 5 Performance of the SVM model

Table 4 The results of the ARIMA model

Model	Mean absolute error MAE (per 1000 cases)	Mean squared log error (MSE)	Latency	R^2 value (model score)
ARIMA	55.807	0.0054	10.89	99.74%

The Y axis represents the number of confirmed cases and the X axis represents the number of days. The dotted lines represent the number of actual cases that have been confirmed and the dotted lines represent the performance of the SVM model.

6.4 Results of ARIMA

Table 4 shows that the model predicts the growth of the virus accurately to some extent. For this model the Mean Absolute Error (per 1000 cases) is 55.807 and the Mean Squared Log Error (MSE) is 0.0054 and Model Score is very high 99.74%. Figure 6 represents the COVID-19 actual occurrences versus the ARIMA performance for the predictions. The ARIMA curve is able to predict the cases of COVID-19 much better than the other three models.

6.5 Results of Prophet

Table 5 predicts that the performance parameters of the model using the Prophet model is far better compared to all the other models. Figure 7 shows the performance

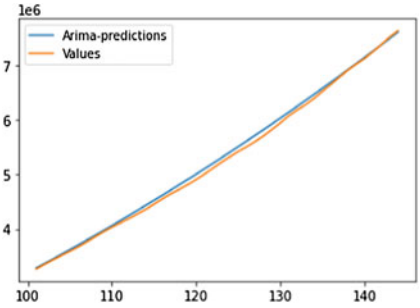

Fig. 6 Performance of the ARIMA model

Table 5 The results of the prophet model

Model	Mean absolute error MAE (per 1000 cases)	Mean squared log error (MSE)	Latency	R^2 value (model score)
Prophet model	64.807	0.0064	10.89	98.33%

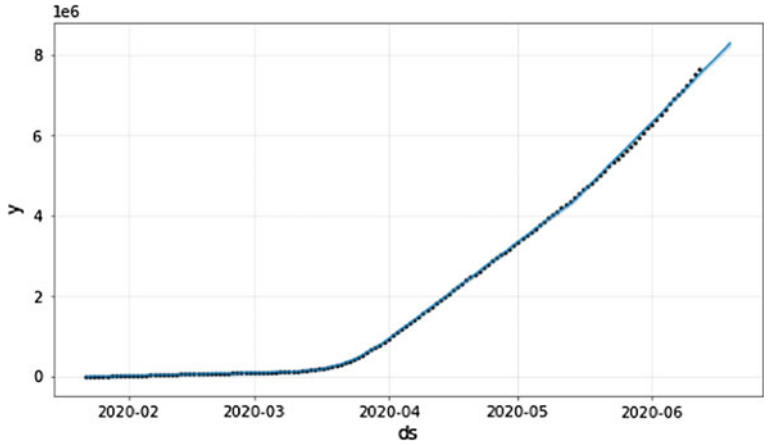

Fig. 7 Performance of the Prophet model

of the Prophet model. The *Y* axis represents the number of confirmed cases and the *X* axis represents the number of days. The curve signifies better accuracy with a model score of 98.33%. This shows better performances in the non-linear predictions.

7 Conclusion

The growth of the virus is erratic in the end stages and unpredictable in many cases. A recent form of linear classifier as Linear Regression, Polynomial Regression, SVM, ARIMA and nonlinear classifiers like the Prophet Model have been able to predict the

growth of the virus and act as an early warning to several countries. The conventional methods produce an error of over a hundred thousand making the predictions much undesirable. In this work a comparative study is also performed to decide which type of models can be useful for the better prediction of the spread of the virus. The obtained results clearly show that only such kind of models which can increase quadratically can provide a better estimate of the growth of the virus. The prophet model shows the best accuracy of 98.33% and suitable for prediction of non-linear spreading & growth of the virus. Only by the prevention of community transmission of the virus the growth of the virus can be stopped at stage one that is the stage of linear increase in the spread of the virus.

References

1. Huang, C., Wang, Y., Li, X., et al.: Clinical Features of Patients Infected with 2019 Novel Coronavirus in Wuhan, China. Lancet (2020).https://doi.org/10.1016/S01406736(20)30183-5
2. WHO: Coronavirus Disease (COVID-19) Outbreak Situation [online] (2020). Available https://www.who.int/emergencies/diseases/novelcoronavirus-2019
3. Jenssen, H.B.: China National Health Commission Diagnosis and Treatment of Pneumonitis Caused by New Coronavirus (Trial Version 6). Accessed Sep. 8, 2020 [online]. Available http://www.nhc.gov.cn/yzygj/s7653p/202002/8334a8326dd94d329df351d7da8ae%fc2.shtml
4. Zu, Z.Y., Jiang, M.D., Xu, P.P., Chen, W., Ni, Q.Q., Lu, G.M., Zhang, L.J.: Coronavirus disease 2019 (COVID-19): a perspective from china. Radiology (2020). https://doi.org/10.1148/radiol.2020200490
5. Chhaya, K., Sandipan, D., Vandana, J.: 7 discovery of robust distributions of COVID-19 spread. In: Use of AI, Robotics, and Modern Tools to Fight Covid-19, pp. 89–110. River Publishers (2021)
6. Predicting the time period of extension of lockdown due to increase in rate of covid-19 cases in India using machine learning-ScienceDirect. https://www.sciencedirect.com/science/article/pii/S2214785320363914. Accessed on 12/15/2020
7. Li, L., et al.: Artificial intelligence distinguishes COVID-19 from community acquired pneumonia on chest CT. Radiology **296**(2), E65–E71 (2020). https://doi.org/10.1148/radiol.2020200905
8. Samanta, P.K., Mukherjee, S., Rout, N.K.: Susceptibility analysis of novel corona virus using hadoop distributed file system. In: Banerjee, S., Mandal, J.K. (eds.) Advances in Smart Communication Technology and Information Processing. Lecture Notes in Networks and Systems, vol. 165. Springer, Singapore. https://doi.org/10.1007/978-981-15-9433-5_33
9. Abhinav, S., Arpit, J., Mangey, R.: 3 AI for COVID-19: the journey so far. In: Use of AI, Robotics, and Modern Tools to Fight Covid-19, pp. 29–43. River Publishers (2021)
10. Poleneni, V., Rao, J.K., Afshana Hidayathulla, S.: COVID-19 prediction using ARIMA model. In: 2021 11th International Conference on Cloud Computing, Data Science & Engineering (Confluence), pp. 860–865 (2021). https://doi.org/10.1109/Confluence51648.2021.9377038
11. Prophet—prophet is a forecasting procedure implemented in rand python. It is fast and provides completely automated forecasts that can be tuned by hand by data scientists and analysts. https://facebook.github.io/prophet/
12. Taylor, S.J., Letham, B.: Forecasting at scale. Am. Stat. **72**(1), 37–45 (2018)
13. https://www.mygov.in/covid-19
14. Rustam, F., et al.: COVID-19 future forecasting using supervised machine learning models. IEEE Access **8**, 101489–101499 (2020). https://doi.org/10.1109/ACCESS.2020.2997311

15. Jain, M., Bhati, P.K., Kataria, P., Kumar, R.: Modelling logistic growth model for COVID-19 pandemic in India. In: 2020 5th International Conference on Communication and Electronics Systems (ICCES), Coimbatore, India, pp. 784–789 (2020). https://doi.org/10.1109/ICCES48766.2020.9138049
16. Di Giamberardino, P., Iacoviello, D., Papa, F., Sinisgalli, C.: Dynamical evolution of COVID-19 in Italy with an evaluation of the size of the asymptomatic infective population. IEEE J. Biomed. Health Inform. https://doi.org/10.1109/JBHI.2020.3009038
17. Sear, R.F., et al.: Quantifying COVID-19 content in the online health opinion war using machine learning. IEEE Access **8**, 91886–91893 (2020). https://doi.org/10.1109/ACCESS.2020.2993967
18. Kang, H., et al.: Diagnosis of coronavirus disease 2019 (COVID-19) with structured latent multi-view representation learning. IEEE Trans. Med. Imaging. https://doi.org/10.1109/TMI.2020.2992546
19. Rajaraman, S., Siegelman, J., Alderson, P.O., Folio, L.S., Folio, L.R., Antani, S.K.: Iteratively pruned deep learning ensembles for COVID-19 detection in chest X-rays. IEEE Access **8**, 115041–115050 (2020). https://doi.org/10.1109/ACCESS.2020.3003810
20. Pathak, Y., Shukla, P.K., Arya, K.V.: Deep bidirectional classification model for COVID-19 disease infected patients. IEEE/ACM Trans. Comput. Biol. Bioinform. https://doi.org/10.1109/TCBB.2020.3009859
21. Hu, S., et al.: Weakly supervised deep learning for COVID-19 infection detection and classification from CT images. IEEE Access **8**, 118869–118883 (2020). https://doi.org/10.1109/ACCESS.2020.3005510

An Advanced Irrigation System for Smart Agriculture Using the Internet of Things

M. Nagarajapandian, R. Savitha, and D. Shanthi

Abstract In the present scenario, technological advancements play a crucial role in the development of all the fields. Automation greatly reduces the human work. Agriculture is the primary sector in India. Automation in agricultural sector will be very helpful for the farmers. The proposed work focuses on designing and implementation of an efficient automation system for agricultural field maintenance. With the use of embedded system the whole irrigation system can be automated. Moisture and temperature sensors are used to promote efficient watering of crops. There are three irrigation methods in this scheme: manual mode, auto mode, and IoT mode. With the help of the keyboard, the farmer may alter the ways of irrigation. The user's Android mobile with the help of WiFi module displays the data values of all sensors.

Keywords Irrigation system · Embedded system · WiFi module · Android mobile

1 Introduction

Technologies provide simplicity in mechanisms by overcoming the complexities in handling the process. Nowadays many people are moving to urban areas in search of better jobs, so they are unable to maintain their field. In turn many conclude to sell their farm as they can't maintain it. Technological advancement makes our daily chores move smoothly. Automation in agro field maintenance will be very useful for farmers as they can easily maintain their fields irrespective of their location. The proposed system helps the farmers in easy maintenance of the irrigation system. Thus

M. Nagarajapandian · R. Savitha · D. Shanthi (✉)
Department of Electronics and Instrumentation Engineering, Sri Ramakrishna Engineering College, Coimbatore, Tamil Nadu, India
e-mail: shanthi.1806041@srec.ac.in

M. Nagarajapandian
e-mail: nagarajapandian.m@srec.ac.in

R. Savitha
e-mail: savitha.1806040@srec.ac.in

B. Sikdar et al. (eds.), *Proceedings of the 3rd International Conference on Communication, Devices and Computing*, Lecture Notes in Electrical Engineering 851,
https://doi.org/10.1007/978-981-16-9154-6_57

farmers can engage themselves in other activities without spending much of their time for field maintenance.

Mostly irrigation is done by tradition methods of stream flows from one end to other. Depending on the water supply, the moisture levels in the fields may vary. The administration of the water system can be enhanced utilising programmed watering framework. This paper proposes a programmed water system with framework for the terrains which will reduce manual labour and optimising water usage increasing productivity of crops. For formulating the setup, Arduino kit is used with moisture sensor with WiFi module. Our experimental setup is connected with cloud framework and data acquisition is done. Then data is analysed by cloud services and appropriate recommendations are given [1].

In automation system water availability to crop is monitored through sensors and as per need watering is done through the controlled irrigation. The almost infinite capabilities of storage and processing, the rapid elasticity makes cloud computing an attractive solution to the large amount of data generated. The idea is to focus on parameters such as temperature and soil moisture. This is a Mobile Integrated and smart irrigation system using IOT based on application controlled monitoring system. The main objective of this project is to control the water supply and monitor the plants through a Smartphone [2].

Irrigation is one of the traditional practice and involves higher percentage of labours in daily agriculture sector. To water the plants automatically, sensors and microcontrollers are available to determine when the plants need water. Automation involves improving the speed of production, reduction of cost, effective use of resources. The main role of this project is to develop a Microcontroller system to irrigate the plant automatically and the information is been sent to the farmers [3]. The creation of an irrigation system directed to the automation of crop irrigation through the use of technology instruments for precision agriculture, with a focus on crop irrigation processes, is presented in this paper. For this, an autonomous hydraulic irrigation system with a storage system and self-sustaining energy regulation was designed, allowing irrigation decision-making in places where it is needed at all times. For decision-making, this irrigation system uses a service that uses sensors to analyze environmental factors like as ambient temperature, soil moisture, and relative humidity. For self-supply, the irrigation system was constructed using solenoid valves as actuators that were controlled by relays, as well as two solar panels and a set of lithium batteries that were managed by a battery management system [4]. An intelligent water-saving irrigation plan based on ZigBee-WiFi dual-protocol communication technology is presented. The researchers explain an intelligent water-saving irrigation plan based on ZigBee-WiFi dual-protocol communication technology. Create and install C#-based monitoring platform software that includes automated or manual watering based on the optimal humidity for the crop's growth stage [5]. The aim of the paper, titled "Automatic Irrigation System on Soil Moisture Content," is to create an automated irrigation system that detects the earth's moisture content and switches the pumping motor ON and OFF. In the farming industry, proper irrigation procedures are necessary. The advantage of using these systems is that they reduce human meddling while still ensuring proper irrigation. This automated irrigation

project uses an Arduino board with an ATmega328 microcontroller configured to receive input signals from the earth's changing dampness conditions using a dampness detecting device [6]. Water availability to the crop is monitored by sensors in the automation system, and watering is done as needed through controlled irrigation. Because of its effectively unlimited storage and processing capabilities, as well as its quick flexibility, cloud computing is an enticing response to the massive quantity of data created. Irrigation is a traditional agricultural activity that employs a more significant number of people daily. Sensors and microcontrollers may be utilized to automatically determine when the plants need to be watered. Increased manufacturing speed, lower prices, and more efficient resources are part of automation. The primary purpose of this research is to develop a microcontroller system that will autonomously irrigate plants and provide data to farmers [7]. To solve the waste of physical and human resources, a significant waste of water resources, and a low utilization rate in traditional agriculture irrigation, a low-cost intelligent irrigation system is constructed using sensor technology and wireless data transmission technology. The system can remotely monitor irrigation water volume, receive feedback from the field controller, and turn on or off the irrigation system solenoid valve, allowing for precise and timely irrigation. It has been validated by the Institute of Water Resources and Hydropower Research. The designed system has a high level of stability, reliability, and application value and can efficiently conduct real-time monitoring, data feedback, and analysis [8]. The objective is to focus on factors like temperature and soil moisture. This is a mobile, integrated, innovative irrigation system based on an Internet of Things-enabled monitoring system. The primary purpose is to regulate the water supply and monitor the plants using smart phones [9]. To run a weather monitoring system and irrigation controller, the user must measure various variables, including atmospheric temperature, humidity, wind speed, wind direction, radiation, soil conditions, brightness, and rainfall. The primary purpose of this paper is to present a low-cost microcontroller-based irrigation scheduler that executes user-defined tasks and provides commands to activate appropriate actuators (relay, solenoid valves, motor). A soil moisture sensor was created, simulated, and tested to deliver exact and trustworthy findings at a reasonable cost. The sensor is a low-cost, high-performance, a small temperature sensor that can also measure humidity [10].

2 Advanced Irrigation System

The main objectives are to conserve water and reduce human resources in agriculture, especially irrigating fields. Use of communication technologies on farmland, such as Wi-Fi modules, to develop a remote control and monitoring system for farmers, which will improve water conservation.

Our proposed paper mainly focuses on providing efficient automation for irrigation and field maintenance. Features such as automated control and monitoring using

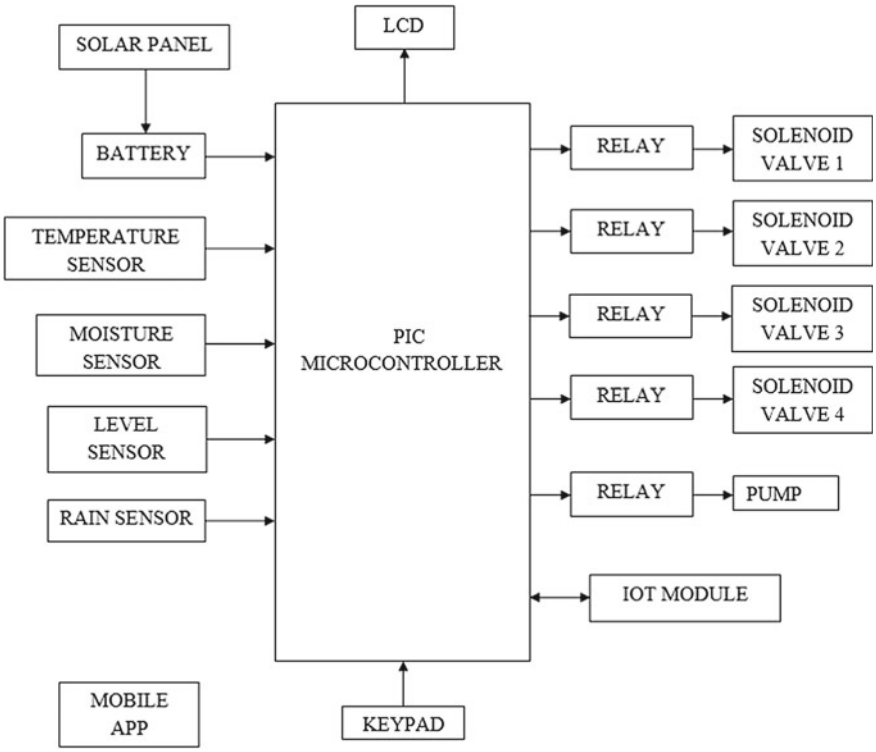

Fig. 1 Block diagram of proposed system

IoT make maintenance tasks easier for farmers. The solar panel supplies a power for its operation Three methods are used to control the irrigation system.

The main processor in the proposed system is the peripheral interface controller PIC16F877A, as shown in Fig. 1. It is a 40-pin IC with a low cost and flexibility of operation. The reason for selecting this PIC IC is that it supports both hardware and timer interrupts and is well suited for various application protocols like I2C, Serial, and parallel. A relay switch is used to electronically controlled open and close a circuit. The results were shown on the 16 $\times$ 2 LCD panel. Four different types of sensors are employed in this research. Temperature Sensor, Humidity Sensor, Rain Sensor, and Level Sensor are the four sensors.

A level sensor is mounted in the tank to measure the water level. In the proposed method, a solenoid valve is utilised to open or shut circulation in a valve body. A plunger, coil, and sleeve assembly make up a solenoid valve. In this paper, four solenoid valves are used. The farmer can use the solenoid valve as a requirement of the feed. If farmers grow four types of crops in their field, all four types of crops do

not need the same amount of water. So now each valve is used to supply different amounts of water to each type of crop. Solenoid valve is connected to the pump.

3 Model Description

3.1 Microcontroller

The microcontroller utilised in this project is from the PIC family. The PIC microcontroller is the first RISC based microcontroller made in CMOS (Complementary metal oxide semiconductor) that uses a separate instruction and data bus to provide simultaneous access to programme and data memory. The key benefit of combining CMOS and RISC is the reduced power consumption, which results in a relatively tiny chip size with a low pin count. The main advantage of CMOS over other fabrication techniques is that it is noise resistant. Microcontrollers are smaller, use less power, and are less expensive.

A microcontroller is a self-contained unit that can perform functions without the use of additional hardware such as I/O ports or external memory. The CPU core, which has historically been built on an 8-bit microcontroller device, is the heart of the microcontroller. Microcontrollers have been developed in recent years around specific designed CPU cores, such as the microchip PIC family of microcontrollers.

The PIC16F877A has 8 KB of flash programme memory, 368 KB of data memory, 256 KB of EEPROM data memory, 15 interrupts, in-circuit programming, 3 internal hardware timers, Capture/Compare/PWM modules, and 15 interrupts. Up to eight 10-bit A/D channels, 5 digital I/O ports (up to 22 lines) and a built-in USART for serial connection.

3.2 Power Supply Board

The ac voltage, which is usually 220 V rms, is linked to a transformer, which reduces the ac voltage to the desired dc output level. Figure 2 shows the flow of the power supply. A full-wave rectified voltage is then produced by a diode rectifier, which is first filtered by a simple capacitor filter to produce a dc voltage. There is frequently some ripple or ac voltage change in the resulting dc voltage. Even though the input dc voltage changes, a regulator circuit removes the ripples and maintains the same

Fig. 2 Block diagram of power supply

dc value. One of the most common voltage regulator IC modules is used to provide is this voltage regulation.

3.3 Solenoid Valve and Submersible Water Pump

A solenoid valve is a type of electro-mechanical valve that is often used to control the flow of liquid or gas. There are several varieties of solenoid valves, but the two most common are pilot operated and direct acting. The most common type of pilot controlled valve uses system line pressure to open and close the main orifice in the valve body. A coil, plunger, and sleeve assembly make up a solenoid valve. A plunger return spring inhibits flow in usually closed valves by holding the plunger against the opening. The magnetic field created by energising the solenoid coil elevates the plunger, allowing flow. When the solenoid coil in a normally open valve is activated, the plunger closes the aperture, preventing flow. To control the fluids in the system, most flow control applications require starting or stopping the flow in the circuit. This is commonly done with an electrically controlled solenoid valve. Solenoid valves can be placed in remote places and controlled by simple electrical switches since they are solenoid actuated.

MicroSubmersible Pump, DC (3–6)V DIY project to make a mini water pump for a fountain garden. This is a low-cost, small-size Submersible Pump Motor that can be powered by a 3-V power supply, as shown in Fig. 4. It can process up to 120 L per hour while only consuming 220 milliamps of power. Simply connect a tube pipe to the motor output, submerge it in water, and activate it. At all times, make sure the water level is higher than the motor. Dry running can damage the motor by overheating it and making noise. The operational current is (130–220) mA and the operational voltage is (3–6) V. The water flow rate in the pump is (80–120) L/H. And the total amount of time spent working is 500 h. Pumps can be driven in two ways: DC or magnetically. The submersible pump is depicted in Fig. 3.

Fig. 3 Submersible pump

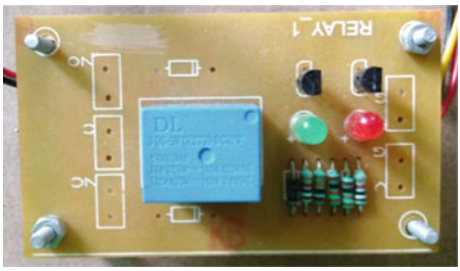

Fig. 4 Relay module

3.4 Solar Panel

Solar panels can be photovoltaic modules, solar hot water panels, or a group of solar photovoltaic (PV) modules electrically connected and mounted on a supporting structure. A PV module is a solar cell assembly that is packed and linked solar panels can be used in commercial and residential applications to generate and deliver electricity as part of a larger solar system. Each module's DC output power is rated under standard test conditions (STC) and typically ranges between 100 and 320 W. The efficiency of a module influences its size when the rated output is the same: an 8% efficient 230 W module will have twice the area of a 16% efficient 230 W module. On the market, there are a few solar panels that are more efficient than 19%. Because a single solar module can only generate a certain amount of energy, most systems employ many modules. A solar panel or array, an inverter, and, in certain situations, a battery and/or solar tracker, as well as interconnecting cables, make up a photovoltaic system.

3.5 Temperature Sensor and Level Sensor

The LM35 series of temperature sensors are precision integrated-circuit 2 sensors with a linearly proportional output voltage to the temperature in degrees Celsius. As a result, the LM35 has an advantage over linear temperature sensors calibrated in degrees Kelvin in that it does not require the user to subtract a large constant voltage from the output in order to achieve proper Centigrade scaling. The LM35 provides typical accuracies of 14 °C at room temperature and 34 °C over an entire temperature range of 55 to + 150 °C without the need for external calibration or trimming. The temperature range of + 150 °C ensures low costs. The LM35's output impedance, linear output, and flawless intrinsic calibration make connection to readout or control circuits a snap, thanks to its inexpensive cost. The gadget can be used with either a single power supply or a plus and minus supply.

Liquids, other fluids, and fluidized solids with an upper free surface, such as slurries, granular materials, and powder, are detected by level sensors Flowing liquids become almost horizontal in their containers (or other physical restrictions) due to

gravity, whereas most bulk solids pile up at an angle of repose to a peak due to gravity. The substance to be measured can either be in its natural state or contained within a container (e.g., a river or a lake). Continuous or point values can be used to measure the level. Continuous level sensors identify the exact amount of material in a given location by measuring the level within a specific range, whereas point-level sensors merely tell whether the material is above or below the detecting point. The latter, in general, detects levels that are abnormally high or low.

3.6 Wifi Module and Relay Module

Expressive developed the ESP8266 WiFi enabled system on chip (SoC) module. It's primarily used to create embedded IoT (Internet of Things) applications. It runs at 80 MHz on a 32-bit RISC CPU based on the Tensilica Xtensa L106 (or over clocked to 160 MHz). It has a 64-kilobyte boot ROM, 64-kilobyte instruction RAM, and 96-kilobyte data RAM. SPI can be used to access external flash memory. The ESP8266 module is a low-cost wireless transceiver that can be utilised in IoT end-point applications. The microcontroller must use a series of AT commands to connect with the ESP8266 module. The microcontroller connects with the ESP8266-01 module using a UART with a set Baud rate.

The Relay module is a distinct hardware device that is used to switch between remote devices. The relay module is shown in Fig. 4. It allows you to control gadgets remotely across a network or the Internet. With commands from Clock watch Enterprise given over a local or wide area network, devices can be remotely switched on or off. From across the office or around the world, you can operate computers, peripherals, and other powered devices. The Relay module can sense and operate a range of external devices by sensing external on/off conditions. The serial port is used to connect the PC interface.

3.7 MPLAB IDE and Proteus

MPLAB IDE is a Microchip microcontroller application development environment for PCs. It's called an Integrated Development Environment, or IDE, since it provides a single integrated "environment" for developing code for embedded microcontrollers. The MPLAB Integrated Development Environment (IDE) is a full-featured editor, project manager, and design workspace for Microchip PICmicro MCUs and dsPIC DSCs embedded designs.

Simone Zanella designed Proteus (easy-to-use text processor) in 1998. It is a fully complete procedural programming language. It integrates functions from other languages, including C, BASIC, Assembly, and Clipper/dbase; it is exceptionally versatile when dealing with strings, with hundreds of dedicated functions, making it one of the most powerful text manipulation languages. Proteus is named after Proteus,

a Greek sea god who looked after Neptune's entourage and provided responses; he was known for his ability to shift into several forms. The fundamental purpose of this language is to convert data from one form to another.

4 Result and Discussion

Figure 5 shows the snapshot of the proposed model with a mobile app-based advanced irrigation system using a moisture sensor, WiFi module, microcontroller. There are three irrigation methods in this scheme: manual mode, auto mode, and IoT mode. With the help of the keyboard, the farmer may alter the ways of irrigation. Auto mode operates based on sensor value. The motor pump is turned on or off depending on the field's abnormal climatic conditions. The water content is measured, and the field is irrigated and maintained according to the crop pattern. In auto mode, before irrigation, the water level in the well is checked. The user's Android mobile displays the data values of all sensors with the help of a WiFi module. If the climatic conditions are such that it has begun to rain, the microcontroller will turn off the pump until it has stopped raining. In manual mode, the water supply can be change by changing the valve if the farmer is in the field. In IoT mode, the farmer can fully control and monitor the entire irrigation system on a user Android mobile. Farmers can control farmland if it is too far from the field. This improves the conservation of water. Thus the system works.

The valve on/off condition is shown in Fig. 6 from the WiFi module to the user's mobile app. They employ a variety of irrigation techniques in agriculture. As a result, we can easily water the crops with this method. In the display, we can view the sensor values. Based on moisture and rain value, we can determine which crops require irrigation. In manual mode, we can change the mode manually by pressing the keypad. In auto mode, the crops will irrigate themselves based on sensor readings. In the display, we can observe the current status. The IoT mode is depicted in Fig. 6.

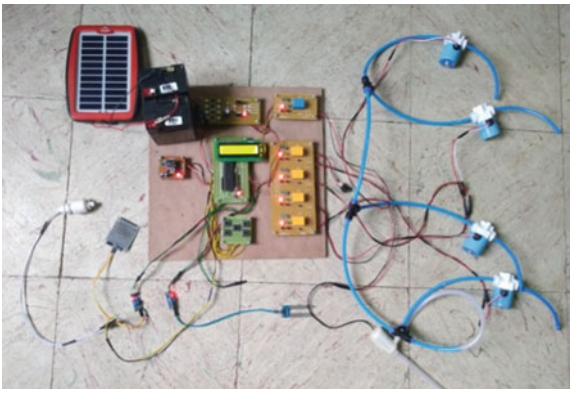

Fig. 5 Snap shot of proposed system

Fig. 6 Screenshot of mobile control app

Fig. 7 LCD displsy in agriculture field

The valves are controlled via a mobile app in this mode. This image depicts the temperature, moisture, rain, and water level in the tank. All of the valves are turned off in this situation. If necessary, we can turn on the valve.

The LCD display in the agriculture field is shown in Fig. 7. This display indicates the temperature, moisture value, and the value of rain if there is any. The three modes are selectable. The second setting, AUTO MODE, is selected in this display.

5 Conclusion and Future Scope

The microcontroller-based Advanced Irrigation System efficiently regulates and monitors all types of irrigation system activity. By implementing this technology need of man power can be reduced. Farmers can get proper irrigation facilities with prior knowledge of it. We are going to make the whole agro field automated by including facilities for automatic manuring to crops.

In terms of maximising water resources for agricultural production, the contemporary irrigation system that was installed is both appropriate and cost-effective. The proposed technique saves time, which results in higher profits for farmers. The technology is very flexible as well as cost-effective. It is so simple and dependable that no one needs to be on duty to use it.

Acknowledgements This resarch work was performed at the department of Electronics and Instrumentation Engineering, Sri Ramakrishna Engineering College, we would be obligated to the Management, Principal for implementing our research work, thank you.

References

1. Dweepayan, M., Arzeena, K., Rajeev, T., Shuchi, U.: Automated ırrigation system-IoT based approach. In: 2018 3rd International Conference On Internet of Things: Smart Innovation and Usages (IoT-SIU), vol. 1, pp. 2197–2201 (2018)
2. Vaishali, S., Suraj, S., Vignesh, G., Dhivya, S., Udhayakumar, S.: Mobile integrated smart irrigation management and monitoring system using IOT. In: 2017 International Conference on Communication and Signal Processing (ICCSP), vol. 1, pp. 2569–2579 (2017)
3. Karpagam, J., Infranta Merlin, I., Bavithra, P., Kousalya, J.: Smart irrigation system using IoT. In: 2020 6th International Conference on Advanced Computing and Communication Systems (ICACCS), vol. 1, p. 229 (2020)
4. Amaury, C., Cristian, A.: Irrigation system for precision agriculture supported in the measurement of environmental variables. Int. Eng. Sci. Technol. Conf. (IESTEC) **1**, 2–112 (2019)
5. Nyoman Rudy, H., Luh Putu, Y., Gede Angga, P.: Fuzzy based internet of things irrigation system. Int. Conf. Cybern. Intell. Syst. (ICORIS) **1**, 2–124 (2019)
6. Nagarajapandian, M., Ram Prasanth, U.: Automatic irrigation system on sensing soil moisture content. IJIREEICE **3**(3), 96–98 (2015)
7. Pranita, A.: Water saving—irrigation automatic agricultural controller. Int. J. Sci. Technol. Res. Lett. **1** (2012)
8. Priyanka, D., Hande: Microcontroller based irrigation. Int. J. Microcircuits Electron. **15**, 1 (2012)
9. Joaquin Gutierrez, J.: Smartphone irrigation sensor. IEEE Sens. J. **15**, 5122–5127 (2015)
10. Venkata Naga Rohit, G.: Micro controller based automatic plant irrigation system. Int. J. Adv. Res. Technol. **2** (2013)

Design of Fork Antenna

Samiran Chatterjee, Kulsum Khanam Nayyar, Vemireddy Ramya Sree, and S. Teja

Abstract Here, we propose single layer, triple-feed four elements fork array antenna which uses transmission line feed and suitable for different application. The proposed design presents with high return loss and 2:1 VSWR range. This project achieves good result when port 1 and 2 acts as an active port, and port 3 acts as a parasitic element. At the above-mentioned condition, we achieved two resonant frequencies of about 4.37 GHz and 5.31 GHz with − 37.2 dB and − 65.36 dB return loss, respectively. Also − 10 dB bandwidth of about 4.69 GHz shows the proposed structure uses as wide bandwidth for the above-mentioned condition. But when any one port is active and others acts as parasitic elements, that condition also achieves a considerable result in terms of bandwidth. The proposed antenna uses as wide bandwidth antenna for any combination of feeds. But the antenna does not work properly when port 1 or port 3 active individually and other ports acts as parasitic elements. At this condition, the proposed structure has good resonant frequency with good return loss but the bandwidth not sufficient for the application for which it is intended. Also got the absolute gain ranges from − 1.68 to − 21.52 dBi for all the resonant frequencies. The main achievement is increased frequency ratio with no intersymbol interference (ISI).

Keywords Fork · Port · ISI · Gain · VSWR

1 Introduction

Current era shows the increased demand for small antennas on wireless communication design among microwaves and wireless engineers with high bandwidth. For getting the more bandwidth, the young engineers design several antennas [1–5].

S. Chatterjee (✉)
Professor, ECE Department, Amrita Sai Institute of Science and Technology, Vijayawada, Paritala, India

K. K. Nayyar · V. R. Sree · S. Teja
Department of ECE, Vignan's Institute of Management and Technology for Women (Affiliated to JNTU, Hyderabad), Rangareddy, Telangana 500031, India

B. Sikdar et al. (eds.), *Proceedings of the 3rd International Conference on Communication, Devices and Computing*, Lecture Notes in Electrical Engineering 851,
https://doi.org/10.1007/978-981-16-9154-6_58

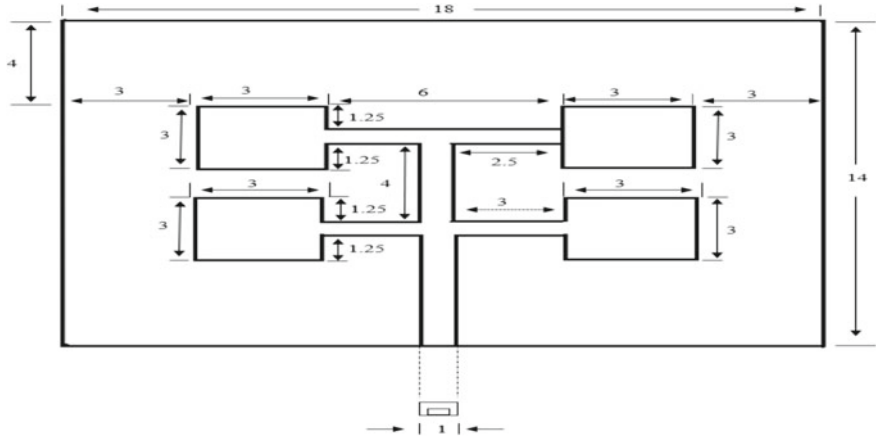

Fig. 1 Structure of four elements fork

Among all the design, fork antenna design creates more interest which gives the large bandwidth [7–9], and this antenna design consists of minimum two patches. The patches are connected in both horizontal and vertical combination [6] to achieve the high bandwidth with deep return loss. The proposed design makes the interest on wireless engineers [10–12] and the new trends proposed in here which uses the MoM-based software IE3D [13].

2 Fork Antenna Structure

Figure 1 illustrated the fork antenna design with detailed dimensions. The insulation materials specified for this design are epoxy FR_4 substrate. For this design, we choose transmission line feeding techniques.

The proposed fork designed with 14 mm × 18 mm rectangular patch. Figure 2 shows fork antenna with shows feeding arrangements.

3 Result Analysis

All kinds of parameters of the designed fork antenna were analyzed here for the bandwidth, gain and S parameters of the antenna. Figures 3, 4, 5, 6, 7 and 8 point return losses. We also achieved large bandwidth which discussed in below tables.

The designed fork array antenna shows good performance of impedance matching on all ports. The results point up that the return losses for each resonant frequency are less than − 10 dB. Some antenna parameters have been investigated to improve the bandwidth, return loss and gain.

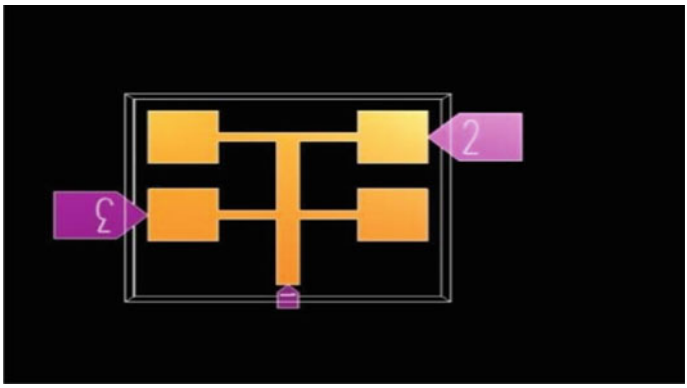

Fig. 2 Antenna with feeding arrangements

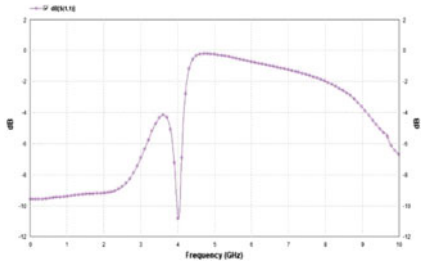

Fig. 3 Return loss when port 1 is active

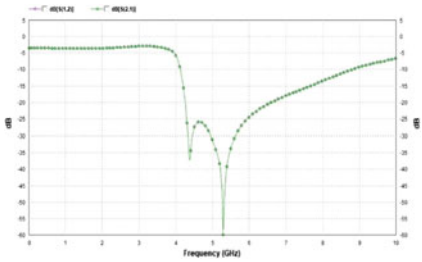

Fig. 4 Return loss when port 1 and port 2 are active

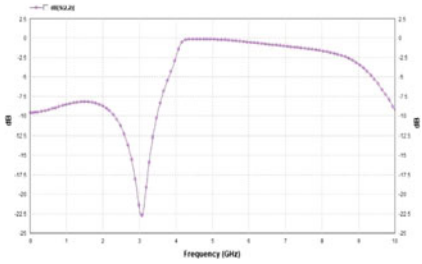

Fig. 5 Return loss when port 2 is active

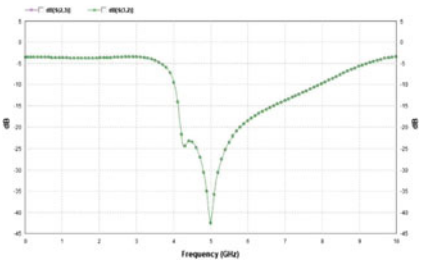

Fig. 6 Return loss when port 2 and port 3 are active

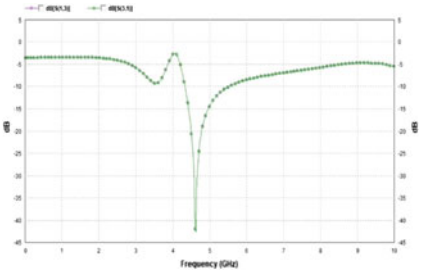

Fig. 7 Return loss when port 1 and port 3 are active

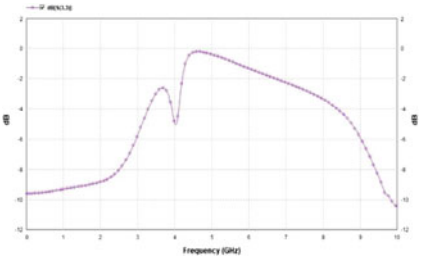

Fig. 8 Return loss when port 3 is active

3.1 Electric and Magnetic Field Pattern

Electric and magnetic field patterns for fork antenna are shown in Figs. 9, 10, 11, 12, 13, 14, 15, 16, 17, 18, 19 and 20 for all the resonance (Tables 1 and 2).

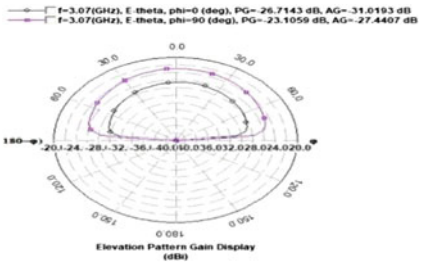

Fig. 9 Electric field pattern at 3.07 GHz

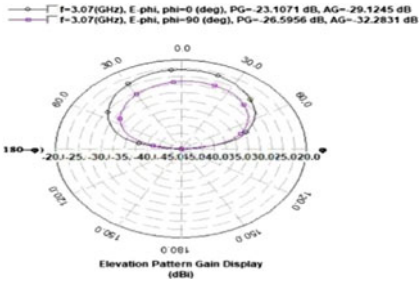

Fig. 10 Magnetic field pattern at 3.07 GHz

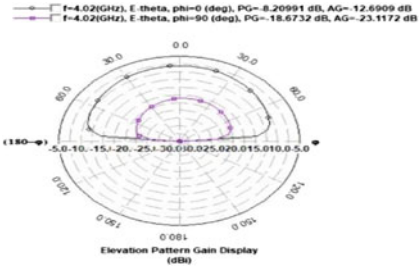

Fig. 11 Electric field pattern at 4.02 GHz

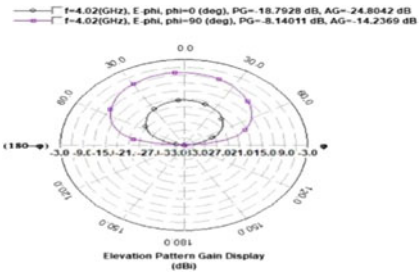

Fig. 12 Magnetic field pattern at 4.02 GHz

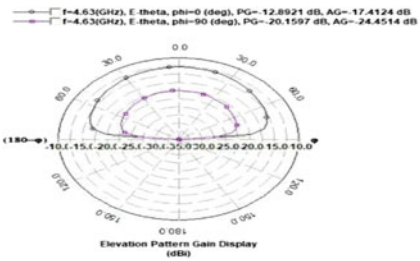

Fig. 13 Electric field pattern at 4.63 GHz

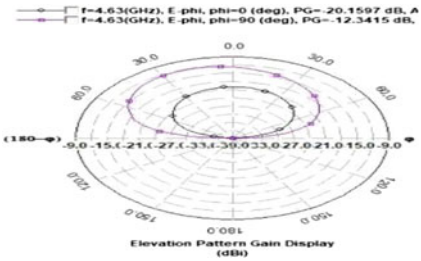

Fig. 14 Magnetic field pattern at 4.63 GHz

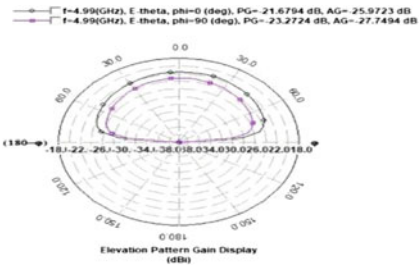

Fig. 15 Electric field pattern at 4.99 GHz

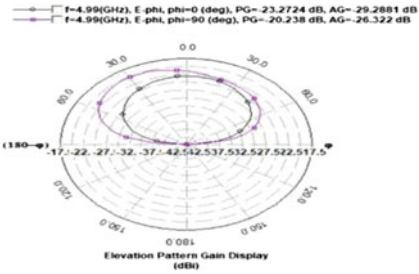

Fig. 16 Magnetic field pattern at 4.99 GHz

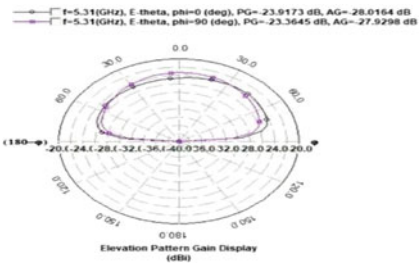

Fig. 17 Electric field pattern at 5.31 GHz

4 Conclusion

The integrated four-element fork assembly antenna was proposed in this project. All four rectangular spots are connected via transmission line feeding technology. In

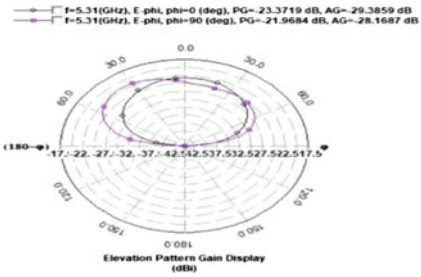

Fig. 18 Magnetic field pattern at 5.31 GHz

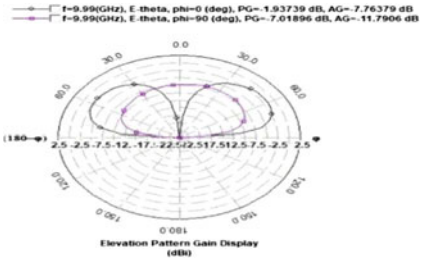

Fig. 19 Electric field pattern at 9.99 GHz

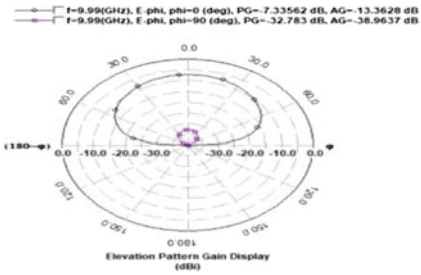

Fig. 20 Magnetic field pattern at 9.99 GHz

Table 1 Summary of bandwidth and resonant frequency

Input port	Output port	S parameter	Port as an parasitic element	Resonant frequency (GHz)	Return loss (dB)	− 10 dB bandwidth (Hz)	VSWR
1	1	S_{11}	2, 3	$f_1 = 4.02$	− 10.88	73.02 M	1.81
1	2	S_{12}	3	$f_1 = 4.37$	− 37.2	4.69 G	–
2	1	S_{21}		$f_2 = 5.31$	− 65.36		–
3	1	S_{31}	2	$f_1 = 4.63$	− 42.31	1.19 G	–
1	3	S_{13}					
2	2	S_{22}	1, 3	$f_1 = 3.07$	− 22.78	1.17 G	1.16
2	3	S_{23}	1	$f_1 = 4.99$	− 42.42	3.92 G	–
3	2	S_{32}					–
3	3	S_{33}	1, 2	$f_1 = 9.99$	− 10.46	–	1.86

Table 2 Summary of gain and beamwidth

(S-parameters)	Resonant frequency (GHz)	Frequency ratio	Absolute gain (dBi)	− 3d beam width (°)
S_{22}	$f_1 = 3.07$	$f_1/f_1 = 1$	− 21.52	130.962
S_{11}	$f_2 = 4.02$	$f_2/f_1 = 1.36$	− 7.828	91.1976
S_{13}, S_{31}	$f_3 = 4.63$	$f_3/f_1 = 1.50$	− 11.74	94.6467
S_{23}, S_{32}	$f_4 = 4.99$	$f_4 = 4.99$	− 18.684	113.084
S_{21}, S_{12}	$f_5 = 5.31$	$f_5 = 5.31$	− 20.004	125.943
S_{33}	$f_6 = 9.99$	$f_6 = 9.99$	− 1.68	152.3

the designed fork antenna, we achieved multiple resonant frequencies belonging to the application of different microwave frequency bands. This project achieves good result when port 2 and 1 act as an active port and port 3 acts as a parasite. In the above case, two resonant frequencies of about 4.37 GHz and 5.31 GHz were achieved with a return loss of − 37.2 dB and − 65.36 dB, respectively. The − 10 dB bandwidth of about 4.69 GHz also illustrates the uses of the architecture proposed as broadband for the above case. But when any port is active and the other is acting as parasitic, this condition also brings great result in terms of bandwidth. But the antenna does not work properly when port 1 or port 3 is individually active and other ports act as parasites. In this case, the proposed architecture has a good resonant frequency with good return loss, but the bandwidth is not sufficient for its intended application. The proposed matrix achieved an increasing frequency ratio with a 2:1 VSWR and HPBW ranges from 91.20° to 152.30° on average for all resonant frequencies. The proposed antenna is applicable in radio astronomy, long-range radio communication, amateur radio and the application of molecular rotational spectroscopy depending on the different feed set. The bandwidth is also sufficient for the intended application.

References

1. Sarkar, I., Sarkar, P.P., Chowdhury, S.K.: A new compact printed antenna for mobile communication. In: 2009 Loughborough Antennas & Propagation Conference, 16–17 Nov. 2009, Loughborough, UK
2. Chatterjee, S., Paul, J., Ghosh, K., Sarkar, P.P., Chanda (Sarkar), D., Chowdhury, S.K.: A compact micro strip antenna for WLAN communication. In: National Conference of Electronics, Communication and Signal Processing, 2011, Paper ID: 116
3. Chatterjee, S., Paul, J., Ghosh, K., Sarkar, P.P., Chowdhury, S.K.: A printed patch antenna for mobile communication. In: Convergence of Optics and Electronics Conference, 2011, pp. 102–107, Paper ID: 15
4. Fallahi, R., Kalteh, A.-A., Golparvar Roozbahani, M.: A novel UWB elliptical slot antenna with band-notched characteristics. Progr. Electromagn. Res. C **18**, 211–220 (2011)
5. Chatterjee, S., Chowdhury, S.K., Sarkar, P.P., Sarkar, D.C.: Compact micro strip patch antenna for microwave communication. Indian J. Pure Appl. Phys. **51**, 800–807 (2013)
6. Balanis, C.A.: Advanced Engineering Electromagnetic. John Wiley & Sons, New York (1989)

7. Petosa, A., Ittipiboon, A.: Dielectric resonator antennas: a historical review and the current state of the art. IEEE Antennas Propag. Mag. **52**(5), 91–116 (2010)
8. Chatterjee, S., Paul, J., Ghosh, K., Chowdhury, S.K., Sarkar, P.P., Chanda (Sarkar), D.: Compact microstrip antenna for mobile communication. Microwave Opt. Technol. Lett. (MOTL) **55**(5), 954–957 (2013)
9. Chatterjee, S., Chowdhury, S.K., Sarkar, P.P., Chanda (Sarkar), D.: Comparison between two CPW-FED UWB antennas based on dielectric constant of substrate. Int. J. Electron. Commun. Technol. (IJECT) **IV**(I), 49–58 (2013)
10. Chatterjee, S., Chowdhury, S.K., Sarkar, P.P., Sarkar, D.C.: Bevel microstrip printed antenna for satellite communication. Indian J. Pure Appl. Phys. (IJPAP) **52**, 760–766 (2014)
11. Chatterjee, S., Sarkar, P.P., Chanda (Sarkar), D., Chowdhury, S.K.: Compact microstrip antenna for WLAN and H-LAN communication. Int. J. Soft Comput. Eng. **2**(3), 270–274 (2012)
12. Chatterjee, Chowdhury, S.K., Chanda (Sarkar), D., Sarkar, P.P.: A compact CPW-FED UWB antenna. In: Second (2nd) National Conference of Control, Communication and Signal Processing, 2012 (NCECS-2012), Paper ID: NCECS-1219; Chatterjee, S., Chowdhury, S.K., Sarkar, P.P., Chanda (Sarkar), D.: Compact microstrip antenna for C-band microwave communication. In: National Conference of Electronics, Communication and Device Electronics (N3CD-2013), pp. 99–104, Paper ID: ID0262N25
13. Zeland Software Inc.: IE3D: MOM-Based EM Simulator. http://www.zeland.com

Design of Wilkinson Power Divider

Samiran Chatterjee, Yasaswi Sowmya Tungaturti, Rachana Mahendrakar, G. Naga Sai Bhavani, and P. Priyanka

Abstract Here, proposes single sided Wilkinson power divider with three transmission line feed. One feed uses as an input port and other two uses as an output port. Here also analyzed that there will be no coupling error between two output ports. The power divider presents in this project with high return loss and VSWR in between 2:1 range. This work achieves good result when port 1 acts as an active port, and other two ports act as a parasitic element. At the above mentioned, condition achieved a resonant frequency of about 5.23 GHz with − 17.69 dB return loss. For the above frequency also achieved a − 10 dB bandwidth of about 5.90 GHz which shows is an ultrawide bandwidth. Also get the gain of about − 6 dBi with 170.142° bandwidth (− 3dB HPBW). Also the main achievement is to get increased frequency ratio (IFR), so that the power divider gives no inter symbol interference (ISI). This Wilkinson power divider is specially designed for C band microwave frequency region and also applicable for terrestrial broadband and military telemetry applications. Finally, the proposed power divider is operating for multi-frequency operation.

Keywords Port · Power divider · Parasitic element · Feed · IFR · Return loss

1 Introduction

The Wilkinson power divider [1–5] is one type of power divider which do not have any isolation between output ports for any conditions. The electromagnetic engineer designed this power divider or power joiner by the help of printed antenna [6–12] to reduce the cross talk between transmitter and receiver. Nowadays, all the researchers try to design the power divider from the previous printed antenna design [13–16] and

S. Chatterjee (✉)
Professor, ECE Department, Amrita Sai Institute of Science and Technology, Vijayawada, Paritala, India

Y. S. Tungaturti · R. Mahendrakar · G. Naga Sai Bhavani · P. Priyanka
Department of ECE, Vignan's Institute of Management and Technology for Women (Affiliated to JNTU, Hyderabad), Kondapur, Hyderabad, Telangana 501301, India

B. Sikdar et al. (eds.), *Proceedings of the 3rd International Conference on Communication, Devices and Computing*, Lecture Notes in Electrical Engineering 851,
https://doi.org/10.1007/978-981-16-9154-6_59

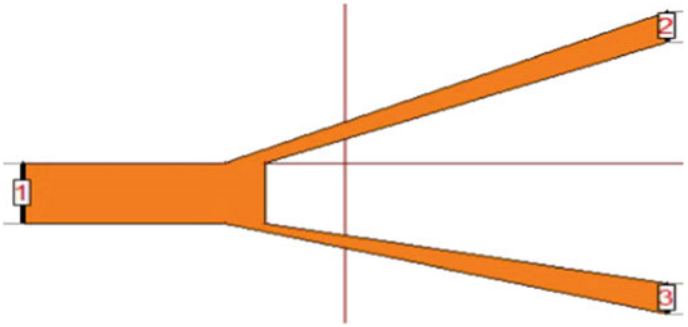

Fig. 1 Wilkinson power divider configuration

analyzed all parameters of power divider. The scattering matrix for general WPD is defined by [17]:

$$|S| = \frac{-j}{\sqrt{2}} \begin{vmatrix} 0 & 1 & 1 \\ 1 & 0 & 0 \\ 1 & 0 & 0 \end{vmatrix}$$

For ideal design of WPD, we use IE3D software [18] for our power divider design and after design, all parameters analyzed and discussed in this paper.

2 Wilkinson Power Divider Design

Figure 1 pointed out the designed Wilkinson power divider with feeding techniques. We simulate the ideal WPD with three transmission line feed in which one is use as an input port and other two uses as an output port. The insulation materials specified for this WPD is epoxy FR_4 substrate.

3 Analysis with Simulated Results

Figures 2, 3, 4, 5, 6 and 7 lighted the return loss result of proposed WPD design and all the analysis related to return loss described in below tables. Some parameters are investigated for improved bandwidth and return loss of Wilkinson power divider.

3.1 Electric and Magnetic Field Pattern

The electric and magnetic field patterns are described in Figs. 8 and 9. The electric and magnetic field patterns are taken across different center frequencies, and for all

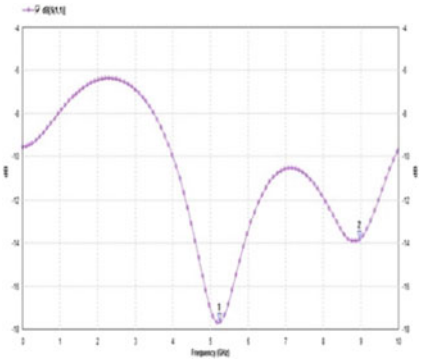

Fig. 2 Return loss when port 1 is active

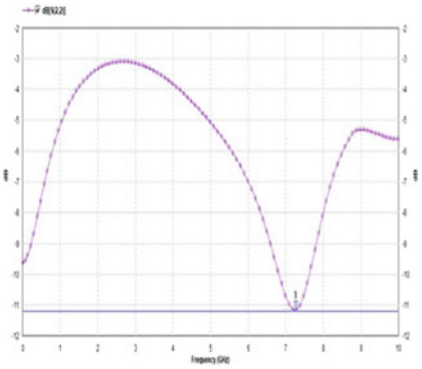

Fig. 3 Return loss when port 2 is active

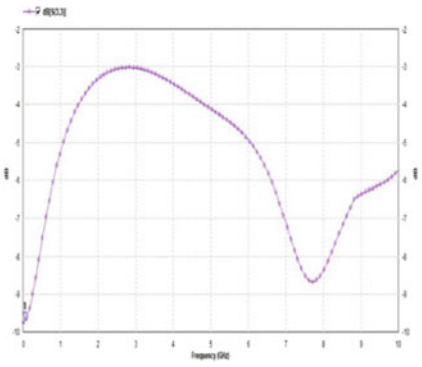

Fig. 4 Return loss when port 3 is active

the resonant frequencies, the calculation mentioned in the below table of this section (Fig. 10; Tables 1 and 2).

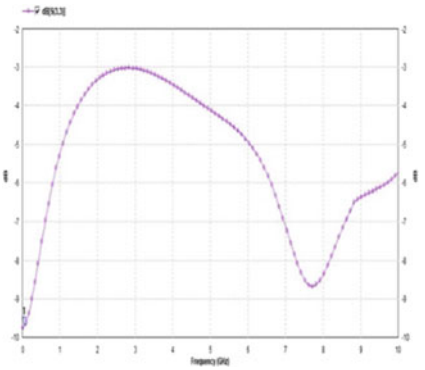

Fig. 5 Return loss when ports 1 and 2 are active

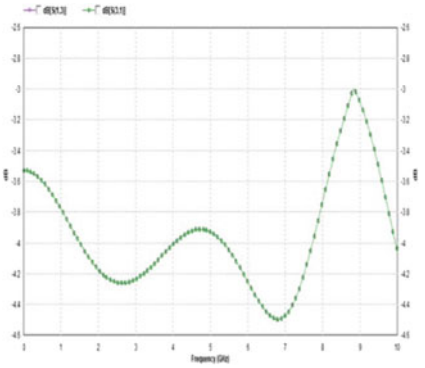

Fig. 6 Return loss when ports 1 and 3 are active

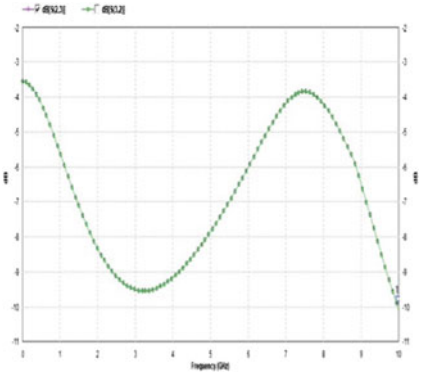

Fig. 7 Return loss when ports 2 and 3 are active

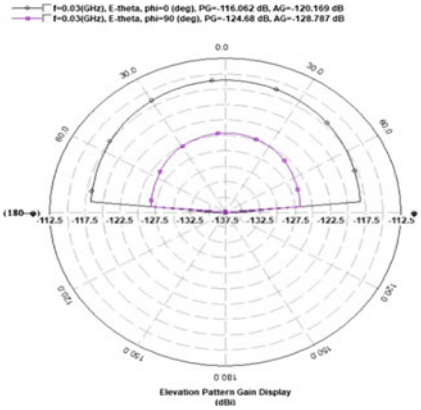

Fig. 8 E-plane 2D radiation pattern with transmission line feed at $f = 0.03$ GHz

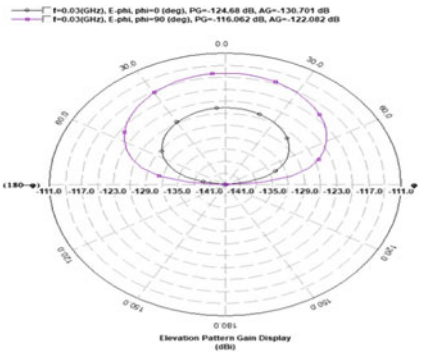

Fig. 9 H-plane 2D radiation pattern with transmission line feed at $f = 0.03$ GHz

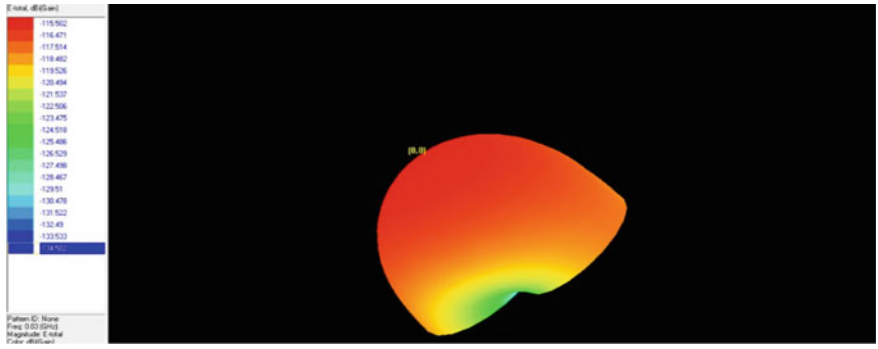

Fig. 10 Total 3D radiation pattern with transmission line feed at $f = 0.03$ GHz

Table 1 Simulated results of resonant frequency versus return loss

Antenna structure	Input port	Output port	Frequency (GHz)	Return loss (dB)	Bandwidth (Hz)	VSWR
S_{11}	1	1	$f_1 = 5.23$	− 17.69	5.90 G	1.30
			$f_2 = 8.90$	− 13.88		1.51
S_{12}	1	2	–	–	–	–
S_{21}	2	1				
S_{13}	1	3	–	–	–	–
S_{31}	3	1				
S_{22}	2	2	$f_1 = 0.03$	− 9.74	–	1.97
S_{23}	2	3	$f_1 = 9.99$	− 10.08	–	–
S_{32}	3	2				
S_{33}	3	3	$f_1 = 7.26$	− 11.16	809.87 M	1.76

Table 2 Analyze of antenna w.r.t gain and beam width for different resonant frequency

Return loss parameters	Frequency (GHz)	Frequency ratio	Gain (dBi)	Beamwidth (°)
S_{22}	$f_1 = 0.03$	1	− 115.5	170.142
S_{11}	$f_2 = 5.23$	174.33	− 12.7	61.579
S_{33}	$f_3 = 7.26$	242	− 7.02	153.997
S_{11}	$f_4 = 8.90$	296.6	− 6	153.937
S_{23}	$f_5 = 9.99$	333	− 5.25	152.151

4 Conclusion

In this paper, it proposes power divider with three microstrip line feeding at the both ends of antenna structure which shows that this WPD is working for the desired application for which for it is intended. Proposed power divider has achieved the resonant frequency at 5.23 GHz with return loss of − 17.69 dB when port 1 is active and other two output ports act as parasitic elements and 0.03 GHz with return loss of − 9.74 dB when port 2 is active and other two ports act as an parasitic elements. And when port 3 is active, the other two output ports act as parasitic elements, the power divider achieves the resonant frequency at 7.26 GHz with return loss of − 11.16 db. It is observed that there will be no resonant frequency when input port and any one output port are active. So it is conclude that there will be no ISI for the proposed power divider. This power divider shows a bandwidth of 5.90 GHz which acts as ultrawide band (UWB) antenna. It achieved increased frequency ratio with 2:1 VSWR range and 170.14° of HPBW on an average on all resonant frequencies. The final conclusion of the proposed antenna works for C band microwave frequency region and also applicable for terrestrial broadband and military telemetry applications. The beamwidth is enough for the application for which it is intended.

References

1. Wilkinson, E.: An N-way hybrid power divider. IRE Trans. Microwave. Theory Tech. **8**(1), 116–118 (1960)
2. Parad, L.I., Moynihan, R.L.: Split-tee power divider. IRE Trans. Microwave Theory Tech. **8**, 91–95 (1965)
3. Cohn, S.B.: A class of broadband three-port TEM- mode hybrids. IEEE Trans. Microwave Theory Tech. **MTT-16**, 110–116 (1968)
4. Ekinge, R.B.: A new method of synthesizing matched broadband TEM-mode three-ports. IEEE Trans. Microw. Theory Tech. **19**(1), 81–88 (1971)
5. Tang, X., Mouthaan, K.: Analysis and design of compact two-way Wilkinson power dividers using coupled lines. In: Asia-Pacific Microwave Conference, pp. 1319–1322, Dec 7–10, 2009
6. Sarkar, I., Sarkar, P.P., Chowdhury, S.K.: A new compact printed antenna for mobile communication. In: 2009 Loughborough Antennas & Propagation Conference 16–17 Nov 2009, Loughborough, UK
7. Wu, J.-W., Hsiao, H.-M., Lu, J.-H., Chang, S.-H.: Dual broadband design of rectangular slot antenna for 2.4 and 5 GHz wireless communication. IEE Electron. Lett. **40**(23) (2004)
8. Chatterjee, S., Paul, J., Ghosh, K., Sarkar, P.P., Chanda (Sarkar), D., Chowdhury, S.K.: A compact micro strip antenna for WLAN communication. In: National Conference of Electronics, Communication and Signal Processing, 2011, Paper ID: 116
9. Raj, R.K., Joseph, M., Anandan, C.K., Vasudevan, K., Mohanan, P.: A new compact microstrip-fed dual-band coplaner antenna for WLAN applications. IEEE Trans. Antennas Propag. **54**(12), 3755–3762 (2006)
10. Chakraborty, U., Chatterjee, S., Chowdhury, S.K., Sarkar, P.P.: Triangular slot micro strip patch antenna for mobile communication. In: India Conference (INDICON), 2010 Annual IEEE, pp. 4–7, Paper ID: 511
11. Chatterjee, S., Paul, J., Ghosh, K., Sarkar, P.P., Chowdhury, S.K.: A Printed patch antenna for mobile communication. In: Convergence of Optics and Electronics conference, pp. 102–107, 2011, Paper ID: 15
12. Chatterjee, S., Chowdhury, S.K., Sarkar, P.P., Sarkar, D.C.: Compact micro strip patch antenna for microwave communication. Indian J. Pure Appl. Phys. **51**, 800–807 (2013)
13. Chatterjee, S., Paul, J., Ghosh, K., Chowdhury, S.K., Sarkar, P.P., Chanda (Sarkar), D.: Compact microstrip antenna for mobile communication. Microw. Opt. Technol. Lett. (MOTL). **55**(5), 954–957 (2013)
14. Chatterjee, S., Chowdhury, S.K., Sarkar, P.P., Sarkar, D.C.: Bevel microstrip printed antenna for satellite communication. Indian J. Pure Appl. Phys. (IJPAP). **52**, 760–766 (2014)
15. Chatterjee, S., Sarkar, P.P., Chanda (Sarkar), D., Chowdhury, S.K.: Compact microstrip antenna for WLAN and H-LAN communication. Int. J. Soft Comput. Eng. **2**(3), 270–274 (2012)
16. Chatterjee, Chowdhury, S.K., Chanda (Sarkar), D., Sarkar, P.P.: A compact CPW-FED UWB antenna. In: Second (2nd) National Conference of Control, Communication and Signal Processing, 2012 (NCECS-2012), Paper ID: NCECS-1219
17. Balanis, C.A.: Advanced Engineering Electromagnetic. John Wiley & Sons, New York (1989)
18. Zeland Software Inc. IE3D: MOM-Based EM Simulator. http://www.zeland.com

Mathematical Modeling of Respiratory System Introducing Electrical Control Function Analogy

Moupali Roy, Arpan Das, Rounak Biswas, Biswarup Neogi, and Prabir Saha

Abstract The lung analogy concept is essential for the design of a respiratory model, thereby its electrical analysis is of utmost importance for researchers. An electrical circuit has been introduced through the representation of the stable lung dynamics system applying various control system tools. The mathematical model of such a respiratory system has been redesigned to reach a stable system. Suitable control algorithms have been introduced in this system and proper observation has been taken care of through the applicable software and response has been examined to determine the stability through the Bode plot. Moreover, to get satisfactory results Ziegler-Nichols rule (Z-N rule) as well as PID simulator tuning has been introduced in this proposed system. In addition, controllability (CTRB) and observability (OBSV) testing have been performed on this redesigned system. After continuous domain analysis, the proposed system has been converted to a discrete domain and incorporated Jury's algorithm to obtain a stable system.

Keywords Lung modeling · Electrical circuit · Continuous signal · Discrete signal · Stability analysis

1 Introduction

Nowadays, mathematical modeling of the respiratory system is an emerging research topic. The respiratory model analysis through electrical control circuit is essential to evaluate the lung condition of human beings [1]. Several researches have already been established by various researchers based on this topic. Such as Rayan A. et al.

M. Roy · A. Das · R. Biswas
Narula Institute of Technology, Kolkata, India
e-mail: moupaliroy@nitm.ac.in

B. Neogi
JIS College of Engineering, Kalyani, India

P. Saha (✉)
National Institute of Technology, Shillong, Meghalaya, India

B. Sikdar et al. (eds.), *Proceedings of the 3rd International Conference on Communication, Devices and Computing*, Lecture Notes in Electrical Engineering 851,
https://doi.org/10.1007/978-981-16-9154-6_60

introduced thoracic transplantation and aspect of artificial lungs [1], Scott D. Lick et al. had proposed a complete perioperative management protocol where studied Paracorporeal Artificial Lungs in [2], Iterative integral parameter identification of a respiratory mechanics model had studied by Paul D. et al. [3] and Surajit Baghchi explained electrical modeling of the respiratory system and identification of common COPD diseases [4], the same way, Adma et al. researched about forced oscillations and respiratory system modeling in adults [6], Blanca E. published advancement of technologies for chronic pulmonary diseases [7]. In 2012, A. D. Freed et al. conversed about the connection among these balances of modeling that had been a source of insight and inspiration for the lung parenchyma viscoelastic model [8]. Vibration and analysis for lung hemorrhage discussed by D. John Jabaraj et al. in the year 2013 where numerous revisions had been ruled out the mechanism of respiratory depletion [9]. In the year 2013, by Anand Santhanam, expressed in 3D lung modeling, reproduction, conception obtained characterized by lung structure and function [10].

Here, all these researches have been found in various topics related to the respiratory system. Such like that, research under the category of a respiratory model in a collaboration with biomedical and electronics depending on the stability, controllability, observability has been created a research gap.

However, the focal determination of such a study has to explore the electrical circuit modeling for the human respiratory control system [11]. The foremost objective of this control model is to firstly, stem one electrical circuit of the human respiratory system and convert it into its transfer function so that the circuit can be analyzed in a mathematical way. Secondly, to observe the step output of this transfer function to relook the control parameters like stability, controllability, and observability. In order to pave the way for additional development in this aspect, the model has to be stable first [7].

In this paper, the previous model has been [10] re-evaluated and stability has been verified. For the verification of the stability, several techniques like PID tuning (Ziegler-Nichol's tuning method), etc. have been incorporated. After eventually receiving the final transfer model, the stability of the structure needs to be re-analyzed, and the Bode plot has been measured. Moreover, the transfer function needs to be converted into state space where the system stability can be patterned by evaluating the controllability and observability matrix. At this point, the final transfer function has been converted into a discrete domain so that the stability can be analyzed in a discrete domain also. The stability can be examined with a method called the Jury's stability criterion. In the discrete domain, the model has been satisfied the stability condition.

2 Review of the Previous Model

2.1 Control Block Representation of Human Respiratory System

The exchange of gas with respiratory mechanics is depicted by the reference electrical model and the model target to implement the total control mechanisms of lungs. A representation block of the prototypical is shown in Fig. 1, wherever the connections midst the diverse subsystems are tinted. The cardiovascular arrangement and the respiratory structure cooperate via the gas exchange and transport segment. This part defines the gas exchange progressions in the lungs and the complete tissues, along with the gas conveyance throughout the vascular structure.

A correspondence is observed to the range that permits an acquaintance of one arena to be pragmatic in the additional ground. It is quite significant to analyze a machine-driven system in terms of its electrical equivalent since a heap of information is available about the characteristics of electrical circuits compared to other categories of mechanical systems. The difficulty to practice the conventional mechanical–electrical analogy due to its in-completion in certain important particulars is shown here in detail. A novel generous of mechanical–electrical correspondence is presented below which is more comprehensive than any of its ancient variants. These analogy authorizations a correspondent electrical circuit to be pinched in a much added forthright and commonsensical method, not demanding such cautious reasoning at apiece period. Therefore, apparent that a novel equivalence is possible where force is recognized with current somewhat than with e.m.f. as observed in the ancient equivalence. In what shadows, it will be exposed that the novel equivalence is additional complete and supplementary convenient than the ancient one.

First, an electrical circuit model of the human respiratory system has been taken [10]. Now the transfer function of the electrical circuit model is needed. At first, the

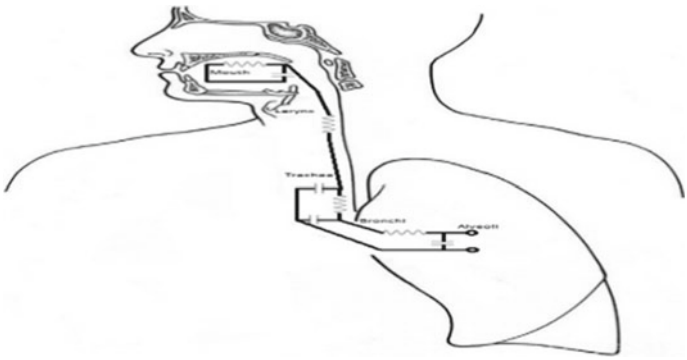

Fig. 1 Electrical lung model circuit implementation in the human body

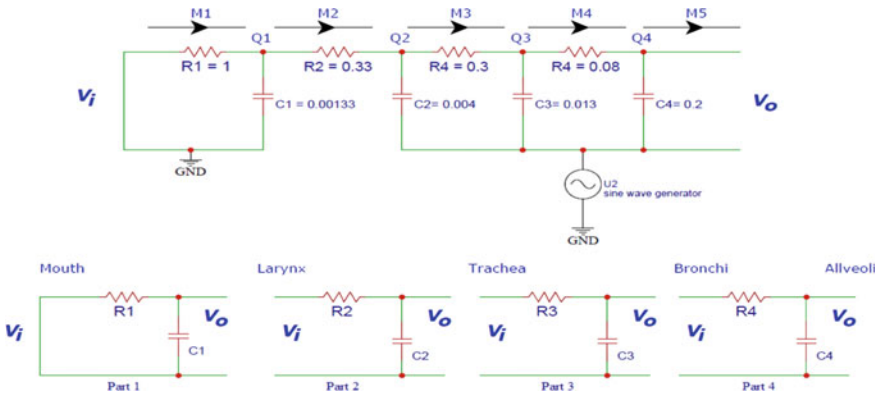

Fig. 2 Respiratory system analogy circuit [10, 12]

electrical circuit has to be divided into four parts. Then the current and voltage equations have to be found out for each part of the circuit followed by taking the Laplace for each and every equation. Comparing those Laplace equations for each part, the transfer function for all four parts of this electrical circuit has to be determined (Fig. 2).

Here, v_i = input voltage; v_o = output voltage; $r1$ = resistor with value 1 Ω; $r2$ = resistor with value 0.33 Ω; $r3$ = resistor with value 0.3 Ω; $r4$ = resistor with value 0.08 Ω; $c1$ = capacitor with value 0.0013 F; $c2$ = capacitor with value 0.004 F; $c3$ = capacitor with value 0.013 F; $c4$ = capacitor with value 0.2 F; $Q1$ = node between $r1$ and $r2$; $Q2$ = node between $r2$ and $r3$; $Q3$ = node between $r3$ and $r4$; $Q4$ = node between $r4$ and $c4$; M1 = input signal across $r1$; M2 = input signal across $r2$; M3 = input signal across $r3$; M4 = input signal across $r4$; M5 = input signal across v_o.

For the 1st part of the circuit,

$$V_i(S) = R_1 I(S) + \frac{1}{C_1 S I(S)} \tag{1}$$

$$V_o(S) = \frac{1}{C_1 S I(S)} \tag{2}$$

$$\text{TF} = \frac{V_o(S)}{V_i(S)} = \frac{1}{R_1 C_1 S + 1} \tag{3}$$

For the 2nd part of the circuit,

$$V_i(S) = R_2 I(S) + \frac{1}{C_2 S I(S)} \tag{4}$$

$$V_o(S) = \frac{1}{C_2 S I(S)} \tag{5}$$

$$\mathrm{TF} = \frac{V_o(S)}{V_i(S)} = \frac{1}{R_2C_2S + 1} \tag{6}$$

For the 3rd part of the circuit,

$$V_i(S) = R_3I(S) + \frac{1}{C_3SI(S)} \tag{7}$$

$$V_o(S) = \frac{1}{C_3SI(S)} \tag{8}$$

$$\mathrm{TF} = \frac{V_o(S)}{V_i(S)} = \frac{1}{R_3C_3S + 1} \tag{9}$$

For the 4th part of the circuit,

$$V_i(S) = R_4I(S) + \frac{1}{C_4SI(S)} \tag{10}$$

$$V_o(S) = \frac{1}{C_4SI(S)} \tag{11}$$

$$\mathrm{TF} = \frac{V_o(S)}{V_i(S)} = \frac{1}{R_4C_4S + 1} \tag{12}$$

After getting the transfer function for each part of the electrical circuit, represent the electrical circuit into a control block system. Once the control block representation of the system has been made, then the system's transfer function can be determined easily through the block diagram reduction technique (Fig. 3).

Finally, the transfer function of that system is state as

$$\mathrm{TF}_1 = \frac{1}{[(R_1C_1S + 1)(R_2C_2S + 1)(R_3C_3S + 1)(R_4C_4S + 1)]}$$

From the circuit putting these values: $R_1 = 1$, $R_2 = 0.33$, $R_3 = 0.3$, $R_4 = 0.08$, $C_1 = 0.0013$, $C_2 = 0.004$, $C_3 = 0.013$, $C_4 = 0.2$. Now the transfer function of the electric circuit is,

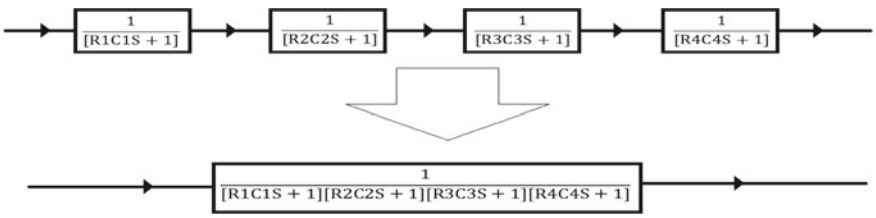

Fig. 3 Block representation of respiratory circuit

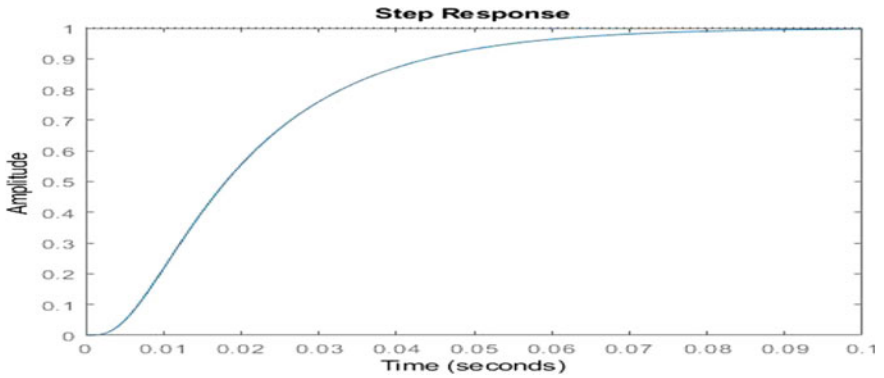

Fig. 4 Step response of respiratory system analogy circuit

$$\mathrm{TF}_1 = \frac{1}{\left[(0.0013S+1)\left(1.32\times10^{-3}S+1\right)\left(3.9\times10^{-3}S+1\right)(0.016S+1)\right]}$$
$$= \frac{1}{\left(1.07\times10^{-10}S^4\right)+\left(1.976\times10^{-7}S^3\right)+\left(1.163\times10^{-4}S^2\right)+\left(2.252\times10^{-2}S\right)+1}$$

2.2 Analysis of Control Block of Human Respiratory System

This is the step response of the transfer function. Step Response of a system is essential to determine if the system is stable or not [7]. For that reason, this transfer function has been passed into a step input (Fig. 4).

After analyzing the time domain of the step response output, the stability of the system can be checked. Here, the system is unstable. An unstable system can't be used to design any model. Anyhow the system has to be stable. There is a method called the Ziegler-Nichols tuning approach. It produces upright values for three PID gain parameters. Those are controller path gain (K_p), integrator time constant (T_i), derivative time constant (T_d) [6]. Using those parameters, the system can be tuned to make it a stable system.

3 Proposed Model

Characteristics Equation: $1 + kG(s) = 0$; Here $G(s)$ is the TF_1 (Table 1).

Table 1 Routh Hurwitz (R-H) criterion table for the transfer function TF_1

Power	Array1	Array2	Array3
S4	(1.07×10^{-10})	(1.163×10^{-4})	$(1 + k)$
S3	(1.976×10^{-7})	(2.252×10^{-2})	0
S2	(1.041×10^{-4})	$(1 + k)$	0
S1	$\frac{(2.147\times10^{-6})-k(1.976\times10^{-7})}{(1.041\times10^{-4})}$	0	0
S0	$(1 + k)$	0	0

$$\mathrm{TF}_1 = \left(1.07 \times 10^{-10} S^4\right) + \left(1.976 \times 10^{-7} S^3\right) + \left(1.163 \times 10^{-4} S^2\right) + \left(2.252 \times 10^{-2} S\right) + 1 + k = 0$$

The range of K for stability is: $\frac{(2.147\times10^{-6})-k(1.976\times10^{-7})}{(1.041\times10^{-4})} > 0$ and, $(1 + k) > 0$. After calculating those equations, the value of k is; $k < 10.86$ and $k > -1$. So, consider the value of $K_{\mathrm{cr}} = 10.86$. Now the auxiliary equation became $\left(1.041 \times 10^{-4}\right) S^2 + 1 + k = 0$. Through the calculation the value of $S = \pm(337.53)$. $P_{\mathrm{cr}} = \left(2\pi/\omega\right)$ where the value of ω has been assumed $\omega = 337.53$ Value of $P_{\mathrm{cr}} = 0.0186$. From K_{cr} and P_{cr}, those three values can be calculated in Matlab; $K_{\mathrm{p}} = 6.561$, $T_i = 0.0093$, $T_{\mathrm{d}} = 2.325 \times 10^{-3}$. So now the Transfer Function $\mathrm{TF_{RS}}$ is (Fig. 5),

$$\mathrm{TF_{RS}} = \frac{\left(2.16 \times 10^{-5} S^2\right) + (0.0699S) + 1}{\left(9.958 \times 10^{-13} S^5\right) + \left(1.838 \times 10^{-9} S^4\right) + \left(1.081 \times 10^{-6} S^3\right) + \left(2.311 \times 10^{-4} S^2\right) + (0.0792S) + 1}$$

The system is still unstable. So, this tuning method has been introduced in this system.

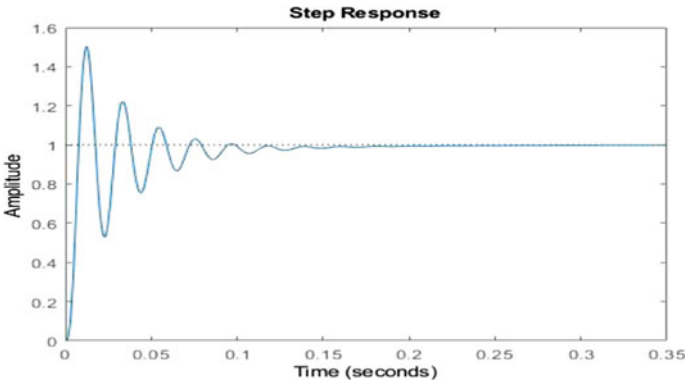

Fig. 5 Using Z-N rules in the transfer function of analogy circuit

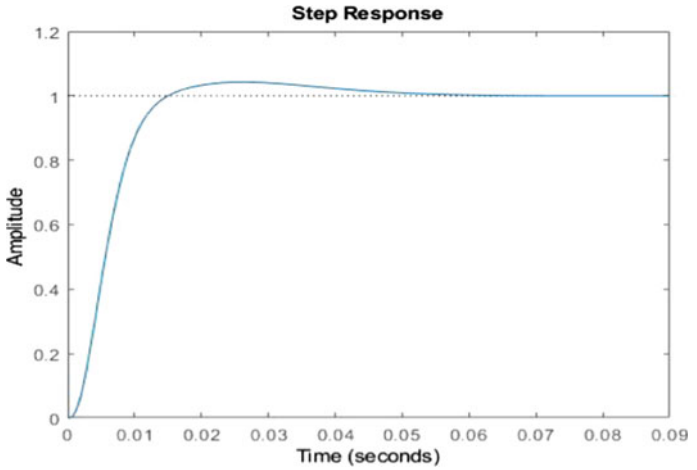

Fig. 6 Step response after using PID tuning in the respiratory system analogy circuit

There is another tuning method called PID tuning which allows the transfer function to be tuned directly in MATLAB software. So, the transfer function needs to be passed into a PID controller which eventually tries to stabilize any unstable system. There is an option to change the response time and the transient behavior. It automatically sets the values of proportional gain $\left(K_{\mathrm{p}}\right)$, integral gain (K_i), Derivative gain (K_{d}) of a PID controller to achieve desired performance [5].

This is the procedure to perform the PID tuning method. After PID tuning, we got those values, $K_{\mathrm{p}} = 2.1993$, $K_i = 143.8628$, $K_{\mathrm{d}} = 0.0081482$. So now the transfer function is (Fig. 6),

$$\mathrm{TF_{RST}} = \frac{\left(8.148 \times 10^{-3} S^2\right) + (2.199S) + 143.9}{\left(1.071 \times 10^{-10} S^5\right) + \left(1.976 \times 10^{-7} S^4\right) + \left(1.163 \times 10^{-4} S^3\right) + \left(3.067 \times 10^{-2} S^2\right) + (3.199S) + 143.9}$$

4 Result Analysis

Finally, the system is in a stable region. So, this transfer function can be used to analyze the lung circuit. Consider it as the final transfer function for further analysis.

$$\mathrm{TF_{RST}} = \frac{\left(8.148 \times 10^{-3} S^2\right) + (2.199S) + 143.9}{\left(1.071 \times 10^{-10} S^5\right) + \left(1.976 \times 10^{-7} S^4\right) + \left(1.163 \times 10^{-4} S^3\right) + \left(3.067 \times 10^{-2} S^2\right) + (3.199S) + 143.9}$$

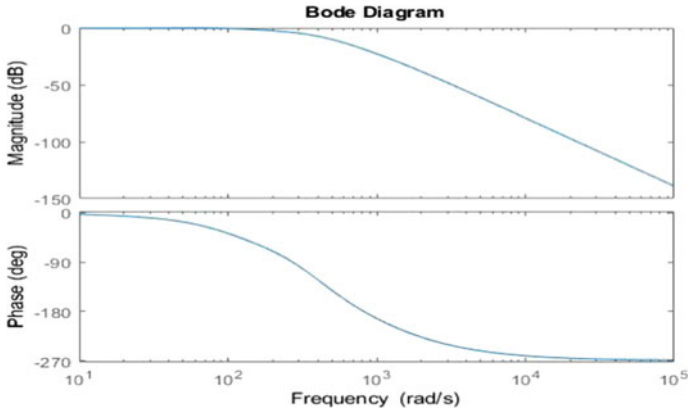

Fig. 7 Bode plot of respiratory system analogy circuit

Now, the stability of the system needs to be checked. Bode plot has been used to analyze the system's stability which is a more advanced level stability checking process. "Bode" command is used to plot the Bode diagram in MATLAB software (Fig. 7).

Observing the gain margin and phase margin, the stability of that system can be defined. The system is marginally stable.

State space is cast-off for representing a linear time-invariant system and also for scrutinizing system concert in a time domain and frequency domain. "tf2ss" command is used to convert the transfer function into state space. At the output, there are four different matrices.

$$A = 1.0e^{+10} \times \begin{bmatrix} 0\ 0 & -0.03 & -2.99 & -134.36 \\ 0\ 0 & 0 & 0 & 0 \\ 0\ 0 & 0 & 0 & 0 \\ 0\ 0 & 0 & 0 & 0 \\ 0\ 0 & 0 & 0 & 0 \end{bmatrix}$$

$$B = \begin{bmatrix} 1 \\ 0 \\ 0 \\ 0 \\ 0 \end{bmatrix}$$

$$C = 1.0e^{+10} \times \begin{bmatrix} 0\ 0\ 0.01\ 2.05\ 134.36 \end{bmatrix}$$

$$D = \begin{bmatrix} 0 \end{bmatrix}$$

"Controllability and Observability" are two important properties of state space models to check the stability of the system. "ctrb" and "obsv" these two commands are used to determine the matrices.

$$\mathrm{CO} = 1.0e^{+10} \times \begin{bmatrix} 0\,0\,0 & -0.26 & 270.42 \\ 0\,0\,0 & 0 & -0.26 \\ 0\,0\,0 & 0 & 0 \\ 0\,0\,0 & 0 & 0 \\ 0\,0\,0 & 0 & 0 \end{bmatrix}$$

$$\mathrm{OB} = 1.0e^{+21} \times \begin{bmatrix} 0\,0 & 0 & 0 & 0 \\ 0\,0 & 0 & 0 & 0 \\ 0\,0 & 0 & 0 & 0 \\ 0\,0 & 0 & 0 & 0 \\ 0\,0\,0.03 & 3.48 & 161.01 \end{bmatrix}$$

From here, the rank of the matrices can be determined. If the rank of the Controllability Matrix was identical to the degree of the close loop Transfer Function, then the system was Controllable. In the same way, if the rank of the Observability Matrix was equivalent to the degree of the close loop Transfer Function, then the system was Observable. This was also one of the stability checking processes in the control system.

Now the transfer function needs to be converted into a discrete domain. The target was to convert the system into a mechanical device. For that reason, the analysis of the system in the Z domain is also required. This was also essential for checking if the system work in the digital domain or not. If it did not work then further study could not be done for that system. So, the transfer function requirements to be transformed from S domain to Z domain. "c2d" command was used to do the conversion in MATLAB tools. As the transfer function was represented in the Z domain, it also needs a sampling time. So, the discrete-time transfer function was (Table 2),

$$= \frac{\begin{array}{c}\left(0.9894Z^4\right) - \left(0.1174Z^3\right) + \left(3.308 \times 10^{-3}Z^2\right) \\ -\left(2.797 \times 10^{-5}Z\right) + \left(1.238 \times 10^{-8}\right)\end{array}}{\begin{array}{c}Z^5 - \left(0.1706Z^4\right) + \left(4.581 \times 10^{-2}Z^3\right) + \left(1.195 \times 10^{-4}Z^2\right) \\ +\left(1.059 \times 10^{-7}Z\right) - \left(9.296 \times 10^{-17}\right)\end{array}}$$

Sample time: 0.02 s. The characteristics equation is:

$$\begin{array}{c} Z^5 - \left(0.1706Z^4\right) + \left(4.581 \times 10^{-2}Z^3\right) + \left(1.195 \times 10^{-4}Z^2\right) \\ + \left(1.059 \times 10^{-7}Z\right) - \left(9.296 \times 10^{-17}\right) = 0 \end{array}$$

Stability conditions are given below

- $|a_n| < a_0$; i.e. $\left(9.296 \times 10^{-17}\right) < 1$
- $f(1) = 0.875 > 0$
- $f(-1) = -1.216 < 0$
- $|b_{n-1}| \langle |b_0|$; i.e. $1\rangle\left(1.059 \times 10^{-7}\right)$

Table 2 Jury table of the discrete-time transfer function

Row	Z^0	Z^1	Z^2	Z^3	Z^4	Z^5
1	$-(9.296 \times 10^{-17})$	(1.059×10^{-7})	(1.195×10^{-4})	(4.581×10^{-2})	$-(0.1706)$	1
2	1	$-(0.1706)$	(4.581×10^{-2})	(1.195×10^{-4})	(1.059×10^{-7})	$-(9.296 \times 10^{-17})$
3	-1	(0.1706)	$-(4.581 \times 10^{-2})$	$-(1.195 \times 10^{-4})$	$-(1.059 \times 10^{-7})$	
4	$-(1.059 \times 10^{-7})$	$-(1.195 \times 10^{-4})$	$-(4.581 \times 10^{-2})$	0.1706	-1	
5	1	$-(0.1706)$	(4.581×10^{-2})	(1.195×10^{-4})		
6	(1.195×10^{-4})	(4.581×10^{-2})	-0.1706	1		
7	0.999	$-(0.1706)$	0.046			

- $|c_{n-2}| > |c_0|$; i.e. $1 > \left(1.195 \times 10^{-4}\right)$
- $|d_{n-3}| > |d_0| 0.999 > 0.046$

It satisfies all the conditions of the Jury's stability criterion. Thereby the system became stable.

5 Conclusion

An electrical model of the human respiratory system has been reintroduced in this paper with the help of control analysis. The continuous domain stability test of the reference respiratory model has been analyzed in this paper where marginal stability has been observed. In addition, the performance analysis introducing controllability and observability testing has been implemented. Furthermore, discrete domain stability analysis has been performed through Jury's stability test and obtained the desired stability condition.

References

1. Orizondo, R.A., Cardounel, A.J., Kormos, R., Sanchez, P.G.: Artificial Lungs: Current Status and Future Directions, pp. 307–315, published online: 11 Nov 2019. Springer Nature Switzerland AG 2019. https://doi.org/10.1007/s40472-019-00255-0
2. Lick, S.D., Deyo, D.J., Wang, D., Witt, S.A., Alpard, S.K., Harper, D.D., Zwischenberger, J.B.: Paracorporeal artificial lung: perioperative management for survival study in sheep. J. Investigative Surgery **16**(3), 177–184 (2009). https://doi.org/10.1080/08941930390205818
3. Schranz, C., Docherty, P.D., Chiew, Y.S., Möller, K., Geoffrey Chase, J.: Iterative integral parameter identification of a respiratory mechanics model, BioMed. Eng. OnLine, 1–14 (2012). https://doi.org/10.1186/1475-925X-11-38
4. Bagchi, S., Chattopadhyay, M.: Electrical modelling of respiratory system and identification of two common COPD diseases through stability analysis technique. In: 2012 IEEE International Conference on Advanced Communication Control and Computing Technologies (ICACCCT), pp. 23–25, Aug 2012, India
5. Lima, A.N., Faria, A.C.D., Lopes, A.J., Jansen, J.M., Melo, P.L., Lima et al.: Forced oscillations and respiratory system modeling in adults with cystic fibrosis, BioMed. Eng. OnLine (2015). https://doi.org/10.1186/s12938-015-0007-7
6. Himes, B.E., Weitzman, E.R.: Innovations in health information technologies for chronic pulmonary diseases. Respir. Res. (2016).https://doi.org/10.1186/s12931-016-0354-3
7. Pitt-Developed Artificial Lung Shows Promise in Pre-Clinical Trials. The McGowan Institute for Regenerative Medicine [online], 13 Apr 2017. Available from https://mirm-pitt.net/news-archive/pittdeveloped-artificial-lung-shows-promise-in-pre-clinical-trials/
8. Freed, A.D., Einstein, D.R., Carson, J.P., Jacob, R.E.: Viscoelastic Model for Lung Parenchyma for Multi-Scale Modeling of Respiratory System Phase II: Dodecahedral Micro-Model (2012)
9. John Jabaraj, D., Jaafar, M.S.: Vibration Analysis of Circular Membrane Model of Alveolar Wall in Examining Ultrasound-induced Lung Hemorrhage (2013)
10. Santhanam, A.P.: Modeling, Simulation, and Visualization of 3d Lung Dynamics. B.E. University of Madras, India, 11 Mar 2014. Available from https://www.researchgate.net/publication/47714999_MODELING_SIMULATION_AND_VISUALIZATION_OF_3D_LUNG_DYNAMICS

11. Wearable Artificial Lung Designed to Help Sick Children Remain Mobile While Hospitalized. The McGowan Institute for Regenerative Medicine [online], 24 Jan 2018. Available from https://mirm-pitt.net/news-archive/wearable-artificial-lung-designed-to-help-sick-children-remain-mobile-while-hospitalized/#:~:text=Wearable%20Artificial%20Lung%20Designed%20to%20Help%20Sick%20Chi
12. Wood, A.W.: Physiology, Biophysics, and Biomedical Engineering. CRC Press, Taylor & Francis Group (2012)

Analyze Different Types of Connector for Design of MSA

Samiran Chatterjee, Mukundu Mounika, Patlolla Akhila, Veeramalla Pratyusha, and Korni Madhavi

Abstract In this major project, proposed the analysis of different feeding techniques and try to find that which feeding technique is better in terms of connector. Here in this project proposed antenna analyzed by use of different connector with different feeding techniques. In antenna structure, is applying two feeding methods i.e. Transmission Line feeding and co-axial feeding and also use different connector for different feeding methods. For transmission line feeding uses both transmission line connector and CPW (Co-planar waveguide) connector and in coaxial feeding connects the connector by soldering method. In this project, the antenna is analyzed for different feeding with different connectors for the same antenna structure. The proposed antenna presents in this project with high return loss and 2:1 VSWR range for any feeding technique analysis. This project achieves good result by applying the transmission line feed with CPW connector. At the above mentioned condition achieved four resonant frequencies of about 2.54 GHz, 6.73 GHz, 7.66 GHz and 9.85 GHz with −22.45 dB, −27.94 dB, −10.62 dB and −16.69 dB return loss respectively. Whereas for the Transmission line feed with transmission line connector the proposed structure achieves single resonant frequency for the above mentioned condition. But when using the coaxial feeding method, the proposed antenna does not work properly and does not achieve a single resonant frequency. The proposed structure has good resonant frequency for which it is intended. The main achievement is increased frequency ratio which has no ISI (Inter Symbol Interference).

Keywords CPW · Feed · Layer · Connector · Transmission line · VSWR

S. Chatterjee (✉)
Professor, ECE Department, Amrita Sai Institute of Science and Technology, Vijayawada, Paritala, India

M. Mounika · P. Akhila · V. Pratyusha · K. Madhavi
ECE Department, Vignan's Institute of Management and Technology for Women (Affiliated to JNTU, Hyderabad, Approved by AICTE, New Delhi), Kondapur, Gatkesar, Medchal-Malkajgiri, Telangana 501301, India

B. Sikdar et al. (eds.), *Proceedings of the 3rd International Conference on Communication, Devices and Computing*, Lecture Notes in Electrical Engineering 851,
https://doi.org/10.1007/978-981-16-9154-6_61

1 Introduction

Microstrip antenna is essentially limited to some substrate [1–4]. For simple design of microstrip antennas we use only the top layer, it does not give off bandwidth [5–7]. To get the bandwidth, it requires cutting slots and cracks in the top layer as well as the bottom layer [8]. When cutting only some of the top and bottom layer, at that time we do not create any disturbance to the ground layer. This type of ground layer is called infinite earth layer and it has some conductivity so it behaves like a ground layer [9–12]. But for the DGS structure, we need to make a disturbance in the ground layer in the form of cutting some holes and cracks. This type of ground plane is called finite ground plane and has zero conductivity. Here in this project, we design both antenna structure and parameter analyzes for both finite and unlimited ground plane. All the results are performed using IE3D software [13].

2 Design of Proposed Structure

The proposed antenna having an asymmetrical rectangular patch [14] on both layers is shown in Fig. 1 with dielectric substrate. The insulation material specified herein is an epoxy polytetrafluoroethylene based substrate with FR_4 [15–18]. The designed antenna structure is shown in Figs. 2, 3, 4, 5 and 6.

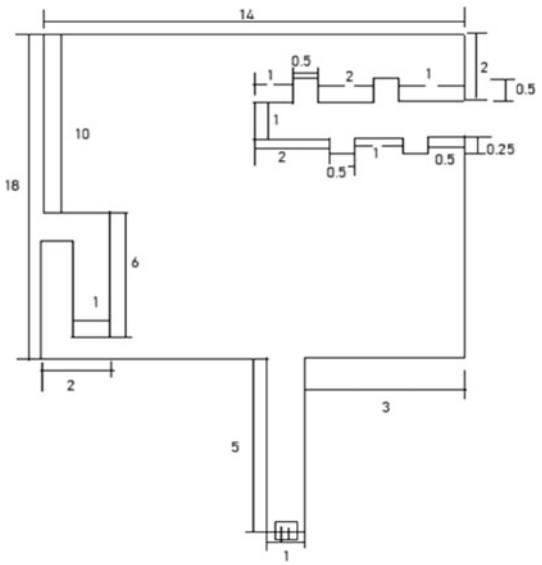

Fig. 1 Designed antenna with CPW connector (top layer)

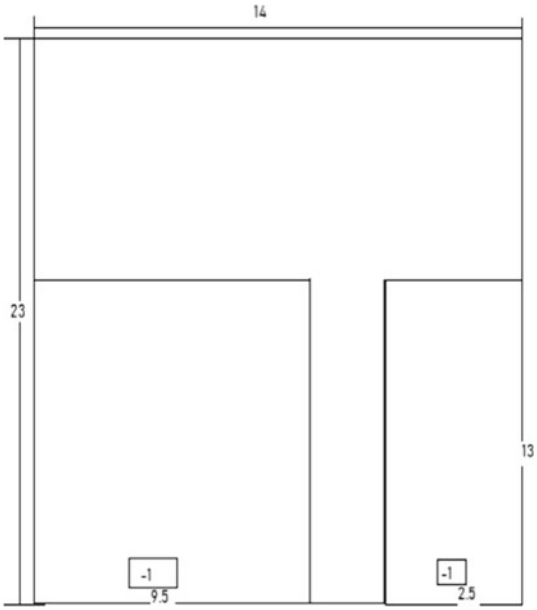

Fig. 2 Designed antenna with CPW connector (bottom layer)

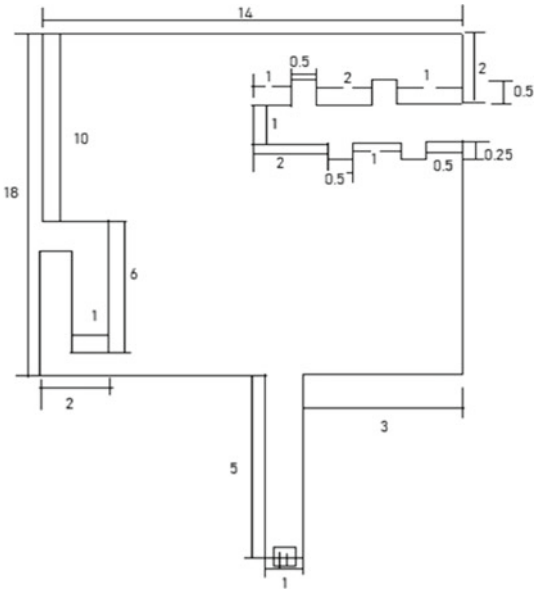

Fig. 3 Designed antenna with SMA connector (top layer)

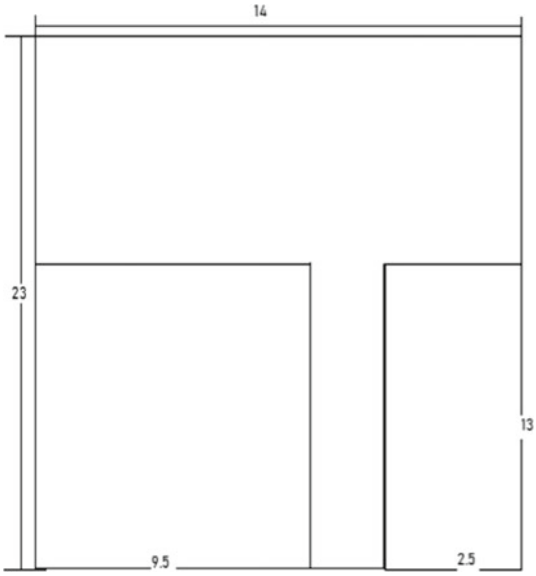

Fig. 4 Designed antenna with SMA connector (bottom layer)

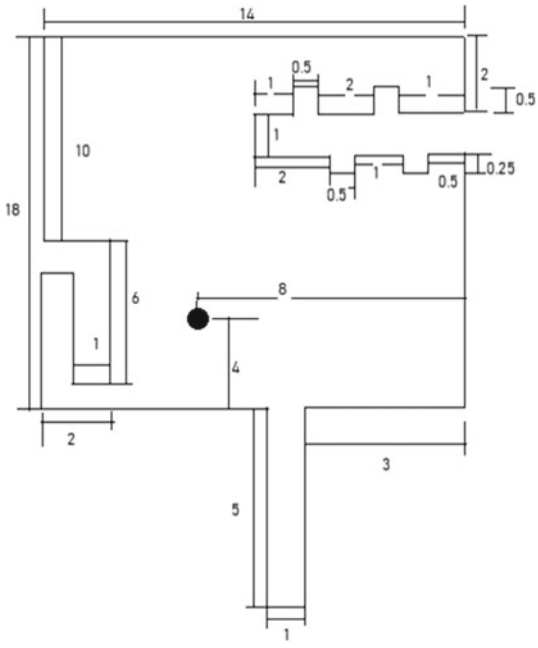

Fig. 5 Designed antenna for SMA connector as co-axial feed (top view)

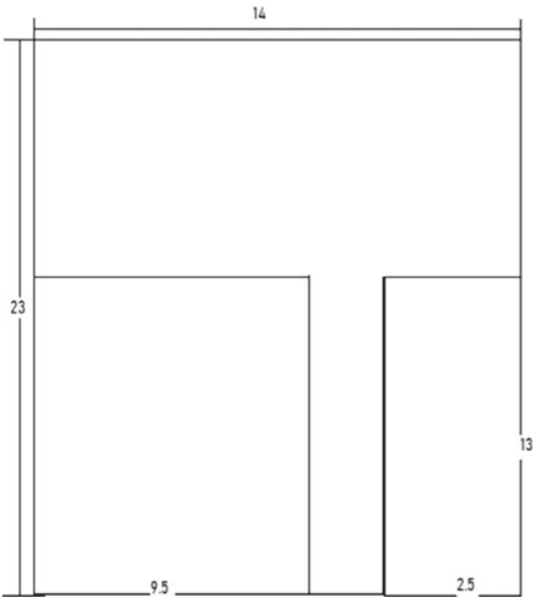

Fig. 6 Designed antenna for SMA connector as co-axial feed (bottom view)

The rectangular patch dimensions of 18 mm × 14 mm in top layer and 23 mm × 14 mm dimension in bottom layer.

3 Result and Discussion

In this section detailed antenna parameters are analyzed. Figures 7, 8 and 9 illustrated the return loss of proposed antenna for different connectors.

As cutting slots, the resonance frequencies are obtained with large frequency ratio. All the results are shown in Tables 1, 2, 3 and 4.

3.1 Analysis of Radiation Pattern

The radiation patterns for all resonant frequencies are displayed in Figs. 10, 11, 12, 13 and 14.

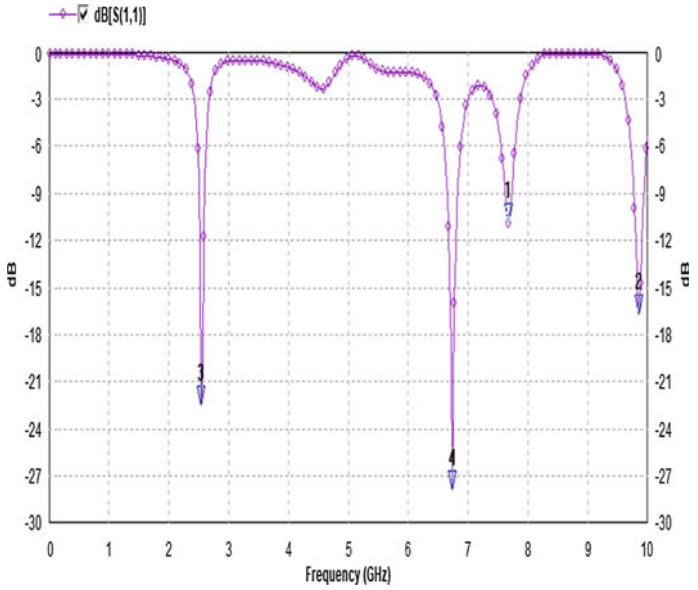

Fig. 7 Return loss for CPW connector

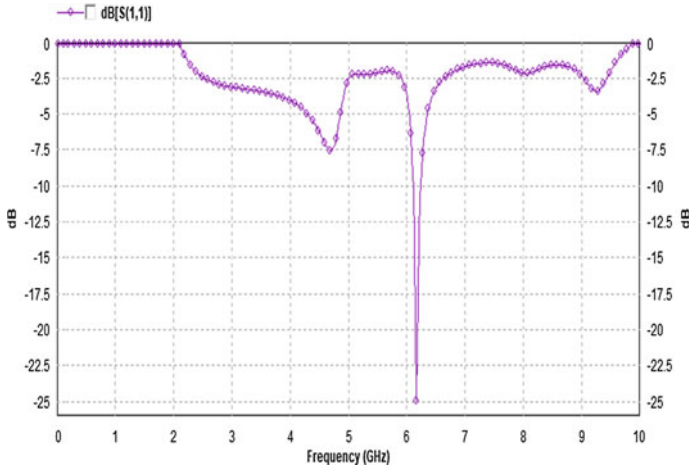

Fig. 8 Return loss for SMA connector as transmission line feed

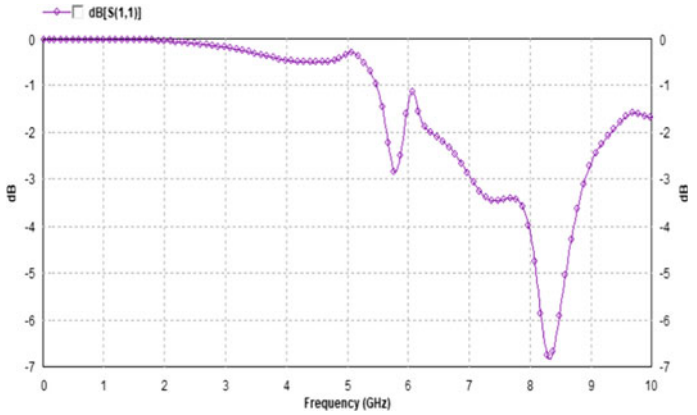

Fig. 9 Return loss for SMA connector as co-axial feed

Table 1 Summary of pattern with CPW connector

Frequency (GHz)	Ratio of frequency	HPBW (Deg)	Absolute gain (dBi)
$f_1 = 2.545$	1	274.781°	−1.34
$f_2 = 6.7332$	2.645	92.107°	4.584
$f_3 = 7.6613$	3.01	88.905°	2.56
$f_4 = 9.85$	3.87	30.83°	2.656

Table 2 Summary of reflection coefficient with CPW connector

Frequency (GHz)	Reflection coefficient (dB)	Band-width (MHz)
$f_1 = 2.545$	−22.45	0.08824
$f_2 = 6.7332$	−27.94	0.1528
$f_3 = 76{,}613$	−10.63	0.068
$f_4 = 9.85$	−16.6887	0.314

Table 3 Summary of pattern for SMA connector as transmission line feed

Frequency (GHz)	Ratio of frequency	HPBW (Deg)	Absolute gain (dBi)
$f_1 = 6.172$	1	81.584°	4.572

Table 4 Summary of reflection coefficient for SMA connector as transmission line feed

Frequency (GHz)	Reflection coefficient (dB)	Band-width (MHz)
$f_1 = 6.172$	−24.93	0.13

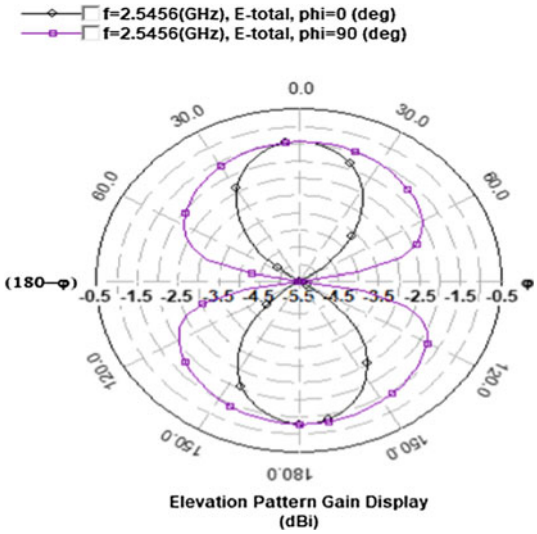

Fig. 10 Radiation pattern for E-total at 2.545 GHz for CPW connector

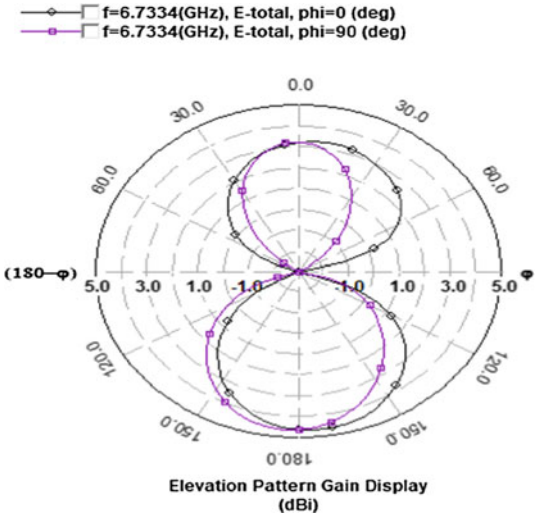

Fig. 11 Radiation pattern for E-total at 6.7337 GHz for CPW connector

4 Conclusion

The compact microstrip antenna with different parametric analysis is proposed in this project. Here proposed antenna structure is analyzed by use of different connectors with different feeding techniques. In proposed antenna structure is applying two feeding methods i.e. Transmission Line feeding and co-axial feeding and also use different connector for different feeding methods. For transmission line feeding uses both transmission line connector and CPW (Co-planar waveguide) connector and

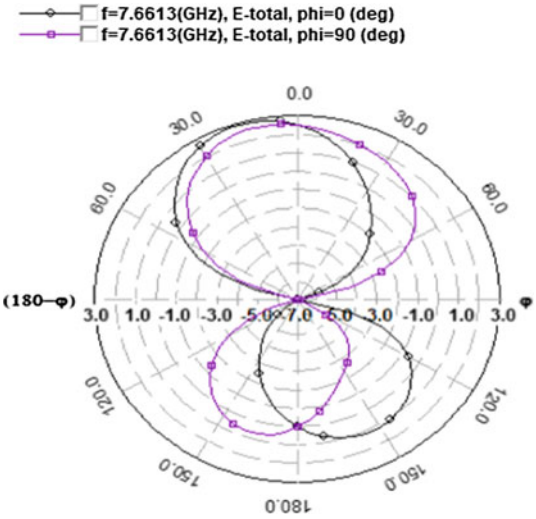

Fig. 12 Radiation pattern for E-total at 7.664 GHz for CPW connector

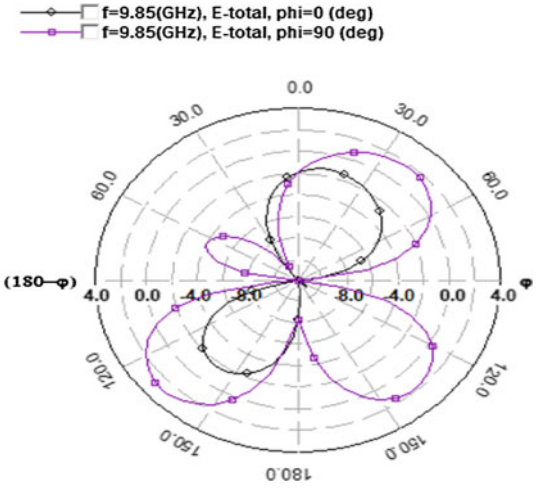

Fig. 13 Radiation pattern for E-total at 9.85 GHz for CPW connector

in coaxial feeding connects the connector by soldering method. Also the antenna is analyzed for different feeding with different connectors for the same antenna structure. This project achieves good result by applying the transmission line feed with CPW connector. At the above mentioned condition achieved four resonant frequencies of about 2.54 GHz, 6.73 GHz, 7.66 GHz and 9.85 GHz with −22.45 dB, −27.94 dB, −10.62 dB and −16.69 dB return loss respectively. Also the VSWR value is very close to its minimum value for all the resonant frequencies what achieves for the above mentioned condition. Also for the transmission line feed with transmission line connector got single resonant frequency of about 6.17 GHz with −24.93 dB return loss. For this above mentioned condition it achieves VSWR of 1.12. But for

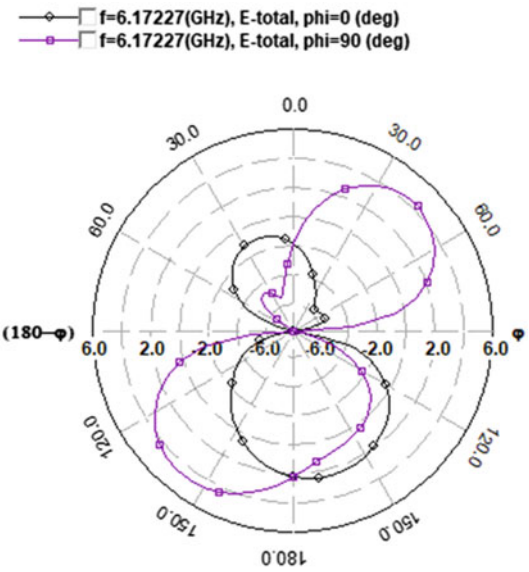

Fig. 14 Radiation pattern for E-total at 6.172 GHz for SMA connector as transmission line feed

co-axial feeding technique, the proposed structure does not work properly because at this condition the structure doesn't have any resonant frequency. The proposed antenna achieved increased frequency ratio with maximum gain of 4.58 dBi and HPBW ranges from 30.830 to 274.780 for CPW condition whereas the proposed structure got maximum gain of 4.57 dBi with HPBW of about 81.580 for transmission line feed condition. The proposed antenna is applicable for long distance radio telecommunications application when using transmission line feed. The proposed structure is also applicable for surface ship radar, C-Band microwave communication, space communications and amateur radio for CPW connector connected with the structure. The beamwidth is also enough for the application for which it is intended for any transmission line feed technique with any types of connector connected with the structure. So final conclusion is CPW connector with transmission line feed gives the better result out of all types of feeding techniques and feeding connectors.

References

1. Sarkar, I., Sarkar, P.P., Chowdhury, S.K.: A new compact printed antenna for mobile communication. In: 2009 Loughborough Antennas & Propagation Conference, 16–17 Nov. 2009, Loughborough, UK (2009)
2. Wu, J.-W., Hsiao, H.-M., Lu, J.-H., Chang, S.-H.: Dual broadband design of rectangular slot antenna for 2.4 and 5 GHz wireless communication. IEE Electron. Lett. **40**(23) (2004)
3. Chatterjee, S., Paul, J., Ghosh, K., Sarkar, P.P., Chanda (Sarkar), D., Chowdhury, S.K.: A compact micro strip antenna for WLAN communication. In: National Conference of Electronics, Communication and Signal Processing, Paper ID: 116 (2011)

4. Raj, R.K., Joseph, M., Anandan, C.K., Vasudevan, K., Mohanan, P.: A new compact microstrip-fed dual-band coplaner antenna for WLAN applications. IEEE Trans. Antennas Propag. **54**(12), 3755–3762 (2006)
5. Jan, J.-Y., Tseng, L.-C.: Small planar monopole Antenna with a shorted parasitic inverted-L wire for wireless communications in the 2.4, 5.2 and 5.8 GHz bands. IEEE Trans. Antennas Propag. **52**(7), 1903–1905 (2004)
6. Chatterjee, S., Chakraborty, U., Sarkar, I., Chowdhury, S.K., Sarkar, P.P.: A compact microstrip antenna for mobile communication. In: India Conference (INDICON), 2010 Annual IEEE, pp. 1–3, Paper ID: 510 (2010)
7. Danideh, A., Fakhr, R.S., Hassani, H.R.: Wideband coplanar micro strip patch antenna. Prog. Electromagn. Res. Lett. PIER **4**, 81–89 (2008)
8. Bahl, J., Bhartia, P.: Micro strip antennas. Artech House, Dedham, MA (1980)
9. Chakraborty, U., Chatterjee, S., Chowdhury, S.K., Sarkar, P.P.: A compact micro strip patch antenna for wireless communication. Prog. Electromagn. Res. C **18**, 211–220 (2011)
10. Fallahi, R., Kalteh, A.-A., GolparvarRoozbahani, M.: A novel UWB elliptical slot antenna with band-notched characteristics. Prog. Electromagn. Res. C **18**, 211–220 (2011)
11. Chatterjee, S., Chowdhury, S.K., Sarkar, P.P., Sarkar, D.C.: Compact micro strip patch antenna for microwave communication. Indian J. Pure Appl. Phys. **51**, 800–807
12. Chatterjee, S., Paul, J., Ghosh, K., Chowdhury, S.K., Sarkar, P.P., Chanda (Sarkar), D.: Compact microstrip antenna for mobile communication. Microw. Opt. Technol. Lett. (MOTL) **55**(5), 954–957 (2013)
13. Zeland Software Inc. IE3D: MOM-Based EM Simulator. Web: http://www.zeland.com
14. Chatterjee, S., Chowdhury, S.K., Chanda (Sarkar), D., Sarkar, P.P.: A compact CPW-FED UWB antenna. In: Second (2nd) national conference of control, communication and signal processing, 2012 (NCECS-2012), Paper ID: NCECS-1219 (2012); [32] Chatterjee, S., Chowdhury, S.K., Sarkar, P.P., Chanda (Sarkar), D.: Compact microstrip antenna for c-band microwave communication. In: National conference of electronics, communication and device electronics (N3CD-2013), Paper ID: ID0262N25, pp. 99–104 (2013)
15. Chatterjee, S., Chowdhury, S.K., Sarkar, P.P., Chanda (Sarkar), D.: Comparison between two CPW-FED UWB antennas based on dielectric constant of substrate. Int. J. Electron. Commun. Technol. (IJECT) IV(I), 49–58, VER. 1, Jan–March (2013)
16. Chatterjee, S., Chowdhury, S.K., Sarkar, P.P., Sarkar, D.C.: Bevel microstrip printed antenna for satellite communication. Indian J. Pure Appl. Phys. (IJPAP) **52**, 760–766 (2014)
17. Chatterjee, S., Sarkar, P.P., Chanda (Sarkar), D., Chowdhury, S.K.: Compact microstrip antenna for WLAN and H-LAN communication. Int. J. Soft Comput. Eng. **2**(3), 270–274 (2012)
18. Chatterjee, S., Chowdhury, S.K., Chanda (Sarkar), D., Sarkar, P.P.: Design of compact microstrip antenna for s-band microwave communication. Special Issue Int. J. Comput. Appl. (0975–8887), International conference on computing, communication and sensor network (CCSN), pp. 13–17 (2012)

Arrhythmia Detection and Classification Using Two Stage Median Filter Through Dynamic Features of ECG Signals

S. Dhanunjay Reddy, R. Murugan, Arnab Nandi, and Tripti Goel

Abstract An electrocardiogram (ECG) is a non-invasive method that uses electrical signals produced by pacemakers to examine and visualize the heart's functionality, quick identification of arrhythmia aids in proper care and reduction of the risk factor. This paper's main aim is to use machine learning algorithms, to detect and identify arrhythmia types by extracting simple dynamic features from the ECG. This aids medical professional in the early detection of certain common arrhythmia forms that appear to be expected. A simple flow is built into this work to achieve a better result with less computational complexity. The workflow will go through three stages: preprocessing, feature extraction, and classification. An LPF and a two-stage median filter are used to eliminate all artifacts for successful feature extraction. The preprocessed signal is then fed into the next step, which extracts dynamic ECG features. With the aid of extracted features, the classification block predicts the form of arrhythmia. The proposed method was tested with all eleven types of heartbeats from the MIT-BIH arrhythmia database, as stated in the Association for Advancement of Medical Instrumentation's recommendations. 97% overall accuracy is achieved using Random forest and dynamic features of ECG Morphology in the time-domain.

Keywords Electrocardiogram · Arrhythmia · Two-stage median filter · Dynamic features

1 Introduction

The cardiac activity can be analyzed easily using a non-invasive electrocardiogram (ECG) [1]. Atrial depolarization and ventricle depolarization are two major phases in a heartbeat cycle. The viscus activity of transferring ions in the heart through the atrial

S. D. Reddy · R. Murugan (✉) · A. Nandi · T. Goel
Bio-Medical Imaging Lab., Department of Electronics and Communication Engineering, National Institute of Technology Silchar, Silchar, Assam 788010, India
e-mail: murugan.rmn@ece.nits.ac.in

B. Sikdar et al. (eds.), *Proceedings of the 3rd International Conference on Communication, Devices and Computing*, Lecture Notes in Electrical Engineering 851,
https://doi.org/10.1007/978-981-16-9154-6_62

sinus node is observed and taken from the skin's surface by attaching surface electrodes at the chest part of a person. Received electrical signals are diagrammatically portrayed within the cardiogram record.

P, *Q*, *R*, *S*, *T*, and *U* are individual notated waves in the ECG signal. Peak amplitudes, QRS-width, wave duration, and intervals like *PP*, *PR*, *RR*, *ST* intervals are the main features. Malfunction of pacemakers, ventricular region blockage, and associate position in the ectopic center give an irregular form of QRS-complex. QRS-complex is a vital segment to detect irregularities. The general form of ECG waveform is shown in Fig. 1. [2]. From this, a medical practitioner will notice numerous varieties of arrhythmia, such as Atrial Fibrillation (AFIB), Atrial Flutter (AF), Bigeminy (B), Trigeminy (T), Ventricular Tachycardia (VT) through the irregularities in ECG waveforms.

Various noises in continuous control distort the ECG signal. Low frequency and high-frequency noises give an inaccurate estimation of results in long-term readings of ECG. Baseline wander (BW), Powerline interference (PLI), and Myographic noise (MN) have frequency ranges of (0.5–0.6) Hz, (50–60) Hz, and (15–40) Hz, respectively. After removing these artifacts, the process of feature extraction, detection, and classification will begin. Although manual heartbeat classification of ECG recordings takes a long time and a lot of practice for junior doctors, a trained identification and classification system is a more efficient way to diagnose and, as a result, improve treatment quality.

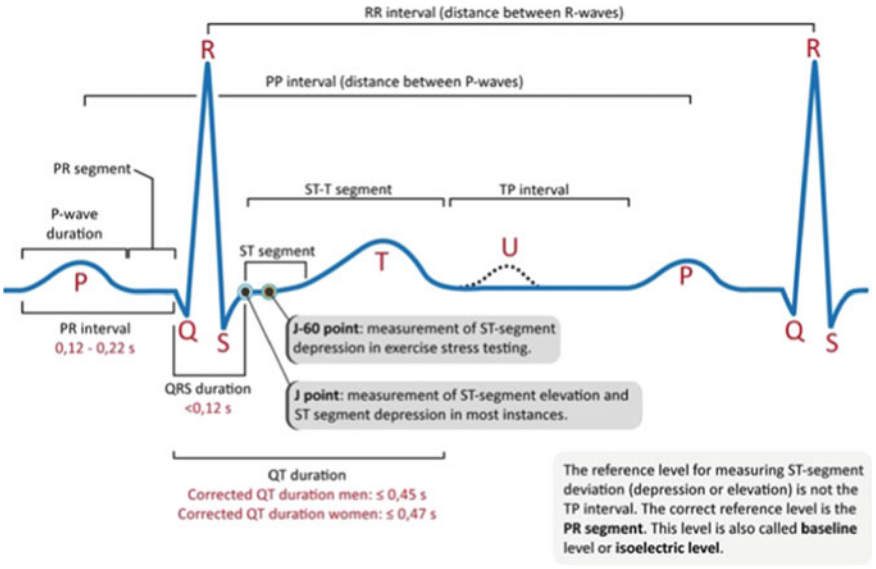

Fig. 1 General structure of ECG waveform [2]

Various noises in continuous control distort the ECG signal. Low frequency and high-frequency noises give an inaccurate estimation of results in long-term readings of ECG. Baseline wander (BW), Powerline interference (PLI), and Myographic noise (MN) have frequency ranges of (0.5–0.6) Hz, (50–60) Hz, and (15–40) Hz, respectively. After removing these artifacts, the process of feature extraction, detection, and classification will begin. Although manual heartbeat classification of ECG recordings takes a long time and a lot of practice for junior doctors, a trained identification and classification system is a more efficient way to diagnose and, as a result, improve treatment quality.

Arrhythmia is an issue of irregular rhythm of the heartbeat may be too high or too low. Tachycardia is an irregularity in which the heart beats very quickly. Bradycardia is an irregularity in which the heart beats too slowly. An irregular ECG is a crucial factor in predicting cardiovascular diseases (CVDs) in both the elderly and the young [1]. Cardiovascular arrhythmia is a common untreated disorder. In some instances, this can result in accidental death. Early detection of such irregular activity assists the patient and doctor in suitable medication.

At first, various artifacts, such as PLI, BW, and MN, influence ECG signals. The ECG is assessed by physiological artifacts and noises, which is complicated in the automated computerized system. Furthermore, the inconsistency of classifying various subjects is assured by the differences in each individual's ECG signal. Also, the time-varying dynamic features of the same individual's ECG signals add to the automatic assessment process's complexity.

For ECG classification, several automated methods have been developed. A random forest is a content estimator that helps classify non-uniform data with a better accuracy rate and reduces the overfitting problem. Support vector machine (SVM) is also one of the most widely used versions of a classifier to classify the labeled data based on the kernel function.

2 Related Works

Preprocessing, feature extraction, and heartbeat classification are the three main sections of a complete ECG arrhythmia identification and classification system. For removing BW, PLI, and MN, various methods are proposed. Band-pass filter [3] approach for removing PLI and MN. Adaptive filters [4], Empirical Mode Decomposition (EMD) [5], and wavelet transform method [6] for BW removal. This research focuses primarily on the feature extraction point, which is critical for ECG signal arrhythmia classification. Literature gives a brief idea about the independent works on ECG feature extraction techniques.

Deriving features from ECG signals in the time domain is an easy and effective way to analyze the arrhythmia type. The critical disadvantage of this approach is processing and dealing with high-dimensional vectors. The signal scale of displacement may also influence it in terms of a fiducial point of the QRS-complex. As

a result, an 85 percent accuracy of classification was recorded. Beat-interval (RR-interval) is the most commonly documented function in the literature. For example, Lin and Yang [2] found that using a normalized RR interval boosts classification accuracy. RR-based characteristics are mentioned in [7]. Because of the less noise influence on RR interval can also be used for constructing HRV signal [5].

Venkatesan et al. [8] found that using statistical HRV parameters, arrhythmia could be classified into standard and irregular classes using an abnormality detection scheme based on an SVM classifier. With a maximum accuracy of 96.00 percent. Amplitudes, intervals, and durations have all been clinically studied among these morphological features [9]. Zhang et al. [10] classified heartbeats with an accuracy of 86.66% using ECG features such as inter and intra-beat intervals, amplitude, and area and verified the RR interval's discrimination power *P* wave and QRS complex. A new technique for lowering error rates and improving classification accuracy in the time domain is proposed in this paper.

3 Methodology

The proposed arrhythmia recognition and classification method have three phases: preprocessing, feature extraction, and arrhythmia classification. Figure 2 shows a block diagram of the proposed heartbeat classification algorithm.

3.1 Preprocessing

Axis corrections are needed for preprocessing because the amplitude and time axis values in the MIT-BIH arrhythmia database raw data are not available in measurable units. Changed real-time units are generated using the database's gain and sampling frequency values. The proposed preprocessing flow is shown in Fig. 3. The signal is then fed through an LPF to eliminate myographic noise after the axis corrections have

Fig. 2 Arrhythmia detection and classification flow

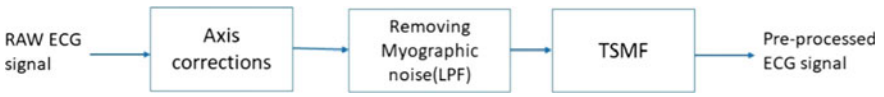

Fig. 3 Flow of Preprocessing

Table 1 LPF transfer function

Order	Transfer function
2	$H(s) = \frac{1}{s^2+0.658s+0.8659}$
4	$H(s) = \frac{1}{(s^2+0.712s+0.866)(s^2+1.72s+0.866)}$

been made. A simple Butterworth filter with a cut-off frequency of 40 Hz is designed to eliminate PLI and MN without affecting the characteristics of ECG signals. The transfer function of the filter is shown in Table 1 with their orders.

To estimate and extract the baseline wander of the noisy ECG signal, the LPF output is fed to a two-stage median filter (TSMF). The steps of the proposed TSMF algorithm are presented in Algorithm 1.

Algorithm 1: Proposed TSMF algorithm

1. Input: Noisy signal- $(n) = x(n) + N(n)$

   (n) – ECG signal without noise (n) – Baseline wander noise

   L = length of (n)

   fs = sampling frequency

2. Defining window length at each stage

   $n1 = 0.2*fs$

   $n2 = 0.6*fs$

3. Removing mean error

   $M = \frac{1}{L}\sum_{n=1}^{L} x(n)$

   $P(n) = x(n) - M$

4. Estimating baseline wander

$$\widehat{N}(n) = \begin{cases} Med(P(j:j+n_1-1)) & ; \quad X_1(j) \\ Med(X_1(j:j+n_2-1)) & ; \quad X_2(j) \end{cases}$$

5. Removing the estimated noise from the noisy signal

$$\hat{x}(n) = X(n) - \widehat{N}(n)$$
$$\hat{x}(n) \approx x(n)$$

3.2 Feature Extraction

Feature extraction is fed with preprocessed signals to extract the critical features for recognizing and classifying arrhythmia types. This section will extract features like *R*-peaks location and amplitude, *RR*-interval, Heart rate, *P*, *Q*, *S*, *T*-peaks, *P*-wave existence, *S*-peak amplitude Regularity, QRS-width.

Discrete Wavelet Transform (DWT) is used to find R-peak locations and amplitude. DWT plays a key role in precise event detection. Symlet wavelet is used in the basis function because its symmetry and morphological features resemble the QRS-complex. Dilation and translation parameters (a, b) are taken in powers of two to avoid the redundant coefficients as shown in the Eqs. (1), (2), and (3).

$$D(n) = \sum_{-\infty}^{\infty} x(k)\emptyset(m,n) \tag{1}$$

$$\emptyset(m,n) = a^{-\frac{m}{2}}\varphi^*\left(a^{-m}k - nb\right) \tag{2}$$

$$\emptyset(m,n) = 2^{-\frac{m}{2}}\varphi^*(2^{-m}k - n \tag{3}$$

DWT concept is implemented using the undecimated filter bank theory. LPF details are taken as approximated coefficients and HPF as detailed coefficients. Coefficients and their frequency ranges are discussed in Table 2. Our main motive is to highlight the signal's frequency components, which have the QRS-complex details. QRS-complex resides in a frequency range of (15–45) Hz. From Table 2 d_3 and d_4 having these frequency components. The flow of R-peak detection using DWT is displayed in Fig. 4.

We are making a new signal which is the summation of d_3 and d_4 coefficients. Using the thresholding method, we detect the peaks of R-peaks with a threshold value greater than 0.2 times of max $(d_3 + d_4)$. As a next step, we will remove the same QRS complex by checking based on the R-peak interval. If any two peaks are detected within the interval of 100 ms, the peak having low amplitude is eliminated because consecutive heartbeats within 0.1 s are impossible. At last R-peak location and amplitude are noted if they are obeying the threshold and R-peak interval conditions. After saving the *R*-peak locations (*RR*(*j*)) as an array, we will use that array to

Table 2 Coefficients and frequency ranges

Coefficients	Frequency (Hz)
d_1	90–180
d_2	45–90
d_3	27.5–45
d_4	13.7–27.5
a_4	0–13.7

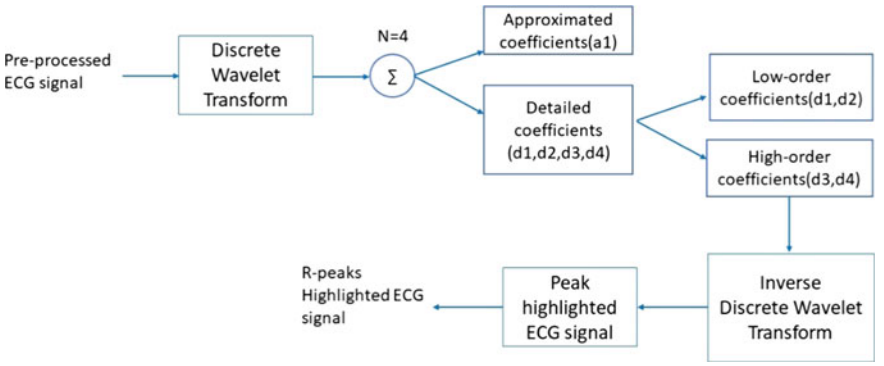

Fig. 4 R-peak detection flow

find the average *RR*-interval. From $RR(j)$, $RR_{\text{int}}(j)$ is calculated, Where $RR_{\text{int}}(j)$ is an array of intervals for successive R-peaks. $\text{RR}_{\max}$ and $\text{RR}_{\min}$ are calculated. If $|RR_{\max} - RR_{\min}| > 2$ ms, the signal is said to be irregular; otherwise, regular, this feature can be used in classification. From $RR_{\text{int}}(j)$ average *RR*-interval is calculated based on Eq. (4).

$$\text{AVG\_RR} = \frac{1}{L}\sum_{j=1}^{L} RR_{\text{int}}(j) \tag{4}$$

In this paper, a particular method is used for finding the heart rate of arrhythmia patients. We had taken our ECG signals from the database of 10-s length with 3600 samples. In that 3600 samples, we will segment 2160 samples to get 6 s ECG signal. Again *R*-peak detection procedure is applied, and we will find the number of peaks for segmented ECG signals. One *R*-peak represents one ECG cycle, and one ECG cycle represents the completion of one heartbeat. We will normalize the heartbeats of 6 s to one minute by multiplying them by 10.

Then other peaks of ECG signal are calculated by using *R*-peak locations. In general, the QRS-width value is in the range of 80–125 ms for finding the *Q* and *S* peaks by applying local minima after and before the location of *R*-peaks at 50 ms range (30 samples). And from *Q*, *S* peaks by using the local maxima before and after 100 ms range (60 samples), *P* and *T* wave peaks are detected. In particular, arrhythmias like atrial fibrillation and atrial flutter *P*-waves don't exist because of advanced atrial depolarization. *P*-wave doesn't exist when this advanced atrial depolarization happens. This can be detected by comparing the locations of *P*-peaks and *T*-peaks. If more than 3 *P*-peaks and *T*-peaks are coinciding and that is too occurring in between two *R*-peaks, we can finalize *P*-waves in existence. After finding the *S*-peak amplitude, each amplitude of *S*-peak is compared and classified to use in classification as follows.

$$S\_\text{amp}(i) \geq 10 * 0.1\,\text{mV} - \text{More negative}$$
$$5 * 0.1\,\text{mV} \leq S\_\text{amp}(i) \geq 0.1\,\text{mV} - \text{Negative}$$
$$0.1\,\text{mV} \leq S\_\text{amp}(i) \geq 0.1\,\text{mV} - \text{Normal}$$

The interval between *S*-peak and *Q*-peak is calculated, and it is said to be QRS-width. A wide and narrow QRS-complex is defined as follows.

$$\text{QRS} - \text{width} \geq 120\,\text{ms} - \text{wide QRS - complex}$$
$$\text{QRS} - \text{width} \leq 120\,\text{ms} - \text{narrow QRS - complex}$$

All these feature extracted data are used as classification characteristics to detect and classify the arrhythmia type.

3.3 Classification

A non-uniform dataset causes a challenge to classifiers. Random forest (RF) has been invoked here to deal with non-uniform data and handle the overfitting problem. It does so as it can correctly classify the samples even when the class samples are unequal. The noise resistance and gain inaccuracy is also observed when the ensemble-based approach is incorporated. SVM is well known for classification tasks. So, we have also used a support vector machine (SVM) over-extracted features. The arrhythmia has been classified based on the characteristics that is shown in Table 3.

Table 3 Characteristics table of arrhythmia types

Arrhythmia type	Heartrate (bpm)	Regular	*S*-amplitude	QRS-width	*P*-wave
AFIB	90–170	RIR	Normal	narrow	No
AFL	300	RIR	Normal	Narrow	No
B	<60	IR	Negative	Wide	Yes
IVR	20–40	R	Negative	Wide	No
NSR	60–100	R	Normal	Narrow	Yes
PVC	60–80	IR	More negative	Wide	Yes
SVTA	140–250	R	Normal	Narrow	No
T	>100	IR	Negative	Wide	Yes
VFL	–	IR	–	–	No
VT	170	IR	More negative	Wide	Yes
WPW	75–100	R	Normal	Wide	Yes

Table 4 Database used for classification

S. No.	MIT-BIH dataset	Number of samples
1	Atrial fibrillation (AFIB)	135
2	Atrial flutter (AFL)	20
3	Bigeminy (B)	55
4	Idioventricular rhythm (IVR)	10
5	Normal sinus rhythm (NSR)	283
6	Premature ventricular contraction (PVC)	133
7	Supraventricular tachycardia (SVTA)	13
8	Trigeminy (T)	13
9	Ventricular flutter (VF)	10
10	Ventricular tachycardia (VT)	10
11	Wolff-Parkinson-white (WPW)	21

4 Result and Discussion

4.1 Dataset

MIT-BIH arrhythmia database samples are trained and tested to classify arrhythmia types. MATLAB (2018b) prototype was used to run the algorithm developed for the Arrhythmia detection and classification for each signal on a laptop 1.00 GHz Intel(R) Core (TM) i5-1035G1 CPU and 8.00 GB RAM).

The dataset used for arrhythmia classification is shown in Table 4. Thus, 703 ECG signals are tried in which 283 signals are Normal Sinus Beats, and 420 ECG signals belong to different arrhythmia types.

The raw signal and preprocessed signal after removing all the artifacts from the raw signal is shown in Fig. 5. *R*-peak detected ECG signal using DWT and *P*, *Q*, *R*, *S*, *T* waves peak detected output is shown in Fig. 6. All the other dynamic features are taken and collectively used for the training and testing of classifiers. The confusion matrix and ROC curve for Random forest and SVM are shown in Figs. 7 and 8, with 97% and 94.2% accuracy, respectively. Area Under Convergence (AUC), sensitivity, and specificity (shown in Eq. (5), (6) and (7)) are calculated based on the True Positive (TP), True Negative (TN), False Positive (FP), False Negative (FN).

$$\text{Sensitivity} = \frac{\text{TP}}{\text{TP} + \text{FN}} \tag{5}$$

$$\text{Specificity} = \frac{\text{TN}}{\text{TN} + \text{FT}} \tag{6}$$

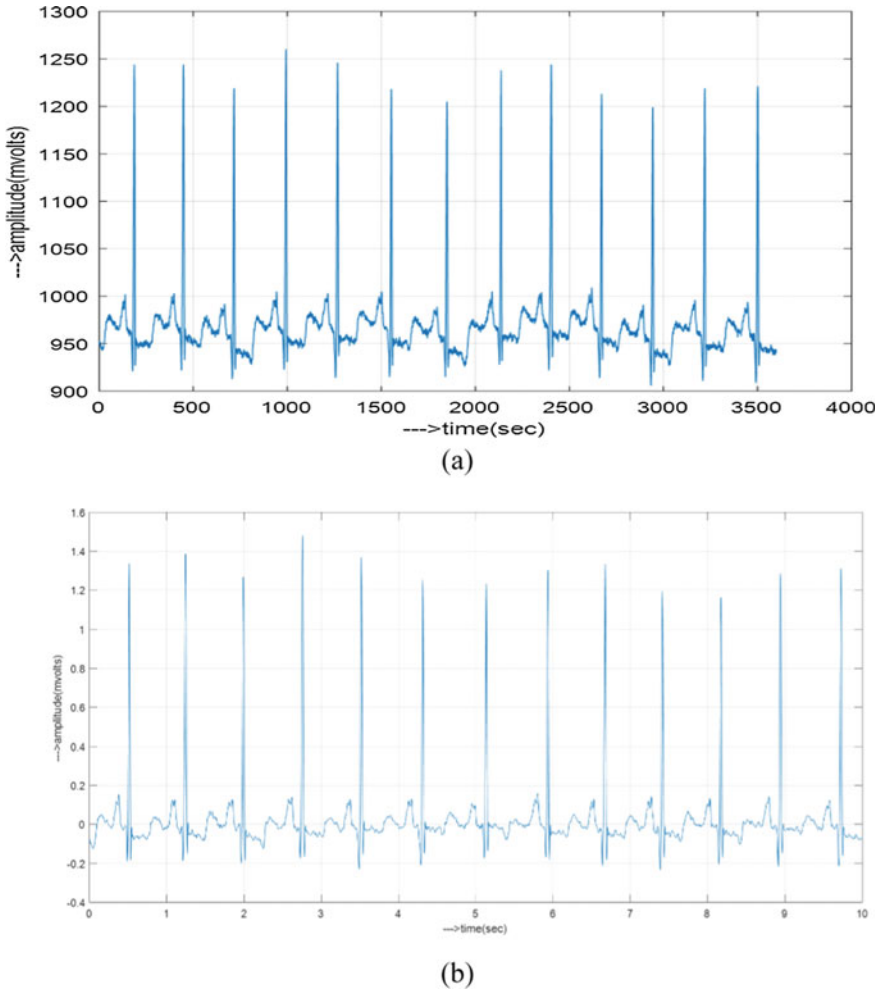

Fig. 5 **a** Raw signal, **b** Preprocessed signal after removing baseline wander and PLI

$$\text{AUC} = \frac{2\text{TP}}{\text{FP} + \text{FN} + 2\text{TP}} \tag{7}$$

A high-performance work Comparison was also conducted to verify the proposed method's performance improvement for the classification of arrhythmia. The comparison result is presented in Table 5.

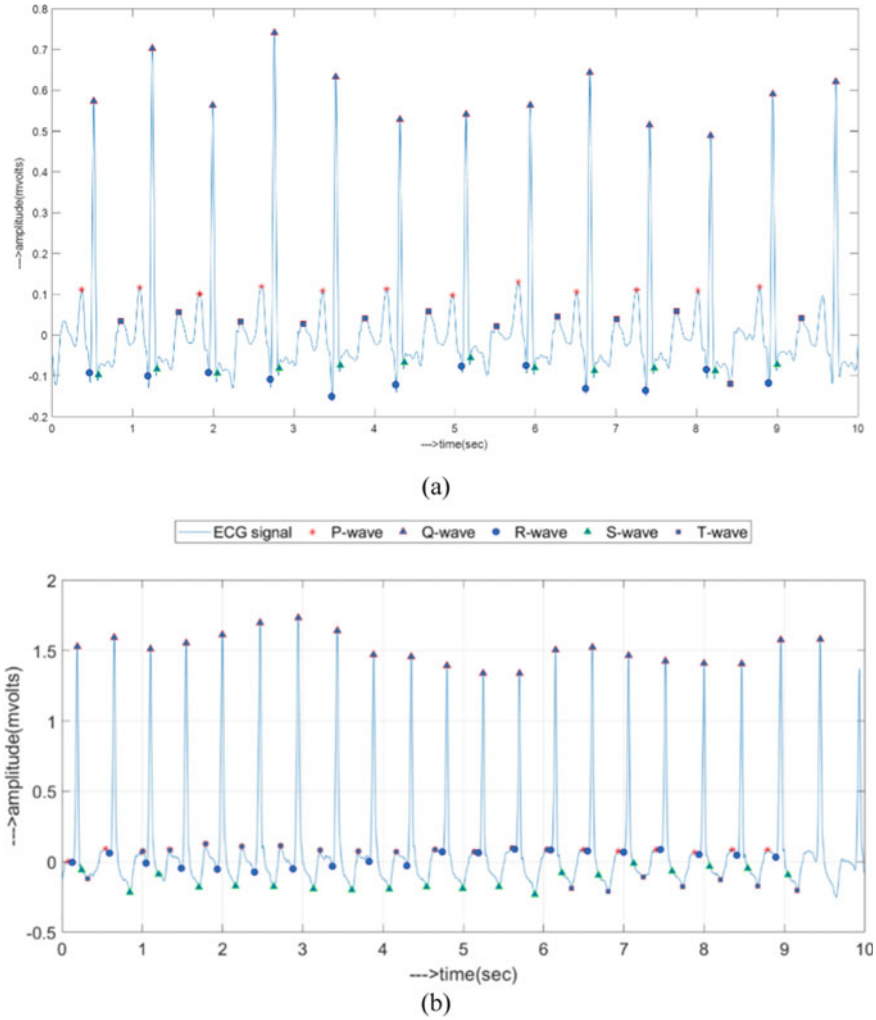

Fig. 6 **a** *R*-peak detected output using DWT, **b** Fiducial points detected output

5 Conclusion and Future Work

ECG is a non-invasive technique for checking the heart's functionality. Early recognition and classification of arrhythmia will help patients and medical practitioners with suitable medication. This paper proposes recognizing and classifying the arrhythmia type by using simple dynamic feature extraction techniques. 97% accuracy is achieved with the non-uniform database samples of MIT-BIH. Further, this approach can be extended toward the more and benchmark uniform dataset.

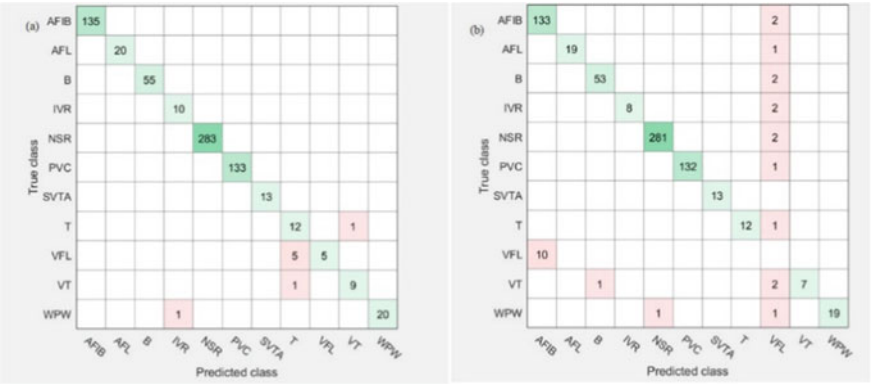

Fig. 7 Confusion matrices for **a** Random forest, **b** Support vector machine

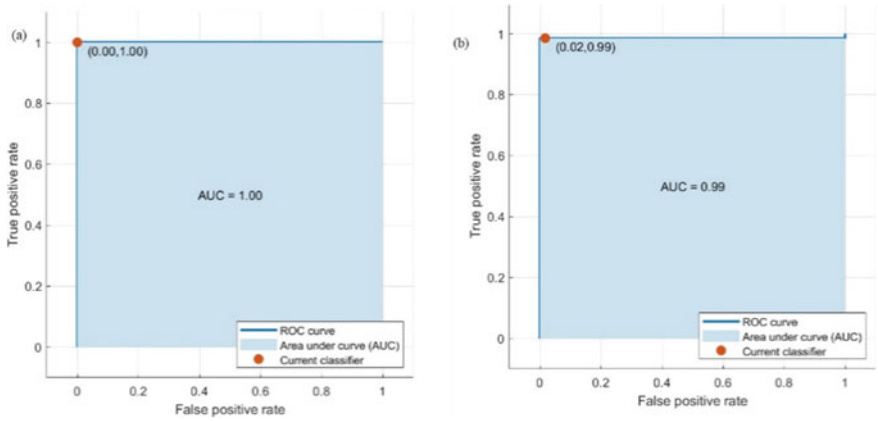

Fig. 8 ROC for **a** Random forest, **b** Support vector machine

Table 5 Comparison of the proposed method

Author	Features	Classifier	Data size	Accuracy (%)
Zhang et al. [11]	ECG morphology	SVM-RBF	101,398	86.66
Venkatesan et al. [8]	HRV parameters	SVM	NA	96
Yang et al. [12]	Raw data	DL-CCANeT	3350	95.25
This study	Dynamic features	Random forest	703	97

References

1. H Yang Z Wei 2020 Arrhythmia recognition and classification using combined parametric and visual pattern features of ECG morphology IEEE Access 8 47103 47117 https://doi.org/10.1109/ACCESS.2020.2979256

2. Lin, C.-C., Yang, C.-M.: Heartbeat classification using normalized RR intervals and morphological features. Math. Problems Eng. **2014**, May 2014, Art. no. 712474 (2014)
3. Gotchev, A., Nikolaev, N., Egiazarian, K.: Improving the transform domain ECG denoising performance by applying inter-beat and intra-beat decorrelating transforms. In: Proceedings of IEEE International Symposium on Circuits and Systems (ISCAS), Sydney, NSW, Australia, May 2001, pp. 17–20 (2001)
4. M Thomas MK Das S Ari 2015 Automatic ECG arrhythmia classification using dual tree complex wavelet-based features AEU-Int. J. Electron. Commun. 69 4 715 721
5. M Rakshit S Das 2018 An efficient ECG denoising methodology using empirical mode decomposition and adaptive switching mean filter Biomed. Signal Process. Control 40 140 148
6. Wang, L., Sun, W., Chen, Y., Li, P., Zhao, L.: Wavelet transform based ECG denoising using adaptive thresholding. In: Proceedings of 7th International Conference on Bioinformatics and Biomedical Science (ICBBS), Shenzhen, China, Jun 2018, pp. 35–40 (2018)
7. Jung, W.-H., Lee, S.-G.: ECG identification based on non-fiducial feature extraction using window removal method. Appl. Sci. **7**(11), Nov. 2017, Art. no. 1205 (2017). https://doi.org/10.3390/app7111205
8. C Venkatesan P Karthigaikumar A Paul S Satheeskumaran R Kumar 2018 ECG signal preprocessing and SVM classifier-based abnormality detection in remote healthcare applications IEEE Access 6 9767 9773
9. LB Marinho NDMM Nascimento JWM Souza MV Gurgel PPR Filho VHC Albuquerque de 2019 A novel electrocardiogram feature extraction approach for cardiac arrhythmia classification Future Gener. Comput. Syst. 97 564 577
10. Z Zhang J Dong X Luo K-S Choi X Wu 2014 Heartbeat classification using disease-specific feature selection Comput. Biol. Med. 46 1 79 89
11. Ye, C., Kumar, B.V., Coimbra, M.T.: Combining general multi-class and specific two-class classifiers for improved customized ECG heartbeat classification. In: Proceedings of 21st International Conference on Pattern Recognition (ICPR), Tsukuba, Japan, Nov. 2012, pp. 2428–2431 (2012)
12. Yang, W., Si, Y., Wang, D., Zhang, G.: A novel approach for multi-lead ECG classification using DL-CCANet and TL-CCANet. Sensors **19**(14), Jul. 2019, Art. no. 3214 (2019)
13. SL Oh EYK Ng RS Tan UR Acharya 2018 Automated diagnosis of arrhythmia using combination of CNN and LSTM techniques with variable length heart beats Comput. Biol. Med. 102 278 287

An Efficient Decoding of SEC-DED-DAEC Code with Odd-Column-Weight *H*-matrix

Raj Kumar Maity, Jagannath Samanta, and Jaydeb Bhaumik

Abstract The most familiar way to minimize the influence of soft error in the memories is the employment of suitable error correcting codes (ECCs). The codes like single error correction (SEC) and single error correction-double error detection (SEC-DED) have been enormously employed for the detection and correction of double and single errors, respectively, in the memory systems. Single error correction-double error detection-double adjacent error correction (SEC-DED-DAEC) codes are the simplest form of adjacent ECCs which are proficient of correcting adjacent double errors along with the SEC-DED capability. An assortment of SEC-DED-DAEC codes have already been presented in this regard. But the major limitations of these codes are higher decoding complexities and mis-correction rate. In this paper, an efficient decoding technique has been presented to minimize the area and delay requirement of SEC-DED-DAEC codes with odd-column-weight *H*-matrix.

Keywords Memory · Soft errors · ECCs · SEC-DED-DAEC · FPGA

1 Introduction

Radiation induced soft errors are the main origin of defects in modern memory systems [1]. These defects in the memory systems are generally minimized by applying suitable error correcting codes (ECCs) which have been explored by Chen et al. in [2] for the first time. Single bit error in the memory cells are corrected by single error correction (SEC) and single error correction-double error detection (SEC-DED) codes [3, 4]. Single error correction-double error detection-double adjacent error correction (SEC-DED-DAEC) codes [5–11] have been widely employed to diminish the

R. K. Maity (✉) · J. Samanta
Haldia Institute of Technology,Haldia, India

J. Bhaumik
Department of ETCE, Jadavpur University, Kolkata, India
e-mail: jaydeb.bhaumik@jadavpuruniversity.in

B. Sikdar et al. (eds.), *Proceedings of the 3rd International Conference on Communication, Devices and Computing*, Lecture Notes in Electrical Engineering 851,
https://doi.org/10.1007/978-981-16-9154-6_63

effects of soft errors in memory systems. The first SEC-DED-DAEC codes for memory systems have been offered by Dutta et al. [9] with minimum redundancy. But higher rates of considering nonadjacent double errors as adjacent double errors is the main restriction of Dutta codes. Capability of scalable adjacent error detection and lower mis-correction rates have been the main characteristic of SEC-DED-DAEC codes presented by Neale et al. [7, 8]. Two techniques for reducing the area and delay overheads, respectively, of SEC-DED-DAEC decoder have been illustrated in [10]. A compact decoding of SEC-DED-DAEC code has been presented in [11] for designing SEC-DED-DAEC codec. Whereas K-map-based approach to diminish the hardware complexity of error location detection (ELD) circuitry of SEC-DED-DAEC decoders have been explored by Maity et al. in [12]. So the main considerations for constructing SEC-DED-DAEC decoder are lower mis-correction probability and hardware complexities.

In this article, an efficient design of SEC-DED-DAEC decoder for odd-column-weight H-matrix has been proposed. The synthesis results of proposed and existing associated schemes have been compared based on FPGA platform and the proposed decoders have moderate area and delay requirements for various word lengths.

The rest of this brief is ordered as follows. Section 2 describes the existing decoding schemes of SEC-DED-DAEC codes with odd-column-weight H-matrix. The proposed scheme of designing the SEC-DED-DAEC decoder is presented in Sect. 3. The synthesis results which are based on FPGA platform for the proposed and existing schemes of decoders are presented in Sect. 4 and finally, Sect. 5 concludes the paper.

2 Existing Decoding Schemes of SEC-DED-DAEC Codes with Odd-Column-Weight H-matrix

In this section, two existing decoding schemes of SEC-DED-DAEC code with odd-column-weight H-matrix as presented by Reviriego et al. in [10] have been summarized in brief.

2.1 The First Scheme of Decoding by Reviriego et al.

The weight of syndromes for single error correcting (SEC) and double adjacent error correcting (DAEC) have a fixed value of 3 and 4, respectively, in [10]. In the first scheme of decoding in [10], the locations of single and adjacent double errors have been determined by allowing for only the 1's in the corresponding error correcting syndromes. Also, a $not\,DED$ signal has been applied in this first decoding method to avoid the interpretation of double adjacent errors as single error. This $not\,DED$

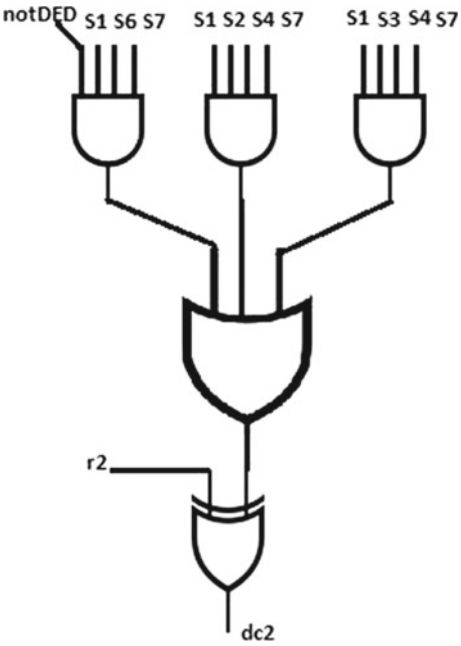

Fig. 1 Logic diagram of first scheme of decoding the 2nd data bit for (23, 16) SEC-DED-DAEC code

signal has been expressed as the XOR sums of all the syndrome bits. The logic diagram of this scheme of decoding for second data bit of (23, 16) SEC-DED-DAEC code in [10] is shown in Fig. 1.

The main advantage of this decoding scheme as reported by Reviriego et al. is the reduction in area overhead of the SEC-DED-DAEC decoder. On the other hand, the delay overhead of this scheme is higher due to the use of $notDED$ signal. So the first scheme of decoding of SEC-DED-DAEC code by Reviriego et al. reduces the area overhead in the expense of delay overhead.

2.2 The Second Scheme of Decoding by Reviriego et al.

In the second scheme of decoding in [10], the location of single error has been determined by allowing for both 1's and 0's in the single error correcting syndrome values but without the $notDED$ signal. Whereas,, the adjacent double errors have been located by employing the same technique of first scheme of decoding, i.e., by allowing for only the 1's in the corresponding error correcting syndromes. The logical diagram of this scheme of decoding for second data bit of (23, 16) SEC-DED-DAEC code in [10] is shown in Fig. 2.

The main advantage of this decoding scheme as reported by Reviriego et al. is the reduction in delay overhead of the SEC-DED-DAEC decoder. And this is due to

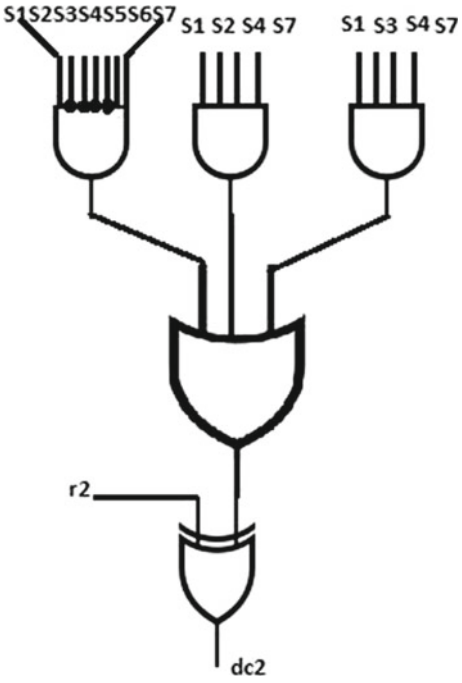

Fig. 2 Logic diagram of second scheme of decoding the second data bit for (23, 16) SEC-DED-DAEC code

absence of $not\,DED$ signal in this scheme. On the other hand, the area overhead of this scheme is higher. So the second scheme of decoding of SEC-DED-DAEC code by [10] reduces the delay overhead in the expense of area overhead.

So the two existing schemes of decoding of SEC-DED-DAEC codes with odd-column-weight H-matrix are capable of reducing either the area overhead or the delay overhead of the decoder. But none of them are capable of reducing both area and delay overheads of decoder. The main objective of the present work is to design an efficient decoding scheme for SEC-DED-DAEC codes with odd-column-weight H-matrix so that both the area and delay overheads of the decoder can be reduced upto a moderate level.

3 Proposed Decoding Scheme of SEC-DED-DAEC Code with Odd-Column-Weight H-matrix

In this section, the proposed decoding scheme for SEC-DED-DAEC code with odd-column-weight H-matrix has been presented in details. The proposed decoding rules are as follows:

Step-1: The syndrome bits are computed.
Step-2: The single error is located for each data bit position by considering both 1's and 0's in the syndrome value but with the properly selected variable length syndrome bits.
Step-3: The adjacent double errors are located in each data bit position by considering only the 1's the corresponding syndrome bits.
Step-4: The located single and adjacent double errors are corrected for each data bit positions.

The main difference between the proposed and existing second scheme of decoding of SEC-DED-DAEC code by Reviriego et al. lies in the step-2 of the proposed decoding rules. All the syndrome bits have been utilized in the second scheme of decoding by Reviriego et al. for locating single error. Whereas, the proposed scheme of decoding utilizes a variable length syndrome bits for locating single error in each data bit. These variable length syndrome bits for locating single error in each data bit have been selected properly by avoiding any conflicts from other single and double adjacent errors locating syndromes. So they are unique from each others and from DAEC syndromes. The logical expressions for locating single error in each data bit for the proposed and the second scheme of decoding by Reviriego et al. have been summarized in Table 1 for (23, 16) SEC-DED-DAEC decoder in [10].

Table 1 Comparison of single error locating logical expressions of (23, 16) SEC-DED-DAEC Decoder by Reviriego et al. with the proposed and existing Schemes

Data bit	Second scheme by Reviriego et al. [10]	Proposed scheme
d_1	$s'_1.s_2.s'_3.s_4.s'_5.s_6.s'_7$	$s_2.s_4.s'_5.s_6.s'_7$
d_2	$s_1.s'_2.s'_3.s'_4.s'_5.s_6.s_7$	$s_1.s'_5.s_6.s_7$
d_3	$s'_1.s'_2.s_3.s_4.s'_5.s_6.s'_7$	$s_3.s_4.s'_5.s_6.s'_7$
d_4	$s'_1.s_2.s'_3.s_4.s'_5.s'_6.s_7$	$s'_1.s_2.s'_3.s_4.s'_5.s'_6.s_7$
d_5	$s'_1.s'_2.s_3.s'_4.s_5.s'_6.s_7$	$s'_2.s_3.s'_4.s_5.s'_6.s_7$
d_6	$s'_1.s_2.s'_3.s'_4.s'_5.s_6.s_7$	$s_2.s'_3.s'_4.s_6.s_7$
d_7	$s'_1.s'_2.s_3.s'_4.s_5.s_6.s'_7$	$s'_2.s_3.s'_4.s_5.s_6.s'_7$
d_8	$s'_1.s'_2.s'_3.s_4.s_5.s'_6.s_7$	$s'_2.s'_3.s_4.s_5.s'_6.s_7$
d_9	$s'_1.s_2.s'_3.s'_4.s_5.s_6.s'_7$	$s_2.s'_3.s'_4.s_5.s_6$
d_{10}	$s'_1.s'_2.s'_3.s_4.s'_5.s_6.s_7$	$s'_2.s'_3.s_4.s'_5.s_6.s_7$
d_{11}	$s'_1.s_2.s'_3.s'_4.s_5.s'_6.s_7$	$s_2.s'_3.s'_4.s_5.s_7$
d_{12}	$s'_1.s'_2.s_3.s_4.s_5.s'_6.s'_7$	$s'_2.s_3.s_4.s_5.s'_6.s'_7$
d_{13}	$s'_1.s'_2.s_3.s'_4.s'_5.s_6.s_7$	$s'_2.s_3.s'_4.s'_5.s_6.s_7$
d_{14}	$s'_1.s'_2.s'_3.s_4.s_5.s_6.s'_7$	$s'_2.s'_3.s_4.s_5.s_6.s'_7$
d_{15}	$s'_1.s'_2.s_3.s_4.s'_5.s'_6.s_7$	$s'_1.s'_2.s_3.s_4.s'_5.s'_6.s_7$
d_{16}	$s'_1.s'_2.s'_3.s'_4.s_5.s_6.s_7$	$s'_1.s'_3.s'_4.s_5.s_6.s_7$

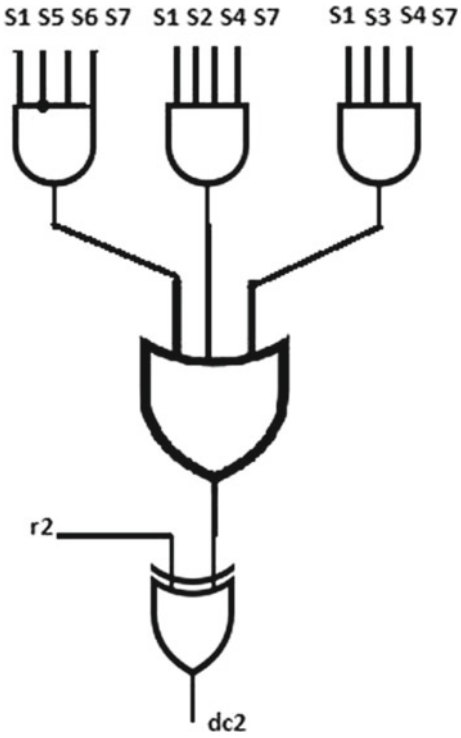

Fig. 3 Logic diagram of proposed scheme of decoding the 2nd data bit for (23, 16) SEC-DED-DAEC code

As shown in Table 1, the expressions for locating single error are more compact in the proposed scheme of decoding. So lesser number of AND and NOT logic gates are required for designing the proposed decoding scheme compared to the second decoding scheme by Reviriego et al. The proposed decoder circuit for correcting the second data bit of (23, 16) SEC-DED-DAEC code in [10] is shown in Fig. 3.

The theoretical area complexity of any logical circuitry is generally measured by counting the total number of equivalent two-input NAND (NAND2) gates of the circuitry. The comparison of theoretical area complexities of proposed and existing related decoding schemes is presented in Table 2. As shown in Table 2, the first scheme of decoding by Reviriego et al. and the decoding scheme by Neale et al. require lowest and highest number of equivalent NAND2 gates, respectively, for all the word lengths. The theoretical area complexity of the proposed decoding scheme is lower compared to Neale et al. scheme and the second scheme of decoding by Reviriego et al. for all the word lengths. But the proposed scheme of decoding have slightly higher theoretical area complexity compared to first scheme of decoding by Reviriego et al. So the theoretical area complexity of proposed decoding scheme is positioned in the middle of both the decoding schemes by Reviriego et al.

Table 2 Theoretical area complexities of proposed and existing decoding schemes

k	Decoder	XOR2	OR2	AND2	NOT	Equiv. NAND2
16	Reviriego et al. scheme1 [10]	70	31	151	0	675
	Reviriego et al. scheme2 [10]	64	31	189	64	791
	Neal et al. scheme [7, 8]	58	31	282	173	1062
	Proposed scheme	64	31	170	42	731
32	Reviriego et al. scheme1 [10]	134	62	285	0	1292
	Reviriego et al. scheme2 [10]	128	62	381	128	1588
	Neal et al. scheme [7, 8]	130	62	564	305	2139
	Proposed scheme	128	62	362	112	1534
64	Reviriego et al. scheme1 [10]	264	127	573	0	2583
	Reviriego et al. scheme2 [10]	256	127	893	384	3575
	Neal et al. scheme [7, 8]	275	126	1330	714	4852
	Proposed scheme	275	126	717	207	3119

4 Synthesis Results Based on FPGA Platform

The proposed decoding scheme has been applied to the odd-column-weight H-matrices presented in [10] for SEC-DED-DAEC codes. The proposed SEC-DED-DAEC decoders for the word length of 16, 32 and 64 bits have been characterized in verilog hardware description language (HDL). These decoders have been simulated and synthesized on field programmable gate array (FPGA)-based Virtex6 (XC6VCX75T-2ff484) device family. The synthesis results based on FPGA platform of proposed and existing SEC-DED-DAEC decoders in [7, 8, 10] are compared in Table 3.

The area requirement of proposed decoding scheme with 16-bit word length is lower compared to the other existing schemes in Table 3. Also, the proposed scheme with word lengths 32 and 64 bits has lower area requirement compared to the Neale et al. scheme and second scheme of decoding by Reviriego et al. for the same word lengths. But the area requirement of proposed scheme with 64-bit word length is slightly higher with respect to the first scheme of decoding of Reviriego et al. So the area requirement of the proposed decoding scheme lies in between the area and delay optimized decoding schemes by Reviriego et al. for the world length of 32 and 64

Table 3 Comparison of FPGA-based synthesis results for proposed and existing schemes of decoding

Word length (k)	Decoding schemes	Area (LUTs)	Delay (ns)
16	Reviriego et al. scheme1 [10]	55	3.20
	Reviriego et al. scheme2 [10]	53	3.44
	Neal et al. scheme [7, 8]	51	3.31
	Proposed scheme	47	3.39
32	Reviriego et al. scheme1 [10]	93	4.39
	Reviriego et al. scheme2 [10]	102	3.96
	Neal et al. scheme [7, 8]	108	5.29
	Proposed scheme	97	4.02
64	Reviriego et al. scheme1 [10]	175	5.15
	Reviriego et al. Scheme2 [10]	216	4.05
	Neal et al. scheme [7, 8]	210	5.40
	Proposed scheme	202	3.95

bits. The proposed scheme of decoding exhibits the delay requirement which stands in between the delay requirement of both the existing schemes by Reviriego et al. for the word lengths of 16 and 32 bits. The existing decoding scheme by Neale et al. provides slightly better delay performance compared to proposed scheme for these word lengths. But the proposed scheme with 64-bit word length has the lowest delay requirement compared to all the existing schemes in Table 3.

5 Conclusion

In this paper, an efficient scheme of decoding for SEC-DED-DAEC code with odd-column-weight H-matrix has been proposed for memory application. The proposed and existing three related schemes have been simulated and synthesized by using FPGA platform. The comparison of this synthesis results exhibits that the proposed decoding scheme have moderate area and delay requirements compared to the existing related schemes. The application of proposed decoding scheme includes the protection of memories against the data corruption due to soft errors.

References

1. R. C. Baumann, Soft errors in advanced computer systems. IEEE Des. Test. Comput. **22**(3), 258266 (2005)
2. Chen, C.L., Hsiao, M.Y.: Error-correcting codes for semiconductor memory applications: a state-of-the-art review. IBM J. Res. Develop. **28**(2), 124134 (1984)

3. Hsiao, M.Y.: A class of optimal minimum odd-weight-column SEC-DED codes. IBM J. Res. Develop. **14**(4), 301395 (1970)
4. J. Samanta, Kewet, A.: Compact and high speed hsiao based SEC-DED code for cache memory. J. Circ. Syst. Comput. (World Sci.) **31**(01), 1793–6454 (2021)
5. Tripathi, S., Maity, R.K., Jana, J., Samanta, J., Bhaumik, J.: FPGA based low area multi-bit adjacent error correcting codec for SRAM application. Radioelectro. Commun. Syst. J. **63**(10), 543–552 (2020). Dec
6. Tripathi, S., Jana, J., Samanta, J., Anand, A., Kumar, C., Raj, G.: FPGA and ASIC implementation of SEC-DED-DAEC codes for SRAM application. In: Proceedings of the 2nd International Conference on Communication, Devices and Computing. Lecture Notes in Electrical Engineering, pp. 237–248, vol. 602. Springer, Singapore (2019)
7. Neale, A., Sachdev, M.: A new SEC-DED error correction code subclass for adjacent MBU tolerance in embedded memory. IEEE Trans. Device Mater. Rel. **13**(1), 223230 (2013)
8. Neale, A.: Design and Analysis of an Adjacent Multi-bit Error Correcting Code for Nanoscale SRAMs. Ph.D. Thesis (2014)
9. Dutta, A., Touba, N.A.: Multiple bit upset tolerant memory using a selective cycle avoidance based SEC-DED-DAEC code. In: Proceedings of 25th IEEE VLSI Test Symposium 2007, pp. 349–354
10. Reviriego, P., Martnez, J., Pontarelli, S., Maestro, J.A.: A method to design SEC-DED-DAEC codes with optimized decoding. IEEE Trans. Dev. Mater. Reliab. **14**(3), 884–889 (2014)
11. Maity, R.K., Samanta, J., Bhaumik, J.: New compact SEC-DED-DAEC code for memory applications. In: Proceedings of the 2nd International Conference on Communication, Devices and Computing, pp. 321–329. Springer, Singapore (2020)
12. Maity, R.K., Tripathi, S., Samanta, J., Bhaumik, J.: Lower complexity error location detection block of adjacent error correcting decoder for SRAMs. IET Comput. Dig. Techn. **14**(5), 210–216 (2020)

Study of Automatic Solar Power-Based Micro-Irrigation System

Avijnan Bardhan, Partha Kumar Mondal, Ayan Karmakar, Suraj Kumar Prasad, Sushri Mukherjee, Dharmbir Prasad, and Rudra Pratap Singh

Abstract With the continuous increase in population, there is a rapid increase in food demand to feed people. This requires some innovations to improve farmers' agricultural production methodology, so that maximum yield is achieved without much difficulty. Nowadays, farmers often face many problems when pouring water into their fields in the stipulated time. They have to remain in their fields to manually operate the water pumps until the water is filled in their growing area to the required amount, which is difficult work if productivity is to be high. A person cannot remain in the field for long hours, and therefore, the uneven distribution of water takes place in the crop fields. Sometimes, excess water can lead to water clogging and, eventually, large production losses. To obtain an optimal result, we plan to propose a project. We have proposed the design for a solar power-based irrigation system. This would lead us to successfully achieve a few goals including conservation of water and energy. It can also turn barren land into productive land. Furthermore, as our project is based on solar energy, we can use it efficiently in remote locations where electricity is barely available.

Keywords Irrigation · Solar power · Automatic · Renewable energy · Agriculture

1 Introduction

The basic working principle of the irrigation system based on solar energy is quite simple. A motor that is controlled by an Arduino Uno microprocessor and powered by a solar panel pumps water from a distant source into irrigation channels cut into the fields being cultivated. This ensures system automation and energy availability.

A. Bardhan · P. K. Mondal · A. Karmakar · D. Prasad (✉) · R. P. Singh
Asansol Engineering College, Asansol, West Bengal 713305, India

S. K. Prasad
Santiniketan Polytechnic, Burdwan, West Bengal 713204, India

S. Mukherjee
Indian Institute of Technology Delhi, New Delhi 110016, India

B. Sikdar et al. (eds.), *Proceedings of the 3rd International Conference on Communication, Devices and Computing*, Lecture Notes in Electrical Engineering 851,
https://doi.org/10.1007/978-981-16-9154-6_64

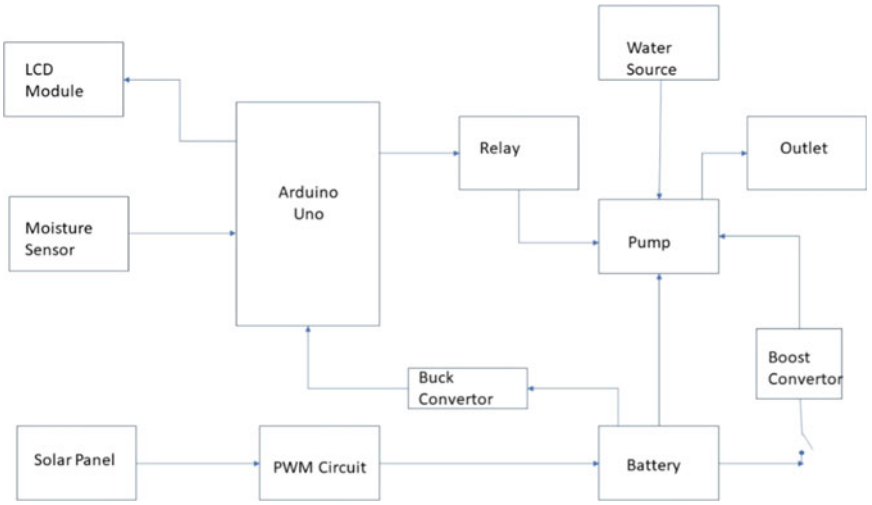

Fig. 1 Architecture of android application

A moisture sensor is introduced into the field under study and sends a signal to a terminal of the Arduino Uno microprocessor. When moisture is absent or low in the soil, the sensor sends a signal to the microprocessor terminal, which is programmed to rotate in the motor when the signal is detected. The energy consumed by the motor is solar, eliminating the need for grid connection. Batteries can be used to store the extra amount of energy produced as well as fed for local household uses. An additional benefit of this system is that, in most cases, energy is usually available when it is needed, that is, when the soil moisture level is low, as the intense sunlight and accompanying heat usually dry out, even the cultivated fields. Our system uses this same sunlight to generate solar energy that pumps water back into the field. However, should it be necessary to irrigate the field at a time when there is no sunlight available, an energy storage mechanism can be easily integrated into the system. The process flowchart of undertaking works is portrayed in Fig. 1.This whole study has been organized as follows: in Sect. 1: Introducing current study and citing literature survey, Sect. 2: Solution approach for efficient irrigation, Sect. 3: Result and discussion, and Sect. 4: Conclusion.

1.1 Survey of Recent Literatures

Recently, several research works have been pursued on greener means of irrigation. The financial analysis of the emerging and promising technology, the solar-powered irrigation system has been conducted in [1]. Experiments in the field of solar PV technology came up with the revelation that a 1 HP solar PV pumping system whether

AC or DC type has the potential to be successfully used in the operation of mini-sprinklers, micro-sprinklers, and drippers with good irrigation uniformity. Ahead of this, a self-sustainable module that can be deployed in judicial use of water and energy is designed in which both water and energy can be harvested and recycled [2]. The solar PV technologies despite having visible advantages, especially in terms of payback period, reduction in greenhouse gases, fails to gain popularity and thereby the rampant installation due to the higher initial investment cost involved. The focus of current research, however, is to find out potential and affordable solar-powered drip irrigation by leveraging the existing local resources [3, 4]. Cost comparison of AC and DC loads depicts that, for small-scale irrigation systems powered by renewable energy, DC pumps get a higher acceptance by proving too be to economical and reliable against pumps which, along with excess generation yields uneconomic results [5, 6].

MPPT based on incremental conductance algorithm pushing the PV panel to obtain the high peak in power coupled with a boost converter and inverter can come up with an alternative highly economical, low-price solar-powered drip irrigation system [7]. This combined with intelligent watering of plants or needed based on the requirement is developed by the installation of soil parameter sensor and thus soil status monitoring for good yields in the field by triggering optimized operation of water pump electric motor [8–13]. A gravity-fed type micro-irrigation system integrated with low-cost solar-based pumping has the potential to add to this purpose at the same time [14].

A real-time model called the smart photovoltaic irrigation manager is said to synchronize the photovoltaic power availability with the energy needed to pump the irrigation requirements for different sectors of irrigation networks [15]. This can further be accelerated with a new type of solar panel, i.e., spin cell, which has the capability to harvest 20 times more current than the traditional flat panel [16]. Adoption of higher efficiency irrigation systems allays water stress and can eliminate the need for additional water supply [17]. The BLDC pump set in the off-grid application can be used in solar irrigation systems which can lead to huge power savings. It uses the optimal amount of DC power from the solar panels feeding the excess amount to the local grid [18].

2 Mathematical Formulation

In this study, major associated aspects have been formulated in the succeeding sections. The PV cell current could be obtained by Eq. (1) [3],

$$I = I_{\text{ph}} - I_s\left[e\frac{qV_{\text{oc}}}{N_s K A_D T_O} - 1\right] \tag{1}$$

where V_{oc}: open circuit voltage, K: proportionality constant, N_s: number of cell, q: flow of charge.

Solar photovoltaic array power is given by Eq. (2) [9, 10],

$$P_{\text{pv}} = \frac{E_w}{\left(I_T \eta_{\text{mp}} F\right)} \tag{2}$$

where I_T: average daily solar irradiation, F: array mismatch factor, η_{mp}: daily subsystem efficiency.

The overall solar water pumped may be given by Eq. (3) [9, 10],

$$V = \left(\frac{P_{\text{pv}} I_T \eta_{\text{mp}} F}{\rho g.TDH}\right) \tag{3}$$

where TDH: total dynamic head.

Solar PV pumping system helps to reduce the emission of a large amounts of carbon dioxide, which can be quantified by Eq. (4) [9, 10],

$$\text{Carbon footprint}\,(\text{kg}\,\text{CO}_2 - \text{eq}\,\text{kWh}^{-1}) = \frac{\text{EF}(\text{kg}\,\text{CO}_2 - \text{eq}\,\text{kWh}^{-1})}{\text{Effeiciency of Pumping System}} \tag{4}$$

3 Solution Approach for Efficient Irrigation

The main objective of this project was to create a system that is efficient, cost-effective, easy to maintain and repair, and a viable solution to the economic problems faced by the government and farmers. We strive to create a system built from readily available equipment that is inexpensive and readily available. Most importantly, it can be modified to easily serve specific geographic purposes. Added to this, the system has very low installation costs and mobile connectivity. Combining all these factors, the proposed system can be implemented widely, quickly, and cost-effectively. In this regard, the list of major components are as follows: solar panel, PWM circuit, battery, buck convertor, boost convertor, Arduino Uno, moisture sensor, pH sensor, LCD module, relay, pump, and sprinkler. Its circuit diagram is presented in Fig. 2. However, circuital representation for boost converter is given in Fig. 3.

3.1 Working Theory

In this paper, a solar power-based irrigation system has been used, which is self-sustained/ self-powered. And the main controller have been used Arduino Uno. In

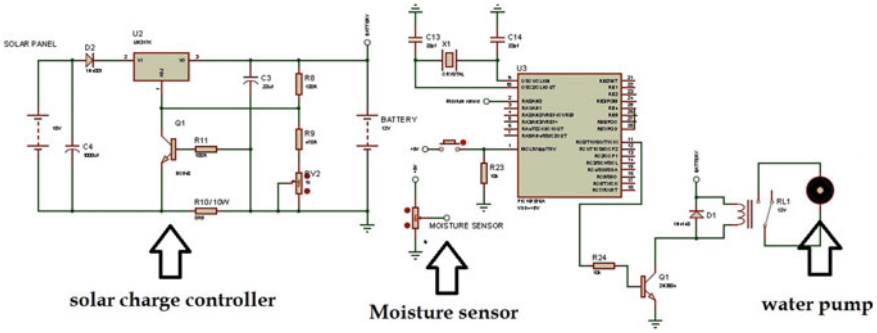

Fig. 2 Circuit representation of proposed micro-irrigation system

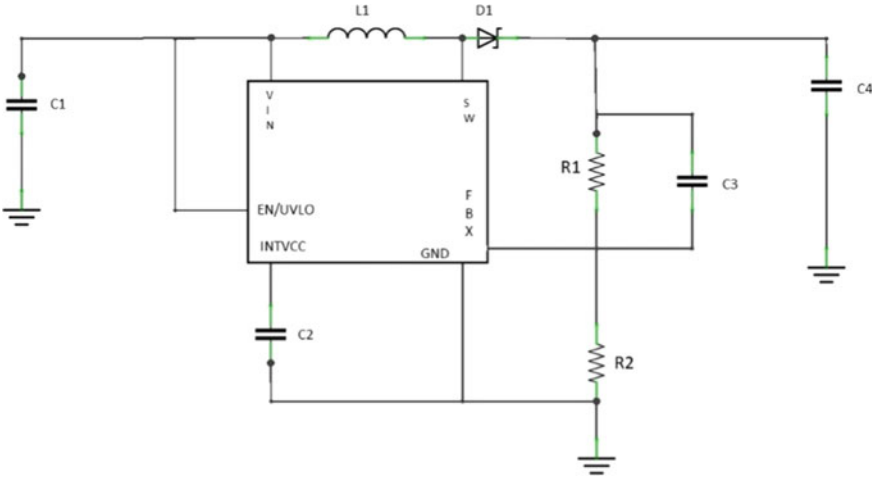

Fig. 3 Circuit schematic for boost convertor

the barren land or in the remote areas, there is no electricity and the supply is very limited. In these places, the system we propose can work very efficiently as it is self-sustained. Solar panels generate electricity from the sunlight, which is a renewable source of energy. Then, it is stored in the rechargeable battery. From the battery, we have used the buck converter to reduce the voltage and send it to the Arduino as it takes low voltage as its supply energy source. From the Arduino, we connected the soil moisture sensor to get the data on whether the soil is dry or not. If the soil moisture sends "high" as output to the Arduino, then the Arduino turns the relay in "ON" state and the pump gets the power to function, directly from the battery. Now, when the soil gets enough moisture in it, then the soil moisture sensor sends the output as "Low" to the Arduino. Then, Arduino cuts the power of the pump through the relay.

4 Result and Discussion

With the help of the proposed system, there are lots of benefits for the government and as well as for the farmers also. A solution to the energy crisis is proposed to the government with the help of the use of solar power-based system. Using the automatic irrigation system, we optimize water usage, reduce waste, and reduce human intervention for farmers. The excess energy produced by solar panels can also be delivered to the accumulator, which can be reused for domestic use, promoting agriculture in India, and at the same time providing a solution to the energy crisis. The proposed system is an ecologically correct and easy to implement solution for field irrigation. Solar pumps also offer clean solutions without the danger of well contamination as presented in Table 1. The system requires minimal maintenance and attention as it starts automatically. To further improve daily pump rates, tracking matrices can be implemented. Although a high capital investment is required to implement this system, the overall benefits are high, and, in the long run, this system is cheap as illustrated in Fig. 4.

Table 1 Monthly energy saving using proposed solution

Period	Unit (kW/month)	Period	Unit (kW/month)
Jan	320	Jul	400
Feb	230	Aug	310
Mar	150	Sep	240
Apr	170	Oct	120
May	250	Nov	200
Jun	360	Dec	290

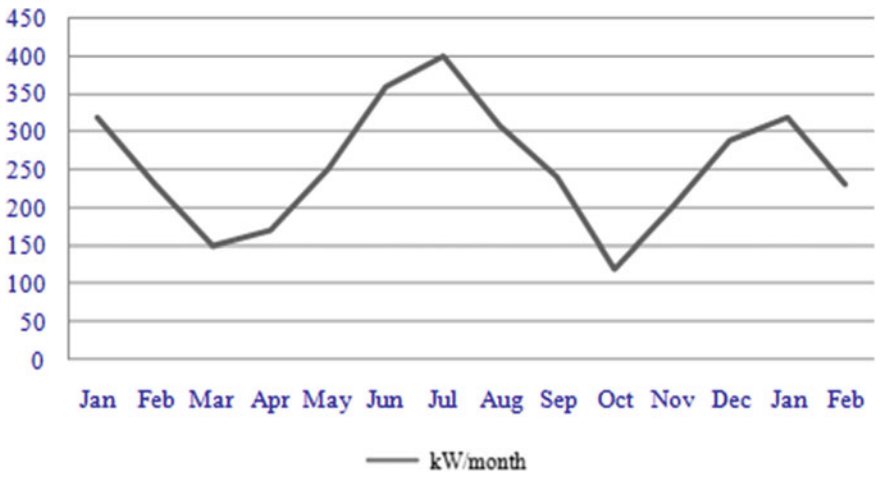

Fig. 4 Characteristics for monthly energy savings

5 Conclusion

A solar-powered irrigation system has been successfully developed and can use soil moisture to analyze soil conditions and decide whether or not to irrigate the farm. The design of this system responds to the concerns of traditional irrigation systems, with the considerable waste of resources. The need for excessive labor was resolved with the introduction of an automated function to check soil conditions, water pumping needs, etc. The proposed system is economical and can be easily installed in gardens, roofs, as well as in large areas for planting. End users can be trained to perform basic maintenance that ensures that once the system is installed, it runs smoothly. The simple design also ensures that the system is less prone to complicated failures. In the future, this project can be expanded to fit the actual size of the farms and support the operation without the need for human intervention and irrigation labor, and can also be used to optimize the cost of the accessories used in the implementation and in maintaining the irrigation system. In conclusion, we can say that the solar energy-based irrigation system is a versatile, simple, easily modifiable, robust, and reliable system that aims to solve one of the main problems that afflict farmers, the economy, the government, and us.

References

1. Rana, J., Kamruzzaman, M., Oliver, M.H., Akhi, K.: Financial and factors demand analysis of solar powered irrigation system in Boro rice production: a case study in Meherpur district of Bangladesh. Renew. Enj. **167**, 433–439 (2021)
2. Santra, P.: Performance evaluation of solar PV pumping system for providing irrigation through micro-irrigation techniques using surface water resources in hot arid region of India. Agric. Water Manag. **1**, 106554 (2021)
3. Verma, S., Mishra, S., Chowdhury, S., Gaur, A., Mohapatra, S., Soni, A., Verma, P.: Solar PV powered water pumping system–A review. Mater. Today Proc. (2020)
4. Wazed, S.M., Hughes, B.R., O'Connor, D., Calautit, J.K.: Solar driven irrigation systems for remote rural farms. Enj. Procedia. **142**, 184–191 (2017)
5. Ronad, B.F., Jangamshetti, S.H.: Optimal cost analysis of wind-solar hybrid system powered AC and DC irrigation pumps using HOMER. Int. Con. Renew. Eng. Res. App. **8**, 1038–1042 (2015)
6. Wazed, S.M., Hughes, B.R., O'Connor, D., Calautit, J.K.: A review of sustainable solar irrigation systems for Sub-Saharan Africa. Renew. Sustain. Eng. Rev. **81**, 1206–1225 (2018)
7. WanQuan, S., Niringiyimana, E., Simiyu, P., Ndayishimiye, V., Dushimimana, G.: Modelling a 30 kw standalone solar powered irrigation system. PES/IAS Power Africa, pp. 1–5 (2020)
8. Uddin, J., Reza, S.T., Newaz, Q., Uddin, J., Islam, T., Kim, J.M.: Automated irrigation system using solar power. Int. Con. Electr. Comput. Eng. **7**, 228–231 (2012)
9. Al-Ali, A.R., Al Nabulsi, A., Mukhopadhyay, S., Awal, MS., Fernandes, S., Ailabouni, K.: IoT-solar energy powered smart farm irrigation system. J. Electr. Sci. Tech. **17**, 100017 (2019)
10. Eragamreddy, G., Sree, K.R.: Solar powered auto watering system for irrigation using embedded controller. Int. Con. Energy Commun. Data Anal. Soft Comput., 2424–2428 (2017)
11. Adamsab, K., Saif, M., Saif, S., Khamis, I., Talib, W.: Hybrid powered intelligent irrigation system using Oman Falaj and solar energy. Mater. Today Proc. **41**, 260–264 (2021)

12. Das, P., Patton, C., Devi, S.F., Marak, W.C., Yaker, T.: Design of solar powered automatic irrigation system. Int. Con. Electr. Comput. Commun. Technol. 1–5 (2020)
13. Xiaochu, L., Jingpeng, L., Li, Y., Hualong, W., Jianhua, T.: Engineering quality control of solar-powered intelligent water-saving irrigation. Int. Asia Con. Info. Control, Auto. Rob. **3**, 254–257 (2010)
14. Kumar, M., Reddy, K.S., Adake, R.V., Rao, C.V.: Solar powered micro-irrigation system for small holders of dryland agriculture in India. Agr. Water Mange. **9**, 158–112 (2015)
15. García, A.M., García, I.F., Poyato, E.C., Barrios, P.M., Díaz, J.R.: Coupling irrigation scheduling with solar energy production in a smart irrigation management system. J. Cleaner Prod. **82**, 670–682 (2018)
16. Alex, G., Janakiranimathi, M.: Solar based plant irrigation system. Int. Con. Adv Electr. Electr. Inf. Comm. Bio-Info. **2**, 425–428 (2016)
17. Caldera, U., Breyer, C.: Assessing the potential for renewable energy powered desalination for the global irrigation sector. Sci. Total Environ. **1**, 133598 (2019)
18. Krishna, M.H., Manmadharao, S.: Grid integrated solar irrigation system by using BLDC motor pump set. Int. Con. Inventive Res. Comput. App., 1261–1264 (2018)

Compact Microstrip Printed Antenna Design Using Square Root-Shaped Slot in the Patch

Nikita Dey, Akash Dhakal, Ashim Das, Laishram Manali Devi, and Sunandan Bhunia

Abstract A design of a square root-shaped slot loaded compact printed microstrip printed antenna has been presented in this literature. A conventional rectangle-shaped microstrip printed antenna with dimension of 18×14 mm^2 has been taken as reference antenna which radiates at 5.7 GHz. The presence of the square root-shaped slot on the patch lengthens the electrical path on the patch for which the resonant frequency has been decreased considerably. The resonating frequency of the proposed slotted antenna has been found as 2.89 GHz with 28 dB return loss and maximum peak gain at 2.89 GHz has been obtained as 2 dBi. With respect to the conventional size of the antenna radiated at 2.8 GHz, the proposed antenna has obtained the compactness by 76.66%. The proposed design has been simulated using commercially available software IE3D.

Keywords Slotted patch · Compact · Microstrip patch antenna · IE3D

1 Introduction

A rapid growth on advancement of wireless communicating systems is observed nowadays. To fulfill the demand of making the wireless communication devices more portable, the antennas are required to be very small, as antennas are very essential part of the wireless communication systems. Microstrip printed antennas are widely used in those portable wireless communication devices like portable cell phones, laptops etc., due to its remarkable features which includes light weight, compact, easy to fabrication capabilities with microwave circuits, low fabrication cost, conformal etc. [1, 2]

The conventional microstrip patch antennas have different shapes like rectangular, square, circular, hexagonal etc., which radiates at single frequency depending on the electrical length on the patch. Several techniques have been used by the researchers to decrease the resonant frequency among which cutting the slots on the patch may be

N. Dey · A. Dhakal · A. Das · L. M. Devi · S. Bhunia (✉)
Central Institute of Technology, BTAD, Kokarajhar, Assam, India
e-mail: s.bhunia@cit.ac.in

B. Sikdar et al. (eds.), *Proceedings of the 3rd International Conference on Communication, Devices and Computing*, Lecture Notes in Electrical Engineering 851,
https://doi.org/10.1007/978-981-16-9154-6_65

considered as most simple and mostly used in some research articles. The different slots patterns present on the patch surface disturb the surface electrical current distribution and mostly lengthen the electrical current path and thus the resonant frequency has been decreased. Many research articles have presented different types of design techniques to achieve compact and reduced size microstrip antennas [3–10]. Bhunia et al. [3, 4] has designed compact rectangular microstrip patch antennas using some rectangular slots on the patch with the size reduction of 85 and 67%. Miniaturization of microstrip patch antennas has also been obtained by etching the different shapes of slots on the infinite or finite ground plane, use of spur lines on the radiating upper patch etc. [5–9]. In the article [10], it has been presented that the notches in the opposite non-radiating edges affect more on resonant frequency than the notches in the same non-radiating side or edge of a microstrip patch antenna.

In this article, a design of a square root-shaped slotted rectangular microstrip printed small compact antenna has been presented. The antenna structure has been simulated in commercially available software IE3D. The radiating frequency of the proposed antenna has been observed as 2.89 GHz and simulated maximum gain has been obtained as 2 dBi. After comparison with the regular shaped microstrip antenna radiated at 2.89 GHz, the miniaturization of the proposed and designed antenna has been calculated as 76.66%.

2 Antenna Design

The overall size of the radiating copper patch in the reference rectangle-shaped microstrip printed antenna has been considered as 18×14 mm^2; consider the rectangular ground back plane having dimension of almost three times bigger than the radiating element to gain the requirement of infinite back plane. The total radiator has been designed on Arlon Epoxy substrate with dielectric constant $\varepsilon_r = 3$ and thickness $h = 1.524$mm. The coaxial cable has been used for feeding to the antenna at optimum location. The antenna taken as a reference structure is depicted in Fig. 1.

To lengthen the surface electrical path on the upper radiator, a square root-shaped slot has been introduced on the upper surface. The designed and presented antenna structure along with all the dimensions of the slot on patch has been given in Fig. 2. The back plane size has been remained same as the reference antenna and the feeding with coax cable has been used at optimum location (from top 0.1 mm and from right edge 0.8 mm) to achieve the desired result.

3 Simulated Data and Graph

The antennas taken as reference and modified configurations have been designed and simulated in IE3D simulator. The reference conventional antenna radiates at 5.7 GHz

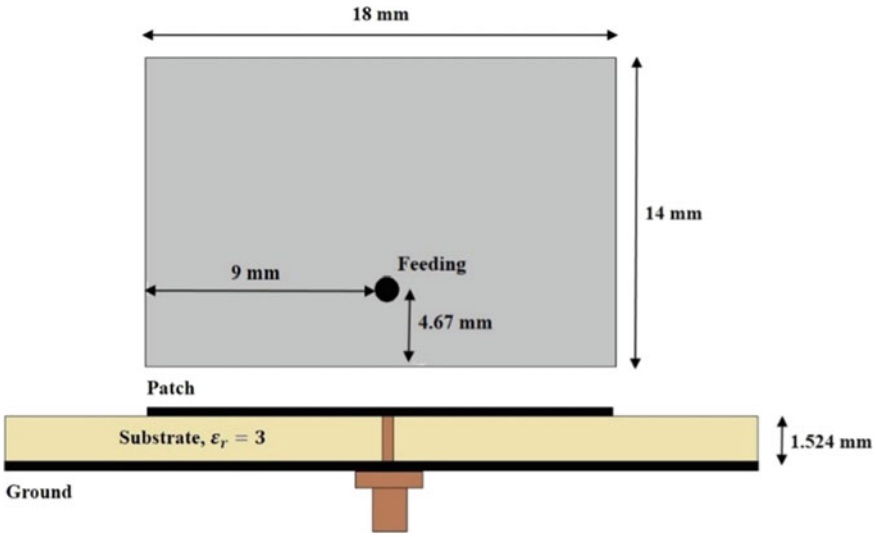

Fig. 1 Radiating element taken as reference structure

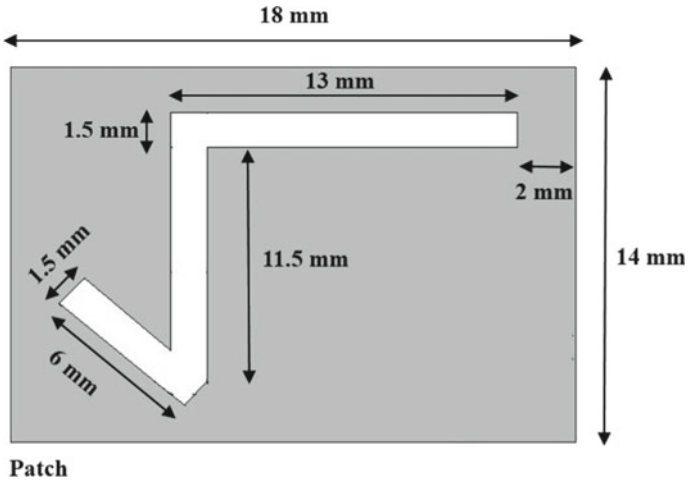

Fig. 2 Upper radiating element with square root slot

with 24 dB return loss. With square root slotted design, the proposed antenna radiates at 2.89 GHz with 28 dB return loss. The simulated results are shown in Table 1.

The simulated return loss versus operating frequencies graph of the conventional antenna for reference and proposed antenna are illustrated in Figs. 3 and 4, respectively. The frequency vs. gain graph of the proposed antenna is shown in Fig. 5, and normalized radiation patterns of the reference antenna at 5.7 GHz and proposed antenna at 2.89 GHz are depicted in Figs. 6 and 7.

Table 1 Simulated results of reference and proposed antenna

Antenna	Resonating frequencies (GHz)	Return Losses (dB)	Bandwidth in (MHz, %)	Peak Gain in (dBi)
Conventional reference	5.7	24	182, 3.2	4.6
Modified and proposed	2.89	28	155, 5.5	2

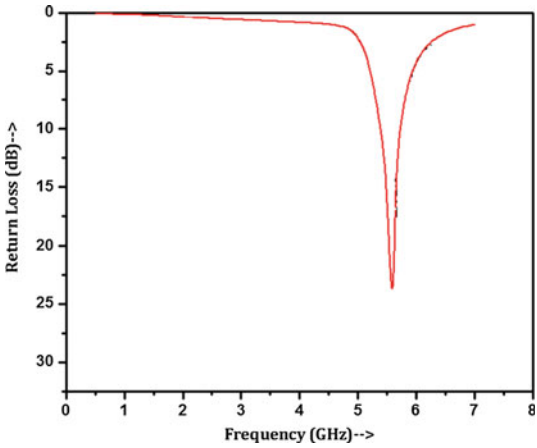

Fig. 3 Return loss versus operating frequencies graph of reference antenna

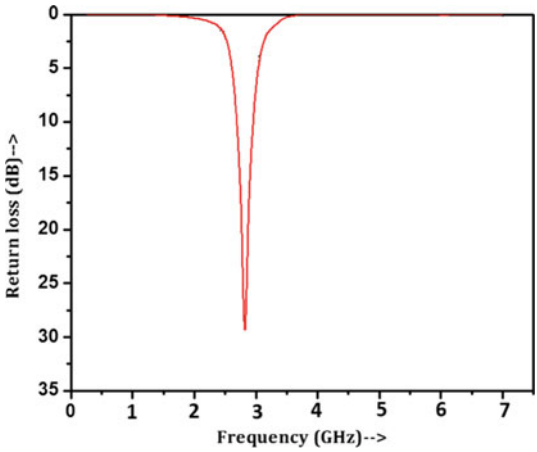

Fig. 4 Return loss versus operating frequencies graph of the modified antenna

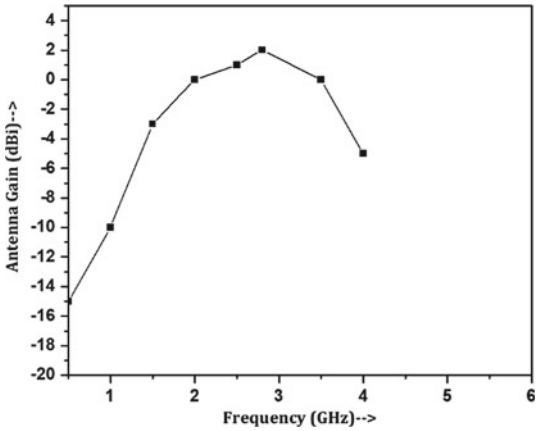

Fig. 5 Frequency versus antenna gain graph of the proposed antenna

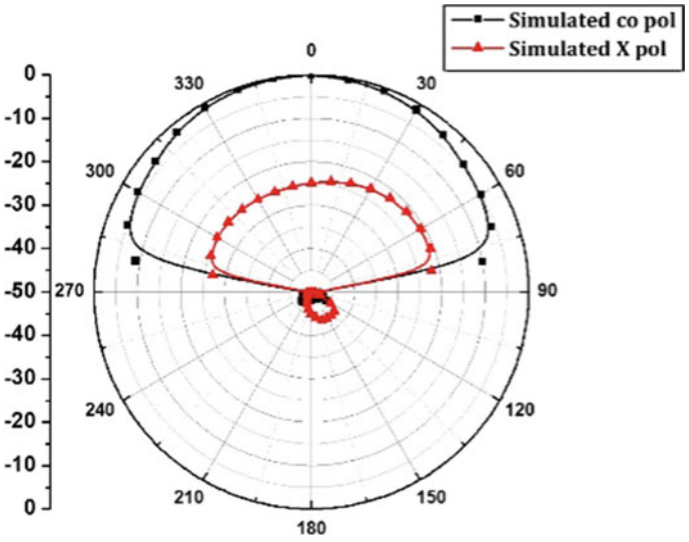

Fig. 6 Normalized radiation pattern of the reference antenna at 5.7 GHz

4 Conclusion

A design of a square root-shaped slot loaded compact microstrip radiating antenna has been reported in this literature. By using the square root-shaped slot on the upper radiating element, the surface electrical path length has been increased and thus the resonating frequency has been lowered. The proposed antenna resonates at 2.89 GHz and comparing with the conventional antenna, 76.66% compact miniaturization has

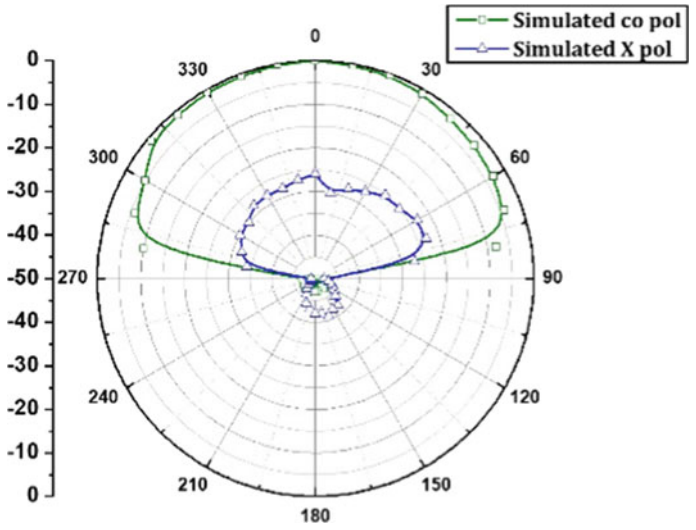

Fig. 7 Normalized radiation pattern of the proposed antenna at 2.89 GHz

been found. The peak gain of the designed antenna has been observed as 2 dBi. The antennas have been designed and simulated in IE3D simulator.

References

1. Wong, K. L.: Planer Antennas for Wireless Communications. Wiley (2003)
2. Chen, Z. N.: Antennas for Portable Devices. Wiley (2007)
3. Bhunia, S., Sarkar, D., Biswas, S., Sarkar, P.P., Gupta, B., Yasumoto, K.: Reduced size small dual and multi-frequency microstrip antenna. Microw. Opt. Technol. Lett. **50**, 961–965 (2008)
4. Bhunia, S., Sarkar, P.P.: Reduced sized dual frequency microstrip antenna. Indian J. Phys. **83**, 1–5 (2009)
5. Chatterjee, S., Chowdhury, S.K., Sarkar, P.P., Sarkar, D.C.: Compact microstrip patch antenna for microwave communication. Indian J. Pure Appl. Phys. **51**, 800–807 (2013)
6. Sarkar, S., Das, M.A., Mondal, S., Biswas, S., Sarkar, D., Sarkar, P.P.: Miniaturization of rectangular microstrip patch antenna using optimized single-slotted ground plane. Microw. Opt. Technol. Lett. **53**, 111–115 (2011)
7. Chakraborty, U., Kundu, A., Chowdhury, S. K., Bhattacharjee, A. K.: Compact Dual-Band Microstrip Antenna for IEEE 802.11a WLAN Application, *IEEE Antennas and Wireless Propag. Lett.*, **13** (2014), 407–410.
8. Roy, A., Bhunia, S., Sarkar, D. Chanda, Sarkar, P.P., Chowdhury, S.K.: Compact multi frequency strip loaded microstrip patch antenna with spur lines. Int. J. Microw. Wirel. Technol. **9**, 1111–1121 (2016)
9. Roy, A., Bhunia, S., Sarkar, D. Chanda, Sarkar, P.P.: Slot loaded compact microstrip patch antenna for dual band operation. Prog. Electromagn. Res. C (PIER C), **73,** 145–156 (2017)
10. Bhunia, S., Roy, A., Sarkar, D. Chanda, Sarkar, P.P.: Effects of two identical notches in the same and opposite non radiating edges of a rectangular microstrip patch antenna. Int. J. Signal Proces. Image Process. Patt. Recogn. **11**, 15–28 (2018)

Design of Compact Microstrip Patch Antenna Introducing V-Shaped Slot in the Patch

Akash Dhakal, Nikita Dey, Ashim Das, Laishram Manali Devi, and Sunandan Bhunia

Abstract In this article, a single-layer mono-feed compact rectangular-shape microstrip antenna has been proposed. The resonant frequency of the antenna has been minimized by introducing an inverted V-shaped slot on the metallic radiating patch. The size of the antenna has been scaled down by 72% in comparison with the conventional microstrip rectangular patch antenna. The proposed antenna characteristics have been studied using the IE3D electromagnetic solver. The analysis of the return loss, gain, and radiation properties has been reported in this paper. The proposed antenna operates at 3.18 GHz which will be useful for S-band radiolocation application. The simulated reflection coefficient at resonant frequency has been observed as 22.75 dB. The proposed antenna possess a gain of 2.05 dBi.

Keywords Slotted patch · Compact · Microstrip patch antenna · IE3D

1 Introduction

Recent communication devices are noticeably reduced in terms of size. Mostly, consumers are looking for compact, lightweight, handheld devices. In space communication and military applications, miniaturized devices are also in priority. In IoT applications, several devices are communicating simultaneously during mobility. All these must have an antenna with having desired properties that will mitigate the technological demand. Microstrip antenna is one of the prominent choices due to its several advantages like low profile, conformal, easy to fabricate, and low cost. The concept of size reduction of the conventional microstrip antenna is a challenging task. Many researchers have been proposed various techniques to miniaturize the dimension of the antenna.

The concept of decreasing the size of the antenna is linked to the reduction of the resonance frequency of the conventional type [1]. Different mechanisms have been identified and reported. These include etching of slots on the radiating metallic

A. Dhakal · N. Dey · A. Das · L. M. Devi · S. Bhunia (✉)
Central Institute of Technology, BTAD, Kokarajhar, Assam, India
e-mail: s.bhunia@cit.ac.in

B. Sikdar et al. (eds.), *Proceedings of the 3rd International Conference on Communication, Devices and Computing*, Lecture Notes in Electrical Engineering 851,
https://doi.org/10.1007/978-981-16-9154-6_66

layer [2–4], slotted or defected ground plane [5–7], shorting pin-loaded antenna [8], dielectric resonator antenna [9], and fractal antenna [10]. Among the mentioned techniques, cutting slots on radiating metallic layer and ground plane are the simplest. They are easy to fabricate and integrate with the systems. Defected ground structure affects the overall gain and bandwidth performance of the antenna. Hence, this method is not well accepted. The slots on the radiating patch will be a suitable option. This method results in good gain-bandwidth performance and better return loss.

The proposed work represents the miniaturization of a rectangular microstrip antenna. In this work, the conventional rectangular patch has been modified by removing the metal in a particular geometric manner which results in an inverted V-shaped slot on the patch. The optimized dimension has been applied to achieve the desired performance to apply this antenna for S-band geo-location application. The proposed structure provides resonance at 3.18 GHz. The antenna has been designed, and the characteristics have been observed through the simulation using electromagnetic solver IE3D. The gain response, return loss, and radiation attributes have been documented in the following sections.

2 Antenna Design and Geometry

The structure of the reference and proposed antenna has been depicted in Fig. 1 and Fig. 2, respectively. Arlon AD300 of having dielectric constant $\varepsilon_r = 3$ has been chosen as the dielectric material for the designing of the antenna. The height

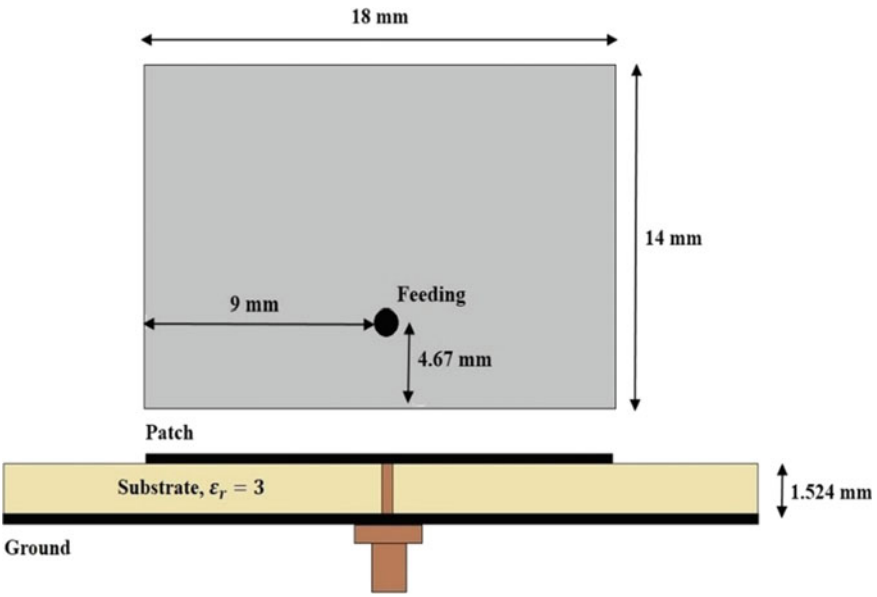

Fig. 1 Structure of the reference antenna

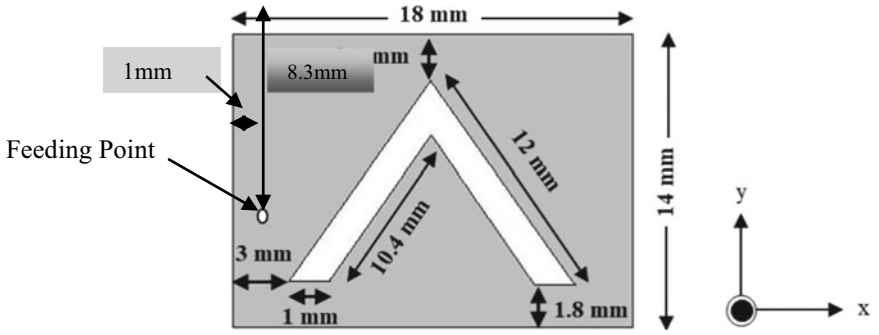

Fig. 2 Structure of the proposed antenna

of the dielectric material is 1.524 mm and having loss tangent value of 0.002. The dimension of the antenna has been figured out by employing the transmission line method [1]. The width and the length of the rectangular patch have been calculated by using the available standard expressions [1].

3 Results and Discussion

The optimum dimension of the proposed antenna has been realized by simulating the structure using an electromagnetic solver IE3D. The reflection coefficient of the reference antenna and the proposed antenna has been depicted in Fig. 3. Initially, without the slot on the patch, the antenna has a resonance frequency of 5.56 GHz. Further, after implementing the inverted V-shape slot on the patch, the resonance frequency has been reduced to 3.18 GHz. The reduction in resonant frequency is due to the extension of the path of surface current flowing through the patch. The proposed antenna has a gain of 2.05 dB with omnidirectional radiation characteristics. The simulated gain of the proposed antenna has been displayed in Fig. 4. The E-plane co-polarization and cross polarization radiation characteristics for both reference and proposed antenna have been displayed in Fig. 5.

4 Conclusion

In this article, a compact microstrip antenna utilizing the slot on the radiating patch has been designed and presented. An electromagnetic solver IE3D has been used to design the proposed structure. The reduction on the resonance frequency of the antenna has been achieved by introducing an inverted V-shaped slot on the radiating patch. The resultant compactness has been calculated as 72% as compared to

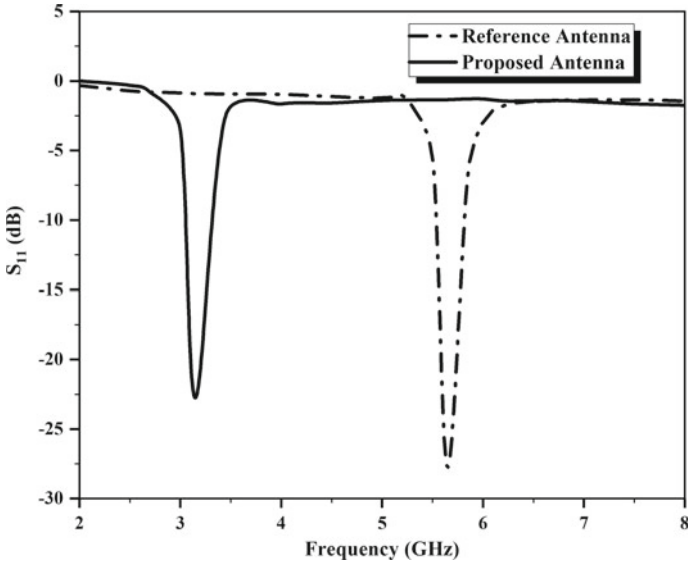

Fig. 3 Reflection coefficient of the reference and proposed antenna

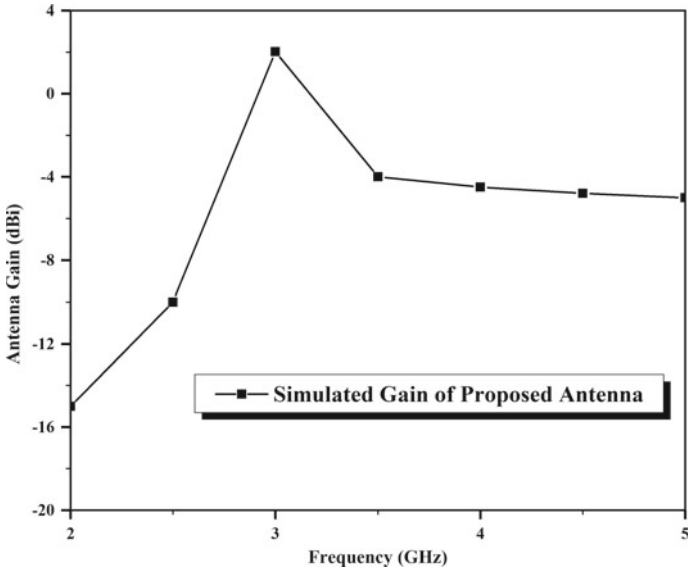

Fig. 4 Simulated gain of the proposed antenna

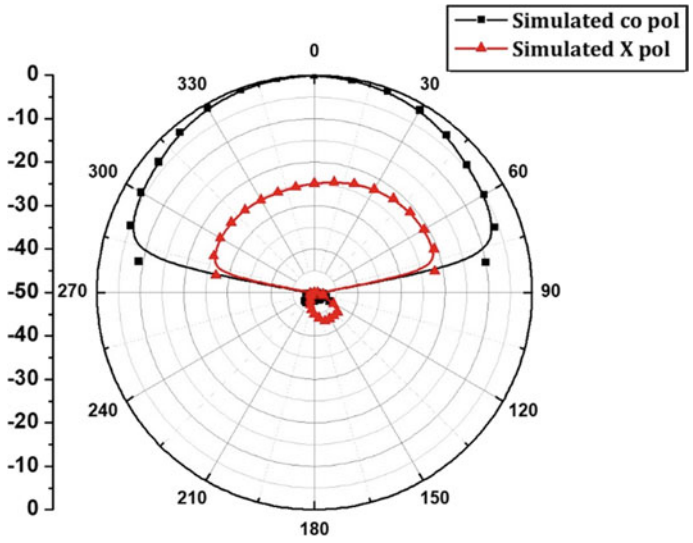

(a)

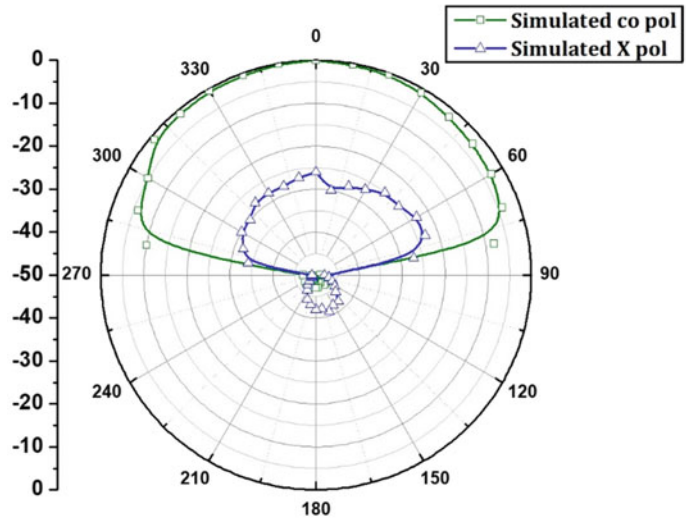

(b)

Fig. 5 Radiation pattern of the reference antenna **a** and Proposed antenna **b**

the reference antenna. The proposed antenna has gain of 2.05 dBi with the reflection coefficient value of 22.75 dB. The operating center frequency of the proposed design is obtained as 3.18 GHz. The antenna will be useful for S-band radiolocation application.

References

1. Garg, R., Bhartia, P., Bahl, I., Ittipiboon, A.: Microstrip Antenna Design Handbook. Artech House Publishers, Boston, London (2001)
2. Bhunia, S., Sarkar, D., Biswas, S., Sarkar, P.P., Gupta, B., Yasumoto, K.: Reduced size small dual and multi-frequency microstrip antenna. Microw. Opt. Technol. Lett. **50**, 961–965 (2008)
3. Bhunia, S., Sarkar, P.P.: Reduced sized dual frequency microstrip antenna. Indian J. Phys. **83**, 1–5 (2009)
4. Chatterjee, S., Chowdhury, S.K., Sarkar, P.P., Sarkar, D.C.: Compact microstrip patch antenna for microwave communication. Indian J. Pure Appl. Phys. **51,** 800–807 (2013)
5. Sarkar, S., Das, M.A., Mondal, S., Biswas, S., Sarkar, D., Sarkar, P.P.: Miniaturization of rectangular microstrip patch antenna using optimized single-slotted ground plane. Microw. Opt. Technol. Lett., **53**, 111–115 (2011)
6. Mukherjee, S., Roy, A., Bhunia, S., Sarkar, D.C., Sarkar, P.P.: Compact multi frequency microstrip antenna with enhanced gain using multiple U-shaped slotted modified ground plane. In: Intelligent Techniques and Applications in Science and Technology. ICIMSAT 2019. Learning and Analytics in Intelligent Systems, vol. 12. Springer. (2020)
7. Roy, A., Mukherjee, S., Bhunia, S.: Design of modified grounded microstrip antenna for dual band operation in wireless communication. IEEE VLSI Device Circ. Syst. (VLSI DCS) **2020**, 263–266 (2020)
8. Luan, X., Fang, S., Tan, K.: Analysis and optimization design of compact microstrip patch antennas loaded with shorting pins. In: IWAT 2005 IEEE International Workshop on Antenna Technology: Small Antennas and Novel Metamaterials, pp. 529–533 (2005)
9. Petosa, A., Ittipiboon, A.: Dielectric resonator antennas: a historical review and the current state of the art. IEEE Antennas Propag. Mag. **52**, 91–116 (2010)
10. Gianvittorrio, J.P., Rahmat-Samii, Y.: Fractal antennas: a novel antenna miniaturization technique and applications. IEEE Antennas Propag. Mag. **44**, 20–36 (2002)

Performance Analysis of a Solar Power Plant

Danyal Rizvi, Roopa Manjunatha, Niranjan Polai, and Debasis De

Abstract Solar photovoltaic (PV) system has the versatility and flexibility for developing off-grid as well as on-grid residential solar systems but the performance of the system over the time is always a concern. Performance analysis is a measure to study the existing output with the help of certain parameters. For this project, a 10 kW on-grid solar PV system situated on the rooftop of Accrete Electromech private limited has been taken into consideration, located in Waluj Aurangabad, Maharashtra, India. Performance analysis of the solar PV setup has been performed with the site loggers data during the year 2017. 30 solar PV modules (Trinia solar, 320 Wpeak) are placed with 15 each connected in series making one string, two such strings are connected to a dual maximum power point tracker (MPPT) inverter (Fronius symo, 10 kW). Analysis was performed on various parameters including performance ratio, capacity utilization factor, inverter efficiency, total loss, weather conditions, and energy supplied to grid. Average module efficiency, performance ratio (PR), and capacity utilization factor were 11.614%, 56.6%, and 12.5%, respectively. Correlation values for: (i) PR and total loss were 0.82, (ii) output array power and humidity were 0.71.

Keywords Solar photovoltaic · On-grid solar power plant · Performance analysis · Efficiency of plant

1 Introduction

Indian government has planned to install around 20 GW on-grid solar power plant by 2022 [1]. Installed grid connected non-conventional energy generation capacity in India stands at 77.6 GW, which is 22% of the total installed generation base in India. As on March 2019, non-conventional energy has 20% share in the installed generation capacity in India [2]. A performance analysis is required to effectively

D. Rizvi · R. Manjunatha · N. Polai · D. De (✉)
Energy Institute, Bengaluru (Centre of Rajiv Gandhi Institute of Petroleum Technology), Bengaluru, India
e-mail: debasisd@rgipt.ac.in

B. Sikdar et al. (eds.), *Proceedings of the 3rd International Conference on Communication, Devices and Computing*, Lecture Notes in Electrical Engineering 851,
https://doi.org/10.1007/978-981-16-9154-6_67

check the working of a solar PV system of a specific capacity so that its reliability in future can be maintained. The 10 kW on-grid PV system was installed on the rooftop of Accrete Electromech limited, Waluj Aurangabad, Maharashtra, India. Latitude and longitude of the location are as follows 19.48 and 75. 846. The system was installed in late 2016. Data of 2017 and 2018 have been collected by the Fronius Private Limited. Tilt angle was 25, and azimuth was zero in this site viewed in Fig. 1.

Solar irradiance varies from 4.09 to 7.10 (kWh/m^2/day) with the maximum irradiance in May 2017. Maximum humidity (88%) occurred in July 2017 due to the rainy overcast weather, and maximum wind speed was observed in the month of June. The meteorological observed data are given in Table 1. Tables 2 and 3 show the solar panel specifications and inverter specifications use in the plant.

A model representation of the plant is given in Fig. 2. Two strings are present and each string comprises of 15 solar modules connected in series. Each of the string generates (15 * 320 W_{peak}) power, such that two strings are connected to a

Fig. 1 Plant site view

Table 1 Meteorological observation of the site

Month	Ambient temperature (°C)	Humidity (%)	Solar irradiance (kWh/m^2/day)	Weather	Wind speed (km/h)
April	40	15	6.74	Sunny	6
May	40	48	7.10	Partly sunny	9
June	34	56	5.352	Partly sunny	15
July	27	88	4.09	Rainy, overcast	11
August	30	70	4.13	Partly sunny	9
September	30	66	4.89	Overcast	6
October	23	76	5.287	Haze	6
November	39	40	4.52	Sunny	7
December	28	48	4.41	Passing clouds	4
January	29	27	4.69	Sunny	11
February	30	35	5.10	Passing clouds	9
March	36	19	6.40	Scattered	9

Table 2 Solar panel specifications used in the plant

Electrical data STC	
Peak power watts-PMAX (W_p)*	320
Power output tolerance-PMAX (W)	0~+5
Maximum power voltage-VMPP (V)	37.1
Maximum power current-IMPP (A)	8.63
Open circuit voltage-V_{OC} (V)	45.5
Short circuit current-I_{SC} (A)	9.15
Module efficiency n (%)	16.5
Mechanical specifications	
Solar cells	Multicrystalline 156 × 156 mm (6 inches)
Cell orientation	156.75 × 156.75 mm (6 inches), 72 cells (6 × 12)
Module dimensions	1960 × 992 × 40 mm (77.2 × 39.1 × 1.57 in.)
Weight	22.5 kg (49.6 lb)
Glass	3.2 mm (0.13 inches), AR coated tempered glass
Backsheet	White

Table 3 Inverter specifications used in the plant

Number of MPP trackers	2
Max input current ($I_{dc\ max}$)	27.0/16.5
Max. short circuit current, module array	40.5/24.8 A
DC input voltage range ($V_{dc\ min} - V_{dc\ max}$)	200–1000 V
Feed-in start voltage ($V_{dc\ start}$)	200 V
Nominal input voltage ($V_{dc,r}$)	600 V
MPP voltage range ($V_{mpp\ min} - V_{mpp\ max}$)	270–800 V
Usable MPP voltage range	200–800 V
Number of DC connections	3 + 3
Max. PV generator power ($P_{dc\ max}$)	15 kW_{peak}

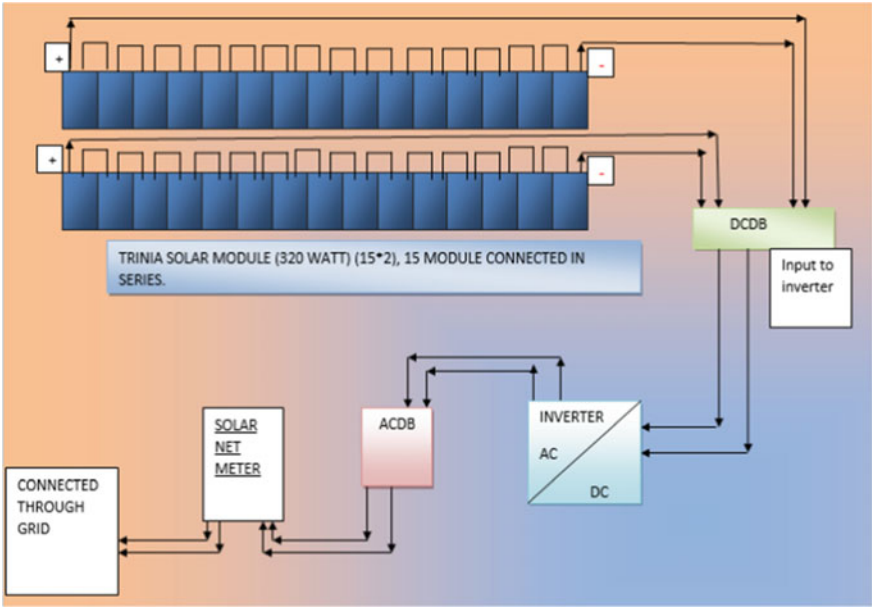

Fig. 2 Model representation of the PV

dual maximum power point tracking (MPPT) inverter with a rated input capacity of 10 kW. One string provides power of 4.8 kW, so the total DC power going into inverter input from solar array is 9.6 kW which is less than the inverter max input capacity. Array junction box (AJB) also known as direct current distribution box (DCDB), component of an electricity supply system which divides an electrical power feed into subordinate circuits, it also provides circuit breaker and a protective fuse for every circuit. DC power coming from array is handled by AJB. Surge protection devices along with fuse are installed to protect the solar panel string as well as other components from any sort of hazard. The alternative current distribution box (ACDB) collects AC power coming from the solar inverter and directs it toward the load via distribution box and it comprises of surge protection devices as well as molded case circuit breakers to provide protection against overload. Inverter used has dual MPPT tracking system where each string is connected to a particular MPPT of the inverter.

1.1 System Parameters

Array yield describes the DC power generated by the PV setup with respect to its rated power capacity in the form of day, month, or year [1].

$$Y_A = \frac{E_{\text{dc}}}{P_{\text{pv,rated}}}, Y_{A,d} = \frac{E_{\text{dc},d}}{P_{\text{pv,rated}}} \tag{1}$$

where

E_{dc} is the DC power output from solar array (E_{dc} is in kWh/day).
The daily array yield ($Y_{A,D}$) and daily final yield ($Y_{f,D}$) in $\frac{h}{d}$.
monthly average daily array yield ($Y_{A,M}$) and monthly array yield ($Y_{f,M}$) in $\frac{h}{d}$.

Final yield: It basically tells about the actual output we get with respect to the total capacity of the plant, it can be calculated on daily basis as well as on monthly and yearly basis, according to the need. This is a comparative parameter that allows comparison of comparable PV systems during a specific geographical region. It is captivated with the kind of mounting, inclination on a roof, and conjointly on the situation [3].

$$Y_{f,D} = \frac{E_{\text{ac},d}}{P_{\text{pv,rated}}}, \text{and } Y_{f,M} = \frac{1}{N}\sum_{d=1}^{N} Y_{f,D} \tag{2}$$

Reference yield: The reference yield is the summation of solar irradiance at a specific place with respect to its area, H_t, (kWh/m^2) divided by the array reference irradiance (1 kW/m^2). It is the number of peak sun-hours and is given by [1]

$$Y_R = \frac{H_t}{B}, \text{ where } B \text{ is } 1\left(\frac{\text{kW}}{\text{m}^2}\right) \tag{3}$$

where H_t (total in plane solar insolation) is in $\frac{\text{kWh}}{\text{m}^2}$.

PV Module Efficiency: The instantaneous PV module conversion efficiency is calculated as

$$n_{\text{pv}} = \frac{E_{\text{dc}}}{H_t \times A_m} \times 100, \tag{4}$$

where E_{dc} is in (kWh), A_m (area of module) is in m^2.

Module Temperature:

$$T = T_{\text{ambient}} + C \times H_t \tag{5}$$

C is a constant representing $\frac{(\text{NOCT}-\text{Tstc})}{A}$, NOCT is nominal operating cell temperature [4] was

$$A \text{ is } 800\frac{\text{kWh}}{\text{m}^2} \tag{6}$$

Daily inverter efficiency is calculated as

$$n_{\text{inv}}\left(\frac{E_{\text{ac},d}}{E_{\text{dc},d}}\right) \times 100 \tag{7}$$

System efficiency [3, 5] **is calculated as**

$$n_{\text{sys},}\left(\frac{E_{\text{ac},d}}{H_t \times A_m}\right) \times 100 \tag{8}$$

$$n_{\text{sys},} = n_{\text{pv}} \times n_{\text{inv}} \tag{9}$$

The capacity factor (CF):

Capacity factor is an important aspect which tells the user about the generation capacity of its solar power setup with respect to its optimum working capacity.

The demonstration of CF as per reference [1] shows that the PV plant has worked upon its maximum capacity for the given month or year, similarly if CF for the month becomes 0.5, it shows that PV plant is working on half of its rated capacity for the given month or year. In the denominator, we assume the ideal condition that the plant works on its rated capacity for the given month/year for 24 h a day [1, 3].

$$\text{CF} = \frac{E_{\text{ac}}(\text{annual})}{P_{\text{pv(rated)}\times 24\times 365}} \tag{10}$$

Losses occurred in the system (inverter):

Thermal capture loss and effect of cell temperature on loss—power generation in solar pv module is inversely proportional to the cell temperature as when temperature of the solar PV cell exceeds more than 25, its power generating capacity gets decreased by a factor mentioned in the solar panel data sheet. Instantaneous power loss corresponds to the difference between ideal and actual power generation at 25 °C. The losses in inverters are due to various reasons like due to DC voltage, frequency, and the noise that are generated in the system also leads to losses in inverter, and the range goes from 7 to 38% [6].

Capture losses are also evident in a solar PV system and are represented as.

$$L_c = Y_r - Y_a \quad [3] \tag{11}$$

where Y_r represents reference yield and Y_a is array yield

$$\text{Total losses} = L_c + L_s \tag{12}$$

Performance Ratio:

Performance ratio tells about the losses occurred in a system, losses can be in the inverter or in the wirings connecting the entire system. Performance ratio varies inversely to losses occurred in the system. It has no relation to array output power generation. A system can have high array output with a low performance ratio which system is going through enough losses [3].

$$\mathrm{PR} = Y_f / Y_R \tag{13}$$

2 Methodology

Average monthly data have been collected from data loggers ID, and an excel file has been made, the same excel file been imported to "Python Jupyter notebook" and libraries were installed in the same for reading the file as well for calculation. Libraries installed include "pandas" which helps for reading the data set in Python as well as for making the new data frames. "Matplot lib" has been installed for making graphs and visualization. "NumPy" has been installed to do mathematical calculation. Figure 3 shows the importing libraries in the Python from Jupyter notebook database.

3 Results and Discussion

The following results have been obtained after the analysis:

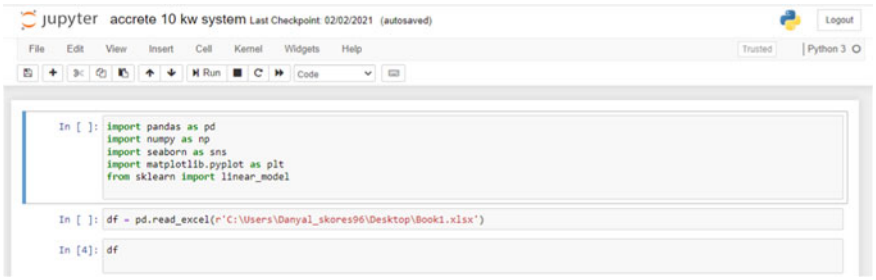

Fig. 3 Importing libraries in Python from Jupyter notebook database

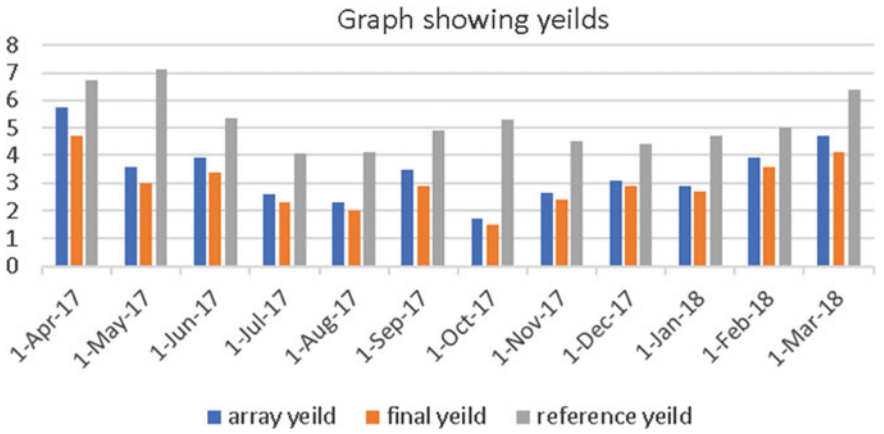

Fig. 4 Monthly average yield of installed solar photovoltaic system

3.1 Inverter Efficiency and System Efficiency

The annual monthly average of the inverter and system efficiency was 88.717% and 10.28%, respectively. This system generated a 10.28% system efficiency which is considerably better than most of the present systems here as the variation we see in system efficiencies in India ranges from 8.52 to 9.77%, the mean inverter efficiency is 90.54% with respect to its rated capacity, and the module power generation shows a effectiveness of around 70.23% with respect to optimum producing capacity.

3.2 Results for the Yields

The final yield, reference yield, and array yield generated were found to be 2.9583, 5.22, and 3.377 kWh/kWp/day, respectively. The highest final yield of 4.7 kWh/kWp/day was observed during April 2017 as depicted in the graph of Fig. 4. The graph shows the variation in yield values with respect to change in time interval (monthly basis).

3.3 Variation of Total Loss with Performance Ratio

Performance ratio is a factor which tells user about the total loss incurred the system and it has no relation to DC array power output, losses occurred can be due to loss in inverters or due to the loss occurred in cables. In Fig. 5, a graph is drawn taking the performance ratio, total loss, and time interval (in months). The red line indicates different performance ratios, and blue line indicates the total loss. After plotting,

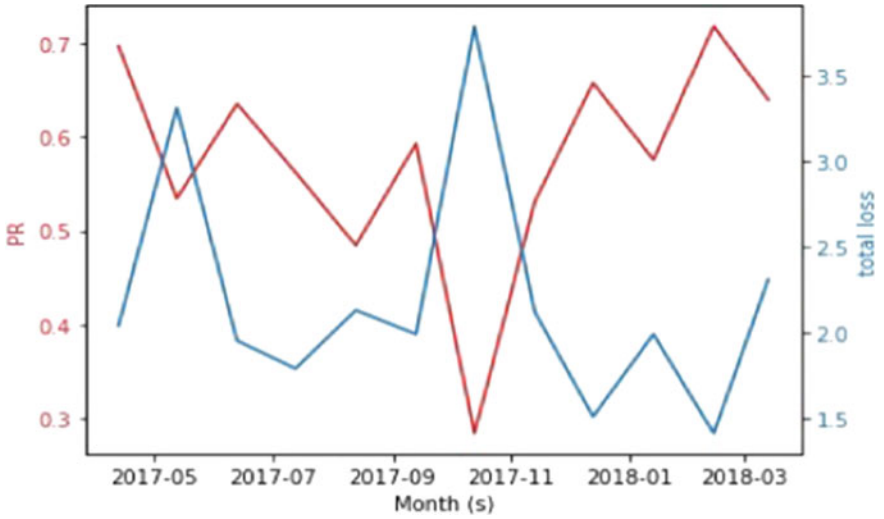

Fig. 5 Variation of performance ratio of the solar photovoltaic system with total loss occurred

the total loss was found to be maximum in the month of October (3.787), and as it is inversely proportional to performance ratio, therefore, the minimum performance ratio was also found to be in the same month (0.283) or 28.3%, while minimum total loss (1.41) and maximum performance ratio (71.85) were observed in the month of Feb 2018.

3.4 Variation of Array Power Output with Respect to Humidity

Humidity plays a major role in altering DC power produced from the arrays, humidity generates moisture in the form of water droplets upon the panels which, therefore, shows refraction and absorption of incident solar irradiance on the solar module as a result decreasing the array power output [7].

A plot is made between output power, humidity, and time interval. The bar graph shows the output power, and the line graph shows the changes in humidity. Humidity was found to be minimum in the month of April (03/2018), and power generated was maximum in that period. Decrement has been observed in the array output in the months of July (07/2017) and August (08/2017) when the humidity was at its peak (Fig. 6).

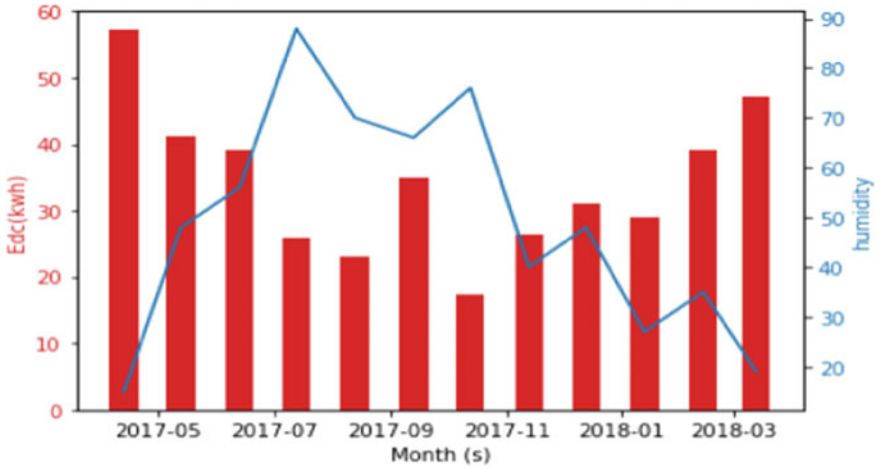

Fig. 6 Variation of array output power of solar photovoltaic system with humidity

3.5 Variation of Array Power Output with Cell Temperature

Temperature increment reduces the bandgap of the structure which in turn increases the short circuit current. Increase in cell temperature reduces open circuit voltage but increases short circuit current slightly. But increment in short circuit current does not balances the decrement in open circuit voltage, as a result, overall power decreases with increase in cell temperature. Although cell temperature is high in the month of April but due to the high irradiance value in April 2017, E_{DC} value is high. Trend from June to December 2017 shows a significant decrement in the array power output with increase in cell temperature (Fig. 7).

4 Conclusions

The conclusions are drawn from the performance analysis, and the results obtained after calculation by taking system parameters as the basics. The parameters include temperature, humidity, and wind speed. As the humidity increases, it was found that the array power gets decreased. Similar is the case with temperature also, when the cell temperature rises the overall power decreases. Again, the system efficiency of the plant and capacity utilization factor was found to be 10.38% and 12.5%, respectively. The mean module efficiency was 70.30% of its rated efficiency while the inverter efficiency 88.71% which is 90.52% of its rated efficiency. This shows that the PV power plant taken is running efficiently and effectively as of present world scenario but lot of research is still required in this field so that we can extract more power and hence techniques like performance analysis is a must to learn about our power

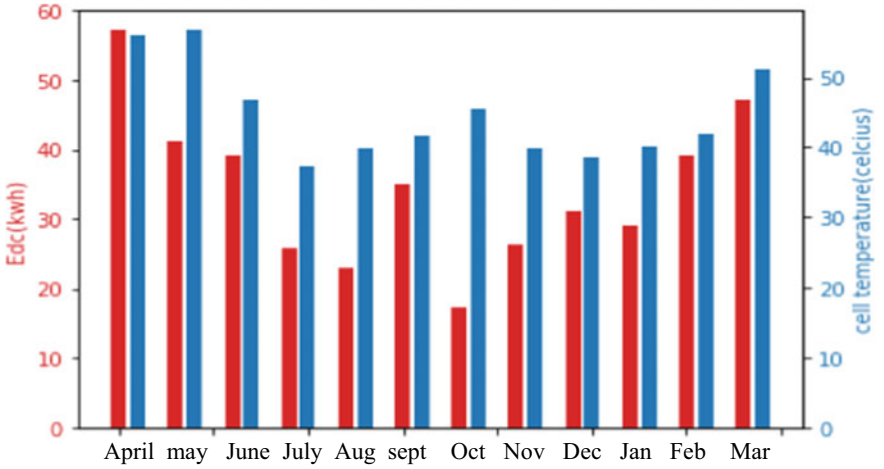

Fig. 7 Variation of array output power with cell temperature

plant better. Also, the average performance ratio of the system was found to 56.6% which indicates high losses in the system which requires proper maintenance of the system.

References

1. Niti Ayog, India action plan report: https://niti.gov.in/writereaddata/files/coop/IndiaActionPlan. Accessed on 23 Apr 2017
2. Renew power limited: https://links.sgx.com/FileOpen/ReNew%20Power%20Limited%20-%20OM%20-%20Sept%205,%202019.ashx?App=Prospectus&FileID=39793. Accessed on 5 Sept 2019
3. Ayompe, L.M., Duffy, A., McCormack, S.J., Conlon, M.: Measured performance of a 1.72 kW rooftop grid connected photovoltaic system in Ireland. Energy Convers. Manage. **52,** 816–825 (2011)
4. Drif, M., Pérez, P.J., Aguilera, J., Almonacid, G., Gomez, P., De la Casa, J., Aguilar, J.D.: A grid connected photovoltaic system of at Jaén University. Overview and performance analysis. Sol. Energy Mater. Sol. Cells **91**, 670–683 (2007)
5. Vasisht, M.S., Srinivasan, J., Ramasesha, S.K.: Performance of solar photovoltaic installations: effect of seasonal variations. Sol. Energy **131**, 39–46 (2016)
6. Marion, B., Adelstein, J., Boyle, K., Hayden, H., Hammond, B., Fletcher, T., Rich, G.: Performance parameters for grid-connected PV systems. IEEE Photovoltaic Spec. Conf. **31**, 1601–1606 (2005)
7. Panjwani, M.K., Narejo, B.G.: Effect of humidity on the efficiency of solar cell (photovoltaic). Int. J. Eng. Res. Gen. Sci. **2**, 2091–2730 (2014)

Evaluation of Kernel-Level IoT Security and QoS Aware Models from an Empirical Perspective

Bharat S. Dhak and Prabhakar L. Ramteke

Abstract Internet of Things (IoT) based devices have proven to be highly useful during this pandemic. From home automation to industrial monitoring, these devices have become an integral part of day-to-day activities. Thus, it is essential that these devices must be highly secure and must possess high Quality of Service (QoS) performance. To integrate these optimizations to IoT devices, a wide variety of options are available; which include application-layer enhancements, network-level patches, and kernel-level modules. Out of these, application-layer enhancements are neither secure nor efficient when large-scale IoT devices are deployed, while network-level patches are focused toward fixing network performance, and have limited node-level enhancement capabilities. Moreover, kernel-level patches have high computational efficiency due to their proximity to IoT BIOS and can be used to trace both node-level and network-level parameters. Thus, in this text recent kernel-level security and QoS models are discussed, and their performance in terms of attack resilience, computational complexity, reaction delay, etc. is evaluated and compared. From the review, it is observed that various soft computing models can be used to further improve the QoS and security performance of IoT networks. These models include but are not limited to fuzzy logic models, neural network models, linear programming models, etc. This evaluation will assist network designers and researchers to select the best possible algorithms for their given network, thereby reducing the time and cost needed for optimum network design. Moreover, this text also recommends various improvements for the compared models, thereby assisting in further optimization of overall IoT performance.

Keywords IoT · Security · Kernel · Machine · Learning · QoS

Present Address:
B. S. Dhak (✉) · P. L. Ramteke
HVPM's College of Engineering and Technology, Amravati, Maharashtra, India

B. Sikdar et al. (eds.), *Proceedings of the 3rd International Conference on Communication, Devices and Computing*, Lecture Notes in Electrical Engineering 851,
https://doi.org/10.1007/978-981-16-9154-6_68

1 Introduction

The efficient design of IoT kernels is a multidomain task, that involves power management, sensing device design, design of security models, queueing modes, routing models, etc. The design of these interfaces must be done in a manner such that each of the components is seamlessly compatible with each other. Moreover, each of these components is designed and integrated such that Quality of Service (QoS) parameters like end-to-end delay, energy consumption, and routing load are reduced; while parameters like throughput, packet delivery ratio, and scalability are improved. It is also recommended that the designed IoT kernels must have high attack resilience, thereby making them secure for both large-scale and small-scale networks. An example of such a kernel which is based on the Barbara architecture model can be observed from Fig. 1, wherein standard Linux Kernel is combined with IoT drivers, industrial drivers, security layer, communication protocols, etc. in order to form an IoT specific kernel design. The Barbara model uses IoT drivers like WiFi, Ethernet, Bluetooth, LORA, etc. in order to communicate from device to device or to the cloud. This communication interface integrates security and routing components, wherein different encryption models, hashing models, routing models, and scalability models are integrated. The main aim of this layer is to securely communicate data between devices (or clouds) with high routing efficiency. This model is guided and accompanied by the industrial driver layer, wherein industry-specific communication protocols are implemented for short-range and long-range communication. This layer uses results from the security layer, wherein system integrity models, encryption models, monitoring and auto fixing models, permission management models, error management models, and certificate management models are designed. This

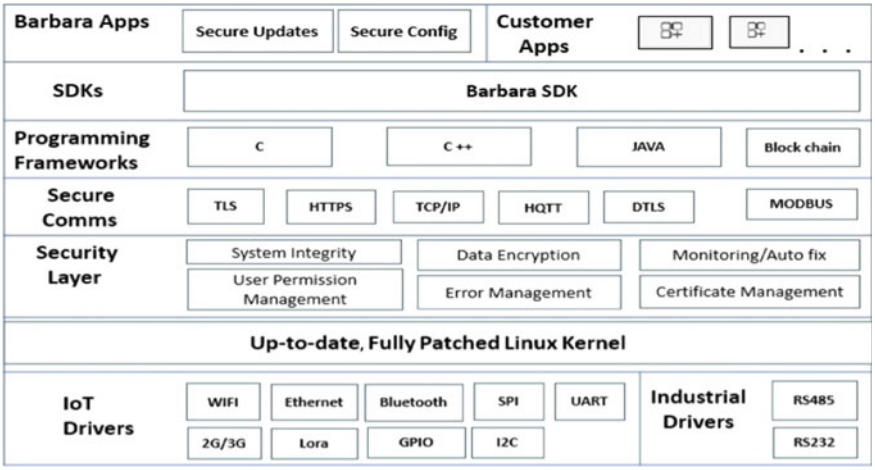

Fig. 1 Barbara IoT kernel model

layer takes its data from the secure communication layer, wherein standard device-to-device communication protocols are implemented. Finally, a programming frameworks layer is implemented, wherein application-specific models are programmed and stored onto the kernel. In this layer, various machine learning and optimization models are implemented for further improving QoS and security performance.

A large number of kernel-level implementations are available for IoT networks; thus, it becomes difficult for IoT designers to select and audit [1] the best possible combination of protocols to be used at the kernel level for optimum security and QoS performance. In order to resolve this ambiguity, the next section reviews some of the most recent and efficient IoT kernel implementations and evaluates their performance in terms of various security and QoS parameters. This is followed by an empirical comparison between these kernels, via which their strengths and weaknesses can be identified. Finally, this text concludes with some interesting observations about the reviewed models and recommends methods to improve their performance.

2 Literature Review

Securing IoT devices against internal and external attacks has become a crucial design aspect for IoT manufacturers. This has motivated kernel-level security upgrades, which make IoT devices resilient to application-level or network-level security issues. For instance, the work in [2] proposes a kernel-level Intrusion Detection System (IDS), wherein information from IoT kernels is used in order to detect attacks. The model uses parameters like resource usage, load capacity, swap space, etc. in order to perform pattern analysis via machine learning models. This allows the kernel to estimate pattern changes between normal and abnormal packets, thereby assisting in the identification of attacks with 95% accuracy. The system uses Message Queue Telemetry Transport (MQTT) broker as observed from Fig. 2, in order to transfer data from IoT kernel to IoT hub, wherein various machine learning models are deployed for intrusion detection. The data is stored on the hub for temporal analysis, wherein it assists in the accurate estimation of future attacks from other IoT nodes. Parameters

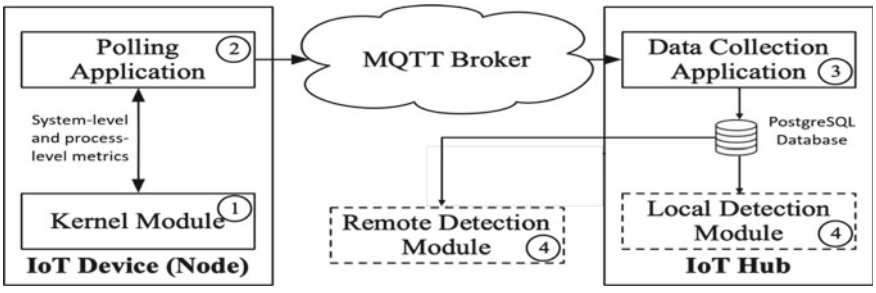

Fig. 2 Kernel-level parametric analysis for intrusion detection [2]

at the system level and process level are aggregated and processed using machine learning for pattern analysis. These parameters include number of logical CPUs, bandwidth of each machine, available RAM and swap memory, loads at different time instances, total running processes, physical and virtual memory used, total files opened, and other memory parameters. Attacks like network pivoting, exfiltration, black and grey hole, Distributed Denial of Service (DDoS), etc. are emulated on the network. The kernel model is able to remove most of these attacks with 100% accuracy. Only network pivoting and exfiltration attacks need further analysis, which can be done via the use of deep learning models.

These attacks can be further mitigated via the use of transport layer security (TLS), and Datagram TLS; which assist in establishing preliminary security models in the network. Implementation of these protocols at the kernel level can be observed from [3], wherein the Zephyr kernel is modified. TLS and DTLS provide security against DDoS and key exchange attacks, thereby making the network resilient to these external entities. This security performance can be further improved by the use of execution code analysis at kernel level as suggested in [4], wherein Binary Static Analysis (BSA) is used. The BSA model is applied along with fuzzy sandboxing, wherein each program is executed in a sandbox space; and its security performance is measured. In this model, the binary patterns are converted into blocks; and each block undergoes transition analysis for estimating data shift patterns. These patterns are combined with analysis of library functions used by the program in order to find inherent vulnerabilities. As a result of this, memory corruption attacks and application attacks are mitigated with high accuracy. This work is limited to Linux kernels, but can be extended to other kernels via efficient signature analysis and deep learning models.

Discovering backdoor attacks and verifying security protocols is also one of the most important aspects of IoT devices. The work in [5] proposes such a model, wherein a firmware vulnerability observer module is deployed at the kernel level. It is able to efficiently analyze reversing firmware binary attacks by 96%, password hijacking by 85%, and backdoor attacks by 94% using the shell script dependency checker module. The module analyzes the inter-dependency of different shell scripts and estimates their impact at the kernel level. Due to which any mismatch with normal working behavior is immediately flagged, and the program is filtered for further scrutiny. If the underlying program is injected with any kind of trapdoor, then its previous trace is scanned; and any changes made by it are reversed while preserving any important data files. This property of maintaining stored data, while mitigating malicious behavior enables the model to perform attack detection with high accuracy, thereby improving security performance. This performance can be further improved via the use of a separation kernel as suggested in [6], wherein each application on the IoT device is executed in its own micro kernel environment, thereby limiting its access to the whole device. This property allows the system to execute tasks with high efficiency, and block micro kernel which has been compromised. The micro kernel model is able to segregate internal execution layers into admin, virtual sensor, actuator, processing, and access control mini models. Each of these mini models is deployed for individual IoT devices, thereby limiting their data communication

capabilities with each other. This limits peer-to-peer communications (which can happen via IoT hub nodes under controlled conditions) but enables devices to have better security performance.

An application of micro kernel architecture can be observed from [7], wherein electric-powered vehicles are secured in terms of fault tolerance, permission access, trust establishment, and external attacks. This model can be further improved via the use of code analysis as proposed in [8], wherein binaries are decoded via the process of code disassembly. The model compares application-level algorithmic models with symbolic data in order to generate a control flow graph. This graph is annotated via disassembling process, and abstract syntax trees are generated. These trees are analyzed for any ambiguous patterns, and irregularities in terms of data access, code execution, memory access, etc. are estimated. Aggregation of these irregularities at the kernel level assists in improving system security performance. The model is able to provide an accuracy between 85 and 95% for various vulnerabilities on different IoT applications including Ardupilot, Marlin, Tmon, SmartPID, etc. A survey of these vulnerabilities can be observed from [9], wherein breaking of address space layout randomization (ASLR), kernel ALSR, keystroke timing, and covert channels are discussed. These vulnerabilities can be removed using secure sandboxes, wherein each program is executed in its own space, thereby limiting its attack probability. An example of such a model can be observed from [10], wherein a model for hardened memory data protection framework is discussed. The model uses a 5-step process for sandbox creation, which can be described as follows,

- For any request, protect the code pages via read-only model permissions.
- Create a secure sandbox by granting permissions which are analyzed via decoding application binaries.
- Execute the binaries on the sandbox.
- Check for any invalid access request, and block the application if these requests go beyond a certain threshold.
- Upon completion, disable the secure box, and remove code protection for normal execution.

These steps are executed on the hypervisor as observed from Fig. 3, thereby further limiting access control for the executing models.

The same hypervisor model can be applied for other security components at the kernel level as discussed in [11], wherein integrity enforcement, monitoring, and security management components are discussed. These components allow for secure updates, micro kernel operation, and sandboxed execution for improved efficiency. The model is tested on SylixOS, which is based on Linux Kernel, and is found to be effective against a large number of attacks which include DDoS, authentication prevention, spoofing, and spying with over 85% accuracy. This accuracy can be improved via the use of machine learning classifiers like support vector machines (SVM) as discussed in [12]. The proposed model is able to achieve over 97% accuracy for Block Node attack, Selective Forward attack, blackhole attack, sinkhole attack, sink in the middle attack, and DDoS attacks, but the model is computationally complex, and thus cannot be applied to low power IoT devices. A similar

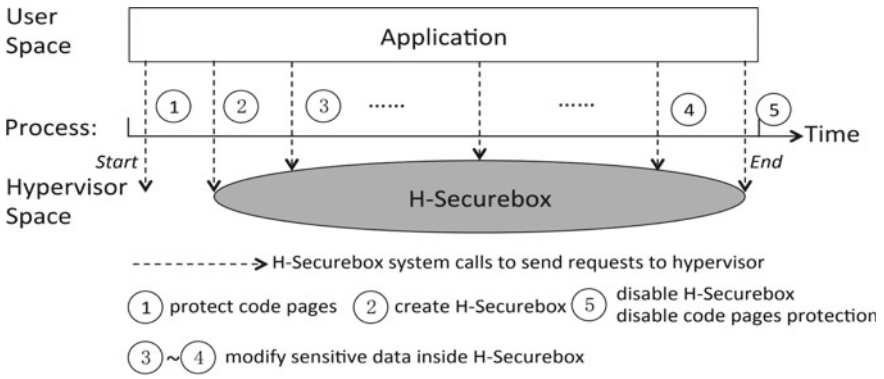

Fig. 3 Kernel-level-hypervisor-based sandboxes for enhanced security [10]

model can be observed from [13], wherein Intel Processor Trace (IPT) is used for kernel-level intrusion and malware analysis.

In order to strengthen kernel security, work in [14] proposes the use of Double Arbiter Physical Unclonable Functions (DAPuFs) for keyless data exchange. The main idea is to design separate functions for each IoT device, which cannot be cloned by machine learning attacks. Due to the use of DAPuF, the IoT kernels are able to seamlessly communicate data between each other, thereby improving security performance. An example of a double arbiter PuF can be observed in [14], wherein instead of one output, the system is able to generate two separate outputs, thereby assisting in the provision of a stronger security model which is difficult to crack. The model showcases 99.65% attack detection accuracy, which is higher than other security models, thereby the use of DAPuFs is encouraged during kernel design. The speed of DAPuFs is slow due to complex calculations, which can be improved via zero-cost system calls as suggested in [15], wherein an 11% improvement in speed is observed. An application of high-speed PuF design can be observed from [16], wherein session key security is improved via a universally composable framework. These identities assist in safeguarding the network against active and passive attacks, thereby improving overall system security.

A real-time implementation of a secure IoT kernel that uses traffic ontology for security analysis can be observed from [17], where the Chamel-IoT design is described. The design is capable of detecting various IoT attacks via kernel-level reconfiguration, thereby making it highly secure and scalable. This security performance can be further improved via the use of machine learning and blockchain architectures as described in [18], wherein threats like DDoS, Man-in-the-middle, Malware, Botnet, Sybil, Spoofing, Injection, and intrusion detection are discussed. These threats are accompanied by Data Privacy Attacks, like Eavesdropping, Impersonation, Sniffing, Authorization, Re-identification, Identity Theft, and Data Leakage. It is observed that deep learning models like convolutional neural networks (CNNs), long-short-term-memory (LSTM), Multi-Variate Correlation Analysis, Class-wise Information Gain, Deep Feature Embedding Learning,

online sequential extreme learning machine, Oblivious Evaluation of Multi-variate Polynomial model, etc. are able to counter one or more of these attacks. But blockchain-based models are able to mitigate all of these attacks with 100% efficiency due to their immutability, traceability, transparency, and distributed nature. The only issue with this technology is its limited scalability due to mining and verification complexity, which can be tackled via the use of machine learning-based blockchain implementations. The use of machine learning models can optimize blockchains and reduce computational and execution delay, but it increases memory and energy consumption due to continuous training. To resolve this issue, the use of transfer learning and incremental learning must be performed, thereby assisting in improved security and Quality of Service (QoS) performance. The performance can also be improved via the use of intelligent process migration as suggested in [19], wherein particle swarm optimization (PSO) is used. The PSO Model tuned for high security via optimization of service-level agreements, bandwidth reduction, and optimizing CPU utilization. The model is able to identify security threats with more than 85% accuracy for the detection of DDoS, Sybil, and other IoT-related attacks.

Machine learning models might be very effective against security vulnerabilities, but they increase exponential system complexity during execution. To reduce this complexity, work in [20] proposes the use of software fault isolation, wherein tightly coupled software modules are provided low profile and low overhead sandboxing. The model showcases 91% security performance in terms of attack detection, with 25% reduced complexity due to low overhead process sandboxing. Similar models are discussed in [21–23] wherein domain parameters, multiple kernels with meta-heuristic feature selection, and selective adversarial sampling are used. These models are able to achieve an accuracy of 95%, 99.72%, and 86.55%, respectively on the application of various intrusions and malwares. The model in [23] uses incremental deep transfer learning as observed in Fig. 4, due to which it has low running overheads. The model uses both static and dynamic analysis for training, and combines Jacobian

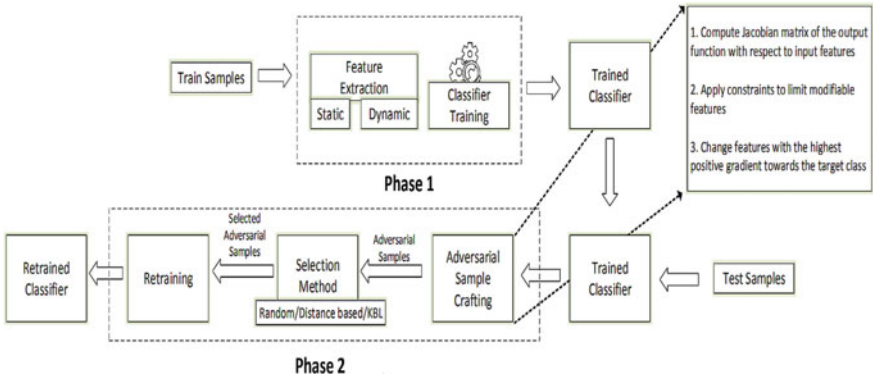

Fig. 4 Deep incremental transfer learning for kernel security [23]

analysis, constrained modifiable feature estimation, and modification of feature selection process for adversarial sample crafting. After this process, different methods for feature selection including random feature selection, distance-based selection, and kernel-based learning are used for re-training the network to perform incremental learning. These models can be pre-trained and deployed on IoT kernels for improved security. Regular kernel model upgradations can be done for enhancing the security performance of the system. Work in [24–26] can be combined with this approach, wherein sequence scanning for feature extraction, memory-based checking, and pairing-free-ID-based proxy re-signature schemes are discussed. These schemes are combined with various machine learning models to mitigate DDoS, malware, signature, Sybil, and other data and network-related attacks with over 95% accuracy. Security computations can be offloaded to edge devices in order to facilitate collaborative learning.

The work in [27–30] proposes the use of edge computing for improving performance efficiency, machine learning security performance, and cache optimization. Each of these applications is capable of detecting and mitigating various security vulnerabilities at the node and network-level due to a collaborative learning mechanism. The memory and processing requirements of these models can be further reduced via the use of Trusted Execution Environment (TEE) based minimum demand paging system as suggested in [31], wherein the Merkle tree is used for memory protection, and sandboxing is used for process protection. This combination is able to reduce the probability of board-level physical attacks, thereby making the IoT devices resilient against physical access vulnerabilities. Due to the use of the Merkle tree and TEE, the system is secured against Direct Kernel Object Manipulation (DKOM) as discussed in [32], thereby reducing the number of errors during device deployment. Other vulnerabilities can be detected using various monitoring processes as discussed in [33, 34] wherein Blackbox Fuzzing and Rocket-fast System for Log Processing. These models allow kernels to self-correct themselves via adaptive machine learning analysis, and control. Such a system can be observed from [35], wherein an object-level security model is deployed. This model is activated adaptively when the system senses internal or external vulnerabilities, which adds dynamic security to the network, and improves its attack mitigation performance. These system models are evaluated on various performance metrics, and these metrics are compared with each other in order to find the best combination of kernel-level modifications for highly secure IoT deployment. This analysis can be observed from the next section of this text.

3 Empirical Analysis

From the literature survey, it is observed that the reviewed models have their own nuances, advantages, and limitations. In order to empirically analyze the performance of the proposed models, they are compared in terms of accuracy of attack detection, security level (in terms of the number of attacks detected and mitigated),

the complexity of the deployment, and QoS performance. These parameters are estimated for each of the reviewed models and can be observed from the following Tables 1 and 2. Table 1 showcases security performance, while Table 2 showcases the QoS performance of the reviewed models. In Table 1, the security level is evaluated using the following conditions,

- Low (when the system is focused on only one attack)
- Medium (when the system can mitigate between 2 and 3 attacks or malwares)
- High (when the system can mitigate between 4 and 8 attacks or malwares)
- Very high (when the system can tackle virtually any attack or malware).

Table 1 Security analysis of the compared models

Model	Accuracy (%)	Security level
MQTT with ML [2]	95	High
TLS & DTLS [3]	74	Low
BSA [4]	91	Medium
Firmware vulnerability [5]	94	High
Separation kernel [6]	93	Medium
Code disassembly [8]	91	High
Hardened memory protection [10]	90	High
Integrity enforcement [11]	85	High
SVM [12]	97	Very high
DAPuFs [14]	99.65	Very high
PuF [16]	97	High
Chamel-IoT [17]	76	Medium
CNN [18]	94	Very high
LSTM [18]	92	High
Blockchain [18]	99.8	Very high
Blockchain ML [18]	99.8	Very high
PSO [19]	85	High
Fault isolation [20]	91	Medium
Domain parameter optimization [21]	95	Medium
Multiple kernels [22]	99.72	High
Selective adversarial sampling [23]	86.55	Very high
Sequence scanning [24]	76	Medium
Memory-based checking [25]	71	Medium
Pairing-free ID [26]	91	High
TEE [31]	80	High
BLESS [35]	92	Very high

Table 2 QoS analysis of the compared models

Model	Complexity	QoS
MQTT with ML [2]	High	Medium
TLS & DTLS [3]	Low	High
BSA [4]	Medium	H igh
Firmware vulnerability [5]	Medium	Medium
Separation kernel [6]	Low	Medium
Code disassembly [8]	High	Medium
Hardened memory protection [10]	Low	High
Integrity enforcement [11]	Medium	High
SVM [12]	Medium	High
DAPuFs [14]	Medium	Medium
PuF [16]	Medium	Medium
Chamel-IoT [17]	Medium	Medium
CNN [18]	Very high	Low
LSTM [18]	High	Medium
Blockchain [18]	Very high	Low
Blockchain ML [18]	Very high	Low
PSO [19]	High	Medium
Fault Isolation [20]	Medium	Medium
Domain parameter optimization [21]	Medium	Medium
Multiple kernels [22]	Medium	High
Selective adversarial sampling [23]	Medium	Medium
Sequence scanning [24]	Low	Medium
Memory-based checking [25]	Medium	Low
Pairing-free ID [26]	Medium	Medium
TEE [31]	Low	Medium
BLESS [35]	Medium	Medium

The security level is given a weight of 0.2, 0.4, 0.7, and 1.0 for low, medium, high, and very high respectively. Based on this weight, the final weighted accuracy is evaluated and visualized from Fig. 5, wherein best performing models can be observed.

From the analysis, it can be observed that blockchain-based systems [18], DAPuFs [14], SVM [12], CNN [18], and BLESS [35] models outperform other models in terms of security. This analysis is followed by the QoS performance analysis as observed from Table 2, wherein QoS and complexity are divided into three levels of low, medium, high, and very high depending upon their post-deployment performance.

These values are normalized similar to security levels, and their normalized QoS performance is estimated using Eq. 1 and can be visualized from Fig. 6.

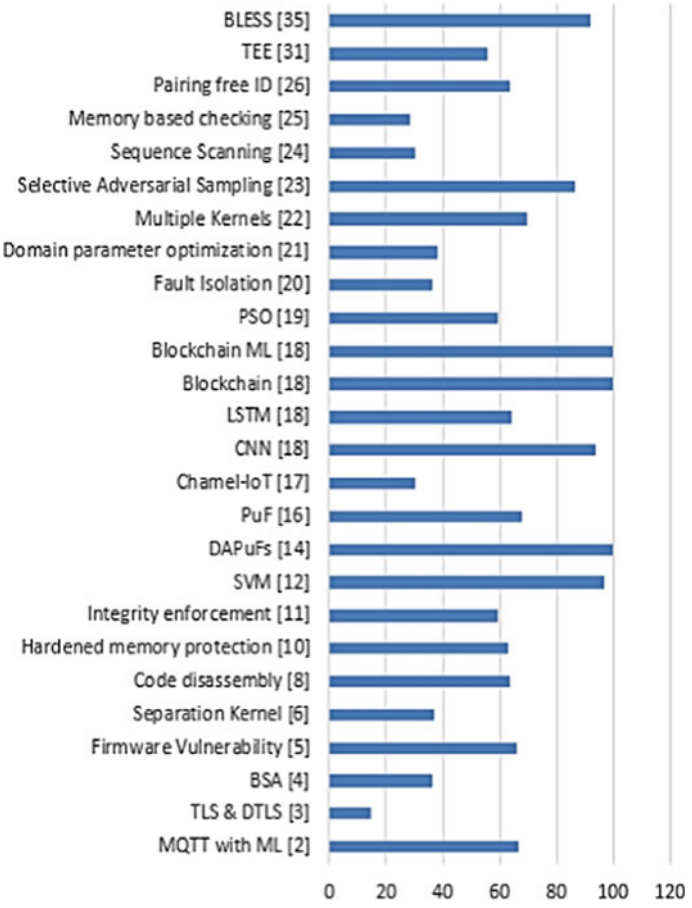

Fig. 5 Normalized accuracy (%)

$$N_{\text{qos}} = \frac{\text{QoS Level}}{\text{Complexity Level}} \tag{1}$$

The normalized QoS values are fused with normalized accuracy values using Eq. 2, and QoS to security performance values are estimated. These values can be visualized from Fig. 7, wherein researchers can observe the most suitable methods for their application.

$$\text{QoS}_{\text{security}} = \text{Normalized Accuracy} * \frac{N_{\text{qos}}}{\text{Max}\left(N_{\text{qos}}\right)} a \tag{2}$$

From the comparison, it can be observed that Hardened Memory Protection [10], Sequence Scanning [24], Separation Kernel [6], and SVM [12] outperforms all

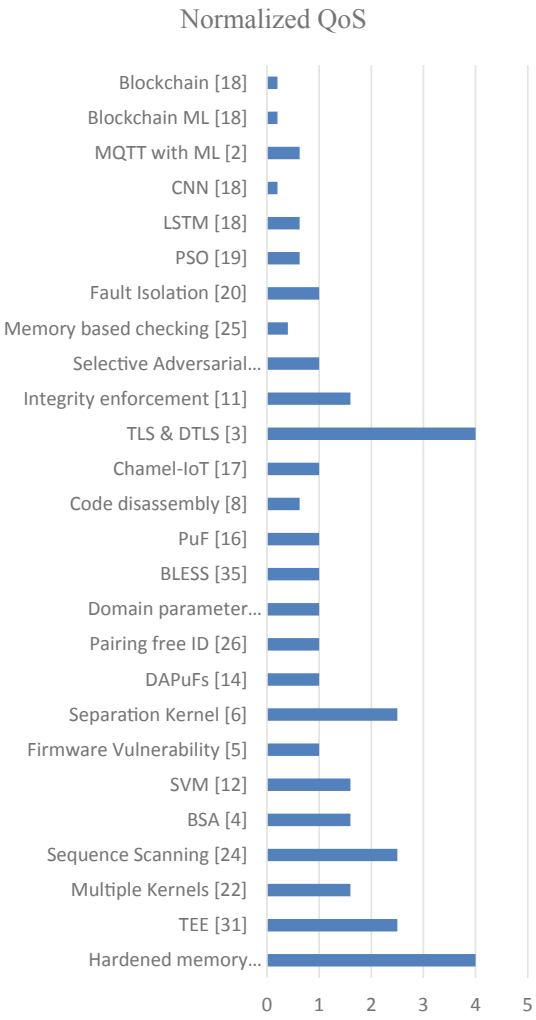

Fig. 6 Normalized QoS for various models

other models, while Chamel-IoT [17], Pairing-free ID [26], DAPuFs [14], Integrity enforcement [11], and PuF [16] have optimum security and QoS performance levels. Thus, these protocols must be used for large-scale IoT deployment where both security and QoS performance is needed.

4 Conclusion and Future Scope

Based on the performance evaluation, it is observed that Blockchain [18], DAPuFs [14], SVM [12], CNN [18], BLESS [35], and Selective Adversarial Sampling [23]

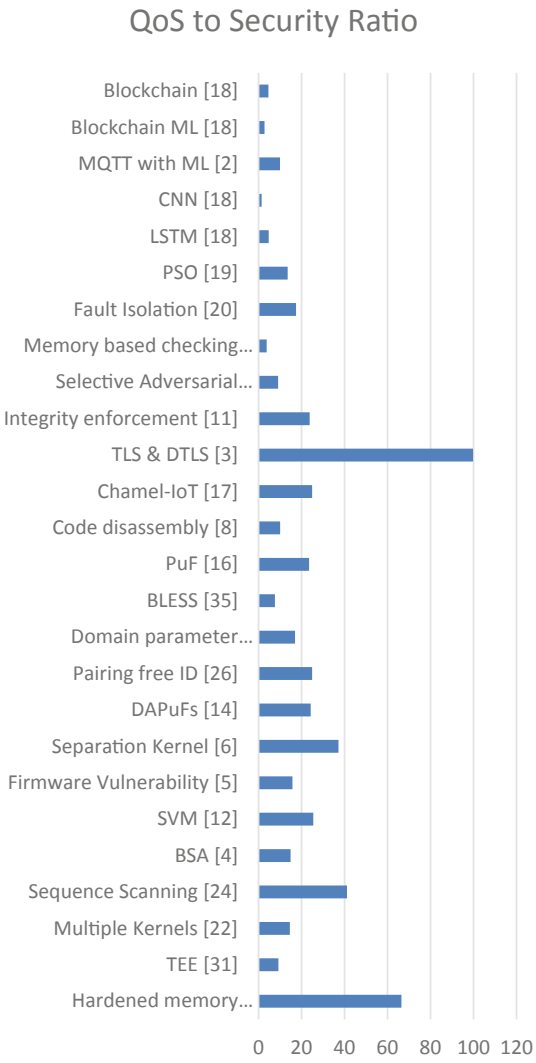

Fig. 7 QoS to Security Ratio of different algorithms

are the most secure protocols. While, Hardened Memory Protection [10], TEE [31], Sequence Scanning [24], Separation Kernel [6], Multiple Kernels [22], Integrity enforcement [11], and SVM [12] are the most QoS optimum security models. System designers can select from these models when only single parameter optimization is needed. But in order to optimize both security and QoS performance, a combination of these metrics is taken, and algorithms like DAPuFs [14], Integrity enforcement [11], PuF [16], Fault Isolation [20], Domain parameter optimization [21], Firmware Vulnerability [5], BSA [4], Multiple Kernels [22], PSO [19], and MQTT with ML [2] are identified. These algorithms provide high security and high QoS performance,

thus they have a moderate QoS to security ratio. The use of these kernel-level security models in real-time IoT deployments would yield highly optimum QoS and security-aware networks. The efficiency of these networks can be improved via the integration of lightweight blockchain and sidechain networks. These networks can be managed via pre-trained CNN Models and incremental learning for continuous kernel upgradation. Exploration of soft computing models with security and QoS aware fitness function design can also be explored. From a kernel perspective, there are no bottlenecks in terms of security and QoS performance, but blockchain-based models can be used to further contemplate and improve security at the kernel level. This will allow the system to operate at high QoS with better security, without any performance saturation.

References

1. Li, D., Zhang, Z., Liao, W., Xu, Z.: KLRA: a kernel level resource auditing tool for IoT operating system security. In: 2018 IEEE/ACM Symposium on Edge Computing (SEC), pp. 427–432 (2018).https://doi.org/10.1109/SEC.2018.00058
2. Cosson, A., Sikder, A.K., Babun, L., Celik, Z.B., McDaniel, P., Uluagac, S.: Sentinel: a robust intrusion detection system for IoT networks using kernel-level system information, pp. 53–66 (2021). https://doi.org/10.1145/3450268.3453533
3. Lee, Y., Kim, Y., Kim, J.: Implementation of TLS and DTLS on Zephyr OS for IoT devices. In: 2018 International Conference on Information and Communication Technology Convergence (ICTC), pp. 1292–1294 (2018). https://doi.org/10.1109/ICTC.2018.8539493
4. Zheng, Y., Song, Z., Sun, Y., Cheng, K., Zhu, H., Sun, L.: An efficient Greybox fuzzing scheme for Linux-based IoT programs through binary static analysis. In: 2019 IEEE 38th International Performance Computing and Communications Conference (IPCCC), pp. 1–8 (2019). https://doi.org/10.1109/IPCCC47392.2019.8958740
5. Tien, C., Tsai, T., Chen, I., Kuo, S.: UFO—hidden backdoor discovery and security verification in IoT device firmware. In: IEEE International Symposium on Software Reliability Engineering Workshops (ISSREW), pp. 18–23 (2018).https://doi.org/10.1109/ISSREW.2018.00-37
6. Yaker, M., et al.: Ensuring IoT security with an architecture based on a separation kernel. In: 2018 IEEE 6th International Conference on Future Internet of Things and Cloud (FiCloud), pp. 120–127 (2018). https://doi.org/10.1109/FiCloud.2018.00025
7. Yang, W., et al.: Micro-Kernel OS architecture and its ecosystem construction for ubiquitous electric power IoT. In: IEEE International Conference on Energy Internet (ICEI), pp. 179–184 (2019).https://doi.org/10.1109/ICEI.2019.00038
8. Sun, P., Garcia, L., Zonouz, S.: Tell me more than just assembly! reversing cyber-physical execution semantics of embedded IoT controller software binaries. In: 2019 49th Annual IEEE/IFIP International Conference on Dependable Systems and Networks (DSN), pp. 349–361 (2019). https://doi.org/10.1109/DSN.2019.00045
9. Radovici, Rusu, C., Şerban, R.: A survey of IoT security threats and solutions. In: 2018 17th RoEduNet conference: networking in education and research (RoEduNet), pp. 1–5 (2018). https://doi.org/10.1109/ROEDUNET.2018.8514146
10. Zhang, Z., Li, Z., Xia, C., Cui, J., Ma, J.: H-Securebox: A hardened memory data protection framework on ARM devices. In: IEEE Third International Conference on Data Science in Cyberspace (DSC), pp. 325–332 (2018).https://doi.org/10.1109/DSC.2018.00053
11. Liu, W., et al.: Research on technology of embedded system security protection component. In: IEEE International Conference on Advances in Electrical Engineering and Computer

Applications (AEECA), pp. 21–27 (2020). https://doi.org/10.1109/AEECA49918.2020.9213603
12. Ioannou, C., Vassiliou, V.: Classifying security attacks in IoT networks using supervised learning. In: 2019 15th International Conference on Distributed Computing in Sensor Systems (DCOSS), pp. 652–658 (2019). https://doi.org/10.1109/DCOSS.2019.00118
13. Seo, J., Bang, I., You, J., Cho, Y., Paek, Y.: SBGen: a framework to efficiently supply runtime information for a learning-based HIDS for multiple virtual machines. IEEE Access **8**, 225356–225369 (2020). https://doi.org/10.1109/ACCESS.2020.3041302
14. Alamro, M.A., Zhuang, Y., Aseeri, A.O., Alkatheiri, M.S.: Examination of double arbiter PUFs on security against machine learning attacks In: IEEE International Conference on Big Data (Big Data), pp. 3165–3171 (2019).https://doi.org/10.1109/BigData47090.2019.9006041
15. Wen, E., Weber, G.: Wasmachine: bring IoT up to speed with a web assembly OS. In: IEEE international conference on pervasive computing and communications workshops (PerCom Workshops), pp. 1–4 (2020).https://doi.org/10.1109/PerComWorkshops48775.2020.9156135
16. Chatterjee, U., Chakraborty, R., Mukhopadhyay, D.: A PUF-based secure communication protocol for IoT. ACM Trans. Embed. Comput. Syst. **16**, 1–25 (2017). https://doi.org/10.1145/3005715
17. Silva, M., Tavares, A., Gomes, T., Pinto, S.: ChamelIoT: an agnostic operating system framework for reconfigurable IoT devices. IEEE Internet Things J. **6**(1), 1291–1292 (2019). https://doi.org/10.1109/JIOT.2018.2863545
18. Waheed, N., He, X., Usman, M.: Security & privacy in IoT using machine learning & blockchain: threats & countermeasures (2020)
19. Ma, T., Xu, C., Zhou, Z., Kuang, X., Zhong, L.: SE-PSO: resource scheduling strategy for multimedia cloud platform based on security enhanced virtual migration. In: 2019 15th International Wireless Communications & Mobile Computing Conference (IWCMC), pp. 650–655 (2019). https://doi.org/10.1109/IWCMC.2019.8766781
20. Aweke, Z.B., Austin, T.: uSFI: ultra-lightweight software fault isolation for IoT-class devices. In: 2018 design automation & test in Europe conference & exhibition (DATE), pp. 1015–1020 (2018).https://doi.org/10.23919/DATE.2018.8342161
21. Misic, J., Misic, V.B., Chang, X.: Kernel based estimation of domain parameters at IoT proxy. In: IEEE Global Communication Conference (GLOBECOM), pp. 1–6 (2018).https://doi.org/10.1109/GLOCOM.2018.8648071
22. Haddadpajouh, H., Mohtadi, A., Dehghantanaha, A., Karimipour, H., Lin, X., Choo, K.-K.R.: A multikernel and metaheuristic feature selection approach for IoT malware threat hunting in the edge layer. IEEE Internet Things J. **8**(6), 4540–4547 (2021). https://doi.org/10.1109/JIOT.2020.3026660
23. Khoda, M., Imam, T., Kamruzzaman, J., Gondal, I., Rahman, A.: Robust Malware defense in industrial IoT applications using machine learning with selective adversarial samples. IEEE Trans. Ind. Appl. **56**(4), 4415–4424 (2020). https://doi.org/10.1109/TIA.2019.2958530
24. Wan, T.-L., et al.: IoT-malware detection based on byte sequences of executable files. In: 2020 15th Asia Joint Conference on Information Security (AsiaJCIS), 2020, pp. 143–150 (2020). https://doi.org/10.1109/AsiaJCIS50894.2020.00033
25. Myers, J., Babun, L., Yao, E., Helble, S., Allen, P.: MAD-IoT: memory anomaly detection for the Internet of Things. IEEE Globecom Workshops (GC Wkshps) **2019**, 1–6 (2019). https://doi.org/10.1109/GCWkshps45667.2019.9024539
26. Zhang, J., Bai, W., Wang, Y.: Non-interactive ID-based proxy re-signature scheme for IoT based on mobile edge computing. IEEE Access **7**, 37865–37875 (2019). https://doi.org/10.1109/ACCESS.2019.2899828
27. Filgueras et al.: The AXIOM Project: IoT on heterogeneous embedded platforms. IEEE Des. Test. https://doi.org/10.1109/MDAT.2019.2952335
28. Dash, P.B., Nayak, J,. Naik, B., Oram, E., Islam, S.K.H.: Model based IoT security framework using multiclass adaptive boosting with SMOTE. Secur. Privacy 3, e112 (2020). https://doi.org/10.1002/spy2.112

29. Lv, Z.: Security of Internet of Things edge devices.Softw: Pract. Exper. 1–11 (2020). https://doi.org/10.1002/spe.2806
30. Tahsien, S., Karimipour, H., Spachos, P.: Machine learning based solutions for security of Internet of Things (IoT): a survey. J. Netw. Comput. Appl. 161, 102630 (2020).https://doi.org/10.1016/j.jnca.2020.102630
31. Zhao, S., Zhang, Q., Qin, Y., Feng, W., Feng, D.: Minimal kernel: an operating system architecture for TEE to resist board level physical attacks. RAID (2019)
32. Eresheim, S., Luh, R., Schrittwieser, S.: On the impact of kernel code vulnerabilities in IoT devices. In: International Conference on Software Security and Assurance (ICSSA), pp. 1–5 (2017).https://doi.org/10.1109/ICSSA.2017.16
33. Wang, D., Zhang, X., Chen, T., Li, J.: Discovering vulnerabilities in COTS IoT devices through blackbox fuzzing web management interface. Secur. Commun. Netw. Article ID 5076324, p, 19 (2019). https://doi.org/10.1155/2019/5076324
34. Lee, J., Kim, T., Cho, W., Lee, H.: Lightweight built-in network monitor in Linux kernel for self-adaptive IoT devices. In: 2015 17th International Conference on Advanced Communication Technology (ICACT), pp. 609–612 (2015). https://doi.org/10.1109/ICACT.2015.7224869
35. BLESS:Object level encryption security for object-based storage system, https://www.sciencedirect.com/science/article/pii/S0895717711001142

A Review of Intelligent Techniques for Implementing SMART Learning Environments

Roopesh Kevin Sungkur and Manoj Maharaj

Abstract The world is facing an unprecedented situation with the rapid rise in Covid-19, impacting on all spheres of life. The world of Education has not been spared of this phenomenon, with millions of learners not being able to attend schools and universities. It is clear that e-learning and technology-enhanced-learning remains the way forward in this difficult situation. However, the concept of one-size-fits-all is ever-present and the teaching and learning process does not consider the individualities of the learners which might be in terms of prior knowledge, learning style, level of maturity, pace of learning and emotional state. This research advocates the usage of SMART Learning Environments which are able to consider the individualities of the learners and are able to provide personalised learning. This research highlights key technologies that can be used to develop SMART Learning Environments which the researchers perceive as being the way forward given the actual context.

Keywords Smart learning environments · Personalised learning · Technology enhanced learning · One-size-fits-all · Artificial intelligence

1 Introduction

E-learning advocates have long been fighting for e-learning to have its place in the education sector but little did they knew that Covid-19 would be this catalysing factor for the adoption of e-learning worldwide. The solution to educate this massive amount of learners outside the four walls of the classroom, lies within the provision of e-learning and other modes of technology-enhanced learning. The advantages of e-learning are numerous and undebatable but there are currently some pressing issues that need to be addressed to ensure the effectiveness of the teaching and

R. K. Sungkur (✉)
University of Mauritius, Reduit, Mauritius
e-mail: r.sungkur@uom.ac.mu

M. Maharaj
University of KwaZulu-Natal, Durban, South Africa
e-mail: Maharajms@ukzn.ac.za

B. Sikdar et al. (eds.), *Proceedings of the 3rd International Conference on Communication, Devices and Computing*, Lecture Notes in Electrical Engineering 851,
https://doi.org/10.1007/978-981-16-9154-6_69

learning process. It is beyond doubt that teacher-centred learning has significantly transformed our society and has had its load of contribution. Our present digital era is radically transforming the educational landscape and education for the future would perhaps require a new paradigm shift.

Challenges in the field of Technology Enhanced Learning (TEL)

It should be understood that every learner has their own specificities and abilities. This phenomenon is even more clearly visible with the concept of Massive Open Online Courses (MOOCs) such as Coursera or edX where the dropout rate is high and very often the learners are 'disconnected' [14]. The emergence of all these new technologies in the educational arena is interesting but the real challenge lies in the learner's need rather than the technological possibilities. The current teaching and learning system adopts the concept of 'one-size-fits-all' where it is expected that all learners are equal and learn in the same way; which is definitely not true.

2 Literature Review

SMART Learning Environments: Proposed Techniques and Technologies

A number of techniques and technologies can be used to develop SMART Learning Environments. Some will respond to the extrinsic factors influencing the learning process of a learner whereas others can be used to address the intrinsic factors. This section touches the different possibilities with an understanding that the use of all of them to formulate the proposed SMART Learning Environment will not be feasible due to the scope of the project. However an understanding of the different techniques and technologies are important to comprehend the wide range of possibilities available to develop SMART Learning Environments providing personalisation. Depending on the context and scope of the development of a SMART Learning Environment, some of these technologies and techniques can be used in isolation whereas others may be used in conjunction with each other, so as to provide a more comprehensive SMART Learning Environment.

2.1 Artificial Intelligence

Artificial Intelligence (AI), inspired from human intelligence aims to reach still further, by not only, understanding and depicting features of intelligence but by also building intelligent entities [13]. AI uses the patterns identified to create insights and knowledge that are more accurate. There exists a whole array of AI techniques as discussed in Table 1.

Table 1 AI techniques

Techniques	Brief description
Fuzzy logic	Fuzzy Logic can be depicted as an extension of multivalued logic that can help in modelling the vague modes of reasoning. Some view it as being helpful in situations where there is no absolute truth [20]. Fuzzy logic has successfully been used in areas ranging from Finance to Earthquake Engineering
Decision trees	Decision Trees are very useful to build classification models which are easy to understand and an effective way of representing human reasoning. Decision trees operate in a sequential manner and combine a logical sequence of simple tests in the form of a comparison with some threshold values [10]. If is often argued that decision trees provide much comprehensibility in the sense that it is easier to interpret as compared to models such as neural nets, which provide much opacity. This makes Decision Trees a prime choice for decision makers
Bayesian networks	Bayesian networks have been successfully used to model complex systems and to make diagnosis and predictions. This technique involves the computation of distribution probabilities in a set of variables. The limitation of Bayesian Networks includes the fact that there is no well-defined semantic to drive the development of a coherent model [19]
Genetic algorithms	A Genetic Algorithm is often used to solve hard optimising problems which is inspired by living beings and the theory of the 'survival of the fittest'. The robustness of the algorithm by giving consistent results with a broad range of problem types is perhaps one of its main advantage. Population size is an important determent of success, as a small population size may not present an adequate solution space to provide accurate results [16]
Hidden Markov models (HMM)	A Markov Process or Model consists of states and fixed, known probabilities for the state transitions [17]. In contrast, a Hidden Markov Process has states that are not directly visible. HMM has proved to be a successful technique for statistical pattern analysis [3]. The major limitation of HMM stems from the Markov property itself, in the sense that HMM is memoryless and does not give the possibility to model dependencies between distant events [15]

2.2 Machine Learning

Machine Learning is a sub field of Artificial Intelligence which consists of algorithms designed to emulate human intelligence and which are able to determine patterns/trends [8]. In this era characterised by big data analytics, Machine Learning is expected to play a pivotal role by making reliable predictions. Machine Learning techniques have been successfully applied to fields such as computer vision, pattern recognition, finance and computational biology, just to name a few. In simple terms,

Machine Learning can be pictured as a set of algorithms that parse data, learn from the set of data and then eventually apply their understanding to take decisions. Machine Learning can be classified into three categories, namely, supervised, unsupervised and semi-supervised learning. There is still another category of Machine Learning, termed Reinforcement Learning. This one, though, substantially different from structured and unstructured learning is worth some discussion. This is shown in Table 2.

The basic machine learning framework consists of two sets of data. The first is the Training Data, that is used to train the classifier and the Test Data that is used to evaluate the classifier. The success of a particular algorithm also depends on two criteria. The first one is its ability to tackle repetitive tasks and the second one, lies in its ability to uncover subtle and complicated patterns, difficulty seen by the human eye. Both of these are issues that definitely need to be addressed in the field of education.

Table 2 Categories of machine learning

Classification	Description
Supervised learning	Supervised learning is used to estimate an unknown (input, output) mapping from known (input, output) samples, where the output is labelled [8, 9]. A very simple example that can be used to explain this is to train a system to recognise an apple from an orange. Human beings, understand that oranges and apples have certain distinctive characteristics and are able to differentiate them
Unsupervised learning	Another category of machine learning happens through unsupervised learning. The algorithm finds its own way through the training input data. This type of data is unlabelled and the algorithm tries to make some sense on its own by extracting patterns and features. For example, questions such as 'are there any correlations between the features' might be asked
Semi-supervised learning	Another category of machine learning lies in between structured and unstructured and is termed semi-structured. This category has seen some progress in the recent years and operates through the fact that part of the data is labelled and other parts are unlabelled. The labelled part can be used to aid the learning of the unlabelled part [8]
Reinforcement learning	This is another category of Machine Learning Algorithms that controls learning by using a feedback system through the use of an agent which takes a sequence of actions so as to maximise a cumulative reward. [4, 8, 18] describe Reinforcement Learning as a system where a Reinforcement Learning Agent identifies the best way of learning a task through repeated interactions with its environment. An analogy that can be used to explain Reinforcement Learning is that of a child's brain that can be taught what is right and what is wrong through the use of punishments and rewards. The child's brain subject to appropriate education will thereafter develop into an adult's brain

2.3 Neural Networks

Neural Networks are computing systems inspired by biological neural networks that help machines reason like a human would [1, 7]. An Artificial Neural Network (ANN) comprises of processing elements namely: nodes, neurons and the connections and can be imagined as a circuit of neurons. The nodes are related layer-wise. This is shown in Fig. 1. The learning process of the Artificial Neural Network can be supervised or unsupervised.

The most popular learning algorithm used for prediction purposes is the Backpropagation Algorithm, which is a supervised learning algorithm [7]. Though Artificial Neural Networks have been around for years, the advent of the Backpropagation Algorithm has given a definite boost to the use of ANN. The Backpropagation (BP) algorithm uses a layered neural network approach. That is, the input layer, the hidden layer and the output layer. The network learns by adjusting the interconnection between the layers.

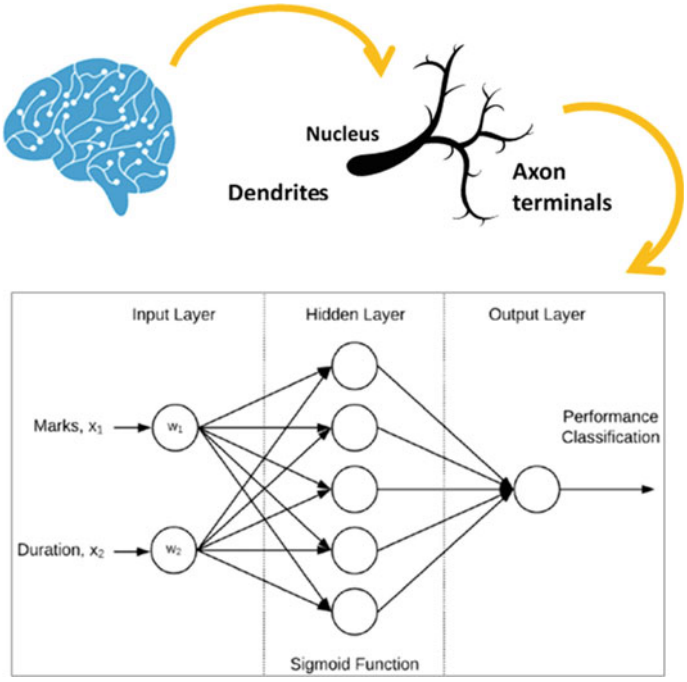

Fig. 1 Analogy between human brain and ANN

2.4 Deep Learning

Deep learning is a subset of machine learning and has had significant contributions in applications, the most well-known being, self-driving cars, image recognition, object recognition and storm detection. The development of its computational model was inspired by the human brain. It is often referred as deep neural networks (DNN) but usually called convolutional neural networks (CNN), since it is a representation of very large neural networks. The deep neural network consists of more than one hidden layer and complex algorithms which do not need to be explicitly coded [12, 13]. When the labelled dataset is input in the DNN, it firstly identifies the features. The advanced and beneficial part of the DNN is that it trains the dataset by itself for the recognition of patterns and more data is fed into the DNN, more computation will occur resulting into better algorithms, better recognition of features and more accurate output [6].

2.5 Agent Based Technology

A software agent is an autonomous and independent high-level software abstraction, capable of performing a process without the user's intervention [2, 5]. Software agents can be used to implement an Agent-Based Learning Environment that will eventually provide a more customised and unified learning environment. This can in turn provide the learners with a more transparent process [11].

3 Proposed Solution

SMART Learning is becoming increasingly relevant in the actual context of online learning. It can be seen at the intersection of technology, content and pedagogy. This is shown in Fig. 2.

Features of the Proposed SMART Learning Environment

The proposed SMART Leasrning Environment for this research provides the following features:

- Determination of the current Competency Level of the learner.
- Evaluation of Learning Performance of the learner done mostly through the use of online tests, activities and tasks.
- Adaptation of Learning Materials.
- Visualisation of the progress of the learner.
- Recommendation System for Individual Learners to reach desired level through Learning Analytics.
- Interaction with the learner through Ubiquitous Computing.

Fig. 2 SMART learning

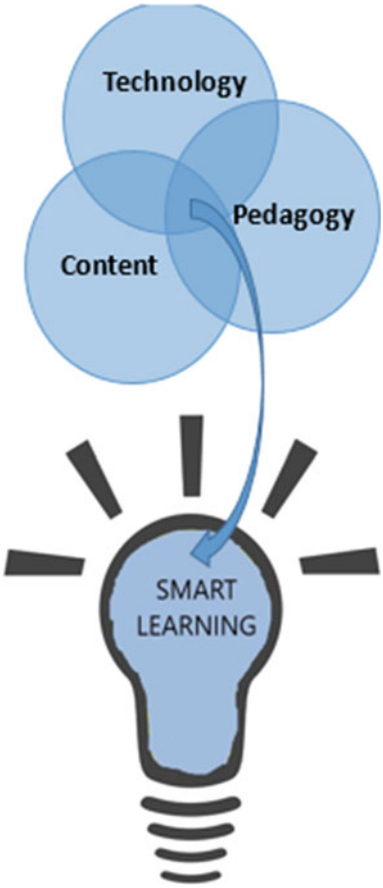

The proposed SMART Learning Environment is shown in Fig. 3 and also offers visualisation features in the form of graphs and charts that are able to show the progress and eventually provide timely feedback to the learner. Learners that are lagging behind are provided with consolidation exercises and materials as identified by the recommendation module so that they are able to reach to the desired level. Important messages can also be sent through the use of notifications.

4 Conclusion

With the current situation of Covid-19, education specialists are trying to find ways and means so as to continue inculcating knowledge to learners using means available at hand. Common means that are used involve the use of video-conferencing software such as Zoom or Google Meet. These have proved to be very much helpful but

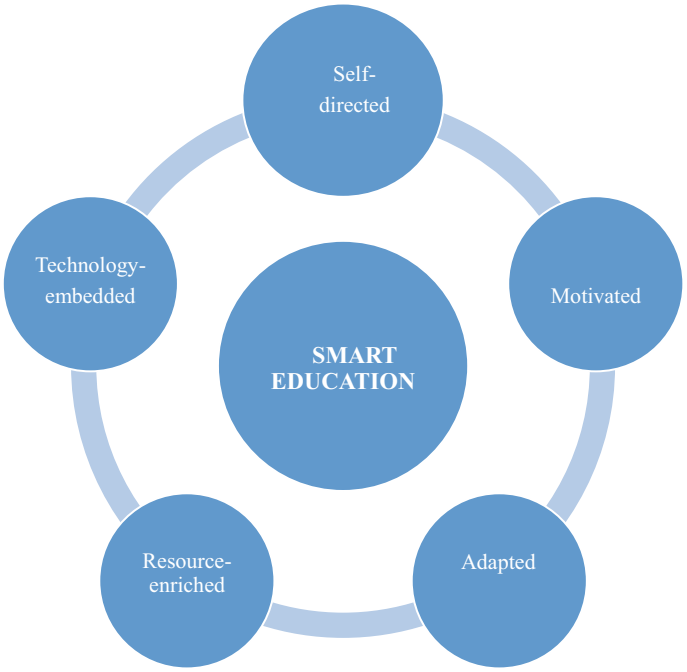

Fig. 3 SMART education

many education specialists argue that the use of such video-conferencing software is possibly more appropriate to conduct business meetings and often lack pedagogical incentives required for proper teaching and learning to take place. Alternatively, the use of Learning Content Management Systems (LCMS) or platforms such as Massive Open Online Courses (MOOCs) encourage on-size-fits-all learning and do not account for the individualities and specificities of different learners. It has been shown that the level of engagement of the learners on these platform can be very low, resulting in dropouts or having 'disconnected learners'. The use of SMART Learning Environments is seen as the way forward, hence making the learning process more engaging, motivating and effective.

References

1. Acharya, U.R., Bhatt, P.S., Iyenger, S.S., Rao, A., Dua, S.: Classification of heart rate data using neural networks and fuzzy equivalence relation. Pattern Recogn. **36**, 61–68 (2019)
2. Alexandru, A., Tirziu, E., Tudora, E., Bica, O.: Enhanced education by using intelligent agents in multi-agent adaptive e-learning systems. Stud. Inform. Control **24**, 13–22 (2015). https://doi.org/10.24846/v24i1y201502
3. Annachhatre, C., Austin, T.H., Stamp, M.: Hidden Markov models for malware classification. J. Comput. Virol. Hack. Techn. **11**(2), 59–73 (2014). https://doi.org/10.1007/s11416-014-0215-x

4. Badgwell, T.A., Lee, J.H., Liu, K.: Reinforcement learning—overview of recent progress and implications for process control. Comput. Aided Chem. Eng. **44**, 71–85. ISSN 1570-7946, ISBN 9780444642417 (2018). https://doi.org/10.1016/B978-0-444-64241-7.50008-2
5. Bellifemine, F., Caire, G., Greenwood, D.: Developing Multi-Agent System with JADE. Wiley Online Library (2017)
6. Brownlee, J.: What is deep learning?—Machine learning mastery. [Online] Machine Learning Mastery. Available at: https://machinelearningmastery.com/what-is-deep-learning/ (2016). Accessed on 12 July 2021
7. Chattopadhyay, S., Bandyopadhyay, G.: Artificial neural network with backpropagation learning to predict mean monthly total ozone in Arosa Switzerland. Int. J. Remote Sens. **28**(20), 4471–4482 (2017). https://doi.org/10.1080/01431160701250440
8. EI Naqa, I., Murphy, M.J.: What is machine learning? Mach. Learn. Radiat. Oncol. 3–11 (2015).https://doi.org/10.1007/978-3-319-18305-3_1
9. Juan, A., Daradoumis, T., Faulin, J., Xhafa, F.: SAMOS: a model for monitoring students' and groups' activities in collaborative e-learning. Int. J. Learn. Technol. **4**(1/2), 53–72 (2019). https://doi.org/10.1504/IJLT.2009.024716
10. Kotsiantis, S.B.: Decision trees: a recent overview. Artif. Intell. Rev. **39**, 261 (2013). https://doi.org/10.1007/s10462-011-9272-4
11. Lavendelis, E., Grundspenkibrowns, J.: MIPITS—an agent based intelligent tutoring system. In: Proceedings of the Second International Conference on Agents and Artificial Intelligence (ICAART 2010), Valencia, Spain, Jan 22–24 2010, pp. 5–13 (2018)
12. LeCun, Y., Bengio, Y., Hinton, G.: Deep learning. Nature **521**(7553), 436–444 (2015). https://doi.org/10.1038/nature14539
13. Nicholson, C.: Artificial intelligence, machine learning and deep learning—deeplearning4j: open-source, distributed deep learning for the JVM. [online] Deeplearning4j.org. Available at: https://deeplearning4j.org/ai-machinelearning-deeplearning (2017). Accessed on 12 July 2021
14. Onah, D.F.O, Sinclair, J., Boyatt, R.: Dropout rates of massive open online courses: behavioural patterns. The University of Warwick (United Kingdom) (2014)
15. Schuster-Bockler, B., Bateman, A.: An Introduction to Hidden Markov Models. Current Protocols in Bioinformatics. A.3A.1–A.3A.9 (2017)
16. Sivanandam, N.S., Deepa, N.S.: Introduction to Genetic Algorithms. Springer, Berlin, Heidelberg (2018)
17. Stamp, M.: A revealing introduction to hidden Markov models. Available at http://www.cs.sjsu.edu/faculty/stamp/RUA/HMM.pdf (2012). Accessed on 11 Oct 2019
18. Sutton, R., Barto, A.: Reinforcement Learning: An Introduction, 2nd edn. MIT Press (2016)
19. Weber, P., Medina-Oliva, G., Simon, C., Iung, B.: Overview on Bayesian networks applications for dependability, risk analysis and maintenance areas. Eng. Appl. Artif. Intell. 25(4), 671–682. ISSN: 0952-1976 (2012).https://doi.org/10.1016/j.engappai.2010.06.002
20. Zadeh, L.A.: Fuzzy logic. Computer **21**(4) (1988)

Investigating the Behavioral and Physiological Analysis of Learners While Interacting in Online Educational Platforms

Oorvashee Dasruth and Roopesh Kevin Sungkur

Abstract Currently, online learning is widely being used due to the Covid-19 pandemic with more than 1.2 billion learners being affected by school closures and confinement. This paper presents a web-based system that will be able to monitor the behavioral and physiological aspects of learners while interacting with online education platforms. At times, the interaction of the learner with the online education platform is not straightforward and the learner can be lost and become disconnected from the learning process. In an era where massive data can be collected and analyzed, vast amount of data can also be collected from the learner's interaction with the learning platform. This data collected can eventually be transformed into information that can guide in making the learning process more effective and engaging. This research makes use of convolutional neural network and demonstrates that the teaching and learning process can be improved by analyzing the learners' behavior and physiological traits.

Keywords Online learning · Physiological · Behavioral · Convolutional neural network · Technology enhanced learning

1 Introduction

Online learning is growing at a faster rate and is expected to grow continuously over the years. Research shows due to the Covid-19 pandemic, e-learning has been increasing drastically. In 2018, around 6 million students enrolled in distance learning in America's degree-granting institutions. Technology Enhanced Learning makes use of innovative technologies to help students increase their knowledge and develop new learning skills. Technology Enhanced learning plays an important role in helping

O. Dasruth · R. K. Sungkur (✉)
Department of Software and Information Systems, Faculty of Information Communication and Digital Technologies, University of Mauritius, Reduit, Mauritius
e-mail: r.sungkur@uom.ac.mu

O. Dasruth
e-mail: oorvashee.dasrut@umail.uom.ac.mu

B. Sikdar et al. (eds.), *Proceedings of the 3rd International Conference on Communication, Devices and Computing*, Lecture Notes in Electrical Engineering 851,
https://doi.org/10.1007/978-981-16-9154-6_70

teachers and students to reach course objectives. Studying online requires dedication and motivation and on the other hand, there are lots of distractions that are already present on the internet; YouTube, Social media and so on. At times during the learning process, the interaction of the learners with the online education platforms is not straightforward and the learner can be lost and become disconnected from the learning process. Analyzing emotions, behavioral and physiological traits can greatly help education specialists understand the mindset and level of receptiveness of learners [1–4].

2 Literature Review

2.1 Emotions

There are 6 universal human emotions and they are divided into two main categories; positive and negative emotion. Positive emotions such as happiness, surprise tend to improve mood and reduce stress whereas negative emotions tend to increase stress and recognize risks and deal with difficult situations. Examples of negative emotion are sadness, fear, anger, disgust and contempt. When analyzing a person's emotions, all these factors must take into consideration; their facial expression, tone of voice and general behavior. Facial expression is one of the most important ways to express emotion. Eye contact is necessary when having a conversation. People often tend to show emotion through their tone of voice but some emotion cannot be conveyed through voice such as fear, sadness. A person's voice can change according to their emotional state, their voice tends to increase and decrease in rate, volume and tone. General behavior includes body movement and posture that is to focus on the entire body rather than just reading the facial expressions. For example; when a person is shaking their legs, they might be anxious, annoyed or in a hurry.

2.2 Related Work in Emotion Recognition and Its Application

Real-Time Speech Emotion Recognition System

This system aims to detect emotions from continuous speech. It is composed of six parts: voice detection, segmentation of speech, signal preprocessing, extraction of features, classification of emotions and statistical analysis of emotion frequency. The application of the real-time emotion recognition system is very helpful in the online learning environment. The learning process becomes more effective as the teaching content and delivery speech are adjusted to fit students' learning abilities [5].

2.3 Emotion Recognition System Using Facial Expressions

2.3.1 Facial Expression

Facial expression system is used to analyze behavioral and physiology of students while interacting in online platforms movements. Facial Expression Recognition System is an effective technology that uses biometric identifiers, that is unique to each and every individual. The facial expression movement shows the emotional state of students to teachers. It is a way to transmit information on online platforms. Researchers have found that technology can have a positive impact on teaching and learning by increasing student achievement and satisfaction. It can promote and sustain student learning, extend access and flexibility of students and facilitate students to discuss group work. The teachers can track student behavior by asking questions during the online courses. Facial expression plays an important role while interacting on an online platform, as it is a direct means to communicate with humans via the internet. A facial expression shows the behavior and human emotions such as smile, anger, sadness, disgust, fear, surprise and contempt. In the context of online learning, a smile on the student's face shows happiness and looks healthier and comfortable in the learning environment [6]. Generally, facial expression recognition system (FERs), as shown in Fig. 1, consists of three main stages namely [7];

- Image Preprocessing
- Feature Extraction
- Classification.

Image Preprocessing

Image preprocessing are the steps to convert an image in its raw form into a form that a model is ready to use for training and inference. Images can be of various sizes, different contrast levels, they might be oriented in wrong and different ways. Image preprocessing are all the rules based to make sure all images are formatted correctly.

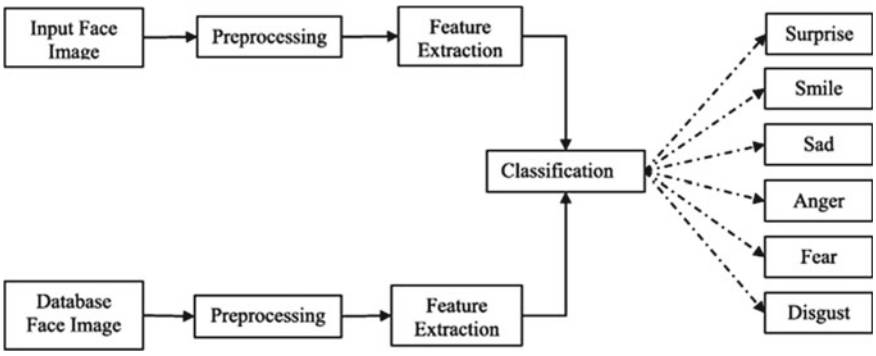

Fig. 1 Facial expression recognition system

It is the data cleaning of computer vision. Image preprocessing is used to improve an image data that increases image features for future processing and to analyze results.

Feature Extraction

Feature Extraction is one of the most important processes in the whole emotion recognition system. There are two common approaches in feature extraction are discussed below [8].

- Appearance-based methods

Facial expression features that are extracted by using appearance-based methods have a strong anti-interference ability.

- Geometric-based methods

Geometric-based methods are used to represent the shape and location of a human face. However, when there is a low image quality and complex background, it is very challenging to achieve accurate positioning of feature points. It does not take care of other important elements of the face such as skin texture changes which lead to low accuracy rate in facial expression recognition. Both appearance-based methods and Geometric-based methods belong to a single feature-based method. Studies show a lot of fusion feature-based methods are common nowadays and they later found that neural networks have greater ability to express emotion. An effective facial feature extraction will increase the accuracy of the facial expression recognition system.

Classification

The last phase of the facial expression recognition system is the classification stage. Extracted Facial features from the captured image are then processed to the classifier. The main important role of the Classifiers is to recognize the different emotions based on the face image. There are three main problems in the classification task, they are as follows;

- Choose good facial feature
- Choose the efficient machine learning techniques
- Database for training set.

2.4 Algorithm for Emotion Recognition System Using Facial Expressions

Nowadays, researchers are covering substantial information about facial emotion recognition to understand the state of human emotion; that is; happy, sad, angry, surprise, fear, disgust and contempt [9]. The challenges faced with the FER is to detect facial emotion which have a higher accuracy. Every person is different compared to other people in terms of skin color, age, background and surroundings. Normally, FER is divided into three main stage; Face Detection, Feature Extraction and Emotion

classification. First stage consists of pre-processing technique that is the facial image is detected and the facial components such as eyes, brows, nose and mouth. The second stage all important features will be extracted from the image captured. Finally, the last stage is to train data using a classifier. Moreover, there is another approach to analyze facial emotion known as Facial Action Coding System (FACs). It has been proposed by Paul Ekman to detect emotions based on facial muscle movement [10].

2.4.1 Face Detection

Face detection is the process to recognize facial emotion of human beings. A captured image is divided into two parts; faces and background regions. Table 1 shows different algorithms to detect faces in real-time [11].

Haar Classifier

The Haar cascade classifier is used to detect images in various sizes. It identifies a set of features which are contributed for the face detection problem in the training phase. Haar features are measured by resizing the size of pixels. Moreover, the Haar cascade classifier is more suitable to detect faces in the training phase since the computation complexity is small [12].

Adaptive skin color

Adaptive skin color algorithm is based on skin-color to detect a human face. It has a high accuracy as skin color is used for segmentation. However, it is not suitable with different levels of illumination. To avoid this problem adaptive gamma corrective method is used.

Adaboost contour points

Adaboost contour points can be used in real-time to detect faces. It has a high accuracy and a low computational complexity. The contour points give a higher accuracy and

Table 1 Different algorithms to detect faces

Algorithm	Accuracy	Performance in real-time
Haar classifier	It has suitable Haar features leading to high accuracy	In the training phase, computational complexity is very less
Adaptive skin color	Accuracy is good based on skin color however it fails due to different levels of illumination	It leads to high computational complexity. It is used to get rid of illumination problems. However, it is not suitable in real-time
Adaboost contour points	Strong classifier to detect single face by using contour points leading to a good accuracy	Low computational complexity as it has less number of features

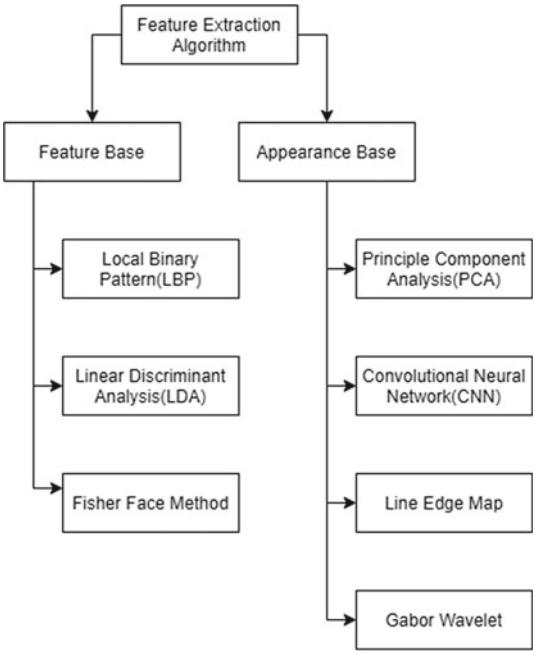

Fig. 2 Feature extraction techniques

performance because the features extracted are less leading to low computational complexity.

2.4.2 Feature Extraction

Feature Extraction process gives a higher-level of representation of shape, color and texture of an image. It processed only the most important features so as to give a better emotion classification. Figure 2 shows the feature extraction techniques.

2.5 Benefits and Drawbacks of Facial Expression Recognition System

2.5.1 Benefits of Facial Expression Recognition System

By using a webcam during an online course, the teacher can detect the emotions of students by their behavior whether they are attentive or not. The teacher can ask specific questions to a particular student and see the reaction of the student. If he is scared, confused and unable to answer the question. The teacher would be able to see the face expression of the student, if he sees some students are lost during the

online courses, he will therefore explain the topic with more examples so that the student can understand.

2.5.2 Drawbacks of the Facial Expression Recognition System

The students may act normal as if they have understood the concept well, but in reality they have not. Therefore, it would be difficult for the teachers to understand the facial expressions of the students. The facial emotion recognition algorithm depends on the location of the camera, for example; if the camera is lower, the eyebrow seems more up than the normal state and indicates that the student is surprised about a concept whereas if the camera is upper, then the teacher will get a different perspective [13].

3 Proposed Solution

3.1 Architectural Design

The web-based Facial Emotion Recognition System will consist of a series of different phases such as capturing faces from a web camera, carry out image preprocessing stage, the facial features are extracted and then finally facial emotion of the student will be identified. This is shown in Fig. 3.

3.2 Detailed Description of the System

The online web-based system analyzes the behavior and psychological aspects of online learners during e-learning by using emotion recognition systems. Emotion Detection is the process to analyze a human's emotion. Emotions are directly related to the psychological aspects of a human being.

3.3 Dataset Used

The dataset that has been used for this project is FER 2013. It is a well-known face emotion recognition dataset; it is a part of Kaggle competition. The problems encounter with the dataset are as follows:

Imbalance problem

This dataset was generated by cropping the posted videos and images on the internet, it has a lot of public dataset. Based on deep learning, they specify and divide into

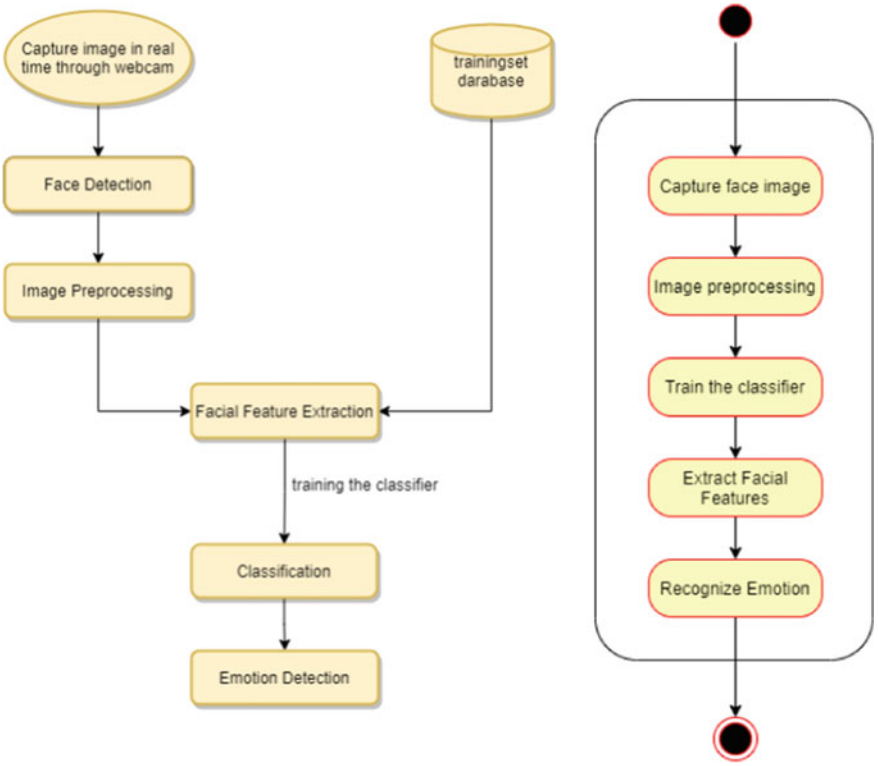

Fig. 3 System design

different categories such as angry, happy, fear, surprise, disgust, sad, neutral. The solution for the imbalance problem is data augmentation. One of the techniques used in data augmentation is generative adversarial neural network. For example, an image can be rotated and regenerate fictitious images. It can also crop, padding, scale, translate, rotate any image and generate more data.

Intra-class variation of FER

It means when a category such as happy, it has face images, sketch image and painting and cartoon images, and hence lead to intra-class variation as it contains a large variety of images. Intra-class variation can be resolved by avoiding over fitting. For example, a deep learning architecture is performing well on training dataset but once deploy it in a testing or unknown dataset, it does not perform. Therefore, it has a class variation and over fitting should be avoided.

Table 2 Tools and platforms

Environment used	Ubuntu 16
Libraries used	OpenCV OpenCV is an open source computer vision library. It is used to capture face image, detect Face and perform image preprocessing techniques
Hardware used	Integrated webcam

3.4 Implementation

The different tools and platforms used for this research is summarized in Table 2.

3.5 Building Keras Model

Convolutional Neural Network (CNN): A CNN is a deep learning technique which takes an input image and then assigns importance to various aspects of the image [14]. Sample code is shown in Fig. 4.

emotiondetection-master > build_dataset.py > ...

```
# USAGE
# python build_dataset.py

# import the necessary packages
from config import emotion_config as config
from pyimagesearch.io import HDF5DatasetWriter
import numpy as np

# open the input file for reading (skipping the header), then
# initialize the list of data and labels for the training,
# validation, and testing sets
print("[INFO] loading input data...")
f = open(config.INPUT_PATH)
f.__next__()
(trainImages, trainLabels) = ([], [])
(valImages, valLabels) = ([], [])
(testImages, testLabels) = ([], [])

# loop over the rows in the input file
for row in f:
    # extract the label, image, and usage from the row
    (label, image, usage) = row.strip().split(",")
    label = int(label)

    # if we are ignoring the "disgust" class there will be 6 total
    # class labels instead of 7
    if config.NUM_CLASSES == 6:
        # merge together the "anger" and "disgust classes
        if label == 1:
            label = 0
```

Fig. 4 Sample code

4 Results and Interpretation

Step 1: Log into the deep learning for computer vision virtual environment

Once the user has opened and logged into VM, he/she needs to open command line and type following command to open the set up tools for emotion recognition "work on emo_recog". Screen should look like this with the name of the virtual environment that contains the tools in brackets.

Step 2: Face detection and emotion classification

Provide a path to where your emotion recognition python file resides on your computer. Then you type in the following command and execute "python emotion_detector.py—cascade haarcascade_frontalface_alt.xml\—model checkpoints/epoch_75.hdf5". The application will start capturing a human face. The app will have a rectangle drawn on the detected face and also display the recognized emotion on top. It will also have the emotion probabilities displayed at the bottom of the same display frame.

Step 3: Multiple face detection

The application also allows multiple face detection. Rectangles will be drawn on faces that display full frontal face features such as eyes, nose, mouth and jaws. Every face detected will have a colored rectangle with corresponding emotion exhibited by the person's face and probabilities with the same color.

Step 4: Classification on saved video

Users who wish to apply the application to a video file will run the command "python emotion_detector.py—cascade haarcascade_frontalface_default.xml\—model checkpoints/epoch_75.hdf5—video path/to/your/video.mp4". Provide a path to where the video file resides on your computer.

Step 5: Classification using ethernet camera

Acquire IP address of a supported ethernet camera. Follow the steps above used to run the application under normal conditions then execute the command "python emotion_detector.py—cascade haarcascade_frontalface_alt.xml—model checkpoints/epoch_75.hdf5—source ip—address https://172.25.68.15".

5 Conclusion

The web-based system is implemented that will be able to monitor the behavioral and physiological aspects of learners while interacting with online education platforms. This research is able to identify the specific emotion of every student in the class. The system can monitor the facial expressions of the learner leading to an effective learning process. The system will therefore analyze every learner whether they are

concentrating or not. Besides, the proposed system is low cost and is adapted for any computer equipment which has a web camera. However, one of the limitations of the system is that the dataset that has been used is for white skin people and this research is carried out on black and brown skin people. It does not provide the same accuracy compared to white skin people. Future works include the improvement of accuracy of the system to any cultural environment.

References

1. Yoon, M., Lee, J., Joe, I.: Video learning analytics: Investigating the behavioral patterns and learner clusters in video-based online learning. Internet High. Educ. **50**(100806), 1096–7516.https://doi.org/10.1016/j.iheduc.2021.100806
2. Sungkur, R.K., Antoaroo, M.A., Beeharry, A.: Eye tracking system for enhanced learning experiences. Educ. Inf. Technol. **21**, 1785–1806 (2016). https://doi.org/10.1007/s10639-015-9418-0
3. Taurah, S., Bhoyedhur, J., Sungkur, R.K.: Emotion-based adaptive learning system. In: Machine Learning for Networking: Second IFIP TC 6 International Conference, Paris, France (2019)
4. Mohabeer, H., & Soyjaudah, K.M.S.: Application of predictive coding in the evolution of artificial neural network. In: 2012 IEEE 3rd International Conference on Cognitive Infocommunications (CogInfoCom), pp. 775–780 (2012). https://doi.org/10.1109/CogInfoCom.2012.6421958
5. Cene, L., Wu, F., Yu, Z., Hu, F.:A real time speech emotion recognition system and its application in online learning (2016).https://doi.org/10.1016/B978-0-12-801856-9.00002-5
6. Dewan, M.A.A., Murshed, M., Lin, F.: Engagement detection in online learning: a review. Smart Learn. Environ. **6**, 1 (2019). https://doi.org/10.1186/s40561-018-0080-z
7. Dagher, I., Dahdah, E., Al Shakik, M.: Facial expression recognition using three-stage support vector machines. Vis. Comput. Ind. Biomed. Art **2**, 24 (2019). https://doi.org/10.1186/s42492-019-0034-5
8. Do, N.T., Kim, S.H., Yang, H.J., Lee, G.S., Yeom, S.: Context-aware emotion recognition in the wild using spatio-temporal and temporal-pyramid models. Sensors **21**, 2344 (2021). https://doi.org/10.3390/s21072344
9. Hasouneh, A., Mutawa, A.M., Murugappan, M.: Development of a real-time emotion recognition system using facial expressions and EEG based on machine learning and deep neural network methods. Inform. Med. Unlocked **20**, 100372. ISSN 2352-9148 (2020).https://doi.org/10.1016/j.imu.2020.100372
10. Wojdel, A.: Knowledge Driven Facial Modelling. Available at http://www.kbs.twi.tudelft.nl/docs/syllabi/Thesis-ANIA.pdf (2015). Accessed on 20 July 2021
11. Deshmukh, S., Patwardhan, M., Mahajan, A.: Survey on real-time facial expression recognition techniques. IET Biometr **5**(3), 155 (2016). https://doi.org/10.1049/iet-bmt.2014.0104
12. Thirumaleshwari, B.D., Shitharth, S.: IOP Conf. Ser.: Mater. Sci. Eng. **1042** 012017 (2021)
13. Ravina, I.M., Emmanuel, W.R.S.: A survey on human face expression recognition techniques, Journal of King Saud University. Comput. Inform. Sci. **33**(6), 619–628. ISSN: 1319 1578 (2021).https://doi.org/10.1016/j.jksuci.2018.09.002
14. Chiang, S.C.: Fluency in real-time video streaming by learning human perceptive traits to reveal the expected section in outstanding quality. Available at http://waseda.repo.nii.ac.jp (2020). Accessed on 21 July 2021